ISSN 1348-8236

# USE2008

The 29th Symposium
on
ULTRASONIC
ELECTRONICS

Nov.11-13, 2008 / Sendai

# 第29回
# 超音波エレクトロニクス
## の基礎と応用に関するシンポジウム

# 講演論文集

平成20年11月11日～13日　仙台

主催：超音波シンポジウム運営委員会
共催：応用物理学会
協賛：映像情報メディア学会，海洋音響学会，精密工学会，超音波工業会
電気学会，電子情報通信学会，日本音響学会，日本化学会
日本学術振興会弾性波素子技術第150委員会，日本機械学会
日本金属学会，日本生体医工学会，日本超音波医学会
日本非破壊検査協会，日本物理学会，日本分光学会
日本分析化学会，日本分析機器工業会，IEEE UFFC Society Japan Chapter

# Program of USE2008

The 29th Symposium
on
ULTRASONIC
ELECTRONICS

Nov.11-13, 2008

Sendai, Japan

URL: http://www.use-jp.org

第２９回 超音波エレクトロニクスの基礎と応用に関するシンポジウム プログラム

†講演者　*奨励賞応募講演
【 】付の題目は論文委員による和訳

## 第１日：11 月 11 日(火)

09:00 受付開始

09:50 開会式

10:00-10:45 超音波物性・材料・フォノン物理　座長：山中一司（東北大）

1J1-1* 超音波共鳴法を用いた金属薄膜の弾性定数の高速回復現象に関する研究 1
中島丈雄† 中村暢伴 荻博次 平尾雅彦 西山雅祥（大阪大）

1J1-2 光音響分光法による CdSe 量子ドットを吸着したナノ結晶 Si の熱拡散率評価 3
小鹿倉淳† 加藤侑志 沈青 豊田太郎（電通大）

1J1-3* 水熱合成法による $KNbO_3$ エピタキシャル膜の作製と特性評価 5
石河睦生† 宇津木覚 藤澤隆志 安井伸太郎 山田智明 黒澤実 森田剛[1] 舟窪浩（東工大 [1]東大）

10:45-10:50 休憩

10:50-11:50 光ー超音波エレクトロニクス / 水中音響　座長：土屋健伸（神奈川大）

1J3-1* FBG を用いたファブリ・ペロー干渉計による振動センシングの検討 7
和田篤† 杣友宏行 田中哲 高橋信明（防衛大）

1J3-2* ラム波を用いた高効率な光モード変換器 9
齋藤光希† 中川恭彦 垣尾省司（山梨大）

1J9-1 タイムリバーサルによる陰影領域中の物体の探知 11
鶴ヶ谷芳昭† 菊池年晃[1] 水谷孝一[2]（NEC [1]防衛大 [2]筑波大）

1J9-2* アプラナートフレネル音響レンズの設計 13
佐藤裕治† 水谷孝一 若槻尚斗 中村敏明[1]（筑波大 [1]防衛大）

11:50-13:00 昼食

13:00-14:00 測定技術　座長：大野正弘（千葉工大）

1J2a-1* LFB 超音波材料解析システムによる漏洩弾性表面波伝搬特性の測定モデル 15
大津賢治† 荒川元孝 櫛引淳一（東北大）

1J2a-2 光熱分光法と表面光起電力法による GaAs/AlAs-MQW の電子遷移過程の研究 17
王萍† 境健太郎 福山敦彦 碇哲雄（宮大）

1J2a-3* 半導体ナノピラーにおける振動モードのピコ秒音響法による観測 19
佐久間洋宇† 友田基信 松田理 福井孝志 富岡克広 Oliver B. Wright（北大）

1J2a-4 水平すべり波（ＳＨ）波の表面励振 21
尾上守夫†（東大）

14:00-16:00 ポスターセッション

1P1-8 矩形断面を持つナノワイヤー超格子に生じる振動モード 23
水野誠司† 中村祐史（北大）

1P1-9 粒子配向型$(Bi_{1/2}K_{1/2})TiO_3$-$BaTiO_3$ セラミックスの電気的諸特性 25
根本正博† 晝間裕二 永田肇 竹中正（東理大）

1P1-10 【離散電極を有する圧電体メンブレン内のラム波の精密解析】 27
Yung Yu Chen†（Tatung Univ.）

1P1-11* 【大気圧プラズマ処理の超音波バンプボンディングにおよぼす影響】 29
Jung-Lae Jo† Ja-Myeong Koo Jong-Bum Lee Seung-Boo Jung Jeong-Hoon Moon[1]
（Sungkyunkwan Univ. [1]Suwon Sci. Coll.）

1P1-12 【フレキシブル電極パターンのガラス基板上への超音波ボンディングと諸条件の影響】 31
Jong-Bum Lee† Jong-Gun Lee Jung-Lae Jo Ja-Myeong Koo Seung-Boo Jung（Sungkyunkwan Univ.）

1P1-13 球回転式粘度計による界面活性剤水溶液のレオロジー測定 33
細田真妃子† 小川英生 野村浩康 酒井啓司[1]（東京電機大 [1]東大）

16:00-17:15 バルク波デバイス / 弾性表面波デバイス 座長：近藤淳 (静岡大)



第 2 日：11 月 12 日(水)

9:00 受付開始

9:10-10:10 一般英語口演Ⅰ 座長：酒井啓司 (東大)



10:10-10:15 休憩

10:15-11:00 一般英語口演Ⅱ 座長：中村健太郎 (東工大)



11:00-11:05 休憩

11:05-11:50 一般英語口演Ⅲ　　座長：黒澤実（東工大）



11:50-13:00 昼食

13:00-15:00 ポスターセッション

15:00-15:50 招待講演 I　　座長：山中一司（東北大）

15:50-16:40 招待講演Ⅱ　　座長：梅村晋一郎（東北大）

2INV2 【マイクロバブルと超音波：医用イメージングにおける新しいパートナー】 341
Peter N. Burns† (University of Toronto)

16:40-16:45 休憩

16:45-17:15 一般英語口演Ⅳ　　座長：松川 真美（同志社大）

2E7a 【2 次ボルテラシステム同定に基づいた非線形超音波信号の分離】 343
Pornchai Phukpattaranont† (Prince Songkla Univ.)

2E7b 【超音波顕微鏡を用いた骨の微小領域の弾性評価：ナノインデンテーションとの比較】 345
Pascal Laugier† Fabienne Rupin Davy Dalmas[1] Francoise Peyrin[2] Kay Raum[3] Etienne Barthel[1] Amena Said
(Univ. Paris 06 [1]Unite Mixte CNRS/Saint-Gobain [2]CNRS [3]Martin Luther Univ. Halle-Wittenberg)

17:15-17:30 表彰式

17:45- 懇親会

## 第 3 日：11 月 13 日(木)

9:00 受付開始

9:10-10:10 映像法 / 非破壊検査　　座長：荻博次（大阪大）

3J2b-1* 紫外励起光熱変換顕微鏡の開発と無染色生細胞の観察 347
藤井宣行† 原田明（九大）

3J2b-2 超音波による電気・磁気特性の画像化 349
生嶋健司† 樋田啓[1] 小宮山進[1]（農工大 [1]東大）

3J2c-1 サブハーモニック超音波フェーズドアレイ SPACE を用いた閉じた応力腐食割れの計測 351
小原良和† 遠藤宏明 三原毅[1] 山中一司（東北大 [1]富山大）

3J2c-2* 二層型圧電振動子を用いた閉じた亀裂から発生する Lamb 波の非線形成分の検出 353
福田誠† 今野和彦（秋田大）

10:10-10:15 休憩

10:15-10:45 ソノケミストリー　　座長：松岡辰郎（名古屋大）

3J6-1 超音波反応槽内における気泡構造形成過程の観察 355
飯田康夫† 砥綿篤哉 安井久一 小塚晃透 辻内亨 Judy Lee（産総研）

3J6-2 超音波照射時間の変化によるナノダイヤモンド微粒子の分散への影響 357
内田武吉† 菊池恒男 青木貴宏[1] 川島徳道[1] 竹内真一[1]（産総研 [1]桐蔭横浜大）

10:45-10:50 休憩

10:50-11:50 強力超音波　　座長：工藤すばる（石巻専修大）

3J8-1 V 型超音波モータを用いた高速高分解能ステージ 359
阿隅一将† 福永了一 藤村健 黒澤実[1]（太平洋セメント [1]東工大）

3J8-2 導波路管型超音波洗浄機用振動子の CMP 後洗浄への適用-スポット型振動子の洗浄評価- 361
鈴木一成 潘毅† 岡野勝一 副島潤一郎 小池義和[1]（カイジョー [1]芝浦工大）

3J8-3 無鉛圧電セラミックスと超音波洗浄機への応用 363
董敦灼† 浜口佑樹 舞田雄一 山森春男 高橋和利[1] 寺嶋良充[1]（本多電子 [1]富士チタン工業）

3J8-4* エアロゾルデポジション法による PZT 膜を用いた高周波超音波プローブの音響特性 365
遠藤聡人† 明渡純（産総研）

11:50-13:00 昼食

13:00-15:00 ポスターセッション

†Speaker
*Applying to Young Scientists Award

## Tuesday, November 11

09:00- Registration

09:50 Opening Ceremony

10:00-10:45 Ultrasonic properties of materials, Phonon physics  Chair: Kazushi Yamanaka (Tohoku Univ.)



10:45-10:50 Break

10:50-11:50 Acousto-optics / Underwater ultrasound  Chair: Takenobu Tsuchiya (Kanagawa Univ.)



11:50-13:00 Lunch

13:00-14:00 Measurement techniques  Chair: Masahiro Ohno (Chiba Inst. of Tech.)



14:00-16:00 Poster Session

## Wednesday, November 12

9:00- Registration

9:10-10:10 Aural English Session Ⅰ  Chair: Keiji Sakai (Univ. Tokyo)



10:10-10:15 Break

10:15-11:00 Aural English Session Ⅱ  Chair: Kentaro Nakamura (Tokyo Inst. Tech.)



11:00-11:05 Break

11:05-11:50 Aural English Session Ⅲ  Chair: Minoru Kurosawa (Tokyo Inst. Tech.)



11:50-13:00 Lunch

13:00-15:00 Poster Session

15:00-15:50 Invited Lecture I Chair: Kazushi Yamanaka (Tohoku Univ.)

## Thursday, November 13

# USE2008

The 29th Symposium
on
ULTRASONIC
ELECTRONICS

Tuesday, November 11, 2008

Proceedings of Symposium on Ultrasonic Electronics, Vol. 29 (2008) pp. 1-2
11-13 November, 2008

# Study on Fast Recovery of Elastic Constants of Metallic Thin Films by Resonant-Ultrasound Spectroscopy.

超音波共鳴法を用いた金属薄膜の弾性定数の高速回復現象に関する研究

Takeo Nakashima[1‡], Nobutomo Nakamura[1], Hirotsugu Ogi[1], Masahiko Hirao[1], Masayoshi Nishiyama[2] ([1] Grad. Sch. Eng. Sci., Osaka Univ.; [2] Reno. Cent. Instru., Osaka Univ.)
中島丈雄[1‡], 中村暢伴[1], 荻博次[1], 平尾雅彦[1], 西山雅祥[2] ([1]大阪大 基礎工; [2]大阪大 機器セ)

## 1. Introduction

It has been reported that the recovery and recrystallization occur in thin films after the deposition, and they continue for several hours or several days. During this period, the microstructure and residual stress evolve. X-ray diffraction,[1)] positron annihilation,[2)] atomic-force microscopy,[3)] and curvature measurement[4)] have been used for studying the mechanism of them. However, recovery behavior of elastic constants has not been studied because of difficulty of the measurement, despite that the elastic constants are required for designing the devices.

In this study, we propose a new method for studying the recovery of the elastic constants, which is based on the resonant-ultrasound spectroscopy.[5)] This method enables the continuous monitoring of the change in the elastic constants during and after the deposition. Considering that the elastic constants change with the microstructure, we can evaluate the microstructure by measuring the elastic constants, and it gives us the valuable knowledge to clarify the recovery mechanism of thin films. We show the measurement setup integrated in a sputtering system, and the recovery of the elastic constants of Ag thin films on Si substrate.

## 2. Specimens and Experiment

Metallic thin films such as Cu, Ag, Au and Al were deposited on (001) plane of a single-crystal Si substrate (3.000 mm × 3.500 mm × 0.100 mm) by the RF (or DC) magnetron sputtering method at room temperature. Background pressure was 1.7 × $10^{-4}$ ~ 6.3 × $10^{-3}$ Pa, and the deposition was performed in Ar gas at a pressure of 0.4 Pa. Deposition time was 15 ~120 min at the sputtering rate of 0.4 ~ 0.8 Å/s. Film thickness, which was measured by the x-ray reflectivity measurements[8)] after the measurement, was 82 ~ 400 nm.

Resonance frequencies of the free vibration of a layered specimen consisting of a substrate and a thin film depend on their elastic constants.[6)] By monitoring the resonance frequency, we can evaluate the change of the thin-film elastic constants before, during and after deposition. **Figure 1** shows our measurement setup. Resonance frequency is measured by a tripod needle-shape sensor, which is placed in the deposition chamber. The sensor consists of two piezoelectric transducers and a thermocouple, and a substrate is put on them. The synthesizer inputs cw signal into one of the transducers to oscillate the film/substrate, and the other detects the oscillation amplitude. We sweep the excitation frequency. When the cw frequency equals the resonance frequency of the specimen, a standing wave is generated, and a resonance peak appears in the resonance spectrum. The resonance frequency is measured by fitting a

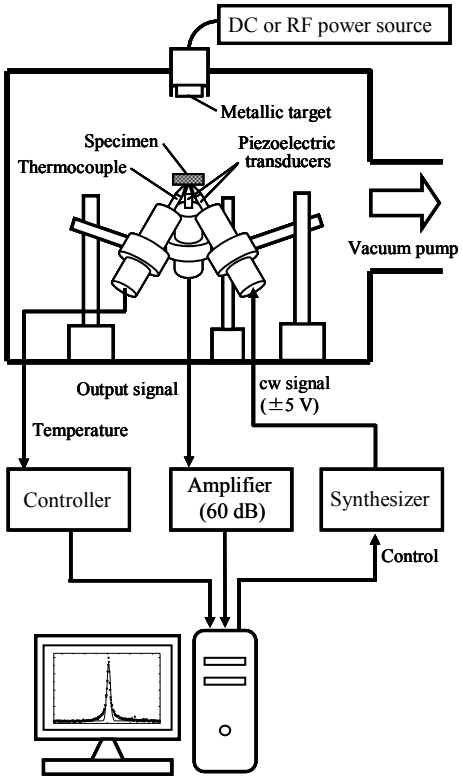


Fig. 1 Setup of sputtering/RUS monitoring system.

Gaussian function to the peak. The thermocouple measures the temperature at the back of substrate. The resonance frequencies and the temperature are measured every 10 seconds. The vibration mode of monitored resonance frequency was identified by measuring the distribution of the out-of plane displacement by the laser-Doppler interferometry.[7)]

### 3. Results and discussions

**Figure 2** shows the typical changes of temperature and the resonance frequency ($\Delta f/f_0$) of the Ag/Si specimen before, during and after deposition. During the deposition, the temperature increased linearly (Fig.2 (a)) and the frequency decreased (Fig.2 (b)). After finishing the deposition, the temperature decreased gradually, and the frequency increased rapidly by 0.06 %. This frequency increment originates from the following factors: (i) temperature dependence of elastic constants of the substrate and the thin film and (ii) the change of thin-film elastic constants. We can calculate the temperature dependence of the resonance frequency of Si substrate from the temperature dependence of the bulk Si elastic constants, and it is shown in Fig. 2(c) by open triangles (△). That of the thin film is assumed negligible because the volume fraction of the thin film is very small (less than 0.3 %). We observed that the temperature dependence of the elastic constants hardly affect the resonance frequency, and the recovery of the thin-film elastic constants governs the change of the resonance frequency. We then estimate the fractional change of the elastic constant reflecting the recovery. **Figure 3** shows

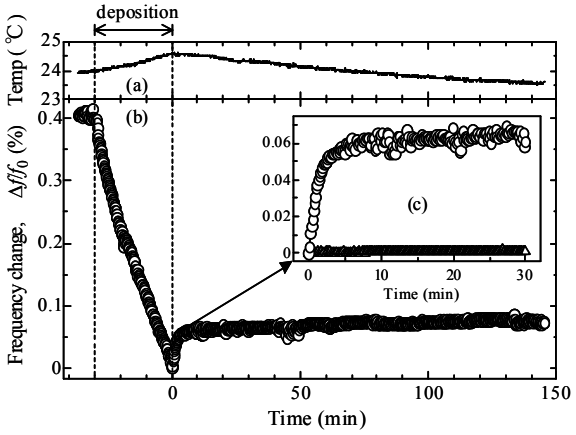


Fig. 2 Changes of (a) temperature and (b) resonance frequency of the Ag/Si specimen before, during, and after the deposition. Ag film is 255 nm thick. (c) An inset enlarges the measured resonance frequency (○) and temperature dependence of the resonance frequency calculated from that of the elastic constants of the Si substrate (△).

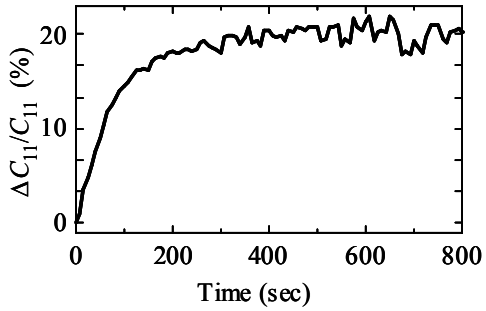


Fig. 3 Elastic constant change, $\Delta C_{11}/C_{11}$, calculated from measured frequency change, $\Delta f/f_0$ of Ag thin film.

the fractional change of the in-plane longitudinal elastic constant ($\Delta C_{11}/C_{11}$) of Ag thin-film after deposition, which was calculated from the contribution ratio of $C_{11}$ to the resonance frequency, $\partial C_{11}/\partial f$, and the measured frequency change, $\Delta f/f_0$.[5)] From this result, we found that the elastic constant increased about 20 % in 5 minutes after finishing the deposition.

The increment behavior of $C_{11}$ in Fig. 3 is similar to the change of the residual stress in Ag thin film reported by Chason *et al*.[4)] As a cause of the evolution of the residual stress, they proposed a model that is based on the flow of the excess atoms into the grain boundaries of the polycrystalline film due to a nonequilibrium surface chemical potential during deposition. In the present study, we consider that the flow of the atoms improve the binding condition at the grain boundaries, which results in the recovery of the elastic constants.

### References


1. J. W. Pattern, E. D. McClanahan and J. W. Johnston: J. Appl. Phys. **42** (1971) 4371.
2. A. Uedono, T. Suzuki, T. Nakamura, T. Ohdaira and R. Suzuki: J. Appl. Phys. **98** (2005) 043504.
3. D. N. Buckley and S. Ahmed: Electrochem. Solid-State Lett. **6**, 3 (2003) C33.
4. E. Chason, B. W. Sheldon and L. B. Freund: Phys. Rev. Lett. **88** (2002) 156103.
5. N. Nakamura, H. Ogi, T. Nakashima, M. Hirao and M. Nishiyama: Jpn. J. Appl. Phys. **46** (2007) 4450.
6. N. Nakamura, H. Ogi, N. Nitta, H. Tanei, M. Fujii, T. Yasui and M. Hirao: Jpn. J. Appl. Phys. **45** (2006) 4580.
7. H. Ogi, K. Sato, T. Asada, and M. Hirao: J. Acoust. Soc. Am. **112** (2002) 2553.
8. L. G. Parratt: Phys. Rev. **95** (1954) 359.

1J1-2

Proceedings of Symposium on Ultrasonic Electronics, Vol. 29 (2008) pp. 3-4
11-13 November, 2008

# 光音響分光法による CdSe 量子ドットを吸着した ナノ結晶 Si の熱拡散率評価

# Characterization of thermal properties of porous Si film adsorbed with CdSe quantum dots using photoacoustic technique

小鹿倉淳†、加藤侑志、沈青、豊田太郎（電通大 量子・物質工）

Jun Kogakura, Yushi Kato, Qing Shen and Taro Toyoda (Depertment of Appl. Phys. and Chem., The Univ. of Electro-Com.)

A strong interest has been attracted on nanocrystalline Si (NSi) since it was found to show efficient luminescence at room temperature. In addition, NSi has the thermal conductivity much smaller than that of Si. Therefore, the NSi has been expected to be applied to light emitting devices, thermal insulators, and optical devices. But there are few reports about the thermal property of NSi. In particular, the mechanism of thermal conductive process in the NSi adsorbed with molecules and/or quantum dots is not clear. In this paper, we report our experimental results on the measurements of thermal properties of NSi film adsorbed with CdSe quantum dots using photoacousic technique.

## 1. はじめに

ナノ結晶 Si (NSi)は可視発光特性が発見されて以来[1]、発光デバイスへの応用が研究されてきた。また NSi の持つ興味深い特性の一つとして、熱伝導率が Si と比べ極めて小さいことが挙げられる。そのため、マイクロシステムなどに適用可能な新しい熱絶縁材料としても注目されている。ここで光音響(PA)分光法は、光励起後の無輻射遷移緩和による熱エネルギーを測定するため、半導体の光物性・熱物性・電子物性を非破壊的に評価することに対して有効である[2,3]。PA 法は、光熱変換現象に基づいた手法の一つである。PA 法を利用する測定手段には様々な利点がある。その特徴として次のようなことが挙げられる。

(1)不透明、散乱が大きい試料に対しても光吸収評価が可能。
(2)非破壊、非接触の分析が可能。
(3)熱定数、光学定数や、緩和現象の同時評価が可能。
(4)光源の変調周波数を変化させることで、試料の深さ方向の分析が可能。

これまで我々は PA 法を利用して NSi/Si の２層構造試料における熱拡散率・熱伝導率を測定してきた[4]。一方、ナノ結晶化されている Si とその表面に吸着された分子やナノ粒子間での熱伝導過程についてのメカニズムは、まだ十分には解明されていない。そこで今回、NSi 表面に CdSe 量子ドットを吸着させた系での熱拡散率について評価を行った。CdSe 量子ドットの物性はよく知られており、今回の試料作製法では吸着時間に応じて粒径と吸着量を変化できることから、ナノ粒子のモデル材料として選んだ。透過型 PA 法を用いて PA 信号の変調周波数依存性を測定し、その結果から試料を均一と仮定した実効的な熱拡散率を計算し評価を行った。

E-mail: kogakura@jupiter.pc.uec.ac.jp

## 2. 実験法

### 2.1 試料作製法

p型Si単結晶基板（ホウ素ドープ、厚さ 525 μm、面方位〈100〉、抵抗率 1～10 Ω・cm）を基板として陽極化成法によりNSi試料を作製した。陽極化成法とは陽極にSi、陰極にPtを用いた電気溶解反応である。電流密度は 10 mA/cm$^2$、陽極化成時間は 30 分の条件下で反応させた。

また、化学吸着法によりCdSe量子ドットを吸着した[5]。$CdSO_4$水溶液、$N(CH_2COOHNa)_3$水溶液、$Na_2SeSO_4$水溶液を混合して作られる吸着溶液にNSiを浸漬させ、恒温槽で 10℃に温度を保った状態で吸着を行った。今回、吸着時間は２時間と

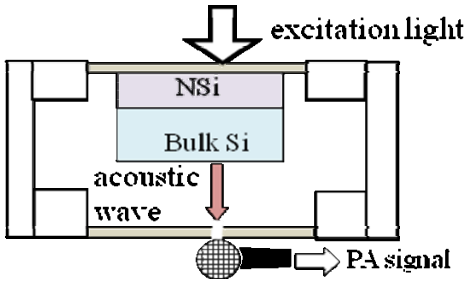


Figure 1 Arrangement of the transmission PA method.

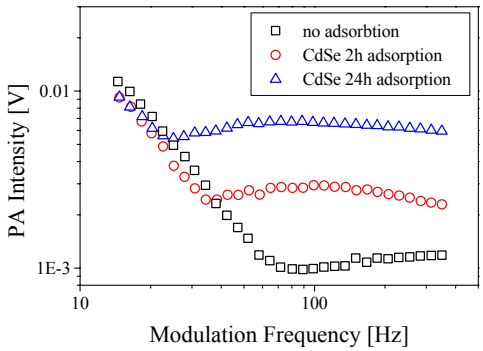


Figure 2 Modulation frequency dependence of PA signal intensity of NSi adsorbed with CdSe QDs.

24 時間に限定した。

## 2.2 PA 法の測定系

光源に 300W の Xe ランプからの白色光を分光器で単色化し、チョッパーを通して変調して試料に照射した。試料表面では光照射により熱が発生し、表面層の空気が膨張と収縮を繰り返し、この空気の圧力変化を音響信号としてマイクロフォンで検出する。検出された音響信号はロックインアンプでチョッパーの周波数と同期させ検出した。

今回の測定は光照射面と信号検出面が異なる側の面で行われる透過型 PA 法を用いた[6](**Fig. 1**)。励起光変調周波数を変化させることによって試料の熱的性質を見積もることができる。光照射によって発生じた熱またはキャリアが試料内を拡散し、光照射面とは反対側の面で音響波を発生し、これを検出する。今回は励起光の波長を 400 nm、変調周波数を 15 ~ 350 Hz と設定して PA 信号の変調周波数依存性の測定を行った。

## 3. 結果と考察

**Fig. 2** に、CdSe 量子ドットを吸着した NSi 試料の PA 信号の変調周波数依存性を示す。PA信号はある周波数$f_{min}$ において極小値を示し、この値を境に低周波数側を熱拡散が支配的な過程、高周波数側は光励起キャリア拡散によって生じる発熱が支配的な過程と考えることができる[6, 7]。$f_{min}$の値から試料を均一と仮定した実効的な熱拡散率を下記に示す解析式(1)を用いて導出した[6]。

Table 1 Value of $f_{min}$ and effective thermal diffusivity of NSi adsorbed with CdSe QDs.

| CdSe adsorbtion time [h] | 0 | 2 | 24 |
|---|---|---|---|
| $f_{min}$ [Hz] | 80 | 34 | 25 |
| Effective Thermal diffusivity [$\times 10^{-3}$ $cm^2/s$] | 28 | 12 | 8.6 |

$$\sqrt{\alpha/\pi f_{min}} \approx L/5 \qquad (1)$$

ここで、α、Lはそれぞれ熱拡散率と試料の厚さを表す。$f_{min}$の値と、その値を用いて算出した熱拡散率の値を表1に示す。これらの結果から、CdSe量子ドットの吸着時間の増加に応じて$f_{min}$の値が低周波数側にシフトすることが確認された。すなわち、CdSe量子ドットを吸着したNSiの熱拡散率がCdSeの吸着時間の増加に従い減少することを示している。この原因としては、CdSe-NSiもしくはCdSe-CdSe粒子間の界面抵抗により熱拡散が妨げられることが考えられる。

今後は過渡応答評価からキャリアの寿命や緩和過程を調べ、さらに詳細な熱物性とキャリアの移動特性の評価を行っていく。

引用文献

1) L.T.Canham: Appl. Phys. Lett. **57** (1990) 1046.

2) A. Rosencwaing, A. Gersho: J. Appl. Phys. **47** (1976) 64.

3) 沢田嗣郎; 「光音響分光法とその応用—PAS」 (学会出版センター, 1982).

4) 加藤侑志: 学士論文: 電気通信大学量子物質工学科(2007).

5) S. Gorer, G. Hose: J. Phys. Chem. **98** (1994) 5338.

6) Q. Shen, T. Toyoda: Jpn. J. Appl. Phys. **39** (2000) 3164

7) M. D. Dramicanin, Z. D. Ristovski, P. M. Nikolic, D. G. Vasiljevic D. M. Todorovic: Phys. Rev. B **51** (1995) 14226

Proceedings of Symposium on Ultrasonic Electronics, Vol. 29 (2008) pp. 5-6
11-13 November, 2008

# 水熱合成法による $KNbO_3$ エピタキシャル膜の作製と特性評価

Epitaxial $KNbO_3$ Films Grown on $SrRuO_3/SrTiO_3$ using Hydrothermal Method and Their Electromechanical Properties

石河睦生[1‡]，宇津木覚[1]，藤澤隆志[1]，安井伸太郎[1]，山田智明[1]，黒澤実[1]，森田剛[2]，舟窪浩[1] ([1]東工大 総理工; [2]東大 新領域)
Mutsuo Ishikawa[1†], Satoru Utsugi[1], Takashi Fujisawa[1], Shintaro Yasui[1], Tomoaki Yamada[1], Minoru Kuribayashi Kurosawa[1], Takeshi Morita[2], Hiroshi Funakubo[1], ([1]Institute of Technology; [2]Frontire science, The Univ. of Tokyo)

High quality epitaxial $KNbO_3$ films were successfully grown on (100)$SrRuO_3$//(100)$SrTiO_3$ substrates by hydrothermal method. The $KNbO_3$ or $KNbO_3$-based materials are one of the promising lead-free piezoelectric materials as an environmental friendly material; however, the main interest in the $KNbO_3$-based piezoelectric materials have limited on bulk ceramics materials owing to the difficulty in thin or thick films preparation. Therefore the hydrothermal method has utilized for the growth of $KNbO_3$ films. Because, hydrothermal method has number of advantages for fabrication method of ultrasonic transducers; low deposition temperature, good conformability, high-purity deposition on a substrate. In this study, epitaxial $SrRuO_3$ film was used as bottom electrodes, which were grown on (100) $SrTiO_3$ substrate by sputter method. $KNbO_3$ films were prepared on (100) $SrRrO_3$//$SrTiO_3$ substrates at 210 °C by hydrothermal method. The $KNbO_3$ films were 7.5 μm thicknesses, and the K/Nb ratio measured by EDS was 50/50. The piezoelectric performance and material constants of the prepared $KNbO_3$ thick film were measured.

## 1. はじめに

$KNbO_3$は有力な非鉛系圧電材料の一つであり、また、大きな電気機械結合係数を有する[1]ことから、超音波トランスデューサ材料として魅力的である。近年、開発が進む数十MHz以上の周波数の超音波送受信を行うデバイスを想定した場合、構造上は厚膜や薄膜の$KNbO_3$結晶の利用が望ましい。しかし、$KNbO_3$結晶は基板上への成膜が困難で、報告例が少なく、基板上へ成膜された$KNbO_3$結晶膜[2]の圧電特性は不明な点が多かった。最近、$NaNbO_3$及び$(K,Na)NbO_3$結晶膜の優れた圧電特性の報告[3]があり、純粋な$KNbO_3$結晶膜における圧電特性の評価は重要となっている。そこで本研究では水熱合成法[4,5]を用いることで高品質な単結晶$KNbO_3$の成膜を行った。

## 2. 実験方法

本研究では、$KNbO_3$単結晶膜を成膜する基板として、(100)$SrRuO_3$ を成膜した(100)$SrTiO_3$ 基板を用いた。$SrRuO_3$は導電性酸化物であり、下部電極として用いることが可能である。はじめに厚み 0.5 mm の(100)$SrTiO_3$ 基板上に、スパッタ法により厚み 60 nm の(100)$SrRuO_3$ 膜を成膜した。次に、得られた(100)$SrRuO_3$ //(100)$SrTiO_3$ 基板を保持具に固定し、出発原料と共にオートクレーブ内に投入し密閉した後、温度 210 度で 30 時間の水熱合成を行った。出発原料には 1.56 g の $Nb_2O_5$ を 9 mol/*l* の KOH 水溶液中に混合したものを用いた。

## 3. 実験結果

Figure 1 に(100)$SrRuO_3$ //(100)$SrTiO_3$ 基板上に水熱合成した$KNbO_3$膜のX線回析(XRD, Philips X'Pert MRD system）パターンを示す。

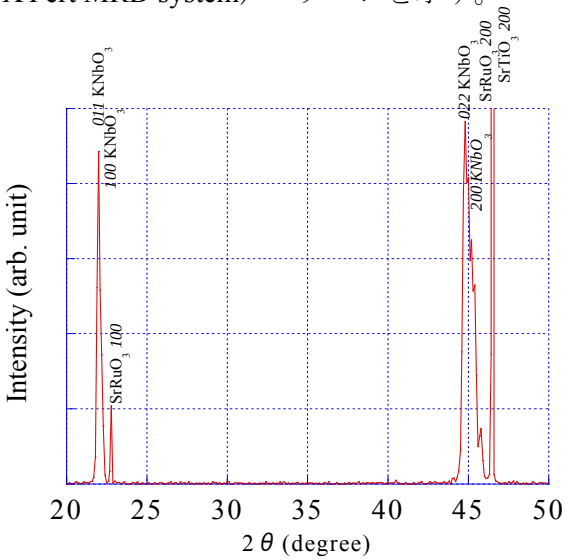


Fig.1 XRD pattern of $KNbO_3$ film grown on (100)$SrRuO_3$//$SrTiO_3$ substrate using hydrothermal method.

XRD パターンからは、(100)$SrRuO_3$ //(100) $SrTiO_3$ および $KNbO_3$ の(100)と(011)が観察された。また、(101)面による X 線極点図形から、得られた $KNbO_3$ 膜の面内配向を確認し、基板に対してエピタキシャル成長していることが分かった。次に走査型電子顕微鏡(FE-SEM, HITACH S-4800)を用い、$KNbO_3$膜の断面観察を行った結果を Fig.2 に示す。FE-SEM 像から、得られた(100)/( 011)配向エピタキシャル $KNbO_3$ 膜の膜

---

Ishikawa.m.ai@m.titech.ac.jp

厚は約 7.5μm (成膜速度、7.5μm /30h)であった。膜の組成は、EDX ( HORIBA, 7593H )を用いて分析した結果、K/Nb 比は 50/50 であった。

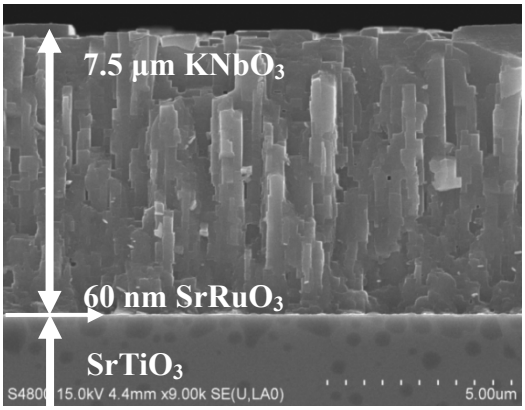


Fig.2 Cross-sectional SEM photograph of 7.5 μm-thick epitaxial $KNbO_3$ film.

次に、(100)/(011) $KNbO_3$ 膜の表面をメタルマスクで覆い、電子ビーム蒸着装置（ANELVA）を用いて直径 100μm の Pt 上部電極を作製した。この Pt 上部電極と $SrRuO_3$ 下部電極を用い、$KNbO_3$ 膜の分極－電界（P-E）特性を、周波数 100 kHz において測定した。得られた結果から、Fig. 3 のようにヒステリシスループおよび約-40 kV/cm のインプリントが観察された。また、電圧 150 V(電界 200 kV/cm)加えた残留分極値は約 28 μC/cm$^2$ であった。

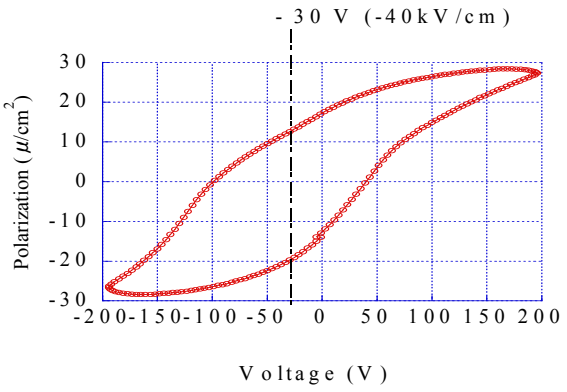


Fig.3 *P* - *E* hysteresis loops for (100)/(011)-oriented epitaxial $KNbO_3$ films grown on (100)$SrRuO_3$//(100)$SrTiO_3$.

次に、Dicing saw(Disco DAD321) を用いて (100)/(011)$KNbO_3$//(100)$SrRuO_3$//(100)$SrTiO_3$ 基板を幅 1.5mm×7mm で切断し、片端を固定することで長さ 3.53mm のユニモルフ振動子を作製した。振動子の表面には真空蒸着装置（ULVAC）により幅 1mm の Au 上部電極を形成している。作製したユニモルフ振動子の先端の振動変位を Laser Doppler Velocimeter（LDV, Polytec OFV 3001）を用いて測定した結果を Fig.4 に示す。駆動周波数については、ユニモルフ振動子の共振周波数の影響を受けていない 50Hz とした。

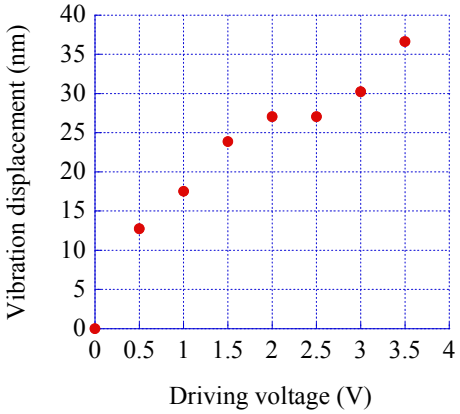


Fig.4 Relationship between vibration displacement and applied voltage at 50 Hz.

以上の結果から、振動変位は駆動電圧に対して線形的に増加することが分かった。

## 4. 考察

水熱合成法を用いて膜厚 7.5μm の(100)/(011)配向したエピタキシャル $KNbO_3$ 膜を成膜した。組成は K/Nb = 50/50 であり、高品質な $KNbO_3$ の厚膜が得られることが分かった。水熱合成法によりエピタキシャル $KNbO_3$ 膜を用いて試作したユニモルフ振動子の圧電効果を利用し、振動変位を測定することが可能であり、今後は、圧電定数等の材料定数を測定し報告を行う予定である。また、(111) $SrRuO_3$//(111)$SrTiO_3$ 基板等を用いることで結晶方位依存について、比較検討を行いたいと考えている。

## 謝辞

本研究の一部は井上科学振興財団の研究助成を受けて行われました。

## 引用文献

1. K. Nakamura, *et al*, J. Appl. Phys., **91**, 11, pp.9272-9276 (2002)
2. T. Arai *et al*, JJAP., **42**, pp.6019-6022 (2003)
3. I. Kanno, *et al.*, IEEE Transaction on UFFC., **54**(12), pp.2562 – 2566 (2007)
4. T. Morita, *et al.*, J. Mater. Res., **19**(6), pp. 1862-1868 (2004)
5. Wojciech L. Suchanek, Chem. Mater. vol.16, pp.1083-1090 (2004)

Proceedings of Symposium on Ultrasonic Electronics, Vol. 29 (2008) pp. 7-8
11-13 November, 2008

# FBG を用いたファブリ・ペロー干渉計による振動センシングの検討

Vibration sensing by using Fabry-Perot interferometer with FBG reflectors

和田篤†, 杣友宏行, 田中哲, 高橋信明 (防衛大)
Atsushi Wada, Hiroyuki Somatomo, Satoshi Tanaka, and Nobuaki Takahashi (National Defense Academy)

In vibration sensing by use of a FBG based on intensity modulation, light incident on a FBG is narrow-band light tuned to the slope in a transmittance spectrum of the FBG. Since the sensor sensitivity is proportional to the slope of the spectrum curve, enhancement of the sensitivity requires steeper slope of the curve. In this paper, vibration sensing by use of Fabry-Perot interferometer with FBG reflectors (FBG-FPI) is numerically investigated. Because a transmittance spectrum of an FBG-FPI has steeper slope, the FBG-FPI can yield improvement in sensitivity of the sensing.

## 1. はじめに

これまで我々は, 固体振動や水中音響の計測を行うため, 強度変調方式に基づいた各種の FBG センサの提示を行ってきた. この方式では, FBG の透過(あるいは反射)スペクトルの傾斜部に同調した狭帯域光を FBG に入射させると, FBG に振動や音圧を印加したときに透過光(反射光)が強度変調を受けることを利用し, 簡単な構成でひずみや圧力の波形を直接観測することができる. また, この方式によるセンサの感度は FBG の透過(反射)スペクトルの傾斜部分の傾きに依存し, 高感度な計測を行うためには, この傾斜が急峻であることが必要となる. 本研究では FBG を用いて構成したファブリ・ペロー干渉計 (FBG-FPI) による振動計測の検討を数値計算によって行った. FBG を用いたファブリ・ペロー干渉計の透過スペクトルは単一の FBG によるものよりも急峻な傾きを持つ為, 計測の高感度化が期待できる.

## 2. 数値計算

数値計算によって FBG と FBG-FPI の反射率スペクトルを算出し, 両者を比較する. 数値計算には特性マトリックスの手法を用いた[1]. 算出した FBG の反射率スペクトルを **Fig. 1** に示す. 数値計算のパラメータは紫外光に感度を持つファイバに周期 1060 nm の位相マスクを用いて紫外光を照射して屈折率分布を構成する作製手法を想定して選択した. FBG の周期 $\Lambda$ を 530 nm, 長さ $L_{FBG}$ を 4 mm, ファイバの屈折率 $n$ を 1.458, 紫外光感光によるファイバ屈折率の増加率 $\Delta n/n$ を 0.01% とした.

FBG 2 つを反射鏡として用いて共振器を構成しているファブリ・ペロー干渉計 (FBG-FPI) の反射率スペクトルを **Fig. 2** に示す. FBG-FPI のモデルを **Fig. 3** に示す. このモデルでは同じ条件の共振器の鏡として用いる FBG 間の距離 $L_{FPI}$ は 4 mm とした. また, 両端の FBG については Fig. 1 に示した計算と同様に, 周期 $\Lambda$ を 530 nm, 長さ $L_{FBG}$ を 4 mm, ファイバの屈折率 $n$ を 1.458, 紫外光感光によるファイバ屈折率の増加率 $\Delta n/n$ を 0.01 % とした. Fig. 2 を見ると FBG-FPI の反射率スペクトルが Fig. 1 に示した単一の FBG

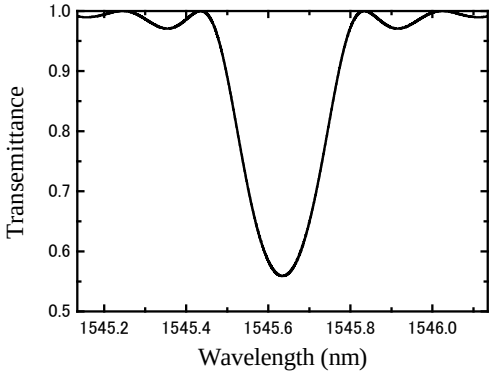


Fig.1 Transmittance spectrum of FBG.

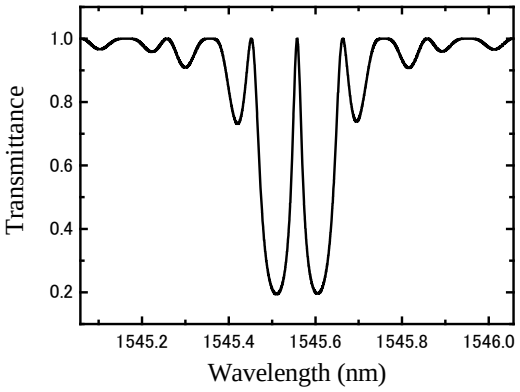


Fig. 2 Transmittance spectrum of FPI with FBG mirrors.

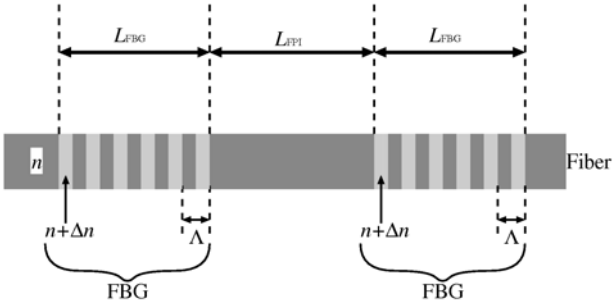


Fig.3 FPI with FBG mirrors.

---

†a24wada@nda.ac.jp

の反射率スペクトルよりも急峻な傾斜部を持っていることを確認できる.

傾斜の急峻さを比較するため, 単一の FBG と FBG-FPI のそれぞれについて反射率スペクトルの傾きを算出した. 算出した傾きを **Fig. 4** に示す. Fig. 4 を見ると, FBG-FPI の反射率スペクトルの傾きは単一の FBG の反射率スペクトルの傾きの約 10 倍であることがわかる.

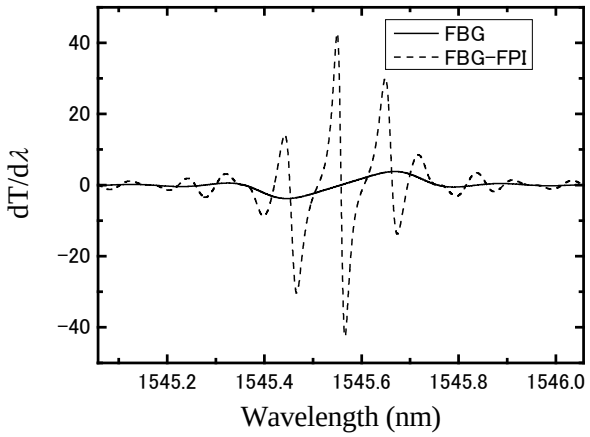


Fig. 4 Slope of transmittance spectra of FBG and FBG-FPI.

FBG-FPI にひずみを加えた場合の反射率スペクトルを算出した. ひずみは 2 つの FBG を含む共振器全体に加えるものとした. 結果を **Fig. 5** に示す. 算出した反射率スペクトルを基にひずみに対するスペクトル関数の波長シフト量を計算したところ, 1.6 pm/με であった. 一方, 単一の FBG に対してもひずみを加えた場合の反射率スペクトルを計算し, 波長シフト量を計算したところ, FBG-FPI と同様に 1.6 pm/με であり, 今回示した条件下では両者の間に有意な差は見られなかった. FBG-FPI の波長シフト量は FBG 間の距離に依存しており, $L_{FPI}$ が大きい場合には単一の FBG よりも大きな波長シフト量が得られた.

強度変調方式の計測を想定し, 単一の FBG と FBG-FPI のそれぞれについて, 反射率スペクトルの勾配が大きな点を動作点に選び, ひずみに対する透過率の変化を調べた. 算出した透過率のひずみ依存性を **Fig. 6** に示す. 10 με 程度のひずみに対して単一の FBG の透過率が 5% 程度しか変動していないのに対し, ファブリ・ペロー干渉計の透過率は 60% 程度変動しており, 強度変調方式の計測の高感度化が期待できることが確認できる.

## 3. まとめ

FBG を用いて構成したファブリ・ペロー干渉計による高感度振動センサの検討を数値計算によって行った. 数値計算には特性マトリックスの手法を用いた. FBG-FPI の透過スペクトルが単一の FBG よりも急峻な傾きの傾斜部を持ち, 計測の高感度化が期待できることが確認できた.

## 参考文献

1. 田中　哲, 横須賀　泰輝, 高橋　信明, 第52回春季応物講演会予稿集, 31p-D-7, p.1354, 2005.

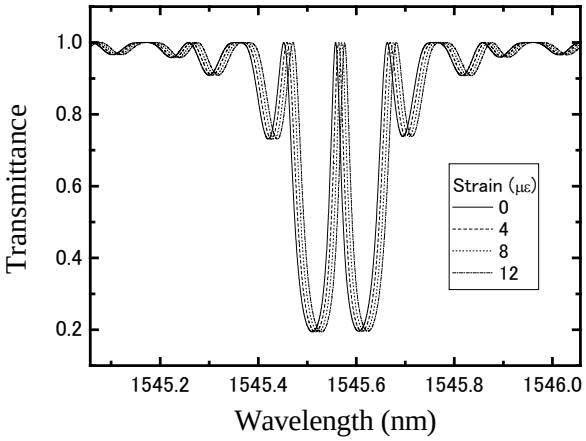


Fig. 5 Strain dependence of transmittance spectrum of FBG-FPI.

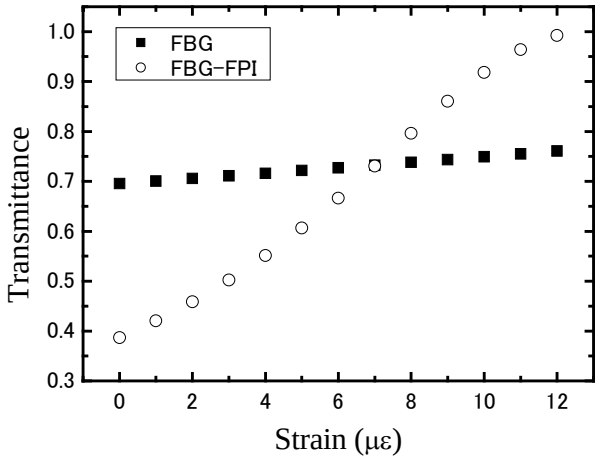


Fig. 6 Strain dependence of transmittance of FBG and FBG-FPI.

1J3-2

Proceedings of Symposium on Ultrasonic Electronics, Vol. 29 (2008) pp. 9-10
11-13 November, 2008

# ラム波を用いた高効率な光モード変換器

High efficient optical mode converter using Lamb wave

齋藤光希†, 中川恭彦, 垣尾省司（山梨大院・医工）

Koki Saito† , Yasuhiko Nakagawa and Shoji Kakio(Interdisciplinary Graduate School of Med. Eng., Univ. of Yamanashi)

When Lamb wave propagates in a crystal, the photo-elastic effect induces a refractive index change in a crystal and makes phase grating in a crystal. Therefore optical mode conversion occurs in the crystals which Lamb wave propagating. Using this phenomenon, it can be expect the Lamb wave type crystal substrate apply to the optical communication system. In this study, we had theoretically examined the optical mode conversion during refractive index period structure. The theoretical calculation result predicted a least power for the mode conversion at a mode1 in various modes. Furthermore, when Lamb wave Λ =270μm and substrate thickness H=20μm in mode 1, Lamb wave power $P_{100}$ to need for 100% optical mode conversion was 12.8mW. Which is very small power for the optical mode converter.

## 1. はじめに

本報では、ラム波型結晶基板の光通信への応用を目指し、ラム波[1,2]による屈折率周期構造中の光波伝搬について理論的な検討を行った。ラム波型結晶基板に光を入射すると、結晶中のラム波と光波との相互作用により、モード変換が生じる。これらについて検討を行った結果、高効率でモード変換が行えることを確認した。

## 2. ラム波による屈折率周期構造

ラム波解析に用いる座標系を図１に示す。ラム波の伝搬方向を $X_1$ 方向、基板表面に垂直な方向を $X_3$ 方向、ラム波波長が $\Lambda$、基板の厚さ $H$ として波動解析を行った。ラム波は,圧電基本式を満たし、(1)、(2)式の運動方程式とラプラスの方程式を満す。

$$\rho \frac{\partial^2 u_j}{\partial t^2} = c^E_{ijkl} \frac{\partial^2 u_k}{\partial x_i \partial x_l} + e_{kij} \frac{\partial^2 \phi}{\partial x_i \partial x_k} \quad \cdots(1)$$

$$e_{ikl} \frac{\partial^2 u_k}{\partial x_i \partial x_l} - \varepsilon^S_{ik} \frac{\partial^2 \phi}{\partial x_i \partial x_k} = 0 \quad \cdots(2)$$

基板表面と裏面による粒子変位、応力、電気的変位、電位の連続性による８つの境界条件下で一般解(3),(4)式が求まる。

$$u_j = \alpha_j \exp(ikbx_3) \exp(ikx_1 - i\omega t) \quad \cdots(3)$$

$$\phi = \alpha_4 \exp(ikbx_3) \exp(ikx_1 - i\omega t) \quad \cdots(4)$$

ラム波による結晶中の屈折率は，(4),(5)式により求まる。

$$\Delta B_{ij} = \frac{1}{2}\left( p_{ijkl} S_{kl} + \gamma_{ijk} E_k + c.c. \right) \quad \cdots(5)$$

$$\Delta B_I = p_{IJ} S_J + \gamma_{Ik} E_k = p_{IJ} S_J - \gamma_{Ik} \phi_{,k} \quad \cdots(6)$$

## 3. ラム波による光モード変換理論

光モード変換は図１の $LiTaO_3$ 基板を用いた。$X_2$ 方向偏波光と $X_3$ 方向偏波光の $X_1$ 軸に沿った振幅,波数ベクトルを

$$(\phi_2(x_1), \beta_2), (\phi_3(x_1), \beta_3) \quad \cdots(7)$$

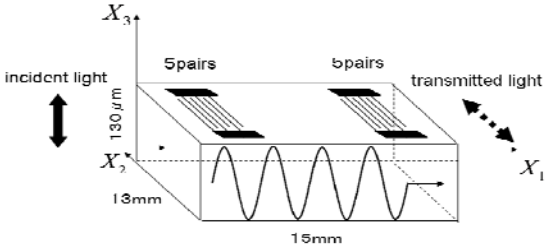


Fig.1 polarized wave rotation experimental Lamb wave substrate.

とすると、媒質中のトータル場は次式となる。

$$\mathbf{E}_T = \phi_2(x_1)\mathbf{E}_2 + \phi_3(x_1)\mathbf{E}_3$$

$$\mathbf{H}_T = \phi_2(x_1)\mathbf{H}_2 + \phi_3(x_1)\mathbf{H}_3 \quad \cdots(8)$$

ここで,ラム波による屈折率周期場の波数を $\mathbf{K}$ とすると、波数整合条件は次式となる。

$$\beta_2 + \mathbf{K} = \beta_3 \quad \cdots(9)$$

$$\mathbf{K} = \beta_3 - \beta_2 = \frac{2\pi n_{33}}{\lambda_0} - \frac{2\pi n_{33}}{\lambda_0} = \frac{2\pi(n_{33} - n_{22})}{\lambda_0}$$

$$\Lambda = \lambda_0 / (n_{33} - n_{22}) \quad \cdots(10),(11)$$

この関係を用い、振幅に関する関係式は、以下のように求まる。[3]

$$\frac{d}{dx_1}\phi_2(x_1) 2(-j\beta_2)\mathbf{E}_{20} = -\omega^2 \mu_0 \varepsilon_0 \frac{1}{2}\{\Delta\varepsilon_{23} \cdot \mathbf{E}_{30}\}\phi_3(x_1)$$

$$\frac{d}{dx_1}\phi_3(x_1) 2(-j\beta_3)\mathbf{E}_{30} = -\omega^2 \mu_0 \varepsilon_0 \frac{1}{2}\{\Delta\varepsilon_{32} \cdot \mathbf{E}_{20}\}\phi_2(x_1) \quad \cdots(12)$$

(12)式を解くと、$X_2$ 方向偏波光と $X_3$ 方向偏波光の振幅はそれぞれ

$$\phi_2(x_1) = \cos(\alpha x_1),\ \phi_3(x_1) = j\sqrt{C_{32}/C_{23}}\sin(\alpha x_1) \quad \cdots(13)$$

ここで、$C_{23}$ と $C_{32}$ は結合係数であり、

$$C_{23} = C^*_{32} = [\, j \frac{1}{480\ \lambda_0} \int_{-H}^{0} (E^*_{20} \Delta\varepsilon_{23} \cdot E_{30}) dx_3 \,]$$

$$\alpha = \sqrt{C_{23} C_{32}} \quad \cdots(14)$$

100%モード変換するに要するラム波パワーを $P_{100}$ とすると、

$$P_{100} = \eta(D/L^2), \eta = \pi^2/(2\alpha)^2 \quad \cdots(15)$$

ここで、$D$：IDT の交差幅、$L$：相互作用長である。

nakagawa@es.yamanashi.ac.jp

## 4. 計算結果

図 2 に $H$=130μm, $\Lambda$=132μm の LT.X-Y 伝搬ラム波の各モードの $K^2$ の計算値を示す。また図 3 に各モードの $\eta$ の計算値を示す。図 4 には図 3 で最も $\eta$ が小さかった Mode 1 (23.29MHz)での基板中の歪みの分布を示す。図から歪み $S_{13}$ が基板中に大きく分布しているため、小さなラム波パワーで光モード変換が起こることがわかった。図 5 に $H$=130μm としたときの $\eta$ の $\Lambda$依存性を示す。図 6,7 に、$\Lambda$ をそれぞれ 132μm( $\lambda_0$ =0.63μm),270μm( $\lambda_0$ =1.3μm)としたときの $\eta$ の $H$ 依存性を示す。

ここで、$D$=1mm,$L$=10mm とすると(15)式より $\Lambda$=270μm,$H$=20μm,の時 $P_{100}$=12.8mW と小さいラム波パワーで光モード変換できる。

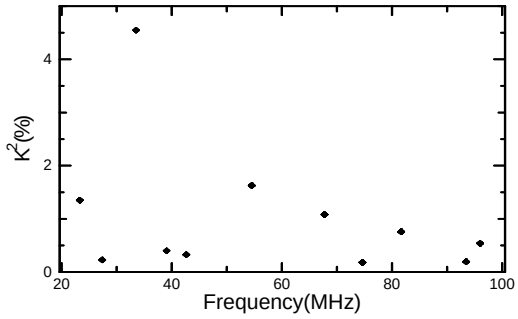


Fig.2 Analytical result of $K^2$ in each mode for lamb wave.

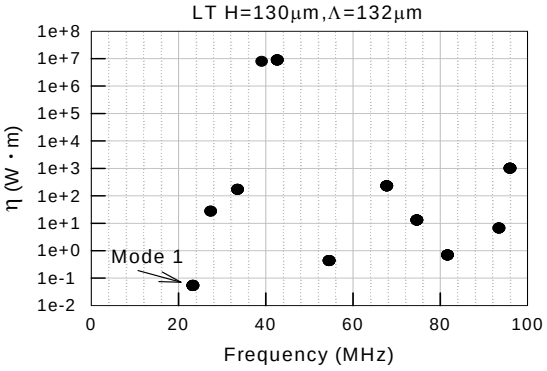


Fig.3 Analytical result of Lamb wave power in each mode for polarized wave rotation.

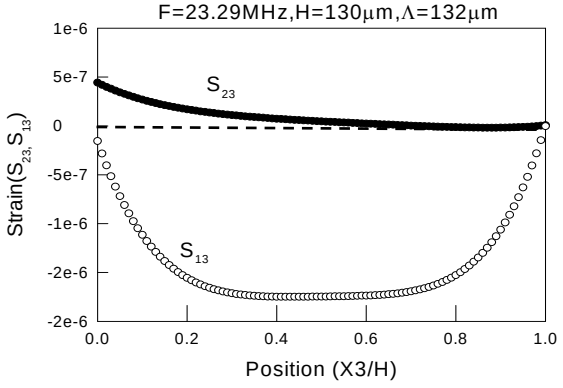


Fig.4 Strain distribution for mode1.

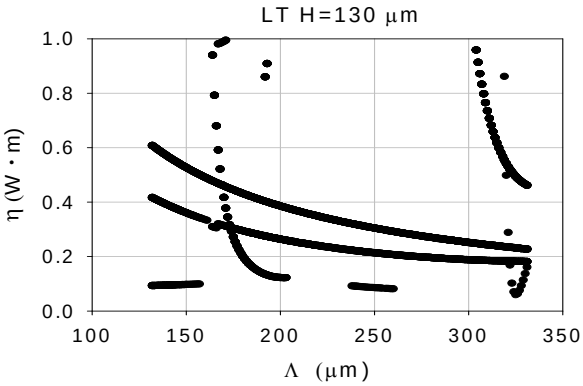


Fig.5 Λ dependency with $\eta$ .(H=130μm)

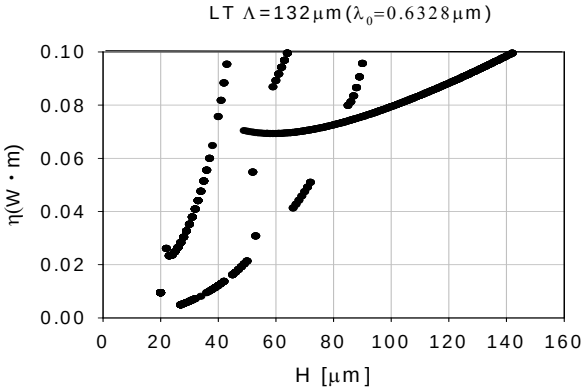


Fig.6 H dependency with $\eta$ .(Λ=132μm)

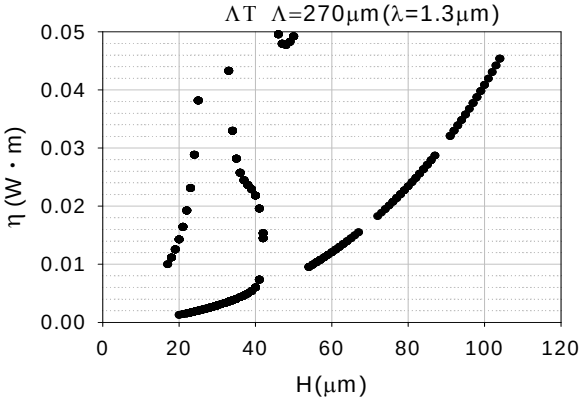


Fig.7 H dependency with $\eta$ .(Λ=270 $\mu$ m)

## 5. あとがき

本報告では、ラム波による光モード変換について検討を行い、論理計算の結果から、高効率な光モード変換器を提案した。

今後は、さらに高い変換効率を得るための設計指針を理論的、実験的に求める予定である。

### 参考文献


[1] Y. Nakagawa *et al.* Jpn.J.Appl.Phys., 42(5B), 3086-3090, 2003.

[2] Y. Nakagawa *et al.* Jpn.J.Appl.Phys., 43(5B), 3020-3023, 2004.

[3] 小山次郎,西原浩共著, “光波電子工学”, コロナ社

Proceedings of Symposium on Ultrasonic Electronics, Vol. 29 (2008) pp. 11-12
11-13 November, 2008

# タイムリバーサルによる陰影領域中の物体の探知

Detection of objects in shadow region using time reversal

鶴ヶ谷芳昭[1‡]，菊池年晃[2]，水谷孝一[3]（[1]NEC; [2]防衛大;[3]筑波大）
Yoshiaki Tsurugaya[1†], Toshiaki Kikuchi[2] and Koichi Mizutani[3] ([1]NEC; [2]NDA; [3]Univ. of Tsukuba.)

A method of detecting targets present in the shadow area of an obstacle like a seamount by applying a time reversal is described. Transmission signals of two types with a different phase are used. First, the signal of a normal phase is transmitted in the propagation environment without a target, and the signal received with each element of a transducer array is preserved. Next, the signal of an anti-phase is transmitted in the propagation environment with the target, and the signals received with each element of the transducer array are preserved. The received signals of two types are added in the vector. The time reversal sound field (TRSF) to the target is formed by time-reversing and re-emitting the added signal.

## 1. はしがき

最近、タイムリバーサルを利用した水中物体の探知に関する研究が注目されている[1,2]。C. Prada らは、複数ターゲットからの反射波にタイムリバーサルを適用した波を放射して、ターゲットに収束する波を生起させた。その波に対する反射波に再びタイムリバーサルを適用して再放射する。この操作を繰り返すことによって、個々のターゲットに収束する波を生起させた。この方法は、タイムリバーサルを反復する必要がある。一方、鶴ヶ谷ら[3]は、音源からの進行波を除去して、ターゲットからの前方散乱波に対してタイムリバーサルを適用して、個々のターゲットに収束させた。この方法では単純な参照音場を用いたが、ターゲットの配置によって、一部のターゲットの識別が困難になることがある。そこで、今回は複雑な伝搬環境における参照音場について検討する。

## 2. タイムリバーサル音場

浅海中に設置された音源と変換器アレイを用いて、次式に従って、タイムリバーサル音場を求める。

$$P_{pc}(r,z;t)=\sum_{j=1}^{J}\int G_{\omega}(r,z,z_j)G_{\omega}^{*}(R;z_j,z_{ps})\times e^{i\omega T}S^{*}(\omega)e^{-i\omega t}d\omega \qquad (1)$$

ここで$G_{\omega}(R;z_j,z_{ps})$は、音源からアレイ素子に及ぼすグリーン関数で、$G_{\omega}(r,z,z_j)$はアレイ素子から点(r,z)に及ぼすグリーン関数である。$S(\omega)$は音源から放射されるパルスの周波数スペクトルである。放射されるパルスは中心周波数 500Hz のトーンバースト波である。グリーン関数の算出には結合モード法を用いる。

## 3. シミュレーション

### 3.1 海山の陰影にある物体

複雑な伝搬環境の一つとして、**Fig. 1** に示したような、海山を有する浅海域を設定する。平坦部の水深は 100m、海山頂部の深さは 50m である。音源から海山と変換器アレイまでの距離はそれぞれ 1km と 3km である。はじめは、海山を有する海域で、ターゲットを挿入せずに、タイムリバーサル音場を求める。すなわち、(1)式を用いて、音源からアレイの間の点(r,z)での音圧を求め、その音圧振幅分布を **Fig. 2** に示す。距離 3km に位置する変換器アレイから放射されたタイムリバーサル波は、距離 1km に位置する海山を越えて音源位置(距離 0m、深度 50m)に収束することが分かる。

次に、ターゲットを挿入した場合のタイムリバーサル音場を求める。ターゲットの大きさは縦横共に 2m で、その音速は 4350m/s である。それを音源からみて海山の陰影部に相当する位置(距離 1.5km 深度 70m)に挿入する。そのときのタイムリバーサル音場は Fig. 2 とほとんど

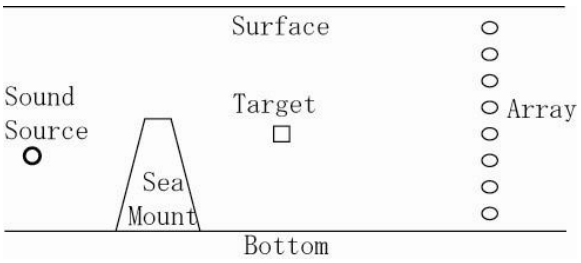


Fig. 1 Schematic representation of the simulation model.

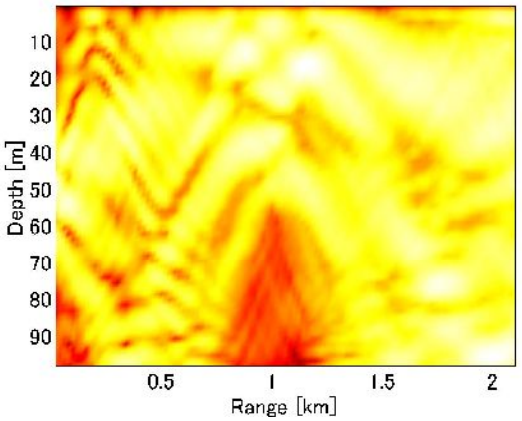


Fig. 2 TRSF in shallow water with a seamount by a normal method.

y-tsurugaya@bp.jp.nec.com

同じで、ターゲットの付近の音場には全く変化が見られない(図は省略する)。その理由は、音源から変換器アレイへ進行する進行波のレベルがターゲットによる散乱波のレベルより大きいためと考えられる。

次に、進行波の成分を除去して、散乱波のみのタイムリバーサル音場を求める。進行波成分を除去するために、音源から放射する二種類の音波パルスを用いる。まず、始めに、ターゲットが挿入されない状態(参照音場)で、音源から正相の音波パルスを放射して、変換器アレイの各素子で受波して、保存する(参照波)。次に、ターゲットを挿入した状態(ターゲット音場)で、逆相の音波パルスを放射して、変換器アレイの各素子で受波する(ターゲット波)。そして先に保存した参照波とターゲット波をベクトル的に加算する。この操作によって、進行波の成分は打ち消されて、変換器アレイの各素子にはターゲットからの散乱波の成分のみが残される。この残された成分を、各素子から放射することにより、散乱波のみのタイムリバーサル音場が求められる。

求められた散乱波に対するタイムリバーサル音場を **Fig. 3** に示す。この図から明らかなように、ターゲットの位置にのみ収束し、音源位置への収束はみられない。また、Fig.2 と比較すると、収束点の上部のレベルがかなり低い。すなわち、進行波成分がほとんど現れていないことが分かる。更に、Fig. 2 と比較すると、Fig. 2 で見られる海山は Fig. 3 では全く見ることが出来ない。このことから、散乱波のタイムリバーサル波には、海山などの伝搬環境は影響しないことが分かる。

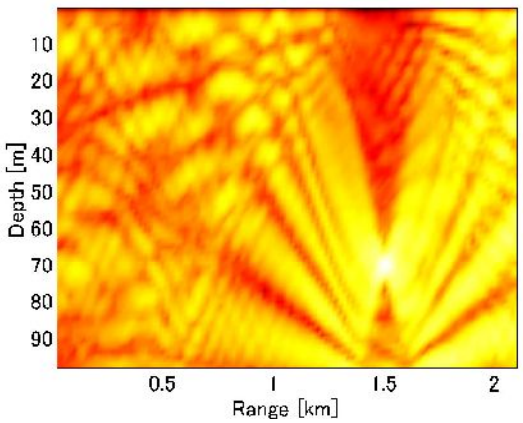


Fig. 3　TRSF for the target after traveling wave is deleted.

### 3-2　物体の陰影にある物体

我々は先に [3]、参照波を作成する伝搬環境として単純な伝搬環境を用いた。しかし、前項に示したように、複雑な伝搬環境でも、参照波の作成が可能であることが明らかになった。そこで、ここでは一部のターゲットを伝搬環境に含めることを検討する。二つのターゲットがほぼ水平に配置した場合、**Fig. 4** に示したように、距離 1.7km、深度 50m にあるターゲット(第 2 ターゲット)の識別が困難になりやすい。これは第 2 ターゲットには、音源からの進行波と距離 1.5km、50m 音源にある第 1 ターゲットの散乱波が当たるためと考えられる。そこで、第 1 ターゲットを伝搬環境の中に含めて、参照波を求める。そして第 2 ターゲットに対するタイムリバーサル音場を求めた結果を **Fig. 5** に示す。第 2 ターゲットのみに収束していることが分かる。

## 4. まとめ

ターゲットのタイムリバーサル音場を求める際の参照音場について検討した。その結果、海山のある伝搬環境や、不要なターゲットを含む伝搬環境をも参照音場として利用出来ることが明らかになった。

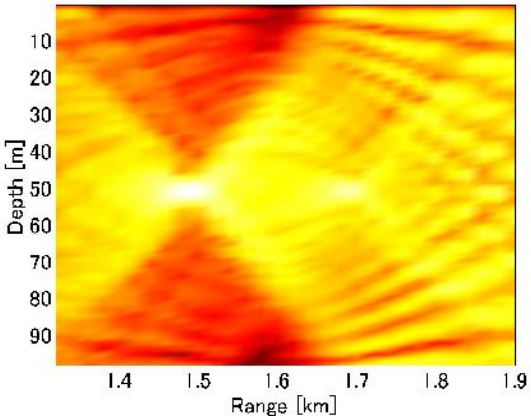


Fig. 4　TRSF for two targets that queue up horizontally.

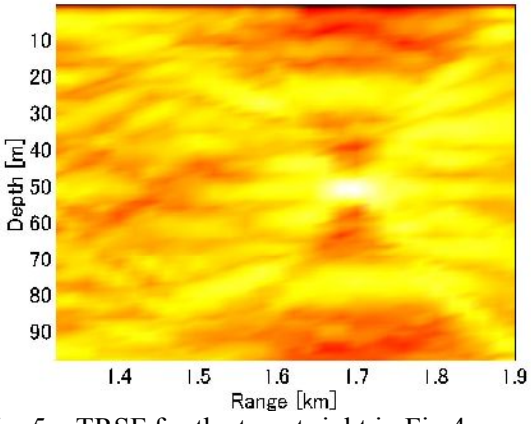


Fig. 5　TRSF for the target right in Fig.4.

### 引用文献

1. C. Prada, et al : J.Acoust.Soc.Am. 99(1996) 2067.
2. G. Montaldo et al : J. Acoust. Soc. Am. 115 (2004) 776
3. Y. Tsurugaya et al: Acoustics'08 Paris. 2aSPb (2008) 1395

1J9-2

Proceedings of Symposium on Ultrasonic Electronics, Vol. 29 (2008) pp. 13-14
11-13 November, 2008

# Design for Aplanatic Fresnel Acoustic Lens
アプラナートフレネル音響レンズの設計

Yuji Sato[1‡], Koichi Mizutani[1] , Naoto Wakatsuki[1] , and Toshiaki Nakamura[2]
([1]University of Tsukuba; [2]National Defense Academy)
佐藤裕治[1‡], 水谷孝一[1], 若槻尚斗[1], 中村敏明[2] ([1]筑波大院 シス情工; [2]防衛大 地球海洋)

## 1. Introduction

Underwater acoustic lenses are useful device for the beam forming of an underwater imaging system because the lenses can make the system size small. An Autonomous Underwater Vehicle "URASHIMA" equipped the acoustic lens for the obstacle avoidance sonar for an actual example[1)].

A low-frequency sound must be used for long range detection. The aperture of lens should be enough larger than the wavelength and the lens becomes thick. It is a problem because the sound pressure is seriously attenuated in the lens and it becomes heavy. A Fresnel lens which has stair-like surface is useful to reduce the thickness and it can focus higher sound pressure than an ordinary convex lens[2)]. Another problem is an aberration. A spherical lens has a spherical aberration. The spherical aberration is compensated in aspherical lenses but a coma aberration appears in case of an oblique incidence. An aplanatic lens has two aspherical surfaces and the spherical and coma aberrations are both compensated in paraxial area[3)].

Thus, it is considered that an aplanatic Fresnel lens is better than the aplanatic lens. We designed an aplanatic Fresnel lens using an optical method and evaluated it using ray tracing method and the 2 dimensional finite difference time domain (2D FDTD) method.

## 2. Design for aplanatic Fresnel lens

An aplanatic lens is designed by solving following equations.

$$\sin u_2 = \frac{h}{f}, \tag{1}$$

$$a + nb + c = nd + s, \tag{2}$$

$$e = d + s - f\cos u_2 - a, \tag{3}$$

$$b^2 = e^2 + (f-c)^2 - 2e(f-c)\cos u^2, \tag{4}$$

$$\frac{f-c}{\sin u_1} = \frac{b}{\sin u_2}, \tag{5}$$

$$\frac{da}{dh} = \frac{n\sin u_1}{n\cos u_1 - 1}. \tag{6}$$

Here, $n$ is the refractive index of the lens and other parameters are shown in **Fig. 1**. The 1st surface is determined by $a$ and $h$, and the 2nd surface is determined by $c$ and $u_2$. There is an infinite shape of lens which has same $d$ and $f$. The shapes are determined by the central curvature radius of the 1st surface $r_1$. It is called as bending. A spherical aberration and the thickness of the rim become smallest when the $r_1$ satisfies the following relation[4)].

$$\frac{1}{r_1} = \frac{(2n+1)n}{2(n-1)(n+2)f}. \tag{7}$$

An aplanatic Fresnel lens is designed by combining some lenses, which are designed to have the same focal point. Additionally, if the 1st or 2nd surfaces of these lenses are overlapped each other the shape becomes simple. **Fig. 2** shows an instance of the 2nd surfaces overlapping. The lens 1 which is smaller than lens 2 is assigned to the inner part of the combined lens and the lens 2 is assigned the outer part. $d_1$ is determined arbitrarily. $d_2$, $d_3$, … ,$d_N$ are derived by the following equation.

$$d_N = \frac{(N-1)\lambda_w}{n-1} + d_1. \tag{8}$$

Here, $\lambda_w$ is the wavelength in water.

Designed lenses are shown in **Fig. 3**. The lenses in Fig. 3 (b) and 3 (c) are named as "the First surface Stepped aplanatic Fresnel lens (FSF)" and "the Second surface Stepped aplanatic Fresnel lens (SSF)", respectively. Fig. 3 (a) shows the outer lens of the FSF which is named as "the Aplanatic Convex lens (AC)". FSF and SSF are thinner than AC and each lens has 12 steps.

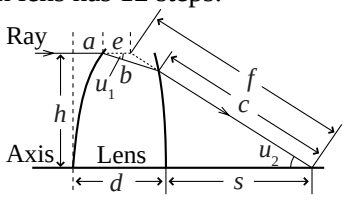


Fig. 1 Diagram of an aplanatic lens.

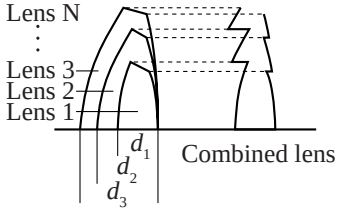


Fig. 2 Combining lenses for a Fresnel lens.

yuji@aclab.esys.tsukuba.ac.jp

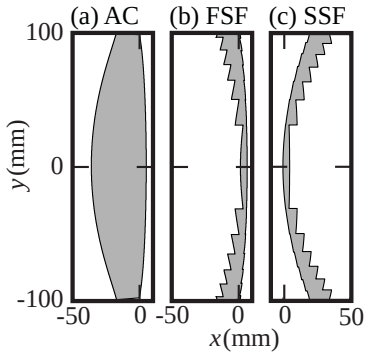


Fig. 3 Shapes of lenses.
(a) Aplanatic Convex lens (AC),
(b) First surface Stepped aplanatic Fresnel lens (FSF),
(c) Second surface Stepped aplanatic Fresnel lens (SSF).

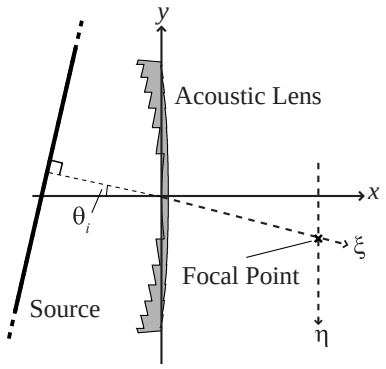


Fig. 4 Arrangement of the 2D FDTD analysis.

## 3. 2D FDTD analysis

Converged sound pressure fields of the 3 lenses are evaluated by the 2D FDTD method. An arrangement of the 2D FDTD analysis is shown in **Fig . 4**. The origin is located on the center of the 1st surface of FSF or SSF. The *x* axis is identical to the lens axis and the *y* axis lies on the radial direction. The ξ axis is passing through the origin and the focal point and η axis is parallel to the *y* axis and passing through the focal point. The lens is assumed to be made of silicone rubber which has 1000 m/s sound speed, 1490 kg/m$^3$ density and 1 dB/$\lambda$ attenuation. Here, $\lambda$ is the wavelength in the lens. The lens is surrounded by water which has 1500 m/s sound speed and 1000 kg/m$^3$ density. A plane wave is incident to the lens with the incidence angle $\theta_i$. The incident wave is 500 kHz and 25 cycles burst wave. The discretizing interval is 0.2 mm in space and 0.02 ms in time. The sound field is surrounded by the absorbing layer and the exterior boundary is Mur's 1st order non-reflective boundary.

The characteristics on ξ and η axes with $\theta_i$ = 0 and 10 ($^o$) are shown in **Fig. 5** and **6**, respectively. These are the integrated RMS of the sound pressure normalized by the maximum sound pressure of the FSF with $\theta_i = 0^o$. The sound pressures of FSF and SSF are larger than AC. Thus, the 2 aplanatic

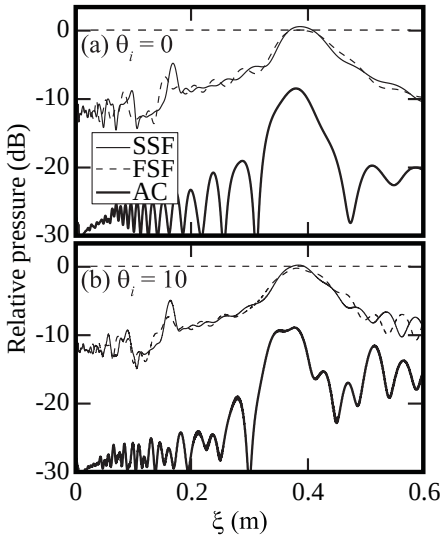


Fig. 5 On ξ axis characteristics.

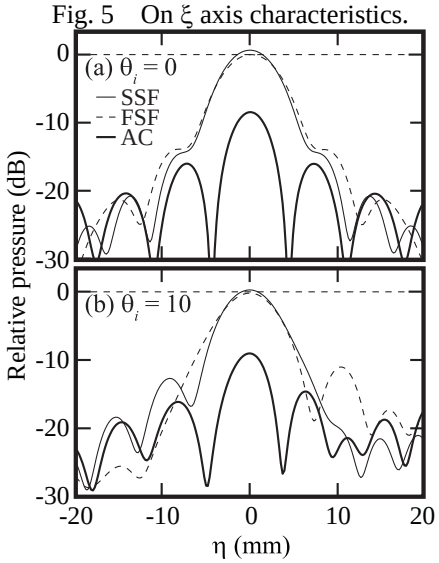


Fig. 6 On η axis characteristics.

Fresnel lenses have better property than AC. The sound pressure of SSF is slightly larger than that of FSF. The focal sound pressure of the SSF is larger than that of FSF about 0.5dB.

## 4. Conclusion

The 2 shapes of the aplanatic Fresnel lenses were designed and evaluated using the 2D FDTD method. In conclusion, the property of SSF is best of all. It is future problems to design the most appropriate lens shape because the SSF designed in this report is one of the extreme shapes.

**References**

1). S. Tsukioka, T. Aoki, H. Ochi, T. Shimura, T. Sawa, T. Nakamura, T. Anada, I. Kaihou and H. Noda: Jpn. J. Appl. Phys. **41** (2002) 3970.
2). Y. Sato, K. Mizutani, N. Wakatsuki, and T. Nakamura: Jpn. J. Appl. Phys. **47** (2008) 4354.
3). Y. Sato, A. Miyazaki, K. mori, and T. Nakamura: Jpn. J. Appl. Phys. **46** (2007) 4982.
4). Y. Tanaka, M. Yamagata, and T. sasano: Kogaku **27** (1998) 720 [in Japanese].

1J2a-1

Proceedings of Symposium on Ultrasonic Electronics, Vol. 29 (2008) pp. 15-16
11-13 November, 2008

# LFB 超音波材料解析システムによる漏洩弾性表面波伝搬特性の測定モデル

## Measurement model for propagation characteristics of leaky surface acoustic waves by the line-focus-beam ultrasonic material characterization system

大津賢治[1‡]，荒川元孝[2]，櫛引淳一[2]　([1]東北大院 医工; [2]東北大院 工)
Kenji Otsu[1], Mototaka Arakawa[2], and Jun-ichi Kushibiki[2] ([1]Graduate School of Biomedical Engineering, Tohoku Univ.; [2]Graduate School of Engineering, Tohoku Univ.)

The line-focus-beam ultrasonic material characterization system can perform material characterization by accurately measuring the propagation characteristics (viz., phase velocity $V_{\mathrm{LSAW}}$ and attenuation $\alpha_{\mathrm{LSAW}}$) of leaky surface acoustic waves (LSAWs) excited on the water-loaded specimen surface. In the conventional theoretical calculations, water was treated as an ideal fluid and the shear-wave component was not considered for the boundary conditions. In this paper, we studied an exact measurement model of LSAW propagation characteristics for synthetic silica glass and borosilicate glass, considering the shear-wave component in the water-loading effect and viscosities of longitudinal and shear waves for both specimen and water. The calculated results for this advanced measurement model exhibit dispersion for both LSAW velocities and normalized attenuation coefficient factors. This is mainly caused by the effect of shear-wave component of water.

### 1. まえがき

直線集束ビーム超音波材料解析（line-focus-beam ultrasonic material characterization: LFB-UMC）システム[1)]は，水を負荷した試料表面を伝搬する漏洩弾性表面波（leaky surface acoustic wave: LSAW）の伝搬特性（位相速度$V_{\mathrm{LSAW}}$，規格化伝搬減衰$\alpha_{\mathrm{LSAW}}$）を高精度に計測でき，材料評価に用いられている．従来の測定モデルでは水を理想流体と仮定し，水の横波の効果を無視していた．本研究ではその効果を測定モデルに導入して検討を行ったところ，従来の解析値との間に顕著な差が見られたので報告する．

### 2. 漏洩弾性表面波の伝搬特性の理論解析モデル

**Fig. 1** は水の横波を考慮したLSAW伝搬特性の解析モデルとその新しい概念を示すものであり，基板深さ方向を $+z$ 方向とし，$+x$ 方向に伝搬するLSAWの伝搬解を与える境界条件[2)]は，水と試料の境界において以下のように表される．

$$\begin{cases} T_{zz}^{s} = T_{zz}^{w} & (1) \\ U_{z}^{s} = U_{z}^{w} & (2) \\ T_{zx}^{s} = T_{zx}^{w} & (3) \\ U_{x}^{s} = U_{x}^{w} & (4) \end{cases}$$

ただし，上付き添え字 $s$ は試料（specimen），$w$ は水（water）のパラメータであることを意味する．

水を理想流体として取り扱う場合，境界条件は式(1), (2)および式(3)において $T_{zx}^{s} = 0$ とする 3 式で与えられる．水の横波の効果に対して考慮しなければならない境界条件として式(3), (4)が加わり，これら 4 式を解くことで新しい測定モデルにおける LSAW 伝搬特性が得られる．

ここで複素弾性率は一般に $c = c' + jc''$ と表せ，これに関係する定数は Fig. 1 に示すパラメータにより計算される．ここでは試料として 2 種類の等方性固体，すなわち合成石英ガラス C-7980 と硼珪酸ガラス C-7740 を取り上げる．試料のバルク音響特性を **Table I**, **II** [3, 4)]に，水に対するそれを**Table III** [5-8)]にまとめ，これらのデータをもとに，新しい測定モデルを用いたLSAW伝搬特性の数値計算を行った．

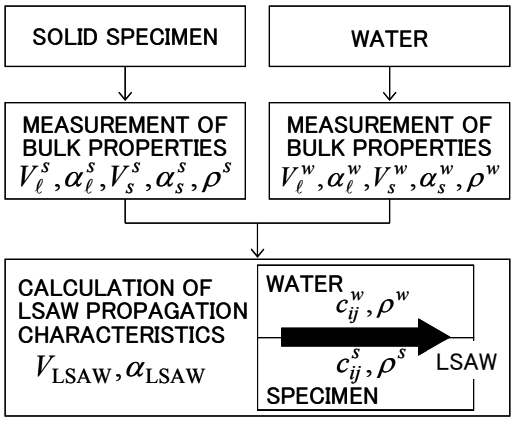


Fig. 1 New concept of theoretical analysis of LSAW propagation characteristics.

Table I Bulk propagation characteristics of C-7980. [Refs.[3],[4]]

| | Longitudinal | Shear |
|---|---|---|
| Velocity [m/s] | 5929.13 | 3767.62 |
| Attenuation coefficient [m$^{-1}$] | $1.1\times10^{-16}\times f^2$ | $1.9\times10^{-16}\times f^2$ |
| Density [kg/m$^3$] | 2199.82 | |

Table II Bulk propagation characteristics of C-7740. [Refs.[3],[4]]

| | Longitudinal | Shear |
|---|---|---|
| Velocity [m/s] | $5538.29+0.0328\times f^{0.27}$ | $3401.95+1.53\times f^{0.10}$ |
| Attenuation coefficient [m$^{-1}$] | $2.30\times10^{-9}\times f^{1.29}$ | $1.82\times10^{-9}\times f^{1.33}$ |
| Density [kg/m$^3$] | 2222.48 | |

Table III Bulk propagation characteristics of water. [Refs.[5]-[8]]

| | Longitudinal | Shear |
|---|---|---|
| Velocity [m/s] | 1491.23 | $10.5+2.42\times10^{-7}\times f$ |
| Attenuation coefficient [m$^{-1}$] | $2.23\times10^{-14}\times f^2$ | $2.64\times10^{3}\times f^{0.48}$ |
| Density [kg/m$^3$] | 997.54 | |

otsu@ecei.tohoku.ac.jp

## 3. 数値計算結果

**Fig. 2** に 100 ~ 300 MHz における LSAW 伝搬特性の数値計算結果を示す．実線は式(1)~(4)の境界条件を適用し，Fig. 1 に示した全ての成分を考慮した新しい測定モデルの計算値，破線は水を理想流体と仮定した従来の測定モデルの計算値を表す．C-7980 の場合，周波数が増加するにつれて，$V_{\mathrm{LSAW}}$ および $\alpha_{\mathrm{LSAW}}$ はともに単調に増加した．従来の方法と今回の方法による数値計算結果と比較すると，225 MHz において $V_{\mathrm{LSAW}}$ は 3426.22 m/s から 3428.76 m/s へ 0.07 % 増加し，$\alpha_{\mathrm{LSAW}}$ は 0.03896 から 0.03934 へ 1.0 % 増加した．また C-7740 の場合も同様の傾向を示し，225 MHzにおいて，$V_{\mathrm{LSAW}}$ は 0.09 % 増加し，$\alpha_{\mathrm{LSAW}}$ は 2.9 % 増加した．

## 4. 検討

従来の理論解析法では水の音響特性については水の縦波音速 $V_\ell^w$ のみを考慮している．そこで，水の負荷効果として水の縦波減衰係数 $\alpha_\ell^w$ , 横波音速 $V_s^w$ , 横波減衰係数 $\alpha_s^w$ の各パラメータが LSAW 伝搬特性に与える影響を数値計算により検討した．考慮したパラメータの組み合わせを **Table IV** に示す. Case① は水を理想流体と仮定した従来の測定モデルであり，Case②と①の差が $\alpha_\ell^w$ の影響，同様に③と②の差が $V_s^w$ の影響，④と③の差が $\alpha_s^w$ の影響を表す.

C-7980 および C-7740 の 2 種類の等方性固体試料に対して周波数特性を求めた．225 MHz における値を **Table V** に示す．その結果，いずれの試料に対しても水の負荷効果として $V_s^w$ および $\alpha_s^w$ の影響が大きく， $\alpha_\ell^w$ の影響は十分に小さいことが示された．また，Fig. 2 において $V_{\mathrm{LSAW}}$ ，$\alpha_{\mathrm{LSAW}}$ がともに単調増加の傾向を示したことは，Table III より水の音響インピーダンスの周波数特性がこの周波数範囲で増加したため，漏洩波が大きくなったと考えられる．

さらに Fig. 1 に示した全てのパラメータを考慮した場合を Case⑤とすると，Case⑤と④の差が試料の吸収減衰 $\alpha_b$ による影響を表し，それを Table V に併記した．C-7740 の変化は C-7980 のそれより大きく，C-7740 のバルク損の特性を反映している．

## 5. あとがき

本報では LSAW 伝搬特性の測定モデルにおいて，これまで考慮されていなかった水の横波の効果についてガラスを対象に数値計算を行った. その結果，得られた分散特性は水の横波成分が支配的であることが示された．本研究が測定モデルの完成へ貢献できるものと考える．

Table IV　Considered parameters as water-loading effect on calculation of LSAW propagation characteristics.
○: considered, ×: ignored

| | $V_\ell^w$ | $\alpha_\ell^w$ | $V_s^w$ | $\alpha_s^w$ |
|---|---|---|---|---|
| Case① | ○ | × | × | × |
| Case② | ○ | ○ | × | × |
| Case③ | ○ | ○ | ○ | × |
| Case④ | ○ | ○ | ○ | ○ |

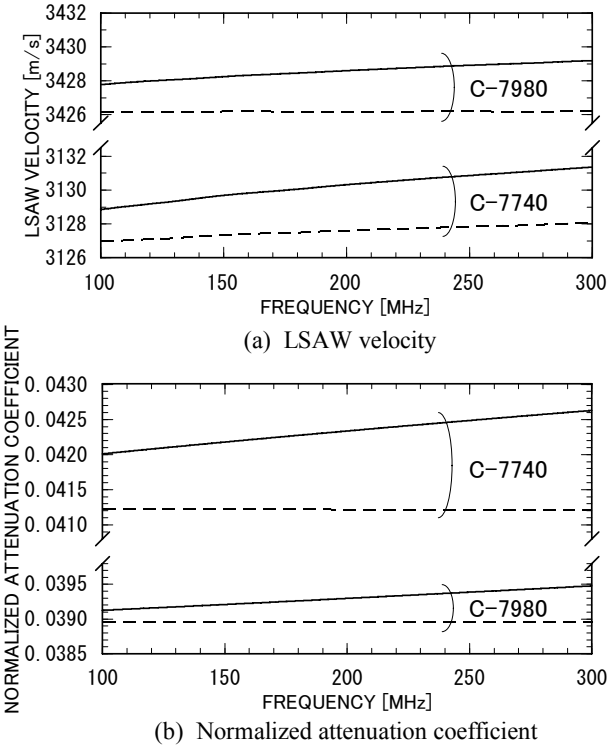

(a) LSAW velocity

(b) Normalized attenuation coefficient

Fig. 2　Calculated results of LSAW propagation characteristics for C-7980 and C-7740. Solid lines denote the results considering the shear-wave component of water, broken lines denote the results treating water as an ideal fluid.

Table V　Water-loading effect of each parameter on LSAW propagation characteristics at 225 MHz.

| | C-7980 | | C-7740 | |
|---|---|---|---|---|
| | Diff.($V_{\mathrm{LSAW}}$) | Diff.($\alpha_{\mathrm{LSAW}}$) | Diff.($V_{\mathrm{LSAW}}$) | Diff.($\alpha_{\mathrm{LSAW}}$) |
| ②−① ($\alpha_\ell^w$) | –0.19 m/s (–0.01 %) | $1.5\times10^{-5}$ (0.04 %) | –0.19 m/s (–0.01 %) | $2.0\times10^{-5}$ (0.05 %) |
| ③−② ($V_s^w$) | –3.51 m/s (–0.10 %) | $6.6\times10^{-4}$ (1.70 %) | –3.78 m/s (–0.12 %) | $6.1\times10^{-4}$ (1.48 %) |
| ④−③ ($\alpha_s^w$) | 6.23 m/s (0.18 %) | $-3.3\times10^{-4}$ (–0.85 %) | 6.46 m/s (0.21 %) | $-1.6\times10^{-4}$ (–0.40 %) |
| ⑤−④ ($\alpha_b$) | 0.01 m/s (0.00 %) | $3.1\times10^{-5}$ (0.08 %) | 0.35 m/s (0.01 %) | $7.2\times10^{-4}$ (1.76 %) |

## 引用文献


1. J. Kushibiki and N. Chubachi: IEEE Trans. Sonics Ultrason. **SU-32** (1985) 189.
2. J. J. Campbell and W. R. Jones: IEEE Trans. Sonics Ultrason. **SU-17** (1970) 71.
3. J. Kushibiki, R. Okabe, and M. Arakawa: J. Acoust. Soc. Am. **113** (2003) 3171.
4. 櫛引, 荒川, 鈴木, 小野: 信学技報 **US2007-52** (2007) 55.
5. W. Kroebel and K.-H. Mahrt: Acustica **35** (1976) 154.
6. F. E. Jones and G. L. Harris: J. Res. Natl. Inst. Stand. Technol. **97** (1992) 335.
7. 橋本, 明石, 櫛引: 信学技報 **US97-50** (1997) 37.
8. 小林, 明石, 櫛引: 電気学会計測研究会資料 **IM-96-89** (1996).

Proceedings of Symposium on Ultrasonic Electronics, Vol. 29 (2008) pp. 17-18
11-13 November, 2008

# Investigation of carrier recombination processes in GaAs/AlAs multiple quantum wells using piezoelectric photothermal and surface photovoltage techniques

# 光熱分光法と表面光起電力法による GaAs/AlAs-MQW の電子遷移過程の研究

Ping Wang†, Kentaro Sakai, Atsuhiko Fukuyama, Tetsuo Ikari (Facult. Eng., Miyazaki Univ.)
王萍‡, 境健太郎, 福山敦彦, 碇哲雄 （宮大 工）

## 1. Introduction

For improving the performance of quantum structure optical devices, it is important to investigate the carrier generation, confinement, and recombination processes in quantum wells. We have reported that the excitonic and two-dimensional step-like subband absorptions up to 3rd order subband of GaAs/AlAs multiple quantum wells (MQW) were successfully obtained by using the piezoelectric photothermal (PPT) and the surface photovoltage (SPV) methods at room temperature (As shown in the insets of **Fig. 1**).[1)] We also concluded that the subtracted SPV signal detected the photoexcited carriers confined in MQW, whereas the subtracted PPT signal implies the radiative recombination of carriers in MQW. In this study, we investigate the temperature dependence of confinement, radiative, and nonradiative recombinations of photoexcited carriers in MQW.

## 2. Experimental procedure

A high-quality undoped GaAs/AlAs MQW sample was grown on a semi-insulating (SI) GaAs (100) substrate by molecular beam epitaxy. The MQW layer was composed of 50 periods of 12.8-nm-thick GaAs wells and 5.9-nm-thick AlAs barriers. [2)]

For the SPV measurements, the sample was first mounted on the cold finger as the grounded back electrode with an insulating sheet, and an indium tin oxide (ITO) film, as a transparent front electrode, was placed on this sample.[1, 3)] The voltage between the ITO film and the cold finger generated by the photoinduced changes in the surface potential was detected as a SPV signal.

For the PPT measurements, a disk-shaped piezoelectric transducer (PZT) was directly attached to the sample surface using a conducting paste to detect the heat and/or strain generated by nonradiative transitions. The detailed PPT experimental setup has already been reported. [4, 5)]

The subtracted PPT and SPV spectra were measured at temperature range from 80 to 300K by deducing the background signal from GaAs substrate.[1)] The modulation frequency of the probing light was set at 100 Hz, where the thermal diffusion length was larger than the sample thickness.

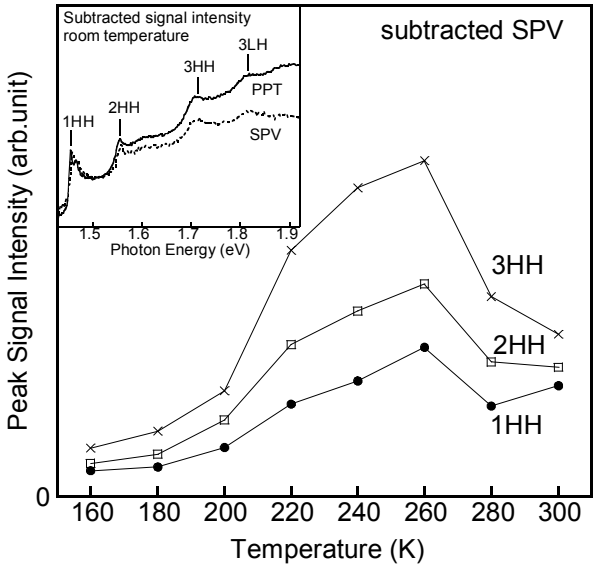


Fig. 1 Temperature dependence of subtracted SPV signal intensities at 1HH, 2HH and 3HH peaks. The insets show the subtracted PPT and SPV spectra at room temperature from Ref.1.

## 3. Results and discussion

**Figure 1** shows the temperature dependence of subtracted SPV signal intensities at 1st- (1HH), 2nd- (2HH), and 3rd- (3HH) subband absorptions, respectively. Since the subtracted SPV implied the carrier confinement within MQW,[1)] the carrier confinement showed the maximum at around 260K, and then decreased with decreasing temperature. In this situation, the confined carriers should come back to the ground states both through radiative and nonradiative recombinations. **Figure 2** shows the temperature dependence of subtracted PPT signal intensities at same point. The subtracted PPT spectra indicated the radiative recombination component of confined carriers in MQW.[1)] As the temperature decreased, a significant decrease of

wping@ssp.phys.miyazaki-u.ac.jp

radiative recombination component was observed. Below 220K, the radiative recombination component showed negative signals. This behavior should be interpreted as an increase of the nonradiative recombination component in the MQW. This behavior was remarkable in the higher order subband such as 3HH. It is considered as follows. When the photoexcited carriers in the higher order subband relax to the lowest subband, phonons will be emitted. These phonons can be detected as the nonradiative recombination signals. If this relaxation process dominant at low temperature, the nonradiative recombination component will increase and then subtracted PPT will show the negative signal at low temperature.

**Figure 3** shows the temperature dependence of photoluminescence (PL) peak intensities associated with 1HH, 1LH, and 2HH transitions. It is obvious that the higher subband luminescence of 2HH can only be observed at higher temperature above 220K. It can be explained that carriers pohotoexcited in 2nd electron subband first relaxed to the 1st electron subband emitting with phonons, and finally recombined radiatively as 1HH PL signal. This phonon emitting inter-subband relaxation process may become dominant when the temperature decreased. These experimental results also give an additional evidence for the increase of nonradiative recombination component at low temperature. Detailed explanation of this relaxation process is now in progress.

In conclusion, we had investigate the temperature dependence of confinement, radiative, and nonradiative recombinations of photoexcited carriers in MQW. As the temperature decreased, decrease of carrier con-

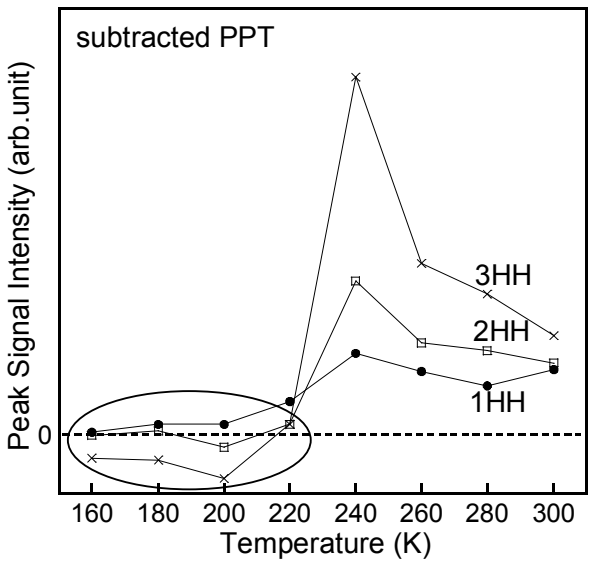


Fig. 2 Temperature dependence of subtracted PPT signal intensities at 1HH, 2HH and 3HH peaks.

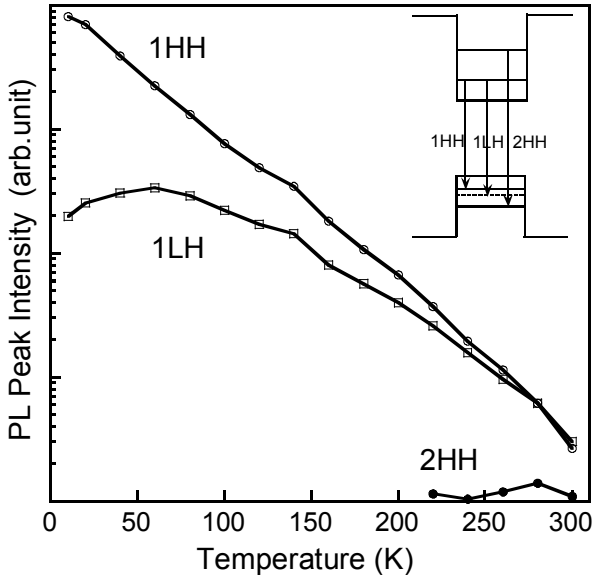


Fig. 2 Temperature dependence of 1HH, 1LH, and 2HH PL peak intensities

finement and increase of nonradiative recombination were observed. It was found that the phonon emitting inter-subband relaxation was dominant at low temperature.

**Acknowledgment**

This work was partly supported by a Grant-in-Aid for Scientific Research from the Ministry of Education, Culture, Sports, Science and Technology. The authors wish to thank to Dr. Kenzo Fujiwara of Kyushu Institute of Technology for supplying high-quality samples.

**References**

1. P. Wang S. Kurayama, A. Fukuyama,Y. Akashi and T. Ikari: Jpn. J. Appl. Phys. **46** (2007) 6857.
2. K. Fujiwara, N. Tsukada, and T. Nakayama: Jpn. J. Appl. Phys. **27** (1988) L1832.
3. L. Kronik, and Y. Shapira: Surface Science Reports **37** (1999) 1.
4. T. Ikari, S. Shigetomi, Y. Koga, H. Nishimura, H. Yayama, and A. Tomokiyo: Phys. Rev. B **37** (1988) 886.
5. T. Ikari and A. Fukuyama: in *Progress in Photothermal and Photoacoustic Science and Technology Vol. IV*, ed. A. Mandelis and P. Hess (SPIE, Washington, 2000), Chap. 5, p. 145.

1J2a-3

Proceedings of Symposium on Ultrasonic Electronics, Vol. 29 (2008) pp. 19-20
11-13 November, 2008

# 半導体ナノピラーにおける振動モードのピコ秒音響法による観測

## Vibrational modes of semiconductor nanopillars studied by picosecond ultrasonics

佐久間洋宇[1‡], 友田基信[1], 松田理[1], 福井孝志[2], 富岡克広[2], Oliver B. Wright[1]
([1]北大院工 ; [2]北大院情科研及び量集センター )

Hirotaka Sakuma[1‡], Motonobu Tomoda[1], Osamu Matsuda[1], Takashi Fukui[2], Katsuhiro Tomioka[2] and Oliver B. Wright[1] ([1]Grad. Sch. Eng., Hokkaido Univ.; [2]Grad. Sch. Info. and RCIQE, Hokkaido Univ.)

We investigate the vibrational modes of GaAs nanopillars of hexagonal cross section on a GaAs substrate using an ultrafast optical technique. The motions of the pillars after excitation with visible light pulses are detected using a time-delayed infrared light pulses. Thickness modes of the pillars are detected in the 10-30 GHz range.

## 1. はじめに

近年、ナノマテリアルすなわちナノサイズの物質あるいは構造物に対する振動の研究がなされている。例えば、超短パルスレーザーによるピコ秒音響法を用いて非破壊的に、ナノキューブ[1,2]、ナノディスク[3]、ナノロッド[4]の構造の情報がその GHz 振動から解明されている。

本研究では、新しい形のナノ構造、六角形の GaAs ナノピラーに注目する。ピコ秒音響法を用いてこのナノピラーのピコ秒時間領域の反射率測定を行い、固有振動数を得た。今回の実験で用いたナノピラーの振動数は 10 ~ 30 GHz 程度である。

ナノマテリアルの~10 GHz オーダーにおける振動の測定方法としては、ピコ秒音響法が最も適切である。他にも固有振動数を観測する方法としてはピエゾ素子を用いた振動数領域での測定方法[5]、ラマン散乱分光法[6]などが考えられるが、~10 GHz の固有振動数に対して、前者は観測可能振動数領域が低すぎ、後者はラマンシフト量が小さすぎ困難である。

## 2. 試料

本研究では、試料として GaAs(111)B 面基板に有機金属気相選択成長法により作製した六角形の GaAs ナノピラーを用いた。有機金属気相選択成長法とは半導体ウェハ上に堆積した誘電体マスクに予めパターニングを施し、マスク開口部にのみ所望のナノ構造を自在に形成させる半導体結晶成長法である[7]。この試料の特徴としては、ナノピラーは直径 100 ~ 200 nm、高さ 300 ~ 800 nm、ナノピラーの間隔 200 ~ 1000 nm で、空間的周期性を持って配置されている (**Fig. 1**)。

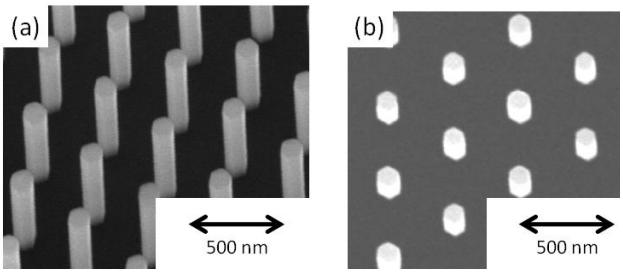


Fig.1 (a), (b) Typical scanning electron microscope images of GaAs nanopillars taken from different angles.

## 3. 実験

測定は、光源にモードロック Ti-サファイアレーザーを用いたピコ秒音響法によって行った[1-4]。ピコ秒音響法とは、ポンプ・プローブ法の一種であり、光パルスを２つに分け、1 つの光パルス（ポンプ光）を用いて試料に GHz-THz の振動を起こし、その振動によって試料に起こった過渡的光反射率変化をもう１つの光パルス(プローブ光)を用いて測定する方法である。実験に用いた光学系を **Fig. 2** に示す。ポンプ光、プローブ光の中心波長はそれぞれ 415 nm、830 nm で光パルス幅は 150 fs、繰り返し周波数は 80 MHz（12.5 ns 周期）である。ポンプ光パルスを対物レンズで直径数 μm に集光し、試料に垂直入射する。このとき熱弾性的または変形ポテンシャルによりナノピラー群に振動が励起される。測定されるプローブ

loghiro@eng.hokudai.ac.jp

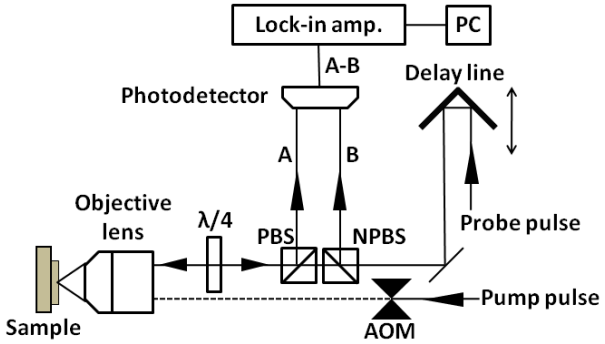


Fig. 2 Experimental setup for generation and detection of nanopillar vibrations. AOM: acousto-optic modulator, PBS: polarizing beam splitter, NPBS: non-polarizing beam splitter, PC: personal computer, λ/4: quarter-wave plate.

光の反射率変化は微小なので、ポンプ光パルス列を、音響光学素子(AOM)を用いて 1 MHz に変調し、ロックイン増幅器を用いてプローブ光の検出信号の中から、この変調周波数成分のみを検出する。この方法によりピコ秒の時間領域で試料の $10^{-6}$程度の微小な反射率変化が得られる。

## 4. 結果と考察

様々なサイズのナノピラーに対してデータを取得した。一例として、直径 180 nm、高さ 290 nm のナノピラーの過渡的な光反射率変化を **Fig. 3** に挙げた。0 ps においてポンプ光が当たり、キャリア励起によるプローブ光の急激な反射率変化が起こっている。その後、0 ～ 400 ps 程度の時間範囲においてナノピラーの振動による反射率変化が観測されている。

そのデータに対して、フーリエ変換を行うことにより **Fig. 4** に示すような周波数スペクトルを得た。20 GHz 付近に表れている反射率変化の最も大きなピークについて取得したデータを検証したところ、このピークがとる振動数がナノピラーの直径に反比例しているという特性を得た。これは六角柱断面における動径方向に振動する単ナノピラーモードであることを示唆している。このナノピラー振動の減衰時間は~100 ps である。また 50 GHz 付近にあるピークは基板内を伝播する縦波音響波からのブリルアン散乱によるものである[8]。

## 5. まとめ

私たちは有機金属気相選択成長法を用いて作られた六角形断面の GaAs ナノピラーの振動モードを励起・検出する実験を行った。ナノピラーの断面において動径方向に伸縮するモードが立つことを確認した。

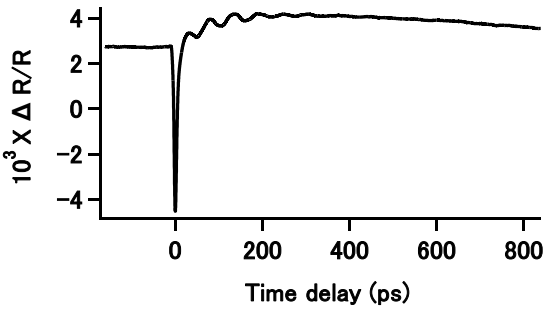


Fig. 3 Relative reflectivity change versus the time delay between the pump and the probe pulses. The nanopillar has a height of 290 nm and a width of 180 nm.

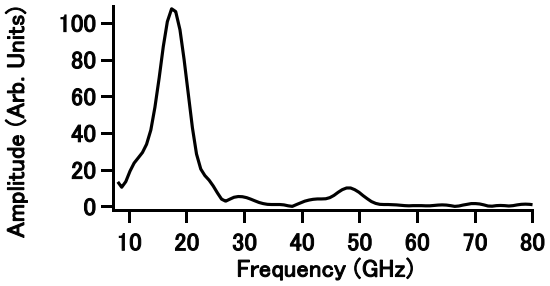


Fig. 4 Vibrational amplitude spectrum obtained from the modulus of the Fourier transform of the data in Fig. 3.

今後は今回観測した以外の振動モードを観測する方法、減衰機構の解明、ナノピラーの周期性による連成的な振動の探求を行っていく予定である。

## 引用文献

1. H. Petrova *et al.*: J. Chem. Phys. **126** (2007) 094709.
2. J. F. Robillard *et al.*: Phys. Rev. B **76** (2007) 092301.
3. C. Giannetti *et al.*: Phys. Rev. B **76** (2007) 125301.
4. G. M. Sando *et al.*: J. Chem. Phys. **127** (2007) 074705
5. J. Fujita *et al.*: J. Vac. Sci. Technol. B **19** (2001) 2834.
6. H. Portales *et al.*: Phys. Rev. B **65** (2002) 165422.
7. J. Motohisa *et al.*: Physica E **23** (2004) 298.
8. C. Thomsen *et al.*: Opt. Commun. **60** (1986) 55.

1J2a-4

Proceedings of Symposium on Ultrasonic Electronics, Vol. 29 (2008) pp. 21-22
11-13 November, 2008

# Surface Excitation of Shear Horizontal Waves
# 水平すべり波（ＳＨ）波の表面励振

Morio Onoe (Professor Emeritus, University of Tokyo)
尾上守夫 （東京大学名誉教授）

## 1. Introduction

Shear horizontal (SH) waves guided in a plate and torsional waves guided in a rod or pipe have been widely used in electronic devices for frequency control and selection and in ultrasonic non-destructive testing (NDT). The lowest (fundamental) mode of propagation of both types of waves is non-dispersive, namely its phase and group velocity are independent of frequency, and hence it can propagate for a long distance without distortion of waveform. This is a desirable feature for NDT of such elongated objects as beams and pipes.

In previous papers, a new ultrasonic guided wave testing were presented. [1 - 3)] A trapped energy mode of vibration of a portion under inspection is excited by mode conversion from a propagating mode. The resonant freqency and Q are sensitive to such changes in the portion as thickness, surface corrosion, etc. It can be remotely measured by reflection of a propagating mode at the boudary of the portion. Although a higher mode of propagatin may be used, the use of the foundamental mode has a tangible advantage mentioned above in order to avoid complexity of intepretation of test results due to waveform distortion and multiple propagation of plural modes of propagation.

In such an electronic device as ultrasonic delay line, a transducer is mounted on a side edge of a plate. A particular mode can be selectively excited by a design of configuratin of a transducer. A transducer fully covered the edge can excite only the fundamental mode. [4)] In NDT, however, it is often required to mount transducers on the sureface of a plate or a pipe. Transducers on the surface usually excites plural modes but not selectively a single mode.

Hence it is important to study a configuration of transducers, which effectively excites a desired mode, specifically the fundamental mode.

This paper presents an analysis of excitation of SH waves by transducers mounted on the surface of a plate. A multiple transmission line model previously used in an analysis of remote excitation of trapped energy mode is also useful in the present study.

---

e-mail: m.onoe@ieee.org

As previously reported, dispersion curves of torsional waves in a rod or a pipe, axially symmetric waves in a plate and circumferential SH waves in a pipe are similar to those of SH waves in a plate. Hence the present analysis yield a good approximation for all these waves, when the thickness is small.

## 2. Multiple transmission line model

SH waves in a plate consists of plural modes. Their dispersion curves are shown in **Fig. 1.** The vertical axis is for normalized frequency, the horizontal axis is for normalized wave number and m is the order of mode. The fundamental (m=0) mode is non-dispersive, whereas higher modes are dispersive. A higher mode has a cutoff frequency, which corresponds to an overtone resonance of thickness shear mode in an infinite plate. At a frequency higher than a cutoff frequency, the wave number becomes real as shown in the right half plane of Fig. 1 and hence waves can freely propagate. At a frequency lower than a cutoff frequency, the wave number becomes pure imaginary (evanescent) as shown in the left half plane and hence waves cannot propagate. A tangent to a dispersion curve in the right half plane yields group velocity, which is close to zero at near a cutoff frequency with severe dispersion.

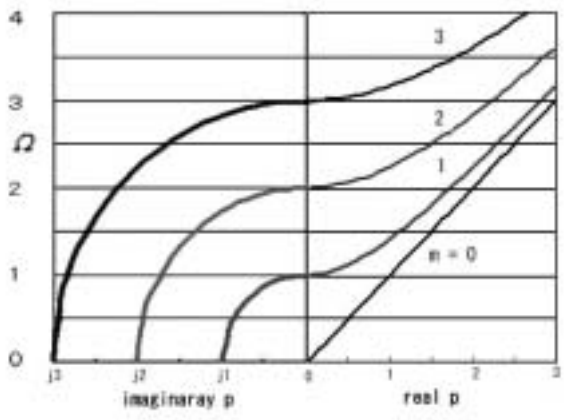


Fig. 1 Dispersion curves of SH waves in a plate

Propagation characteristics of each mode can be represented by a transmission line, based on the force-voltage and particle velocity-current analogue as shown in **Fig. 2.** Frequency response of each line is also included. Distribution of displacement across the thickness of each mode constitutes a Fourier cos series, which can expand any distribution. across a cross section. [4)] Specifically impulse excitation at surface is expanded into impulses of equal amplitude (like white noise) as input for each line.

Impulse response of each line can be obtained from frequency characteristics. For any input waveform, an output waveform of each line after a certain propagation distance can be obtained as a convolution of input waveform and impulse response of each line. (Alternatively a product in frequency domain. ) A summation of all the output as a cosine series yields a whole distribution at the cross section.

If all the frequency components of an input waveform are below the first cutoff frequency, only the fundamental (m=0) mode remains and all the higher modes decay out in the far distance. In order to excite a trapped energy mode, however, an input waveform should contain some frequency components above the first cutoff frequency. These components propagate in the first (m=1) mode as well as the fundamental (m=0) mode. But these components near the cutoff frequency in the first mode have very small group velocity and also encounter severe dispersion and hence spread out in a wide time span. Hence only the fundamental mode remains after some distance of propagation.

**Fig. 3** shows output waveforms after propagation of normalized distance (x = distance/ plate thickness) of 2 and 10, respectively. The input waveform is a burst sine wave with envelope of raised cosine starting at the time step of 50. Its normalized frequency is 0.7 and bandwidth is 52 %. The output waveform of the fundamental mode is the same as the input waveform. Output waveform of the first mode at x = 10 shows more spread than waveform at x = 2 as expected. Hence, practically speaking, it is possible to generate only the fundamental mode by surface excitation. Characteristics of a transducer with any configuration can be calculated from impulse response. Design techniques of interdigital transducer for SAW devices can be utilized to realize more efficient or unidirectional excitation.

**References**


1. M. Onoe: IEICE Technical Report, US2006-78, (2006). (in Japanese).
2. M. Onoe: Proc. FCS, (2007) pp.488-493.
3. M. Onoe, K. Oka, T. Suzuki: Proc. USE, (2008) pp.75-80. (in Japanese)
4. M. Onoe: J. Acoust. Soc. Am., 35 (1963) pp. 1003-1008.


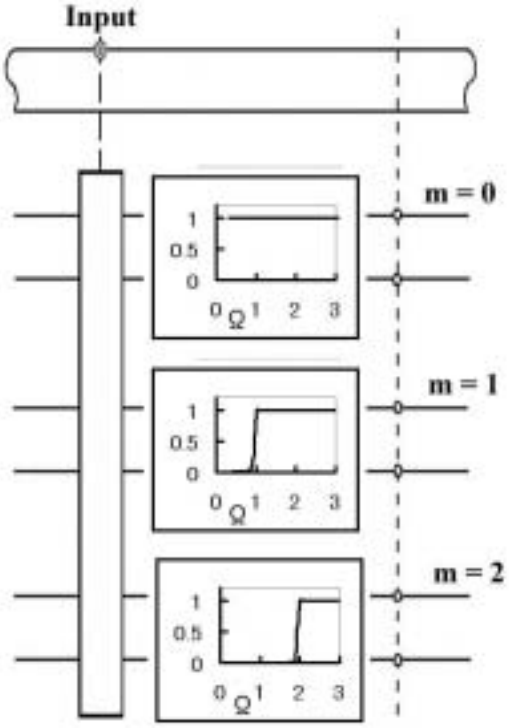


Fig. 2 Multiple transmission line model

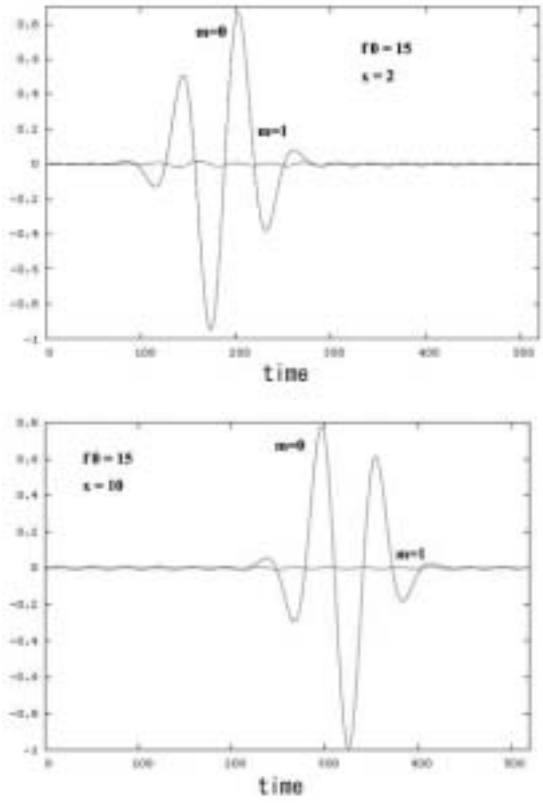


Fig. 3 Output waveforms for x = 2 and 10.

Proceedings of Symposium on Ultrasonic Electronics, Vol. 29 (2008) pp. 23-24
11-13 November, 2008

# Vibrational Modes in Rectangular Cross-Section Nanowire Superlattices
# 矩形断面を持つナノワイヤー超格子に生じる振動モード

Seiji Mizuno† and Yushi Nakamura (Dept. Appl. Phys., Hokkaido Univ.)
水野誠司，中村祐史（北大院工）

## 1. Introduction

Recently, advances in fabrication methods enable realization of one-dimensional compositionally modulated nanowires. For example, GaAs/GaP, Si/SiGe, InAs/InP, and ZnSe/CdSe nanowire superlattices (NWSLs) were synthesized, and their electronic, optical, and transport properties were studied [1-4]. It has been shown that the NWSLs offer unique features, which are radically different from plain nanowires and quantum wells in their electronic, optical, and transport properties [5]. The NWSLs lead to a variety of possible applications [6, 7]. Moreover, it is expected that the NWSLs yield interesting physical effects on phonon properties.

In previous papers [8, 9], we studied the torsional modes generated in isotropic NWSLs. In the present work, we theoretically study all the acoustic phonon modes in NWSLs composed of "anisotropic" materials. Based on the group theory, the acoustic phonon modes are classified and discussed.

## 2. Symmetry and vibrational modes

Here, we consider acoustic phonon modes in a rectangular cross-section NWSL consisting of cubic materials [**Fig. 1**].

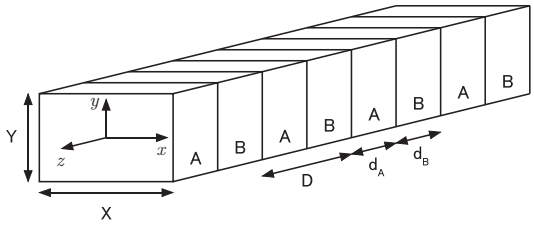


**Fig. 1.** Rectangular cross-section nanowire superlattice.

The point group of the rectangular cross-section is $C_{2v}$, whose irreducible representations are $A_1$, $A_2$, $B_1$, and $B_2$. Using their projection operators, we can construct symmetry-adopted basis functions belonging to the irreducible representations of this group. The symmetries of these basis functions are schematically illustrated in **Fig. 2**, in which only the phonon displacements at the corners of the rectangular section are shown. These modes are named as follows: $A_1$ mode is the dilatational mode, $A_2$ mode is the torsional or shear mode, and $B_1$ and $B_2$ modes are the flexural modes.

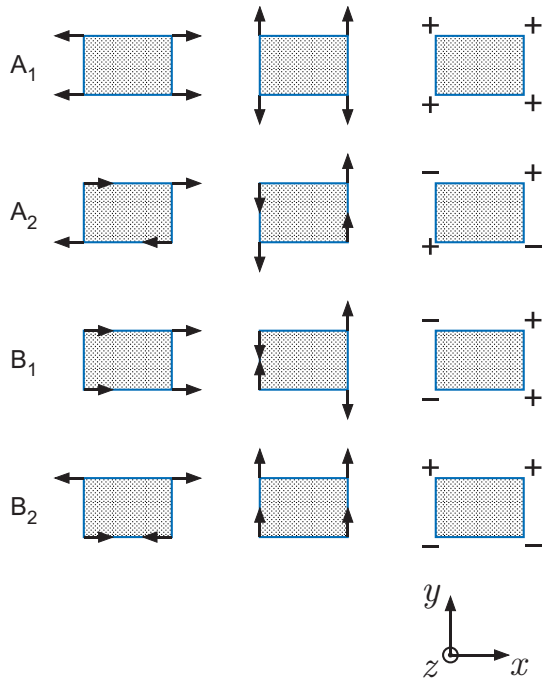


**Fig. 2.** Symmetry-adopted basis functions belonging to the irreducible representations of $C_{2v}$. Arrows and ± show the phonon displacements at the corners.

## 3. Mathematical method

We calculate numerically all the acoustic phonon modes generated in the free-standing NWSL with the use of the XYZ algorithm [10]. This method was developed in resonant ultrasound spectroscopy for deriving the free vibrational modes of inhomogeneous objects and later applied to homogeneous plain wires [11]. We modify this method and apply to the present problems.

By solving the elastic wave equation with the symmetry-adopted basis functions, the dispersion relations and phonon displacements are obtained for each phonon mode.

†e-mail address: mizuno@eng.hokudai.ac.jp

## 4. Numerical examples

As a numerical example, we consider a NWSL consisting of the alternate stacking of GaAs and AlAs, i.e. A = GaAs and B = AlAs. The size of this NWSL is as follows: X = 5 nm, Y = 10 nm, and $d_A = d_B = D/2 = 50$ nm (see Fig. 1).

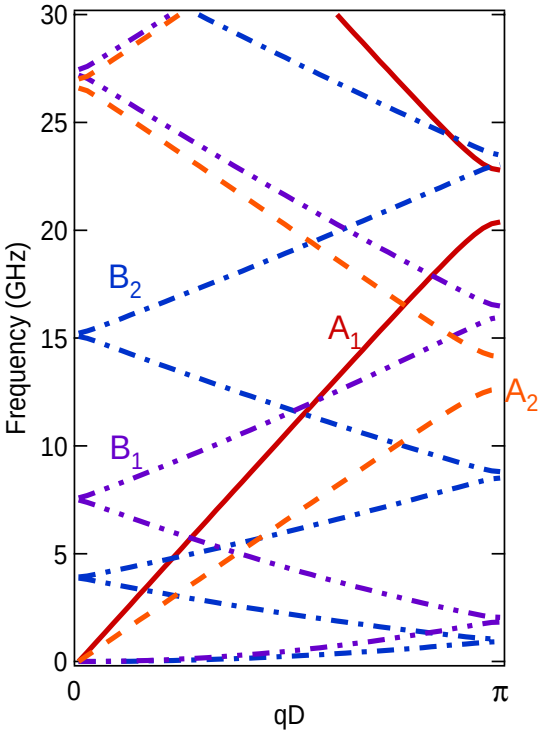


**Fig. 3.** Phonon dispersion relations of the rectangular cross-section nanowire superlattice consisting of GaAs and AlAs.

The calculated dispersion relations are shown in **Fig. 3**. Here, *q* is the Bloch wave number in the z direction. The numbers of basis functions used in the present calculation is empirically selected to be 336 for each mode. These dispersion relations become complicated structure due to the effects of both the confinement of phonons in the lateral direction and superlattice modulation in the longitudinal direction. However, the overall structure of each phonon dispersion relation can be approximately understood by the folding of the dispersion curves for a homogeneous cylinder into the mini-Brillouin zone (BZ) determined by the periodicity D of the NWSL.

Subband structure exists originally in the dispersion relation of the homogeneous plain nanowire. This is due to the fact that the wave vectors in the lateral direction are discretized because of the lateral confinement. Each dispersion curve in this subband structure is folded into the mini-BZ. In the folded dispersion relation, phononic band gaps are generated at the center and edges of the mini-BZ. In the present example, the frequency gaps of $B_1$ and $B_2$ modes (flexural modes) are small compared with the other modes.

## 5. Summary

In the present work, we theoretically studied the acoustic phonon modes in a NWSL composed of cubic materials. Based on the group theory, the acoustic phonon modes were classified. We found there exist four independent phonon modes in the rectangular cross-section GaAs/AlAs NWSLs. Using the XYZ algorithm, we calculated dispersion relations for each mode. The overall structure of the phonon dispersion relations can be understood by the folding of the dispersion curves in the subband structure of a homogeneous plain wire. Phononic band gaps are generated at the center and edges of the mini-BZ.

Here, we note that dispersion relations depend on the shape of the cross-section of a NWSL. The results for square and circular cross-section NWSLs will be given elsewhere. Furthermore, it would be interesting to consider a phononic crystal consisting of two-dimensional arrays of NWSLs.


## Acknowledgment

The authors had useful discussion with N. Nishiguchi.


## References


1. M. S. Gudikson L. J. Lauhon, J. Wang, D. C. Smith, and C. M. Lieber, Nature (London) **415**, 617 (2002).
2. Y. Wu, R. Fan, and P. Yang, Nano Lett. **2**, 83 (2002).
3. M. T. Bjork, B. J. Ohlosson, T. Sass, A. I. Persson, C. Thelander, M. H. Magnusson, K. Deppert, L. R. Wallenberg, L. Samuelson, Nano Lett. **2**, 87 (2002).
4. R. Solanki, J. Huo, and J. L. Freeouf and B. Miner, Appl. Phys. Lett. **81**, 3864 (2002).
5. L. C. Lew Yan Voon and M.Willatzen, J. Appl. Phys. **93**, 9997 (2003).
6. M. T. Bjork, B. J. Ohlosson, C. Thelander, A. I. Persson, K. Deppert, L. R. Wallenberg, L. Samuelson, Appl. Phys. Lett. **81**, 4458 (2002).
7. C. Thelander, T. Martensson, M. T. Bjork, B. J. Ohlosson, M. W. Larsson, L. R. Wallenberg, L. Samuelson, Appl. Phys. Lett. **81**, 4458 (2002).
8. S. Mizuno, Phys. Rev. B **71**, 085303 (2005).
9. S. Mizuno, Jpn. J. Appl. Phys. **47**, 3817 (2007).
10. W. M. Visscher, A. Migliori, T. M. Bell, and R. A. Reinert, J. Acoust. Soc. Am. **90**, 2154 (1991).
11. N. Nishiguchi, Phys. Rev. B **50**, 10970 (1994).

Proceedings of Symposium on Ultrasonic Electronics, Vol. 29 (2008) pp. 25-26
11-13 November, 2008

# Electrical Properties of Textured $(Bi_{1/2}K_{1/2})TiO_3$-$BaTiO_3$ Ceramics

粒子配向型$(Bi_{1/2}K_{1/2})TiO_3$-$BaTiO_3$ セラミックスの電気的諸特性

Masahiro Nemoto†, Yuji Hiruma, Hajime Nagata and Tadashi Takenaka
(Faculty of Science & Technology, Tokyo University of Science)
根本正博†，晝間裕二，永田肇，竹中正 （東理大 理工）

## 1. Introduction

A $(1-x)(Bi_{1/2}K_{1/2})TiO_3$-$xBaTiO_3$ [abbreviated to BKT-BT100$x$] solid solution attracts attention as a candidate material for lead-free piezoelectric actuator applications. In particularly, the BKT-BT ($x$<0.4) seems to be a considerably promising candidate material for lead-free piezoelectrics with a wide working temperature range because the depolarization temperatures, $T_d$, for BKT-BT100$x$ ($x$=0-0.4) are higher than 300°C. Although the Curie temperature, $T_c$, decreased with increasing the amount of BT in BKT-BT, the larger anisotropy c/a (~1.025) has been obtained at BT content ($x$) less than 30 mol%.[1] Moreover, BKT-BT10 has a relatively high piezoelectric constant ($d_{33}$=73.4 pC/N), however, it is not sufficient for use in practical actuators. For the enhancement of its piezoelectric properties, the grain oriented BKT-BT100$x$ ceramics are prepared by a reactive templated grain growth (RTGG) method.[2-5]

Grain orientation processe are superior method for enhancing piezoelectric properties; particularly, the RTGG is very effective for perovskite-structured ferroelectrics.[2-5] RTGG enables us to prepare textured solid solutions, which is difficulty in making single crystals. Grain orientation process was developed by the growth of template grains at the expense of matrix grains during sintering. In other words, the growth of template grains is responsible for the texture development and the grain growth itself is also very important for obtaining highly textured samples.

In this study, we attempted to prepare grain-oriented 0.9BKT-0.1BT (BKT-BT10) ceramics by the RTGG method with long soaking time (2~200 h) and to investigate their electrical properties.

## 2. Experimental Procedure

Textured specimens were prepared by RTGG with matrix and template of platelike $Bi_4Ti_3O_{12}$ (BiT) particles for BKT-BT. Platelike BiT particles were prepared by a molten salt synthesis. $Bi_2O_3$ and $TiO_2$ were mixed with an equal weight of salt and heated at 1070~1100°C for 0.5 h. Platelike BiT particles with an average diameter of about 10-20 μm and a thickness of about ~0.4 μm were obtained. The starting materials for matrix particles were $BaTiO_3$, $Bi_2O_3$, $TiO_2$, and $K_2CO_3$ with purities of 3-4 N. Calcined BKT-BT10 powders were prepared by a solid-state reaction. Raw powders were mixed by ball milling for 10 h with ethanol. Resulting powders were calcined at 950-1000°C followed by ball milling for 20 h.

The reactive template consists of platelike BiT particles (the template content ≈35 wt %), and the complementary compounds (matrix particles) are $BaTiO_3$, $Bi_2O_3$, $TiO_2$, $K_2CO_3$, and calcined BKT-BT10 powder. The slurries for tape casting were prepared by mixing the starting mixtures, solvent, binder, and plasticizer. The sheets were cut, laminated, and pressed to form green compacts. The green compacts were heated to remove organic ingredients and sintered at 1080°C for 2-200 h. Moreover, nontextured BKT-BT10 ceramic was also prepared by a conventional ceramic fabrication technique for comparisons with textured ceramics. These ceramics were cut and polished for physical measurements. The crystal phase of these ceramics was determined using an X-ray diffractometer (XRD; Rigaku RINT-2000). The orientation factor, $F$, was determined from the XRD pattern by the Lotgering method. Microstructures were observed by a scanning electron microscopy (SEM: Hitachi S-2400). Electric-field-induced strains were measured by unipolar driving at 0.1 Hz using a contact-type displacement sensor (Millitron Model 1240).

## 3. Results and Discussion

X-ray analyses were carried out on the top surface of the specimen in grain-oriented samples. All samples showed a single-phase perovskite structure with a tetragonal symmetry at room temperature. The density in the textured specimen increased with increasing the sintering time. The density ratio to the theoretical density was ~97% for textured specimens sintered at 1080°C-200 h.

**Figure 1** shows the degree of orientation, $F$, for textured BKT-BT10 sintered at 1080°C as a

E-mail : tadashi@ee.noda.tus.ac.jp

function of sintering time. The $F$ increased with increasing the sintering time and almost saturated at the sintering time for 100 h. The specimen sintered for 200 h indicated higher $F$ than 60%.

The $F$ value was closely related to the microstructure. The grain sizes were increased with increasing sintering temperatures and longer soaking times. It is very important to perform long sintering in order to promote the grain growth and improve the orientation factor. The matrix grains remained in textured BKT-BT10 sintered at 1080°C-10 h. The presence of matrix grains reduced the $F$.[4] At 1080°C-40 h, however, almost all matrix grains disappeared, and the microstructure was composed of only template grains at 1080°C-100 h. The largest $F$ obtained by 100~200 h sintering is caused by the disappearance of matrix grains.

**Figure 2** shows field-induced strains, $S$, for textured and nontextured BKT-BT10 in the direction parallel (//) to the tape stacking direction at $E$=0~80 kV/cm. It can be seen that the strain of the textured specimen was higher than that of the nontextured (random) specimen. The field-induced strains of BKT-BT10 ceramic were improved by the grain orientation.

**Figure 3** shows the normalized strain $d_{33}^*$ ($=S_{max}/E_{max}$) of textured and nontextured BKT-BT10 ceramics as a function of the degree of orientation, $F$. The $d_{33}^*$ increased with increasing the $F$. The $d_{33}^*$ of the textured BKT-BT10 ceramic ($F$≈74%) in the direction parallel (//) to the tape stacking direction was 267 pm/V at 80 kV/cm.

## 4. Conclusions

BKT-BT10 ceramics were prepared by the ordinary solid state reaction and the RTGG method. The textured ceramics without matrix grains were obtained by increasing the sintering time to increase the grain growth. Field induced strains of BKT-BT10 ceramic were improved by grain orientation. The $d_{33}^*$ ($=S_{max}/E_{max}$) increased with increasing the degree of orientation, $F$, and reached 267 pm/V at $F$≈74%. The textured BKT-BT10 ceramic seems to be a superior candidate material for lead-free piezoelectric ceramics with large strain and wide working temperature range.


## Acknowledgments

The authors would like to thank Toho Titanium Co., Ltd., for providing high-purity titanium dioxide powders. This work was supported in part by Grants-in-Aid for Scientific Research (B) (No. 19360302) from the Japan Society for the Promotion of Science.


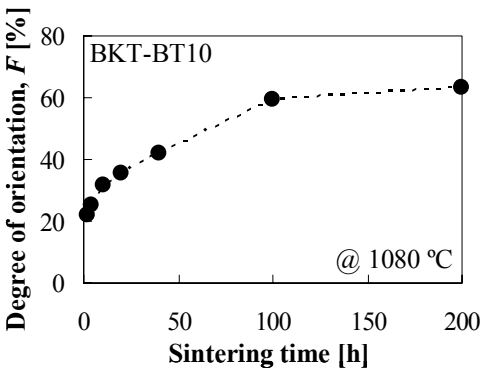


**Fig. 1** Degree of orientation, $F$, for textured BKT-BT10 sintered at 1080°C as a function of sintering time.

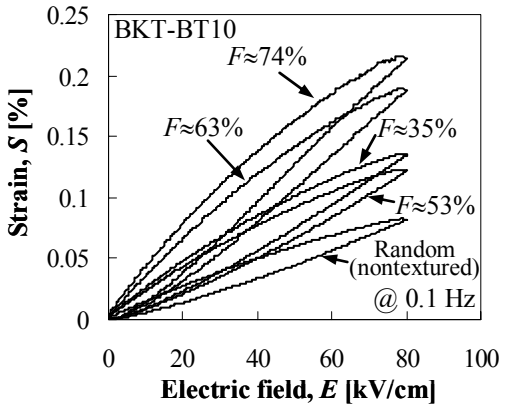


**Fig. 2** The strain behavior of BKT-BT10 ceramic under unipolar driving of electric field, $E$, from 0 to 80 kV/cm.

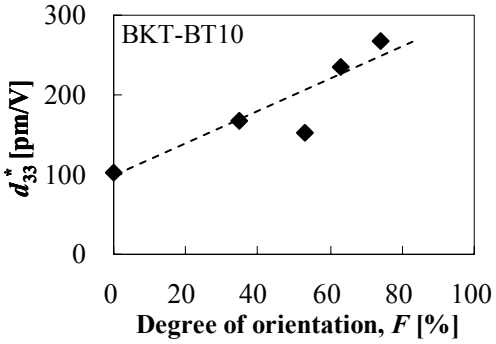


**Fig. 3** The normalized strains $d_{33}^*$ ($=S_{max}/E_{max}$) of textured and nontextured BKT-BT10 ceramics as a function of the degree of orientation, $F$.

## References


[1] Y. Hiruma, R. Aoyagi, H. Nagata, and T. Takenaka: Jpn. J. Appl. Phys. **43** (2004) 7556.
[2] T. Kimura: J. Ceram. Soc. Jpn. **114** (2006) 15.
[3] E. Fukuchi, T. Kimura, T. Tani, T. Takeuchi, and Y. Saito: J. Am. Ceram. Soc. **85** (2002) 1461.
[4] K. Fuse and T. Kimura: J. Am. Ceram. Soc. **89** (2006) 1957.
[5] T. Kimura, T. Takahashi, T. Tani, and Y. Saito: J. Am. Ceram. Soc. **87** (2004) 1424.

1P1-10

Proceedings of Symposium on Ultrasonic Electronics, Vol. 29 (2008) pp. 27-28
11-13 November, 2008

# Exact Analysis of Lamb Waves in Piezoelectric Membranes with Distinct Electrode Arrangements

Yung Yu Chen (Tatung University, Department of Mechanical Engineering)

## 1. Introduction

Piezoelectric membranes have been widely used in electro-acoustic and microfluidic devices [1-4]. When the membrane thickness is less than a wavelength, Lamb wave modes exist and propagate in the membrane; hence, these devices are so-called Lamb wave devices. In order to improve their performances, the phase velocity dispersion and electromechanical coupling coefficient (ECC) of the Lamb wave must be calculated exactly during designing.

Currently, two methods have been widely used to calculate the ECC. One is the acoustic velocity difference method, based on the velocity difference under free-surface and metalized-surface electical boundary conditions. Adler [5] adopted this method to analyze Lamb waves in piezoelectric membranes with distinct electrode arrangements. However, this is an approximation method. The other is the Green's function method. Joshi and Jin [6] adopted this method to calculate the ECC of Lamb waves in single piezoelectric plate; nevertheless, distinct electrode arrangements were not taken into account.

This paper aims at analylzing exactly Lamb waves in a single piezoelectric membrane with distinct electrode arrangements. First, a transfer matrix [5-8] is used to calculate the phase velocity dispersion. For exact analyses, the Green's function method is employed to calculate the ECC under distinct electrical boundry conditions. Finally, the calculated results are compared with that by using the acoustic velocity difference method..

## 2. The electromechanical coupling coefficient

### 2.1 The acoustic velocity difference method

The electromechanical coupling coefficient $K_S^2$ of a piezoelectric membrane is obtained approximately by [6-8]

$$K_S^2 = 2\frac{v_o - v_m}{v_o} \qquad (1)$$

where $v_m$ and $v_o$ are the Lamb wave velocity with metallized and free surface respectively.

### 2.2 The Green's function method

The electromechanical coupling coefficient $K_S^2$ of a piezoelectric medium is obtained exactly by [6-7]

$$K_S^2 = -2\Gamma_s \varepsilon_s^{(\infty)} \qquad (2)$$

where $\varepsilon_s^{(\infty)}$ is the effective permittivity at infinite slowness and $\Gamma_s$ is a coupling parameter.

## 3. Calculation results

ZnO thin films with *c* axis have been widely used to configure electro-acoustic devices due to their high ECCs. Therefore, a ZnO membrane is taken as the calculation example. Moreover, there are two electrode arrangements, shown in **Fig. 1**, in the calculation; the IDTs are deposited on top surface and the down surface can be either electrically free or metallized. The metallization means zero potential and no mechanical loading.

Shown in **Fig. 2** is the phase velocity dispersion of the first three Lamb wave modes with free surface, which was calculated by using the transfer matrix. This result shows that the first two modes are all-pass modes, but the A2 (second antisymmetrial) mode is a high pass mode. We note that except for the A1 (first antisymmetrical) mode, phase velocity is larger than that of surface wave.

**Fig. 3** and **Fig. 4** show the ECCs for the free surface case and metalized surface case calculated by using the Green's function method, respectively. Results show that the ECCs deeply depends on the electrode arrangement. Moreover, at most of the frequency-thickness products, the ECC of the Lamb wave is larger than that of surface wave. This is one of the reasons why the Lamb wave devices attract increasing attentions recently. It is worth noting that the ECC of the A2 mode for the free surface case increases with decreasing the frequency-thickness product and is much larger than that of other modes. However, the dispersions of not only phase velocity but ECC for this mode are obvious. This will increase the fabrication difficulty.

**Fig. 5** and **Fig. 6** show the ECCs for the free surface case and metalized surface case calculated by using the acoustic velocity difference method. Although most of the results is close to that calculated by using the Green's function method, the difference exists for the S1 (first symmetrical) mode with metalized surface. This reminds us to use carefully the calculated results of the acoustic velocity difference method during designing even though this method is simple.

---

yychen@ttu.edu.tw

## 4. Conclusions

This paper proposes a exact analysis of Lamb waves in the ZnO membrane with two types of electrode arrangements by the Green's function method. By comparing the calculated results of the two methods, we can see that the difference indeed exists, especially for the S1 mode. Moreover, the coupling coefficients deeply depends on the electrode arrangement. Results show that the S1 mode for the metalized surface case is a better choice for a Lamb wave device due to its larger velocity, higher coupling coefficient and less dispersion.


### Acknowledgment

The author thanks the financial support of this research from the National Science Council of ROC through the grant NSC 97-2221-E-036-020-MY3.


### References


1. R.M. White, P.J. Wicher, S.W. Wenzel, and E.T. Zellers : IEEE Trans. Ultrason. Ferroelectr. Fre. Control **34** (1987) 162.
2. N. Yamamoto, Y. Nakagawa, and S. Kakio : Jpn. J. Appl. Phys. **47** (2008) 4024.
3. Y. Nakagawa, M. Momose, and S. Kakio : Jpn. J. Appl. Phys. **46** (2007) 4665.
4. N.T. Nguyen and R.M. White : Sensor Actuat. A-Phys. **77** (1999) 229.
5. E.L. Adler : IEEE Trans. Ultrason. Ferroelectr. Fre. Control **36** (1989) 223.
6. L. Fan, S.Y. Zhang, K. Zheng, W. Lin and H.D. Gao : Ultrason. **44** (2006) e849.
7. T.T. Wu and Y.Y. Chen : IEEE Trans. Ultrason. Ferroelectr. Fre. Control **49** (2002) 142.
8. T.T. Wu and Y.Y. Chen : J. Mech. **19** (2003) 225.


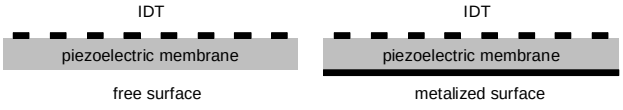


(a) (b)

Fig. 1 Two types of electrode arrangements.

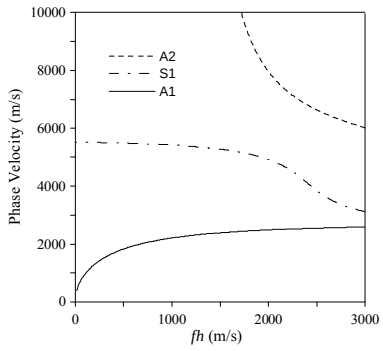


Fig. 2 Phase velocity dispersion of the first three Lamb modes with free surface.

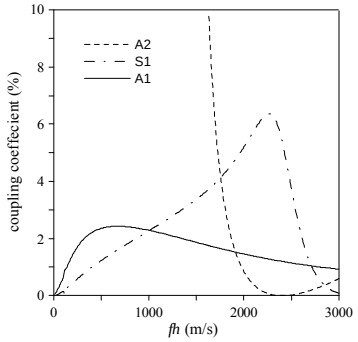


Fig. 3 Coupling coefficient for free surface calculated by the Green's function method.

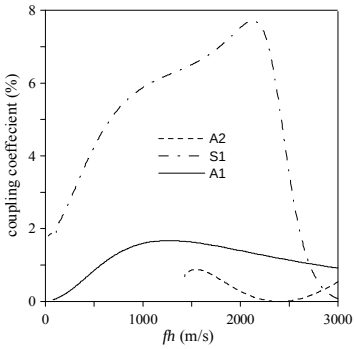


Fig.4 Coupling coefficient for metalized surface calculated by the Green's function method.

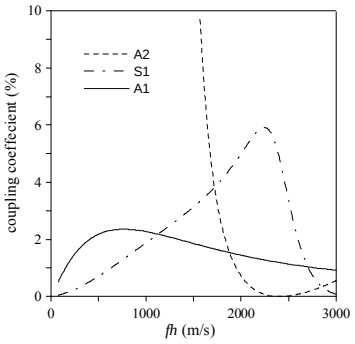


Fig.5 Coupling coefficient for free surface calculated by the acoustic velocity difference method.

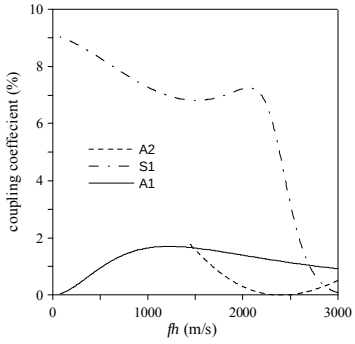


Fig.6 Coupling coefficient for metalized surface calculated by the acoustic velocity difference method.

1P1-11

Proceedings of Symposium on Ultrasonic Electronics, Vol. 29 (2008) pp. 29- 30
11-13 November, 2008

# Effect of atmospheric pressure plasma treatment on ultrasonic bumpless flip chip bonding

Jung-Lae Jo‡, Ja-Myeong Koo, Jong-Bum Lee, Seung-Boo Jung (Sungkyunkwan Univ. , School of Adv. Mat. Sci. & Eng.) and Jeong-Hoon Moon (Suwon Sci. College, Dept. of Mechanical Eng.)

## 1. Abstract

A transverse ultrasonic vibration was employed to bond the Cu flip chip bump with Cu finished glass substrate. This study was focused on the atmospheric pressure plasma treatment conditions on the ultrasonic bonding strength between the Cu bump and Cu finished substrate because the cleanness and roughness of the bonding surface strongly affected the joint integrity. The optimized ultrasonic conditions greatly enhanced the joint strength bonded using ultrasonic energy, while the excessive plasma treatment degraded the joint integrity. In this study, the mechanisms why the joint strength was determined by the treatment conditions were examined and discussed using X-ray photoelectron spectroscopy (XPS), Auger electron spectroscopy (AES).

## 2. Introduction

The miniaturized, multi-functional and portable electronics is realized by the development of flip chip bonding (FCB) technology using solder or adhesive.[1)] Solder bump connections show high electrical and mechanical properties, while the excessive growth of intermetallic compounds(IMCs) at the joint interface significantly degrades the performance and reliability of the solder joint during bonding and system operation.[2)] Furthermore, electronic devices can experience heat damage during bonding due to high bonding temperature of conventional lead-free solders.[3)] Adhesive bonding methods using anisotropic conductive adhesive (ACA) or non-conductive adhesive (NCA) furnish shorter bonding time, lower bonding temperature and finer pitch than the conventional solder bumps, but show poor electrical property and low mechanical reliability.[4)] Additionally, the thin chip die easily broke off during bonding, due to high bonding pressure. Recently, interest in ultrasonic bumpless flip chip bonding technology has been growing, due to its potential advantages such as fast bonding time, low bonding temperature, low bonding pressure, environment-friendly rocess, high electrical and mechanical performances and good reliability. However, the joint strength bonded using ultrasonic vibration is sensitive to roughness and cleanness of the joint surface. The atmospheric pressure plasma cleaning technique is one of the most effective methods to clean the bump surface, because of its simple structure, high productivity and easy configuration of in-line process.[5)] However, plasma cleaning with improper conditions can do more harm than good.[6)] Cu has been used as a good electrode material for ultrasonic bonding. The interest in bumpless flip chip bonding are growing in the portable multi-media electronics, because of its advantages such as great thermo-stability, thinner and lighter, lower resistance and power. However The Cu oxidizes easily. Therefore, the purpose of this study is to optimize the atmospheric pressure plasma treatment conditions, gas and treatment time, for ultrasonic bumpless flip chip bonding.

## 3. Experimental Procedure

Figure 1 shows the cross-sectional schematic structure of the upper flip chip and lower glass substrate. To fabricate the upper substrate, Si wafers were prepared by forming a 0.1 μm-thick $SiO_2$ layer on the bare Si wafer, after which 100 nm-thick Ti and 500 nm-thick Cu layers were subsequently sputtered. The lower substrate was fabricated with 50 nm-thick Cr and 500 nm-thick Cu layers on glass wafer. The $SiO_2$, Ti, and Cu layers acted as a passivation layer, adhesion layer between the $SiO_2$, and Cu and interconnection, respectively. After the photolithography process, 64 Cu bumps, of dimensions 22 (W) x 22 (D) x 11 (H) μm, were electroplated on the sputtered Cu surface. After another photolithography process, the Ti/Cu layers were selectively

etched for the patterning of the Kelvin structure. Four bonding pads were formed in a package, with sixteen bumps on a pad and a pitch size between bumps of 40 μm. After the lower substrate was fabricated by photolithography process, the glass wafer was sputtered with 100 nm-thick Cr and 500 nm-thick Cu, which acted as the adhesion layer between the wafer and Cu and the bonding pad, respectively. Finally, the upper and lower substrates were diced to dimensions of 3 x 3 $mm^2$ and 15 x 15 $mm^2$, respectively.

The samples were cleaned with different gases and times using atmospheric pressure plasma treatment equipment (SE Plasma Co., Korea). The samples underwent plasma treatment without wet etching. All tests and analyses were conducted within 1 hour after the treatment, because the plasma treatment effect is continually reduced over time. The contents and structures of the elements on the surface after the treatment with different gases and times were analyzed using Auger electron spectroscopy (AES: Model 660, Perkin-Elmer Physical Electronics Inc.). The contents of copper, carbon and oxygen were analyzed according to Ar sputtering time.

The spreading test of de-ionized (DI) water was conducted on the lower substrate after the treatment with different gases and treatment times. The distilled DI water was dropped on the Cu substrate, the lateral images were recorded by a spreading angle analyzer, and then the spreading angle was measured using an image tool program (UTHSCSA, U.S.A.).

The upper and lower substrates were directly bonded using an ultrasonic bonder (Fineplacer-Lambda, Germany) after the treatment with different gases and treatment times. After bonding, the samples were die-sheared using a bonding tester (PTR-1000, Rhesca Co., Japan), for which the 5 kgf load cell used in this study was calibrated with a 1 kgf standard weight. The fracture mode was analyzed with scanning electron microscopy (SEM) after the die shear test.

To investigate the effect of the plasma treatment on the Cu surface cleanliness, the elements on the surface underwent quantitative analysis using AES.

**3. Results and Discussion**

The joint strength was strongly dependent on the plasma treatment conditions: gases and treatment time. Too long treatment increased the $O_2$ concentration of the Cu surface, thereby decreasing bonding strength. This showed that the optimization of the cleaning conditions was important to improve the bonding strength between Cu bumps and Cu pad. More studies and results will be discussed in this presentation.

**Acknowledgment**

This work was supported by grant No.RTI04-03-04 from the Regional Technology Innovation Program of the Ministry of Commerce, Industry and Energy (MOCIE).

**References**

1. H. Maruo, Y. Seki and Y. Unami: Assembly 48 (2005) 72.
2. J.W. Yoon, H.S. Chun, J.M. Koo, H.J. Lee and S.B. Jung: Scripta Mater. **56** (2007) 661.
3. J.H. Lee, J.H. Kim and C.D. Yoo: J. Electron. Mater. **34** (2005) 96.
4. H. Maruo, Y. Seki and Y. Unami: *Proc. HDP'04 IEEE,* 2004, p. 307.
5. H.M. Ho, W. Lam, S. Stoukatch, P. Ratchev, C.J. Vath and E. Beyne: Microelectron. Reliab. 43 (2003) 913.
6. Ja-Myeong KOO, Jung-Lae JO, Jong-Bum LEE, Yu-Na KIM, Jong-Woong KIM, Bo-In NOH, Jeong-Hoon MOON, Dae-Up KIM, and Seung-Boo JUNG : Japanese Journal of applied Physics Vol. 47, No. 5, 2008, pp. 4309–4313.

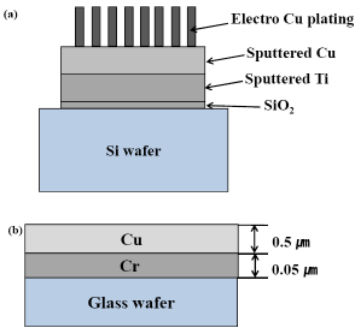


Fig. 1 Schematic diagrams of the upper (a) and lower (b) substrates used in this study.

1P1-12

Proceedings of Symposium on Ultrasonic Electronics, Vol. 29 (2008) pp. 31-32
11-13 November, 2008

# Effect of bonding parameters on ultrasonic bonding of flexible printed board (FPCB) on glass substrate

Jong-Bum Lee, Jong-Gun Lee, Jung-Lae Jo, Ja-Myeong Koo and Seung-Boo Jung†
(Sungkyunkwan Univ., School of Adv. Mat. Sci. & Eng.)

## 1. Abstract

The purpose of this paper is to find bonding parameters of electrodes between the glass and flexible printed circuit board (FPCB) using ultrasonic vibration. The electrodes of FPCB and were electroless-plated with Sn and the glass substrate was sputtered with Cu.

The peel strengths of the joints were investigated with various parameters, such as bonding pressure and time. This study showed that the electrodes between the glass and FPCB were successfully bonded without any adhesive at a low temperature during a short time, compared to other bonding methods: adhesive bonding and thermo-compression bonding.

## 2. Introduction

As the application of the FPCB on glass (FOG) with anisotropic conductive film (ACF) and non-conductive film (NCF) to the liquid crystal displays (LCDs), there are some reliability issues in the industry such as warpage of glass packages, interfacial delamination and increasing contact resistance. Also high cost and low feasibility to fine pitch application issues still exist[1)]. Ultrasonic bonding process is one of the most suitable bonding methods, because of its high mechanical and electrical performance, high reliability, short processing time, low processing temperature and environment-friendly process.[2)] Unfortunately, however, the literature and reliability data about ultrasonic bonding of the electrodes between PCB and glass have rarely been reported. In this study, therefore, the microstructural evolution and mechanical property of the glass to FPCB joint bonded using ultrasonic vibration were investigated with increasing bonding pressure and time.

## 3. Experimental Procedure

In this study, the thickness of FPCB and glass was 18 μm and 1 mm, respectively. The Cu electrodes of FPCB were electroless-plated with Sn and the glass substrate was sputtered with Cu.

The FPCB was bonded with glass After wet cleaning with 10 vol.% $H_2SO_4$ solution. The glass substrate was fixed using a fixture to prevent mis-alignment during bonding. The electrodes were bonded with different bonding time and pressure using ultrasonic energy.

Upon completion of ultrasonic bonding, the samples were mounted in cold epoxy, ground using 100, 800, 1,200, 1,500 and 2,000-grid SiC papers through a row of electrodes and polished with 0.3 μm $Al_2O_3$ powder. The microstructure of the sample was observed using scanning electron microscopy (SEM) in back-scattered electron imaging mode (BEI). Elemental analysis was also carried out using energy dispersive X-ray spectroscopy (EDS).

In-situ temperature variation during ultrasonic bonding was measured to investigate the effect of bonding time. The in-situ NCF temperature measurement was set up with 500 um-thick k-type thermocouples and a thermometer with 500 ms sampling period.

To investigate the effect of bonding conditions on the bonding strength, the peel test was carried out at ambient temperature and humidity. The testing speed and angle were 100 μm/s and 90 °, respectively. The fracture surface was observed and analyzed using SEM and EDS.

## 4. Results and Discussion

Figure 1 shows the changes of the temperature at the interface between the electrodes during ultrasonic bonding. During ultrasonic bonding at room temperature, the temperature reached to 317.4 °C and 489.3 °C within 3 and 4 s, respectively. The electrodes of FPCB were fully bonded on the Cu metallization on glass substrate because of highly increased temperature during ultrasonic bonding.

Excessive ultrasonic energy (long bonding time and high pressure) caused the glass substrate going to pieces. This showed that the optimization of the ultrasonic bonding parameter was important to improve the bonding strength between them.

More studies and results will be discussed in this presentation.

† sbjung@skku.ac.kr (S. B. Jung)

**Acknowledgment**

This work was supported by grant No. RTI04-03-04 from the Regional Technology Innovation Program of the Ministry of Commerce, Industry and Energy (MOCIE).

**References**

1. J.H. Lee, J.H. Kim and C.D. Yoo: J. Electron. Mater. **34** (2005) 96.
2. K. Tanida, M. Umemoto, Y. Tomita, M. Tago, R. Kajiwara, Y. Akiyama and K. Takahashi: Jpn. J. Appl. Phys. **42** (2003) 2198.

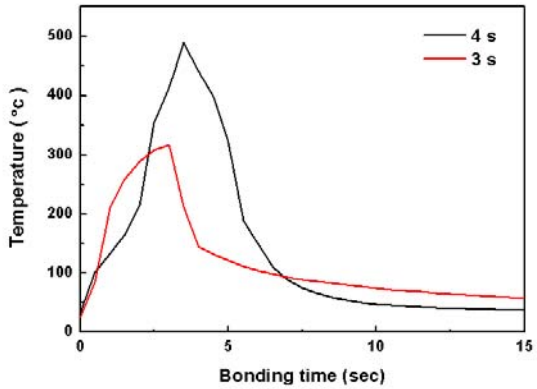


Fig. 1 Temperature rise during 3 and 4 s of ultrasonic bonding

1P1-13

Proceedings of Symposium on Ultrasonic Electronics, Vol. 29 (2008) pp. 33-34
11-13 November, 2008

# Rheology Measurement of Surfactant Solutions by Electro-Magnetically Spinning Viscometer

球回転式粘度計による界面活性剤水溶液のレオロジー測定

Maiko Hosoda[1†], Hideo Ogawa[1], Hiroyasu Nomura[1] and Keiji Sakai[2]
([1] School of Science and Engineering, Tokyo Denki Univ.; [2] Institute of Industrial Science, Univ. of Tokyo.)
細田真妃子[1‡]，小川英生[1]，野村浩康[1]，酒井啓司[2]（[1] 東京電機大 理工; [2] 東大生研）

## 1. Introduction

Ultrasonic spectroscopy is applied to the study of micro-structure and molecular dynamics of materials through the measurement of the visco-elastic characteristics in the frequency domain. The observation of the visco-elasticity at the lower frequency limit is important as it yields the fundamental reference of the frequency spectra observed by the ultrasonic spectroscopy.

In this presentation, we introduce a new experimental technique to give the fundamental visco-elasticity of soft condensed materials, which requires a quite small quantity of samples in a disposable manner. The newly developed viscometer is thus applicable especially to the medical field, such as the rheology measurement of the blood and other body fluids, where the pollution should seriously be prevented.

## 2. Electro-Magnetically Spinning viscometer

We describe here the brief account of newly developed Electro-Magnetically Spinning (EMS) viscometer. The viscometer has a couple of magnets attached on the rotator, which applies the rotating magnetic field. A sample cell is a commercially available small glass tube with smooth concave bottom, in which an aluminum sphere with 2 mm diameter is included and set at the center of the magnets.

The rotating magnetic field causes the induced current in the sphere, and then the Lorentz interaction between the magnetic field and the current applies torque to rotate the sphere. The principle is same as that of the Zimm type viscometer; however, a metal sphere is set at the bottom of the cell in our method. The idea enables the rheology observation with non-contact and disposable manner.

Here, let us consider that the magnetic field is rotating in the horizontal plane and is given in the form, $\mathbf{B} = (B_0 \cos\Omega t, B_0 \sin\Omega t, 0)$. An induced electric field, which satisfies $\mathrm{rot}\,\mathbf{E} = -\mathrm{d}\mathbf{B}/\mathrm{d}t$ drives the current in the metal sphere, that is $\mathbf{I} = \sigma\mathbf{E}$, where σ is the electric conductivity and $\mathbf{E} = \frac{\Omega B_0}{2}(-z\cos\omega t, -z\sin\omega t, x\cos\omega t + y\sin\omega t)$.

Lorentz force **F** then works on the sphere, which is

$$\mathbf{F} = \frac{\omega {B_0}^2 \sigma}{2}\begin{pmatrix} -(x\cos\omega t + y\sin\omega t)\sin\omega t \\ (x\cos\omega t + y\sin\omega t)\cos\omega t \\ 0 \end{pmatrix}$$

We can calculate the torque $T$ to rotate the sphere to $T = \pi^3 \sigma {B_0}^2 R^5 \Omega / 5$, where $R$ is the radius of the sphere.

The feature of the Zimm-type viscometer is that the rotator is floated on the surface of the sample fluid to prevent the rotational friction between the rotator and the bottom. The system has been effective to accurately investigate the rheology especially in the low viscosity region; however, some experimental difficulties still remain: The surface level of the sample must be adjusted severely to maintain the stable floating, and we have to take the effect of the surface visco-elasticity into account.

In our viscometer, instead, we employed a small metal sphere as the rotator and completely immersed it in the sample liquid. Let us consider the resistant torque applied to the rotating sphere: One is the viscous effect and the other is the rotational friction between the sphere and the bottom of the sample cell.

It is known that the resistant torque applied to the rotating sphere in the viscous liquid on the flat bottom is proportional to the sphere volume and the viscosity and given by $T_r = (4\pi/3)\beta R^3 \omega \eta$, where η is the viscosity, β is the coefficient in the order of unity. On the other hand, the torque due to the friction is given by $T_f = (8\pi/9)\alpha\mu\Delta\rho g R^4$. Here, μ is the friction coefficient, Δρ is the difference between the densities of the sphere and sample liquid, $g$ is the gravity acceleration, and we assume that the radius of the real touching area

between the sphere and the bottom is $\alpha R$ ($\alpha$<<1). Note here that $T_f$<$T_r$ holds at the small limit of $R$. Therefore, the effect of friction is overcome by the viscosity if we use a sphere with enough small radius as a rotator. Under the condition of $\eta$=1.0 mPa·s, $\Delta\rho$=2000 kg/m$^3$, $\alpha\approx$1/100, $\beta\approx$1, and $\mu\approx$0.1, the threshold angler velocity giving $T_f$=$T_r$, is calculated to $\Omega_c$=10 s$^{-1}$ for $R$=1 mm.

At the steady state, the torque applied to the sphere satisfies the equation of

$$T_f = (4\pi/3)\beta R^3 \eta\omega + (8\pi/9)\alpha\mu\Delta\rho g R^4 .$$

The torque $T$ is written by the first order function with respect to $\omega$, whose gradient and the $x$-axis intercept give the information on the viscous and frictional force applied to the sphere, respectively.

## 3. Experiment

The torque applied to the sphere is proportional to the difference in the angular velocities of the magnetic field $\Omega_B$ and that of the sphere $\Omega_S$, and the shear rate of the flow is linearly related to $\Omega_S$. We can, therefore, obtain the viscosity depending on the shear rate by measuring $\Omega_S$ changing $\Omega_B$.

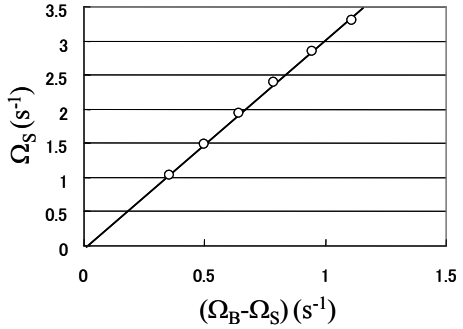


Fig.1 Relation between ($\Omega_B$-$\Omega_S$) giving the applied torque and $\Omega_S$ representing the shear rate.

Figure 1 shows the relation between ($\Omega_B$-$\Omega_S$) giving applied torque, and $\Omega_S$, obtained for the viscosity standard silicone oil with $\eta$=10 mPa·s. As seen, the data are well fitted by the straight line and the intercept on $x$-axis gives the friction force. The logarithmic plot obtained for variety of viscous samples is shown in Fig.2.

Figure 3 shows the relation between the gradient ($\Omega_B$-$\Omega_S$)/ $\Omega_S$, which is expected to be proportional to the viscosity, and the literature value of the viscosity for different standard samples. The linearity is well examined as seen, and we conclude that the system could be used as the viscometer with high accuracy and reproducibility.

The system is applied for the measurement of the viscosity of rod-like-micellar solutions at various concentrations and temperatures. Typical results are shown in Fig.4 and the detailed analysis would be given in the presentation.

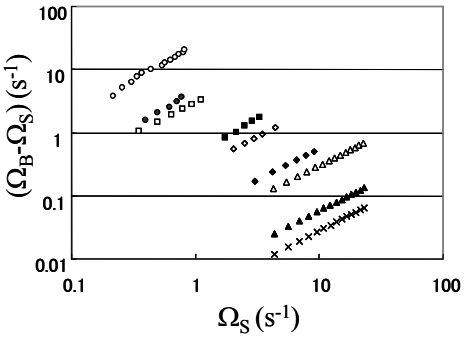


Fig.2 Relation between ($\Omega_B$-$\Omega_S$) and $\Omega_S$ obtained for various viscosities. The viscosities are 5, 10, 50, 100, 500, 1000, 5000 and 10000 cP, respectively, from top to bottom.

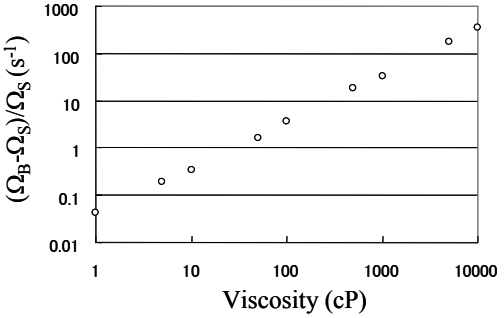


Fig.3 The ratio ($\Omega_B$-$\Omega_S$)/$\Omega_S$ obtained for various viscosities.

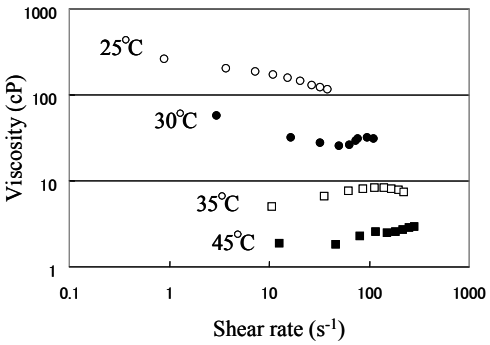


Fig.4 Shear rate dependence of viscosity obtained for aqueous solution of CTAB and Sal-Na.

## Conclusion

The most remarkable feature of the system is that EMS viscometer is completely free from the pollution and the advantage would be useful especially for the medical use. The system is already applied for the medical measurement of the viscosity of human blood, and the results would soon be reported.

Proceedings of Symposium on Ultrasonic Electronics, Vol. 29 (2008) pp. 35-36
11-13 November, 2008

# Phase Relations and Electrical Properties of the Lead-Free $(Bi_{1/2}Na_{1/2})TiO_3$-$(Bi_{1/2}K_{1/2})TiO_3$-$BaTiO_3$ Ternary Systems
# $(Bi_{1/2}Na_{1/2})TiO_3$-$(Bi_{1/2}K_{1/2})TiO_3$-$BaTiO_3$ 三成分系の相関系と電気的諸特性

Yuji Hiruma*, Hajime Nagata and Tadashi Takenaka
( Facult. Sci. Tech., Tokyo Univ. of Sci.)
晝間裕二, 永田肇, 竹中正（東京理科大学 理工）

## 1. Introduction

Piezoelectrics play an important role in electronic devices such as actuators, resonators and sensors. Most of piezoelectric materials were composed of $PbZrO_3$-$PbTiO_3$ (PZT)-based three component system. However, lead-free piezoelectric materials were recently required because of the environmental protection. Therefore, lead-free piezoelectric materials with perovskite structure have been actively studied.

$(Bi_{1/2}Na_{1/2})TiO_3$ (BNT), $(Bi_{1/2}K_{1/2})TiO_3$ (BKT) and $BaTiO_3$ (BT) are well known lead-free ferroelectric materials with relatively high piezoelectric activities in the lead-free piezoelectric materials. Therefore, the BNT-BKT-BT based ternary system has attracted much attention for a candidates of lead-free piezoelectric materials with large piezoelectric properties. The Curie temperatures, $T_C$, of BT, BKT and BNT are 135, 400, and 540ºC, respectively.[1] However, the depolarization temperatures $T_d$ of BKT and BNT are approximately 310 and 185ºC, respectively. In addition, BNT has the rhombohedral-tetragonal phase transition, $T_{R\text{-}T}$, and the temperature of the maximum dielectric constant, $T_m$, at approximately 300 and 340ºC, respectively[1]. There are some studies on the electrical properties for BNT-BT, BNT-BKT, and BT-BKT systems. However, the piezoelectric working temperatures have not been clarified yet. To use for piezoelectric devices, it is very important to clarified the phase transition temperatures.

Thus, in this presentation, we revealed the phase relations and piezoelectric properties of the BNT-BKT-BT ternary system. In particular, depolarization temperatures have been measured from temperature dependence of piezoelectric properties.

e-mail : hirumay@takenaka.ee.noda.tus.ac.jp

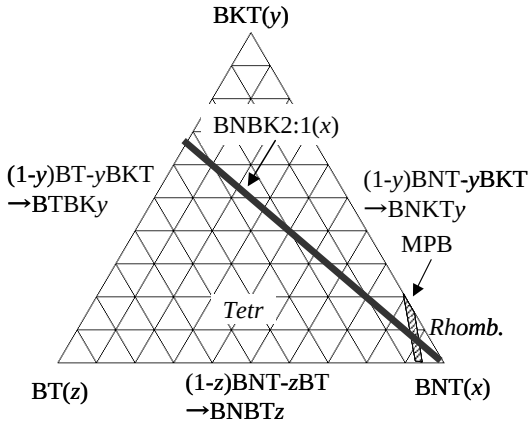


Fig. 1 Schematic diagram of BNT-BKT-BT ternary systems.

## 2. Experimental

The prepared ceramics of $x(Bi_{1/2}Na_{1/2})TiO_3$-$y(Bi_{1/2}K_{1/2})TiO_3$-$zBaTiO_3$ are shown in Fig. 1. (1-*y*)BNT-*y*BKT, (1-*z*)BNT-*z*BT, (1-*y*)BT-*y*BKT, and the inside of *x*BNT-*y*BKT-*z*BT were named as BNKT*y*, BNBT*z*, BTBK*y*, and BNBK*y*:*z*(*x*) (*y*:*z*=2:1). These ceramics were prepared by a conventional ceramic fabrication process. All higher than 99.9% purity of carbonates and oxides were used as starting materials. The crystal structures were identified by the X-ray powder diffraction patterns using Cu-$K\alpha$ radiation. The phase transition temperatures were determined by the temperature dependence of dielectric and piezoelectric properties[2]. The dielectric properties were measured using an LCR meter (YHP4275 and Wayne Kerr 3440). The piezoelectric properties were measured by the resonance and antiresonance method using an impedance analyzer (HP4294A). The temperature dependences of the piezoelectric properties were measured using 33-mode specimens. In particular, we measured the original sample holder with accuracy of ±2ºC to measure 33-mode because it is very difficult to measure accurate temperature of 33-mode specimens.

## 3. Results and discussion

By summarizing the phase transition temperatures of BNBTz, BNKT*y*, BTBK*y*, and BNBK2:1(*x*),[2-4] the phase relations of BNT-BKT-BT ternary systems were revealed, as shown in Fig. 2. In this study, the variation in $T_C$ for BNT was not clarified; however, $T_m$ of BNT was clarified to achieve $T_C$ of BT and BKT. Meanwhile, the $T_d$ corresponded to the $T_C$ with increasing the amount of BT for BNBTz and BTBK*y*. The highest $T_d$ of BNBTz was approximately 220ºC. On the other hand, the $T_d$ shows approximately 300ºC at the BKT content of $y$>0.6 in *x*BNT-*y*BKT-*z*BT.

Figure 3 show the compositional dependence of $T_d$, rhombohedral distortion, 90º-$\alpha$, and tetragonality, *c*/*a*, for BNKT*y*. It can be seen that $T_d$ is dependent on 90-$\alpha$ at the rhombohedral side and *c*/*a* at the tetragonal side of the MPB composition. On the other hand, in the case of BTBK*y*, the variation in *c*/*a* was also similar to $T_d$ rather than $T_C$.

The $T_d$ and the $d_{33}$ of BNBK2:1(*x*) were summarized in Fig. 4. While the MPB was the highest $d_{33}$ value of 181 pC/N, the $T_d$ was especially low temperature of approximately 100ºC. Although the $d_{33}$ of the tetragonal side is lower than that of the MPB, the $T_d$ of tetragonal side was much higher than that of the MPB composition. Therefore, considering both high $T_d$ and $d_{33}$, slightly the tetragonal side of the MPB composition is the optimum composition for BNT-BKT-BT ternary system. Further tetragonal compositions at $T_d$>250ºC were very difficult to pole fully because of high *c*/*a*. Therefore, it was very difficult to obtain large piezoelectricity by the usual poling process.

## 4. Conclusions

In this study, we clarified the phase diagram of BNT-BKT-BT ternary systems. Considering both high $T_d$ and $d_{33}$, slightly the tetragonal side of the MPB composition is the optimum composition, and it is considered to be promising candidate for lead-free piezoelectric actuator applications.

## 5. Acknowledgment

This study was partially supported by Grants-in-Aid for Scientific Research (B) (No. 19360302) from the Japan Society for the Promotion of Science.

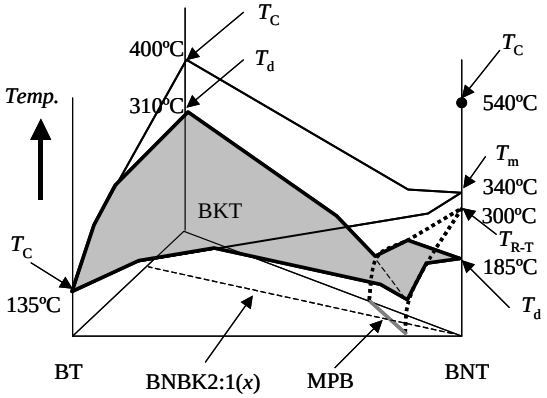


Fig. 2 The phase relations of the BNT-BKT-BT system.

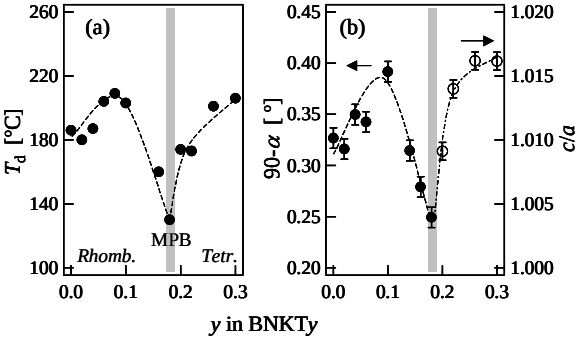


Fig. 3 Compositional dependence of (a) depolarization temperature, $T_d$, and (b) rhombohedral distortion, 90º-$\alpha$, and tetragonality, *c*/*a*, for BNKT*x*.

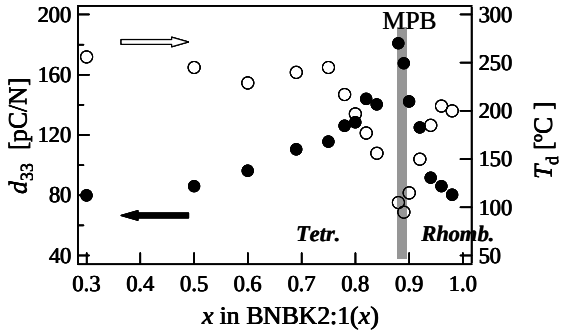


Fig. 4 The piezoelectric constant, $d_{33}$, and depolarization temperature, $T_d$, of BNBK2:1(*x*).

## Reference

1. J. V. Zvirgzds, P. P. Kapostis, and T. V. Kruzina: *Ferroelectrics*. **40** (1982) 75.
2. Y. Hiruma, R. Aoyagi, H. Nagata, and T. Takenka: *Jpn. J. Appl. Phys*. **43** (2004) 7556.
3. Y. Hiruma, R. Aoyagi, H. Nagata, and T. Takenka: *Jpn. J. Appl. Phys*. **44** (2005) 5040.
4. Y. Hiruma, H. Nagata and T. Takenaka: *Jpn. J. Appl. Phys*. **45** (2006) 7049.

Proceedings of Symposium on Ultrasonic Electronics, Vol. 29 (2008) pp. 37-38
11-13 November, 2008

# Elastic and piezoelectric coefficients of $LiNbO_3$ single crystal - RUS measurement and group theoretical analysis -

$LiNbO_3$の弾性・圧電定数計測と群論による解析

Yuki Hayashi[1†], Ryuichi Tarumi[2] and Masahiko Hirao[3]([1]Department of Eng. Science, Osaka Univ.; [2]Graduate School of Eng., Osaka Univ.; [3]Graduate School of Eng. Science, Osaka Univ.)

林勇気[1†], 垂水竜一[2], 平尾雅彦[3] ([1]大阪大学 基礎工; [2]大阪大学 工; [3]大阪大学 基礎工)

## 1. Introduction

Piezoelectric materials are now used in many kinds of sensors, filters and actuators. In addition, they are one of the potential candidate materials for future application to MEMS and/or NEMS devices. Within the framework of linear approximation, the constitutive equation for stress $\sigma_{ij}$, strain $\varepsilon_{ij}$ and electric field $E_i$ can be expressed in the following form,

$$\sigma_{ij} = C_{ijkl}\varepsilon_{kl} + e_{kij}E_k.$$

Where the fourth and the third rank tensors, $C_{ijkl}$ and $e_{kij}$, are the elastic constants and piezoelectric coefficients, respectively. Hereafter, we express them by contractive notations; $C_{IJ}$ and $e_{IJ}$ ($I,J$ = 1~6). From the equation one can see that piezoelectric materials convert electric field $E_i$ into mechanical stress $\sigma_{ij}$ through $e_{IJ}$. Precise measurements of $C_{IJ}$ and $e_{IJ}$ are therefore essential for designing of devices, especially for the above mentioned small-scaled devices.

Resonance ultrasound spectroscopy (RUS) is an attracting method to determine $C_{IJ}$ and $e_{IJ}$ simultaneously from a single crystal specimen.[1-2] Recently, low-temperature $C_{IJ}$ and $e_{IJ}$ of trigonal crystals ($\alpha$-$SiO_2$ and langasite) were measured by the RUS and a notable correlation was confirmed between the temperature dependences of $C_{IJ}$ and $e_{IJ}$.[3] This can be explained with the internal strains induced by thermal contraction. $LiNbO_3$ also belongs to the trigonal class. The low-temperature $C_{IJ}$ and $e_{IJ}$, and their connection with internal strains are, however, still uncertain. In this study, we investigate $C_{IJ}$ and $e_{IJ}$ of $LiNbO_3$ single crystal by RUS from ambient temperature to 6 K and discuss their temperature behaviors from a group theoretical point of view.

## 2. Experiment procedure

### 2-1. Crystallography of $LiNbO_3$

$LiNbO_3$ belongs to trigonal class with its point group symmetry of 3*m* (space group symmetry is *R*3*c*).[4] The independent elastic and piezoelectric components are $C_{11}$, $C_{12}$, $C_{13}$, $C_{14}$, $C_{33}$, $C_{44}$, $e_{15}$, $e_{22}$, $e_{31}$, and $e_{33}$. It has 30 atoms in the unit cell as illustrated in **Fig. 1**. The normal vibration modes can be expressed as a direct sum[4], in case of $LiNbO_3$, is expressed through the three irreducible representations ($A_1$, $A_2$ and $E$) as follow,

$$(A_1+E)_{AM}+(16A_1+13A_2+29E)_{OM}.$$

Where, the subscripts represent the acoustic (AM) and optical (OM) vibration modes, respectively.

The specimen used in this study has a rectangular parallelepiped shape with a dimension of 9.97x10.03x10.01 $mm^3$, respectively. The mass-density is 4631.7 $kg/m^3$.

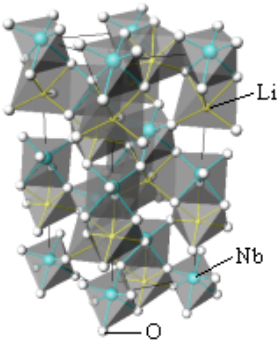


| Wyckoff position | |
|---|---|
| Li | (0, 0, 0.2801) |
| Nb | (0, 0, 0) |
| O | (0.0477, 0.3435, 0.0633) |
| **Wyckoff letter** | |
| (*x*, *y*, *z*) | (-*y*, -*x*, *z*+1/2) |
| (-*y*, *x*-*y*, *z*) | (-*x*+*y*, *y*, *z*+1/2) |
| (-*x*+*y*, -*x*, *z*) | (*x*, *x*-*y*, *z*+1/2) |

Fig. 1 Crystalline structure and Wyckoff position of $LiNbO_3$.

### 2-2. RUS measurements

Complete set of elastic constants $C_{IJ}$ and piezoelectric coefficients $e_{IJ}$ can be determined by RUS. The crystal specimen is mounted on a tripod type of ultrasound transducers. One transducer excites ultrasound vibration in the specimen and the other detects the vibration amplitude while the input frequency is swept. Free vibration resonance spectrum is then obtained. Resonance frequencies are determined by least-square fitting of resonance peaks to Lorenz function. Note that the measurement accuracy of resonance frequency is usually better than $10^{-5}$. The RUS unit is set in a cryogenic chamber, which can control the temperature from 4 to 300 K within the accuracy of 0.1 K.

hayasi-y@mbox.me.es.osaka-u.ac.jp

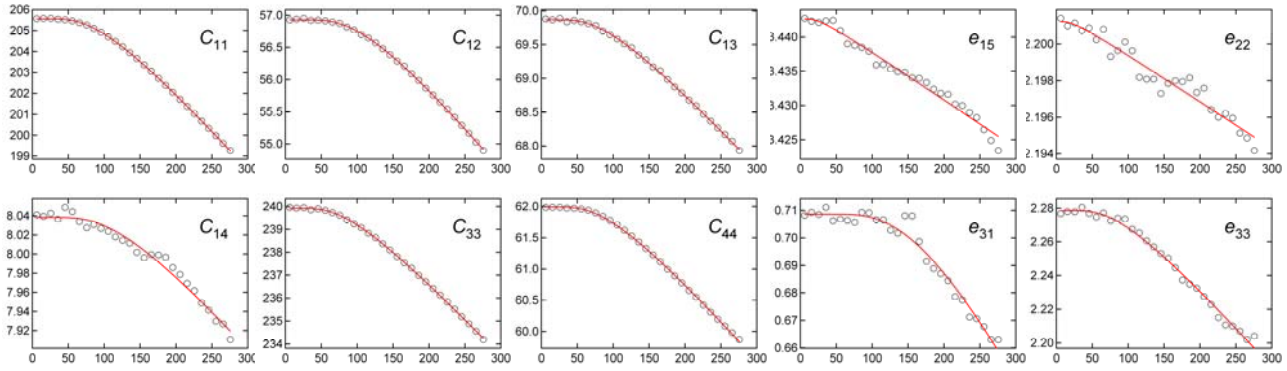


Fig. 2 Temperature dependence of elastic and piezoelectric coefficients of $LiNbO_3$. The units are GPa for $C_{IJ}$ and $C/m^2$ for $e_{IJ}$.

## 3. Results and discussion

**Figure 2** summarizes the temperature dependence of $C_{IJ}$ and $e_{IJ}$ obtained by RUS. We observe that all components show monotonic increase with temperature decreasing. Solid curves represent the least square fitting results to Varshni's function,

$$C_{ij}(T) = C_{ij}(0) - \frac{s}{\exp(\Theta_E - T)}.$$

Here, $C_{IJ}(0)$ is zero-temperature elastic constant (or piezoelectric coefficient), which includes zero-point lattice vibration effect. $\Theta_E$ can be interpreted as an Einstein temperature. Results of the present analysis are summarized in **Table I**. We note that $\Theta_E$ of two piezoelectric components, $e_{15}$ and $e_{22}$, are relatively small among the $C_{IJ}$ and $e_{IJ}$ and also that the temperature coefficients, $s$, of these components are extremely small.

Table I Einstein temperature $\Theta_E$ (K) and fitting parameter $s$ of $LiNbO_3$.

| | $C_{11}$ | $C_{12}$ | $C_{13}$ | $C_{14}$ | $C_{33}$ |
|---|---|---|---|---|---|
| $\Theta_E$ | 276.2 | 328.8 | 261.0 | 367.0 | 252.8 |
| $s$ | 10.9 | 4.7 | 3.0 | 0.3 | 8.5 |
| | $C_{44}$ | $e_{15}$ | $e_{22}$ | $e_{31}$ | $e_{33}$ |
| $\Theta_E$ | 267.92 | 67.3 | 57.7 | 551.2 | 256.3 |
| $s$ | 3.5 | 0.005 | 0.002 | 0.3 | 0.1 |

$LiNbO_3$ has positive thermal expansion coefficients so that thermal contraction occurs at low temperatures. Since the 3$m$ group does not have inversion symmetry, internal strains are expected to occur with the contraction. According to group theory, internal strains can be expressed as a direct sum of irreducible representations, namely, superposition of optical-mode phonon type atomic displacements. On the other hand, lattice dynamics perturbation analysis reveals contribution of the normal displacements on $C_{IJ}$ and $e_{IJ}$. Results of the analysis are summarized in **Table II**, where we see that $E$ mode internal strain can affect $C_{11}$, $C_{12}$, $C_{14}$, $C_{44}$, $e_{15}$ and $e_{22}$. Here, the contributions on $e_{15}$ and $e_{22}$ are $P_1F_{23}$ and $P_2F_{11}$, whereas both $A_1$ and $A_2$ cannot influence these components. It is therefore reasonable to suppose that the notable properties of $e_{15}$ and $e_{22}$ would be originated from $E$ type internal strain, which appears due to thermal contraction at low temperatures.

Table II Effects of internal strains on elastic constants $C_{IJ}$ and piezoelectric coefficients $e_{IJ}$.

| $C_{IJ}$, $e_{IJ}$ | $A_1$ | $A_2$ | $E$ |
|---|---|---|---|
| $C_{11}$ | $F_{11}F_{11}$ | - | $F_{11}F_{11}$ |
| $C_{12}$ | $F_{11}F_{11}$ | - | $-F_{11}F_{11}$ |
| $C_{13}$ | $F_{11}F_{33}$ | - | - |
| $C_{14}$ | - | - | $\pm F_{11}F_{23}$ |
| $C_{33}$ | $F_{33}F_{33}$ | - | - |
| $C_{44}$ | - | - | $F_{23}F_{23}$ |
| $e_{15}$ | - | - | $P_1F_{23}$ |
| $e_{22}$ | - | - | $P_2F_{11}$ |
| $e_{31}$ | $P_3F_{11}$ | - | - |
| $e_{33}$ | $P_3F_{33}$ | - | - |

## 4. Conclusions

In summary, we have determined the complete set of elastic constants $C_{IJ}$ and piezoelectric coefficients $e_{IJ}$ of $LiNbO_3$ single crystal using resonance ultrasound spectroscopy from ambient temperature down to 6 K. Most of $C_{IJ}$ and $e_{IJ}$ showed usual temperature dependence while slightly peculiar properties are found in $e_{15}$ and $e_{22}$. Group theoretical lattice dynamics perturbation analysis revealed that the origin would be the thermal-contraction induced $E$ mode internal strain.

## References

1. I. Ohno: J. Phys. Earth **24** (1976) 335.
2. A. Migliori: Phys. B **183** (1993) 1.
3. R. Tarumi, K. Nakamura, H. Ogi and M. Hirao: J. Appl. Phys., **102** (2007) 113508.
4. T. Inui and Y. Tanabe and Y. Onodera: *Group Theory of Crystal Lattice and Its Applications in Physics* (Spinger-Verlag, Berlin, 1996).

Proceedings of Symposium on Ultrasonic Electronics, Vol. 29 (2008) pp. 39-40
11-13 November, 2008

# Study on viscoelastic properties of polystyrene films by a QCM-D technique

## QCM-D 法によるポリスチレンフィルムの粘弾性評価

Aiko Shirai, [1†] Yohei Asano, [1] Masahiro Maebayashi[2] and Shinobu Koda[1] ([1] Graduate School of Eng., Nagoya Univ.; [2]Facult. Agric., Meijo Univ.)
白井愛子 [1‡], 浅野洋平 [1], 前林正弘 [2], 香田忍 [1] ([1] 名大 院工; [2] 名城大 農)

### 1. Introduction

It is very important to know dynamic properties of polymers in the melting region for the molding and drawing processes. Extensive works of bulk plymer have been done. However, the expermental methods to evaluate the dynamic properties of films at higher temperatures are limmited. In this work, we develop a QCM-D (Quartz Crystal Microbalance with Dissipation)[1-3] technique operated at higher temperatures and examine the viscoelastic properties of polystyrene thin films around glass transition and melting temperatures.

### 2. Experimental

QCM-D measurement: the experimental setup was shown in **Fig. 1**. A 5 MHz AT-cut quartz was driven by a signal generator (WF1943, NF ELECTRIC Instruments). The transducer was disconnected from a driving circuit by a relay (G6Z-1PE-A, Omron) controlled by a function generator (FG-272, KENWOOD). The decay curve of the QCM oscillation is recorded on an oscilloscope (DSO3062A, Agelent). The envelope of the representative decay curve was shown in **Fig. 2**. It is shown that when the driving power to the quartz oscillator is switched off at time $t$ = 0, the voltage over the crystal, $U(t)$, decays as an exponentially damped sinusoidal:

$$U(t) = U_0 e^{-t/\tau} \sin(2\pi f t + \phi) \qquad (1)$$

where $U_0$ is the amplitude at $t$ = 0, $\tau$ is the decay time constant, and $\varphi$ is the phase.[2] The frequency when the amplitude of decay curve becomes the maximum is defined as the resonant frequency $f$. the dissipation factor $D$ is related to the decay time constant as

$$D = \frac{1}{\pi f \tau} \qquad (2)$$

For each samples, $\Delta f$ ($\Delta f = f - f_0$) and $\Delta D$ ($\Delta D = D - D_0$) were measured. $\Delta f$ is the change of resonant frequency. $f$ and $f_0$ are the resonant frequency in measurement samples, and the resonant frequency of the quartz oscillator, respectively. $\Delta D$ is the change of dissipation. $D$ and $D_0$ are the dissipation in measurement and dissipation of only quartz, respectively.

The temperature was regulated by a heater around the sample cell made of brass involving the quartz crystal. The measurements were carried out in the temperature range from 25 to 200 °C.

Sample Preparation: Polystyrene (PS) with molecular weight of 45,000 was purchased from SCIENTIFIC POLYMER PRODUCTS, INC., and was used as received. PS films were prepared by a casting method from PS-toluene solutions at ambient temperature under air atmosphere. Those concentrations were 0.3, 0.5, and 1wt %.

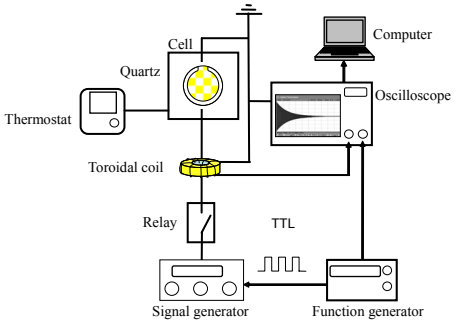


Fig. 1 A schematic illustration of the experimental setup

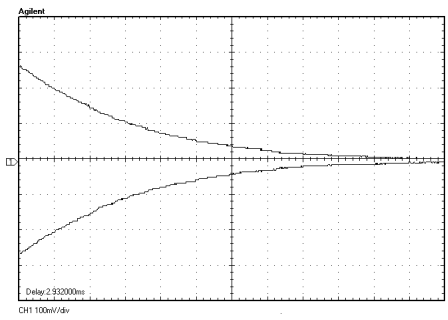


Fig. 2 An envelope of decay curve

---

A.Shirai: shirai.aiko@d.mbox.nagoya-u.ac.jp

## 3. Results and Discussion

The temperature dependence of $\Delta f$ was investigated through three heating and cooling cycles for the same sample at a temperature change rate of 1°C /min and the results shown in **Fig. 3**. In the case of the first cycle, a difference in the initial and final $\Delta f$ was noticed and it is reasonable to assume that this difference is caused by the evaporation of the residual solvent in the film after casting. Moreover, the quantity of the evaporated solvent measured by us counts for 12% of the sample. It was also noticed that this difference is dramatically reduced with increasing the number of cycles carried out for the same sample, this clearly indicates that the residual solvent in the films after casting is almost entirely removed during the first heating process. Hereafter, we present the results of the second cycle.

**Figures 4** and **5** show the temperature dependence of resonant frequency shifts and dissipation for three PS films. The magnitude of $\Delta f$ depends on the concentration of PS solutions. The glass transition temperature and melting temperature of polystyrene is around 100°C and 230°C, respectively. In the heating and cooling processes, the $\Delta f$ at temperature below ca. 100°C in Fig. 5 shows a very weak temperature dependence and above this temperature, the absolute value of $\Delta f$ decreases. At the low temperature region, $\Delta f$ mainly reflects the quantity of polymers mounted on the quartz oscillator, that is the thickness of the films. In this work, the thickness of the PS film prepared with 0.5 wt% PS solution are roughly estimated as 300 nm. The theoretical study of $\Delta f$ and $\Delta D$ by Voinova et al. shows that $\Delta f$ and $\Delta D$ of polymer films are expressed by functions of viscosity, shear modulus, density, and thickness of polymer films.[3] Therefore, the changes in viscoelastic properties contribute to the decrease or increase in $\Delta f$ and $\Delta D$. The $\Delta D$ increases above the glass transition temperature, attains the maximum around 160°C and then decreases. The magnitude of $\Delta D$ increases with increasing the PS concentration. $\Delta D$ is considered to be due to the increase in the thickness and in the fluidity.

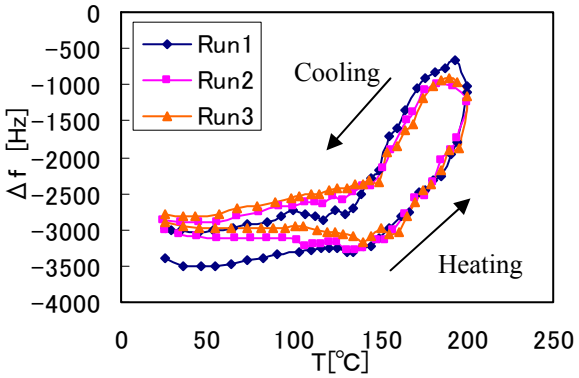


Fig. 3 Temperature dependence of $\Delta f$ for PS film prepared with 0.5 wt% solution.

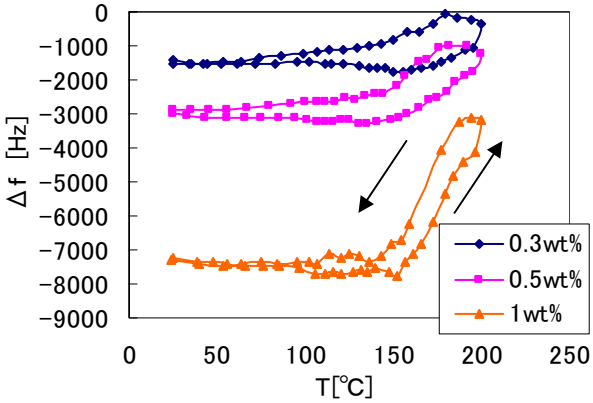


Fig. 4 Temperature dependence of $\Delta f$ of PS films.

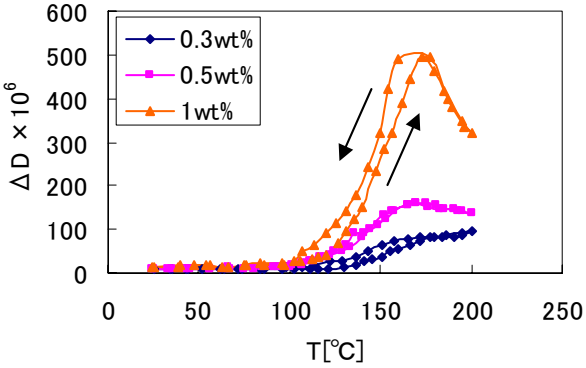


Fig. 5 Temperature dependence of $\Delta D$ of PS films.

### References


1. M. Rodahl and B.Kasemo: Rev. Sci. Instrum. **67** (1996) 9.
2. M. Rodahl and B. Kasemo: Sensors Actuators **B37** (1999) 111.
3. M.V.Voinova, M. Rodahl, M. Jonson and B. Kasemo: Physica Scripta, **59** (1999) 391.

Proceedings of Symposium on Ultrasonic Electronics, Vol. 29 (2008) pp. 41-42
11-13 November, 2008

# Electromechanical coupling coefficient of semiconducting piezoelectric crystal measured by Brillouin scattering

Brillouin 散乱法による圧電半導体の電気機械結合係数の評価

Taisuke Yoshida [1†], Takahiko Yanagitani [2] and Mami Matsukawa [1] ([1] Doshisha Univ.; [2]Nagoya Institute of Technology)
吉田泰祐 [1‡], 柳谷隆彦 [2], 松川真美 [1] ([1] 同志社大学; [2] 名古屋工業大学)

## 1. Introduction

Semiconducting hexagonal crystals such as AlGaN, GaN, ZnO have been extensively used for transistors and LEDs. Electronic and optical properties in these devices are strongly affected by the internal piezoelectric field induced by the strain at boundary of the heterostructure [1]. Therefore, it is important to know piezoelectric properties of these crystals. In this study, we have demonstrated the measurement of piezoelectric properties of semiconducting ZnO crystal by Brillouin scattering method.

## 2. Measurement of piezoelectric property

In general, piezoelectric properties of a crystal are measured by comparing piezoelectrically *"unstiffened"* and *"stiffened"* acoustic wave velocities, $V^E$ and $V^D$ [2]. Electromechanical coupling coefficient $k$ of the crystal is written as $k^2 = 1-(V^E/V^D)^2$. However, in a semiconducting crystal, $V^D$ value cannot be determined by well-known ultrasonic method below UHF ranges, such as pulse-echo methods, resonance method, and acoustic microscopy. The *"piezoelectric stiffening"* is caused by internal electric field due to piezoelectric polarization. In the case that acoustic wave frequency is much lower than the carrier mobility, the space charge distribution due to the piezoelectric polarization should be screened by the carriers, and *"piezoelectric stiffening"* does not occur. **Figure 1** shows theoretically estimated resistivity and frequency dependence of the shear wave velocities of a ZnO crystal, neglecting carrier diffusion. As can be seen in the figure, high frequency measurement above the GHz range is required to detemine $V^D$ value (black part) in the semiconducting piezoelectric crystal whose resistivity is less than $10^1$ Ω·m range. Acurally, VHF acoustic microscopy suffers from the conductivity in the piezoelectric measurement for ZnO crystal. [3] Phonon spectroscopy such as Brillouin scattering method [4] is suitable for measuring piezoelectric properties in the semiconducting crystal.

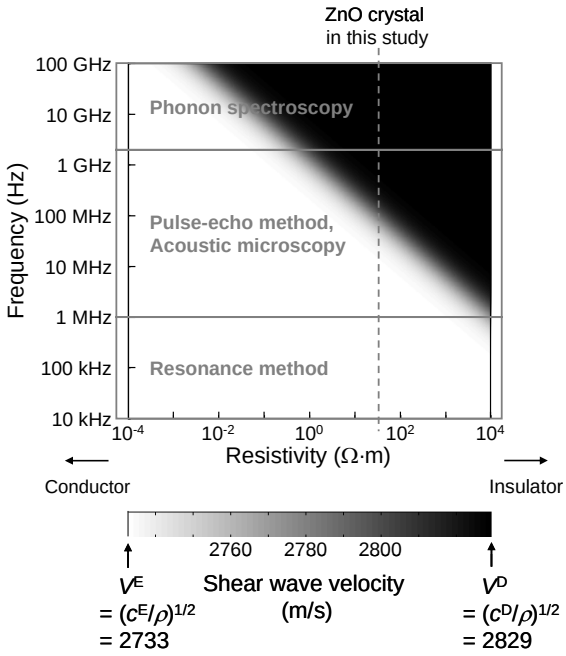


Fig. 1 Theoretically estimated resistivity and frequency dependence of the shear wave velocities of a ZnO crystal. White part and black part correspond to the $V^E$ and $V^D$ values, respectively.

## 3. Method

A semiconducting ZnO single crystal ($10\times10\times0.5$ mm$^3$, MTI Corporation) was used for the measurement. Resistivity (dc) of the crystal was 30 Ω·m at room temperature, which was simply measured using Au/ZnO/Au sandwich structure.

For a-plane hexagonal plate, $V^E$ and $V^D$ correspond to the velocity of shear horizontal waves: propagating along c-axis ($V_{//}$) and perpendicular to the c-axis ($V_{\perp}$), respectively. These two velocities of in-plane direction $\boldsymbol{q}^{\Theta A}$ were measured by reflection induced ΘA (RIΘA) scattering geometry [5,6] as shown in **Fig. 2**. Typical Brillouin spectra are shown in **Fig. 3**. Peaks around 7.5 GHz and 17 GHz correspond to the scattering from shear phonon and longitudinal phonon which travel in-plane direction. Acoustic velocities $V^{\Theta A}$

---

mmatsuka@mail.doshisha.ac.jp

can be determined from shift frequencies of these peaks using following equation.

$$V^{\Theta A} = f^{\Theta A} \frac{\lambda_i}{2 \cdot \sin\left(\frac{\Theta}{2}\right)}$$

Here, the $f^{\Theta A}$ is shift frequency, $\lambda_i$ is wavelength of the incident light, and Θ/2 is incident angle. The Brillouin scattering measurement was performed using a six-pass tandem Fabry-Perot interferometer (JRS Scientific Instruments) with an Argon ion laser at a wavelength of 514.5 nm. The laser power near the sample was 54 mW. We have confirmed the heating effect of laser beam was very few from long time continuous measurements. The actual diameter of the focused laser beam in the sample was approximately 50 $\mu$m.

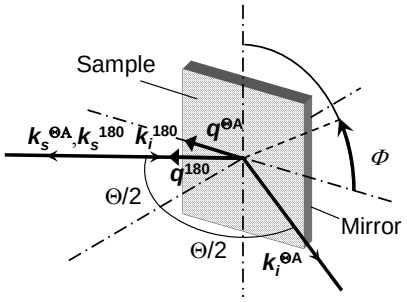


Fig. 2 RIΘA scattering geometry where $\Phi$ is the in-plane rotation angle.

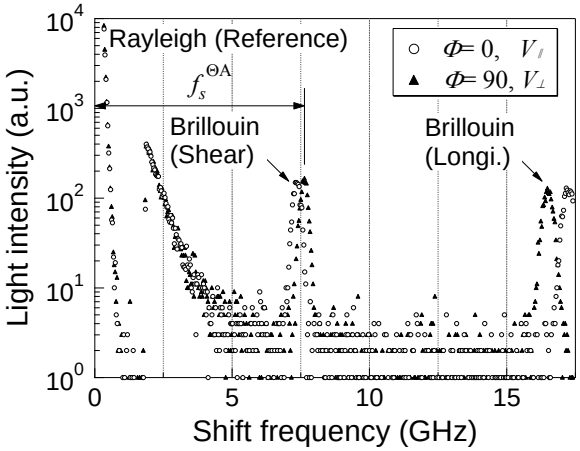


Fig. 3 Typical Brillouin spectra obtained from the ZnO single crystal. Open circle and solid triangle show the spectra measured at $\Phi$= 0º($V_{//}$), $\Phi$= 90º($V_{\perp}$), respectively.

## 4. Results

In-plane anisotropy of shear horizontal wave velocity of the ZnO single crystal was plotted in **Fig. 4**. Calculated curve with or without piezoelecity using the Smith's constant [7] was also shown. Measured values of $V^{E}$ and $V^{D}$ are 2738 m/s and 2838 m/s, respectively, which almost correspond to the calculated curve. Error bar of the velocity is approximately 1.6 m/s. $k_{15}$ value determined from these velocities was in good accordance with the Smith's constant ($k_{15}$=0.26).

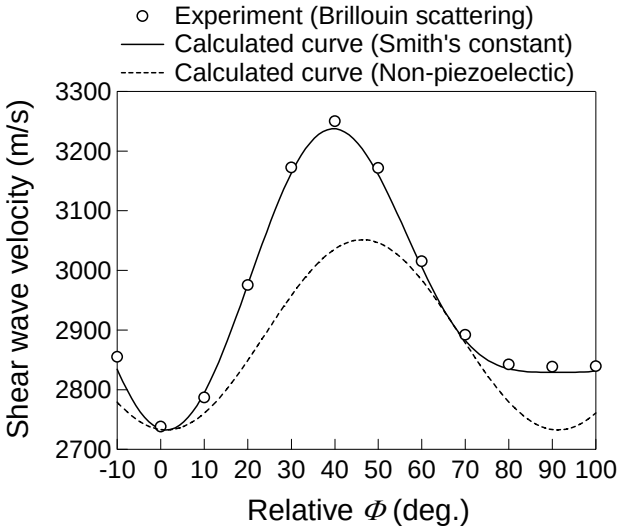


Fig. 4 In-plane anisotropy of shear horizontal wave velocity of the ZnO single crystal measured by Brillouin scattering.

## 5. Conclusion

We have succeeded in the simple and local measurement of electromechanical coupling coefficient $k_{15}$ of a ZnO crystal by using Brillouin scattering method. Brillouin scattering enables the simultaneous measurement of in-plane longitudinal and shear wave velocities at hypersonic frequencies. Moreover, using a microscope system, we will be able to observe much smaller regions. In case of low resistivity samples, this technique makes precise and easy nondestructive measurement of $k_{15}$ distribution possible.

## References


1. O. Ambacher, et. al.: J. Appl. Phys. **87** (2000) 334.
2. B. A. Auld: *Acoustic fields and waves in solids* (John Wiley & Sons, Inc., New York, 1973) pp. 296-307.
3. T. Tanaka, Y. Ohashi, M. Arakawa, J. Kushibiki, and N. Sakagami: Proc. Piezoelect. Mater. & Device Symp., (2008) 41.
4. K. Shintani, T. Yanagitani, M. Matsukawa, and T. Otani: Proc. IEEE Ultrason. Symp., **3** (2004) 1864.
5. J. K. Krüger, J. Embs, J. Brierley and R. Jiménez: J. Phys. D: Appl. Phys., **31** (1998) 1913.
6. S. Murata, T. Kawamoto, M. Matsukawa, T. Yanagitani, and N. Ohtori: Jpn. J. Appl. Phys. **46** (2007) 4626.
7. R T. Smith and V. E. Stubblefield, J. Acoust. Soc. Am., **46** (1969) 105.

Proceedings of Symposium on Ultrasonic Electronics, Vol. 29 (2008) pp. 43-44
11-13 November, 2008

# Shear Mode Piezoelectric Properties of $KNbO_3$-based Ferroelectric Ceramics

$KNbO_3$系強誘電体セラミックスのシェアモード圧電特性

Kouhei Hikita†, Yuji Hiruma, Hajime Nagata and Tadashi Takenaka
(Faculty of Sience and Technology, Tokyo University of Science)
疋田康平，畫間裕二，永田肇，竹中正　（東理大 理工）

## INTRODUCTION

Lead-free piezoelectric materials have recently been demanded from the viewpoint of environmental protection. Potassium niobate, $KNbO_3$ (KN), has attracted considerable attention as a candidate material for lead-free piezoelectric applications, because the KN single-crystal has a large piezoelectricity and a high Curie point.[1] The electromechanical coupling factor, $k_{24}$ and the piezoelectric strain constant, $d_{24}$, in the thickness-shear mode of the KN crystal show as high as 0.88 and 205 pC/N, respectively, which are the highest among those values of current lead-free piezoelectrics.[1] In terms of KN ceramic, there are few reports on the piezoelectric properties [2-3], because of the poor sinterability and the low resistivity of KN ceramic. To solve these problems, the modified processes such as hot-press method, doping effect, atmosphere control have been carried out so far. Also, our group have successfully obtained the dense and non-deliquescent KN ceramic by the modified conventional ceramic fabrication process in air and it indicated high resistivity enough to be poled under the high electric field [4]. Then, we reported that the $k_{33}$ of the KN ceramic was 0.50 [4]. However, the piezoelectric properties for the thickness-shear mode have not made enough investigation, even though the KN single crystal shows large shear mode piezoelectric properties such as $k_{24}$ and $d_{24}$ [1]. In this study, $MnCO_3$ (0.1 wt%)-doped KN (KN-Mn0.1) ceramic wes prepared by a modified conventional processing route in air. Also, the shear mode piezoelectric properties such as $k_{15}$, $d_{15}$, and the mechanical quality factor, $Q_m$, were investigated for the dense KN-Mn0.1 ceramic.

## EXPERIMENTAL PROCEDURE

$KNbO_3$+$MnCO_3$ 0.1 wt % (KN-Mn0.1) ceramic prepared by the modified conventional ceramic fabrication process[4]. Calcination temperatures were 600ºC for 4 h as the first stage and 1000°C for 4 h as the second stage. And the final sintering was carried out at 1047 ºC for 2 h in air.

The density of the sintered sample was measured by the Archimedes technique. The sintered sample was characterized using an X-ray diffractometer (Rigaku RINT2000). For the measurements of electrical properties such as dielectric and piezoelectric properties, the samples were electroded with sputtered gold. Resistivity was measured with a high-resistance meter (HP 4339B). The samples were cut and polished into appropriate shapes for the determination of their piezoelectric properties in the (15) mode. Specimens for the piezoelectric measurements were poled in silicone oil bath heated at 150 ºC. A dc electric field of 5 kV/mm was applied to the samples for 5 min during the poling. Piezoelectric properties were measured by the resonance-antiresonance method on the basis of the EMAS standard using an impedance analyzer (HP4294A). The $k_{15}$ was calculated from the resonance and antiresonance frequencies, using Onoe's formula. Also, the $k_{15}$ was found by the ratio between fundamental and odd-overtone frequencies, $f_r^{(3)}/f_r^{(1)}$, $f_r^{(5)}/f_r^{(1)}$ or $f_r^{(5)}/f_r^{(3)}$ on the basis of EMAS-6005. The free permittivities, $\varepsilon_{11}^{T}$, was determined from the capacitances at 1 kHz of the poled specimen. The elastic compliance constant, $s_{55}^{E}$, was calculated from the frequency constant, $N_{15}$, and the measured density $\rho_0$. Finally, the piezoelectric strain constant, $d_{15}$, was calculated from $k_{15}$, $\varepsilon_{11}^{T}$ and $s_{55}^{E}$ as follow.

$$d_{15} = k_{15}\sqrt{\varepsilon_{11}^{T} \cdot s_{55}^{E}},$$

## RESULTS and DISCUSSION

X-ray diffraction pattern of KN-Mn0.1 ceramic showed a single phase of perovskite structure with an orthorhombic symmetry at RT. A density ratio of the KN-Mn0.1 ceramic was higher than 96%. From the temperature dependence of dielectric properties, Curie temperature, $T_c$, was 424°C, which is almost the same as that of pure KN ceramic [5]. The resistivity, $\rho$, of the KN-Mn0.1 is higher than $10^{12}$ Ω·cm.

**Figure 1** shows the frequency dependence of impedance, $Z$, in the (15) mode for the KN–Mn0.1. Generally, it is very difficult for the (15) mode to

show a good resonance and anti-resonance characteristic without spurious peaks because of the thickness errors. As can be seen in Fig. 1, there are some spurious peaks in the impedance, $|Z|$, and phase, $\theta$. The sample shape in Fig. 1 is a rectangular plate with 0.5×3×8 mm$^3$. The length of the poling direction is $l$=8 mm and the thickness of the shear mode is $t$=0.5 mm. When we changed the sample dimensions, longer $l$ minimized the intensity of spurious peaks without arrows in Fig. 1. From this result, the frequencies with arrows seem to be the resonance and antiresonance frequencies of the (15) mode. Also, spurious peaks may relate to the length of the poling direction. It is still unclear for the origin of the spurious peaks, so that further studies are required. Anyhow, the $k_{15}$ was calculated using the frequencies with arrows and the value was $k_{15}$=0.50. To confirm the accuracy of the $k_{15}$ value, we checked this value from the ratio between fundamental and odd-overtone frequencies, $fs^{(3)}/fs^{(1)}$, $fs^{(5)}/fs^{(1)}$ or $fs^{(5)}/fs^{(3)}$ on the basis of EMAS-6005. **Figure 2** shows frequency dependence of impedance, $Z$, in the (15) mode for KN-Mn0.1 with wide frequency range. The fundamental frequency, $f^{(1)}$, third and fifth harmonics, $f^{(3)}$ and $f^{(5)}$ can be clearly observed. The $k_{15}$ values from $f^{(3)}/f^{(1)}$ and $f^{(5)}/f^{(3)}$ were 0.48 and 0.50, respectively, which were almost consistent with that from calculated by resonance and antiresonance method. Additionally, we compare the $k_{15}$ value with those from the KN single crystal. Considering the $k_{15}$ (0.44) and $k_{24}$ (0.88) in the KN single crystal [1], the $k_{15}$ value in the ceramic places to the mean value between $k_{15}$ and $k_{24}$ in the single crystal. From these considerations, the $k_{15}$ of 0.50 is thought to be reasonable.

**Table I** summarized piezoelectric properties of KN-Mn-0.1 ceramic. The relative free permittivity, $\varepsilon_{11}^T/\varepsilon_0$ was 544, which was larger than the non-poled dielectric constant, $\varepsilon_r$, (=468). Piezoelectric strain constant, $d_{15}$, was 169 pC/N which is lager because of large $\varepsilon_{11}^T/\varepsilon_0$ (544) and $s_{55}^E$ (24.1 pm$^2$/N). The shear mode vibration of KN-Mn0.1 ceramic seems to be a considerably promising candidate for actuator and high power applications.

## CONCLUSIONS

$MnCO_3$ (0.1 wt%)-doped $KNbO_3$ (KN-Mn0.1) ceramic was prepared by the modified conventional processing route. Also, the shear mode piezoelectric properties such as the electromechanical coupling factor, $k_{15}$, and the piezoelectric strain constant, $d_{15}$, were investigated for the dense KN-Mn0.1 ceramic. We first revealed accurate value of the $k_{15}$=0.50 and the $d_{15}$=169 pC/N, respectively, for KN-Mn0.1 ceramic in this study. The shear mode vibration of KN-based ceramics seems to be a considerably promising candidate for actuator and high power applications.

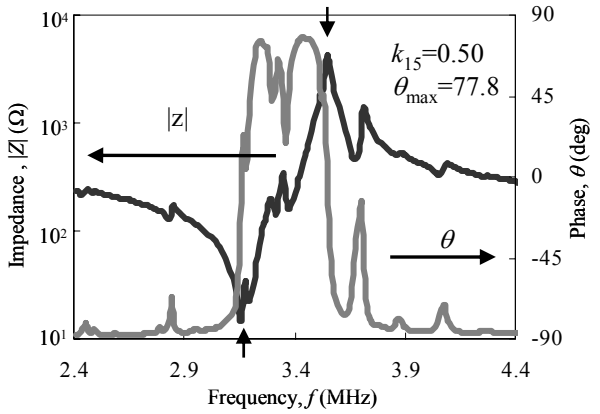


Fig. 1 Frequency dependence of impedance, $Z$, in the (15) mode for KN-Mn0.1.

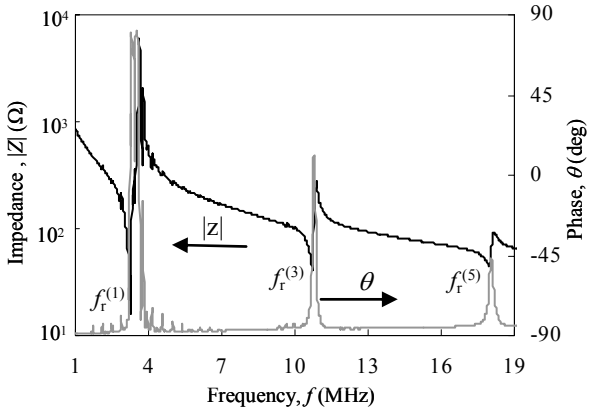


Fig. 2 Frequency dependence of impedance, $Z$, in the (15) mode for KN-Mn0.1 with wide frequency range.

Table I Piezoelectric properties of KN-Mn0.1 ceramic.

| $\varepsilon_{11}^T/\varepsilon_0$ | $k_{15}$ | $N_{15}$ [Hz·m] | $d_{15}$ [pC/N] | $s_{55}^E$ [pm$^2$/N] | $Q_m$ |
|---|---|---|---|---|---|
| 544 | 0.50 | 1798 | 169 | 24.1 | 132 |


## ACKNOWLEDGEMENTS

This study was partially supported by Grants-in-Aid for Scientific Research (B) (No. 19360302) from the Japan Society for the Promotion of Science.


## REFERENCES


[1] S. Wada, A. Seike, and T. Tsurumi: Jpn. J. Appl. Phys. **40** (2001) 5690.

[2] T. Yoshida, Y. Hiruma, R. Aoyagi, H. Nagata, and T. Takenaka: Key Eng. Mater. **301** (2006) 19.

[3] H. Matsumoto, Y. Hiruma, H. Nagata, and T. Takenaka: Jpn. J. Appl. Phys. **45** (2006) 4479.

[4] H. Nagata, T. Hirosue, K. Matsumoto, Y. Hiruma and T. Takenaka, Jpn. J. Appl. Phys. **46** (2007) 7084.

Proceedings of Symposium on Ultrasonic Electronics, Vol. 29 (2008) pp. 45-46
11-13 November, 2008

# Evaluation of Synthetic Silica Glasses by the Ultrasonic Microspectroscopy Technology

超音波マイクロスペクトロスコピー技術による合成石英ガラスの評価

Mototaka Arakawa†, Hideki Shimamura, and Jun-ichi Kushibiki
(Graduate School of Engineering, Tohoku Univ.)
荒川元孝†，島村秀樹，櫛引淳一 （東北大院工）

## 1. Introduction

We have been developing an evaluation method of glass materials by the ultrasonic microspectroscopy (UMS) technology. Variations in acoustic properties, viz., bulk-wave velocities, leaky surface acoustic wave (LSAW) velocity $V_{LSAW}$, and density $\rho$, caused by small amounts of impurities, such as hydroxyl (OH) and chlorine (Cl), were detected by applying the UMS technology to silica glasses[1]. Various physical properties of glasses depend on the fictive temperature $T_f$ that is a representative parameter related to the thermal history.[2, 3] In this paper, relationships among acoustic properties, $T_f$, and Cl concentration $C$(Cl) are discussed.

## 2. Specimen

Specimens were prepared from commercial silica glasses (ED-B and ED-C, Nippon Silica Glass Co. Ltd.) manufactured by the vapor phase axial deposition (VAD) method. Three specimens A, B, and C were prepared from the different lots of each glass. Impurities of the glasses were less than 10 wtppm except for OH and Cl from the catalog.

## 3. Results

LSAW and bulk-wave velocities were measured by the line-focus-beam and plane-wave ultrasonic material characterization system.[4, 5] Density was measured by the Archimedes method. OH concentration was measured by FT-IR[6], and $C$(Cl) was measured by X-ray fluorescence analysis.

Measurement results of longitudinal velocities $V_l$, shear velocities $V_s$, $\rho$, $V_{LSAW}$, and $C$(Cl) were summarized in **Table I**. Measurement errors were within ±0.11 m/s, ±0.09 m/s, ±0.05 kg/m$^3$, ±0.32 m/s, and ±100 wtppm, respectively. Velocity dispersions were not observed for bulk velocities measured in the VHF range. OH concentrations were 0 wtppm for all specimens. Maximum differences among specimens were 7.86 m/s for $V_l$, 11.75 m/s for $V_s$, 8.17 m/s for $V_{LSAW}$, and 0.48 kg/m$^3$ for $\rho$. Maximum difference of $C$(Cl) was 460 wtppm among the ED-C specimens. The differences of acoustic properties among the ED-B specimens could be caused by the difference of $T_f$, and those among the ED-C specimens could be caused by the differences in both $T_f$ and $C$(Cl).

E-mail: arakawa@ecei.tohoku.ac.jp

## 4. Discussion

The relationship between $\rho$ and $T_f$ was obtained from refs. 2 and 3 as follows.

$$\rho = 0.0094 \times (T_f - 1132) + 2202.93 \quad (1)$$

$T_f$ of ED-B(A, B, C) were obtained as 1038°C, 1085°C, and 1083°C, respectively, by substituting the densities into eq. (1). The relationships between acoustic properties and $T_f$ were shown in **Fig. 1**. The sensitivities of the acoustic properties to $T_f$ were shown in **Table II**. The resolutions to $T_f$ were also shown in Table II, where the measurement accuracies of $V_l$, $V_s$, $V_{LSAW}$, and $\rho$ were ±0.1 m/s, ±0.1 m/s, ±0.3 m/s, and ±0.1 kg/m$^3$, respectively.

$C$(Cl) dependence of density was determined in ref. 3 as follows.

$$\rho / T_f = \{-2.44 \cdot C(\mathrm{Cl}) + 9.10\} \times 10^{-3} \quad (2)$$

The sensitivity of density to $C$(Cl) was obtained as -2.64 (kg/m$^3$)/wt% by substituting $T_f$ of ED-B(C), 1083°C, into eq. (2). $\rho$ of ED-C(A, B, C) were calculated from the sensitivity, $\rho$ of ED-B(C), and $C$(Cl) of ED-C (A, B, C). Tentative $T_f$ were obtained using eq. (1) by comparing the measured and calculated densities. Then, sensitivities of $V_l$, $V_s$, and $\rho$ to $C$(Cl) and $T_f$ of ED-C(A, B, C) were obtained with the least squares method for the measured results of ED-B(C) and ED-C(A, B, C). The results are shown in **Fig. 2**. $T_f$ of ED-C(A, B, C) were estimated as 1111°C, 1112°C, and 1114°C, respectively. The sensitivities and resolutions to $C$(Cl) by acoustic property measurements were shown in Table II. $V_l$ has highest resolutions for both $T_f$ and $C$(Cl).

## 5. Summary

In this paper, relationships among acoustic properties, fictive temperatures, and chlorine concentrations were discussed for silica glasses. Hereafter, we will investigate relationships between the acoustic properties and OH concentrations.

**Acknowledgements**

The authors are very grateful to H. Sudo and M. Kudo of Nippon Silica Glass Co. Ltd. for preparation of the specimens, Dr. Y. Kimura of Research Institute of Electrical Communication, Tohoku University, for

Table I. Acoustic properties at 23°C and Cl concentrations for synthetic silica glass specimens.

| Specimen | $\rho$ [kg/m$^3$] | $V_l$ [m/s] | $V_s$ [m/s] | $V_{\mathrm{LSAW}}$ [m/s] | $C$(Cl) [wtppm] |
|---|---|---|---|---|---|
| ED-B (A) | 2202.01 | 5957.15 | 3768.31 | 3429.69 | 0 |
| ED-B (B) | 2202.46 | 5964.84 | 3764.60 | 3428.26 | 0 |
| ED-B (C) | 2202.44 | 5965.01 | 3764.66 | 3428.33 | 0 |
| ED-C (A) | 2202.49 | 5959.39 | 3756.56 | 3421.52 | 1740 |
| ED-C (B) | 2202.24 | 5961.50 | 3758.29 | 3423.30 | 1390 |
| ED-C (C) | 2202.29 | 5961.89 | 3758.52 | 3423.59 | 1280 |

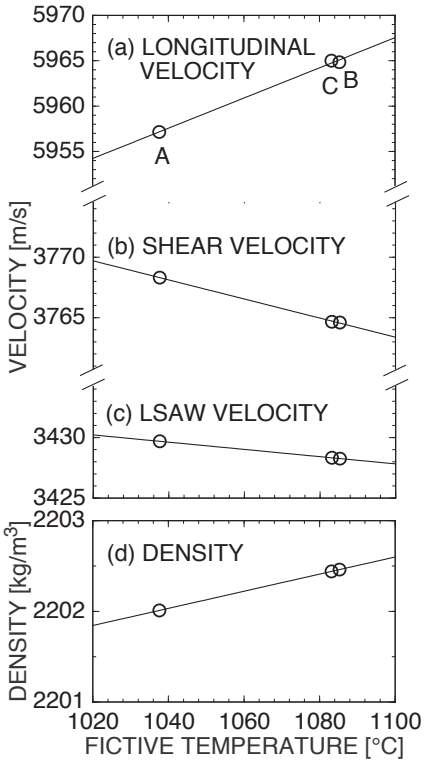


Fig. 1. Fictive temperature dependences of acoustic properties of ED-B specimens.

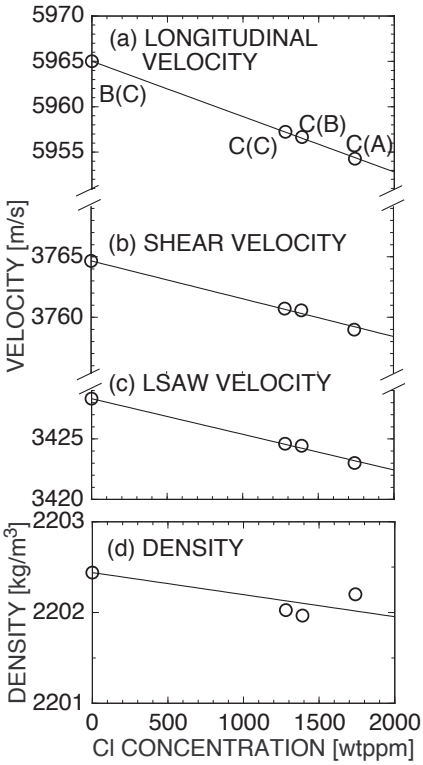


Fig. 2. Cl concentration dependences of acoustic properties of synthetic silica glass specimens.

Table II. Sensitivities and resolutions to fictive temperature and Cl concentration for synthetic silica glasses by acoustic property measurements.

| | $T_{\mathrm{f}}$ | | $C$(Cl) | |
|---|---|---|---|---|
| | Sensitivity | Resolution | Sensitivity | Resolution |
| $V_l$ | 5.99°C/(m/s) | 0.6°C | -164 wtppm/(m/s) | 16 wtppm |
| $V_s$ | -12.7°C/(m/s) | 1.3°C | -320 wtppm/(m/s) | 32 wtppm |
| $V_{\mathrm{LSAW}}$ | -33.4°C/(m/s) | 10°C | -339 wtppm/(m/s) | 102 wtppm |
| $\rho$ | 106°C/(kg/m$^3$) | 11°C | -4116 wtppm/(kg/m$^3$) | 412 wtppm |

measurements of OH concentrations. This work was partially supported by a Grant in Aid for the GCOE Program.

**References**

1. J. Kushibiki et al.: J. Appl. Phys. **87** (2000) 3113.
2. J. E. Shelby: J. Non-Cryst. Solids **349** (2004) 331.
3. H. Kakiuchida et al.: Appl. Phys. Lett. **86** (2005) 161907.
4. J. Kushibiki et al.: IEEE Trans. Ultrason., Ferroelect., Freq. Contr. **49** (2002) 827.
5. J. Kushibiki and M. Arakawa: J. Acoust. Soc. Am. **108** (2000) 564 .
6. K. M. Davis et al.: J. Non-Cryst. Solids **203** (1996) 27.

Proceedings of Symposium on Ultrasonic Electronics, Vol. 29 (2008) pp. 47-48
11-13 November, 2008

# Thermal diffusivities of high polymer transparent films investigated by laser induced thermal wave probing

## レーザ熱波プローブによる高分子透明膜の熱拡散率の推定

Yoshiaki Tokunaga, Hiroyuki Kobayshi †and Koji Aizawa ( Kanazawa Inst. Tech)
得永嘉昭，小林弘幸‡，會澤康治 （金工大）

### 1. Introduction

Recently, remarkable attention of the industrial and academic fields is transiting from characterization of solid material such as a ceramic or a single crystal to characterization of high polymer transparent films such as poly (ethylene terephthalate) (hereafter called PET) ,polyimide （ hereafter called PI ） and poly(vinylidene fluoride) (hereafter called PVDF). Since 1989, we have developed a scanning photo-acoustic microscope (hereafter called SPAM) and studied material characters using it [1-2]. Although our SPAM can be used to the characterization of bulk materials, unfortunately it cannot be done to those of these films [3-5]. The main goal of our present research is to develop a multi-purpose type of laser induced thermal wave microscope (hereafter called LITWM) which can be fully used for these films and bio materials. As a first step to develop, we intend to develop measurement technique of thermal diffusivity of the high polymer transparent film. Actual thermal diffusivity, α, may be different remarkably with a value estimated from physical parameters of film published by maker because it depends strongly on the crystallization temperature, mechanical stress, casting solvent, electric field and other conditions. In this paper we describe the experimental results on values of the α of high polymer transparent films measured by our proposed method.

### 2. Sample preparation and Experimental Setup

Figure 1 shows a photograph of our experimental sample and a principle of measurement, respectively [6]. We employed a carbon material (Touyoutanso Co.Ltd. , ISEM-3) as a black substrate. The representative dimension of the substrate was 1.0cm×1.0cm×0.5cm.

Figure 2 shows an illustration of the experimental setup. A CW laser (Spectra Physics Co. Ltd. model 127) at the wavelength of 632 nm was used as an energy source. The laser power and the beam diameter at the irradiated surface were about 9 mW and 300 μm, respectively. The laser light was modulated by using an acousto-optic modulator (Hoya Co.Ltd, A-100). A microphone (RION Co.Ltd, NC53A) was used for detecting the PA signal. A digital oscilloscope (Iwatsu-Lecroy Co.Ltd, LC6840) was used for the observation of the detected signal and signal processing.

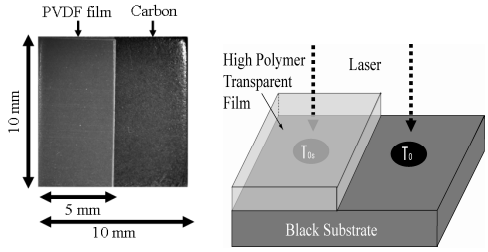


Fig.1 Principle of measurement

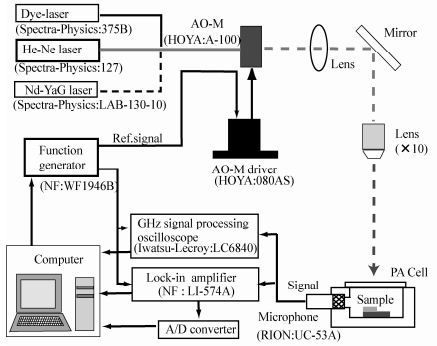


Fig.2 LITW microsocpe

### 3. Experimental results and discussion

Our method has advantage in that the α can be estimated simply by obtaining a relation of phase difference of the LITW signal generated on the substrate with transparent film or without it.

Figure 3 shows an experimental result on a relation of surface temperature, θ, and $\sqrt{f}$ when the 28-μm-thick PVDF film is used. In this case, the $d/\mu_0$ values of 1.2 and 2.0 correspond to modulation frequency of about 49 and 130 Hz, respectively. From a slope of solid line by a least square fitting, we can calculate value of the α and obtain value of $3.9\times10^{-8}$ $m^2/s$. Figure 4 shows an experimental result on a relation between θ and $\sqrt{f}$ in the film with the thickness of 52 μm. In this

---

toklab@mlist.kanazawa-it.ac.jp

case, the modulation frequencies corresponding the thermal diffusion length from $\mu_0$=42 to 26 μm were about 14 to 36 Hz. The value of the α evaluated from a slope of solid line in this region was about $3.4\times10^{-8}$ $m^2/s$.

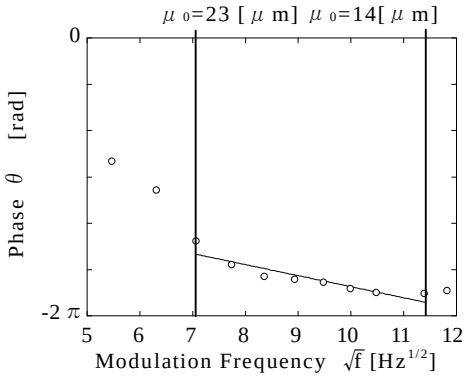


Fig.3 Relation between θ and $\sqrt{f}$ in the 28μm.

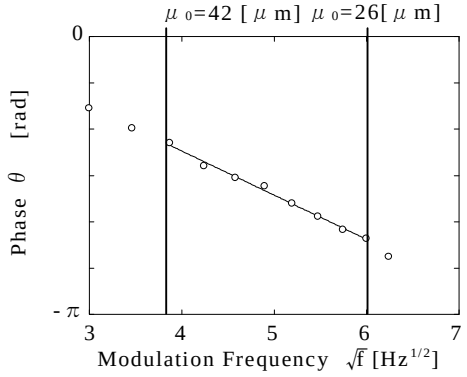


Fig.4 Relation between θ and $\sqrt{f}$ in the 52μm

The measured values of the α in the 28 and 52-mm-thick PVDF film were fairly closed to the predicted value evaluated indirectly from representative parameters of the PVDF polymer published by production maker [7].

Figure 5 shows an experimental result on a relation between θ and $\sqrt{f}$ in the PET film. From this result we could get the $\alpha = 1.25\times10^{-7}$ $m^2/s$. This value was also closed to the predicted one evaluated indirectly from maker's publication parameters [8].

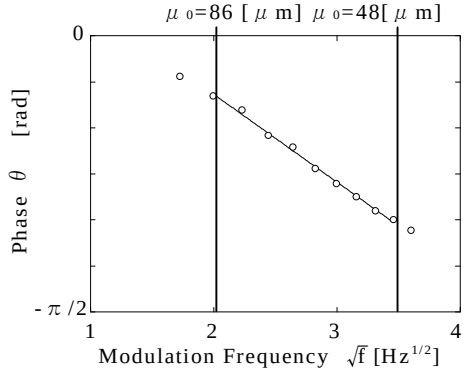


Fig.5 Relation between θ and $\sqrt{f}$ in the PET film

Table I shows representative data on measured films. In this table a symbol " d " represents film thickness of polymer.

Table I. Measured results of α on various films

| film | d[μm] | α [$m^2/s$] | Company |
|---|---|---|---|
| PVDF | 28 | $3.9\times10^{-8}$ | Tokyo Sensor |
| PVDF | 52 | $3.4\times10^{-8}$ | Tokyo Sensor |
| PET | 100 | $1.25\times10^{-7}$ | Teijin Chemicals |
| PI | 25 | $1.29\times10^{-7}$ | DuPont Toray |
| Araldite | 54 | $1.13\times10^{-7}$ | Cemedine |

## 4. Conclusions

We described the experimental results on values of the α of high polymer transparent films such as PVDF, PET, and PI measured by our proposed method.


## Acknowledgements

This work was partially supported by a High-Tech Research Center Project Grant.


## References


1). Y. Tokunaga, A. Minamide, K. Tamura and S. Teraoka: Jpn. J. Appl. Phys. **29**(1990) Suppl 29-1 283

2). Y. Tokunaga and A. Minamide : Jpn. J. Appl. Phys. **31**(1992) Suppl 31-1 149

3). Y. Tokunaga, A. Minamide, K. Tamura and N. Nakada : Jpn. J. Appl. Phys. **32** (1993) 2573.

4). Y. Tokunaga, A. Minamide, K. Tamura and N. Nakada : Jpn. J. Appl. Phys. **33** (1994) 3246.

5). Y. Tokunaga, A. Minamide, and N. Nakada : Jpn. J. Appl. Phys. **34** (1995) 2900.

6). Y. Tokunaga, M. Imai, M. Suzuki and A. Minamide : J. Acoust. Soc. Jpn, **63** No.5 (2007) 262[in Japanese].

7). KYNAR PIEZO FILM TECNICAL MANUAL (1987).

8). K. Yugi : Saturated polyester resins handbook. Nikkan Kogyo Shimbun ,LTD. (1989)233. [in Japanese]

Proceedings of Symposium on Ultrasonic Electronics, Vol. 29 (2008) pp. 49-50
11-13 November, 2008

# Copper precipitation process of thermally aged Fe-Cu alloys evaluated by EMAR method

電磁超音波共鳴法による熱時効 Fe-Cu 合金の Cu 析出挙動評価

Yasuhiro Kamada[1†], Shigehiko Chigusa[1], Toshihiro Ohtani[2], Hiroaki Kikuchi[1] and Satoru Kobayashi[1] ([1] Faculty of Eng., Iwate Univ.; [2]Shounan Insitute of Technology)
鎌田康寛 [1‡], 千種成彦 [1], 大谷俊博 [2], 菊池弘昭 [1], 小林悟 [1] ([1]岩手大工; [2]湘南工科大)

## 1. Introduction

It is known that Cu-rich precipitates are one of the origins of the irradiation embrittlement of nuclear reactor pressure vessels (RPV) steels [1–3]. The clarification of the degradation mechanism and the development of nondestructive evaluation (NDE) techniques are important for prolonging the lifetime of present nuclear power plants. Ultrasonic characterization is one of the candidates of NDE methods and several studies have been reported [4, 5]. Although ultrasonic velocity and attenuation seem to be promising parameters, there has been little discussion on the effect of Cu precipitation. Moreover, most of the previous studies were carried out using conventional ultrasonic techniques using a piezoelectric transducer that inherently includes contact problems. In order to clarify the irradiation effects, precise measurement is necessity to suppress data scatter and improve reliability. Recently, an electromagnetic acoustic resonance (EMAR) method, a contactless measurement, attracts much attention in precise ultrasonic characterization [6, 7]. The purpose of this study is to investigate the copper precipitation process of thermally aged Fe–Cu model alloys, simulating the irradiation embrittlement of RPV steels, by EMAR method.

## 2. Experimental Procedure

The specimens of Fe–1wt.%Cu model alloy were quenched from 1123 K for preparing the supersaturated solid solution state. They were thermally aged at 773 K and the aging time was systematically varied. In this study, plate-shaped specimens ($L_1 \times L_2 \times L_3$ = 12.1 mm × 11.5 mm × 2.0 mm) were used. **Figure 1** shows the setup for EMAR measurement and the specimen orientations. The specimen is inserted into the exciting and detecting coils located between the magnets. In the case of ferromagnetic metals, elastic waves are excited by dynamic magnetic fields from an RF burst current through the magnetostriction mechanism [6]. The signal of the excited vibration was detected by the coil and pre-amplified. Amplitude and phase information of the signal were acquired by a personal computer through analog superheterodyne processing. All the above measurements were carried out using a RITEC RAM system at room temperature. For another series of specimens, the dependence of hardness and conductivity on aging time were also measured at room temperature.

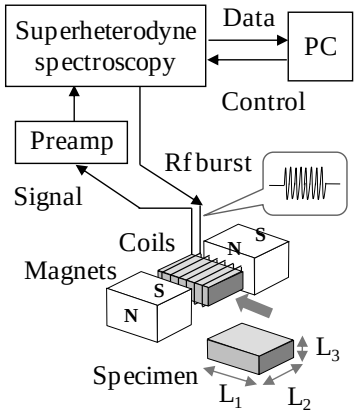


Fig. 1 Schematic representation of the measurement setup.

## 3. Results and Discussion

**Figure 2** shows the aging time dependence of the Vickers hardness [8], conductivity, and a typical resonant frequency of the Fe–1wt.%Cu specimen. Hardness of the alloy initially increased with increasing aging time, but started to decrease after $10^3$ min aging (Fig. 2 (a)). This peaking trend was directly caused by the change of Cu precipitates state, formation, growth, structural transformation, and coarsening [8, 9]. On the other hand, conductivity of the alloy gradually increased with increasing aging time and approached to the value of pure iron at the longer aging time (Fig. 2 (b)). It has been reported that the conductivity of Fe–Cu alloys in a solid-solution state decreases linearly with Cu content due to the electron scattering by Cu solute atoms [10]. This characteristic suggests that the observed change of conductivity would be a result of matrix solute depletion by thermal aging. The resonant frequency also increased with increasing aging time, and did not decrease even

after long-time aging (Fig. 2 (c)). This trend is similar to the change of conductivity caused by a depletion of Cu solute atoms in the matrix. The resonant frequency is related to the elastic constant of the specimens. Therefore, the similarity of the trend indicates that the elastic constant of aged Fe–Cu alloys correlates to the state of solute atoms, not to that of precipitates. According to the first principles calculation, the elastic constant of bcc Fe–Cu alloys are smaller than that of bcc Fe, and it increases with decreasing Cu content [11]. Therefore, the observed behavior of resonance frequency is attributable to the increase of the elastic constant of the matrix due to Cu solute depletion during copper precipitation process.

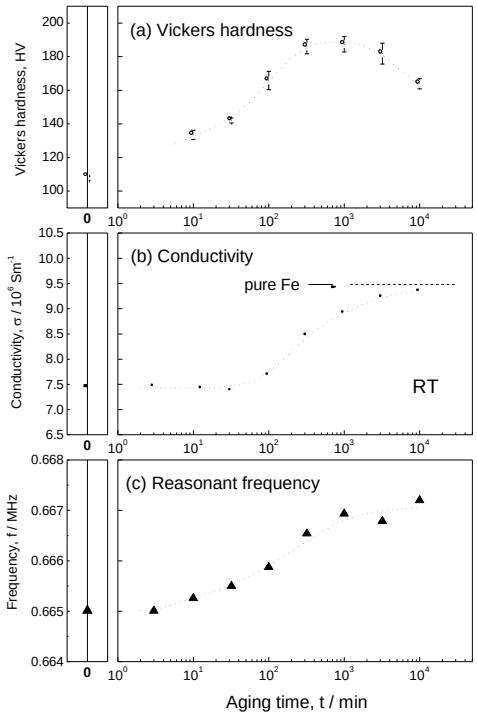


Fig. 2 Aging time dependence of the Vickers hardness, conductivity and typical resonant frequency.

Attenuation coefficients, $\alpha$, were evaluated from the analysis of the ring-down curves, and the dependence of attenuation coefficient against aging time was also investigated. A clear trend was not observed, but it seemed to show a slightly increasing behavior, which would be due to the increase of mobile dislocation density [12] and/or the reduction of Cu solute atoms that enhances the movement of each mobile dislocation. Further studies are desirable to understand the details.

The present study shows that the solute depletion during copper precipitation processes would change the elastic constant of model alloys, which suggests the potential of EMAR measurement as a tool for NDE of irradiated RPV steels especially on solute depletion.

## 4. Conclusion

Precipitation process of thermally aged Fe–1wt.%Cu alloys were evaluated by the EMAR method. The aging time dependence of resonance frequencies showed an increasing behavior, which is different from the peaking trend of the hardness. This phenomenon relates to the increase of elastic constant originated from the depletion of Cu solute atoms in matrix, not from the formation of Cu precipitates. This study suggests a possibility of the application of the EMAR method for NDE of the matrix state of irradiated RPV steels.


## Acknowledgment

This work was supported in part by a Grant-in-Aid for Young Scientists (A), No.19686058, from the Ministry of Education, Culture, Sports, Science and Technology of Japan. The authors would like to thank Dr. H. Ogi for useful discussions.


## References


1. G. R. Odette and G. E. Lucas, Radiat. Eff. Defects Solids, **144** (1998) 189.
2. K. Fukuya, K. Ohno, H. Nakata, S. Dumbill, and J. M. Hyde, J. Nucl. Mater. **312**, (2003) 163.
3. Y. Nagai, T. Toyama, Y. Nishiyama, M. Suzuki, *et al*, Appl. Phys. Lett. **87** (2005) 261920.
4. T. Ishii, N. Ooka, T. Hoshiya, H. Kobayashi, J. Saito, *et al*, J.Nucl.Mater. **307-311**, (2002) 240.
5. A.L. Hiser and R.E. Jr Green, Mat. Res. Soc. Symp. Proc., **503**, (1998) 175.
6. M. Hirao and H. Ogi, *EMATs for Science and Industry*, (Kluwar Academic Publishers, Boston, 2003)
7. T. Ohtani and K. Takei, J. Soc. Mat. Sci., Japan, **54**, (2005) 607.
8. Y. Kamada, D. G. Park, S. Takahashi, *et al*, IEEE Trans. Magn. **43** (2007) 2701.
9. A. Deschamps, M. Militzer, and W. J. Poole, ISIJ International, **41** (2001) 196.
10. M. H. Mathon, A. Barbu, F. Dunstetter, F. Maury, *et al*, J. Nucl. Mater. **245** (1997) 224.
11. J. Z. Liu, A. van de Walle, G. Ghosh and M. Asta, Phys.Rev. B, **72**, (2005) 144109.
12. H. Ogi, H. Ledbetter and S. Kim, Metall. Mater. Trans. A, **32A** (2001) 1671.

Proceedings of Symposium on Ultrasonic Electronics, Vol. 29 (2008) pp. 51-52
11-13 November, 2008

# Non-Radiative Investigation of Photodecomposition of Poly(di-hexyl silane) Thin Films by Using the Piezoelectric Photo-Thermal Spectroscopy

# 非発光遷移検出によるポリジヘキシルシランの光分解性評価

Atsuhiko Fukuyama[1†], Takahiro Kuroki[1], Kentaro Sakai[2], Tomohisa Iwamoto[3], Shoji Furukawa[3] and Tetsuo Ikari[1] ([1] Facult. Eng., Univ. of Miyazaki; [2] CRC, Univ. of Miyazaki; [3] Graduate School of Computer Science and Sys. Eng., Kyushu Ins. Tech.)
福山敦彦[1], 黒木貴裕[1], 境健太郎[2], 岩本朋久[3], 古川昌司[3], 碇哲雄[1]（[1]宮崎大 工; [2]宮崎大 産連セ, [3]九工大 情報工学研究院）

## 1. Introduction

Polysilanes, as one dimensional semi-conductors, have attracted much attention as new materials for future optical and electonic devices due to their unique properties resulting from the delocalization of σ electrons along the silicon backbone. For example, polysilanes exhibit an ultraviolet (UV) absorption assigned to a σ-σ* electronic transition, its wavelength and intensity are strongly related to the conformation of the silicon backbone.[1)] Among them, Poly(di-*n*-hexyl silane) (PDHS) has been investigated by many researchers because it shows the phase transition above room temperature with the thermochromism. We have succesfully described the crystal structure of PDHS, silicon backbone has an all-*trans* conformation, whereas the *n*-hexyl substituents have an asymmetical conformation.[2)] However, a photodecomposition caused by the UV-light irradiation in air, has not been understood yet.

In this study, we have investigate the photodecomposition mechanism from the electron non-radiative recombination view point. We then adopted the piezoelectric photo-thermal (PPT) spectroscopy.[3)] By monitoring the non-radiative electron recombination, the PPT is a high-sensitive method for investigating the optical property especially for the very low absorption region. From the UV-light irradiation time dependent measurement in vacuum, the photodecomposition mechanism are discussed.

## 2. Experimental Procedures

PDHS thin films were prepared by using spin coating method. After the 2 wt.% PDHS solution was placed on the quartz glass substrate, substrate was then rotated at 500, 1000, and 1500 rpm for 10 s followed by additional rotation at 2000 rpm for 30 s, respectively. The film thickness were measured to be 211, 178, and 142 nm by using a contact type film thickness meter, respectively.

---

a-fukuyama@cc.miyazaki-u.ac.jp

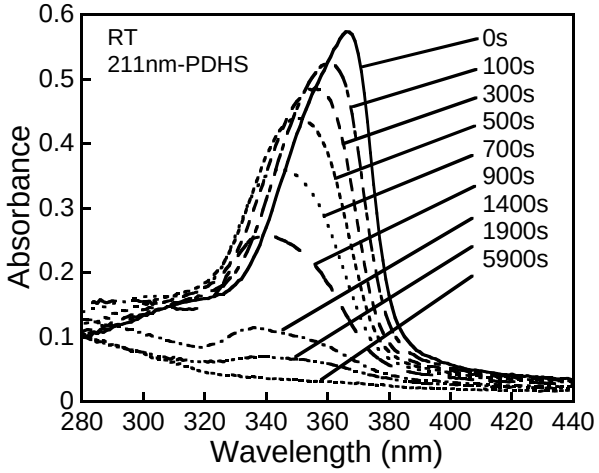


Fig. 1 Effects of UV-light irradiation on the OA spectrum of 211-nm-thickness sample

A 150-W Xe lamp attached with a monochromator was used as the probing light (20 μW/cm$^2$ at 380 nm) for the convensional optical absorption (OA) and PPT measurements. In the PPT measurements, the probing light was focused on the substrate side and the PZT detector was directly attatched to PDHS film surface of the sample. Details of the PPT experimental procedure and setup have already been reported.[3)] All the measurements were performed in vacuum at room temperature. When the effects of UV-light irradiation were measured, the intensity of the probing light was set at 70 μW/cm$^2$ at 380 nm to cause the photodecomposition of PDHS.

## 3. Results and Discussion

**Figure 1** shows the effects of UV-light irradiation on the OA spectrum of 211-nm-thicnkess sample. Irradiation time was defined as the time during the probing light of 350-380 nm were irradiated on the sample. A strong absorption peak at about 370 nm and a broad absorption band around 320 nm that appeared in the 0-s spectrum come from the σ-σ* electron transition in the all-*trans* and *helical* conformations, respectively.[1)]

With increasing the UV-light irradiation time, decreasing their intensities and blue-shifts were observed. These behaviors were caused by the decrease of grain size of PDHS crystal, or decrease of the effective length of the Si backbone chain.[4] Same behaviors were also observed in 178- and 142-nm-thickness samples.

**Figure 2** shows the effects of UV-light irradiation on the PPT spectrum of same sample. As in the case for OA measurements, a strong peak at about 370 nm was also observed, this is caused by the electron non-radiative recombination of σ-σ* transition in the all-*trans* conformation. Most important finding was that the PPT signal around 290 nm increased after irradiation. This peak is due to σ-σ* electron transition in the *helical* conformation. We have already reported an increase of optical absorption around 267 nm in poly(di-methyl silane) thin film after UV-light irradiation.[5] We also concluded that this caused by an increase of Si-O bonds due to the oxidization.

To investigate Si-O bonds, we measured the FTIR spectra from 1500 to 4000 $cm^{-1}$ before (0 s) and after (5900 s) the UV-light irradiation. Results are shown in **Fig. 3**. Unfortunately, an absorption of quartz glass substrate hindered the measurement of Si-O bond absorption about 1050 $cm^{-1}$. However, since all the measurements in the present study were carried out in vacuum, the possibility of the oxidization of film may be very low.

As shown in Fig. 3, a fine structured absorption around 2800 $cm^{-1}$ was observed after irradiation, this is due to C-H bonds.[6] To increase the C-H bonds, Si-C bond between backbone and side chain or C-C bond in the side chain group should be cut off. In this situation, Si-C bond having lower binding energy is a candidate for cut by the UV-light irradiation. It seems reasonable to suppose that the Si dangling bonds (DB) was formed as a result of cut the Si-C bond by the UV-light irradiation.[7] In general, non-radiative recombination provability via DB is high, this may provide an increase of the PPT signal intensities corresponding to σ-σ* transition in the *helical* conformation.

To conclude, effects of the UV-light irradiation in vacuum on the OA, PPT, and FTIR spectra of PDHS were investigated. In addition to cut of Si-Si main chain, a cut of Si-C bond was suggested. This may yielded a formation of DB resulting in the increase of PPT signal around 290 nm.

**Acknowledgment**
This work was supported in part by The Iwatani Naoji Foundation's Research Grant and by The Saneyoshi Scholarship Foundation.

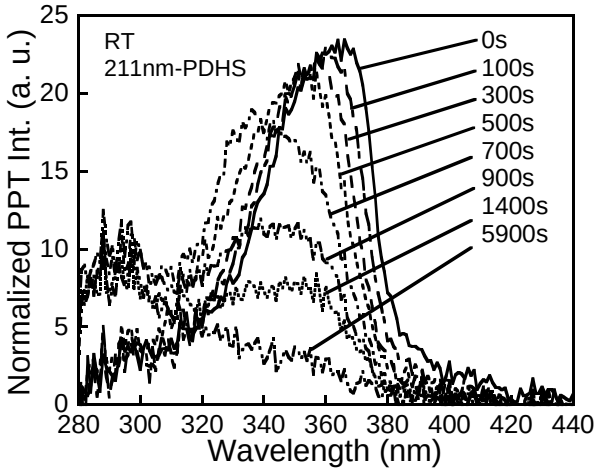


Fig. 2 Effect of UV-light irradiation on the PPT spectrum of 211-nm-thickness sample

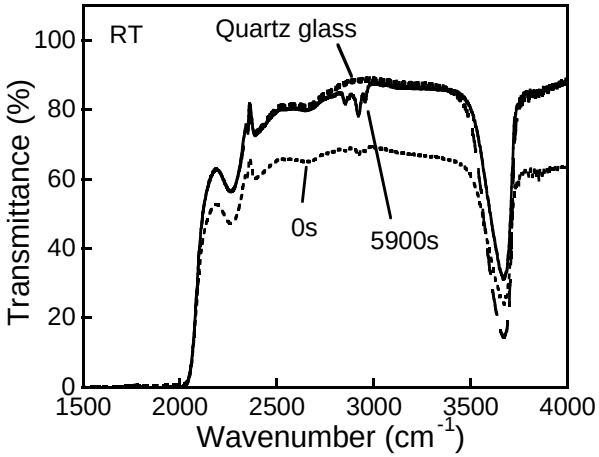


Fig. 3 FTIR spectra before and after UV-light irradiation

**References**

1. R. D. Miller and J. Michl: Chem. Rev. **89** (1989) 1359.
2. K. Takeuchi and S. Furukawa: J. Phys.: Condens. Matter **5** (1993) L601.
3. T. Ikari and A. Fukuyama: *Progress in Photothermal and Photoacoustic Science and Technology, Vol. IV*, ed. A. Mandelis and P. Hess (SPIE, Washington, 2000) p. 145.
4. S. Furukawa and H. Ohta: Thin Solid Films **438-439** (2003) 48.
5. H. Ohta, T. Takamoto, T. Yasuda and S. Furukawa: Thin Solid Films **449** (2006) 129.
6. N. Ostapenko, N. Kotova, V. Lukashenko, G. Telbiz, V. Gerda, S. Suto and A. Watanabe: J. Lumin. **112** (2005) 381.
7. F. Schauer, I. Kuřitka, P. Sáha, S. Nešpůrek, and S. Lipson: J. Non-Cryst. Solids **352** (2006) 1679.

Proceedings of Symposium on Ultrasonic Electronics, Vol. 29 (2008) pp. 53-54
11-13 November, 2008

# Frequency characteristics of the polyurea ultrasonic variable-line-focus-beam-transducer

ポリ尿素可変線集束トランスデューサの周波数特性

Takahiro Aoyagi†, Marie Nakazawa and Kentaro Nakamura (Tokyo Inst. of Tech.)
青柳貴洋†，中澤麻梨江，中村健太郎（東工大）

## 1. Introduction

Polyurea piezoelectric polymer films can be easily fabricated by evaporative polymerization through a complete dry process.[1] The authors have studied the applications of polyurea piezoelectric films such as ultrasonic transducers,[2] a film-shaped earphone[3] and a three-axis-motion sensor.[4] For the application of the ultrasonic transducer, the authors have proposed the variable-line-focus-beam-transducer to measure surface acoustic wave velocities,[5] and theoretically analyzed the radiated ultrasonic beam[6] as like in the V(z) curve method.[7] The calculated surface acoustic velocity has good agreement with measured one[8),9]. However, the frequency characteristics of the polyurea transducer and V($W$) curve were not described before. In this report, the detail of the polyurea film and the frequency characteristics of the V($W$) curve are described.

## 2. Characteristics of the polyurea film ultrasonic transducer.

**Figure 1** shows the geometry of the polyurea film transducer. The top aluminum (Al) electrode (thickness, 3.3 μm), polyurea (PU) piezoelectric material (thickness, 3.5 μm), and bottom aluminum electrode (thickness 1.7 um), were deposited on a polyimide (PI) film (thickness, 25 μm). The active region of the PU film where the electric field is applied is confined to a rectangle of 2 mm×3 mm area.

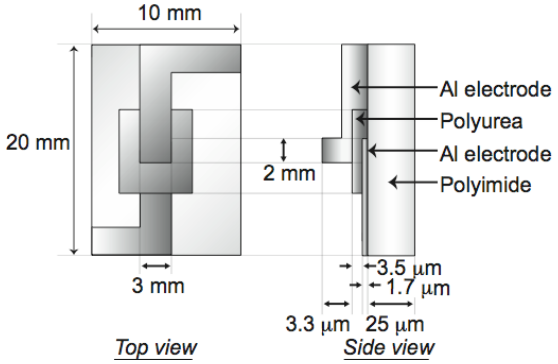


Fig. 1 Geometry of a polyurea ultrasonic transducer.

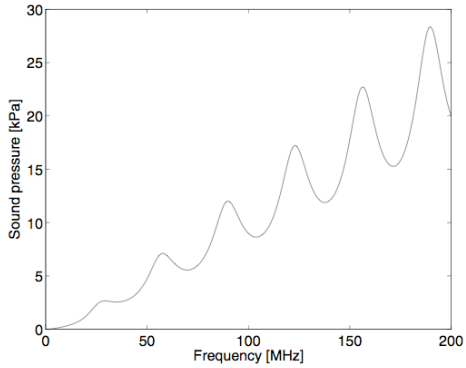


Fig. 2 Frequency characteristics for sound pressure of the water loaded polyurea ultrasonic transducer.

**Figure 2** shows frequency characteristics for sound pressure of the transducer when it is loaded with the water. The sound pressure is analyzed by an equivalent circuit of a Langevin type vibrator[10]. As shown in the figure, resonance frequencies are obtained at about 30 MHz intervals. The resonance frequency of the polyurea layer shown in the Fig. 1 is very high, such as GHz order. Essentially, the principle of the transducer is a Langevin type vibrator that has four layers. Thus, the transducer has multiple thickness resonance characteristics. In this report, V($W$) curves of frequencies 30, 60, and 120 MHz are theoretically calculated.

## 3. Measurement system

**Figure 3** shows the geometry for the surface acoustic wave velocity measurements system. Movable fixtures buckle the transducer to a curved shape so that a focus beam is radiated from the transducer. In this report, the transducer curvature is assumed to the sinusoidal shape described below.[6]

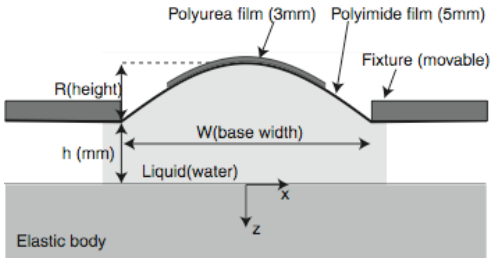


Fig. 3 Geometry of the surface acoustic wave velocity measurement.

$$y = -R\sin(\frac{\pi}{W}x) \qquad (1)$$

Where $x$ and $y$ are coordinates of the transducer surface, $W$ is an interval of the movable fixtures, $R$ is the curve height that depends on $W$. A distance between the transducer curve base and the specimen varies from 0.1 mm to 0.8 mm. The water fills between the transducer and the specimen. The radiated beam reflects on the specimen surface, while some parts of the radiated wave excites the leaky surface acoustic wave on the specimen-water boundary. By measuring the transducer output for each width $W$, we can observe the ripple caused by the interference between the reflected wave and the radiation of leaky surface acoustic wave. The surface acoustic wave velocity can be estimated by the ripple period and amplitude change.

## 3. Numerical calculations of the surface acoustic velocity

**Figure 4** shows calculated responses for several frequencies using the calculation method described in ref. 6. The height $h$ is 0.5 mm. The leaky surface acoustic wave velocity is assumed 3000 m/s. A solid line shows the case that there is no surface acoustic wave. Dotted lines show the cases of frequencies 30, 60, and 120 MHz. Amplitude of each curves are normalized by the peak value of without-LSAW case for each frequencies. The ripples caused by interference are observed. Locations and amplitudes of the ripple are varied depending on the frequency. The ripple of the V($W$) curve decreases as the frequency increases, and the number of the ripple increases as the frequency increases.

**Figure 5** shows a calculated V($W$) curves for 120 MHz. The height $h$ is 0.1 mm. The solid line shows the without-LSAW case. Dotted lines show the case LSAW velocity $v_{LSAW}$ is 2500, 3000, 4000 m/s respectively. As shown in the figure, locations of the peak of ripples vary with $v_{LSAW}$.

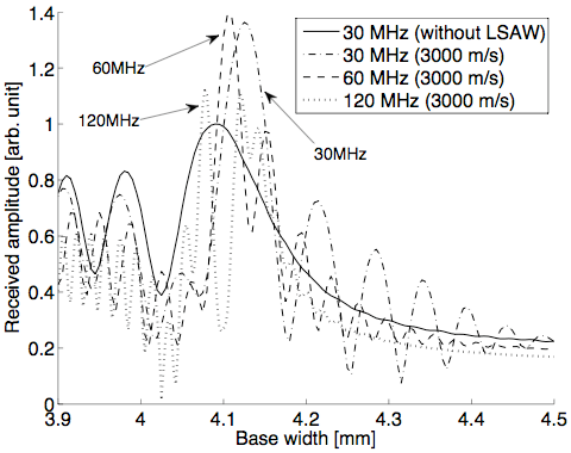


Fig. 4 Frequency characteristics of V($W$) curve ($h$=0.5 mm, Frequency=30, 60, 120MHz, $v_{LSAW}$=3000 m/s).

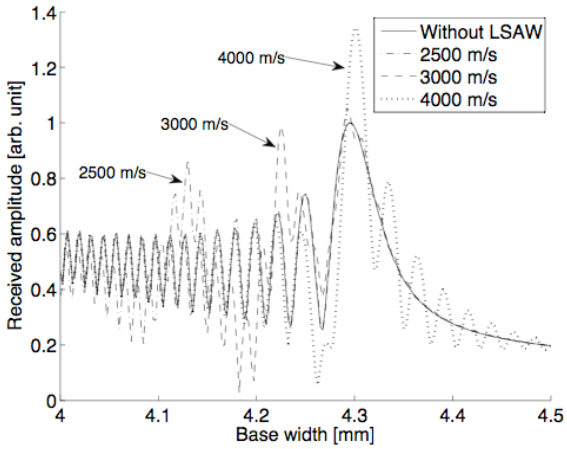


Fig. 5 V($W$) curve for several LSAW velocities ($h$=0.1 mm, Frequency=120MHz, $v_{LSAW}$=2500, 3000, 4000 m/s).

## 4. Conclusion

In this report, we presented the frequency characteristics of the surface acoustic wave velocity measurement using a polyurea piezoelectric variable-line-focus-beam-transducer.
The interference ripple caused by the leaky surface acoustic wave radiation varies as the input frequency and the LSAW velocity. Optimal transducer size and frequency for measurements should be carried out for future study.

## References


1. M. Iijima, S. Ukishima, K. Iida, Y. Takahashi and E. Fukuda : Jpn. J. Appl. Phys. **34** (1995) L65.
2. M. Nakazawa, M. Tabaru, K. Nakamura and S. Ueha : Jpn J. Appl. Phys. **46** (2007) 4466.
3. M. Nakazawa, K. Nakamura and S. Ueha : IEICE Tech. Rep. EA2006-40 (2006) [in Japanese].
4. M. Tabaru, M. Nakazawa, K. Nakamura and S. Ueha : Jpn J. Appl. Phys. **47** (2008) 4044.
5. M. Nakazawa, T. Kosugi, A. Maezawa, K. Nakamura and S. Ueha : Proc. Spring Meet. Acoust. Soc. Jpn, 2006, p. 973 [in Japanese].
6. T. Aoyagi, M. Nakazawa, K. Nakamura and S. Ueha : Jpn. J. Appl. Phys. **46** (2007) 4486.
7. J. Kushibiki and N. Chubachi : IEEE Trans. Sonics Ultrason. **32** (1985) 189.
8. T. Aoyagi, M. Nakazawa, M. Tabaru, K. Nakamura and S. Ueha: Proc. Symp. Ultrason. Electron, **28** (2007) 353.
9. T. Aoyagi, M. Nakazawa, M. Tabaru, K. Nakamura and S. Ueha: Proc. IEICE general conf. A-9-3 (2007) [in Japanese].
10. K. Nakamura, et al.: Chouonpa (Ultrasonics) (Corona publishing, Tokyo, 2001) p. 54 [in Japanese].

Proceedings of Symposium on Ultrasonic Electronics, Vol. 29 (2008) pp. 55-56
11-13 November, 2008

# Optical observation of Lamb Wave in Metal Plate Having a Stepped Thickness
# 光学的方法を用いた段付き平板を伝搬する Lamb 波の測定

Ryota Kudo ‡ and Kazuhiko Imano (Faculty of Engineering and Resource Science, Akita University)
工藤良太‡，今野和彦(秋田大・工学資源)

## 1. Introduction

Propagation characteristic of Lamb wave is affected by both the thickness of material and frequency.[1),2)] The propagation behaviors in the plate having different thicknesses might be useful to obtain the defect information, however their behaviors are very complex. Theoretical research of the propagation of Lamb wave in plate having variation thickness have been presented.[3)] On the other hand, there are few number of experimental researches have been reported. The propagation characteristic of Lamb wave having different thicknesses is very important for the nondestructive testing to understand the properties such as flaw, hole, crack and abrasion.

In this paper, the propagation characteristic of Lamb wave which propagating in aluminum plate having a step variation of thickness is measured by an optical observation method.

## 2. Propagation characteristic of Lamb wave

The propagation modes of Lamb wave depend on the thickness of materials and frequency of the ultrasonic waves. The propagation characteristic of Lamb waves can be theoretically calculated by the Rayleigh-Lamb equation. The dispersion curves of phase velocity $c$ and group velocity $c_g$ in aluminum plate ($c_L$=6410 m/s, $c_T$=3040 m/s) as shown in **Figs. 1(a)** and **1(b)**, respectively. Lamb wave can be efficiently excited when the incident angle satisfies the phase matching condition. This angle, which is critical angle $\theta_c$, is calculated from the Snell's law as,

$$\theta_c = \sin^{-1}\frac{c_w}{c} \quad , \qquad (1)$$

where $c$ is the phase velocity of Lamb wave, and $c_w$(= 2500 m/s) is the velocity of the wedge. The dispersion curves of the critical angle in aluminum plate as shown in **Fig.1(c)**. Thickness $d$ and frequency $f$ used in this study are 1.0 mm and 2.0 MHz, respectively. In case of $fd$ = 2.0 MHz mm, the incidence angle $\theta_c$ was set to 72°(A0-mode), to launch the A0-mode Lamb wave in the aluminum plate.

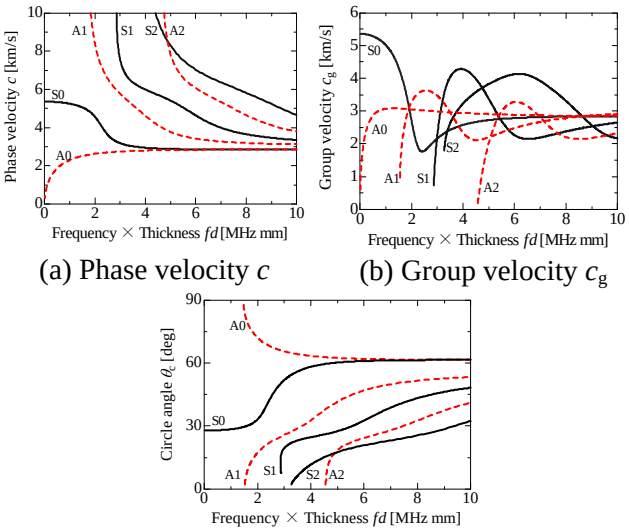


(a) Phase velocity $c$ (b) Group velocity $c_g$

(c) Critical angle $\theta_c$

Fig.1 Dispersion curves of Lamb wave in aluminum.

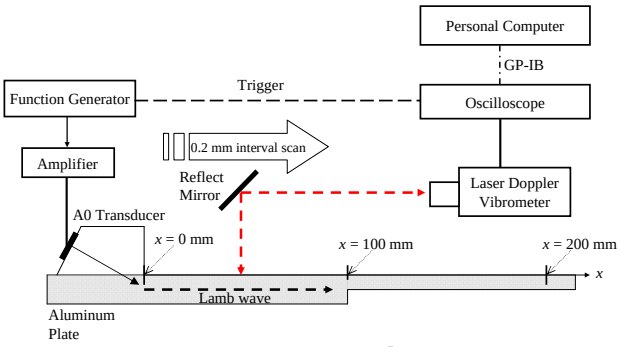


Fig.2 Experimental setup.

## 3. Experimental Method and Results

Lamb wave measurement system is shown in **Fig.2**. Transmission signal of 2.0 MHz, 1.0 Vp-p and 10 cycles burst sin wave were applied to the A0-mode transducer. The laser vibrometer is scanned along the propagation direction of Lamb wave from $x$ = 0mm to $x$ = 200.0 mm at intervals of 0.2 mm. In each point the surface vibrations of Lamb waves are measured. The received vibrating

---

imanoken@ee.akita-u.ac.jp

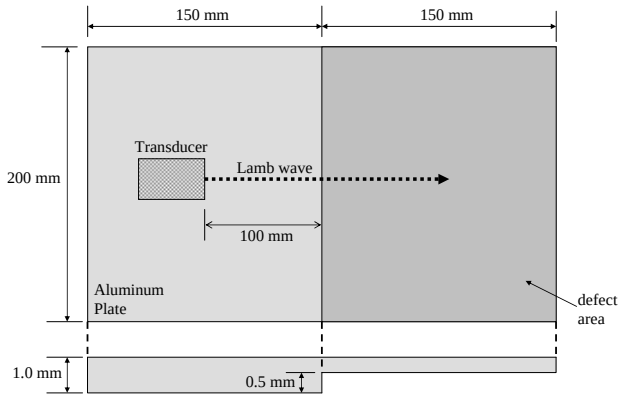


Fig.3 Aluminum plate used in this experiment.

waveforms are digitized and fed to a personal computer via a general purpose interface bus (GPIB).

The geometry of the aluminum plate used in this study is illustrated in **Fig.3**, which has a step of 0.5 mm at the center of plate. Two dimensions distribution of propagation distance *x* - time *t* of the waveform received by the measurement system is shown **Fig.4**.

The *k-f* charts using two dimension Fourier transform of *x-t* data are shown **Figs.5(a)** and **5(b)**, respectively. The peak of *k-f* distribution was corresponded to the dispersion curve of the A0-mode in *d* = 1.0 mm. On the other hand, the peaks were also corresponded to the dispersion curves both A0-mode and S0-mode in *d*=0.5 mm. The results were implied that A0-mode Lamb wave converted to the S0-mode, in different thickness area. The peak values of the spectrum of each mode are shown in **Fig.6**. The amplitude of A0-mode is decreased by approximately 5 dB and that of S0-mode is conversely increased by approximately 12 dB between 45 and 50 μs, so that mode conversion would be occurred around the step of the aluminum plate.

## 4. Conclusions

A0-mode Lamb wave converts to S0 mode in aluminum plate having a stepped thickness was observed. The mode conversion from A0-mode to S0-mode would be occurred by the thickness change, so that the mode properties of Lamb wave become useful index to find the defect such as abrasion.

## References

1.K.Horie *et al*.: Jpn. J. Appl. Phys. **44** (2005) 4333.
2.M.Watanabe *et al*.: Jpn. J. Appl. Phys. **45**(2006) 4565.
3.P.Marical *et al*.: Ultrasonics **47**, (2007)1.

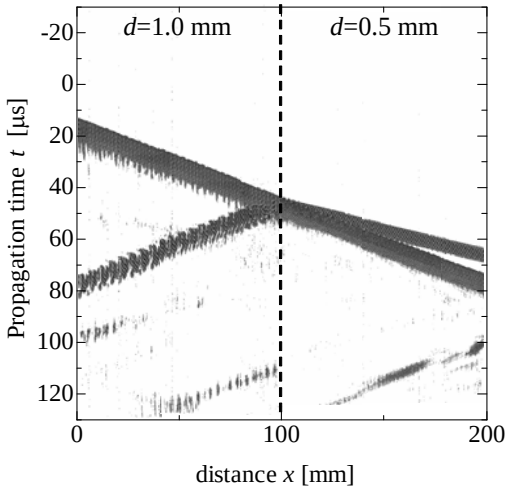


Fig.4 *x-t* distribution.

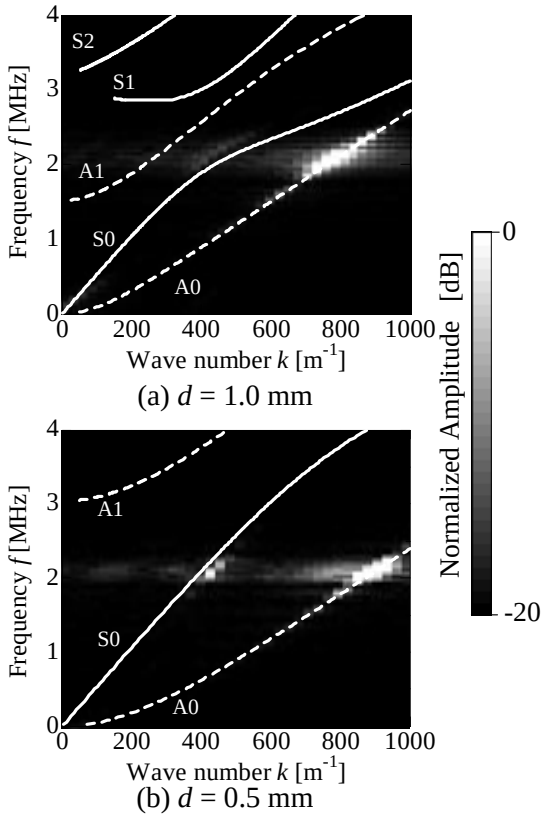


Fig.5 *k-f* image lapped dispersion curves.

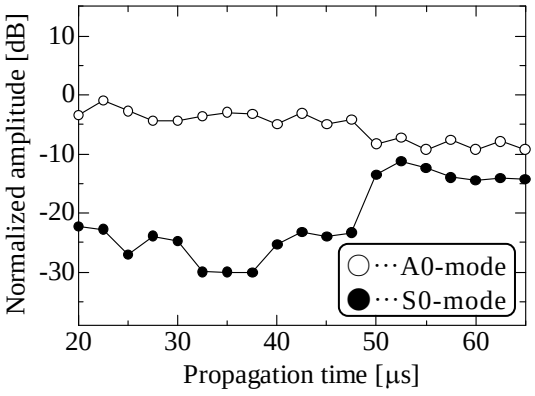


Fig.6 Time - spectrum characteristic.

Proceedings of Symposium on Ultrasonic Electronics, Vol. 29 (2008) pp. 57-58
11-13 November, 2008

# Evaluation of Acousto-optic Effect in Underwater Ultrasonic Pressure Measurement Using an Optical Interferometer
# 光干渉計を用いた水中超音波音圧計測における音響光学効果の評価

Youichi MATSUDA, Masahiro YOSHIOKA and Tsuneo KIKUCHI (NMIJ/AIST)
松田洋一，吉岡正裕，菊池恒男 （産総研）

## 1. Introduction

A combination of a homodyne interferometer and a pellicle normally arranged to the ultrasonic propagation direction, featuring non-contact and a small active element, has been adopted for absolute pressure measurement [1,2] and visualization [3,4] of underwater ultrasound. Because the interferometer probe beam transverses and interacts with ultrasound, the interferometer outputs include both pellicle displacement and the change in the refractive index caused by the ultrasound. The two effects have been evaluated quantitatively using theoretical analyses [1,3,4], but only for far-field ultrasound. Consequently, evaluation of the two effects for near-field or focused ultrasound is necessary. For this study, we developed a system to discriminate the two effects. Measurement results in a far-field ultrasound for system validation and in a small amplitude focused ultrasound are described herein.

## 2. Experimental

In this experiment, a tone burst ultrasound from a transducer is detected using a combination of a path-stabilized Michelson interferometer and a pellicle stretched over a circular frame in water. A 1-μm-thick polyester film with a 300 nm gold coating is used as the pellicle, which is acoustically transparent and optically reflective. Generated ultrasound is detected at almost identical positions using two methods—a transmission method and a reflection method—to discriminate ultrasonic displacement from the acousto-optic effect. Figure 1 depicts a sketch of the two methods. Because only the pellicle is arranged in the transmission method, ultrasound travels in water, passes through the pellicle, and interacts with the probe beam of the interferometer. Both ultrasonic displacement and the acousto-optic effect are observed there. Meanwhile, because an air layer is introduced behind the pellicle in the reflection method, ultrasound travels in water, is almost perfectly reflected at the pellicle–air interface; it does not interact with the interferometer probe beam. Only ultrasonic displacement is observed there. Comparing changes of the optical path length observed using the two methods, the acousto-optic effect was extracted.

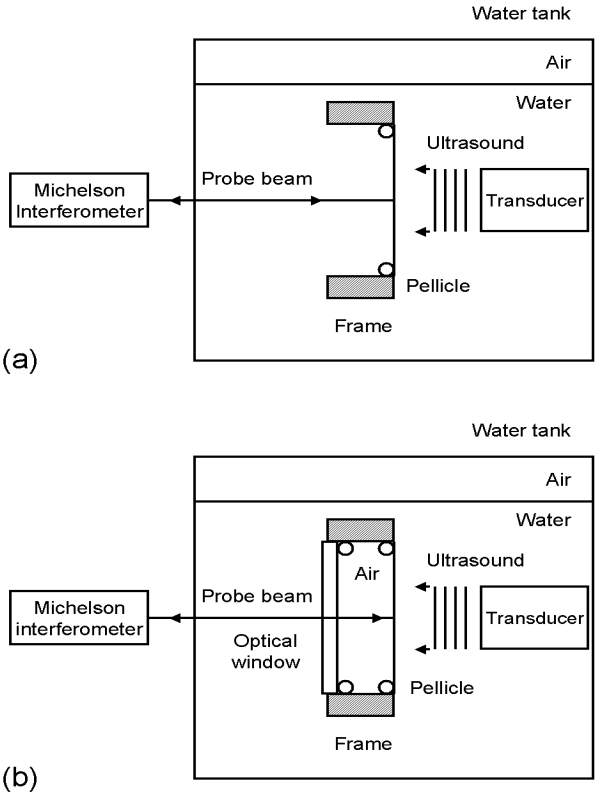


Fig. 1 Two methods for underwater ultrasound detection using a Michelson interferometer: (a) Transmission method and (b) Reflection method.

## 3. Result for far-field ultrasound

For this study, the effective refractive index of water using far-field ultrasound is measured and compared with the theoretical value for the developed system validation. A planar transducer with a radius $a$ of 6.3 mm generates tone burst ultrasound. Ultrasonic frequency $f$ is 1–10 MHz. The transducer-detection point distance $z$ is approximately 37 cm i.e. the normalized distance $S = z\lambda/a^2$ is 1.5–15. Here, $\lambda$ is ultrasonic wavelength. Sound pressures at the

detection point with no pellicle are 5–80 kPa for water temperature of 22±0.5°C. The effective refractive index $n^*$ is given as

$$n^* = \frac{2 \times OP_T(f) \times t_R(f)}{OP_R(f) \times t_T(f)}, \quad (1)$$

where $OP_T(f)$ and $OP_R(f)$ are changes of the optical path length obtained using the interferometer, and $t_R(f)$ and $t_T(f)$ are the displacement transmission coefficients through the pellicle. Subscripts T and R respectively represent the values for the transmission method and the reflection method. The theoretical effective refractive index $n^*$ for a light wavelength of 633 nm at 20°C is $n^* = 1.009 \pm 0.003$ and is expected to vary by 0.01% for temperatures of 15°C to 25°C [1,4]. Figure 2 portrays the experimental results. The standard deviations of four independent measurements are about 1%. Measured values were 1.008–1.010, except for those at 7 MHz, 9 MHz, and 10 MHz. Furthermore, differences between these three values and the theoretical value are within 1%. The measured values are roughly equivalent to the theoretical ones.

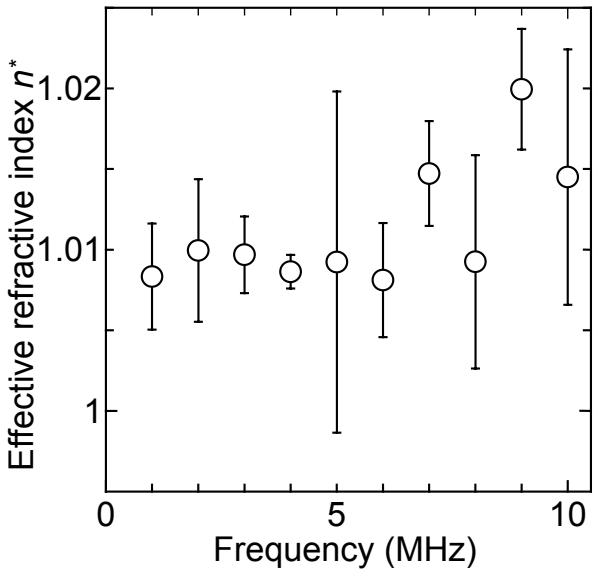


Fig. 2 Measured effective refractive index for far-field ultrasound (Light wavelength = 633 nm, Water temperature = 22.0°C).

## 4. Results for focused ultrasound

The effective refractive index of water for a small amplitude focused ultrasound near the focal point is measured. A 6.3 mm radius point focusing transducer with a 10 cm focal length generates tone burst ultrasound. The transducer-detection point distance $z$ is approximately 10 cm. Sound pressures at the detection point are 5–200 kPa. Ultrasonic frequency $f$ and water temperature are identical to those described in the previous section. Results confirmed that the coefficients of $t_R(f)$ and $t_T(f)$ are regarded as the same as those for the previous section. Figure 3 presents experimental results of eight independent measurements. Measured values were 1.000–1.008; their standard deviations are about 1% at frequencies of 1–5 MHz. However, measured values changed rapidly; their standard deviations increased at frequencies of 6–10 MHz, probably because of the increasing complexity of a focused ultrasonic field near the focal point at high frequencies.

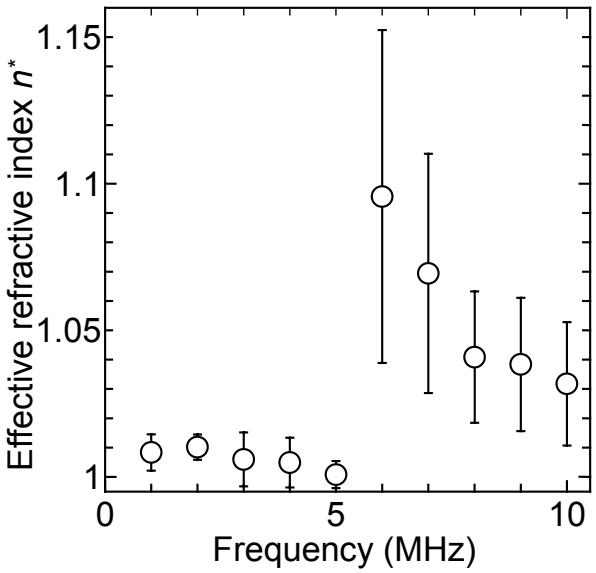


Fig. 3 Measured effective refractive index for small amplitude focused ultrasound (Light wavelength = 633 nm, Water temperature = 22.0°C).

## 5. Conclusion

A system to discriminate ultrasonic displacement from the acousto-optic effect was developed. The measured effective refractive index of water for far-field ultrasound was roughly equivalent to the theoretical value. The acousto-optic effect in a small amplitude focused ultrasound was also evaluated using the system.

## References

1. D. R. Bacon: NPL Report (AC 109) (1986).
2. T. J. Esward and S. P. Robinson: IEEE Trans. Ultrason. Ferroelectr. Freq. Control **46**(3), 737-744 (1999).
3. R. S. Mezrich, K. F. Etzold, and D. H. R. Vilkomerson: RCA Review **35**, 483-519 (1974)
4. C. B. Scruby and L. E. Drain: *Laser Ultrasonic: Techniques and Applications*. (Hilger, Bristol, 1990), 148-164.

Proceedings of Symposium on Ultrasonic Electronics, Vol. 29 (2008) pp. 59- 60
11-13 November, 2008

# Abnormal Frequency Jump of Quartz Crystal Microbalance in Liquid

Sunhee Choi, Mikyung Lim*, Young.H. Kim (Korea Science Academy)

## 1. Introduction

Since Pierre and Marie Curie had discovered piezoelectric effect, a quartz crystal has been widely used for an accurate oscillator. Especially AT-cut quartz crystal is mostly used because of the great stability against temperature change. A quartz crystal microbalance (QCM) is a device which measures very small mass changes with the frequency change of the quartz crystal in real-time. The major application of QCM is thickness monitoring in thin film deposition and a gas detector.

Nowadays QCM is being developed as biological sensors and therefore the behavior of quartz crystal in a liquid has been studied. For example, Kanazawa has proposed an equation which described the frequency shift related to density and viscosity of the liquid which quartz crystal is immersed in [1]. König reported influence of water droplet on the crystal and it seems contact area have a relationship with the frequency shift [2].

In the present work, however, we observed the frequency jump from near 6MHz to 9MHz when quartz crystal is immersed in water. The frequency will be changed in a small amount along the contact area according to König's research, but it just jumped regardless of the contact area. This work tried to investigate this abnormal phenomenon and to explain the reason.

## 2. Experimental details

Fig.1 shows AT-cut quartz crystal of 6MHz resonant frequency and 14mm diameter (Tangidyne, TAN06IG). A dip holder is fabricated in order to isolate electrodes in liquid. Sycon VSO-100 was employed for exciting quartz crystal, and its output is ready for connection to the frequency counter.

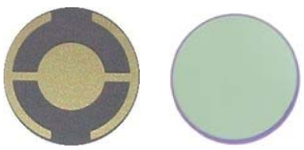

Fig. 1 The electrode shape of TAN06IG [3]

cjtwo120@hanmail.net
* current address : KAIST, Dae-jeon, Korea

In order to clarify the frequency jump, time domain waveform as well as frequency counting were investigated. Frequency spectrum obtained by FFT (Fast Fourier Transform) of time-domain waveform was also investigated. For these purpose, the frequency counter (Agilent 53132A) and A/D board (NI PXI-5124) were employed in the present work.

## 3. Result and discussion

Frequencies of quartz crystal were measured 1000 times for 10 minutes using frequency counter. The average value and standard deviation of frequency of quartz crystal are listed in Table 1. As shown in Table 1, quartz crystal in air vibrates at about 6MHz, whereas frequency of quartz crystal in water jumped to the 9.5MHz. It was also found that oscillation in water is more

**Table I** the average and the standard deviation of the frequency of quartz crystal in air and in water

| | average(Hz) | standard deviation(Hz) |
|---|---|---|
| in air | $5.989507\times10^{6}$ | 5.25 |
| in water | $9.540\times10^{6}$ | $2.297\times10^{3}$ |

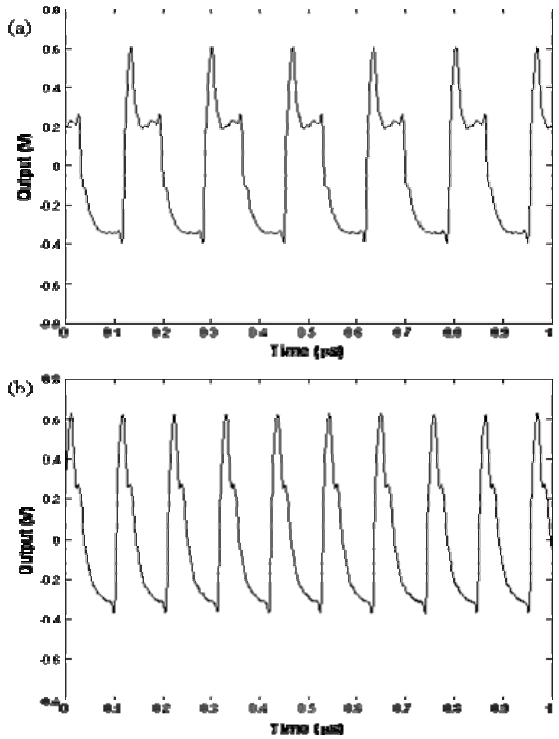


Fig. 2 The waveform of the signals from quartz crystal (a) in air, (b) in water

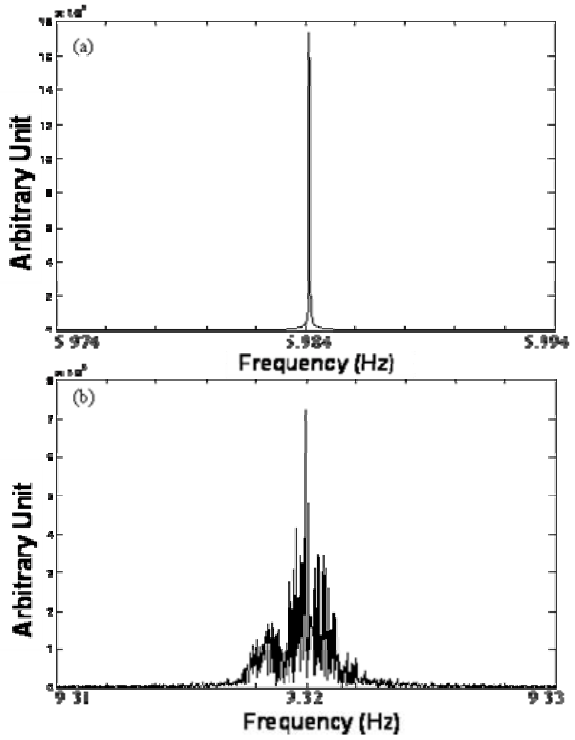


Fig. 3 FFT of the waves from quartz crystal (a) in air (b) in water

unstable compared to that in air.

Time domain waveform was captured by A/D board. In order to observe the detail of waveform, sampling rate was set to 1GS/s. In order to capture waveform for frequency spectrum, sampling rate was set 200MS/s with $10^7$ data points so that frequency resolution was 20 Hz.

The waveforms of the signals from the quartz crystal in air and water are shown in Fig 2. The waveform in air is similar to the square wave with one high peak. The waveform in water is sharper and takes shape of triangle. It is also found that the frequency is shifted from 6MHz to 9.5MHz.

Fig. 3 shows the frequency spectra. The frequency spectrum shows a narrow resonant peak near 6MHz in Fig. 3(a). On the contrary, those in Fig. 3(b) shows broadly spread frequency components near 9.5MHz.

Considering the measured results, there is no doubt that water contact to quartz crystal makes resonant frequency jump to higher frequency. It implies that the water changes the vibration mode of crystal. Abnormal frequency jump to higher frequency will be concerned with a higher wave speed mode. AT cut quartz crystal is normally oscillating in shear mode, and longitudinal wave speed is faster than shear wave speed. Therefore longitudinal vibration crystal is one of possible explanation of abnormal frequency jump. Since shear and longitudinal wave speeds are $3.52\times10^3$m/s and $5.57\times10^3$m/s, respectively, the ratio of jumped frequency will be equal to the ratio of wave speeds, $5.57\times10^3$ / $3.52\times10^3$ = 1.58 [4]. The measured frequency ratio, 1.59, shows good agreement with the wave speed ratio.

## 4. Conclusion

In the present work, we investigated the behavior of quartz crystal when it is immersed in liquid. The frequency was very unstable and jumped to near 9MHz in liquid. It was found that water makes frequency of quartz crystal jump to higher frequency. Abnormal frequency jump seems to be concerned with the longitudinal wave mode even though the mechanism of mode change is not explained.

## References

1. K. K. Kanazawa, J. G. Gordon Ⅱ : Anal. Chem. **52**, 1929 (1980)
2. A. M. K önig, M. Düwel, B. Du, M. Kunze, and D. Johannsmann : Langmuir **22** (2006) 229-233
3. http://www.tangidyne.com/replacement.html
4. J. Krautkrämer, H. Krautkrämer : Ultrasonic testing of Materials 4th Edition, (Springer-Verlag, Berlin, 1990) p.561

1P2a-9

Proceedings of Symposium on Ultrasonic Electronics, Vol. 29 (2008) pp. 61-62
11-13 November, 2008

# Development of Micro-LFB Ultrasonic Device
マイクロ LFB 超音波デバイスの開発

Jun-ichi Kushibiki, Yuji Ohashi, Mototaka Arakawa, Tomoya Tanaka, and Sho Yoshida‡ (Grad. Sch. Eng., Tohoku Univ.)
櫛引淳一, 大橋雄二, 荒川元孝, 田中智也, 吉田翔‡（東北大院・工）

## 1. Introduction

The line-focus-beam ultrasonic material characterization (LFB-UMC) system[1] is capable of quantitatively evaluating various solid materials, including single crystals, by measuring the phase velocity of leaky surface acoustic waves (LSAWs) propagating on a water-loaded specimen surface. Perfect directionality of the LSAW propagation direction that is realized by converging ultrasonic beam into a wedge shape using a cylindrical ultrasonic lens enables measuring the LSAW velocity precisely. The spatial resolution of this system depends on a measurement region of ultrasonic beam widths along the focused direction, $W$, and the along unfocused direction, $D$, formed by the LFB device[2]. $W$ is defined as $W=2|z|\tan\theta_{LSAW}$ where $z$ is the defocus distance in V($z$) curve measurements and $\theta_{LSAW}$ is the critical angle of LSAW. As $D$ for the normal LFB device is relatively large, it is difficult to detect steep variations of acoustic properties along the unfocused direction on specimen surface. Besides, higher spatial resolution is required to evaluate small crystals in a developmental stage. Although directional point-focus-beam (PFB) device has been developed in a viewpoint of the higher spatial resolution,[3,4] this is not sufficient for quantitative evaluation because of imperfect directionality of the LSAW propagation direction in principle. It is also insufficient to simply reduce the transducer width along the unfocused direction because of diffraction effect of the acoustic field.

In this paper, we develop a micro-LFB ultrasonic device to improve the spatial resolution along the unfocused direction.

## 2. Micro-LFB Device

Configuration of the micro-LFB device and its measurement region on a specimen surface are illustrated in **Fig. 1**. A different point from the normal-LFB device is that the micro-LFB device has a cylindrically convex surface with a large curvature radius $R_T$ for fabricating a ZnO-film transducer. We made a micro-LFB device with the following parameters: lens curvature radius

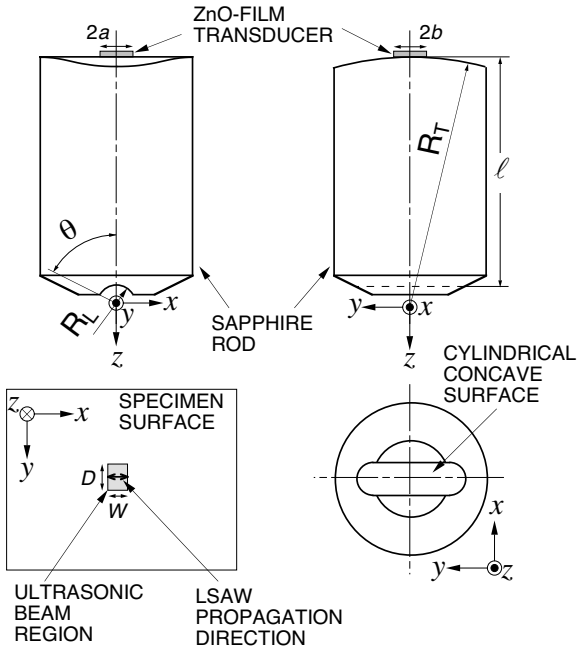


Fig. 1. Illustration of micro-LFB device and measurement region on specimen surface.

$R_L$=1.0 mm, half-aperture angle $\theta$=60°, transducer curvature radius $R_T$=13.0 mm, rod length $\ell$=12.0 mm, and transducer widths of 2$a$=1.73 mm along focused direction and 2$b$=1.50 mm along unfocused direction.

## 3. Experiments and Discussion

We evaluate spatial resolution of the device at 225 MHz by measuring focused acoustic fields using a PFB device as a detecting probe. Results for the normal-LFB and micro-LFB devices are shown in **Fig. 2**. 3dB-down width of the acoustic fields along unfocused direction was improved to 0.26 mm for the micro-LFB device, as compared with that of 0.92 mm for the normal LFB device.

We also verified a capability of anisotropy detection through measurements of angular dependence of LSAW velocities for anisotropic crystal [(110)Ge standard specimen[5]]. The measured and calculated results are shown in **Fig. 3**. Although measured velocities without calibration do not coincide with those of calculated ones, velocity variations reflect crystal symmetry as

E-mail: kushi@ecei.tohoku.ac.jp

predicted by theoretical calculations. We could confirm the capability of anisotropy detection in this micro-LFB device.

Furthermore, we demonstrated spatial detectability through measurements of LSAW velocity distributions for a *Z*-cut ZnO single crystal specimen with large inhomogeneity. Results are shown in **Fig. 4**. Measurements were conducted in 0.25-mm steps along *x*-axis and *y*-axis directions with LSAW propagation direction parallel to the *x*-axis direction. As the ZnO single crystal specimen employed has large inhomogeneity in resistivity, we can observe LSAW velocity distributions of more than 60 m/s in both results. However, configuration of a region with low LSAW velocities spreading around (*x*, *y*)=(-1.5 mm, 0 mm) obtained by the micro-LFB device is clear triangle form while that by the normal-LFB device is in blurred form. Besides, the lower velocity area extended from (*x*, *y*)=(-1.0 mm, +2.5 mm) to obliquely right downward in Fig. 4(b) could be detected only by the micro-LFB device. These results demonstrate that the micro-LFB device can detect finer velocity variations and inhomogeneities, which could not be observed by the normal-LFB device.

## 4. Conclusion

We proposed a micro-LFB device with higher spatial resolution and demonstrated its performance. We succeeded in developing the device with measurement region of smaller than 1/3 in comparison with that for the normal-LFB device, maintaining perfect directionality of the LFB device. This device will be useful for characterizing small precious samples.


## Acknowledgement

The authors thank K. Asano for his great effort with the experiments at the beginning of this work.


## References


1) J. Kushibiki and N. Chubachi: IEEE Trans. Sonics Ultrason. **SU-32** (1985) 189.
2) J. Kushibiki, A. Ohkubo, and N. Chubachi: Electron. Lett. **17** (1981) 520.
3) J. A. Hildebrand and L. K. Lam: Appl. Phys. Lett. **42** (1983) 413.
4) J. Kushibiki, N. Chubachi, and E. Tejima: Ultrason. Inter. 89 Conf. Proc. (1989) 736.
5) J. Kushibiki, M. Arakawa, and R. Okabe: IEEE Trans. Ultrason., Ferroelectr., Freq. Control **49** (2002) 827.


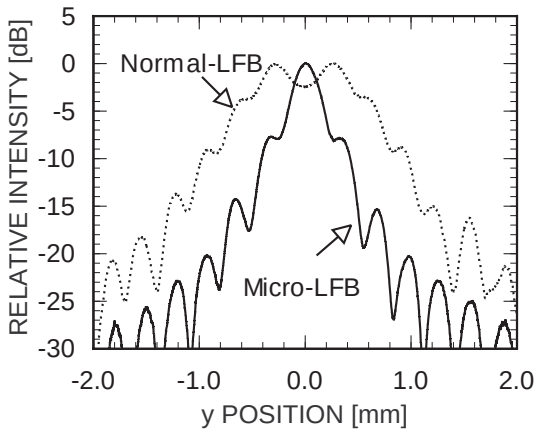


Fig. 2. Acoustic field along *y*-axis direction (ultrasonic frequency: 225 MHz, transducer width along *y*-axis direction: 1.50 mm).

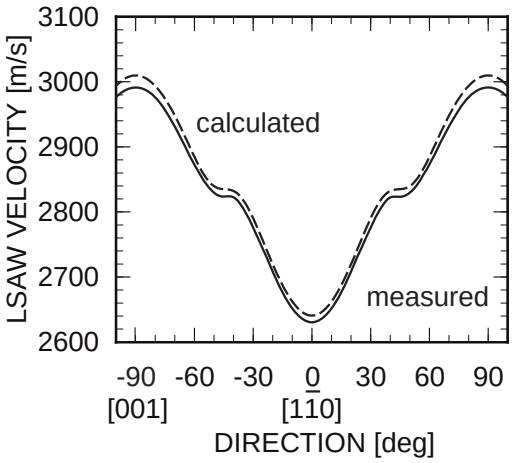


Fig. 3. Angular dependences of LSAW velocities measured for (110)Ge standard specimen using micro-LFB device.

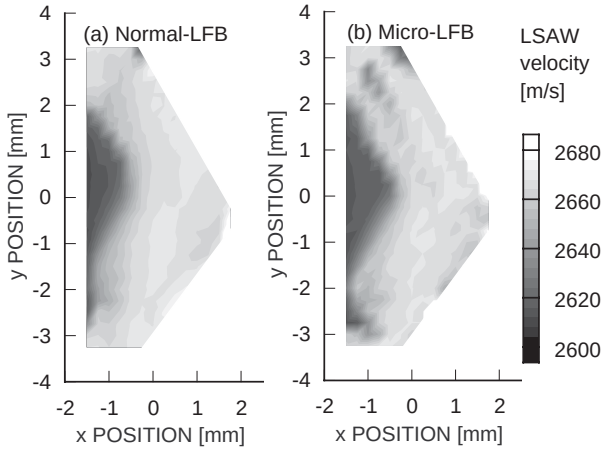


Fig. 4. LSAW velocity distributions measured for Z-cut ZnO single crystal specimen.

Proceedings of Symposium on Ultrasonic Electronics, Vol. 29 (2008) pp. 63-64
11-13 November, 2008

# Automatic Measurement of Nonlinearity Parameter *B*/*A* for Small Volume Liquid Samples

少量液体試料の非線形パラメータ *B*/*A* の自動測定

Shigemi Saito[1†] and Jung-Ho Kim[2] ([1] School of Marine Science and Technology, Tokai University [2] GW Corporation)
斎藤繁実[1†]，金正鎬[2]（[1] 東海大・海洋; [2] ジーダブリュー）

## 1. Introduction

The automatic measurement method for acoustic nonlinearity parameter *B*/*A* in liquid sample has previously been presented.[1] However the method is only available to samples with attenuation coefficients much lower than 200 Np/m at 19 MHz. By setting a thin sample in the focal region of a focused Gaussian beam, *B*/*A* in a more dissipative sample has been successfully measured lately.[2,3] With the aim to generate the image of *B*/*A* distribution, the automatization of the measurement is examined in this work.

## 2. Measurement System

As shown in **Fig.1**, the LN transducer with an inverted polarization layer driven by 7-cycle burst voltages of frequency $f$=18.6 MHz radiates a focused Gaussian beam of 10.65 mm focal length in water (density $\rho_W$=1000 kg/m$^3$, sound speed $c_W$=1483 m/s) through a solid acoustic lens. A space in a sample container provided by a ring spacer inserted between a PS plate and tungsten rod is filled with a liquid sample that forms a layer of thickness $L\approx$1 mm. In PS, the density $\rho_d$, longitudinal sound speed $c_d$, transverse sound speed $c_t$ and *B*/*A* are assumed to be 1049 kg/m$^3$, 2333 m/s, 1120 m/s and 11.4.[4] The 7 cycle burst waves take roundtrips across the sample. The distance $z_R$ of the end of a brass rod from the lens surface is controlled with a stepping motor.

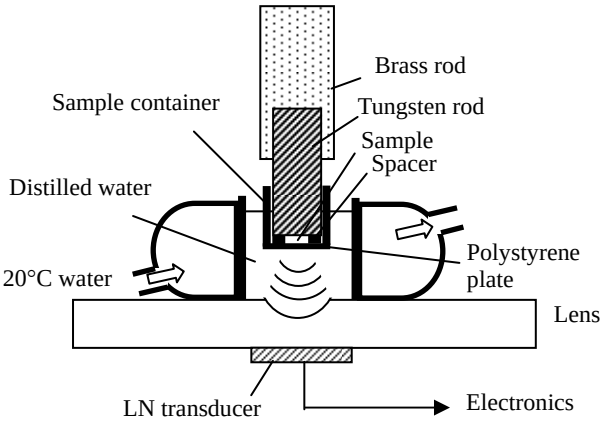


Fig.1. Experimental setup of acoustic system.

ssaito@scc.u-tokai.ac.jp

To measure the magnitude of the reflected sound from any boundary, $z_R$ is adjusted so that the boundary locates on the focal plane. Since the sound reflected at the focal plane returns to the transducer in phase, the signal obtained with the highest sensitivity is accurately proportional to the magnitude of the reflected waves. All the acoustic system is settled in an incubator at 20°C. In addition, the sample and water couplant is held at 20°C with circulation of cooling water.

## 3. Procedure of Automatic Measurement

The sound speed $c$ and attenuation coefficient $\alpha$ are determined by the time of flight and the reduction rate of the sound passing through the sample, respectively. The density $\rho$ is estimated from the reflection coefficient at the interface between the polystyrene plate and the sample. Summarizing all the linear properties and amplitude data of the second harmonic component in the sound transmitted through the sample, the *B*/*A* value is finally determined from the magnitude of second harmonic generation. To compensate the influence on the second harmonic generation, the velocity dispersion is measured using a phase delay of 2$f$ sounds relative to $f$ sounds in dual-frequency sounds. To derive the acoustic properties, the parameters such as amplitudes, phases and time intervals are automatically measured and executed using LabVIEW programs constructed on the basis of the previous method.[1]

The range to maximize the amplitude of the wave reflected from the rear surface of the PS plate, $z_R=D+(1-c_d/c_W)d$, is registered as the reference position of the $z$ stage. The tungsten rod is immersed alone in water, the waveform of the sound reflected from its surface is recorded first as the reference waveform used in cross-correlation computations. Further, the amplitude $P_{RB}$ of the reflected wave from the rear surface of the PS plate directly attached to the tungsten rod is also obtained from the maximum value of the cross-correlation function.

After setting the container filled with the sample, the amplitude $P_{SB}$ of the reflected wave from the rear surface of the PS plate is measured. The time interval $\tau_S$ to the subsequent wave reflected from the

tungsten rod is simultaneously measured. Furthermore, the following process is carried out.

(i) The tungsten rod is lowered by $cL/c_W$. Then the amplitudes $P_{S1}$ and $P_{S2}$ are obtained with FFT for the signal receiving the wave reflected from the tungsten rod during the radiation of dual frequency wave consisting of frequencies $f$ and $2f$. The phase delay $\Phi_S$ of $2f$ component relative to $f$ component is simultaneously measured.

(ii) The second harmonic component $P_{SN2}$ is obtained by the FFT of the reflected wave during the sound radiation of frequency $f$.

Prior to the sample measurement, the process of (i) and (ii) is applied to distilled water filling the container, where $c$ in (i) is $c_W$. The corresponding values $P_{W1}$, $P_{W2}$, $\Phi_W$ and $P_{WN2}$ are then obtained.

**a) Determination of sound speed** The sound speed $c$ is determined with the following equation.

$$c = \frac{2L}{\tau_S} \qquad (1)$$

**b) Determination of density** Considering the transformation from longitudinal to transverse waves, the reflection coefficient $S=P_{SB}/P_{RB}$ at the rear surface of the PS plate must satisfy

$$S = R\left|\frac{\rho c - \rho_d c_d}{\rho c + \rho_d c_d}\right|, \qquad (2)$$

where $R$ is defined by $\rho$ and $c$ as follows[5]:

$$\left.\begin{array}{ll} R=A_0-A_1x-A_2x^2; & c\le 794 \text{ [m/s]} \\ =B_0-B_1y-B_2y^2-B_3y^3-B_4y^4-B_5y^5; & c>794 \text{ [m/s]} \end{array}\right\} \quad (3)$$

where $x=\log_{10}c-3.4377\times10^{-2}q-2.4718\times10^{-3}3q^2$, $y=\log_{10}c-3.7138\times10^{-2}q-1.425\times10^{-3}q^2$ and $q=(1000-\rho)/100$. The coefficients in Eq.(3) are $A_0=0.9087$, $A_1=0.114$, $A_2=0.1181$, $B_0=0.9047$, $B_1=0.1842$, $B_2=0.5079$、$B_3=1.2389$, $B_4=6.884$ and $B_5=21.126$. By substituting the measured values of $S$ and $c$ into Eq.(2), the unknown $\rho$ is determined.

**c) Determination of attenuation coefficient** The diffeence of $P_{S1}$ and $P_{S2}$ from $P_{W1}$ and $P_{W2}$ is primarily attributed to the difference of the sample from distilled water in its attenuation. Considering the impedance mismatching and focal shifting, the attenuation coefficients at $f$ and $2f$ are derived as

$$\alpha_n = n^2\alpha_W\frac{c}{c_W} + \frac{1}{2L}\ln(Q\frac{P_{Wn}}{P_{Sn}}),(n=1,2), \qquad (4)$$

where $Q=\rho c(\rho_d c_d+\rho_W c_W)^2/[\rho_W c_W(\rho_d c_d+\rho c)^2]$ and $\alpha_W$ is the attenuation coefficient in water at 18.6 MHz, namely, 8.65 Np/m.

**d) Determination of *B*/*A*** The amplitude $P_{SN2}$ theoretically depends on $B/A$ and velocity dispersion of the sample $\Phi_W$-$\Phi_S$ as well as other linear properties such as $\rho$, $c$, $\alpha_1$ and $\alpha_2$.[3] Although both the amplitudes $P_{SN2}$ and $P_{WN2}$ are dependent on the transmitting and receiving sensitivities of the transducer, the ratio $P_{SN2}/P_{WN2}$ becomes the function of the unknown parameter $B/A$ in dependent of such sensitivities. When $B/A$ is adjusted so that the theoretical $P_{SN2}/P_{WN2}$ equals to the experimental one, $B/A$ is determined to be the value.

## 4. Example of Measurement Results

The measurement result for the concentration dependence of $B/A$ in aqueous solutions of bovine hemoglobin is shown in **Fig.2**. The trend of $B/A$ increasing with the concentration agrees with the value measured with thermodynamic method.[6] Further study is necessary for interpreting the reason of discrepancy in $B/A$ at high concentrations. The manual operation of the measurement system would require a time as long as 15 minutes for each point except for the computation. This automatic measurement including computations, however, was completed in 14 seconds.

## 5. Conclusions

By using an acoustic window of polystyrene plate, the automatic measurement for $B/A$ of the sample with a volume as small as 0.1 ml was carried out. The imaging of the $B/A$ distribution will be investigated later as well as the speedup of this automated method.


## Acknowledgment

This work was supported by a Grant-in-Aid for Scientific Research (C) 19560429 from the Japan Society for the Promotion of Science.


## References


1. S. Saito, J.-H. Kim and K. Nakamura: Ultrasonics **44** (2006) e1429-e1433.
2. S. Saito, K. Saida and S. Takahashi: Jpn. J. Appl. Phys. **47** (2008) 3859.
3. S. Saito, T. Watanabe and J.-H. Kim: IEICE Tech. Rep. US2008-5 (April, 2008).
4. S. Saito and Y. Motohashi: Jpn. J. Appl. Phys. **47** (2008) to be published.
5. S. Saito and T. Watanabe: IEICE Tech. Rep. US2007-105 (January, 2008).
6. W. K. Law, L. A. Frizzell and F. Dunn: Ultrasound Med. Biol. **11** (1985) 307.


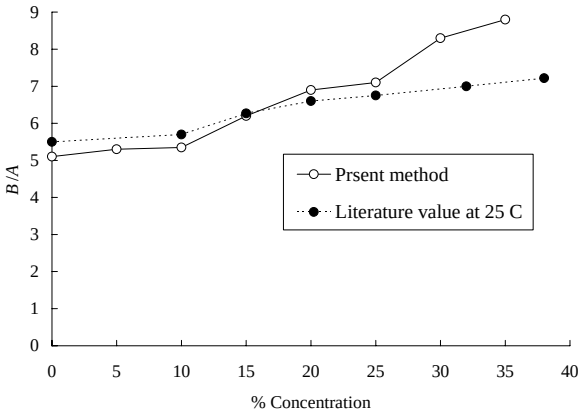


Fig.2. Measured $B/A$ of aqueous hemoglobin solution.

Proceedings of Symposium on Ultrasonic Electronics, Vol. 29 (2008) pp. 65-66
11-13 November, 2008

# Sensing Grid for Air Temperature Composed of Asynchronous-Type Sound Probe

非同期型音響波プローブで構成するセンシンググリッドによる気温計測

Yosuke Katano‡, Naoto Wakatsuki and Koichi Mizutani (Univ. Tsukuba)
片野洋介‡,若槻尚斗,水谷孝一（筑波大院 シス情工）

## 1. Introduction

In recent years, a thermal environmental measurement is required in various fields to maintain an optimum environment for life space, large-scale farm, and so on.[1,2] And, the heat island phenomenon and global warming progress. Therefore, the temperature management in the building group in the big city or the large-scale facilities are regarded as very important.

In conventional temperature measurement method in large-scale space, contact-type sensors like thermocouples and thermistor have been used. Although the temperature distribution measurement using these sensors is easy, a lot of sensors are required for large-scale measurement.[3] In addition, the disturbances such as direct sunshine and radiant heats influence the measurement. Because contact-type sensors are required to be installed in the measurement area, they consume some space there. On the other hand, temperature measurement using sound probe is non-contact and non-destructive measurement, and a measurement method is tolerant of such a disturbance. Sound probes have an advantage of measurement ability by a little number of sensors and less space consumption.[4]

The network of the measurement system for temperature distribution in a large-scale space has been suggested by the authors.[5] In the network, a trigger line was wired by cable for accurate synchronization while data communication was done by wireless. It becomes easy to construct a sensing grid if trigger cables are omitted. This gives flexibility to the sensor arrangement. Therefore, we suggest a temperature measurement by acoustical means without trigger signal as the former stage of the large-scale space measurement. The validity of the measurement principle is confirmed by experiment.

## 2. Principle

The temperature measurement principle using sound probe is transferred to reference.[5] In the conventional temperature measurement using sound probe, the operation beginnings of two acoustic sensors are completely synchronized to measure time of flight (TOF), $t_f$. Synchronous accuracy influences the measurement accuracy at the TOF. Because wireless LAN causes the variation of the delay of a few milliseconds, it cannot be used to transmit and receive the trigger signal. In former research of authors, synchronization was taken by the trigger line using a coaxial cable. To achieve completely wireless sensing grid in this research, the measurement method without trigger signal was investigated. The delays caused in wireless LAN are compensated by using the round-trip TOF.

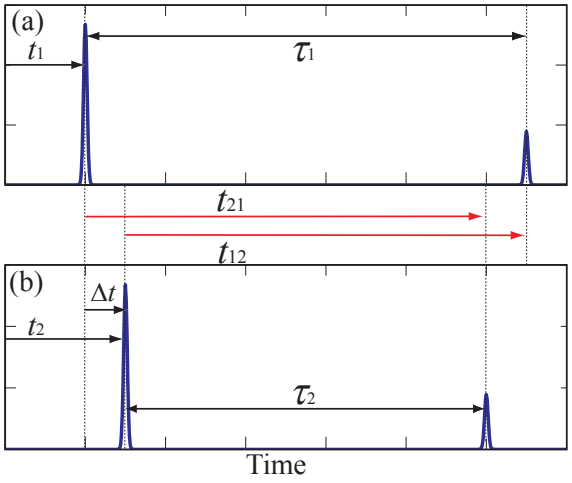


Fig.1 Measurement principle Outline
(a) :Reception waveform of MIC1
(b) :Reception waveform of MIC2

**Figure 1** shows the timings of signal receptions. The times between the transmissions of command to start the measurement and actual beginnings of measurement on MIC1 and MIC2 are defined as $t_1$ and $t_2$, respectively. The difference between $t_1$ and $t_2$ is defined as $\Delta t$. TOFs from the speaker 1, 2 to the microphone 2, 1 are respectively defined as $t_{12}$ and $t_{21}$. Signal arrival times from two speakers are defined as $\tau_1$ and $\tau_2$. These relations are described as

$$\begin{cases} \tau_1 = t_{12} + \Delta t \\ \tau_2 = t_{21} - \Delta t \end{cases} \tag{1}$$

$$\begin{aligned} t_{\text{total}} &= \tau_1 + \tau_2 \\ &= t_{12} + t_{21} \end{aligned} \tag{2}$$

$$t_{total} \approx \frac{2L\bar{c}}{\bar{c}^2 - V_d^2} \approx \frac{2L}{\bar{c}} \tag{3}$$

Adding $\tau_1$ to $\tau_2$ can eliminate the influence of the delay be eliminated, and gives the round-trip TOF $t_{total}$. Thus, the sound speed is obtained from eq. (3), and air temperature is derived.

The component of the wind velocity parallel to the propagation path is defined as $V_d$. When the velocity of the wind is substantially smaller than sound speed, the influence can be disregarded.

## 3. Experimental validation

### *3.1 Experiment Setup*

**Figure 2** illustrates a composition of the experiment. Air temperature are measured in the room (7.16 × 7.44 × 3.08 (m)). Four acoustic sensors are set at the corner of the 4.55 × 4.54 $m^2$ square and form the network by wireless LAN (IEEE802.11b). Each sensor, which consists of a microphone and loudspeaker and amplifiers, is connected to the PC via A-D/D-A converter. The experiment was carried out at 10s intervals from local time of 0:00 to 5:30. The temperature at the center of the room has been changed by heating wire from 2:30 to 3:30. The Reference used thermocouple. The thermocouple was set up in nine points as shown in Figure 2. For separating from the signal received on each acoustic sensor, four kinds of signals were used. First and second signal was a ten-wavelength burst sound modulated from 7 to 3 kHz and from 3 to 7 kHz in linear frequency at sensor 1, 2. Third and Fourth signal was used a 22-wavelength curst sound modulated from 7 to 17 kHz and from 17 to 7 kHz in linear frequency at sensor 3, 4. Because the sampling rate of the A-D/D-A was 250 kHz, the time resolution was 4 μs.

### *3.2 Results of temperature measurement*

**Figure 3** shows measured temperatures along acoustic paths. The solid lines and broken lines represent the temperatures measured by sound probes and thermocouples, respectively. Similar behaviors are observed by both asynchronous-type sound probe and thermocouple. Because of the variation of $\Delta t$, the measurement fails to detect a peak in cross-correlation once in a while.

## 4. Conclusions

In order to measure the air temperature of the large space, we examined the measurement method using the asynchronous-type sound probe. We experimentally verified the adequacy of this measurement method in a room as the primary stage. The wiring is omitted using the asynchronous-type sound probe and the flexibility of the composition of the sensing grid increases. The conclusive peak detection technique would be required in order to eliminate measurement failures.

.

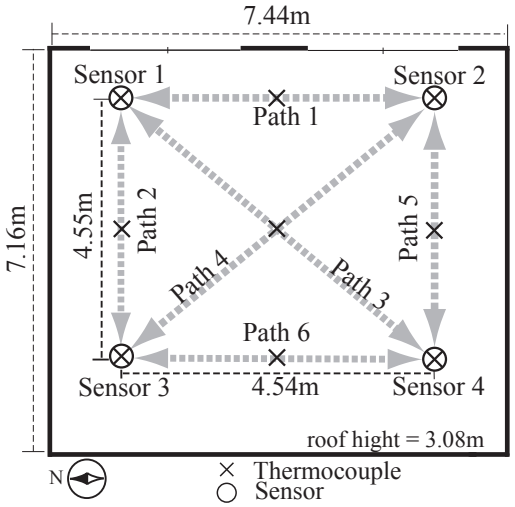


Fig.2 Experimental composition.

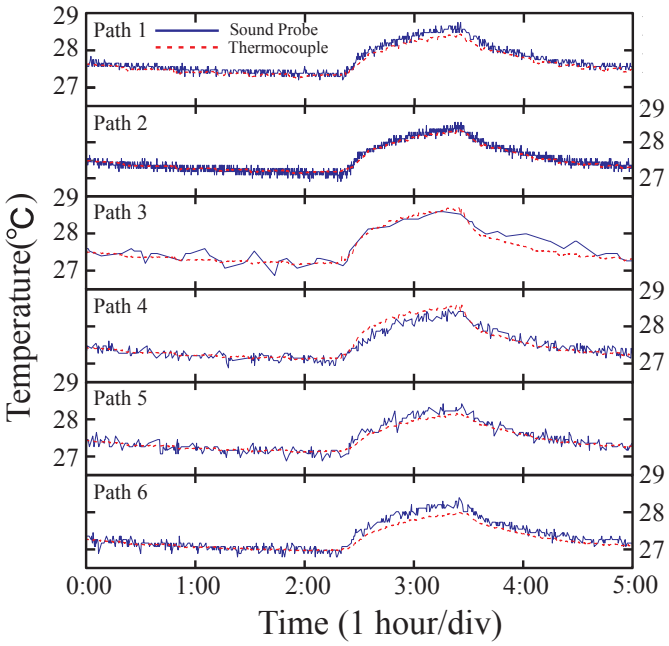


Fig.3 Temperature transitions along six acoustic paths.

## References


1). J. E. Son, J. S. Park and H. Lee: Acta Hort. **578** (2002) 257.

2). D. J. Tanner and N. D. Amos: Acta Hort. **599** (2002) 193.

3). I. Saito, N. Wakatsuki, K. Mizutani, M. Ishii, L. Okushima and S. Sase: Jpn. J. Appl. Phys. 47 (2008) 4329.

4). K. Mizutani, K. Itoga, K. Kudo, L. Okushima, and N. Wakatsuki: Jpn. J. Appl. Phys. **43** , (2004) 3090.

5). K. Sawamura, K.Mizutani, Kashiwazaki, and I. Odanaka: The 26th Symposium on Ultrasonic Electronics, P2-13, (2005) 237.

Proceedings of Symposium on Ultrasonic Electronics, Vol. 29 (2008) pp. 67-68
11-13 November, 2008

# Ultrasonic Measurements of Temperature Distributions of the Inside and Surface of Materials

超音波による材料内部および表面の温度分布計測

Manabu Takahashi[1‡] and Ikuo Ihara[2] ([1]Graduate Student of Nagaoka Univ. of Tech.; [2]Dept. of Mech. Eng., Nagaoka Univ. of Tech.)
高橋学[1‡], 井原郁夫[2] ([1]長岡技科大院; [2]長岡技科大)

## 1. Introduction

In various fields of science and engineering, there are growing demands for noninvasive measurements of the temperature distribution and its transient variation of a material being heated. In our previous work[1)], an ultrasonic inverse method to determine the temperature distribution inside material was proposed and its validity was demonstrated.

In this work, an improved ultrasonic method that can be used for practical and versatile applications has been developed. The method consists of an ultrasonic pulse-echo measurement and an inverse analysis coupled with a one-dimensional finite difference calculation. To demonstrate the practical feasibility of the method, temperature distributions of internal and surface of a material are evaluated.

## 2. Ultrasonic Inversion Method for Determining Temperature Distributions

The principle of temperature measurement by ultrasound is based on temperature dependence of the velocity of the ultrasonic wave that propagates through a medium. Assuming a one-dimensional temperature distribution in a medium, the transit time of ultrasonic pulse-echo in the direction of the temperature distribution can be given by

$$t_L = 2\int_0^L \frac{1}{v(T)}dx, \tag{1}$$

where $L$ is half the transit distance of ultrasound, $v(T)$ is the ultrasonic velocity that is a function of temperature $T$. In general, the $T$ in a medium being heated can be given as a function of location $x$ and time $t$. It is also noted that the temperature dependence of the velocity $v(T)$ may have an approximate linear relation in a certain temperature range and can be given by

$$v(T) = -aT+b, \tag{2}$$

where, $a$ and $b$ are constants.

We now consider a one-dimensional finite difference model consisting of a large number of small elements and grids, for the medium to be evaluated. Using a concept of trapezoidal integration, the transit time $t_L$ given in equation (1) can be calculated from

$$t_L = h\left(\frac{1}{v_1^n}+\frac{1}{v_N^n}\right)+2h\sum_{i=2}^{N-1}\frac{1}{v_i^n}, \tag{3}$$

where $h$ is the grid interval, $N$ is the number of the grid, $v_i^n$ is the ultrasonic velocity at each grid position, $i$ and $n$ are indices corresponding to spatial coordinate and consecutive time, respectively. Considering that the single side of the medium having a uniform temperature $T^n$ at time step $n$ is being heated, temperatures at each grid point in the medium at time step $n$+1 that is a very short elapsed time can be given by[2)]

$$T_i^{n+1} = T_i^n + r\left(T_{i+1}^n + T_{i-1}^n - 2T_i^n\right) \quad (i=2,\cdots,N-1) \tag{4}$$

$$r = \frac{\alpha\tau}{h^2} \tag{5}$$

where $\alpha$ is the thermal diffusivity, $\tau$ is the time step. Using equation (3) and the relation between temperature and ultrasonic velocity, the temperature of the heated surface at time step $n$+1, $T_1^{n+1}$, can be given by

$$T_1^{n+1} = -\frac{1}{a\left\{\frac{t_L}{h}-\left(\frac{1}{v_N^{n+1}}+2\sum_{i=2}^{N-1}\frac{1}{v_i^{n+1}}\right)\right\}}+\frac{b}{a}, \tag{6}$$

where $t_L$ is the transit time of ultrasonic wave measured at the time step $n$+1. It is noted that the temperature of the other side of the medium, $T_N^{n+1}$, is assumed to be known because such temperature at a low temperature side can be easily obtained using any conventional technique such as a thermocouple. Once the temperatures of all grid points in the medium at the time step $n$+1, $T_1^{n+1}$,$^{\cdots}$, $T_N^{n+1}$ are obtained, the temperature distribution at time step $n$+2 can also be determined by the same procedure using the transit time $t_L$ measured at the time step $n$+2. Thus, we can continuously obtain the temperature distribution.

## 3. Experiments and Results

At first, the proposed method has been applied to an internal temperature measurement of a thick

E-mail address: ihara@mech.nagaokaut.ac.jp

steel plate being heated and cooled. A surface of a steel plate of 30 mm thickness is heated by contacting with a heater of 200 °C for 100 s, and then the surface is cooled by water. Ultrasonic pulse-echo measurements at 2 MHz are made for the plate and the transit time $t_L$ through the plate is measured during the heating and cooling. The internal temperature and its variation estimated from the $t_L$ is shown in **Fig. 1**. It can be seen that the ultrasonically estimated results almost agree with those measured using thermocouples.

Next, we attempt surface temperature measurements by a surface acoustic wave (SAW). **Figure 2** shows a schematic of the experimental setup used for SAW measurements. Using a laser ultrasound system consisting of a pulse laser generator (Nd:YAG, 1064 nm, 20 mJ, 10 ns) and a laser interferometer based on photorefractive two-wave mixing (Nd:YAG, 532 nm, 200 mW), the SAW propagating on the surface of a steel plate being heated is measured. Taking the difference in the transit time between SAW1 and SAW2, the transit time $t_L$ of the SAW propagating through the distance between A and B can be determined. An infrared camera is used to obtain a reference value of surface temperature distribution of the plate.

**Figure 3** shows the variations of the temperatures at A and B and the $t_L$ of SAW on the steel surface during heating. As we expected, the temperatures start to rise just after the heating starts and we can see that the transit time increases drastically with the rise in temperature of the plate.

**Figure 5** shows the variations of the estimated surface temperature distributions with the elapsed time, where the ultrasonically estimated results are compared with those measured using an infrared camera. It can be seen that both temperature distributions almost agree.


## Acknowledgment

Financial supports by the Grant-In-Aid for Scientific Research (B19360330) from the JSPS, and Toyota Motor Co. are greatly appreciated.


## References


1. M. Takahashi and I. Ihara. Jpn J. Appl. Phys. **47** (2008) 3894.
2. W. Press, S. Teukolsky, W. Vetterling and B. Flannery: *NUMERICAL RECIPES in C++* (Cambridge Univ., NY, 2003) p.849.


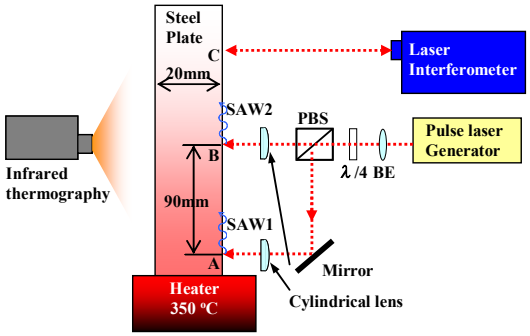


Fig. 2 Schematic of the laser ultrasonic system used for measuring SAWs on a steel plate being heated.

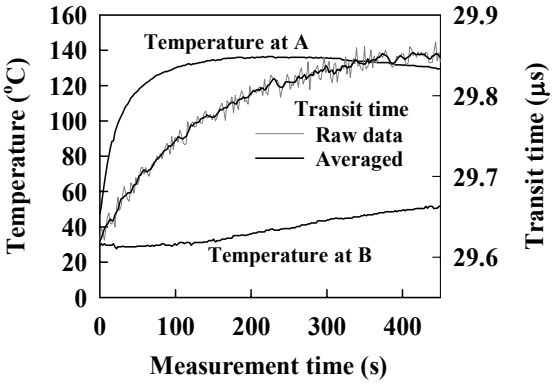


Fig. 3 Variations of the temperatures and the transit time of the SAW on the steel surface during heating.

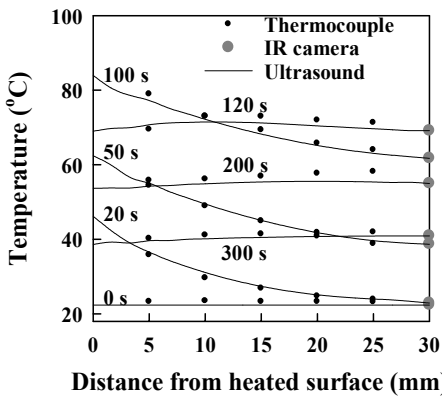


Fig. 1 Internal temperature distribution of the steel plate and its variation during heating and cooling.

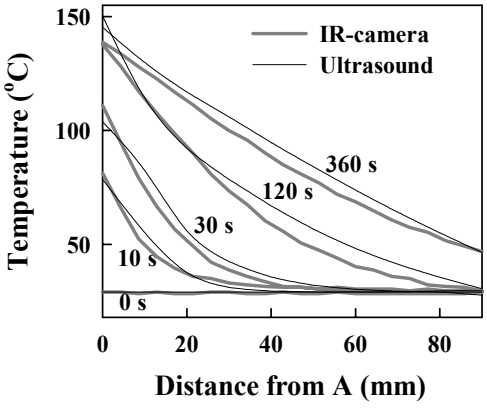


Fig. 4 Surface temperature distribution of the steel plate and its variation during heating.

1P2a-13

Proceedings of Symposium on Ultrasonic Electronics, Vol. 29 (2008) pp. 69- 70
11-13 November, 2008

# Measurement of Air Humidity Using Ultrasonic Delay Line
音響遅延線による湿度計測

Akihiko Kon† (Univ. of Tsukuba/Yamatake),
Naoto Wakatsuki and Koichi Mizutani (Univ. of Tsukuba)
昆昭彦† （筑波大院･シス情工/山武）、若槻尚斗、水谷孝一 （筑波大院･シス情工）

## 1. Introduction

To measure many physical factors like distance[1], sound velocity[2], temperature[3,4] and humidity[5] using ultrasound are widely used because of the features of the ultrasound such as non-contact and non-disturbing for the measured environment. Measurement method of the air temperature using a time of flight (TOF) or an ultrasound velocity measured has been accepted. When the condition of the air humidity becomes nearly saturated and temperature has higher values than the temperature without humidity namely "dry temperature ($T_d$)", the value of TOF becomes smaller and the sound travels faster. This decreased TOF induces errors for measurement of distance, temperature and humidity. There are several works[6,7] on the relation between humidity and properties of the sound in a closed space but the measurement of humidity were not described. New non-contact measurement method of relative humidity is described and experimentally verified at several humidity and temperatures.

## 2. Principle Measurement

When an ultrasound with frequency $f$ (kHz) is transmitted from a speaker (SP) to a microphone (MIC), which makes the ultrasonic delay line with length $L$ (m), the measured TOF introduces sound velocity $c$ (m/s) as $c = L$ / TOF. The sound velocity has relation with air temperature $T$ (°C) as $c = 331.5 \times [(273.17+T) / 273.15]^{1/2} = 20.067 \times (273.17+T)^{1/2}$. This temperature must be virtual temperature. A new equation of relative humidity $U$ (%) is introduced as following: Parameters $\gamma$ (=1.4 air), $P$ (Pa), $P_v$ (Pa) and $P_d$ (Pa) are ratio of specific heats, atmospheric pressure, vapor pressure and dry air pressure, respectively. Parameters $\rho$ (kg/m$^3$), $\rho_v$ (kg/m$^3$) and $\rho_d = 1.29 \times 273.15 / (273.15 + T_d) \times P / 101325$ (kg/m$^3$) are air density, density of vapor and density of dry air, respectively. And parameters $M$ (kg/mol), $M_d$ (=0.028966) (kg/mol), $M_V$ (=0.018) (kg/mol) and $R$ (=8.324472) (J/mol·K) are mass of air, molecular mass of vapor, molecular mass of dry air and gas constant, respectively. $P_v$ and $P_d$ are presented as $P_v = \gamma \times R \times (273.15 + T_d) / M_v$ and $P_d = \gamma \times R \times (273.15+T_d) / M_d$. With saturated vapor pressure $P_m$ (Pa), the relative humidity $U$ is defined as $U=100\times P_v/P_m$. Using sound velocity $c = (\gamma \times P / \rho)^{1/2}$, the ratio $P_v / P_m$ is presented as

$$\frac{P_V}{P_m} = \frac{P_d \times M_d \times \rho_V}{P_m \times M_V \times \rho_d} = \frac{P_d}{P_m} \times \left( \frac{\frac{c^2 \times M_d}{\gamma \times R \times (273.15+T_d)} - 1}{1 - \frac{c^2 \times M_V}{\gamma \times R \times (273.15+T_d)}} \right). \quad (1)$$

When the empirical Antoine equation is adopted to the saturated vapor pressure and an assumption $P=P_d$ is considered because $P_v$ is smaller than $P_d$, the relative humidity is obtained as

$$U = \frac{100 \times P}{133.322 \times \exp\left(18.6686 - \frac{4030.183}{253+T_d}\right)} \times \left( \frac{\frac{c^2 \times 1.293 \times 273.15}{\gamma \times (273.15+T_d) \times 101325} - 1}{1 - \frac{M_V}{M_d} \times \frac{c^2 \times 1.293 \times 273.15}{\gamma \times (273.15+T_d) \times 101325}} \right). \quad (2)$$

Our experiments are validated using eq. (2), which shows the principle for the non-contact measurement of the relative humidity using sound velocity.

## 3. Experimental setup and Results

**Figure 1** shows experimental layout of SP and MIC and equipments for measurement. The SP and MIC (PT40-18N, PR40-18N/Nippon Ceramic) operate for sinusoidal ultrasound at 40 kHz. The pair of SP and MIC was fixed on a rail for optical use. The SP and MIC constitute an ultrasonic delay line whose length $L$ was set to 89.45 mm. A function generator (AGF310/Sony Tektronix) and a digital oscilloscope (2230/Tektronix) were used for generating probing signal and for comparing phase difference $\Delta\phi$ (rad) between transmitted and received ultrasound. Calibrated a humidity sensor/ thermometer (MS-6503/Mastech) and a pressure sensor (TSD01V/VITEC) were used for the references.

kon-akihiko@jp.yamatake.com

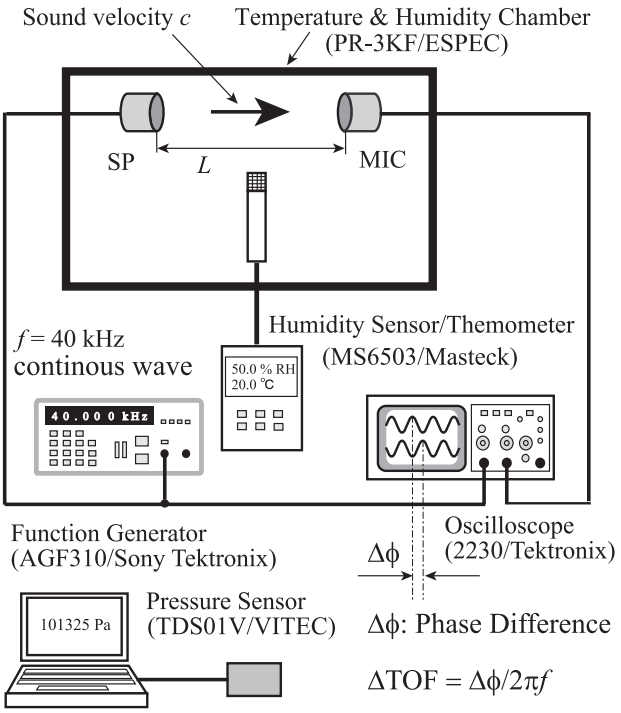


**Fig. 1** Schematic of experiment.
Δϕ is measured and converted into ΔTOF. Reference humidity and reference temperature in the chamber are also measured. Humidity is set at 30, 50, 75 and 100 % RH and temperature is set at 10, 20, 35 and 50 °C.

In order to change the environments at temperature and humidity a temperature & humidity chamber (PR-3KF/ESPEC) was used. The temperature was set to 10, 20, 35 and 50 °C. The relative humidity was set to 30, 50, 75 and 100 %RH. The pair of SP and MIC and the probe of the humidity sensor/thermometer were put in the chamber. The humidity affects the TOF of ultrasound. The base of TOF is that measured at 0 °C. The change of sound velocity $\Delta c$ (m/s) from 331.5 m/s is determined from the difference of TOF (ΔTOF) from the base TOF as

$$\Delta c = 20.067 \times \left( \frac{1}{\sqrt{273.15}} - \frac{20.067}{L} \times \Delta TOF \right)^{-1} \quad (3)$$

**Figure 2** shows measured relative humidity. The experimental data were 54.2, 59.7, 63.7 and 40.0 %RH, whereas reference data were 48.9, 48.2, 51.7 and 53.2 % RH for set value of 50 % RH for example. Nevertheless the differences between the reference and experimental data at 50 °C appear clearly and the errors between the reference and the experiment data are 17.8 % or less, the experimental data have same tendency with the reference data and are close to the reference data. These results suggest the experiments were valid and the

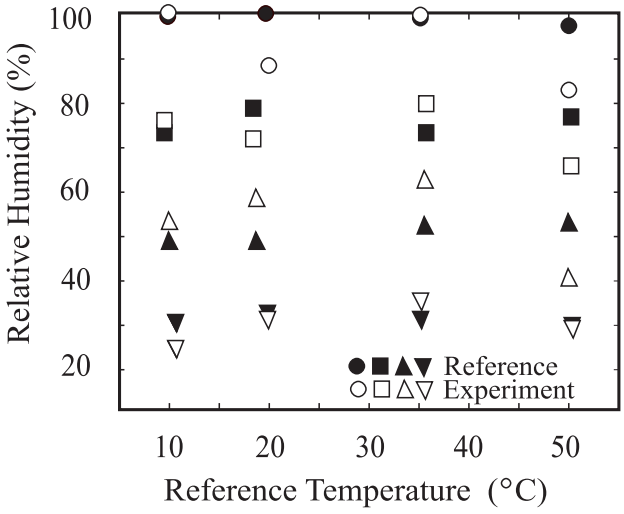


**Fig. 2** Relative humidity measured in the chamber at various temperatures.
Experiment data are obtained using eq. (2) at reference temperatures.

non-contact measurement of the relative humidity using eq. (2) is useful and acceptable.

## 4. Conclusion

Conventional method of humidity measurement using ultrasound velocity measured has some errors because of the increased sound velocity caused by the air humidity. A new equation is introduced for non-contact measurement of relative humidity using reference temperature, atmospheric pressure and sound velocity measured. Experiments based on the method using the equation (2) were carried out. The experimental data of relative humidity approximately agree with the reference data so that it suggests that this non-contact measurement of the relative humidity using the sound velocity affected by the humidity could be adaptable for practical use. We will perform experiments for data to establish more accurate measurement method of relative humidity.

## References

1. F. E. Gueuing et al.: IEEE Trans. Instrum. Meas. **46** (1997) 1236.
2. K. Ikeda: Jpn. J. Appl. Phys. **37**(1998) 3047.
3. K. Mizutani, S. Kawabe, I. Saito and H. Masuyama: Jpn. J. Appl. Phys. **45** (2006) 4516.
4. K. Mizutani, K. Itoga, K. Kudo, L. Okushima and N. Wakatsuki: Jpn. J. Appl. Phys. **43** (2004) 3090.
5. E.J.Evans and E.N.Bazley: Acoustica **6**(1956) 238
6 R. Raspt, C.J. Hickey and J. M. Sabatier: J.Acoust.Soc.Am. **105** (1999) 65.
7. Y. Mao: J.Acoust.Soc.Am. **104** (1998) 664.

Proceedings of Symposium on Ultrasonic Electronics, Vol. 29 (2008) pp. 71-72
11-13 November, 2008

# Measurement of Flow Velocity in Circular Tube Using a Fourier Transform Spectrometer

フーリエ変換スペクトロメータを用いる円管内の流速測定

Tomoyuki Izumi[1†], Naoto Wakatsuki[1] and Koichi Mizutani[1] ([1] Univ. Tsukuba)
泉知行[1‡], 若槻尚斗[1], 水谷孝一[1] ([1]筑波大院・シス情工)

## 1. Introduction

Measurement of flow velocity and flow rate is widely applied technique in plant engeneering and so on, and many measurement method for each measued object is established. In recent years, transposing technique for fine particle using ultrasonic manipulator is well investigated and is expected to applied in medical field.[1] As the peripheral technology of that, flow velocity measurement of liquid contains fine particle or micro bubble is required. Common velocity measurement methods for such a object are particle image velocimetry (PIV)[2] and laser Doppler velocimeter (LDV)[3]. However, LDV requires large and high-precision system. On the other hand, PIV only requires small and simple sensor and other component, but have a low sensitivity with fine particle.

In this study, we suppose a measurement method using Fourier transform spectrometer and apply this method for flow velocity in circular tube, which is taken as commonly measured object. As the object is treated not as a direct image but as a spectrum, our present method gets enough sensitivity for fine particle and does not require large complicated system. The operational principle and experimental results are described in following sections.

## 2. Principle

**Figure 1** shows typical configuration of Fourier transform spectrometer. An object is located between slits and a lens, and in order to be projected by parallel light, the object is assumed to be located on input plane P1. Spectrum of object on P2 that is focal plane of Fourier transform lens. Using transparency distribution of input plane P1 $g(x, y)$, light intensity distribution of focal plane P2 $u(x_0, y_0)$ is directly proportional to power spectrum of $g(x, y)$. It is said that a power spectrum does not contain information of object location $(x, y)$ and its spatial frequency is inversely proportional to object size as the feature. Therefore, even if a particle in P1 moves on this plane, intensity of light on P2 does not change. It is assumed that shape of a particle is sphere, and then $u(x_0, y_0)$ is expressed as follow using polar coordinates $(r, \theta)$.

$$u(r,\theta) \propto r^2\left[\frac{J(k\omega r)}{k\omega r}\right]. \qquad (1)$$

Where $J$ is Bessel function of the first kind, $k$ is $2\pi/\lambda f$, $\lambda$ is wave length of light, $f$ is focal length, $\omega$ is distance from axis of lens on P2. As this formula does not have parameter $\theta$, $u(r, \theta)$ is axial symmetry around the lens axis.

In order to measure flow velocity with that feature, we use a slit array. These slits align at regular intervals $d$ in the direction of flow with particle. It is assumed that velocity of a particle is constant when it passes behind small area of the slits, the particle is illuminated and focus into an image on P2 in regular time interval $\Delta t$. Therefore on P2, intensity of light change at frequency $f = 1/\Delta t$, additionally, form of change does not depend on the place of a slit. Then this variation is converted to electric signal by photo diode placed on P2 near the focal point. As there are a lot of particle in flow, signal is converted to spectrum by FFT in order to calculate variation frequency $f$. If the spectrum has first peak in frequency $f$, flow velocity $v$ is calculated by multiplying $f$ and slit interval $d$.

$$v = fd\,. \qquad (2)$$

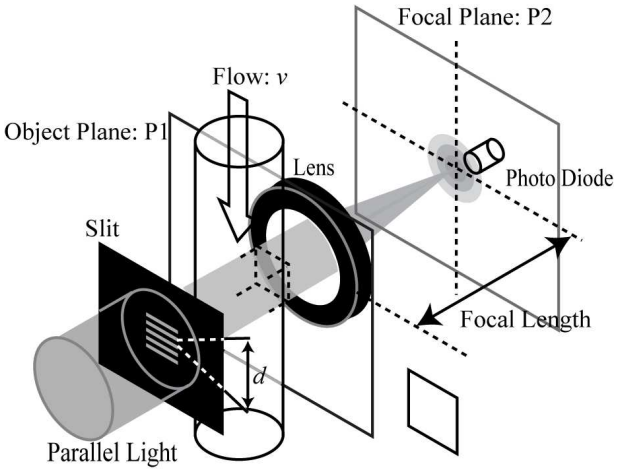


Fig.1 Configuration of a Fourier transform spectrometer

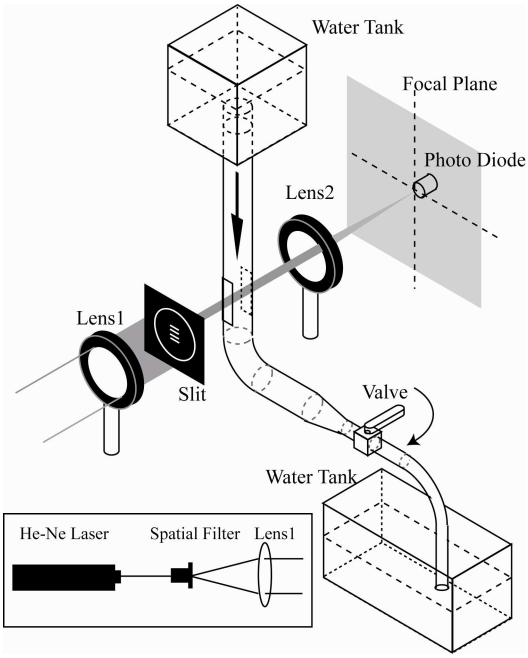


Fig.2 Experimental setup of a spectrometer and a flow system

## 3. Experiments

**Figure 2** shows an experimental setup. Light from 5 mW He-Ne Laser is converted in wide parallel light by a Spatial Filter and the Lens1, and through four slits whoed width is 1.2 mm, interval is 2.4 mm and height is 7.0 mm on P1, projects the image of particles in circular tube flow. Then this light is focused on P2 by convex lens of $f$ = 200 mm. Signal of light intensity variation is picked up by a photo diode placed near the focal point, amplified, A-D converted at 10 kHz sampling rate, and analyzed on computer. Cornstarch of 15 μm average particle size is used as particle. The flow system consists of 10 *l* water tank, circular tube of 590 mm in length and 45 mm in internal diameter, bend duct, diameter convert duct, a hose of 15 mm in internal diameter, a flow adjustment valve, and a drain tank. The inlet height of the tube is 1290 mm from the floor. Several flow velocities are measured for applied velocity in the range from 8.8 mm/s to 120 mm/s. Applied flow velocity is measured by taking a shot of water surface with scale marks using a USB camera..

**Figure 3** shows the spectrum of photo detected signal when reference of flow velocity was 61.2 mm/s. The frequency of a peak $f$ = 26.9 Hz is got from the figure and converted into velocity 64.6 mm/s. **Figure.4** shows comparison between the measured velocity through the present system and the applied velocity. The absolute average of measurement error was 14.1 %. The main cause of error was velocity distribution and rotational flow in the circular tube.

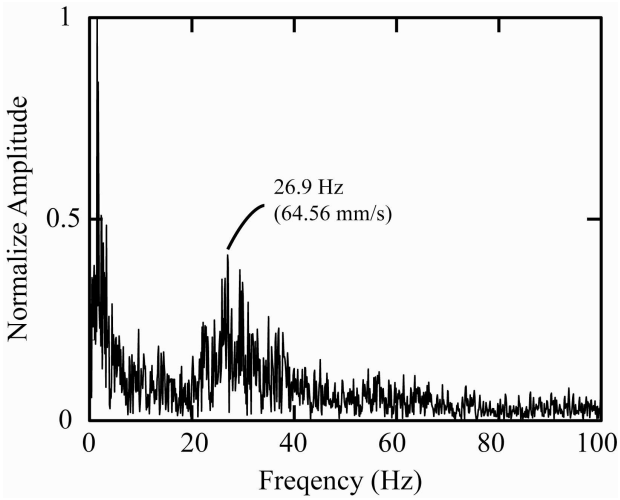


Fig.3 Example of a spectrum in the range of 0 Hz to 100 Hz from a photo-detected signal.

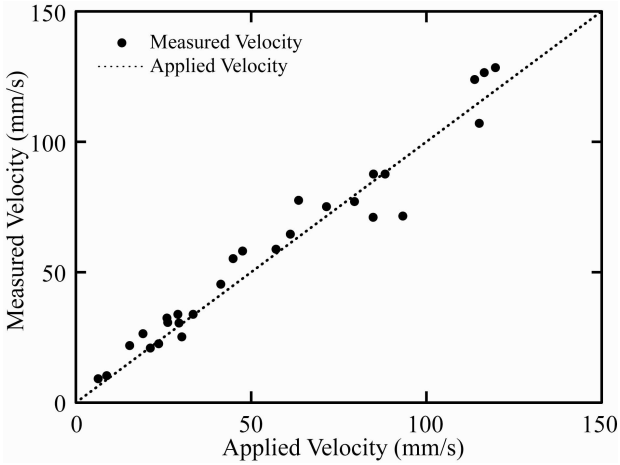


Fig.4 Relationship between applied velocity and measured velocity.

## 4. Conclusions

A simple technique for measuring flow velocity in circular tube using Fourier transform spectrometer has been introduced. Measurement range of the velocity is the experiment is 8.8 mm/s to 120 mm/s. The result of comparing measured and applied velocities is basically conformable. This technique has the advantage of noncontact and real-time sensing and can be used in micro-analyzing of industrial measurements, and biological engineering.

## References

1. Y. Yamakoshi and T. Miwa: Jpn. J. Appl. Phys. **47** (2008) 4127.
2. R. J. Wang, J. Z. Lin, H. B. Xie: Journal of Visualization, **9**, (2006) 209.
3. K. Matsubara, W. Stork, A. wagner, J. Drescher and K. D. M. Glaser: Appl. Opt. **36** (1997) 4516.
4. K. Mizutani, M. Yamazaki, M. Yoshioka and K. Nagai: Jpn. J. Appl. Phys. **38**, (1999) 3116.

1P2a-15

Proceedings of Symposium on Ultrasonic Electronics, Vol. 29 (2008) pp. 73- 74
11-13 November, 2008

# Measurement of Vertical Temperature Distribution Using Sound Probe with Reflectors

反射を用いる音響波プローブによる垂直温度分布計測

Ikumi Saito‡, Koichi Mizutani, Naoto Wakatsuki and Satoshi Kawabe (Univ. Tsukuba)
齋藤育‡，水谷孝一，若槻尚斗，川辺聡 （筑波大院・シス情工）

## 1. Introduction

Efficient airconditioning systems are needed from various perspectives such as realization of comfortable working conditions and energy saving[1,2]. To maintain adequate indoor temperature is the most important. In recent years, facilities tend to grow in size for the mechanization and automation. Therefore, it is difficult to keep adequate indoor temperature in whole spaces. It is necessary to measure temperature distribution for realization of the efficient airconditioning systems[3,4]. In particular, the vertical temperature distribution is more apparent more than the horizontal one. However, the vertical temperature distribution is difficult to measure in large scale spaces. In this paper, we discribe a measurement system of a vertical temperature distribution using sound probes with reflectors. By using the reflectors, the temperature distribution can be measured by a single pair of a loudspeaker (SP) and a microphone (MIC).

## 2. Principle of measurement

**Figure 1** shows a schematic of the measurement of the vertical temperature distribution using sound probes with reflectors. This measurement system consists of a single pair of a SP, MIC and *n* reflectors. Therefore, this system has *n* sound probes. Here, areas bounded by reflectors are defined as Area 1, Area 2, … and Area *n*. The propagation paths between the acoustic sensor and each reflector are defined as $L_1$, $L_2$, … and $L_n$ (m) and times of flights (TOFs) of each sound probe are defined as $t_1$, $t_2$, … and $t_n$ (s). In addition, the mean sound velocity of each area is defined as $c_1$, $c_2$, … and $c_n$ (m/s) and the mean temperature of that is defined as $T_1$, $T_2$, … and $T_n$ (°C). The temperature distribution can be measured from the temperatures of these areas. The sound velocity in Area 1, $c_1$ is expressed as

$$c_1 = \frac{2L_1}{t_1}. \tag{1}$$

E-mail:saitou@aclab.esys.tsukuba.ac.jp

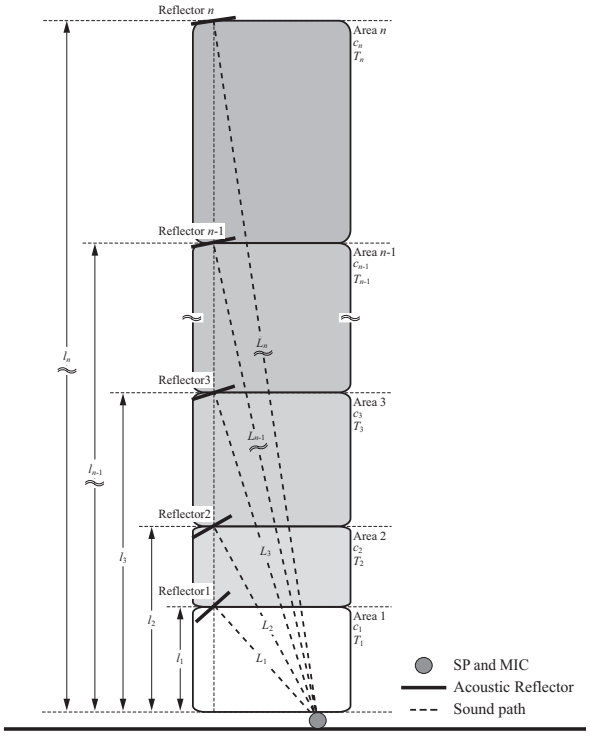


**Fig. 1** Schematic of a measurement of temperature distribution using sound probes with reflectors.

The sound velocity depends on the mean temperature on the propagation path. Therefore, the mean temperature $T$ (°C) is expressed as

$$T = \frac{\mathrm{T}_0}{331.32^2}c^2 - \mathrm{T}_0 \quad (\mathrm{T}_0 = 273.15\ \mathrm{K}). \tag{2}$$

The mean temperature in Area 1, $T_1$ can be obtained from eq. (2) by substituting the sound velocity, $c_1$. In addition, the TOF in Area 2, $t_2$ is expressed as

$$t_2 = \frac{2l_1L_2}{l_1c_1} + \frac{2(l_2 - l_1)L_2}{l_2c_2}, \tag{3}$$

where $l_1$, $l_2$, … and $l_n$ denote the heights of reflectors from the acoustic sensor. $c_2$ is given by solving eq. (3),

$$c_2 = \frac{2(l_2 - l_1)L_2c_1}{l_2t_2c_1 - 2l_1L_2}, \tag{4}$$

$c_1$ has already been obtained by eq. (1). Thus, the mean temperature in Area 2, $T_2$ can be calculated. Here, the general form of eq. (3) is expressed as

$$t_n = \frac{2l_{n-1}L_n}{l_n c'_{n-1}} + \frac{2(l_n - l_{n-1})L_n}{l_n c_n}, \quad (5)$$

where $c'_{n-1}$ is the apparent velocity of the sound reflected by Reflector $n$-1, $c'_{n-1}$ is expressed as

$$c'_{n-1} = \frac{2L_{n-1}}{t_{n-1}}. \quad (6)$$

The general form of eq. (4) is expressed as

$$c_n = 2(l_n - l_{n-1})\left(\frac{t_n l_n}{L_n} - \frac{t_{n-1}l_{n-1}}{L_{n-1}}\right)^{-1}. \quad (7)$$

The mean sound velocity in each area is calculated sequentially. Therefore, the mean temperature of each area is obtained by use of eqs. (2) and (7).

## 3. Experimental verification and result

**Figure 2** shows a schematic of the experimental setup. The experiment was carried out in an anechoic room. A SP and MIC was located on the floor and three acoustic reflectors were located at the heights 1.00, 1.45 and 1.95 (m) from the acoustic sensor, respectively. That is, this measurement system has three sound probes. The reflectors are made of plastic disks of 0.2 m (H) × 0.3 m (V). The transmitted and received signals were processed using a personal computer. The received signals are sampled by the A-D and D-A converter (National Instruments) with the sampling frequency at 250 kHz. The transmitted signals were chirp signals of 5.0 ± 2.5 kHz with ten waves. The TOFs were determined from the cross correlation of the transmitted and received signals. The measured

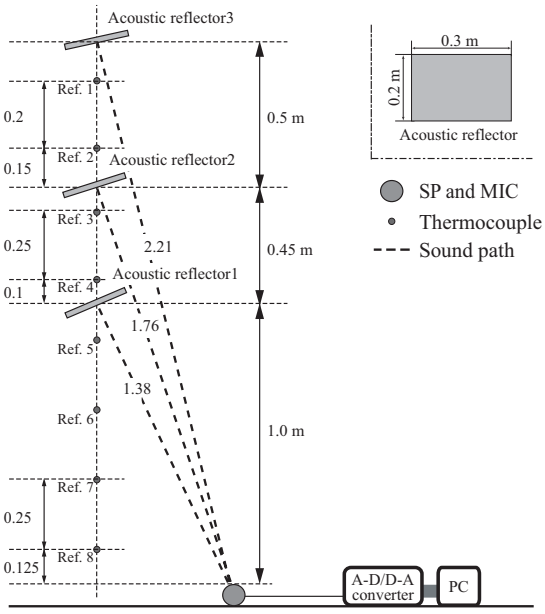


**Fig. 2** Experimental setup. Vertical temperature distribution was measured by three sound probes.

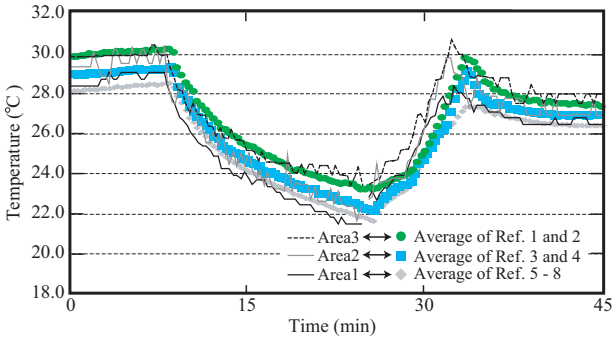


**Fig. 3** Experimental result of mean temperature in each area.

**Table I** Mean temperature results for 45 minutes in each area.

| | Area1 | Area2 | Area3 |
|---|---|---|---|
| Measured (℃) | 26.4 | 27.1 | 27.7 |
| References (℃) | 25.5 | 26.0 | 26.8 |
| Error (℃) | 1.1 | 1.1 | 0.9 |

TOFs were obtained by averaging from five measurements. The temperature was measured every 20 seconds for 45 minutes. Reference values of the temperature were measured using eight thermocouples.

**Figure 3** shows the experimental result of mean temperature in each area. **Table I** shows the mean temperature results for 45 minutes in each area. The mean temperature in each area contains error within 1.1 °C. From these results, it was verified that this measurement system using the reflectors is superior to the response against the temperature change and it can measure the vertical temperature distribution.

## 4. Conclusion

In this paper, we described a measurement of a vertical temperature distribution using sound probes with reflectors. The mean temperature in each area could be measured with errors within 1.1 °C. In addition, we verified the response of sound probes against the temperature change and could simplify the system to measure the temperature distribution. It is considered that the constitution of this system can more simplify by using the wall and ceiling of spaces.

## References


1. G. C. Bakos, E. Tsioliaridou and N. F. Tsagas: Energy Build. **38** (2006) 45.
2. I. Saito, N. Wakatsuki, K. Mizutani, M. Ishii, L. Okushima and S. Sase: Jpn. J. Appl. Phys. **47** (2008) 4329.
3. K. Mizutani, S. Kawabe, I. Saito and H. Masuyama: Jpn. J. Appl. Phys. **45** (2006) 4516.
4. K. Kudo and K. Mizutani: Jpn. J. Appl. Phys. **43** (2004) 3095.

1P2a-16

Proceedings of Symposium on Ultrasonic Electronics, Vol. 29 (2008) pp. 75- 76
11-13 November, 2008

# Preconsolidation stress determination of clay by using ultrasonic waves

Hyung-Koo Yoon [1‡], Joon Han Kim [1], Young-Uk Kim [2], Jong-Sub Lee[1]
([1] Korea University, [2] Myongji University)

## 1. Introduction

When the load or stress is applied, soil starts to deform. The vertical deformation under no lateral strain is related to the compressibility of the soils. The compressibility increases dramatically at preconsolidation stress. The preconsolidation stress is the maximum stress, which was applied into the soil.

Many methods, such as Casagrnade and Onitsuka methods, have been proposed to evaluate the preconsolidation stress. These methods use the global settlement without considering the micro-strain behavior. In this paper, the new method for the evaluation of the preconsolidation stress using ultrasonic shear waves is suggested. This paper includes, the currently used methods for the preconsolidation stress evaluation, the new method, experiments, result analyses, and conclusion.

## 2. Preconsolidation stress evaluation

The preconsolidation stress has been evaluated by several methods, such as Casagrande, Janbu, Onitsuka, and so on. One of the most commonly used methods is the Casagrande method [1]. Casagrande method is based on the void ratio e and the vertical effective stress p' in logarithmic scale (log). The void ratio is the ratio of the net volume of the void to the total solid volume. Because the lateral strain is not allowed in this system, the void ratio is directly calculated by measuring the vertical settlement. In e-log p' curve, the minimum radius of curvature is selected; the horizontal and tangential lines are drawn at the minimum radius; the bisector line between horizontal and bisector lines is drawn; and the tangential line is drawn in e-log p' curve. The intersection is preconsolidation stress. This method, however, is user dependent. The Casagrande method produces 15~50% higher value [2].

Janbu proposed the constrained modulus method. The constrained modulus M is the reciprocal value of the column compressibility coefficient $m_v$ ($M=1/m_v$). The huge drop of the constrained modulus, which is the breakdown of soil resistance stress, captures the preconsolidation stress. The Janbu's constrained modulus method is mainly used for the high sensitive and low overconsolidation ratio(OCR) clay.

‡ Email: jongsub@korea.ac.kr

Another method was suggested by Jose [2]. In Jose's method, log e is used instead of e in e-log p' curve. The Jose's method determines the preconsolidation stress based on the intersection between pre-yield and post-yield. The Jose's method was modified by Onitsuka [3]. Onitsuka use ln(1+e)-log p' instead of log e-log p' to avoid the negative value in void ratio term. The preconsolidation stress in Onitsuka method is the intersection of pre-yield and post-yield lines. It is known that the Onitsuka method produces the most precise preconsolidation stress.

## 3. Shear wave velocity method

The previous methods are based on the void ratio, which reflects the global vertical settlement. The global vertical settlement results in the rearrangement, rotation, and sliding of particles. The strain level of the global vertical settlement is middle strain.

The small strain instead of the middle or large strain may be captured by the ultrasonic waves. The ultrasonic waves in this study are shear waves, which can capture inter-particle contact behavior. The inter-particle contact behavior changes dramatically at the preconsolidadtion stress because the inter-particle forces such as cementation or bonding are broken. The shear wave velocity versus the vertical effective stress (Vs-log p') is plotted during consolidadtion test. Vs-log p' produces the bilinear curve and intersection of the bilinear curve is corresponding to the preconsolidation stress. At the preconsolidation stress, inter-particle contact starts to break. Thus, the shear wave velocity method considers the small strain inter-particle contact behavior.

## 4. Experiment program

A series of the verification tests are carried out by using undisturbed specimen obtained at Incheon(I), Busan(B) and Kwangyang(K) in Korea. The conventional oedometer cell, which is equipped with bender elements, is used to measure the settlement and the shear wave velocity. Note the bender elements are double-layer PZT elements. The dimension of oedometer cell is 74mm in diameter and 63mm in height. And the bender element is 11 mm in length, 4 mm in width, and 0.6 mm in thickness. For the generation and detection

of the shear waves in the soil, the signal generator, filter-amplifier, and oscilloscope are used.

After soil specimen is placed into the oedometer cell, the normal stress is applied. The load increment ratio is about one. Each loading steps is about 24~48 hours to ensure the dissipation of the all excess pore pressure when the settlement does not proceed after the dissipation of the excess pore pressure, the vertical settlement and shear waves are measured.

## 5. Analyses of experimental results

At each loading stage, the vertical settlement and shear waves are measured. The measured shear wave signatures are plotted in Fig. 1 for clays obtained at Incheon and Busan. As the vertical effective stress p' increases, the first arrival of shear waves decreases and the resonant frequency increases.

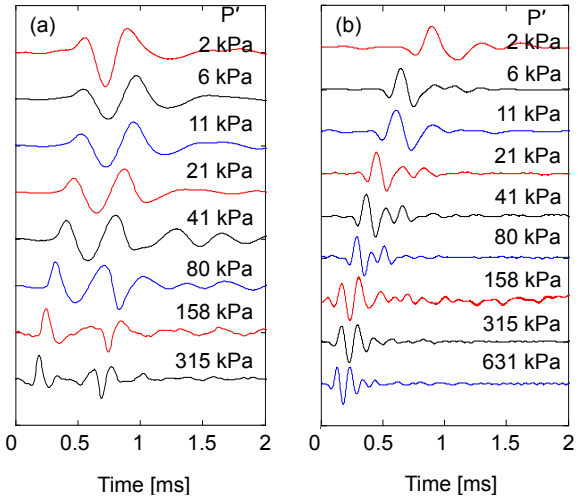


Fig. 1 Measured shear wave signatures: (a) Incheon ; (b) Busan.

The evaluation of the preconsolidadtion stress is demonstrated in Fig. 2 by using Casagende, Onitsuka, and shear wave velocity methods for Incheon clay. The preconsolidation stress evaluated by the shear wave velocity method is almost identical with that estimated by Onitsuka method. The Casagrande method, however, produces the highest preconsolidation stress. The preconsolidation stresses evaluated by three methods are summarized in Table I. Table I confirms again that the Onitsuka and shear wave velocity method produce the similar preconsolidation stress, and the Casagrande method yields the highest value.

## 6. Conclusion

This paper reviews the preconsolidation stress evaluation methods, which are commonly used, and new method using ultrasonic shear wave velocity. The currently used method evaluates the preoconsolidation stress based on the global vertical settlement. The preconsolidation stress by the shear wave velocity is the intersection point at the bilinear curve of Vs-log p'. The preconsolidation stresses estimated by the new shear wave velocity method produce the very similar values evaluated by the Onitsuka method, which yields the almost real preconsolidation stress. This study confirms that the new method is simple, easy, and producing the reliable preconsolidation stress.

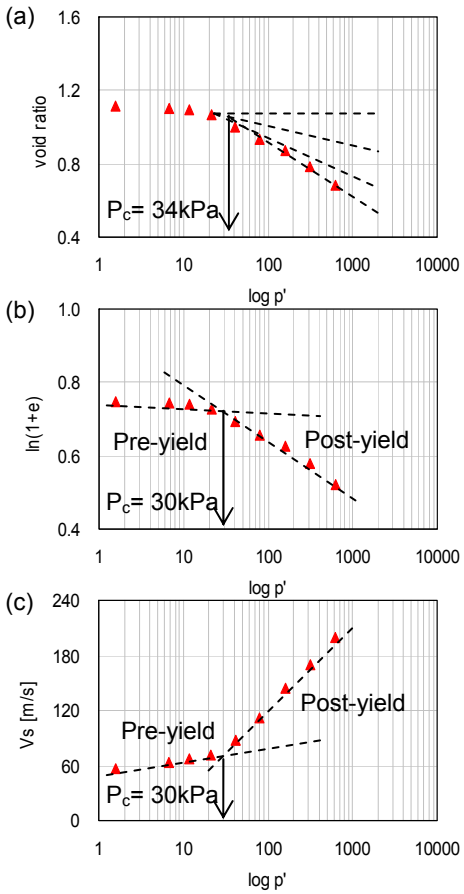


Fig. 2 Determinating preconsolidation stress at Incheon site: (a) Casagrande; (b) Onitsuka; (C) shear wave method.

Table I. Preconsolidation stress comparison.

| Site | depth | Casagrande | Onitsuka | Shear wave |
|---|---|---|---|---|
| I | 6m | 34 kPa | 30 kPa | 30 kPa |
| B | 10m | 28 kPa | 19 kPa | 18 kPa |
| K | 3m | 20 kPa | 18 kPa | 18 kPa |

**References**

1. A. Casagrande: BSCE, April(1932) 72.
2. B. T. Jose, A. Sridharan and B. M. Abraham: ASTM. 12(1989).230.
3. K. Onitsuka, Z. Hong, Y. Hara and S. Yoshitake: 35(1995).61.

Proceedings of Symposium on Ultrasonic Electronics, Vol. 29 (2008) pp. 77- 78
11-13 November, 2008

# Nondestructive Evaluation of Compound Weld Defect by Photoacoustic Microscopy

光音響顕微鏡による複合溶接欠陥の非破壊評価

Daijiroh Shiraishi†, Haruo Endoh and Tsutomu Hoshimiya (Facult. Eng., Tohoku Gakuin Univ.)
白石大二郎，遠藤春男，星宮　務　（東北学院大 工）

## 1. Introduction

In indutry, the nondestructive inspection (NDI) of the existence of surface and internal defects at their early stage has become more and more important. The photoacoustic microscopy (PAM) [1] has been applicable to the NDI at the circumstance in which the X-ray penetration or intersectional side-view inspection is not available but front-view illumination is only available.

In this paper, nondestructive evaluation of compound defect in weld metal of aluminum plates was carried out using PAM and the results were compared with those obtained by the X-ray micrograph obtained by tomography and the scanning laser microscope (SLM).

## 2. Experimental Apparatus and Specimen

The basic arrangement of the PAM system constructed for this experiment is the same as that described in a previous publication.[2] The specimens used in the experiments were aluminum plates. The aluminum specimen sampled from welded plates was chosen to include the compound weld defect in which the surface and internal defects were combined together. Two 45 degree-cut aluminum plates with the dimension of 25mm× 40mm and a thickness of 4mm were welded along y-direction as shown in **Fig. 1**. Reconstructed X-ray tomographic images with the intersection of xy-plane viewed from z-direction and xz-plane viewed from y-direction were shown in **Figs. 2 (a) and (b),** respectively. A dark area at the center of the X-ray photograph corresponds to the internal weld defect located in the position of approximately 0.5mm depth from the specimen surface. The region shown by the arrow in Fig. 2 (a) corresponds to the measured area by the PAM. The dotted line surrounded in the round in Fig.2 (a) shows approximate position and size of surface defect. **Fig. 3** shows the cross sectional view of the defect obtained by SLM measurement. The defect width, length and depth are approximately 300μm, 530μm and 790μm, respectively. Welded aluminum plate was mechanically fined with the thickness of 3mm and set in the photoacoustic (PA) cell.

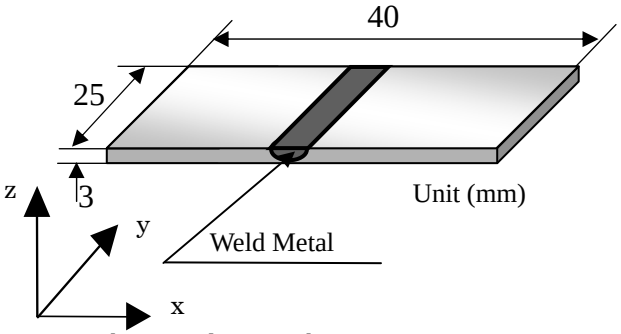


Fig. 1 Schematic drawing showing specimen preparation

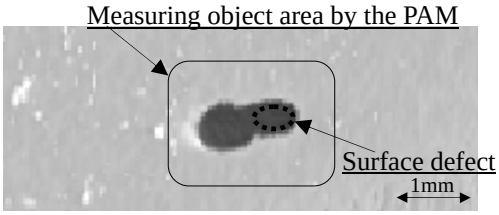


(a) xy-plane view from z-direction

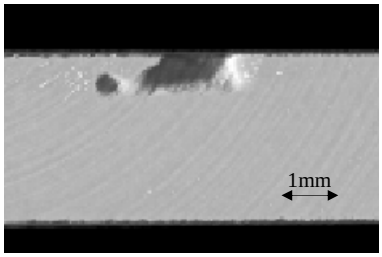


(b) xz-plane view from y-direction

Fig. 2 Photograph of compound weld defect by the lack of joint penetration by X-ray permeation testing

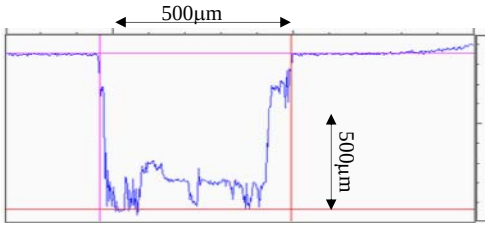


Fig. 3 Cross sectional view of the surface defect obtained by scanning laser microscopy

E-mail : enpal@tjcc.tohoku-gakuin.ac.jp

### 3. Experimental Results and Discussions

The experiments were carried out at different modulation frequencies to obtain the depth profiling by changing the thermal diffusion length.

**Fig. 4** (a) shows the amplitude image obtained at the modulation frequency of 90 Hz for the specimen for the compound weld defect in which the surface defect combined with internal defect and the measured area was 3.0 mm× 3.0 mm. The thermal diffusion length at the modulation frequency of 90 Hz is about 566 μm. A bright area at the center of the PA amplitude image in Fig. 4(a) corresponds to the compound weld defect. In this amplitude image, a particularly round bright area is the surface defect region. In the SLM analysis result, the depth of the surface defect is about 790μm from the specimen surface to internal defect bottom. In the meantime, the internal defect is detected by the X-ray analysis at about 5mm depth. Therefore, the thermal diffusion length is sufficiently long for the thermal wave to penetrate and reach the internal defect. In Fig. 4(a), length of the compound weld defect and size of the surface defect were obtained. Figures 4(b) and 4(c) show the signal distributions along the A-A' line and B-B' line of the PA amplitude image in Fig. 4(a), respectively. The size of compound defect length is guessed again in Fig. 4(b), and it is possible to estimate the measurement of the surface defect in Fig.4(c). **Fig. 5(a)** shows the PA amplitude image obtained at the modulation frequency of 270 Hz for the same specimen for the compound defect. **Fig. 5(b)** shows the signal intensity distribution on the A-A' line of the PA amplitude image in Fig. 5(a). The thermal diffusion length is approximately 327 μm. It is found that the size of internal defect detected from both of Fig. 5(a) and (b) generally decreases. **Fig. 6** shows the PA amplitude image obtained at the modulation frequency of 450 Hz for the specimen for the compound defect and the thermal diffusion length is about 253 μm. In Fig. 6, it is found that the PA signal for the surface defect dominated in the image.

### 4. Conclusion

In this study, we carried out the nondestructive evaluation of the compound defect generated by the welding by PAM, and compared it with X-ray tomographic image and SLM. The separation of surface and internal defects were well performed by changing modulation frequency, and PAM measurement agreed well with X-ray micrograph and SLM measurements.

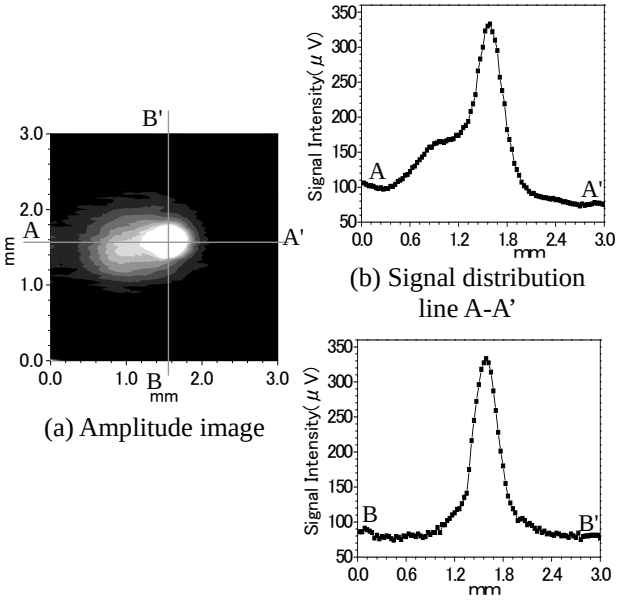


Fig. 4 PA amplitude image and signal distribution for the specimen with compound weld defect (modulation frequencies: 90Hz)

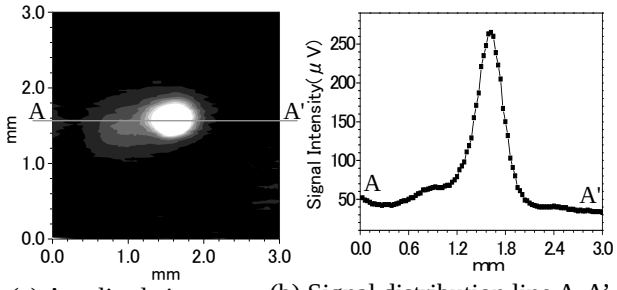


Fig. 5 PA amplitude image and signal distribution for the specimen with compound weld defect (modulation frequencies: 270Hz)

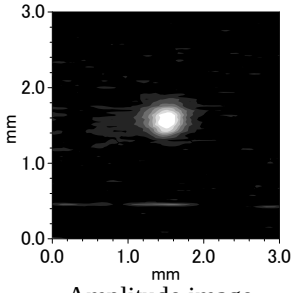


Fig. 6 PA amplitude image and signal distribution for the specimen with compound weld defect (modulation frequencies: 450Hz)

### References

1. H.Endoh, Y.Hiwatashi and T.Hoshimiya: Jpn. J. Appl. Phys. **36**(1997)3312.
2. T. Hoshimiya and K. Miyamoto: Jpn. J. Appl. Phys. **39** (2000) 3172.

Proceedings of Symposium on Ultrasonic Electronics, Vol. 29 (2008) pp. 79- 80
11-13 November, 2008

# Relationship between Photoacoustic Spectra and Thermoelectric Properties of Amorphous Si-Ge-Au Thin Film

アモルファス Si-Ge-Au 薄膜の光音響スペクトルと熱電特性の相関

Hiroaki Takiguchi‡, Makoto Abe, Yoichi Okamoto, Hisashi Miyazaki, and Jun Morimoto (Dept. of MSE, NDA)
滝口　裕章‡, 阿部　誠, 岡本　庸一, 宮崎　尚, 守本　純（防衛大機能材料）

## 1. Introduction

Recently, thermoelectric materials have attracted great deals of attention from the point of the saving energy and the environmental protection. The thermoelectric power generation is the technique to use the wasted heat, which is exhausted from electric power plants, factories, and auto mobiles.

The characteristicts of thermoelectric materials are evaluated by dimensionless figure of merit $ZT= \alpha^2T/(\rho\kappa)$, where $\alpha$, T, $\rho$, and $\kappa$ are thermoelectric power, absolute temperature, electrical resistivity, and thermal conductivity, respectively. One of the criteria for the practical use of the thermoelectric materials is ZT >1. However, the thermal conductivity of thin film is difficult to measure. Therefore, the power factor $P = \alpha^2/\rho$ is commonly used.

We have reported extremely large thermoelectric power of Si-Ge-Au amorphous thin film which maximum ZT value reached around $10^3$.[1,2] It was reported that quasi-stable amorphous phase and/or mixture of microcrystal would be responsible for the large thermoelectric power.[3,4] But the mechanism and appropriate composition ratio of Si, Ge and Au were not clarified sufficiently. In the previous paper,[5] the compostion ratio of Si and Ge was fixed, and photoacoustic (PA) spectra and thermoelectric properties with various Au concentration were measured.

In this paper, we show photoacoustic spectra and thermoelectric properties with various Si and Ge composition ratio, where the Au concentration is fixed at the value where the sign of a thermoelectric power changed.

## 2. Experiments

The sample preparation procedure was almost same as previous paper.[5] Samples were prepared by alternate deposition of Si, Ge and Au in the ultra high vacuum system. The samples were deposited at room temperature. They have 4 layers of Si/Au/Ge/Au as 1 period of deposition. The artificial intervals and total number of periods were kept in 10 nm and 30, respectively. The thickness of the samples was 300 nm. We denoted the samples as (Si layer (nm)/ Au layer (nm)/ Ge layer (nm)/ Au (nm)/ number of intervals) = (x/ 0.2/ 9.6 -x/ 0.2/ 30), where x ranged from 0 to 9.6.

The thermoelectric power and electrical resistivity were measured by four terminal methods during annealing cycles. Annealing temperature was set at 673 K, and one annealing cycle was heat up and cool down between room temperature and 673 K at a rate of 10 K/min.

PA spectra were measured using gas-microphone photoacoustic spectroscopy (PAS) system. The wavelength of excitation light was scanned from 400 nm to 1600 nm with 5 nm step. Measurements were carried out at room temperature.

## 3. Results and Discussion

**Figure 1** shows Si concentration dependence of electrical resistivity at the second annealing cycle. The electrical resistivity decreases with Si concentration increasing. However, the electrical resistivity of one sample of Si: 50 % was one order of magnitude smaller than that of the other samples.

**Figure 2** shows PA spectra of as-deposited samples. Sample (5.3/ 0.2/ 4.3/ 0.2/ 30) has electrical resistivity which smoothly depends on Si concentration. Sample (4.8/ 0.2/ 4.8/ 0.2 /30) has electrical resistivity around one order lower than that of the other samples. The peaks at around 1400 nm come from the absorption of surface adsorbed water. The arrows indicate absorption edge wavelength corresponding to amorphous Si.[5] The wavelengths are 1115 nm in sample (5.3/ 0.2/ 4.3/ 0.2/ 30) and 930 nm in sample (4.8/ 0.2/ 4.8/ 0.2 /30). The composition of two samples is almost the same, but the wavelength is apparently different.

**Figure 3** shows Si concentration dependence of absorption edge wavelength of samples corresponding to amorphous Si. The absorption edge wavelength data could be separated into two

---

g47097@nda.ac.jp

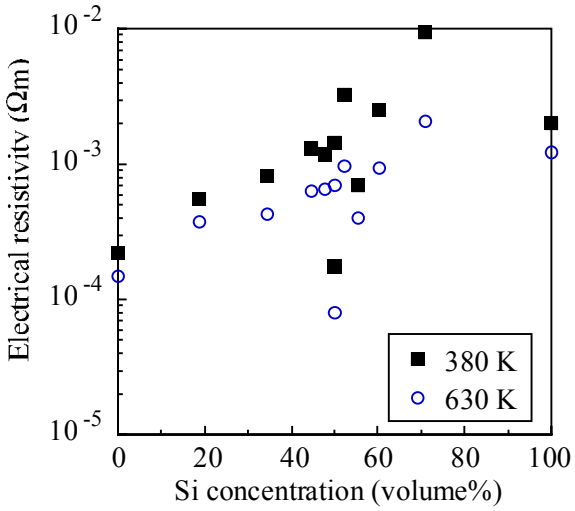


Fig. 1 Si concentration dependence of electrical resistivity at second annealing cycle.

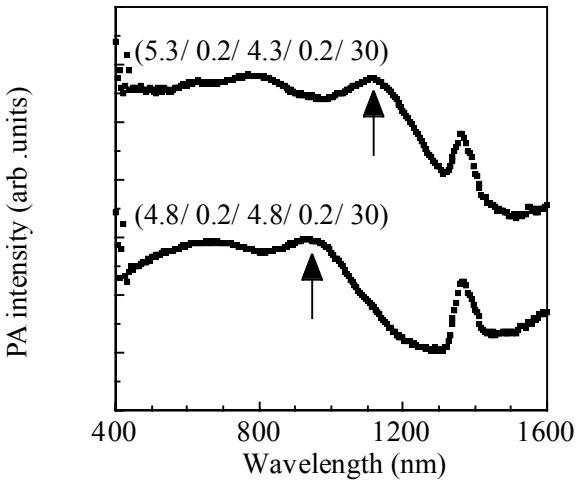


Fig. 2 PA spectra of as-deposited samples.

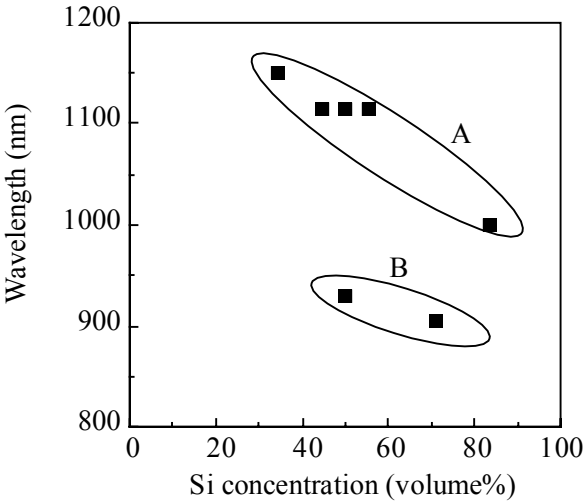


Fig. 3 Si concentration dependence of absorption band edge wavelength of amorphous Si.

groups. In the samples which has longer wavelength (marked by "A"), electrical resistivity increases with Si concentration increasing. In the shorter wavelength samples (marked by "B"), sample of Si: 70 % has electrical resistivity which smoothly depends on Si concentration, and sample of Si: 50 % has lower electrical resistivity than the other samples.

These results would indicate existence of two or more amorphous phases. When electrical resistivity and absorption edge wavelength smoothly depend on Si concentration, the single amorphous phase would be formed, not multi phases. In the other case (electrical resistivity or the wavelength of sample distinctively change with Si concentration), different amorphous phase would be made. Especially, from PAS measurements, the existence of different optical band gaps was found. This fact suggests the formation of the other amorphous phases.

It is well known that substrate temperature has large effects on the degree of crystallinity (or "degree of amorphous") of deposited thin film. In ref. 6, substrate temperature dependence of power factor was reported. Even if samples had same composition, thermoelectric properties changed with changing substrate temperature. We deduced that "degree of amorphous" influenced thermoelectric properties. To control "degree of amorphous", the change of substrate temperature would be effective.

## 4. Conclusion

Optical band gap changed when electrical resistivity changed distinctively. Therefore, the existence of different amorphous phase could be confirmed. Especially, the difference of optical band gap by PAS suggested the existence of two or more amorphous phase. Amorphous phase that was appropriate to thermoelectric materials existed. To control amorphous phase, the change of substrate temperature was one of the effective ways.

## References


1. Y. Okamoto, H. Uchino, T. Kawahara, and J. Morimoto: Jpn. J. Appl. Phys. **38** (1999) L945.
2. H. Uchino, Y. Okamoto, T. Kawahara, and J. Morimoto: Jpn. J. Appl. Phys. **39** (2000) 1675.
3. K. Fukui, M. Nakamori, Y. Okamoto, and J. Morimoto: Proc. 24th Int. Conf. Thermoelectrics, 2005, p. 172.
4. H. Takiguchi, Y. Okamoto, and A. Aruga: Jpn. J. Appl. Phys. **46** (2007) 4622.
5. H. Takiguchi, Y. Okamoto, H. Miyazaki, and J. Morimoto: Jpn. J. Appl. Phys. **47** (2008) 3980.
6. A. Miyata, Y. Sato, Y. Okamoto, T. Kawahara, and J. Morimoto: Proc. 21st Int. Conf. Thermoelectrics , 2002, p. 442.

Proceedings of Symposium on Ultrasonic Electronics, Vol. 29 (2008) pp. 81-82
11-13 November, 2008

# Detection and Analysis of Photothermal Signal Generated in Capillary Channel flow

キャピラリー流路中の光熱変換信号の検出と解析

Satoshi Hirashima, Hitoshi Katae, Akira Harata
(Univ. Kyushu, Development of Molecular and Material Sciences.)
平島諭，片江等、原田明 （九大院 総理工）

## 1. Introduction

Recently, microfluidic devices, called lab-on-chip or μ-TAS atracts great attention. These devices have more advantages, include reduction of reagent, reaction time, and cost than traditional devices. Highly sensitive detection technique is necessary for these devices, because smaller volume are disadvantage to detect target chemical substances. Laser induced fluorescence (LIF) method has excellent sensitivity. However, the LIF can detect only fluorescent chemicals; unfortunately most chemicals are generally nonfluorescent. Photothermal spectroscopy containing photothermal lens (PTL) method is one of the most sensitive detection methods for nonfluorescent chemicals[1-2].

Conventionally, visible laser have been utilized for excitation beam source of PTL system. Ultraviolet excitation laser is desired to detect more kinds of chemicals, which absorb only UV light and are transparent to visible light. We designed and manufactured ultraviolet excitation-visible enhancement photothermal lens system utilized ultraviolet excitation beam in the range of 212 to 220nm, and detected non-labeled amino acids in aqueous solution.[3)]

Ultraviolet laser excited PTL system enables to detect many nonfluorescent chemicals, while separation techniques to distinguish many kinds of nonfluorescent chemicals are desired. High performance liquid chromatography adapting capillary channel flow and micro-separation column (μ-HPLC) is one of the separation techniques suited to PTL. The linear flow rate of capillary channel flow dominates sensitivity of PTL system and separation performance. In addition to linear flow rate, excitation beam chopping frequency is important factor, affecting thermal diffusion length, signal amplitude, and back ground noise. In this work we investigated dependence of linear flow rate and chopping frequency on the PTL signal

## 2. Theory

Photothermal lens signal ($S$)can be written as

$$S \propto \frac{1}{vf} \qquad (1)$$

$v$ is linear flow rate, and $f$ is excitation beam chopping frequency.

## 3. Experimental

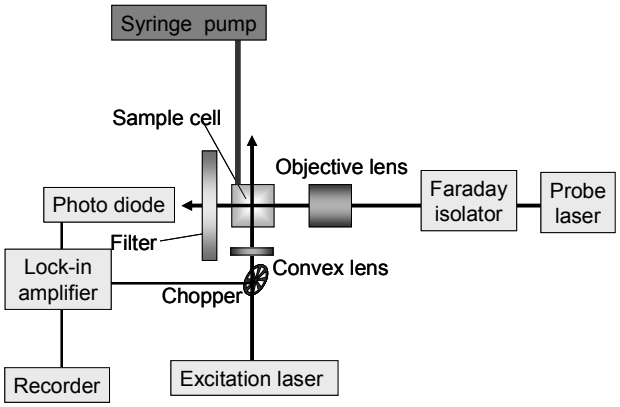


**Figure1.** Schematic diagram of photothermal lens detection system

**Figure 1** shows the schematic diagram of photothermal lens system. It consisted of a diode laser (λ=408nm) as excitation laser and a diode laser (λ=682nm) as the probe laser. Excitation beam irradiated the sample solution in the capirally cell (ID 100μm) with a convex lens (focal length, 100mm). Photothermally generated heat in the sample solution was monitored with probe beam, which was focused with an objective lens (x40). Excitation and probe beams were crossed in the solution. Reducing the reflected light of probe beam is achieved with a Faraday isolator. The light intensity was measured with a photodiode, and the PTL signal intensity was measured with a lock-in amplifier. The sample solution was run through the sample cell at a linear flow rate of 3.5-35 mm/sec with using a syringe pump. Chopping frequency of excitation beam was adjusted 20-600 Hz with a function generator. All experiments were carried out with rhodamine B in methanol as the sample solution (sample concentration, 14μM).

## 4. Results and discussion

4.1 Chopping frequency dependence

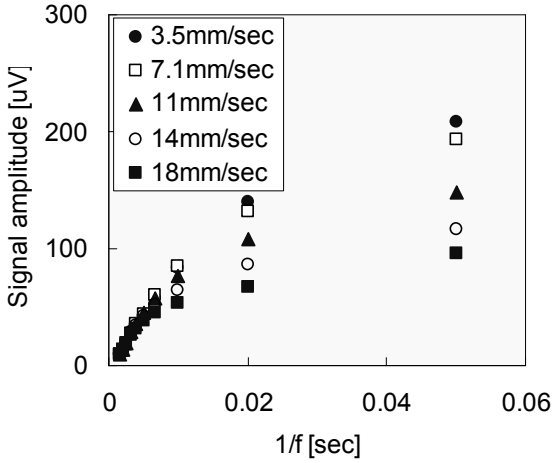


**Figure 2.** Inverse of chopping frequency (f) dependence of signal amplitude
(flow rate=3.5-18mm/sec)

**Figure.2** shows chopping frequency dependence of signal amplitude. Signal was average value measured in 30 sec. In a high chopping frequency, signal amplitude was inversely proportional to chopping frequency. This shows that increase of chopping frequency decrease signal amplitude as decreasing of irradiates time. In a low chopping frequency, signal amplitude reached to a steady state strongly affected by the flow rate. This is due to heat diffusion form the excitation laser spot to the surroundings and motion of the heated area.

4.2 Linear flow rate dependence

**Figure.3** shows linear flow rate dependence of signal amplitude. In a fast linear flow rate, signal amplitude was inversely proportional to the flow rate. This is because increase of the flow rate increases the volume of the heated region. In a slow linear flow rate, signal amplitude reached to a steady state. This is due to a size balance of the heated volume and the thermal diffusion length.

4.3 Sensitivity and separation performance

To evaluate of sensitivity of system, back ground noise was measured for 20-600 Hz of chopping frequency, and for 3.5-21 mm/sec of linear flow rate. This result shows that decreasing of chopping frequency contributes increasing of background noise, while linear flow rate doesn't effect

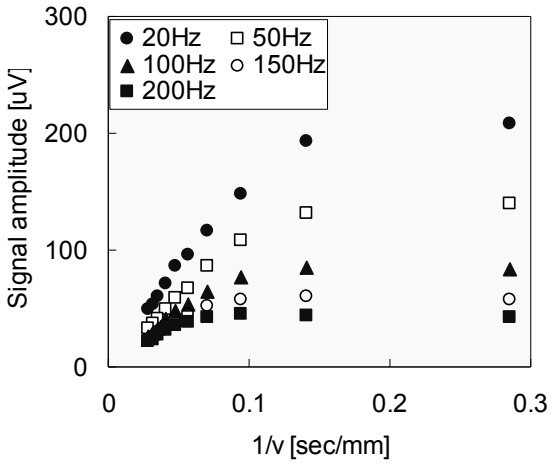


**Figure3.** Inverse of linear flow rate (v) dependence of signal amplitude
(chopping frequency=20-200Hz)

background noise. Therefore, the optimum chopping frequency is consider to 50-100Hz, and the optimum linear flow rate is consider to slower as possible. However a slow linear flow rate contributes negative effects to separation performance in μ-HPLC, photolysis of reagents, and collection time of experimental data. Increase of the capillary crosssection for the sample cell decrease collection time, while harms the separation performance. We investigated effect of increasing capillary crosssection on separation performance, indicated that allowable maximum crosssection size is lower than 960mm$^2$.

## 5. Conclusion

To optimize experimental conditions of photothermal detection for a μ-HPLC separation technique, chopping frequency of excitation beam and linear flow rate were investigated. It is showed that decreasing of chopping frequency and linear flow rate contributes is required to increase of signal amplitude. Optimum chopping frequency is considered to 50-100Hz to decrease back ground noise. A slow linear flow rate with a large cross size capillary cell is the best solution for the photothermal detection. Optimization of flow condition contributes development microfluidic devices.

## References

1. A. Harata, K. Fukushima, Y. Hatano, : Anal. Sci., 18 (2002) 13.
2. S.Hirashima, A.Harata : Proc. Symp. Ultrason. Electron., Vol.26,(2005) pp.333 16-18 Nov,2005
3. S.Hirashima, A.Harata : Jpn. J. Appl. Phys. 47 (2007) 3970.

Proceedings of Symposium on Ultrasonic Electronics, Vol. 29 (2008) pp. 83- 84
11-13 November, 2008

# Millisecond Brillouin Scattering Spectroscopy in Solid and Gas Materials
# 固体と気体のブリュアン散乱のミリ秒観察

Yasuo Minami‡ and Keiji Sakai
(Inst. Indust. Sci., Univ. of Tokyo)
南康夫, 酒井啓司
（東大生研）

## 1. Introduction

We improved sensitivity of the millisecond optical beating Brillouin spectroscopy, and observed the Brillouin scattering spectra in solid (polymethylmethacrylate, PMMA) and gas (air) materials. Though the measurable sample has been restricted to liquid materials due to poor scattering efficiencies of solids and gases, it is now possible to apply the technique to all kinds of materials.

This technique enables us to observe slow dynamics in frequency range from 3 MHz to 300 MHz in non-contact manner.

## 2. Experiment

The measurement were carried out with the millisecond optical beating spectroscopy.[1] **Figure. 1** shows the block diagram of the experimental setup. The incident light and the reference light intersect in the specimen. Then, the scattered light collinear with the reference light is detected by a high-speed photo detector, and they make the optical beating signal. The beating signal is captured by digital oscilloscope in time domain. Finally, we obtain the power spectrum of the phonon by FFT of the signal.

To demonstrate the improved sensitivity, we performed the millisecond Brillouin scattering experiments in PMMA as solid specimen and air as gas specimen.

## 3. Results and discussions

**Figure 2** shows the typical Brillouin peak observed with the millisecond optical beating Brillouin spectroscopy in PMMA. Since an increased instrumental width would be dominant in the Brillouin line, a typical spectrum of the Brillouin peak obtained is expected to be a curve of Gaussian shape.[2] The scattering efficiency of this specimen is very poor and is about 1/5 of that of liquid. As shown in the figure, the observed spectrum is well fitted by Gaussian curve representing the instrumental broadening caused by the focusing the Gaussian beams of the incident and reference lights. We could improve the detection sensitivity and determine the phonon velocity within a few ms at the cost of decay measurement. We observed the dispersion relation in PMMA over the wavenumber range from $k = 8.1\times10^{4}$ m$^{-1}$ to $k = 5.3\times10^{5}$ m$^{-1}$ at 300 K and the result is shown in **Fig. 3**. The solid line shows the best fitted relation of $\omega = vk$ giving 2860 m/s for PMMA. This phonon velocity agrees with the value of 2770 m/s obtained with the conventional optical beating spectroscopy at 100 MHz.[3]

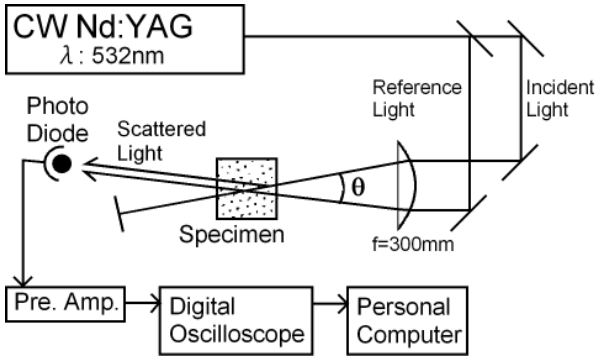


Fig. 1 Block diagram of the millisecond optical beating Brillouin spectroscopy.

We carried out the real time Brillouin scattering experiment also for air, and the typical Brillouin peak observed is shown in **Fig. 4**. The scattering efficiency of air is only about 1/100 of that of liquid. As shown in the figure, the observed spectra are also well fitted by Gaussian curve. The dispersion relation obtained for air at 300 K is shown in **Fig. 5**. The solid line shows the best fitted relation of $\omega = vk$ giving 350 m/s for air. This value is close to the literature value of 348 m/s at 300 K.

E-mail: yminami@iis.u-tokyo.ac.jp

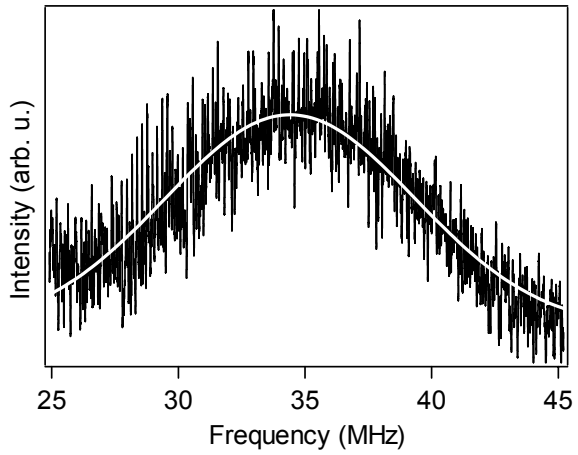


Fig. 2 Brillouin peak in PMMA observed with the millisecond Brillouin spectroscopy. The white solid line is the best-fitted Gaussian curve. The sampling rate and measurement time are 500 MS/s and 10 ms, respectively. The scattering wavenumber is $k = 8.1 \times 10^4$ m$^{-1}$.

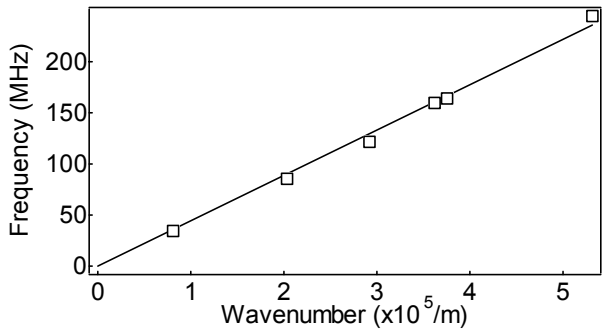


Fig. 3 Dispersion relation of acoustic phonon in PMMA obtained with the millisecond Brillouin spectroscopy over the wavenumber range from $k = 8.1 \times 10^4$ m$^{-1}$ to $k = 5.3 \times 10^5$ m$^{-1}$ at 300 K. The experimental points (□) are well fitted by a straight line, of which the gradient yields the phase velocity, 2860 m/s for PMMA.

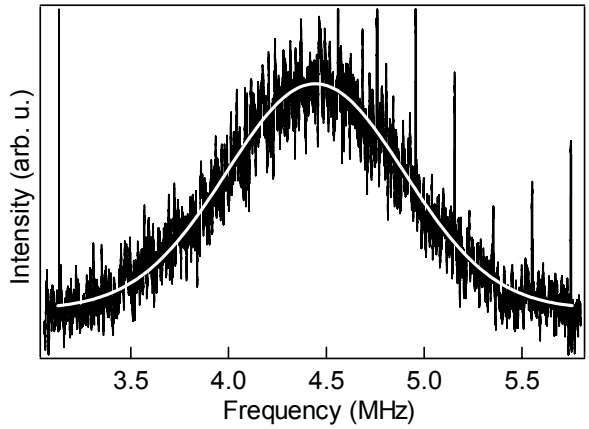


Fig. 4 Brillouin peak observed with the millisecond Brillouin spectroscopy in air. The white solid line is the best-fitted Gaussian curve. The sampling rate and measurement time are 250 MS/s and 200 ms, respectively. The scattering wavenumber is $k = 8.1 \times 10^4$ m$^{-1}$.

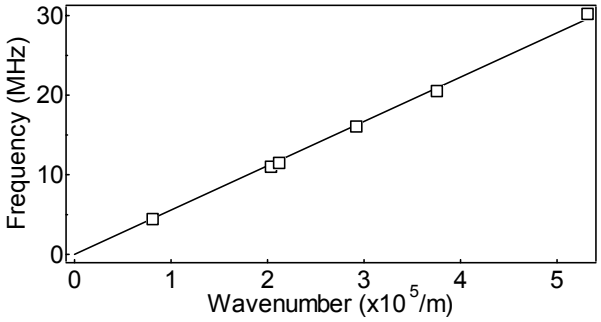


Fig. 5 Dispersion relation of acoustic phonon in air obtained with the millisecond Brillouin spectroscopy over the wavenumber range from $k = 8.1 \times 10^4$ m$^{-1}$ to $k = 5.3 \times 10^5$ m$^{-1}$ at 300 K. The experimental points (□) are well fitted by a straight line, of which the gradient yields the phase velocity, 350 m/s for air.

Error in determining the phonon velocity at a certain frequency can be estimated from the scatter of the data from the line, which is better than 3 %.

## 4. Conclusion

We performed millisecond observation of Brillouin scattering from solid and gas materials with optical beating method, and obtain appropriate dispersion relations of them.

This technique is applicable to the observation of the dynamics of fast reaction and phase transitions, and so on.

## Acknowledgment

This work was partly supported by a Grant-in-Aid for Scientific Research from the Ministry of Education, Culture, Sports, Science and Technology of Japan. This work was also partly supported by Research Fellowships of the Japan Society for the Promotion of Science for Young Scientists.

## References

1) Y. Minami, T. Yogi, S. Mitani, and Keiji Sakai: J. Appl. Phys. **102** (2007) 013111.
2) Y. Minami, T. Yogi and K. Sakai: Jpn. J. Appl. Phys. **45** (2006) 4469.
3) K. Hattori, T. Matsuoka, K. Sakai, and K. Takagi: Jpn. J. Appl. Phys. **33** (1994) 3217.

Proceedings of Symposium on Ultrasonic Electronics, Vol. 29 (2008) pp. 85- 86
11-13 November, 2008

# Cladding-Mode Dependence of Long-Period Fiber Grating Vibration Sensor

# 異なるクラッドモード次数を用いた長周期光ファイバグレーティング振動センサの特性

Hiroyuki Somatomo, Atsushi Wada, Satoshi Tanaka and Nobuaki Takahashi
(National Defwnse Academy)

杣友 宏行，和田 篤，田中 哲，高橋 信明 （防衛大学校）

## 1. Introduction

In recent years there has been attracted much attention in application of fiber-optic sensors for environmental monitoring, smart structure, smart manufacturing, and so on. This is because such sensors have various practical advantages: low loss, immunity to electromagnetic interference, distributed or quasi-distributed sensing capability, etc [1].

In these circumstances we have proposed various fiber-optic sensors using specially designed fiber-optic component so-called fiber Bragg gratings (FBGs) [2-3]. In addition, we have fabricated another type of grating-based fiber components, long period fiber gratings (LPGs), and have applied to fiber-optic sensors for vibration of solid and underwater acoustic waves. In the present paper, we have investigated characteristics of LPG depending on the order of cladding-mode and have demonstrated sensitivity enhancement of LPG vibration sensor.

## 2. Operation Principle

In general, grating-based fiber-optic components, in which periodic refractive index modulation is applied to core of single-mode fiber, are divided into two types, FBG and LPG. The period of the refractive index modulation is less than 1 μm for FBG whereas for LPG the period is several tens ~ hundreds μm. In typical FBGs, incident light wave is totally reflected at the specific wavelength, Bragg wavelength ($\lambda_B$), so that the there is a sharp spectral dip in the transmittance at $\lambda_B$. On the other hand, LPG has several dips in the transmission spectrum due to mode-couplings from core-mode to leaky cladding- modes. The wavelengths of the dips $\lambda^{(m)}_p$ are given by the following equation

$$\lambda^{(m)}_p = \Lambda\ (n_{core} - n^{(m)}_{clad}) \qquad (1)$$

where $\Lambda$ is the period of refractive index modulation, $n_{core}$ and $n^{(m)}_{clad}$ denote effective refractive indices for core mode and $m$-th cladding mode respectively. Since several cladding-modes exist in normal fiber, there are several dips in the transmission spectrum.

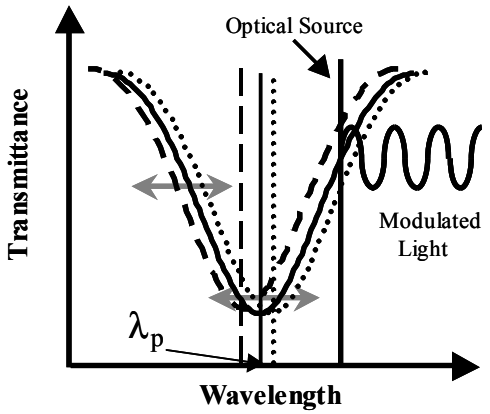


Fig.1. Principle of LPG vibration sensor.

Conceptual scheme for the operation principle of the LPG vibration sensor is shown in **Fig. 1**. With reference to the figure, when a vibration is applied to LPG, the grating period $\Lambda$ as well as the indices $n_{core}$ and $n^{(m)}_{clad}$ change periodically due to the vibration- induced strain. As a result, the spectral dip $\lambda^{(m)}_p$ shifts periodically in wavelength domain. In this situation, if an incident light from a laser source of which wavelength is tuned to a slope of a spectral dip is launched into the LPG, the transmitted light through the LPG is modulated in intensity according to the vibration. Since the intensity modulation depends on strain-sensitivity of $\lambda^{(m)}_p$ and gradient of the slope of the spectral dip, higher sensitive operation can be achieved by using LPGs having steeper dips with high strain-sensitive wavelength-shift for $\lambda^{(m)}_p$.

## 3. Experiment and Results

We fabricated LPG by illuminating 248 nm KrF excimer laser light to a single-mode optical fiber that was photosensitized with boron doping. **Figure 2** shows the transmission spectrum of typical LPG we fabricated. In the figure, Dip1, Dip2, and Dip3 denote the spectral dips due to mode couplings from core-mode to cladding-modes; the dips caused by higher cladding-modes

g46011@nda.ac.jp

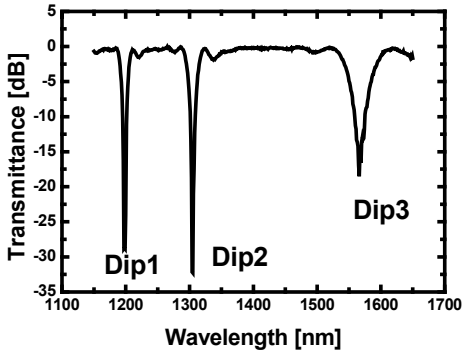


Fig.2. Typical transmission spectrum of LPG.

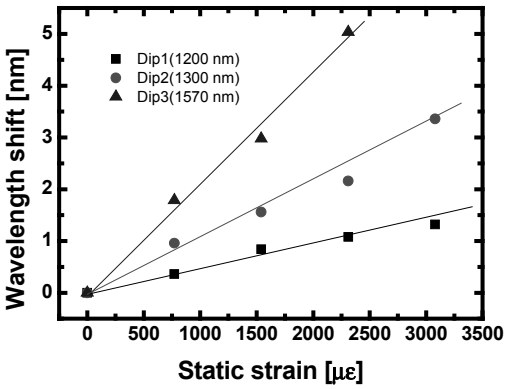


Fig.3. Strain-induced wavelength-shifts for Dip1, Dip2 and Dip3.

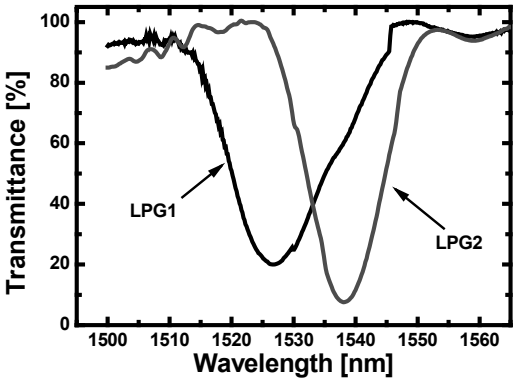


Fig.4. Transmission spectra of sensing LPGs.

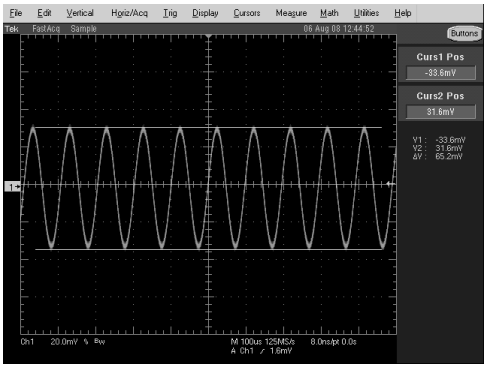

Fig.5. Waveform of sensor output using LPG2.

appears at longer wave- length. The dependence of wavelength shift of the dips on static strain applied to the LPG is shown in **Fig. 3**. As can be seen from the figure, dip with higher cladding-modes shows higher sensitive wavelength- shift to applied strain.

In order to construct LPG vibration sensor, we fabricated two LPGs in which spectral dip is adjusted within a wavelength region of a tunable laser we used, from 1520 to 1590 nm, by changing $\Lambda$ in the writing processes. As shown in **Fig. 4**., Dip2 is adjusted to 1525 nm for LPG1 and Dip3 is 1538 nm for LPG2. For a demonstration of LPG vibration sensor, LPG1 and LPG2 are exerted by a PZT; LPGs are fixed to a rectangular type PZT (140×5×10 mm) and driven by sinusoidal electric signal at its resonant frequency (10.22 kHz). Typical sensor output using LPG2 is shown in **Fig. 4**. As can be seen from the figure, waveform due to applied vibration is observed clearly. Comparing the sensor outputs between for LPG1 and LPG2, the sensitivity of the sensor with LPG2 is about 4 times higher than that with LPG1. The experimental result is in good agreement with the relationship estimated from the strain sensitivity of the wavelength shift and gradient of the slope of dips as indicated in **Table 1**. Accordingly, it was confirmed that higher sensitive operation of LPG vibration sensor can be achieved by utilizing the spectral dip due to higher cladding-mode.

Table 1. Characteristics of sensing LPG.

| Sensing LPG | Strain sensitivity [pm/με] | Slope ($\Delta T/\Delta\lambda$) [%/pm] |
|---|---|---|
| LPG1 (Dip2) | 0.86 | 0.0057 |
| LPG2 (Dip3) | 2.00 | 0.0100 |

## 4. Concluding Remarks

In this research, we have investigated sensitivity of wavelength shift of spectral dip for LPG depending on order of cladding modes in order to enhance the sensitivity of LPG vibration sensor. In addition, we have demonstrated that higher sensitive operation can be achieved by adopting higher cladding-mode.

## References

[1] A.D. Kersey, M.A. Davis, H.J. Patrick, M. LeBlanc, K.P. Koo, C.G. Askins, M.A. Putnam, E.J. Friebele, J. Lightwave Technol. **15,** 1442 (1997).

[2] N. Takahashi, K. Yoshimura, S. Takahashi, K. Imamura, Ultrasonics **38,** 581 (2000).

[3] S. Tanaka, T. Ogawa, H. Yokosuka and N. Takahashi, Jpn. J. Appl. Phys. **43**, 2969 (2004).

Proceedings of Symposium on Ultrasonic Electronics, Vol. 29 (2008) pp. 87- 88
11-13 November, 2008

# Recognition of Wavelength-Multiplexed Hierarchical Label with Acoustooptic Waveguide Circuit

波長多重階層化光ラベルの音響光学導波路回路による認識

Nobuo Goto[1†]and Yasumitsu Miyazaki [2]([1]Univ. of Tokushima, Dept. of Optical Sci. & Tech., [2]Aichi Univ. of Tech., Dept. of Media Informatics)
後藤信夫[1†]，宮崎保光[2]（[1]徳島大　光応用工学科，[2]愛知工科大 情報メディア学科）

## 1. Introduction

High-speed optical processing for packet routing can overcome bottleneck in large-capacity photonic networks. In label routing networks, various label processing methods have been proposed to use effectively the potential of optical signal processing. The authors have studied on collinear acoustooptic (AO) switches[1,2] and applications to optical label recognition.[3-6] Since parallel combination of collinear AO switches can handle wavelength-division-multiplexed (WDM) optical pulses, recognition for optical labels encoded in spectral and time domains can be realized. In this paper, we discuss recognition of layer-structure labels for hierarchical routing control.

## 2. Routing in hierarchical network

**Fig.1** illustrates an example of hierarchical networks. In the layer-structure label routing network, processing of the labels can be simpler and faster.

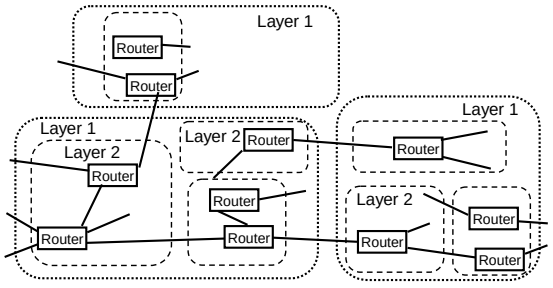


Fig.1 Two-layer photonic network.

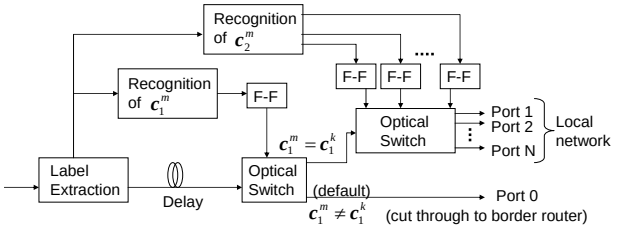


Fig.2 Configuration of optical label router

goto@opt.tokushima-u.ac.jp

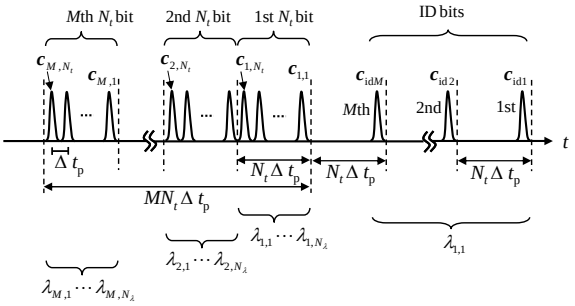


Fig.3 Structure of layer label.

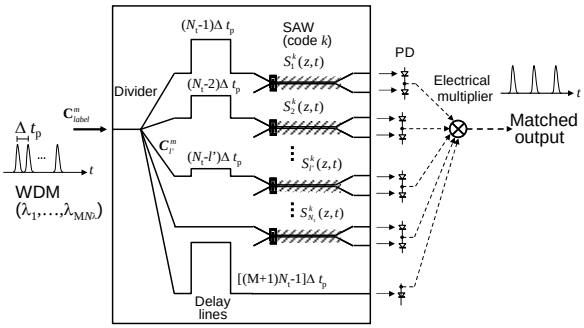


Fig.4 Configuration of collinear AO processor.

Only a partial label corresponding to layer 1 can be used for global routing, where the rest of detail label information is used for local routing. A configuration of the optical label router is shown in **Fig.2**. The extracted label of a packet is optically processed and the label information is used to reconfigure optical switches to forward the packet. We consider *M*-layer label as shown in **Fig.3**, where *M* identifying bits are placed ahead of the routing coded labels. Each of the $N_t$-bit layered codes has different wavelengths. In the next section, we discuss recognition of the partial label.

## 3. AO processor and layer labels

An integrated-optic processor consisting of parallel AO switches and delay lines is shown in **Fig.4**. The incident label is divided into $N_t$ +1 pulse trains. The partial labels or the whole label to be matched in this device are represented by frequency-multiplexed

SAWs. The label pulse trains are wavelength-selectively switched and the outputs are balanced detected with photodiodes (PDs). The electrical output signals are electrically multiplied. The $M$ matched output pulses correspond to label matching of each layer codes.

## 4. Simulation

As a numerical example, we assume a bandwidth limited optical pulse train with pulse period 12 ps, pulse width 5.9 ps, bandwidth 160 GHz and $N_t$ = 3. The interaction length of collinear AO switch is assumed to be $l_{SW}$ = 16 mm. We assume an OOK orthogonal code set as given by

$$\boldsymbol{c}_i^m = \{\boldsymbol{a}_1, \boldsymbol{a}_2, \boldsymbol{a}_3\} = \left\{ \begin{pmatrix} 1 \\ 0 \\ 1 \end{pmatrix}, \begin{pmatrix} 0 \\ 1 \\ 1 \end{pmatrix}, \begin{pmatrix} 1 \\ 1 \\ 0 \end{pmatrix} \right\} \quad (1)$$

Optical incident pulses $E^m(t)$ are shown for the case of $C^m$ = ($a_1$ , $a_1$ , $a_1$ ,$a_1$ , $a_2$ , $a_3$ ,$a_1$ , $a_2$ , $a_3$ ) in **Fig. 5**. When the SAW represents a different code $C^k$= ($a_1$ , $a_1$ , $a_1$ ,$a_2$ , $a_2$ , $a_2$ ,$a_1$ , $a_2$ , $a_3$ ), the output electrical pulse train is obtained as shown in **Fig.6**. Since the second partial label is different, no second pulse is output. Thus, these code matching can be used for routing in layer-structure networks. If only the first partial label is required as the routing information, the SAWs of just the frequencies corresponding to the first label are required. The output current for matching the first label is shown in **Fig.7**. The signals at the timing of the second and the third ID bits are minus current. Similarly, the output for matching the second label is shown in **Fig.8**, where the second label is unmatched.

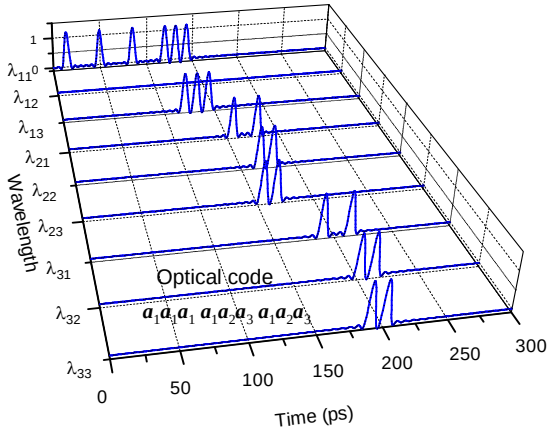


Fig.5 Incident pulse train of an optical label.

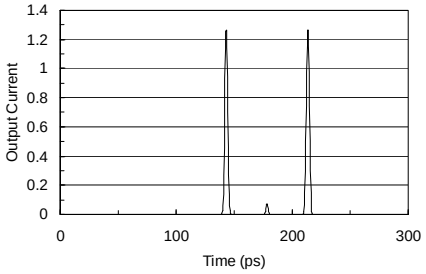


Fig.6 Output when the second partial label is unmatched.

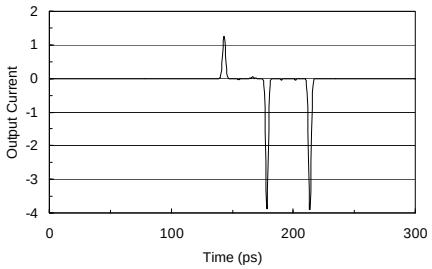


Fig.7 The output for matching the first matched label.

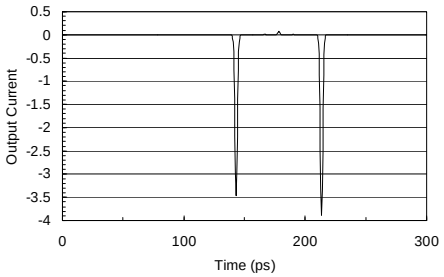


Fig. 8 The output for matching the second unmatched label.

## 5. Conclusions

We discussed optical label matching using an integrated-optic device and an electrical multiplier. By introducing WDM address bits and identifying bits, partial label matching is performed. We will further investigate the layer-structure routing.

## References


[1] T. Kondo, Y. Miyazaki and Y. Akao, Jpn. J. Appl. Phys. vol.17, no.7, pp.1231-1243, 1978.

[2] N. Goto and Y. Miyazaki, Trans. IEICE Electron., vol.J86-C, no.12, pp.1272-1281, 2003.

[3] N. Goto and Y. Miyazaki, Jpn. J. Appl. Phys., vol.44, no.6B, pp.4449-4454, 2005.

[4] N. Goto and Y. Miyazaki, Jpn. J. Appl. Phys., vol.45, no.5B, pp.4625-4630, 2006.

[5] N. Goto and Y. Miyazaki, Jpn. J. Appl. Phys., vol.46, no.7B, pp.4602-4607, 2007.

[6] N. Goto and Y. Miyazaki, Jpn. J. Appl. Phys., vol.47, no.5, pp.3974-3979, 2008.

Proceedings of Symposium on Ultrasonic Electronics, Vol. 29 (2008) pp. 89-90
11-13 November, 2008

# Improvement of Diffraction Efficiency in Surface-Acoustic-Wave-Driven Tandem Acoustooptic Frequency Shifter

弾性表面波を用いたタンデム音響光学周波数シフタの高効率化

Susumu Shinkai‡, Shoji Kakio, Yasuhiko Nakagawa, (Univ. of Yamanashi)
Takefumi Hara and Hiromasa Ito (Tohoku University)
新海 進‡，垣尾省司，中川恭彦（山梨大院・医工） 原 武文，伊藤弘昌（東北大院・工）

## 1. Introduction

The optical frequency of laser beam diffracted by an elastic wave through an acoustooptic effect is Doppler shifted by the acoustical frequency. This phenomenon can be used as an acoustooptic frequency shifter (AOFS). However, the frequency shift of a simple AOFS is almost fixed at around the center frequency of the transducer. To solve this problem, we proposed a monolithically integrated tandem waveguide-type AOFS driven by a surface acoustic wave (SAW) and observed frequency shifted lights corresponding to sum of two driving frequencies and the difference frequency.[1] Moreover, using this tandem AOFS, the frequency-shifted-feedback (FSF) fiber laser oscillation was realized and an optical frequency domain range was demonstrated.[2] The practical applications of the FSF fiber laser with the tandem AOFS, such as that to the optical three-dimensional shape measurement with high accuracy,[3] can be expected upon increasing diffraction efficiency.

In this paper, to improve the diffraction properties of the tandem AOFS, a novel waveguide shape, hereafter called "3-output-ports type", was designed and the diffraction properties were simulated using the beam-propagation method (BPM).

## 2. Design of Tandem AOFS

As a tandem AOFS with a novel waveguide shape, the 3-output-ports type AOFS was designed on 128°-rotated Y-cut $LiNbO_3$ substrate for an optical wavelength of 1.55 μm and SAW wavelength Λ of 32 μm (the driving frequency of 125MHz). The analytical model in the diffraction region is shown in **Fig. 1**. An output port O2 which is not needed to obtain the doubly diffracted light was removed from the waveguide pattern of the previous tandem AOFS[1]. It can shorten the length of the straight waveguide between the 1st and 2nd gratings. By utilizing this margin, the length of a tapered waveguide can be increased from 3.3 mm of the previous tandem AOFS to 9 mm while the total length size of 30 mm was maintained. As a result, the vertex angle of the tapered waveguide can be decreased from 0.78° of the previous tandem AOFS to 0.32°. It may improve a complicated optical interference[4] in the tapered waveguide. Therefore, the improvement of the diffraction properties can be expected.

## 3. Simulated Diffraction Properties

OptiBPM6.0 of Optiwave was used for the analysis. Port I2 was defined as the input port and a Gaussian beam with an optical wavelength of 1.55 μm and a beam waist diameter of 5 μm was assumed as the incident light. The analysis of the diffraction properties resulting from the SAW was performed by setting the refractive index grating expressed as $\Delta n_g \sin(2\pi x/\Lambda)$ in the 1st and 2nd

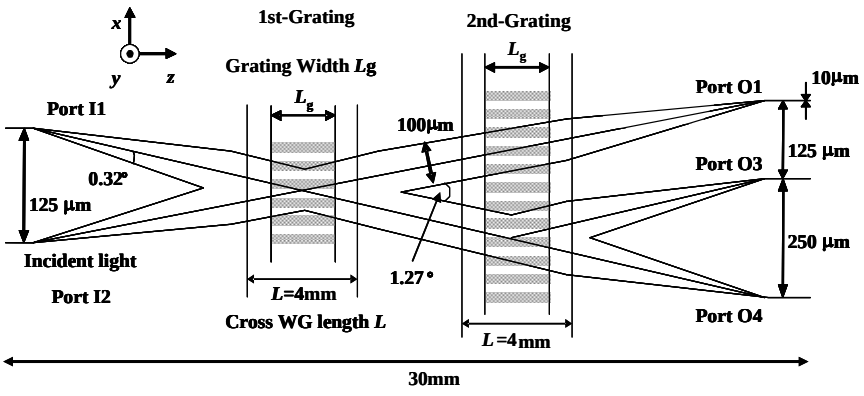


Fig. 1 Analytical model of 3-output-ports type tandem AOFS.

g08me017@yamanashi.ac.jp

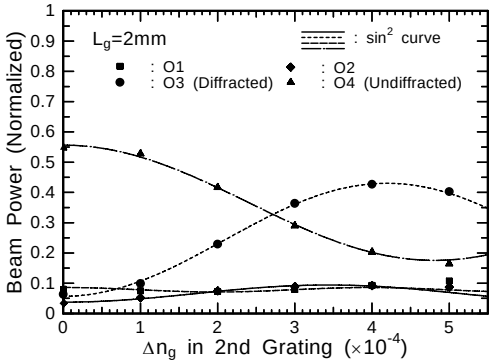


(a) Previous 4-output-ports type.

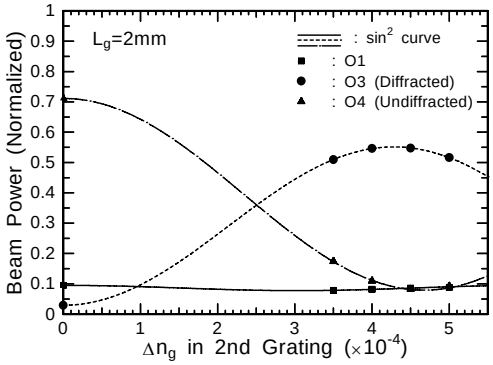


(b) Novel 3-output-ports type.

Fig. 2 Simulated diffraction properties.

AO interaction regions with the width $L_g$ of 2 mm for TM-mode propagation.

**Figures 2(a)** and **2(b)** show the light powers of Ports O1, O3, and O4 power as a function of $\Delta n_g$ in the 2nd grating at the maximum diffraction efficiency by the 1st grating, in the previous 4-output-ports type and the novel 3-output-ports type, respectively. The values of output beam power were normalized by incident light power. The beam power in Port O3 corresponds to the doubly diffracted beam power. The maximum doubly diffraction beam power was increased from 0.43 in the previous type to 0.55. The minimum undiffracted beam power in Port O4 was also improved from 0.20 to 0.08.

**Figure 3** shows the three-dimensional display of the simulated optical field distribution of $E_y$ for the maximum doubly diffraction efficiency. It can be seen that the beam power of the undiffracted beam in the 2nd grating was reduced by adopting the 3-output-ports type. It may be caused by decreasing the vertex angle of the tapered waveguide because the incident beam thorough the tapered waveguide can generate the diffracted beam with the maintained equiphase surface in the 1st grating. Moreover, an influence to other ports due to the removal of the output port O2 was not observed.

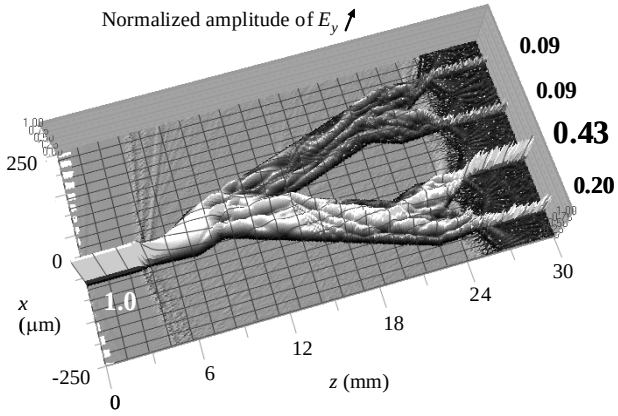


(a) Previous (4-output-ports) type.

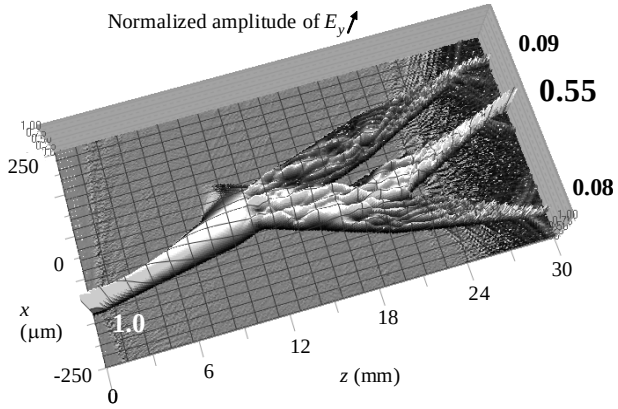


(b) Novel 3-output-ports type.

Fig. 3 Amplitude distribution of $E_y$ simulated by BPM.

## 4. Conclusions

The novel 3-output-ports type AOFS was designed and the diffraction properties were simulated. The diffraction properties were improved by decreasing the vertex angle of the tapered waveguide. The maximum doubly diffraction beam power was increased from 0.43 in the previous type AOFS to 0.55.

In the future, the novel tandem AOFS will be fabricated and the optical diffraction properties will be evaluated.

## References

1. S. Kakio, S. Uotani, M. Kitamura Y . Nakagawa, T. Hara, H. Ito, T. Kobayashi and M. Watanabe, Jpn. J. Appl. Phys. **46** (2007) 4608.
2. S. Kakio, M. Kitamura, Y . Nakagawa, T. Hara and H. Ito, Jpn. J. Appl. Phys. **47** (2008) 3992.
3. C. Ndiaye, T. Hara, N. Hamada and H. Ito, Proc. 23rd Int. Laser Radar Conf. (ILRC23) 8O-1 (2006) 719.
4. S. Kakio, S. Uotani, Y . Nakagawa, T. Hara, H. Ito, T. Kobayashi and M. Watanabe, Jpn. J. Appl. Phys. **46** (2007) 669.

Proceedings of Symposium on Ultrasonic Electronics, Vol. 29 (2008) pp. 91-92
11-13 November, 2008

# Surface-Acoustic-Wave-Driven Acoustooptic Modulator with Wide Wavelength Range for Visible Laser Light

弾性表面波を用いた広帯域可視光変調素子

Shoji Kakio, Susumu Shinkai, Hiroyuki Kawate and Yasuhiko Nakagawa
(Univ. Yamanashi)
垣尾 省司，新海 進，川手 寛之，中川 恭彦（山梨大院・医工）

## 1. Introduction

The authors have proposed a waveguide-type acoustooptic modulator (AOM) driven by a surface acoustic wave (SAW) in a tapered crossed-channel proton-exchanged (PE) waveguide on a 128° Y-cut $LiNbO_3$ substrate for an optical wavelength of 1.55 μm.[1] One of the features of the waveguide-type AOM is that it has a wide wavelength range compared with a bulk-type AOM.[2] By applying the waveguide-type AOM to the visible range, an AOM can be realized in which laser light of the three primary colors of red, green, and blue can be modulated by the same modulator.

In this paper, we first designed the waveguide-type AOM and simulated the optical diffraction properties using the beam-propagation method (BPM). Next, the waveguide-type AOM was fabricated and the optical diffraction properties and the driving SAW power were measured.

## 2. BPM analysis

The overall configuration and the analytical model used for the diffraction region of the waveguide-type AOM are shown in **Figs. 1** and **2**, respectively. Ports 1, 3, and 4 were defined as the input, diffracted output, and undiffracted output ports, respectively. The width of the waveguide of each port was designed to be 3 or 6 μm. These waveguides were expanded to the waveguide width $W$ using tapered waveguides that crossed each other with the Bragg angle $2\theta_B$. The SAW wavelength Λ was designed to be 16 μm.

The extraordinary refractive index change $\Delta n_e$ in the waveguide was assumed to be 0.02. The Bragg angle $2\theta_B$ was determined by the optical wavelength of blue light or the average wavelengths of red and

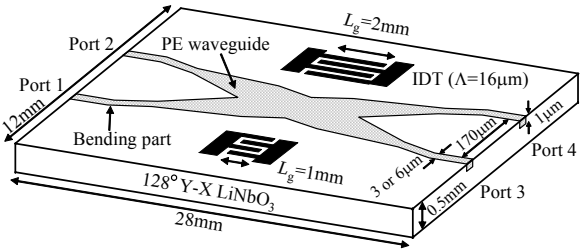


Fig. 1 Configuration of waveguide-type AOM.

blue light, that is, green light. The refractive index change was assumed to be induced by the SAW by setting up a refractive index grating, which was expressed as $\Delta n_g \sin(2\pi x/\Lambda)$. OptiBPM 6.0 of Optiwave was used for the analysis. Optical wavelengths of 633, 532, and 473 nm were used for red, green, and blue light, respectively.

First, the leakage power of Port 3 without the grating ($\Delta n_g$=0) was calculated. The leakage power decreased with increasing waveguide width $W$. For $W$>60 μm, the leakage power, which was normalized by the input light power, was less than 1%. Therefore, $W$ was designated as 60 μm and the lengths of the diffraction region on the waveguide $L$ for blue and green light were determined to be 4.1 and 4.7 mm, respectively.

Second, the output beam power $P_3$ in the diffracted output port, Port 3, was calculated for TM mode propagation as a function of the amplitude of $\Delta n_g$. **Figure 3** shows the optical diffraction properties for $L_g$=1 mm. The maximum values $P_3^{max}$ for optical wavelengths of 633, 532, and 473 nm were 78, 77, and 65%, respectively. The optical wavelength dependence of $P_3^{max}$ is shown in **Fig. 4**, together with the experimental results. The peak of $P_3^{max}$ appeared at the optical wavelength for which the Bragg angle was designed.

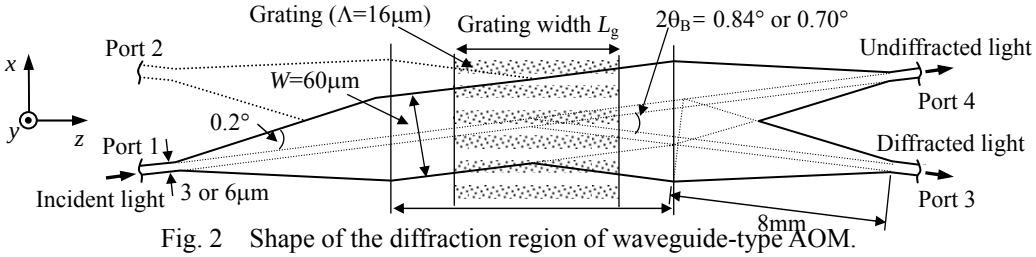


Fig. 2 Shape of the diffraction region of waveguide-type AOM.

kakio@yamanashi.ac.jp

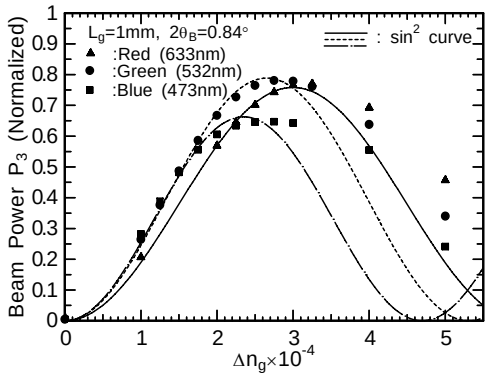


Fig. 3 Calculated diffraction properties.

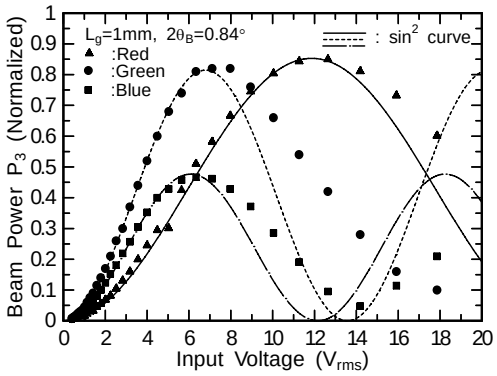


Fig. 5 Measured diffraction properties.

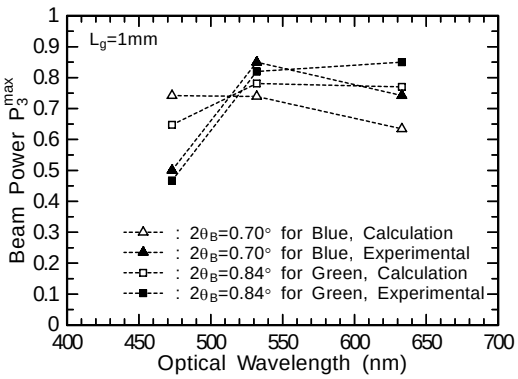


Fig. 4 $P_3^{max}$ vs optical wavelength.

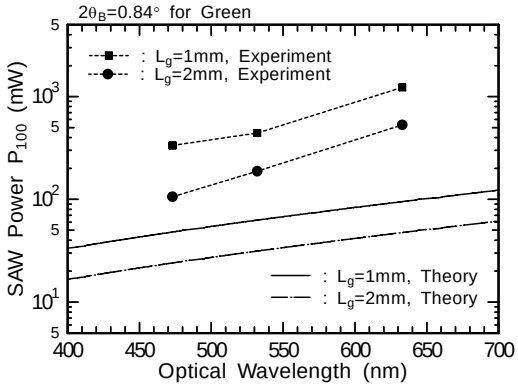


Fig. 6 SAW power $P_{100}$ vs optical wavelength.

## 3. Experiment

The channel waveguide was fabricated by first forming an RF-sputtered $SiO_2$ mask with a film thickness of 0.25 μm by the liftoff method on a 128° Y-cut $LiNbO_3$ substrate followed by the PE process and postannealing. The PE was carried out for 4 min in a solution of benzoic acid containing 0.2 mol% lithium benzoate at 240°C, and the annealing time was 2 h at 400°C. A Gaussian index profile with $\Delta n_e$=0.02 and a waveguide depth of 1.0 μm were obtained.

After polishing the end face of the waveguide, a pair of normal interdigital transducers (IDTs) with a period length Λ of 16 μm and an overlap length $L_g$ of 1 (30 finger pairs) or 2 mm (20 finger pairs) were formed on the substrate. A red (633 nm), green (532 nm), or blue (473 nm) laser beam was guided into the end face of the PE waveguide through an objective lens with a magnification of x40. The diffracted light power as a function of the input voltage of an RF burst signal of 245 MHz was measured using a photomultiplier. **Figure 5** shows the measured diffraction properties for $L_g$=1 mm. The measured $P_3$ was normalized by the output light power in Port 4 without an input voltage.

The peak diffraction efficiencies for optical wavelengths of 633, 532, and 473 nm were 85, 82, and 47%, respectively. As shown in **Fig. 4**, for optical wavelengths of 633 and 532 nm, similar optical wavelength dependences to those in the analytical results were obtained. On the other hand, compared with the analytical results, the maximum diffraction efficiency for the optical wavelength of 473 nm was relatively small.

**Figure 6** shows the optical wavelength dependence of the measured driving SAW power ($P_{100}$) required to obtain the maximum diffraction efficiency. The theoretical results obtained from coupled-mode theory[3], in which a planar waveguide was assumed, are also shown in this figure. The values of the experimentally obtained $P_{100}$ were an order of magnitude larger than the theoretical values. The causes of the difference between the theoretical and experimental values in the waveguide-type AOM will be investigated.

## 4. Conclusions

The diffraction properties of a waveguide-type AOM were evaluated. For 633 and 532 nm, according to the analytical results, a maximum diffraction efficiency ranging from 74 to 85% was obtained. On the other hand, in contrast with the analytical results, the maximum diffraction efficiency for 473 nm was as small as 47%. The values of the $P_{100}$ were an order of magnitude larger than the theoretical values.

## References

1. S. Kakio *et al*, Jpn. J. Appl. Phys. **42** (2003) 3063.
2. S. Kakio *et al*, IEICE Trans. **J-86-C** (2003) 1263 [in Japanese].
3. K. W. Loh *et al*, Appl. Opt. **15** (1976) 156.

Proceedings of Symposium on Ultrasonic Electronics, Vol. 29 (2008) pp. 93-94
11-13 November, 2008

# Fabrication of Magneto-optic Thin Films on $LiTaO_3$ and/or $LiNbO_3$ Substrates by Contact Epitaxy

$LiTaO_3$ および $LiNbO_3$ 基板上へのコンタクトエピタキシーによる磁気光学薄膜の形成

Hiroyuki Tashiro[1†], Satoru Noge[2] and Takehiko Uno[1] ([1] Facult. Eng., Kanagawa Inst. Tech, [2] Numazu Nation. College Tech.)
田代博之 [1‡], 野毛悟 [2], 宇野武彦 [1] ([1] 神奈川工大 工; [2] 沼津高専)

## 1. Introduction

We propose multifunctional thin films for integration of optical and acoustic-wave devices. $LiTaO_3$ (LT) and $LiNbO_3$ (LN) crystals have been widely utilized for piezoelectric and electro-optical (EO) devices. However, magneto-optical devices have not been realized on LT and/or LN substrates. Because the magneto-optical (MO) effect exists in special materials such as YIG (yttrium iron garnet), integration of MO and EO or acousto-optical (AO) effects is difficult to realize.

We have been studied a method to control crystal orientations of thin films by contact epitaxy method[1]. By this method, we obtained cerium substituted yttrium iron garnet (Ce:YIG) films with large Faraday rotation on silica glass substrates. Furthermore, we observed a sign of orientation control for $LiNbO_3$ thin films. In this paper, we discuss the possibility of integration of EO, AO and MO effects on $LiTaO_3$ and/or $LINbO_3$ substrates.

## 2. Cerium substituted YIG films

We investigated fabrication of cerium substituted yttrium iron garnet (Ce:YIG) film on LT and/or LN substrates. It is well known that YIG ($Y_3Fe_5O_{12}$) have a superior Faraday rotation for visible light. However, the Faraday rotation of YIG is not so larage for use of thin-film type MO devices. To improve Faraday rotation characteristic, bismuth substituted or rare-earth matal substituted YIG have been developed. Ce substituted YIG[2-4] ($Ce_xY_{3-x}Fe_5O_{12}$) is one of the promissing materials for a thin-film MO device in near-infrared band.

Ce:YIG with a large substitution amount can fabricate by thermal nonequilibrium processes such as sputtering deposition. Therefore, Ce:YIG can be obtained in the form of thin films. To obtain a superior MO characteristic, single crystal thin film of Ce:YIG is needed, and epitaxial growth technique of Ce:YIG on gadolinium-gallium-garnet (GGG) substrate had been established[4]. To realize thin-film type MO devices, a method to fabricate single crystal films on various substrates must be developed. We have been studied a method to control film orientation deposited on silica substrated. We call the method "contact-epitaxy" and a sign of epitaxial growth of Ce:YIG on silica glass have been obtaied[1].

By use of the contact-epitaxy technique for fabrication of Ce:YIG on LT and/or LN substrates, multifunctional thin films of EO, AO and MO effects may be realized.

hiloyuki@ele.kanagawa-it.ac.jp

## 3. Configuration of the film

Figure 1 shows a configuration of a Ce:YIG film on a LT or LN substrate. The Ce:YIG thin film is not directly formed on the substrate, but a very thin $SiO_2$ layer is interleaved between the substrate and the film. The $SiO_2$ layer prevents the affect of the substrate on crystallization of the film during thermal treatment process of contact-epitaxy. Furthermore, it suppresses the diffusion of Li to the film. The thickness of the $SiO_2$ film must be thin enough to avoid optical and mechanical affects.

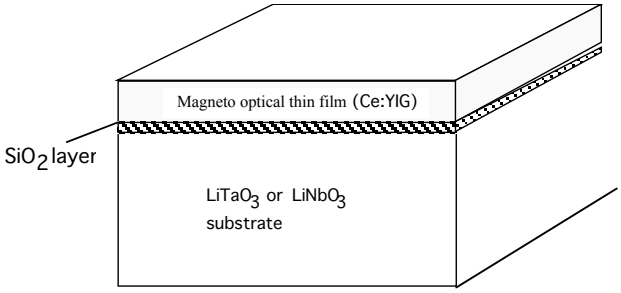


Fig. 1 Configuration of the MO film on LT or LN substrates.

To utilize the Ce:YIG film as optical wave-guide, refractive index of the film, $n_f$, must be larger than that of the substrate, $n_s$. Refractive index of $Ce_1Y_2Fe_5O_{12}$ is 2.21, and the indices for LT and LN are,

LT: $n_o$=2.178, $n_e$=2.18
LN: $n_o$=2.29, $n_e$=2.20.

Therefore, optical wave-guide can be formed on LT substrates. To utilize acousto-optical effect, LT substrate of around 124° or 36° rotated Y-cut

(RY-cut) is suitable. In 36° RY-cut LT substrate, leaky SAW having a large electromechanical coupling constant is excited[5], and propagation loss is small enough for practical use. Dependencies of SAW velocity and electromechanical coupling constant on the film thickness are shown in **Figs. 2 and 3**.

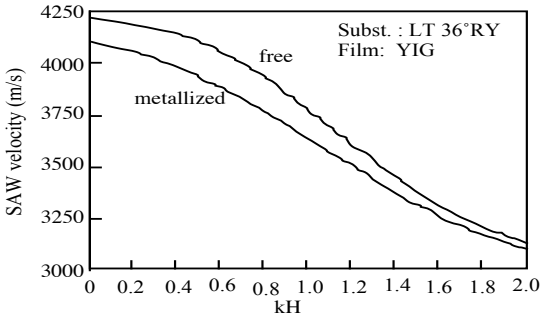


Fig. 2 Dependency of SAW velocity on Ce:YIG film thickness.

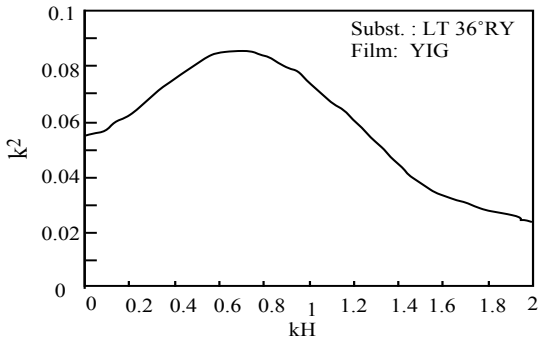


Fig. 3 Dependency of coupling constant on Ce:YIG film thickness

For a case of 1.2□m film thickness, kH=1.5 for 1GHz. In this case coupling constant of about 0.04 can be obtained.

Figure 4 shows an example of field distribution for TE-mode guided light. From this distribution, control of the guided light wave by EO, MO and AO effects will possible with enough efficiency.

## 4. Fabrication technique

The Ce:YIG films can be fabricated by the contact-epitaxy shown in **Fig. 5**. Both of (100) and (111) direction Ce:YIG films having high Faraday rotation constants are possible to prepare.

## 5. Conclusion

We have basically studied multifunctional films having EO, MO and AO effects. Cerium substituted YIG films on rotated Y-cut $LiTaO_3$ substrates will be a suitable configuration for it.


## Acknowledgement

This work is supported by a Grant-in Aid for Scientific Research from the Japanese Ministry of Education, Culture, Sports, Science and Technology.


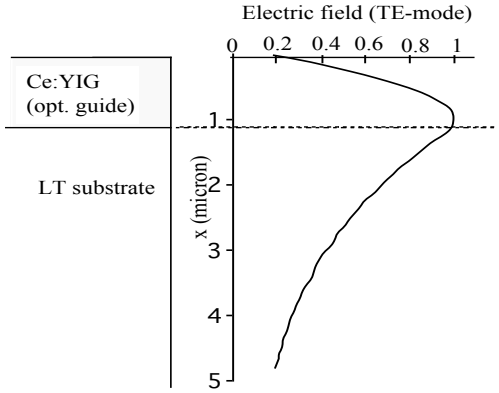


Fig. 4 Electric field distribution of TE-mode. (Calculated)
Film thickness: 1.2 □m, □=1.55 □m

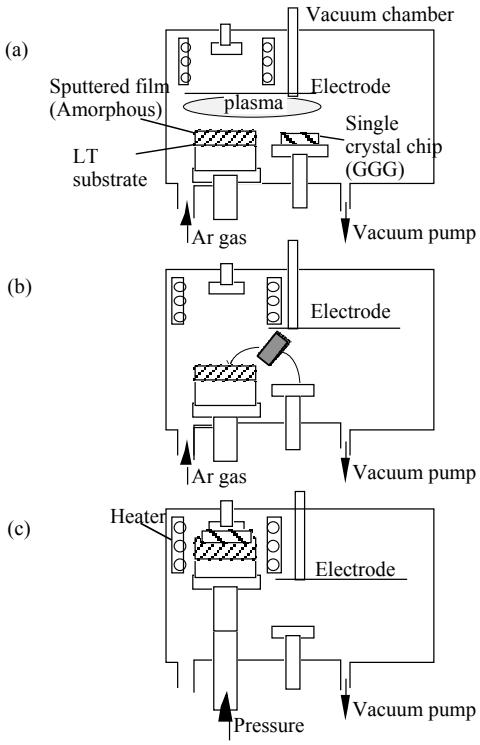


Fig. 5. Fabrication process by the contact-epitaxy

## References


1. T. Uno, S. Ohta and S. Noge: Int. Conf. Electroceramics, (2003, Boston) OS2-CRY-4-0.
2. M. Gomi, K. Satoh and M. Abe: Proc. Fifth Intern. Conf. Ferrites (1989, India) p.919.
3. T. Shintaku and T. Uno: J. Appl. Phys. **76**(1994) 8155
4. A. Tate, T. Uno, S. Mino, A. Shibukawa, and T. Shintaku: Jpn. J. Appl. Phys. **35(**1996), 3419.
5. K. Nakamura, M. Kazumi and H. Shimizu: Proc. IEEE Ultrason. Symp.(1997) p.819

Proceedings of Symposium on Ultrasonic Electronics, Vol. 29 (2008) pp. 95-96
11-13 November, 2008

# Propagation Characteristics of Substrates for Lamb Wave Type Elastic Wave Devices

ラム波型弾性波素子基板の伝搬特性

Hitoshi Yoshida, Yasuhiko Nakagawa and Shoji Kakio ( Interdisciplinary Graduate School of Med. Eng., Univ. of Yamanashi )
吉田斉師，中川恭彦，垣尾省司 (山梨大院 医工)

## 1. Introduction

Quartz is a physically and chemically stable crystalline substrance. It has been used as a crystal occilator that is little affected by aging. It is also widely used in devices such as a frequency generator becausse quartz operates stably with very little thermal frequency shift compared with other substances.[1,2] Therefore, putting an oscillator and a resonator to practical use as an electronic device requires stable operation with good frequency-temperature characteristics. In recent studies, researchers have specifically examined a plate wave propagating on a quartz substrate.[3,4,5] The characteristics of this Lamb wave type substrate include the following: it performs high frequency operations with phase velocity that is 2-3 times higher than that of a surface acoustic wave (SAW); it allows easy excitation and reception with a greater electromechanical coupling coefficient ($K^2$); and it has an extermely high coefficient of reflection from reflectors such as a grating on the propagation path.

We aim at exploiting the application of a substrate for Lamb wave type acoustic wave devices and the frequency-temperature characteristics of Lamb wave propagating on a quartz substrate were discussed theoretically.

## 2. Theoretical Analysis

Fig.1 shows the coordinate system employed for Lamb wave analysis. The Lamb wave to be analyzed is presumed to propagate along the $x_1$ direction, and the direction perpendicular to the substrate surface was set as the $x_3$ direction. The substrate thickness was set to $H$, and wave analyses were conducted. A wave propagating in a piezoelectric medium must satisfy the piezoelectric basic equation, and satisfy the equation of motion and Laplace's equation shown below.

$$\rho \frac{\partial^2 u_j}{\partial t^2} = C_{ijkl}^E \frac{\partial^2 u_k}{\partial x_i \partial x_l} + e_{kij} \frac{\partial^2 \phi}{\partial x_i \partial x_k} \qquad (1)$$

$$e_{ikl} \frac{\partial^2 u_k}{\partial x_i \partial x_l} - \varepsilon_{ik}^S \frac{\partial^2 \phi}{\partial x_i \partial x_k} = 0 \qquad (2)$$

Particle displacement and electric potential were assumed as a solution set of equations (3) and (4).

$$u_j = \alpha_j \exp\left(ikbx_3 + ikx_1 - i\omega t\right) \qquad (3)$$

$$\phi = \alpha_4 \exp\left(ikbx_3 + ikx_1 - i\omega t\right) \qquad (4)$$

Equations (3) and (4) must satisfy equations (1) and (2). Therefore, the latter are substituted into the former. Furthermore, theoretical analysis was conducted under eight boundary conditions: particle displacement, stress, electric displacement and the continuity of electric potential at the top and bottom surfaces of the substrate.

As for frequency-temperature characteristics, assuming a phase velocity at 20 degrees Celsius and an arbitrary temperature as $v_0$ and $v_t$, respectively, frequency variation is expressed as follows:

$$\frac{\Delta f}{f_o} = \frac{v_t - v_o}{v_o} - \alpha \qquad (5)$$

where $\alpha$ is the expansion coefficients at the temperature t = 20 °C, respectively.

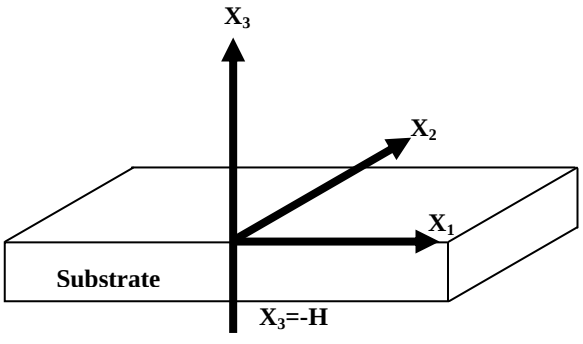


Fig. 1 Coordinate system used for analysis.

nakagawa@es.yamanashi.ac.jp

Table I Characteristics of three new cuts

| | New Cut 1 | New Cut 2 | New Cut 3 |
|---|---|---|---|
| Euler angles ($\lambda$, $\mu$, $\theta$) [°] | (22.95, 124.9, 42.2) | (90.0, 18.997, 7.5) | (90.0, 14.715, 0.0) |
| $v$ [m/s] | 3804 | 4296 | 3775 |
| $K^2$ [%] | 0.107 | 0.130 | 0.115 |
| $\Delta f/f$ [ppm] | 0.7 | 1.37 | 1.22 |
| $H/\Lambda$ | 0.968 | 0.900 | 1.010 |
| PFA [°] | -25.66 | -18.00 | -25.22 |

## 3. Theoretical Analysis Results

Three new cuts with excellent cubic frequency-temperature characteristics were discovered. Theoretical analysis results of frequency-temperature characteristics for three cuts were shown in Fig.2. It shows complete third order curve and these frequency variation were about 1 ppm. The characteristics of three new cuts were shown in Table I.

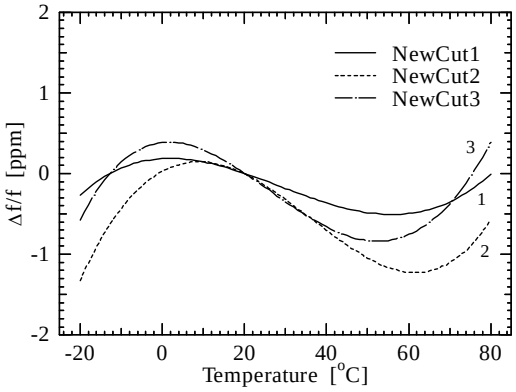


Fig. 2 Theoretical analyses results of frequency-temperature characteristics

## 4. Measurement Result of New Cut 2

Measuring element was made, forming an interdigital transducer (IDT) on a New Cut 2 quartz substrate using photolithographic technique. Frequency response was measured using a network analyzer. The temperature was changed from -20 to 80 °C at steps of 5 °C.

Comparing measurement and theoretical analysis were shown in Fig.3. It shows experimental value was not as good as the calculated value. However the experimental value was well in agreement with theoretical calculation at $\theta$ = 7.45 °. Consequently, change in $\theta$ by 0.05 ° proves to provide more favorable temperature characteristics.

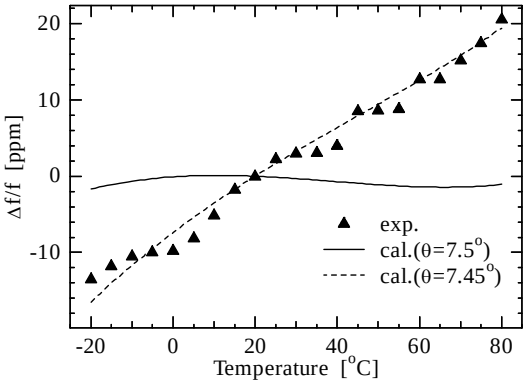


Fig.3 Comparing measurement and theoretical analyses of frequency-temperature characteristics

## 5. Conclusions

In this paper, searching new cuts with excellent frequency-temperature characteristics of Lamb wave propagating on a quartz substrate were conducted. Three new cuts with excellent cubic frequency-temperature characteristics were developed by theoretical analysis and these frequency variation were about 1 ppm. Experimental value of New Cut 2 was well in agreement with theoretical calculation at $\theta$ = 7.45 °. Consequently, change in $\theta$ by 0.05 ° proves to provide more favorable temperature characteristics.

## References


1. H. F. Tiersten: J Acoust. Soc. Am. **59** (1970) 879.
2. M. Matsusita, H. Yao, K. Goohara, I. Hatta and N.; Kato: J. Phys. Soc. Jpn. **54** (1985)
3. Y.Nakagawa, S. Tanaka and S. Kakio: Jpn. J. Appl. Phys. **42** (2003)
4. Y.Nakagawa, M. Momose and S. Kakio: Jpn. J. Appl. Phys. **43** (2003)
5. Y.Nakagawa, M. Shigeta and S. Kakio: Jpn. J. Appl. Phys. **45** (2003)

Proceedings of Symposium on Ultrasonic Electronics, Vol. 29 (2008) pp. 97-98
11-13 November, 2008

# Matrix Formulation for Calculating Spatial Transfer Characteristics in Mechanical Impedance Mismatch System

機械的インピーダンス不整合系における空間伝達特性計算の行列定式化

Michio Ohki (Natl. Def. Acad.)　　大木 道生（防大）

## 1. Introduction

It is practically important and useful to analyze a vibration system with some mechanical impedance mismatch layers inside the system, using a simple and systematic mathematical method. We have already treated such a system with the following tactics:[1,2] The system is always regarded as a 2*N*-layered system (*N*=1,2,...), and the way of propagation, reflection/transmission, and input/output of the wave inside the system are represented with some matrix operations. A multiplication of the matrices in appropriate order represents a path of energy flow, and the sum of these paths, represented with a kind of infinite geometric series of matrices or "Neumann series", is interpreted as a probabilistic superposition of energy modes, which enables us to obtain characteristics of frequency response[1] or impulse response[2], according to the way of superposition.

It is also important to investigate the spatial shape of a mode, for example, the positions of nodes and loops, which influence a spatial transfer frequency response when a (pinpoint) transmitter and receiver are located on the system. However, in general, such an analysis requires matrices of larger size, as its spatial resolution is improved.

In this study, we adopt a concept of "spatial dipole delta function" discussed in ref. 3 along with the foregoing tactics for that purpose. Then, the spatial transfer function can be obtained using (2*N*+4)-by-(2*N*+4) matrices for 2*N*-layered system, and the matrix size does not enlarge, even if the size of a transmitter and receiver becomes smaller.

## 2. Matrix Construction and Operation

We consider an example of 2*N*-layered system, as shown in **Fig. 1(a)** for *N*=1. Mechanical impedance of *i*th layer is denoted by $Z_{[i]}$ (*i* =0 and *i*=2*N*+1 are also allocated outside the system), and the position of boundary between *i*th and (*i*+1)th layers is indicated by $\xi_{[i]}$, where $\xi$ is a coordinate based on propagation time of the wave. A transmitter for input and a receiver for output are located at $\xi = \lambda_T$ and $\xi = \lambda_R$, respectively.

In this study, the effect of a transmitter and receiver is interpreted as insertion of new layers, as shown in **Fig. 1(b)**, each of which has the property of spatial dipole delta function discussed in ref. 3 (the polarity is depicted in the figure), and the length of the inserted layer is given by

$$d\lambda = d\lambda_0 / \omega \qquad (1)$$

where $d\lambda_0$ is a constant sufficiently smaller than the wavelength of wave, and $\omega$ is an angular frequency of wave. (The resolution is preserved for higher $\omega$ with smaller wavelength. The situation of $\omega \to 0$ is not considered.) The layers are renumbered as $Z_1$, $Z_2$, ... , $Z_{2N+4}$. In Fig. 1, $Z_1 = Z_2 = Z_3 = Z_{[1]}$, and $Z_4 = Z_5 = Z_6 = Z_{[2]}$.

Some exceptional examples are shown in **Fig. 2**. In **Fig. 2(a)**, a transmitter is located on an original boundary of layers, and a newly inserted layer is

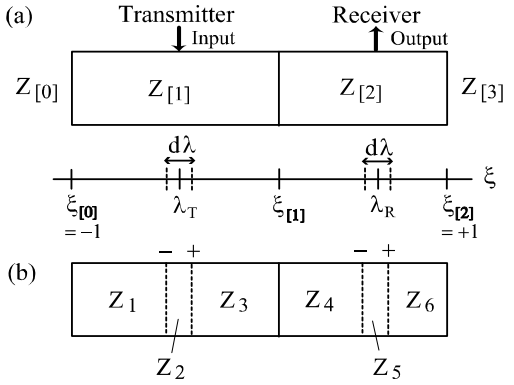


Fig. 1 (a) Transmitter and receiver located on a 2*N*-layered system (in the case of *N*=1). (b) Representation of transmitter and receiver.

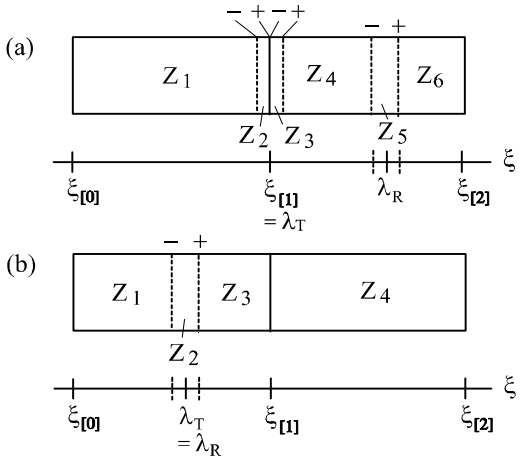


Fig. 2　Some exceptional cases. (a) When $\lambda_T = \xi_{[1]}$. (b) When $\lambda_T = \lambda_R$.

divided into two parts with different mechanical impedance. In **Fig. 2(b)**, when a transmitter and receiver are located on the same position, which is used for the calculation of driving-point frequency response, the degeneration from $2N$+4 layers to $2N$+2 layers occurs.

In any case, the number of layers must be an even number in this methodology. The transformation between layer numbers before and after the insertion of new layers, as well as new layer numbers for transmitter (T) and receiver (R), should be stored for the matrix construction below. In the case of Fig. 2(a), that may be written as {[1]}⇔{1,2}; {[2]}⇔{3,4,5,6}; {T}⇔{2,3}; {R}⇔{5}, where { } denotes a mathematical set, or a mapping $f$ as $f(1) = f(2) = [1]$, $f(3) = \ldots = f(6) = [2]$, and a mapping $g$ as $g(2) = g(3) = \mathrm{T}$, $g(5) = \mathrm{R}$, are defined.

On the system with renumbered layers, three kinds of matrices, with two types, respectively, are constructed, the behaviors of which are illustrated in **Fig. 3**. $D_1$ and $D_2$ represent the propagation of energy mode $\boldsymbol{\eta} = (\eta_1, \eta_2, ..., \eta_{2N+4})^t$, considering the loss due to (irreversible) dissipation processes. $S_1$ and $S_2$ represent the reflection and transmission of $\boldsymbol{\eta}$ based on energy-conserving processes. $K_1$ and $K_2$ are devoted to the input and output processes. See ref. 1 for details with regard to those matrices.

Using the data of mappings $f$ and $g$ and other information on the system, those matrices are constructed; for example, in the case of Fig. 1(b), they have the following forms:

$$D_1 = D_2 = \mathrm{blkdiag}(d_1, \delta, d_3, d_4, \delta, d_6), \tag{2}$$

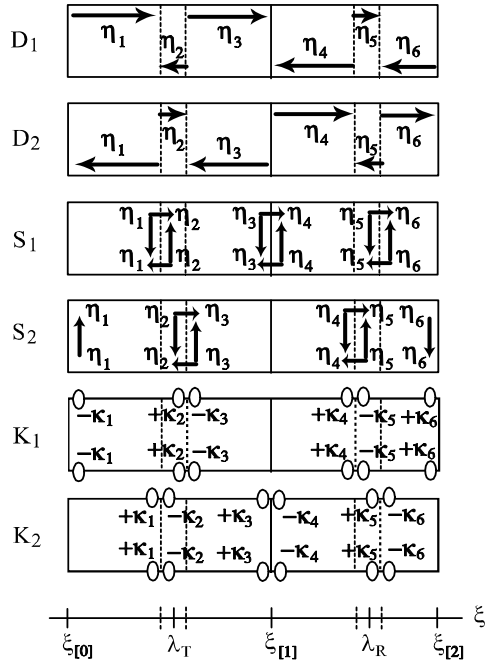


Fig. 3 Diagram of behaviors of matrices $D_1$, $D_2$, $S_1$, $S_2$, $K_1$ and $K_2$ (in Fig. 1(b)).

where "blkdiag" is a function to construct a block diagonal matrix from its arguments, and $d_i$ and $\delta$ are complex propagation factors on $i$th layer and on transmitter or receiver, respectively, and

$$\begin{aligned} S_1 &= \mathrm{blkdiag}(S_{\mathrm{trans}}, S_{[1,2]}, S_{\mathrm{trans}}), \\ S_2 &= \mathrm{blkdiag}(-r_{[0,1]}, S_{\mathrm{trans}}, S_{\mathrm{trans}}, r_{[2,3]}), \end{aligned} \tag{3}$$

where

$$S_{\mathrm{trans}} = \begin{pmatrix} 0 & 1 \\ 1 & 0 \end{pmatrix}, \quad S_{[i-1,i]} = \begin{pmatrix} r_{[i-1,i]} & \sqrt{1-r_{[i-1,i]}^2} \\ \sqrt{1-r_{[i-1,i]}^2} & -r_{[i-1,i]} \end{pmatrix},$$

$$r_{[i-1,i]} = (Z_{[i-1]} - Z_{[i]})/(Z_{[i-1]} + Z_{[i]}),$$

and

$$\begin{aligned} K_{1\,\mathrm{in}} &= -K_{2\,\mathrm{in}} = \mathrm{blkdiag}(0, +\kappa_{[1]}, 0, 0, 0, 0), \\ K_{1\,\mathrm{out}} &= -K_{2\,\mathrm{out}} = \mathrm{blkdiag}(0, 0, 0, 0, -\kappa_{[2]}, 0), \end{aligned} \tag{4}$$

where $\kappa_{[i]}$ is the square root of a kind of driving (and detecting) force on [$i$]-th layer. (Input and output processes are expressed with different matrices, since an input and an output are performed on different layers, when a spatial transfer response is considered.)

Using these matrices, the following Neumann series[1)] is calculated, leading to the spatial transfer frequency response of the system in this study.

$$\boldsymbol{\eta}(\omega) = \sum_{j=1}^{16} \sum_{n=0}^{\infty} K_{\mathrm{out}}^{(j)} \left(R^{(j)}\right)^n A_0^{(j)} K_{\mathrm{in}}^{(j)} \boldsymbol{\eta}_0, \tag{5}$$

where $\boldsymbol{\eta}_0 = (1,1,...,1)^t$, and $A_0^{(j)}$, $R^{(j)}$, and ($K_{\mathrm{in}}^{(j)}$, $K_{\mathrm{out}}^{(j)}$) for 16 probabilistic paths are listed in **Table I**.

## References


1. M. Ohki: Jpn. J. Appl. Phys. **45** (2006) 4462.
2. M. Ohki: Jpn. J. Appl. Phys. **46** (2007) 4474.
3. M. Ohki and K. Toda: Jpn. J. Appl. Phys. **42** (2003) 3102.


Table I. 16 cases of probabilistic paths ($j$ = 1--16).

| $j$ | $A_0^{(j)}$ | $R^{(j)}$ | ($K_{\mathrm{in}}^{(j)}$, $K_{\mathrm{out}}^{(j)}$) |
|---|---|---|---|
| 1 | $D_1$ | $R_1=D_1S_2D_2S_1$ | ($K_{1\,\mathrm{in}}$, $K_{2\,\mathrm{out}}$) |
| 2 | $D_2$ | $R_2=D_2S_1D_1S_2$ | ($K_{2\,\mathrm{in}}$, $K_{1\,\mathrm{out}}$) |
| 3 | $S_1D_1$ | $R_3=S_1D_1S_2D_2$ | ($K_{1\,\mathrm{in}}$, $K_{2\,\mathrm{out}}$) |
| 4 | $S_2D_2$ | $R_4=S_2D_2S_1D_1$ | ($K_{2\,\mathrm{in}}$, $K_{1\,\mathrm{out}}$) |
| 5 | $D_2S_1$ | $R_2$ | ($K_{2\,\mathrm{in}}$, $K_{1\,\mathrm{out}}$) |
| 6 | $D_1S_2$ | $R_1$ | ($K_{1\,\mathrm{in}}$, $K_{2\,\mathrm{out}}$) |
| 7 | $S_2D_2S_1$ | $R_4$ | ($K_{2\,\mathrm{in}}$, $K_{1\,\mathrm{out}}$) |
| 8 | $S_1D_1S_2$ | $R_3$ | ($K_{1\,\mathrm{in}}$, $K_{2\,\mathrm{out}}$) |
| 9 | $D_2S_1D_1$ | $R_2$ | ($K_{1\,\mathrm{in}}$, $K_{1\,\mathrm{out}}$) |
| 10 | $D_1S_2D_2$ | $R_1$ | ($K_{2\,\mathrm{in}}$, $K_{2\,\mathrm{out}}$) |
| 11 | $R_1$ | $R_1$ | ($K_{2\,\mathrm{in}}$, $K_{2\,\mathrm{out}}$) |
| 12 | $R_2$ | $R_2$ | ($K_{1\,\mathrm{in}}$, $K_{1\,\mathrm{out}}$) |
| 13 | $R_3$ | $R_3$ | ($K_{2\,\mathrm{in}}$, $K_{2\,\mathrm{out}}$) |
| 14 | $R_4$ | $R_4$ | ($K_{1\,\mathrm{in}}$, $K_{1\,\mathrm{out}}$) |
| 15 | $R_3S_1$ | $R_3$ | ($K_{2\,\mathrm{in}}$, $K_{2\,\mathrm{out}}$) |
| 16 | $R_4S_2$ | $R_4$ | ($K_{1\,\mathrm{in}}$, $K_{1\,\mathrm{out}}$) |

1P4-3

Proceedings of Symposium on Ultrasonic Electronics, Vol. 29 (2008) pp. 99-100
11-13 November, 2008

# Characteristics of piezoelectric ceramic transducers tapered with exponential function

Jungsoon Kim[1‡], Moojoon Kim[2], Kanglyeol Ha[2]
([1]Dept. of Multimedia Eng., Tongmyong Univ.; [2]Dept. of Physics, Pukyong Univ.)

## 1. Introduction

In order to obtain wide frequency bandwidth, the ultrasonic transducers with tapered piezoelectric ceramics have been studied[1~4]. An ultrasonic probe for medical diagnosis was made of the arrayed piezoelectric elements with non-uniform thickness because of high resolution and wideband characteristics[5]. However, in these approaches, the characteristic evaluation has reported on the specific shape such as an arc or a type with linearly changed thickness[4]. The studies which estimate the performance of the transducer for each design factors are not enough so far.

In this study, an exponential function to give selective variation in thickness along the length of the piezoelectric ceramic was newly introduced. The electro-mechanical characteristics were theoretically analyzed for two transducers of which thickness is changed exponentially according to the function. To confirm the efficacy of the analysis method, some piezoelectric ceramic transducers tapered in accordance with the exponential function were fabricated, and the power transfer functions of the transducers were investigated with experiment.

## 2. Theory

When the thickness of slander type rectangular piezoelectric vibrator is changed exponentially along the length as shown in **Fig. 1**, the thickness can be represented by the function of the position $x$ as following equation.

$$l(x)=\frac{l_{\min}\left(e^{gT}-e^{gx}\right)+l_{\max}\left(e^{gx}-1\right)}{e^{gT}-1} \qquad (1)$$

Here, $l_{max}$ and $l_{min}$ are thickness at $x$=$T$ and $x$=0, respectively. The parameter $g$ is shape index. The equation (1) has the following values for each limitation of $g$.

$$\lim_{g\to-\infty} l(x)=l_{\max} \qquad (2a)$$

$$\lim_{g\to 0} l(x)=\frac{\left(l_{\max}-l_{\min}\right)}{T}x+l_{\min} \qquad (2b)$$

$$\lim_{g\to\infty} l(x)=l_{\min} \qquad (2c)$$

To analyze the characteristics of the vibrator, we assumed that the piezoelectric ceramic with length $T$ is divided by $N$. When the divide number $N$ goes to infinite, the input admittance of the vibrator is

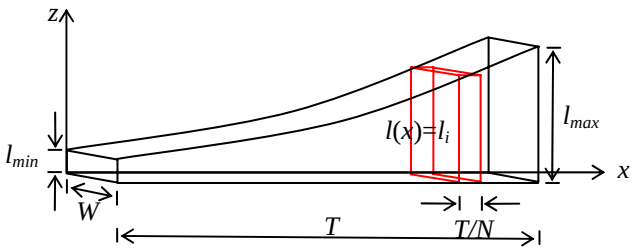


Fig. 1. Calculation model for piezoelectric vibrator with exponentially tapered thickness.

given by

$$Y_3\big|_{0,T}=\int_0^T \frac{j\omega\dfrac{\varepsilon_{33}^S}{l(x)}W}{1+\dfrac{k_T^2}{\left(\dfrac{\omega l(x)}{v_{33}^D}\right)}\dfrac{j\dfrac{\overline{Z}_l}{\overline{Z}_0}-2\tan\left(\dfrac{\omega l(x)}{2v_{33}^D}\right)}{1-j\dfrac{\overline{Z}_l}{\overline{Z}_0}\cot\left(\dfrac{\omega l(x)}{v_{33}^D}\right)}}dx, \qquad (3)$$

where, $\omega$: angular frequency, $\varepsilon_{33}{}^S$: dielectric constant, $W$: width of the vibrator, $k_T$: electro-mechanical coupling coefficient, $v_{33}{}^D$: sound velocity of the piezoelectric vibrator, $Z_0$: characteristic impedance of the piezoelectric vibrator, and $dx=\lim_{N\to\infty} T/N$.

Using the Eq. (3), the power transfer function of the transducer is given by

$$H_p(\omega)=\frac{4R_gR_m}{\left\{R_g+R_m\right\}^2+\left\{X_m-\dfrac{1}{\omega C_0}\right\}^2}, \qquad (4)$$

where $R_g$ is internal resistance of the electric source and the clamped impedance $Z_0\big|_{0,T}$ and the motional impedance $Z_m\big|_{0,T}$ are given as follows:

$$Z_0\big|_{0,T}=\frac{1}{\displaystyle\int_0^T j\omega\frac{\varepsilon_{33}^S}{l(x)}Wdx}, \qquad (5)$$

$$Z_m\big|_{0,T}=\frac{1}{Y_3\big|_{0,T}}-Z_0\big|_{0,T}=R_m+jX_m. \qquad (6)$$

## 3. Experiment and Results

Two transducers with exponentially tapered thickness was obtained from a rectangular

kimmj@pknu.ac.kr

piezoelectric bulk ceramic of 21.85(L) x 13.05(W) x 12.10(H) $mm^3$ size by cutting as shown in **Fig. 2**. The ceramic is uniformly polarized along *z*-axis. A CNC(computer numerical control) milling machine with CAD/CAM software was used in the cutting process, and the very slow cutting progress rate of 0.016mm/s in cooling water was taken to prevent depolarization due to the mechanical stress and heat during the process. The material constants of the ceramic are shown in **Table 1**.

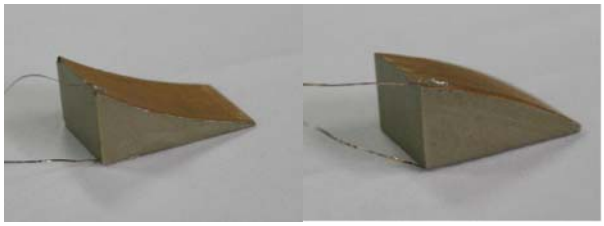

(a) $g$=50 (b) $g$=-50

Fig. 2. Photograph of piezoelectric vibrators with exponentially tapered thickness.

Table 1. Material constants of the piezoelectric vibrator.

| | |
|---|---|
| Density [$kg/m^3$] | 7649.9 |
| Electro-mechanical Coupling constant $k_T$ | 0.381 |
| Dielectric constant $\varepsilon^S_{33}/\varepsilon_0$ | 839 |
| Phase velocity $v^D_{33}$ [m/s] | 4116.3 |

The shape index and size of the vibrators shown in Fig. 2 are listed in **Table 2**.

Table 2. Size and $g$-values of the fabricated transducers.

| $g$ | $l_{max}$[mm] | $l_{min}$[mm] | $W$[mm] | $T$[mm] |
|---|---|---|---|---|
| 50 | 10.9 | 0.8 | 13.0 | 20.8 |
| -50 | 9.9 | 1.0 | 13.0 | 19.2 |

The theoretical and experimental power transfer functions which reveal the frequency bandwidth characteristics are shown in **Fig. 3**. The -3dB bandwidth of the transducer of $g$=50 is about 68.4% in the experimental result. In case of $g$=-50, though the bandwidth is over than 118.4%, the peak of transfer function is less 10 dB than the transducer of $g$=50 in the given frequency range. The center frequencies of the transducers of $g$=50 and $g$=-50 are 2319.3 kHz and 1709.0 kHz, respectively. The tendency of frequency change with shape index $g$ in given frequency range is consistent with the theoretical one.

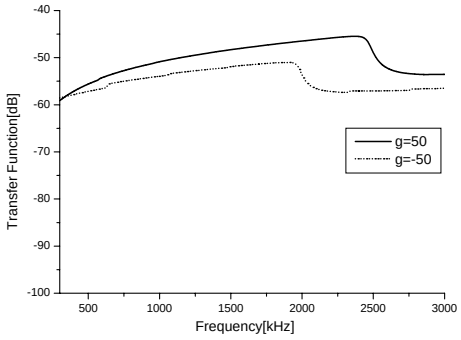


(a) Theory

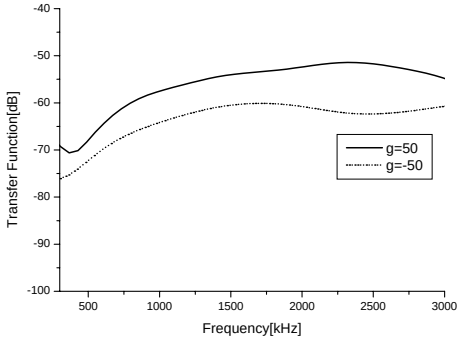


(b) Experiment

Fig. 3. Power transfer function change with vibrator shape.

**Acknowledgment**

This work was supported by the Korea Research Foundation Grant funded by the Korean Government (MOEHRD, Basic Research Promotion Fund) (KRF-2006-531-D0005).

**References**

1. Y. Tomikawa. A. Yamada. and M. Onoe, "Wide Band Ultrasonic Transducer Using Tapered Piezoelectric Ceramics for Non-Destructive Inspection," Jpn. Jour. Appl. Phys., vol. 23, suppl. 23-1, pp. 113-115 (1984).
2. P. G. Barthe and P. J. Benkeser, “A Staircase Model of Tapered-thickness Piezo-electric Ceramics," J. Acoust. Soc. Amer., 89, pp. 1434-1442 (1991).
3. B. N. Alekseev, D. B. Dianov, and S.P. Karuzo, "Tapered-Bar Transducer," in Proceedings of the Eighth All-Union Acoustics Conference [in Russian], Moscow, (1973).
4. D. Kim, J. Han, J. Yang, M. Kim, K. Ha, "Characteristic Evaluation for a PZT Transducer with Cylindrical Rear Surface, " Journal of the Acoustical Society of Korea, vol. 26, no. 1E, pp. 14-20 (2007).
5. A. M. Hanafy, "Broadband Phased Array Transducer Design with Frequency-Controlled Two-Dimensional Capability," SPIE 3341, pp. 64-82, (1998).

Proceedings of Symposium on Ultrasonic Electronics, Vol. 29 (2008) pp. 101-102
11-13 November, 2008

# Analysis of Q-value of Quartz Crystal Tuning Fork Using Thermoelastic Coupling Equations

熱弾性方程式による音叉型水晶振動子のQ値の解析

Hideaki Itoh and Yuhya Tamaki（Shinshu Univ. Dep. Electr & Elect. Eng）
伊藤秀明，玉木悠也（信州大 電気電子工）

## 1. Introduction

Zener [1)2)] investigated a damping coefficient and Q-value of a cantilever beam in bending vibration by using thermoelastic coupling equations and derived a formula for the damping coefficient due to thermoelastic damping. To date, many researchers [3)4)5)] have been developing Zener's works more precisely. The comparison between the measured and the calculated value on the damping coefficient of cantilever beams has been made and the good consistency between them has been shown[4)].

In this study, we derived a formula for Q-value of quartz crystal tuning fork theoretically by using thermoelastic coupling equations given by Sieh[4)]. The comparison between the measured and the calculated values of Q-value for etching processed quartz crystal tuning fork is carried out.

## 2. Analysis and discussion

We pay attention to the transverse vibration of one arm as cantilever beam, in order to obtain Q-value of the quartz crystal tuning fork which consists of two arms undergoing flexural vibration each other in opposite direction as shown in Fig.1.

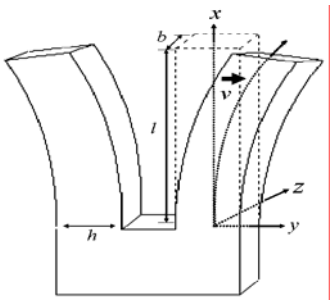


Fig.1 Configuration of Quartz Crystal Tuning Fork

The deflection displacement of the right arm in the y direction, thickness, length, and width of the arm are shown as v(x,t), b, l, and h in Fig.1. Time and the coordinate of longitudinal direction of the arm is set to be t and x, respectively. When the quartz crystal tuning fork undergoes in flexural vibration, temperature at compressing side of the arm increases because of adiabatic thermal compression and at lengthening side decreases because of adiabatic thermal expansion. Therefore, temperature gradient occurs in the y direction of the arm according to compression-expansion behavior and the thermal energy diffuses at the quartz crystal surface by heat conduction. At last, the thermal energy dissipates to the external environment from the surface.

In this study, we rearranged the thermoelatic coupling equations given by Sieh[4)] and adopted the rearranged equations described as

$$EI\frac{\partial^4 v}{\partial x^4}+\rho bh\frac{\partial^2 v}{\partial t^2}+E\alpha b\int_{-h/2}^{h/2} y\frac{\partial^2\theta}{\partial x^2}dy=0, \quad (1)$$

$$k\left(\frac{\partial^2\theta}{\partial x^2}+\frac{\partial^2\theta}{\partial y^2}\right)-\rho c_E\frac{\partial\theta}{\partial t} + E\alpha T_0 y\frac{\partial^3 v}{\partial x^2\partial t}-\frac{E\alpha^2 T_0}{h}\int_{-h/2}^{h/2}\frac{\partial\theta}{\partial t}dy=0, \quad (2)$$

where E, I, α, θ, k, $T_0$, $c_E$, ρ are Young modulus, moment of inertia, thermal expansion coefficient, temperature change from absolute room temperature, thermal conductivity, absolute room temperature, heat capacity, and density of the beam, respectively. When we solve eqs.(1) and (2), the boundary conditions are applied to the arm shown in Fig.1 as follows: (a) the boundary conditions of the arm are fixed at x=0 and expressed by

$$v(x,t)=\frac{\partial v}{\partial x}(x,t)=0 \quad (3),$$

(b) the boundary conditions of the arm are free at x=l and expressed by

$$EI\frac{\partial^2 v}{\partial x^2}+E\alpha b\int_{-h/2}^{h/2} y\theta(x,y,t)dy=0 \quad \text{and}$$

$$EI\frac{\partial^3 v}{\partial x^3}+E\alpha b\int_{-h/2}^{h/2} y\frac{\partial\theta}{\partial x}(x,y,t)dy=0 \quad (4),$$

(c) the adiabatic thermal boundary conditions of the arm are described as

$$\frac{\partial\theta}{\partial x}=0 \ \text{ at } x=0,l \text{ and } \frac{\partial\theta}{\partial y}=0 \ \text{ at } \ y=\pm\frac{h}{2} \quad (5),$$

(d) the isothermal boundary conditions of the arm are described as

$$\theta=0 \ \text{ at } \ x=0,l \ \text{ and } \ y=\pm\frac{h}{2} \quad (6).$$

Using the definition of Q-value[5)] given by

$$Q^{-1}=2\left|\frac{\mathrm{Im}(\omega)}{\mathrm{Re}(\omega)}\right| \quad (7),$$

we can derive Q-value formula using complex angular frequency $\omega$ which is determined by the

---

E-mail: rokuro1@gipwc.shinshu-u.ac.jp

eigenvalue equation obtained by substituting the boundary conditions eqs.(3)～(6) into eqs.(1) and (2)[6].

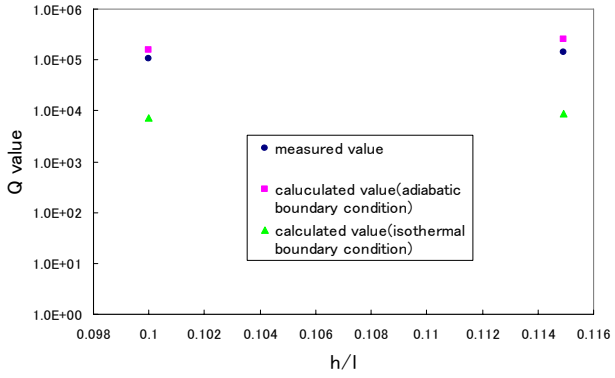


Fig.2 Comparison between calculated and measured Q value as a function of the parameter h/l

Figure 2 shows the comparison between calculated and measured Q-value as a function of the parameter h/l. As shown in Fig.2, the measured value is very close to the calculated value using adiabatic approximation. Therefore, Q-value of quartz crystal tuning fork can be calculated by using a formula for Q-value obtained under adiabatic boundary condition. Furthermore, the difference between the calculated Q-value based on the thermoelasticity and the measured Q-value is responsible for the effect of both heat conduction to the length direction and vibration leakage from the base.

Figure 3 show a temperature-CI value characteristics[7] for an etching processed quartz crystal tuning fork. As shown in Fig. 3, the temperature-CI value characteristics shows V-shaped curve becoming a bottom at about 20℃. Linear increase response in CI value with rising temperature is based on the thermoelasticity because the reciprocal of Q-value formula is proportional to absolute temperature[5]. On the other hand, linear decrease response in CI value with rising temperature seems to be based on the vibration leakage. In Fig.3, the whole CI value was estimated to be 39.0kΩ at 25℃. From the data of Fig.3, we can estimate CI value based on the thermoelasticity at 25℃, by the least squares method applied to experimental data over 25℃, to be 37.0kΩ which is about 95% of the whole CI value at 25℃. By omitting the effect of heat conduction to the length direction, the remainder subtracted the calculated CI value based on the thermoelasticity from the measured CI value becomes a calculated CI value based on the vibration leakage.

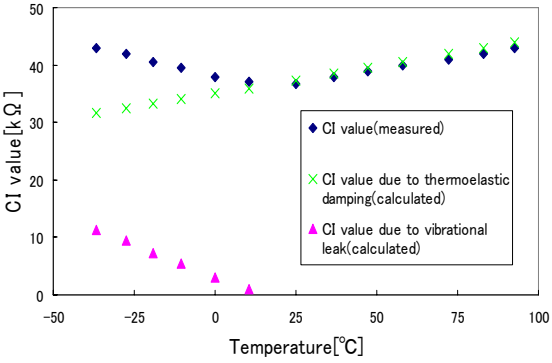


Fig.3 Temperature-CI value characteristics

We calculated the remainder to be 2kΩ, which was about 5% of the whole CI value and was CI value based on the vibration leakage from the base to the holder at 25℃.

## 3. Conclusion

We could derive a formula for Q-value of a quartz crystal tuning fork by using the thermelastic coupling equations for a cantilever beam from the viewpoint of the thermoelasticity. As a result of calculating Q-value under both adiabatic and isothermal boundary conditions, it was clear that the calculated value under adiabatic boundary condition was more close to the measured value on Q-value of an etching processed quartz crystal tuning fork than that under isothermal boundary condition. It is concluded that the phenomenon that CI value increases with rising temperature in high temperature region is due to the effect of the thermoelasticity and that CI value decreases with rising temperature in low temperature region is due to the effect of the vibration leakage from the base of a quartz crystal tuning fork to the holder.

## References

1. C.Zener, Phys. Rev. **52**, 230 (1937).
2. C.Zener, Phys. Rev. **53**, 90 (1938).
3.L.D.Landau and E.M.Lifshitz, Theory of Elasticity (Pergamon Press, Oxford, 1959).
4. R.C.Shieh, J. Appl. Mech. **38**, 839 (1971).
5. R.Lifshitz and M.L.Roukes, Phys. Rev. B **61**, 5600 (2000).
6. H. Itoh et. al., Proc. 36th EM Symp., (2007) p.5.
7. O.Kawauchi et. al., Proc. 32th EM Symp., (2003) p.39.

Proceedings of Symposium on Ultrasonic Electronics, Vol. 29 (2008) pp. 103- 104
11-13 November, 2008

# Analytical Study on Load Effects of $LiNbO_3$ Vibrator for Ultrasonic Motor Using Vibration Mode Coupling

$LiNbO_3$結合モード利用モータ振動子の負荷影響に関する解析的検討

Kyousuke Shibata‡, Hideki Tamura*, Manabu Aoyagi[1], Takehiro Takano[2],
Yoshiro Tomikawa and Seiji Hirose
(Yamagata Univ., [1]Muroran Inst. of Tech., [2]Tohoku Inst. of Tech.)
柴田恭佑‡, 田村英樹*, 青柳学[1], 高野剛浩[2], 富川義朗, 広瀬精二（山形大・工、[1]室蘭工大、[2]東北工大）

## 1. Introduction

The authors have investigated ultrasonic motors using the piezoelectric single-crystal $LiNbO_3$. [1-4] One of them, we proposed the single phase driving motor using the coupling-mode combined with a longitudinal and flexural in-plane modes in a rectangular plate. An additional rotated X-rotated Y-cut rectangular plate can provide the coupling-modes caused by the crystal anisotropy. Rotational direction of the single phase motor can be reversed by switching the two modes. To obtain the same characteristics between the both rotation, we designed the vibrational displacements of both modes to be equal by FEM analysis. [3] However, experimental results showed large difference of the revolution characteristics between the both direction. Because the generative force of the $LiNbO_3$ is small, and the vibrator easily takes the influence of the preload and external load. The condition of modes are changed by the loads from the designed it. This paper shows the analytical investigation for the influence of the loads using a FEM model with spring elements.

## 2. FEM analysis with the spring element to load

**Figure.1** illustrate an experimental construction of stator. The center points on the top and bottom surfaces of the $LiNbO_3$ rectabgular vibrator are fixed for support and are used for electric power feed. The vibrator is based on the 135° X-rotated Y-plate, length $L$, width $W$ and thickness $t$=0.5 mm, and applied second rotation Φ in the y'-axis as shown in Fig. 1(b) .

We had analyzed the vibrator by FEM method using the simple rectangular crystal model. In this study, we try to apply an influence of loads for the analysis model, and it is assumed that a mechanical spring which is attached at the contact point of the vibrator acts the load by its reaction force. Therefore, the springs of the vertical and horizontal

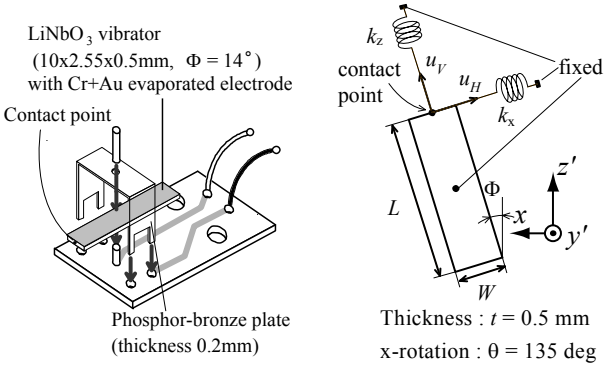


(a) Support configuration of stator vibrator for a trial. (b) Parameters of vibrator and applied spring loads.

Fig.1 Stator vibrator of an ultrasonic motor using vibration mode coupling in $LiNbO_3$ rectangular vibrator.

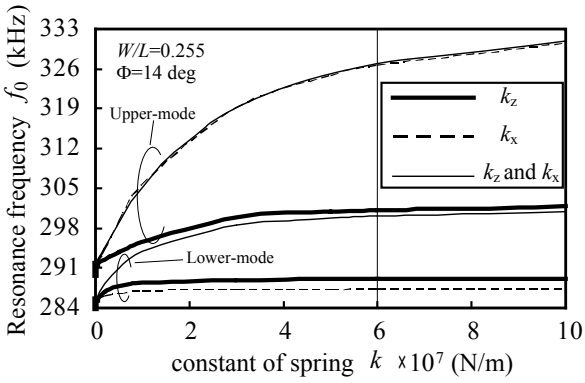


Fig.2 Analysis result of the resonance frequency correlated with spring constant $k$ of loads.

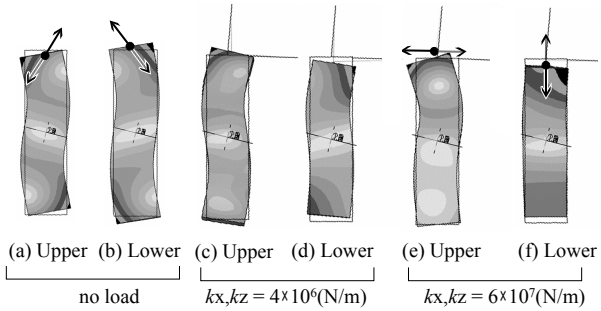


Fig.3 Load influence of the vibration resonance mode.($W/L$=0.255)

*E-mail : htamura@yz.yamagata-u.ac.jp

components are applied using "COMBIN14" element of ANSYS as shown in Fig. 1(b), and the spring constants are $k_z$ and $k_x$, respectively. The another side of the springs is fixed.

Two coupling-modes are caused by the originated longitudinal 1st and flexural 2nd modes. The coupling mode with the higher resonance frequency is called the upper mode, and the another is called the lower mode. The resonance frequencies of the coupling-modes are changed by strength of the springs as shown in **Fig.2**. The frequencies increase with the strength of springs, and its tendency accords with the experimental experience. The load influence not only changes the resonant frequency but also deforms of each mode as shown in **Fig.3**. These influences are one of the reasons of the large difference of the motor characteristics between the both rotation directions.

We require the conditions of the displacement at the contact point for the vibrator design as follows:

(a) the upper and lower modes have to same displacement ratio $u_H/u_V$,

(b) and the vertical and horizontal components have to be equal each other ($u_H/u_V$ =1).

The vibrator designed on no-load fulfills above conditions as shown in Fig.3(a) and (b). However, the loaded vibrator shown in Fig. 3(e) to 3(f) distinctly deviates from the request. The analysis results for the load influence of the resonance frequencies and displacement ratio $u_H/u_V$ correlated with the width-to-length ratio *W/L* are shown in **Fig. 4** and **5**, respectively. The both characteristics are shifted by load; therefore, determinate value of *W/L* =0.255 when Φ =14 $^{o}$ is not suitable under the loading. For example, when the loaded spring constants $k_z$ and $k_x$ equal 4x10$^6$ N/m, the both displacement ratios of the upper and lower modes are on the same at *W/L* =0.244. However, its displacement ratio $u_H/u_V$ is about 1.55 and not equals one; therefore, it is necessary to design the suitable width-to-length ratio and crystal cut-angle with the load influence.

Additionally, in case of the large loading, for instance when $k_z$ and $k_x$ equal 6x10$^7$ N/m, the displacement ratios between the upper and lower modes are not crossing any more. Thus, a loading limit will be able to be estimated by this method.

## 3. Conclusions

Our previous designed stator vibrator using the coupling-mode has problems in experimental characteristics. In this study, the load influence for the vibrator is considered in the FEM analysis using a simple spring element, and we provide the analytical results that the single crystal vibrator is large affected by the external loads and the previous

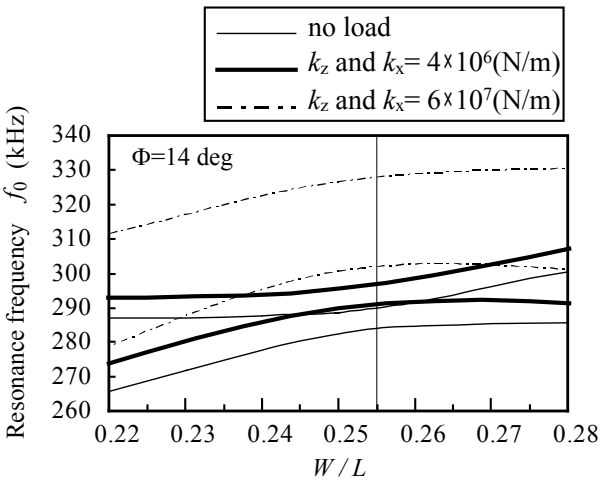


Fig.4 Resonance frequency correlated with the width-to-length ratio *W/L* depended on the load of springs.

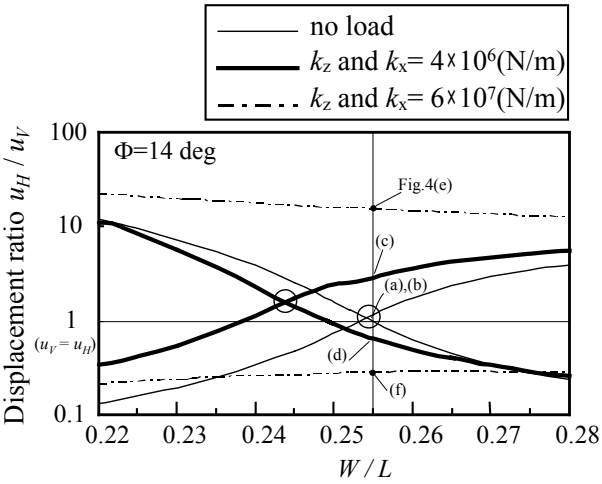


Fig.5 Displacement ratio at the contact point correlated with width-to-length ratio *W/L* depended on the load of springs.

dimensions of vibrator are not suitable for an actual condition in loading.

For future work, the correlation between the values of spring constant as the load and the actual load force have to be clear, and it is necessary to establish the design method of the vibrator corresponding to the applied load.


## Acknowledgment

This research was partially supported by the Ministry of Education, Culture, Sports, Science and Technology, Grantin-Aid for Scientific Research on Priority Areas (No.438)No.19016001.


## References


(1) T. Takano *et. al*., Proc. 10th Int. Conf. Actuators 2006, pp.453-456, 2006.

(2) H. Tamura *et. al*., Jpn. J. Appl. Phys. Vol. 46, 7B pp.4698-4703, 2007

(3) H. Tamura *et. al*., Jpn. J. Appl. Phys. Vol. 47, No.5 pp.4015-4020, 2008

(4) H. Tamura *et. al*., Jpn. J. Appl. Phys. Vol. 47, No.5 pp.4034-4040, 2008

Proceedings of Symposium on Ultrasonic Electronics, Vol. 29 (2008) pp. 105-106
11-13 November, 2008

# A Study on the Shape of Longitudinal Bar Resonators used as Piezoelectric Vibratory Tactile Sensors

圧電振動型触覚センサの振動子形状の検討

Subaru Kudo (Ishinomaki Senshu Univ.)
工藤すばる（石巻専修大 理工）

## 1. Introduction

Various piezoelectric vibratory tactile sensors have been proposed for measuring the softness and hardness of an object 1-7). These tactile sensors utilize the longitudinal-mode, flexural-mode or edge-mode vibration of the resonators. They make use of changes in the resonance frequencies of the resonators, which are induced when their vibrating sections are brought into contact with an object. In these tactile sensors, the longitudinal bar type sensor has been the most studied 1,4,7), and the sensitivity of the resonance frequency change on the tactile sensor was investigated using the distributed constant-circuit model of the resonator 8).

In this study, the shape of the longitudinal bar resonator is considered for improving the sensitivity on the piezoelectric vibratory tactile sensor. First, the approximate equation of the frequency change of the tactile sensor in case of contacting with a softer object is derived. The experimental results of sensitivities for the tactile sensor are discussed from the viewpoint of the mass of the resonator. Then, the equivalent masses of the horn type resonators are calculated using the finite element method.

## 2. Sensitivity of tactile sensor

Figure 1 shows the construction of tactile sensor with a longitudinal bar resonator. When the tactile sensor, which is driven in the longitudinal mode, touches an object, the softness and hardness of the object are detected as changes in resonance frequencies.

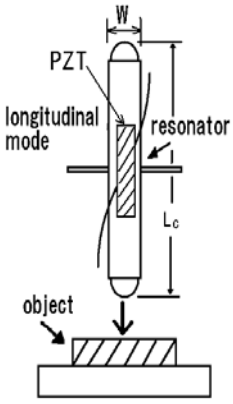


Fig.1 Construction of tactile sensor with longitudinal bar resonator.

In general, the resonance angular frequency $\omega_0$ of a resonator is shown by $\omega^2{}_0 = s/m_0$. Here, $m_0$ and s are the equivalent mass and stiffness of the resonator, respectively. When the resonator is contacted with a softer object, the resonant frequency changes by an additional mass effect. In this case, the resonance angular frequency $\omega$ is approximately given by $\omega^2 = s/(m_0+m_e)$, where $m_e$ is an additional mass. Then, the resonance frequency change is expressed by

$$\frac{f}{f_0} = \left(1+\frac{m_e}{m_0}\right)^{-\frac{1}{2}} . \qquad (1)$$

Moreover, in the case of assuming that $1 \gg m_e/m_0$, the sensitivity of the frequency change ratio is expressed as

$$\frac{\Delta f}{f_0} \cong -\frac{m_e}{2m_0} = -\frac{m_e}{2\delta M_0} \qquad (2)$$

, where $\Delta f = f - f_0$ and $\delta$ ($=m_0/M_0$ ; $M_0$:total mass) is the equivalent mass coefficient.

This approximate equation means that the sensitivity of tactile sensor is inversely proportional to the equivalent mass of the resonator. Then, the resonator with small $\delta$ is suitable for increasing the sensitivity.

Figure 2 shows the experimental results for the tactile sensor with the longitudinal bar resonator, where Lc=50mm and resonance frequency $f_0$=51.55kHz. When the load added to test pieces increased, the resonance frequencies of the resonator gradually decreased. The amount of decrease of resonance frequency is expressed as $\Delta f$ ($=f_L-f_0$), where $f_L$ is the resonance frequency when a load is applied and $f_0$ is the resonance frequency with no load. The characteristics between the load and $\Delta f$ show the tendency that the amount of decrease for the soft test piece S1 is larger than the hard test pieces S2 and S3. Figure 3 shows the relationship between the frequency change ratio $|\Delta f/f_0|$ at load W=4gf and the mass $M_0$ of the resonator. It is clear that the sensitivity of $|\Delta f/f_0|$ is inversely proportional to the mass of the resonator as shown by eq.(2). The relationship between $|\Delta f/f_0|$ and $M_0$ is estimated to be $|\Delta f/f_0| \propto M_0^{-0.799}$ by curve fitting.

kudou@isenshu-u.ac.jp

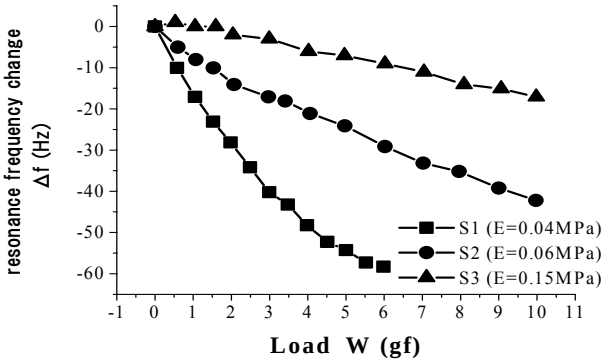


Fig.2 Characteristics of longitudinal-bar type tactile sensor. (Lc=50mm, $f_0$=51.55kHz, first mode)

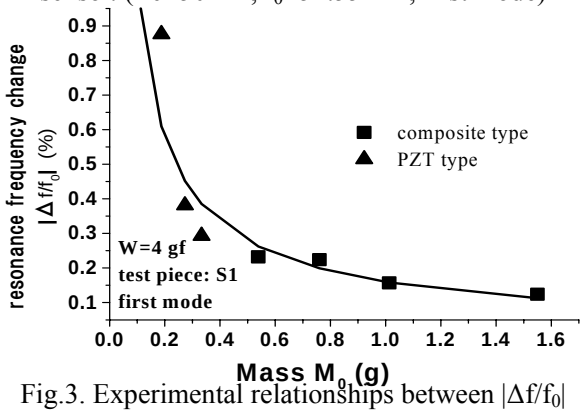


Fig.3. Experimental relationships between $|\Delta f/f_0|$ and Mass.

## 3. Calculated results of the equivalent mass

To consider the effect on a shape of the bar resonator, the equivalent masses of the horn type resonators in Fig.4 are calculated using the finite element method. Table I shows the calculated results of the equivalent mass of the resonator in Fig.4(a). It is clarified that the equivalent mass $m_0$ and the equivalent mass coefficient $\delta$ are small as the width W2 of the sensor tip becomes smaller. On the other hand, Figs. 4 and 5 show the calculated results of the equivalent mass and the eqivalent mass coefficent in Fig.4(b). The values of $m_0$ and $\delta$ become small when $L_A \fallingdotseq 6$mm. From these calculated results, it became clear that there is a possibility to improve sensitivity by designing the shape of the longitudinal bar resonator.

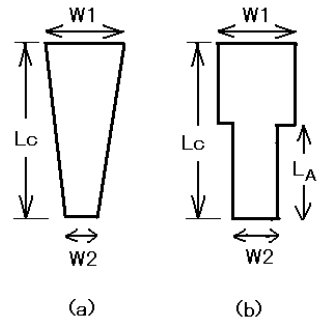


Fig.4 Horn type longitudinal bar resonator.

Table I. Calculated results of equivalent mass. (Lc=16mm, W1=4mm, t=2mm, $\rho$ =7900kg/m$^3$)

| W2 (mm) | 4.0 | 2.0 | 1.0 |
|---|---|---|---|
| Equivalent mass $m_0$ (g) | 0.494 | 0.262 | 0.158 |
| Total mass $M_0$ (g) | 1.011 | 0.758 | 0.632 |
| Equivalent mass coefficient $\delta$ | 0.49 | 0.35 | 0.25 |

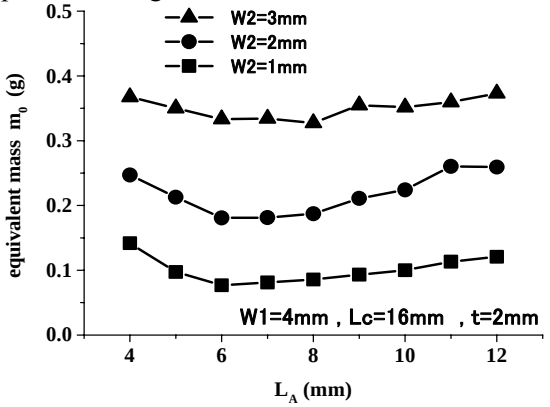


Fig.5 Calculated relationship between $L_A$ and $m_0$.

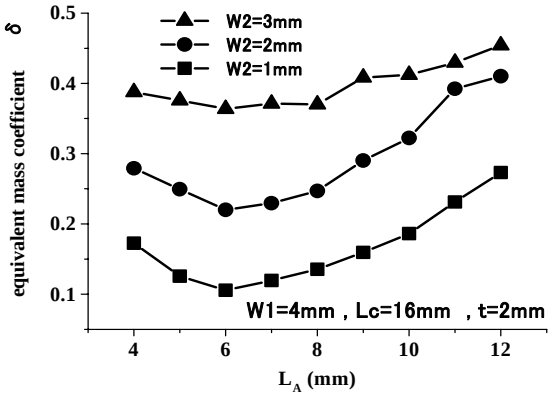


Fig.6 Calculated relationship between $L_A$ and $\delta$ .

## 4. Conclusion

The shape of the longitudinal bar resonator was studied for improving the sensitivity on the piezoelectric vibratory tactile sensor. This work was partially supported by a Grant-in-Aid for Scientific Research C2(No.19560426) from the Japan Society for the Promotion of Science, and a Grant from Ishinomaki Senshu University.

## References

1. S.Omata and Y.Terumura:Sensors and Actuators A, **35**(1992) 9.
2. M.Maesawa, et al : Proc.1997 Int. Cof. Solid-State Sen. & Actu. (1997) 117.
3. H.Itoh, et al : Jpn.J.Appl.Phys **38** (1999) 3225.
4. Y.Murayama and S.Omata:IEEE Trans. Ultra. Fero. & Freq. Cont.(2005)434.
5. S.Kudo : Jpn.J.Appl.Phys **44** (2005) 4501.
6. H.Watanabe : Jpn.J.Appl.Phys **40** (2001) 3704.
7. C.Kleesattel and G.M.L.Gladwell: ULTRASONICS (1968)175.
8. S.Kudo : Jpn.J.Appl.Phys **46** (2007) 4704.

Proceedings of Symposium on Ultrasonic Electronics, Vol. 29 (2008) pp. 107-108
11-13 November, 2008

# A Study on Sensitivity of Frequency-Change-Type Force Sensor
# 周波数変化型力センサの感度に関する研究

Sumio Sugawara, Masaki Yamakawa†, Subaru Kudo (Ishinomaki Senshu Univ.)
菅原澄夫，山川将貴†，工藤すばる（石巻専修大 理工）

## 1. Introduction

A high-sensitivity frequency-change-type force sensor has been required for application to the attitude control and navigation systems of moving objects such as vehicles. As such a sensor, some structures have been proposed.[1] However, because the change of the resonance frequency by axial force is very small, these structures are unsuitable for the required specification. Therefore, the authors have proposed the force sensor utilizing an out-of-plane mode to realize high sensitivity[2]. The acceleration sensor[3)-5)] and the inclination angle sensor[6] can be also realized using this sensor.

In this paper, some frequency-change-type force sensors are designed using the finite-element method. The sensor sensitivity is analyzed and compared.

## 2. Structures of force sensor

**Fig. 1** shows some force sensors utilizing the phenomenon that the resonance frequency of a bending vibrator changes by axial force. **Fig. 1(a)** is the structure utilizing an out-of-plane mode[2]. As shown in **Fig. 2(a)**, the sensor vibrates along the direction which is vertical to its surface. On the other hand, **Figs. 1(b)** and **1(c)** are the structures utilizing an in-plane mode. The sensors vibrate along the direction which is horizontal to its surface, as shown in **Figs. 2(b)** and **2(c)**. **Figs. 1(d)** and **1(e)** are the structures which are utilizing an in-plane mode that two arms vibrate symmetrically, as shown in **Figs. 2(d)** and **2(e)**.

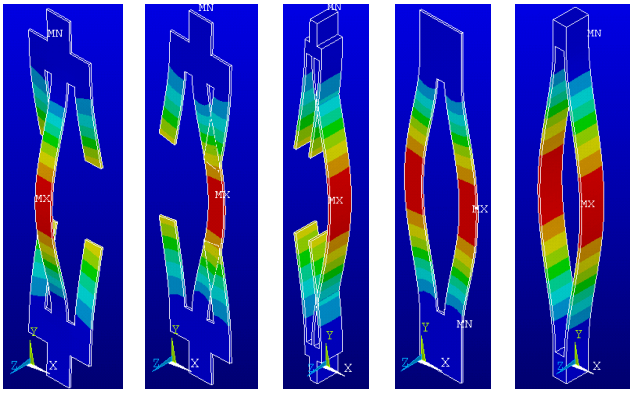

(a) Type (a) (b) Type (b) (c) Type (c) (d) Type (d) (e) Type (e)

Fig. 2 Vibration modes of force sensor.

## 3. Analysis of Sensor Characteristics

The sensor material is stainless steel (SUS304), and the dimensions in **Figs. 3(a)** and **3(b)** are listed in **Table Ⅰ**. Ansys 11.0 is used as software for the finite-element analysis. The displacements at the both ends of the sensor are decreased, and the frequency change rate of $\Delta f/f_0$ is analyzed using the finite-element method when the axial force along the y axis is applied to the sensor.

### 3.1 Displacements at base end

To support the sensor, the displacements at both ends of the sensor must be decreased by changing the shape of the base part. The analyzed results of the displacements $u_i$(i=x, y, z) at the base end are shown as the ratio $u_i/u_{i0}$ to the maximum displacement $u_{i0}$ at the central part of the arm. The value of $u_i/u_{i0}$ must be made less than $10^{-3}$. The calculated values of $u_i/u_{i0}$ are listed in **Table Ⅱ**,

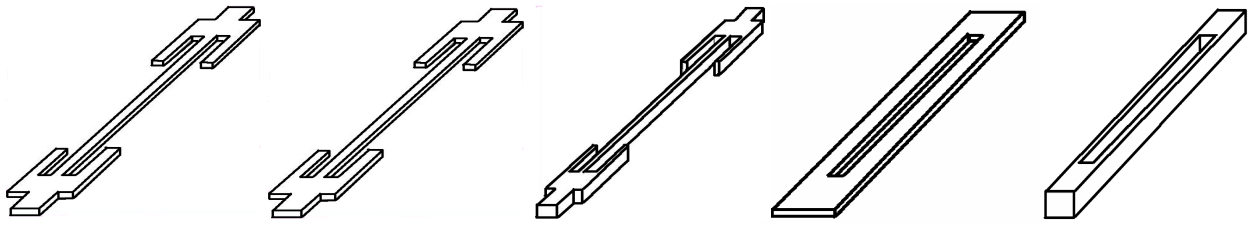

(a) Type (a) (b) Type (b) (c) Type (c) (d) Type (d) (e) Type (e)

Fig. 1 Structures of frequency-change-type force sensor.

E-mail address: ssumio@isenshu-u.ac.jp

and very small in the case of the sensors of types (a) and (e). The ratios at the base center are different from the ratios at the base edge generally.

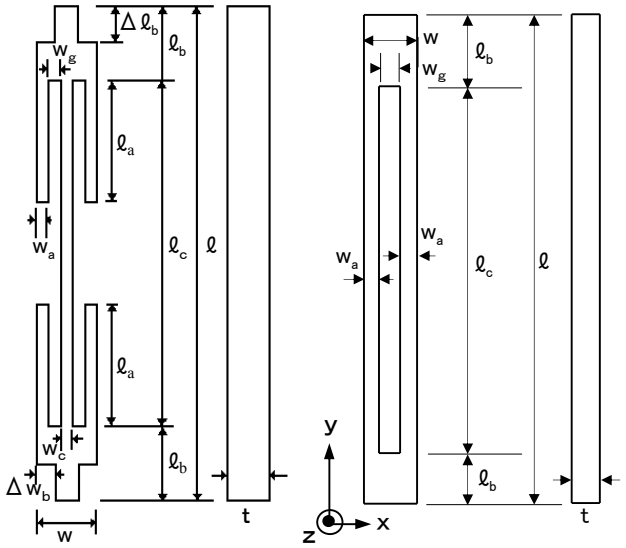


Fig. 3 Symbols for dimensions.

Table Ⅰ Dimensions of sensor (mm).

(a) Types (a)～(c)

| | |
|---|---|
| $\ell$ | 30～38 |
| $\ell_a$ | 8.0, 8.5 |
| $\ell_b$ | 3.0～7.4 |
| $\ell_c$ | 24 |
| $\Delta\ell_b$ | 1.5～1.9 |
| w | 1.6, 7.6 |
| $w_a$ | 0.2, 2.0 |
| $w_c$ | 0.2, 2.0 |
| $w_g$ | 0.5, 0.8 |
| $\Delta w_b$ | 0.45, 2.4 |
| t | 0.2, 2.0 |

(b) Types (d) and (e)

| | |
|---|---|
| $\ell$ | 32, 36 |
| $\ell_a$ | |
| $\ell_b$ | 4.0, 6.0 |
| $\ell_c$ | 24 |
| $\Delta\ell_b$ | 2.0, 3.0 |
| w | 0.9, 4.8 |
| $w_a$ | 0.2, 2.0 |
| $w_c$ | |
| $w_g$ | 0.5, 0.8 |
| $\Delta w_b$ | 0 |
| t | 0.2, 2.0 |

### 3.2 Sensitivity of sensor

When the force $F$ along the y axis was applied to the sensor, and the change $\Delta f$ of the resonance frequency of the sensor was analyzed. **Fig. 4** shows a relationship between $F$ and $\Delta f/f_0$. Here, $f_0$ is the resonance frequency. The change rate $\Delta f/f_0$ in the case of $F$=1N, that is, the sensor sensitivity is also listed in **Table Ⅱ**. The sensors of types, (c), (a) and (e), are the high-sensitivity structures.

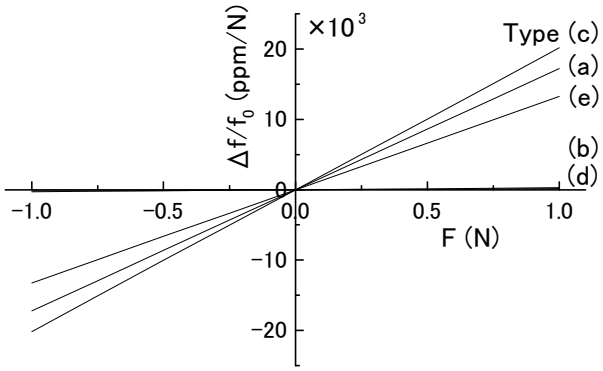


Fig. 4 Calculated characteristics of $F$–$\Delta f/f_0$ of force sensor.

## 4. Conclusions

The sensitivity of the frequency-change-type force sensor was analyzed using the finite-element method. The sensors of types, (c), (a) and (e), are the high-sensitivity structures and the displacement ratios at both ends of types (a) and (e) are less than $10^{-3}$. As a result, the sensors of types (a) and (e) can be used because of high-sensitivity and small displacements. From the standpoint of realizing a MEMS sensor, the sensor of type (a) is preferable.


### Acknowledgments

The work was partially supported by a Grant-in-Aid for Scientific Research (No. 19560047) from the Ministry of Education, Culture, Sports, Science, and Technology, Japan.


### References


1) L. Weisbond: US Patent 4,479,385 (1984).
2) S. Sugawara, et al.: Jpn. J. Appl. Phys., **41** (2002) 3433.
3) J. Takahashi, et al.: Jpn. J. Appl. Phys., **42** (2003) 3124.
4) J. Takahashi, et al.: Jpn. J. Appl. Phys., **43** (2004) 3035.
5) S. Sugawara, et al.: Jpn. J. Appl. Phys., **46** (2007) 4652.
6) S. Sugawara, et al.: Jpn. J. Appl. Phys., **47** (2008) 4048.


Table Ⅱ Calculated characteristics of force sensor.

| Type | Resonance frequency | | Sensitivity | Displacement ratio at base center | | | Displacement ratio at base edge | | |
|---|---|---|---|---|---|---|---|---|---|
| | $f_0$(Hz) | Δf(Hz/N) | Δf/f(ppm/N) | $u_x/u_{x0}\times10^{-3}$ | $u_y/u_{x0}\times10^{-3}$ | $u_z/u_{x0}\times10^{-3}$ | $u_x/u_{x0}\times10^{-3}$ | $u_y/u_{x0}\times10^{-3}$ | $u_z/u_{x0}\times10^{-3}$ |
| (a) | 1,707 | 29.4 | 17,223 | 0 | 0 | −0.344 | 0 | 0 | −0.704 |
| (b) | 14,997 | 4.2 | 279 | 0.884 | 0 | 0 | 0.884 | 8.392 | 0 |
| (c) | 1,870 | 37.7 | 20,194 | 0.039 | 0 | 0 | 0.039 | 4.744 | 0 |
| (d) | 14,481 | 2.5 | 172 | 0 | −6.825 | 0 | 0.346 | −6.825 | 0 |
| (e) | 1,789 | 23.8 | 13,280 | 0 | −0.218 | 0 | 0 | −0.218 | 0 |

1P4-8

Proceedings of Symposium on Ultrasonic Electronics, Vol. 29 (2008) pp. 109-110
11-13 November, 2008

# Characterization of Electrical Probe for Measuring Induced Charge on Surface of Piezoelectric Vibrator
# 圧電振動子表面誘起電荷測定用探針の量的評価

Shigetaka Kaga[1†] and Morio Onoe[2]
([1]Nihon Denpa Kogyo Co. Ltd.; [2]Professor Emeritus, University of Tokyo)
加賀重隆[1†]，尾上守夫[2]　([1]日本電波工業株式会社；　[2]東京大学名誉教授)

## 1. Introduction

Electrical probe method developed by Fukuyo is an excellent tool to identify various vibration modes of a piezoelectric vibrator. [1, 2] Piezoelectrically induced charge of a mode is picked up by a small needle probe embeded in the lower electrode as shown in **Fig. 1**. Mechanical scanning of the vibrator by an X-Y stage allowed to obtain a distribution of induced charge over the surface. Fukuyo measured only the amplitude of induced charge. Watanabe, et al. [3, 4] introduced a network analyzer, which allowed the measurement of phase as well as amplitude and the scanning of frequency. Their works, however, were limited to qualitative observation of distribution pattern.

This paper presents more quantitative characterization of a probe. Impedance of a probe is kept as low as possible, so that the probe is accounted to be a part of grounded lower electrode with litttle disturbance of surrounding electrical field. Hence the input to the network analyzer is essentially proportional to the current flowing the probe. It consists of a desired piezoelectrically induced part and an undesired part caused mainly by stray capacitances. The latter has to be subtracted from the observed value. On a circle diagram (vector) plot as a function of frequency, the former part at a resonance is essentially a circle, whereas the latter part is essentially constant, which we call here "reference origin". The reference origin is a slow varying function of frequency. Watanabe, et al. determined a reference orgin at each resonance in the following manner. First scan the frequency in a wide range, second remove parts of observed values corresponding to resonannces, third approximate remaining values by a polynomial function of frequency and finally calculte an estimated value of reference origin at a particular resonant frequency. [4]

The present paper shows that a reference origin can be directly determined from observed values obtained by a frequency scanning in a narrow range around a resonance itself.

A probe picks up surface charge not only at an infinitesimal point but also at surrounding points due to fringing in electrical field. Its characteristics can be exptressed by a spatial point spread function similar to an optical point spread function of a lens. Spacial distribution of surface charge of a main thickness-shear mode usually contains components of high spacial frequency due to effects of high overtones of contour modes. A spread function reduces the observed amplitude of these high spacial frequency components.

In previous papers, distributions of surface charge were analytically obtained and compaired with experiments. A good agreement between analyses and experiments was obtained, when a spread function is taking into an account. [5, 6, 7]

This paper presents relationships between a spread function and geometrical configurations of a probe.

## 2. Estimation of reference origin

Movements of a mechanical stage is slow in time. Hence a frequency scanning in a narrow range can be completed at each point of mechanical scanning with no extra time. This allows to draw circle diagrams of several spurious modes with only one mechanical scan. The use of circle diagrams allows a sensitive detection of any irregularity during mechanical scan

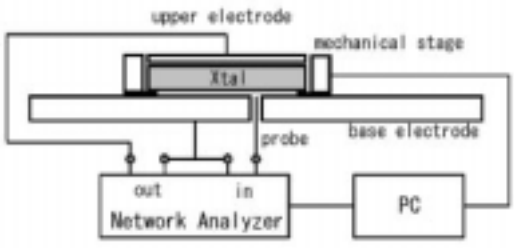


Fig. 1　Probe system to pick up induced charge

e-mail: [1] kagas@ndk.com; [2] m.onoe@ieee.org

Since reference origin is essentially constant during a narrow frequecy scanning, it contributes only to DC componet in Fourier domain. Hence a desired piezoelectrically induced part of a circle diagram can be obtained as follows: first apply Fourier trasform (FT) to circle diagram, second remove DC component and third apply inverse FT.

**Fig. 2** shows an experimental plot of circle diagrams of the main (1,1,0) mode of an AT-cut vibrator (x: 22.0 mm, y': 0.552 mm, z': 27.0 mm). The vertical axis is distance in mechanical scan along the x axis. Only a few circle digagrams are shown here in order to avoid congestion. It can be seen that their reference origins coincide with each other. In terms of DC component of FT, standard deiation of their spread is 1 %.

## 3. Point spread function

Point spread functions are experimentally evaluated for several combinations of the diameter of needle, the diameter of embedding hole and gap between the surface of a vibrator and needle point.

**Fig. 3** is an example showing the amplitude ratio between the main component and a high spatial frequency component as a function of the diameter of embedding hole. The diameter of needle is kept to be a constant of 0.3 mm. The larger the hole diameter, the broader the point spread function. Experimental observations agree with FEM analysis of electrostatic field around the probe by Dr. Y. Watanabe of Ricoh. [8)]

## 4. Conclusion

Characteristics of electrical probe for measuring piezoelectrically induced charge on the surface of a vibrator quantitatively evaluated.

First a new method to estimate reference origin of circle diagram is presented.

Second effects of geometrical configuration of a probe on its point spread function are discussed.


## Acknowledgment

The authors thank Mr. Okazaki of Nihon Dempa Kogyo Co. for his constant support and encouragement and Dr. Y. Watanabe of Ricoh Co., for his FEM analysis of electrostatic field around the probe.


## References


1. H. Fukuyo: Bull. Tokyo Inst. Tech., series A (1955) no. 1.
2. I. Koga and H. Fukuyo: Jour. Inst. Comm. Eng. 36 (1953) 59. (in Japanese)
3. Ya. Watanabe, et al.: Proc. Ultrasonics Symp., (1993) 571.
4. Ya. Watanabe, et al.: Trans. Inst. Comm. Eng. J77-A, (1994) 285. (in Japanese)
5. R. D. Miundlin：Quart. Appl. Math. **19** (1961) 51.
6. R. D. Miundlin and D. C. Gazis: 4 th US Nat. Congress Appl, Mech. (1962) 305.
7. M.Onoe and S. Kaga: Proc. Frequency Control Symp. (2008) .
8. Yo. Watanabe: Ricoh Co. Ltd., private communication.


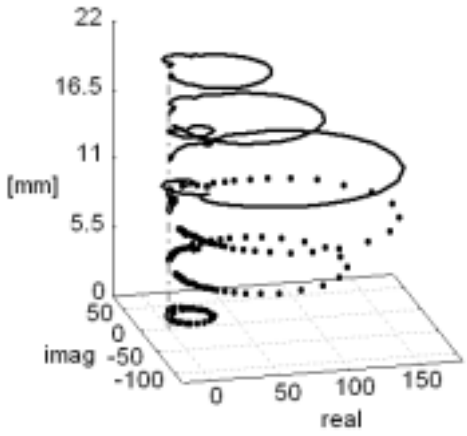


Fig. 2 Circle diagrams of the main mode.

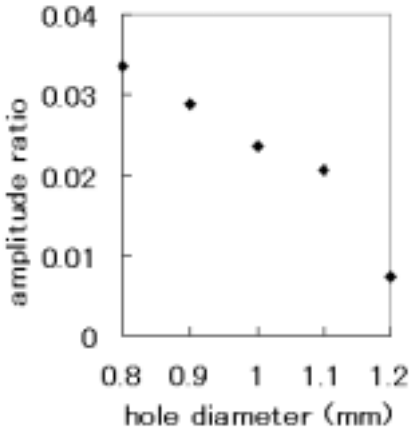


Fig. 3 Effect of hole diameter on point spread function

Proceedings of Symposium on Ultrasonic Electronics, Vol. 29 (2008) pp. 111-112
11-13 November, 2008

# Pure-shear mode BAW resonator consisting of (11$\bar{2}$0) textured AlN films

(11$\bar{2}$0)配向 AlN 薄膜を用いた純横波モード共振子

Takahiko Yanagitani [1†] and Masato Kiuchi [2] ([1] Nagoya Institute of Technology, [2] National Institute of Advanced Industrial Science and Technology)
柳谷隆彦 [1‡]，木内正人 [2] ([1] 名古屋工業大学; [2] 産業技術総合研究所）

## 1. Introduction

(0001) textured hexagonal films such as ZnO and AlN films have been widely used for longitudinal wave or Rayleigh wave mode piezoelectric devices. We have previously shown that (11$\bar{2}$0) textured ZnO films can be formed using various ion beam asisted deposition technique [1-3]. This film can be used for pure-shear mode FBAR [4] or SH-SAW devices [5]. On the other hand, (11$\bar{2}$0) textured AlN films have a number of potential advantages compared to the ZnO films:

- High chemical stability and resistance. This is important for sensor application
- Low intrinsic mechanical loss. This result in high Q resonator.
- Low temperature coefficient of elastic constant.
- High electrical breakdown strength, High power operation.
- High heat conductivty. This realize high power operation.
- High acoustic velocity, High frequency operation

Takada et al. have reported that $H_2$ gas introduction during deposition induces (11$\bar{2}$0) texture formation in a RF magnetron sputtering [6]. However, in-plane crystalline orientation, which is essential for shear wave excitation, have not been achieved. From our previous study on the ZnO film, it is known that ion bombardment during deposion induces preferential (11$\bar{2}$0) or (10$\bar{1}$0) texture formation. This is caused by an crystalline anisotropy of sputtering yield (difference of damage tolerance for ion bombardment among crystal planes) [2]. We considered that the same holds for AlN which have same wurtzite structure as ZnO. In this study, we then tried to fabricate (11$\bar{2}$0) AlN film using ion beam sputtering technique [3]. Crystalline orientation and piezoelectric properties of the film have been also reported.

---

yana@nitech.ac.jp

## 2. AlN film deposition

As shown in **Fig.1**, ion beam sputtering deposition system with single ion gun was used for AlN film deposition. This ion gun plays two roles, sputtering nitrided Al metal target and bombarding the substrate surface. Nitrogen ion beam with 3 keV was irradiated normal to the target surface and parallel to the substrate surface simultaneously during the deposition. A gas pressure of 0.02 Pa , and a nitrogen gas flow of 10 ccm were set during the deposition. AlN films were deposited on the two types of substrates: silica glass substrate (sample A) and Al electrode film/silica glass structured substrate (sample B). Substrate temperatures during the deposition of sample A and B were around 160 ºC and 340 ºC, respectively.

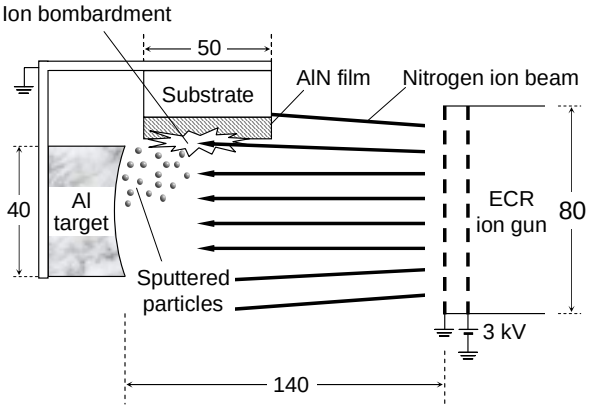


Fig. 1 Ion beam sputtering deposition system with single ion gun.

## 3. Crystalline orientation

**Figure. 2** show the XRD patterns of the sample A and B. (10$\bar{1}$0) and (11$\bar{2}$0) peaks were observed. (0002) peak was not observed in the both sample. Discrepancies between the experimental and expected (JCPDS card) peak position are probably caused by internal stress in the films. FWHM values of the (11$\bar{2}$0) $\omega$-scan rocking curve were found to be 4.6º. **Figure 3** shows the (11$\bar{2}$2) pole figure of the sample A. FWHM values of $\phi$-scan profile curve in (11$\bar{2}$2) pole of the film were

found to be 23º. These results show high in-plane and out-of-plane $(11\bar{2}0)$ preferred orientation.

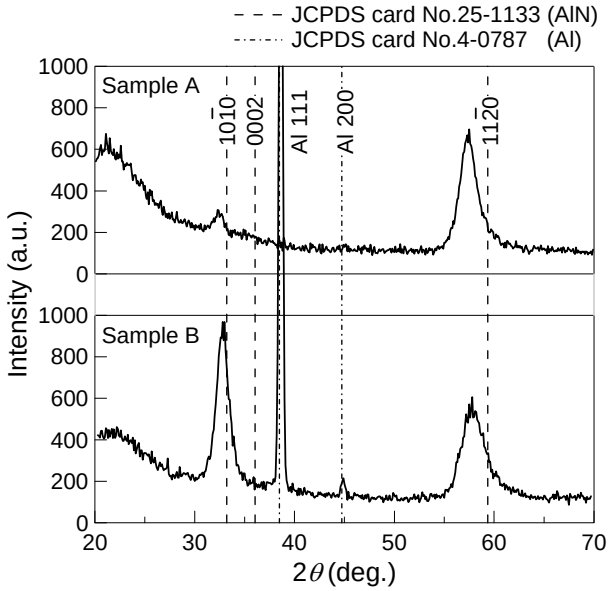


Fig. 2 XRD patterns of sample A (AlN/Silica glass substrate) and B (AlN/Al/Silica glass substrate)

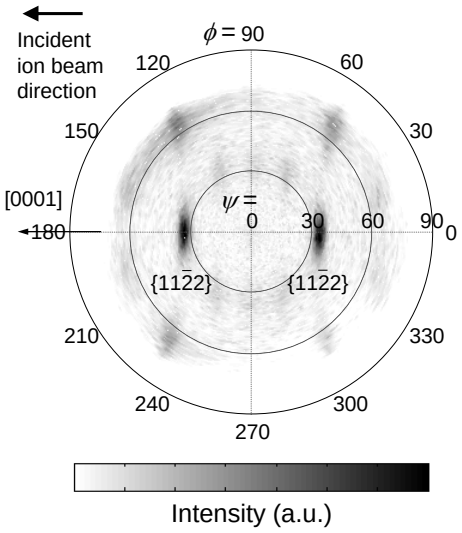


Fig. 3 $(11\bar{2}2)$ pole figure of $(11\bar{2}0)$ textured AlN film (sample A). The arrows indicate the [0001] direction in the substrate plane and the incident ion beam direction.

## 4. Piezoelectric properties

A Cu film was then evaporated on the sample B as a top electrode of the HBAR. **Figure 4** shows the impulse response of the resonator, which was obtained by taking the inverse Fourier transform of the reflection coefficient $S_{11}$. Shear wave echo train reflected from the bottom substrate surface and the top film surface was clearly observed without any excitation of longitudinal waves.

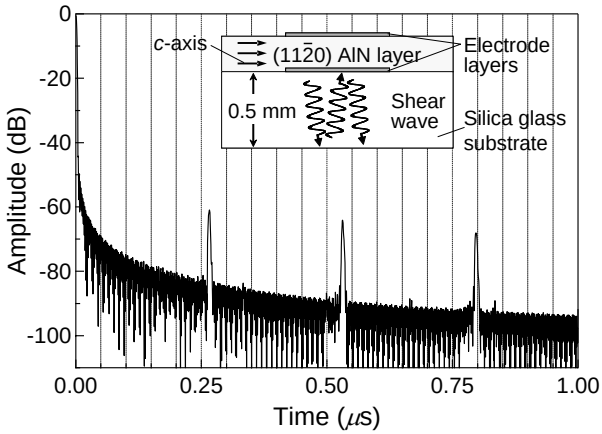


Fig. 4 Schematic diagram of pure thickness shear mode HBAR and impulse response of the resonator. Longitudinal and shear waves propagate in the 0.5-mm-thick silica glass substrate at respective velocities of 3770 m/s and 5960 m/s so that their echoes should be observed at 168 ns and 265 ns, respectively.

## 5. Conclusions

This presentation reports the first synthesis of the in-plane oriented $(11\bar{2}0)$ AlN film on a non-crystalline substrate. Pure-shear wave excitation was clearly observed in the thin film HBAR structure. This film would be suitable for use in shear mode FBAR sensor or SH-SAW sensors for measuring liquid. In addtion, this film can be faricated on various substrate and curved surface.

## Acknowledgment

The authors thank Professor Yoshaki Watanabe and Professor Mami Matsukawa of Doshisha University for their valuable collaboration in measuring the piezoelectric properties of samples.

## References

1. T. Yanagitani, M. Kiuchi, M. Matsukawa, and Y. Watanabe: J. Appl. Phys., **102** (2007) 024110.
2. T. Yanagitani and M. Kiuchi: J. Appl. Phys., **102** (2007) 044115.
3. T. Yanagitani and M. Kiuchi: Jpn. J. Appl. Phys., **46** (2007) L1167.
4. T. Yanagitani, M. Kiuchi, M. Matsukawa and Y. Watanabe: IEEE Trans. Ultrason., Ferroelect., Freq. Contr. **54** (2007) 1680.
5. A. Tanaka, T. Yanagitani, M. Matsukawa, and Y. Watanabe: IEEE Trans. Ultrason., Ferroelect., Freq. Contr. *in press*
6. F. Takeda, T. Mori, and T. Takahashi: Jpn. J. Appl. Phys., **20** (1981) L169.

1P4-10

Proceedings of Symposium on Ultrasonic Electronics, Vol. 29 (2008) pp. 113-114
11-13 November, 2008

# Development of the Ultrasonic Information Transmission System using One-Chip Microcomputer for Wearable Devices

ワンチップマイコンを用いたウェアラブルデバイス用超音波通信システムの開発

Shin-nosuke Suzuki[1‡], Manabu Ishihara[1], Yukio Kobayashi[1], Tamotsu Katane[2], Osami Saito[2] and Kazuto Kobayashi[3] ([1]Dept. of Elec. and Comp., Oyama N. C. T; [2]Faculty of Eng., Chiba Univ. ; [3]Honda Electronics co., ltd.)

鈴木真ノ介[1‡]，石原学[1]，小林幸夫[1]，片根保[2]，斉藤制海[2]，小林和人[3]（[1]小山高専 電気情報; [2]千葉大 工；[3](株)本多電子）

## 1. Introduction

In these days, our daily life is being “Ubiquitous society” that we can use computers at “any time” and “any place”. One of the resason is spread of the cellular phones. They are installed with many functions, such as music player, digital camera, IC card and electric money. It has evolved from an only mobile phone to a small computer. In the near future, it will been mounted into wearing instrument like a wrist watch. The authors define it “Wearable Device”.

We have been studied about the digital information transmission using modulated ultrasonic[1)-2)] and applied it to the communication of the wearable device. In our previous study, the transmission speed of 115.2 kbps is obtained in the prototype transmitter, which is using one-chip microcomputer and assumed the transmission from the wearable device to the data reader-writer[2)].

In this time, we have improved the prototype. The inprovement points are that adding the receiver function and higher transmissoin speed, although using one piece of same microcomputer. We have carried out the communication experiment by new prototype and obtained the speed of about 2 times higher than previous model (250 kbps).

## 2. System configuration

**Figure 1** shows the configuration of the proposed system. The system transmits interactive information using a single path with half-duplex communication through the human body. The path is consisting of a pair of piezoelectric ceramic oscillators. One oscillator is mounted in the wearable device (WD), and another is in the reader-writer (R/W). The communication method is as follows. When the user touches the R/W with the finger or the palm of the hand, the digital information in the each side is transferred bi-directionally. Since the WD can also read and write the data, the communication is performed from one WD to another with the shake hands. It is assumed that the WD has a solar and a rechargeable battery and is provided the energy from them.

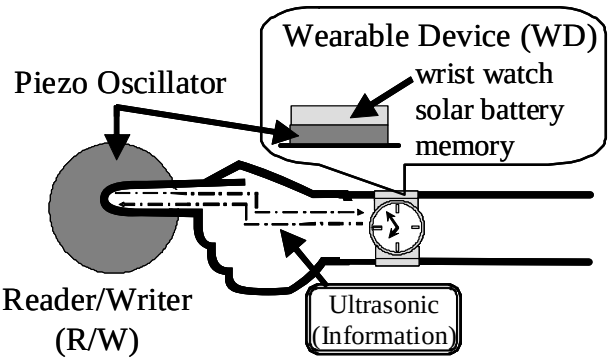


Fig. 1 Communication System for Wearable Device.

The system prevents from the leaking of the wearing information because ultrasonic has a large attenuation in the air. In addition, so the WD can store several data and include the IC card function that the user get rid of the botheration of taking out the card from the pocket. Furthermore, the system is effective for the handicap people who have visual impairments and are using an invalid wheel chairs. So they wear the WD and hold hands with the third person who touches the R/W, that the communication is enable.

## 3. The improved prototype using microcomputer

**Figure 2** shows the circuit diagram of the improved prototype. The one-chip microcomputer “PIC” (Microchip Technology Inc., PIC16F84A), is also used previous prototype. It can transmit and receive the information in order to change the mode of PIC, and communicate between two prototypes interactively. In this time, They deal with the 8 bit signel assumed half size character information. The information transmission of the system is according to the amplitude shift keying modulation (ASK) and the detail is as follows.

E-mail: shin-s@oyama-ct.ac.jp

The PIC in the one prototype output 0 V from the terminal RB2 for changing the mode “send”. According to the digital information that stored the memory, the power source voltage is switched. As a result, the modulated signal is produced. The wave form is like impluse signal, because of battery power saving. The signal is input the piezo oscillator and the modulated ultrasonic wave is transmitted to receiver side through the human body. The PIC in the another prototype output 5 V from RB2 for changing the mode “receive”. The receiver side oscillator transforms the received ultrasonic into electrical signal. The signal is demodulated thorough the filter, amplifier and comparator. The demodulated signal input RB0 and the PIC output the results to RA0~3 (lower 4 bit) and RB4~7 (upper 4 bit). The received condition is confermed from the LEDs that are connected the terminals,.

The piezoelectric ceramic oscillators configuration in this prototype is as follows: Pb (Zr, Ti) $O_3$: PZT, Resonance frequency 1 MHz, Diameter 20 mm, thickness 2 mm.

## 4. Experimental Results

Using two sets of the prototype, the experiment assumed the WD-WD communication is carried out. It is experimented in a person and one PZT set the wrist and another PZT is touched on the nearest forefinger. The digtal information is the several kind of 8bit signal, such as “01010101”. After the adjustment of the demodulator, signals are transmitted and the proper LEDs are always lighted. Therefore, the transmission is success. Then, the transmission speed is obtained corresponding 250 kbps. The waveform sample is shown in **Fig. 3**. The signal can be received not only between a wrist and a finger, but also all over the point in the person.

However, the error rate cannot be mesured, because the same series signal is transmitted and the received condition is observed only LEDs in this experiment. For improving the communication accuracy, mesuring the error rate is absolutly neccesary. Next step, the constructing the mesuring system is need , for example, the personal computer is utilized in the recever side..

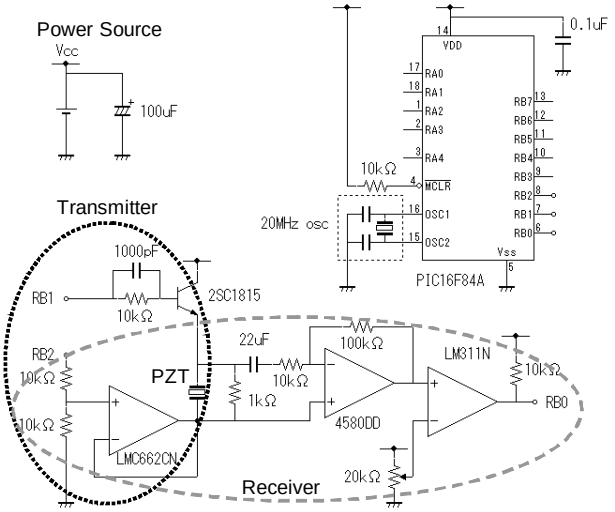


Fig. 2 Transmitter and Receiver Circuit.

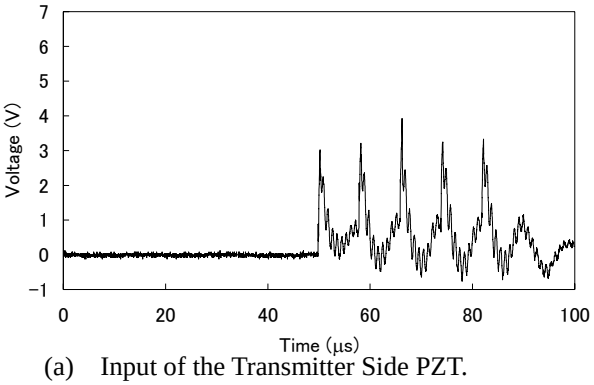


(a) Input of the Transmitter Side PZT.

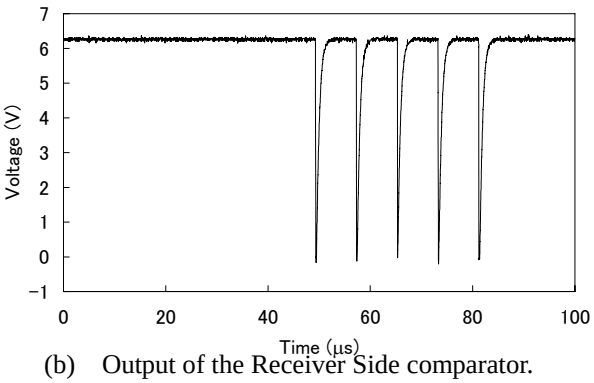


(b) Output of the Receiver Side comparator.

Fig.3. Waveforms on the Prototype Experiment. (250kbps, “01010101”, Finger - Wrist)

## 5. Conclusions

In this paper, we proposed the new prototye with transmitter and receiver using PIC. It can transmit 8 bit signal at the speed of 250 kbps between the two arbitrary point in a human body. Next step, we plan to construct the mesuring system introducing personal computer. In addition, we will try to communicate several electrical files in this system.


## Acknowledgment

This work was supported by Grant-in-Aid for scientific research from the Ministry of Education, Culture, Sports, Science and Technology of Japan (No. 19760241)


## References


1) S. Suzuki, M. Ishihara, T. Katane, O. Saito and K. Kobayashi: Jpn. J. Appl. Phys. **45** (2006) 4550.

2) S. Suzuki, M. Ishihara, T. Katane, O. Saito and K. Kobayashi: USE2007 (2007) 1-10P-54

1P4-11

Proceedings of Symposium on Ultrasonic Electronics, Vol. 29 (2008) pp. 115-116
11-13 November, 2008

# Mechanical Transient Analysis of Breaking Contact in a Magnetic Relay

電磁リレーにおける開離接点の動的挙動の解析

Nobuo Takatsu[1†], Noboru Wakatsuki[1] and Masahiro Oikawa[1] ([1] School of Sci. Eng., Ishimomaki Senshu Univ.)
高津　宣夫[1†]，若月昇[1]，及川　雅弘[1]　([1]石巻専修大 理工)

## 1. Introduction

Breaking arc as well as bounce in a magnetic relay are difficult problems that have not been solved. There are many reports on studies of arc where opening speed of contact is said to be one of the most important parameters and conventional designs aim to increase opening velocity to avoid arc. Nevertheless, there are few reports on estimating the transient motion of contacts during a break operation of magnetic relay. One of the authors developed a device named "Transient Current Switch (TCS)", which can suppress break arcing[1] and using it he has started building a new model of an opening contact. In this study, a conventional hinged magnetic relay is modeled by a lumped parameter system of 2-DOF and its dynamic characteristics especially at eary stage of opening are analyzed numerically.

## 2. Model of hinged magnetic relay

A hinged magnetic power relay, Fuji Electric HH62P, is modeled by lumped parameters as shown in **Fig.1 (a)**. The movable contact assembly can be seen as a rotating rigid bar (iron armature) with a pair of contacts and leaf springs installed at one end and a return spring with stiffness $k_r$ at the other end. The moment of inertia $J_a$ of the armature around support O is represented with an equivalent mass $m_a$. The movable contact and leaf spring is assumed to be a cantilever with an equivalent mass $m$ of the contact at its free end. Neglecting higher modes of the cantilever, its stiffness $k$ can be defined from deflection under a concentrated load at the free end. Then $m$ is estimated from the natural frequency $\omega_n$ of the system, which can be determined experimentally. Both a- and b- fixed contacts are modeled by contact stiffnesses $k_{ca}$ and $k_{cb}$, respectively, including related movable contact. Assuming the foregoing model, equations of motion for $m_a$ and $m$ are derived. $G$ and $G_s$ are gaps of contact and armature, respectively.

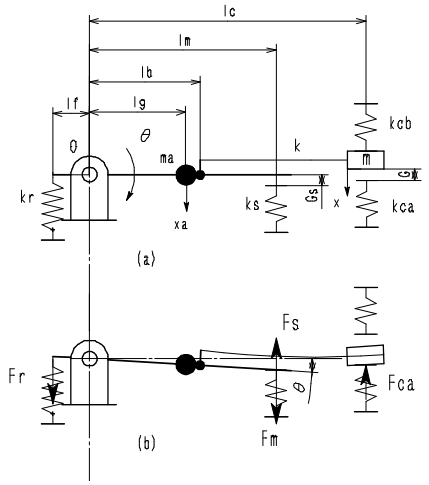


Fig. 1 Lumped parameter model of a hinged magnetic relay, (a) free state, (b) make state

## 3. Modeling contact stiffness

A stiffness model of contact is required in the foregoing model. Mechanical modeling of a relay contact with a rough surface is not a new problem, but has not been well established. Multi-contact model [2] seems to be preferable, but estimation of contact stiffness for practical application has not been verified. Hertz contact between two identical virtual spheres with radius $R$ is assumed in this study. $R$ is estimated as follows: So-called Holm's radius $\alpha$ of known material (Ag alloy) is estimated from measured value of contact resistance under known contact force. Then $R$ can be estimated if $\alpha$ is assumed to be equal to Hertz's contact radius [3]. For simplicity, a linear contact stiffness $k_{ca} = 250$ N/mm is introduced by linearizing the nonlinear relation between the force and relative approach of the two spheres in the range of actual contact force.

## 4. Analysis of break operation

Equations of motion were solved numerically under the initial state of "make" shown in Fig.1 (b), where both gaps are fully closed, by removing magnetic force $F_m$. Velocities were assumed to be zero. All electrical effects were ignored. Main constants of the relay are shown in **Table I**.

Table I Constants of the target relay

| |
|---|
| $k = 0.77 \times 10^3$ N/m |
| $m = 0.19 \times 10^3$ kg |
| $J_a = 72.3 \times 10^3$ kg mm$^2$ |
| $G = 0.6$mm, $G_s = 0.45$mm |
| $k_r = 0.787$N/mm |

**Fig.2** show the behavior of moving contact where all variables are shown in non-dimensional variables. The contact remains at rest as shown in Fig.2 (a) and (b) till the elastic deformation at the contact disappears (Fig.2(c)). Then contact is accelerated rapidly at almost constant acceleration as shown in Fig.2 (b) because the variation of the restoring force at return spring is small. Fig.2 (d) shows repetitive bounce motion at b-contact after break.

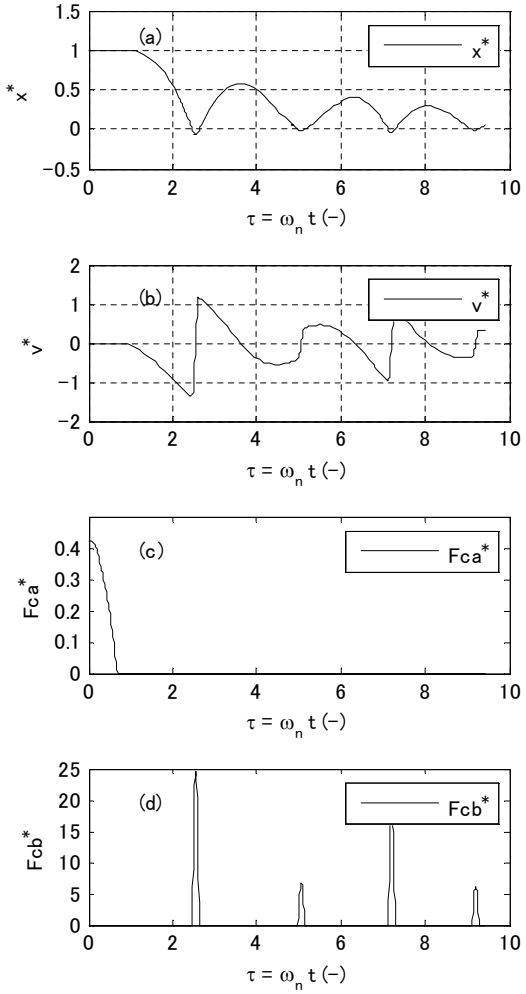


Fig.2 Time history of non-dimensional variables of contact. (a) Displacement $x^* = x/G$ . (b) Velocity $v^* = v/(\omega_n G)$ . (c) Contact force $F_{ca}^* = F_{ca}/(kG)$ . (d) Contact force $F_{cb}^* = F_{cb}/(kG)$ .

We are interested in the dynamic behavior of the contact at an early stage of break**. Fig.3** shows it in real values during one milli-second after the initiation of break. Displacement and velocity of the contact are displayed in (a) and (b) respectively by a magnified scale. Contact force plotted in (c) shows that elastic contact breaks at $t = 0.35$ ms. The value of displacement and velocity at that instant (indicated by a broken line) are 0.7 $\mu$ m and 5 mm/s, respectively. Fig.3 (d) shows contact resistance obtained from Holm's radius.

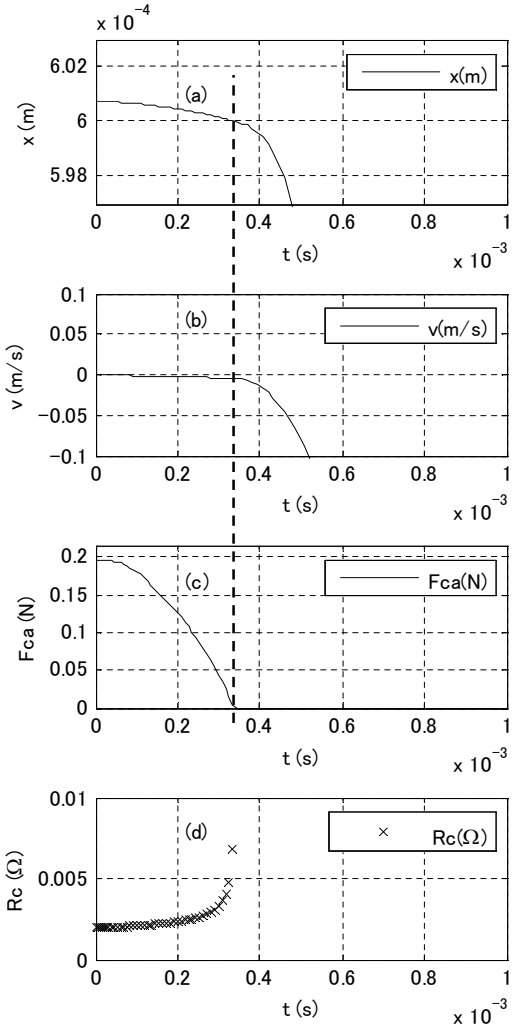


Fig.3 Behavior of the contact at early stage of break in real values. (a) Displacement $x$ . (b) Velocity $v$ . (c) Contact force $F_{ca}$ . (d) Contact resistance $R_c$ .

**Acknowledgment**
The authors express their great gratitude to Fuji Electric FA Components & Systems Co. Ltd. for relay samples.

**References**

1. Y. Yonezawa and N. Wakatsuki: IEICE Trans. Electron. E87-C (2004) 1324.
2. J. A. Greenwood and J. H. Tripp: Trans. ASME, J. Appl. Mech., March (1967) 153.
3. S. P. Timoshenko and J. N. Goodier: *Theory of Elasticity*, Third Edition (McGRAW-HILL KOGAKUSHA, 1970) p.409.

Proceedings of Symposium on Ultrasonic Electronics, Vol. 29 (2008) pp. 117-118
11-13 November, 2008

# Basic Study on Effect of Current Flow to Time-Reversal Communication

位相共役通信への流れの影響の基礎検討

Takuya Shimura[1], Yoshitaka Watanabe[1], Hiroshi Ochi[1], and Takehito Hattori[2]
([1] Advanced Marine Technology Research Program, JAMSTEC;
[2] Nippon Marine Enterprises, LTD.)
志村拓也[1]，渡邊佳孝[1]，越智寛[1]，服部岳人[2]
（[1] 海洋研究開発機構, 先端技術研究プログラム; [2] 日本海洋事業）

## 1. Introduction

The researches on uderwater acoustic technologies are assigned to our group in Japan Agency for Marine-Earth Science and Technology (JAMSTEC). Time reveresal communication has a possibility to realize long horizontal communication by utilizing multipath signals. We have studied its basic focusing property [1-5] and executed at-sea experiments [6-9].

It is presupposed that the reciprocity of the media is retained for time reversal process. So, it is necessary to invesigate the effects of non-reciprocal disturbances due to, for example, a moving source-receiver or current flow. The effect of the source-receiver movement has been researched in the previous works [4, 5]. In this paper, the current flow-induced effect are discussed through simulations.

## 2. Propagation in moving media

The numerical solution of a wide-angle parabolic equation (WAPE) for moving media are developed by Godin [10] and Mikhin [11]. In the coordinate as shown in Fig. 1, its parabolic equation takes the following form

$$\frac{\partial}{\partial x}\left[\frac{1}{\sqrt{\rho\beta^3}}\left(1+\gamma\hat{X}\right)\psi\right] = \frac{2j\alpha k_0}{\sqrt{\rho\beta^3}}\hat{X}\psi + \frac{j}{2k_0\sqrt{\rho\beta^3}}\left(1+\gamma\hat{X}\right)^{-1}\beta B, \quad (1)$$

where $\rho(x,z)$ is the medium density, $\beta$ is defined as $\beta = 1 - u/c_0$, $c_0$ is a reference sound speed, and $u(x, z)$ is the horizontal flow component. The second order differenctial operator $\hat{X}$ is given by

$$\hat{X} = \frac{\beta}{k_0^2}\left[\rho\beta^2\frac{\partial}{\partial z}\left(\frac{1}{\rho\beta^2}\frac{\partial}{\partial z}\right) + k^2\beta^2 - k_0^2\right] \quad (2)$$

where $k_0 = \omega/c_0$ and $k = \omega/c$ are the representative and local wave number, repectively. The horizontal flow velocity affects sound propagation through $\beta$ and the vertical flow effect is indirectly included through the derivatives of $\rho$, $c$, and $\beta$, although the vertical flow is not considered directly.

## 3. Simulation conditions

Simulatoins under current flow in shallow water using the mehod as described in the previous section are executed. The environmental conditions are illustrated in Fig. 1. The flow velocity profiles (FVPs), sound velocity profile (SVP), and the time reversal array (TRA) configurations are shown in Fig. 2.

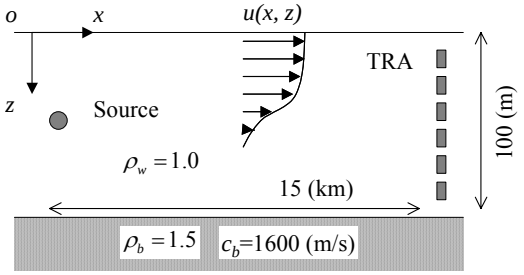


Fig. 1 Simulation condition.

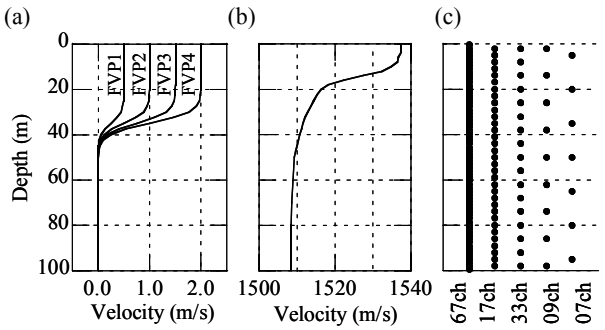


Fig. 2 (a) FVPs (b) SVP (c) TRA configurations.

shimurat@jamstec.go.jp

## 4. Simulation results

Figure 3 is the demodulation result of binary phase shift keying (BPSK) in the case of 9 channel TRA. The titles on the left graphs, TR, indicate using only time reversal focusing effect, while the titles, TR+AE, on the right graphs indicate using the proposed method of combining time reversal and adaptive equalizer [2-9]. In the case of TR, it is observed that the performance becomes degraded and demodulated symbols get indistinguishable as the flow velocity is faster. In the meantime, in the case of TR+AE, such flow-induced effect is compensated and demodulation can be achieved. In these results, the phase rotation due to current flow is time-invariant not like in communication with a moving source-receiver [4, 5].

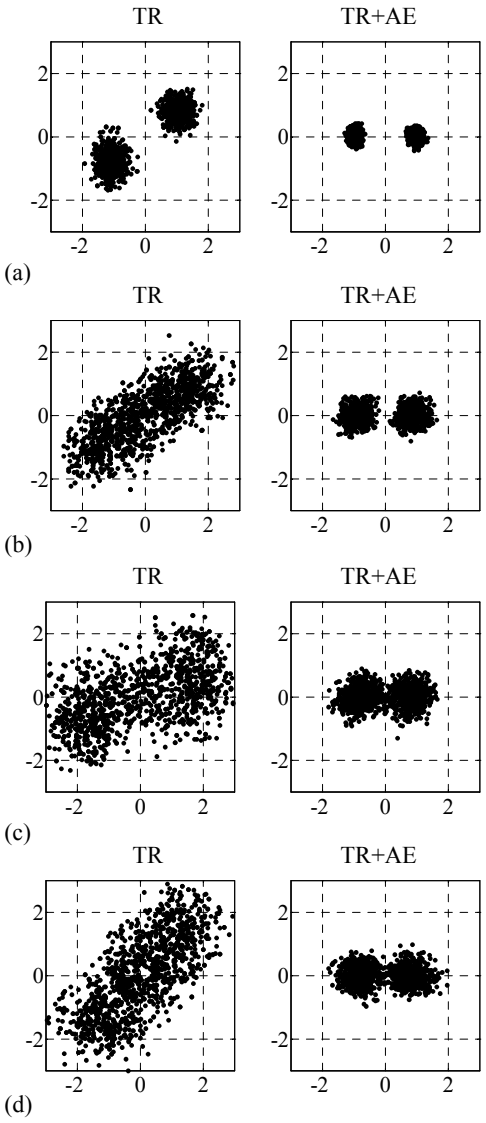


Fig. 3 demodulation results in the case of 9 channel TRA under the flow velocity
(a) FVP1, (b) FVP2, (c) FVP3, and (d) FVP4.

The bit error rates (BERs) and output SNRs of the proposed method are plotted in Fig. 4, when TRA channel number is changed. In the case of each FVP, it is possible to achieve communication with no error with at least 17 channel TRA.

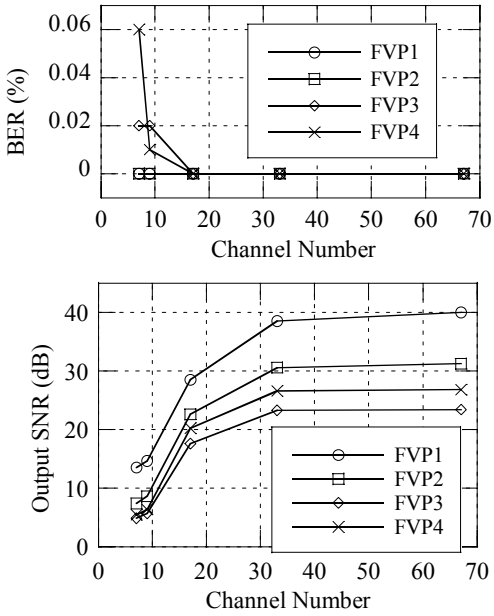


Fig. 4 BER and output SNR in case of TR+AE.

## 5. Summary

Simulatoins of time reversal communication considering current flow are executed. It is shown that the flow-induced effect can be compensated and communication can be achieved by the proposed method. Simulations with other various conditions will be carried out and at-sea experiments under current flow will be performed.

## References

1. T. Shimura: Acoust. Sci. Technol. **25** (2004) 364.
2. T. Shimura et al.: Jpn. J. Appl. Phys. **44** (2005) 4722.
3. T. Shimura et al.: Acoust. Sci. Technol. **26** (2005) 526.
4. T. Shimura et al.: Jpn. J. Appl. Phys. **45** (2006) 4847.
5. T. Shimura et al.: ECUA2006 (2006) 879.
6. T. Shimura et al.: Jpn. J. Appl. Phys. **46** (2007) 4956.
7. T. Shimura et al.: Jpn. J. Appl. Phys. **47** (2008) 4360.
8. T. Shimura et al.: Oceans/Techno Ocean 2008 (2008).
9. T. Shimura et al.: Acoustics'08 (2008) 699.
10. O. A. Godin: ICTCA '97 (1997) 329.
11. D. Mikhin: ECUA'98 (1998) 581.

Proceedings of Symposium on Ultrasonic Electronics, Vol. 29 (2008) pp. 119-120
11-13 November, 2008

# The Effect of the Number of Receiving Channels in Wideband Acoustic Communication at Deep Sea

深海域の広帯域音響通信における受信チャンネル数の影響について

Hiroshi Ochi[1†], Yoshitaka Watanabe[1], Takuya Shimura[1] and Takehito Hattori[2] ([1] Marine Technology Center, JAMSTEC; [2] Nippon Marine Enterprises Inc.)
越智寛[1†]，渡邊佳孝[1]，志村拓也[1]，服部岳人[2]　([1]海洋研究開発機構　海洋工学センター; [2]日本海洋事業)

## 1. Introduction

There are various research of underwater acoustic communication.[1,2)] Authors also are researching underwater acoustic communication, especially short range wideband acoustic communication.[3,4)] For controlling ROV by acoustic signal, it is required high update rate image transmission. Our goal is to develop a color image transmission system, which can transmit more than 1 color image per second. For this objective, the research is in progress based on sea experiment. Considering the operation response, transmission range is limited to approximately 500 m. We assume that the operator will accept transmission delay of less than 1 second in round trip. In consideration of this limitation and absorption loss, the carrier frequency was set to 80 kHz.
An acoustic data transmission experiment using 4-channel receiver was carried out at the depth of 1,000 m in November 2007. Received signals were recorded in each channel, and results of postprocessed demodulation were obtained. In this paper, it is described that characteristics of the demodulation with changing the number of channels.

## 2. Outline of the experiment

**Fig.1** shows geometry of the sea experiment. The transmitter was moored at the near bottom. The receiver was suspended from R/V "KAIYO" by armored coaxial cable. Parameters of transmitted signal are as follows. Carrier frequency is 80 kHz, band width is 40 kHz, and modulation method is quadrature phase shift keying (QPSK). Transmission rate is 80 kbps. For realizing such a wideband transmission, tilted toroidal beam wideband transducer[5)] is used. The receiver has 4 omni-directional hydrophones. And received signals are recorded in each channel. Demodulation processing is post-processed by software after recovering test equipments. Demodulator is composed of an adaptive multichannel decision feedback equalizer (M-DFE), a phase compensator and a JPEG image decompression unit. Least mean square (LMS) is selected as an adaptive algorithm.
The receiver position was shifted along with the line of 77º from vertical by controlling ship position and cable length. Relative received positions are shown in **Fig.2**. The x-y origin (0, 0) means the position of the transmitter. Because all of recorded data were same direction, there is no need for considering directivity pattern of the transducer.

## 3. Results and discussions

Typical channel response is shown in **Fig.3**. There are small multi-paths, which are bottom reflected wave.
The received data were recorded each 4 channels respectively, demodulation was processed with

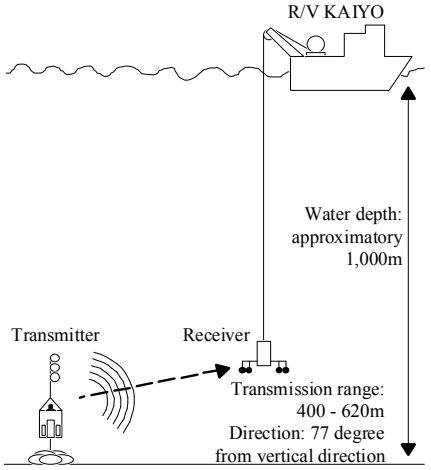


Fig.1　Geometry of the sea experiment.

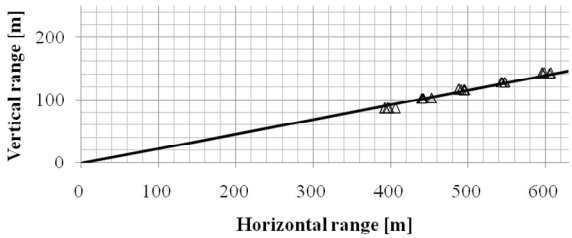


Fig.2　Relative position of the receiver. (0,0) as the transmitter position. △: relative position of the receiver. Solid line: 77º from vertical.

changing the number of channels for the same packet. And the total number of transmitted packet was 20. **Fig.4** shows performance of the demodulator. The x-axis shows average input SNR and the y-axis shows symbol error rate. In case of error free, its result is plotted as $10^{-5}$ of symbol error rate. The solid line is calculated value with additive white Gaussian noise (AWGN) channel. The result of a single-channel demodulation was approximately 3 dB worse than AWGN case. The result of two-channel demodulation was almost the same as AWGN case. When the number of channels become larger, the result of demodulation performance becomes better. Output SNR is defined as eq. (1), which shows convergence performance of the demodulator output.

$$\text{outputSNR} = 10\log\frac{E\left\{\left|d(n)\right|^2\right\}}{\frac{1}{N_d}\sum_{n=1}^{N_d}\left|d(n)-\hat{d}(n)\right|^2}, \quad (1)$$

where, $N_d$ is the number of symbols in one packet, $d(n)$ is the correct symbol value, $\hat{d}(n)$ is estimated value by M-DFE. **Fig.5** shows output SNR vs average input SNR characteristic. The result of the multi-channel demodulation shows a good characteristic than less number of receiving channel. When average input SNR is 8 dB, it can't demodulate in single channel demodulation. But in 4-channel demodulation, it still keep $10^{-4}$ order symbol error rate.

## 4. Conclusion

Wideband short range underwater acoustic data transmission experiment was carried out at 1,000 m depth area. Propagated data was recorded along with same direction, and 4 channels respectively. By changing the number of the channels to use for the demodulation, its characteristic was provided. When average input SNR is larger than 10 dB, the result of 4-channel demodulation was approximately 6 dB better than single channel case.

## References


1. M. Stojanovic: IEEE J. Oceanic Eng. **21** (1996) 125.
2. D. B. Kilfoyle and B. Baggeroer: IEEE J. Oceanic Eng. **25** (2000) 4.
3. H. Ochi, Y. Watanabe and T. Shimura: Jpn. J. Appl. Phys. **44** (2005) 4689.
4. H. Ochi, Y. Watanabe and T. Shimura: Proc. 8th ECUA (2006) 849.
5. H. Ochi and T. Fukuchi: Jpn. J. Appl. Phys. 46 (2007) 4961.


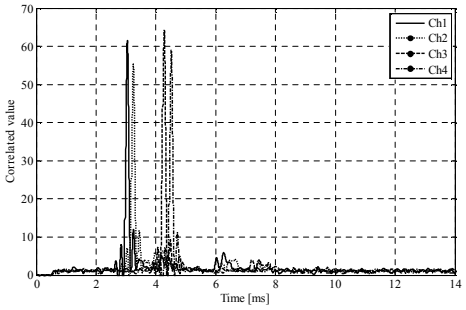


Fig.3 Typical channel response. (Slant range: 410 m)

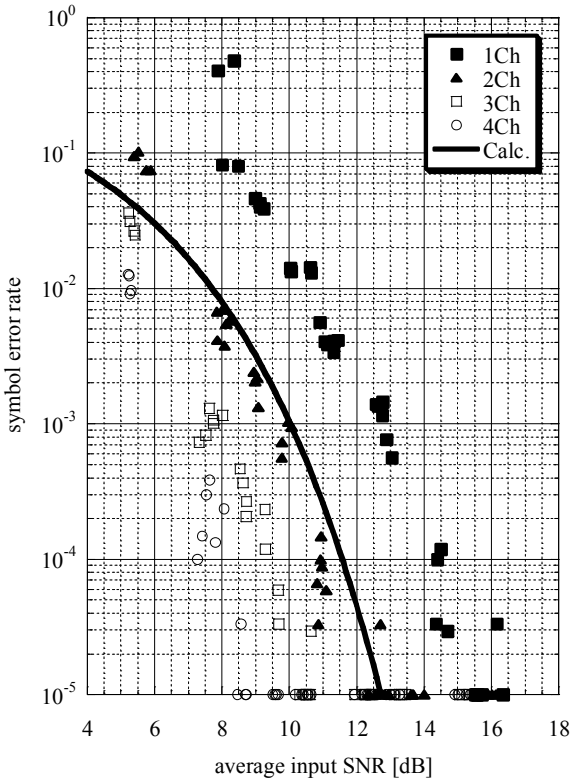


Fig.4 Symbol error rate vs average input SNR. (transmission rate: 80 kbps)

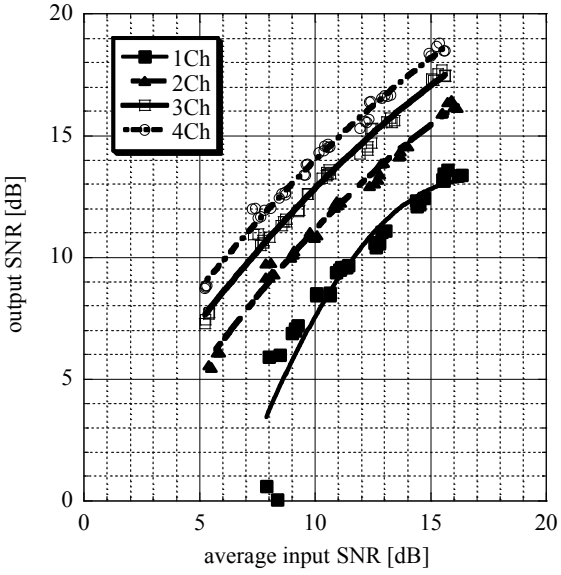


Fig.5 Output SNR vs average input SNR

Proceedings of Symposium on Ultrasonic Electronics, Vol. 29 (2008) pp. 121-122
11-13 November, 2008

# Temporal Coherence Variation for Sea Surface Fluctuation

Jihyun Park, Jong R. Yoon†, Kyongbeak Ryu and [1]Joung-Soo Park
(Pukyong National University, Korea; [1]Agency for Defense Development, Korea)

## 1. Introduction

Temporal coherence of acoustic signals in the ocean has an effect on the performance of underwater communication systems and it has been studied experimentally in the ocean [1-4]. In this paper, temporal coherence variation due to only the sea surface fluctuation is presented. By using directional source and with highly absorptive bottom, bottom scattering effect could be ignored. Volume scattering from such as biological scatters are also ignored.

## 2. Experimental conditions

**Figs. 1** and **2** show schematic diagram of experimental configuration and sound speed profiles derived from XBT casts over the period of 5 hours experiment, respectively. Water depth is about 170m. Wind speed is about 15~16 knots at 15.5m height from sea level. Surface wave direction to source to receiver direction is parallel in initial stage and 70 degree direction in final stage of 5 hrs experiment.

7kHz tone burst signals are transmitted from the source which consists of 21 elements to give directional beam. The length of the burst is variable from 1ms to 1s. The burst interval is also variable from 1s to 30s. The vertical line array of the receiver consists of 10 elements with 10.7cm spacing.

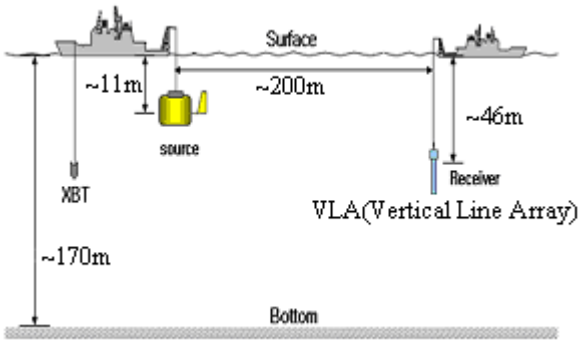


Fig.1 Schematic diagram of experimental configuration.

**Fig. 3** shows ray traces and time delays from source to receiver assuming a constant 1500m/s sound speed and 170m depth of water with mud bottom.

jryoon@pknu.ac.kr

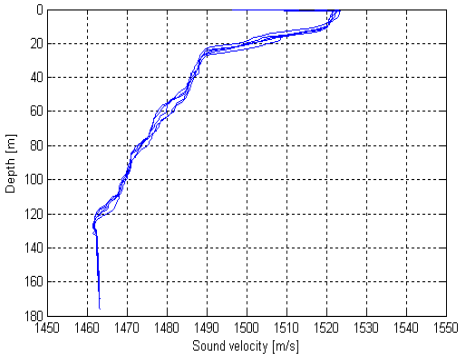


Fig. 2. Sound speed profiles derived from XBT casts over the period of 5 hours experiment.

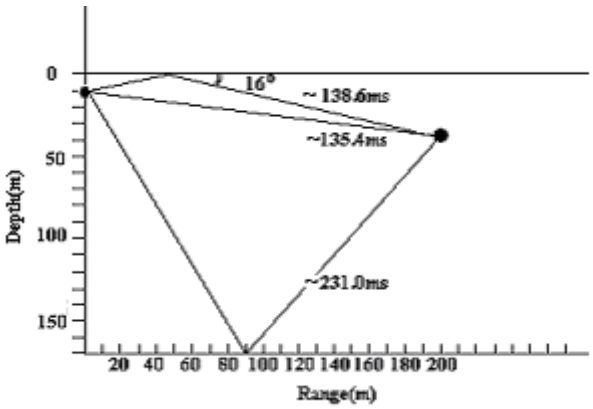


Fig. 3 Ray traces from source to receiver.

## 3. Temporal coherence

For this study, 2ms CW bursts whose bandwidth is about 1kHz, are transmitted at a temporal delay rate of 2s. **Figs. 4** and **5** show received signal samples in which the direct and the surface reflection paths are dominant paths and surface reflection paths are variant with temporal delay. The coherence between direct path signal $R_d(t)$ and surface reflection path signal $R_s(t)$ at each transmitted pulse, is defined in terms of the cross correlation function

$$C_{d,s}(\tau) = \sum_{k=-K}^{K} R_d(\tau) R_s(k+\tau) . \qquad (1)$$

The cross correlation function is then normalized to give a correlation coefficient

$$\rho_{d,s}(\tau) = C_{d,s}(\tau) / \sqrt{C_{d,d}(0) C_{s,s}(0)} \,. \qquad (2)$$

Temporal coherence is given by maximum value of the correlation coefficient $\left|\rho_{d,s}(\tau)\right|_{\max}$ . The temporal coherence as a function of temporal delay is examined for 150 delays of 5min. **Fig. 6** shows the mean coherence of all receivers as a function of temporal delay. Its mean for 150 delay of 5min is about 0.9.

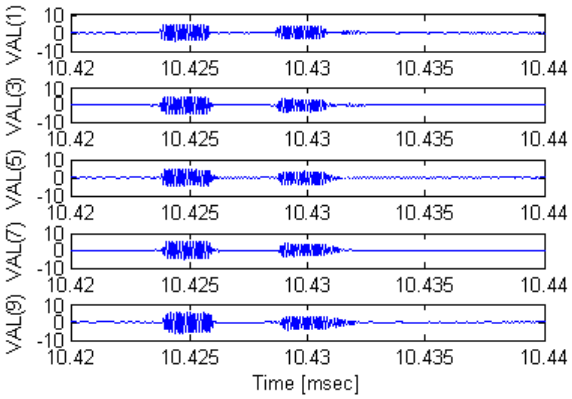


Fig. 4 Received signal samples of order number receivers of VLA.

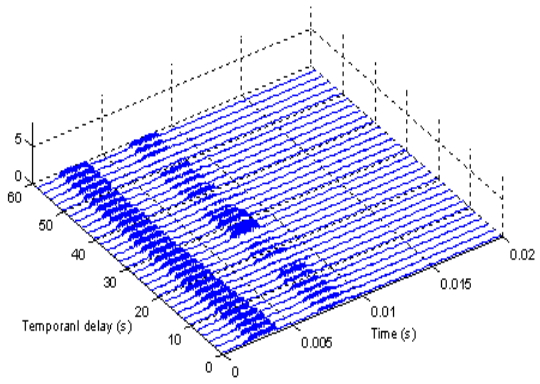


Fig. 5 Signal variation with temporal delay.

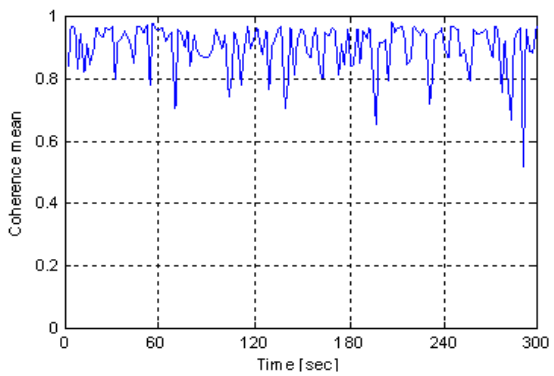


Figure 6. Mean coherence of all receivers with respect to temporal delay.

The fluctuation of the coherence with temporal delay will be consistent with sea surface fluctuation. Dominant wave height and frequency by Pierson-Moskowitz sea surface spectrum are 1.34m, and 0.177Hz for experimental wind speed about 15~16 knots at 15.5m above sea level. **Fig. 7** shows the spectrum of the mean coherence variation and its dominant frequency is well consistent with the sea surface dominant frequency of 0.177Hz.

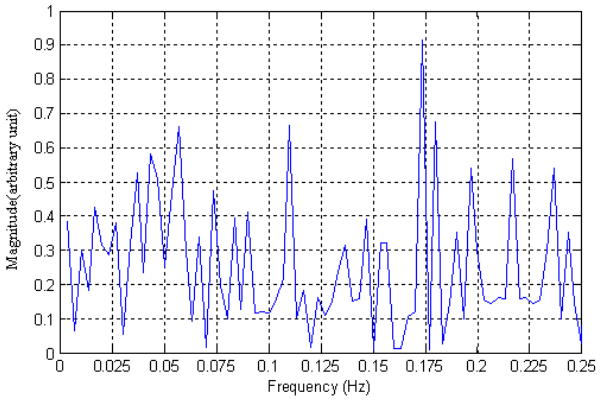


Figure 7. Mean coherence spectrum.

## 4. Conclusions

Temporal coherence variation due to sea surface fluctuation is examined experimentally. 7 kHz, 2ms CW burst signal whose bandwidth is about 1kHz, is used. Mean coherence is about 0.9 for grazing angle of $16^0$ and wind speed of 15~16 knots. Its dominant variation frequency is well consistent with dominant sea surface wave frequency.

**Acknowledgment**

This work was supported by Defense Acquisition Program Administration and Agency for Defense Development under the contract UD070054AD.

**References**

1. L. Culver and D. Bradley : High Frequency Ocean Acoustics Conference AIP Conference Proceedings Vol. 728(2004) p. 204.
2. R. Heitsenrether and M. Badiey : High Frequency Ocean Acoustics Conference AIP Conference Proceedings Vol. 728(2004) p. 214.
3. T. Ruppel, S. Stanic, G. Norton, R. Meredith, E. Kennedy, R. Goodman and M. Wilson : High Frequency Ocean Acoustics Conference AIP Conference Proceedings Vol. 728(2004) p. 413.
4. H. Chandler, E. Kennedy, R. Meredith, R. Goodman and S. Stanic : High Frequency Ocean Acoustics Conference AIP Conference Proceedings Vol. 728(2004) p. 420.

Proceedings of Symposium on Ultrasonic Electronics, Vol. 29 (2008) pp. 123-124
11-13 November, 2008

# Numerical Analysis of Pulse Wave Propagated in Luzow-Holm Bay of Antarctic Ocean

南極リツォホルム湾における伝搬パルス波の数値解析

Takenobu Tsuchiya[1], Mari Takahashi[1†], Shuki Ushio[2], Tetsuo Anada[1] and Nobuyuki Endoh[1] ([1] Facult. Eng., Kanagawa Univ.; [2]NIPR)
土屋健伸[1]，高橋茉里[1†]，牛尾収輝[2]，穴田哲夫[1]，遠藤信行[1]（[1]神奈川大 工; [2]国立極地研究所）

## 1. Introduction

It is important to know the phenomenon of Ocean climate in the Antarctic Ocean, because polar region was large influenced to the energy circulation of the global climate. Therefore, measurement of oceanic environment carried out in the Antarctic Ocean by many countries. For example, in 1991, the Japanese Antarctic Research Expedition (JARE-31) conducted a two-year program of atmosphere /sea-ice/ocean study in the Antarctic Ocean [1]. However, the large area observation under the sea ice is very difficult, because it is very hard to go in site to the research ship, and to measure environmental data under sea-ice floor.

Recently, the climate research of Ocean using Autonomous Underwater Vogel (AUV) is being planned in the Antarctic Ocean[2]. The underwater communication is the only method to distant control AUV in sea-water, and the research of the improvement of the transmission rate in underwater communication was developed. In order to know the characteristics of sound propagation in the Antarctic Ocean for communicate to AUV, we were calculated propagation time and amplitude of pulse used by parabolic equation method. We have investigated about the influence of barthmetry for sound propagation in the Antarctic Ocean model that was covered ice surface for 33 km in range.

## 2. Environment of Lűtzow-Holm bay

Observations of marine environments are being by the national polar region laboratory in the South Pole from 1989 to 1992. The Japanese Antarctic Research Expedition (JARE-31) conducted a two-year program of atmosphere /sea-ice/ocean study in Lűtzow-Holm bay and in its surrounding sea of the Antarctic Ocean. The purpose of this study is to understand a geophysical role of ice-covered ocean in the processes of the Antarctic Ocean climate.

The sound velocity profiles of Lűtzow-Holm bay are shown in **Fig. 1**. The profile was calculated by measurement data using Del-Grosso equation. As shown in Fig. 1(a), the bottom depth of OW5 is about 785 m which measured water temperature and the salinity at the ocean side. The water temperature of sea surface about -1.8 degrees C, and it is changed rapidly near sea surface. When depth is higher than 100 m, water temperature was constant value which is about -0.5 degrees C. Sound velocity profile has changed almost linearly. In Generic Ocean, velocity profile of depth direction depends on the water pressure, water temperature, and salinity of this ocean. Measurement point OW5 has constant value of temperature higher than 100 m of depth. Therefore, sound velocity only depends on water pressure in OW5. The bottom depth of OW1, which is located near bay side, is about 185 m as shown in Fig. 1 (b). The difference of sound velocity by the season is very small.

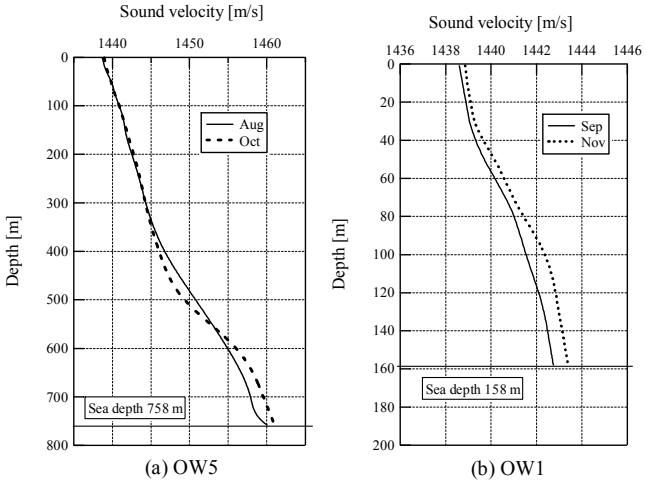


Fig. 1 Sound velocity profile of Lűtzow-Holm bay

## 3. Calculation results

In this simulation, in order to investigate of the characteristics of sound propagation in Lűtzow-Holm bay, we calculated sound pressure filed by PE method with two ocean bottom models that were varied the depth of sea bottom and acoustical parameter. In the case1, sea bottom is flat, which was defined by Range-Independent (RI) model. In the case2, the depth of sea bottom was

---

kenshin@kanagawa-u.ac.jp

assumed by measurement data which was defined by Range-Dependent (RD) model. The depth of the sound source was assumed to be 100m in both traverse line. In these cases of RD model and RI model, acoustical parameter of bottom assumed 1700 m/s in sound velocity and 1.5 g/cm$^3$ in density.

**Figure 2** shows the calculation results of sound pressure distribution of transverse line OW in Lűtzow-Holm bay by PE method in the cases of RD model. The d istribution of sound pressure were changed near source depth, because amplitude of sound pulse reflected from sea bottom is large, so that RD model has upslope bottom shape.

**Figure 3** shows estimated waveform to propagate in the Antarctic Ocean by parabolic equation method with inversion Fourier transfer. In this case, we calculated sound propagation assumed three bottom models Fig. 3 (a) shows estimated pulse waveform in the case of RD model. It is assumed that bottom depth data was used by measurement data. Fig. 3 (b) shows estimated pulse waveform in the case of RI model. This model was assumed the float bottom shape in the bottom depth in source point. The difference value was -3dB between RD model and RI model.

## 4. Conclusions

In order to know the characteristics of sound propagation in Antarctic Ocean, we will know the characteristics of sound propagation in the Antarctic Ocean. We calculated to obtain the characteristics of sound propagation in the Antarctic Ocean using PE method.

It is shown that sound pressure distribution obtained by PE method was influenced by bottom shape. In order to obtain the accuracy heavier of sound propagation in Antarctic Ocean, we calculate pulse waveform by PE method to propagate in the Antarctic Ocean using inversion Fourier transfer in three bottom model. As a result, amplitude of sound pulse was different to three cases. The difference value was -3dB between RD model and RI model. In order to know the characteristics of sound propagation in Antarctic Ocean more accurately, it is necessary to use measurement data of environment.

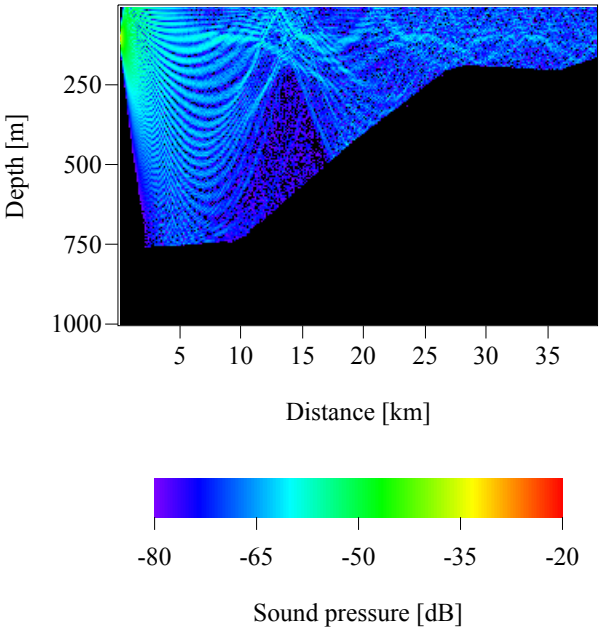


Fig. 2 calculation results of sound pressure distribution of transverse line OW in Lűtzow-Holm bay by PE method in the cases of RD model.

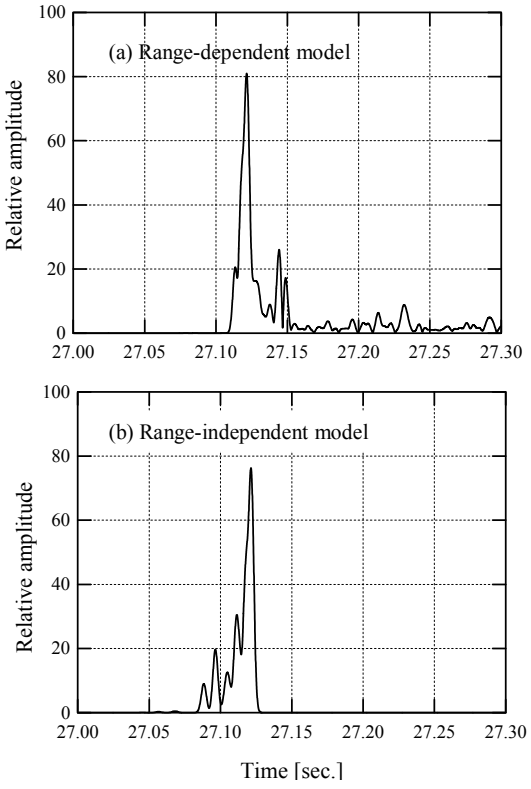


Fig. 3 Estimation of pulse waveform propagated in Lutzow -Holm bay on transverse line 'OW'.


## Acknowledgment

This study was partly supported by High-Tech Research Centre Project from the Ministry of Education, Culture, Sports, Science and Technology, Japan.


## References


1. T. Shimura, et. al., JJAP, **45** (5B), 4847-4852, 2006.
2. S. USHIO and T. TAKIZAWA, "JARE DATA REPORTS NO. 184 (Oceanography 13)," NIPR, 1993.

Proceedings of Symposium on Ultrasonic Electronics, Vol. 29 (2008) pp. 125-126
11-13 November, 2008

# Influence on Sound Field by Number and Interval of Internal Waves
# 音場に対する内部波の数と間隔の影響

Yoshiaki Tsurugaya[1†], Toshiaki Kikuchi[2] and Koichi Mizutani[3] ([1]NEC; [2]NDA; [3]Univ. of Tsukuba.)
鶴ヶ谷芳昭 [1‡]，菊池年晃 [2]，水谷孝一 [3] ([1]NEC; [2]防衛大; [3]筑波大)

## 1. Introduction

Internal waves in the ocean is a wave motion generated on the density interface in underwater. Many studies has been performed in the field of geophysics for a physical property of internal waves (IWs)[1]. In recent years, IWs in the continental shelf and the littoral region is widely confirmed with the sensor equipped with a satellite, and it pays attention to an influence on sound propagation[2]. The studies of the influence to the sound propagation are performed about the fluctuation to the propagation time and the remote sensing of IW using acoustics. However, a study of the influence on sound field by the modification in the state of IWs has not being performed. Then, in relatively short range (<10km) using active sonar such as fish finders, the influence on sound field is examined by the state variation of the number of IWs and the interval between IWs. The influence by IWs was examined by assuming IWs approaching to the sound source, and comparing the sound field with IWs and the sound field without one.

## 2. Internal waves (IWs)

The echo-sounder trace of IWs taken New York Bight, southeast of New York near the edge of the continental shelf[3] is shown in **Fig. 1**. The character of the waves is clearly visible, with only downgoing pulses appearing and very little upgoing excursion. In many cases, an internal wave train (a solibore) is formed rather than a single IW.

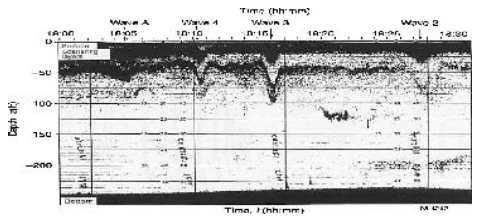

Fig. 1 Echo-sounder trace of IWs.

## 3. Parameters of IWs

The parameters used to examine of IWs are shown in **Fig. 2**. Sound speed profile in shallow water is used the value of reference[4], and sound speed and density in the bottom is 1500m/s and 1500kg/m$^3$ of sandy silt, respectively. Absorption coefficient is 1.0dB/λ. Wavelength and amplitude of IW are 100m and 22.5m referring to the value of IWs[5] , respectively. As for the examination of the influence, the sound fields of one IW and two IWs with the intervals of 0m, 100m, and 200m were compared respectively. Water depth is 200m.

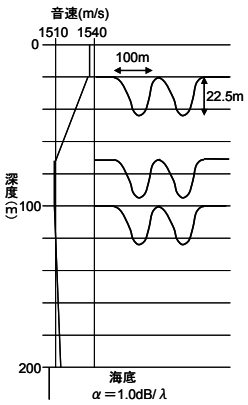


Fig. 2 Sound speed profile and parameters.

## 4. Sound field without IW

For the simulation, used frequency is 600Hz and the simulation model is FOR3D[6] of the PE model. The sound field by sound source in the thermocline, 50m in depth, is shown in **Fig. 3**. In 200m to 2km, there is an overlap of the sound wave that reflect at the surface or refract in the vicinity of surface and changes the direction to downward. And, the propagation of sound wave iterates the reflection at the bottom and the surface. Moreover, the surface duct is formed between sea surface and the lower side of the thermocline. In the area of 6km or more, sound field below the thermocline is formed with the propagation by reflections and the leakage from the lower side of the thermocline

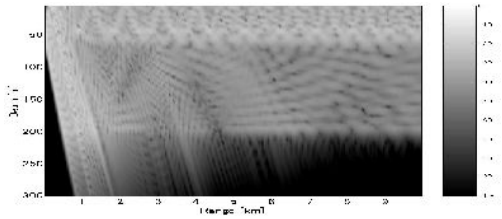

Fig. 3 Sound field without IW in sound source depth 50m.

## 5. Sound field with IWs

Subtracted sound field that the sound field without IW was subtracted from the sound field with IW is shown in **Fig. 4**. The refraction of the

y-tsurugaya@bp.jp.nec.com

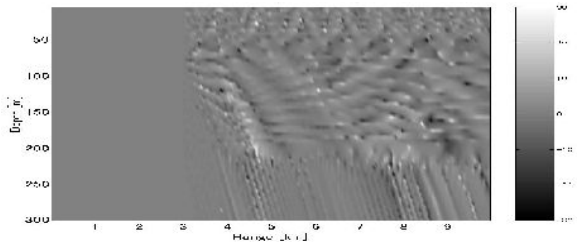

Fig. 4 Subtracted sound field without IW from sound field with IW. range; 3km sound source depth; 50m

sound wave to the upper part and to the under is emphasized by IW fields because of sound source 50m in depth. Considering the change in phase, in depth that is shallower than sound source, modes is shifted to the low-order mode because of the shallower angle of refraction, and in depth that is deeper than sound source, modes is shifted to the high-order mode because of the deeper angle of refraction. Therefore, the sound field under the thermocline is formed with sound wave changing the direction of propagation and sound wave leaking from under the thermocline. The sound field where the sound field of one IW was subtracted from the sound field of two IWs and the sound field where the sound field of two IWs with 100m intervals subtracted from the sound field of that with 200m intervals are shown in **Fig. 5**. As shown in Fig. 5(a), the strength and the range of refraction increase in sound field with consecutive IWs because the consecutive IWs fields broadens more than the one IW fields. Moreover, the sound pressure level under the thermocline increases because the refraction of the sound wave from the duct is emphasized. In Fig. 5(b)), there is no substantial change in upward refraction in sound field with 100m intervals, but three strong sound fields are generated in downward refraction. As for this, because the internal wave is only 100m away, the refraction by the second internal wave is superimposed. On the interval 200m（Fig. 5(c)）, compared with the case of the interval 100m, the strength pattern does not become clear though the influence of the refraction by two IWs is generated. In the difference of the sound field of the interval 100m and the interval 200m(Fig. 5(d)), sound field of the intervals 100m is appeared strongly because the sound wave reflected at sea surface and the second internal wave fields was overlapped.

## 6. Summary

The influence on the sound field of the consecutive IWs was examined. The sound field without IW and with IWs were compared, and the

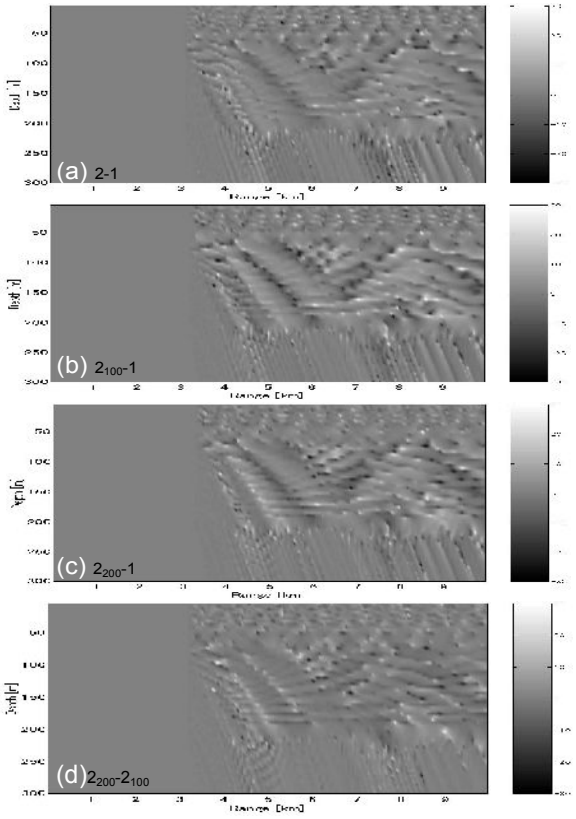


Fig. 5 Subtracted sound field. (a)sound field of 2 consecutive IWs and that of 1 IW (b) 2 consecutive IWS with the 100m intervals and 1 IW (c) 2 consecutive IWs with the 200m intervals and 1 IW (d) 2 consecutive IWs with 100 and 200m intervals

sound field having different intervals of IWs are compared respectively. As a result, the position between the position of sound field without IW and the internal wave fields is important in the sound field formation. Moreover, considering from the states of the phase, the shifting to the low-order mode by the refraction to the upper side and to the high-order mode by the refraction to the lower side became clear.

## References


1. C. R. Jackson *et al*., *Internalwave Atlas*. 2nd ed., (2004).
2. J. R. Apel *et al*., J. Acoust. Soc. Am., 121(2) (2007)696.
3. R. F. Gasparovic *et al*., Science, 232(1986)1529.
4. F. B. Jensen *et al*., "*Computational Ocean Acoustics*", AIP PRESS, 1994.
5. J. R. Apel, "*Oceanographic Applications of Remote Sensing*", CRC Press, 1995.
6. D. Lee *et al*., "*Numerical Ocean Acoustic Propagation in Three Dimension*", World Scientific, 1995.

1P9-11

Proceedings of Symposium on Ultrasonic Electronics, Vol. 29 (2008) pp. 127-128
11-13 November, 2008

# Tidal Effect of Sound Propagation at Hashirimizu Port
走水港内音波伝搬における潮汐の影響

Hanako Ogasawara[1‡], Toshiaki Nakamura[1], Kazuyoshi Mori[1] and Koichi Mizutani[2]
([1] National Defense Academy; [2]Univ. Tsukuba)
小笠原英子[1‡]，中村敏明[1]，森和義[1]，水谷孝一[2] ([1]防衛大 地球海洋; [2]筑波大 シス情工)

## 1. Introduction

At the ocean, acoustic methods have been used in many ways such as signal communication, environmental monitoring tools, and detection system because of its advantage that it is less attenuation than optics or radiowave. We had analyzed reciprocal sound data which was traveling more than 100 km retrieved in the equatorial central Pacific Ocean while a whole year in 2000[1-4]. However, refraction and reflection from the sea surface and seabed complicate the received signals especially at the shallow water. Therefore, many ocean experiment[5, 6] and simulation[7] were executed to clarify these effect and sound propagation. As sea surface level dynamically change because of the tidal effect, the effects of refraction and reflection also alter with time. In this study, we show some results caused by tidal changes from a small scale sound propagation experiment at Hashirimizu port.

## 2. Experimental result

A pair of a sound propagation system was placed on either bank of Hashirmizu port with the distance of about 120 m. Depth of the port is about 5 m in average as shown in **Fig. 1**. Depth of the propagation area was measured every 5 m between the propagation systems. As the seabed covers with mad and sand, the shape of the seabed is very smooth. Transducer was placed at the depth of about 0.9 m from the seabed. Sending signal is seventh order M-sequence and repeated for four times. The signal was sent with the career frequency of 80 kHz.

The systems alternate sending and receiving every 30 s; we can get reciprocal sound propagation data every 1 min. Received signal is recorded for 300 ms after the sending start with the sampling rate of 1 MHz. To synchronize both side of the system, a global positioning system (GPS) clock generates 1 pulse per second signal with accuracy of ± 200 ns. Therefore, it is able to detect the accurate travel time between the systems.

M-sequence modulated signal has an advantage in measuring accurate travel time in the noisy environment because it can be treated as a pulse after demodulation by the original M-sequence. As sending signal include 4 times of M-sequence signal, recorded signal was cut the length of one cycle M-sequence and added all of the cut signals. Effects of spicular noises and other noises can be almost removed by these processes. The added signal were demodulated with M-sequence and transformed to get amplitude components.

**Figure 2** shows the travel time changing through the experimental period of 4th-20th August in 2007. At the same time, water temperature at the sea surface, depth around the transducer, and the seabed were measured every 2 min and plotted by dashed line, gray line and solid line, respectively on Fig. 2(b). Figure 2(c) shows the depth between the transducer and the sea surface monitored by conductivity temperature depth meter (CTD) near the transducer every 5 min. Gray scale indicates the amplitude of the signals in Fig. 2(a). White part means strong amplitude and black part means weak amplitude. The first strong amplitude appeared around 75 ms. The first white band located at the front of the black part around 75.2 ms are the point of the direct pass. Distance between the systems is calculated as 114.5 m from the sound speed calculated by McKenzie's equation[8] with average temperature 24 ℃ and average salinity 30.5 ‰ at the depth of 2 m. As the accurate measurement between the systems by a laser distance meter shows 116.3 m, acoustic monitoring result has validity.

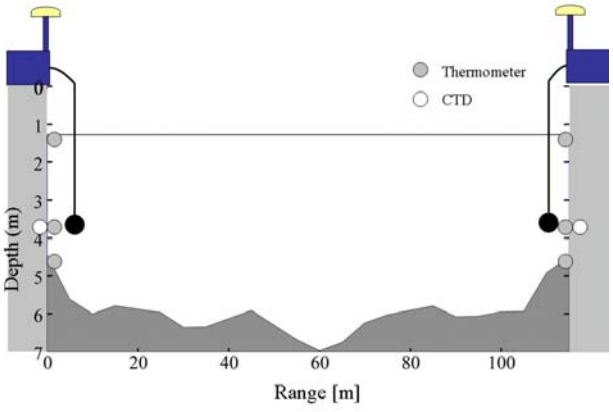


Fig. 1 Propagation area and arrangement of experimental equipments.

ogasawar@nda.ac.jp

## 3. Discussion

Tracking the first white band, travel time varies according to the changes of water temperature in Fig. 2(b). But in some part, the first arrival amplitude suddenly disappeared such as around noon of 15th and 16th August as indicated by white arrows in Fig. 2(a). In such period, it is confirmed that water vertical gradient of water temperature is steep shown as arrows in Fig. 2(b) and depth from the transducer to the sea surface is very shallow given as Fig. 2(c). It is assumed that the direct pass could not reach the received transducer because high vertical temperature gradient refracts the propagating sound. Furthermore, the very shallow depth because of the tidal effect seems to make refracted sound into the seabed.

Ray paths in two characteristic conditions are calculated by a ray tracing program, Bellhop[9] are figured in **Fig. 3**. Sound speed profiles, which are shown on the right side of Fig. 3, are calculated with temperature profiles which are created by liner interpolation with the three measured temperature by thermometers. Temperature at points deeper than the measured depth assumed as the same temperature of the measured at seabed. As depth of the water is decided from CTD data, depth of 0 m means sea surface. In Fig.3(a), temperature gradient is small and high tide. On the other hand, temperature gradient near sea surface has high gradient at low tide in Fig. 3(b). Though we can confirm direct pass in Fig. 3(a), all passes are refracted and cannot propagate directly in Fig. 3(b). Because of low tide, high temperature gradient caused by sun-warmed water directly affects sound propagation. If it had enough depth between the transducer and the surface, some rays would travel directly without any reflection.

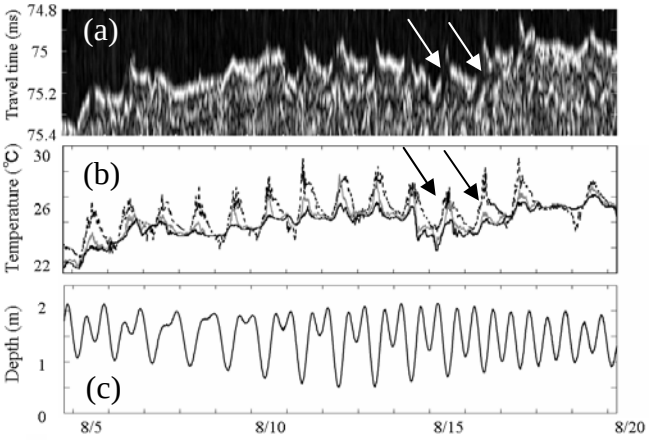


Fig.2 (a) Extracted amplitude of received signals correlated with M-sequence. (b) Water temperature at sea side. (Solid line) water temperature around seabed, (gray line) water temperature near the transducer, (dashed line) water temperature near the sea surface. (c) Distance between the surface and the transducer.

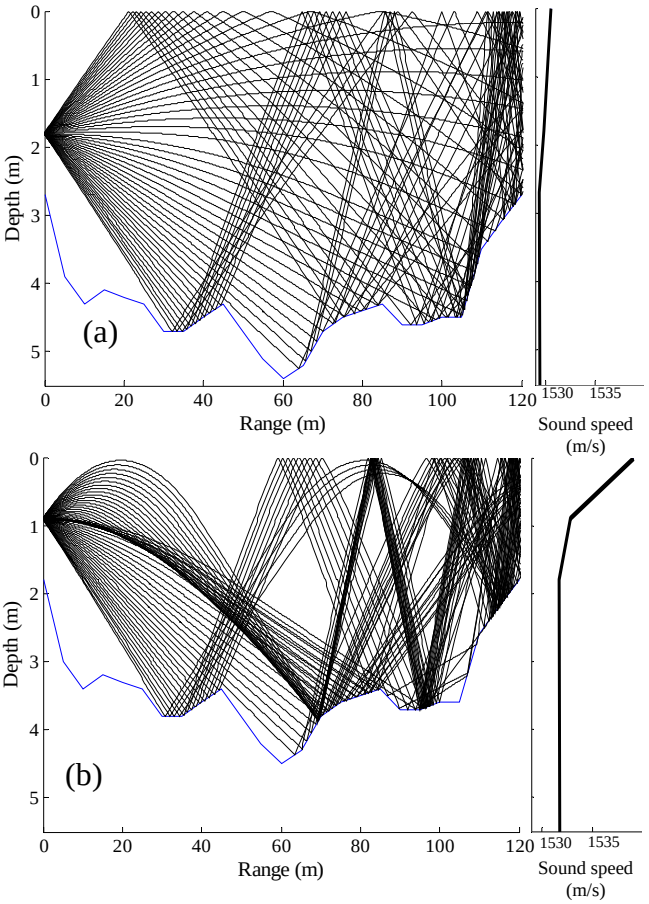


Fig. 3 Rays calculated by Bellhop under the parameters of temperature and depth at (a) 6:00 and (b) 14:00 on August 16, 2007. Graph on the right side shows sound speed profile in the water used for calculation.

## 4. Conclusion

Travel time changes related to the depth of the transducers and temperature gradient. Under the condition of high temperature gradient and low tide, direct passes disappeared because all passes are refracted to downward and reflect at the seabed. Bellhop model explains this result. We will calculate other conditons of depth and temperature gradient for detail explanation.

## References


1. H. Ogasawara, T. Nakamura, H. Hachiya, H. Fujimori, K. Mizutani, Jpn. J. Appl. Phys. 47, (2008) 4349-4353.
2. H. Ogasawara, T. Nakamura, H. Fujimori, K. Mizutani, Proc. Int. Congress on Ultrasonics, (2007) ID 1254.
3. H. Ogasawara, T. Nakamura, H. Fujimori, K. Mizutani, Jpn. J. Appl. Phys. 46, (2007) 4998-5003.
4. H. Ogasawara, T. Nakamura, H. Hachiya, H. Fujimori, K. Mizutani, Jpn. J. Appl. Phys. 45, (2006) 4842-4846.
5. B. D. Dushaw, B. D. Cornuelle, P. F. Worcester, B. M. Howe, D. S. Juther, J. Phys. Oceanogr. **25**, (2005) 631-647.
6. B. D. Dushaw, Deep-Sea Res. I 53, (2006) 449-473.
7. F. Iijima, T. Tsuchiya, N. Endoh, Jpn. J. Appl. Phys. 39, (2000) 3200-3204.
8. K. V. Mackenzie, J. Acoust. Soc. Am. 70, (1981) 807-812.
9. M. B. Porter and Y. Liu: in *Theoretical and Computational Acoustics Vol. 2*, ed. D. Lee and M. H. Schultz (World Scientific Publishing, 1994) pp.947-956.

Proceedings of Symposium on Ultrasonic Electronics, Vol. 29 (2008) pp. 129-130
11-13 November, 2008

# Development of Small-sized SAW Duplexer on $SiO_2/Al/LiNbO_3$ structure for Band IV system

## $SiO_2/Al/LiNbO_3$構造を用いたBand IV用小型SAWデュプレクサの開発

Hidekazu Nakanishi†, Hiroyuki Nakamura, Tetsuya Tsurunari, Hiroki Kamiguchi, Yosuke Hamaoka, Rei Goto and Yukio Iwasaki (Panasonic Electronic Devices Co., Ltd.)
中西秀和‡，中村弘幸，鶴成哲也，上口洋輝，濱岡陽介，後藤令，岩崎行緒 （ﾊﾟﾅｿﾆｯｸ ｴﾚｸﾄﾛﾆｯｸﾃﾞﾊﾞｲｽ㈱）

## 1. Introduction

The SAW duplexer is a key device of the mobile phones for miniaturization and high performances. In UMTS (Universal Mobile Telecommunication System), each band can be separated into three groups, which have wide duplex gap, moderate duplex gap and narrow duplex gap according to features. Band I and Band IV systems have a wide duplex gap. Therefore, to realize the small-sized SAW duplexers with low insertion loss and high attenuation, the substrate with high electro-mechanical coupling coefficient (K2) and small temperature coefficient of frequency (TCF) is needed. Recently, a combination of a rotated Y-cut $LiNbO_3$ substrate and $SiO_2$ film for wideband applications is reported.[1)] For Band I duplexer application, a flattened $SiO_2$ film /Cu electrode/$LiNbO_3$ structure[2)] and a shape controlled $SiO_2$ film /Al electrode/$LiNbO_3$ structure[3)] were reported. On the other hands, for Band IV duplexer application, these substrates have never been reported. In this report, the Al electrode thickness was optimized to realize excellent duplexer for Band IV by using a shape controlled $SiO_2$ film/Al electrode/$LiNbO_3$ structure. And, we developed small-sized SAW duplexer for Band IV system.

## 2. Characteristics of SAW resonator of Band I and Band IV frequency bands

**Table 1** shows frequency allocations of Band I and Band IV. Rx band is the same frequency band. On the other hand, Tx band of Band IV is much lower than one of Band I. When the same electrode thickness (160nm) of Band I is applied to Band IV, as shown **Fig.1**, the characteristic of SAW resonator of Band IV degrades. Especially, an attenuation at anti-resonant frequency degrades.

Firstly, we studied the degrading factor of SAW resonator. We focused on a phase velocity of anti-resonant frequency (Va) for resonators. A phase velocity is calculated by Eq. (1).

nakanishi.hidekazu@jp.panasonic.com

Table 1 Frequency allocations

| Operation band | Tx band | Rx band |
|---|---|---|
| Band **I** | 1920MHz-1980MHz | 2110MHz-2170MHz |
| Band**IV** | 1710MHz-1755MHz | 2110MHz-2155MHz |

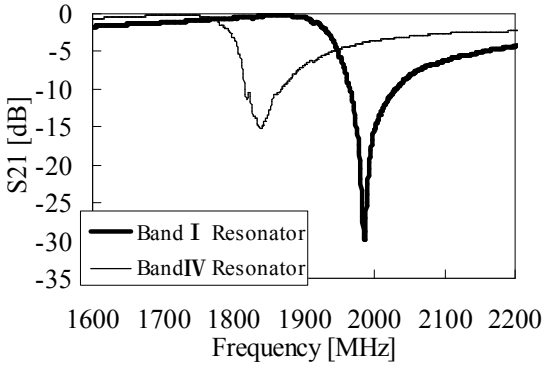


Fig. 1 Characteristics of SAW resonator

$$Va = f \times (2 \times p) \qquad (1)$$

f: anti-resonant frequency
p: IDT pitch
(Band I : 1.0μm, Band IV: 1.1μm)

As a result, Va of SAW resonator of Band I is 4007m/sec, Va of SAW resonator of Band IV is 4072m/sec. Va of SAW resonator of Band IV is faster than a phase velocity of slow shear wave of $LiNbO_3$ (4024m/sec). This is attributed to thin electrode thickness for Band IV. Thus, a bulk radiation occurs at anti-resonant frequency of SAW resonator of Band IV. Because of a bulk radiation, an attenuation at anti-resonant frequency degrades. Therefore, to realize a good performance SAW resonator of Band IV, it is necessary to determine the electrode thickness or $SiO_2$ thickness so that Va is slower than a phase velocity of slow shear wave of the $LiNbO_3$ substrate.

## 2. Optimization the electrode thickness

We optimized the electrode thickness so that Va is slower than a phase velocity of slow shear wave of $LiNbO_3$ substrate. Here, $SiO_2$ thickness is constant of 400nm. **Fig.2** shows the characteristics of SAW resonator when the electrode thickness is 160nm, 200nm and 240nm. **Fig.3** shows a phase velocity at anti-resonant frequency of each condition. And, dashed-line is a phase velocity of slow shear wave $LiNbO_3$. When the electrode thickness is 200nm and 240nm, attenuations at anti-resonant frequency are better. However, when the electrode thickness is 160nm, it degrades. Because, as shown Fig.3, Va becomes slower than a phase velocity of slow shear wave of $LiNbO_3$ when the electrode thickness is 200nm and 240nm. Especially, a characteristic of SAW resonator is excellent when the electrode thickness is 200nm. And, coupling factor is enough large of 14%

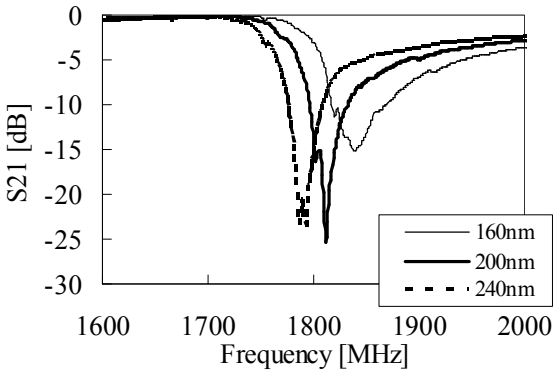


Fig. 2 Characteristics of SAW resonator of Band IV

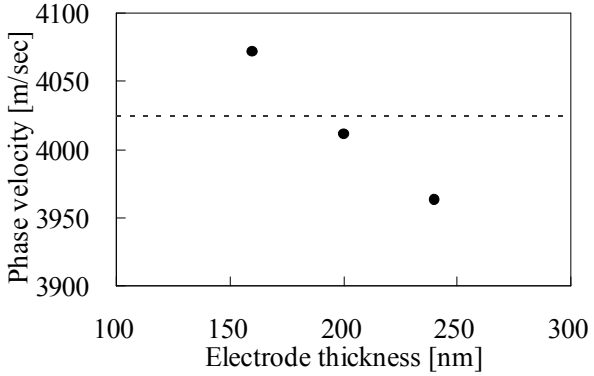


Fig. 3 A phase velocity dependence of the electrode thickness

## 3. Characteristics of the SAW Duplexer

The small-sized Band IV SAW duplexer was fabricated by using the resonator with optimized $SiO_2/Al/LiNbO_3$ structure. The package size of the duplexer is small of 2.5×2.0×0.5mm. **Fig.4** and **Fig.5** show Tx and Rx characteristics, respectively. In Tx characteristics, insertion loss and attenuation in Rx band are 1.2dB and 45dB. In Rx characteristics, insertion loss and attenuation in Tx band are 2.2dB and 42dB. The duplexer has small TCF, which is almost same value of Band I duplexer. [3)]

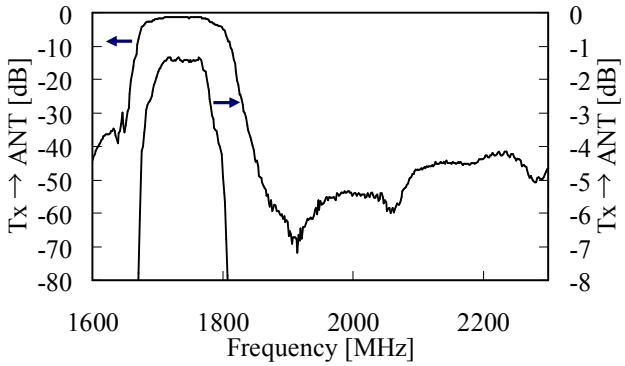


Fig. 4 Tx characteristic of the SAW duplexer

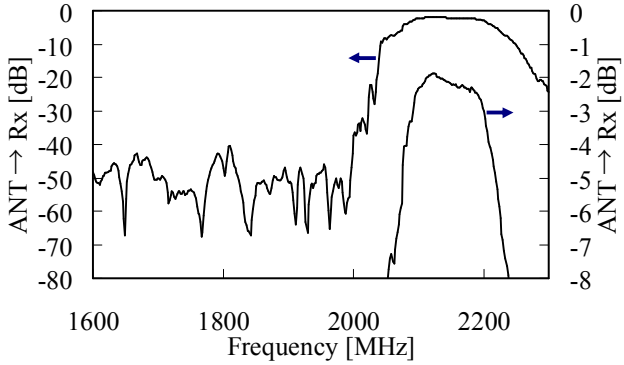


Fig. 5 Rx characteristic of the SAW duplexer

## 4. Conclusion

The SAW resonator with good performance was realized by optimizing the electrode thickness on $SiO_2/Al/LiNbO_3$ structure from a viewpoint of a phase velocity. Applying the SAW resonator, the SAW duplexer, which has excellent performances of low insertion loss, high attenuation and small-sized, could be realized.

## References


1. K. Yamanouchi, Y. Satoh, H. Isono and D. Kawasaki: Jpn. J. Appl. Phys. **44** (2005) 4520.
2. M. Kadota, T. Nakao, K. Nishiyama, S. Kido, M. Kato, R. Omote, H. Yonekura, N. Takada and R. Kita: Jpn. J. Appl. Phys. **46** (2007) 4714.
3. H. Nakamura, H. Nakanishi, T. Tsurunari, K. Matsunami, Y. Iwasaki, K. Hashimoto and M. Yamaguchi: Jpn. J. Appl. Phys. **47** (2008) 4052.

1P5-2

Proceedings of Symposium on Ultrasonic Electronics, Vol. 29 (2008) pp. 131-132
11-13 November, 2008

# Improvement of Shape Factor of SAW Resonator Filter composed of $SiO_2$/High-density-electrode/$LiTaO_3$

# $SiO_2$/高密度電極 /$LiTaO_3$構造共振子 SAW フィルタの肩特性改善

Takaki Murata‡, Michio Kadota, Takeshi Nakao, and Kenji Matsuda
(Murata Mfg. Co., Ltd.)
村田崇基，門田道雄，中尾武志，松田賢二（村田製作所）

## 1. Background

Recent years, surface acoustic wave (SAW) filters such as radio frequency (RF) ones and duplexers have been applied to mobile phones, global positioning system (GPS), Bluetooth (BT) and so on, because of their small size, good performance, and reasonable price. A leaky SAW (LSAW) on a 36º-48ºY·X-$LiTaO_3$ and a 50º-70ºY·X-$LiNbO_3$ substrates are widely used to their applications with wideband characteristic. However, they are not so suitable for some of the applications, because their temperature coefficient of frequency (TCF) are poor as about -40 and -80ppm/ºC, respectively. By depositing a $SiO_2$ film with positive TCF on $LiNbO_3$ and $LiTaO_3$ substrates with negative TCF, the TCF of transversal filters using their Rayleigh wave and LSAW were improved [1)-3)]. However, in case of the resonator devices such as a double mode SAW resonator filter (DMS) and a ladder filter, it is important to flatten the $SiO_2$ surface to obtain good frequency characteristics. The LSAW and Rayleigh wave on flattened $SiO_2$ film/high density metal electrode/$LiTaO_3$ or $LiNbO_3$ with excellent TCF were applied to SAW duplexers composed of ladder filters [4)-7)] Therefore, depositing the $SiO_2$ film onto the substrate with negative TCF and flatting its substrate are effective to improve TCF.

The authors previously applied this flattened $SiO_2$ film/high density metal electrode/36º-48ºY·X-$LiTaO_3$ substrate to the DMS that requires a narrow pass band and a sharp attenuation for RF range, for instance, "MediaFLO™," which is developed by Qualcomm. Inc. or "Terrestrial Mobile Multimedia Broadcasting (T-MMB), which is one of the mobile TV system candidates in China market.[8)] The report was mainly focused on optimizing substrate material to obtain best value of the coupling factor ($k^2$) and nearly zero TCF. In this report, filter design on the substrate will be discussed. By modifying the filter design, shape factor of SAW resonator filter is improved.

## 2. Filter Design

### 2.1 Suppression of transverse response

The filter characteristic for MediaFLO™ using the conventional Al-electrode/36º-48ºY·X-$LiTaO_3$ substrate is shown in **Fig. 1**. A transversal response is observed at higher frequency from pass band. The filter consists of a cascaded two DMS filters, where each DMS filter is a longitudinally coupled resonator as roughly shown in **Fig. 2**. **Figures 3** and **4** show the calculated reflection coefficients and coupling factors of Al/36ºY·X-$LiTaO_3$ and flattened $SiO_2$/high density metal electrode/36ºY·X-$LiTaO_3$, respectively. The data was calculated by Finite Element Method (FEM) including thickness (0.25λ) and shapes of electrode and $SiO_2$ (0.05λ). Where λ is wave length. In case of the filter in **Fig. 1**, the Al electrode thickness is 0.04λ to satisfy both enough reflection coefficient and small coupling factor to realize narrow bandwidth. The reflection coefficient and the bandwidth of stopband are slightly small of 0.05 (• mark in Fig. 3) and 0.03, respectively, and it results in the transversal response. Therefore, it is difficult to design a narrow band pass filter by Al/$LiTaO_3$ without any transversal responses. On the other hand, the bandwidth of the stopband is 0.06 to 0.07 by the flattened $SiO_2$/high density metal electrode/36ºY·X-$LiTaO_3$ with the electrode thickness ( ○ marks in Fig.3) where the reflection coefficient is doubled from the filter in **Fig. 1**. The stop bandwidth is sufficient to suppress the transversal responses. Moreover, $SiO_2$ film has the merits of not only improving TCF but also being the coupling factor smaller to realize narrow band, so that this structure is suitable to design a narrow band pass filter. Then a filter is designed by this structure.

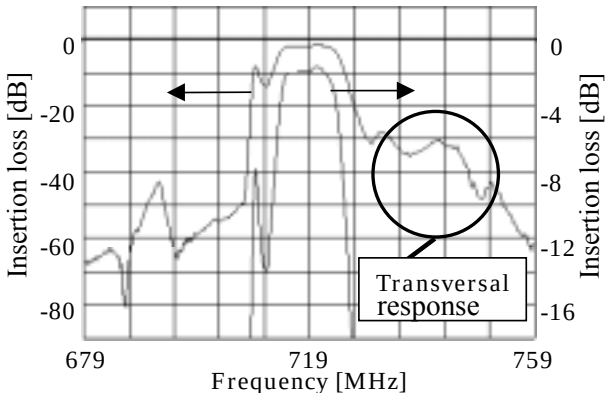


Fig. 1 Frequency characteristic of RF filter with conventional Al/36º-48ºY·X-$LiTaO_3$ substrate.

Each DMS filter consists of two IDTs and two reflectors as shown in Fig. 2, where λ is about 5μm, the aperture is about 16λ, the gap between IDTs is about 0.5λ, the number of pairs of the IDT is around 20, the number of fingers of the reflectors is around 50, and the metallization ratio is about 0.6. The thickness of $SiO_2$ is 0.27λ. The total size of SAW package is 1.4 × 1.1 × 0.6 mm by using Chip Size Package (CSP) structure.

By using the above-mentioned structure, the

‡ takaki_murata@murata.co.jp

transversal response can be suppressed as shown by solid line in Fig.6. However, some of the application requires more severe specification for attenuation. In order to improve the attenuation slope more sharply, the authors modified the IDT design of the DMS filter to improve the shape factor.

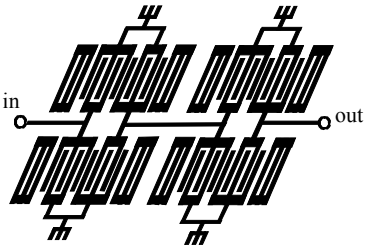


Fig. 2: Composition of RF filter composed of DMS.

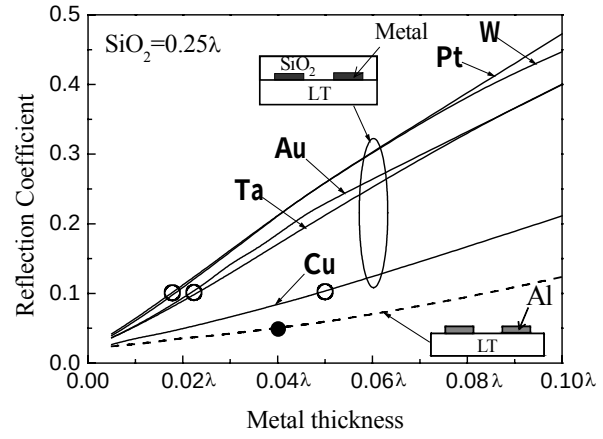


Fig. 3 Calculated reflection coefficients on flattened $SiO_2$/various electrode/36ºY·X-$LiTaO_3$ and Al/36º Y·X-$LiTaO_3$ as function of electrode thickness.

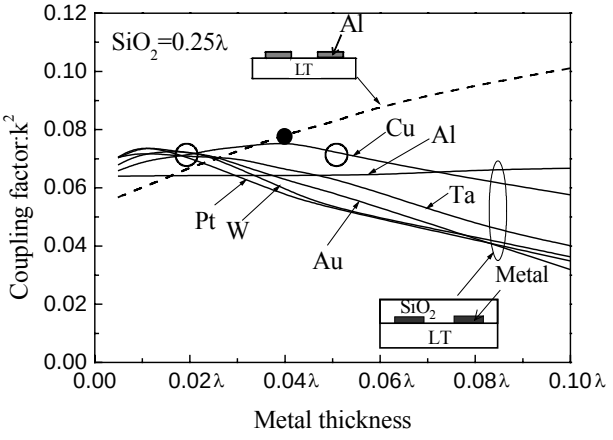


Fig. 4 Calculated coupling factors on flattened $SiO_2$/various electrode/36ºY·X-$LiTaO_3$ and Al/36º Y·X-$LiTaO_3$ as function of electrode thickness.

## 2.2 Improvement of shape factor

The fingers of normal IDT is designed alternately on a substrate as shown in Fig. 5(a). If the order is broken, the SAW resonance is not excited so well and the filter performance is degraded. But when the disadvantage effect from disorder is quite small, there are some possibilities to modify IDT finger order. The authors optimized it and found a certain case that was possible to improve the attenuation slope without performance degradation. It is achieved by putting a couple of adjacent fingers near the gap of two IDTs onto the same direction and same electric potential. The phase of some SAW is inverted around these fingers (phase inverse design) and it results in the sharper attenuation slope as shown in **Fig. 5 (b)**. **Fig. 6** shows the comparison between normal design (solid line) and phase inverse design (broken line). The shape factor has been improved.

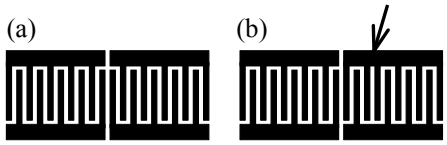


Fig. 5: IDT structure - (a)Normal design, (b)Phase inverse design.

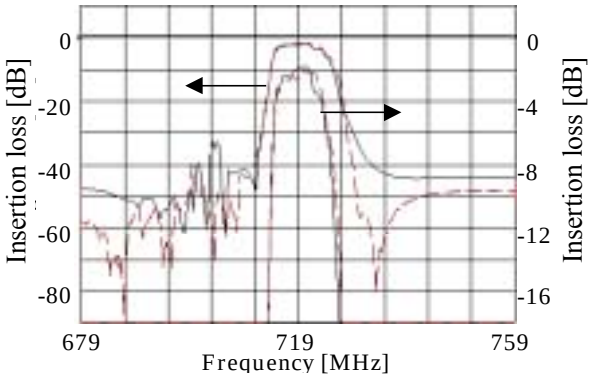


Fig. 6: Frequency characteristic of RF filter with flattened $SiO_2$ film/high density metal electrode/36º-48ºY·X-$LiTaO_3$ substrate. (broken line: Phase inverse design, solid line: Normal design)

## 3. Conclusion

The optimizing filter design results in improving shape factor of SAW resonator filter. This design is suitable for flattened $SiO_2$ film/high density metal electrode/36º-48ºY·X-$LiTaO_3$ substrate with a narrow pass band and a sharp attenuation.

### References

1. T. E. Parker and H. Wichansky: Proc. IEEE Ultrason. Symp., (1974)5031.
2. T. E. Parker and M. B. Schulz: Proc. IEEE US. Symp., (1975) 295.
3. K. Iwasaki, K. Yamanouchi, and K. Shibayama: Tech. Rep. of IEICE of Jpn., US-77-43 (1977)37 [in Japanese].
4. M. Kadota, T. Nakao, N. Taniguchi, E. Takata, M. Mimura, K. Nishiyama, T. Hada, and T. Komura: Proc. of IEEE Ultrason. Symp., (2004) 1970.
5. M. Kadota, T. Nakao, N. Taniguchi, E. Takata, M. Mimura, K. Nishiyama, T. Hada, and T. Komura: Jpn. J. Appl. Phys. **44** (2005) 4527.
6. T. Nakao, M. Kadota, K. Nishiyama, Y. Nakai, D. Yamamoto, Y. Ishiura, T. Komura, N. Takata, and R. Kita: Jpn. J. Appl. Phys. **46**, Part I, 7B (2007) 4760.
7. M. Kadota, T. Nakao, K. Nishiyama, Y. Nakai, D. Yamamoto, Y. Ishiura, T. Komura, N. Takata, and R. Kita: Jpn. J. Appl. Phys. **46**, Part I, 7B (2007) 4714.
8. T. Murata, M. Kadota, T. Nakao, and K. Matsuda: Jpn. J. Appl. Phys. **47** (2008) 4101.

1P5-3

Proceedings of Symposium on Ultrasonic Electronics, Vol. 29 (2008) pp. 133- 134
11-13 November, 2008

# A Full-Wave Analysis of Surface Acoustic Waves Propagating on a $SiO_2$ Overlay/Metal Grating/Rotated YX-$LiNbO_3$ Substrate Structure

Yiliu Wang[†‡], Ken-ya Hashimoto, Tatsuya Omori and Masatsune Yamaguchi (Graduate School of Engineering, Chiba University)

## 1. Introduction

The authors have recently reported a full wave analysis of piezoelectric boundary acoustic waves (PBAWs) [1] propagating in a semi-infinite $SiO_2$ overlay/Cu grating/rotated YX-$LiNbO_3$ (LN) substrate structure [2]. In this paper, instead of the semi-infinite $SiO_2$ overlay, we make an analysis of $SiO_2$ overlay of finite thickness/metal grating/ rotated YX-LN substrate structure. The influence of thickness and surface topology of the $SiO_2$ overlay upon acoustic wave excitation and propagation characteristics are discussed.

## 2. Simulation and Analysis

*1. Simulation Steps:*

The simulation is carried out for two types of structures shown in **Fig. 1** and **Fig. 2**, where the YX-LN substrate is of semi-infinite. For metal grating materials, either Cu or Al grating is assumed. For the Cu and Al gratings, the thickness is fixed at $0.2p$ [2] and $0.16p$ [3], respectively. Different from ref [2], the $SiO_2$ thickness is assumed to be finite in Figs. 1 and 2.

Using the software – SYNCO, we calculated $\hat{Y}(\omega)$ of an infinitely long metal IDT sandwiched in between the $SiO_2$ and YX–LN as a function of the relative frequency $fp/V_B$ ($V_B$ = 4,752 m/s is the fast-shear BAW velocity in LN). **Fig. 3** shows the result for the flattened-$SiO_2$ overlay structure where $h_2 = 3.2p$ with the Cu grating. It is seen that there propagate several modes. Some are caused by thickness resonance modes in the $SiO_2$ overlay, some by Rayleigh- and SH-type acoustic waves.

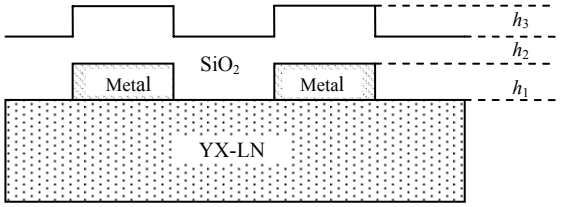


Fig. 1 Controlled shape $SiO_2$ overlay/metal grating /rotated YX-LN structure

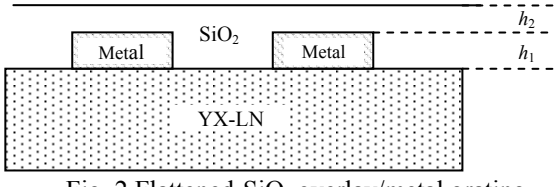


Fig. 2 Flattened-$SiO_2$ overlay/metal grating /rotated YX-LN structure

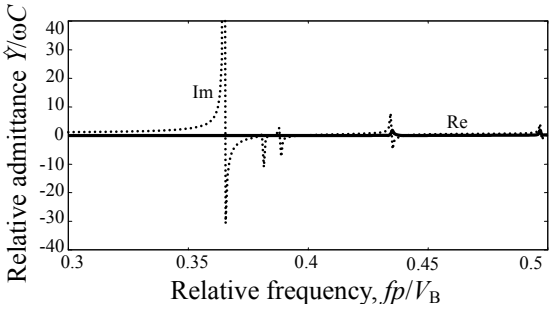


Fig. 3 Input admittance of infinitely-long Cu IDT

We calculated relative admittance for various $SiO_2$ thickness ($0<h_2/2p<2$) to help distinguish the modes. As shown in Fig. 3, the modes whose relative frequency is less than 0.43 are non-leaky, because their $Re[\hat{Y}/\omega C]$ is zero. From Fig. 3, we can get the resonance and anti-resonance frequency of a certain mode ($f_r$ and $f_a$). The electro-mechanical coupling factor of this mode can be evaluated by the difference of $f_r$ and $f_a$. Besides the flattened-$SiO_2$ overlay structure, we also make an analysis of the controlled shape $SiO_2$ controlled shape $SiO_2$ overlay structure, where $SiO_2$ thickness $h_2/2p$ varies from 0 to 2, with $h_1$ and $h_3$ being fixed at $0.2p$. On the other hand, for the Al grating, the thickness $h_2/2p$ is changed from 0 to 2, with $h_1$ and $h_3$ being fixed at $0.16p$.

*2. Simulation Results and Analysis*

**Fig. 4** shows the change in the effective velocities ($V_r=2f_rp$, $V_a=2f_ap$) with the $SiO_2$ thickness for the controlled shape $SiO_2$ overlay structure using the Cu grating, where $V_1$ (=4,031m/s) represents the slow shear bulk acoustic wave velocity in LN. $V_2$ (=3,766 m/s) is for the shear bulk acoustic wave velocity in $SiO_2$, which determines

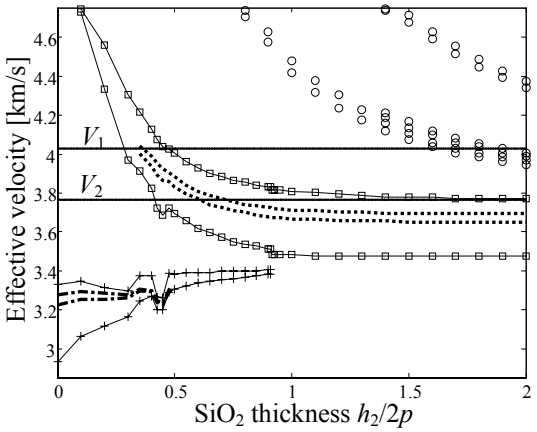


Fig. 4 Variation of the effective velocities of acoustic waves with $h_2/2p$ (Controlled: Cu $h_1=h_3=0.2\ p$)

whether the acoustic wave is leaky or not; when $V<V_2$, it is non-leaky. Otherwise, it is leaky. In the figure, "□" shows $V_r$ and $V_a$ of the SH-type PBAW, while the dotted lines are for those of the Rayleigh-type PBAW. Their effective velocities become unchanged when $SiO_2$ thickness is large,

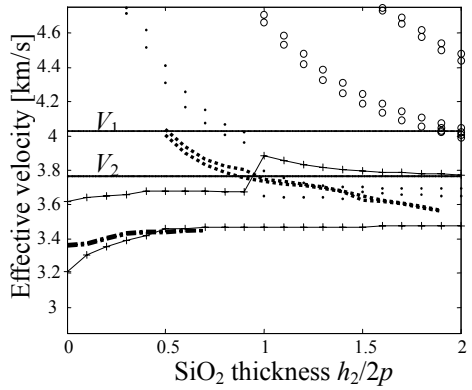


Fig. 5 Variation of the effective velocities of acoustic waves with $h_2/2p$ (Flattened: Cu $h_1$=0.2 $p$)

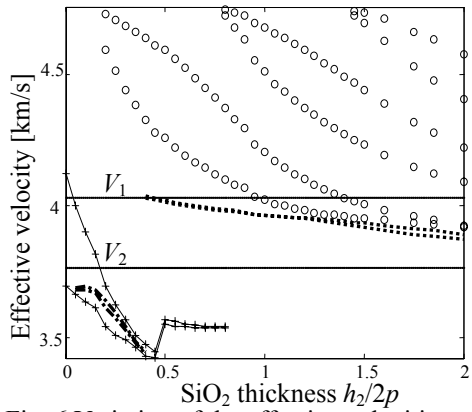


Fig. 6 Variation of the effective velocities of acoustic waves with $h_2/2p$ (Controlled: Al $h_1$=$h_3$=0.16 $p$)

with coupling factor being kept almost the same. The results definitely reveal that there propagate two kinds of PBAWs in the controlled shape $SiO_2$ overlay structure. The mark "o" represents the thickness resonance modes in the $SiO_2$ overlay, which could be suppressed by sand-blasting the $SiO_2$ surface. The lines with "+" represent the SH-type surface acoustic wave (SAW) propagating on the $SiO_2$ top surface. It is crystal clear that this mode vanishes with an increase in the $SiO_2$ thickness ($h_2/2p$>1). The dash-dotted lines are for the Rayleigh-type SAW, coupling factor of which also decreases with an increase in $h_2$. This suggests that $h_2/2p$ should be greater than 1 in device implementation.

For comparison with the controlled shape $SiO_2$ overlay structure, **Fig. 5** shows the result for the flattened-$SiO_2$ structure. Similar to Fig. 4, there propagate PBAWs when the $SiO_2$ thickness $h_2/2p$ is from 1 to 2. The mark "o" on the upper right represents the thickness resonance modes in the $SiO_2$ overlay. The line with "+" represent the SH-type SAW, while the dash-dotted lines are for the Rayleigh-type SAW on the $SiO_2$ top surface. The sparse dotted points are for the Rayleigh-type PBAW. When $0.8<h_2/2p<1.2$, it seems that the Rayleigh-type PBAW couples with different modes. This behaviour is not yet clearly understood which branch corresponds to which mode. From Figs. 4 and 5, it is suggested for the implementation of potential PBAW devices, the $SiO_2$ thickness $h_2/2p$ should be made relatively large (say, greater than 1.9), so that the Rayleigh-type SAW on the top surface of the $SiO_2$ overlay may be suppressed. The thickness resonance modes (shown as "o" markers) in the $SiO_2$ overlay could be suppressed by sand-blasting the $SiO_2$ surface.

In the controlled shape $SiO_2$ structure, the Al grating is also applied to the comparison with the Cu grating. The results are shown in **Fig. 6**. Similarly, "o" marks the thickness resonance modes in $SiO_2$. Sand-blasting is needed for the $SiO_2$ surface. The lines with "+" are for the SH-type SAW, whilst the dash-dotted lines are for the Rayleigh-type SAW. Fig. 6 suggests that SH-type SAW may be effective in device implementation. If the $SiO_2$ thickness $h_2/2p$ is relatively small (i.e., less than 0.5), the Rayleigh-type SAW is barely excited. From Fig. 6, therefore, the $SiO_2$ thickness of $0<h_2/2p<0.5$ is of interest, which agrees fairly well with the result shown in ref [3].

## 3. Conclusion

In this paper, numerical analysis on finite $SiO_2$ overlay/metal grating/rotated YX-LN structure was conducted and results were analysed in details. Two types of structures are compared with each other to check the influence of thickness and surface topology of the $SiO_2$ overlay upon acoustic waves excitation and propagation characteristics. For metal gratings, Cu and Al are applied. The results showed that there propagate PBAWs in both structures with Cu as the grating, but not with the Al grating.

**Acknowledgment**

This work was partly supported by TriQuint Semiconductor, Inc. It is our pleasure to thank Dr. Benjamin P. Abbott of TriQuint for his suggestions and discussion.

**References**

1. H. Kando, *et al* : Jpn. J. Appl. Phys. **45** (2006) 4651. Or H. Kando, *et al* : Proc. IEEE Ultrasonic Symp., (2006) 188.
2. Y. Wang, *et al* : Proc. IEEE Freq. Contr. Symp., (2008) [to be published].
3. H. Nakamura, *et al* : Proc. IEEE Ultrasonic Symp., (2007) 488. Or H. Nakamura, *et al* : Jpn. J. Appl. Phys. **47** (2008) 4052~4055.

1P5-4

Proceedings of Symposium on Ultrasonic Electronics, Vol. 29 (2008) pp. 135-136
11-13 November, 2008

# Interpolation Technique for Fast Analysis of SAW and Lamb Wave Devices

Jan H. Kuypers‡ and Albert P. Pisano
(Berkeley Sensor & Actuator Center, University of California at Berkeley)

## 1. Introduction

The development of high performance acoustic devices for RF filters and sensors requires the precise simulation for the design and analysis. The design procedure generally consists of running iterations on a given layout to achieve given filter or sensor specifications. In order to obtain an optimization in a reasonable time the computation speed is very important. Increasing the computation power and optimization of the program code are useful, but generally not sufficient. Very often the complexity of the simulation or the number of output points are reduced to speed up the computation, both at the cost of sacrificing accuracy of the simulation output.

## 2. Background

Modern acoustic device simulation is performed in the frequency domain, as various input parameters are frequency dependent, i.e. phase velocity, mass loading, propagation loss, electrode resistivity, etc. Very often the frequency spacing for the simulation has to be chosen to be very small, in order to obtain an accurate estimation of high Q resonators and reflective SAW delay line sensors [1]. Especially for the wideband simulation of high Q resonators (and filters) the correct estimation of impedance at series and anti-resonance requires a very fine frequency discretization. In case of a time domain analysis based on a frequency domain simulation and subsequent FFT, as used for time-gating procedures and reflective SAW delay line sensors, requires a high frequency discretization in order to be able to resolve long enough time delays in the time domain. Therefore, it is highly desirable to find a method that reduces the number of points to be simulated, but at the same time does not affect the accuracy of the simulation output.

## 2. Interpolation Technique

In this paper we present an interpolation technique that reduces the number of frequencies at which the device has to be simulated, with a minimum effect on the accuracy of the output. Obviously, simply reducing the number of frequencies in the simulation and interpolating the direct output does not yield a good estimate of the resonator or filter. Fitting an equivalent circuit to the supporting points and using this to increase the frequency resolution defeats the purpose of a general simulation, as the accuracy of the output is now determined by how well the chosen circuit fits the actual device under consideration.

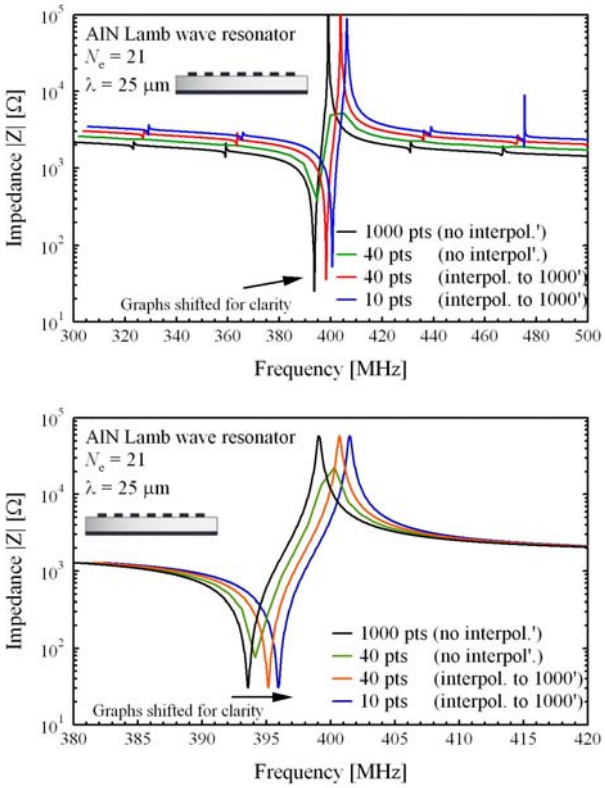


Fig. 1 Simulated impedance of a Lamb wave resonator on AlN using different interpolation schemes.

The P-Matrix and K-Matrix Model [2, 3] are both based on deriving nine $K_{ij}$ entries of (3×3) matrices representing single electrode cells. Examining the frequency dependence of these entries reveals that all coefficients $K_{ij}$ if separated into real and imaginary part are continuous functions and are easily fitted by higher order polynomials and therefore easily interpolated. Phase jumps in the transmission coefficients $K_{12}$ and $K_{21}$ are removed by multiplying with the sign of $Im\{K_{11}\}$. The key is to perform the interpolation on a level, where no singularities exist. As soon as the single electrode cells are cascaded the interaction of the electrodes causes singularities, which cannot be interpolated in any accurate fashion.

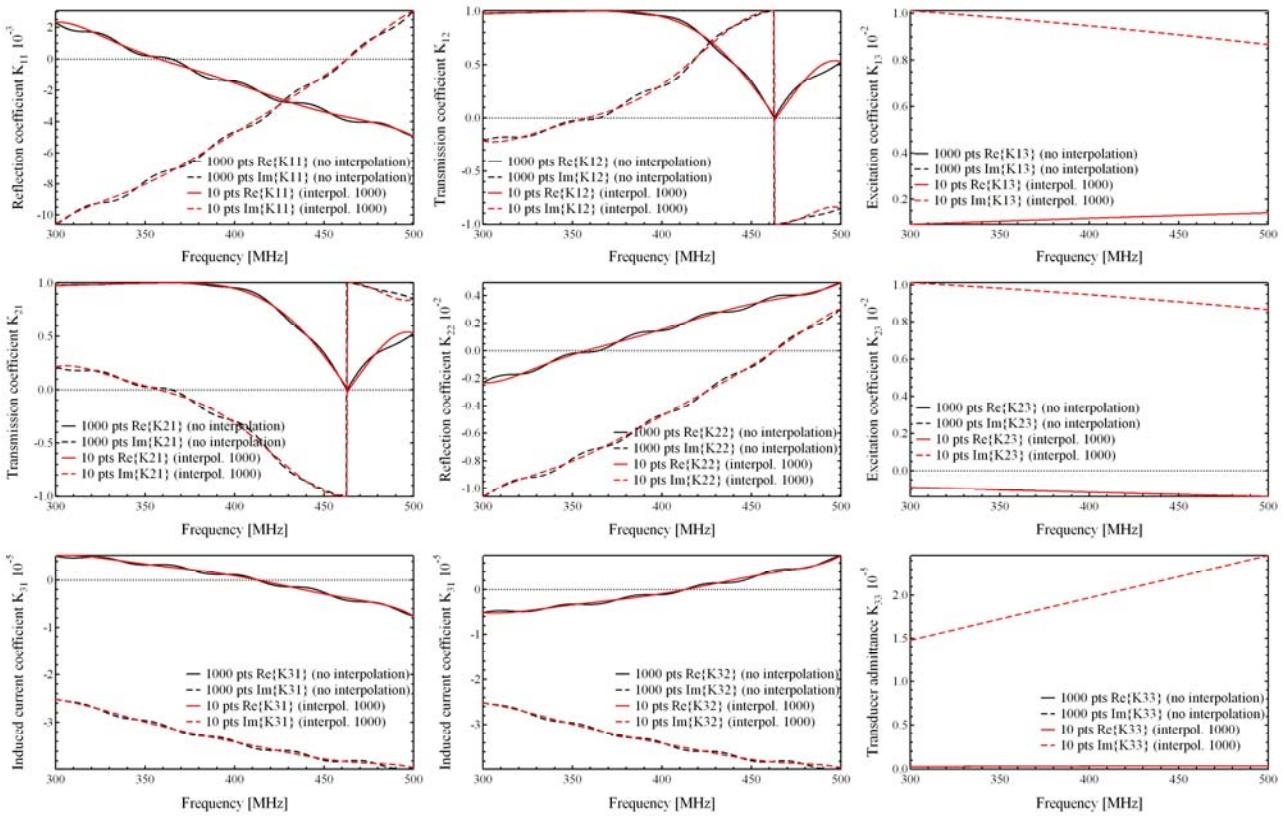


## 3. Results

For this study we computed the impedance of a Lamb wave resonator on a 1 μm thick aluminum nitride plate with bottom metallization using a single electrode design with 21 electrodes, $\lambda$ = 25 μm, and acoustic aperture of 100 μm. The results are shown in **Fig. 1**. Details of the K-Model simulation of Lamb wave resonators are given in [4]. The first curve in **Fig. 1** refers to a brute-force simulation of 1000 points. The second case is for a reduced computation of using only 40 points, which leads to a very poor estimation of the resonator around resonance and anti-resonance. By using the proposed interpolation technique using only 40 computed points the accuracy demonstrated with the third plot is obtained, which is almost identical to the original brute force result. Even using only ten points leads to a very good prediction of the resonator.

The frequency dependence of the $K_{ij}$ entries for the brute force case and the interpolation based on only ten points for an edge electrode are shown in **Fig. 2**. The edge-electrode case is the most challenging, as edge effects lead to a stronger frequency dependence and require a higher order polynomial fit than for a center electrode. The polynomial order has to be chosen according to the number of simulation points or might otherwise cause errors in fitting. The only inaccuracy of the interpolation is the signature swing of the $K_{ij}$ related to the end effects and electrode geometry [5].

## 4. Conclusion

We have proposed an interpolation scheme that can be applied to the P-Matrix and K-Matrix model and significantly reduces the computation time. In the presented example the numerous spurious resonances observed in Lamb wave resonators with low number of electrodes are well predicted by the simulation using this interpolation technique, although the device was only simulated at ten frequencies points.


## Acknowledgment

This work was supported by the DARPA M/NEMS S&T Fundamentals award (HR0011-06-1-0041) under the DARPA Center for Micro/Nano Scaling-Induced Physics (MiNaSIP).


## References


1. J. H. Kuypers, L. M. Reindl, S. Tanaka and M. Esashi, IEEE Trans. Ultrason., Ferroelect., Freq. Contr., **55**, (2008), 1640-1652.
2. C. W. Ruppel, W. Ruile, G. Scholl, K. Wagner, and O. Männer, Proc. IEEE Ultrason. Symp. 1994, 313-324.
3. J. H. Kuypers, D. A. Eisele, L. M. Reindl, Proc. IEEE Ultrason. Symp. 2005, 1550-1555.
4. J. H. Kuypers, A. P. Pisano, to be presented at IEEE Ultrason. Symp. 2008.
5. J. H. Kuypers, Ph.D. thesis, Tohoku University (2007), 80-81.

1P5-5

Proceedings of Symposium on Ultrasonic Electronics, Vol. 29 (2008) pp. 137-138
11-13 November, 2008

# High Frequency Lamb Wave Device of $LiNbO_3$ Thin Film

## $LiNbO_3$ 薄膜を用いた高周波ラム波デバイス

Michio Kadota, Takashi Ogami†, Kansho Yamamoto, Yasuhiro Negoro, and Hikari Tochishita (Murata Mfg. Co., Ltd.)
門田道雄, 小上貴史, 山本観照, 根来泰宏, 栃下光（村田製作所）

## 1. Introduction

Substrates for surface acoustic wave (SAW) devices doing currently a important role for handy telephone have a low velocity as about 4,000 m/s, so it is considered that it is difficult to apply for a higher frequency device. The Lamb wave device can be operated at a high frequency. The waves propagating in a thin plate are called the plate waves, which are classfied Lamb wave and Shear Horizontal (SH) wave according to direction of these displacements. The plate waves can be excited by interdigital transducer (IDT). The design method for SAW device can be also applied for the plate wave devices. As the devices using plate waves, the Quartz single crystal[1], ZnO-film/pyrex-glass composite structure[2], AlN-film/Si structure[3], $LiNbO_3$ thin single crystal plate[4] and $LiTaO_3$ thin single crystal plate[5] have been reported. The reported frequencies are lower than 600MHz in the Quartz single crystal[1], 300 MHz in ZnO-film/pyrex-glass composite structure[2] and 100 MHz in AlN-film/Si structure[3]. In addition, these materials have a small electromechanical coupling factor, and therefore can't apply the devices required wide band. On the other hand, the reported frequencies in the plate wave devices using $LiNbO_3$ and $LiTaO_3$ single crystal plate are lower than 100 MHz[4,5], but these devices have a large electromechanical coupling factor which realizes wide band. It is difficult to make very thin plate of $LiNbO_3$ or $LiTaO_3$ crystals, though $A_1$ mode of Lamb wave in the Z-cut $LiNbO_3$ or $LiTaO_3$ has a high phase velocity and a high coupling factor. If a highly orientated thin film can be realized, a high frequency such as 5 GHz and wide band device could be realized.

In this time, authors have tried to realize the high frequency device by using an anti-symmetric $A_1$ mode of Lamb wave propagating in Z-X thin $LiNbO_3$ film having high velocity and high electromechanical coupling factor. As the result, we have realized a 4.5 GHz high frequency Lamb wave resonator composed of thin $LiNbO_3$ epitaxial film/air-gap/substrate deposited chemical vapor deposition method (CVD).

ogami@murata.co.jp

## 2. Phase Velocities of Plate Waves

**Figure 1** shows the calculated phase velocities of plate waves propagating in Z-cut thin $LiNbO_3$ plate along X-axis as a function of plate thickness[6]. $A_1$ mode of Lamb wave has high velocity over 10,000 m/s, when the $LiNbO_3$ plate thickness is thinner than 0.2 λ ( λ : wavelength). Finite Element Method (FEM) was used in this calculation.

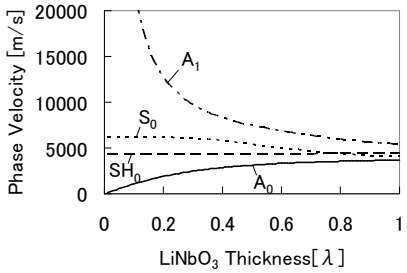


**Fig. 1 Calculated phase velocities of plate waves as a function of $LiNbO_3$ thickness**

## 3. Device Structure

To make air-gap type membrane[7] and obtain high orientated $LiNbO_3$ film, the buffer layer has been grown on a substrate. The thin $LiNbO_3$ film with thickness of about 480 nm has been deposited on the buffer layer under the condition of the heated substrate temperature of 600 to 700 degrees. The deposition rate was 12 nm/minite. After the IDT has been fablicated, the air gap has been made by remove the buffer layer. **Figure 2** (a) and (b) show a measured rocking curve and a pole figure of the thin $LiNbO_3$ film, which show good c-axis orientated epitaxial twin film because of narrow full width of half maximum (FWHM) of 0.2 degrees and 6 spots in the pole figure.

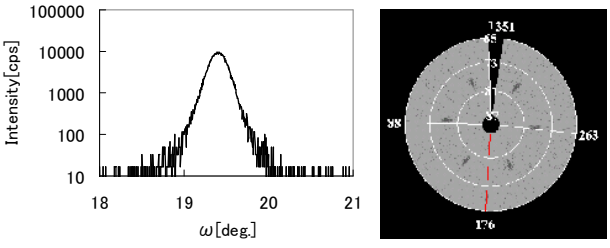


**Fig. 2 (a) Measured rocking curve and (b) pole figure of thin $LiNbO_3$ film with X-Ray Deffraction**

**Figure 3** (a) and (b) show side view and top view of a fabricated Lamb wave device, respectively. The membrane with size of 200 $\mu$m squares has been warped, so interference fringes have been seen.

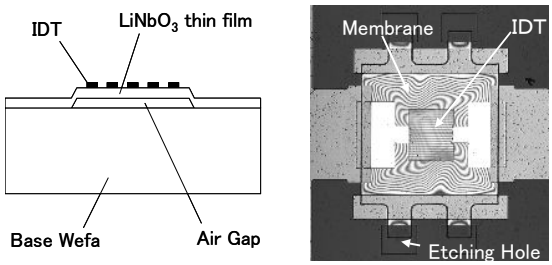


(a) (b)

**Fig. 3 Device structure (a) side view and (b) Top view**

## 4. Propaties of 1-port resonator

Thickness of the thin $LiNbO_3$ film is 0.15 $\lambda$ and Al-electrode thickness is 0.03 $\lambda$, which the IDT wavelength $\lambda$ is 3.2 $\mu$m. 1-port resonator has aperture of 15 $\lambda$ and 60 finger pairs. **Figure 4** shows the measured impedance and phase characteristics. A response seen at 4 to 5 GHz is $A_1$ mode of Lamb wave, and that seen at 0.5 GHz is $A_0$ mode one as a result of comparison with simulation. $SH_0$ mode, which should be excited at 1 to 1.5 GHz in simulation result, is not excited because of the twin crystal effect[6]. **Figure 5** shows the measured impedance and the phase characteristics around the $A_1$ mode of Lamb wave response at narrow range. The $A_1$ mode of Lamb wave has a high resonant frequency of about 4.5 GHz, which correspond high phase velocity of 14,000 m/s, and large impedance ratio of 52dB. Where the impedance ratio is $20 \times \log_{10}$(anti-resonant impedance/resonant impedance). The mechanical quality factor[8] at resonant frequency is about 170, and that at anti-resonant frequency is about 90. As a result of fitthing, electromechanical coupling factor $k^2$ has been evaluated about 18 %, which is 0.8 times of theoretical one. It is considered that quality of the thin $LiNbO_3$ film deposited by CVD is little inferior to $LiNbO_3$ single crystal.

## 5. Conclusion

Authors have tried to realize the high frequency device by using Lamb wave propagating on Z-X thin $LiNbO_3$ film deposited by CVD having high velocity and high electromechanical coupling factor. As the result, we have realized a 4.5 GHz high frequency Lamb wave resonator with high velocity of 14,000 m/s, large impedance ratio of 52dB, and wide bandwidth of 7.2 % composed of thin $LiNbO_3$ epitaxial film/air-gap/substrate.

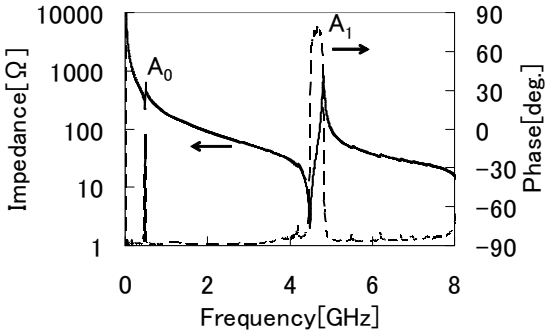


**Fig. 4 Measured impedance and phase characteristics of 1-port resonator (wide range)**

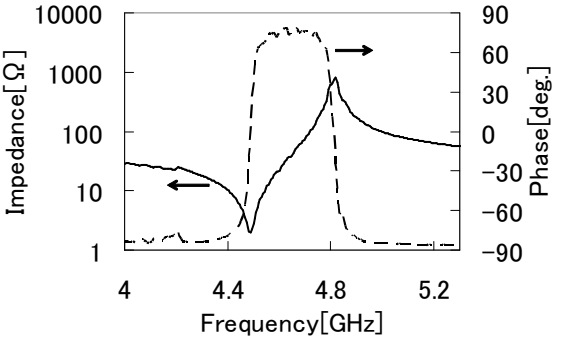


**Fig. 5 Measured impedance and phase characteristics near $A_1$ mode of Lamb wave response( narrow range)**

## References


1. Y.Nakagawa, S.Tanaka and S.Kakio: Jpn. J. Appl. Phys. **42** (2003) 3086.
2. A.Tanaka, M.Koike, F.Saito, K.Hashimoto and M.Yamaguchi: Technical Report of IEICE Japan **US91-89** (1992) [in Japanese]
3. N.Tirole, A.Choujaa, D.Hauden, G.Martin, P.Blind, M.Froelicher, J.C.Pommier and A.Cachard: Proc. IEEE Ultrason. Symp. (1993) 371.
4. K.Mizutani and K.Toda: Trans. IECE Japan **J68-A** (1985) 496. [in Japanese]
5. K.Toda and K.Mizutani: Trans. IEICE Japan **J71-A** (1988) 1225. [in Japanese]
6. M.Kadota, T.Ogami, K.Yamamoto, Y.Negoro and H.Tochishita: EM Symp. (2008) 69. [in Japanese].
7. H.Satoh, H.Suzuki, C.Takahashi, C.Narahara and Y.Ebata: Proc. IEEE Ultrason. Symp. (1987) 363.
8. K.Hashimoto: An Introduction to Simulation Technique for Surface Acoustic Wave Device (1997) 140. [in Japanese]

Proceedings of Symposium on Ultrasonic Electronics, Vol. 29 (2008) pp. 139-140
11-13 November, 2008

# A Basic Study on Face to Face Bonded SAW Devices
# 表面張り合わせによる SAW 素子の基礎検討

Takanori Yamazaki, Keishin Koh and Kohji Hohkawa (Kanagawa Institute of Technology)
山崎貴紀　黄啓新　宝川幸司　（神工大 工学部）

## 1. Introduction

Many reports on packaging of SAW devices have been reported so far [(1) – (3)]. For packaging SAW devices, we must form capping structure to cover the surface of the SAW propagating substrate. Sometimes, these capping structures effect on SAW characteristics caused by many effects, such as inherent stress, temperature dependent variation on SAW propagation characteristics and aging. These problems could be simply improved, if we would use the same substrate with SAW substrate as the capping material of the device. In this situation, we can also use capping structure as the SAW substrate. If we would form the structure of the packaging close enough to couple with each other, we could produce many new functional device using coupling modes.

In this paper, we report a simple coupled device using face to face bonded structure.

## 2. Face to Face Bonded SAW (FFB) device

As the first device, we introduce the simplest face to face bonding (FFB) device structure, shown in **Fig. 1**. Most SAW devices have IDT finger electrodes with much wider overlapping length than that required for avoiding insertion loss, due to beam spreading, which causes plane wave limit of propagation path length. If we connect in parallel two devices whose overlap length is a half size of that of the original device, they could produce almost the same response as that of original device. The device size with half overlapping length is slightly larger than the half size of original device due to increase in terminal electrodes. However, total cost of substrate would not be increased, because smaller chip size enables to reduce thickness of the substrate.

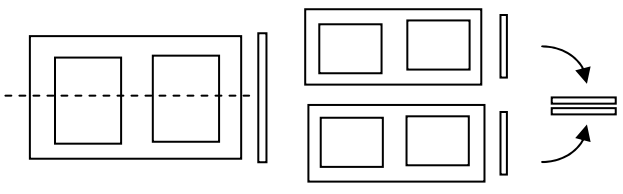


Fig. 1 FFB device

hk-yama@ele.kanagawa-it.ac.jp

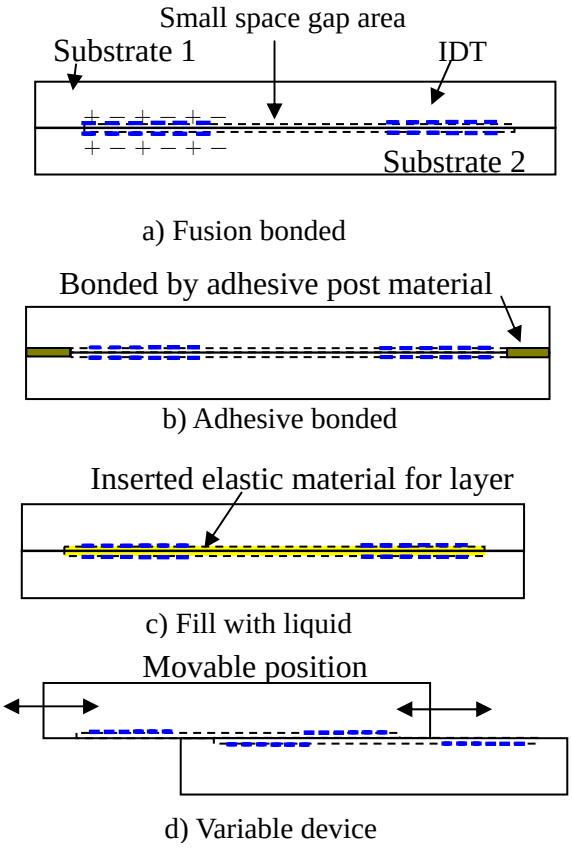


Fig. 2 FFB devices under consideration

From simple device structures shown in **Fig. 2**, it is clear that the FFB device is one of waveguide coupled device, similar to the MSC devices[(4)], when the separation of the surfaces of two propagation path is closed. It is clear that the same functional devices as that of MSC devices could be formed. On the other hand, if the spacing of two substrates is designed to be relatively large, it could be a packaging structure with relatively high performance, as discussed in the following section.

## 3. Fabrication process of FFB SAW device

There are several device fabrication methods depending on the function of the device. **Fig. 3** illustrates typical process step for FFB-SAW device. In these process steps, difficulty exists how to dice bonded wafers into multiple chips, maintaining electrical lead line connection to the external space. This is especially difficult for the mode coupled device which utilizes face to face coupled operation

with narrow spacing between substrates. We form dimple on the substrates surface to make spacing on the surface edge of counter chip. This process could be carried out by chemical etching process or mechanical technology such as sand blast milling.

## 4. Basic Experiment

We fabricated test devices using Quartz substrate and buried IDT electrode which is formed using dry etching technology and lithograph technology. **Tab. 1** shows device parameters of test devices. We investigated boned method using adhesive materials, such as film resist and water glass ($SiO2:Na_2O$) **Fig. 4** shows photograph of test devices. We estimated basic characteristics of FFB-SAW devices. **Fig. 5** shows measured results. The SAW devices with buried IDT electrode show relatively good frequency characteristics. After bonding, there is no change in the frequency characteristics. We are studying dependence of frequency characteristics on bonding conditions.

## 5. Conclusion

We proposed a small, low cost and simple packaging method for SAW device in which two devices chips with a half overlapping length with an original device, are bonded in face to face. We investigated process condition such as adhesive materials heating method etc. and fabricated test devices. The basic experiments results indicate possibility of FFB technology for realizing coupled devices.

**Acknowledgment**

We would like to thank Mr. Okitsu and Mr. Oshiyama for their contribution on the process. This work is partially supported by the fund from Education Culture, Sports, Science and Technology.

**References**

1. M. Goetz and C. Jones, Proceeding of Electronics manufacturing technology Symposium, 2002, pp. 63-69.
2. O. Ikata, Y. Kaneda, S. Ono, K. Sakinada, O. Kawachi, Y. Tanimoto, Third International Symposium on Acoustic Wave devices for Future Communication System CD-ROM, 2007
3. K. Koh, T. Yamasaki, and K. Hohkawa, Proceedings of 2007 IEEE Ultrasonic Symposium, （CD media）, pp.1890-1893, 2007.
4. O. Kawachi, K. Sakinada, Y. Kaneda and S. Ono, Proceeding IEEE Ultrasonic Symposium, 2006, pp. 2289-2292.
5. F. G. Marshall, C.O. Newton and H. I. S. Paige, IEEE Trans., MTT 21, PP.195-205 (1973)

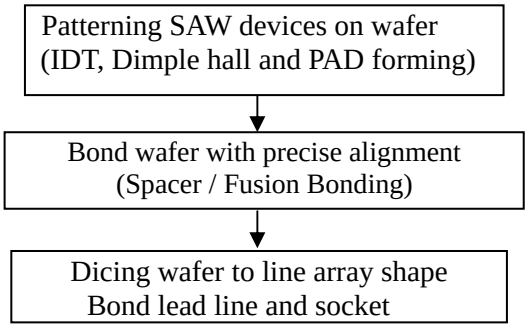


Fig. 3 Fabrication process steps

Tab. 1 Device parameters

| | |
|---|---|
| Substrate | Quartz ST cut |
| IDT line & space | 2μm:2μm |
| Electrode material | Al thickness 100nm |
| Overlap. length | 178 μm |
| Number of pairs | 100-100 pairs |
| Dry etching condition | $CF_4$:Ar 100W 5min |
| Bonding condition | 100℃, 10min 0.05MPa |

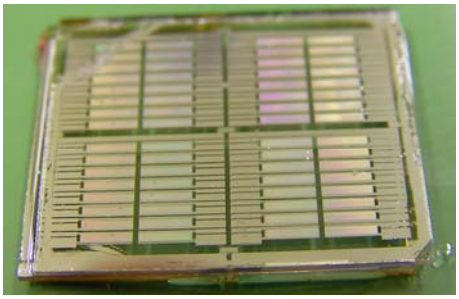

Fig. 4 Photograph of test devices

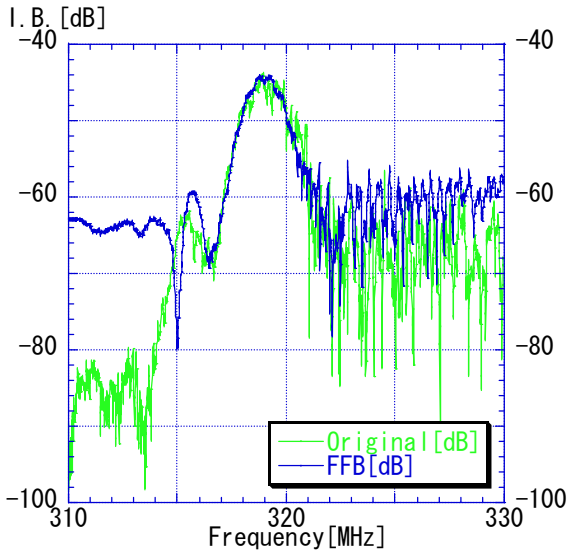


Fig. 5 Frequency characteristics of SAW devices after face to face bonding.

Proceedings of Symposium on Ultrasonic Electronics, Vol. 29 (2008) pp. 141-142
11-13 November, 2008

# Experimental study of SAW propagation characteristics on a slotted $SiO_2$ film/embedded grating electrodes/128° YX-$LiNbO_3$ structure

# $SiO_2$ 装荷による SAW 伝搬特性制御に関する実験的検討

Kumiko Konishi†, Akitoshi Omata, Tatsuya Omori, Ken-ya Hashimoto, and Masatsune Yamaguchi (Graduate School of Engineering, Chiba University)
小西くみこ†，小俣晋紀，大森達也，橋本研也，山口正恆 （千葉大学　大学院工学研究科）

## 1. Introduction

Surface acoustic wave (SAW) devices are widely used in various mobile communication systems because of their excellent performances in frequency selectivity, physical size, insertion loss,etc.

In particular, when developing wide band SAW devices, one should mind their temperature stability; in general, highly piezoelectric substrates employed to maximize their bandwidth possess a poor temperature coefficient of frequency (TCF). Previous work[1][2][3] has shown that $SiO_2$ films deposited on an SAW propagation surface are most effective in improving TCF.

Fabricating a slotted $SiO_2$ film on a 128° YX-$LiNbO_3$ substrate, the paper attempts to control an SAW reflection coefficient of grating electrodes to be embedded in the slots as well as to improve TCF.

First, the fabrication process making skillful use of ion milling and reactive ion etching (RIE) techniques is discussed, which enables to control the thicknesses of the slotted $SiO_2$ film and grating electrodes embedded in the slots independently. This suggests that SAW devices may be developed suitable for various applications.

Next, the process is applied to the fabrication of an SAW transversal filter. The result shows that the reflection coefficient is able to be controlled without deteriorating the filter performance.

## 2. Fabrication process

**Fig. 1** shows the process applied to the fabrication of a slotted $SiO_2$ film on a 128° YX-$LiNbO_3$ structure.

1. Deposition of a $SiO_2$ film on a 128° YX-$LiNbO_3$ substrate by chemical vapor deposition (CVD).
2. Resist coating.
3. Drawing of a resist pattern by electron beam lithography.
4. Development of the resist pattern.
5. Evaporation of Cu and Cr layers used as a mask for ion milling and RIE.
6. Resist removal by a lift-off technique.
7. Slotting of the $SiO_2$ film by ion milling and RIE.
8. Evaporation of Al grating electrode layers.
9. Removal of the Cu and Cr mask.

The process makes it possible to control the thicknesses of the slotted $SiO_2$ film and Al grating electrodes embedded in the slots independently.

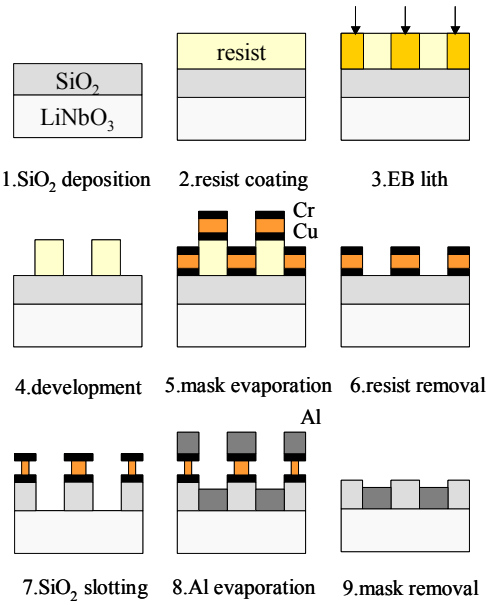


Fig.1 Fabrication process

## 3. Slotting of $SiO_2$

The mask used for ion milling consists of a composite Cr/Cu/Cr layer (see Process 6 in Fig. 1). Due to a faster etching rate for Cu than Cr, accordingly, both side faces of the mask layer are expected to be etched in such shape of "**I**" as shown in Process 7 in Fig. 1. This under-etched "**I**" shape is effective in removing the Al layer on the top Cr layer, leaving the embedded Al electrodes in the slots as they are.

In addition, the application of RIE after ion milling is proposed, by which residual substances left in the slots are effectively removed. **Fig. 2(a)** shows the SEM image of the etched substrate and mask surfaces, while Fig. 2(b) shows the cross-sectional view of the mask layer etched in

---

cumico@graduate.chiba-u.jp

the shape of "**I**". Both images confirm the successful application of ion milling and RIE techniques to the fabrication of the slotted $SiO_2$ film.

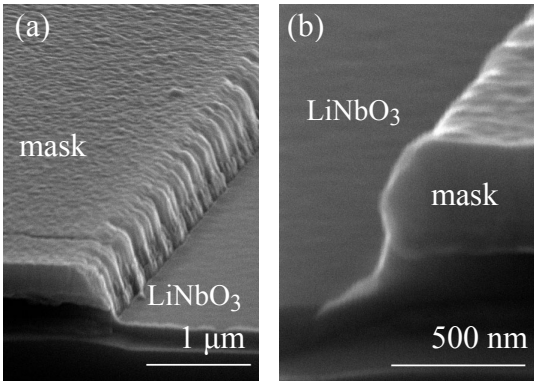


Fig.2 SEM images after the ion milling and RIE

## 4. Fabrication of an SAW transversal filter

The developed process was applied to the fabrication of an SAW transversal filter consisting of two identical interdigital transducers (IDTs), which are embedded in the slotted $SiO_2$ film.

**Fig. 3** shows the optical microscope and SEM images of the fabricated filter. Here the thicknesses of the Al grating and $SiO_2$ film are 100 nm and 200 nm, respectively. As to the IDT, the electrode periodicity (=one wavelength of an SAW), the number of the electrodes and the aperture length are 16 μm, 10 and 120 μm, respectively.

It is clearly seen from Fig. 3 that the Al IDT electrodes are successfully embedded in the slotted $SiO_2$ film without any defects. This shows that the process discussed above enables to fabricate SAW devices having specified structures.

**Fig.4** compares the frequency response of the filter consisting of the embedded IDTs with that of the filter employing non-embedded IDTs. As can be seen in the figure, both center frequency and insertion loss are almost identical with each other. On the other hand, the small distortion of the passband shape suggests that the reflection coefficient of the grating electrodes could have approximately been doubled by embedding the IDTs.

## 5. Conclusion

This paper proposed the fabrication of a slotted $SiO_2$ film on a 128° YX-$LiNbO_3$ substrate, by which SAW reflection characteristics can be controlled with improved temperature stability.

The process employing both ion milling and RIE techniques was applied to the fabrication of the slotted $SiO_2$ film. This makes it possible to embed grating electrodes in the slotted $SiO_2$ film.

The process is applied to the fabrication of an SAW transversal filter consisting of two embedded IDTs. The result suggested that the reflection coefficient could be controlled without deteriorating filter performances.

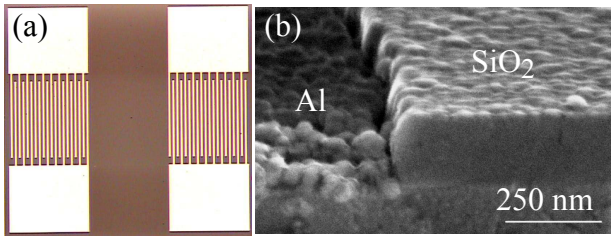


Fig.3 Fabricated filter

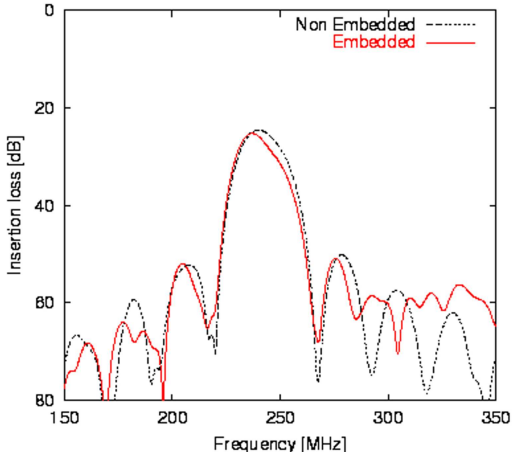


Fig.4 Frequency response of the filter using embedded and non-embedded IDTs

**Acknowledgment**

The authors are indebted to Mr. Yuzo Murasawa of Chiba University for his assistance. We also thank the members of Venture Business Laboratory of Chiba University for providing the experimental facilities. This work was partially supported by the Grant-in-Aid for Scientific Research from the Japanese Society for the Promotion of Science, and the Project to Develop "Innovative Seeds" from the Japanese Science and Technology Agency.

**References**

1. K.Yamanouchi and T.Ishii: Jpn. J. Appl. Phys. **41** (2002) pp.3480-3482
2. T.Nakao, M.Kadota, K.Nishiyama, Y.Nakai, D.yamamoto, Y.Ishiura, T.Komura, N.Nakada, and R.Kita: Jpn. J. Appl. Phys. **46** (2007) pp.4760-4763
3. H.Nakamura, H.Nakanishi, T.Tsurunari, K.matsunami and Y.Iwasaki: Proc. Ultrason. Symp. (2007) pp.488-491

Proceedings of Symposium on Ultrasonic Electronics, Vol. 29 (2008) pp. 143-144
11-13 November, 2008

# Leaky-SAW Properties on Reverse-Proton-Exchanged $LiNbO_3$
# 逆プロトン交換$LiNbO_3$基板上のリーキー表面波伝搬特性

Hidenori Shimizu‡, Shoji Kakio and Yasuhiko Nakagawa (Univ. of Yamanashi)
清水秀徳‡，垣尾省司，中川恭彦 （山梨大院・医工）

## 1. Introduction

Leaky surface acoustic waves (LSAWs) have an inherent attenuation because LSAWs lose energy by continuously radiating the bulk wave into the substrate. Because of this property, the cut of the substrate with a smaller attenuation is used in the LSAW device. The authors reported that, in a certain range of rotation angles for rotated Y-X $LiNbO_3$ (LN), the attenuation can be reduced by forming a proton-exchanged (PE) layer with an elastically soft property on the substrate.[1] However, by carrying out the PE process, the piezoelectric property is nearly eliminated and the coupling factor $K^2$ is reduced.

On the other hand, reverse proton exchange (RPE) has been proposed as a method of exchange lithium ions and protons on the PE layer to fabricate buried optical waveguides.[2] It can be expected that the RPE layer with a property similar to that of bulk LN prevents the degradation of $K^2$ and the buried PE layer reduces the LSAW attenuation.[3]

In this study, first, a layered structure of air/bulk LN/softened LN was assumed for the rotated Y-X LN and the LSAW attenuation was calculated. Next, the RPE layer and the buried PE layer were formed on the 41° Y-X LN and the LSAW propagation loss (*PL*) was measured.

## 2. Theory

The substrate structure after RPE process has a four-layered structure as shown in **Fig. 1(a)**. For convenient calculation, a three-layered structure of air/bulk LN/softened LN was assumed as shown in **Fig. 1(b)**. The elastic constants $c'_{ij}$ of the softened LN were expressed by $Ac_{ij}$, where $c'_{ij}$ are bulk values and $A$ is a parameter. The elastic constant of the PE layer are approximately 60% of those of bulk LN. The elastic constant is considered to be recovered by annealing effect during the PRE process. Therefore, the parameter $A$ was set to be ranged from 0.6 to 1.0.

**Figure 2** shows the calculated phase velocity as a function of the rotation angle from Y-axis when the normalized depth $d/\lambda$ of the bulk LN layer was fixed to be 0.2 λ, for (a) the free and (b) metallized surface cases. The corresponding attenuations are shown in **Fig. 3**.

g08me015@yamanashi.ac.jp

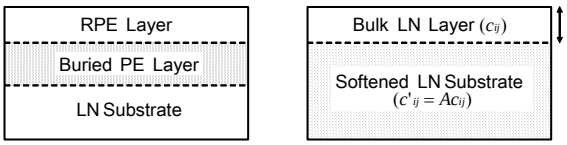


(a) RPE LN (b) Analytical model

Fig. 1 Structures of RPE LN and analytical model.

According to the decrease of the elastic constant of the substrate, it seems that the range of rotation angles giving zero attenuation markedly expanded for free surface [Fig. 3(a)]. It appears in a wide range of -30°~95° at $A$=0.6. The phase velocity decreases monotonously with the decrease of the elastic constant [Fig. 2(a)]. The phase velocity of a fast shear bulk wave in the softened LN is also decreased. The range of the rotation angles which the LSAW phase velocity exceeds that of the bulk wave expanded. The LSAW solution is not obtained in this range. However, the attenuation is vanished to zero immediately before the LSAW phase velocity exceeds that of the bulk wave.

On the other hand, for the metallized surface, the

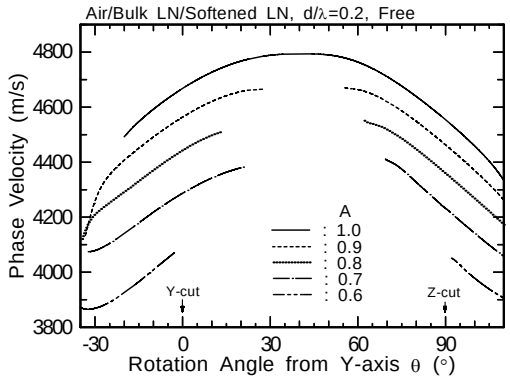


(a) Free

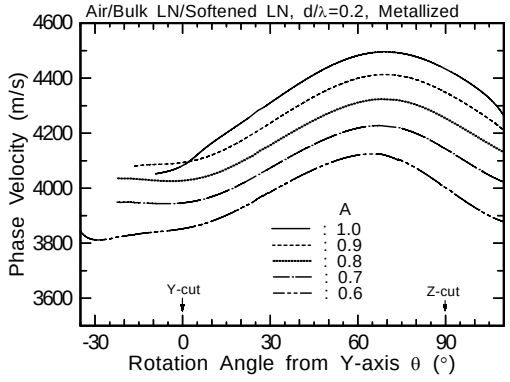


(b) Metallized

Fig. 2 Calculated phase velocity.

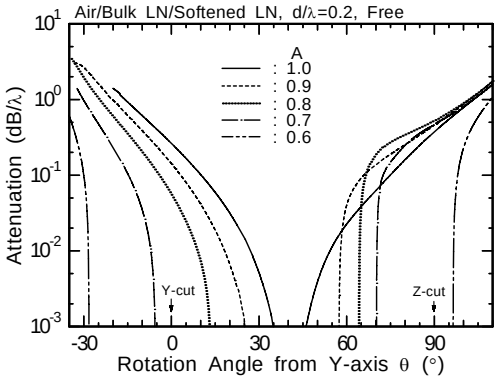


(a) Free

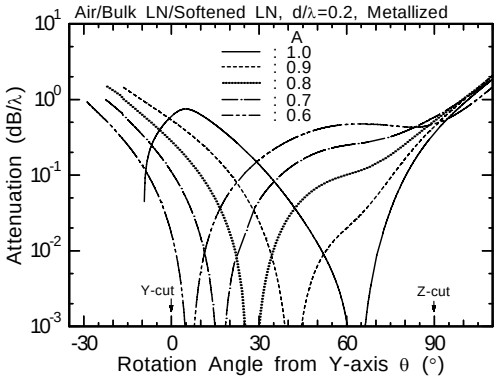


(b) Metallized

Fig. 3 Calculated attenuation.

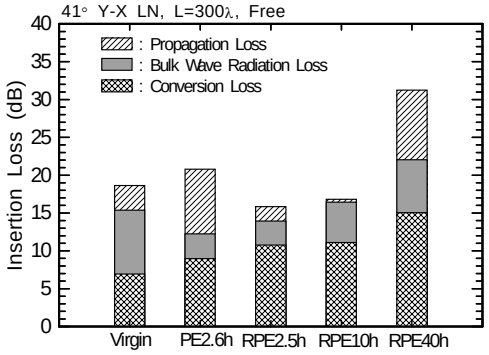


(a) Free

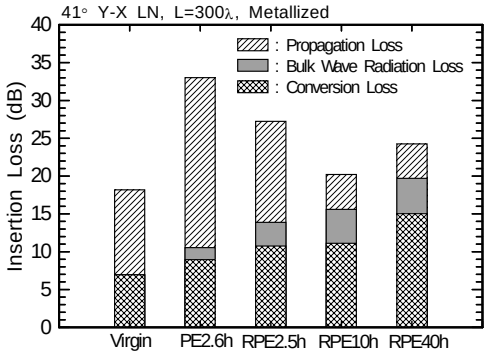


(b) Metallized

Fig. 4 Details of insertion loss of 41° Y-X LN sample.

solution exists in the rotation angle range because the phase velocity is slower than that of the bulk wave [Fig. 2(b)]. The rotation angle giving zero attenuation shifts from 64° toward 5° [Fig 3(b)].

## 3. Experiment

A simple delay-line sample with different depths of the RPE layer was fabricated on 41° Y-X LN substrate. First, the PE layer with a depth of 1.9 μm was formed by immersing the LN substrate in a solution of benzoic acid (Li 0.1 mol%) at 240°C for 160 min. Next, the RPE layer was formed by immersing the PE sample in an equimolar mixture of $LiNO_3$-$NaNO_3$-$KNO_3$ at 300°C for 2.5 h, 10 h, or 40 h. Finally, interdigital transducers (IDTs) with a period length λ of 20 μm and 8 split-finger pairs were fabricated on the sample using Al film.

Using a network analyzer, the frequency response was measured. **Figure 4** shows the insertion loss (*IL*) for *L*=300 λ as a histogram. The *IL* for both surface cases that increased after the PE process was recovered by carrying out the RPE process. Further RPE process increases the value. The *PL* was estimated by subtracting the *IL* with a path length of 100 λ from that of 300 λ. The values of the *PL*, the conversion loss (C*L*), and the bulk wave radiation loss are also shown in Fig. 4. The *PL* for the metallized surface was decreased by carrying out the RPE process for 10 h from 0.036 dB/λ of a virgin sample to 0.015 dB/λ. The decrease of the *PL* for the free surface was also observed. The *CL* was increased after the RPE process because the $K^2$ was reduced in above fabricating conditions.

## 4. Conclusion

The LSAW properties on the rotated Y-X LN substrate with the RPE layer and the buried PE layer were investigated. First, a layered structure of air/bulk LN/softend LN was assumed the LSAW attenuation was calculated. The rotation angle from Y-axis giving zero attenuation shifted from 64° toward 5° for a metallized surface. The range of the rotation angles which the LSAW phase velocity exceeds that of a fast shear bulk wave markedly expanded in a wide range of -30°~95° for a free surface while the attenuation was vanished at these boundaries. Next, the measured *PL* on 41° Y-X LN was decreased by carrying out RPE process.

We will experimentally apply the layered structure to a 5°~15° rotated Y-X LN substrate with a large $K^2$.

## References

1. S. Kakio *et al.*, IEICE Trans. **J80-A** (1997) 1830 [in Japanese].
2. J. Olivares and J. M. Cabrera, Appl. Phys. Lett. **62** (1993) 2468.
3. M. Maeda, S. Kakio, and Y. Nakagawa, Proc. USE2007 (2007) 93.

Proceedings of Symposium on Ultrasonic Electronics, Vol. 29 (2008) pp. 145-146
11-13 November, 2008

# AlGaN/GaN device using buried electrode structure
# 埋め込み形電極構造を用いた AlGaN/GaN 素子

Yuji Terao, Satoshi Oshiyama, Keishin Koh and Kohji Hohkawa
(Kanagawa Institute of Technology.)
寺尾有司　押山聡　黄啓新　宝川幸司　（神工大 工学部）

## 1．Introduction

AlGaN/GaN film has been expected and used for high speed systems such as satellite communication and ultra high speed optical transmission systems [1]. Focused on its piezoelectric properties, it is also expected for SAW devices at the same high frequency range and many research results are reported so far [2-4]. This paper investigates new surface acoustic wave devices which consist of transducers having 2 DEG layer electrodes.

There exists a thin 2 DEG layer with relatively high conductivity in the interface of the AlGaN/GaN film. Difference of this structure from conventional transducers with metal electrodes, is the transparency nature of the conductive layer and existing of AlGaN laver over it. This structure would simplify the device fabrication process. In addition, this structure might have produced a new functional operation by changing 2 DEG layer as conductive electrodes.

## 2. SAW device structures consisting of 2DEG electrodes

It is possible to form many kinds of device structures for making SAW device consisting of 2 DEG conductive electrodes. Here, we consider three structures illustrated in **Fig. 1**.

a) We form this structure by simply etching AlGaN film layer existing on the space region of transducer using gas plasma etching equipment. .
b) We fabricate simply metal space patterns on the AlGaN/GaN film. The 2 DEG electrodes are formed by applying negative bias potential on it so that carriers under electrodes may move to the region of transducer.
c) We form comb shaped AlGaN layer and place gate electrodes to enhance carrier densities in 2 DEG layer corresponding finger electrodes. By applying positive potential, we can enhance carrier density of finger electrodes.

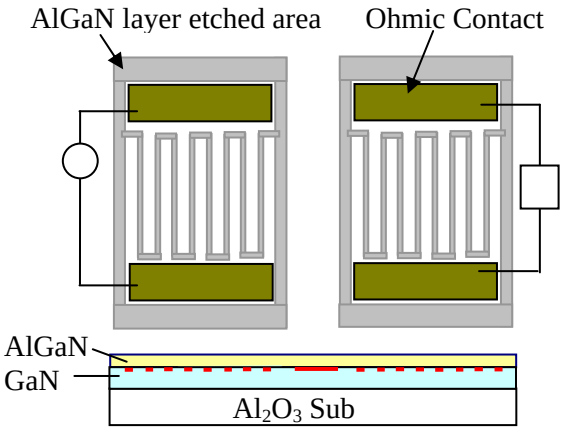


a) AlGaN layer IDT

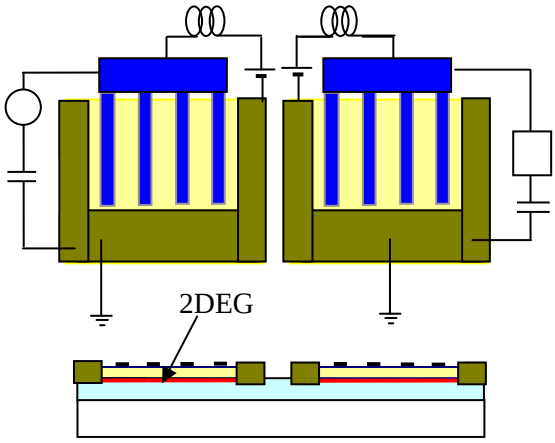


b) Suppress by metal

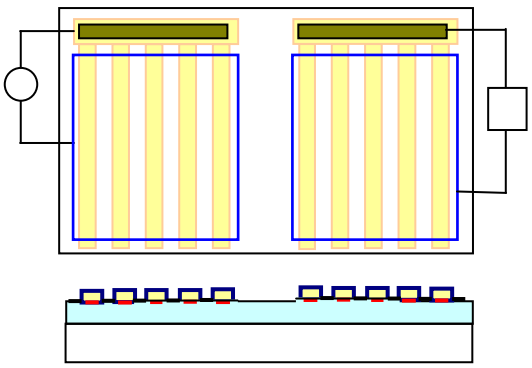

c) Metal cover

Fig. 1 Various type of 2DEG IDT

oshiyama@ele.kanagawa-it.ac.jp

### 3. Experimental and result

We fabricated test devices with structure as shown in **Fig. 1**. Table I shows their parameters. The film with the layer with AlGaN film thickness of 0.02 μm correspond the layer used for HEMT. An AlGaN/GaN film was deposited on a (0001) sapphire substrate by metal organic chemical vapor deposition, and the aluminum mole fraction of the AlGaN layer was nominally 0.255. The space area of transducer in **Fig. 1** is formed by using dry etching process. We formed Aluminum electrode patterns using liftoff method and also formed Ohmic contact pads consisting of Ti/Al by heating samples at 800℃, for 45s. An example of test devices photograph show in **Fig. 2**.

We used microwave probes and a network analyzer (Anritsu MS4623B) to estimate the frequency characteristics of test devices. **Fig. 3** shows an example of frequency characteristics for a test device. The experimental results of devices with 2 DEG electrodes, especially devices with thick AlGaN layers, have shown a relatively large insertion loss due to poor conductivity of films. These devices seem to be rather pessimistic for passive device application, such as resonator and filters. However, when the carrier densities under 2 DEG are increased by DC bias or light induced method, the filed effect due to SAW could be enhanced and the good frequency characteristics could be expected. We are now investigating

### 4. Conclusion

We estimated AlGaN/ GaN SAW devices consisting of 2 DEG layer electrodes. We fabricated test devices with various electrodes patterns and estimated basic characteristics. We observed generation and detection of SAW in AlGaN/GaN system by electrode of 2 DEG. It is very poor compared with the metal electrode. But, some results indicated that AlGaN/GaN system with this structure would realize variable SAW devices operating at high frequency using field modulation. In enhance preference of the device, we are preparing higher frequency devices by electron beam lithograph technology and investigating optimum electrode structure. We also discuss possibility of application as optical sensor.


### Acknowledgment

We would like to thank Mr. Okitsu and Mr. Oshiyama for their contribution on the process. This work is partially supported by the fund from Education Culture, Sports, Science and Technology.


### References


1. C. Deger, E. Born, H. Angere, O. Ambacher, M. Stutzmann, J. Hornsteiner: Applied Phyisics. Letters, **72**, (1998) 2400.
2. N. Shigekawa, K. Nishimura, H. Yokoyama and K. Hohkawa: Applied. Phyisics Letters, **87** (2005) 084102
3. N. Shigekawa, K. Nishimura, T. Suemitsu, H. Yokoyama and K. Hohkawa; Applied Phyisics Letters, **89**, (2006) 033.
4. T. Mizusawa, M. Wada, K. Koh, K. Nishimura, N. Sigekawa, and K. Hohkawa: Proc. Symposium on Ultrasonic Electronics, **26**, (2005) 223.


Table 1. Parameters used for the experiments

| | |
|---|---|
| Substrate | AlGaN / GaN / $Al_2O_3$ |
| Thickness of AlGaN film | 0.02 , 0.1, 0.3 μm |
| Thickness of GaN film | 2 μm |
| IDT line &space | 2μm:2μm |
| Overlap. length | 200 μm |
| Number of pairs | 50-50 pairs |

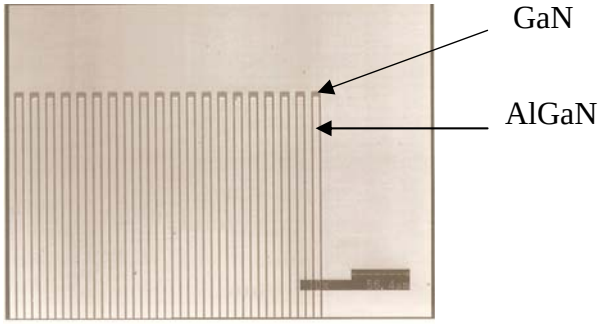


Fig. 2 Photograph of test device.

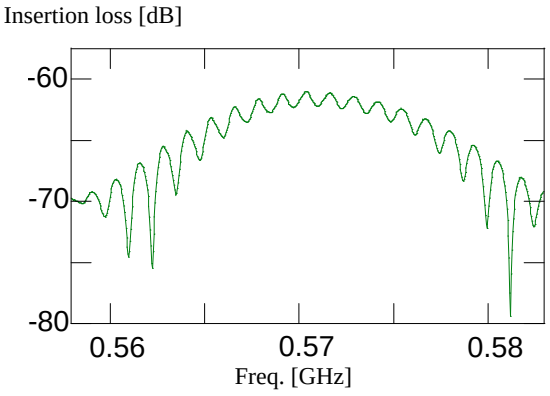


Fig. 3 Frequency characteristics of AlGaN/GaN SAW device used 2 DEG as electrodes.

Proceedings of Symposium on Ultrasonic Electronics, Vol. 29 (2008) pp. 147-148
11-13 November, 2008

# Fabrication of Highly Oriented $Ta_2O_5$ Piezoelectric Thin Films by RF-Magnetron Sputtering

高周波スパッタリング法による高配向$Ta_2O_5$圧電薄膜の作製

Takeshi Mitsui‡, Akinori Tsuchiya, Shoji Kakio and Yasuhiko Nakagawa (Univ. of Yamanashi)
三井 剛‡，土屋彰教，垣尾省司，中川恭彦（山梨大院・医工）

## 1. Introduction

For the development of high-performance piezoelectric devices, such as surface acoustic wave (SAW) and film bulk acoustic resonator (FBAR) devices, piezoelectric thin films required to realize high coupling, high stability, low loss and high frequency have been widely studied. An *X*-axis-oriented tantalum pentoxide $Ta_2O_5$ piezoelectric thin film is a relatively new material developed by one of the authors, and has features, such as a large piezoelectric property similar to that of ZnO thin films and a high dielectric constant.[1,2] Investigations on the preparation conditions to improve the properties have been carried out.[3-5]

On the other hand, the authors reported that, in the deposition of potassium niobate $KNbO_3$ thin films using an RF-magnetron sputtering system with a long-throw sputter (LTS) cathode and an $O_2$-radical source, a high (110)-orientation and a smooth surface were obtained.[6]

In this paper, the *X*-axis-oriented $Ta_2O_5$ thin films were deposited on a fused quartz substrate using the RF-magnetron sputtering system. The degree of orientation and the electromechanical coupling factor ($K^2$) for the Rayleigh-type SAW were evaluated.

## 2. Deposition of $Ta_2O_5$ thin film

**Figure 1** shows the configuration of the RF-magnetron sputtering system with long-throw sputter (LTS) cathodes and the $O_2$-radical source used for the deposition of the $Ta_2O_5$ thin film on a fused quartz substrate.

The sputtering parameters are shown in **Table I**. A metal tantalum target with 50 mm diameter was used and the distance between the target and the substrate was 100 mm. The substrate temperature $T_S$ was varied from 650˚C to 750˚C. The RF power applied to the cathode and radical source was 150 W. The atmosphere gas flow rate Ar:Ar for the two cathodes with/without the target was 30:3 ccm and the $O_2$ flow rate for the radical source was varied from 4 to 10 ccm, while the atmosphere gas pressure was fixed to be 0.75 Pa. The deposition time was 5 h and the deposition rate ranged from 0.54 to 1.73 μm/h.

---

g08me030@yamanashi.ac.jp

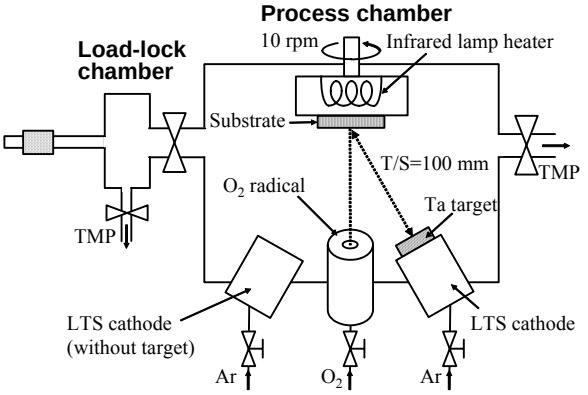


Fig. 1 Configuration of RF-magnetron sputtering system.

Table I Sputtering parameters.

| | |
|---|---|
| Substrate | Fused quartz |
| Substrate temperature (˚C) | 650 ~ 750 |
| Gas flow rate, Ar : Ar : $O_2$ (ccm) | 30 : 3 : 4 ~ 10 |
| Gas pressure (Pa) | 0.75 |
| Target-substrate distance T/S (mm) | 100 |
| Target power (W) | 150 |
| $O_2$-radical power (W) | 0 ~ 150 |
| Deposition time (h) | 5 |
| Film thickness (μm) | 2.70 ~ 8.65 |
| Deposition rate (μm/h) | 0.54 ~ 1.73 |

## 3. Evaluation of $Ta_2O_5$ thin film

The degree of orientation was evaluated from X-ray diffraction (XRD) patterns. **Figure 2** shows XRD patterns for the $O_2$-radical power of (a) 150 W and (b) 0 W when $T_S$ and the $O_2$ flow rate were 700˚C and 6 ccm, respectively. As can be seen from these XRD patterns, it was found that supplying the RF power to the $O_2$-radical source markedly activated the preferred (200)-axis orientation.

The degree of orientation was sensitive to changes of $T_S$ and the $O_2$ flow rate. The full width at half maximum of the peak at 750˚C decreased to a half value of that at 700˚C. However, the peak almost disappeared at 650˚C. Moreover, when the $O_2$ flow rate was 10 ccm, the orientation similar to that for 6 ccm was obtained. On the other hand, when the $O_2$ flow rate was 4 ccm, several spurious peaks were observed in the XRD pattern and a polycrystalline thin film was deposited.

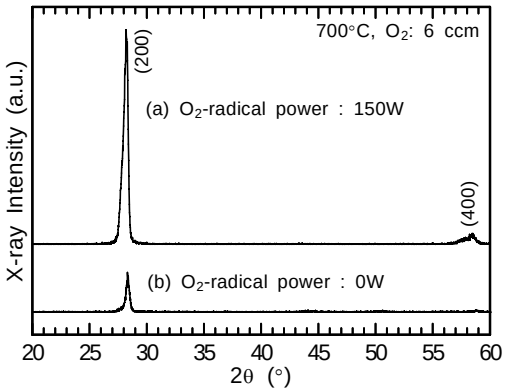


Fig. 2 XRD patterns of $Ta_2O_5$ thin film deposited by $O_2$-radical power of (a) 150 W and (b) 0 W.

Table II Measured coupling factor $K^2$.

| | $T_S$ (°C) | $O_2$-radical power (W) | $O_2$ (ccm) | $h$ (μm) | $h/\lambda$ | $K^2$ (%) |
|---|---|---|---|---|---|---|
| (a) | 700 | 150 | 6 | 5.50 | 0.275 | 0.12 |
| (b) | 700 | 0 | 6 | 2.58* | 0.129 | 0.02 |
| (c) | 700 | 150 | 10 | 2.70 | 0.135 | 0.23 |
| (d) | 650 | 150 | 6 | 3.63 | 0.182 | ~ 0 |
| (e) | 750 | 150 | 6 | 3.43 | 0.172 | ~ 0 |

*deposition time: 3.5 h

Interdigital transducers (IDTs) with a period length λ of 20 μm and 30 single-finger pairs were fabricated on the deposited film using Al film. The electromechanical coupling factor ($K^2$) for the Rayleigh-type SAW was evaluated from the measured admittance property.

**Table II** shows the measured $K^2$ corresponding to the above-mentioned sputtering parameters. When the substrate temperature $T_S$ was 700˚C, the piezoelectric property in the deposited thin film was observed. The $K^2$ of the sample (c) with the $O_2$ flow rate of 10 ccm was measured to be 0.23% for the normalized thickness $h/\lambda$ of 0.135. This value is about half of that for the previously obtained *X*-axis-oriented $Ta_2O_5$ thin film using a DC diode sputtering system.[2] On the other hand, the $K^2$ of the sample deposited at 750˚C was negligible small in spite of its high orientation. Therefore, the piezoelectric property was sensitive to substrate temperature.

**Figure 3** shows the measured frequency response for the sample (c) with the $K^2$ of 0.23%. The propagation loss was estimated to be approximately 0.05 dB/λ from the minimum insertion loss of 26.1 dB, the conversion loss of 20.3 dB, and the propagation length of 130 λ.

**Figure 4** shows a surface morphology image obtained by atomic force microscopy (AFM) for the sample (c). The root-mean-square roughness *Rq* was measured to be 9.8 nm over a typical 10 x 10 $\mu m^2$ region.

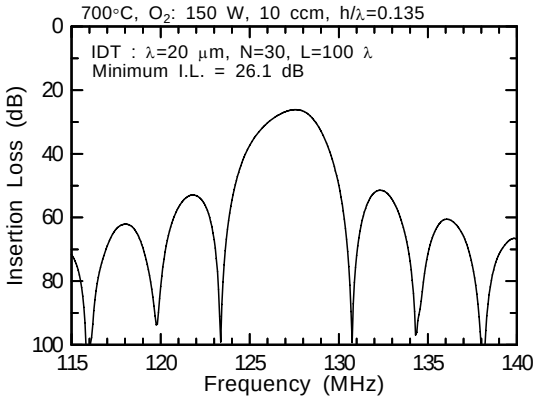


Fig. 3 Frequency response of IDT/$Ta_2O_5$ thin film/fused quartz sample (c).

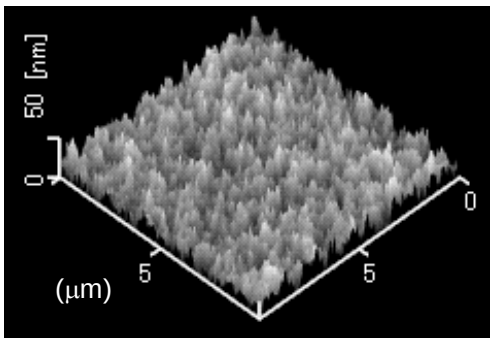


Fig. 4 AFM image for $Ta_2O_5$ thin film sample (c).

## 4. Conclusions

The *X*-axis-oriented $Ta_2O_5$ piezoelectric thin films were deposited using an RF-magnetron sputtering system. Supplying the RF power to the $O_2$-radical source markedly activated the preferred (200)-axis orientation. When the substrate temperature was 700˚C, the coupling factor $K^2$ was measured to be 0.23% for the normalized thickness $h/\lambda$ of 0.135.

Further optimization of sputtering condition will be investigated to obtain a higher piezoelectric property.

## References

1. Y. Nakagawa and Y. Gomi: Appl. Phys. Lett. **46** (1985) 139.
2. Y. Nakagawa and T. Okada: J. Appl. Phys. **68** (1990) 556.
3. Y. Nakagawa and T. Igarashi: Jpn. J. Appl. Phys. **41** (2002) 3285.
4. Y. Nakagawa, I. Morita, M. Takahashi and S. Kakio: Jpn. J. Appl. Phys. **46** (2007) 4441.
5. S. Wu and B. Houng: Proc. Japan-Taiwan Workshop on Future Frequency Control Devices (2007) 57.
6. S. Kakio, H. Kurosawa, T. Suzuki and Y. Nakagawa: Jpn. J. Appl. Phys. **47** (2008) 3802.

1P5-11

Proceedings of Symposium on Ultrasonic Electronics, Vol. 29 (2008) pp. 149-150
11-13 November, 2008

# Variation of SAW velocity and propagation loss by grain boundaries

## 結晶粒界による薄膜 SAW 速度と損失の変化

Shingo Chida[1†], Tomoaki Karaki[1], Masatoshi Adachi[1],
Makoto Furuhata[2], Takamitsu Higuchi[2] and Tsukasa Funasaka[2]
([1]Toyama Prefectural Univ.; [2]SEIKO EPSON CORPORATION)
千田進悟 [1†], 唐木智明 [1], 安達正利 [1], 古畑誠 [2], 樋口天光 [2], 舩坂司 [2]
([1] 富山県立大, [2] セイコーエプソン株式会社)

### 1. Abstract

High frequency communication devices including thin film surface acoustic wave (SAW) filter, film bulk acoustic resonator (FBAR), as well as micro-electromechanical systems (MEMS) use piezo-electric thin films (PZT, $LiNbO_3$, AlN, ZnO) as actuating elements.

However, sound velocity of polycrystalline piezo-electric films is sometimes different from that calculated using published single-crystal elastic constants. There is reason to believe that that was caused by grain boundaries. In this work, elastic constants of thin films were calculated by using a composite model. In addition, because complex elastic constants were introduced in the calculation, propagation loss was evaluated, and a good result was obtained.

### 2. Difference between measured value and simulation

The structure of SAW filter used in this work is Si/ZnO/IDT. Figure 1 shows the simulation values (solid line), measured values of Rayleigh and Sezawa waves (point) vs. the *kh* value of ZnO film from 0.1 to 3.0. There is a tendency that the difference between the measured values and the simulation values increases with the film thickness. It seems that the influence of the elastic constants is quite large in the case.

### 3. Reason of the difference

Scanning electron microscopy (SEM) image of etched surface of the ZnO film is shown in Fig. 2. The black areas are the grain boundary of the ZnO film. The grain boundary is considered the reason of the difference in propagation velocity and loss. Therefore, a composite model was used to calculate the material elastic constants for simulation of SAW propagation properties.

---

s754008@st.pu-toyama.ac.jp

### 4. Calculation of elastic constants

It is effective to apply the micro-elastic theory for calculating elastic constants of a composite material. The ratio of grain boundary to grain volume was readout from Fig. 2. We considered that the two kinds of materials were series-arranging in film plane and parallel-arranging in film thickness direction. So that the composite-modeled elastic constants will be much different to the crystal values, resulting in a change of the velocity.

### 5. Simulation results

Figure 3 shows the simulation results of wave velocity (line) using composite-modeled elastic constants. The simulation values got closer to the measured values for both Rayleigh and Sezawa waves than those of before.

### 6. Evaluation of propagation loss

Complex elastic constants were introduced into this model and used for evaluation of propagation loss. The calculated values showed a good agreement with the measured values, as plotted in Fig. 4.

### 7. Summary

We considered that the velocity difference between simulated and measured values was caused by the grain boundary of the ZnO thin film. Therefore, a composite model based on micro-elastic theory was applied to calculate elastic constants of the ZnO film, followed by simulation of the SAW propagation properties. As a result, it is known that existence of the grain boundary was the reason of the difference between the simulation and measurement. Moreover, the loss was roughly estimated by introducing complex elastic constants and a good result was obtained. However, the difference between simulation and measurement of ZnO film with thicker thickness should be investigated in further work.

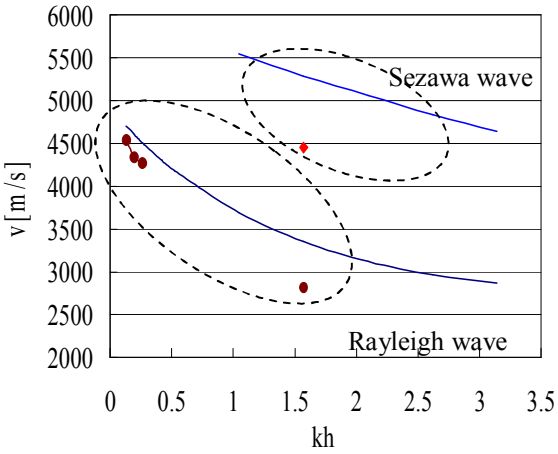


Fig.1 Difference of measured and simulated SAW velocity vs *kh*.

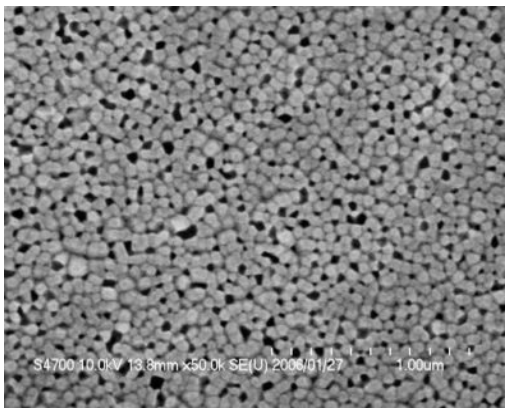


Fig. 2 SEM image of etched surface of ZnO film.

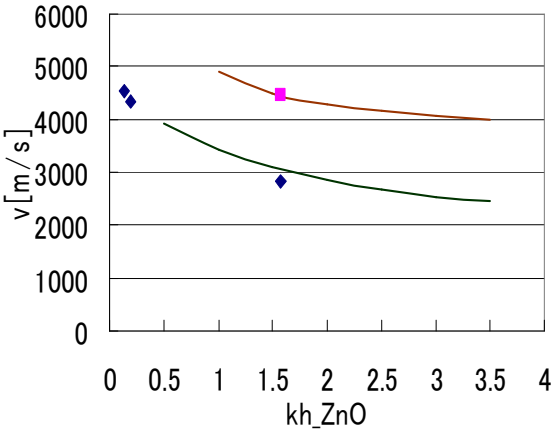


Fig. 3 Velocity simulation using composite-modeled elastic constants.

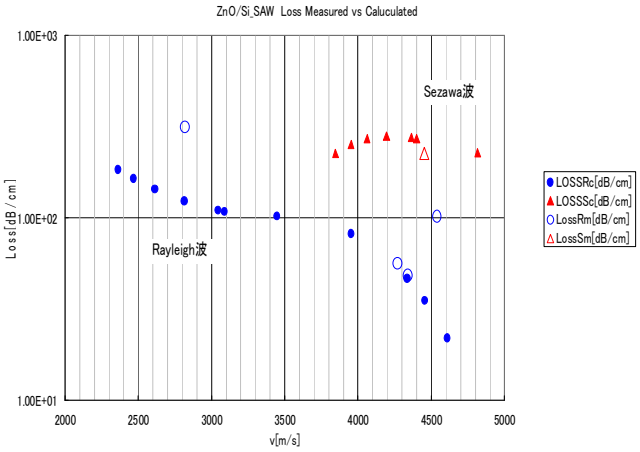


Fig. 4 Calculation result of loss vs velocity.

## 8. Reference

1. J. J. Campbell, et al.: IEEE Trans. Sonics and Ultrason. pp. 209-217, (1968)
2. F. Takeda, T. Shiosaki, and A. Kawabata: The 5th symposium on USE (1984)
3. F. Takeda et al.: JJAP. Vol.24 (1985) pp. 124-124
4. Respondent the 50th meetings of JSAP 27a-ZM-4(2003.3)
5. Respondent the 51st meetings of JSAP 31p-YG-1(2003.9)
6. T.Karaki and et al.: JHES, (2003)
7. M. Furuhata, et al.: Proc. Symp. Ultrason. Electron. Vol. 25 (2004) pp. 211-212
8. M. Furuhata, et al.: (2005) IEEE Ultrason. Symp. pp. 2194-2197
9. H. Fukuda and G. BEN: Mechanics introduction of composite materials: ISBN-10, 4-7722-1373-2 (1989) P210
10. JSME Computational Mechanics Handbook (Vol I):ISBN-10, 4-8889-8085-3 (1999) P240
11. Elasticity element technological handbook: ISBN-10, 4-2740-3365-1 (1991) P319 Table 4.21
12. Elasticity element technological handbook: ISBN-10, 4-2740-3365-1 (1991) p320 Fig. 4.91

1P5-12

Proceedings of Symposium on Ultrasonic Electronics, Vol. 29 (2008) pp. 151-152
11-13 November, 2008

# Speeding-up effects of aluminum oxide films on surface acoustic wave on cystalline quartz

Wen-Ching Shih, Tzyy-Long Wang*, and Yi-Ling Kuo (Graduate Program in Electro-Optical Engineering, Tatung University, Taiwan, R.O.C.)

**Abstract**

Aluminum oxide ($Al_2O_3$) films have been successfully deposited on ST-cut quartz substrates by electron beam evaporation without any interlayer between them to ensure a good adhesion of the $Al_2O_3$ films to quartz substrates The $Al_2O_3$ thin films increase the surface acoustic wave (SAW) velocity sufficiently, and they can be used for improvement of the performance of the SAW devices. The effect of accelerating SAW by the $Al_2O_3$ thin films has been measured and discussed. The results show that SAW phase velocity in the $Al_2O_3$/quartz structure increases with inserting an $Al_2O_3$ film. It is observed that the 1.45μm thick $Al_2O_3$ film is able to speed up SAW by 3.28% at 271 MHz for $Al_2O_3$/quartz sample.

## 1. Introduction

It has been reported that high hardness diamond-like carbon (DLC) films deposited on the surface of $LiNbO_3$, quartz and $LiTaO_3$ substrates can speed up the surface acoustic wave (SAW) [1-5]. The velocity change obtained has been shown to reach a level that is sufficient for application in SAW devices. An efficient SAW reflector, containing DLC reflecting arrays on $LiNbO_3$ substrate, has been prepared making use of this speeding-up effect [6]. $Al_2O_3$ also possess many attractive properties including: high hardness property, chemical stability, high thermal conductivity and electrical isolation. In this paper, we will examine the speeding-up effect of $Al_2O_3$ films on SAW on crystalline quartz substrates.

## 2. Experimental procedure

Interdigital transducers (IDTs) with 3 μm line-width and line-to-line spacing were fabricated on the ST-cut quartz substrates by a conventional photolithographic technique and the etching process. Each transducer has a 12 μm period and 1.2 mm aperture. The number of the finger pair is 100 and the propagation distance between the input and output transducers is 3 mm. After the fabrication of the IDTs, we deposited the $Al_2O_3$ films on above. The $Al_2O_3$ films used in this study were prepared using electron beam (e-beam) evaporation of the $Al_2O_3$ pellet. The background pressure was below $5\times10^{-5}$ torr. The deposition conditions are DC current of 70 mA, substrate temperature of 300°C and distance of evaporation source to substrate of 15 cm.

The thickness of the $Al_2O_3$ film was measured by Dektak$^3$STα-step surface profiler. The stoichiometry of the $Al_2O_3$ buffer layer was measured by energy dispersive spectroscopy (EDS). The cross-sectional morphology of the films was examined by using field emission scanning electron microscope（FE-SEM, JEOL JSM-6500F）, whereas the surface roughness was estimated using the atomic force microscopic micrograph（AFM, Digital Instruments）under tapping mode. The frequency response of the fabricated SAW devices was measured by Agilent 8720ES network analyzer.

## 3. Result and discussions

From the EDS measurement of the $Al_2O_3$ overlayer, we can see that the atomic ratio of Al/O of the $Al_2O_3$ buffer layer is about 2/3, which means that the quality of the $Al_2O_3$ overlayer deposited by e-beam evaporation is acceptable for further application. Figures 1 and 2 show the measured frequency responses for ST-cut quartz and $Al_2O_3$ (1.45μm thick)/ST-cut quartz substrates, respectively.

The center frequency of SAW device without $Al_2O_3$ overlayer layer was measured to be about 263 MHz, and the corresponding phase velocity ($v=f\times\lambda$) calculated from the center frequency is 3156 m/s. On the other hand, the center frequency of SAW device with $Al_2O_3$ (1.45 μm) overlayer layer was measured to be about 271 MHz, and the corresponding phase velocity calculated from the center frequency is 3252 m/s. From Figures 1 and 2, we can see that when we add an $Al_2O_3$ film layer, the center frequency and the phase velocity of the fabricated SAW devices were also increased. It is observed that the 1.45μm thick $Al_2O_3$ film is able to speed up SAW by 3.28% at 271 MHz for $Al_2O_3$/quartz sample. The result is better than those published in the literatures for diamond-like carbon/quartz structure.

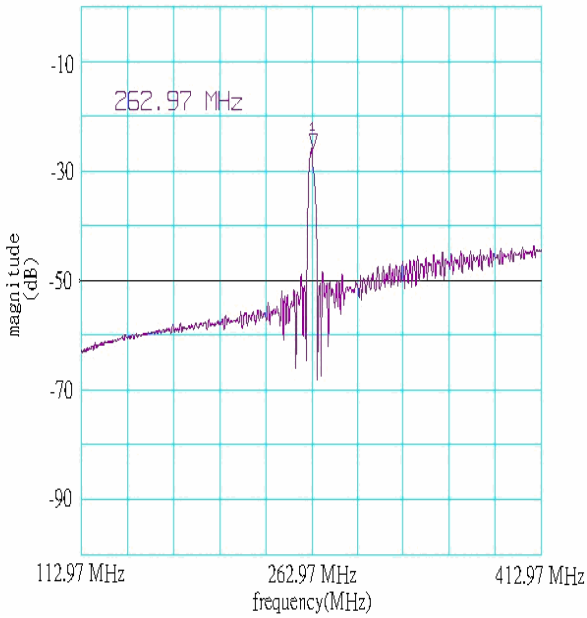


Fig. 1. The measured frequency response of the SAW filter for ST-cut quartz substrate with electrode width of 3 μm.

## 4. Conclusions

The $Al_2O_3$ films with thickness up to 2.4μm have been successfully deposited on ST-cut quartz substrates by e-beam evaporation without any interlayer between them to ensure the adhesion. The effect of the thickness of the $Al_2O_3$ films on speeding up the SAW has been confirmed. The phase velocity of the fabricated SAW device in the $Al_2O_3$/quartz structure was increased with increasing the thickness of the $Al_2O_3$ film. The SAW is accelerated by 3.28% at 271 MHz for $Al_2O_3$/quartz sample with 1.45 μm thick $Al_2O_3$ film. The result is better than those published in the literatures [3,4] for diamond-like carbon (1 μm)/SiC buffer layer/quartz structure with the velocity change ratio of 2.3 % .

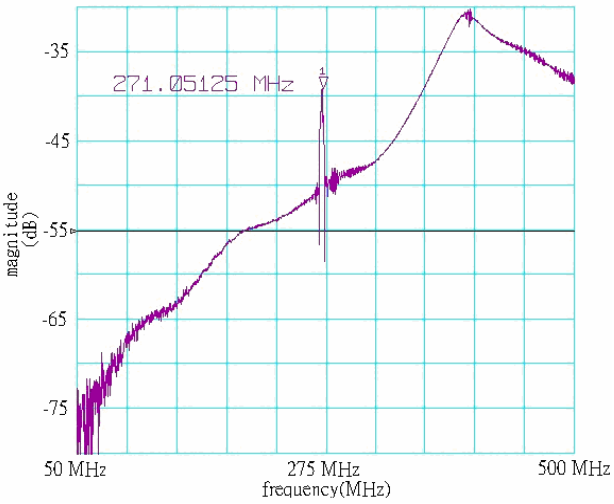


Fig. 2. The measured frequency response of the SAW filter for $Al_2O_3$ (1.45 $\mu$ m thick)/ST-cut quartz substrate with electrode width of 3 μm.


## Acknowledgements

This work was sponsored by the Tatung University, Taiwan, R.O.C.. The authors deeply appreciated their financial and technical support.


## References


[1] Q. Zhang, S.F. Yoon, S. Zhgoon, B. Gan, J. Ahn, A. Revkov, Rusli, Thin Solid Films 360 (2000) 274.

[2] S. Zhgoon, Q. Zhang, S.F. Yoon, A. Revkov, B. Gan, J. Ahn, Rusli, Diamond Relat. Mater. 9 (2000) 1430.

[3] Q. Zhang, S. F. Yoon, S. Zhgoon, V. Ligatchev, M. B. Yu, J. Ahn, Rusli, Diamond Relat. Mater. 10 (2001) 1843.

[4] Qing Zhang, S. F. Yoon, S. Zhgoon, V. Ligatchev, J. Ahn, Rusli, Z. Sun, Thin Solid Films 397 (2001) 276.

[5] Jingze Tian, Qing Zhang, Q. Zhou, R. Gruenwald, M. Huesgen, S.F. Yoon, J. Ahn, Surf.Coatings Technol. 198 (2005) 198.

[6] S. Zhgoon, Q. Zhang, S.F. Yoon, A. Revkov, B. Gan, J. Ahn, Rusli, IEEE 48 (2001) 202.

Proceedings of Symposium on Ultrasonic Electronics, Vol. 29 (2008) pp. 153-154
11-13 November, 2008

# Research on photo-thermal signal of a scheffelera arboricola caused by Dye laser radiation

Dye レーザ照射によるカポックの熱波信号に関する研究

Yoshiaki Tokunaga, Masatoshi Yoshimura, Yukihiro Ishimaru†,
and Junji Hirama (Kanazawa Inst. Tech)
得永嘉昭，吉村政俊，石丸幸大‡，平間淳司（金工大）

## 1. Introduction

Recently, it has been focused the spotlight of attention upon environment and life. Saying specifically, they may be problems on $CO_2$ increment, on energy crisis and on food less production. One of keys for solving of these problems is to find out method on effective usage of plant's potential capabilities. We begin on a new research on photo-thermal effect of a plant and a scheffelera arboricola (hereafter called kapok) is selected to study. Although electrical behavior of a kapok by photo-irradiation has been done in details by one of present authors[1], photo-thermal effect of it caused by laser radiation has been investigated scarcely. In this paper we describe experimental results of "in vivo" measurement on photo-thermal effect caused by irradiation wavelengths with 633nm or 570 nm on a costa or an edge of the kapok's leaf.

## 2. Sample preparation and sensing system

Figure 1 shows a principle of "in vivo" measurement of photo-thermal signal. In this figure, a schematic position between laser irradiation and poly(vinylidene fluoride) (hereafter called PVDF) sensor at the kapok's leaf is shown.

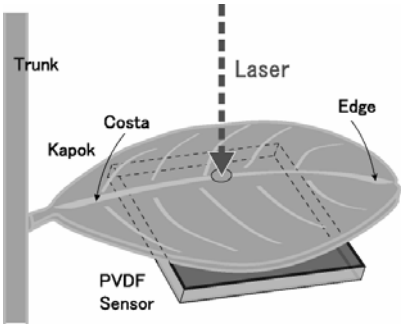


**Fig.1 "In vivo" measurement of the leaf**

---

toklab@mlist.kanazawa-it.ac.jp

In this configuration thermal wave from the irradiated surface of the leaf to opposite side of it can be measured.

Figure 2 shows a sensing system. Dye laser (Spectra Physics: 375B) by Ar laser pumping was used as an excitation source for changing continuously from 570nm to 700nm. An acousto-optical modulator (Gooch&Housego: M080-2B) was used for frequency modulation of the Dye laser light. PVDF film (Tokyo sensor Co.Ltd,3-1003702-4) with 110μm was used as a sensor material. Lock-in amplifier (NF: LI-574A) was used for signal processing.

An energy transfer optical fiber (Edmund Optics: UV/VIS 1000[μm]) was used to lead laser light on the leaf. Irradiation beam diameter on the leaf was about 3mm and it's energy density was about 1.41[mW/mm$^2$] in order to prevent irradiation damage.

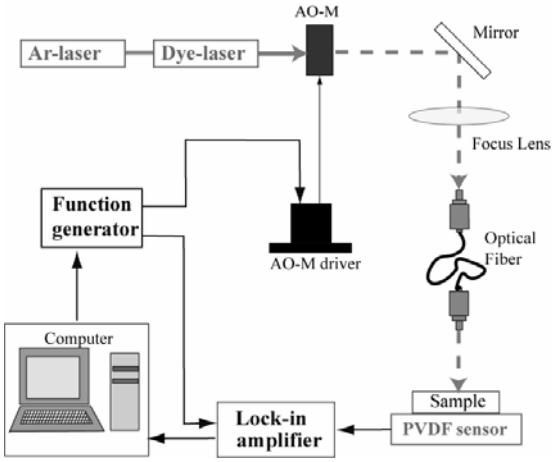


**Fig.2 Sensing system**

## 3. Experimental results and discussion

We can do total and detail discussions on optical stimulus of kapok by adding experimental data on the photo-thermal effect since we have already collected many experimental data on bio-electrical potential [1].

Figures 3(a) and (b) represent amplitude dependence of the signal on modulation frequency of laser induced thermal wave (hereafter called LITW) when irradiation wavelengths are 570nm and 633nm. In these figures ordinate represents signal amplitude of LITW and abscissa delineates laser modulation frequency. In the case of irradiation on a costa of the leaf, the frequency dependence was $f^{-0.80}$ for 570nm irradiation and $f^{-0.51}$ for 633nm one when the modulation frequency was changed continuously from 10Hz to 100Hz. On the other hand, in the irradiation near the edge of the leaf, amplitude dependence was $f^{-0.92}$ for 570nm irradiation and $f^{-0.74}$ for 633nm one as shown in Figs. 4(a) and (b). From these experimental results the amplitude dependence was different between the costa and the edge of the leaf. In addition we found that phase in the 633nm irradiation was delayed about 20 degree in comparison with that of the 570nm irradiation.

## 4. Conclusions

We described "in vivo" measurement on photo-thermal effect of leaf of the kapok caused by 633nm irradiation or 570 nm one.

## References

1). J.Hirama et.al., J.SHITA. 9(2) (1997), pp.103-106.[in Japanese]

## Acknowledgments

The authors would like to thank prof. N.Miyamoto at Kanazawa Institute of technology for his valuable cooperation and suggestions.

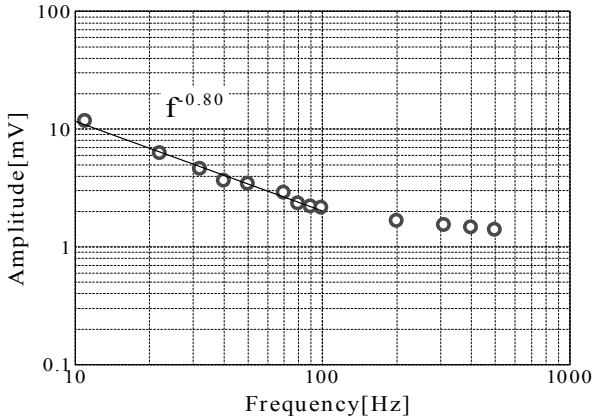


(a) 570nm irradiation

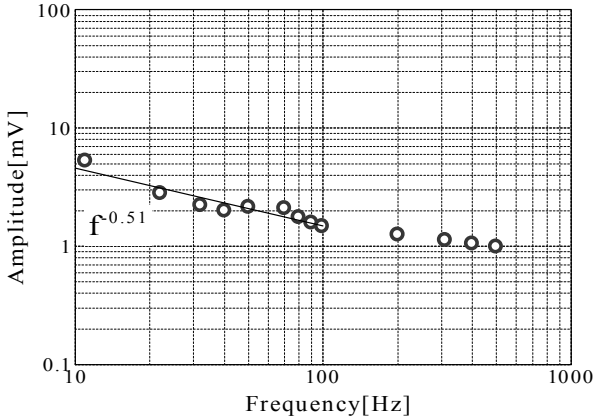


(b) 633nm irradiation

**Fig.3 case of costa**

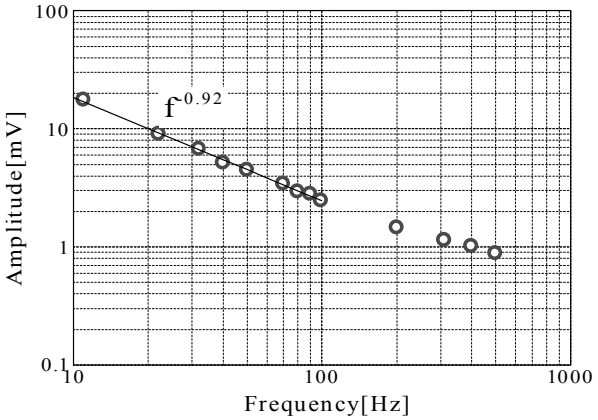


(a) 570nm irradiation

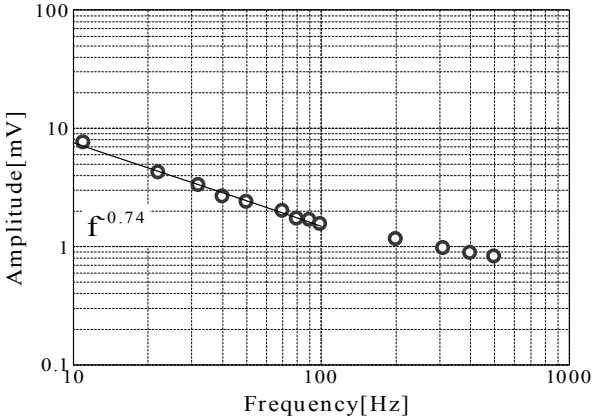


(b) 633nm irradiation

**Fig. 4 case of edge**

Proceedings of Symposium on Ultrasonic Electronics, Vol. 29 (2008) pp. 155-156
11-13 November, 2008

# Active ultrasonic SONAR system of bat
## - Relationship between 3-D flight path and acoustical characteristics of echolocation sounds during foraging -

生物超音波によるアクティブソナーシステム
～採餌行動時における野生コウモリの３次元飛行ルートと放射パルスの関係～

Emyo Fujioka [1‡], Shigeki Mantani [1], Shizuko Hiryu [2], Hiroshi Riquimaroux [2] and Yoshiaki Watanabe [2] ([1]Facult. Eng., Doshisha Univ.; [2]Facult. Life and Medi. Sci., Doshisha Univ.)

藤岡慧明 [1‡], 萬谷重樹 [1], 飛龍志津子 [2], 力丸裕 [2], 渡辺好章 [2] ([1] 同志社大 工; [2] 同志社大 生命医科)

## 1. Introduction

Bats and dolphins emit ultrasonic sonar sounds to obtain surrounding information. The systems they use are called bio-SONAR, and our final purpose is to reveal highly developed ultrasonic SONAR system established by bats from viewpoints of biology and engineering [1].

Amount of daily energy consumption of the echolocating bats is known to be much greater than that of other small mammals, and especially foraging activity requires a greater part [2]. In addition, since the bats have to capture a plenty of insect preys everyday, they are supposed to effectively exhibit foraging, i.e. selecting rational flight path to a target prey of interest.

In this study, the ultrasonic emitted sonar sounds were examined for wild bats during foraging, combined with measurement of their 3-D flight paths by using a four-microphone array system. We investigated how the bats selected their flight paths to capture small airborne insects effectively by interacting echolocation and flight simultaneously.

## 2. Materials and Methods

The Japanese house bats (*Pipistrellus abramus*) were used in this study. The fundamental component of the pulse is downwardly modulated from 100 kHz to 40 kHz [3].

Sound recordings were conducted for 6 days during a 1-hour period before and after the sunset. Emitted echolocation pulses were recorded with 4 omni-directional condenser microphones (Knowles, FG-3329) positioned about 2 m above the ground (Fig. 1A). The signals were digitized with 16 bit at sampling rate of 500 kHz by using a DAQ device (NI PXI-6250, Tokyo, Japan). Theoretical range error of the 3-D position measurement was estimated to be less than 10 cm within target range of 7 m in front of the microphone array (Fig. 1B). Prior to recording, the range error was measured by using a loudspeaker (Pioneer, PT-R7, Tokyo, Japan). We confirmed that maximum range error was small enough; less than 3 % within target range of 5 m (Fig. 1C).

## 3. Results

Echolocation of the bats during foraging can be generally divided into three phases; search, approach and terminal (Fig. 2A) [4]. The bats emitted CF-like (Constant-Frequency-like) pulses during search phase. However, the frequency

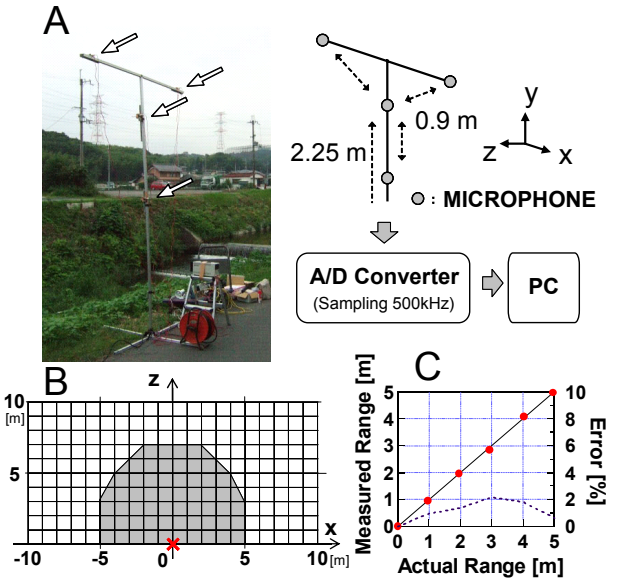


Fig. 1 (A) Four-microphone array system. Open arrow indicates the position of each microphone. (B) Theoretical range error of the microphone array system. The error was estimated to be less than 10 cm (gray area). Cross mark indicates the position of the microphone array. (C) Calibration measurement for the microphone array. Circles indicate the measured ranges and dotted line indicates the position error (see text).

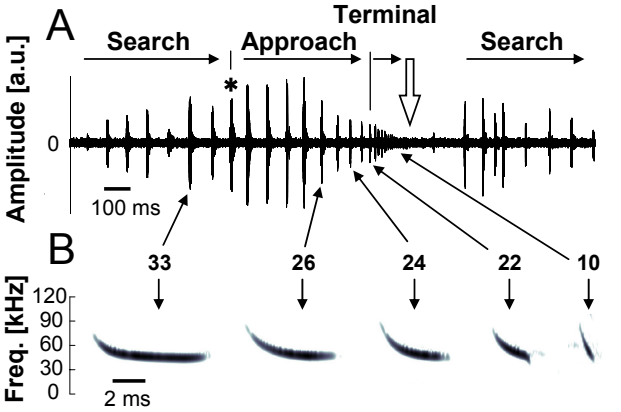


Fig. 2 (A) Representative sequence of echolocation pulses during foraging in the field. The pulses were numbered beginning at the timing of capture (open arrow). (B) Change in the frequency structure of echolocation pulses before capturing. Asterisk indicates the phase transition to approach.

dth0902@mail4.doshisha.ac.jp

structure varied from CF-like to FM (Frequency Modulation) and the bats shortened the pulse duration after approach phase started (Fig. 2B ∗). Fig. 3 shows a 3-D flight trajectory of a bat before capturing a prey (numbers correspond to those of the pulses in Fig. 2). The bat changed its flight direction soon after starting approach phase (Fig. 3 ∗), and then approached the target prey linearly. We calculated the target distances from the bat to the target (capture point) from two different ways; direct distance to capture (DDC; dashed lines in Fig. 3) and actual distance along the flight path to capture (ADC; solid curve). If the bats exhibited a straight-ahead approach to the target, DDC coincided with ADC. From three representative flights shown in Fig. 4, we found that DDC identical with ADC after the approach phase started. In addition, the bats lengthened the pulse duration at the coincident timing between DDC and ADC (Fig. 4C ∗). These findings suggest that the bats immediately select a straight-ahead approach a target prey before capturing and emission of long CF-like pulse is required for the bats to start their final approach to the target.

## 4. Discussion

*P. abramus* in the field repeated capturing insects every 2-3 seconds [3]. Therefore, the bats are supposed to effectively find and approach a target prey for a short amount of time. Our results show that the flying bats lengthened the pulse duration just before phase transition to approach (Fig. 4). Since the CF-like pulse (Fig. 2) is assumed to be useful for detecting an insect's fluttering [5], the bats may confirm the presence of a target prey by emitting a long CF-like pulse, and then start their final approach to capture the target. We also found

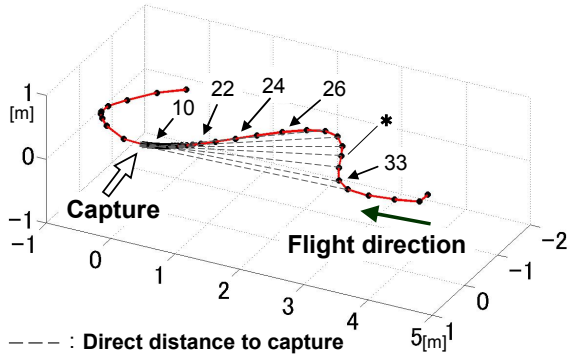


Fig. 3 Three-dimensional flight trajectory of the bat during the capturing flight shown in Fig. 2. Positions of pulse emission were plotted along with the flight trajectory.

that the flying bats selected a straight-ahead path to a target after the phase transition (Fig. 4). This implies that the bats forecast the moving direction and velocity of the insect prey. In addition, the coincidence between DDC and ADC between flights (Fig. 4) indicates that the bats start approach phase according to the relative direction or velocity to the target prey. We will investigate how the bats select their flight paths according to the movement of a target prey for effective foraging.


## Acknowledgments

This work was partly supported by a grant to RCAST at Doshisha Univ. from MEXT of Japan: Special Research Grants for Development of Characteristic Education from the Promotion and Mutual Aid Corporation for Private Schools Japan, Innovative Cluster Creation Project.


## Reference


1. S. Hiryu et al.: J. Acoust. Soc. Am., **121**, No. 3, (2007) 1749.
2. G. Neuweiler: *The biology of bats* (Oxford University Press, NY, 2000) p.98.
3. E. Fujioka et al.: Proc. of Acoustics'08 Paris, (2008) 5933.
4. H. U. Schnitzler et al.: J. Comp. Physiol. A, **161**, (1987) 267.
5. H. U. Schnitzler et al.: *Advances in neuroethology*, (1983) p. 801.


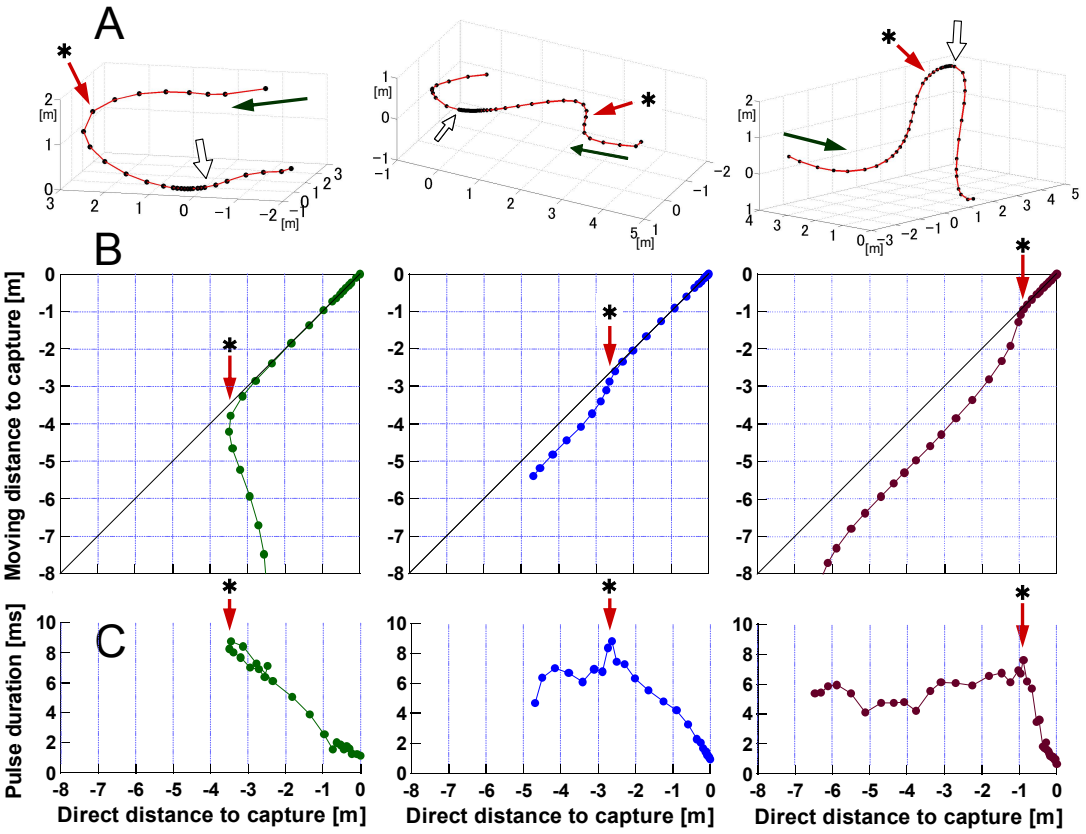


Fig. 4 Three-dimensional flight trajectories (A) and changes in moving distance to capture (B) and pulse duration (C) during foraging behavior from the distance of 8 m to capturing point.

1P10-3

Proceedings of Symposium on Ultrasonic Electronics, Vol. 29 (2008) pp. 157-158
11-13 November, 2008

# Development of ultrasonic sensor for mobile robot to measure the normal direction and parallel of walls
# 壁面と平行移動するロボット用の超音波センサについて

Manabu Ishihara[1†], Makoto Shiina[2] and Shin-nosuke Suzuki[1] ([1] Oyama National College of Tech. ;[2] Advanced Courses, Oyama National College of Tech. Eng.)
石原学 [1‡]，椎名誠 [2]，鈴木真ノ介 [2] （[1] 小山高専電気情報; [2] 小山高専専攻科）

## 1. Introduction

Ultrasonic sensors are used in various fields because of their unique characteristics. One such use is to provide positioning control for robots. Although ultrasonic ranging provides excellent distance resolution, one of its shortcomings is that it provides low directionality when compared to optical sensors. Various attempts have been made to improve measurement resolution, including the use of rotating and/or multiple frequency sensors, as well as the adoption of a sophisticated signal processing technique [1][2].

In this study, We investigated a method believed to be capable of controlling a moving body in a way that allows it to maintain a user-specified distance from nearby walls. The method uses multiple ultrasonic sensors and a simple signal processing method.

## 2. Sensor Outline

### 2.1 Ultrasonic Sensor Characteristics

One of the characteristics of ultrasonic sensors is that their aerial transmission speed is slower than light, which makes its signal processing easier. Furthermore, ultrasonic wavelengths are relatively short (approximately 8.6 mm at 40 kHz), which allows for high resolution in the direction of distance. This makes it possible to conduct highly accurate distance measurements. Another advantage is that ultrasound is unaffected by the color of an object and can thus be used to measure the distance from a sensor to a transparent body such as a glass object. Ultrasound is also relatively immune to effects of light and airborne dust, which makes it useful for performing measurements in outdoor environments. Because of these characteristics, ultrasonic sensors are also used for automobile navigation and ranging systems, etc.

### 2.2 Conventional Sensor System

One example of a conventional ultrasonic sensor system is an ultrasonic rangefinder. Ultrasonic rangefinders emit ultrasonic pings, which travel to an object and are then reflected back to the rangefinder. Distance is calculated by measuring the time between the emission and reception of the reflected ping.

Figure 2 shows this scheme. Ultrasonic sensors of this type are often used for collision avoidance by measuring the distance from a moving vehicle to a potential obstacle. While it is possible to use multiple units for this type of echo-ranging, as shown in Fig. 3, adequate distance between the sensors as well as careful consideration of the arrangement of multiple sensors is required in situations where the robot is cylindrically shaped.

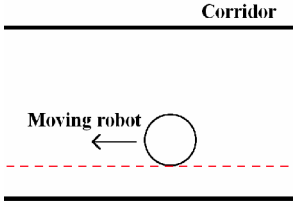


Fig. 1 Equidistant control

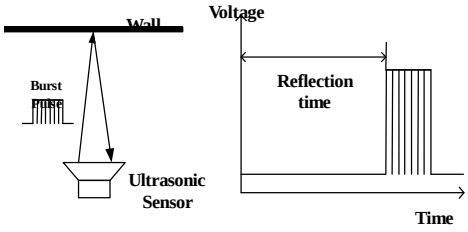


Fig. 2 Ultrasonic measurement system

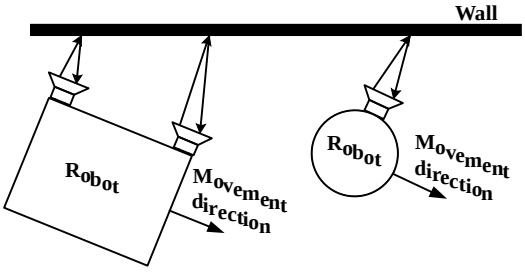


Fig. 3 An idea of sensor arrangement

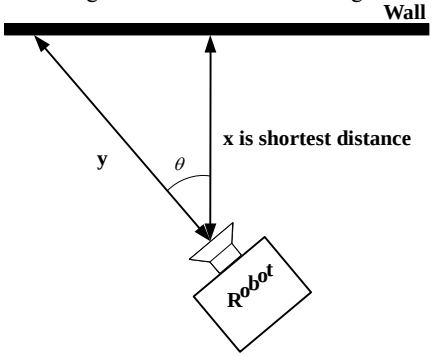


Fig. 4 Outline of measurement system

## 3. Proposed System

3.1 Measurement Principle

We will now examine a situation where a robot is required to move parallel to a wall, as shown in Fig. 1. If we can somehow simultaneously measure the minimum distance x between the system and the wall, and the distance to the wall y in the frontal direction of the system, we then know that the robot is moving parallel to the wall when x and y are equal. Using these measurements, we can determine the system's inclination angle as well.

The relation between the angle θ, x and y is expressed as:

Equation $\quad \cos\theta = X/Y \qquad (1)$

Then,

Equation $\quad \theta = \cos^{-1}(X/Y) \qquad (2)$

Thus, the system is controlled to satisfy the relation θ= 0 [deg] in the equation (2). When a robot is controlled in a real system, the x and y values are measured constantly and the robot's movements are controlled to ensure they stay within the given threshold values. In addition, because this method uses measured angles as parameters, positioning control can be determined easily.

3.2 Minimum Distance Measurement

The minimum distance between the wall and the system x has to be measured even when the system (the axis of the sensor) is somewhat tilted, as described above. Here we will call the sensor for measuring the distance x as X. When measuring the minimum distance, the broad directional angle of the ultrasonic sensor is utilized. As shown in Fig. 5 (a), ultrasonic sensors typically have a wide measurable range, i.e. directional angle. In other words, even when the ultrasonic sensor is slightly tilted, as shown in Fig. 5 (b), the measured distance is approximately equal to the minimum distance x. In our system, the minimum distance is measured using this feature.

3.3 Tilted Distance Measurement

If the system (the axis of the sensor) is not precisely perpendicular to the wall, x ≠ y, and it is necessary to measure the tilted distance to the wall y. We will call the sensor for measuring the distance y as Y, which is shown in Fig. 6. In this situation, the distance y is measured from the outermost part of the measuring range of sensor Y. An experiment was therefore conducted to determine the directionality of the sensor.

## 4. Discussion

Using the proposed sensor system, the distance between the sensor and the wall and the angle of the sensor relative to the wall were measured at distances of 50 - 250 cm and at angles of 0 – 15 degrees (0 degree indicates that the sensor axis is perpendicular to the wall). From these results, it was concluded that the proposed system is suitable for use as the positioning control of a robot that is designed to travel along a passage, such as a corridor.

Since the proposed system can be connected to the position control circuit of a robot using other microcontrollers via I2C, or to a PC via RS-232, it can easily be installed and used in other systems as a position-detecting module.

From these observations, we feel it is safe to say that the proposed sensor system offers sufficient functionality to allow its use as a position controlling platform for a robot, and that it can be applied to small traveling robots.

## 5. Conclusion

A sensor system was developed using only inexpensive and easily available components. Based on the information obtained while designing, manufacturing and testing the prototype, we conclude the system proved to be sufficiently capable for use in robots.

Future research will include achieving positioning control of a small robot using the present system.

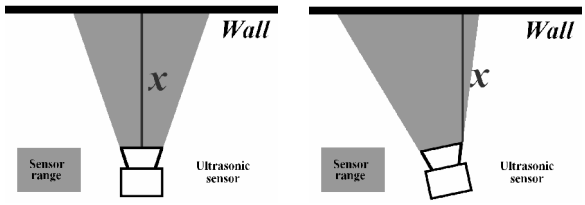


(a) Perpendicular with a wall (b) Change a direction

Fig. 5 Shortest distance measurement by the Ultrasonic sensor

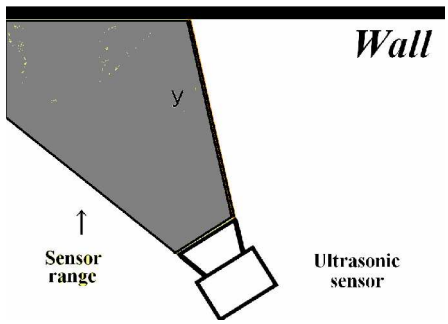


Fig. 6 Change the direction of rotation by the Ultrasonic sensor

## References

1. Y.Nagashima, A.Ohya and S.Yuta: The Journal of the Acoustical Society of Japan. **51** (1994)39.
2. M. Okuyuki, A. Kimura, M. Ohki and M.Ohkita: IEEJ-C, **128** (2008) 55.

Proceedings of Symposium on Ultrasonic Electronics, Vol. 29 (2008) pp. 159-160
11-13 November, 2008

# Target Detection Using Multiple M-sequence Signals in Indoor Environments

M 系列信号の同時送波による室内ターゲット検出能の検討

Hiroshi Matsuo[1‡], Tadashi Yamaguchi[2] and Hiroyuki Hachiya[3] ([1] Graduate school of Advanced Integration Science, Chiba Univ.; [2]Resarch Center for Frontier Medical Engineering, Chiba Univ.; [3]Graduate School of Sci. and Eng., Tokyo Institute of Technology)
松尾宏[1‡]，山口匡[2]，蜂屋弘之[3] （[1]千葉大 融合科学; [2]千葉大 CFME; [3]東工大 理工）

## 1. Introduction

An acoustic method in air has the potential to allow for the fast and accurate characterization of object in air. Nevertheless, it is difficult to identify acoustic signal from small objects clearly because of environmental noise and the scattering of the signal on the object surface.

In this paper, we present the target detection using multiple M-sequence signals in indoor environments. By using M-sequence signal that is one of coded signals, we are able to improve SN ratio and to measure the reflected waves from a small object that cannot be detected using a conventional impulse. Simultaneous transmission of multiple M-sequence signals enable an effective data acquisition. We discuss the cross-correlation characteristics between different codes. Acoustic imaging results of cylinder targets are presented.

## 2. Method

M-sequences of degree n which have a sharp auto- correlation peak can be generated by different binary feedback shift registers of length n. Cross-correlation properties are important when multiple M-sequence signals are transmitted. Pairs which have low cross-correlation value especially called preferred pair (PP) exist except in degree of multiples of 4. **Table 1** shows cross-correlation values of preferred pair of degree *k*.

The experiment was conducted in an indoor environment using the measurement system shown in **Fig. 1**. In this measurement, the phase modulated M-sequence signals of degree 10, centered at 25 kHz were used. The sequence is repeated three times during each transmission to eliminate the effect of sequence truncation. Stainless steel pipes with diameters of 13 mm were used as targets.

Table 1 Cross-correlated value of preferred pair.

| Degree | Value | Probability |
|---|---|---|
| *k* : odd number | $-(2^{(k+1)/2}+1)$ | ~0.25 |
| | -1 | ~0.5 |
| | $2^{(k+1)/2}-1$ | ~0.25 |
| k : even number (except in multiples of 4) | $-(2^{(k+2)/2}+1)$ | ~0.125 |
| | -1 | ~0.75 |
| | $2^{(k+2)/2}-1$ | ~0.125 |

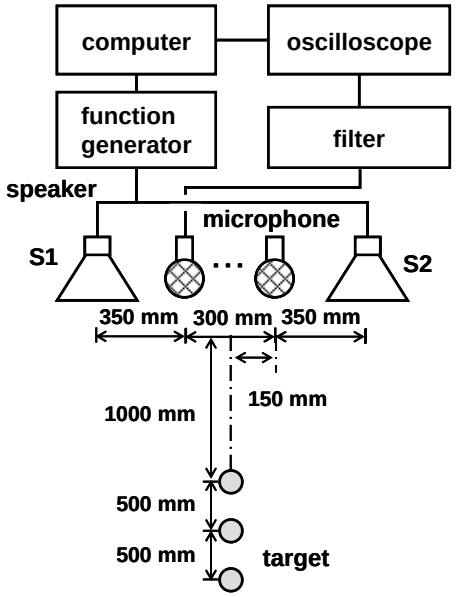


Fig. 1 Measurement system.

## 3. Results and discussion

M-sequence signal of code- number ‘3265’ was transmitted from a speaker (S1) to estimate cross-correlation properties in real environment. A code-number such as ‘3265’ written in octal form shows the pickup position of the feedback signal from the shift register. Received signals were correlated with same code as the transmitted M-sequence ’3265’. Then the signals were correlated with M-sequences of a code name ‘3575’ and ‘2011’. A pair of codes ‘3265’ and ‘3575’ is a preferred pair. A pair of cods ‘3265’ and ‘2011’ is not a preferred pair. The amplitude of correlated signals with ‘3265’, ‘3575’ and ‘2011’ are shown in **Fig. 2**, **Fig. 3** and **Fig. 4**. In Fig. 3 and Fig. 4, signals from 0 to 500 ms are the result of a correlation with the direct waves at 100, 220, 340 ms shown in Fig. 2. Correlated results are equivalent to a random noise which can be called correlated noise. This noise causes the fall of the SN ratio when multiple M-sequence signals are transmitted.

**Table 2** shows maximum and average of the amplitude of the range from 100 to 222.76 ms where there is not the influence of sequence truncation. The frequency distribution of the

amplitude is shown in **Fig. 5**. In Fig. 5, the solid line shows the frequency distribution of correlated signals with '3575' (PP) and the dotted line show that of correlated signals with '2011' (not PP). The average of the amplitude of '3575' result is lower than that of '2011' result and the frequency of low amplitude is high. These results agree well with theoretical characteristics of M-sequence.

We transmitted M-sequence of code '3265' and '3575' which are preferred pair from each speaker in Fig.1 and captured reflected signals from the targets. The image using the received signals is shown in **Fig. 6**. It is difficult to detect the reflected signals from a distant target due to influence of cross-correlation noise.

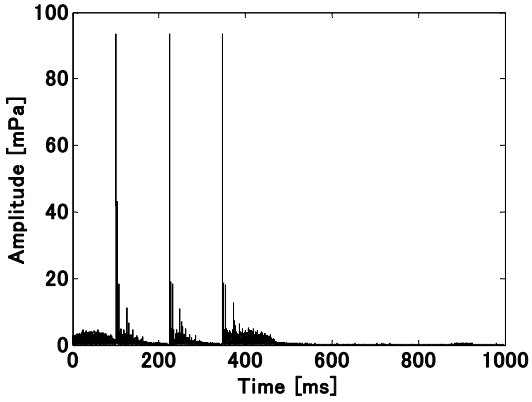


Fig. 2 Correlated signal using code '3265'.

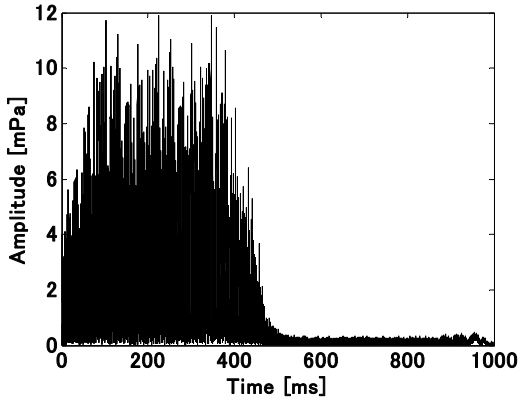


Fig. 3 Correlated signal using code '3575'.

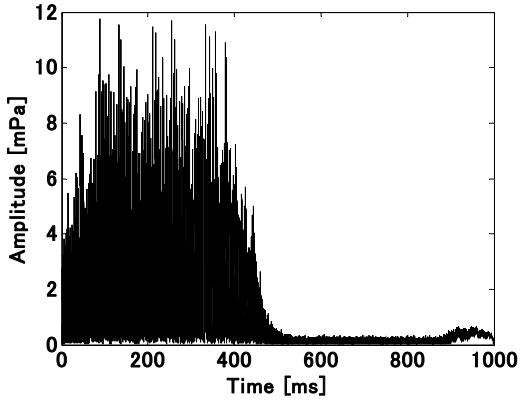


Fig. 4 Correlated signal using code '2011'.

Table 2 Statistical value of amplitude.

| Code | Maximum [mPa] | Average [mPa] |
|---|---|---|
| 3265 | 93.66 | 0.93 |
| 2011 | 11.71 | 2.90 |
| 3575 | 11.92 | 2.79 |

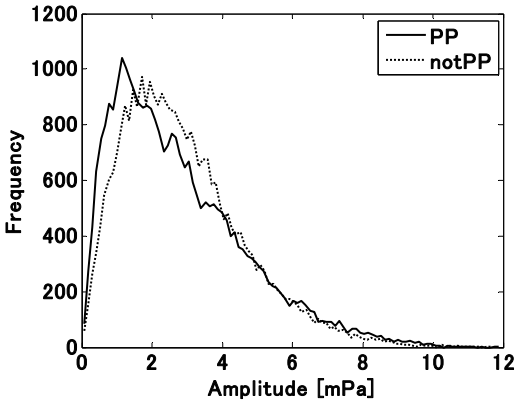


Fig. 5 Amplitude distribution.

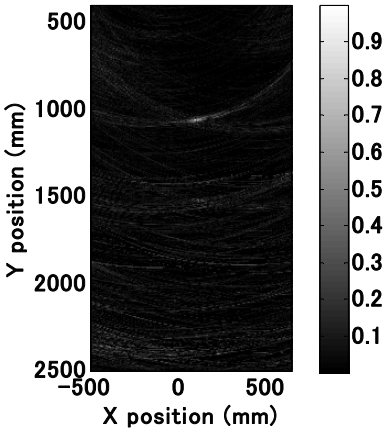


Fig. 6 Acoustic image.

## 4. Conclusion

In this paper, we present the target detection using multiple M-sequence signals in indoor environments. As a result of estimation of correlated signals using a different code from a transmitted code, in the case of the preferred pair, the frequency of low amplitude is higher than other pairs.

## References

1. Y. Wang *et al.*: Jpn. J. Appl. Phys. **42** (2003) No. 5B 3206-3211.
2. K. Nishihara *et al.*: Acoust. Sci. Technol. **29** (2008) 15-20.
3. H. Matsuo *et al.*: Jpn. J. Appl. Phys. **47** (2008) No. 5B 4325-4328.
4. Y. Wang *et al.*: Jpn. J. Appl. Phys. **47** (2008) No. 5B 4319-4324.
5. Y. Wang *et al.*: Jpn. J. Appl. Phys. **46** (2007) No. 7B 4490-4496.

1P10-5

Proceedings of Symposium on Ultrasonic Electronics, Vol. 29 (2008) pp. 161-162
11-13 November, 2008

# Design for High-Accurate Numerical Simulation of Acoustic Field in Time Domain Using Finite Difference Time Domain (FDTD) Method and Pseudospectral Time Domain (PSTD) Method

FDTD 法と PSTD 法による時間領域における音場数値解析の高精度設計法

Kan Okubo[1†], Masaki Omiya[1], Takao Tsuchiya[2] and Norio Tagawa[1]
([1] Faculty of System Design, Tokyo Met. Univ.; [2]Faculty of Eng., Univ. of Doshisha.)
大久保寛 [1‡]，大宮理生 [1]，土屋隆生 [2]，田川憲男 [1]（[1] 首都大システムデザイン; [2] 同志社大工）

## 1. Introduction

Time domain numerical analysis of acoustic fields has become investigated widely as a result of recent computational progress. To date, accurate schemes are developed for acoustic simulation.

Some techniques have been proposed as an acoustic field calculation method; the finite difference time domain (FDTD) method[1-3] is very widely used for time domain numerical analysis. The FDTD method by Yee, however, causes numerical dispersion error due to using 2nd order finite difference (FD) approximation. To overcome this problem, FDTD methods using higher order spatial FD[1] have been proposed.

Meanwhile, a pseudospectral time-domain (PSTD) method[4] is examined. This method uses Fourier transform to represent spatial derivatives in the governing equations for the acoustic field.

Higher order FDTD and PSTD methods yield superior accuracy in exchange for a more complicated formulation. However, both methods require to set a smaller time step than Yee-FDTD method in order to maintain the accuracy. Therefore, in some cases, these methods may use more total CPU time; we need to consider the balance between the accuracy in space and required CPU time in design for high-accurate time domain numerical simulation.

This study examines a design method for acoustic numerical simulation in time domain using FDTD and PSTD, considering numerical dispersion relation.

## 2. Dispersion relation

For simplicity, we consider one-dimensional (1-D) case. Then, in acoustic FDTD simulation, the numerical sound velocity normalized by theoretical sound velocity in medium is given as

$$c_n' = c_0 \sqrt{\left(\frac{k}{\omega}\right)^2 \left( \frac{A\sin\left(\frac{k\Delta x}{2}\right)}{\frac{k\Delta x}{2}} + \frac{B\sin\left(\frac{3k\Delta x}{2}\right)}{\frac{3k\Delta x}{2}} \right)^2 \left( \frac{\frac{\omega\Delta t}{2}}{\sin\left(\frac{\omega\Delta t}{2}\right)} \right)^2} . \quad (1)$$

In those equation, $c_n'$ is the normalized sound velocity, $c_0$ is the theoretical sound velocity, $k$ is the numerical wave number, $\omega$ is the angular frequency, $\Delta t$ is the time step, and $\Delta x$ is grid size. The coefficients are defined as $A = 9/8$ and $B = -1/8$ in FDTD (2, 4) method[1]. If $A = 1$ and $B = 0$ are used, Eq. (1) shows the normalized velocity of FDTD method by Yee[2].

In Eq. (1), discritization in space and time causes the numerical phase error. That is, if there is no error in regard to spatial discretization,

$$c_{(s)n}' = c_0 \sqrt{\left(\frac{k}{\omega}\right)^2 \left( \frac{\frac{\omega\Delta t}{2}}{\sin\left(\frac{\omega\Delta t}{2}\right)} \right)^2} . \quad (2)$$

On the other hand, if no error in time,

$$c_{(t)n}' = c_0 \sqrt{\left(\frac{k}{\omega}\right)^2 \left( \frac{A\sin\left(\frac{k\Delta x}{2}\right) + B\sin\left(\frac{3k\Delta x}{2}\right)}{\frac{k\Delta x}{2}} \right)^2} . \quad (3)$$

Additionally, the numerical sound velocity of PSTD method is given as Eq. (2), because it theoretically causes no error in regard to spatial discretization.

## 3. Results and discussion

Assuming that the Courant number is $C_n = v\Delta t / \Delta x$, we can obtain

$$C_n \cdot d\,[\mathrm{GPW}] = d\,[\mathrm{TPP}], \quad (4)$$

where GPW and TPP represent grids per wavelength and timesteps per period, respectively.

**Figure 1** shows numerical sound velocity versus GPW calculated by Eq. (3) for $A = 1, B = 0$ (2nd-order FD) and $A = 9/8, B = -1/8$ (4th-order FD). Results calculated using Eq. (2) for $C_n = 0.25$, 0.5 and 1 are also plotted in Fig. 1. Here, considering the relationship of Eq. (4), we can illustrate different three top axes as shown in Fig. 4.

In this figure, if

$$c_{(t)n}' \cdot c_{(s)n}' = 1, \qquad (5)$$

then there is no numerical dispersion. That is, FDTD algorithm provides exact solutions at the so-called magic time step ( $A=1$ , $B=0$ and $C_n=1$ ). Now, Eq. (5) is substitute into

$$c_{(t)n}' - 1/c_{(s)n}' = 0. \qquad (6)$$

Equation (6) demonstrates that it is required to reduce the value of $D = c_{(t)n}' - 1/c_{(s)n}'$ in order to realize an accurate FDTD simulation.

**Figure 2** shows $c_{(t)n}'$ and $1/c_{(s)n}'$ versus GPW or TPP. In addition, numerical velocity of compact 4th-order FD is also illustrated in this figure. $c_{(t)n}'$ for 2nd-order FD and $1/c_{(s)n}'$ for $C_n=1$ are identical values. Moreover, we compare the two results; $c_{(t)n}'$ for 2nd-order FD and $1/c_{(s)n}'$ for $C_n=0.25$.

**Figure 3** shows total numerical velocity $c_n'$ calculated from Eq. (2). In this case, even if a small time step is used to improve the accuracy of the time integration, numerical velocity deviates from the theoretical value in total, as is seen from Figs. 2 and 3(a). On the other hand, In the case of 4th-order FD with $C_n=0.85$, numerical phase error is also caused in total due to a large time step, as is shown in Fig. 3 (b).

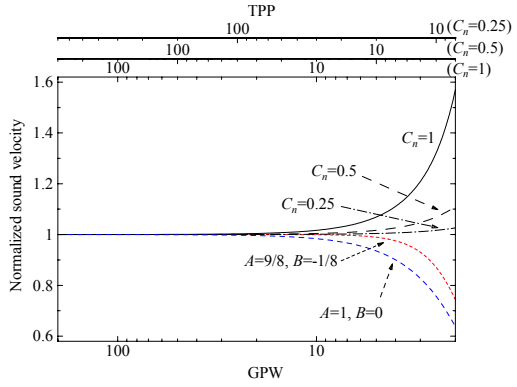


Fig.1 Numerical sound velocity v.s. GPW or TPP.

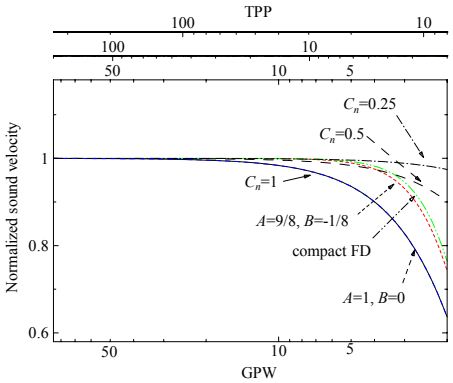


Fig.2 Numerical sound velocity v.s. GPW or TPP.

Next, we will discuss the multi-dimensional calculation. There is no magic time step for FDTD in two or three dimensional (2-D/3-D) simulation. Because FDTD has numerical anisotropic behaviors due to the difference of numerical wave number for a propagation angle. $c_{(t)n}'$ for 4th-order FD (azimuthal angle of 45 deg. and 0 deg. in 2-D calculation) and $1/c_{(s)n}'$ for $C_n=0.25$ , 0.4 and 0.5 are shown in **Fig. 4**. This figure indicates that in 2-D simulation, we must choose an appropriate time step for the accuracy of spatial FD.

Additionally describing, PSTD method has theoretically causes no error in regard to spatial discretization. Therefore, it provides higher accuracy, as time step is smaller.

## 4. Conclusion

This study investigated a design method for acoustic numerical simulation using FDTD and PSTD. By separately considering numerical dispersion relation in space and time, we can choose an appropriate time step for spatial FD. We will examine a design for asymmetric FDTD method in near future.

## References


1. A. Taflove: Computational Electrodynamics: The Finite-Difference Time-Domain Method (Artech House, Boston, MA, 1995)
2. K. S. Ye: IEEE Trans. on AP, AP-14 (1966) 302
3. M. Sato: Jpn. J. Appl. Phys. 44 (2005) pp. 4490
4. Q. H. Liu: Microw. Opt. Technol. Lett., 15(1997) 158


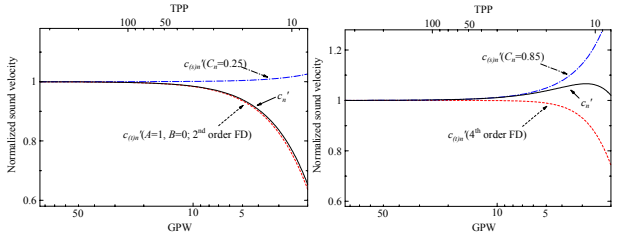


(a) (b)

Fig.3 Numerical sound velocity v.s. GPW or TPP.

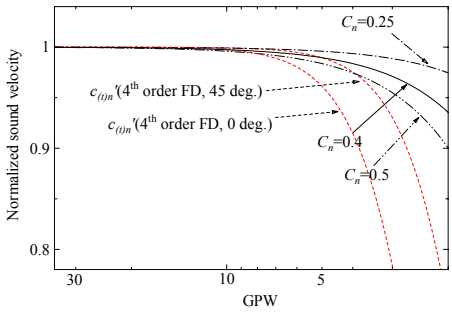


Fig.4 Numerical sound velocity in 2-D simulation.

1P10-6

Proceedings of Symposium on Ultrasonic Electronics, Vol. 29 (2008) pp. 163-164
11-13 November, 2008

# Two Dimensional Simulation of Nonlinear Acoustic Wave Propagation Using Constrained Interpolation Profile (CIP) Method

CIP 法を用いた非線形音波伝搬の 2 次元数値解析

Masahito Konno[1†], Kan Okubo[1], Takao Tuchiya[2] and Norio Tagawa[1] ([1] Facult. System Design, Tokyo Met. Univ.; [2]Facult. Eng., Dosisha Univ.)
紺野正仁 [1‡], 大久保寛 [1], 土屋隆生 [2], 田川憲男 [1] ([1] 首都大院　システムデザイン; [2] 同志社大 工)

## 1. Introduction

To date, Numerical analysis has been investigated for sound wave propagation. Now, development of accurate numerical schemes is an important technical issue. The Constrained Interpolation Profile (CIP) method is a novel numerical scheme recently proposed by Yabe[1,2]. It is a kind of method of characteristics (MOC) and is a numerical scheme with high accuracy that hardly caused numerical dispersion errors[1-5]. It uses not only the value at the grid point but also their derivatives to solve the problem of wave propagation. Some of the authors reported application of CIP method to the one-dimensional (1-D) nonlinear sound wave propagation in air[6].

In this study, numerical simulation of two-dimensional (2-D) nonlinear sound wave propagation in time domain is performed by CIP method.

## 2. Formulation

The governing equations for nonlinear acoustic fields with velocity dispersion under the assumption of weak shock are given as follows. Equation (1) is the continuity equation and Eq. (2) is the equation of motion.

$$\frac{\partial p}{\partial t} = -\rho_0 c_0^2 \nabla\cdot\vec{v} + \frac{\delta_1}{\rho_0}\nabla^2 p + \frac{\beta}{\rho_0 c_0^2}\frac{\partial p^2}{\partial t}, \quad (1)$$

$$\frac{\partial \vec{v}}{\partial t} = -\frac{1}{\rho_0}\nabla p + \frac{\delta_2}{\rho_0}\nabla^2\vec{v}, \quad (2)$$

where $p$ is the pressure, $\vec{v}$ is the particle velocity, $\rho_0$ is the ambient medium density, $c_0 = \sqrt{\kappa/\rho_0}$ is the sound velocity of small amplitude , $\kappa$ is the bulks modulus and $\beta$ is the nonlinearity parameter. $\delta_1$ and $\delta_2$ are respectively given as

$$\delta_1 = \chi\left(\frac{1}{c_v}-\frac{1}{c_p}\right), \quad \delta_2 = \zeta + \frac{4}{3}\eta. \quad (3)$$

In those equation, $\chi$ is the thermal conductivity, $\zeta$ is the bulk viscosity, $\eta$ is shear viscosity, and $c_v$ and $c_p$ are the specific heat at constant volume and the one at constant pressure, respectively.

Now, we solve Eq. (1) and Eq. (2) using time splitting method. Using this method, the equations are separately solved on advective term and non-advective term. First, we denote the advective term.

For simplicity, we assume $\vec{v} = (\vec{v}_x, 0, 0)$ in order to analyze 1-D sound wave propagation of the x-direction. When the medium dispersion and nonlinearity can be ignored, Eq. (1) and Eq. (2) can be denoted as

$$\frac{\partial p}{\partial t} + c_0\frac{\partial (Zv)}{\partial x} = 0, \quad (4)$$

$$\frac{\partial (Zv)}{\partial t} + c_0\frac{\partial p}{\partial x} = 0, \quad (5)$$

where $Z = \sqrt{\rho_0\kappa}$ is the characteristic impedance. Then we solve Eq. (4) and Eq. (5) using the CIP method[5]. Similarly, propagation in the y-direction as well as in the x-direction can be calculated.

Next, we describe the non-advective terms. We consider the dispersion and nonlinear terms shown as

$$h_p = \frac{\delta_1}{\rho_0}\left(\frac{\partial^2 p}{\partial x^2}+\frac{\partial^2 p}{\partial y^2}\right) + 2\beta p\left(\frac{\partial v_x}{\partial x}+\frac{\partial v_y}{\partial y}\right), \quad (5)$$

$$h_{v_x} = \frac{\delta_2}{\rho_0}\left(\frac{\partial^2 v_x}{\partial x^2}+\frac{\partial^2 v_y}{\partial y^2}\right), \quad (6)$$

$$h_{v_y} = \frac{\delta_2}{\rho_0}\left(\frac{\partial^2 v_x}{\partial x^2}+\frac{\partial^2 v_y}{\partial y^2}\right). \quad (7)$$

Here, we use the linear relation; $\partial p/\partial t = -\rho_0 c_0^2 \partial u/\partial x$, $\nabla\cdot\vec{v} = (-1/(\rho_0 c_0^2))\partial p/\partial t$ an

d $\partial\vec{v}/\partial t = (-1/\rho_0)\nabla p$ . Those non-advective terms are calculated after calculating the advection term [5].

### 3. Results and Discussion

We show the results of calculation for 2-D analysis of the nonlinear sound wave propagation using CIP method. Analytical parameters of calculations are as follows: grid size, $\Delta x$, $\Delta y = 0.005$ [m]; time step, $\Delta t = 4.37$ [μs]; medium, air; the sound speed, $c_0 = 340$ [m/s]; the nonlinear parameter, $\beta = 1.2$ . Consequently, the CFL number is 0.3. A single-shot pulse of sinusoidal whose amplitude and frequency are 500[Pa] and 1[kHz] is given around $(x, y) = (0, 0)$ . **Figure 1** shows the spatial distribution of the initial pressure. Here, the Blackman window is used in *y*-direction as shown in Fig. 1.

**Figure 2** shows spatial distribution of the sound pressure at the time $t = t_s$ where

$$t_s = \frac{\rho_0 c_0^2}{\beta \omega p_0} \tag{8}$$

is the shock formation time. The results of the type-M CIP and the type-C CIP are very similar. Those clearly calculated the shock fronts associated with the nonlinear acoustic wave propagation.

Next, **Fig. 3** shows the sound pressure versus time. The observation point is $(x, y) = (10, 0)$ [m]. i.e., the azimuthal angle is 0 degree. The results demonstrate the generation of the higher harmonic components with wave propagation.

### 4. Conclusion

The study first applies the CIP method to 2-D nonlinear acoustic wave propagation in time domain under the assumption of the weak shock.

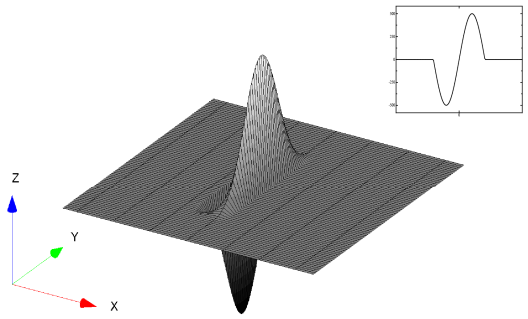


Fig. 1 Initial sound pressure

Numerical demonstrations are made for 2-D nonlinear sound propagation in air. Those verified that the shock front is clearly calculated by the CIP method.

### References


1. H. Takewaki, A. Nishiguchi and T. Yabe: J. Comput. Phys. **61**, (1985) 261.
2. Nakamura T., Tanaka R., Yabe T., Takizawa K: J. Comput. Phys. **174**, (2001) 171.
3. T. Yabe, X. Feng and T. Utsumi: J. of Comput. Phys. **169** (2001) 556.
4. T. Aoki: Comput. Fluid Dynamics Jour. **4** (1995) 279.
5. T. Tsuchiya, K. Okubo and N. Takeuchi: Jpn. J. Appl. Phys. **47**. (2008) 3952.
6. T. Kamakura: *Fundamentals of nonlinear acoustics* (Aichi-shuppan, 1996)
7. M. Konno, K. Okubo, T. Tsuchiya, N. Tagawa: Jpn. J. Appl. Phys. **47** (2008) 3962.


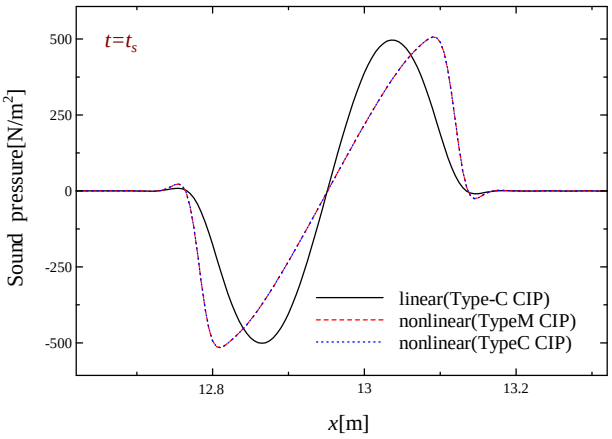


Fig. 2 Sound pressure distribution at $t_s$

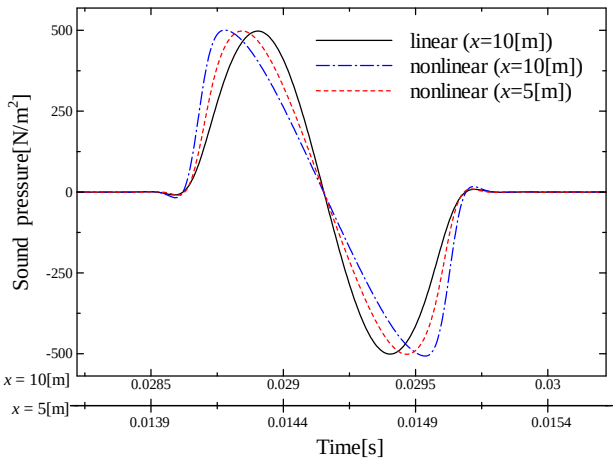


Fig. 3 Sound pressure versus time

Proceedings of Symposium on Ultrasonic Electronics, Vol. 29 (2008) pp. 165-166
11-13 November, 2008

# Shear Mode Type Solidly Mounted Piezoelectric Resonator Using a $LiTaO_3$ Transducer

$LiTaO_3$トランスジューサを用いた横波ＳＭＲの検討

Takehiko Uno, Kei Kasahara and Hiroyuki Tashiro(Facult. Eng., Kanagawa Institute of Technology).
宇野武彦，笠原慧，田代博之 （神奈川工大 工）

## 1. Introduction

Solidly mounted piezoelectric thin film resonator (SMR) is one of the promising bulk acoustic-wave devices for frequency control in a GHz band[1-3]. Thickness extensional mode SMR has been studied up to the present date, because of using the c-axis oriented ZnO thin film for the electromechanical transducer layer. Temperature coefficient of frequency (TCF) is relatively large in SMR because of the negative TCF of ZnO film.

This paper presents the possibility of thickness shear mode SMR having low TCF. Rotated Y-cut (RY-cut) plate of $LiTaO_3$ is used for the piezoelectric layer of the SMR. Thickness shear vibration of low TCF can be excited by parallel electric field in RY-cut $LiTaO_3$ plate. Simulation result shows the possibility of zero TCF shear mode SMR. The simulation result also shows that high effective piezoelectric coupling constant will be realized. Fabrication technique of the shear mode SMR using $LiTaO_3$ plate will be discussed.

## 2. Construction of shear mode SMR

**Figure 1** shows the SMR construction proposed here. $LiTaO_3$ rotated Y-cut plate is used as the piezoelectric transducer. Under the transducer, acoustic multi-layer reflector with low impedance and high impedance layers is formed and mounted on a substrate. Because of the pure shear acoustic wave can be excited by an electric field parallel to the a-axis, two types of electrode configurations may be possible as shown in Fig. 1(a) and (b). In this configuration, mechanical affect on the vibration by electrodes is very small and high resonance Q value will be obtained.

The characteristics of the SMR mainly depend on the piezoelectric transducer. Electro-mechanical coupling constant, $k$, by parallel field excitation can be calculated by ref. 4. For the RY-cut $LiTaO_3$ and $LiNbO_3$, $k$ is given by

$$k = e_{16}' / \sqrt{c_{66}^{E}{}' / \varepsilon_{11}^{S}} \qquad (1).$$

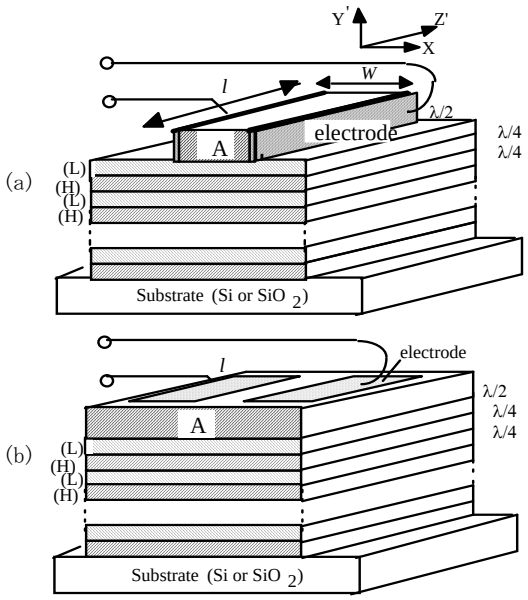


Fig. 1 Shear mode SMR by parallel field excitation.
A: Rotated Y-cut $LiTaO_3$ film.

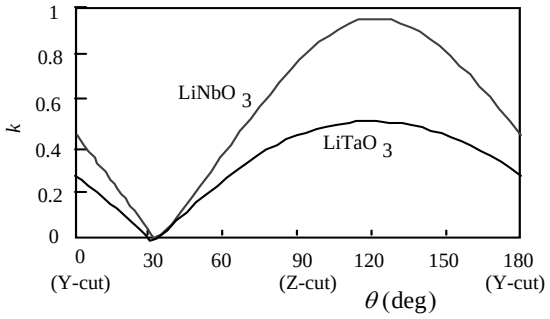


Fig. 2 Coupling constant of parallel field excitation.

**Figure 2** shows cut angle dependency of $k$. The maximum coupling constant value for $LiNbO_3$ (LN) is about 0.9 and that for $LiTaO_3$ (LT) is about 0.5. In spite of high electro-mechanical coupling, frequency temperature characteristic is not so good for LN. On the other hand, zero and positive TCF can be obtained for LT as shown by **Fig.3** curve (a). In the calculation, constant values by Smith and Welsh[5] were used. Temperature characteristics of SMR depend also on the materials

tk_u-no@ele.kanagawa-it.ac.jp

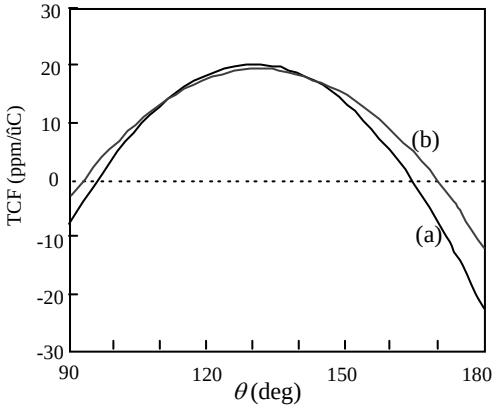


Fig. 3 1st order frequency temperature coefficient.
(a) Rotated Y-cut $LiTaO_3$ shear wave resonator.
(b) SMR by $LiTaO_3$ RY-cut plate.
High Imp.: ZnO
Low Imp. : $SiO_2$(amorphous)
Reflection layers: 8 (ZnO:4 + $SiO_2$:4)

of the reflector.

Curve (b) in Fig. 3 shows the calculated value of the SMR.

Negative TCF of ZnO is almost cancelled by positive TCF of the amorphous $SiO_2$, and the TCF of SMR is almost same as the LT RY-cut plate. However, practical temperature characteristics of LT parallel field excitation resonators are somewhat complicated[6], the cut angle range for positive TCF of SMR may be narrower than the range shown in Fig. 3.

**Figure 4** shows the calculated result of effective electromechanical coupling factor of the SMR. The k value is 85-90% of LT parallel field excitation resonator plate for each cut angle. This means that 75-80% of vibration energy is trapped in the transducer.

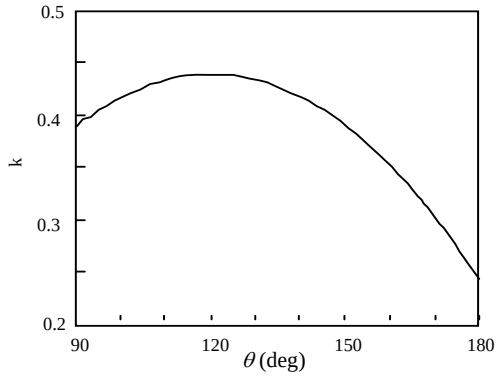


Fig. 4 Effective electromechanical coupling constant of SMR.
Configuration conditions: Same as Fig.3 (b).

## 3. Fabrication process

Thin film of $LiTaO_3$ is impossible at present. Therefore, thin plate of $LiTaO_3$ must be used. The fabrication process of the SMR is shown in **Fig.5**.

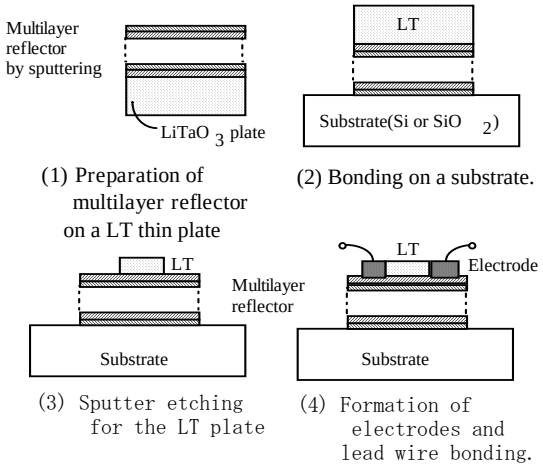


Fig. 5 Fabrication process of the SMR.

First, the multilayer acoustic wave reflector is deposited on a $LiTaO_3$ plate. Next, the resonator is bonded on a substrate. The third step is milling the $LiTaO_3$ plate. Because reactive etching of $LiTaO_3$ impossible, sputter etching by Ar plasma is the only way at present. The last step is electrode deposition and lead wire bonding.

## 4. Conclusion

A configuration of shear mode solidly mounted piezoelectric resonator is proposed. UHF band resonator having low temperature coefficient may be possible to realize. The resonator may be applicable for UHF band resonators, filters and high sensitive gas and liquid sensors.


## Acknowledgment

This work is supported by a Grant-in Aid for Scientific Research from the Japanese Ministry of Education, Culture, Sports, Science and Technology.


## References


1. K. M. Lakin, K. T. McCarron and R. E. Rose: Proc. IEEE Ultrasonics Symp. 1995, p.905
2. H. Kobayashi, Y. Ishida, K. Ishikawa, A. Doi and K. Nakamura: Jpn. J. Appl. Phys. **41**(2002)3455
3. K. Nakamura, S. Sato, S. Ohta, K. Yamada and A. Doi: Proc. IEEE Ultrasonics Symp. 2003, p.1438
4. T. Yamada and N. Niizeki: J. Appl Phys. **41**(1970)3604
5. R. T. Smith and F. S. Welsh: J. Appl. Phys. **42**(1971)2219
6. T. Uno: Proc. Intern. Symp. Circuit and systems, 1979 ,p. 892.

Proceedings of Symposium on Ultrasonic Electronics, Vol. 29 (2008) pp. 167-168
11-13 November, 2008

# Monitoring of aggregation behavior of amyloid β peptide using wireless-electrodeless quartz-crystal microbalance

無線・無電極 QCM を用いたアミロイドβ凝集過程のモニタリング

Yuji Fukunishi[1†], Kenichi Hatanaka[1] Hirotsugu Ogi[1, 2], Masahiko Hirao[1], Masayoshi Nishiyama[3]
[1] Graduate School of Engineering Science, Osaka University.
[2] Life Phenomena and Measurement Analysis, JST PRESTO
[2]Renovation Center of Instruments for Science Education and Technology, Osaka University.
福西勇志 [1‡], 畑中健一 [1], 荻博次 [1, 2],平尾雅彦 [1], 西山雅祥 [3]
[1] 大阪大学 大学院基礎工学研究科, [2] JST さきがけ, [3] 大阪大学科学技術機器教育リノベーションセンター

## 1. Introduction

Alzheimer disease (AD) is a kind of dementia that causes the decline of cognitive faculty and change in the personal character. Recent intensive studies [1-3] demonstrated that Aβ peptide is the dominant pathogeny of AD. In a healthy people, the concentration of the Aβ peptide is controlled by specific enzymes and antibodies in the cortical area of the brain. However, several factors make the concentration of Aβ higher, and when it exceeds a critical value, agglutinates of Aβ peptides are formed, resulting in neurotoxicity and cell cytotoxicity [4]. Therefore, the aggregation mechanism of Aβ peptide is very important for the development of drugs for AD. Many relative studies were reported, but quantitative and real-time monitoring of the aggregation process of Aβ peptides has not been achieved because of the measurement difficulty.

In this study, we focus on using quartz-crystal microbalance (QCM) biosensor for the study of the aggregation behavior of Aβ peptides. QCM has shown pronounced ability for studying recognition behavior among biochemical molecules through changes of resonance frequencies of the quartz plate. The surface-modified quartz plate adsorbs target molecules, resulting in the increase of the effective mass of the resonator system and then in the decrease of the mechanical resonance frequencies. The resonance frequency can be monitored during the binding reactions in real time without any labeling, yielding thermodynamic binding constants. The QCM is a mass-sensitive biosensor, and its sensitivity deteriorates for Aβ peptides because Aβ has a low molar weight (~4 kDa). Thus, it is required to improve the QCM sensitivity. Most reliable approach is making the quartz-plate thickness diminished, because the QCM sensitivity is inversely proportional to the square of the thickness. We propose a wireless-electrodeless technique for this and achieved advanced QCM systems with much higher fundamental frequencies up to 90 MHz [5-7].

Here, we study the aggregation behavior of Aβ peptides using a 55-MHz wireless QCM we developed and discuss their aggregation mechanism quantitatively.

## 2. Experimental Procedure

The 30-μm thick AT-cut quartz plate, whose fundamental resonance frequency is near 55 MHz, was used. For the gold-alkanethiol binding reaction, we deposited 9-nm Au films after 1-nm Cr films on both surfaces of the quartz plate. The crystal was cleaned in the piranha solution (98%$H_2SO_4$: 33% $H_2O_2$=3 : 7) , and after rinsing with ultrapure water, it was immersed in a 10 mM 10-carboxy- 1-pentanethiol solution for 24 h. The surfaces of the sensor were then activated using a 100 mM 1-ethyl-3-(3-dimethyl aminopropyl) carbodiimide (EDC) solution. Then, the crystal plate was immersed in a 50 μg/ml 1-42-Amyloid-β-peptide ($Aβ_{1-42}$)/DMSO-PBS solution for 24h. After blocking the crystal sensor for 1 h using a 50 mM glycine, the sensor crystal was set in the handmade sensor cell, and the sensor cell was incorporated in the homebuilt flow-injection system as shown **Fig. 1**. The micropump provided a constant flow of buffer solution (PBS; pH7.4) at flow rate of 500 μl/min. The solution flowed sensor cell through degasifier and 3 m Teflon tube that made the solution temperature stable at a set value (37℃).

The rf-bursts were applied to the generation

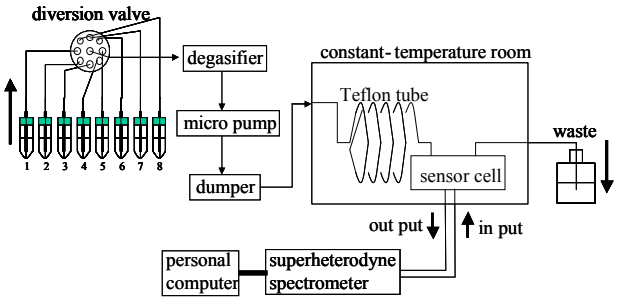


Fig. 1 Homebuilt flow injection system

antenna to generate the shear-horizontal vibration of the quartz in a noncontact manner. After the excitation, the reverberating signals were received by the receiving antenna, which entered into the superheterodyne spectrometer to measure the phase and amplitude of received signal. As an analyte to be injected, we used a 50 μg/ml $A\beta_{1-42}$/PBS solution.

## 3. Result

**Fig. 2** shows an example of observed resonance-frequency change during the aggregation of the Aβ peptide. We succeed in monitoring the aggregation of the Aβ peptide despite its smaller molecular mass. After the injection, the resonance frequency monotonically decreased, without showing a saturation. Thus, the aggregation of the peptide is clearly demonstrated.

## 4. Discussion

According to the Sauerbrey equation [8], the rate of the change in the resonance frequency equals the rate of the absorbed mass of the protein to the oscillator mass. The expression is shown as follows.

$$\frac{\Delta f}{f} = -\frac{\Delta m}{M} \qquad (1)$$

Here , $f$ , $\Delta f$, $M$, and $\Delta M$ denote the resonance frequency, the decrement of resonance frequency, mass of the oscillator, and mass of the adsorbed protein on oscillator, respectively. According to this concern, the amount of the Aβ peptide that adsorbed on the oscillator for 9 h is calculated as 3.55 pmol. This leads to the prediction of the aggregation rate that 144 Aβ monomers will agglutinate in the brain on the area of 1 $nm^2$ every year. The previous study [9] showed that the Aβ monomer changed into the Aβ fibril for 6 h after the Aβ monomer was incubated, indicating that 0.1 Aβ monomers agglutinate in the area 1 $nm^2$ for 6 h after. Thus, our measurement showed that nearly 1500 times Aβ monomers agglutinated for making fibril compared with the previous study. Some study reported that Aβ fibrils have cell cytotoxicity, and their cell cytotoxicity kill cells and cause AD [10]. Therefore, the concentration of the Aβ peptide we used in this study can cause AD. As above, measuring the aggregation of Aβ peptides quantitatively can provide us with important information about the inherent biochemical property of Aβ peptides, and it helps us to understand AD.

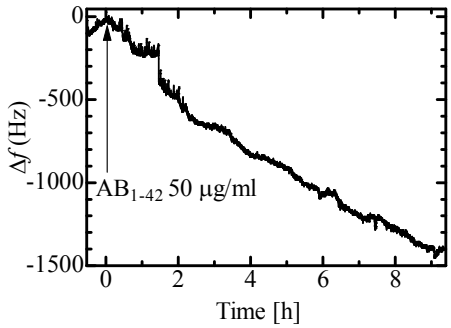


Fig. 2 Frequency response during the aggregation of the $A\beta_{1-42}$ peptide

## 4. Conclusion

We developed a high sensitivity QCM by excluding wires and electrodes, and succeed in monitoring the aggregate behavior of $A\beta_{1-42}$ (molecular weight 4kDa) without labeling. The aggregation rate was estimated to be 144 molecules/(year・$nm^2$), following the Sauerbrey equation. The wireless-electrodeless QCM will contribute to the study of the aggregation mechanism of Aβ peptides.

**Acknowledgment**
This study was supported by Life Phenomena and Measurement Analysis, PRESTO, by Japan Science and Technology Agency.

**References**

1. D. J. Selkoe: Neuron **6** (1991) 487.
2. E. Bossy-Wetzel, R. Schwarzenbacher, S. A. Lipton:, Nat. Med. **10** (2004) S2.
3. D.J. Selkoe: Physiol. Rev. **81** (2001) 741.
4. D. Loo, A. Copani, C. Pike, E. Whittemore, A. Walencewicz, and C. Cotman: Proc. Natl. Acad. Sci. USA **90** (1993) 7951.
5. H. Ogi, Y. Fukunishi, T. Omori, K. Hatanaka, M. Hirao, and M. Nishiyama: Anal. Chem. **80**, (2008) 5494.
6. H. Ogi, T. Omori, K. Hatanaka, M. Hirao, and M. Nishiyama: Jpn. J. Appl. Phys. **47** (2008) 4021.
7. H. Ogi, K. Motohisa, K. Hatanaka, T. Ohmori, M. Hirao, and M. Nishiyama: Biosens. Bioelectron. **22**, (2007) 3238.
8. G. Sauerbrey: Z.Phys. **155** (1959) 206.
9. Nuria Benseny-Cases, Mercedes Cocera, Josep Cladera: Biochem. Bioph. Res. Commu. **361** (2007) 916.
10. K. Girigoswami, S. Ku, J. Ryu, and C. Park: Biomat. **29** (2008) 2813

Proceedings of Symposium on Ultrasonic Electronics, Vol. 29 (2008) pp. 169-170
11-13 November, 2008

# 凹凸 $SiO_2$/Cu 電極/ $LiNbO_3$構造弾性表面波デュプレクサ

**Surface Acoustic Wave Duplexer composed of $SiO_2$/Cu-electrode/$LiNbO_3$ Structure having convex and concave portions**

中井 康晴†, 中尾 武志, 西山 健次, 門田 道雄 (村田製作所)
Yasuharu Nakai, Takeshi Nakao, Kenji Nishiyama, Michio Kadota (Murata MFG. Co.,Ltd.)

A transition bandwidth between a transmission (Tx: 1850-1910MHz) and a receiving (Rx: 1930-1990MHz) of Personal Communication Services (PCS) handy phone in US is very narrow as 20MHz compared with other systems. Authors have already realized the 5.0×5.0×1.7 or 3.0×2.5×1.2mm$^3$ size SAW duplexer for US-PCS which has a good temperature coefficient of frequency (TCF) by using the SH wave on flattened-$SiO_2$/Cu-electrode/36～48° YX-$LiTaO_3$ structure and Rayleigh wave on $SiO_2$/Cu-electrode/120～128° YX-$LiNbO_3$ structure. Though the surface of above-mentioned structures is the flattened $SiO_2$, authors also studied the shape of the surface of the $SiO_2$. As a result, in addition to increase of reflection coefficient, the TCF and power durability have been improved by making convex portions on the surface of the $SiO_2$ over the IDT's gap.

## 1. はじめに

USのPersonal Communication Service(PCS)の規格は、送信側と受信側の周波数間隔が20MHzと非常に狭いため、適した電気機械結合係数、良好な周波数温度特性(TCF)、大きい反射係数をもつSAW基板が必要である。著者らはこれまでに、$SiO_2$膜表面に凸部のない平坦化$SiO_2$/Cu電極/36～48° YX-$LiTaO_3$構造のSH波を用いた温度特性の良好な 5.0×5.0×1.7mm$^3$のワイヤボンディング型SAWデュプレクサや、さらに小型化のために送信側に$SiO_2$/Cu電極/120～128° $LiNbO_3$構造のレイリー波を用いたフリップチップボンディング型の小型 3.0×2.5×1.2mm$^3$ サイズや 2.5×2.0×0.48mm$^3$ サイズSAWデュプレクサの開発や実用化を行っている[1][2]。

フリップチップボンディング型の送信側の開発過程において、$SiO_2$/Cu 電極/120～128° YX-$LiNbO_3$構造の表面$SiO_2$の形状について検討を行った。その結果、ギャップ部分の$SiO_2$表面を凸形状にすることにより、$SiO_2$表面が平坦な構造に比べ、電気機械結合係数の劣化なしに反射係数が増大した。また、従来の平坦構造に比べ耐電力性の面でより長寿命化することができた[3]。本稿ではそれらの結果について報告を行う。なお、$SiO_2$を用いた凹凸構造についてはいくつかの提案例があるが[4][5]、著者らは、電極が Cu である点と表面を$SiO_2$で被覆した構造についての測定結果がある点で異なっている。本稿の構造や計測結果などについては2006年に出願済である[3]。

## 2. 計算結果

これまで著者らによって、$SiO_2$、電極、基板の組み合せのうち、Fig1(a)に示すような電極指に起因した$SiO_2$の凸部をもつ構造や(b)のように $SiO_2$表面を平坦化した $SiO_2$/Cu 電極/圧電基板構造が報告されている[1][2]。平坦化は特性劣化防止のため、Cu電極は大きな反射係数を得るために使用されている。今回、新たにFig 1 (c)(d) のようにIDTのギャップ上部の$SiO_2$をIDT膜厚と異なる厚さの凹凸形状にした構造の検討を行った。ここで、Fig1のように基準となる第1の$SiO_2$膜厚を$h_1$、基準膜厚からの追加した第2の$SiO_2$膜厚を$h_2$とする。これらの構造について有限要素法を用いて、温度特性、電気機械結合係数、反射係数の計算を行った。計算は、基板 126° YX-$LiNbO_3$、電極 Cu、厚さ 0.04λ、メタライゼイションレシオ 0.5 で行った。λはSAWの波長である。第1の$SiO_2$膜厚$h_1$を 0.25λとして、平坦及び凹、凸形状の第2の$SiO_2$膜厚$h_2$を上に追加した構造で計算した。

計算の結果、温度特性はいずれの構造においても第2の$SiO_2$膜厚$h_2$の増加すると、改善することがわかった。電気機械結合係数については、(d)構造では第2の$SiO_2$膜厚$h_2$の増加に対して、大きく減少するが、(b)・(c)構造では第2の$SiO_2$膜厚$h_2$の増加に対して、電気機械結合係数の減少は小さいことがわかった。反射係数については第2の$SiO_2$膜厚$h_2$の増加に対して、(b)・(d)構造で減少するが、(b)構造ではその減少量はわずかにすぎない。一方、(c)構造では第2の$SiO_2$膜厚$h_2$の増加に対して、反射係数が増大することがわかった。

以上のことから、$SiO_2$/Cu 電極/128° YX-$LiNbO_3$構造のレイリー波では、(c)構造にすることで、電気機械結合係数の減少なしにTCFを改善し、反射係数も大きくすることが期待できる。(b)構造で、単に Cu 電極膜厚を厚くしても反射係数は得られるが、(c)構造で得られるもう一つの利点については後述する。

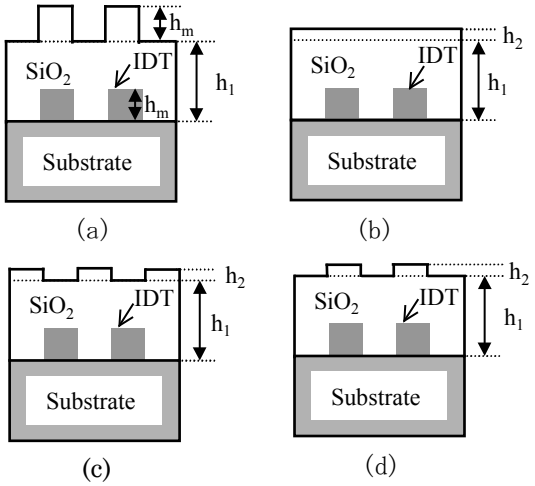


Fig1. $SiO_2$/Cu-electrode/$LiNbO_3$ structure

y_nakai@murata.co.jp

## 3.1port 共振子の試作結果

126° YX- $LiNbO_3$ 基板上に波長 1.95μm、対数 120 対、交叉幅 32.3μm、膜厚 0.04λの Cu 電極と、膜厚 0.25λの $SiO_2$ を用い 1port 共振子を作製した。作製した構造は、(b)・(c)構造の 2 つの構造である。

Fig2 に試作した 1port 共振子の温度特性測定結果を示す。両構造とも、第 2 の $SiO_2$ 膜厚 $h_2$ の増加とともに温度特性が改善することが確認できた。

Fig3 に試作した 1port 共振子の比帯域幅を示す。両構造とも、第 2 の $SiO_2$ 膜厚 $h_2$ の増加に対する比帯域幅の変化が小さいことが確認できた。

Fig4 に試作した 1port 共振子のストップバンド幅を示す。(b)構造では、第 2 の $SiO_2$ 膜厚 $h_2$ の増加とともにストップバンド幅が減少するが、(c)構造では増加することが確認できた。

## 4.デュプレクサの試作結果

1port 共振子の試作結果をもとにデュプレクサの試作を行った。第 2 の $SiO_2$ 膜厚 $h_2$ が 0.02λのときの(b)・(c)構造の送信側フィルタの特性を Fig5 に示す。ほぼ同等の特性を持ちながら、(c)構造では温度特性が 3～5ppm/℃改善することを確認した。

## 5.耐電力性の評価結果

試作した 1port 共振子を用いて耐電力性の評価を行った。評価の結果、(c)構造で第 2 の $SiO_2$ 膜厚が増加するに従い耐電力寿命が、約 3 倍程度に改善することを確認した(6)。有限要素法を用いて、応力解析を行ったところ(c)構造にすることで、IDT に波の伝播方向にかかる応力が、小さくなることがわかった。この応力の低減が、耐電力性改善の一つの要因だと推定する。

## 6.むすび

$SiO_2$/Cu 電極/$LiNbO_3$ 構造の LN レイリー波においてギャップ部分の $SiO_2$ 表面を凸形状にすることで、反射係数や耐電力性が改善することを実測により確認した。また、デュプレクサを試作したところ同等の常温特性で温度特性が 3～5ppm/℃程度改善した。

これらの結果をもとに、US-PCS 向けデュプレクサの実用化にあたって、この凹構造を採用している。

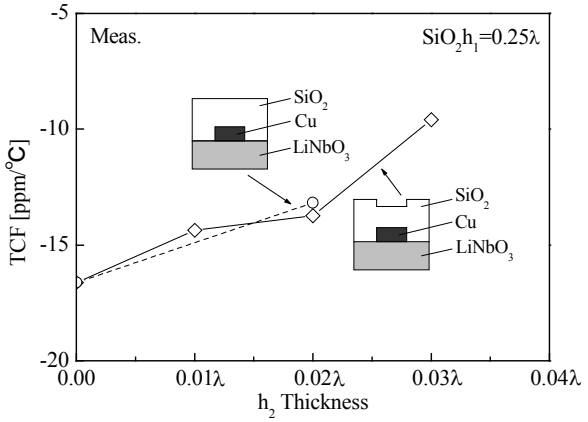


Fig2. Temperature coefficient of frequency as a function of $h_2$ thickness

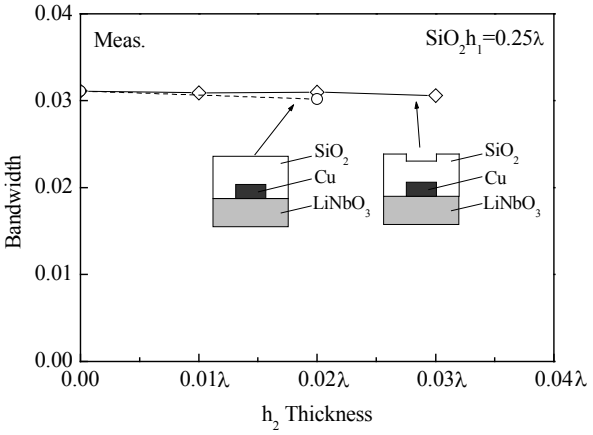


Fig3. Bandwidth as a function of $h_2$ thickness

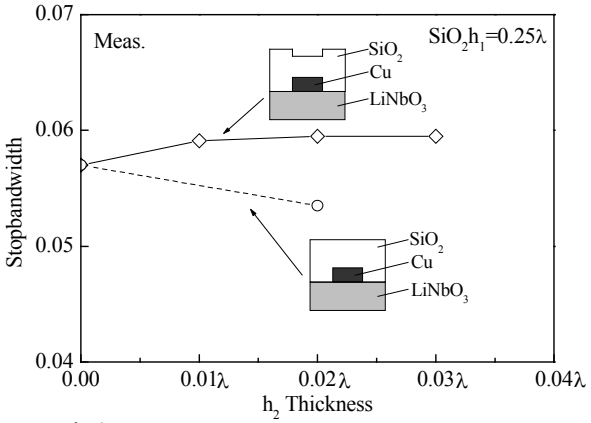


Fig4. Stopbandwidth as a function of $h_2$ thickness

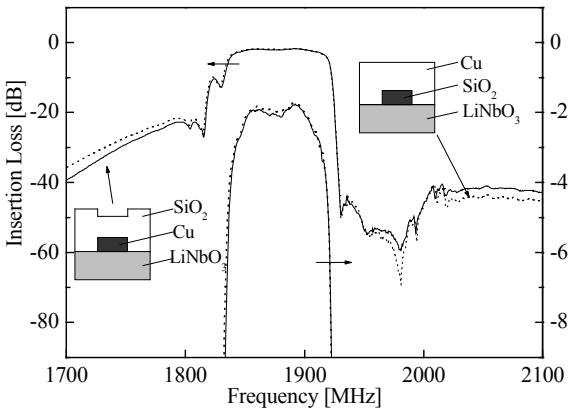


Fig5. Tx filter response of flattened structure and conex structure

## 文 献


(1) M.Kadota, T.Nakao, N.Taniguchi, E.Takata, M. Mimura,K.Nishiyama,T.Hada,and T.Komura: Jpn. J. Appl. Phys., 44, (2005)p.4527-4531.

(2) T.Nakao, M.Kadota, K.Nishiyama, Y.Nakai, D. Yamamoto, Y.Ishiura, T.Komura, N.Takada, R.Kita : Jpn. J. Appl. Phys.,46,(2007)p4760-p4763.

(3)木戸,中尾,中井,西山,門田：特願 2006-056378 (2006.3.20)及び PCT/JP2007/051995(2007,2,6)

(4)村沢,小西,大森,橋本,山口：圧電材料・デバイスシンポジウム 2008,P123-126.

(5)竹内,山之内：電子情報通信学会論文誌 Vol.J85-C No.9 p709-p716

(6)中井,中尾,西山,門田:信学技報 Vol.108.No19(2008.3) p11-p15

Proceedings of Symposium on Ultrasonic Electronics, Vol. 29 (2008) pp. 171-172
11-13 November, 2008

# ZnO/高密度電極/水晶構造高周波共振子型フィルタ

High Frequency SAW Resonator Filter composed of ZnO/High-density-electrode/quartz Structure

門田 道雄, 中尾 武志, 松田 賢二†, 村田 崇基 (村田製作所)
Michio Kadota, Takeshi Nakao, Kenji Matsuda, Takaki Murata, (Murata MFG. Co.,Ltd.)

Radio frequency filters with a narrow band width.and high attenuations are required in recent years. One of the substrates with a suitable coupling factor and an excellent TCF for this filter is a ZnO film/Al electrode/quartz substrate. However, the reflection coefficient of this substrate has not reported, and both the RF SAW filter and the multiple mode resonator one using this substrate have not been reported. In this report, an RF narrow band SAW resonator filter composed of the ZnO/high density metal electrode/quartz structure was realized to obtain a suitable reflection coefficient, and it has minimum insertion loss of 2.08 dB, bandwidths of 3.9MHz (0.054%), and excellent TCF of 4.0ppm/°C.

## 1. はじめに

近年、MediaFLO™ や TD-SCDMA 等、RF 帯において高減衰で狭帯域(0.7%程度)なフィルタ特性が求められているものがある[1]。このようなフィルタ特性を実現するためには、適した電気機械結合係数と良好な周波数温度特性(TCF)をもつ弾性表面波(SAW)基板が必要であり、平坦化 $SiO_2$ 膜/高密度電極/$LiTaO_3$ 基板を用いた狭帯域 RF フィルタの報告がある[1]。一方、この狭帯域フィルタに適した結合係数と良好な TCF をもつ他の材料として ZnO 膜/すだれ状電極(IDT)/水晶基板があり[2][3]、著者の 1 人等によりこの構造を用いた携帯電話の IF 用 SAW トランスバーサル型フィルタの報告がある[2][3]。しかし、これまで、この構造を用いた RF フィルタや多重モード共振子型フィルタの報告はない。本報告では、この ZnO/IDT/水晶構造を用いて RF 用共振子型 SAW フィルタの検討を行ったので報告する。

## 2. 解析結果

**Fig.1** に ZnO 膜/ST-35ºX 水晶構造における電気機械結合係数の ZnO 膜厚依存性を示す。著者の 1 人等が報告した ZnO/Al 電極/26ºYX 水晶構造トランスバーサル型 SAW フィルタでは、ZnO=0.27λ、Al=0.026λにて 0.37ppm/°C の良好な TCF を得ているが、今回多少 TCF を犠牲にしてでももう少し大きい結合係数を得たいので、ZnO 膜厚は 0.5λを用いることにした。多重モード共振子型フィルタを設計する場合には、反射係数は重要なパラメータであり、上述の ZnO 膜と水晶を用いた IF 用トランスバーサル型 SAW フィルタでは Al 電極を用いていたが、他の高密度な電極材料についても、反射係数の検討を行った。**Fig.2、3** に ZnO 膜厚が 0.5λ、電極指のメタライゼーション比 0.5 における、各種電極の厚みに対する反射係数と結合係数を示す。図中に示した形状で FEM で求めた Al における反射係数はマイナスを示し、Cu、Ni は 0.05λ近傍でプラスからマイナスに変化する。Au は示した範囲ではプラスを示したままである。一方、電気機械結合係数は電極間で多少差があり、示した電極の中では Al は大きいが Au は小さい。Al 電極、Au 電極の厚みが 0.03λ、0.04λ、0.05λにおける反射係数の ZnO 膜厚依存性を **Fig.4** に示す。ZnO 膜を厚くすることにより Fig.4 に示したように、反射係数は小さくなることがわかる。

ken2_matsuda@murata.co.jp

**Fig.5** に ZnO 膜 0.5λ、電極膜 0.03λにおける反射係数のメタライゼーション比を示す。メタライゼーション比 0.37 以上で Al の場合マイナスの反射係数を示し、Au の場合はメタライゼーション比 0.5 より 0.3～0.4 の方が大きい反射係数を示している。また、その結合係数は図示していないが、Au の場合メタライゼーション比 0.5 のときよりごくわずかに大きくなる。以上よりプラスを示す反射係数と電気機械結合係数を考慮し、ZnO 膜 0.5λ、Au 電極 0.03λ、メタライゼーション比 0.3～0.4 近傍で設計することにした。

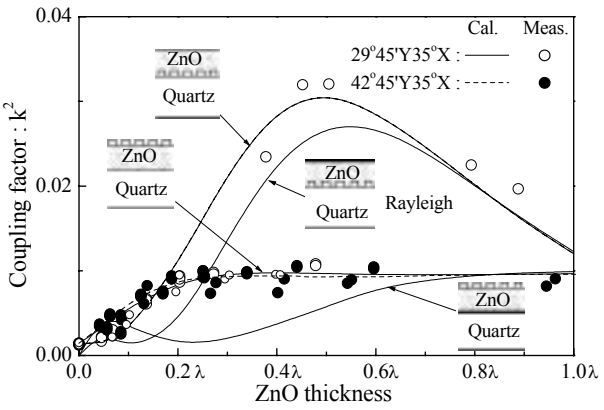


Fig.1 Electromechanical coupling factor of ZnO/quartz as a function of ZnO thickness.

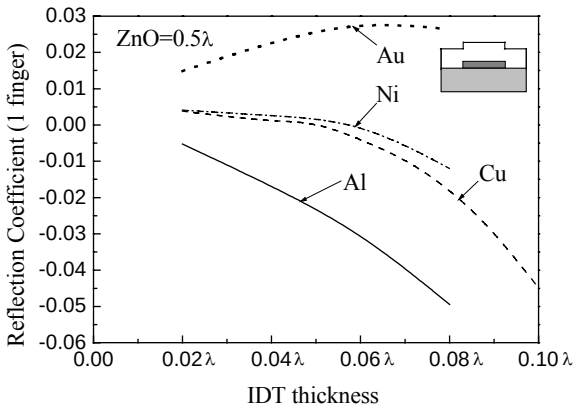


Fig.2 Reflection coefficient (1 finger) of ZnO/various IDT/27ºYX quartz as function of IDT thickness at ZnO thickness of 0.5λ.

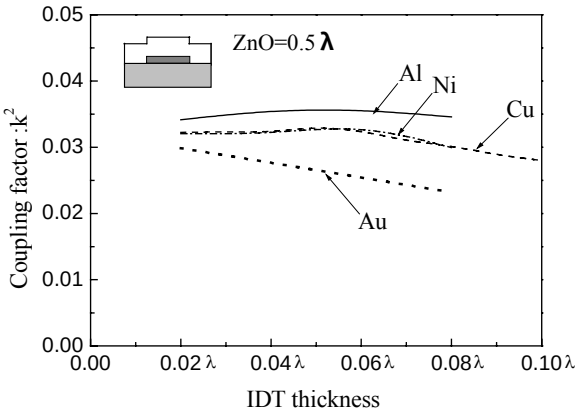


Fig.3 Coupling factor of ZnO/ various IDT/27ºYX quartz as function of IDT thickness at ZnO thickness of 0.5λ.

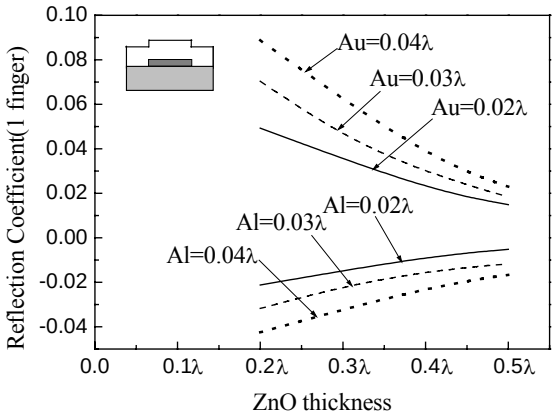


Fig.4 Reflection coefficient of ZnO/IDT/27ºYX quartz as function of ZnO thickness at Au and Al thickness of 0.2, 0.3, 0.4λ.(Metalization ratio)

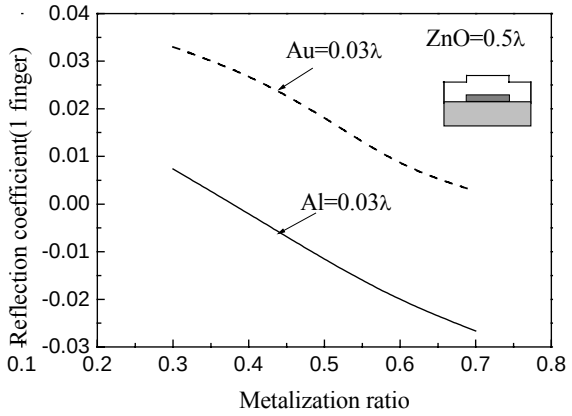


Fig.5 Reflection coefficient as function of the metalization ratio.

## 3.フィルタの試作結果

ZnO/Au-IDT/水晶構造を用いて MediaFLO(中心周波数 719MHz、、帯域幅 5MHz)向け RF 帯における共振子型 SAW フィルタを試作し、**Fig.7** にその特性を示す。ここで、設計パラメータは ZnO 膜厚 0.5λ、Au 電極 0.028λ、λ=3.62μm、メタライゼーション比=0.3～0.4 であり段数は 1 段である。**Fig.6** より、最小挿入損失 2.08dB、3dB 帯域幅 3.9MHz(0.54%)の特性が得られた。所望の帯域より狭いが、ZnO 膜質の向上やより詳細な設計を今後行っていく予定である。**Fig.8** に-30～85℃におけるフィルタの周波数変化を示す。その TCF は 4.0ppm/℃となっており良好な温度特性を得られている。

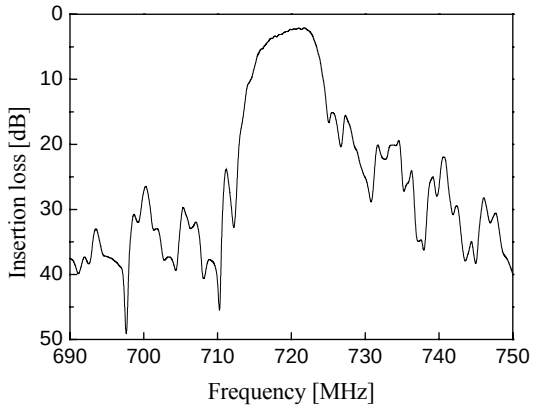


Fig.7 Frequency Characteristic of the fabricated filter.

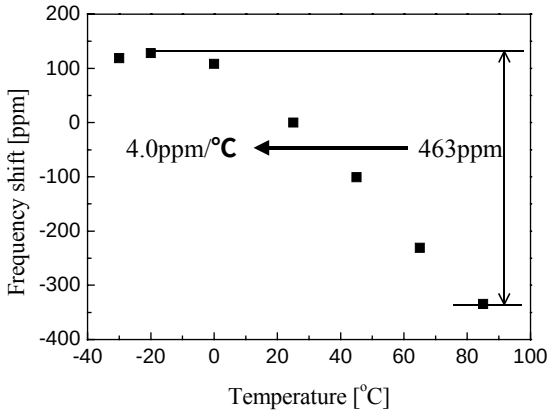


Fig.8 Frequency shift of the fabricated filter relative to temperature.

## 4.むすび

RF 帯での狭帯域フィルタの材料として、適した結合係数と良好な TCF を持つ ZnO/Au-IDT/水晶構造について検討を行った。まず、計算により Au 電極を用いると比較的大きなプラスの反射係数が得られることがわかった。次に、メタライゼーション比について検討を行い、Au 電極ではメタライゼーション比を小さくするほど、反射係数が大きくなることが分かった。そして ZnO/Au/水晶構造を用いて共振子型 SAW フィルタの試作を行い、最小挿入損失 2.08dB、帯域幅 3.9MHz(0.054%)、良好な TCF 4.0ppm/℃を得た。

## 引用文献

(1)T. Murata, M. Kadota, T. Nakao, and K. Matsuda: Jpn. J. Apply. Phys. **47**(2008)4101.
(2) M. Kadota, H. Kando: Jpn. J. Apply. Phys. **42**(2003),3139.
(3)M. Kadota, H. Kando: IEEE Trans. Ultrason. Ferroelectr. Freq. Control **51** (2004) 464.

1J5-3

Proceedings of Symposium on Ultrasonic Electronics, Vol. 29 (2008) pp. 173-174
11-13 November, 2008

# 変調 IDT を用いた Cu 電極/15°YX-$LiNbO_3$ 基板構造広帯域 DMS フィルタ

Wideband DMS Filter Employing Pitch Modulated IDTs on Cu-Grating/15°YX-$LiNbO_3$-Substrate Structure

宮本宗†，大森達也，橋本研也，山口正恆　(千葉大 院工)

Takashi Miyamoto†, Tatsuya Omori, Ken-ya Hashimoto and Masatsune Yamaguchi
(Graduate School of Eng., Chiba Univ.)

This paper discusses the application of Cu-grating/15°YX-$LiNbO_3$(15-LN)-substrate structure to the development of wideband Double-Mode SAW (DMS) filters. This structure seems suitable for the current purpose because of its distinctive features such as extremely large electromechanical coupling factor (circa 30%) and small attenuation with propagation. We applied the pitch modulation technique for the design of IDTs to arrange multiple resonances properly. This arrangement is essential for the realization of flat and wide passband. The result indicates relative bandwidth more than 12% and good out of band rejection are simultaneously achievable. A DMS filter was fabricated on Cu-grating/15-LN substrate. The measured result agreed well with the design, and the passband width of 11.9% and the minimum insertion loss of 1.7 dB were obtained at 900 MHz range.

## 1. まえがき

現在、携帯電話に代表される移動体通信機器の RF 段には DMS フィルタが多用されている。これはこの素子が優れた帯域外抑圧を持つフィルタ機能に加えて、バラン機能やインピーダンス変換機能を併せて実現できることによる。しかし、現行の DMS フィルタでは実現できる-3 dB 比帯域幅が、高圧電性結晶基板に $LiTaO_3$ を用いた場合でも数%程度と狭い。今後の移動体通信機器のデータ伝送量増加および高速化を見据えると、さらに広帯域なフィルタの実現が必要である。

一方、筆者らは Cu 電極/15-LN 基板構造上の高結合非漏洩 SH 型(高結合ラブ波型)SAW を利用すると、非常に広帯域で低損失なラダー型 SAW フィルタが実現できることを報告している[1]。この構造では、約 30%の非常に大きな電気機械結合係数 $K^2$ が得られるため、比帯域幅 20%という非常に広帯域なフィルタを実現できる。また、約 1,000 の高い品質係数 $Q$ と小さな容量比 $\gamma$ も同時に実現できるため、0.5 dB 程度の最小挿入損失を併せて実現できる。

そこで、広帯域 DMS フィルタ実現を目的とし、本構造の適用を以下検討した。

## 2. DMS フィルタの動作原理

2IDT 構成の基本的な DMS フィルタは、**Fig.1** のように共振周波数の等しい 2 つの同一な SAW 共振子を近接配置し、音響的に結合させた電極構造をとっている。これに生じる共振は、構造が左右対称なため、対称な界分布を持つ対称モードと、斜対称な界分布を持ち共振周波数が異なる反対称モードに分類できる。

ここで、両 IDT を並列もしくはたすき掛けに並列接続した際に得られる実行的な 1 ポート共振子のアドミタンスをそれぞれ $Y_e$、$Y_o$ とする。この時、$Y_o$=0 となる反対称モードに対する反共振周波数 $\omega_a^o$ と $Y_e^{-1}$=0 となる対称モードに対する共振周波数 $\omega_r^e$ が一致するか、$Y_e$=0 となる対称モードに対する反共振周波数 $\omega_a^e$ と $Y_o^{-1}$=0 となる反対称モードに対する共振周波数 $\omega_r^o$ が一致するとき、入出力間を無損失伝送できる。一般に、$\omega_r^e$ と $\omega_r^o$ は交互に現れる。また、$\omega_a^e$ は $\omega_r^e$ より若干高い。そのため、複数の連続する共振周波数で上記の無損失伝送条件を満足するように設計できれば、その周波数範囲で平坦な通過域が形成できる[2]。なお、一般的な DMS フィルタ設計法では、反射器間の 2 種類の共振と IDT が反射器として動作する際に中央の空隙間で生じる共振の計 3 種を利用することが多い[3]。

Cu 電極/15-LN 基板構造を適用した DMS フィルタを設計したところ、-3 dB 比帯域幅 10%以上の非常に広帯域な通過特性を計算できることがわかった。しかし、それには $\omega_r^e$ と $\omega_r^o$ の間隔を拡げるため、IDT 対数を数対と極端に少なく設計する必要があった[4]。この場合、インピーダンス整合のため開口長を極端に長くする必要があり、IDT における電気抵抗が増大してしまうので現実的ではない。

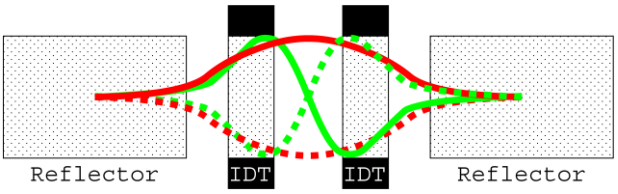


Fig. 1　Two-port DMS resonator.

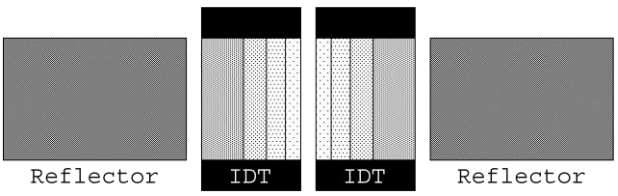


Fig. 2　DMS filter using pitch-modulated IDTs.

†walla-walla@graduate.chiba-u.jp

## 3. 変調 IDT の利用

上述した問題を解決するため、**Fig.2** の様に IDT をいくつかに分割し、IDT 並びに反射器の電極周期を空間的に変調する手法[3]を素子構造に適用した。

この構造では、外側程 IDT の電極周期が大きくなるように設計すると、$\omega$ の増加と共に IDT の外側から順次反射器として動作する。従って、IDT 周期と共にその対数を調節することにより、数多くの周波数で上記の無損失伝送条件を満足できるため、$\omega_r^e$ と $\omega_r^o$ の間隔をあまり拡げなくとも広帯域フィルタが設計可能となる。これにより、IDT の開口長を現実的な値にまで低減できる。また、利用する共振の数の増加によりフィルタのスカート特性が急峻になるという特長も生じる。さらに、設計の自由度が増大するため、あえて中央のスペースを与える必要がなくなる[4]。なお、SH 型 SAW を利用する場合、中央の空隙部における SAW の散乱損失が無視できない[5]ので、フィルタの低損失化にもこの手法は非常に有効だと言える。

## 4. 試作結果

今回、IDT を 4 分割して電極周期を変調した Cu 電極/15-LN 基板構造 DMS フィルタを設計し、実際に試作を行った。

ただし、設計の際に用いるシミュレータには、Abbott らが提案した SH 型 SAW に対する COM モデル[6]を適用した。なお、シミュレータ精度向上を図るため、別途用意した試作 1 ポート共振子のアドミタンス特性と COM 解析結果との比較により決定したパラメータ[7]を計算には用いている。一方、試作には、走査型電子顕微鏡をベースとした電子線露光装置とリフトオフ法を組み合わせた方法[8]を採用した。

まず、試作素子の表面写真を **Fig.3** に示す。バスバーを除いた実質的なデバイスサイズは 180 μm × 129 μm となっており、堆積させた Cu 膜厚は約 250 nm である。次に、試作素子の通過特性 $S_{21}$ を、計算値と併せて **Fig.4** に示す。今回の試作では横モードの対策[1]を施していないため通過域に細かいリップルが見られるものの、最小挿入損失は 880.5 MHz において 1.7 dB であり、-3 dB 比帯域幅が 11.9%と低損失かつ非常に広帯域な特性となっている。

以上のように、Cu 電極/15-LN 基板構造と変調 IDT の利用により、非常に広帯域な DMS フィルタが実現できることを実験的に示せた。

## 5. まとめ

本研究では、広帯域 DMS フィルタ実現を目的とし、Cu 電極/15-LN 基板構造上の高結合ラブ波型 SAW の利用を検討した。また、素子構造に IDT の電極周期を空間的に変調する手法[3]を採用して試作を行った。その結果、最小挿入損失 1.7 dB (880.5 MHz), -3 dB 比帯域幅 11.9%の非常に広帯域な通過特性が得られた。

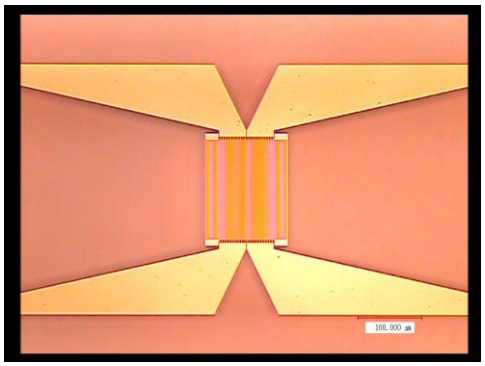

Fig. 3 Microscope photo of fabricated device. (400 μm × 700 μm)

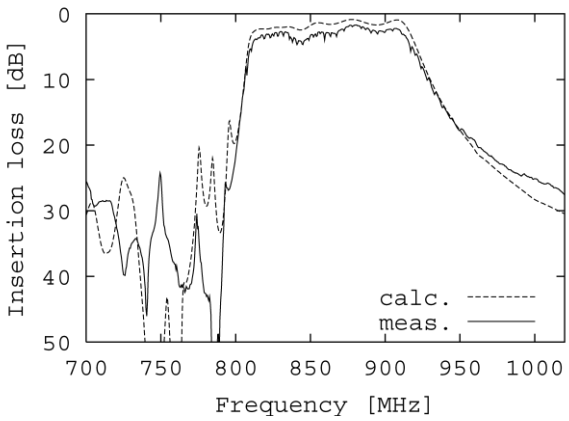


Fig. 4 Frequency response of fabricated DMS filter.


## 謝辞

本研究の一部は独立行政法人日本学術振興会科学研究費補助金並びに独立行政法人科学技術振興機構シーズ発掘試験研究の補助を受けた。


## 引用文献


[1] T.Omori, et al: Proc. IEEE Ultrason. Symp. (2006) 1874-1877.

[2] K.Hashimoto, et al: IEEE Trans. Ultrason., Ferroelec. and Freq. Cont. **51** (2004) 1394-1403.

[3] K.Hashimoto, et al: IEEE Trans. Ultrason., Ferroelec. and Freq. Cont. **54** (2007) 2152-2157.

[4] 宮本 他: 第 36 回 EM シンポジウム予稿集 (2007) 63-68.

[5] O.Kawachi, et al: IEEE Trans. Ultrason., Ferroelec. and Freq. Cont. **54** (2007) 2159-2164.

[6] B.P.Abbott and K.Hashimoto: Proc. IEEE Ultrason. Symp. (1995) 239-245.

[7] 宮本 他: 日本学術振興会弾性波素子技術第 150 委員会第 106 回研究会資料 (2008) 17-22.

[8] H.Hatakeyama, et al, IEEE Ultrason. Symp. (2004) 1896-1900.

# USE2008

The 29th Symposium
on
ULTRASONIC
ELECTRONICS

Wednesday, November 12, 2008

2E1

Proceedings of Symposium on Ultrasonic Electronics, Vol. 29 (2008) pp. 175-176
11-13 November, 2008

# Elastic Constant and Microstructure of Oxide Thin Films Studied by Picosecond Laser Ultrasounds

ピコ秒レーザー超音波法による酸化物薄膜の弾性定数測定と組織評価

Tomohiro Shagawa[1†], Hirotsugu Ogi[1], Nobutomo Nakamura[1], Masahiko Hirao[1], Hidefumi Odaka[2] and Naoto Kihara[2] ([1]Grad. Sch. Eng. Sci., Osaka Univ.; [2]Asahi Glass Co., LTD)

舎川知広[1‡]，荻博次[1]，中村暢伴[1]，平尾雅彦[1]，小高秀文[2]，木原直人[2]（[1]阪大基礎工; [2]旭硝子）

## 1. Introduction

Oxide thin films are used in many devices because of their specific functions such as piezoelectricity, transparency, and insulation ability, and they have been recognized as important industrial materials. Recently, oxide thin films are applied to acoustic devices such as film bulk acoustic resonator (FBAR), achieving an ultrahigh-frequency bulk-wave filter. These devices must have an index of their reliability. Elastic constants can be the index, because the elastic constants of films are significantly decreased by defects. Furthermore, they are important parameters required in designing acoustic devices. Thus, measurement of the elastic constants of thin oxide films is a very important issue. However, conventional techniques (microtensile tests, microbending tests, nanoidentation, and so on) have shown difficulty for determining accurate elastic moduli because they are too much sensitive to the dimension errors and to many ambiguous parameters.

In previous work, we revealed that picosecond laser ultrasounds (PSLU)[1, 2] is an effective method for the measurement of the elastic constants of thin metal films[3, 4]. PSLU technique is classified into three methods; the pulse-echo method[3], the phonon-resonance method[4], and the Brillouin oscillation method[2, 5]. Here, we use the last one because it is effective for transparent materials and it does not require the thickness measurement, which has been troublesome. There is no report determining the elastic constants of thin films using the Brillouin-oscillation method.

There are two purposes in this study. First, we establish the accurate measurement method of oxide thin films by Brillouin oscillation. Second, evaluate of microstructure of oxide thin films, through the elastic constant. We measured the elastic constants of amorphous silica ($a$-$SiO_2$) films by Brillouin oscillations method. Measured elastic constants highly depend on the microstructure. We quantitatively discuss the relationship between elastic constants and microstructure.

E-mail: shagawa@mbox.me.es.osaka-u.ac.jp

## 2. Brillouin Oscillations

Brillouin Oscillations arises in the reflectivity change of the probe light from the interference between the reflected light at the film and the diffracted light by the ultrasound grating in the transparent material. Because the grating moves at the sound velocity, the interference light intensity is oscillated as the ultrasound propagates. Its frequency is determined by Bragg's law. When the probe light enters the material perpendicularly, the Brillouin oscillation frequency $f_a$ takes the form

$$f_a = \frac{2nv}{\lambda_o}, \tag{1}$$

where, $n$ is refractive index of material, $v$ is sound velocity, and $\lambda_o$ is wavelength of the probe light. Thus, measuring the frequency and refractive index, we can determine the sound velocity and then the longitudinal-wave elastic constant.

## 3. Experiments

We deposited $a$-$SiO_2$ films on (001) Si substrate by a reactive sputtering method. We changed sputtering parameter such as sputtering pressure, $O_2$/Ar gas ratio, and sputtering voltage for making various microstructures. Film thicknesses were 200-1000 nm. The results of the x-ray diffraction measurements showed that all samples were amorphous. We observed the cross-section by field-emission scanning electron microscopy (FE-SEM). For generating ultrasound, a 10-nm Al film was sputtered on $a$-SiO2 films.

We used Ti-sapphire pulse laser with 100 fs pulse width, 80 MHz repetition frequency, and 800 nm wavelength. The light pulse was split two pulses. One was the pomp light and the other was the probe light. The pomp light was focused on the Al film to generate ultrasounds through thermal expansion. The probe light was frequency-doubled (400 nm wavelength) and irradiated the sample to detect Brillouin oscillations ($\lambda o$=400 nm in Eq. (1)). The refractive index $n$ was measured by ellipsometry, assuming the Lorentz-oscillator model.

The probe light and ultrasound pulse penetrated to the Si substrate. Hence, two Brillouin oscillations were usually observed. One was from $a$-$SiO_2$, the other was from Si. Since, $n$ of Si is

four times larger than that of $a$-$SiO_2$, the Brillouin-oscillation frequency of Si was significantly larger than that of $a$-$SiO_2$.

## 4. Results

**Figures 1** and **2** show typical reflectivity changes of the probe light, including Brillouin oscillations, and the determined elastic constants of the $a$-$SiO_2$ films, respectively. We observed no Brillouin oscillations of Si from samples S3 and S4, and their elastic constants of the $a$-$SiO_2$ films were lower than the others by up to 30 %. The SEM images showed that S1 and S2 exhibited smooth and flat microstructures, while S3 and S4 exhibited rough and granular microstructures.

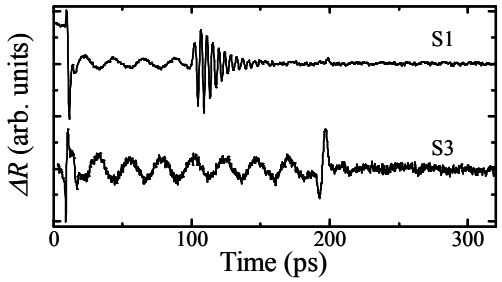


Fig. 1 Reflectivity changes from S1 and S2, showing Brillouin oscillations.

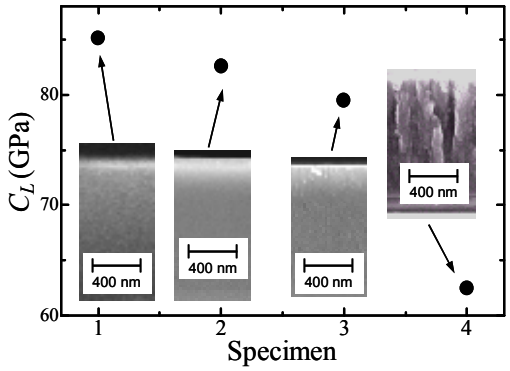


Fig. 2 Elastic constants $C_L$ and cross-section microstructures of $a$-$SiO_2$ films.

## 5. Discussion

S3 and S4 had granular microstructure, indicating scattering loss for the sound wave. Attenuation of ultrasounds by scattering is proportional to the fourth power of the frequency assuming Rayleigh scattering. Therefore, as ultrasound propagates $SiO_2$ film, high-frequency components of ultrasound is attenuated drastically. There are many factors of granular microstructure. However, concerning an amorphous, they are limited to defects and precipitates. Especially, thin defects (nano-micro cracks) decrease elastic constants of materials severely, despite nearly zero volume fraction.

We therefore develop a model to realize the stiffness decrease with defects of very small volume fraction using micromechanics calculation. Eshelby's equivalent-inclusion method and Mori-Tanaka mean-field theory yield the macroscopic stiffness of a composite composed of isotropic matrix and inclusions as

$$\mathbf{C}^{\mathrm{C}} = \mathbf{C}^{\mathrm{M}} + \left[f_{\mathrm{I}}\left(\mathbf{C}^{\mathrm{I}} - \mathbf{C}^{\mathrm{M}}\right)\mathbf{A}^{\mathrm{d}}\right]\left[f_{\mathrm{M}}\mathbf{I} + f_{\mathrm{I}}\mathbf{A}^{\mathrm{d}}\right]^{-1},$$
$$\mathbf{A}^{\mathrm{d}} = \left[\mathbf{S}(\mathbf{C}^{\mathrm{M}})^{-1}\left(\mathbf{C}^{\mathrm{I}} - \mathbf{C}^{\mathrm{M}}\right) + \mathbf{I}\right]^{-1}. \quad (2)$$

Where, $\mathbf{C}^{\mathbf{C}}$, $\mathbf{C}^{\mathbf{M}}$ and $\mathbf{C}^{\mathbf{I}}$ are the elastic-stiffness tensors of the composite, matrix, and inclusions, respectively. $\mathbf{S}$ is the Eshelby tensor determined by Poisson's ratio of the matrix and the shape of the inclusion. $f_{\mathrm{M}}$ and $f_{\mathrm{I}}$ are volume fractions of the matrix and inclusion, respectively. We assumed pan-cake shape air inclusions for defects. **Figure 3** shows the calculation result and estimated volume fraction of measurement elastic constants of samples. These results explain severely decrease of the elastic constant by small volume fraction of the inclusion.

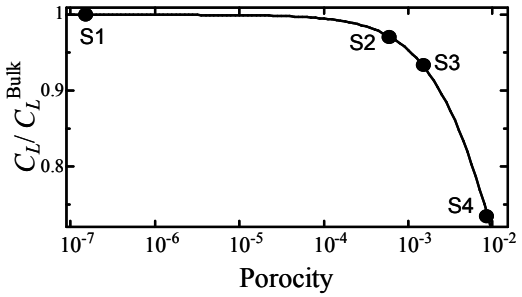


Fig. 3 Relationship between the measured and calculated elastic constants $C_L$ for the defects with the aspect ratio 1/100.

## 6. Conclusion

We studied the elasticity of sputtered $a$-$SiO_2$ thin films using Brillouin oscillations. Granular samples showed smaller elastic constants by 30% and high sound attenuation. Using the micromechanics modeling, we estimated volume fraction of microcracks at lower than 1 %.

## References


1. C. Thomsen *et al.*, *Phys. Rev. Lett.* **53**, 989 (1984).
2. C. Thomsen *et al.*, *Phys. Rev. B* **34**, 4129 (1986).
3. N. Nakamura *et al.*, *Phys. Rev. Lett.* **99**, 035502 (2007).
4. H. Ogi et al., *Phys. Rev. Lett.* **98**, 195503 (2007).
5. A. Devos and R. Côte, *Phys. Rev. B* **70** 125208 (2004).

2E2a

Proceedings of Symposium on Ultrasonic Electronics, Vol. 29 (2008) pp. 177-178
11-13 November, 2008

# High Temperature Integrated Ultrasonic Transducers for Light-Weight Metal Process Monitoring

高温一体型超音波トランスジューサによる
軽金属成形モニタリングの検討

Makiko Kobayashi† and Cheng-Kuei Jen (Industrial Materials Institute, National Research Council Canada)
小林牧子†，任正魁 （工業材料研究所　カナダ国立研究所）

## 1. Introduction

Light weight and high mechanical strength metals such as magnesium (Mg) and aluminum (Al) alloys have become increasingly used for manufacturers in automobile industry in order to enhance fuel-efficiency for ecology purpose. Liquid and semi-solid diecasting and thixmolding (injection molding of Mg alloys) are commonly used production technologies for such materials. High production rate and yield, and quality assurance are crucial factors to ensure the success of these technologies and the increase of the use of these materials.

Due to high pressure and high temperature (HT) and corrosive natures of Mg and Al in the molten state during the above mentioned production processes, it is not simple to perform on-line monitoring of temperature, pressure, microstructure, filling conditions and solidifcaton of the melt. In the past delayed line ultrasonic probes [1] have been utilzied to perform real-time monitoring of Al and Mg alloy diecasting processes, however, these probes needed cooling and were bulky. Holes were required to be made in the die so that these probes can be acommodated. It means that they are invasive sensors. Furthermore, due to the HT and high pressure of the diecasting and thixomolding processes the safety requirements prohibit the use of the above mentioned invasive delay line ultrasonic probes at the nozzle. Any leak of molten metals at any hole which accommodates the invasive probe may lead to serious hazards to human lives. However, current commercially available broadband ultrasonic transducers (UTs) have limitations for HT operations due to the lack of appropriate HT couplant and backing material. They are also not convenient for use at curved surfaces and not reliable under thermal shock or vibration condtions. Therefore HT non-invasive UTs are desired for above mentioned real-time process monitoring applications.

HT integrated UT (IUT) using piezoelectric composite ceramic films made by sol-gel spray technique were reported [2,3]. These IUTs can be directly fabricated onto curved surfaces such as nozzles and die or mold inserts, do not need ultrasonic couplant and have high signal strength and broadband width. They seem suitable for real-time non-invasive monitoring of diecasting and thixomolding processes.

Toward the demonstration of IUTs' suitability for the above mentioned application directions, in this study, two kinds of IUTs were fabricated onto different substrates. Lithium niobate (LN)/ lead-zirconate-titanate (PZT) IUTs [3] were fabricated onto a titanium rod and a steel pipe, and bismuth titanate (BIT)/PZT IUTs were fabricated onto a real thixomolding mold insert in order to investigate their HT ultrasonic performance, thermal shock and cycling resistance.

## 2. LN/PZT IUT onto a titanium substrate

A LN/PZT IUT was fabricated onto a 25.4mm diameter and 26.3mm height titanium rod with around 10mm square platinum top electrode as shown in **Fig.1**. The detail description of fabrication procedure for sol-gel spray technique can be found in elsewhere [2, 3].Titanium rod and platinum paste top electrode were selected because of their high temperature durability.

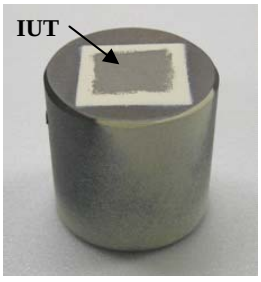


Fig.1 LN/PZT IUT onto a titanium rod.

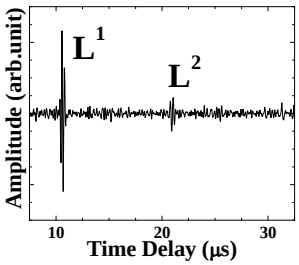


Fig.2 Ultrasonic performance of IUT in Fig.1 at 800°C

To examine the thermal shock resistance and HT operation capability, a propane gas torch was used to heat the LN/PZT IUT shown in Fig. 1. **Fig.2** shows the 1st , $L^1$, and 2nd round-trip, $L^2$, reflected echoes from the bottom of substrate through the thickness of the rod. The center frequency. 6dB bandwidth and signal to noise ratio (SNR) of the $L^1$

Makiko.kobayashi@cnrc-nrc.gc.ca

echo are 4.5MHz, 3.1MHz and 21dB, respectively. It is noted that thermal cycling using the propane gas torch as the heating source was executed 5 times between room temperature and 800°C and no signal deterioration was observed. Since the temperature at the nozzle of the thixomolding or that of a diecasting machine is up to a maximum of about 620°C, it is expected that LN/PZT IUTs are attractive and practical non-invasive ultrasonic sensors for process monitoring at those locations.

## 3. LN/PZT IUTs onto a steel pipe

In order to simulate the nozzle, a steel pipe with an inner diameter of 14.3mm, outer diameter of 38.2mm, and length of 43.5mm was chosen as a substrate. It is noted that normally the nozzle of the thixomolding and diecasting machine can be detached from the machine for IUT fabrication. Two LN/PZT IUTs were then fabricated onto this steel pipe at two opposite cylindrical convex sides facing each other, as shown in **Fig. 3**. This configuration could allow the use of transmission as well as reflection mode operation during process monitoring. .

In order to simulate on-line monitoring at the nozzle, the pipe with LN/PZT IUTs in Fig. 3 was filled in silicone oil and ultrasonic measurement was performed in transmission mode. The result is shown in **Fig. 4**. The transmitted signal through silicone oil was clearly observed at 200°C. The real-time non-invasive process monitoring of thixomolding and Al diecasting at the nozzle is being prepared and the results will be reported in future.

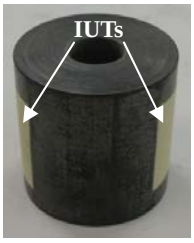


Fig.3 LN/PZT IUTs onto a steel pipe.

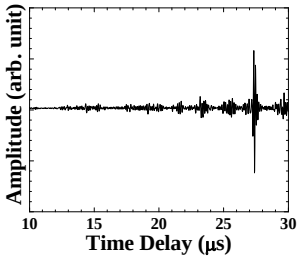


Fig.4 Transmission mode of Fig. 3 with oil at 200°C

## 4. BIT/PZT IUTs onto a mold insert

Filling completion monitoring has been demonstrated in [1] using the invasive and bulky delay line probes installed in the die. One objective of this study is to develop an on-site fabrication technique to deposit the non-invasive and miniature HT IUTs onto a large size metallic mold insert, e.g. of thixomolding machine for process monitoring purposes. It is noted that a large size mold insert has huge thermal capacitance, it needs great care to develop heating and cooling methods as well as electric poling technique to treat the sol-gel fabricated piezoelectric composite films.

Since the temperature of mold insert as shown in **Fig. 5** is lower than 450°C, BIT/PZT IUTs were chosen. The dimensions of this die are of 46cm width, 61cm length and 5cm height, respectively. Several BIT/PZT IUTs were fabricated onto the mold insert. The ultrasonic performance of the IUT fabricated onto the surface is shown in **Fig. 6**. The 1st, 2nd, and 3rd reflected round-trip echoes represented by $L^1$, $L^2$ and $L^3$, respectively through the thickness of the die were clearly observed. The center frequency. 6dB bandwidth and SNR of the $L^1$ echo are 11.9MHz, 15.4MHz and 31dB, respectively. It is believed that BIT/PZT IUTs are suitable for process monitoring of thixomolding and diecasting at the mold insert and the die.

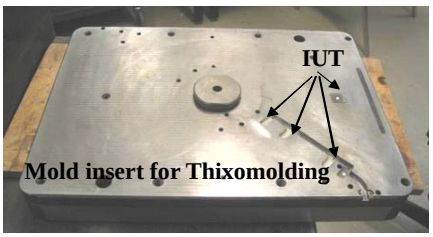


Fig. 5 BIT/PZT IUTs fabricated onto a mold insert for Mg thixomolding machine.

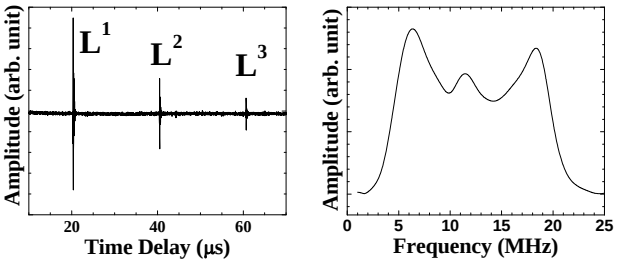


Fig. 6 Ultrasonic performance of BIT/PZT IUT fabricated onto the surface of a thixomolding mold.

## 5. Conclusions

800°C LN/PZT [3] and 450°C BIT/PZT IUTs [2] were fabricated onto a titanium substrate and a steel pipe, and a thixomolding mold insert, respectively by a sol-gel spray technique suitable for on-site fabrication. The ultrasonic measurement results indicated that these IUTs are suitable for real-time non-invasive ultrasonic process monitoring at the nozzle and die of thixomolding and die casting machines.

## References

1. J.-F. Moisan, C.-K. Jen, J.-W. Liaw, C.-Q. Zheng, T.-F. Chen, Z. Sun and C.A. Loong; Measurement Science and Tech. **11** (2001) 1956.
2. M. Kobayashi, C.-K. Jen, Y. Ono, K.-T. Wu and I. Shih: Jpn. J. Apl. Phys. **46** (2007) 4688-4692.
3. M. Kobayashi, H. Nagata, Y. Hiruma, T. Tokutsu, T. Takenaka and C.-K. Jen: Proc. IEEE Ultrasonics Symp (2007) 953.

2E2b

Proceedings of Symposium on Ultrasonic Electronics, Vol. 29 (2008) pp. 179-180
11-13 November, 2008

# Imaging the Acoustic Rectification of Surface Acoustic Waves

音響整流器構造における表面音響波伝播の実時間イメージング

*Sorasak Danworaphong[1†], Timothy A. Kelf[1], Osamu Matsuda[1], Oliver B. Wright[1], Kosei Ueno[2], Yoshiaki Nishijima[2], Saulius Juodkazis[2], and Hiroaki Misawa[2]
([1]Graduate School of Engineering, Hokkaido University, [2]Research Institute for Electronic Science, Hokkaido University)

*Sorasak Danworaphong[1†], Timothy A. Kelf[1], 松田 理[1], Oliver B. Wright[1], 上野 貢生[1], 西島 喜明[2], サリウス ジュドゥカジス[2], 三澤 弘明[2]
([1]北大院工; [2]北大電科研)

## 1. Introduction

Acoustic rectification is the process, analogous to that used in diodes in electronics, in which acoustic waves in a structure are preferentially transmitted in one direction. Recently, acoustic rectifying structures for bulk acoustic waves based on triangular holes were proposed and numerically studied by Krishnan *et al.*[1,2] They used single and double rows of triangular holes on an elastically isotropic and homogeneous material. The transmission coefficients and rectification efficiencies of such waves were calculated, and comparison between the single and double arrays showed that the double arrays had better efficiencies in general. The simulations also indicated the existence of a threshold frequency above which the rectification sets in. This was explained as due to the Bragg diffraction of the acoustic waves, which also gives rise to periodic frequency dips in the transmission and rectification efficiency. Here we experimentally demonstrate acoustic rectification at frequencies ~100 MHz-1 GHz for surface acoustic waves (SAW) on surfaces containing rows of triangular holes.

We make use of an ultrafast imaging technique that combines a time-domain Sagnac interferometer with the optical pump and probe technique.[3,4] Temporal and spatial resolutions are ~1 ps and ~1 $\mu$m, respectively. Spatiotemporal Fourier transforms of the data allow the acoustic dispersion relations to be derived, as well as the acoustic fields in two dimensions at individual frequencies. This allows the acoustic reflection and transmission coefficients and rectification efficiencies to be extracted.

## 2. Experiment

Micro-fabrication methods including lithography and dry etching are used to make the rectifier samples. The samples are fabricated on a silicon (100) wafer by plasma dry etching using a $SF_6$ and $C_4F_8$ gas mixture and coated with polycrystalline chromium film of thickness 30 nm. The depth of the triangular holes is 11.3 μm, and the spacing is 20 μm. **Fig. 1** shows the scanning electron microscope (SEM) images of our single- and double-array rectifiers as well as their orientation with respect to the Si crystal axes. The imaging system is shown in **Fig. 2**. The pump (frequency-doubled at 415 nm) and probe pulses at 830 nm originate from a mode-locked Ti:Sapphire laser at 75.5 MHz repetition rate and have a ~1 ps pulse duration.

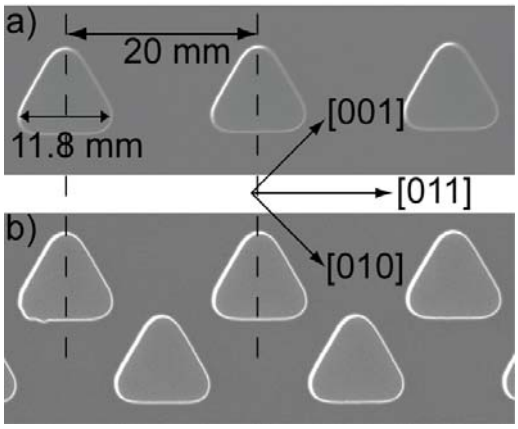


Fig. 1 SEM images of rectifier samples. a) Single row structure and b) Double row structure.

After modulation at 1 MHz by an acousto-optic modulator, the pump beam is reshaped by a cylindrical lens, and is then focused through a microscope objective to create a line source of length ~30 $\mu$m for purposes of acoustic plane wave generation. The aspect ratio of this line source is 10:1 and the average total power of the pump beam after the objective lens is 5 mW. The line source is positioned ~100 μm away from the rectifier structure. Two optical probe pulses temporally separated by 325 ps are focused onto the sample to a spot diameter of ~2 $\mu$m by the same objective lens. The phase difference between the two probe pulses, as measured by the Sagnac interferometer, is detected by the use of two photodiodes. The phase changes, caused by the outward motion of the sample ~10 pm in amplitude, are proportional to the

*On leave from: School of Science, Walailak University Nakhon Si Thammarat, Thailand 80160.

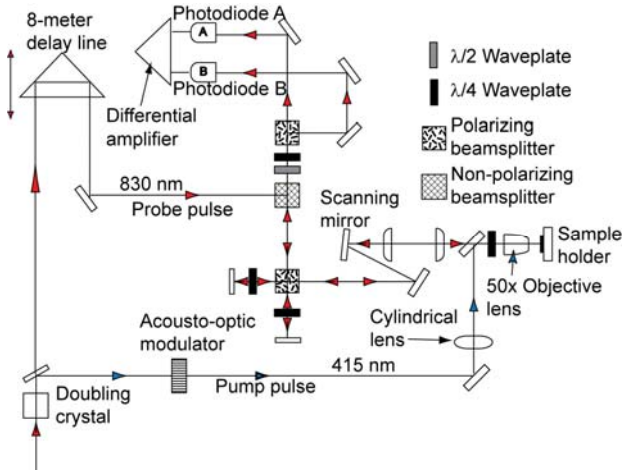


Fig. 2 Experimental setup.

outward surface velocity of the sample. The differential output of these photodiodes is amplified and fed to a lock-in amplifier synchronized to the optical pump beam modulation frequency. The scanned area of the sample covers a region of 80 $\mu$m× 200 $\mu$m. A total of 48 images are taken for each structure at equally spaced intervals in delay time (between the pump and probe pulses) over the period (13.3 ns) between two consecutive pump pulses.

## 3. Results and Discussion

**Figure 3** shows phase-change images at a fixed delay time for the single-row sample of Fig. 1a) for normal acoustic incidence on the single-row structure from two different directions (termed I and II as shown in the figure). The dispersion curves for these two cases are obtained by spatially and temporally Fourier transforming the image data, and are revealed by plotting the modulus of the Fourier transforms in **Fig. 4** in *k* space (where *k* is the acoustic wave number in the vertical direction). In Fig. 4a) the negative slope represents the incoming waves, which in this case are directed towards the triangle bases (and move in the negative vertical direction in Fig. 3). The fainter positive slope represents the reflected waves. The response for the transmitted waves overlaps here with that of the incident waves. The positive slope in Fig. 4b) represents incoming waves, which move in the positive vertical direction towards the tips of the triangles. The negative slope corresponds to the reflected waves.

The data of Fig. 4a) and 4b), representing the intensity of corresponding waves, are used to evaluate transmission and reflection coefficients, including rectification efficiencies. Preliminary results show a periodic response in frequency in both single and double array structures, similar to that predicted by Krishnan *et al*. However, there are certain differences between the experiment and the

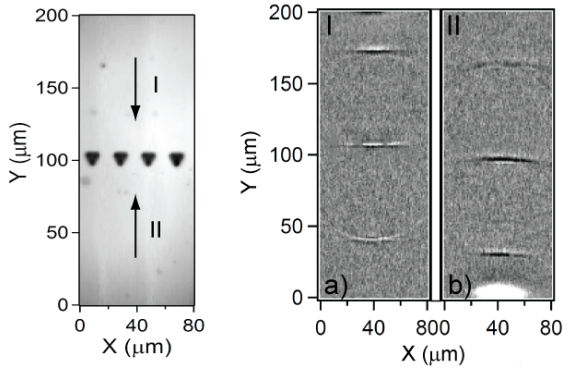


Fig. 3 Optical reflectance of the single row rectifier structure: I and II indicate the direction of incident SAW's. a) and b) are the phase difference images at delay time 0.51 ns for cases I and II, respectively. The bright spot b) is the pump position.

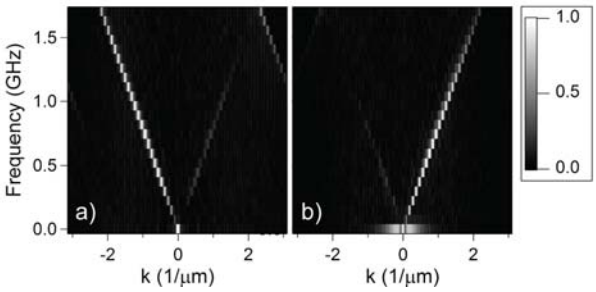


Fig. 4 a) and b): modulus of spatiotemporal Fourier transform for case I and case II, respectively, for the single row structure.

theory due to the anisotropic nature of our silicon substrate and the use of surface acoustic waves here rather than bulk acoustic waves. Further modelling should elucidate the differences.

## Acknowledgement

The authors would like to express their gratitude to N. Nishiguchi and Y. Tanaka for fruitful discussions.

## References

1. R. Krishnan, S. Shirota, Y. Tanaka, N. Nishiguchi : Solid State Commun. **144** (2007) 194
2. S. Shirota, R. Krishnan, Y. Tanaka, N. Nishiguchi : Jpn. J. Appl. Phys. **46** (2007) L1025
3. T. Tachizaki, T. Muroya, O. Matsuda, Y. Sugawara, D.H. Hurley, O.B. Wright : Rev. Sci. Instrum. **77** (2006) 043713
4. Y. Sugawara, O.B. Wright, O. Matsuda, V.E. Gusev : Ultrasonics **40** (2002) 55

Proceedings of Symposium on Ultrasonic Electronics, Vol. 29 (2008) pp. 181-182
11-13 November, 2008

# Development of inspection equipment for bottom edges of rails with guided waves
ガイド波によるレール底端部検査装置の開発

Junjie Chang†, Takahiro Hayashi, Morimasa Murase (Nagoya Inst. Tech.)
Keita Kataoka (East Japan Railway Company, Technical Center)
常俊傑‡，林高弘，村瀬守正（名工大），片岡慶太（JR 東日本）

## 1. Introduction

Inspections for railway rails are now done by an ultrasonic pulse echo method where transducers on a rail inspection car input ultrasonic waves from a rail head with wheel probes. This technique is very effective for inspecting defects in rail heads and webs, but bottom edges of rails are blind zones in this technique. Therefore, visual inspection is carried out for bottom edges of rails except in crossings where the bottom edges of rails are hidden by cover plates. Thus, the inspection technique for bottom edges of rails, especially in crossings, is indispensable in order to ensure the reliability as well as safety of transportation.

On the other hand, the ultrasonic guided wave technology attracts lots of attentions in recent years because it can propagate along the bar-like structures in the long distance. The “guided waves” have been widely used as a fast screening technique for such structures. And measurement of guided wave propagation echo is a quite effective method of NDE of bottom edge of rail.

This paper firstly describes the effective guided wave modes for inspecting bottom edges of a rail using guided wave dispersion curves software developed by the authors[1)]. A special angle beam transducer for bottom edge inspection was developed. The developed transducer was checked with both the influences of fastenings and the defect inspection capability.

## 2. Suitable modes for inspecting bottom edges of a rail

Dispersion curves and wave structures for JIS 50kgN rail were obtained using our software based on the SAFE method[1-2)] as shown in Figs.1 and 2. Looking at the wave structures of modes in Fig.2, we can find that these modes concentrate at the bottom edges and vibrate in both horizontal and vertical directions. Comparing vibration direction of the wave structures the horizontally vibrating mode in Fig. 2 (a) can be expected that this mode can avoid the interference with fastenings, and we can conclude that this mode is the one of the most suitable modes for inspecting bottom edges of a rail.

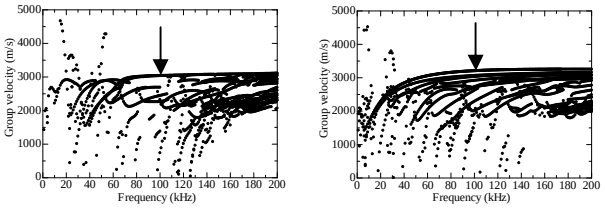


(a) horizontally dominant modes (b) vertically dominant modes

Fig.1 Group velocity dispersion curves at bottom edges of a rail.

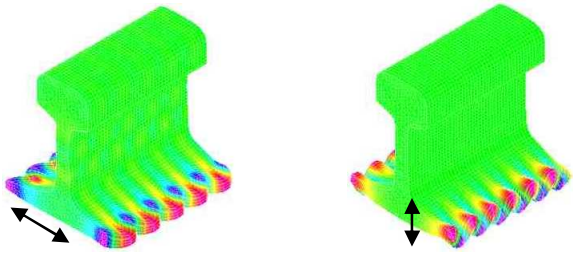

(a) horizontally vibrating mode (b) vertically vibrating mode

Fig.2 Visualization of the vibrating modes corresponding to the arrow positions in Fig.1 (a) and (b).

## 3. Development of a transducer for bottom edge inspection

Since Rayleigh waves are generally excited and received by an angle beam transducer, we fabricated an angle beam transducer consisting of an epoxy resin wedge (longitudinal wave $c_w$=2500m/s) and a PZT disk (100 kHz). The incident angle of the wedge is determined to approximately 55° by Snell’ law for the phase velocity of the Rayleigh-like mode , about 3000 m/s at 100 kHz. The developed transducer for bottom edge inspection is shown in Fig.3.

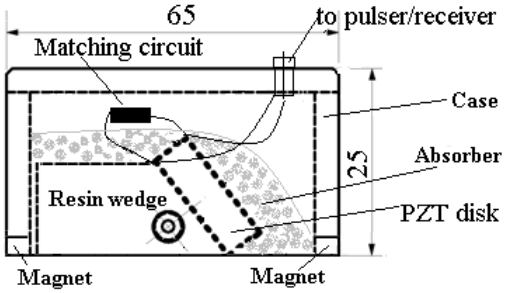


Fig. 3 Transducer for a rail bottom edges.

## 4. Experimental result by developed transducer

Using the transducer, inspection experiments for the bottom edges of a rail were conducted. The configuration of the experiment is shown in Fig. 4. In these experiments we use plates of 4.0m × 125mm × 12mm instead of real rails, because the Rayleigh like mode propagates with vibrating only at the edges of the bottom plate like region. 6 fastenings were fastened about at every 60cm and the plates are placed on the rubber plates on the sleepers. There were three fastenings (a) - (c) between the transducer and the defect. The other three fastenings were always fastened. The artificial defect is located at 2.2m from the left end of the plates. Incident signals are a 10-cycle square burst wave at the center frequency of 100 kHz.

First, the influence of the fastenings on the defect echo was investigated using the developed transducer. Figure 5 shows waveforms for various fastening conditions. The upper horizontal axis denotes distance between the transducer and a defect calculated by the group velocity of the Rayleigh-like mode 3000m/s.When fastenings (a) - (c) were fastened in this order, waveforms were obtained as shown from the bottom to top. The upper horizontal axis denotes distance between the transducer and a defect calculated by the group velocity of the Rayleigh-like mode 3000m/s. The defect echoes were observed in all signals at the correct location, the overlapping waves at the left end are reverberations within transducers and within epoxy resin wedge. As the number of fastenings increases, the defect echoes become smaller. This is because the plates and the sleepers contact more tightly as the number of fastenings increases and ultrasonic energy leak out and absorb at the sleepers. Although the influence of fastenings was observed in the signals, defect echoes are sufficiently detected.

Next, in order to investigate the ability of defect detection using the developed technique, echoes from defects with various depths were detected. The artificial defects are made by electric saw with the depth from 2 mm to 10mm in 2 mm increment. The width of the defect is about 2mm. Fig. 6 shows the detected waveforms for various depths of the defects. Although all fastenings were fastened, the obvious echo was obtained from all the defects at the correct locations calculated from the group velocity of 3000m/s. And the amplitudes of the echoes gradually increase for deeper defects. The bigger waves at about 2.2m are from artificial defects, and the small waves between reverberating incident waves and defect echoes are from fastenings.

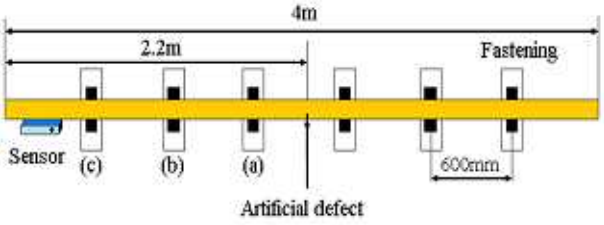


Fig. 4 Configuration of a test plate and fastenings.

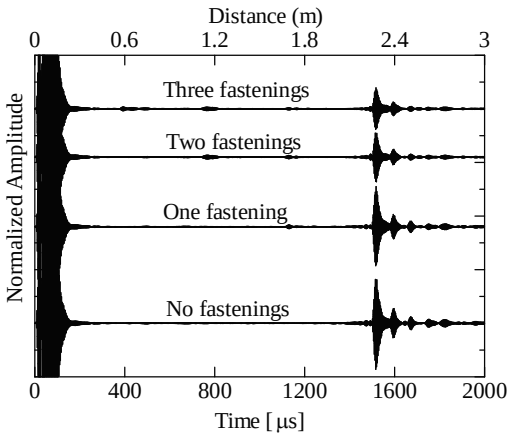


Fig. 5 Normalized amplitude with propagation time for different fastenings.

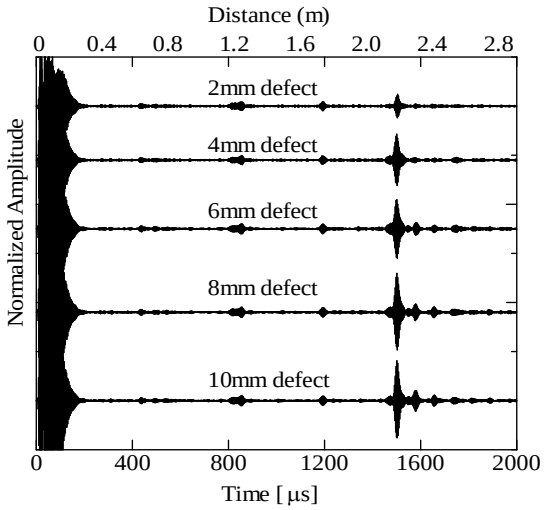


Fig. 6 Normalized amplitude with propagation time for different defect order.

## 5. Conclusions

In this report, a transducer was designed by following the analysis of mode selection and mode excitation. In the experiments using the newly designed transducer, the influences of fastenings were investigated and defect inspection capability of the developed transducer was checked. Good pulse echo signals were obtained with the transducer at the correct location of a defect at a bottom edge of rail.

**References**

1. T. Hayashi: Ultrasonics **41**(2003) 175
2. T. Hayashi: Jpn. J. Appl. Phys. **47**(2008) 3865.

2E4

Proceedings of Symposium on Ultrasonic Electronics, Vol. 29 (2008) pp. 183-184
11-13 November, 2008

# Modeling of Thermoelastic Damping in Piezoelectric Aluminum Nitride Tuning Forks

Gabriele Vigevani‡, Jan H. Kuypers and Albert P. Pisano
(Berkeley Sensor & Actuator Center, University of California at Berkeley)

## 1. Introduction

The accuracy and performance of consumer electronic devices is determined by the performances of their electromechanical components, including micrelectromechanical systems (MEMS) devices. A key to enhance the performance of MEMS resonators is to increase the *Q* and hence to minimize the impact of energy loss mechanisms. Increasing the *Q* factor is also a key to improve phase noise performances for frequency reference and to improve the signal-to-noise ratio (SNR) for sensors.

The *Q* is the result of many energy losses of different origin and different magnitude. It is therefore extremely important to have accurate design guidelines for each of the damping sources in order to minimize their impact. For beam based resonators like a double ended tuning fork (DETF) the air damping is usually the dominant energy loss mechanism [1]. However, if these types of resonators are operated in vacuum the ultimate *Q* is largely determined by thermo elastic damping (TED) [1].

There is an increasing interest in piezoelectric actuation compared to electrostatic driven MEMS, because of their better capacitance ratio ($C_0/C_m$) and more suitable impedances for interfacing with circuits. For the first time the piezoelectric contribution is included in the TED. Starting from the Euler Bernoulli theory for simple thermoelastic beams developed by Lifshitz and Roukes [2] we consider the piezoelectric constitutive equations and derive a closed-form expression for the *Q*-factor of the beam. Because of its CMOS compatible properties the following theory is applied to aluminum nitride (AlN), a piezoelectric and pyroelectric material of class 6mm.

## 2. Equations of Linear Thermo Piezo Elasticity

*Beam Orientation*

Consider a DETF of AlN with uniform rectangular cross section and oriented as shown in **Fig. 1** with electrodes patterned on the top and the bottom surface. The strain of the in-plane deformation along the *x*-axis ($S_{11}$) leads to an electric field along the *z*-direction via $d_{31}$.

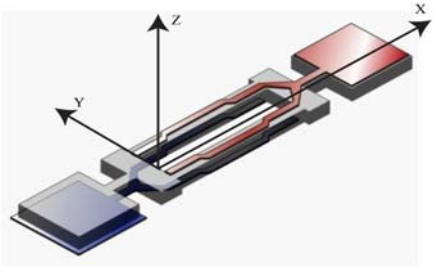


Fig.1 Illustration of the DETF orientation.

*Divergence Gradient and Constitutive Equations*

The physics of thermo piezo elastic damping (TPED) are the result of the interaction of three fields: A mechanical strain field, an electric field and a temperature field. In order to study the beam dynamics we must consider the divergence and the gradient equations [3]. In addition to these equations we have to consider the thermo piezo elastic constitutive equations [4]:

$$S_{ij} = \alpha_{ij}^{E}\theta + s_{jkl}^{E,\Theta}T_{kl} + d_{mij}^{\Theta}E_k \qquad (1)$$

$$D_n = p_n^{T}\theta + d_{mkl}^{\Theta}T_{kl} + \varepsilon_{nm}^{T,\Theta}E_m \qquad (2)$$

$$\delta\sigma = \left(\frac{\rho C^{T,E}}{\Theta}\right)\theta + \alpha_{ij}^{E}T_{ij} + p_m^{T}E_m \qquad (3)$$

where in (1) $S_{ij}$ is the strain, $\alpha_{ij}$ is the thermal expansion coefficient, $s_{ijkl}$ is the compliance tensor, $T_{kl}$ is the stress tensor, $\theta$ is the temperature increment, $d_{mij}$ is the piezoelectric strain tensor and $E_m$ is the electric field. In (2) $p_n$ is the pyroelectric coefficient and $\varepsilon_{nm}$ is the dielectric tensor. In (3) $\delta\sigma$ is the increment in entropy, $\rho$ is the density and $C$ is the specific heat capacity and $\Theta$ is the reference temperature.

*Mechanical Domain: Euler Bernoulli Kinematics*

The Euler Bernoulli theory considers only the stress in the axial direction ($S_{11}$). According to the assumptions of the Euler Bernoulli kinematics, we can write the following equation for the strain and the balance of linear momentum [5]:

$$S_{11} = -y\frac{d^2Y}{dx^2}, \qquad \frac{\partial^2 M}{\partial x^2} - \rho A\cdot\frac{\partial^2 Y}{\partial t^2} = 0, \qquad (4)$$

Where $Y$ is the mechanical displacement of the neutral axis, $M$ is the moment of the beam, $A$ is the cross section of the beam and $y$ is the distance of a point from the beam neutral axis.

Combining (4) with the constitutive equation (1) we get the following Euler Bernoulli formulation for a piezoelectric material:

$$\frac{\partial^2}{\partial x^2}\left(\frac{I_M}{s_{11}}\frac{\partial^2 Y}{\partial x^2}+\frac{d_{31}}{s_{11}}I_E+\frac{\alpha_{11}^E}{s_{11}}I_T\right)+\rho A\cdot\frac{\partial^2 Y}{\partial t^2}=0, \qquad (5)$$

where we define the following terms of inertia:

$$I_M=\int_A y^2 dzdy;\quad I_E=\int_A y\cdot E_3 dzdy;\quad I_T=\int_A y\cdot\theta dzdy$$

*Electrical Domain*

To derive the electrical domain equation we must use the constitutive equation (2). If the electrodes are short-circuited the piezoelectric contribution is eliminated and the analytical solution coincides with the classic TED solution for a non-piezoelectric material [2]. If the electrodes are not short circuited we set $D_3 = 0$ [4], in this case the electrical domain equation is given by:

$$E_3=\Gamma_1 y\frac{d^2Y}{dx^2}+\Gamma_2\theta, \qquad (6)$$

where

$$\Gamma_1=\frac{1}{\varepsilon_{33}^{T,\Theta}-d_{31}^{\,2}/s_{11}}\cdot\frac{d_{31}}{s_{11}}\quad \Gamma_2=\frac{1}{\varepsilon_{33}^{T,\Theta}-d_{31}^{\,2}/s_{11}}\cdot\left(\frac{d_{31}}{s_{11}}\alpha_{11}-p_3^T\right)$$

*Thermal Domain*

The thermal domain equation can be derived by using the thermodynamic divergence and gradient equations and substituting the entropy given by the constitutive equation (3). As in [2] we can assume the following simplifications:

- For motion in the *xy*-plane: $\frac{\partial\theta}{\partial z}=0$
- For low order mode of vibration: $\frac{\partial\theta}{\partial y}>>\frac{\partial\theta}{\partial x}$

Resulting in the thermodynamic equation:

$$\frac{\partial\theta}{\partial t}\Delta_1=\chi\cdot\frac{\partial^2\theta}{\partial y^2}+\Delta_2\frac{\partial E_3}{\partial t}+y\Delta_3\frac{\partial}{\partial t}\left(\frac{\partial^2 Y}{\partial x^2}\right), \qquad (7)$$

where: $\Delta_1=\left(1+\frac{\Theta}{\rho C^{T,E}}\frac{\alpha_{11}^{\,2}}{s_{11}}\right)$

$$\Delta_2=\frac{\Theta}{\rho C^{T,E}}\left(\alpha_{11}^E\frac{d_{31}}{s_{11}}+p_3^T\right)\qquad \Delta_3=\frac{\Theta}{\rho C^{T,E}}\frac{\alpha_{11}^E}{s_{11}}$$

## 3. Results

Using harmonic ansatz functions for the temperature $\theta$, displacement $Y$ and electric field $E$ in (5), (6) and (7) we obtain:

$$\omega^2 Y_0(x)=\frac{I_M E_\omega}{\rho A}\frac{\partial^4 Y_0(x)}{\partial x^4}, \qquad (8)$$

where $E_\omega$ is an equivalent Young modulus for a thermo piezoelectric material and has the following form:

$$E_\omega=\frac{1}{s_{11}}\left(1+\frac{d_{31}}{I_M}f_1(\omega)+\frac{\alpha_{11}^E}{I_M}f_2(\omega)\right), \qquad (9)$$

where $f_1(\omega)$ and $f_2(\omega)$ are complex functions of the frequency of vibration. The natural frequency of (8) is therefore given by:

$$\omega=(\beta L)^2\sqrt{\frac{I_M E_\omega}{\rho A L^4}}, \qquad (10)$$

where $\beta L$ is a numerical value and depends on the boundary conditions at the ends of the beam [5]. The quality factor is given by [2]

$$Q^{-1}=2\left|\frac{\mathrm{Im}(\omega)}{\mathrm{Re}(\omega)}\right|. \qquad (11)$$

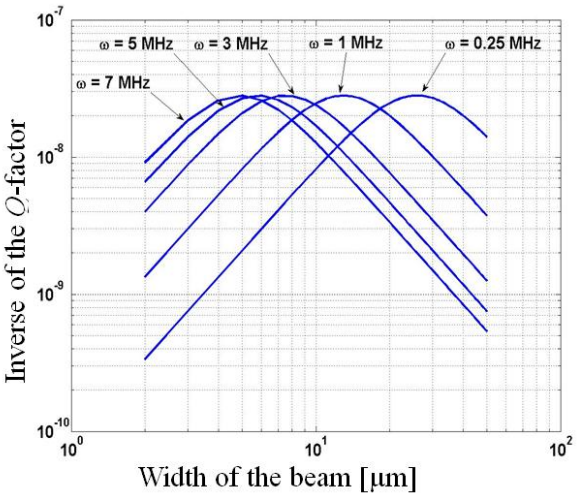


Fig.2 Inverse of $Q$ as function of the beam width.

In **Fig.2** we plot the $Q$-factor as function of the beam width for several natural frequencies.

## Conclusion

Our results demonstrate the importance of TPED as energy loss mechanism for miniature resonators. The model shows that the piezoelectric and pyroelectric effects for a fixed-fixed beam reduce the Q-factor by an amount of 15%.


## Acknowledgment

This work was supported by DARPA M/NEMS S&T Fundamentals award (HR0011-06-1-0041) under the DARPA Center for Micro/Nano Scaling-Induced Physics (MiNaSiP).


## References


1. W.E. Newell: *Science*, **161** (1968), 1320.
2. R. Lifshitz and M.L. Roukes: Phys. Rev. B **61**, (2000-II), 5600.
3. R. D. Mindlin: *J. Solids Structures* **10**, 625.
4. T. Ikeda: *Fundamentals of Piezoelectricity* (Oxford Science Publications), 12.
5. Meirovitch: *Fundamentals of Vibrations* (McGraw Hill) 385.

2E5

Proceedings of Symposium on Ultrasonic Electronics, Vol. 29 (2008) pp. 185-186
11-13 November, 2008

# Study on the Frequency Dependence of Lateral Energy Leakage in RF BAW Device by Laser Probe System

Nan Wu[†‡], Ken-ya Hashimoto, Keisuke Kashiwa, Tatsuya Omori,
and Masatsune Yamaguchi (Graduate School of Engineering, Chiba University)

## 1. Introduction

A variety of laser probes have been applied to the visualizaion of propagating surface and bulk acoustic waves (SAW/BAW)[1-2]. The authors have recently developed a phase-sensitive laser probe system based on Sagnac interferometer for the diagnosis of RF SAW/BAW devices[3]. High quality 2D images of SAW/BAW field patterns can be captured within several minutes. Currently the system operates at frequencies up to 2.5GHz[4-5]. The authors also developed integrated software which can handle and process complex image data acquired by the laser probe under user-friendly man-machine interface[6].

This paper describes the application of the developed hardware and software to the diagnosis of frequency dependent energy leakage occurring in RF BAW devices.

## 2. Experimental Result

**Fig. 1(a)** shows a 2D image obtained by the measurement at 1,816 MHz. In the RF BAW resonator used as a DUT, a piezoelectric AlN thin film is sandwiched in between two Ru electrodes, and the structure is floating on a Si substrate through an air gap. The transversal resonance pattern is clearly observed in the oval region where the resonator is placed. **Fig. 1(b)** shows the result of the 2D FFT of this image. Several concentric circles are seen. The circles indicate the propagation of waves with different lateral wavenumbers. The brightest center circle corresponds to the thickness vibration of the longitudinal wave.

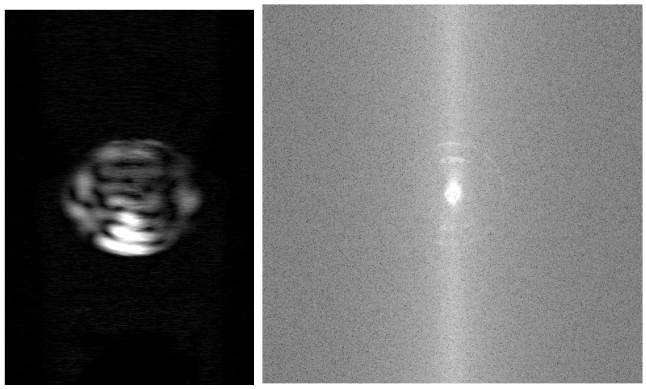

(a) Surface amplitude (b) Wavenumber domain
Fig.1 Field distribution at 1,816MHz

**Fig. 2(b)** shows the result when only the second largest circle was extracted and inverse Fourier transformed. It is seen that the wave energy of the mode leaks away under the upper electrode of the resonator.

**Fig. 2(a)** and **(c)** show the results when the same procedure was applied to the measured data at two different frequencies. From comparison of Figs. 2(a) and (c) with Fig. 2(b), it is clearly seen that the energy leakage is very frequency-dependent.

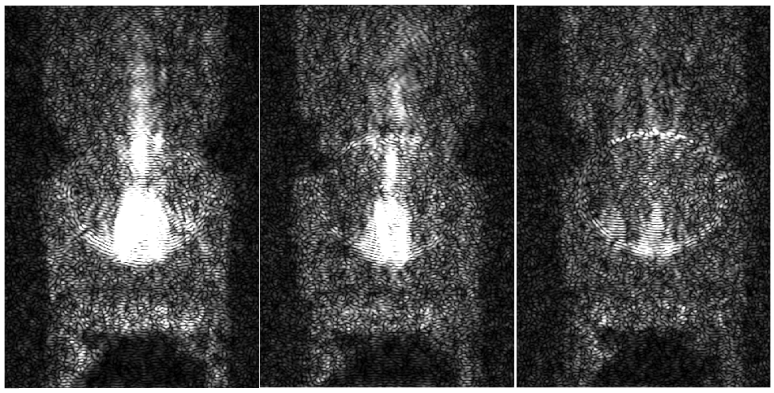

(a) 1,790MHz (b) 1,816MHz (c) 1,840MHz
Fig.2 Results of the IFFT after the extraction

## 3. Analysis

In the following analysis, three distinctive modes having a wavenumber represented by the inner, second largest and outermost circles in the FFT image in Fig. 1(b) are called Mode 1, Mode 2 and Mode 3, respectively.

**Fig. 3** shows the dispersion relation between the frequency $f$ and normalised wavenumber $\beta_x/2\pi$ obtained by the scanned data at different frequencies. The results are represented by "o", "∗" and "+" for Mode 1, 2 and 3, respectively, where the three corresponding lines are obtained by the least squares method for the calculated results. As can be seen from Fig. 3, Mode 1 possesses a cut-off frequency around 1,825 MHz. The negative group velocity of Mode 1 suggests that it is launched with a Poynting vector that is at some angle off of the normal of the resonator surface

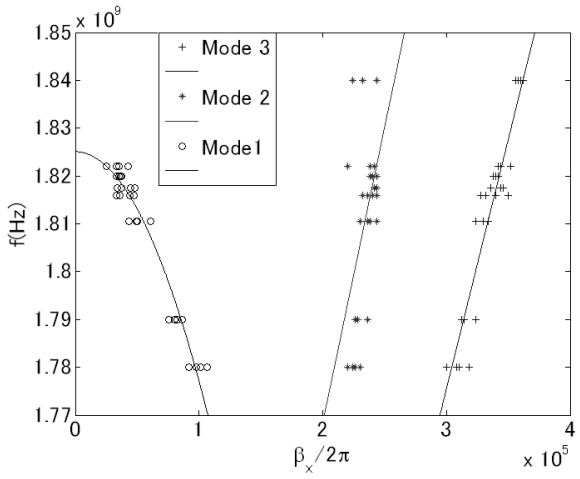


Fig.3 Dispersion curve

which causes the displacement complexity[7].

For the energy leakage analysis, we also calculate the power of each mode at some different frequency points. For this estimation, first we get the IFFT image of Mode 1, 2 or 3, and then sum up the square of each pixel's brightness.

**Fig. 4** shows the relative power thus estimated, where the three lines with "+", "×" and "＊" represent the power of Mode 1, 2 and 3, respectively. For comparison, the power of the original amplitude image is shown by the line with "o". Note here that the power of Mode 1 and the original amplitude image is about 300 times larger than that of Mode 2 and 3 (compare the right and left vertical scales).

It can be seen very clearly that independent of frequency, most of the energy is contributed from Mode 1. This may confirm in conjunction with the discussion in Fig. 3 that Mode 1 is substantially the

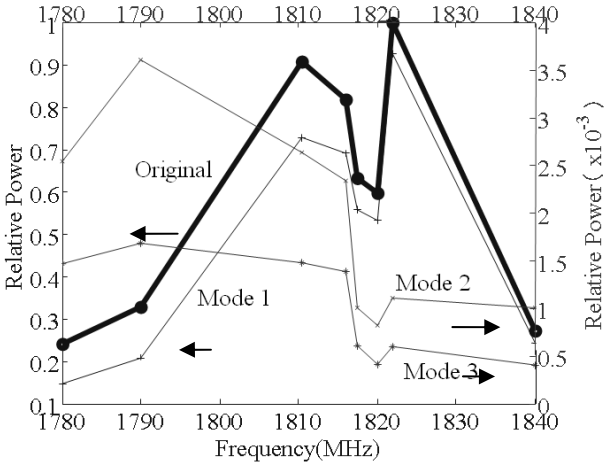


Fig.4 Variation of relative power of each mode with frequency

energy-trapped, main thickness vibration of the longitudinal wave. Meanwhile, compare the behaviours represented by the four lines. One can see that the power of Mode 2 and 3 simply decreases above 1,822 MHz. On the other hand, the power of Mode 1 takes the maximum value at 1,822 MHz just below its cut-off frequency of 1,825 MHz. The above discussion suggests that both Mode 2 and 3 may be excited by the reflection of Mode 1 at the electrode edge. This concludes the reason why the energy leakage can not be seen only in Fig.2(c).

## 4. Conclusion

As an application of laser probe systems to the diagnosis of acoustic wave devices, the paper has discussed one of the mechanisms which cause the lateral energy leakage encountered in RF BAW device. It is suggested in the device used in the experiment that the leakage may be caused by some spurious modes excited by the reflection of the main resonance mode at the electrode edge. The conclusion has successfully explained the experimental result for an RF BAW resonator.


## Acknowledgment

The authors thank Mr. O. Takano, Mr. S. Meguro and Mr. K. Akahane of Neoark Co., Ltd. for their assistance to the system development. We also thank to Fujitsu Laboratories for supplying the device used in the experiment. This work was partly supported by the Mitsubishi Foundation, a Project to Develop "Innovative Seeds" from the Japan Science and Technology Agency, and a Grant-in-Aid for Scientific Research from Japan Society for the Promotion of Science.


## References


1. S. Jen and C.S. Hartmann: *Proc. IEEE Ultrason. Symp.* (1996) pp.33-36
2. H. Kamizuma, *et al*: Jpn. J. Appl. Phys. **44** (2005) pp.4535-4538.
3. K. Hashimoto, *et al*: *Proc. IEEE Micro. Symp.* (2008) pp.851-854
4. K. Kashiwa, *et al*: Jpn. J. Appl. Phys. **47**, 5 (2008) pp.4108-4110
5. K. Hashimoto, *et al*: *IEEE Trans. Ultrason., Ferroelec., and Freq. Contr.* **53**, 5 (2007) pp.1072-1075
6. N. Wu, *et al*: *IEEE Trans. Ultrason., Ferroelec., and Freq. Contr.,* under review
7. R. C. Ruby, *et al*: *Proc. IEEE Ultrason. Symp.* (2005) pp.1832-1835

2E3

Proceedings of Symposium on Ultrasonic Electronics, Vol. 29 (2008) pp. 187-188
11-13 November, 2008

# Acousto-optic Characteristics of Silicon Nanofoam
シリコンナノフォームの音響光学特性

Takeshi Iino‡ and Kentaro Nakamura (P&I Lab., Tokyo Tech.)
飯野剛‡，中村健太郎 （東工大 精研）

## 1. Introduction

Silicon nanofoam[1] is porous material with nano-meter structure produced through sol-gel process, and has been used as heat insulator of electronic circuits. It is expected that the nanofoam may work as a good acoustic matching layer of airborne ultrasonic transducer for highly sensitive and wideband ultrasound transmission/detection since the nanofoam has an extremely low acoustic impedance. The nanofoam may also have a possibility as an acousto-optic device because of its very small sound speed and optical transparency.

We have measured the fundamental acoustic and optical characteristics of the nanofoam through acousto-optic measurements[2,3]. The sound speed and the acoustic attenuation were measured in the frequency range of around 500 kHz using rectangular samples attached on a piezoelectric transducer. Sound speed and acoustic attenuation constant were 150~165 m/s and 2.78 dB/mm, respectively. Optical refractive index and its change rate due to sound pressure were measured at the optical wavelength of 632.8 nm. Refractive index was 1.075~1.080, and the change rate in the refractive index of nanofoam material due to sound pressure was $2.58\sim2.96\times10^{-8}$ 1/Pa. Optical attenuation was 0.92 dB/mm for wavelength of 632.8 nm. Diffraction due to interaction between light and ultrasound was also observed.

This time, among the acousto-optic characteristics, we focus on the polarization rotation of the transmitted light due to sound pressure. First, we investigate the effect of static force on the direction of laser light transmitted through the silicon nanofoam. Second, we measured modulation in the polarization of the transmitted light due to ultrasonic wave.

## 2. Experimental set up

**Figure 1** illustrates the set up for measuring the polarization direction, where the direction is measured as an angle $\phi$ from the horizontal line. Light source is a linearly polarized He-Ne laser. The laser light goes through a half-wave plate, a light chopper, a silicon nanofoam sample, a rotating-analyzer (polarization plate) and a biconvex lens. Intensity of the light is detected by an avalanche photodiode. The nanofoam sample is placed on a bolt-clamped Langevin transducer and statically loaded by 3.3 N. Polarization of the incident light is set parallel to the load direction using the half-wave plate. Dimension of the silicon nanofoam is 10 mm by 10 mm, and the thickness is 5 mm. Bolt-clamped Langevin transducer radiates a 26-kHz longitudinal wave traveling along the polarization direction. The polarization direction of the transmitted light is found by rotating the analyzer.

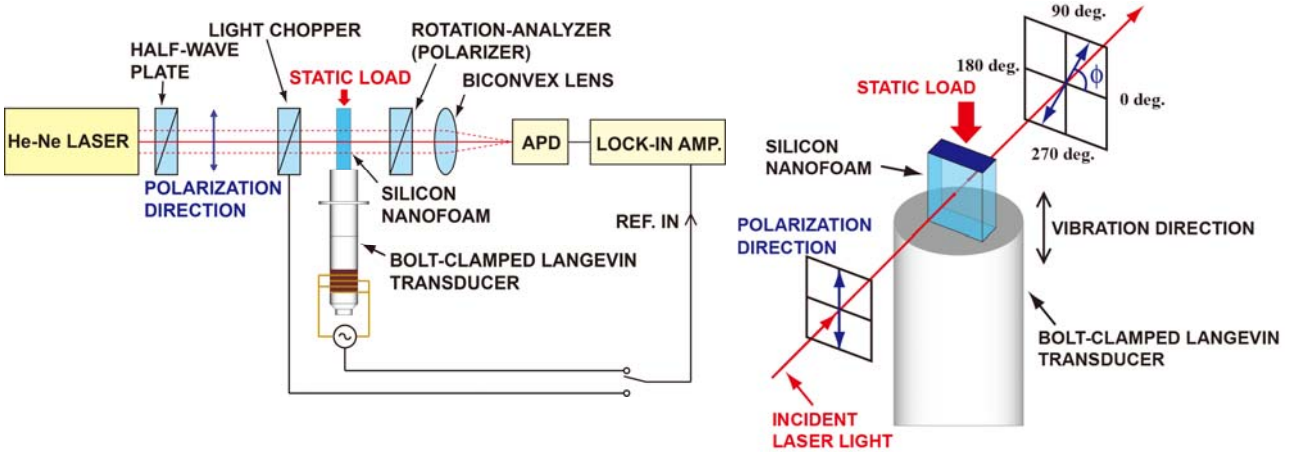


Fig. 1 Experimental set up for measuring the rotation angle of polarization in the laser light transmitted through a loaded silicon nanofom.

---

iino.t.aa@m.titech.ac.jp

## 3. Experimental results

Figure 2 shows the light intensity detected by the APD as a function of the angle of the analyzer for different static load without ultrasonic excitation. Here, the lock-in detection was carried out using the chopper to measure the transmitted light intensity. The polarization direction of the laser light was rotated by the static load by several degrees. The relationship between the rotation angle of the polarization and the applied static force is summarized in Fig. 3. In this case, the polarization is rotated by 1.0 degrees by the load of 1 N in the middle of the curve.

Next, the 26-kHz vibration is added to the static force of 3.3 N, and the AC (26 kHz) component was measured for different angles of the analyzer. Here, the lock-in detection was made with the driving signal of the transducer as a reference signal. Figure 4 shows the intensity and phase of the AC component of the transmitted laser light. Intensity had local maximal values at 45 degrees, 135 degrees, 225 degrees and 315 degrees, because the slope of Fig. 2 was maximum at around these angles. There was a 180-degree phase difference between adjacent peaks in Fig. 4 because the sign of the slope was changed at 0 degrees, 90 degrees, 180 degrees and 270 degrees. If we observe the results carefully, we shall find that the peaks and the nulls in Fig. 4 are shifted by 2 degrees due to the offset caused by the static force of 3.3 N.

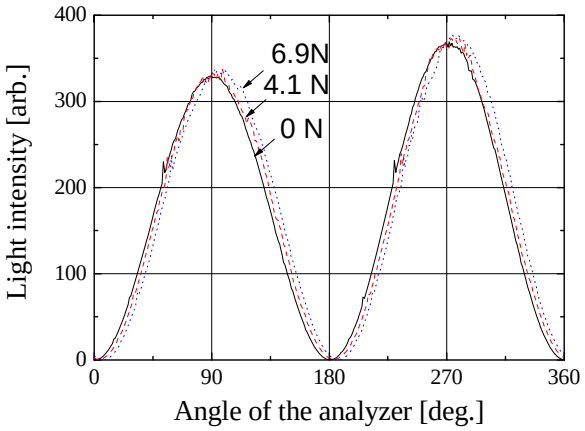


Fig. 2 Light intensity vs. angle of the analyzer.

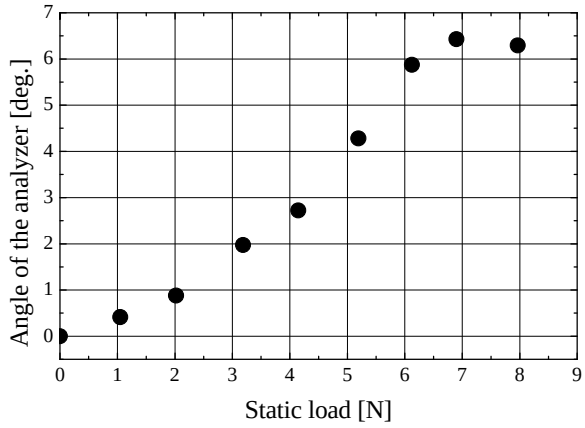


Fig. 3 Angle of the analyzer vs. static load.

## 4. Conclusions

Polarization direction of the laser light transmitted through the nanofaom was changed by static load. We also observed the modulation in the polarization angle due to 26-kHz ultrasonic longitudinal waves.


## Acknowledgment

Authors would like to thank Mr. M. Hashimoto of Panasonic Corporation for providing the silicon nanofoam sample.


## References


1. H. Nagahara, T. Hashida, M. Suzuki and M.Hashimoto: Jpn. J. Appl. Phys. **44** (2005) 4485.
2. T. Iino, K. Nakamura, S. Ueha: Proc. 19th ICA 2007 Madrid, (2007) ULT 02-003.
3. T. Iino, K. Nakamura, S. Ueha: Proc. Autumn Meet. Acoust. Soc. Jpn., pp.1213-1214(2007.9) (In Japanese).


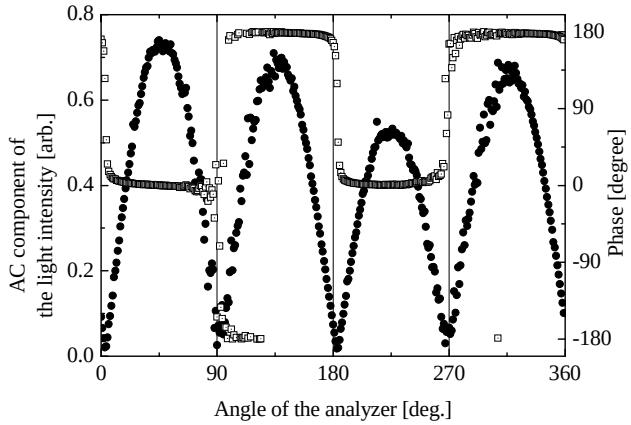


Fig. 4 Intensity and phase of the AC component of the laser light vs. the angle of the analyzer when 26-kHz sound wave is applied.

2E6

Proceedings of Symposium on Ultrasonic Electronics, Vol. 29 (2008) pp. 189-190
11-13 November, 2008

# The Influence of Liquid Height on the Ultrasonic Power Dissipated in Organic Solvents

Maricela Toma [1], Satoshi Fukutomi [1], Yoshiyuki Asakura [2], Shinobu Koda [1]
[1] *Nagoya University, Furo-cho, Chikusa-ku, Nagoya, Aichi, Japan,*
[2] *Honda Electronics Co., Ltd., 20 Oyamazuka, Oiwa-cho, Toyohashi, Aichi, Japan*

## 1. Introduction

It is well known that the intensity of cavitational phenomenon depends on the acoustic pressure generated in the sonochemical reactor vessel. Although the literature is abundant in the reports about the dissipated ultrasonic power only few studies on organic solvent have been reported [1, 2], most of the measurements have been performed for water. Measuring the ''true'' sonochemical power in the fluid is of great importance for understanding and improving the efficiency of the sonochemical reactors. Thus, for a better description of the energy balance our study focuses on the accurate quantification of ultrasonic power dissipated on a sonochemical reactor operating at an ultrasonic frequency of 490 kHz.

## 2. Method and materials

The ultrasonic power dissipated in the bulk liquid were investigated as a function of the liquid height for a cylindrical vessel cell (60mm diameter) when the liquid column ranges from 3 to 30 cm and the results were compared for different organic solvents. In order to obtain accurate data, the electrical power input at the transducer is constant for all measurements. The experimental set-up is shown in **Fig.1**.

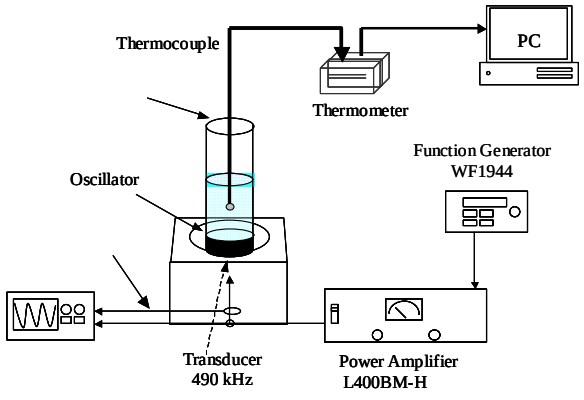


**Fig. 1 Experimental set-up for power measurements.**

The ultrasonic power dissipated in the bulk liquid was measured by calorimetry for water and for the following organic solvents: methane, ethanol, buthanol, propanol, cyclohexane, hexane, benzene, toluene, xilene and 1,2,3,4-tetrahydronaphthalene (tetralin). All solvents employed in this work were of high purity (99,5%) and used as purchased without any purification step. Prior to every experimental measurement the solvents were saturated with air at atmospheric pressure. The dissipated power quantities were recorded calorimetrically at half height of the liquid column with a thermocouple (T-type). The effective power input into the oscillator is regulated at a fixed value of 30W as measured with an oscilloscope, type TDS300B; Tektronix. Measurements were carried out at an initial temperature of 298K and the dissipated power was calculated by the following equation: Power= M·Cp·dT/dt, were *Cp* is the heat capacity of the liquid, *M* is the mass of liquid and *dT/dt* is the rate of increased temperature.

## 3. Results

The dependency of the energy conversion on temperature for different solvents is presented **Fig.2**.

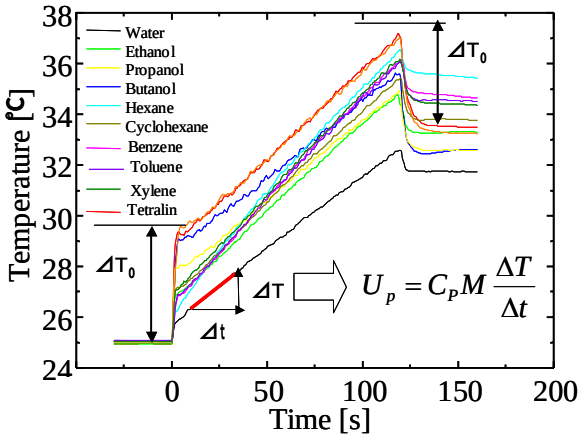


**Fig. 2 The energy conversion for different solvents.**

---

e-mail address: toma@nuce.nagoya-u.ac.jp

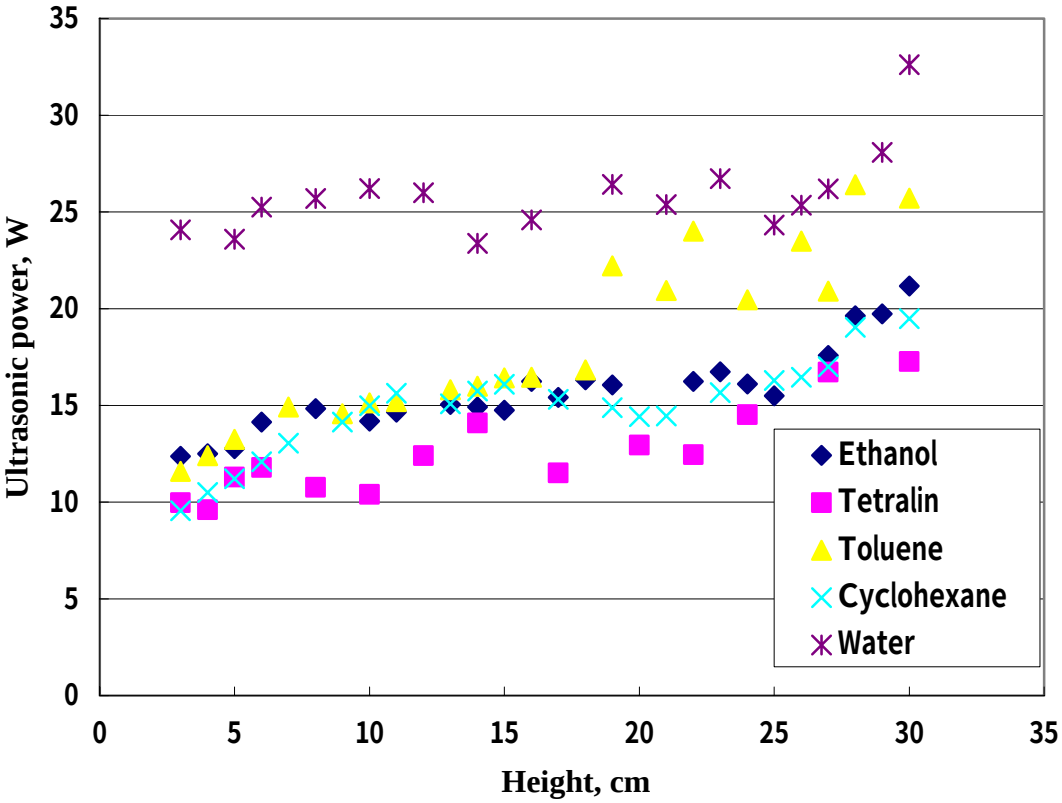


**Fig. 3. Dissipated ultrasonic power as a function of the liquid height.**

**Fig.3** shows the dependence of dissipated ultrasonic power on the height of the liquid for different solvents. The data presented in the **Fig.2** illustrates that the type of organic solvent is an important parameter in the energy conversion process. The details will be discussed in our presentation. For the presented experimental conditions, the efficiency of the sonochemical reactor increases with the increasing of the liquid column height, as shown in **Fig.3**. Based on the literature reports, it is expected that the acoustic power input increases with the increasing of the liquid height [(1)]. By increasing of the liquid column height from 3 to 30 cm, the volume of sonicated samples is increasing by 10 times for the last experimental value presented here. It is meaningful to indicate that with the increasing of the liquid height, the buoyancy of cavitation bubbles and the magnitude of the bubble coalescence increases as well, this phenomenon reduces the number of cavitations and therefore the slope of the calorimetric curve. It was noticed that the intensity of the solvent evaporation and mist formation decreases dramatically as the liquid height increases up to 14-15 cm.

## 4. Conclusions

The intricate coupling between the ultrasound source and the sonicated liquids generated a lack of accurate reports regarding the dissipated ultrasonic power. In this study, calorimetry has been employed to describe the influence of liquid height on the ultrasonic power dissipated on the vessel of a sonochemical reactor operating at a frequency of 490 kHz and the data were compared for different organic solvents in an attempt to define the power conversion basis for scale-up considerations. Based on this data, it is reasonable to conclude that the efficiency of the 490 kHz sonochemical reactor increases as the liquid height increases, mainly due to the thermal effect (associated with cavitational phenomenon) diminution.

## References

1. M.W.A. Kuijpers, M. F. Kemmere, J. T. F. Keurentjes **:** Ultrasonics **40** (2002) 657.
2. Jan-Martin Loninget, C. Horst、U. Hoffmann**:** Ultrasonic Sonochemistry **9** (2002) 169.

Proceedings of Symposium on Ultrasonic Electronics, Vol. 29 (2008) pp. 191-192
11-13 November, 2008

# Heat Pump Placed in the Resonance Tube Connected to the Loop-tube-type Thermoacoustic Cooling System Improves the Cooling Effect

ループ管に接続した共鳴管内にヒートポンプを設置することによる冷却効果の向上

Shin-ichi SAKAMOTO[1†], Hideo YOSHIDA[2], Atsushi Sakaguchi[3], and Yoshiaki WATANABE[4] ([1]University of Shiga Prefecture; [2, 3, 4]Doshisha University)
坂本眞一[1†]，吉田秀穂[2]，坂口敦[3]，渡辺好章[4]（[1]滋賀県立大学; [2, 3, 4]同志社大学）

## 1. Introduction

Thermoacoustic effect enables mutual energy conversion between heat energy and sound energy. Practical application of the "thermoacoustic cooling systems" using such energy conversion creates an eco-friendly cooling system that enables the effective use of energy. Today, the study of thermoacoustic cooling systems is progressing energetically in every corner of the earth[1-5]. Our group is also conducting research to improve the cooling effect of a loop-tube-type thermoacoustic cooling system[6-8].

We discuss the cooling effect of a loop-tube-type thermoacoustic cooling system especially emphasizing the effect of the heat pump placed in the resonance tube, while making the tube resonate at one-wavelength mode.

## 2. Experiment Setups

Three types of loop tube are used: loop tubes A, B, and C. Loop tube A is not connected by the resonance tube and the heat pump is placed upper right in the loop. Loop tube B is connected by the resonance tube and the heat pump is placed in the resonance tube. Loop tube C is connected by the resonance tube and the heat pump is placed upper right in the loop. Figures 1(a) – (c) show schematic illustrations and the experiment setups of loop tubes A, B, and C. The total length of the loop except for the resonance tube is 3740 mm. The inner diameter of the tube is 42.5 mm. Air is filled in the loop tube at atmospheric pressure as the working fluid. The 50 mm long honeycomb-ceramic stack with the channel radius of 0.45 mm is used in the prime mover and that with channel radius of 0.35 mm is used in the heat pump. The resonance tube is connected to the upper right portion of loop tubes B and C, which is near the antinode of the sound pressure. The tube is 935 mm in length which is a

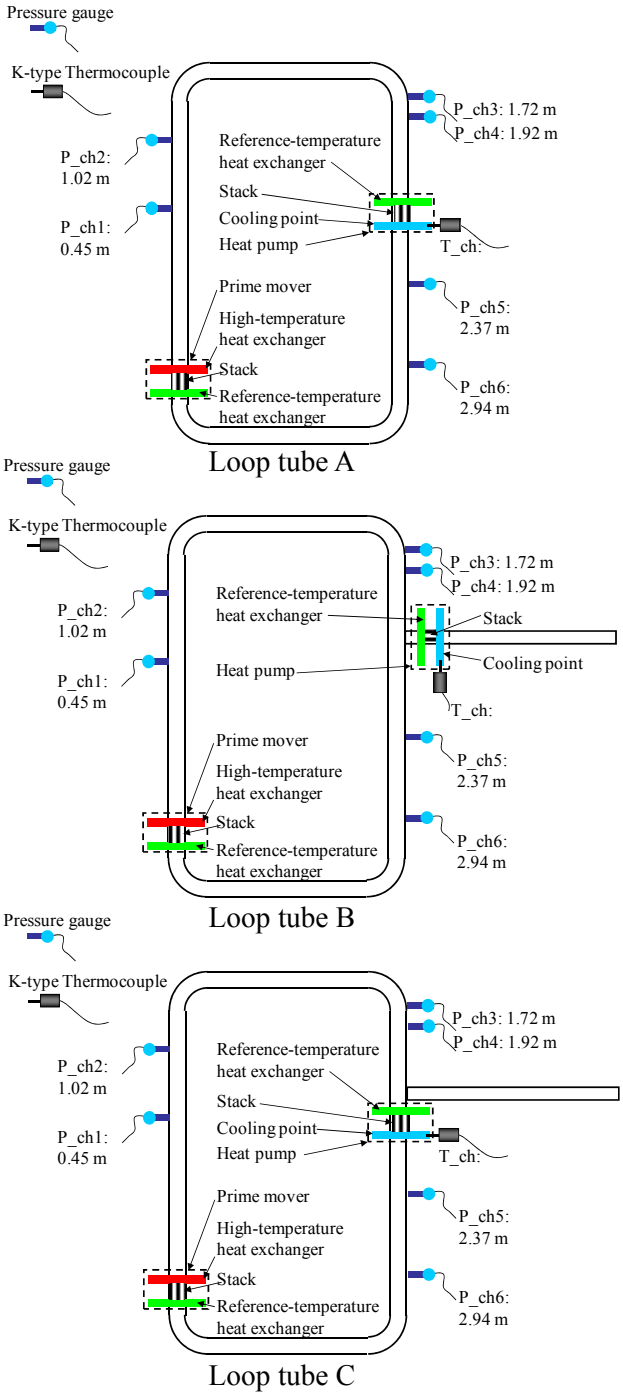


Fig.1 Schematic illustrations and the experiment setups of loop tubes A, B, and C.

quarter of the total length of the loop tube. One end of the tube is open.

The temperature at the cooling point of the heat pump is measured with K-type thermocouple. The sound pressure of the sound generated in the loop tube is measured using six pressure gauges. The measurement is conducted changing the input power of heat energy supplied to the electric heater from 50 W to 330 W for three loop tubes A, B, and C.

## 3. Results

The temperature decrease at the cooling point measured for various input heat energy is shown in Fig. 2. The temperature decrease for loop tube B is the biggest, and those for loop tubes C and A follow. In the case of input heat energy of 330 W, the temperature decrease for loop tube B is approximately 25 °C, while the temperature decrease for loop tube A is only about 9 °C and that for loop tube C is about 11°C.

Figure 3 show the sound intensity distribution for loop tubes A, B, and C. The values in these figures are calculated using the two-sensor power method[3)], based on the observed sound pressures obtained by the pressure gauges.

The sound intensity for loop tube A between P_ch1 and P_ch2 is 310 W/m$^2$, that for loop tube B is 11300 W/m$^2$, and that for loop tube C is 1050 W/m$^2$. The sound intensity shows the efficiency of heat-to-sound energy conversion. The bigger the sound intensity, the more efficiently the heat energy is converted to the sound energy. Since the sound intensity for loop tube B is the biggest, the heat-to-sound energy conversion efficiency for loop tube B is the highest, and consequently, the cooling effect for loop tube B is the greatest.

## 4. Summary

We discuss the cooling effect of a loop-tube-type thermoacoustic cooling system especially emphasizing the effect of the heat pump placed in the resonance tube. The temperature decrease for the loop tube connected by the resonance tube with the heat pump placed in the resonance tube is 25 °C, while the temperature decrease for the loop tube without the resonance tube with the heat pump placed in the loop tube is only 9 °C. This is the effect of the heat pump placed in the resonance tube. The heat pump placed outside of the loop tube suppresses an influence of not only the viscosity effect of the heat-pump stack but also the undesirable heat flow caused by the acoustic streaming. According to this, the connection of the resonance tube contributes to an improvement. Consequently, the heat pump placed in the resonance tube connected to the loop tube improves the cooling effect of the loop tube.

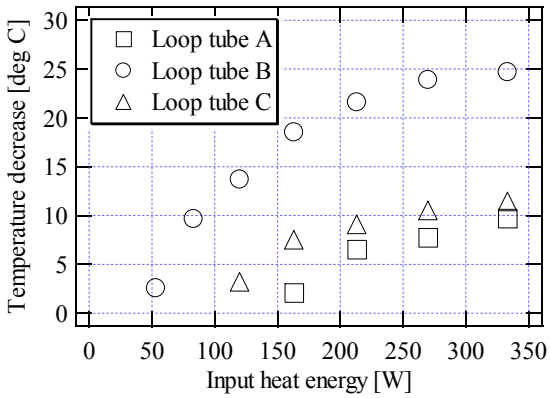


Fig.2 Temperature decrease at the cooling point measured for various input heat energy.

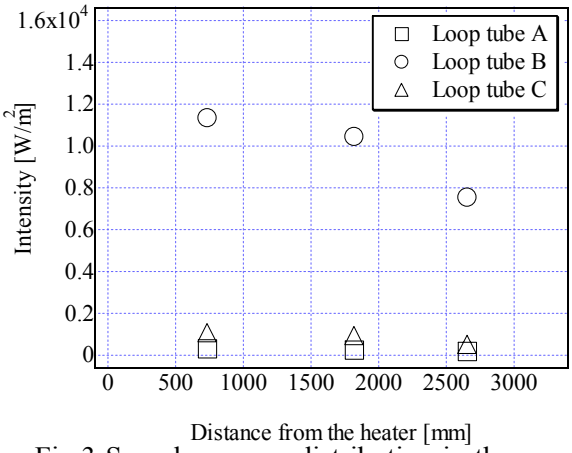


Fig.3 Sound pressure distribution in the case of input heat energy of 330 W for loop tubes A, B, and C.

## References


1. T. Yazaki, A. Iwata, T. Maekawa, and A. Tominaga: Phys. Rev. Lett. **81** (1998) 3128.
2. S. Backhaus and G. W. Swift: Nature **339** (1999) 335.
3. T. Biwa, Y. Ueda, T. Yazaki, and U. Mizutani: Cryogenics **41** (2001) 305.
4. T. Yazaki, T. Biwa, and A. Tominaga: Appl. Phys. Lett. **80** (2002) 157.
5. Y. Ueda, T. Biwa, U. Mizutani, and T. Yazaki: J. Acoust. Soc. Am. **115** (2004) 1134
6. S. Sakamoto and Y. Watanabe: Jpn. J. Appl. Phys. **43** (2004) 2751.
7. S. Sakamoto and Y. Watanabe: Acoust. Sci. Technol. **27** (2006) 361.
8. H. Yoshida, S. Sakamoto, and Y. Watanabe: Jpn. J. Appl. Phys. **46** (2007) 4413.

2E9

Proceedings of Symposium on Ultrasonic Electronics, Vol. 29 (2008) pp. 193-194
11-13 November, 2008

# A Study on SSBL Underwater Positioning Using SS Communication

SS 信号を用いた SSBL 水中音響測位に関する研究

Yoshitaka Watanabe[1†], Hiroshi Ochi[1], Takuya Shimura[1] and Takehito Hattori[2]
([1] Mari-tech., JAMSTEC.; [2]NME.)
渡邊佳孝 [1‡]，越智寛 [1]，志村拓也 [1]，服部岳人 [2] （[1]海洋機構; [2] 日海事）

## 1. Introduction

In recent years precious observations with autonomous underwater vehicle (AUV) have been carried out. The positioning and navigation of AUV is very important. However in acoustic positioning of underwater vehicles as AUV, state of target varies from hour to hour. The Authors are studying of acoustic positioning with communication in that case. The studies of integration of acoustic positioning and inertial navigation system (INS) are being performed in the world[1]. In this paper an integration method are shown. In the method the support ship monitored the AUV with super short baseline (SSBL) acoustic positioning. INS output data are included in the response signal from AUV. The support ship equips a hydrophones array for SSBL and receives the signal. Simulation and experimental results are shown and the cause of error is considered in this paper.

## 2. A method of AUV positioning

In this method the response signal from AUV is continuous which length is few or few dozen seconds. The INS data output in the AUV are included in the signal. Phase shift keying (PSK) is used as the data modulation. And the spread spectrum (SS) technique is applied. The parameters of the signal from AUV are shown in **Table 1.** The relationship of SSBL and INS outputs is shown as

$$\frac{1}{N_I}\sum_{l=0}^{N-1}\left(\mathbf{x}_a(mN_I-l)-\left(\boldsymbol{\delta}\mathbf{x}_I(m-1)+(N_I-l)\frac{\boldsymbol{\delta}\mathbf{x}_I(m)-\boldsymbol{\delta}\mathbf{x}_I(m-1)}{N_I}\right)\right)$$
$$=\mathbf{x}_0(m)+\mathbf{n} \quad .$$

where $\mathbf{x}_0$ : the origin during the continuous signal, $\mathbf{x}_a$ : the SSBL estimation of absolute position of AUV, $\delta\,\mathbf{x}_I$ : relative position to origin obtained from INS output and **n :** random error due to SSBL. $\mathbf{x}_0$ is calculated by a Kalman filtering. The detail is referred in ref. 2. And the absolute position of AUV $\mathbf{x}_{AUV}$ is calculated as

$$\mathbf{x}_{AUV}(m)=\mathbf{x}_0(m)+\boldsymbol{\delta}\mathbf{x}_I(m) \quad .$$

**Fig.1** shows a simulation result. The left shows SSBL estimation. The right shows the result calculated with the method mentioned above. The true track of AUV, starting from the left low to the right upper, is well tracked in Fig.1. And **Fig.2** shows an experimental result. The experiment was implemented in the deep ocean. The depth was around 1,000 meters. The acoustic signal was transmitted from the experimental device moored on the sea bottom. And the signal was received the hydrophones array equipped on the ship. The horizontal range between the ship and the experimental device was around 1,400 meters. The right figure is result applied our method. The estimation is well converged. In the both the results calculated with proposed method were clearly better than simple Kalman filtering using only SSBL estimations[2].

Table1. Parameters of signal from AUV

| | |
|---|---|
| Carrier frequency | 12.5kHz |
| Chip rate | 3.125kHz |
| PN code | M-sequence, length=31 |
| Data modulation | 8PSK |
| Fractional sampling rate | 2 |
| Symbols per INS data | $N_I$=20 |
| Array allocation | 4x4=16ch planer array |

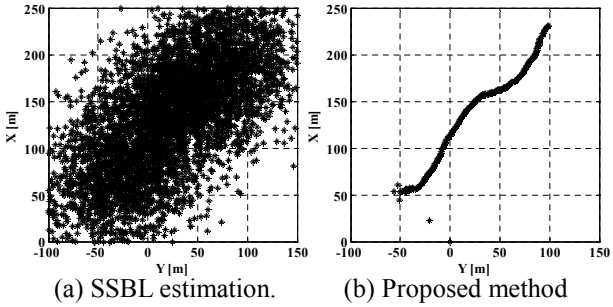


(a) SSBL estimation. (b) Proposed method

Fig. 1 Simulation result of AUV positioning. The true track is well tracked in the right figure.

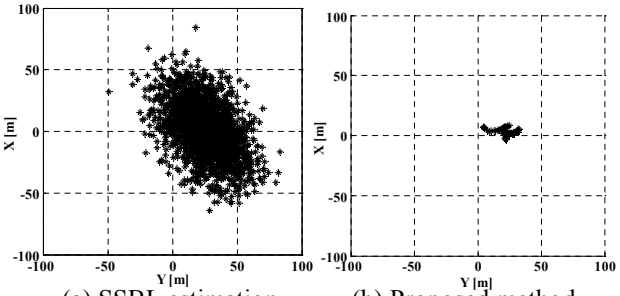


(a) SSBL estimation. (b) Proposed method

Fig. 2 An ocean experimental result. The signal was transmitted from moored device to the ship.

---

yoshitakaw@jamstec.go.jp

## 3. Error due to signal distortion

The acoustic signal for positioning is distorted and the estimation of SSBL is degraded. The causes are considered as noise, Doppler shift and interference due to multipath.

The SSBL estimation is achieved with the mean described in ref. 1. The arrival direction of signal is calculated with phase differences of all combinations of the array elements. If the array is three dimensional, the effect of Doppler shift is negated. On the other hand if the array is two dimensional as planer array in this paper, the Doppler shift degrades the estimation result. **Fig.3** shows the error of estimation arrival angle due to Doppler shift generated at relative velocity $V_p$. When the arrival angle is 30 degrees and Vp is 5 m/s, systematic error of few percents of the slant range is generated. This is lower than other errors. And the degree of error can be estimate with the phase rotation of the signal and AUV speed from INS data. The phase rotation includes both motions of ship and AUV, so the AUV speed is necessary.

The acoustic signal is continuous in this study. When the signal is short pulse, the multipath is not considerable. However in the case as this study, the multipathe becomes a cause of the SSBL estimation error. The arrival directions of the reflection waves from frames are close to that of direct wave. Then the interference is also close for each other element. However for example the arrival direction of the reflection from the sea bottom is obviously different from that of direct wave. Then the SSBL estimation is degraded due to the interference. **Fig. 4** shows the propagation channel in the experiment of Fig. 2. Multipath exists close behind the direct wave. This is seems to be the reflection from the seabed. And around one second after some multipaths exist. These seem to reflect twice at the surface and the seabed. **Fig. 5** shows the each axis output of the SSBL estimation result of Fig.2. It can be found that the variation of output becomes larger at around 100th symbol. This can be guessed to be the interference of the multipaths with twice reflection mentioned above. Although the levels of the multipaths are low, the arrival angle is far different from that of the direct wave. Then the influence of the interference is high. This is the inter-symbol interference (ISI) and the error degrees are different between each interfering symbol. If the symbol sequence is enough random, the error can be compensate with the Kalman filter shown as Fig.2.

## 4. Summary

An integration method of SSBL and INS was introduced. Simulation and experimental results were shown and it was shown that the method

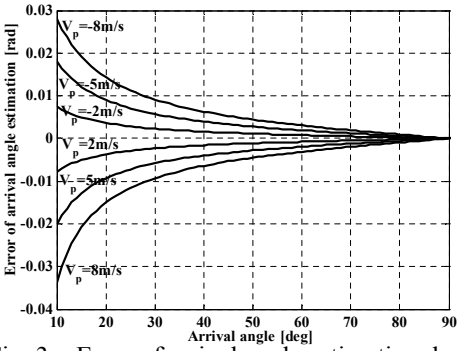


Fig. 3 Error of arrival angle estimation due to the Doppler shift caused by the motion of the array.

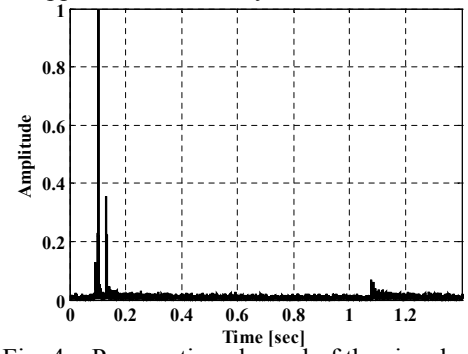


Fig. 4 Propagation channel of the signal of the experiment.

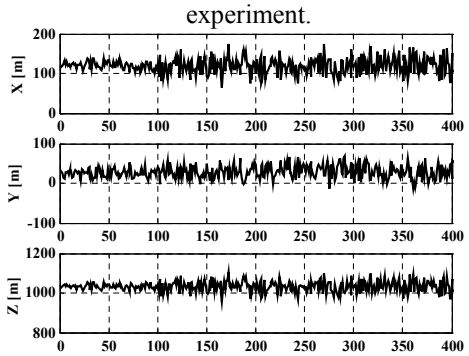


Fig. 5 Outputs of each axis of SSBL estimation.

works well. The estimation errors due to the signal distortion caused the Doppler shift and the ISI were considered. Especially the error of SSBL estimation due to the ISI is generated because of the continuous acoustic signal that is distinguished for the proposed method. Nevertheless the proposed method is useful.

In the future adaptive compensation of the system error and multiple access will be considered.


## Acknowledgment

The ocean experiment was supported by the crews of R/V KAIYO and the support members of Marin Works Japan.


## References


1. M. Morgado, P. Oliveira, C. Silvester and J. F. Vasconcelbs: The 9th International Conference on Information Fusion (2006).
2. Y. Watanabe, H. Ochi. T. Shimura and T. Hattori: IEEE/MTS OCEANS2008, Quebec (2008).

Proceedings of Symposium on Ultrasonic Electronics, Vol. 29 (2008) pp. 195-196
11-13 November, 2008

# Elastic properties of polymorphic protein crystals studied by micro-Brillouin scattering

顕微ブリルアン散乱法によるタンパク質結晶多形の音波物性

Yuichiro Aoki†, Eiji Hashimoto, Hitoshi Kanazawa, Yuji Ike, Seiji Kojima
(Univ. Tsukuba, PAS.)
青木雄一郎†，橋本英二，金沢一史，池祐治，小島誠治 （筑波大 数理物質）

## 1. Introduction

To clarify physical properties of protein crystals are important in various fields, such as biology, pharmacology, and engineering. The protein crystal has a polymorph[1], and they have different physical properties.

The micro-Brillouin scattering is the best solution for the measurement of a small sample by noncontact and nondestructive, and to measure the sample like the protein crystal. Since protein crystals contain a large amount of water molecules, the crystals may deform and damage during the dehydration such as, unwanted stresses, cracks, degradations in mosaicity etc. The Brillouin scattering measurement enables us to determine the sound velocity, elastic constant and damping of sound waves.

We employed glass forming liquid of ethylene-glycerol and glycerol which undergoes a glass transition without crystallization even in slow cooling. Glass transition phenomenon is related to cluster structure formed by hydrogen bond.

By micro-Brillouin scattering over a wide temperature range, we can discuss behavior of intermolecular water and glass transition.

## 2. Experimental

The experimental setup of a micro-Brillouin scattering instrument is shown **Fig. 1**. The Brillouin scattering spectra were measured at the backward scattering geometry. The Sandercock-type 3 + 3 pass tandem Fabry-Perot Interferometer (FPI) was combined with microscope and operated to acquire spectra of scattered light. A free spectral range of 30 GHz was applied and the Brillouin spectra were measured in ± 25 GHz frequency range. The sample temperature was controlled within ± 0.1 °C and increased from room temperature with a cryogenic cell (LINKAM HTMS600).

---

e-mail address: s-aokiy@ims.tsukuba.ac.jp

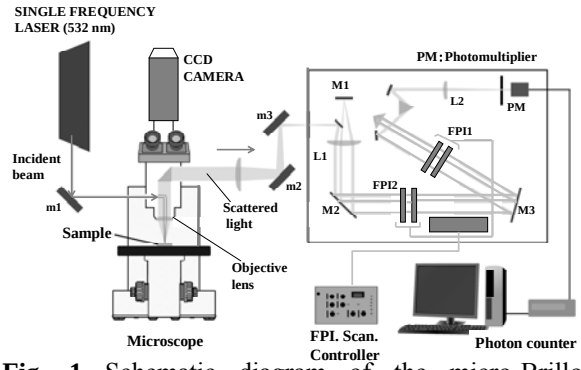


**Fig. 1** Schematic diagram of the micro-Brillouin scattering instrument[2].

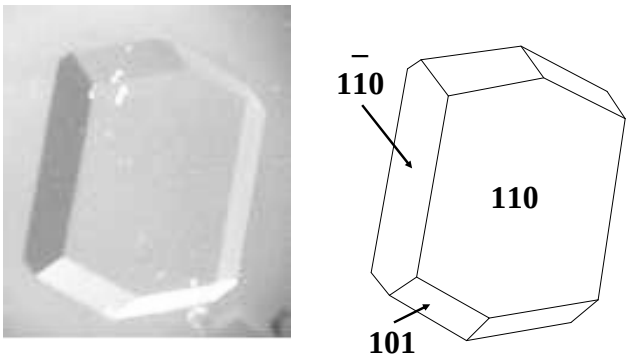


**Fig. 2** The as-grown tetragonal HEWL crystal with habit planes of {110} and {101}.

Hen egg white lysozyme (HEWL) crystals were grown by two liquids interface method that employing an insoluble and dense liquid.[3] Crystals were grown on the interface of two liquids of lysozyme solution and dense liquid such as Fluorinate. We made the lysozyme crystals of tetragonal crystal, monoclinic crystal, and, orthorhombic crystal. For example, the solution to make tetragonal crystal were consisted of 25 mg/ml lysozyme and 5 % (w/v) NaCl in 50 mM acetate buffer solution (pH = 4.5). All crystals were grown in few days and show the crystal habit of {110} and

{101} planes. The micrograph of as-grown crystal was shown in **Fig. 2**. The laser beam was incident perpendicular to the {110} habit plane of the crystal.

## 3. Results and Discussion

The observed Brillouin spectrum of a HEWL crystal shows one broad longitudinal acoustic (LA) mode as shown in **Fig. 3**. As temperature decreases, Brillouin shift increases and full width at half maximum (FWHM) gradually becomes narrow. Brillouin shift and FWHM were determined from the spectra. The longitudinal sound velocity was calculated from the Brillouin shift $v$ (= $qV_l/2\pi$) and the scattering wave vector $q$ (= $2\pi n\sin(\theta/2)/\lambda$), where $n$, $\lambda$ and $\theta$ are the values of refractive index of the sample, the wavelength of the laser and scattering angle, respectively. The value of refractive index of a HEWL crystal[5] was used. The LA mode absorption coefficient $\alpha$ is related to FWHM of Brillouin component by the equation, $\alpha = \pi\Gamma/V_l$ where $\Gamma$ is FWHM. The temperature dependence of Brillouin shift and FWHM is plotted as shown in **Fig. 4.** It shows FWHM peak at about 80 °C. The glass transition occurs at the kink point at about -100 °C. At the high and low temperature, Brillouin shift and FWHM gradually approach the constant value. The behavior of relaxation process is observed when the solution surrounding a crystal vitrified.

From the results, we can discuss the structural relaxation process based on viscoerastic theory. The Brillouin data analyzed by using a Debye function, and, the activation energy is obtained. The relaxation process is relevant to the cooperative motion of alcohol, protein, and, water molecules.

## 4. Summary

By using the micro-Brillouin scattering method, we successfully observe the temperature dependence of Brillouin shift and FWHM in HEWL crystals. We observe glass transition of the protein crystal and alcohol solution. The relaxation process originate from cooperative motion is clearly observed.

The comparison of the relaxation processes of three kinds of HEWL crystal will be discussed.


## Acknowledgments

This research was partially supported by the Ministry of Education, Science, Sports and Culture, Grant-in-Aid for Exploratory Research, 19656005, 2007 and the Research Foundation of the Japan Society for the Promotion of Science for Young Scientists, 18·3811.


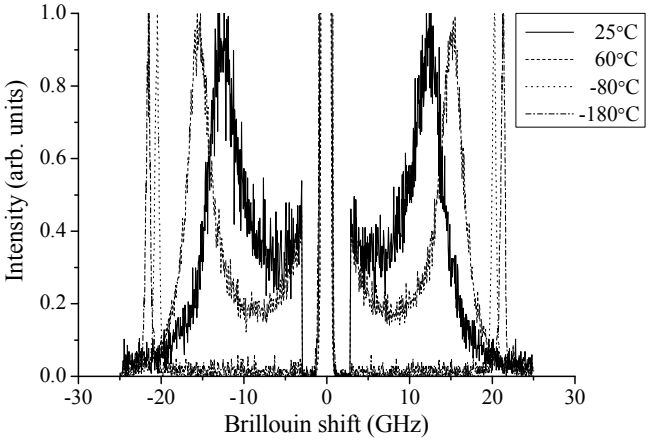


**Fig. 3** Observed Brillouin spectra of a HEWL crystal at 25℃(line), 60℃(broken line), -80℃(dotted line), -180℃ (chain line), which include the scattering from the longitudinal acoustic phonon.

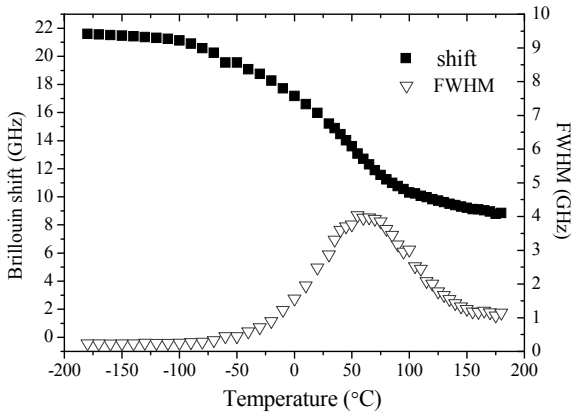


**Fig. 4** Temperature dependences of Brillouin shift and FWHM of a glycerol solution (65 mol %).

## References


1. M. C. R. Heijna, W. J. P. van Enckevort, and E. Vlieg: Cryst. Growth Des., **8** (2008) 270.
2. Y. Ike and S. Kojima: J. Aco. Soc. Jpn. **61** (2005) 461. (in Japanese)
3. H. Adachi, T. Watanabe, M. Yoshimura, Y. Mori and T. Sasaki: Jpn. J. Appl. Phys. **41** (2002) L 726.
4. B. Cervelle, F. Cesbron, J. Berthou and P. Jolles: Acta Cryst. A**30** (1974) 645.
5. E. Hashimoto, Y. Aoki, Y. Seshimo, K. Sasanuma, Y. Ike and S. Kojima: Jpn. J. Appl. Phys. **47** (2008) 3839.
6. K. Sasanuma, Y. Seshimo, E. Hashimoto, Y. Ike and S. Kojima: Jpn. J. Appl. Phys. **47** (2008) 3843.

Proceedings of Symposium on Ultrasonic Electronics, Vol. 29 (2008) pp. 197-198
11-13 November, 2008

# Elastic Properties of Potassium Borate Glasses in a Wide Composition Range Studied by Brillouin Scattering

ブリルアン散乱による広い濃度範囲のカリウムホウ酸塩ガラスの弾性的性質

Mitsuru Kawashima[1,†], Yu Matsuda[1], Yasuteru Fukawa[1], Seiichi Mamiya[1], Masao Kodama[2] and Seiji Kojima[1] [1](Univ. Tsukuba, Inst. Mat. Sci.) [2](Sojo Univ., Dept. Appl. Chem. )

川島充[1,†], 松田裕[1], 布川泰輝[1], 間宮精一[1], 小玉正雄[2], 小島誠治[1] [1]（筑波大 数理物質）[2]（崇城大 応用化学）

## 1. Introduction

The structure and physical properties of alkali metal borate glasses show the anomalous behavior against their composition, such as exhibiting maxima or minima.

The elastic properties of sound velocity and elastic moduli are very sensitive and indicative of the change of the glass structures, therefore it is interesting to investigate the composition dependence of the elastic properties of the potassium borate glass (KB) system. In this context, the composition dependences of the elastic properties of KB are of great interest. We already reported the composition dependence of the elastic properties of KB up to 34 mol% of $K_2O$ studied by the ultrasonic pulse-echo overlap method [1]. The present paper is a sequel of our previous studies [1-2]. Since the glass-forming ability of the high composition samples is poor, the only thin and fragile samples are obtained. It is impossible to perform the ultrasonic pulse-echo overlap method using a transducer. The Brillouin spectroscopy is a powerful tool to investigate the elastic properties of glass of the high composition KB.

## 2. Experimental

The composition formula of potassium borate glasses is denoted by $xK_2O\cdot(100\text{-}x)B_2O_3$, where x is molar composition of $K_2O$. All glasses were prepared with high homogeneity in order to investigate the inherent nature of binary system [1]. To achieve the high homogeneity of the glass forming materials, they were first made to react in an aqueous solution. The compositions of all glasses were analyzed with respect to both x and (100-x) with a neutralization titration [1].

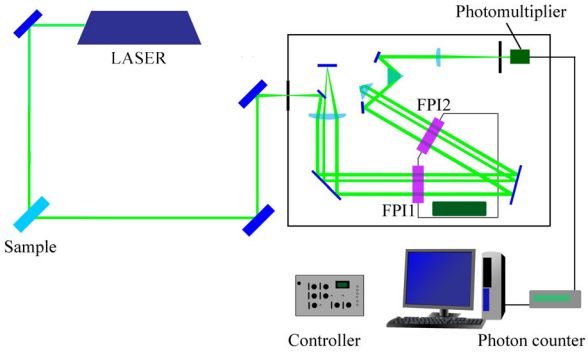


Fig. 1 Schematic diagram of the micro-Brillouin scattering apparatus.

The experimental setup of a Brillouin scattering apparatus is shown in Fig. 1. The features of this system are a combination of a microscope and a Sandercock-type 3 + 3 passes tandem multipass Fabry-Perot interferometer (FPI) [2]. The Brillouin scattering spectra were measured at a backward scattering geometry.

## 3. Results and Discussion

In order to measure not only transverse acoustic (TA) mode but a longitudinal acoustic (LA) mode, the Brillouin scattering spectra were measured at the right-angle ($90^{o}$A) scattering geometry. Figure 2 shows the observe Brillouin spectra of KB. The Brillouin shifts ($\Delta\nu$) and the full width half maximum (FWHM) have been obtained from the fitting procedure of the spectra.

The LA velocity ($V_L$) and TA velocity ($V_T$) are calculated using the Brillouin shifts ($\Delta\nu$) by

---

The corresponding author: s-kawa@ims.tsukuba.ac.jp

$$V_i = \frac{\lambda \cdot \Delta \nu^i}{\sqrt{2}} \quad (i\text{=L, T}), \qquad (1)$$

where $\lambda$ is the wavelength of the incident laser (532 nm). The advantage of the 90°A-scattering geometry is that the determination of sound velocity is independent of the refractive index of the sample [3].

$V_L$ and $V_T$ are shown in Fig. 3 as a function of the composition at room temperature (RT). Since the range of the studied composition in the previous paper was limited up to 34 mol%, information for the wide composition range was lacking. The present study reveals that the composition dependence of sound velocity over a wide composition range. The values of $V_L$ and $V_T$ do not change in a monotonic way with the increase of $K_2O$ but a maximum around 30 mol%. This trend is strongly correlated with the formation of the 4-coordinated boron atoms, studied by NMR [4]. The networks of the pure $B_2O_3$ glass are constructed by the planar 3-coordinated boron atoms. The addition of the $K_2O$ causes the formation of 4-coordinated boron, resulting in the creation of the 3-dimential rigid structural units.

The elastic constants such as longitudinal modulus (L), shear modulus (G), bulk modulus (K), Young's modulus (E) and Poisson's ratio ( $\sigma$ ) are determined by sound velocity. Figure 4 shows the composition dependences of L, G, K, E and $\sigma$ . These elastic contents except $\sigma$ show a maximum at around 30 mol%, and then decrease with the increase of $K_2O$ composition as similar as sound velocity. These behaviors are discussed by occurrence of non-bridging oxygen that destroys the glass network or coordination number change of boron. Poisson's ratio is shown different behavior from other elastic constants such as L, G, K, and E.


## Acknowledgment

The author (Y M) is thankful for the JSPS Research Fellowship 19.574.


## References


[1] M. Kodama et al.: Jpn. J. Appl. Phys. **34** (1995) 2570.

[2] Y. Ike et al.: Jpn. J. Appl. Phys. **45** (2006) 4474.

[3] H. H. Krbecek et al.: Polymer, **37** (1996) 3483.

[4] G. E. Jellison et al.: Phys. Chem Glass, **19** (1978) 52.


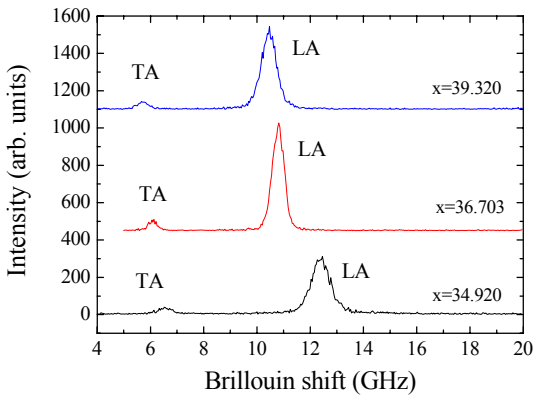


Fig. 2 The Brillouin scattering spectra.

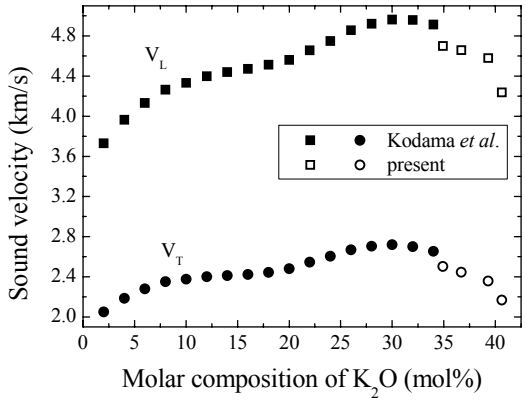


Fig. 3 The composition dependence of sound velocity.

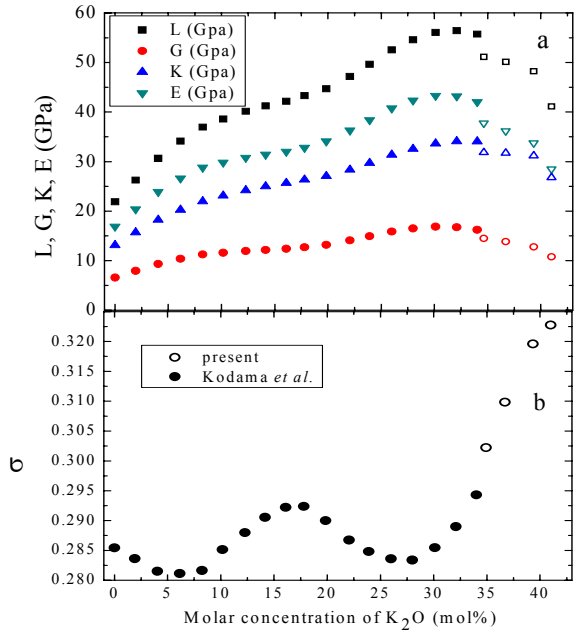


Fig. 4 The composition dependences of (a) L, G, K, E and (b) $\sigma$ .

2P1-3

Proceedings of Symposium on Ultrasonic Electronics, Vol. 29 (2008) pp. 199-200
11-13 November, 2008

# Elastic constants of C12A7 single crystals studied by resonance ultrasound spectroscopy
# 超音波共鳴法を用いた C12A7 単結晶の弾性定数計測

Masataka Yamamoto[1†], Ryuichi Tarumi[2] and Masahiko Hirao[1], Masahiro Hirano[3], Sung Wng Kim[4] and Hideo Hosono[4] ([1]Grad. Sch. Eng. Sci., Osaka Univ., [2]Grad. Sch. Eng., Osaka Univ., [3] FCRC, Tokyo Inst. Tech., [4]Mat. Struct. Lab., Tokyo Inst. Tech.)
山本昌孝 [1‡], 垂水竜一 [2], 平尾雅彦 [1], 平野正浩 [3], 金聖雄 [4], 細野秀雄 [4] ([1] 阪大 基礎工; [2] 阪大 工; [3] 東工大 フロンティア; [4] 東工大 応セラ研)

## 1. Introduction

C12A7:$O^{2-}$ ($Ca_{24}Al_{28}O_{66}$: $12CaO \cdot 7Al_2O_3$) and related compounds are attracting materials for their amazing crystalline structures and wide-varying physical properties. The C12A7:$O^{2-}$ is constructed from two molecules, $2x(12CaO+7Al_2O_3)$, and its chemical formula is given in the following form,

$$[Ca_{24}Al_{28}O_{64}]^{4+}+2O^{2-}.$$

Here, positively charged $[Ca_{24}Al_{28}O_{64}]^{4+}$ ions make a framework structure in its unit cell,[1)] which can be interpreted as an aggregation of 12 empty cages. On the other hand, two $O^{2-}$ ions occupy 2 of the 12 cages so that the C12A7 have 2 occupied and 10 unoccupied cages in its unit cell. Recently, Hosono *et al.* replaced the encapsulated $O^{2-}$ ions by other active anions such as $O_2^-$ (superoxide radicals) and $H^-$ (hydride ions).[2)] Later, they succeeded to replace the $O^{2-}$ by the supreme minus ion, that is, electron $e^-$. The chemical formula of C12A7: $e^-$ is

$$[Ca_{24}Al_{28}O_{64}]^{4+}+4e^-.$$

The C12A7:$e^-$ is called *electride*. This is the first *electride*, which is chemically stable at ambient temperature. Kim *et al.* investigated temperature dependent electrical conductivity of the C12A7:$e^-$ electride and found superconducting transition below 0.2 K.[3)] However, most of fundamental properties of the electride are still unclear yet.

One of the key questions is the occupation site of electron in the 12 cages. As well as C12A7:$O^{2-}$, it is reasonable to suppose that $4e^-$ electrons occupy 4 of 12 different cages. The framework structure (or 12 empty cages) is known to have a cubic type $T_d$ point group symmetry (space group symmetry is $I\bar{4}3m$). According to the Neumann's principle,[4)] microscopic point group symmetry governs macroscopic physical properties. Thus, the symmetry of macroscopic physical properties will not change if 4 electrons do not have predominant occupation site; namely 4 electrons occupy random position in 12 cages. On the other hand, tetragonal symmetry of macroscopic properties will change if and only if 4 electrons have certain predominant occupation sites. Thus, the occupation site of 4e- electrons can be investigated by a precise measurement of macroscopic physical properties. Needless to say, this analysis is also valid for $2O^{2-}$ in C12A7:$O^{2-}$. In this study, we investigate a complete set of elastic constants $C_{ij}$ of C12A7:$O^{2-}$ and C12A7:$e^-$ single crystals to discuss the occupation sites of $2O^{2-}$ and $4e^-$.

y-masa@mbox.me.es.osaka-u.ac.jp

## 2. Experimental procedure

Materials used in this study are rectangular parallelepiped shaped C12A7:$O^{2-}$ and C12A7:$e^-$ single crystals prepared by Czochralski method. **Table I** summarizes dimensions and mass densities of the specimens.

Free vibration resonance frequencies, $f_i$, of a specimen depend on the dimension, mass-density and elastic constants $C_{ij}$. We can inversely determine $C_{ij}$ from the resonance frequencies $f_i$ by Lagrangian minimization scheme solved with Rayleigh-Ritz method. We employed electromagnetic acoustic resonance (EMAR)[5)] to measure the resonance frequencies. Here, we briefly summarize the EMAR measurement procedure. A single crystal specimen is inserted into a solenoid coil, both of which are set in a static magnetic field (~0.2 T). The coil is driven by tone-burst currents (~1 MHz, ~30 μs), which induce the eddy current in the specimen surface. The eddy current and the static magnetic field interact to cause cyclic Lorentz force, which excites ultrasound vibration in the specimen. The reverse process occurs in the detection of ultrasound vibration. Free vibration resonance spectra are then obtained by a frequency sweep of the input current. Resonance frequencies are determined by Lorentz function fitting procedure around the resonance peaks.

Table I. Dimension and mass-density of C12A7: $O^{2-}$ and C12A7: $e^-$ single crystals.

| Specimen | Dimension (mm) | | | Density ($kg/m^3$) |
|---|---|---|---|---|
| C12A7: $O^{2-}$ | 10.02 | 5.54 | 4.72 | 2680 |
| C12A7: $e^-$ | 3.23 | 4.94 | 3.09 | 2648.5 |

## 3. Results and discussion

### 3-1. C12A7: $O^{2-}$

As mentioned above, the point group symmetry (or elastic symmetry) of the C12A7:$O^{2-}$ is unclear because the occupation site of $2O^{2-}$ ions has not been identified yet.

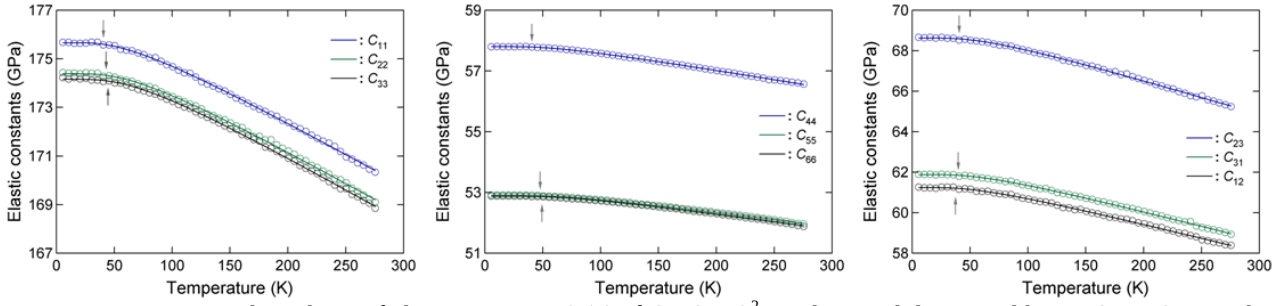


Figure 1. Temperature dependence of elastic constants $C_{ij}(T)$ of C12A7: $O^{2-}$ single crystal determined by EMAR. Arrows show Einstein temperatures estimated from Varshni's equation.[6)]

In this study, we assumed the orthorhombic type elastic symmetry,

$$\boldsymbol{C}_{ij} = \begin{bmatrix} C_{11} & C_{12} & C_{13} & 0 & 0 & 0 \\ & C_{22} & C_{23} & 0 & 0 & 0 \\ & & C_{33} & 0 & 0 & 0 \\ & & & C_{44} & 0 & 0 \\ & \textit{sym.} & & & C_{55} & \\ & & & & & C_{66} \end{bmatrix}$$

The number of independent $C_{ij}$ components is 9.

**Figure 1** shows temperature dependence of elastic constants $C_{ij}$ obtained from C12A7:$O^{2-}$. As mentioned, point group symmetry of the framework structure is $T_d$. In this case, $C_{ij}$ satisfies the following relations,

$C_{11}= C_{22} =C_{33}$, $C_{44}= C_{55} =C_{66}$, $C_{12}= C_{23} =C_{31}$.

From the measurement, however, we find the relation of $C_{22} \fallingdotseq C_{33}$, $C_{55} \fallingdotseq C_{66}$ and $C_{31} \fallingdotseq C_{12}$ throughout the temperature range. This result indicates that the C12A7:$O^{2-}$ has a tetragonal type elastic anisotropy. It is therefore reasonable to conclude that $2O^{2-}$ ions have specific occupation sites in 12 cages. **Figure 2** shows a group–subgroup relationship about the $I\bar{4}3m$. The less-symmetric point groups that belong to tetragonal class are $D_{2d}$ and $S_4$.

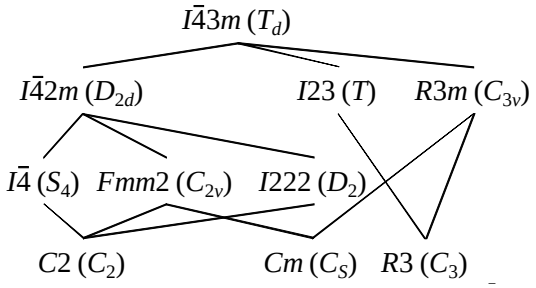


Figure 2. Group–subgroup relationship about the $I\bar{4}3m$ ($T_d$) symmetry. There are two subgroups that have tetragonal symmetry; $D_{2d}$ and $S_4$.

### 3-2. C12A7:$e^-$

**Table II** summarizes elastic constants of C12A7:$e^-$ measured by EMAR at ambient temperature. We observe that $C_{11} \fallingdotseq C_{22} \fallingdotseq C_{33}$, $C_{55} \fallingdotseq C_{66}$ and $C_{31} \fallingdotseq C_{12}$. This result suggests that C12A7:$e^-$ also has a tetragonal type elastic anisotropy. Thus, the point group symmetry expected from the $C_{ij}$ measurement is $D_{2d}$ or $S_4$.

One of the plausible interpretations of the present results is that the positions of $2O^{2-}$ and $4e^-$ in the 12 cages are not random. Namely, there exist predominant occupation sites to minimize the internal energy of the systems. Their accurate positions are still uncertain. This is open for the future work.

Table II Elastic constants $C_{ij}$ (GPa) of C12A7:$e^-$ single crystal obtained by EMAR at ambient temperature.

| $C_{11}$ | $C_{22}$ | $C_{33}$ | $C_{23}$ | $C_{31}$ |
|---|---|---|---|---|
| 166.48 | 173.90 | 171.04 | 69.24 | 57.67 |
| $C_{12}$ | $C_{44}$ | $C_{55}$ | $C_{66}$ | |
| 65.09 | 53.93 | 59.14 | 51.54 | |

## 4. Conclusion

In this study, we investigated complete sets of elastic constants of C12A7:$O^{2-}$ and C12A7:$e^-$ by EMAR. The present results showed that both of the two crystals have a tetragonal type elastic symmetry. Their point group symmetry is $D_{2d}$ or $S_4$, as can be expected from the group-subgroup diagram. These results suggest that $2O^{2-}$ and $4e^-$ have specific occupation sites in the 12 cages.

## References


1 S. Watauchi *et al.*: J. Cryst. Growth, **237** (2002) 496-502.

2 H. Hosono: Sci. Tech. Adv. Mater., **5** (2004) 409-416.

3 M Miyakawa *et al.*: J. Am. Chem. Soc., **129** (2007) 7270 -7271.

4 Neumann's principle; "Any symmetry exhibited by the point group of the crystal (the macroscopic symmetry: rotations, reflections, and inversion) must also be possessed by every physical property of crystal" (A. S. Nowick, Crystal Properties via group theory, Cambridge university press, New York, 1995).

5 M. Hirao and H. Ogi, EMATs for Science and Industry, (Kluwer, Boston, 2003).

6 Y.P. Varshni: Physica, **34** (1967) 149.

2P1-4

Proceedings of Symposium on Ultrasonic Electronics, Vol. 29 (2008) pp. 201-202
11-13 November, 2008

# Ultrasonic Study of h-BN Machinable Ceramic（Ⅲ）
# ｈ－BN セラミックの超音波による研究（Ⅲ）

Nobuo Kashiwagura†, Motoki Satoh, Mitsuo Yamaga, Masayuki Akita and Hiroaki Kamioka（Fac. of Eng., Gigu Univ.）
柏倉伸男†、佐藤元樹、山家光男、秋田正之、上岡宏彰（岐阜大学工学部）

## 1. Introduction

Hexagonal boron nitride (h-BN) has a graphite-like structure, and exhibits cleavage perpendicular to the c-axis. Because of the cleavage nature, the sintered h-BN becomes machinable, i.e. is machined to small tolerances with conventional metal working tools such as a lathe or a drilling machine. The material is also a good insulator, chemically stable, impervious to gas penetration and able to withstand high temperatures (to approximately 1000℃). The excellent properties enable wide application in the fabrication of vacuum components and high pressure and/or high temperature parts in addition to providing various other uses.

Despite numerous studies of the elasticity of the machinable ceramics which can be used as high temperature components, few previous studies have reported the elastic properties in the high- temperature region above 500 ℃. The velocities of compressional waves and shear waves and their attenuation in the material were precisely measured using ultrasonic pulse transmission in the temperature range between 30℃ and 1000℃, and elastic moduli were calculated from the wave velocities. In this study, we focus on the temperature dependence of elastic properties of h-BN machinable ceramic in the high-temperature range. It is interesting to compare elastic properties of h-BN with those of Macor[1)].

## 2. Experimental

A cylindrical sample of h-BN approximately 38.0 mm in diameter and 20.0 mm long was prepared with flat and parallel faces by conventional machining. Its measured density was 2.26 g/cm$^3$.

A schematic diagram of the measurement system which was specially designed for the precise measurement of ultrasonic velocity at high temperatures (to approximately 1000℃) is shown in **Fig.1**. For the measurements, an ultrasonic wave of 0.5 MHz and the pulse transmission method using a dual acoustic path were employed[1-6)]. In this system, one path consists of a vertical mercury delay line, which precisely measures the distance between transducers by use of a micrometer, and is necessary for the precise measurement of ultrasonic velocity, and the other consists of a high-temperature furnace with the sample and stainless steel buffers inside. The temperature of the sample was controlled in the range from 30 ℃ to 1000℃ by a microcomputer. The buffers reduce heat to prevent the destruction of transducers (PZT, resonance frequency : 0.5 MHz) in combination with water jackets. The housing of transducers, buffers and the sample were held together under appropriate pressure (approximately 60 Kgf/cm$^2$) along the sample's cylindrical axis. Thus no acoustic binder was employed at any interface between the

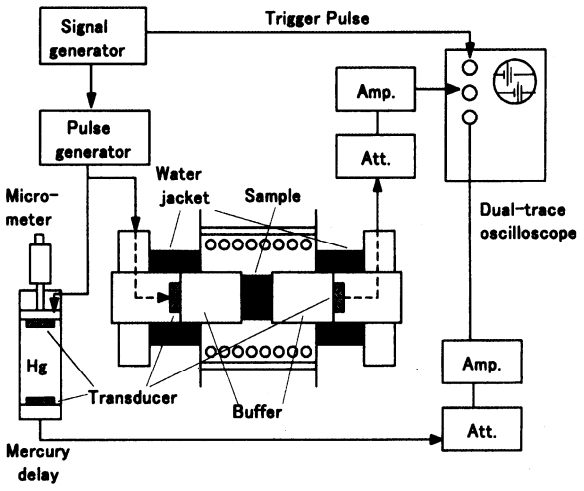


Fig.1. Schematic diagram of the apparatus for measuring ultrasonic velocity and attenuation even at high temperature region.

transducers, the buffers and the sample for ultrasonic measurements.

Tree same samples, DENKA type HC, were prepared. Ultrasonic measurements were carried out tree times for each sample. The results of ultrasonic velocities at a certain temperature are almost the same within errors, and the averaged value is shown.

### 3. Results

The temperature dependence of compressional wave velocity and shear wave velocity was measured during heating and cooling in the temperature range from 30℃ to 1000℃, as is shown in **Fig. 2**. As temperature increases, roughly speaking, compressional wave velocity stays almost constant from room temperature (30℃) to 500℃, increases from 500℃ to 850℃, and then stays almost constant again above 850 ℃. Whereas the shear wave velocity slightly decreases or stays almost constant from room temperature to 800℃, and then increases above 800℃.

Comparing with those of Macor[1)], the ratio of compressional wave velocity change is very large around 30%, in case of Macor, less than 2%).

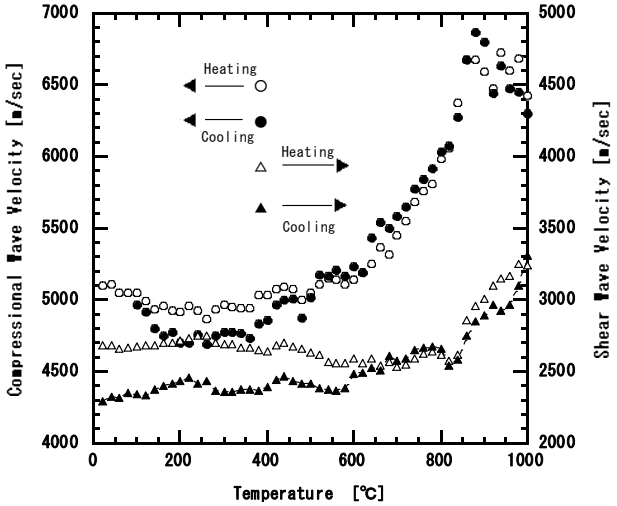


Fig.2. Temperature dependence of compressional wave velocity (○:Heating , ●:Cooling) and shear wave velocity (△:Heating , ▲:Cooling).

Ultrasonic measurement enables us to obtain elastic moduli without the destruction of the sample that is unavoidable in a standard tensile test. Using an appropriate apparatus, wave velocities can be measured over wide range of temperatures. It is significant to investigate elastic properties over the high-temperature region above 500℃ for a machinable ceramic, which is used for parts experiencing temperatures up to 1000℃.

Using the values of the compressional wave velocity and the shear wave velocity as shown in Figs. 2, elastic moduli were computed using equations[2)]. Elastic moduli depend on the density of a material, which is affected by thermal expansion. In a high-temperature region, thermal expansion is no longer negligible. Thus, elastic moduli are corrected for thermal expansion.

The temperature dependence of the bulk modulus, the modulus of rigidity and Young's modulus will be shown in the session. Knowledge of the temperature dependence of elastic moduli of machinable ceramics is useful for predicting the behavior of a material in extensive applications, even at high temperatures.

The ultrasonic wave method was applied to investigate a machinable ceramic, h-BN, across the temperature range from 30℃ to 1000℃. Ultrasonic measurement proved to be sensitive and useful to investigate elastic properties in a machinable ceramic, even at high temperatures.

1)N.Kashiwagura,M.Akita and H.Kamioka: Jpn. J. Appl. Phys. **44**(2005)4339.
2)N.Kashiwagura,Y.Ohsawa,S.Iwata,J.Jin and H.Kamioka:Jpn.J.Appl.Phys.**9**(2000)2928.
3) N.Kashiwagura, S.Sakai and H.Kamioka: Jpn. J. Appl.Phys. **40**(2001)3516.
4) N.Kashiwagura, S.Sakai and H.Kamioka: Jpn. J. Appl. Phys. **41**(2002)3176.
5) N.Kashiwagura, T.Muramatsu and H.Kamioka: Jpn.J.Appl.Phys. **42**(2003)2931.
6) N.Kashiwagura, O.Yoshida, M.Kobayashi, K.Nakata, S.Mizuno and H.Kamioka: Jpn. J. Appl. Phys. **43**(2004)2905.

2P1-5

Proceedings of Symposium on Ultrasonic Electronics, Vol. 29 (2008) pp. 203-204
11-13 November, 2008

# Effect of polling process on property of hydrothermally synthesized PZT polycrystalline film

分極処理が水熱合成 PZT 多結晶膜の特性におよぼす影響

Shinya Irisawa[1†], Akito Endo[2], Minoru Kurosawa[3], Norimichi Kawashima[1] and Shinichi Takeuchi[1] ([1]Toin Univ. of Yokohama , [2]AIST, [3] Tokyo Institute of Technology.)
入澤信哉 [1‡]，遠藤聡人 [2]，黒澤実 [3] ，川島徳道 [1]，竹内真一 [1] ([1] 桐蔭横浜大院; [2] 産総研, [3] 東工大院)

## 1. Introduction

We are developing 10 MHz array type ultrasound probes with 8 elements hydrothermally synthesized PZT polycrystalline film transducers with wide of 35 μm, length of 4 mm. Hydrothermally synthesized PZT polycrystalline film is suitable for deposition on the complex shaped or tiny sized Ti substrate and it shows piezoelectricity without polling process. However, there is a problem with low sensitivity. Therefore, we tried to improve its sensitivity by polling process in spite of above features. Effect of polling process on property of hydrothermally synthesized PZT polycrystalline film is reported in this paper.

## 2. Fabrication of bimorph type vibrator with hydrothermally synthesized PZT polycrystalline film

Bimorph type vibrators were fabricated by deposition of hydrothermally synthesized PZT polycrystalline film on the Ti substrate with thickness of 50 μm. Our hydrothermal method includes nucleation process (NC) and crystal growth process (CG). Nuclei of PZT polycrystals are deposited on the Ti substrate in the material solution under conditions of temperature 160 ℃ and synthesizing time 24 hours in 1 cycle of NC process. The PZT crystals grow up under the condition of temperature 140 ℃ and synthesizing time 24 hours in 1 cycle of CG process. PZT polycrystals are synthesized and deposited by 1 cycle of NC and 4 cycles of CG in this study. The material solution was stirred by the Teflon stirring blade with stirring speed of 245 rpm. Ti substrates were held on the stirring blade directly. Consequently, we obtained PZT polycrystalline film with thickness of about 10 μm. The SEM image of PZT polycrystals deposited on the Ti substrate are illustrated in Fig.1. Au electrodes were deposited on both sides of the bimorph type vibrators with hydrothermally deposited PZT polycrystalline films as shown in Fig. 1.

t17b010@edu.toin.ac.jp

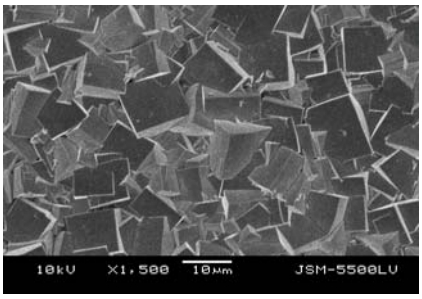


Fig.1 The SEM image of hydrothermally synthesized PZT polycrystalline film on Ti substrate of bimorph type vibrator

## 3. Polling process

We tried to improve the sensitivity of bimorph type vibrators by polling process. The polling process was performed by applying DC 10 and 20 V between both Au electrodes and Ti substrate as shown in Fig. 2 for three hours in 80℃ silicon oil in the oil bath. 2 ways of polling process were tried. DC voltage were applied between Au electrodes as anode electrodes and Ti substrate as cathode electrode as shown in Fig. 2 (a). The other way is shown in Fig. 2 (b).

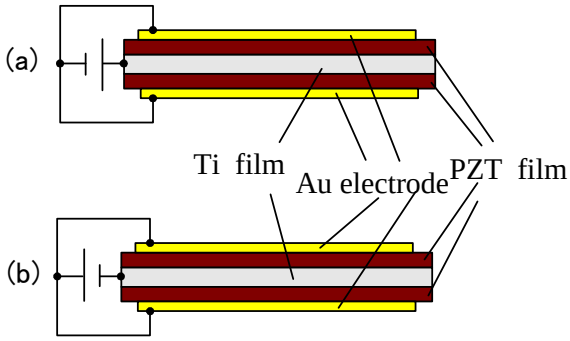


Fig.2 Polling processes for bimorph type vibrators with hydrothermally synthesized PZT polycrystalline films

## 4. Experimentals

### 4-1. Measurement method of vibration velocity

The fabricated bimorph type vibrators were driven electrically as shown in Figs.3 and 4. The sinusoidal wave with amplitude of 5 $V_{0\text{-}P}$ was

applied to the vibrator with a function generator. The vibration velocity was measured with Laser Doppler Velositometer (LDV) as shown in Fig. 4. The distance between free and fixed ends in the bimorph type vibrator was 15mm. The measurement position of vibration velocity is 2mm from the free end.

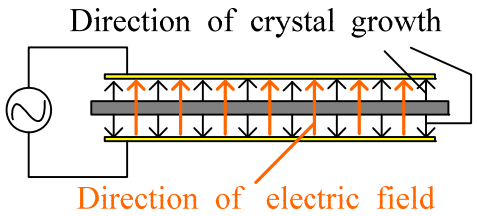


Fig.3 Relationship between directions of crystal growth of deposited PZT and applied electric field

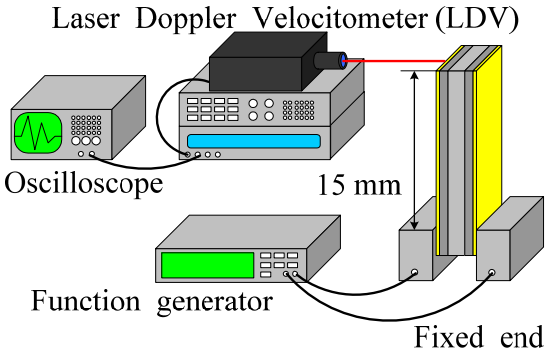


Fig.4 Vibration velocity measurement system of bimorph type vibrator with hydrothermally synthesized PZT polycrystalline film

**4-2.Measurement method of dielectric constant**

Capacity $C_T$ between the Au electrodes deposited on both sides of bimorph type vibrator with hydrothermally synthesized PZT polycrystalline film was measured. The Capacity $C_T$ is expressed as eq. (4-1). Dielectric constant $\varepsilon_r$ is expressed as eq. (4-2). $C$ is of capacity of hydrothermally deposited PZT polycrystalline film on one side of Ti substrate of vibrators, $S$ is cross section of Au electrode, $D$ is thickness of PZT film, $\varepsilon_0$ is dielectric constant in vacuum.

$$C_T = \frac{C}{2} \qquad (4\text{-}1)$$

$$\varepsilon_r = \frac{2C_T}{\varepsilon_0} \cdot \frac{D}{S} \qquad (4\text{-}2)$$

**5. Results**

The vibration velocity increased 50% by polling process with applied voltage of DC 20 V between Ti substrate as a cathode electrode and Au electrode as anode electrode. The effects of polling process on vibration velocity are shown in Fig.5. Dielectric constant decreased by the polling process. The results are illustrated in Fig.6.

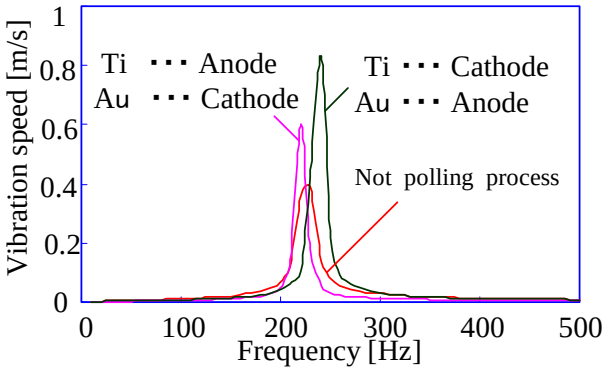


Fig.5 Effects of polling process on vibration velocity of bimorph type vibrator with hydrothermally synthesized PZT polycrystalline film

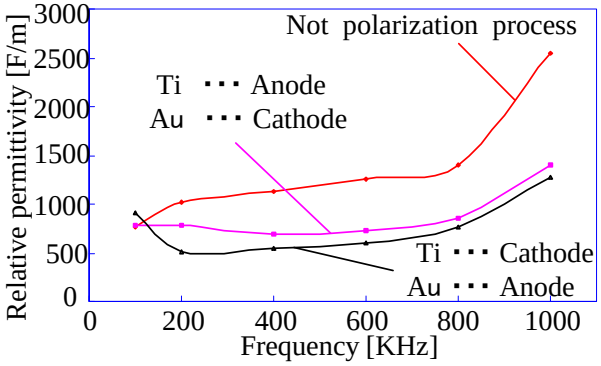


Fig.6 Effects of polling process on dielectric constant of bimorph type vibrator with hydrothermally synthesized PZT polycrystalline film

**6. Conclusions**

It was found that the vibration velocity increased but dielectric constant decreased by polling process. We will consider the effects of polling process by various voltages on the vibration velocity, sensitivity and various material properties in the future.

**References**

1. AEndo, M Ishikawa, N Kashima, M Kurosawa, S Takeuchi, 2006 IEEE International Ultrasonics Symposium. p.611. 2006.
2. M Ishikawa, M K Kurosawa, A Endo, and S Takeuchi: Jpn J Appl Phys. 44 (2005) 4342.
3. A Endo, N Kawashima, S Takeuchi, M Ishikawa, and M K Kurosawa. Jpn J Appl Phys. 46 (2007) 4779.
4. T Hasegawa, H Kitsunai, N Kawashima, S Takeuchi, M Ishikawa, and M K Kurosawa. Jpn J Appl Phys. 46 (2007) 4801.

2P1-6

Proceedings of Symposium on Ultrasonic Electronics, Vol. 29 (2008) pp. 205- 206
11-13 November, 2008

# Shear wave velocity of vanishing materials

Q. Hung Truong[1‡], Yong-Hun Eom[1], Changho Lee[2] Jong-Sub Lee[1]
([1] Korea University, [2] Georgia Institute of Technology)

## 1. Introduction

Soil containing soluble grains, such as salt, limestone, gypsum, dolomite, and halite [1] are susceptible to the change of the properties due to the dissolution of theses particles. Particle dissolution results in changes of the micro-structure of mixtures that can affect the strength and deformation behavior. The dissolution yields the greater hydraulic permeability that plays a crucila role in the safety of structures. For examples, the one of the factors of the St. Francis Dam failure is the dissolution of the partilces. However, there is a lack of information about the changes of shear wave velocity of the vanishing during dissolution under no lateral strain condition. This research includes experiment program, equipment system, experimental results and discussions of shear wave velocity during dissolution.

## 2. Experimental study

The vanishing mixtures are prepared using sieved table salt and Jumunjin 40/50 sand, as shown in Fig. 1. The table salt used sieved using 50/70 sieves is uniform, fine, and cubic grain salt. The mean grain size of the sand particle is about 1.5 times larger than that of salt particle. The smaller salt particles can be placed into the pores between larger sand particles. Thus, the minimum volume change is expected due the vanishing. The use of artificial specimen may provide a valuable insight view in macroscale mechanical response of soil [3]. Vanishing mixtures are prepared with 10% salt contents in volume. The vanishing mixtures are funneled into the oedometer cell in five layers. Each layer is compacted by the same tamping numbers to produce homogeneous specimens and simulate the construction of the earth dam.

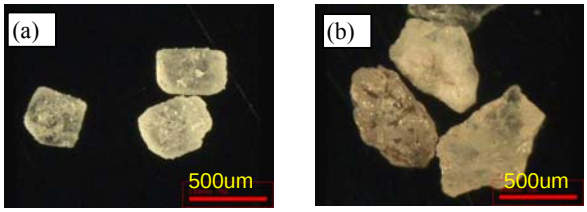


Fig. 1. Photograph Image: (a) Table salt particle; (b) Sand particle.

Email: jongsub@korea.ac.kr

The effects of local void on the micro to macro mechanical behaviors of vanishing mixtures are explored by implementing shear wave in a conventional oedometer cell equipped with bender elements, as shown in Fig. 2 [4]. The vertical load is applied into the cell. When the vertical load is reached to a planned stress (80kPa and 320kPa), the electrolyte, NaCl 0.01M, is slowly and carefully poured into the cylindrical container to dissolve the vanishing minerals. The electrolyte level in the container is kept lower than that in the specimen to prevent the flow of water from top to bottom at the beginning of the vanishing. Thus, the electrolyte gradually flows from the bottom to the top of specimen. The electrolyte in the container is kept to ensure the dissolution of all soluble mineral inside the mixtures. The fabric change due to the non-soluble particle relocation may occur during vanishing.

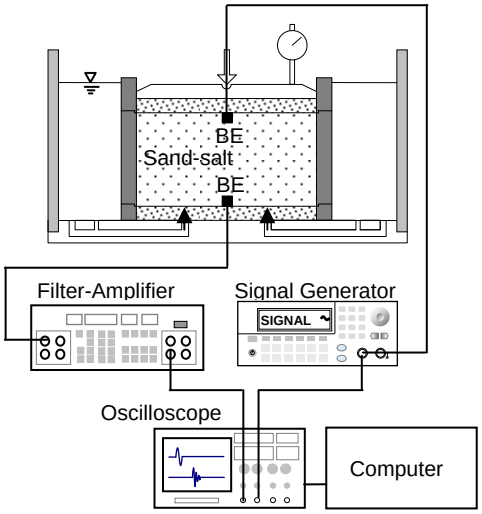


Fig. 2. Experimental setup. BE denotes a bender element.

## 3. Experimental results and discussions

During dissolution of the vanishing materials after the specimen is fully saturated, the vertical strain and shear waves are continuously monitored (see Fig. 3). The process monitoring of vertical strain and shear wave velocity show that the vanishing behavior can be categorized into three regions. In the first region, which ranges 0 ~ 0.3 minutes after saturation started, the vertical strain increases and the shear wave velocity tremendously decreases. When the specimen changes from the dry condition to saturation condition, the change of the

velocity is huge because the shear wave velocity can detect local change within the specimen. The change of the vertical strain, however, is minor because the vertical strain reflects the global change of the specimen. The change of the vertical strain and shear wave velocity results from the electrolyte flow and the vanishing of salt particles. In the second region (0.3~10 minutes), the increment of the vertical strain decreases, and the velocity increases after it decreases. The change of the increment of the shear wave velocity may be related with reorientation of the sand particle after dissolution of the salt particle. In third region (after 10 minutes), only minor vertical strain occurs. Thus, the shear wave velocity becomes stable.

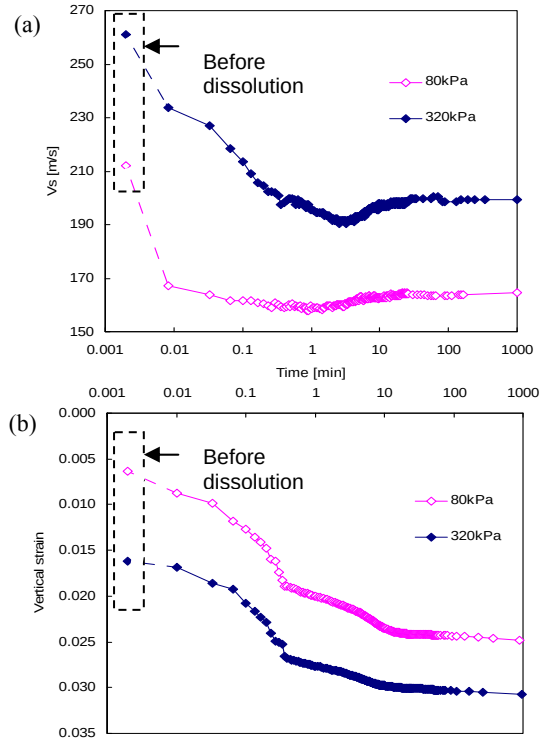


Fig. 3. Process monitoring during dissolution of vanishing materials at the vertical effective stresses of 80 kPa and 320 kPa: (a) Vertical strain versus time; (b) Shear wave velocity versus time.

The small strain shear modulus $G_{max}$ is obtained using the shear wave velocities $V_S$ and the corresponding mass density ρ

$$G_{max} = \rho \cdot V_S^2 \quad (1)$$

The small strain shear modulus during dissolution is plotted in Fig. 4, which shows the decrease of the small strain shear modulus during vanishing. Note the shear wave velocity and the mass density decrease during dissolution.

Empirical relation of shear wave with propagation direction of x and particle motion of y depends on the stresses on the x and y direction $\sigma_x$ and $\sigma_y$ is

$$V_S = \Theta \left( \frac{\sigma_x + \sigma_y}{2\text{kPa}} \right)^{\zeta} \left( \frac{\sigma_x - \sigma_y}{2\text{kPa}} \right)^{\Psi} \quad (2)$$

where Θ, ζ and Ψ are the factors represent material parameters to be experimentally determined [5]. Therefore, the decrease (up to 25%) of shear wave velocity with axial strain increase can be explained due to the change of mass density, the void ratio, mechanical fabric changes and the stress as well as material anisotropy changes.

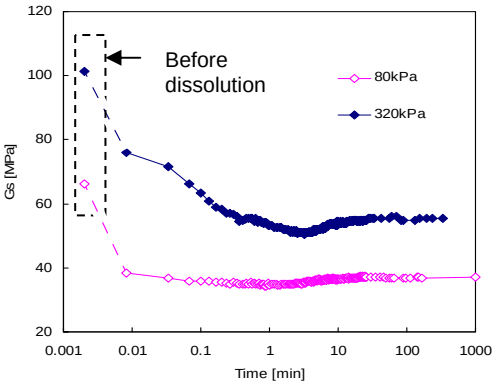


Fig. 4. Evolution of small strain shear modulus during dissolution.

## 4. Conclusions

The effect of the dissolution of the particles was studied using the artificial specimens prepared by mixing sand and granular salt, then dissolving the salt grains. The small strain shear wave velocity changed up to 25% or the small strain shear modulus changed up to 40% during particle dissolution. The small strain shear wave parameters are effective in detecting and quantifying the fabric changes associated with particle-dissolution processes.


## Acknowledgment

This work was supported by BK-21 Global Leaders in Construction Engineering, Korea University, Korea.


## References


1. F.G. Bell: *Engineering Geology* (Elsevier, 2004).
2. D. Craft, C. Cain, and C. Sullivan: Technical Memorandum 86-6829010, U.S. Department of the Interior - Bureau of Reclamation (2006).
3. M. A. Fam, G. Cascante, , and M. B. Dusseault: J. Geotech. Geo.. Eng., **128** (2002).
4. J.S Lee. and J.C. Santamarina: J. Geotech. Geo. Eng. **131** (2005).
5. J.C. Santamarina, K.A. Klein and M.A. Fam: *Soils and Waves* (JohnWiley and Sons, 2001).

2P1-7

Proceedings of Symposium on Ultrasonic Electronics, Vol. 29 (2008) pp. 207- 208
11-13 November, 2008

# Modulus change of rigid-soft mixtures during cementation

Changho Lee[1‡], Q. Hung Truong[2], Hyung-Koo Yoon [2], Jong-Sub Lee[2]
([1] Georgia Institute of Technology, [2] Korea University)

## 1. Introduction

Applications of the shredded tires increase to solve not only environmental but also economical problmes. Addtion of soft particle into the soil decreases in the specific gravity, mass density, permeability of water, strength, and stiffness, and increases in compressibility and damping [2], [3]. Cementation remarkbaly changes the stiffness and strength of the soil so that it is often adopted to a ground improvement. Modulus change is explored to monitor vertical settlement and elastic wave velocities during cementation. This study includes experimental setup with specimen preparation, experimental results and discussions of modulus change during cementation.

## 2. Experimental study

The rigid-soft particle mixtures are prepared using pre-sieved shredded tire and Jumunjin 20/30 sand, as shown in Fig. 1. The mean particle size of two particles is 0.725mm. The rubber is angular and irregularly shaped and the sand is uniform, coarse, and angular. The maximum and minimum void ratios are $e_{min}$=0.60 and $e_{max}$= 0.87, repsectively.
Specimens are prepared with three different volumetric sand fraction (sf=$V_{sand}/V_{total}$=0.2, 0.6, and 0.8). Portland cement is used as the cementation agent. Dried sand and rubber particles are mixed with Portland cement of 20g and deionized water for 5 minutes in the container. Well mixed specimen is carefully scooped into four layers. Each layer is lightly compacted by the same tamping numbers to apply same amount of compact energy. When the mixture is filled in the oedometer cell, the top cap is placed on the mixture. The initial height and weight of the specimen is measured to determine the initial condition of the specimen.

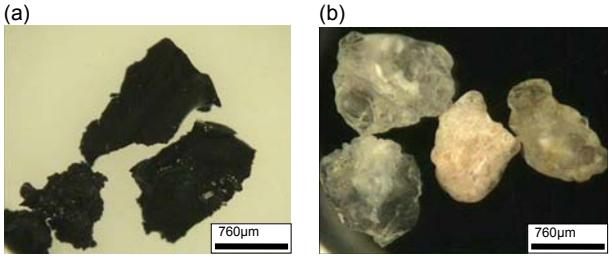


Fig. 1 Photograph Image: (a) Shredded rubber; (b) Jumunjin 20/30 sand.

Email: jongsub@korea.ac.kr

Bender elements 11.0×4.0×0.6 (length × width × thickness in mm) and piezo-disk element 14×20×0.45 (ceramic dia.× sensor dia. ×thickness in mm)) are used as transducers to measure the shear and primary waves. All transducers are waterproofed and electrically shielded. The transducers are installed into the top cap and bottom plate of the odeometer cell to gather elastic waves along vertical direction in the transmission mode as, shown in Fig. 2 [1].
The vertical sitting stress ($\sigma_{sit}$ =21kPa) is applied and maintained for 72 hours during hardening of cementation agent. Axial strain and P- and S- waves are measured to monitor the void ratio change and the evolution of the modulus of the specimens with time under no-lateral deformation.

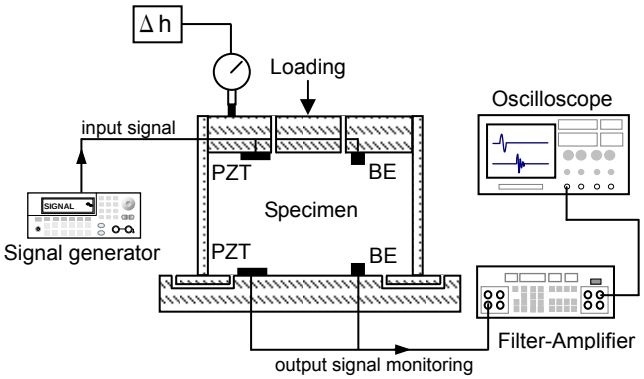


Fig. 2 Experimental setup. BE and PZT denote a bender element and piezo-disk element, respectively

## 3. Experimental results and discussions

The rubber is a typical creep material. Fig. 3 shows the vertical settlement of tested specimens with time. A large deformation is observed in all specimens immediately after applying the vertical load. The vertical settlement increases with a decrease in the sand fraction for an applying vertical stress because the rubber particles easily distort. The vertical settlement approaches gradually asymptotic value about 1~24 hours after loading. Note that as the sand fraction decreases, the settlement increases.
Evolutions of measured elastic wave signals are shown in the Fig. 4 for sf=0.6 at the fixed vertical stress (21kPa) with time. The travel times of P- and S-wave are almost constant for about 30 minute

after applying vertical load. The traveling times of P- and S- waves decease and the resonant frequency of P- and S- waves increases significantly due to the curing process.

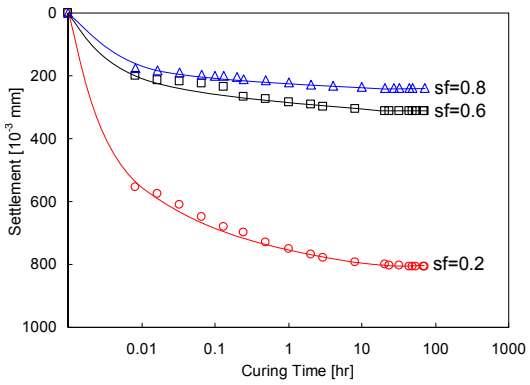


Fig. 3 Vertical settlement with time.

The constraint modulus M and the small strain shear modulus $G_{max}$ can be obtained from the calculated the primary wave velocity $V_P$ and the shear wave velocities $V_S$, and the corresponding mass density ρ

$$M = \rho \cdot V_P^2 \quad (1)$$

$$G_{max} = \rho \cdot Vs^2 \quad (2)$$

The evolutions of constraint and small strain shear modulus are plotted in Fig. 5 during cementation hardening. The moduli is almost constant until 0.3 hour (for sf=0.8) ~ 3 hour (for sf=0.2). The constraint modulus and shear modulus of the specimens increase dramatically due to the curing of cementation agent. The modulus change of the higher sf specimens (sf=0.8) are higher than that of the lower sf specimens (sf=0.2).

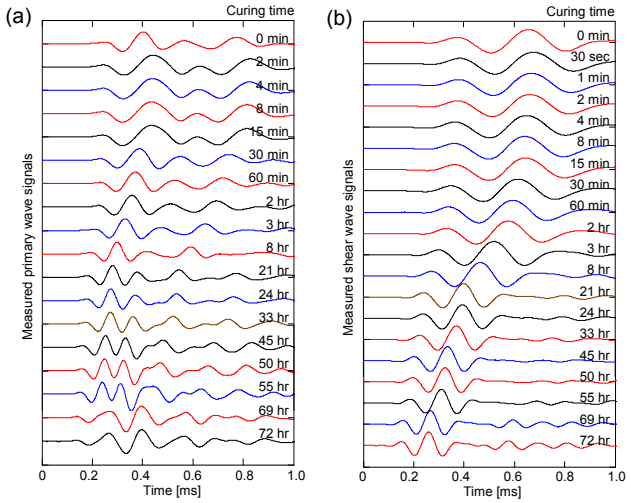


Fig. 4 Evolution of measured signals for sf=0.6 at fixed vertical stress σ'$_v$=21kPa: (a) Primary wave; (b) Shear wave.

The stiffness of granular material is a function of the effective stress on the particle-to-particle contact. However, cementation increases particle contact area so that it remarkably affects the strength and modulus of the specimen.

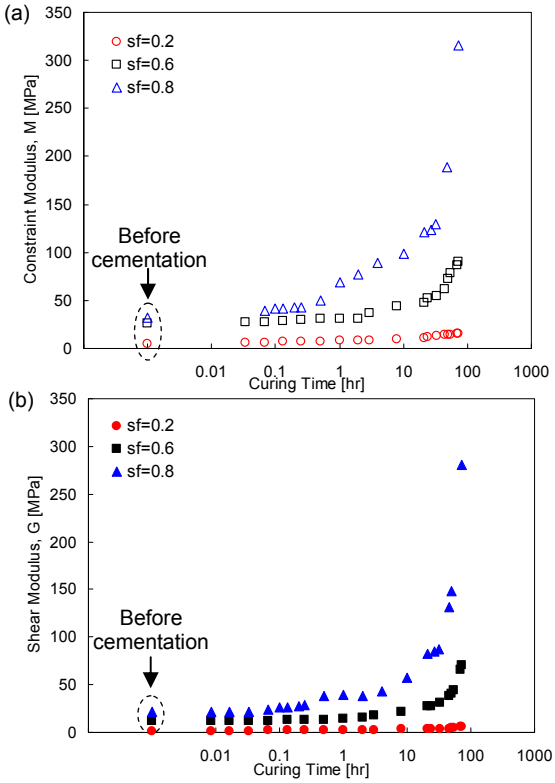


Fig. 5 Modulus change during cementation: (a) constraint modulus; (b) shear modulus.

## 4. Conclusions

Modulus change in rigid-soft particle mixtures is studied by monitoring vertical settlement and elastic wave velocities. The vertical deformation approaches gradually asymptotic value in about 1~24 hours after loading. The effect of cementation increases the constraint modulus and shear modulus under a fixed vertical effective stress because particle level contact area increases with the cementation. The higher the sand fraction, the higher the moduli. This study shows that the ultrasonic wave velocity can be effective tools for monitoring of modulus change during cementation.


## Acknowledgment

This work was supported by BK-21 Global Leaders in Construction Engineering, Korea University, Korea.


## References


1. C. Lee, J.S. Lee, W., Lee, and T.H. Cho: *Geotech. Test. J.*, 31(2), (2008).
2. J. G. Zonberg, A. Canral, and C. Viratjandr: : *Can. Geotech. J.*, 41(2) (2004).
3. Z. Y. Feng K. G. Sutter: *Geotech. Test. J.*, 23(3), (2000).

2P2a-17

Proceedings of Symposium on Ultrasonic Electronics, Vol. 29 (2008) pp. 209-210
11-13 November, 2008

# Accurate distance measurement by pulse compression using linear-period-modulated signals and calibration of Doppler shift

線形周期変調信号を用いたパルス圧縮と
ドップラーシフト補正による高精度距離計測

Shinnosuke Hirata[1†], Minoru Kuribayashi Kurosawa[1] and Takashi Katagiri[2]
([1]Dept. of Information processing, Tokyo Tech; [2]Sutekina Inc.)
平田慎之介[1†], 黒澤実[1], 片桐崇[2] ([1]東工大 総理工; [2]すてきな (有))

## 1. Introduction

The pulse-echo method is the tyipical method of ultrasonic distance measurement. The method is based on determination of the time of flight (TOF) of ultrasonic waves. For improvement of the distance resolution and reduction of white noise of echoes, pulse compression has been employed in the method. A linear-frequency-modulated (LFM) ultrasonic pulse is transmitted in typical pulse compression. A received signal, which includes reflected echoes, is correlated with a reference, which is the transmitted ultrasonic pulse. The signal processing for pulse compression consists of huge iterations of multiplications and accumulations. Real-time distance measurement by pulse compression is difficult because of requirement of high-cost digital signal processing. For reducing the calculation cost of pulse compression, a sensor signal processing method using a delta-sigma modulated single-bit digital signal has been proposed[1]. Cross-correlation by single-bit signal processing of the proposed method can reduce the calculation cost.

However, if an object is moving, due to the Doppler effect introduced by the motion of the object, echoes are Doppler-shifted. The distance of the moving object cannot be accurately measured because the Doppler-shifted LFM signals cannot be correlated with the transmitted LFM signal. In this paper, a low-calculation-cost method for accurate distance measurement of moving objects is proposed. In the proposed method, the TOF and the Doppler velocity of moving objects are measured by pulse compression using linear-period-modulated (LPM) ultrasonic pulses. The distance can be accurately measured by calibration of the TOF with the Doppler velocity.

## 2. Linear-period modulation

Doppler shift is linear compression or expansion of the signal period in proportion to the Doppler velocity of moving objects. Therefore, the Doppler-shifted LFM signals cannot be correlated with the transmitted LFM signal.

Pulse compression using LPM signals has been proposed for ultrasonic distance measurement of moving objects [2]. An LPM signal is written as

$$u(t) = a \sin\left\{2\pi \frac{1}{p_b} \ln\left(t + \frac{l}{b_b} p_0\right) + \varphi_0\right\}, \quad (1)$$

where $a$ is the signal amplitude, $l$ is the signal length, $p_0$ is the initial signal period, $p_b$ is the chirp rate of the signal period, and $\varphi_0$ is the constant of phase. The period of the LPM signal linearly chirps with time. Therefore, the Doppler-shifted LPM signals can be correlated with the transmitted LPM signal. The LPM signal is thus suitable for cross-correlation of Doppler-shifted signals.

## 3. Doppler velocity estimation

The TOF of the Doppler-shifted LPM signal is determined from the peak of cross-correlation function of the Doppler-shifted LPM signal and the transmitted LPM signal. However, the TOF is also Doppler-shifted by three factors, 1: increase or decrease of traveling time of ultrasonic waves, 2: change of correlative period band, and 3: phase shift of the peak of the cross-correlation function. Therefore, calibration of the Doppler-shifted TOF with the Doppler velocity is necessary for accurate distance measurement of moving objects.

In the pulsed Doppler method, the Doppler velocity is estimated from the Doppler-shifted frequency of the echo, which is given by Fourier transform. The disadvantages of Fourier transform are low velocity resolution and high cost digital signal processing. Similar to the frequency, the signal period and signal length of the echo are Doppler-shifted. Therefore, the Doppler velocity can be estimated from the Doppler-shifted length. The Doppler-shifted length is expressed as,

$$l_d = (v/v + v_d) \cdot l, \quad (2)$$

where $l_d$ is the Doppler-shifted signal length, and $l_0$ is the length of the LPM signal. $v_d$ is the Doppler velocity, and $v$ is the velocity of ultrasonic wave in air. Fig. 1 shows a proposed method of accurate distance measurement by transmitting two LPM signals. When two LPM signals are continuously

† hirata.s.ab@m.titech.ac.jp

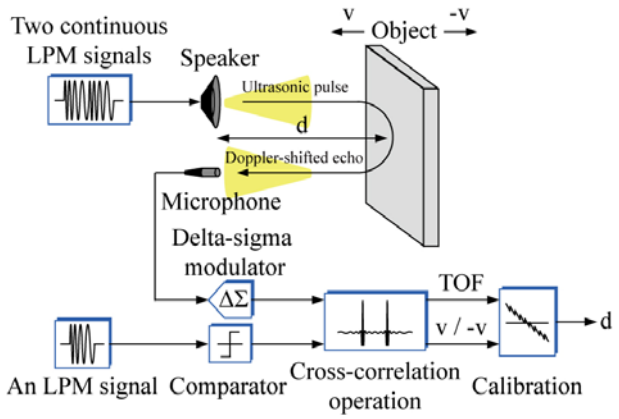


Figure 1: Design of the proposed method of accurate distance measurement

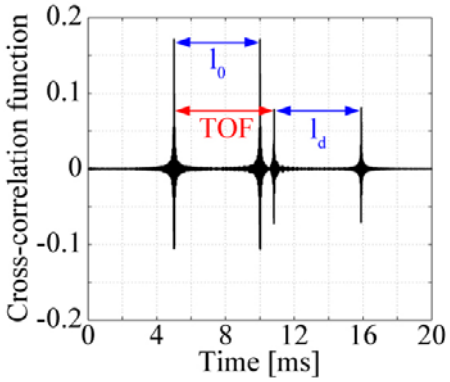


Figure 2: The cross-correlation function of the transmitted two LPM signals and the LPM signal

transmitted, the cross-correlation function of the transmitted two LPM signals and an LPM signal has two peaks, as illustrated in Fig. 2. The interval of the first peak and second peak of the cross-correlation function shows is the Doppler-shifted signal length $l_d$.

## 4. Calibration with Doppler velocity

The proposed method of accurate distance measurement by transmitting two LPM signals was evaluated by a computer simulation using MATLAB. In the simulation, the period of an LPM signal chirps from 16.67 μs to 50 μs, and the duration of the signal was 5 ms. The duration of transmitted two LPM signals was 10 ms. The distance to the object was 1 m. The velocity of ultrasonic wave in air was 344 m/s at approximately 20 ℃. The sampling frequency was 12.5 MHz. The cross-correlation function was obtained from cross-correlation by single-bit signal processing.

The distance, which measured from the Doppler-shifted TOF, is illustrated in Fig. 3. The distance, which calibrated with the Doppler velocity of Fig. 3, is illustrated in Fig. 4. The distance of moving objects can be accurately measured by

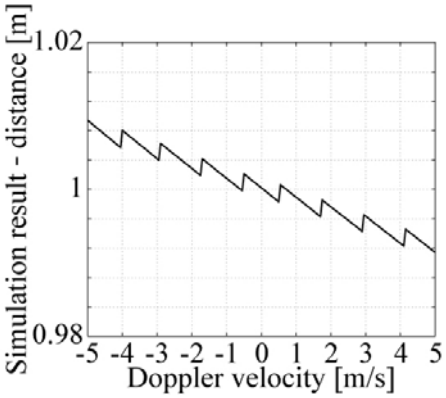


Figure 3: The distance measured from the Doppler-shifted TOF

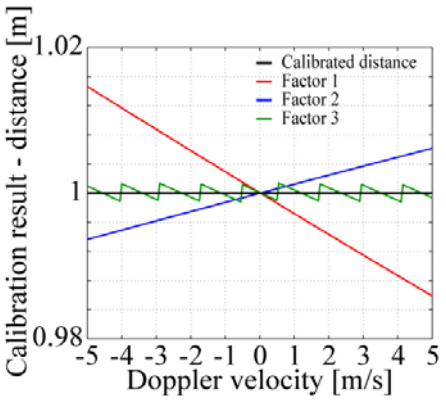


Figure 4: The distance calibrated with the Doppler velocity

calibration of three factors of Doppler shift. The proposed method of accurate distance measurement does not require additional calculation cost beyond the pulse compression.

## 5. Conclusion

A low-calculation-cost method for ultrasonic distance measurement of moving objects is proposed. Pulse compression by transmitting two LPM signals can measure the Doppler-shifted TOF and estimate the Doppler velocity of moving objects with high resolution. By calibrating the Doppler-shifted TOF with the Doppler velocity, the distance of the moving object can be accurately measured.


## Acknowledgments

This work was supported by a Grant-in-Aid for Research Fellowships of the Japan Society for the Promotion of Science for Young Scientists.


## References


1. S. Hirata, M. K. Kurosawa, and T. Katagiri: IEICE Trans. Fundamentals **E91-A, No.4** (2008) p. 1031 - 1037.
2. J. J. Kroszczynski: Proc. of the IEEE, **Vol. 57, No.7** (1969) p. 1260 - 1266.

2P2a-18

Proceedings of Symposium on Ultrasonic Electronics, Vol. 29 (2008) pp. 211-212
11-13 November, 2008

# A Study on Liquid-Level Sensing by Using Trapped-Energy-Mode Thickness Vibrations

エネルギー閉じ込めモード厚み振動を利用した
微小液面レベル変化の検知

Ken Yamada[1,2†], Hisato Honda[1], Shuhei Horiuchi[2], and Tetsuya Kinai[1] ([1]Faculty of Eng., Tohoku gakuin Univ.; [2] Graduate School of Eng., Tohoku Gakuin Univ.)
山田　顕[1,2‡]，本田斐聡[1]，堀内修平[2]，木内哲也[1]（[1]東北学院大・工; [2]東北学院大・院・工）

## 1. Introduction

Detection and/or sensing of the liquid level by using ultrasonic techniques has widely been used so far. Most of the techniques employ the pulse-echo method to detect the variation in the liquid level. In recent years, measurement of liquid level in millimeter scale or less has become an important suject in, for example, biological and chemical fields. However, the pulse-echo method is inadequate for the measurement of variation in such a small scale. As an example of an alternatinve method, liquid level sensing using a self-excited small PZT-cantilever has been proposed[1)]. In this paper, a new method is presented that employs a piezoelectric thickness vibrator operating in a trapped-energy mode for detecting a small-scale variation in the liquid level. The energy-trapping phenomenon in thickness vibration modes was found by Shockley et al.[2)] and has been applied successfully in piezoelectric resonators and/or filters over several tenth of years. Application of this phenomenon to the liquid level sensing should be a new and unique attempt that might have not been tried yet.

## 2. Principle of operation

Let us consider a thickness-mode piezoelectric vibrator having a partially-electroded region at its center such as that shown in **Fig.1(a)**. Because of the piezoelectric effect, the cut-off frequency in the electroded region, $\omega_0$, is slightly lower than that, $\omega_0'$, in the surrounding (unelectroded) region. In this configuration, the resonant vibration occurs between $\omega_0$ and $\omega_0'$. The wavenumber in the electroded region, $\gamma$, is real, whereas that in the surrounding region, $\gamma'$, is imaginary. Therefore, the vibration energy is confined in the central region and decays exponentially in the surrounding region. Thus the energy-trapping works, and an evanescent field is created in the unelectroded region, such as shown in **Fig.1(b)**.

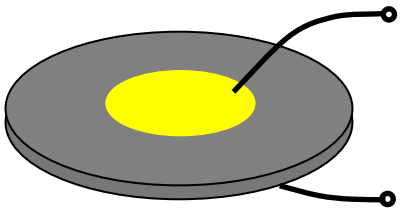

Fig. 1(a)　Trapped-energy-mode vibrator.

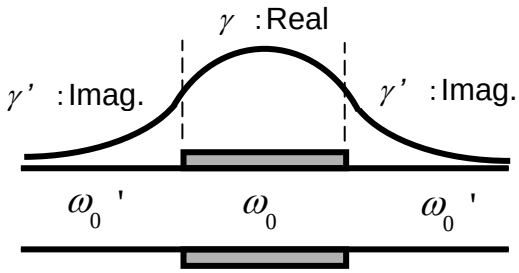


Fig. 1(b) Displacement distribution for trapped-energy mode.

If the unelectroded region is dipped in a liquid, a small amount of leakage of the vibration energy will occur. The amount of the leakage will vary depending on how deep the surrounding region is dipped in the liquid. Therefore, the electric characteristics of the vibrator such as the *Q*-factor and the electric conductance *G* at the resonance will vary in accordance with the immersion depth. This will enable us to the sensitive detection of variation in the liquid level in a small scale.

## 3. Experimental setup

A thickness-poled PZT plate (NEPEC-6) of 30 mm in diameter and 1 mm in thickness having a 4 mm diameter electrode was employed as the vibrator material. **Figure 2** shows the frequency characteristics of the electric admittance |*Y*| and the electric conductance *G*. The resonance frequency was 2.09 MHz and the *Q*-factor was about 400. The plate was supported vertically by clamping its fringe. Because the vibration energy is confined to the electroded region, the clamping does not cause deterioration of the *Q*-factor. Then, the plate was

---

† k-yamada@tjcc.tohoku-gakuin.ac.jp

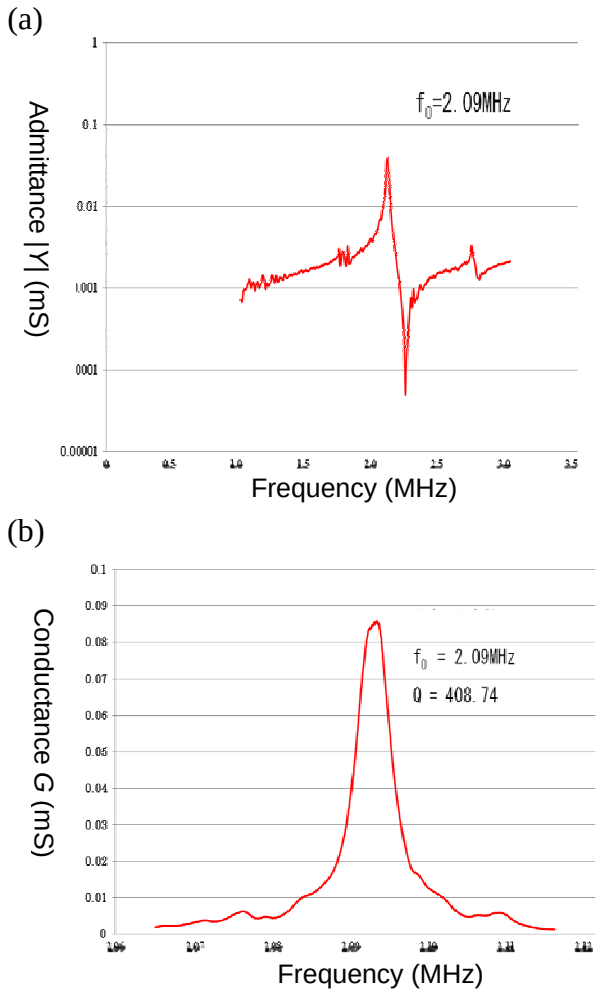


Fig. 2 Frequency response of admittance (a) and Conductance (b) for the vibrator.

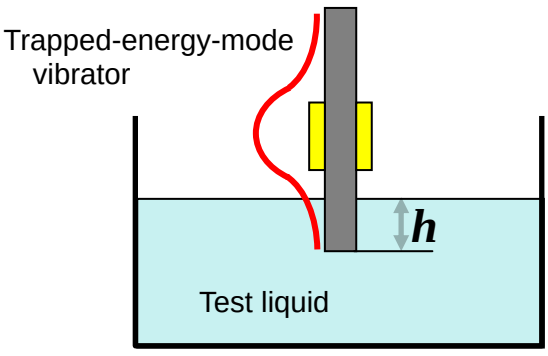


Fig. 3 Experimental setup for measurements.

dipped in a liquid to be tested such as shown in **Fig.3**. The test liquids employed were water, glycerin, castor oil, and honey. The depth *h* of dipping was varied using a stepping-motor stage moved in the vertical direction. Here, the variation in *G* against *h* at the resonance frequency was measured because it corresponds to the variation in *Q*-factor as long as the *Q*-value is high.

## 4. Results

**Figure 4** shows the variations of *G* obtained for the four different kinds of liquids. The vertical axis is normalized to the maximum values $G_{max}$ for each of the liquids. The origin of the horizontal axis corresponds to the boundary between the electroded and the unelectroded regions. The positive value of *h* means that the liquid surface is at the unelectroded (evanescent wave) region, whereas the negative value of *h* means that the liquid surface goes up beyond the electrode edge. In any cases the *G* value decreases gradually according to the increment of the liquid level. The variations of *G* are almost linear in the range ±5 mm from the electrode edge. It might be said that the variation is steeper for the liquid having higher viscosity.

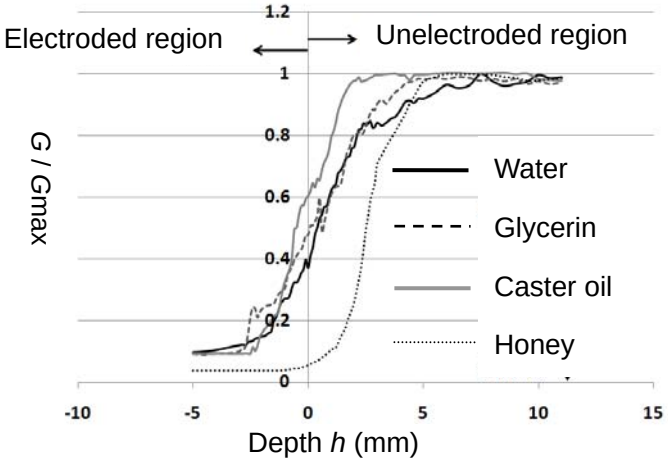


Fig. 4 Variations in normalized *G* vs. depth *h* for 4 different liquids.

## 5. Conclusions

It has been shown that the piezoelectric vibrator operating in a trapped-energy mode will be a novel tool for detecting the liquid level variation in a millimeter scale. Almost linear variation of *G* against the depth of dipping has been obtained within a few millimeter ranges. Further investigation is required for clarifying the effects of hydrophilicity and surface tension of the liquids on the sensing. The use of thickness-shear vibration modes might be more convenient for the liquids having higher viscosity, and is under investigation.

## References

1. G.. A. Campbell and R. Mutharasan.: Sensors and Actuators A **122** (2005) 326.
2. W. Shockley, D. R. Curran, and D. J. Koneval.: Proc. 17th Frequency Control Symposium (1963) 88.

2P2a-19

Proceedings of Symposium on Ultrasonic Electronics, Vol. 29 (2008) pp. 213-214
11-13 November, 2008

# Target Ranging by Using Ultrasonic Adaptive Signal and Pulse Compression

超音波適応信号とパルス圧縮を併用した距離測定

Ryo Toh[1†], Dai Chimura[2] and Seiichi Motooka[1] ([1]Facult. Eng., Chiba Inst. Tech.; [2]Graduate School Eng., Chiba Inst. Tech.)
陶良[1†], 千村大[2], 本岡誠一[1] ([1]千葉工大 工; [2]千葉工大 院)

## 1. Introduction

Ultrasonic pulse-echo method is widely used for target ranging, especially in water or in air where testing environment is not suitable for optical or electromagnetical waves, such as remote sensing of automobile and robot etc. In order to augment both the range resolution and the signal to noise ratio (SNR), pulse compressing technique using coded pulse with long duration is employed. Two kinds of pulse coding methods are commonly used, such as phase coding and frequency modulation (FM). In this paper, the compression of frequency modulated pulse is discussed.

Usually, the linear frequency modulated wave (chirp wave) is used, and the matched filtering method which calculates the cross-correlation of the receiving signal with the transmitting signal is employed for the pulse compression.[1,2] However, especially in the application of ultrasonic wave, the effective bandwidth of receiving signal is affected by the restriction of the sensitivity of sensors.

In order to acquire broader bandwidth with flat spectral amplitudes, an adaptive transmitting wave, which equalizes the affect of sensitivities of sensors, is proposed.[3] The effectiveness of adaptive signal is verified by an example of target ranging in air.

## 2. Adaptive transmitting signal

Neglecting noise, the spectrum of receiving signal $S_r(\omega)$ can be written as

$$S_r(\omega) = S_t(\omega) \cdot R(\omega) \quad (1)$$

where $S_t(\omega)$ and $R(\omega)$ are the transmitting signal and transmission function including the sensitivities of both transmitter and receiver, respectively.

If we use an adaptive transmitting signal $S_{ta}(\omega)$, signal with flat spectrum amplitudes can be received theoretically. It is given as

$$S_{ta}(\omega) = \frac{|S_{r0}(\omega)|}{|S_{r0}(\omega)|^2 + \alpha^2 \cdot |S_{r0}(\omega)|^2_{\max}} \cdot S_{t0}(\omega) \quad (2)$$

where $S_{r0}(\omega)$ is the reference receiving signal by using $S_{t0}(\omega)$ as transmitting signal, $\alpha$ is the stabilization factor to restrain the divergence of the response function at where the value of $S_{r0}(\omega)$ is small.

† Email: liang.tao@it-chiba.ac.jp

## 3. Experiment conditions and methods

The arrangement of sensors and target is shown in **Fig.1**. Two ultrasonic transducers with 1.5 cm in diameter and a 40 kHz resonant peak are employed as transmitter and receiver, which are set at (15, 30, 0) ($x$, $y$, $z$ in cm in the coordinates shown in Fig.1, and same in following) and (-15, 30, 0), respectively. A 5 cm x 5 cm square steel plate is employed as measuring target. The $y$=0 plane is ground surface where reflection should be taken into consideration.

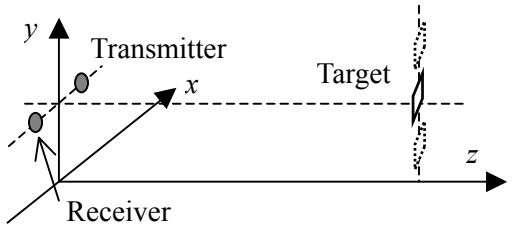


Fig.1 Arrangement of sensors and target.

The chirp wave and the reference receiving signal reflected by the target at (0, 30, 100) are shown in **Fig.2**. Calculated with them, the adaptive signal and the corresponding reference receiving signal reflected by the same target is shown in **Fig.3**.

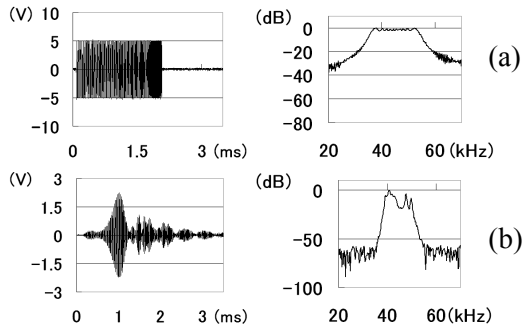


Fig.2 (a): Chirp wave; (b): Reference receiving signal.

It's shown that unevenness is brought forth by the compensation in the spectrum of adaptive signal comparing to the flat range of chirp wave, while the spectrum of receiving signal is compensated to be flatter and broader. Here, the amplitudes of the two kinds of transmitting signals are normalized according to their envelope areas.

The effectiveness of pulse compression using adaptive signal is studied experimentally by setting the target to (0, 50, 100) and (0, 10, 100). Though the positions are symmetric to the sensors, the affect of reflection from ground can be shown in the lower arrangement.

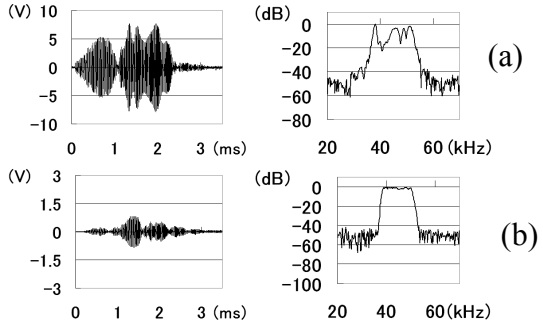


Fig.3 (a): Adaptive signal; (b): Reference receiving signal.

## 4. Results of Measurement

**Fig.4** shows the comparison receiving signals using chirp wave and adaptive signal as transmitting signals, while the target is set at (0, 50, 100). **Fig.5** shows the compressed pulses calculated by cross correlation of receiving signals shown in Fig.4 with those corresponding reference receiving signals shown in Fig.2 (b) and Fig.3 (b), respectively. **Fig.6** shows the comparison pulse compression results while the target is set at (0, 10, 100).

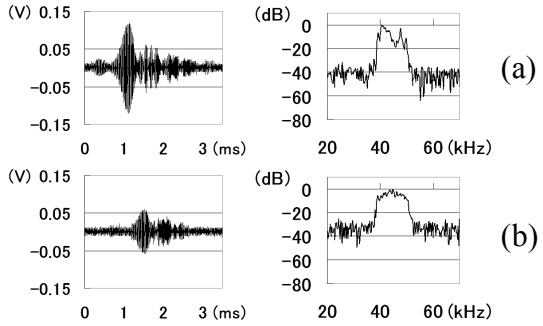


Fig.4 Receiving signals of target at (0, 50, 100) corresponding to (a): Chirp wave; (b): Adaptive signal.

In Fig.5, the effectiveness of adaptive signal is shown clearly. Because of the unevenness in the spectrum of receiving signal shown in Fig.4 (a), the correlation result of Fig.5 (a) shows a narrower bandwidth in its spectrum and more expanding pulse width in its waveform, comparing to those of adaptive signal.

In Fig.6, the positions of pulse propagating time via the target directly, together with that being reflected once by the ground surface (path lengths of transmitting wave reflection and receiving wave reflection are same owing to that the position of the target is set at the center of transmitter and receiver) are also shown. The ground surface reflection shows larger amplitude because of the directivity of the target reflection and double paths summation. In the result of chirp wave, the interference of two pulses causes error at the direct reflection, while in that of the adaptive signal they are distinguished clearly.

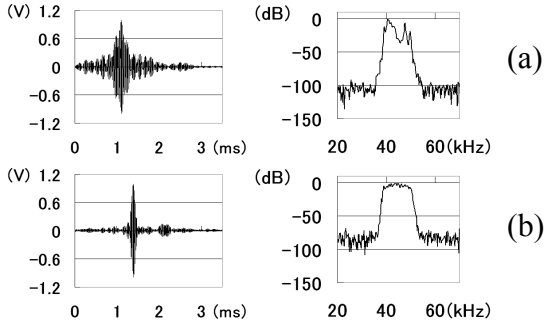


Fig.5 Results of pulse compression of target at (0, 50, 100) corresponding to (a): Chirp wave; (b): Adaptive signal.

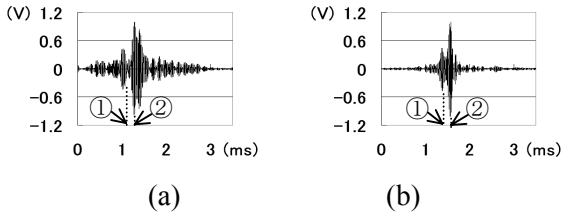


Fig.6 Results of pulse compression of target at (0, 10, 100) corresponding to (a): Chirp wave; (b): Adaptive signal. (①:direct reflection; ②: once ground reflection)

## 6. Conclusions

By using adaptive transmitting signal, the spectrum of receiving signal is compensated to be flatter and broader, which brings forth better resolution in the result of pulse compression. The effectiveness of adaptive signal in improving the accuracy of target raging can be expected.

## References

1. E. Ha, Y. Kawamura, et al. Jpn. J. Appl. Phys. **47** (2008) 3946.
2. K. Toiyama, T. Hayashi, and S. Kamiya. Proc. Symp. Ultrason. Electron., **26** (2005) 441.
3. D. Chimura, R. Toh, and S. Motooka. Proc. Natl. Autumn Meet. Acoustical Society of Japan, 2008, No. 2-Q-28 [in Japanese].

2P2a-20

Proceedings of Symposium on Ultrasonic Electronics, Vol. 29 (2008) pp. 215-216
11-13 November, 2008

# A Hydrogen Sensor using Ultrasonic

## 超音波を用いた水素センサーに関する研究

Yoshimine Kato (Facult. Eng., Kyushu Univ.)
加藤　喜峰　（九大　工）

**Abstract**

A hydrogen sensor using ultrasonic was studied. Sound velocity of hydrogen is about four times larger than that of the air. Therefore, it is possible to measure hydorgen contents in the air by measuring the sound velocity. We have showed that it is possible to measure up to near 100ppm hydrogen content in the air by measuring the sound velocity at 330kHz of ultrasonic.

## 1. Introduction

Using hydrogen gas as a new fuel is important for clean-energy society that does not emmit $CO_2$, $NO_x$, and etc. Especilally, fuel cells and hydrogen gas vehicles are widely studied and developed. Therefore, hydrogen sensors for those applications are very important and will be widly used for safety. Currently, many kinds of hydorgen sensors were developed and used today. For example, solid state sensors[1], electrochemical sensors, catalytic sensors, metal-oxide semiconductor sensors[2], ball surface acoustic wave hydrogen sensors [3], and etc are commercially available or studied. However, some of those sensors require high temperature or the response time is relatively slow as the order of seconds. Also, many of these sensors cannot distinguish hydrogen from other flammable gases such as methane, propane and butane gases.

The sound velocity of hydrogen is about four times larger than that of the air. Therefore, in this study, we have showed that it is possible to measure hydrogen contents close to 100 ppm in the air by measuring sound velocity changing.

## 2. Theory and Experiment

When there is hydrogen content of $\rho$ vol.% in the dry air which mass is 28.96, the sound velocity is expressed as $v_H$,

$$v_H = \sqrt{\frac{kRT}{28.96(1-\rho)+2.016\rho}} \qquad (1)$$

where $k$ is specific heat ratio, $R$ is gas constant and $T$ is temperature in K. To obtain the hydrogen concentration $\rho$ in the dry air, one could measure the sound traveling time difference $\Delta t$ between the dry air and the hydrogen contained dry air with the following equation.

$$\rho = \frac{28.96}{26.94}\{1-(\frac{t-\Delta t}{t})^2\} \qquad (2)$$

By obtaining the ratio of the sound traveling time in the dry air $t$ and the traveling time difference $\Delta t$ from eq. (2) as shown below,

$$\frac{\Delta t}{t} = 1-\sqrt{1-\frac{26.94}{28.96}\rho} \qquad (3)$$

one could plot the curve as shown in Fig. 1.

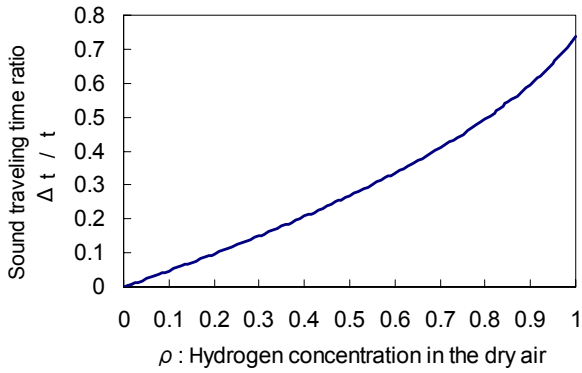


Fig. 1 Dependence of the hydrogen concentration $\rho$ in the dry air, to the ratio of the sound traveling time in the dry air $t$, and traveling time difference $\Delta$t between the dry air and the hydrogen contained dry air according to eq. (3).

From **Fig. 1**. one can see that $\Delta t/t$ and ρ has almost linear relation at lower hydrogen concentration, therefore; it is simple to detect low concentration hydrogen by measuring the traveling time difference $\Delta t$.

For measuring $\Delta t$, an Ultrasonic Pulsar and Receiver (Japan Probe JPR-10bB) at 330kHz was used. A number of pulses was varied form one to four and their voltages were varied form 50 to 200V. Two standard ultrasonic probes were used for transmitting and receiving the pulse. Distance of these two probes was varied from 20 to 54 mm.

---

E-mail: yoshimine.kato@zaiko.kyushu-u.ac.jp

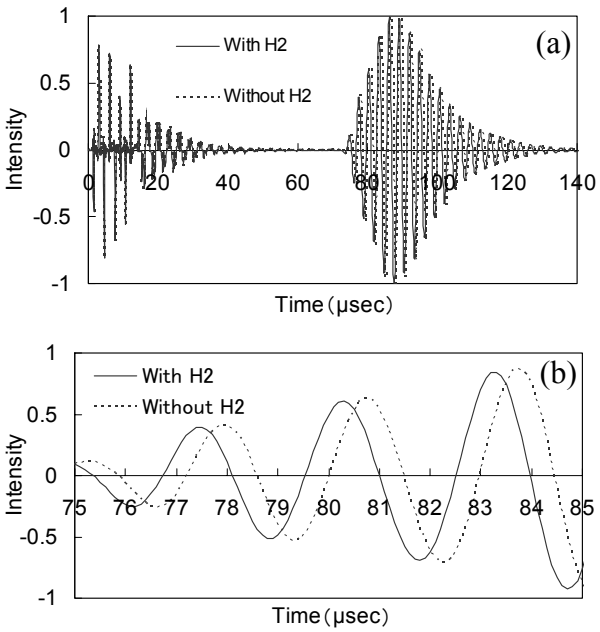


Fig.2 (a) Signal intensity form the ultrasonic receiver. Four pulses of sound wave traveled after 28mm of distance are shown. (b) Enlargement of Fig. 2(a).

## 3. Results and discussions

**Fig.2** shows the experimental result using the Ultrasonic Pulsar and Receiver. Signal intensities of the four pulses sound wave traveled after 28mm are shown. Solid line shows received signal of the hydrogen mixed air and dashed line shows the signal from just the air. Fig. 2(b) is the enlargement of Fig. 2(a). $\Delta t$ the traveling time difference between the air and the hydrogen contained air can be measured as about 0.4 μsec form Fig. 2(b), and assuming that the sound traveling time in the dry air $t$ is about 80 μsec, one can calculate the hydrogen concentration of about 1% from eq. (2). This result was about the same value with the measured hydrogen concentration using a conventional $H_2$ sensor.

Next, ppm order hydrogen concentration measurement was tried. The traveling time difference $\Delta t$ between the air and the hydrogen contained air was able to be measured as small as 0.01 μsec, thus the hydrogen concentration was calculated to be about 140 ppm as show in **Fig. 3**. Fig. 3 shows estimated hydrogen concentration from the measured $\Delta t$ according to eq. (2). The transmitting pulse was one pulse and distance to a receiving probe was 54 mm. These results suggest that it is possible to measure hydrogen concentration by ultrasonic up to near 100 ppm and if one can increase the ultrasonic frequency or

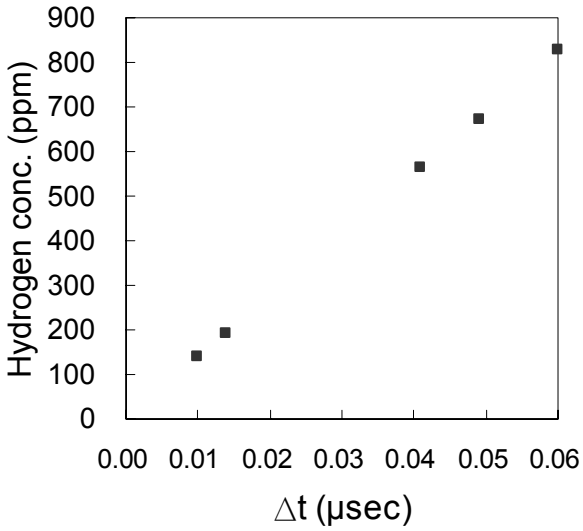


Fig. 3 Hydrogen concentration derived form eq. 2 with the measured $\Delta t$: the traveling time difference between the air and the hydrogen contained air.

distance between transmitting and receiving probes, this limitation can be lowered.

The time for detecting hydrogen can be also faster than conventional $H_2$ sensors. It takes only about 1 or 2 μsec to convert an electrical signal to a sound signal or vice versa in the transmitting and receiving probes. Additionally, it takes less than 150 μsec for sound to travel between the probes of which distance is less than 50mm, for example.

## 4. Summary

In this study we developed a hydrogen sensor using the large sound velocity difference between air and hydrogen. We have showed that it is possible to detect hydrogen concentration up to near 100 ppm with the order of μsec.

**Acknowledgment**

Author would like to thank M. Inoue, H. Baba and K. Ohira for their help in the experiment and discussion. This work was supported by CASIO Science Promotion Foundation, and Japan Science and Technology Agency (JST) digging seeds program.

**References**

1. C. Christofides and A. Mandelis, J. Appl. Phys. **68** (1990) R1-R30.
2. S. Patel, K. Wise, J. Gland, M. Zanini-Fisher and J. Schwank, Sensors and Actuators B **42** (1997) 205-215.
3.. T. Nakatsukasa, S. Akao, T. Ohgi, N. Nakaso, T. Abe and K. Yamanaka, Jpn. J. Appl. Phys. **45** (2006) 4500-4504.

2P2a-21

Proceedings of Symposium on Ultrasonic Electronics, Vol. 29 (2008) pp. 217-218
11-13 November, 2008

# More Precise Estimation of Capacitance Ratio in Electromechanical Coupling System

電気機械結合系における容量比の更に精密な評価

Michio Ohki (Natl. Def. Acad.)　　大木 道生（防大）

## 1. Introduction

The estimation of capacitance ratio $C/C_0$, defined in the equivalent circuit shown in **Fig. 1(a)** with $C = \Sigma_{l=1} C_l$, is important theoretically and practically for the following reasons: (i) The electromechanical coupling coefficient $k^2$ is related with $C/C_0$: In the quasi-static situation shown in **Fig.1(b)**, the ratio of elastically stored energy to electrically inputted energy, or the ratio of dielectrically stored energy to mechanically inputted energy, leads to $k^2_{(qs)} = C/C_0$ for longitudinal (L-) effect and $k^2_{(qs)} = (C/C_0)/(1+C/C_0)$ for transverse (T-) effect, where '(qs)' indicates 'quasi-static.' (ii) Although different values of $C/C_0$ are actually estimated on different modes (more than one mode), the estimates of $C/C_0$ should be identical theoretically regardless of the observed modes. This nature can be utilized for the reduction of errors in the lumped-parameters obtained from the observation of the admittance loops.[1] Therefore, it is desired to pursue more precise estimation formula for $C/C_0$.

When the $n$th mode is observed, as shown in **Fig. 1(c)**, $C_0'$ is observed instead of $C_0$, where

$$C_0' = C_0 \mp g_n C \qquad (1)$$

(upper sign for L-effect and lower sign for T-effect). Therefore, it is necessary to estimate $g_n$ (depending on the mode number $n$ even theoretically) more precisely. Conventionally, $g_n$ has been estimated only from capacitance components $C_l$ ($l > n$) higher than the $n$th mode. In this study, the correction of $g_n$ is investigated, which reduces the errors of the estimates. Since an inference process is needed to determine $g_n$, the influence of the misjudgment of the inference is also discussed.

## 2. Formulation for Correcting $g_n$

First, we define the following quantities on the $n$th mode: $\omega_n = \omega_A$ (electrical anitiresonance frequency) for L-effect, or $\omega_n = \omega_R$ (electrical resonance frequency) for T-effect; $\omega'_n = \omega_R$ for L-effect, or $\omega'_n = \omega_A$ for T-effect; $Y_n \propto (L_n)^{-1}$, resonance intensity of the $n$th mode, from which

$$\hat{Y}_n = \frac{8}{\pi^2}\frac{Y_n}{{\omega_n}^2}, \quad \hat{Y} = \sum_m^{\infty} \hat{Y}_m. \qquad (2)$$

In eq. (1), $g_n$ is derived from the circuit near the $n$th mechanical resonance shown in **Fig.2**. Conventionally, $L_{low}$ is neglected as $L_{low} \to \infty$, and $C_{high} = \Sigma_{l>n} C_l$, which leads to

$$g_{n(conv)} = \frac{C - \sum_{l \le n} C_l}{C} = \frac{\hat{Y} - \sum_{l \le n} \hat{Y}_l}{\hat{Y}}, \qquad (3)$$

where the subscript stands for 'conventional.' The value of $\hat{Y}$ is appropriately inferred from finite values of $\hat{Y}_m$ actually observed, using the nature which the combination of resonance frequencies and intensities ('resonance pattern' in the frequency domain) should follow.[2,3] We can calculate an estimate of capacitance ratio, denoted by $r_n$, on the $n$th mode, using the obtained data of $\omega_n$, $\omega'_n$, $Y_n$ and the inferred value of $\hat{Y}$.[1]

In this study, lower capacitance and inductance

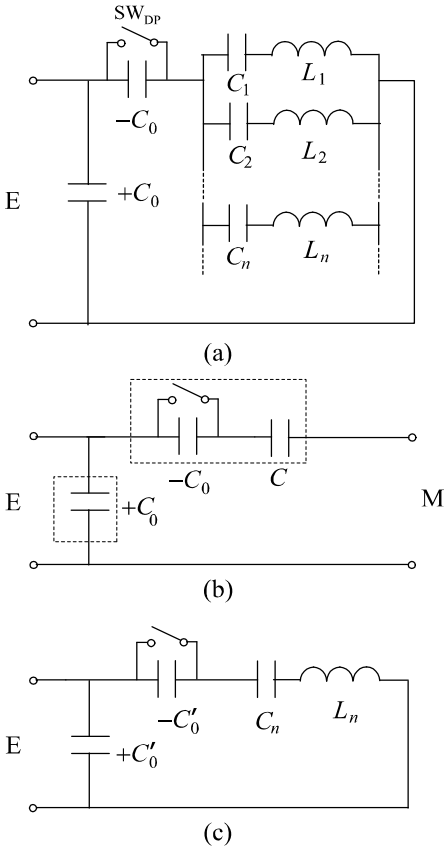


Fig. 1 (a) Lumped-parameter equivalent circuit. The switch $SW_{DP}$ is opened for L-effect and shorted for T-effect. (b) In the quasi-static situation (with mechanical terminal). (c) When the $n$th mode is observed.

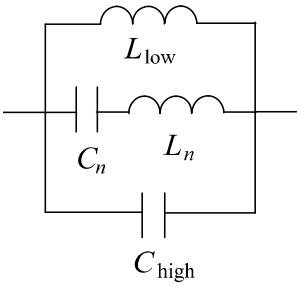


Fig. 2 Near the *n*th mechanical resonance.

components than the *n*th mode, which constitute $L_{\text{low}}$, and higher inductance components, which are included in $C_{\text{high}}$, are considered to correct $g_n$. Then, $g_n$ is corrected as

$$g_{n(\text{corr})} = g_{n(\text{conv})} + \Delta g_{n(\text{low})} + \Delta g_{n(\text{high})}; \quad (4)$$

$$\Delta g_{n(\text{low})} = \sum_{l=1}^{n-1} \frac{\frac{\hat{Y}_l}{\hat{Y}}}{1-\left(\frac{\omega_n}{\omega_l}\right)^2}, \ \Delta g_{n(\text{high})} = \sum_{l=n+1}^{n'} \frac{\left(\frac{\omega_n}{\omega_l}\right)^2 \frac{\hat{Y}_l}{\hat{Y}}}{1-\left(\frac{\omega_n}{\omega_l}\right)^2}.$$

$r_n$ is corrected by replacing $g_n = g_{n(\text{conv})}$ in the formula in ref. 1 with $g_n = g_{n(\text{corr})}$.

### 3. Numerical Examples

A sample of a "nonstandard" boundary condition, denoted by #1, is prepared, the admittance of which is calculated with Mason's equivalent circuit (with transmission lines), and the foregoing formula is applied to obtaining $r_n$, which is compared to the value of $C/C_0$ (independent of $n$) set on Mason's circuit. For lack of space, see ref. 4 for further details about boundary condition of #1.

On the modes of $n$ = 1 to 5(= $n_{\max}$) of this sample ($n$ = 4 is not driven), $g_n$ is corrected, as shown in **Table I**, where we set $n' = n_{\max} + 2$ in $\Delta g_{n(\text{high})}$ for practical reason. The errors between estimated $r_n$ (using $\omega_n$ and $\omega'_n$ of six significant digits) and true value of $C/C_0$ are evaluated before and after the correction of $g_n$, which are shown in **Fig. 3**. On the whole, the errors are reduced after the correction.

Next, the influence of misjudgment of $\hat{Y}$ on the errors of the estimate of capacitance ratio is evaluated. As shown in **Fig. 4**, as the error of $\hat{Y}$ is larger, the mean square error of $r_n$ over $n$ = 1 to $n_{\max}$ also becomes larger, but the variance of the error of $r_n$ over $n$ = 1 to $n_{\max}$ is almost unchanged and still small. This fact means that, when the present estimation method is applied to the correction of lumped parameters $L_n$ using the "principle of least variance" on $r_n$ discussed in ref. 1, this method is robust against the misjudgment of $\hat{Y}$, which is preferable for that purpose.

### References

1. M. Ohki: Jpn. J. Appl. Phys. **47**(2008) 4029.
2. M. Ohki: Jpn. J. Appl. Phys. **44**(2005) 4509.
3. M. Ohki: Jpn. J. Appl. Phys. **46**(2007) 4679.
4. M. Ohki: Cho-onpa Techno **18** (2006) No.5, 1.

Table I Correction of $g_n$.

| $n$ | $g_{n(\text{conv})}$ | $\Delta g_{n(\text{low})}$ | $\Delta g_{n(\text{high})}$ | $g_{n(\text{corr})}$ |
|---|---|---|---|---|
| 1 | 0.53473 | 0 | 0.13900 | 0.67372 |
| 2 | 0.20274 | –0.18221 | 0.04595 | 0.06648 |
| 3 | 0.13052 | –0.23214 | 0.02651 | –0.07512 |
| 5 | 0.10371 | –0.09367 | 0.05868 | 0.06872 |

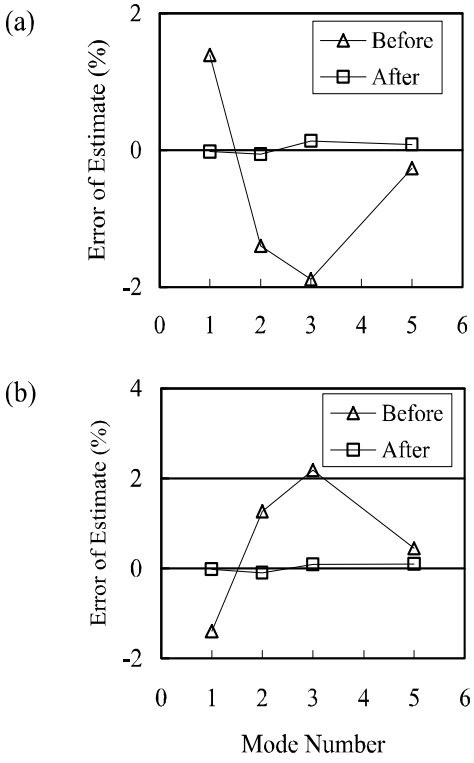


Fig. 3 Errors of the estimated capacitance ratio before and after the correction of $g_n$, in the cases of (a) L-effect and (b) T-effect for #1.

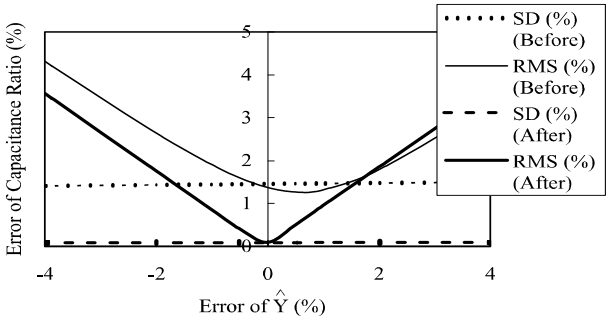


Fig. 4 Dependence of the root-mean-square error (RMS) and standard deviation of error (SD) of the estimated capacitance ratio on the error of inferred $\hat{Y}$, before and after the correction of $g_n$.

2P2a-22

Proceedings of Symposium on Ultrasonic Electronics, Vol. 29 (2008) pp. 219-220
11-13 November, 2008

# Improvement of Impulse Response of Loudspeaker Based on Equivalent Circuit Model

等価回路モデルに基づくラウドスピーカのインパルス応答の改善

Syunji Inoue‡, Naoto Wakatsuki, Koichi Mizutani (Univ. Tsukuba)
井上俊二‡，若槻尚斗，水谷孝一（筑波大院・シス情工）

## 1. Introduction

An impulse response of loudspeaker has a resonance characteristic in auditory area. While the existance of resonance contributes actively to efficient electro-acoustic conversion, the existance of resonance causes deterioration of sound quality especially when input signal is very short like a burst signal. This feature of the loudspeaker is a problem when the burst signal is used for acoustic measurement[1, 2].

In this paper, we propose the system for improvement of impulse response of the loudspeaker. The system consists of passive electrical elements, operational amplifier, and designed based on an equivalent circuit model of the loudspeaker[3, 4].

## 2. Equivalent circuit model of loudspeaker

**Figure 1** is an equivalent circuit of the loudspeaker. Synthetic impedance of the equivalent circuit area is given by

$$Z = R_E + \frac{1}{\dfrac{R_m + R_a}{Bl_E Bl_m} + j\omega \dfrac{M_m + M_a}{Bl_E Bl_m} + \dfrac{1}{j\omega Bl_E Bl_m S_m}} \qquad (1)$$

where $L_E$ is ignored and the acoustical system is included in the mechanical system because efficiency of the mechanical system is much bigger than efficiency of the acoustical system. However, Eq.(1) is enough to describe the impedance of the loudspeaker as for the resonance area. **Figure 2** is equivalent circuit in the resonance area which is simplified based on Eq.(1) and estimated parameters. **Figure 3** is experimental result and equivalent circuit in the resonance area. We estimate parameters of the equivalent circuit using electric impedance method.

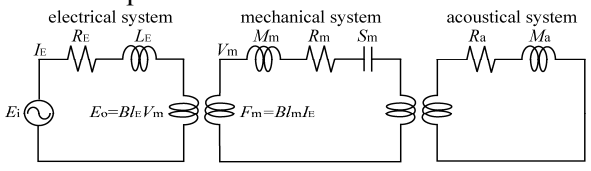


$E_i$ : input voltage
$E_o$ : output voltage
$I_E$ : electrical current
$R_E$, $L_E$ : electrical impedance
$Bl_E$,$Bl_m$ : force facter
$M_m$, $R_m$, $S_m$ : constant of vibration system
$M_a$, $R_a$ : radiation mass, radiation resistance
$V_m$ : vibration velocity of diaphragm
$F_m$ : force to voice coil

**Fig. 1** Equivalent circuit of loudspeaker.

inoue@aclab.esys.tsukuba.ac.jp

## 2. Transfer function

Equation (2) is transfer function of the equivalent circuit. Equations (3) are impulse response of the equivalent circuit. Equations (3) are calculated from Eq.(2) by Laplace transform. Equations.(3) are the impulse response of vibration velocity of diaphragm. Vibration velocity of diaphragm is not proportional to acoustic pressure. Acoustic pressure is proportional to vibration acceleration of diaphragm. So impulse response of vibration acceleration of diaphragm is given by Eq.(4).

$$G = \frac{V_m}{E_i} = \frac{1}{Bl_E} \cdot \frac{1}{R_E\left(\dfrac{R_m+R_a}{Bl_E Bl_m} + j\omega\dfrac{M_m+M_a}{Bl_E Bl_m} + \dfrac{1}{j\omega Bl_E Bl_m S_m}\right)+1} = \frac{1}{Bl_E} \cdot \frac{1}{R_E\left(R + j\omega M + \dfrac{1}{j\omega S}\right)+1} \qquad (2)$$

$$\alpha = \frac{R_E R + 1}{2R_E M},\ \beta = \sqrt{\frac{1}{MS} - \left(\frac{R_E R + 1}{2R_E M}\right)^2} \qquad (3)$$

$$g(t) = \frac{1}{Bl_E R_E M} e^{-\alpha t}\left(\cos\beta t - \frac{\alpha}{\beta}\sin\beta t\right)$$

$$\dot{g}(t) = \frac{1}{Bl_E R_E M} e^{-\alpha t}\left\{\left(\frac{\alpha^2}{\beta} - \beta\right)\sin\beta t - 2\cos\beta t\right\} \qquad (4)$$

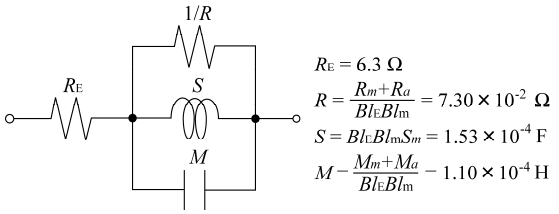


**Fig.2** Equivalent circuit in resonance area.

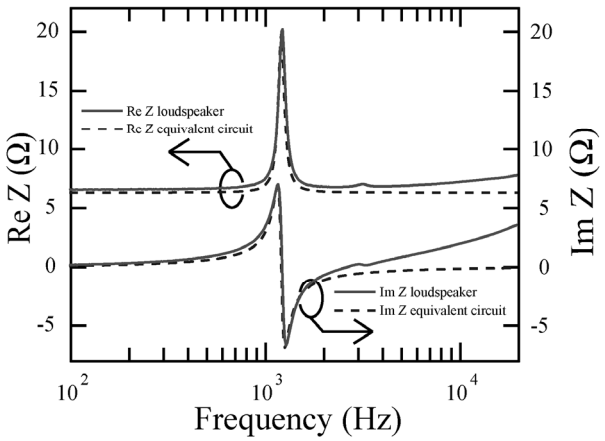


**Fig.3** Impedances of an actual loudspeaker and its equivalent circuit.

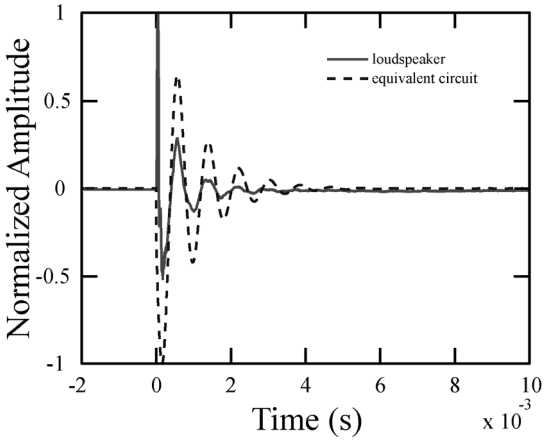


**Fig.4** Impulse response of loudspeaker and equivalent circuit.

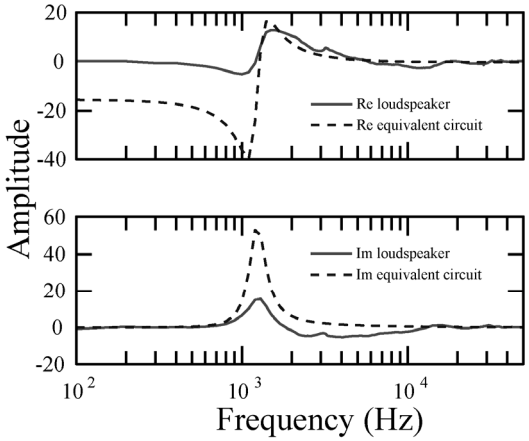


**Fig. 5** Frequency response of loudspeaker and equivalent circuit.

**Figure 4** is acoustic impulse responses of the loudspeaker and transfer function of the equivalent circuit. Using each of the maximum amplitude, Fig.4 is normalized. **Figure 5** is frequency response of Fig.4. Figure 5 shows that we can use the transfer function of the equivalent circuit as transfer function of the loudspeaker in the resonance area.

## 4. System for improvement of impulse response of loudspeaker

**Figure 6** is the system which we propose for improvement of the impulse response of the loudspeaker. The idea of the system is that we control $R_E$ in Eq.(2) using equivalent circuit which can make a same output as an actual loudspeaker. As a result $\beta$ becomes 0 and the impulse response does not resonate. Transfer function of the system is Eq.(5). Equations.(6) are impulse response of the system. Equation.(7) is impulse response of vibration acceleration of diaphragm. When $\beta$ is 0, $X$, $A$ and impulse response are Eqs.(8). **Figure 7** is simulation of the impulse response of the loudspeaker based on the system in the case $R_1$=1 Ω and $R_2$=50 Ω. Figure 7 is normalized using the maximum amplitude of Eq.(4).

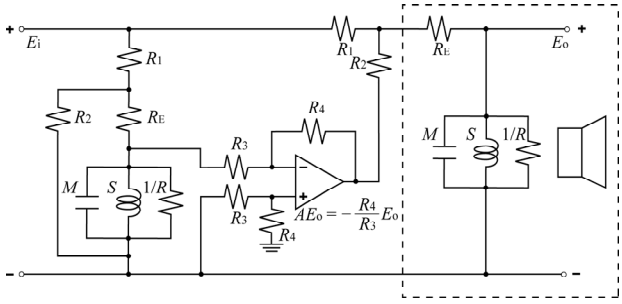


**Fig.6** System for improvement of impulse response of loudspeaker.

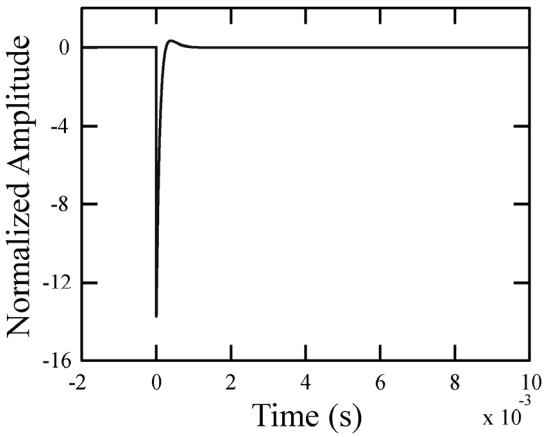


**Fig.7** Simulation of impulse response of loudspeaker based on the system.

$$G=\frac{V_m}{E_i}=\frac{R_2}{Bl_E(R_1+R_2-AR_1)}\cdot\frac{1}{\dfrac{R_E(R_1+R_2)+R_1R_2}{R_1+R_2-AR_1}\left(R+j\omega M+\dfrac{1}{j\omega S}\right)+1} \quad (5)$$

$$X=\frac{R_E(R_1+R_2)+R_1R_2}{R_1+R_2-AR_1},\ \alpha=\frac{XR+1}{2XM},\ \beta=\sqrt{\frac{1}{MS}-\left(\frac{XR+1}{2XM}\right)^2}$$

$$g(t)=\frac{R_2}{Bl_E(R_1+R_2-AR_1)}e^{-\alpha t}\left(\cos\beta t-\frac{\alpha}{\beta}\sin\beta t\right) \quad (6)$$

$$\dot{g}(t)=\frac{R_2}{Bl_E(R_1+R_2-AR_1)}e^{-\alpha t}\left\{\left(\frac{\alpha^2}{\beta}-\beta\right)\sin\beta t-2\cos\beta t\right\} \quad (7)$$

$$X=\left.\frac{\sqrt{MS}}{2M-R\sqrt{MS}}\right|_{\beta=0},\ A=\left.\frac{1}{R_1X}\{(X-R_E)(R_1+R_2)-R_1R_2\}\right|_{\beta=0}$$

$$\dot{g}(t)\to\frac{R_2}{Bl_E(R_1+R_2-AR_1)}e^{-\alpha t}\left(\alpha^2-2\right) \quad (8)$$

## 5. Conclusions

We propose the system for improvement of the resonance characteristic in the impulse response of the loudspeaker. The idea of the system is that we control $R_E$ in Eq.(2) using the equivalent circuit. Then, we establish that the system is useful for improvement of the impulse response of the loudspeaker.

## References

1. I. Odanaka *et al*.: Proc. OfICSV12, (2005) 361.
2. I. Saito *et al*.: Jpn. J. Appl. Phys. **47** (2008) 4329.
3. K. Satoh *et al*: Audio Eng. Soc. 107th Convention, Preprint (1999) 5023.
4. W. Klippel, U. Seidel: Audio Eng. Soc. 110th Convention, Preprint (2001) 5308.

2P2b-10

Proceedings of Symposium on Ultrasonic Electronics, Vol. 29 (2008) pp. 221-222
11-13 November, 2008

# Improvement of Reflection Point Search by Rectangular Sound Source through Introducing Array with Small Number of Element

矩形音源による反射点探索の少数要素アレイの導入による改善

Hiroyuki Masuyama[1‡] and Koichi Mizutani[2] ([1] Electron. Mech. Eng. Dep., Toba Nat. Col. of Mar. Tech.; [2] Grad. Sch. of Sys. Info. Eng., Univ. of Tsukuba)

増山裕之[1‡]，水谷孝一[2]（[1]鳥羽商船高専・電子機械工; [2]筑波大院・シス情工）

## 1. Introduction

In measurement and imaging using ultrasonic waves, a rectangular transducer is widely used as an element of array sound sources. By the effect of four vertices and four sides, the spatial impulse response of the rectangular transducer complicatedly changes in proportion to the position of the observation point of the sound wave[1)]. Therefore, the waveform, that is acquired by driving the sound source actually, also changes with the dependence on the position of the observation point.

Here, a method that searches the position of the reflection point is examined, by analyzing the change of the waveform of the reflected wave from a point reflector, which depends on the position of the reflection point. By introducing a rectangular transducer array with small number of element as a sound source, and forming multiple rectangular sound sources in which the configuration differs, it aims at the improvement on the search result from the method using single rectangular sound source[2)].

## 2. Theory for Searching Reflection Point

As shown in **Fig. 1**, a coordinate system including a rectangular transducer array sound source and a point reflector is considered. As a sound source, the rectangular transducer array with five elements is assigned in the cruciform to a plane that is perpendicular to the $z$-axis so that the center in the central element is the origin of the coordinates. The dimension of each element is $(b_2-a_1)\times 2a_2$ (element 1 and 3), $2a_1\times(b_1-a_2)$ (element 2 and 4), and $2a_1\times 2a_2$ (element 5), respectively. The position of the reflection point is indicated by $P(\boldsymbol{r})$, and, when calculation results are shown, $\boldsymbol{r}$ is expressed using the distance from the center of the sound source ($|\boldsymbol{r}|$), the azimuth angle (azim.), and the elevation angle (elev.).

When the sound source is driven with uniform velocity $v(t)$, the output $e(\boldsymbol{r}, t)$ received at the sound source as a result of the reflection at point $P(\boldsymbol{r})$ can be expressed by the following equation[3)]:

$$e(\boldsymbol{r},t)=-\frac{k\rho A}{2c}v(t)*\frac{\partial}{\partial t}h(\boldsymbol{r},t)*\frac{\partial}{\partial t}h(\boldsymbol{r},t), \qquad (1)$$

where $k$ is the proportionality constant, ρ is the density of the propagation medium of the sound wave, $A$ is the area of the region in which the reflection point contributes to the reflection, $h(\boldsymbol{r}, t)$ is the spatial impulse response of the sound source, and $*$ denotes the convolution integral.

e-mail address: masuyama@toba-cmt.ac.jp

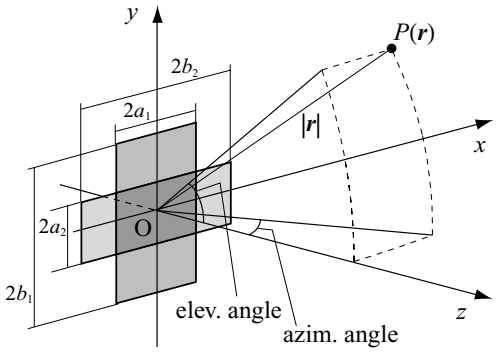


Fig. 1 Geometry of the coordinate system, rectangular array sound source and a reflection point $P$.

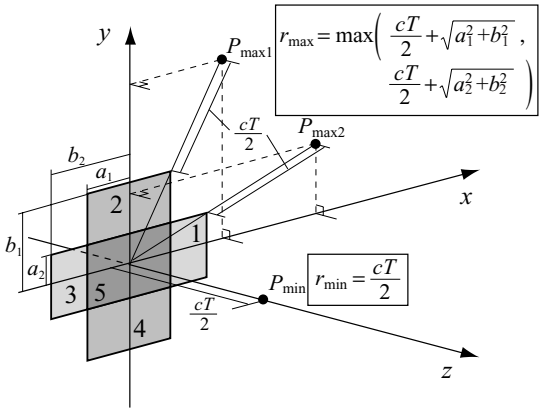


Fig. 2 Calculation range of the distance $|\boldsymbol{r}|$.

Since $v(t)$ is known, and since the rise time of the reflected wave is measurable, the value of $|\boldsymbol{r}|$ can be determined in a certain range. The region is shown in **Fig. 2**. When the rising time of the reflected wave is $T$ and the velocity of sound is $c$, the shortest distance between a certain part of the sound source and the reflection point $P(\boldsymbol{r})$ becomes $cT/2$. When $cT/2$ is adopted as the distance from the center of the sound source, $|\boldsymbol{r}|$, the minimum and maximum value of $|\boldsymbol{r}|$ are obtained when the reflection point $P(\boldsymbol{r})$ is located on $P_{\min}$ and, $P_{\max1}$ or $P_{\max2}$ in Fig. 2. When the value of $\boldsymbol{r}$ is set in an appropriate interval in this range, the spatial impulse re-

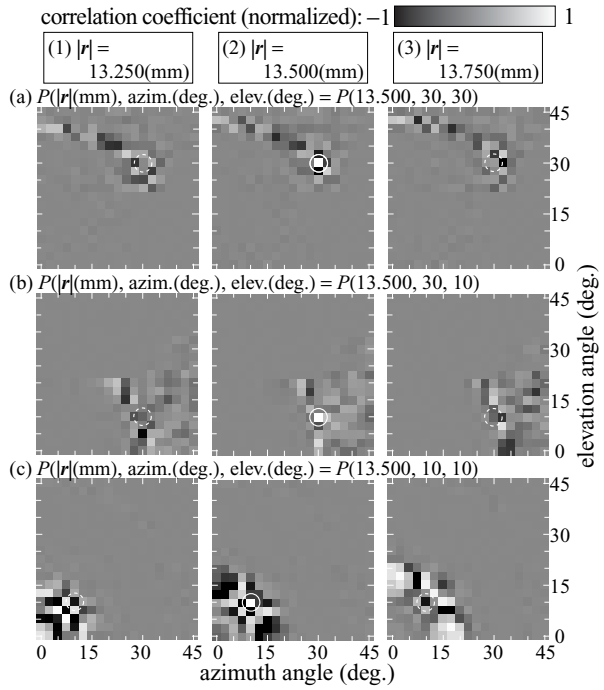


Fig. 3 Calculation results of cross-correlation coefficients: calculated using five-element rectangular array sound source.

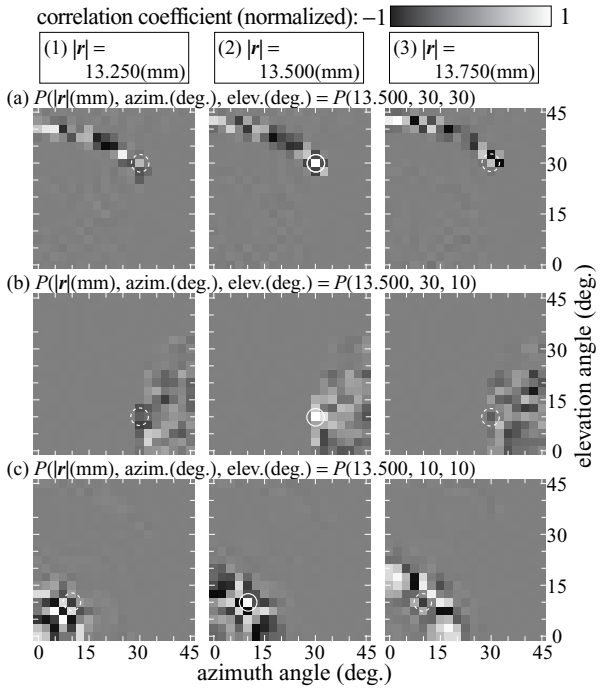


Fig. 4 Calculation results of cross-correlation coefficients: calculated using single rectangular sound source.

sponse $h(\boldsymbol{r}, t)$ corresponding to each $\boldsymbol{r}$ can be obtained, and the output waveform $e(\boldsymbol{r}, t)$ in eq. (1) at each $\boldsymbol{r}$ can be calculated. By deducing the cross-correlation coefficient between the waveform obtained by the calculation and the original (acquired) reflected wave in the sequential order, it becomes possible to estimate the position of reflection point $\boldsymbol{r}$.

## 3. Numerical Calculations

**Figure 3** illustrates the results confirming that the search by the above-mentioned technique is possible. Each result is obtained by calculating $v(t)*(\partial/\partial t)h(\boldsymbol{r}, t)*(\partial/\partial t)h(\boldsymbol{r}, t)$ in eq. (1), and calculating the cross-correlation coefficient at time zero with the calculation result for the points around located reflection points. The dimensions of the array element used for the calculation are $a_1$ = 6.45 mm, $a_2$ = 4.85 mm, $b_1$ = 10.05 mm, and $b_2$ = 9.95 mm, respectively. Using each of element 1, 3, and 5, and element 2, 4, and 5 in Fig. 2, two kinds of the rectangular sound source in which the configuration differs are formed. Then, the correlation coefficient is calculated in each sound source, and the average is taken. For the comparison, the calculation result using a single rectangular element of dimension $2a_1 \times 2b_1$[2)] is shown in **Fig. 4**.

In Fig. 3(a), the result with high correlation except at the reflection point (solid circular mark in each subfigure), obtained when the single element was used (shown in Fig. 4(a)), is not conspicuous, and seemed to improve the search result. The reflection point shown in Fig. 3(b) is what the search was achieved, when single element sound source was used. There is an aspect that the position of the reflection point is searched, when the array sound source is also used. In contrast, in Fig. 3(c), there are many areas of high correlation and inverse correlation except at the reflection point, and there is an aspect of which the search result is not improved.

## 4. Summary

In the reflection point search using rectangular sound sources, a rectangular transducer array with small number of element was introduced, and the improvement on the search result was attempted. Results of numerical calculations show that there is the position where the search result is improved. However, the position where the search result is not improved also exists. In order to attempt the improvement on the search results, it is necessary to conduct further examinations with respect to the conditions of the reflection point and sound sources.


## Acknowledgment

This work was supported in part by a Grant-in-Aid for Young Scientists (B) (No. 19760280) from MEXT, Japan.


## References


1. J. L. San Emeterio and L. G. Ullate: J. Acoust. Soc. Am. **92** (1992) 651.
2. H. Masuyama and K. Mizutani: Jpn. J. Appl. Phys. **46** (2007) 7793.
3. J. P. Weight and A. J. Hayman: J. Acoust. Soc. Am. **63** (1978) 396.

2P2b-11

Proceedings of Symposium on Ultrasonic Electronics, Vol. 29 (2008) pp. 223-224
11-13 November, 2008

# Visualization of Lamb-Type Waves in Glass Plates Using Pulsed Light Source

パルス光源を用いるガラス板内 Lamb－Type Wave の可視化

Kojiro Nishimiya‡, Koichi Mizutani, Naoto Wakatsuki, Takeshi Ohbuchi (Univ. Tsukuba) and Ken Yamamoto (Kansai Univ.)
西宮康治朗‡，水谷孝一，若槻尚斗，大淵武史（筑波大院・シス情工），山本　健（関西大）

## 1. Introduction

Visualizing sound waves is very important in order to understand the condition when the sound waves propagate in various mediums. In recent days, many visualizing methods have been investigated[1]. These results contribute to nondestructive test[2,3], medical fields as shown in the acoustic focusing lens , and so on.

In this study, the visualizing method using photoelasticity is used for observing the stress of elastic waves in the elastic body. Particularly, we considered Lamb-type waves in the elastic plates. The waves in layer structure are observed. Among them, the condition that the layer changes on the way is very interesting. In this condition, not only the Lamb-type waves but also the wave propagating along the boundary exists at the same time. In this study, we can observe these multiple elastic waves at the same time. This boundary wave is slower than the simultaneous Lamb-type waves because the energy of the wave is trapped around the boundary surface. These visualizing results can use for understanding of the behavior of the sound wave in the elastic body.

## 2. Visualization System and Experimental Conditions

**Figure 1** shows the visualization systems of the sound waves. In this system, the stress in the elastic plates is visualized using the birefringence effect arisen from ultrasound stress, through two orthogonal polarization plates. We show the photoelastic optical system and visualization image of the elastic wave in **Fig. 2**. Polarizer and Analyzer are orthogonalized and tilted at 45° to the propagation direction of the elastic wave as shown in Fig.2 (a). Herewith, absolute difference of stress $|T_{xx}\text{-}T_{zz}|$ are visualized. Additionally, by slightly deviating the angle between the polarizer and analyzer from the completely orthogonal condition, the stress difference $T_{xx}\text{-}T_{zz}$ is visualized. The visualized image is shown in Fig. 2 (b) and (c). At this time, the stop motion is obtained by using the pulsed light source synchronized to ultrasound incidence. The transient response is obtained by using the delay time between the light emission and the ultrasound incidence.

In this study, Lamb and Lamb-Type waves in glass plates are visualized. The waves in the plates are excited by the incident ultrasound in water at a particular angle to the plates. The waves in the plate have dispersiveness and various propagation modes[4,5,6]. The modes depend on the wavelength of the incident ultrasound, the incident

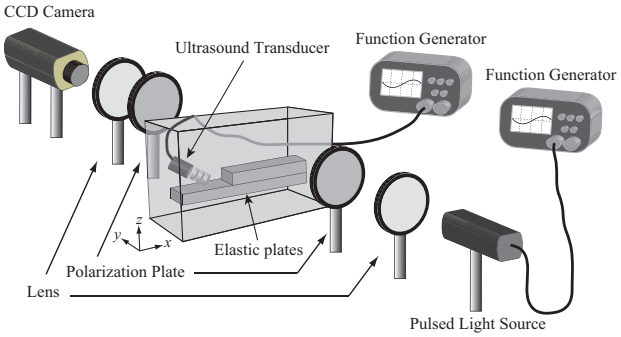


Fig. 1 Visualization systems of sound waves.

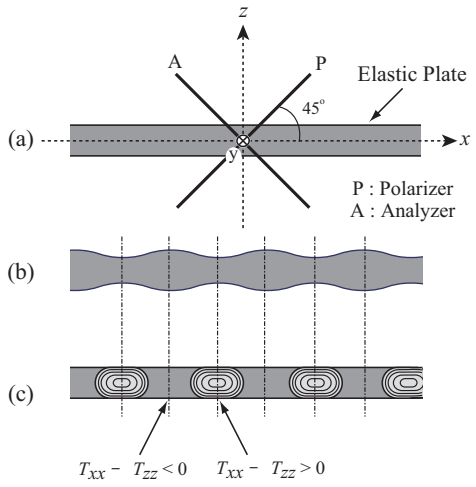


Fig. 2 Photoelastic optical system and visualized image of elastic wave.

nishimiya@aclab.esys.tsukuba.ac.jp

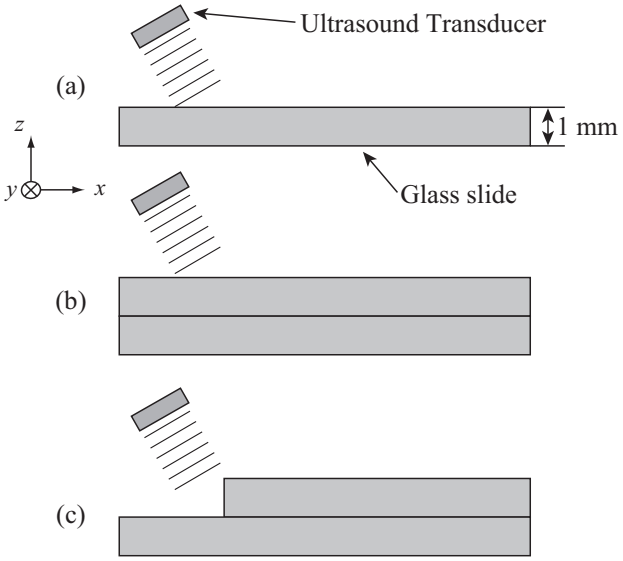


Fig. 3 Experimental setup of visualization.

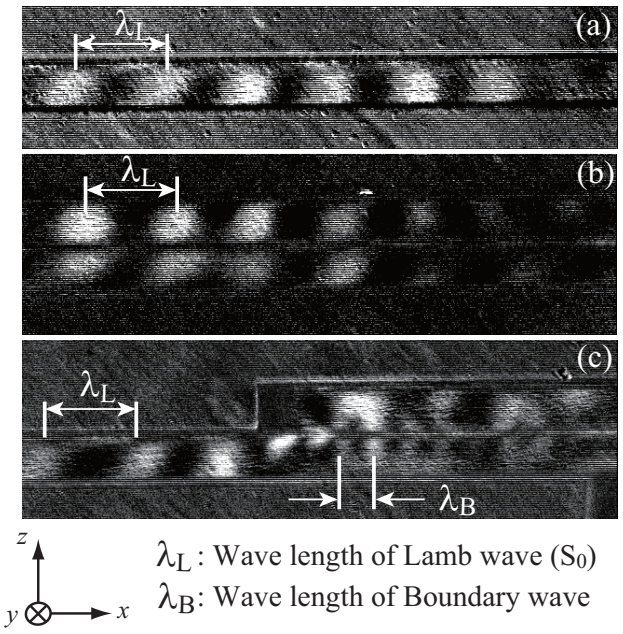


Fig. 4 Visualization results.

angle of the wave and the thickness of the elastic plates. We observed the condition that the Lamb waves in one plate and the layer structure. Particular, we considered the condition that the layer changes on the way. The incident wave frequency is fixed. Also, the glass slides are used as the elastic plates. The thickness of the glass slides are 1 mm. In this experiment, we use the piezoelectric resonator that the thickness is 2 mm, as a transducer. As shown in **Fig. 3**, oblique incidence waves are transformed into the Lamb and Lamb-type waves and propagate in the elastic plate. Lamb-type wave is a kind of plate-mode waves propagating in layered structure[7,8]. At this time, the excitation frequency is about 1.07 MHz. we examined three conditions (a), (b) and (c) in Fig. 3.

## 3. Visualization Results

Observed images of waves in the plates are shown in **Fig. 4**. Bright areas in the images correspond to the high stress areas. $S_0$ mode Lamb wave or symmetrical Lamb-type wave are observed in all cases. As well as these modes, another wave is also observed. We guess the wave is a kind of boundary waves. The wave is slower than the Lamb wave, because shear stress is interrupted by the boundary surface because the boundary surfaces can slip. Consequently, the wavelength of the boundary wave is shorter than that of the Lamb waves. In this way, it was verified that the multiple elastic waves exist in the elastic plate at the same time by using visualization.

## 4. Conclusions

We observed the multiple elastic waves in the elastic plates by using visualization system. In this study, we observed the Lamb and Lamb-type waves of several conditions. Among them, we verified that a kind of boundary waves is excited in the condition that the layer changes on the way. The wavelength of the boundary wave was shorter than that of the Lamb waves.

Visualization of the elastic wave is important to develop the skill in various fields. Particularly, in the nondestructive test, the complex elastic wave depending on the shape of the elastic body must be dealt. In these cases, visualization is available.

## References


**1**. Hyo Ung Li and Katsuo Negishi: Ultrasonics, **32**,(1994) 243

2. H. Sato, M. Lebedev, and J. Akedo: Jpn. J. Appl. Phys. **46** (2007) 4521.

3. Toshinobu Ito and Yasuo Kokubun: Jpn. J. Appl. Phys. **43** (2004) 1002

4. I. Tolstoy and E. Usdin: J. Acoust. Soc. Am. **29 (**1957**) 37**.

5. K. Nishimiya, K. Yamamoto, K. Mizutani, and N. Wakatsuki: Jpn. J. Appl. Phys. **46** (2007) 4483.

6. K.Nishimiya, Koichi Mizutani, Naoto Wakatsuki, and Ken Yamamoto: Jpn. J. Appl. Phys. **47** (2008) 3855.

7. K.Yamamoto: Proc. Symp. Ultrasonic Electronics, **26** (2005) 355 [in Japanese].

8 F. Coulouvrat and M. Rousseau: Acta Acust, **84** (1998) 12.

2P2b-12

Proceedings of Symposium on Ultrasonic Electronics, Vol. 29 (2008) pp. 225-226
11-13 November, 2008

# Reconstruction of 3D sound field from 2D sound field using acoustical holography

音響ホログラフィ法を用いる二次元音場からの三次元音場再構成

Takeshi Ohbuchi[1‡], Koichi Mizutani[1], Naoto Wakatsuki[1], Kojiro Nishimiya[1] and Hiroyuki Masuyama[2] ([1] Univ. Tsukuba; [2]Toba Natl. Coll. Mar. Tech.)

大淵武史 [1‡], 水谷孝一 [1], 若槻尚斗 [1], 西宮康治朗 [1],増山裕之 [2] ([1] 筑波大院シス情工; [2] 鳥羽商船高専)

## 1. Introduction

Ultrasonic waves are widely used for industrial instrumentation, medical diagnosis, and so on. Thereunder, it is important to measure three-dimensional sound fields. Currently, a major instrument for measuring the sound field is a microphone with mechanical scannings. However, the instrument disturbs the sound field and requires time for measurement. So, an optical probe draws attention. Noncontact measurement of the sound field is possible with the opticalprobe [1)].

In this paper, we propose a method for a reconstruction of a radiated three-dimensional sound field. An acoustic hologram is first obtained using optical computerized tomography (O-CT) [1)]. Two-dimensional sound fields are then calculated using near-field acoustical holography [2, 3)] (NAH) from the hologram. Fimally, images of sound field are bound together, and the three-dimensional sound field is reconstructed.

## 2. Principle of measurement

### *2-1. Reconstruction of sound fields using O-CT*

We consider a coordinate system as shown in **Fig.1.** An ultrasonic wave is radiated in the direction of *z*-axis, and a laser is passing through the ultrasonic wave in the direction of *y*-axis. The center of a transducer is located on origin. The laser is influenced on a phase by the ultrasonic wave [2)]. The phase change is quadrature detected using an interferometer with linear scannings so that a single projection is obtained. Then, projections in all the directions are obtained by rotation scannings, and the sound field is reconstructed using CT [1)].

### *2-2. Calculation of sound fields using NAH*

A sound field in a reconstructed plane $z = z$ is expressed as $p_{CT}(x, y, z)$. A sound field in another plane $z = z'$, $p_{AH}(x, y, z')$, is calculated from the experimental data in $z=z$. The relationship between the sound fields in reconstructed and calculated planes is given by

$$p_{AH}(x, y, z') = p_{CT}(x, y, z) * h(x, y, z' - z), \quad (1)$$

ohbuchi@aclab.esys.tsukuba.ac.jp

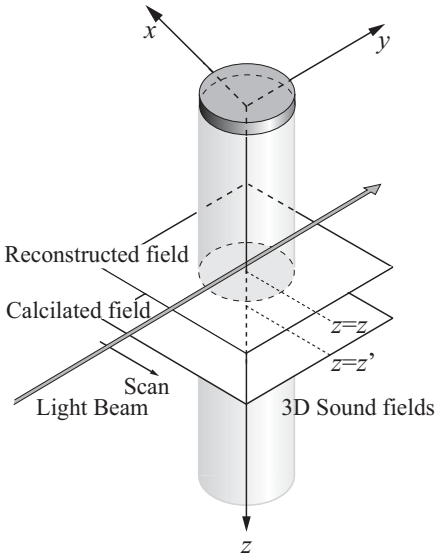


Fig. 1 Schematic of sound velocity measurement using Optical-CT and coordinate system.

where $*$ and $h$ denote convolution integral and a propagation function. Here, the propagation function in wavenumber domain $H$ is expressed as

$$H(k_x, k_y, z'-z) = \exp\{ik_z(z'-z)\}, \quad (2)$$

$$k_z^2 = k^2 - k_x^2 - k_y^2, \quad (3)$$

where $k$ is a wavenumber [3)].

Thus, two-dimensional images are calculated with presumption of the wavenumber[4)], and the three-dimensional sound field is reconstructed.

### *2-3. Determination of the wavenumber*

To calculate the sound field using NAH, the wavenumber is determined. Two sound fields in $z = z$ and $z = z'$ are reconstructed using CT, and a sound field in $z=z'$ is calculated from the sound field in $z=z$ using NAH with a presumption of wavenumber $k_{AH}$. Then, a phase difference $\Phi_d$ is gained between the reconstructed and calculated sound fields, $p_{CT}(x, y, z')$ and $p_{AH}(x, y, z')$ in wavenumber domain. The relationship between the phase difference and the wavenumber is given by

$$k = \sqrt{\left|\frac{\Phi_d}{(z'-z)} - k_{zAH}\right|^2 + k_x^2 + k_y^2}, \quad (4)$$

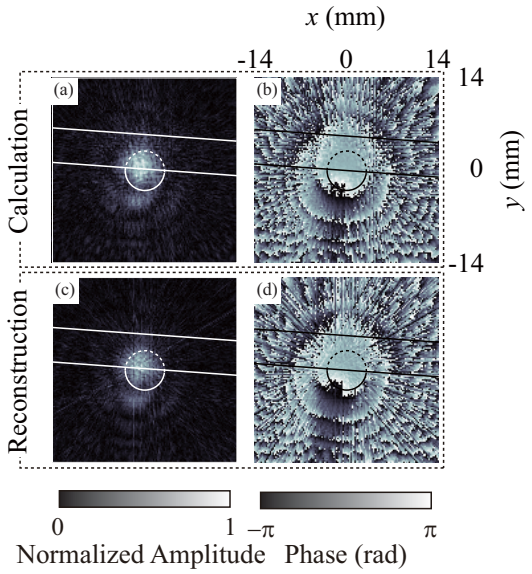


Fig. 2 Experimental results of reconstructed and calculated sound fields. (a) and (b) the calculated sound fields; (c) and (d) the reconstructed sound fields. (a) and (c) the amplitude of sound fields; (b) and (d) the phase.

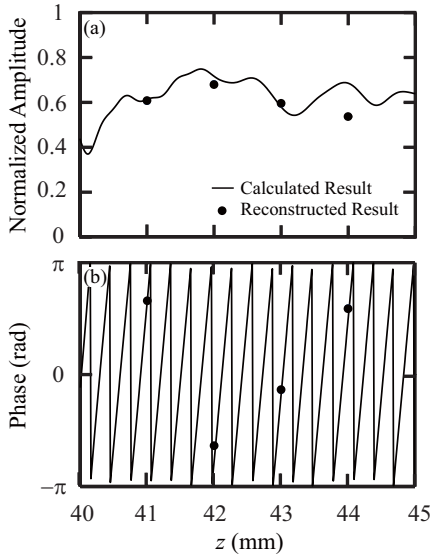


Fig. 3 Reconstructed and calculated sound field on *z*-axis.

$$k_{zAH}{}^2 = k_{AH}^2 - k_x^2 - k_y^2 . \quad (5)$$

Then, the actual wavenumber is obtained [4], and the three-dimensional sound field can be reconstructed.

## 3. Experimental Results

A diameter of a transducer radiating an ultrasonic wave into water is 6.0 mm, and a frequency of the ultrasonic wave is 5.0 MHz. In water, an obstacle exists. The obstacle is a metal bar whose diameter is 5 mm, and located at $z$=20 mm. Two-dimensional sound fields in the range from $z$=40 mm to $z$=44 mm with 1.0 mm step are measured by an optical probe whose light source is a He-Ne laser. The transducer is set to mechanical $x$– and $\theta$–stages and is scanned relatively to the laser beam. A linear scanning range in $x$ direction is $-20 \le x \le 20$ (mm) with 0.2 mm steps, and a range of rotation is $0 \le \theta < \pi$ (rad) with $\pi$ /18 rad rotation step angles; 18 projection data are acquired. The sound field is obtained using CT from these projections. A sound velocity is determined as 1508 m/s by eq. (4) from sound fields in $z$=40 mm and $z$=41 mm. The three-dimensional sound field is obtained in the range from $z$=40 mm to $z$=45 mm, that is 501 images of sound fields reconstructed using NAH from the reconstructed sound field in $z$=40 mm using CT.

**Figure 2** shows an experimental result of sound fields in $z$=44 mm. Circles and parallel lines show the transducer and the metal bar, respectively. Figs. 2(a) and 2(b) show the sound fields calculated using NAH, and Figs. 2(c) and 2(d) show those reconstructed using CT. Figs. 2(a) and 2(c) show normalized amplitudes of the sound field, and Figs. 2 (b) and 2(d) show the phases. Images of the calculated sound field are similar to those of the reconstructed sound field, and influences by the obstacle are expressed in Fig. 2.

**Figure 3** shows an experimental result of the sound field on $z$-axis. Fig. 3(a) and 3(b) show the normalized amplitude and the phase, respectively. The solid line denotes the results using NAH, and dotted line denotes the results using CT. The calculated result is good agreement with the reconstructed result.

## 4. Conclusions

The three-dimensional sound field was reconstructed using O-CT and NAH. The sound field was radiated into water from the circular transducer with the diameter of 6.0 mm and driven at 5.0 MHz, and the obstacle existed on the sound axis. To determine the wavenumber, two-dimensional sound fields at $z$=40 mm and $z$=41 mm were reconstructed using O-CT in the region of 28 × 28 mm$^2$. The determined sound velocity was 1508 m/s. Using NAH with the determined sound velocity, the three-dimensional sound field in the region of 28 × 28 × 5 mm$^3$ was reconstructed using NAH from the two-dimensional sound field in $z$=40 mm. The reconstructed three-dimensional sound field using NAH was good agreement with the reconstructed sound field using CT. The visualization technique presented in this paper is expected to be applicable to an evaluation of transducers, and so forth.


## Acknowledgment

This work was supported by Grant-in-Aid for JSPS Fellows (20.581).


## References


1. T. Ohbuchi *et al*., Jpn. J. Appl. Phys., **45** (2006) 7152.
2. E. G. Williams *et al*., Phys. Rev. Lett., **45** (1980) 554.
3. T. Ohbuchi *et al*., Jpn. J. Appl. Phys., **46** (2007) 4629.
4. T. Ohbuchi *et al*., Jpn. J. Appl. Phys., **47** (2008) 3959.

2P2b-13

Proceedings of Symposium on Ultrasonic Electronics, Vol. 29 (2008) pp. 227-228
11-13 November, 2008

# Study on the extreme shallow underground imaging using SLDV
# SLDV を用いた極浅層地中映像化に関する研究

Touma Abe† and Tsuneyoshi Sugimoto (Faculty of Eng., Toin Univ. of Yokohama)
阿部冬真‡　杉本恒美（桐蔭横浜大 工）

## 1. Introduction

Up to now, Ground Penetrating Radar (GPR) and metal detector are used for the land mine detection. Because a recent land mine hardly includes the metal, these detection methods are not so effective. Besides, these methods can not work in the marshy area and the soil containing the electrolyte, like as the soil in the Kingdom of Cambodia. To enable the exploration under such a condition, the exploration method that uses sound wave has been examined [(1)].

This research has a purpose of extremely shallow underground exploration that including the land mine detection. The vibration velocity distribution of ground surface is measured by Scanning laser Doppler vibrometer (Hereafter, it is simplified with SLDV) [(2)]. This time, the comparison of elastic wave generated by super-magnetostriction vibrator and airborne wave generated by flat speaker are examined. Moreover, outdoor exploration of buried object using flat speaker is examined.

## 2. Exploration method using SLDV

Vibration velocity at the ground surface that energized by sound source is measured by the SLDV (Polytec PSV400-H8). To measure the vibration velocity using the SLDV, distance between the SLDV head unit and ground surface needs more than 0.4m. The measurable range is within ±20 degrees.

Fundamental concept of the exploration method using the SLDV is shown in **Fig.1**. The difference of the vibration velocity will be expected, if a buried object near the ground surface exists.

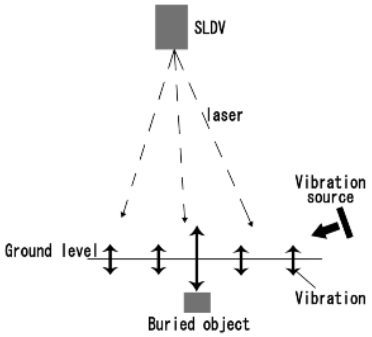


Fig.1 Fundamental concept of exploration method using SLDV

## 3. Comparison of super-magnetostriction vibrator with flat speaker

The vibration velocity distribution of the sand surface is measured in the laboratory. The experimental setup is shown in **Fig.2** Sand tank size is 80cm ×60cm× 50cm,and average sand particle is about 300 $\mu$ m in diameter. super-magnetostriction vibrator (Moritex Corp, AA140Jo13-MS1) and flat speaker (FPS2030M3P1R) were used for the vibration source respectively. Nothing has been buried in sand. Output waveform is burst 10cycle of sine and frequency is 300Hz. **Figure 3** shows the vibration velocity change in each frequency. Form this figure, vibration velocity changes are seen other than the driving frequency (300Hz) when a super-magnetostriction vibrator is used as a sound source. In addition, the velocity amplitude of the airborne wave is smaller than the elastic wave that generated by a vibrator which contact to the sand surface.

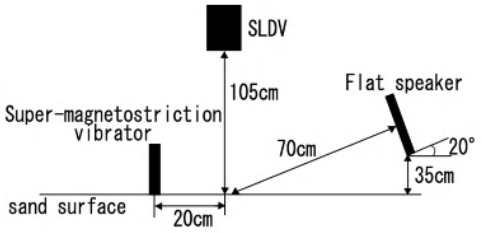


Fig.2 Experimental set up in the laboratory

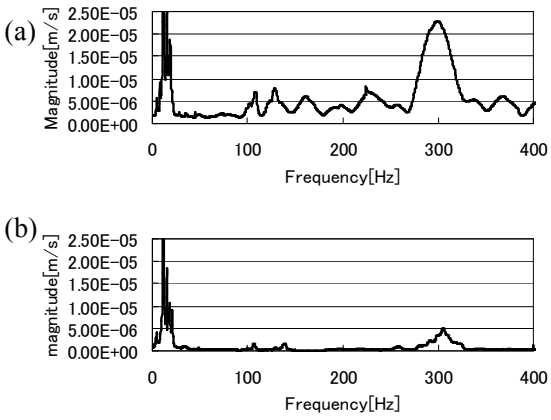


Fig.3 Vibration speed vs. frequency at surface of sand
(a) Used super-magnetostriction vibrator
(b) Used flat speaker

## 4. Experimental exploration buried object for outdoor

Outdoor experiments are carried out at the fallow field in Ibaraki prefecture. To make good coupling with the soil, a plastic container (dia. 10cm, height 9cm) was buried approximately one year ago. Container is filled with sugar, because the specific gravity is comparatively near the TNT gunpowder used for the

kaosunetto@gmail.com

land mine (specific gravity: sugar is 1.59 g/cm$^3$, TNT gunpowder is 1.65 g/cm$^3$).

### 4.1 Experimental set up for outdoor

The numbers of scan points are 143, and the distance between each point is 5cm. The buried object is located at the center of these points. **Figure 4** shows the setup. Flat speaker is tilted at 20° for better generation of the slow wave [(3)]. For the cancellation of the horizontal vibration and the emphasis of the vertical vibration, two flat speakers are facing each other as shown in Fig.4. Output waveform used noise wave and sine-wave burst (150Hz). The noise wave is output for one second. The burst wave number is 50.

### 4.2 Verification of buried object response

**Figure 5** shows the image of the vibration of the ground surface created by each output waveform. They are images by noise wave (156Hz) and burst wave (150Hz of output frequency). A large vibration velocity change is seen at the center of the scan area. Next, to the confirm the difference of the vibration velocity distribution, average vibration velocity of four points on the buried object and around the buried object are compared. **Figure 6** and **Fig.7**shows the average results of using noise wave, and using burst waves, respectively. In the case of the noise waves, some peaks exist around the 150Hz on the buried object. On the other hand, in the case of the burst waves, a strong peak exists at the driving frequency on the buried object.

### 5. Conclusion

For non-contact land mine detection using sound wave, the airborne waves was compared with the elastic waves. From the experimental results, we confirmed that ground surface did not vibrate other than the driving frequency in the case of the airborne waves.
Therefore, considering about the actual exploration, it seems that the following methods are best way. First, using the noise waves, vibration velocity distributions at various frequencies are examined. Next, exploration is made by the burst waves with the frequency that a large change of the vibration velocity is observed.
The buried object respons was able to be imaged by using both noise waves and burst waves. In this time, two flat speakers were facing each other, we will examine a more effective setup in the future. From experimental results, the velocity amplitude became small when the noise waves were used, therefore, we will examine whether we cannot make more big vibration velocity in the future.

## Reference


1. Watanabe and Iyama , MASJ, pp.1215-1216,2007
2. J.M.Sabatier, et al, IEEE Trans. Geosci. & Rem. Sens. 39, pp.1146-1154, (2001)
3. T.Tsurumi and M.Kimura, MASJ,2-9-15, PP.1145-1146, (2003.9)


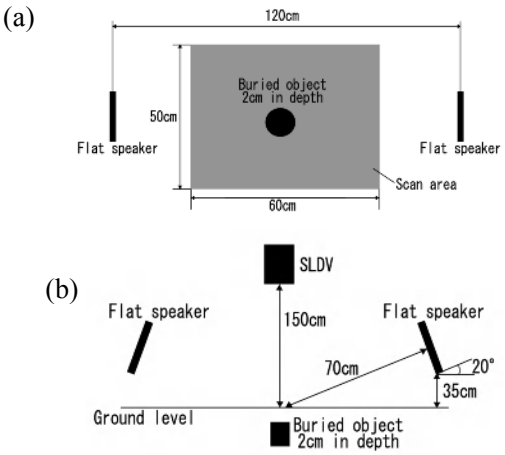


Fig.4 Experimental set up for outdoor experiment
(a) Upper view (b) Side view

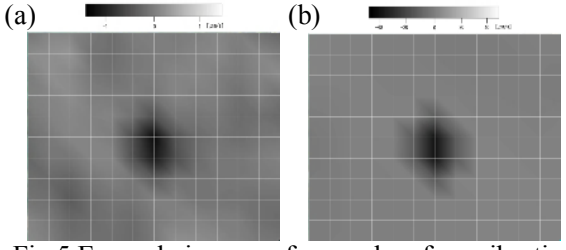


Fig.5 Example images of ground surface vibration
(a) Noise wave (156Hz) (b) Burst wave (150Hz)

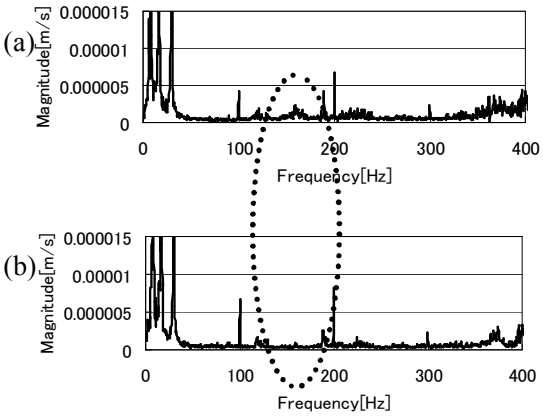


Fig.6 Vibration velocity vs. frequency
at ground surface used noise wave
(a) On buried object (b) Out of buried point

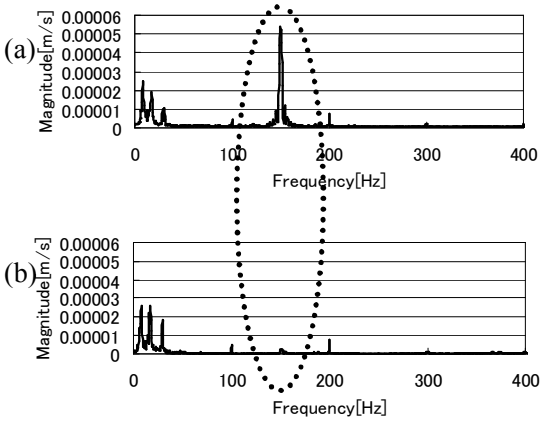


Fig.7 Vibration velocity vs. frequency
at ground surface used noise wave
(a) On buried object (b) Out of buried point

2P2b-14

Proceedings of Symposium on Ultrasonic Electronics, Vol. 29 (2008) pp. 229-230
11-13 November, 2008

# Study on the ultrasonic imaging at the extreme shallow underground in submerged soil

冠水土壌中での極浅層超音波イメージングに関する研究

Kunihiko Seo, Takashi Shirakawa and Tsuneyoshi Sugimoto (Facult.. Eng., Toin Univ. of Yokohama)

瀬尾邦彦‡, 白川貴志, 杉本恒美（桐蔭横浜大・工）

## 1. Introduction

Now a lot of land mines remain buried in the world, so that the clearance of them is required. As a tool of removing those land mines, metallic detectors or Ground Penetrating Radar (GPR) are often used. However, they are not effective in Southeast Asia in the rainy season when most of the land is flooded and change into marshes, because electromagnetic waves are not transmitted well in water. Therefore, using sound waves will be profitable to detect the land mines in the flooded soil. So we have tried to detect buried object at extreme shallow underground in submerged soil by ultrasound. Considering the land mine search, a target area is extreme shallow such as around several cm in the depth. In previous presentation, we tried underground imaging of submerged soil in our lab. using ultrasonic transducers driven at 50 kHz[1]. As a result, higher frequency is thought to be effective to detect the shape of buried object. Then in this research we employ ultrasonic transducers driven at 120 kHz for improvement of axial resolution of images.

## 2. Exploration and imaging method

Our target area is extreme shallow in underground exploration. So we employ two transducers (For transmitter and for receiver) to separate received signals from a input signal. However, the receiver receives the direct wave which has huge amplitude. For cutting the direct wave, We employ an acoustic shielding board. **Fig.1** shows the appearance of the transducers and the shielding board. In this research, transmitter and receiver are fixed as one device.

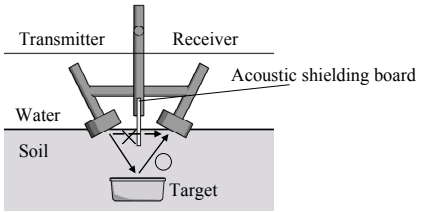


Fig. 1 Appearance of the transducers and the acoustic shielding board

Underground images are made by B-mode imaging method using reflected waves from a buried target. Transducers (Transmitter and receiver) are placed on the ground. Then the transmitter emits ultrasound waves toward downward. And these waves are reflected at the buried object. The relation between the time in received waves and the depth of reflection point is shown by the following equation.

$$Z = \sqrt{\left(\frac{vt}{2}\right)^2 - \left(\frac{d}{2}\right)^2} \qquad (1)$$

Here, $Z$ is the depth from the ground and $d$ is the distance of two transducers and $v$ is the sound velocity. From previous research, the velocity is assumed to be 1500 m/s[1]. We scan transducers on the ground in 2 dimensions at specific distance by hand. At each recorded point, the equation above is applied and 3 dimensional image are calculated.

## 3. Experimental imaging in the lab.

We make underground imaging of submerged sand in the water tank at the lab. The diameter of sand particles are 200-300 micrometers. The depth of water from ground is around 6 cm. To record a data, a set of the transmitter and the receiver is placed on the ground. Then waves are transmitted and recorded. Exploration area and measurement location are shown in **Fig.2**. Target object (10 cm × 15cm × 4 cm, hollow plastic container) is buried around the depth of 10 cm from ground level. We scanned transducers at the interval of 4 cm by hand. And received signals are recorded at each measurement location. Transmission signals are 7 cycles burst waves at 120 kHz.

Calculated image is shown in **Fig.3**. Same numerical value points are connected as a flat surface. Strong waves which have higher amplitude are observed when the transducers are placed on the buried target. As a result, rough buried point dicated graphically in 3D image shown in Fig.3.

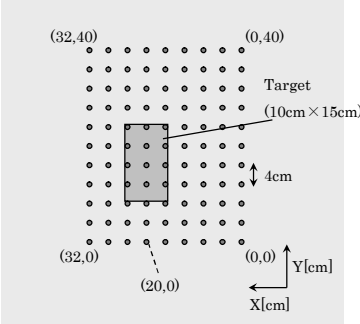


Fig. 2 Exploration area and measurement location

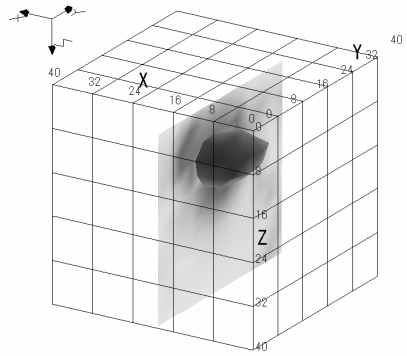


Fig. 3 Calculated 3D image of underground

We change the material and the buried depth of target. Then a similar experimental exploration is carried out. Calculated 3D images are shown in **Fig.4** (a). Fig.4 (b) shows a cross section in underground. Three buried objects are detected. In this experiment, weaker signal is observed from deeper buried object and weakest signal is observed from buried object of resin material. As a result, material of buried target is thought to be effect exploration.

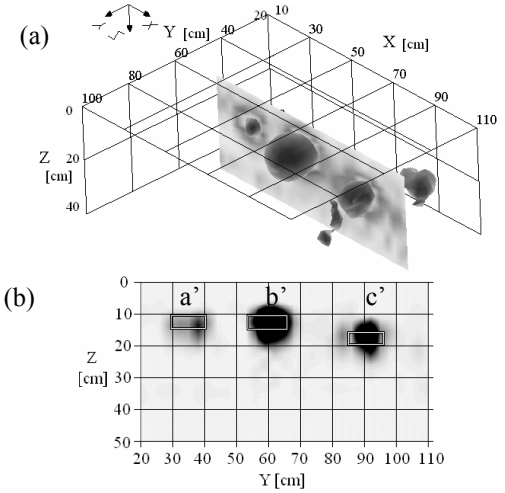


Fig. 4 (a) 3D image of underground. (b) Cross section
materials and buried depth Z[m] are
a' : resin model, 10 cm. b' : hollow container, 10 cm.
c' : hollow container, 15 cm

## 4. Experimental imaging at paddy field

A similar experimental imaging is carried out at the paddy field. We scan the transducers to one line at intervals of 5cm. The total distance of the scan line is 6 m. Hollow plastic container, container filled by water and resin model are buried for target object. The location and the depth of buried targets are shown in **Fig.5**. Exploration result is shown in **Fig.6**. Although hollow plastic container buried at 15.3 cm (a) is imaged clearly, other targets are blurring. This is thought to be caused by the characteristic of the paddy field. The soil in paddy field is not uniform. So ultrasound wave proceeding in the soil is thought to be attenuated or reflected diffusely. As a result, thought image is very unstable, one target object is detected.

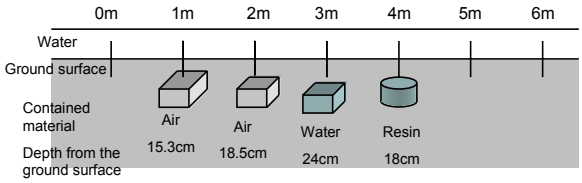


Fig. 5 Buried location of exploration targets

## 5. Discussion

As a result of the experimental imaging in the lab, buried hollow containers are detected clearly. Although the signal from resin model is weaker compared with from hollow container, the signal is possible to distinguish from the non-buried state. Because the soil is ideal condition, ultrasound waves are well transmitted and weak signal could detect. By contrast, in the outdoor experiment at the paddy field, signals from targets are unstable and the distinction is impossible. Because real soil in outdoor is nonuniform, ultrasound waves are thought to be attenuated or reflected diffusely. So countermeasures against high attenuation are necessary. Compensation of amplitude in reflected wave by digital signal processing or amplification of received signal by an amplifier are thought to be effective for high attenuation. In consideration of above, to enable the exploration in the submerged soil in outdoor is future task.

## 6. Conclusions

As a result of experimental imaging in the lab, we succeed to detect the target buried in the extreme shallow area for underground exploration. Our exoloration method using acoustic shielding board enables another mehod for exploration in special situation. However, experimental imaging in outdoor is unstable. For exploration in outdoor, countermeasures to compensate for the attenuated amplitude are necessary.

## References

1. K.Seo, T.Shirakawa and T. sugimoto: Proc. Symp. Ultrason. Electron., 28 (2008), pp.225-226

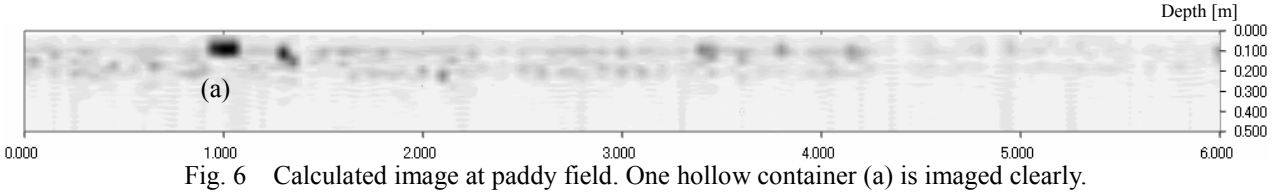


Fig. 6 Calculated image at paddy field. One hollow container (a) is imaged clearly.

2P2b-15

Proceedings of Symposium on Ultrasonic Electronics, Vol. 29 (2008) pp. 231-232
11-13 November, 2008

# Resolution improvement of underground image using pulse compression

パルス圧縮を用いた地中映像分解能の改善

Hiraku, Kawasaki†, Tsuneyoshi Sugimoto (Dept. Elect. Info., Toin Yokohama Univ.)
川﨑拓‡, 杉本恒美 （桐蔭横浜大・工）

## 1. INTRODUCTION

In order to detect the buried relics through underground imaging, a method by using shear waves [1, 2] has been proposed.
In our past research, a hammer method, in which a sound source is hit directly by a hammer, was used for making underground images. Although this method is easy to use, improving the underground image's resolution is difficult because the frequency and the waveform cannot be changed arbitrarily. Therefore, we employ a super-magnetostriction vibrator as a sound source instead of a hammer. And we consider the pulse compression [4]. The axial resolution of underground images when used chirp wave (300 to 800Hz, duration is 100ms) was about 20cm in our simulation results [5].
This time, we confirm the axial resolution in the actual underground, carry out where the buried position has already known.

## 2. EXPERIMENTAL SET-UP

We used the super-magnetostriction vibrator (Moritex Corp, AA140J013-MS1). To generate the shear waves, this vibrator was set on the sound source of aluminum that is attached of spike as is shown in **Fig.1**. Besides, we used the geophones for the shear waves which are the speed sensors as the receivers. The generated sound waves are recorded simultaneously in a seismically operation equipment (Oyo Corp, McSEIS-SX, MODEL-1125R).
The experimental setup is as shown in **Fig.2**. Twelve receivers (geophones) are arranged in a line at 0.5m intervals on the ground. The sound sources are set between all the receivers. The output wave is a down chirp wave that oscillates from 800 to 300Hz (duration 100ms). The position of the buried object is the center (2.75m in width, 0.5m in depth) of the exploration line. The buried object is hollow plastic containers (width 13cm, height 12cm, depth 5cm). We experiment three months after the object buried.

hot.hu2.feel.good@gmail.com
tsugimot@cc.toin.ac.jp

Fig.1 Super-magnetostriction vibrator

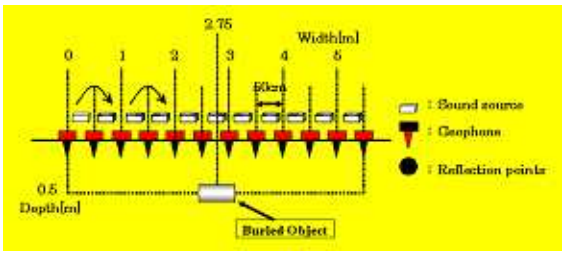


Fig.2 Experimental set-up

## 2. SIGNAL PROCESSING

The damping factor of the start frequency and stop frequency in the chirp are different. Then the chirp signal's spectrum of the high frequency is amplified when the filter is processed. The Fourier transform results that are sample of received wave and driving waveform are shown in **Fig.3**.
The amplitude of the received wave is less than that of driving waveform in the frequency width of 600-800Hz. Therefore, we computed the inverse Fourier transform after amplifying the amplitude of 600-800Hz. Then, the correlation processing is done. The filtered processing as is shown in **eq.1**.
Here, ***fft*** is Fourier transform, ***ifft*** is inverse Fourier transform, **abs** is absolute value.

$$\textit{Filtered wave} = \mathbf{ifft}\left\{ \mathbf{\textit{fft}}(\textit{Received wave}) \times \mathbf{abs}\left(\mathbf{\textit{fft}}(\textit{Received wave})\right) / \mathbf{abs}\left(\mathbf{\textit{fft}}(\textit{Driving waveform})\right) \right\} \quad \cdots \text{(eq.1)}$$

The driving waveforms, the sample of received wave, filtered wave and waveform of correlation result in the time domain are shown in **Fig.4**. Filtered wave is looked like the driving waveform. Then correlation result is compressed the pulse width.

## 3. THE UNDERGROUND IMAGE

We produced two underground images; one by applied pulse compression and another by hammer method. Those images are shown in **Fig.5**. **(a)** is hammer method, **(b)** is underground image by Pulse compression. A boundary rectangle is the buried position (2.75m in width, 0.5m in depth). STC (Sensitivity Time Control) is the value of correction for attenuation. STCT (STC Time) is the time to apply STC. The reason of the sound speed of (a) and (b) is different is the experimental day is different.

In the image the wave appeared the position that the object had been buried. It seems that the resolution seen from the image by the pulse compression is much higher than that of by the hammer method. Axial resolution is about 0.2–0.25 m. This value is almost the same as the simulation result [5].

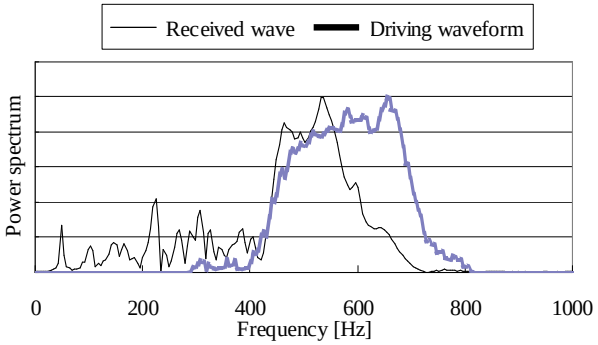


Fig.3 Fourier transforms results

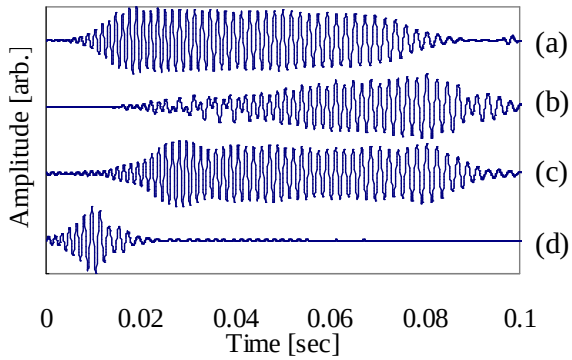


Fig.4 Received waves.
(a) Driving waveform, (b) Received wave,
(c) Filtered wave, (d) Correlation result

## 4. CONCLUSION

We confirm that the validity of the pulse compression method for resolution improvement of underground image. In the exploration experiment, almost the same axial resolution is obtained as a result of the simulation. Then, it was confirmed that axial resolution when the down chirp wave that oscillated 800 to 300Hz (duration 100ms, applied k-flat function) is about 0.2–0.25m in the actual exploration experiment.

This time, duration time of chirp signals is 100ms for the specification of the recorder that we are using. To improve the image resolution, we will investigate the method that the expending the duration time of chirp signals.

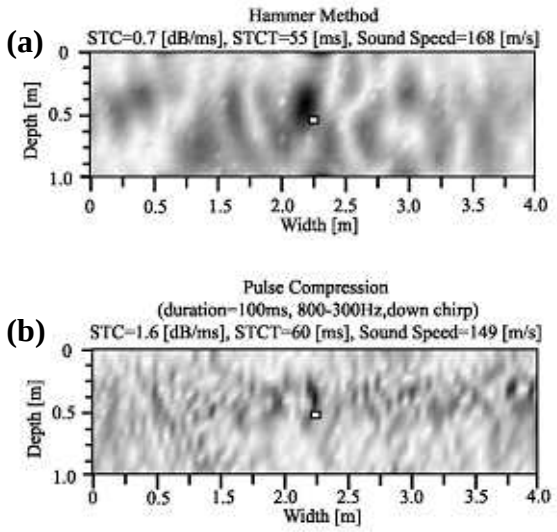


Fig.5 Underground Images
(a) Hammer method
(b) Pulse compression

**Acknowledgment**

This work was supported by a Grant-in-Aid for Scientific Research (B) (No.18300307) from the Japan Society for the Promotion of Science.

**References**

1. T. Sugimoto and M. Okujima: Jpn. J. Appl. Phys. **35** (1996) 3105-3108.
2. T. Sugimoto and H. Saitou, M. Okujima: "Archaeological Prospection", Jpn. March. (2000) Vpl.7 No.4, 249-261.
3. M. Moriya and T. Sugimoto: Jpn. J. Appl. Phys. **41** (2002) part 1, No.5B, 3501-3502.
4. Earth Remote Sensing Data Analysis Center (ERSDAC), "SAR processing algorithm description", [in Japanese] (2005) http://www.palsar.ersdac.or.jp/guide/pdf/sar_algorithm.pdf.
5. H. Kawasaki and T. Sugimoto: Proc. Symp. Ulttrason. Electron., Vol.28,(2007) pp.335-336 14-16 Nov. 2007.

2P2b-16

Proceedings of Symposium on Ultrasonic Electronics, Vol. 29 (2008) pp. 233-234
11-13 November, 2008

# Poisson's Ratio Mapping System Using Immersion Ultrasonic Scanning

SeoYoung Oh‡, Young H. Kim, Yosub Shin [1] (Korea Science Academy), and Hyun-Joon Cho (Advanced Institute of Quality and Safety)

## 1. Introduction

Poisson's ratio is one of the elastic constants, which are material parameters that relate stress and strain[1]. Many elastic constants have been used to determine the materials property, but Poisson's ratio hasn't been given much attention due to its narrow range[2-3]. However recently it has been reported that Poisson's ratio is closely related with the bonding forces and sound wave speeds in a certain material[2]. Thus besides the classical method of measuring Poisson's ratio with mechanical loading, determination from longitudinal and transverse wave speeds can be also used as a nondestructive method. The sound wave speeds have been measured seperately, each longitudinal or transverse wave at one time, because transverse wave is hardly transferred in liquid medium. This method had many difficulties, which were another downsides of Poisson's ratio among the elastic constants, such as pasting or removing solid couplant and damage to the specimen during this[3]. However the mode conversion from longitudinal wave to transverse wave was reported with contact type longitudinal transducer, not only at oblique incident but also at normal angle, using liquid couplant [4]. Longitudinal and transverse wave speeds can be Simultaneously measured using immersion method and Poisson's ratio can be determined from measured wave speeds [3].

In the present work, "μ-scan (Poisson's ratio scan)" system which can determine distribution of Poisson's ratio in a sample using immersion method has been proposed. An immersed transducer scanned over a surface of the specimen. Wave modes were idetified from the pulse-echo signals. The Poisson's ratio was determined from the transit times of longitudinal and transverse wave modes.

## 2. Theoretical Background

Poisson's ratio is defined as the ratio of lateral contraction to longitudinal extension and therefore can be expressed with Lamé constant as below [1].

$$\mu = -\frac{\varepsilon_{22}}{\varepsilon_{11}} = \frac{\lambda}{2(\lambda + G)} \tag{1}$$

Since longitudinal and transverse wave speeds are given as [1]

$$c_\ell = \left(\frac{\lambda + 2G}{\rho}\right)^{1/2} \quad c_t = \left(\frac{G}{\rho}\right)^{1/2} \tag{2}$$

and combining equations (1) and (2), we can get

$$\left(\frac{c_\ell}{c_t}\right)^2 = \frac{\lambda}{G} + 2 = \frac{2-2\mu}{1-2\mu}. \tag{3}$$

The transit times of longitudinal and transverse wave modes are as follows:

$$\tau_\ell = \frac{2d}{c_\ell}, \tau_t = \frac{2d}{c_t}, \tag{4}$$

where $d$ is thickness of specimen. The relationship between ratio of transit times of wave modes and Poisson's ratio is given by

$$\left(\frac{c_\ell}{c_t}\right)^2 = \left(\frac{\tau_t}{\tau_\ell}\right)^2 = \frac{2-2\mu}{1-2\mu}. \tag{5}$$

Therefore, Poisson's ratio can be determined from the ratio of transit time of longitudinal and transverse wave modes without prior information of specimen thickness.

## 3. Experiment

Four specimens of Al, Fe, Cu, and brass were employed in order to verify proposed method. Each of them has parts of two different thicknesses as shown in Fig. 1.

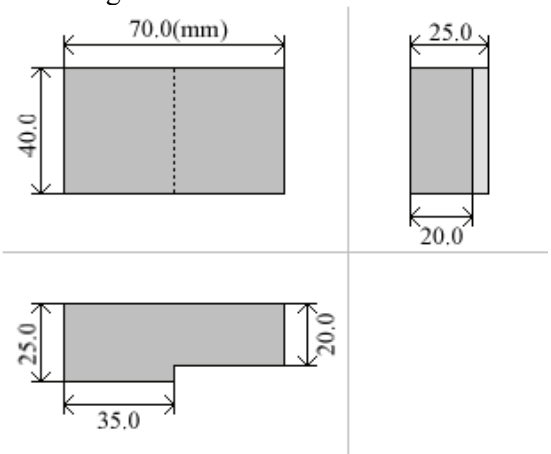


**Fig. 1** Dimensions of the specimen used in the present work.

[1] Present address: University of Illinois at Urbana Champaign

An ultrasonic pulser-receiver (Panametrics 5800) and a broadband longitudinal transducer (5 MHz center frequency and 12.7 mm diameter) were used to obtain pulse-echo signal. The distance from transducer to the top surface of specimen was about 52.5 mm. rf signals were digitized with 12 bit resolution and 200 Ms/s.

## 4. Results

Typical pulse-echo signals obtained from steel specimen are shown in Fig. 2. The echo from the surface is referred to as "Front," and the longitudinal echoes from the bottom are referred to as 2P, 4P, … , and mode converted echoes 1P1S, 2S, 3P1S, …. The numbers in the front of P and S represent the number of wave modes involved in the echoes. Fig. 2(a) and (b) show the different time intervals between echoes due to different thickness at each position. The time intervals between echoes are also different according to different materials properties, as shown in Fig. 2(c), the pulse-echo signals from aluminum specimen.

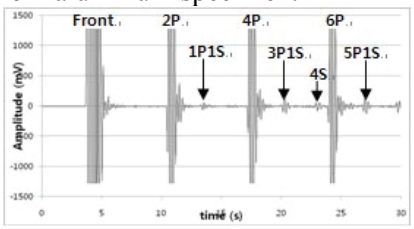

(a)

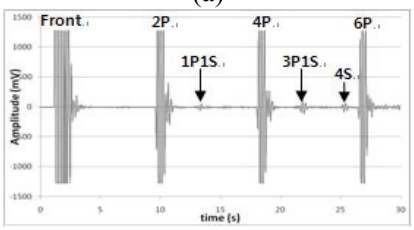

(b)

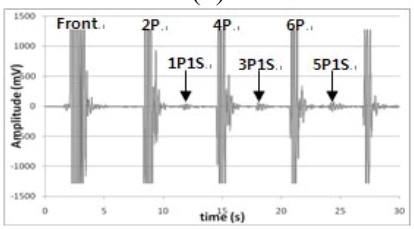

(c)

**Fig. 2** Typical pulse-echo signals from the steel specimen (a) at 20 mm thick and (b) at 25 mm thick, and (c) aluminum specimen at 20 mm thick.

From the scanned results, Poisson's ratios at each point were calculated using equation (5). Although the time intervals change with difference in thickness, Poisson's ratio can be obtained independently of specimen thickness. It is demonstrated more obviously in Fig. 4, which shows the distribution of Poisson's ratio in aluminum and steel specimens. The similar color tone represents similar value of Poisson's ratio, from which can be assumed that Poisson's ratio is the same in one material, regardless of thickness.

When the transducer passes the stepped area, signals from both bottoms with different depths are detected at the same time. Thus it is hard to measure Poisson's ratio.

At copper and brass specimens the mode converted echoes were not evident enough to be located and therefore were difficult to obtain Poisson's ratio at this moment. It is assumed that greater Poisson's ratio influences the speed of transverse wave to become slower and efficiency to be lower[3].

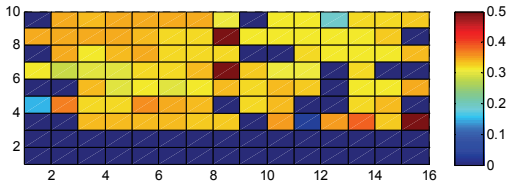

(a)

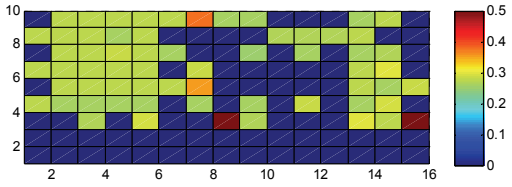

(b)

**Fig. 3** μ-scan results of (a) aluminum and (b) steel specimens.

## 5. Conclusions

From the result of scanning of each specimen, we could determine distribution of Poisson's ratio in the specimen and concluded that Poisson's ratio is irrelevant to the thickness of the specimen. The materials of relatively greater Poisson's ratio were rather hard to obtain accurate Poisson's ratio. In this aspect the further research is required. We expect that this system can be used to identify change of composition in a specimen such as sintering in ceramics and different material characteristics at welded points.


## Acknowledgment

This research was partially supported by the Teacher-Student Research program of Korea Science Academy in 2008.


## References


1. H. F. Pollard: *Sound Waves in Solids* (Pion Ltd, London, 1977) p.15, 25.
2. A. Kumar, T. Jayakumar, B. Raj and K. K. Ray: Acta Materialia **51** (2003) 2417.
3. Y. Shin, Y. H. Yoon and Y. H. Kim: Journal of the Korean Society for Nondestructive Testing **28** (2008) 40.
4. Y. H. Kim, J. K. Lee and H. C. Kim: J. Korean Phys. Soc. **42** (2003) 111.

2P2b-17

Proceedings of Symposium on Ultrasonic Electronics, Vol. 29 (2008) pp. 235-236
11-13 November, 2008

# Development of an ultrasonic face classification system

Zhenwei Miao, Wei Ji, Yong Xu, and Jun Yang† (National Laboratory of Acoustics, Institute of Acoustics, Chinese Academy of Sciences)

## 1. Introduction

Face classification, as an active research area over the last decade[1-2], has its advantages of non-intrusive and being well accepted by users. But the variations of illumination, pose and facial expression etc. always deteriorate the performance of a face classification system. Although many efforts have been put towards improving the classification rate, the face classification in an uncontrolled environment is still a challenging problem. Recently, McKerrow et al.[3-5] employed an active ultrasound sensing technology to classify human face by using a statistical classifier. The classification results indicated that ultrasonic sensing was able to distinguish different faces.

The aim of our work is to develop a robust ultrasonic sensing-based face classification system free of the lighting conditions. Effective feature extraction algorithms are proposed for improving classification rate and verified by experiment results. The rest of this paper is organized as follows. Section 2 presents the basic theory. Section 3 describes the ultrasonic face classification system. Section 4 designs the experiment and then illustrates the test result of classification. Finally, a brief conclusion is made in Section 5.

## 2. Basic Theory

As the ultrasound encounters an object during its propagation, according to the mechanism described by Freedman's 'image pulse' model[6-7], echoes are produced whenever the acoustic impedance or any of the derivatives of it with respect to range is discontinuous. The amplitude of the echo is inverse to the order of the derivatives and proportional to the area of the discontinuity. The discontinuities distribute over range, azimuth and elevation angle. When the ultrasonic beam impinges on a face, echoes from these discontinuities contain information of their respective areas, order of the derivatives and the relative range on the face as show in **Fig.1**.

The bottom area in Fig.1 shows the variation of the echo amplitude corresponding to the distance. The ordinate represents the normalized amplitude while the abscissa represents the distance with the unit of meter. The left bottom part of Fig.1 represents the orthogonal detection of a subject's face. The first peak in the echo spectrum corresponds to the nose, the second peak corresponds to the forehead, the third to the lip, the forth to the cheeks, etc. The right-bottom part of Fig.1 represents the sensing angled at 45° to the same face. According to the alignment between the echo and the face features, our initial idea is that we can classify the faces by using signal processing to analyze the received echoes from them.

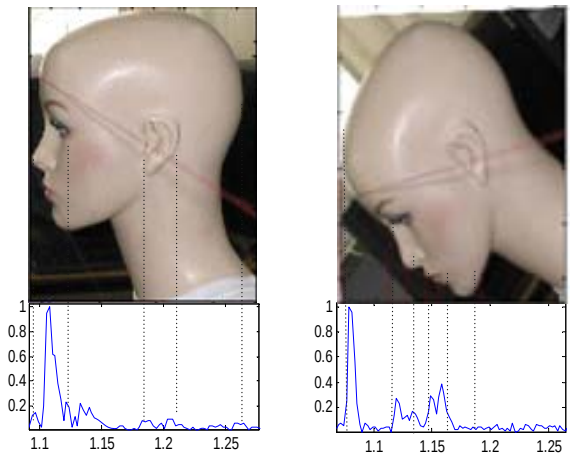


Fig.1. The face and the ultrasonic echo signal

## 3. Ultrasonic face classification system

Based on the above algorithm, we design the ultrasonic face classification system. The block diagram of this system is shown in **Fig. 2**. SensComp's Series 600 electrostatic transducer is used to transmit the chirp signal and G.R.A.S. 1/4" microphone is used to receive the echo. The analog echo signals received by the microphone were converted to digital signal by NI DAQpad-6070E data acquisition card with a sample rate of 500 kHz. Two transmitters are utilized in this system from multi-directions to detect human face. Receivers of the same amount are employed to collect echoes from different angles.

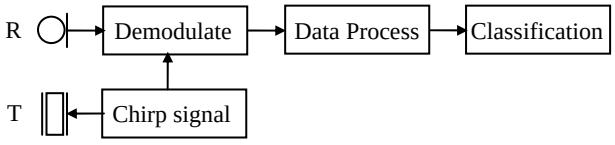


Fig. 2 Block diagram of the face classification system

**Fig. 3** illustrates the experiment setup. One transmitter and one receiver combine a TR-pair. Two TR-pairs, named TR-A and TR-B, are fixed on a spherical frame. They aimed at the front of the

jyang@mail.ioa.ac.cn

face orthogonally and 45°, respectively. One reference point was set 1 meter away from the two TR-pairs to position the subject's faces. One camera was used to record the subject's facial expression and track slight movement of the head so that we can analyze the echo spectrums accordingly.

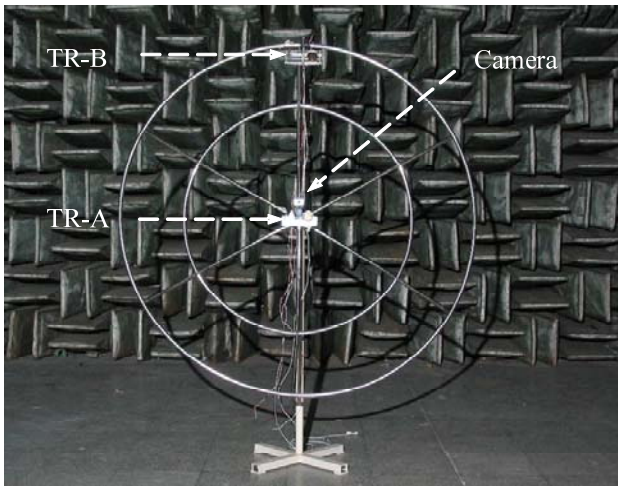


Fig. 3 Experiment setup

## 4. Experiment design and classification

The experiment was carried out with a group of samples including 10 persons (4 females and 6 males). In order to acquire reliable echo data, the subjects were required to cooperate with the test as follows:

1) Keeping head not tilted, looking straight forward, nose tip closely sticking to the reference point;
2) Allowance of head movement such as slightly turn left or right within a small angle range of about 5°;
3) Taking off glasses, earrings, and any other head accessories.

Three methods were used in feature extraction in our work. The first extraction method was McKerrow's method (Method I) in[3]. The second extraction method (Method II) was simplified from McKerrow's method by decreasing the number of thresholds from nine to six with adjustment of threshold values. Furthermore, we proposed a new feature extraction method (Method III). The facial features were picked from the power spectrum of the demodulated echo signal directly.

The features were evaluated by both the classical KNN and Bayes classifiers[8], respectively. For each subject and each detection angle, there were 100 data samples, 67 samples were used as training samples, and the rest were used as testing samples. We set $k = 1$ in the KNN classifier and then compared the classification rate in **Table 1**.

Table 1. Results of the face classification experiment

| Feature extraction method | Data source | KNN classifier | Bayes classifier |
|---|---|---|---|
| Method I | TR-A | 73.3% | 67.0% |
| | TR-B | 89.4% | 82.4% |
| | TR-A&TR-B | 97.9% | 95.8% |
| Method II | TR-A | 77.9% | 71.8% |
| | TR-B | 91.5% | 87.9% |
| | TR-A&TR-B | 98.8% | 97.9% |
| Method III | TR-A | 98.5% | 97.3% |
| | TR-B | 97.6% | 93.3% |
| | TR-A&TR-B | 100% | 99.1% |

From Table 1 we can see that, using the same classifier, the features extracted by Method III can give a better classification result than that by the other two methods in the same experimental condition. Features extracted from echoes collected by TR-B leaded to a higher classification rate than that by TR-A did if they were extracted by Methods I or II, but it was not the case when they were extracted by Method III. Nevertheless, no matter which method was chosen to extract features, data fusion gave the best results.

## 5. Conclusion

A robust ultrasonic sensing-based face classification system free of the lighting conditions is presented in the paper. With effective feature extraction algorithms and proper configurations of TR-pairs designed in this work, the proposed system could achieve a high classification rate in the lab condition.

**Acknowledgment**

This research was partially supported by the National Natural Science Foundations of China under Grant No. 60535030.

**References**

1. R. Chellapa, C. L. Wilson, and S. Srrohey: Proc. of the IEEE, 83 (1995) 704
2. S. Z. Li and A. K. Jain: *Handbook of Face Recognition*. (Springer, Ger., 2005)
3. K. K. Yong and P. J. McKerrow: Proc of Aus. Conf. on Robotics & Automation (2005)
4. P. J. McKerrow and K. K. Yoong: Proc. Towards Autonomous Robotic Systems (2006) 111
5. P. J. McKerrow and K.K. Yoong: Robotics and Autonomous Systems, 55 (2007) 702.
6. A. Freedman: Acustica, 12 (1962) 10.
7. R. Kuc: J. Acoust. Soc. Am. 102 (1997) 689
8. R. O. Duda, P. E. Hart, and D. G. Stork: *Pattern Classification*. (Wiley, Am, 2000). p 174

2P2c-6

Proceedings of Symposium on Ultrasonic Electronics, Vol. 29 (2008) pp. 237-238
11-13 November, 2008

# Development of a Movable Inspection Sensor for a Pipe Using an EMAT

## 電磁超音波探触子を用いた移動型配管探傷センサの開発

Yusuke Okawa [1†], Riichi Murayama [1], Hideaki Morooka [1], and Yusuke Yamashita [1]
([1] Facult. Eng.,Fukuoka Institute of Technology.)
大川悠助[1‡], 村山理一[1], 諸岡秀昭[1], 山下雄介[1] ([1]福岡工業大 工)

## 1. Introduction

In recent years, a nondestructive inspection technique using a pipe wave, a type of ultrasonic wave that can travel a long-distance along a pipe was applied as a nondestructive inspection method. We have tried to develop a pipe wave sensor which is movable and can be easily installed using an Electromagnetic Acoustic Transducer (EMAT).

## 2. Characterization of a pipe wave

Figure 1 shows the theoretical dispersion curve of the group velocities of a pipe wave for a steel pipe with a 43 [mm] diameter and 1 [mm] thickness. We can confirm that there are a T(0,1) mode and T(1,1) mode which vibrate in the circumferential direction of a pipe [2] and travel along the axial direction of a pipe, an L(0,1) mode and L(0,2) mode which vibrate and travel along the axial direction of a pipe.

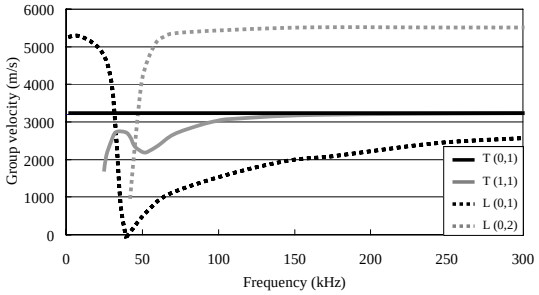


Fig.1 Group velocity dispersion curves

## 3. Drive principle of an EMAT for a pipe wave

The drive principle of an EMAT generating an L-mode pipe wave is shown in Fig.2 (A). The EMAT composed of an electromagnet which can generate a static magnetic field along the axis direction of a pipe and a circular-shaped sensor coil which can generate a dynamic magnetic field along the axis direction of a pipe. We next devised a trial EMAT for a T-mode pipe wave as shown in Fig.2 (B). The EMAT is composed of an electromagnet which can generate a static magnetic field along the axis direction of a pipe and a sensor coil which can generate a dynamic magnetic field along the circumferential direction of a pipe.

E-mail:mcm07002@bene.fit.ac.jp

However, we cannot confirm a T-mode pipe wave using this sensor. Therefore, we developed the EMAT composed of an electromagnet, which can generate a static magnetic field along the circumferential direction, and a circle-shaped sensor coil, which can generate a dynamic magnetic field along the axis direction of a pipe.

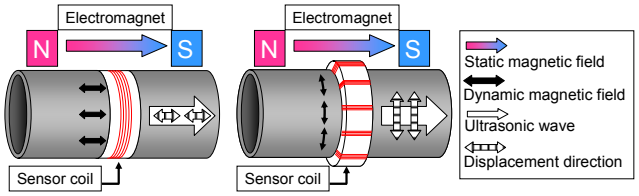


A.L-mode type B.T-mode type

Fig.2 Drive principle of an EMAT for a pipe wave

## 4. Basic structure of the trial EMAT

The displacement distribution of the circumferential direction of the T (0, 1) mode and T (1, 1) modes are shown in Fig.3. It suggests that a uniform static magnetic field along the circumferential direction is necessary to generate a T (0, 1) mode pipe wave. Therefore, we manufactured many electromagnets which could supply a uniform magnetic field in the circumferential direction as shown in Fig.4.

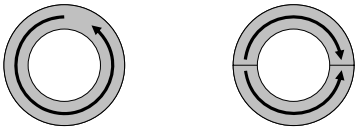

A. T (0, 1) mode B. T (1, 1) mode

Fig.3 Cross-sectional illustrations of circumferential vibration modes

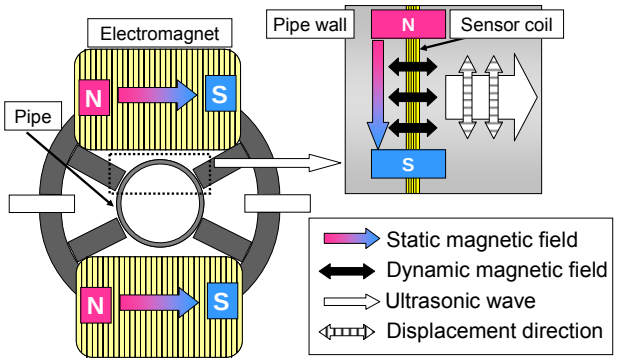


Fig.4 Drive principle of an EMAT for a T-mode pipe wave

## 5. Experimental system

The experimental system is shown in Fig.5. Steel pipes (STKM) of 43 [mm] outside diameter, 2400 [mm] length and 1 [mm] and 2 [mm] pipe wall thicknesses were used as the test specimen.

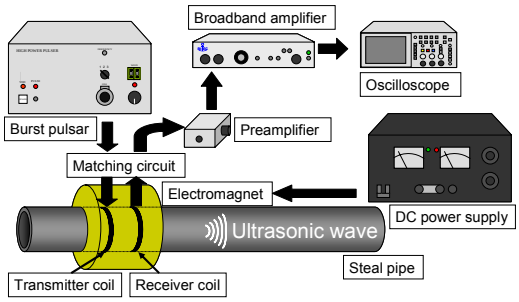


Fig.5 Experimental system

## 6. Experimental results

### 6-1. Optimization of the static magnetic field strength

The static magnetic field strength is then adjusted to become the maximum received ultrasonic signal. Fig.6 shows the relationship between the magnetic field strength and the received ultrasonic wave signal strength. As can be seen, the highest signal was obtained at the magnetic field of 70 [mT].

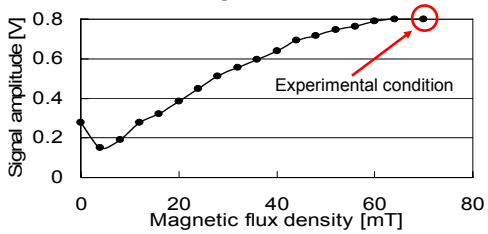


Fig.6 Relationship between the signal amplitude and the magnetic flux density

### 6-2. Confirmation of the pipe wave mode

The static magnetic field distribution in the circumferential direction of a pipe is shown in Fig.7 and the velocity distribution curve due to the drive frequency that ranges from 60 [kHz] to 160 [kHz] is shown in Fig.8. As can be seen, we could not observe the T (1, 1) mode.

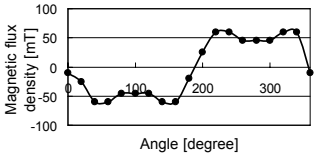


Fig.7 Relationship between the magnetic flux density and the circumferential angle

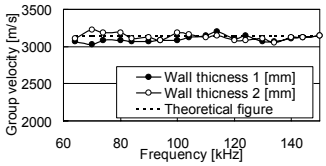


Fig.8 Relationship between the group velocity and the drive frequency

### 6-3. Inspection results

Three kinds of circular through holes (diameters of 5, 10, and 15 [mm]) were machined into the pipe. The cross section area rates of these circular holes are 4%, 8%, and 15%, respectively. The samples of the signal waveform are shown in Fig.9. We could confirm the reflection signal from the 15% circular defect.

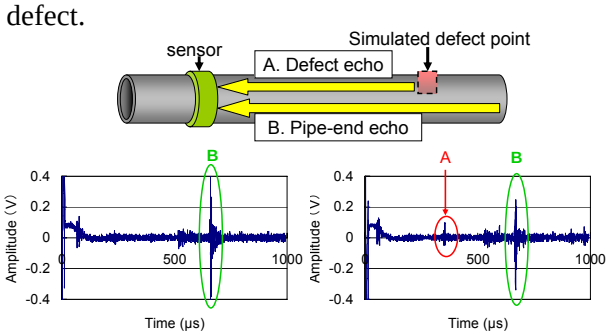


A. Non-defect signal B. Defect signal (15%)

Fig.9 Example of received ultrasonic waveforms

### 6-4. Scanning inspection results

We scanned the trial EMAT in the axis direction of a 500 [mm] pipe. Figure 10 shows the attenuation rates of the reflection signal from a circular hole defect and a slit defect. It was confirmed that the attenuation rate of the reflection echo of a circular hole defect is obviously enlarged when compared to that of a slit defect.

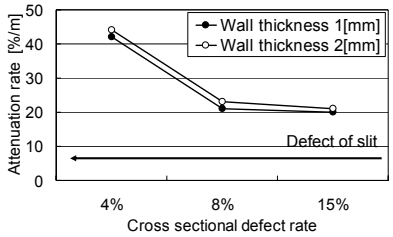


Fig.10 Relationship between the cross-sectional defect rate and attenuation rate

## 7. Conclusion

We developed a trial EMAT for a T-mode pipe waves and could observe a defect echo by certain kinds of defects. We also showed that the potential to distinguish the type, size and depth of the defect. Both the L and T-mode pipe waves will be combined by an L-mode EMAT and a T-mode EMAT in the future.


## Acknowledgements

This work was partially supported by a Grant-In-Aid for Scientific Research (C19560104). We acknowledge Dr. T.Hayashi at the Nagoya Institute of Technology for offering the software to compute the pipe wave velocity dispersion curves.


## References


1. H.Nishino et al., Jpn. J. Appl. Phys. Vol. **40**, pp364-370, 2001.
2. H.Kwun et al., Mater. Eval. Vol.**62**, pp 430-433, 2004.

2P2c-7

Proceedings of Symposium on Ultrasonic Electronics, Vol. 29 (2008) pp. 239-240
11-13 November, 2008

# Development of Circumferential Scan in Pipes by Non Contact Air Coupled Ultrasonic Testing
# 非接触空中超音波によるパイプ円周方向探傷の開発

Masakazu Takahashi[1], Hidekazu hoshino[1], Yukio Ogura[1], Hideaki Kitagawa[2], Junichi Kusumoto[2], Akihiro Kanaya[2], Hideo Nishino[3] ( [1]Japan Probe Co. Ltd; [2]Kyushu Electric Power Co., Inc. [3]Inst. Tech. & Sci., The Univ. of Tokushima )
高橋雅和 [1]，星野秀和 [1]，小倉幸夫 [1]，北川秀昭 [2]，楠元淳一 [2]，金谷章宏 [2]，西野 秀郎 [3] （ [1]ジャパンプローブ㈱, [2]九州電力㈱, [3]徳島大院 ）

## 1. Introduction

A guided wave propagating along circumferential direction of a pipe ( circumferential guided wave; CGW ) has been anticipated for a rapid and efficient screening technique for the monitoring of piping. The CGW is classified into two propagation modes, namely, the circumferential (C-) SH and the C-Lamb waves. Several reports of the propagation phenomena [1–5] and applications for NDT [6, 7] of the CGW have been published.

On the other hand, air coupled transductions of ultrasounds in solid materials have also been expected to apply to any kind of environments and for on-line monitoring because of their non-contacting feature. In this paper, we propose a novel method of defect detections by non contact air coupled ultrasonic testing ( here after called NAUT ) in pipes using the C-Lamb waves generated and detected by a pair of air-coupled probes. A specially designed focusing probe for efficient transductions was also described. Experimental verifications of both defect detections of the method and the special probe were shown.

## 2. Experimental setup

Several 10 cycles of negative rectangular monopole burst pulses generated by the high power tone-burst pulsar / receiver ( Japan Probe JPR – QD ) were employed in the experiments. The pulsar / receiver built-in the 60 dB amplifier has been designed for the NAUT with optimum electronics. Piezoelectric 1-3 composite probes ( PCP's ) were used for the NAUT. Center frequencies of PCP's are 400 kHz ( 0.4K14x20N and 0.4K40x20N – R190 ) and 800 kHz ( 0.8K14x20N ), respectively. The element size is 14x20 mm in a case of 0.4K14x20N, K is the composite material. The suitable matching layers are utilized for the efficient transductions. The test pipe is φ 318.5 mm outer diameter with 14.3 mm thick steel pipe. Incident angle to the pipe surface of the radiated longitudinal waves was set to be optimum value [8, 9, 10] to generate the C-Lamb waves efficiently.

e-mail address : masakazu-takahashi@jp-probe.com

## 3. Constant incident angle method by focusing probe

Incident angle of a plane wave ( normally generated by a flat vibrator ) to a surface of a pipe varies accordingly to the irradiation position as shown in Fig. 1 (a). This phenomenon is ineffective for the C-Lamb wave generations. Therefore, we have developed the constant incident beam angle ( CIBA ) method by using a focusing probe as shown in Fig. 1 (b). In this setting, when the angular aperture θ takes small, the incident angle *i* approximately takes constant value. Fig. 2 shows

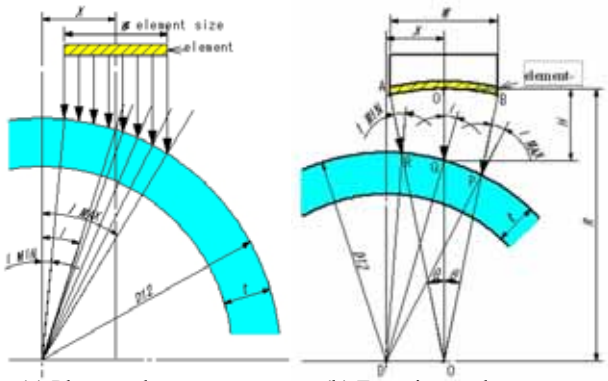


(a) Plane probe (b) Focusing probe

**Fig. 1 Oblique incidence to pipes. by NAUT**

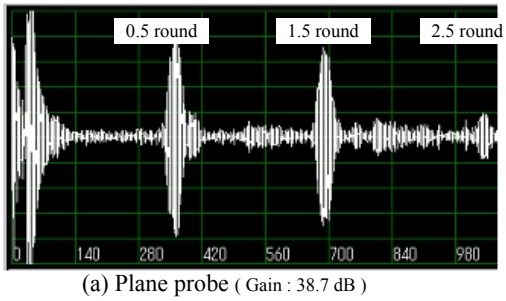


(a) Plane probe ( Gain : 38.7 dB )

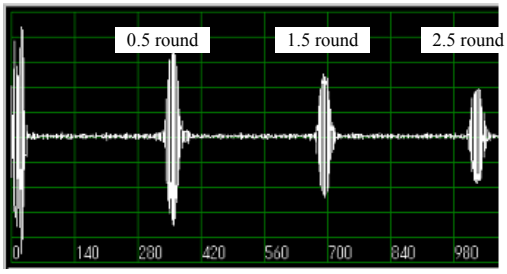


(b) Focusing probe ( Gain : 28.5 dB )

**Fig. 2 Example of transmission waves**

time domain signals obtained by the plane probe (a) and the CIBA method (b). It was obviously confirmed that the obtained amplitude and signal to noise ratio by the CIBA method was improved ( 10 dB gain up ).

## 4. Development of tandem method

Conventional transmission method which two probes being faced each other doesn't identify defect position, however the new developed method enables to determine the defect position. Fig. 3 shows the tandem method using a pair of air-coupled probes and the echo pattern.

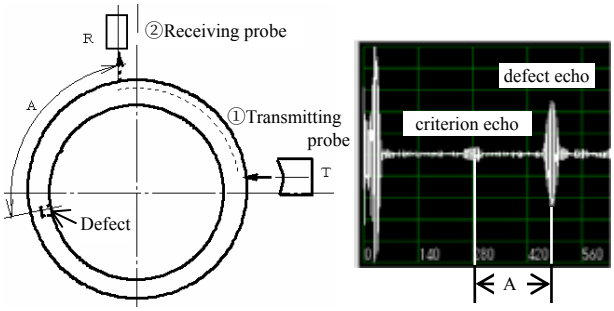


**Fig. 3 The tandem method and the echo pattern**

The transmitting probe ① sends ultrasonic beam to the pipe and the receiving probe ② receives a little diffraction echo from propagated circumferential guided wave in the pipe, the echo is small, and position is constant in time. Therefore we call it "criterion echo" which is important to determine defect position by the distance between criterion echo and the defect echo. Fig. 3 shows the criterion echo and the defect echo in the distance A = 320 mm between defect and probe. Fig. 4 shows the experimental arrangement of the equipment in this method. Fig. 5 shows some examples of detecting defect echoes, to enable to find φ 4 mm × 4 mm deep flat bottom hole.

## 5. Conclusion

High power square tone burst, pulsar/ receiver can make possible to generate the high guided wave into pipe and to receive effectively it in the NAUT. We have developed the effective generating and propagating guided waves in optimum frequency, incident angle and probe. Improvement of signal noise ratio and high sensitivity has been obtained by the NAUT. The tandem method evaluates the defect position from the distance between the criterion echo and the defect echo, to find the defect size of 3 mm deep slit and φ 4 mm × 4 mm deep flat bottom hole.

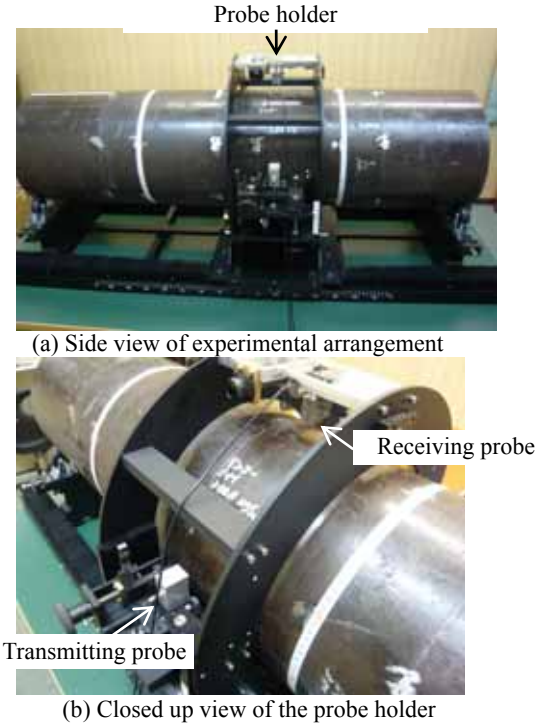


(a) Side view of experimental arrangement

(b) Closed up view of the probe holder

**Fig. 4 Experimental arrangement of the tandem method**

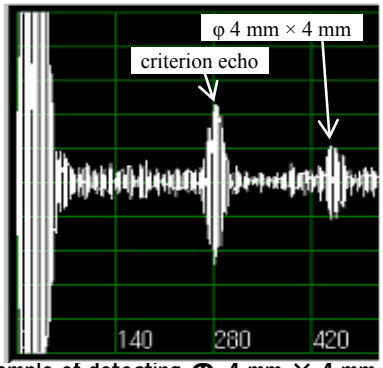


**Fig. 5 Example of detecting Φ 4 mm × 4 mm deep flat bottom hole**

## References


[1] G. Liu and J. Qu: J. Appl. Mech. 65 (1998) 424
[2] X. Zhao and J. L. Rose: JASA 115 (2004) 1912
[3] H. Nishino and K. Yoshida: Acoust. Sci. Tech. 27 (2006) 389
[4] H. Nishino, R. Yokoyama, H. Kondo and K. Yoshida: JJAP 46 (2007) 4586
[5] H. Nishino, R. Yokoyama, K. Ogura, H. Kondo and K. Yoshida: JJAP 47 (2008) 3885
[6] M. Hirao and H. Ogi: NDT&E 32 (1999) 127
[7] W. Luo et al: AIP conf. Proc. 820 (2006) 165
[8] H. Nishino et al: Proc. JSNDI fall meeting (2007) p.27 [in Japanese]
[9] M. Takahashi et al: Proc. JSNDI spring meeting (2008) p.5 [in Japanese]
[10] H. Reissner: Helv. Phys. Acta 7 (1934) 140 [in German]

Proceedings of Symposium on Ultrasonic Electronics, Vol. 29 (2008) pp. 241-242
11-13 November, 2008

# Nonlinear Acoustic Evaluation of Creep Damage in a Cr-Mo-V Steel

非線形超音波法を用いた Cr-Mo-V 鋼のクリープ損傷評価

Toshihiro Ohtani † (Faclut. Eng., Shonan Inst. Tech.)
大谷俊博†(湘南工大 工)

## 1. Introduction

Many of fossil power plants, which were constructed during 1960's and 70's and exceed more than 100,000 working hours, have presently been operating while they have underwent progressive damage, mainly from creep, as the time proceeds[1]. Furthermore, by shifting the base load of power from fossil power plants to nuclear power plants, they are faced to even more severe operating condition such as daily or weekly startup and shut-down in order to correspond to rapid change of the de-mand. As the consequence of this trend, the material's degradation is being accelerated. Therefore, a non-destructive technique is now highly required for safely operating plants and predicting the remaining life. It is also important for the technique to be simple and quick oper-ating to cope with the large number of measuring points.[2]
In this study, we apply an electromagnetic acoustic transducer (EMAT) to monitor the surface-shear-wave nonlinearity throughout creep life of metals. The use of an EMAT makes contactless transduction possible. However, EMATs lack a large transduction efficiency, which the nonlinear measurement needs. To overcome this limitation, we chose to use electromagnetic acoustic resonance (EMAR) [2] so as to excite and enhance the standing wave of the second-harmonic component around a cylindrical specimen. Coherent superposition produces highly magnified amplitude of the second harmonics. The measured surface-wave nonlinearity detected the peak around 20 % of creep life.

## 2. Samples and experimental condition

We performed creep tests using specimens ϕ14 mm in gauge diameter, 60 mm in gauge length [3]. The material of the specimens was commercially available JIS-SNB16. The heat treatment chemical composition and mechanical properties at room temperature are found in Ref. 3 The creep tests were performed at 923 K in the atmosphere by using a vertical single-lever creep machine and a heating electric furnace. Twelve creep specimens are prepared for 25 MPa. The creep test individually carried out until the creep strain reached target value. After the creep tests, the nonlinear ultrasonic characteristics were measured at room temperature.

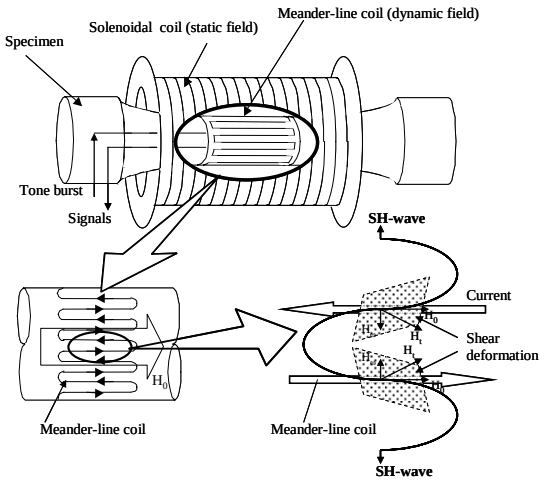


Fig. 1 Configuration and mechanism of the magnetostrictive EMAT for generating and receiving the axial shear wave.

## 3. EMAR for nonlinear acoustics

**Figure 1** shows the magnetostrictively coupled EMAT designed for the axial shear wave in ferromagnetic materials. It consists of a solenoidal coil to supply the biasing magnetic field along the axial direction and a meander-line coil surrounding the cylindrical surface to induce the dynamic field in the circumferential direction. The total field oscillates in the axial direction at the same frequency as the driving currents and produces a shearing vibration through the magnetostriction effect, resulting in the axial-shear-wave excitation. The same coil works as receiver through the reverse mechanism[2].

Driving the meander-line coil with long tone bursts causes interference among the axial shear waves traveling around the cylindrical surface, and a frequency scan detects resonance peaks at unequal

†E-mail: ohtani @mech.shonan-it.ac.jp

frequency intervals, at which all the waves overlap coherently to produce lareg amplitudes.We used the first resonant mode around $f_r$=3.9MHz, whoes amplitude distribution has the miaximu at the surface and a steep gradient with the radius; the penetration depth is estimated to be 0.5 mm [4]. We defined the maximum amplitude of the first resonance peak as the fundamental amplitude, $A_1$ (**Fig. 2**). We then excited the axial shear wave by driving the EMAT at half of resonant frequency ($f_r$/2), keeping the input power unchanged. In this case, the drivng frequency does not satisfty the resonant condition and the fundamental componet does not produce a detactable signal. However, the socond harmonic component having double frequency ($f_r$) satisfies the resoonat condition and the resonance spectrum of the received signal contains a peak at the original resonant frequency as shown in Fig.2. We defind this peak height as socond-harmonic amplitude, $A_2$, to calculated the nonlinearity $A_2/A_1$. These measuremnt were made possible by the system for nonlinear acoustic phenomena (SNAP) manufactured by RITEC Inc...

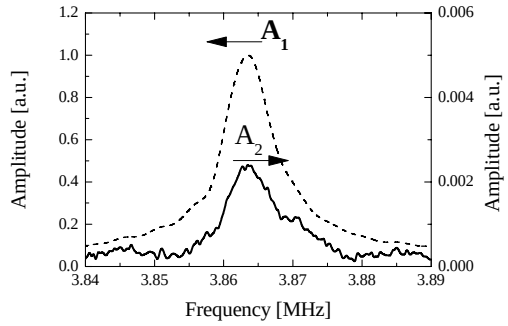


Fig. 2 Resonant spectra for the fundamental and the second-harmonic components.

## 4. Results

**Figure 3** shows the relationship between the nonlinearity $A_2/A_1$, relative velocity, $\Delta V/V_0$ ($V_0$: initial velocity), the creep strain, the strain rate, and estimated life fraction $t/t_r$ (the creep time/ estimated creep life). For the estimation of $t/t_r$ of each sample, we applied the modified θ projection and the rupture parameter [5, 6]. $A_2/A_1$ reached its peak at $t/t_r$ = 0.2, and it dropped to the minimum level at $t/t_r$ = 0.5. The creep strain rate decreased from the start of creep until $t/t_r$ = 0.2, remained steady until $t/t_r$ = 0.5, and then gradually increased before the rupture. These changes correspond to three creep regimes: transient creep, steady creep, and accelerating creep. These results were the same as the change of attenuation coefficient obtained by the bulk shear-wave EMAT [3], possibly suggesting that the change in $A_2/A_1$, as shown in Fig. 3, was due to absorption by dislocation vibrations[7]. Furthermore, we observed the change of dislocation structures with TEM. The evolution of $A_2/A_1$ as creep progress is related to the microstructure change, especially, dislocation structure.

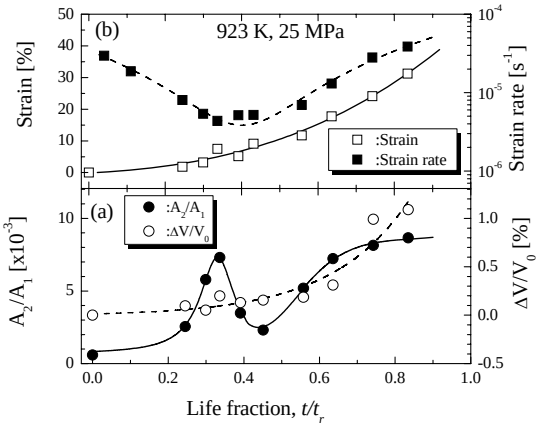


Fig. 3 Relationship between $A_2/A_1$, $\Delta V/V_0$, the creep strain, the strain rate, and life fraction, $t/t_r$.

## 5. Conclusion

Creep damage in Cr-Mo-V steel (JIS-SNB16) at 923 K in air was evaluated through the nonlinearity $A_2/A_1$ measured with the EMAR method. The $A_2/A_1$ showed a peak at around 20% and a minimum value at 50 % of the creep life, which is interpreted as resulting from microstructural changes, especially, dislocation mobility.

## References


1. R. Viswanathan: *Damage Mechanism and Life assessment of High Temperature Componen*t (ASM International, Metals Park, OH, 1989) p.1.
2. M. Hirao and H. Ogi: *EMATs for Science and Industry* (Kluwer Academic, Boston, 2003) p. 1.
3. T. Ohtani, H. Ogi, and M. Hirao: Jpn. J. Appl. Phys. **45** (2006) 4526.
4. H. Ogi, T. Hamaguchi and H. Hirao: Metall. Mater. Trans. A **31A** (2000) 1121.
5. K. Maruyama, C. Harada and H. Oikawa: J.Soc. Mater. Sci. Japan. **34** (1985) 1289.
6. K. Maruyama, H. Oikawa: Trans. ASME, J. Pressure Vessel Techno. **109** (1989) 142.
7. A. Granato and K. Lücke: J. Appl. Phys. **27** (1956) 583.

2P2c-9

Proceedings of Symposium on Ultrasonic Electronics, Vol. 29 (2008) pp. 243-244
11-13 November, 2008

# Nonlinear ultrasonic characterization of thermally damaged Westerly granite

Claude Inserra‡, Shiro Biwa and Youqing Chen (Graduate School of Energy Science, Kyoto University)

## 1. Introduction

The influence of temperature on the mechanical properties of rocks is of relevant importance in geophysical applications, that require heating and cooling of rocks. While the temperature variation imposed to rocks will generate an internal thermal stress large enough to create cracks, the local variation in the temperature gradient will cause the propagation of existing cracks. These two mechanisms lead to the deterioration of the material, and the thermal cracking affects the elastic properties of rocks. As a consequence, in addition to optical measurements of the internal microstructure of rocks[1)], nondestructive ultrasonic methods are of great interest for the characterization of the evolution of elastic properties of rocks under thermal treatment. Usually, P and S-wave velocities are measured to follow the deterioration of material, and by means of the effective medium theory[2,3)], the average characteristics of defects (crack density, crack mean aspect ratio) can be evaluated. These methods assume that cracks are open, randomly distributed and that a linear macroscopic stress-strain relationship of the solid matrix holds. However, several experimental studies have revealed a nonlinear elastic behavior of rocks indicating that the nonlinear acoustic methods are highly sensitive to the defects (cracks, intergrain contacts) than linear ones. In this study, thermally damaged Westerly granite samples are probed by linear and nonlinear ultrasonic methods. First, linear ultrasonic methods are used to follow the P-wave velocity variation during thermal damage. Then, a nonlinear acoustic phenomenon is observed and the results discussed.

## 2. Experimental setup and procedure

The experimetal setup is presented in **Fig.1**. Circular cylindrical samples of Westerly granite, of length 40 mm and diameter 20 mm, are probed by ultrasonic waves. A pulse or toneburst wave was sent to the rock cylinder, using a high-power pulse emitter (RITEC RPR-4000) to excite a piezoelectric transducer (Panametrics) with a 1 MHz nominal frequency. The transmitted wave was then detected at the end of the rod by a wideband transducer with

claude.inserra@at7.ecs.kyoto-u.ac.jp

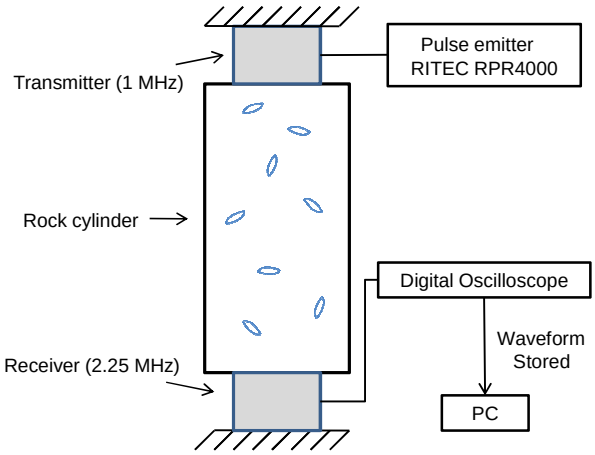


Fig. 1 Schema of the experimental setup.

a 2.25 MHz nomimal frequency. Silicon oil couplant was used between transducers and rock samples. In experiments using toneburst, the time length of the signal was 10 μs (10 periods). The emitted and transmitted waveforms were stored via a digital oscilloscope (Tektronix TDS340AP). In order to observe nonlinear effects, the excitation voltage was varied at 19 steps linearly spaced between 110 V and 450 V.

To investigate the effects of cracks occuring inside Westerly granite when heating, five samples were subjected to a one-cycle heating and cooling test under different holding temperatures. Prior to the ultrasonic measurements, the effective porosity was measured for all the samples by a water evaporation method, which required drying them to 100 °C. So, the samples were all heated above the crack-initiation temperature in the granite, established around 60 °C with acoustic-emission monitoring[4)]. However, the damage occuring in these samples due to this process can be considered as low, and the samples after the porosity measurement are called intact samples. The heating and cooling rate were chosen constant, at 50 °C/hr, and the holding temperature was varied as 200, 300, 400 and 500 °C, with holding time of 30 minutes, for four samples, while keeping one as a reference sample without thermal damage.

## 3. Results

First, wide band pulses were used to measure

the P-wave velocity of the samples, by means of time-of-flight measurement based on zero-crossing method. The P-wave velocity of 4060 m/s, measured in the intact sample, decreased to 2195 m/s for the sample heated at 500 °C, exhibiting a linear decrease of velocity with the holding temperature. These results show a nearly 50% decrease in the P-wave velocity, confirming that linear ultrasonic measurements are a good indicator of the deterioration of the samples. However, it is well known that nonlinear ultrasonic measurements are more sensitive to the presence of defects in materials, like cracks or intergrain contacts. So, in order to check acoustical nonlinear properties of the medium, tonebursts, instead of pulses, were emitted at increasing excitation amplitude. The transmitted waveforms at high excitation amplitude (450 V) for the intact sample and the 500 °C damaged one are shown in **Fig.2**. For the intact sample, the shape of the emitted toneburst is conserved, with slight distorsion. The Fourier spectrum of this signal showed one peak at 1 MHz and no harmonic generation, due to the high attenuation of ultrasonic waves in granite. After heating at 500 °C, the transmitted waveforms contain essentially no frequency components around 1 MHz. The Fourier transform revealed that all the energy of the signal has been transferred to lower frequency components. The waveform appeared to be the time derivative of the envelope of the emitted toneburst, explaining the change in phase of transient peaks (the first and last ones). This nonlinear effect, called "self-demodulation" process, has already been observed in sand[5], and is well known in fluid mechanics[6]. For samples heated below 500 °C, the transmitted waveform are intermediate states between the ones presented in **Fig.2**, and contain

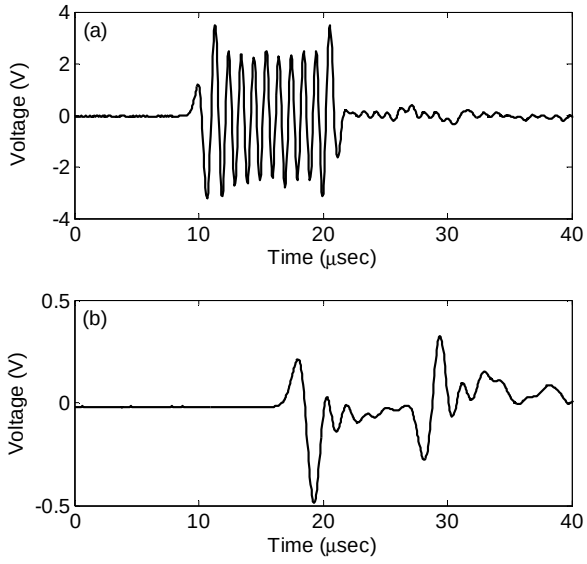


Fig. 2 Evolution of the transmitted toneburst for the intact sample (a) and the thermally damaged one (b).

both the transient peaks corresponding to self-demodulation process, and the high frequency component attenuated due to damage of materials. By increasing the excitation voltage, slight differences appear between the level of the transient peak amplitudes (corresponding to the nonlinear self-demodulation process) and the intermediate high-frequency amplitude (subjected to the linear attenuation). This effect, due to increasing acoustic wave amplitude, is an indicator of the acoustical nonlinearity of the material. To extract such nonlinear information, a damage factor has been defined as the ratio of the mean amplitude of the high frequency components to the maximum of the transient peak amplitudes. This damage factor, scaled between 0 (highly damaged rock) and 1 (intact rock), decreases below 10% of the initial value, at the lowest excitation voltage, for the maximum holding temperature studied.

## 4. Discussion

While the acoustical linear properties are sensitive to the average elastic properties of an inhomogeneous material, nonlinear acoustic methods are highly sensitive to their defects. When heating Westerly granite up to 500 °C, crack appear progressively causing high damage of granite. The nonlinear acoustic method in terms of the introduced damage factor shows higher sensitivity to damage than linear velocity measurements. The self-demodulation process finds its origin in the parametric array theory. It is then possible to describe it by adding a nonlinear quadratic parameter in the stres-strain relationship of the medium. The evolution of the damage factor with increasing amplitude, giving new information about acoustical nonlinearities of rocks, is currently studied in order to extract such nonlinear quadratic parameter and its evolution with thermal damage of granite.


## Acknowledgment

This work was supported by the JSPS Postdoctoral Fellowship.


## References


1. Y. Chen, T. Kobayashi, Y. Kuriki, H. Kusuda and M. Mabuchi : J. Jpn. Soc. Eng. Geol., in press.
2. T. Reuschle, S.G. Haore and M. Darot : Earth. Plan. Sci. Lett. **243** (2006) 692.
3. M.H.B. Nasseri, A. Schubnel and R.P. Young : Int. J. Rock Mech. Min. Sci. **44** (2007) 601.
4. C. Yong and C. Wang : Geophys. Res. Lett. **7** (1980) 1089.
5. V.Yu. Zaitsev, A.B. Kolpakov and V.E. Nazarov : Acoust. Phys. **45** (1999) 202.
6. M.A. Averkiou, Y. Lee and M.F. Hamilton : J. Acoust. Soc. Am. **94** (1993) 2876.

2P2c-10

Proceedings of Symposium on Ultrasonic Electronics, Vol. 29 (2008) pp. 245-246
11-13 November, 2008

# Optimal Time Reversal Focusing of Random Array Using an Iterative Least Squares Pre-filtering Method

Dengyong Ma and Jun Yang† (National Laboratory of Acoustics, Institute of Acoustics, Chinese Academy of Sciences)

## 1. Introduction

The time reversal mirror (TRM) has been widely used to focus ultrasound beams for the detection of defects in solids, ultrasonic medical imaging and therapy[1]. Generally, TRM methods employ uniform linear arrays to achieve the spatiotemporal focusing at a predefined position. The demands of even spacing and frequency response uniformity for the linear array lead to laborious array calibration in practical applications. On the other hand, in real environments, due to the propagation information losses, classical TRM does not behave as an inverse filter, which makes the time reversal (TR) focusing signal different obviously from the source signal. In order to obtain an optimal TR focusing, Tanter *et al.*[2] designed a spatiotemporal inverse filter derived from the reciprocal of a diagonal transfer matrix. Montaldo *et al.*[3] presented an iterative TRM method implemented by using the focusing error signal to correct TR signal iteratively. However, repetitious transmit-receive operations make these methods laborious and time-consuming for real applications.

To overcome the disadvantages of traditional TRM method, we propose an iterative least squares pre-filtering (ILS-PF) method for an optimal TR focusing. Meanwhile, a random array is employed to solve the restriction of the linear array. In this paper, the multiple pre-filters' coefficients are calculated using a least squares criterion, and then the TR signal is pre-filtered successively and reemitted again to achieve inverse filter focusing. Compared with the previous TRM methods, the presented method is simple and fast to implement. Moreover, the use of a random array permits placing transducers liberally according to real need in practice, and retrains from the array response calibration. The optimal focusing of four-element random array is conducted in a reverberation chamber. Experimental results demonstrate the effectiveness of the presented method.

## 2. the Proposed ILS-PF method

The nonreciprocal time reversal (NR-TR) model was presented by Roux e*t al.* [4] Using this model, the TR focusing of random array can be realized. Due to propagation information losses, the autocorrelation of time domain Green's function is not ideal Dirac delta function and the NR-TR focusing signal can not be recovered to the source signal as shown in the Fig.1. For an optimal TR focusing, a least squares pre-filter (LS-PF) is inserted into the emitter end to compensate the autocorrelation of Green's function so that an ideal Dirac delta function can be achieved. The signal flow graph of LS-PF method is shown in Fig.2.

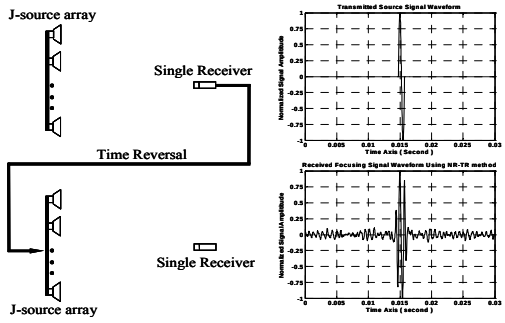


Fig.1 Received focusing signal waveform of four-element random array using NR-TR method

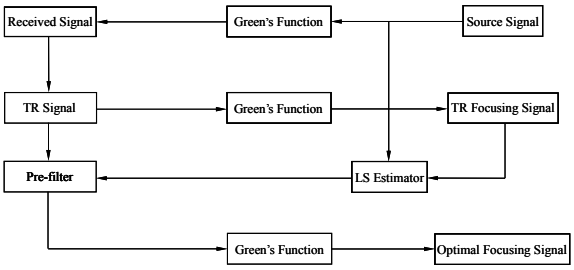


Fig.2 Signal flow graph of LS-PF method

The source signal of *J*-element array can be expressed in time domain by

$$\mathbf{S}=\left[1\ \ 1\ \ \cdots\ \ 1\right]_{1\times J}\otimes\left[s(0)\ \ s(1)\ \ \cdots\ \ s(N-1)\right]^T=\overrightarrow{\mathbf{1}_{1\times J}}\otimes\vec{\mathbf{s}}\,, \quad (1)$$

where "$\otimes$" represents the Kronecker operator. The impulse response of Green's function between *i*-th array element and receiver is defined as

$$\vec{\mathbf{g}}_i=\left[g_i(0)\ \ g_i(1)\ \ \cdots\ \ g_i(L-1)\right]^T, \quad (2)$$

and the received signal is denoted as

$$\vec{\mathbf{r}}_1=\left[r_1(0)\ \ r_1(1)\ \ \cdots\ \ r_1(N-1)\right]^T=\sum_{p=1}^{J}\mathbf{G}_{\mathrm{R},p}\vec{\mathbf{s}}\,. \quad (3)$$

where $\mathbf{G}_{\mathrm{R},p}$ is an $N\times N$ transfer matrix and given by

$$\mathbf{G}_{\mathrm{R},p}(i,j)=\begin{cases}g_p\left[(L-1)-(j-i)\right], & 0\le j-i\le L-1\\ 0, & other\end{cases}. \quad (4)$$

The TR signal is written as

$$\vec{\mathbf{r}}_{1,\mathrm{TR}}=\left[r_1(N-1)\ \ r_1(N-2)\ \ \cdots\ \ r_1(0)\right]^T=\sum_{p=1}^{J}\mathbf{G}_{\mathrm{L},p}\vec{\mathbf{s}}\,, \quad (5)$$

jyang@mail.ioa.ac.cn

where $\mathbf{G}_{\mathrm{L},p}$ is a TR transfer matrix and expressed by

$$\mathbf{G}_{\mathrm{L},p}(i,j)=\begin{cases} g_p\left[(L-1)-(i+j-N-1)\right], & 0\le i+j-N-1\le L-1 \\ 0, & other \end{cases} \quad (6)$$

The TR focusing signal is denoted as

$$\vec{\mathbf{r}}_2=\left[r_2(0)\quad r_2(1)\quad \cdots\quad r_2(N-1)\right]^T=\sum_{q=1}^{J}\mathbf{G}_{\mathrm{R},q}\sum_{p=1}^{J}\mathbf{G}_{\mathrm{L},p}\vec{\mathbf{s}}\,. \quad (7)$$

The impluse response of pre-filter is defined as

$$\vec{\mathbf{w}}=\left[w(0)\quad w(1)\quad \cdots\quad w(M-1)\right]^T. \quad (8)$$

The filtered TR signal is written as

$$\begin{aligned}\overrightarrow{\mathbf{r}_{1,\mathrm{TRF}}}&=\left[r_{1,\mathrm{TRF}}(N-1)\quad r_{1,\mathrm{TRF}}(N-2)\quad \cdots\quad r_{1,\mathrm{TRF}}(0)\right]^T\\&=\mathbf{W}_{\mathrm{F}}\sum_{p=1}^{J}\mathbf{G}_{\mathrm{L},p}\vec{\mathbf{s}}\end{aligned}, \quad (9)$$

where $\mathbf{W}_{\mathrm{F}}$ is an $N\times N$ filter response matrix given by $\mathbf{W}_{\mathrm{F}}(i,j)=\begin{cases} w\left[(M-1)-(j-i)\right], & 0\le j-i\le M-1 \\ 0, & other \end{cases}$. The optimal focusing signal for the filtered TR signal is

$$\begin{aligned}\overrightarrow{\mathbf{r}_{2,\mathrm{opt}}}&=\left[r_{2,\mathrm{opt}}(0)\quad r_{2,\mathrm{opt}}(1)\quad \cdots\quad r_{2,\mathrm{opt}}(N-1)\right]^T\\&=\sum_{q=1}^{J}\mathbf{G}_{\mathrm{R},q}\mathbf{W}_{\mathrm{F}}\sum_{p=1}^{J}\mathbf{G}_{\mathrm{L},p}\vec{\mathbf{s}}=\mathbf{W}_{\mathrm{F}}\vec{\mathbf{r}}_2\end{aligned} \quad (10)$$

Then, according to LS criterion, the filter response vector is estimated by minimizing error power function and denoted as

$$\begin{aligned}\hat{\vec{\mathbf{w}}}&=\arg\min_{\vec{\mathbf{w}}}\left\|\overrightarrow{\mathbf{r}_{2,\mathrm{opt}}}-\vec{\mathbf{s}}\right\|^2=\arg\min_{\vec{\mathbf{w}}}\left\|\mathbf{R}_{N\times M}\vec{\mathbf{w}}-\vec{\mathbf{s}}\right\|^2\\&=\left(\mathbf{R}_{N\times M}^T\mathbf{R}_{N\times M}\right)^{-1}\mathbf{R}_{N\times M}^T\vec{\mathbf{s}},\end{aligned} \quad (11)$$

where $\mathbf{R}_{N\times M}$ is a $N\times M$ data matrix and expressed by $\mathbf{R}_{N\times M}(i,j)=\begin{cases} r_2(M+i-j-1), & 0\le j-i\le M-1 \\ 0, & other \end{cases}$. To improve optimal focusing performance, an iterative LS algorithm is presented to successively estimate multiple pre-filters' coefficients. The estimated pre-filters are used to filter TR reemitted signal in series. The signal-flow graph of this ILS-PF method is illustrated in Fig.3.

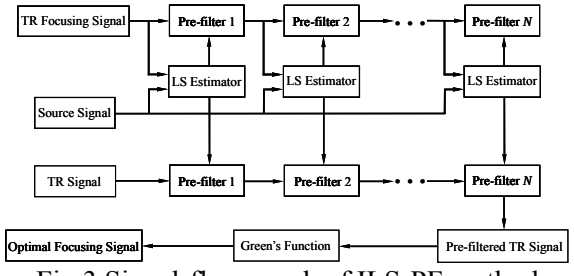


Fig.3 Signal-flow graph of ILS-PF method

## 3. Experiment results

To verify the presented ILS-PF method, we conducted the optimal focusing experiment of four-element random array in a small reverberation chamber with dimensions of 5 m (length)×4.9 m (width)×4 m (height). Four commercial speakers with power of 20 W and resistor of 4 Ω are used as emitters, and a calibrated B&K 4189 microphone is used as a receiver. The B&K 3560C multi-channel pulse analyzer is utilized to transmit/receive and record operations. A widowed 2-cycle sine impulse signal with frequency of 20 kHz is used as the source signal. The speakers are placed randomly on ground and the microphone is mounted on a bracket at a height of 1.42 m. Their corresponding plane coordinates are given as following: speaker 0 (2.92 m, 2.71 m), speaker 1 (2.10 m, 1.92 m), speaker 2 (1.92 m, 2.83 m), speaker 3 (1.56 m, 2.23 m), the microphone (2.34 m, 2.48 m). The pre-filter's length $M$ is 800 and the iterative number is 10. The experiment results of normalized signal waveforms are shown as Fig.4. Obviously, the effectiveness of the ILS-PF method is confirmed by comparing these waveforms in this figure.

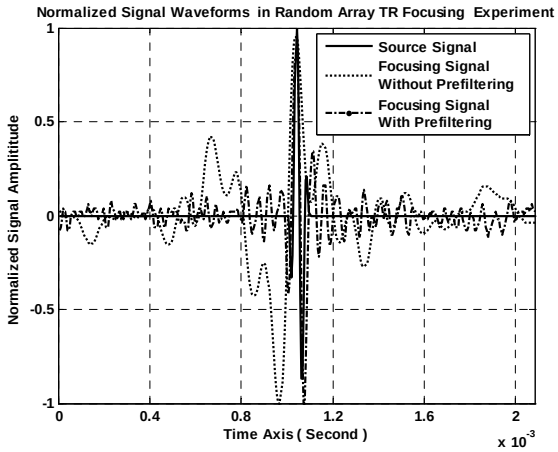


Fig.4. normalized signal waveforms of random array TR focusing experiment

## 4. Conclusion

The presented ILS-PF method can realize rapidly optimal TR focusing by three times transmissions without repetitious transmit-receive operations needed in the previous methods. On the other hand, the use of a random array permits placing transducers liberally according to real needs, which avoids the laborious array calibration.


## Acknowledgment

This research was partially supported by the National Natural Science Foundations of China under Grant No. 60535030.


## References


1. M. Fink : Phys. Today. **50** (1997) 34.
2. M. Tanter, J.-F. Aubry, J. Gerber, J.-L. Thomas, and M. Fink : J. Acoust. Soc. Am. **110** (2001) 37.
3. G. Montaldo, M. Tanter and M. Fink : J. Acoust. Soc. Am. **115** (2004) 768.
4. P. Roux, W. A. Kuperman, W. S. Hodgkiss, H. C. Song, and T. Akal : J. Acoust. Soc. Am. **116** (2004) 1009.

2P5-13

Proceedings of Symposium on Ultrasonic Electronics, Vol. 29 (2008) pp. 247-248
11-13 November, 2008

# Study of SAW Excitation Efficiency for Novel Gas Sensor Installed in "Sensor Network"

センサネットワーク用弾性表面波ガスセンサの高性能化の研究

Y.Hiraizumi , H.Aoki, T.Watanabe, J.Matsuda and M.Hikita (Kogakuin University)
平泉康志, 青木宏融, 渡邊友章, 松田潤治, 疋田光孝 (工学院大学)

## 1. Introduction

A new concept called "Sensor Network (SN)" has been proposed with the development of mobile communications system such as cellular phone, radio LAN and Bluetooth. Signals from many sensor nodes spread in a wide area are gathered to a center node by a technology similar to that used in mobile communications. ZigBee has been proposed as wireless communications medium for SN and regulated by IEEE802.15.4. We have investigated a new SAW gas sensor taking ZigBee as a basic communications medium between sensor nodes. Our proposed SAW gas sensor installed in ZigBee's SN can also monitor the hydrogen gas leakage from future fuel-cell cars.

In this study, we designed a novel structure for a SAW gas sensor. This sensor consists of three delay-lines formed on piezoelectric single crystals. Moreover, we utilize fundamental and 3rd-harmonic frequency signals generated by division and multiplication of ZigBee's 2.4GHz signal. By fundamental/3rd-harmonic frequency method, our sensor can provide large dynamic-range compared to the conventional SAW sensors. Thus this sensor can achieve compatibility between energy saving and high measurement accuracy.

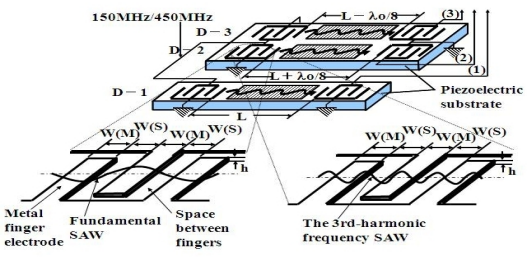


Fig. 1 Proposed SAW gas sensor for "Sensor Network" system

## 2. Novel SAW gas sensor utilizing fundamental/3rd-harmonic waves

Three delay lines whose delay lengths are different to one another are used in our sensor. As shown in **Fig.1**, one length is L for the sensing delay line (D-1). The others are L-λ0/8 and L+λ0/8 for D-2 and D-3 respectively, where λ0 is wavelength of fundamental frequency wave. D-2 and D-3 which provide the standard phases are isolated from measuring gas. We utilize both fundamental/3rd-harmonic waves to detect gas density accurately as shown in Fig.1. SAW energy concentration is about a wavelength toward depth in a substrate. Therefore, the 3rd- harmonic wave is more sensitive than the fundamental wave against change of surface propagation condition. We assume the fundamental and the 3rd- harmonic frequencies to be 150 MHz and 450 MHz, respectively. These signals are generated by 16-time division of ZigBee signal and 3-time multiplication. For instance, in the case of low density of gas, the 3rd-harmonic wave is utilized, and in the other case, fundamental-wave is utilized. By this method, the dynamic-range is extremely extended and the measurement accuracy is improved. However, achieving high excitation efficiencies for both fundamental/3rd-harmonic waves is one of our most concerning problems to be solved.

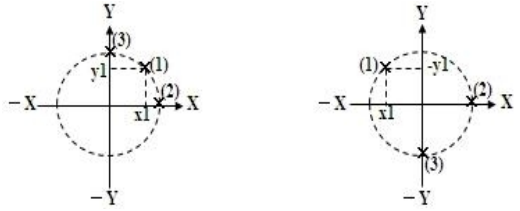


Fundamental　　3rd-harmonic

Fig. 2 Phase relations for Fig.1's three outputs

## 3. Phase relations for three outputs at fundamental/3rd-harmonic waves

**Fig.2** (a) and (b) show relations between output phases at fundamental/3rd-harmonic waves, respectively. In **Fig.(a)** assuming the phase of output (2) to be 0°, output (3) has 90° phase due to λ0/4-length difference between two delay lines. Output (1) is located in between as shown in the figure and moves along the circle depending on

am07051@ns.kogakuin.ac.jp

surface propagation condition. This phase can be measured based on the phases of output (2) and (3). Almost same relations can be achieved at 3rd-harmonic waves as shown **Fig.(b)**. Fig.1's configuration requires no oscillator like conventional ones. Moreover, phase shifts due to temperature are same for these delay lines with any kinds of piezoelectric substrates, which provides self-temperature compensation characteristics.

## 4. Evaluation and experimental results for IDT with fundamental/3rd-harmonic waves

We are designing an IDT which can excite fundamental and 3rd-harmonic waves with almost same amplitudes. We have investigated double-finger type IDT with various width of electrodes. One section schematically illustrated in **Fig.3** as an example is analyzed mathematically. An IDT consisting of multi-sections is formed by connecting this section in cascade. Previous simulation and experimental results for single-finger type IDT are shown in **Fig.4** and **Fig.5**, respectively. Our goal is to achieve much better excitation efficiency using the double-finger type IDT with fine electrode-width adjustments. Basic experimental results for the double-finger type IDT are shown in **Fig.6**. We continue to do farther investigation to improve the characteristics.

## 5. Conclusion

We proposed a novel SAW gas sensor used in sensor network. New technologies such as three-delay line structure and utilization of fundamental/3rd-harmonic waves are introduced in the sensor. We investigated double-finger IDT with various width of electrodes to achieve better excitation efficiencies for both fundamental/3rd-harmonic waves. We continue to improve IDT as well as to make a basic experiment on our sensor.


## Acknowledgment

This study was supported by the Ministry of Education, Culture, Sport, Science, and Technology of Japan.


## References


1. K.Minami, K.Takimoto, Y.Hiraizumi, and M.Hikita: Proc. of Symp. on Ultrasonic Electronics. Vol.28, 2007, pp.99-100
2. S.Ishikawa, N.Nakaso, N.Takeda, T.Mihara, Y.Tsukahara, and K.Yamanaka: The Institute of Electronics. Information and Communication Engineers. Vol.103, No.340, 2003, pp.73-78.
3. T.Mori, H.Noguchi, and T.Sato: The Institute of Electronics, Information and Communication Engineers. Vol.89, No.5, 2006, pp.430-435.


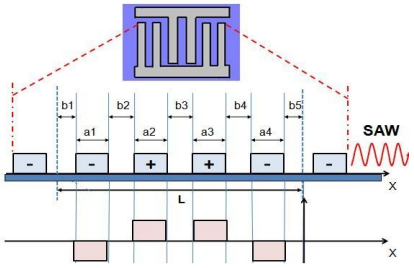


a1,a2,a3,a4: width of electrodes,
b1,b2,b3,b4,b5: interval between electrodes,
L: width of one section

Fig. 3 Investigating double-finger IDT model for SAW

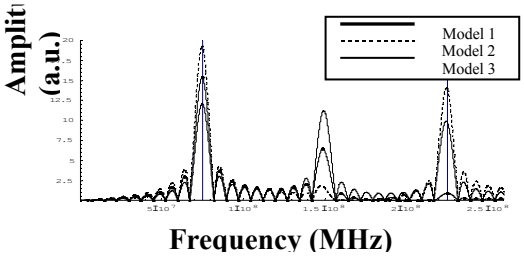


Fig. 4 Calculated excitation characteristics for 3 models of single-finger IDT

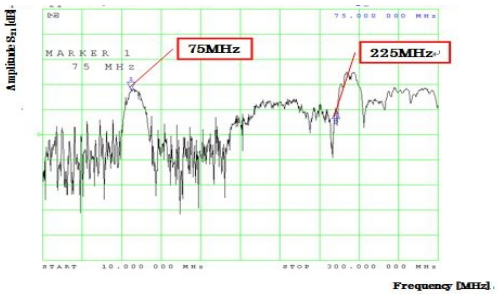


Fig. 5 One result of Fig.4's models


Fig. 6 Experimental result of double-finger IDT model

2P5-14

Proceedings of Symposium on Ultrasonic Electronics, Vol. 29 (2008) pp. 249-250
11-13 November, 2008

# Ball SAW Gas Chromatograph system for Analysis of Mixed Volatile Organic Compounds

多種類の揮発性有機化合物分析のための
ボール SAW ガスクロマトグラフシステム

Yutaro Yamamoto[1], Shingo Akao[1,2,3], Masanori Sakuma[1,2], Kentaro Kobari[1,2], Kazuhiro Noguchi[1,3], Noritaka Nakaso[1,3], Toshihiro Tsuji[1,2] , Kazushi Yamanaka[1,2] ([1] Tohoku University, [2] TOPPAN PRINTING CO., LTD., [3] JST CREST)
山本祐太朗[1], 赤尾慎吾[1,2,3], 佐久間正典[1,3], 小針健太郎[1,3], 野口和洋[2,3], 辻俊宏[1,3], 中曽教尊[2,3], 山中一司[1,3] （[1] 東北大　工; [2] 凸版印刷（株）; [3] JST CREST）

## 1. Introduction

In the field of security and energy exploitation, a wide variety of volatile organic compounds (VOC) are employed. The gas chromatograph (GC) is frequently used for the multiple-gas sensing but is not handy. We have developed the ball surface acoustic wave (SAW) sensor, where SAW with a specific width is naturally collimated and makes multiple roundtrips without diffusing by the diffraction, realizing ultra-high sensitivity. [1, 2].We also succeeded to downsize the gas separation column by micro electro mechanical systems (MEMS) technology [3,4]. Using them, we have proposed the ball SAW GC.

In this study, we show a concept of the new ball SAW GC system using two kinds of MEMS columns (Fig.1), because it is difficult to analyze both heavy and light VOCs by using one kind of column. We use an open tube(O-T) MEMS column coated with 5% phenyl 95% methylpolysilarylene for heavy VOCs and micro packed column with styrenedivinylbenzene (SDB) micro beads for light VOCs. The micro packed column is being replaced by a packed MEMS column fabricated on a silicon wafer.

## 2. Fabrication of MEMS column

We designed a column diameter of 25mm and a column length of 52cm. We touched up existing method of fabrication of MEMS column[4], channel depth was equalize by Deep Reactive Ion Etching (DRIE) using a glass as etched stopped layer. Fabrication of Packed MEMS column is shown in Fig.2 (a). Silicon wafer of 0.5mm thickness was anodically bonded to the pyrex glass of 0.5mm thickness. After that, the positive photo resist OFPR-800-LB 200cp (Tokyo Ohka) was spin coated to achieve a thickness of 6μm on the silicon wafer.

---

a8tm5630@stu.material.tohoku.ac.jp

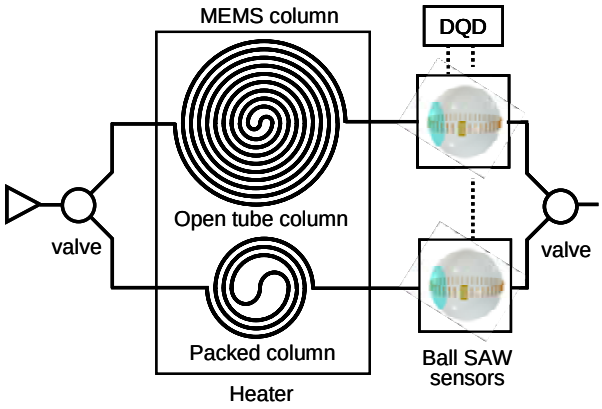


Fig.1 The concept of Dual column ball SAW GC

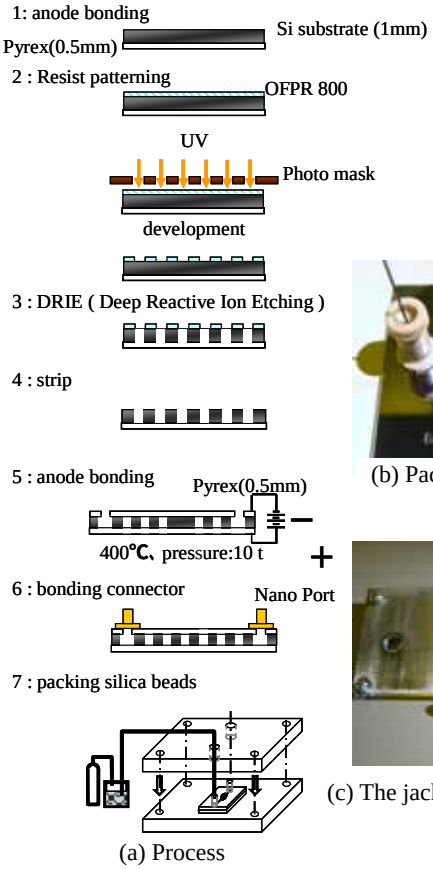


(a) Process

(b) Packed MEMS column

(c) The jacket for withstand pressure

Fig.2 Fabrication of micro separation column that uses MEMS technology

By using a photomask with a channel width of 440μm and a wall thickness of 500μm, a column pattern was exposed. The channel of 500μm depth was etched by DRIE. A pyrex cover glass with holes for the gas inlet/outlet was anodically bonded to the silicon wafer after the alignment. As joint connector to GC, Nano ports（Upchurch Scientific Inc., U.S.A.）were bonded to the column (Fig.2 b).

We fabricated the jacket made of aluminum to safely withstand the very high pressure (100atm) on the MEMS column when packing SDB particles in it (Fig.2 c). We sandwiched a silicon rubber of 0.5mm thickness between an aluminum plate and the column in order to avoid the stress concentration when we apply a pressure on the column. By using this jacket we succeeded to pack SDB particles in the column, similarly to packing in liquid chromatograph.

## 3. Result and discussion

In preliminary experiments, separation of a higher hydrocarbon (tridecance) was achieved by using an OT-MEMS column. A ball SAW sensor made of a 3.3mm Langasite (LGS) single crystal ball was driven at a frequency of a 150MHz. Poly isobutylene (PIB) with a molecular weight of 400,000 was coated on a ball SAW sensor. The signal to noise (S/N) ratio of the amplitude response of ball SAW sensor was 40 times higher than that of a thermal conductivity detector (TCD) used in the state-of-the-art desktop commercial GC (Shimadzu GC-2014)(Fig.3).

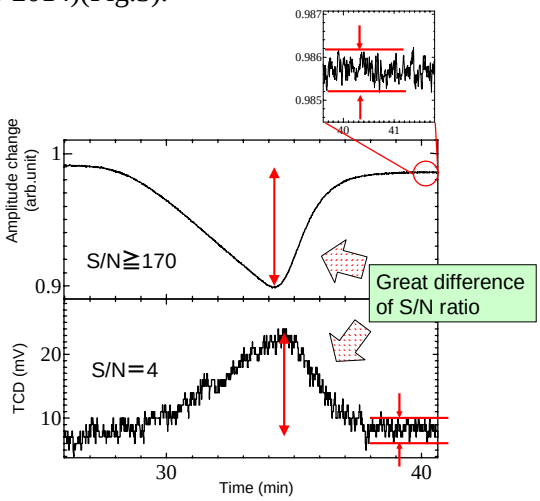


Fig.3 Excellent sensitivity of ball SAW sensor to tridecane

Then, as preliminary experiments of a packed MEMS column, we fabricated a micro packed column made of wide bore capillary of 0.53mm diameters and separation of a lower hydrocarbons were achieved by using it. Fig. 4 shows the chromatogram of the amplitude of a ball SAW sensor and a TCD. The sample gases were city gas including methane ($CH_4$), ethane ($C_2H_6$), and propane ($C_3H_8$). Ball SAW sensor was a 3.3mm LGS single crystal ball without sensitive film. The flow rate of helium carrier gas was 1.8 ml/min, the column temperature was 40℃, the amount of the injected sample was 1μl and the split ratio was 5. We detected three mixed hydrocarbons only by the amplitude change. Then, we successfully separated city gas using the very short column of 50cm length.

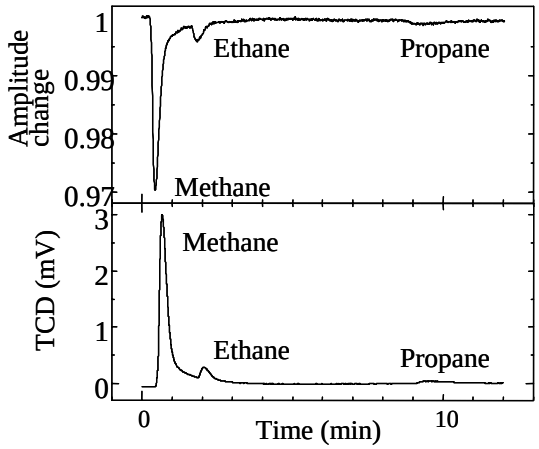


Fig.4 Response for Methane, Ethane, Propane a) Ball SAW Amplitude response b) TCD response

## 4. Conclusion

For the development of handy dual column ball SAW GC, we succeeded separation of higher hydrocarbon by OT MEMS column and showed a excellent sensitivity of ball SAW sensor compared that of a TCD. Meanwhile, lower hydrocarbons were separated by a micro packed column. Then we fabricated a packed MEMS column with MEMS technology. In the next stage, lower hydrocarbons will be analyzed by using a packed MEMS column. In the future, we introduce compact valves and pumps and develop a high performance handy GC system.

## References

[1] K. Yamanaka, H. Cho, and Y. Tsukahara: Appl. Phys. Lett. 76 (2000) 2729.

[2] K. Yamanaka, S. Ishikawa, N. Nakaso, N. Takeda, D-Y. Sim, T. Mihara, A. Mizukami, I. Satoh, S. Akao and Y. Tsukahara: IEEE Trans. UFFC. 53 (2006) 793.

[3] N. Iwata, T. Abe, T. Tsuji, T. Mihara, S. Akao, and K. Yamanaka: Jpn. J. Appl. Phys., 46 (2007) 4532.

[4] S. Akao, N. Iwata, M. Sakuma, H. Onishi, K. Noguchi, T. Tsuji, N. Nakaso, and K. Yamanaka: Jpn. J. Appl. Phys., 47 (2008) 4086.

Proceedings of Symposium on Ultrasonic Electronics, Vol. 29 (2008) pp. 251-252
11-13 November, 2008

# Development of Orientation Controlled Ball Surface Acoustic Wave Device with Optimal IDT Position and Analysis of Propagation Characteristics.

IDT 位置を最適化した方位制御ボール SAW 素子の開発と伝搬特性の評価

Takayuki Yanagisawa[1,3†], Tsuneo Ohgi[1,3], Noritaka Nakaso[1,3], and Kazushi Yamanaka[2,3]
([1]TOPPAN PRINTING CO.,LTD., [2]Tohoku Univeasity, [3]JST.CREST)
柳沢恭行 [1,3†]，大木恒郎 [1,3]，中曽尊教 [1,3], 山中一司 [1,3] （[1] 凸版印刷, [2] 東北大, [3]JST. CREST）

## 1. Introduction

We have discovered a phenomenon that sourface acoustic wave (SAW) on a ball makes ultramultiple roundtrips, [1)] and by using a piezoelectric single-crystal ball, we can efficiently excite SAW merely by fabricating an interdigital transducer (IDT) on a ball. [2)] It is known that piezoelectric crystals have anisotropic acoustic properties, and that on the Z-axis cylinder of a quartz ball, the velocity of SAW and power flow angle (PFA) change periodically. By moving an IDT close to the quartz ball, we confirmed that the SAW velocity varies with a period of 60°, in agreement with the theoretical value, and succeeded in identifying the –Y-axis-equivalent direction. [3)] On the basis of the research findings of the Z-axis cylinder route, [4)] the orientation of the quartz ball was aligned using an orientation control apparatus (OCA) so that roundtrip of SAW attenuates exponentially with the smallest disturbance. [5)] And we found that the exponential attenuation was observed at specific IDT positions distributed in a meander belt with a period of 120° in agreement with PFA period. [6)] In this study, we developed an orientation controlled ball SAW device with an IDT fabricated on the meander belt, and measured the propagation characteristics, and investigated the SAW propagation path on the ball SAW device.

## 2. Fabrication

We evaluated a degree of disturbance of SAW attenuation using the coefficient of determination ($R^2$). [6)] In φ 3.3mm orientation controlled ball SAW device, an IDT was fabricated at the position of the highest SAW velocity, where the meander belt of high $R^2$ position intersected with Z-axis cylinder of the quartz ball. The IDT had ten pairs of electrodes, with a period of 21.38μm and an aperture of 265.59μm. It was designed to create a collimated SAW beam of wavelength 21.38μm and center frequency 150MHz at the position of average velocity of the Z-axis cylinder. We measured the impulse response waveform from the ball SAW device, and the amplitude of the SAW was obtained by quadrature detection. The amplitude of the SAW in the developed device on the log scale as a function of time up to 60 turns is shown in **Fig. 1**.

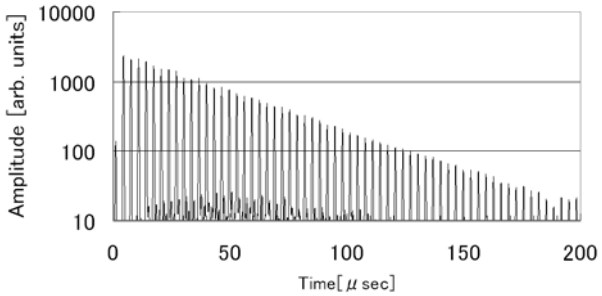


Fig. 1 Multiple roundtrip (60turns) of SAW on a quartz ball SAW device

In Fig. 1, roundtrip of SAW attenuates exponentially well in agreement with the results of proximate concave IDT. [5-6)] In Fig.1, $R^2$ obtained from the SAW amplitude up to 40 turns was 0.9986, with slightly high value compared to the result of proximate concave IDT. [6)] The center frequency of the SAW at the first turn was 151.8MHz. The experimental phase velocity of the SAW, representing the position of the IDT, was estimated from its frequency and the IDT period. The experimental phase velocity was 3245m/s. This result shows that the IDT was fabricated with an error within about 7 degrees in longitude direction by the position where SAW velocity is 3270m/sec, and the velocity is highest on the Z axis cylinder.

## 3. Observation of SAW distribution

The OCA for the measurement of the SAW distribution is shown in **Fig. 2**. The developed ball SAW device was installed in the positioning stage. The pattern of IDT of the glass plate was identical to the IDT of the ball SAW device. The impulse signal was generated with the pulser, and the SAW was generated by the IDT of the ball SAW device. The IDT of the glass plate was moved towards the center of the ball SAW device, and was in slight contact with the device. The SAW on the propagation path was received by the IDT of the glass plate, and transmitted via a matching circuit and Amp. This waveform was recorded by a digital

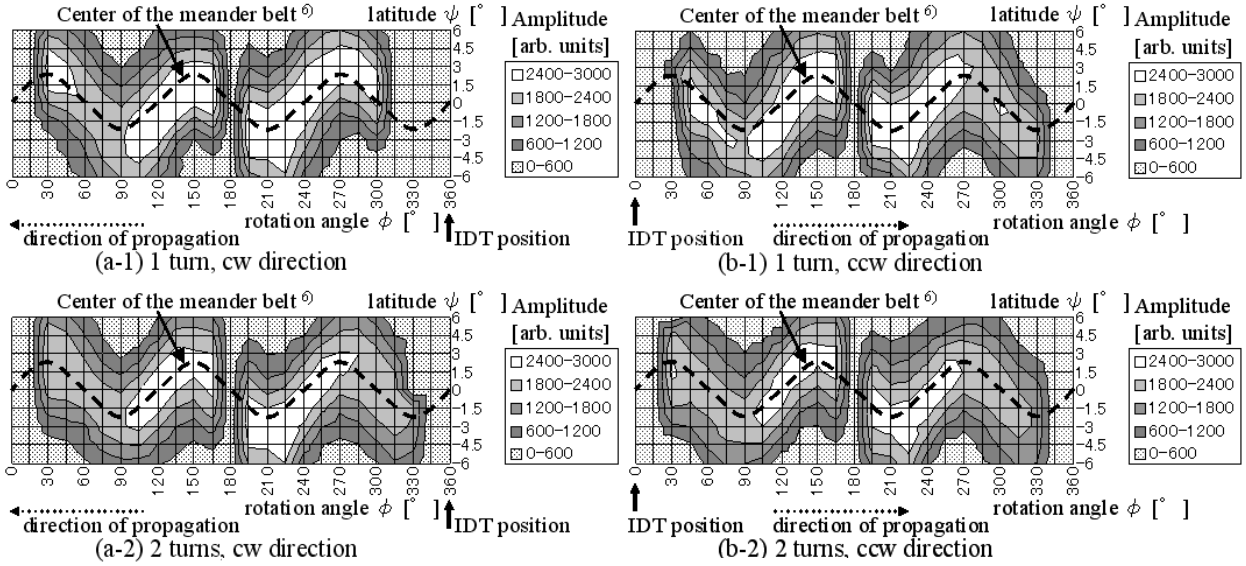


Fig. 3 Amplitude distribution of cw and ccw SAW propagation

oscilloscope and transmitted to PC and analyzed. The ball SAW device was rotated by 360° with 15° steps around the Z-axis (angle φ), and rotated around the x-axis with latitudes of 0°, ±1.5° ±3°, ±4.5°, ±6° (angle ψ) and the waveform at each step was recorded. The amplitude of the cw SAW and the ccw SAW viewed from +Z-axis were obtained from the waveform, and mapped to the SAW distribution at each turn. The cw and ccw SAW distribution at 1 and 2 turns are shown in **Fig.3**. But, because an electrical feedthrough from the IDT of the device, and the interference of cw and ccw SAW, the area near the IDT and different by 180° in φ is not shown in Fig.3. The rotation angle φ= 0° when the IDT of the device was just under that of the glass plate, and the cw rotation was defined as the positive direction. In Fig.3, amplitude of both cw and ccw propagating SAW were distributed in a meander pattern with a period of 120° around the Z-axis cylinder. This pattern was almost identical to the previously observed meander belt [6], where exponential decay of multiple roundtrip SAW was observed without disturbance when SAW was generated and detected by a proximate concave IDT located at each position in it.

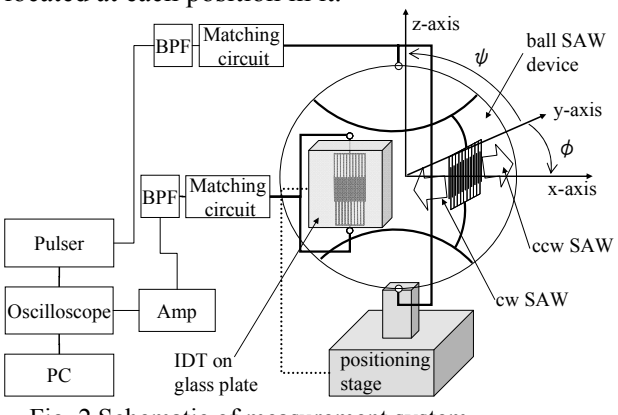


Fig. 2 Schematic of measurement system

In another ball SAW device in which IDT position was uncertain and the attenuation of SAW was disturbed, the propagation path was irregular (not shown in this paper) unlike the path of the developed device. In future work, we will make a test device where an IDT is fabricated at a well-defined position out of the meander belt, and investigate the propagation path.

## 4. Conclusions

Fabricating an IDT at an optimal position proximate IDT, we developed a orientation controlled ball SAW device in which roundtrip of SAW attenuates exponentially with a large $R^2$. The SAW propagation path was identical to the meander belt of the specific positions of proximate IDT where SAW attenuate exponentially without disturbance.

## References

1. K. Yamanaka, H. Cho, and Y. Tsukahara: Appl. Phys.Lett. 76, 2797 (2000)
2. N. Nakaso Y.Tshukahara, S. Ishikawa and K. Yamanaka: Proc. 2002 IEEE Ultrason. Symp. 47.
3. S. Kai, K. Ote, T. Mihara, T. Ohgi, N Nakaso, I. Satoh, T. Fukiura, H. Tanaka, K. Yamanaka: Jpn. J. Apply. Phys. Vol. 46, No. 7B, 2007, pp. 4723-4725
4. S. Kai, K. Ote, T. Mihara, T. Ohgi, N. Nakaso, I. Satoh, T. Fukiura, H. Tanaka, and K. Yamanaka: Jpn. J. Appl. Phys. **46**, No. 7B, (2007), 4723
5. K. Ote, T. Yanagisawa, S. Akao, N. Nakaso, and K. Yamanaka: Technical Report of IEICE US2007-46, (2007), 19-46 [in Japanese]
6. T. Yanagisawa, K. Ote, T. Ohgi, N. Nakaso, and K. Yamanaka Jpn. J. Appl. Phys.**47**, No.7, (2008), 4081

2P5-16

Proceedings of Symposium on Ultrasonic Electronics, Vol. 29 (2008) pp. 253-254
11-13 November, 2008

# Fabrication of Thin Sensitive Film of Ball SAW Sensor Using Off-Axis Spin Coating Method

軸外スピンコート法を用いたボール SAW センサの感応膜の作製

Kentaro Kobari[1, 2‡], Yutaro Yamamoto[1, 2], Masanori Sakuma[1, 2], Shingo Akao[1, 2, 3], Toshihiro Tsuji[1, 2] and Kazushi Yamanaka[1, 2] ([1]Tohoku Univ.; [2]JST,CREST; [3]TOPPAN PRINTING CO., LTD.)

小針健太郎[1, 2‡]，山本祐太朗[1, 2]，佐久間正典[1, 2]，赤尾慎吾[1, 2, 3]，辻俊宏[1, 2]，山中一司[1, 2]
（[1]東北大 工; [2]JST,CREST; [3]凸版印刷）

## 1. Introduction

It is needed to detect hazard gases at low concentration for environment assessment and security, and small portable sensor is needed for monitoring those gases. Ball surface acoustic wave (SAW) sensor is suitable for these purposes, since the ultra-multiple roundtrips (>100 turns) of the collimated SAW along an equator of the ball realizes ultra-high sensitivity [1-3]. Attenuation induced by the sensitive film coated on the roundtrip route must be low not to hinder the ultra-multiple roundtrip, and thus the film must be thin (submicron thickness) and highly uniform. However, conventional spin coating method (Fig.1) where centrifugal force is normal to surface of the route and the liquid (solution of sensitive film) might be left thick there, could not fabricate the film that fulfills these requirements. Therefore, we propose “off-axis spin coating” method and evaluate sensitive films fabricated by this method.

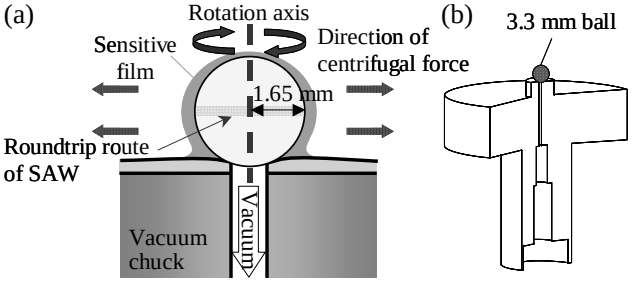


Fig.1 Schematic diagram of conventional spin coating method (a) and cross-section drawing of the vacuum chuck (b)

## 2. Principle of off-axis spin coating method

Centrifugal acceleration $g'$ that act on the rotation body is given by

$$g' = r\omega^2 \qquad (1)$$

where $r$ is the radius of rotation and $\omega$ is the angular velocity. In the conventional method, $r$ is naturally short because it equals to radius of the ball (=1.65 mm). In the off-axis spin coating method, $g'$ is larger than that in the conventional method by a longer $r$. In this method (Fig.2), a ball is clamped at an off axis position ($r$ =6.85 mm). Moreover, the direction of centrifugal force is parallel to surface of the roundtrip route, and it would promote the liquid flow away from the route, then leading to thinner film.

In this study, we applied these methods to langasite (LGS) balls with 3.3 mm diameter. Sensitive film material was polyisopurene (PIP) that has sensitivity to some chemical agents [4], and solvent was benzene. The solution concentrations were 0.2 wt% for conventional method and 1.0 wt% for both methods. Rotation speeds were 5000 rpm in conventional method and 3000 rpm in off-axis method, and then centrifugal accelerations of 46 G and 69 G acted on the route, respectively.

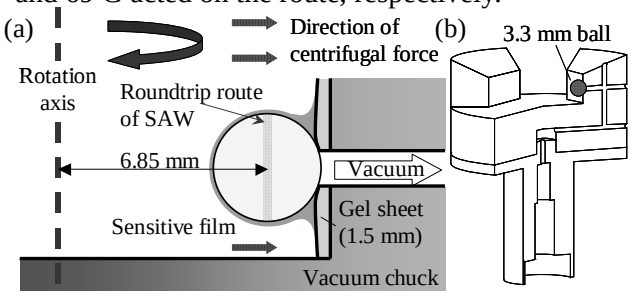


Fig.2 Schematic diagram of off-axis spin coating method (a) and cross-section drawing of the vacuum chuck (b)

## 3. Evaluation of film

The PIP films coated with 1.0 wt% solution were scratched around the route, and the thickness was measured (Fig.3). The film fabricated by the conventional method was about 100 nm thick. On the other hand, the film fabricated by the off-axis method was thinner (~ 40 nm).

Next, sensitive films were coated on two ball SAW sensors by using these methods. And the attenuation changes before and after coating were measured. These were seriously large as 800 dB/m and 3000 dB/m under the conventional method, and available roundtrips were only 2 turns and 1 turn, respectively. Under the off-axis method, in contrast, attenuations were quite low as 60 dB/m and 37 dB/m, and thus available roundtrips were 34 turns and 40 turn, respectively. Therefore the off-axis method proved useful for the multiple roundtrips.

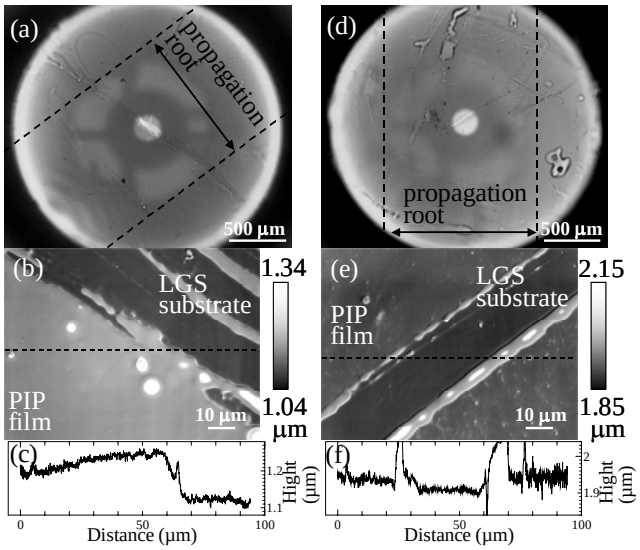


Fig.3 Optical microscope images (a),(d) and topographies (b),(e) of the PIP films coated by conventional method and off-axis method, respectively. (c),(f) Profiles along the dashed lines in (b),(e), respectively.

## 4. Evaluation of sensor coated by off-axis spin coating method

Fig.4 shows the responses of the ball SAW sensor coated by off-axis method (34tunes). The sample gases were four mixed higher hydrocarbons (hexane, heptane, octane and nonane) and a nerve gas simulant (dimethyl methylphosphonate; DMMP). [5]

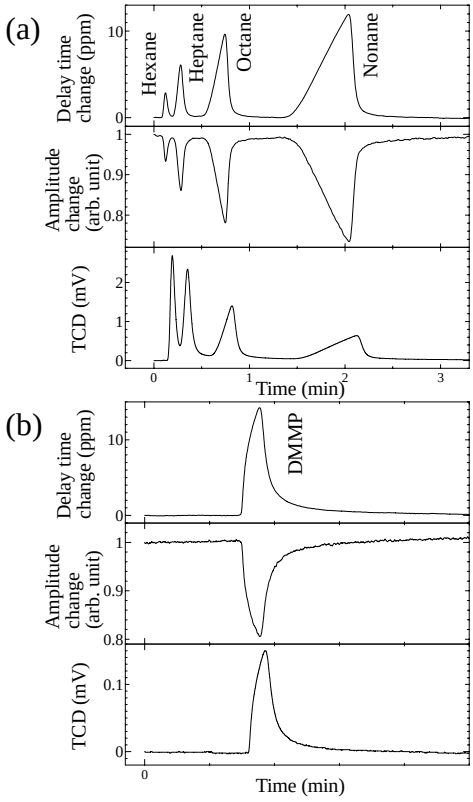


Fig.4 Responses of ball SAW sensor and TCD for detecting four mixed higher hydrocarbons (a) and DMMP (b).

The noise level was 0.02 ppm as an effect of multiple roundtrips (b). The (detection) efficiency defined as the delay time change (ppm) per 1000 ppm gas concentration of DMMP was 23.1 ppm/1000ppm, giving detection limit (sensitivity) of 0.8 ppm.

Fig.5 shows efficiencies and noise levels for DMMP in conventional (a) and off-axis method (b). Whereas efficiencies of sensors coated with 1.0 wt% PIP showed considerable variation in conventional method, these in off-axis method was highly reproducible. The film fabricated by conventional method with 0.2wt% PIP showed low attenuation and allowed 50 turns. This sensor showed low noise level, but the detection efficiency was low and the detection limit was 4 ppm larger than that in the off-axis method.

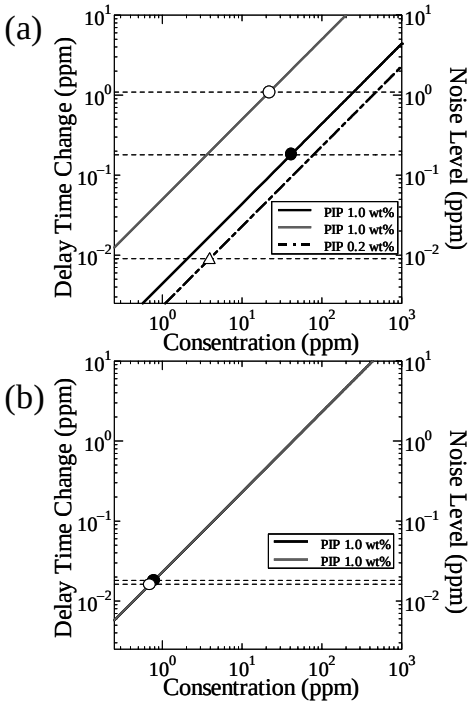


Fig.5 Detection efficiencies and noise levels of delay time change for DMMP obtained with sensors coated by conventional spin coating method (a), and off-axis spin coating method (b). Positions of slope show efficiencies and dashed lines show noise levels. Circles and triangle show detection limits.

## 5. Conclusion

Off-axis spin coating method was proposed to fabricate thin and uniform sensitive films. It enabled enhanced multiple roundtrips, and higher detection efficiency in ball SAW sensors.

**References**


1. K. Yamanaka et al.: Appl. Phys. Lett. **76** (2000) 2797.
2. K. Yamanaka et al.: IEEE Trans. Ultrason. Ferroelecotr. Freq. Control **53** (2006) 793.
3. N. Iwata et al.: Jpn. J. Appl. Phys. **46** (2007) 4572.
4. B.S. Joo et al.: Sens. Actuators B **121** (2007) 47.
5. S. Akao et al.: Jpn. J. Appl. Phys. **47** (2008) 4086.

2P5-17

Proceedings of Symposium on Ultrasonic Electronics, Vol. 29 (2008) pp. 255-256
11-13 November, 2008

# Development of Odor Display Device Using Surface Acoustic Wave
# 弾性表面波を用いた匂い供給装置の開発

Taro Monji†, Atsushi Saitoh and Toru Nomura (Facult. Eng., Shibaura Inst. of Tech.)
文字太郎，齋藤敦史，野村徹 （芝浦工大 工）

## 1. Introduction

Odor sensing system using multiple sensors with different characteristics and pattern recognition technique has studied by many researchers[1]. And, numeric conversion of odors has become possible by such systems. In the result, the demands for the virtualization of olfactory sense have risen to achieve higher reality in the field of virtual reality. There are various types of display systems that can present aural, visual and haptic information, in the field. It is also important to present olfactory information. And, "Olfactory display" will realize that.

Many approaches have been performed the development of olfactory display system, and the odor supplying method[2]. However, the device which enables to synthesize some odors, and to supplies the synthesized odor effectively, rapidly is developing.

In this paper, we describe about an odor supplying device by using surface acoustic wave (SAW) device. The principle of supplying odor is "SAW streaming phenomenon"[3]. SAW streaming is the phenomenon that the liquid on the surface of the SAW is streamed, flight or atomized toward the wave propagating direction. The movement of the liquid depends on the input power of SAW. If the SAW streaming can be used, odor supplying device which enables from the mixture of odor constituents in the liquid state to evaporation in the same motion will be achieved.

## 2. SAW streaming phenomenon

SAW devices are extensively used as analog electrical filters for mobile and wireless communications. A Rayleigh wave is a true SAW, which has an elliptical displacement on the surface due to the combination of a displacement in the direction parallel to the SAW propagation and that normal to the SAW propagation surface. The true SAW is attenuated and radiates the energy into a liquid, if the liquid is placed on the propagation path of SAW. The liquid streams to the propagation direction of SAW by the radiated longitudinal wave by the radiation of the energy. Furthermore, if SAW input voltage is increased, droplet is jet streams in propagation direction. This phenomenon is called as SAW streaming. **Fig. 1** shows the image of SAW streaming phenomenon. The radiation angle $\theta_R$ depends on the ratio at the velocity of the longitudinal wave in the liquid and the propagation velocity of SAW on the piezo-electric substrate. The angle $\theta_R$ is obtained from the following expressions.

$$\theta_R = \sin^{-1} V_L / V_R \qquad (1)$$

Here, $V_L$ is the propagation velocity of the longitudinal wave into a liquid, and $V_R$ is the propagation velocity of the SAW.

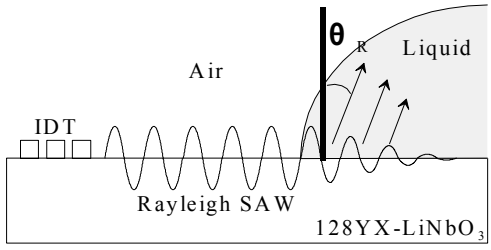


Fig 1. Schematics of SAW steaming

## 3. SAW device for liquid pump

A liquid pump was fabricated for handling odor constituents in liquid state. A 128° rotated Y-cut X-propagating $LiNbO_3$ was used as piezoelectoric substrate. An interdigital transducer (IDT) with 20 finger pairs, apertures of 0.5 mm, and a center frequency of 100 MHz was designed and fabricated on it. And, a grating reflector was also fabricated on the device for propagating SAW in one direction. All electrodes were made of Ti/Pt. **Fig. 2** shows the schematics of the device structure.

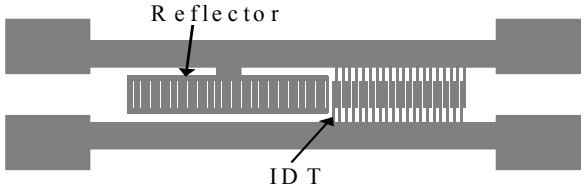


Fig.2 A device for a liquid pump

A volatile organic solvent (VOC) which was odor constituent were loaded on the surface of the device and the flow phenomenon of the liquid was observed with a digital microscope. The volume of a liquid sample was 2μl. The result of observing the flow of a liquid sample is shown in **fig.3**. In this case, the sample is 2- butanone. It was confirmed that the flow of the liquid was caused by ON/OFF of the external input to the device instantaneously. Moreover, the amplitude of input signal was about $5V_{P\text{-}P}$, when the liquid flew at a enough flow

Fig.3 The flow of acetone by SAW streaming

rate. In that time, the electric power was about 0.06W. The flowing was also observed in another samples (Nine kinds of samples were used. alcohols, ketones, and hydrocarbons, etc.).

## 4. SAW device for atomization

In the case of atomizer for VOCs, the same substrate was used as the SAW pump. Two IDTs with 20 finger pairs, apertures of 4.8 mm, and a center frequency of 32 MHz was designed and fabricated on it. And, grating reflectors were also fabricated each outside of IDTs on the device for fabricating a two port resonator. One of the surface of the propagation pass was shorted, and the other was opened. All electrodes were made of Cr/Au. The structure of the device for atomization of VOCs is shown in **fig. 4**. In the case of atomization, RF amplifiers were used, because larger input power was necessary compared with the case of liquid pump.

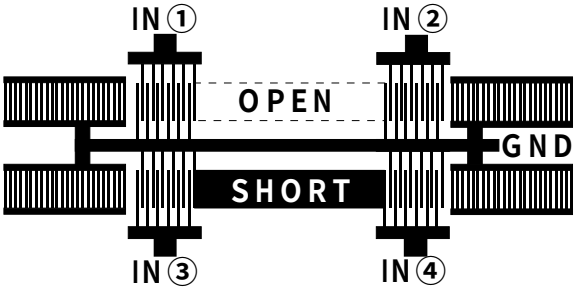


Fig.4 The device for atomization

The appearance of atomization is shown in **fig.5**. Fig.5 is the result that was loaded acetone on the shorted propagation pass. The amplitude of input signal to the SAW device was about $10.81V_{P\text{-}P}$. In the case of the experiments on the shorted channel, All VOCs used at our experiment were atomized by supplying the input signal with the amplitude about $10 \sim 12V_{P\text{-}P}$. However, some VOCs could not be atomized by using the opened surface. We thought that the result was caused by the difference of the interaction between the surface of the device and liquid sample. The contact angle of a liquid on the device surface was measured as an index of the strength of the interaction. The liquid used was pure water in the experiment. When the contact angle had been measured, it was 72 degree on the opened surface, 80 degree on the shorted surface. As a result, it is understood that the shorted surface has stronger hydrophobicity than the opened surface. It is thought that the difference of the hydrophobicity on the surface influenced the phenomenon of atomization.

Fig.5 Atomization by SAW streaming

## 5. Conclusions

Our purpose is development of a odor supplying device which have the function of mixing. The liquid pump and the atomizer for VOCs using SAW streaming was used for the attainment of our purpose. As a result, both of the pump and the atomizer satisfied a basic demand. In the future, multi-channel pumps and an atomizer will be integrated on a substrate for the operation from the mixture of odor constituents in the liquid state to evaporation in the same motion.

**Acknowledgment**
This work was financially supported by the Japan Society for the Promotion of Science, Grant-in-Aid for Exploratory Research, No-166550046.

**References**

1. J.Ide, T.Nakamoto, and T.Moriizumi,: The Technical Digest of the 13th Sensor Symposium, (1995), pp.57 – 60.
2. T.Nakamoto, T.Yamanaka and R.Matsumoto: Proc. Multisensor Fusion and Integration for Intelligent Systems 2001, (2001) pp.13-18.
3. S. Shirakawa, J. Esaki and I. Tomonaga: Jpn. J. Appl. Phys. **46** (2006) 1358.

Proceedings of Symposium on Ultrasonic Electronics, Vol. 29 (2008) pp. 257-258
11-13 November, 2008

# Micro-Laboratory on SAW piezoelectric crystal

SAW 圧電結晶を用いたマイクロ実験室

Noriyuki Yasuda†, Mitsunori Sugimoto and Jun Kondoh (Shizuoka University)
安田宣之‡, 杉本光範, 近藤淳 (静岡大学)

## 1. Introduction

Sensors using microscaled interdigitated electrode arrays (IDEs) have been investigated[1]. Generally, the IDEs are fabricated on a glass ($SiO_2$) plate. Features of the IDEs are high sensitivity and quick response. If a piezoelectric substrate, such as 128YX-$LiNbO_3$, is used as a substrate, a novel device will be realized. An interdigital transducer (IDT) which has the same structure with the IDE is capable of generating a surface acoustic wave (SAW). Liquid droplet is moved by the SAW[2]. Therefore, by fabricating the IDE sensors on the $LiNbO_3$ substrate, an integration system of a liquid sensor and a liquid actuator named the "Micro-Laboratory" is realized. First, the IDE on 128YX-$LiNbO_3$ is compared with it on $SiO_2$. Then a novel micro-laboratory on 128YX-$LiNbO_3$ is fabricated and demonstrated.

## 2. IDE sensor

The IDE sensor system is shown in Fig. 1. The IDE sensors on $SiO_2$ or $LiNbO_3$ are connected to LCR meter (HP 4285A). Fig. 2 shows impedance spectrum at 100 kHz. Samples were glycerol/water mixtures. The results indicate that the impedance is independent of substrate materials.

To evaluate the results, a simplified equivalent circuit model[1] as shown in Fig. 3 was used. The resistance of the solution, $R_{sol}$, and the dielectric capacitance, $C_{de}$, are represented following equations.

$$R_{sol} = \frac{1}{nl}\frac{1}{\kappa}\frac{2K\left(\sin\frac{\pi w}{2L}\right)}{K\left(\cos\frac{\pi w}{2L}\right)} \qquad (1)$$

$$C_{de} = nl\varepsilon\frac{K\left(\cos\frac{\pi w}{2L}\right)}{2K\left(\sin\frac{\pi w}{2L}\right)} \qquad (2)$$

Where n is the number of the interdigitated electrodes, l the length of the fingers, κ the conductivity of the solution, ε the permittivity of the dielectric, w the electrode width, L two times w and K the complete elliptic integral of the first kind.

f0730330@ipc.shizuoka.ac.jp

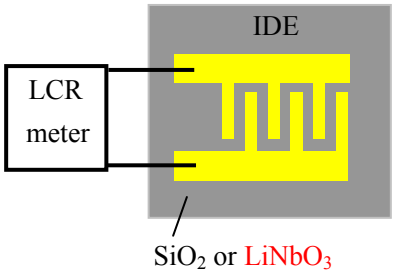


Fig. 1 IDE sensor system.

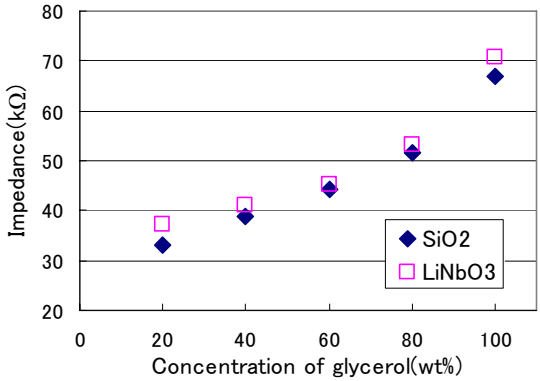


Fig. 2 Impedance spectrum of IDE sensors on $SiO_2$ and $LiNbO_3$.

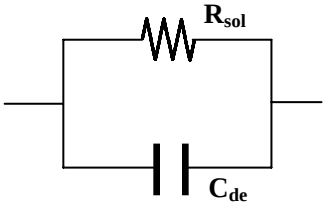


Fig. 3 Model of equivalent circuit.

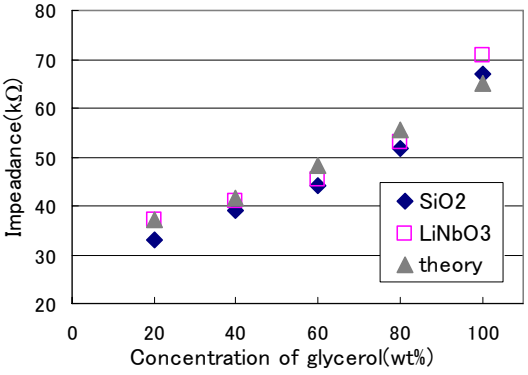


Fig. 4 Comparison of measurements with theory.

Calculated results of eqs.(1) and (2) and the results are plotted on Fig. 4. The measured results agree with the theoretical values. The similar results were obtained at different frequencies (75k, 200k, 300k, 450k, 600k, 1MHz).

### 3. Micro-laboratory on 128YX-$LiNbO_3$

3.1. SAW streaming phenomena

When a liquid is placed on a SAW propagating surface, a longitudinal wave is radiated into liquid as shown Fig. 5. The liquid vibrates, streams and jets with increasing SAW amplitude. This phenomenon is known as SAW streaming[2]. In this work, SAW streaming was used to controlled.

3.2. Mixing of liquid droplets with SAW

Micro-laboratory was fabricated on 128YX-$LiNbO_3$ as shown in Fig. 6. The SAW was generated from the IDT and the measurements were performed by the IDE sensor. Distilled water (DW) and glycerol (100 wt%) were mixed and four different concentrations (20, 40, 60, 80 wt%) of glycerol/water mixtures were produced. Fig. 7 shows the process. Fig. 8 shows the measured results using the IDE sensor at 100kHz. For comparison, the results of premixed glycerol/water mixtures (liquids were not mixed by SAW) are also plotted. In the case of without-SAW, the measurement error of the IDE sensor is large because glycerol/water mixtures have large viscosity. In the case of with-SAW, however, the measurement error was improved because liquids ware uniformly mixed by SAW.

### 4. Conclusion

The "Micro-Laboratory" as a new application on SAW piezoelectric crystal is presented. This "Micro-Laboratory" has a characteristic of which the amount of samples is by the microliter.

In the future, we will perform the study on the disposable SAW device with the three layer structure[3] for the application to the biotechnology.

### References


[1]. Peter Van Gerwen *et al.*, "Nanoscaled interdigitated electrode arrays for biochemical sensors, " Sens. & Act. B, 49, pp.73-80, 1998.

[2]. S. Shiokawa.*et al.*, "Experimental study on liquid streaming by SAW, " Jpn. J. Appl. Phys.,vol. 28, Suppl. 28-1, pp.126-128, 1988.

[3]. M. Satou *et al.*, "SAW streaming phenomen on in isotropic material/liquid/piezo-electric crystal structure, " US2007-80, pp31-35, 2007 [in Japanese].


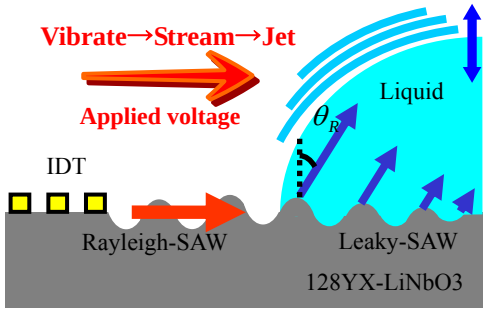


Fig. 5 Principal of SAW streaming.

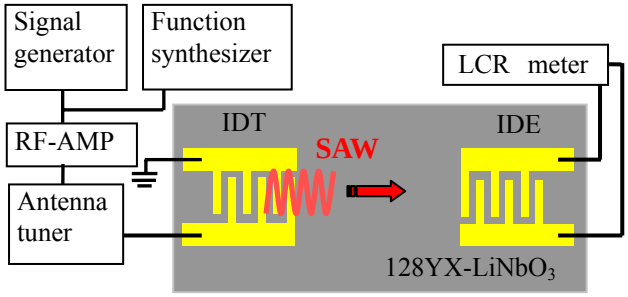


Fig. 6 Mixing and Sensing device.

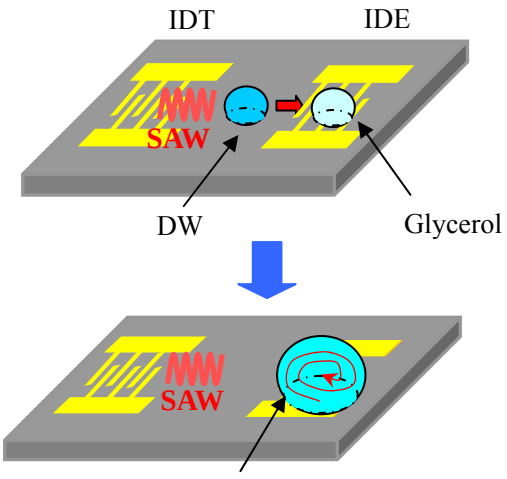


Fig. 7 Process of mixing liquids.

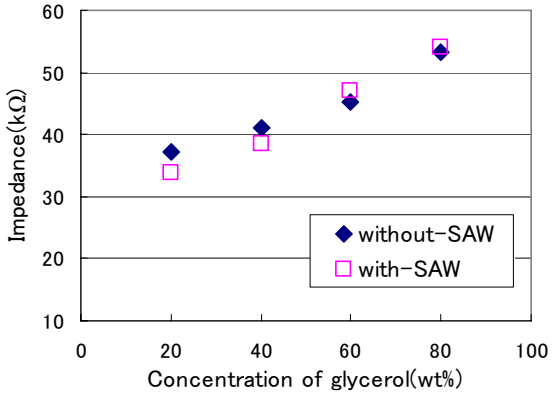


Fig. 8 Impedance spectrum of glycerol/water mixtures without-SAW and with-SAW.

2P5-19

Proceedings of Symposium on Ultrasonic Electronics, Vol. 29 (2008) pp. 259-260
11-13 November, 2008

# Measurements of standard viscosity liquid using shear horizontal surface acoustic wave sensor

横波型弾性表面波を用いた粘度標準液の測定

Takeshi Morita†, Mitsunori Sugimoto and Jun Kondoh (Shizuoka Univ.)
森田武‡，杉本光範，近藤淳 （静岡大学）

## 1. Introduction

A liquid-phase sensor is realized with a shear horizontal surface acoustic wave (SH-SAW) device. As the SH-SAW sensor can detect liquid properties, such as conductivity, dielectric constant, viscosity and density, it has great attractions for liquid evaluations.

In previous works[1], we found that sensor responses for viscosity standard liquids depend on a sensor frequency due to viscoelastic properties of the liquids. In this paper, we report theoretical and experimental consideration about viscosity standard liquids. The SH-SAW sensors with different frequencies are used. A simple viscoelastic model is applied to explain the experimental results.

## 2. Theory

### 2.1 Maxwell model

A viscoelastic liquid has viscous and elastic properties. The liquid is modeled by a Maxwell model[2], as shown in Fig. 1. Maxwell model is expressed in series with spring and dashpot. Behavior of the Maxwell model depends on frequency: at low frequency, it acts a viscous liquid and spring can be ignored. When the frequency increases, influence of the spring appears. In this paper, theoretical equation for the SH-SAW sensor is derived on the basis of the Maxwell model.

### 2.2 Theoretical formula

Relationship between stress, $T$, and strain, $S$, for the Maxwell model is expressed in eq. (1).

$$\frac{\partial S}{\partial t} = \frac{1}{\eta} T + \frac{1}{G}\frac{\partial T}{\partial t} \qquad (1)$$

Here, $\eta$ is viscosity and $G$ is a shear module.

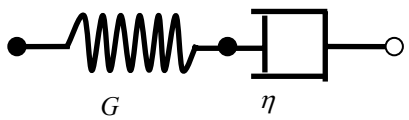


Fig.1 Maxwell model

When time variation of strain is assumed as $e^{j\omega t}$, the relationships between stress and strain are exchanged as following equation.

$$T = \frac{j\omega\eta}{1 + j\omega\tau} S \qquad (2)$$

Here, $\omega$ is the angular frequency and $\tau$ is a relaxation time $(\tau=\eta/G)$. Equation (2) indicates: when $\omega\tau<1$, behavior of the Maxwell model behaves like viscosity fluid. On the other hand, when $\omega\tau>1$, it acts as viscoelasticity.

Surface acoustic impedance, $Z$, for the Maxwell model is given from eq. (2) as follows[2].

$$Z = \begin{bmatrix} -j\frac{\mu}{V}\sqrt{1-\frac{\rho V^2}{\mu}} & 0 & \frac{\mu}{V} \\ 0 & \frac{\omega\eta}{V}\sqrt{1-\frac{\rho V^2}{\mu}} & 0 \\ \frac{\lambda}{V} & 0 & -j\frac{\lambda+2\mu}{V}\sqrt{1-\frac{\rho V^2}{\lambda+2\mu}} \end{bmatrix}$$

Where $V$ is the propagation velocity, and $\rho$ is the density of sample liquid, $\mu$ and $\lambda$ are shown in Ref. [2]. By substituting imaginary part of $Z$ into eq. (3), velocity shift ($\Delta V/V$) for the Maxwell model, eq. (4), is derived.

$$\frac{\Delta V}{V} = -A(v_n \cdot Z_i \cdot v_n + v_n \cdot Z_i' \cdot v_n) \qquad (3)$$

$$\frac{\Delta V}{V} = -A'\left[\frac{1}{V}(M_1^2 + M_2^2)^{\frac{1}{4}}\sin(M_3) - \sqrt{\frac{\omega\rho'\eta'}{2}}\right] \qquad (4)$$

Here,

$$M_1 = \frac{(\omega\eta)^2 - (\omega^2\eta\tau)^2}{\{1-(\omega\tau)^2\}^2 + (2\omega\tau)^2} + \frac{\omega^2\rho\eta\tau V^2}{1+(\omega\tau)^2}$$

$$M_2 = \omega\eta\left(\frac{\rho V^2}{1+(\omega\tau)^2} - \frac{2\omega^2\eta\tau}{\{1-(\omega\tau)^2\}^2 + (2\omega\tau)^2}\right)$$

$$M_3 = \frac{1}{2}\tan^{-1}\left(\frac{M_2}{M_1}\right)$$

Where $\rho'$ and $\eta'$ are density and viscosity of a reference liquid, and $A$ and $A'$ are material constants.

---

f0730329@ipc.shizuoka.ac.jp

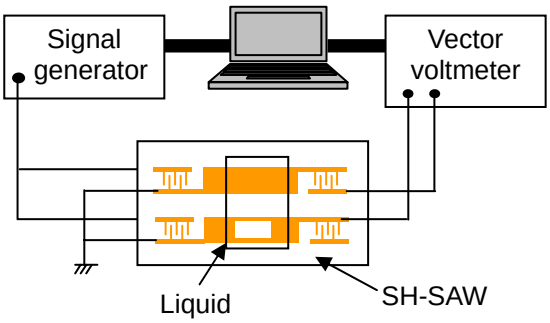


Fig.2 Measurement system

## 3. Experimental

A vector voltmeter measurement system (see Fig. 2) was used to measure viscosity standard liquids. A signal from a signal generator was fed to the SH-SAW sensor. The output from the sensor which is phase shift was monitored using the vector voltmeter.

In this paper, a 36YX-$LiTaO_3$ substrate was used as an SH-SAW sensor substrate. The center frequencies of the SH-SAW sensors were 30, 50, and 100 MHz, respectively.

## 4. Results and discussion

Using the SH-SAW sensors, we measured the viscosity standard liquids. The experimental results are shown in Fig. 3. The abscissa is square root of density and viscosity products. The ordinate is the velocity shift.

For a Newtonian fluid, the velocity shift is proportional in $\sqrt{\rho\eta}$ . At low $\sqrt{\rho\eta}$ , sensor responses are proportional in $\sqrt{\rho\eta}$ . However they are saturated with increasing $\sqrt{\rho\eta}$ due to viscoelastic effect.

As the shear modulus of the viscosity standard liquid is unknown, it is difficult to compare eq. (4) with the experimental results. So, we calculate G using eq. (4). These results are shown in Fig. 4. The abscissa is square root of density and viscosity products. The ordinate is the shear elasticity. The shear moduli are proportional in $\sqrt{\rho\eta}$ and dependent on frequency.

## 5. Conclusions

Using the SH-SAW sensors with different frequencies, we measured the viscosity standard liquids. From the results, we found frequency dependency of the viscosity standard. We found that velocity change depends on the sensor frequency.

Using eq. (4), we estimated the shear moduli. First we tried to compare eq. (4) with experimental

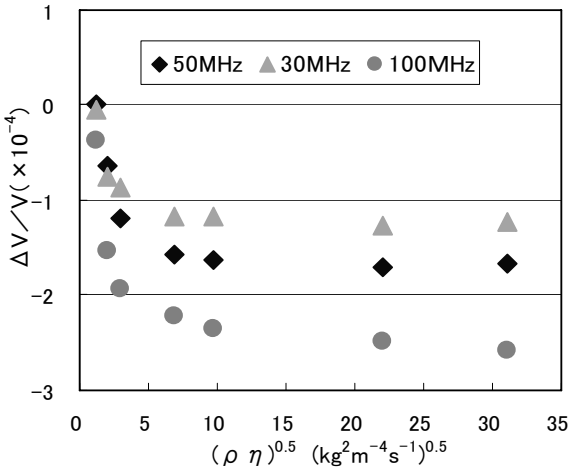


Fig.3 Measurement value for changing the center frequencies

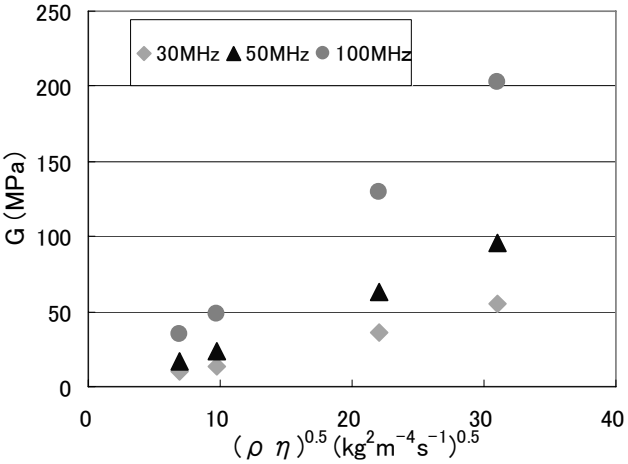


Fig.4 Shear elasticity value for changing the center frequencies

results. However, the shear moduli of the samples at the measured frequencies have not been reported. Therefore, we estimated the shear moduli substituting the results and material constants of sample density and viscosity.

In this paper, we assumed that the density and viscosity of samples are independent of frequency. In future work, simultaneous estimation method of density, viscosity and the shear moduli will be established.

## Acknowledgement

This work was partially supported by NEDO and HFSPO.

## References

[1]. T. Morita et al.: Autumn Meeting of Acoustical Society of Japan, 2-P-15 (2007).
[2]. J. Kondoh: Doctor Thesis, Shizuoka University (1995) (in Japanese)

Proceedings of Symposium on Ultrasonic Electronics, Vol. 29 (2008) pp. 261-262
11-13 November, 2008

# Numerical Simulations of Acoustic Cavitation Noise with Temporal Variation of the Number of Bubbles

気泡数の変動を取り入れたキャビテーション・ノイズの数値シミュレーション

Kyuichi Yasui†, Toru Tuziuti, Judy Lee, Teruyuki Kozuka, Atsuya Towata, and Yasuo Iida (AIST)
安井久一†，辻内　亨，Judy Lee，小塚晃透，砥綿篤哉，飯田康夫（産総研）

## 1. Introduction

Pulsating bubbles under intense ultrasound emit acoustic waves especially at the end of the bubble collapse when shock wave is emitted into the liquid.[1] The noise due to acoustic cavitation is called acoustic cavitation noise. The frequency spectrum of acoustic cavitation noise consists of the driving frequency, its harmonics, subharmonics, ultraharmonics, and the continuum called "white noise".[2] As the origin of the "white noise", two ideas have been proposed. One is the acoustic signals due to the shock-waves emitted from bubbles.[3] The other is the acoustic waves radiated from chaotically pulsating bubbles.[4] In the present study, the origin of the "white noise" is discussed based on the numerical simulations with the temporal variation of the number of bubbles.

Ashokkumar et al.[5] measured the acoustic cavitation noise in pure water and aqueous SDS (surfactant) solutions irradiated by 515 kHz ultrasound. The intensity of the "white noise" is much stronger in pure water than that in low concentration (0.5-2 mM) SDS solutions. Furthermore, the intensity of ultraharmonics is much stronger in pure water than that in low concentration SDS solutions.

## 2. Model

The pressure ($p$) of an acoustic wave radiated from a pulsating bubble is approximately expressed by Eq. (1).[6]

$$p = \rho\left(R^2\ddot{R} + 2R\dot{R}^2\right)/r \qquad (1)$$

where $\rho$ is the liquid density, $R$ is the bubble radius, the dot denotes the time derivative, and $r$ is the distance from a bubble.

Here we consider a bubble cloud in which bubbles are spatially uniformly distributed. Furthermore, the ambient bubble radius, which is defined as the radius of a bubble when ultrasound is absent, is assumed to be the same for all the bubbles. Then, the pressure ($P$) of acoustic waves radiated from the bubbles in the bubble cloud is expressed by Eq. (2).

$$P = \sum_{i=1}^{N} p_i = \rho\left(R^2\ddot{R} + 2R\dot{R}^2\right)\left(\sum_{i=1}^{N} 1/r_i\right) \qquad (2)$$

where the sum is for all the bubbles in the bubble cloud, $p_i$ is the pressure of an acoustic wave radiated from the bubble numbered $i$, and $r_i$ is the distance from the bubble numbered $i$. When the observation point (the position of a hydrophone) is in the bubble cloud, Eq. (2) is expressed by using the "coupling strength" ($S$) of the bubble cloud defined by Eq. (3).[7]

$$S = \sum 1/r_i \qquad (3)$$

$$P = S\rho\left(R^2\ddot{R} + 2R\dot{R}^2\right) \qquad (4)$$

Next, we will discuss the response of the hydrophone. In the experiment of Ashokkumar et al.,[5] the hydrophone has a flat, usable response up to 10 MHz. Such hydrophone characteristics can be approximately modeled by a low-pass filter expressed by Eq. (5).[6]

$$\ddot{U} + 2\gamma\pi f_0\dot{U} + 4\pi^2 f_0^2 U = P(t) + p_S(t) \qquad (5)$$

where $U$ is the hydrophone signal, $\gamma$ is the coefficient for damping, $f_0$ is the cut-off frequency of the hydrophone, $P(t)$ is the instantaneous pressure of acoustic waves radiated from bubbles given by Eq. (4), and $p_s(t)$ is the instantaneous pressure of the driving ultrasound.

The model of the bubble pulsation taking into account the bubble-bubble interaction has been described in Ref. 7.

As a bubble has its own lifetime due to its fragmentation or coalescence, the number of bubbles may vary with time. As the number of bubbles changes, the "coupling strength" defined by Eq. (3) changes because it is a function of the number of bubbles.[7] Thus the temporal fluctuation of the number of bubbles can be modeled by the random variation of the "coupling strength" as Eq. (6).

---

†e-mail address: k.yasui@aist.go.jp

$$S(t+T) = S(t) + (\Delta S) r_n \qquad (6)$$

where $S(t+T)$ and $S(t)$ are the "coupling strength" at time $t+T$ and $t$, respectively, $T$ is the acoustic period, $\Delta S$ is the maximum amplitude of the temporal fluctuation of $S$, and $r_n$ is the random number generated by a computer from -1 to 1. The change of $S$ by Eq. (6) is once an acoustic cycle.

## 3. Results and discussions

In the present study, numerical simulations of the acoustic cavitation noise have been performed under the experimental condition of Ashokkumar et al.[5] According to Lee et al.[8], the ambient radii of sonoluminescing bubbles in pure water range from 2.8 – 3.7 μm at 515 kHz.

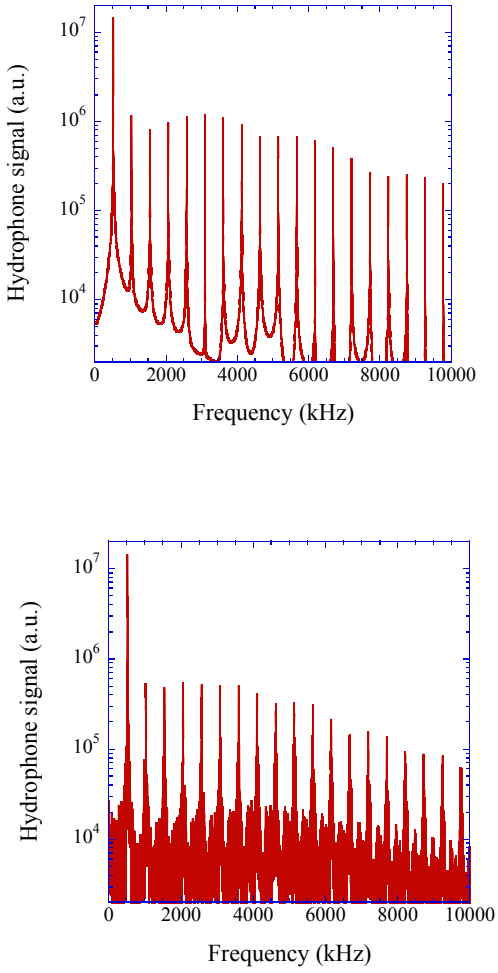


Fig. 1 The calculated frequency spectra of the acoustic cavitation noise without (above) and with (below) the temporal fluctuation of the number of bubbles.

In Fig.1, the calculated frequency spectra of the acoustic cavitation noise have been shown without (the upper graph)) and with (the lower graph) the temporal fluctuation of the number of bubbles when the acoustic pressure is 2.6 bar and the ambient bubble radius is 3 μm. The initial coupling strength is $S_0=10^4$ m$^{-1}$, which corresponds to the number of bubbles of about 50 at around an anti-nodal plane in a cylinder of 30 mm in diameter. For the lower graph, the amplitude of the temporal fluctuation of the coupling strength is 0.2 $S_0$.

With the temporal fluctuation of the number of bubbles, the continuum (white noise) is much stronger than that without it. Thus it is concluded that the temporal fluctuation of the number of bubbles results in the generation of the white noise.

According to the present numerical simulations, the intensity of the white noise is higher for higher acoustic pressure, larger number of bubbles, and larger amplitude of the temporal variation of the number of bubbles. Furthermore, the white noise is stronger for the ambient bubble radius ($R_0$) of 3 μm which is typical in pure water than that for $R_0$=1.5 μm which is typical in low concentration SDS solutions.[8]

## 4. Conclusion

Numerical simulations of acoustic cavitation noise have revealed that the white noise could be generated by the temporal fluctuation of the number of bubbles. The intensity of the white noise increases as the acoustic amplitude, the number of bubbles, and the amplitude of the temporal variation of the number of bubbles increase.

## References


1. T.J.Matula, I.M.Hallaj, R.O.Cleveland, L.A.Crum, W.C.Moss, and R.A.Roy, J.Acoust.Soc.Am. **103** (1998) 1377.
2. P.-K.Choi, Y.Kaneko, and T.Meguro, Jpn.J.Appl.Phys. **47** (2008) 4111.
3. E.A.Neppiras, Phys.Rep. **61** (1980) 159.
4. V.I.Ilyichev, V.L.Koretz, and N.P.Melnikov, Ultrasonics **27** (1989) 357.
5. M.Ashokkumar, M.Hodnett, B.Zeqiri, F.Grieser, and G.Price, J.Am.Chem.Soc. **129** (2007) 2250.
6. S.Luther, M.Sushchik, U.Parlitz, I.Akhatov, and W.Lauterborn, in *Nonlinear Acoustics at the Turn of the Millennium: ISNA15*, edited by W.Lauterborn and T.Kurz, AIP Conf.Proc.No. 524 (AIP, New York, 2000), p.355.
7. K.Yasui, Y.Iida, T.Tuziuti, T.Kozuka, and A.Towata, Phys.Rev.E **77** (2008) 016609.
8. J.Lee, M.Ashokkumar, S.Kentish, and F.Grieser, J.Am.Chem.Soc. **127** (2005) 16810.

Proceedings of Symposium on Ultrasonic Electronics, Vol. 29 (2008) pp. 263-264
11-13 November, 2008

# Dependence of Sonochemiluminescence on Pulsed-wave Conditions at 1 MHz

１MHz ソノケミルミネセンスのパルス波依存性

Ayako Ozawa †and Pak-Kon Choi (Dept. of Phys., Meiji Univ.)
小澤綾子‡，崔博坤 （明大理工）

## 1. Introduction

Pulsed or tone-burst ultrasound is widely used in medical diagnosis and in the study of various effects of cavitation. Previous study have shown that cavitation by pulsed ultrasound can be enhanced by an appropriate choice of pulse length and pulse repetition frequency. [1-3] In this paper, we report the enhancement of multibubble sonochemiluminescence (SCL) intensity in luminol solution using pulsed ultrasound at 987 kHz. The intensity of SCL from luminol solution is larger by two orders of magnitude than that of the sonoluminescence (SL). The SCL intensity depends on the gas content, and few studies have been done on the dependence on the gas content. We have measured sonochemiluminescence (SCL) from luminol solution with various gas contents and various pulse conditions.

## 2. Experiments

Luminol solutions, air-saturated and degassed to 30%, 50%, 70% of saturation, were irradiated in a rectangular quartz cell of 200 mm in length, 130 mm in width, and 150 mm in height. A piezoceramic transducer was bonded to the bottom of the cell. Pulsed ultrasound at 987 kHz with various duty ratios was excited by using a function generator and a power amplifier. The number of pulse-on cycles was fixed to 50, 500, and 5000, and the duty ratio was changed in the range from 0.1 to 100. The duty ratio is defined as pulse-off cycles divided by pulse-on cycles, and is represented by "*D*" hereafter. SCL was measured with a photomultiplier cooled to -20℃, and the signal was monitored with a photon counting system. The SCL signal was detected over 20 seconds, and averaged to obtain the SCL intensity per a finite duration time. The electric input power was in the range from 19 to 121W for continuous wave.

## 3. Results and discussion

Figure 1 shows the results of SCL measurements for the degree of air saturation of 50 % as a typical case. The SCL intensity relative to that for

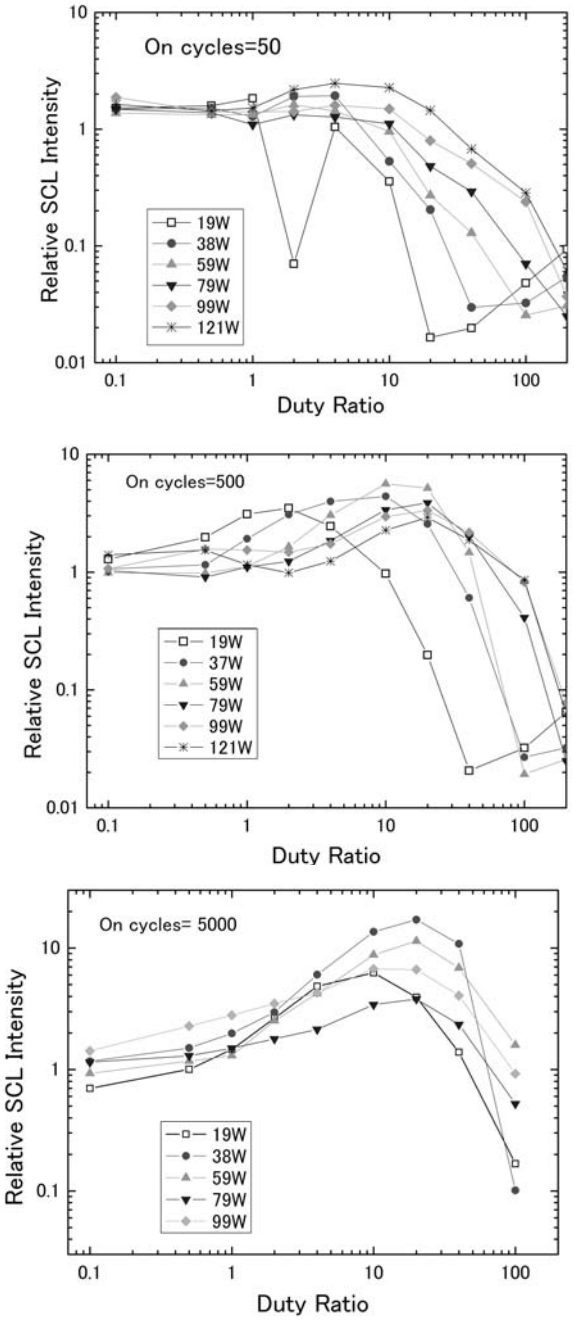


Fig.1. Relative SCL intensity as a function of duty ratio (= off cycle number/on cycle number) for (a) on-cycles=50, (b) on-cycles=500, and (c) on-cycles= 5000.

continuous wave was plotted as a function of duty ratio. Figure 1 (a), (b), and (c) represents the results for pulse on-cycles of 50, 500 and 500, respectively. For the case of on-cycles=50, the relative intensity is 1-2 up to the duty ratio *D*=10 and decreases over *D* =10. For the cases of on-cycles=50 and 500, the maximum relative intensity is 5.6 at D=10 and 17 at D=20, respectively, and *D* value at the peak increases as increasing on-cycles. Ultrasonic power dependence is monotonous for on-cycles=50, and complicated for other cases.

The results for other degrees of air saturation exhibited a similar tendency to have intensity maxima but with different peak values at different *D* values. Figure 2 summarizes the peak value of the relative SCL intensity at *D* =20 for each case of on-cycles. The relative SCL intensity takes a maximum at the degree of about 50 %.

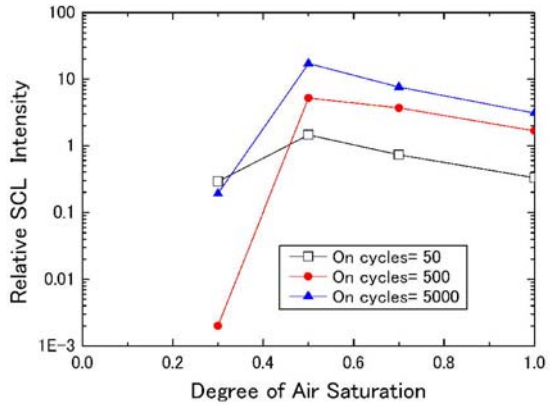


Fig. 2. Maximum relative SCL intensity vs. degree of air saturation for the cases of on-cycles = 50, 500 and 5000.

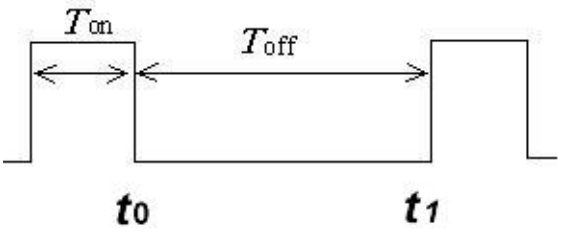


Fig.3. Time sequence of pulse-on and pulse-off times.

Enhancement by pulsed waves have been explained by Flynn and Church [4]. There is a size distribution of bubble nuclei that can grow into transient cavities at a given frequency and acoustic pressure. Only nuclei in a much narrower range of this size distribution grow into transient cavities that contribute to the cavitation activity. The bubbles of initial size in the range of 0.1 – 4 μm show large expansion ratio of $R_m/R_0$ at 7.5 atm and 1 MHz. Here $R_m$ and $R_0$ indicates maximum and initial radius, respectively. During pulse-off time bubbles shrink via gas diffusion into liquid. If the bubble sizes are in this range at the time of $t_1$, indicated in Fig.3, they can contribute to the cavitation activity in the next pulse-on time. Large expanded bubbles fragment to generate many daughter bubbles which contribute to the enhancement of SCL.

In Figs. 1 (a), (b), (c), the SCL intensity decreases at large *D* value where bubble radius may decrease below the critical value of the efficient radius range. Here we assume that the value of *D* =100 corresponds to the critical radius of 0.1 μm. Pulse off times ($T_{0ff}$) calculated from *D* =100 are (a) 5 ms, (b) 50 ms, (c) 500 ms in the three cases. We can roughly estimate the bubble size ($R_x$) at $t_0$ based on the calculation of Epstein and Plesset [5]. A bubble of radius $R_x$ at $t_0$ shrinks to the critical value during the time $T_{off}$. They obtained the value of about 2 s for a bubble of 10 μm for complete dissolving in the case of gas saturation degree of 50 %. Since this time of dissolution is proportional to the square of the initial radius, we can obtain the values of 0.5, 1.5, and 5 μm as $R_x$. This suggests that larger pulse-on time makes a larger bubble size at the end of the pulse-on time. This may resulted by bubble coalescence in long pulse-on time.

The experimental results in the case of saturation degree of 100 % showed that enhancement was observed only at on-cycles= 5000 and low acoustic power. In case of the saturation degree of 30 %, enhancement was observed only at on-cycles= 50 and SCL intensity almost vanishes at *D*= 10. Bubbles do not grow compared to the higher saturation degree because of less rectified diffusion of gas.

**References**


1. T. G. Leighton, “The acoustic bubble” Academic, 1994, p.504.
2. P. Ciuti, N. V. Dezhkunov, G. Iernetti and A. I. Kulak, Ultrasonics, 36(1998)569.
3. P.- K. Choi, Y. Kaneko and T. Meguro, Jpn. J. Appl. Phys. 47(2008)4111.
4. H. G. Flynn and C. C. Church, J. Acoust. Soc. Am.**76** (1984)505.
5. P. S. Epstein and M. S. Plesset, J. Chem. Phys. **18** (1950)1505.

2P6-3

Proceedings of Symposium on Ultrasonic Electronics, Vol. 29 (2008) pp. 265-266
11-13 November, 2008

# Spatio-Temporal Separation of Na-atom Emission and Continuum in Sonoluminescence

ソノルミネセンスにおけるNa発光と連続スペクトル成分の時間空間分離

Pak-Kon Choi and Shogo Abe (Dept. of Physics, Meiji University)
崔 博坤, 阿部将吾 （明大理工）

## 1. Introduction

Multi-bubble sonoluminescence (MBSL) spectrum from NaCl solutions consists of a continuum extending into the UV region and asymmetrically-broadened lines of sodium atoms [1-3]. The origin of the continuum emission is suggested to be bremsstrahlung or blackbody radiation or excited-state molecular emission. We measured the SL spectra of sodium atom emission from ethanol-doped NaCl solutions [4] and showed the quenching and broadening of the Na line upon adding ethanol, which suggested that the sodium atom emission occurs in the gas phase inside bubbles.

In single-bubble SL from NaCl solutions, only the continuum was obtained and the sodium atom emission was not observed [5]. The difference in the results by MBSL and SBSL brings a question that the continuum and sodium atom emission occur in the same bubble or different bubbles. We report here a spatio-temporal separation of the sodium atom emission and continuum in MBSL from argon-saturated NaCl solutions.

## 2. Experiment

We took photographs of MBSL from 2M NaCl aqueous solution using a digital camera (Nikon D70S). The Red-Green-Blue components of the photographs were digitally splitted using a “Image J” software for spatial separation of the continuum and Na emission. The blue component is assumed to be corresponding to the continuum and the red component to the Na emission at 590 nm. The solution was contained in a cylindrical glass cell with 80 mm in diameter and 120 mm in height. A sandwiched transducer was bonded to the bottom of the cell. A continuous signal of 138 kHz was amplified by a power amplifier (NF Circuit Design, HAS4014) and impedance matched by a transformer. Applied voltage to the transducer was 10 – 40 Vpp.

For temporal separation of the continuum and Na emission, we measured the SL pulse spectrally isolated. SL was divided into two spectral components above 500 nm and below 500 nm by using dichroic mirror. Each component was detected with two photomultipliers and displayed with a fast sampling oscilloscope (4 GS/s, Agilent DSO5052A) at the same timing as ultrasound period.

## 3. Results and discussion

Figure 1(a) shows the photograph of SL (full colored in the web version) viewed from the

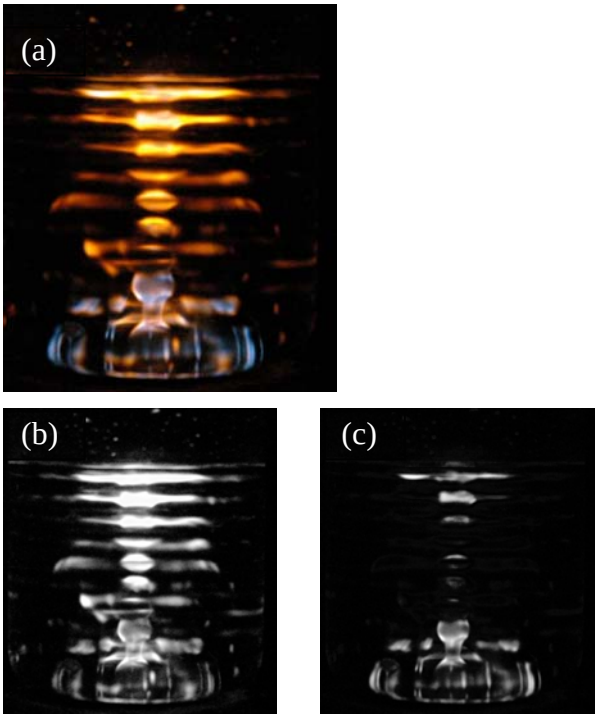


Fig.1 (a): Photograph of sonoluminescence from NaCl solutions at the voltage of 20 Vpp. Red component (b), and blue component (c) of the photo (a).

cylindrical side of the cell at an applied voltage of 20 Vpp. Both orange-colored region and white region are seen in the photograph. At lower voltage only orange-colored SL appeared near the center axis of the cylindrical cell. The orange-colored region expands outward as the applied voltage increases. Red and blue components of the Fig. 1(a) are digitally processed by a software and illustrated in Figs. 1(b) and 1(c), respectively. The red component corresponding to the Na emission spreads over a wide region compared with the blue component which corresponding to the continuum. The regions which emit continuum are near the bottom of the cell and below the surface of the solution. Sound pressure is probably high in these regions. At higher applied voltages the 'continuum region' expands and shows a similar distribution as that in Fig. 1(b). These results indicate that the Na emission originates from bubbles which undergo lower pressure and the continuum originates from bubbles which undergo higher pressure. In other words, the Na emission comes from lower-temperature bubbles and the continuum from higher-temperature bubbles.

The results of the temporal measurement of SL pulse are shown in Fig. 2. Upper and lower oscilloscope tracings are corresponding to the Na emission and continuum emission, respectively. The SL pulses were triggered by ultrasound period and were stored about 1 s. SL in Figs. 2(a), 2(b) and 2(c) were obtained at applied voltages of 16.5, 23.5, and 35 Vpp, respectively. In Fig. 2(a), only the Na emission pulse was obtained, which agrees with the results of spatial measurement. At higher voltage as shown in Fig. 2(b), SL pulses are almost synchronous with ultrasound period and the timing of SL pulse emission has a wide distribution. The timing of the Na emission shows a wider distribution than that of the continuum emission. The distribution of the SL pulse results from a distribution of bubble radius. Then the results suggest that the Na emission originates from bubbles which have a wider distribution of radius. In Fig. 2(c), the Na emission pulse shows chaotic behavior while the continuum emission pulse remains a synchronous property.

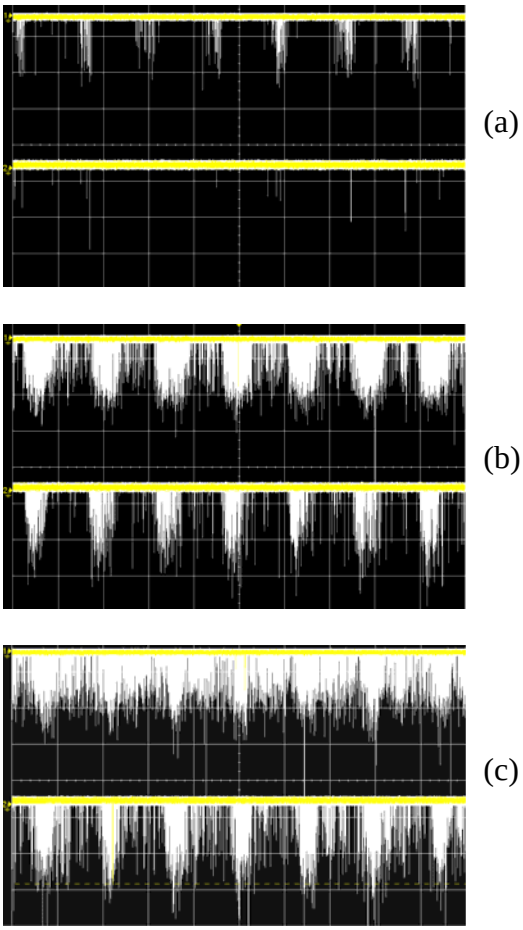

Fig.2. Oscilloscope tracings of SL pulses. Upper: Na emission. Lower: Continuum emission. Applied voltage are (a)16.5 Vpp, (b) 23.5 Vpp, and (c) 35 Vpp.

It is concluded that bubbles which cause Na emission have large radii with a wide distribution. The peak temperature in such bubbles is relatively low compared with bubbles which emit the continuum.

**References**

1. C. Sehgal, R. P. Steer, R. G. Sutherland and R. E. Verrall, *J. Chem. Phys.* **70**, 2242-2248 (1979).
2. E. B. Flint and K. S. Suslick, *J. Phys. Chem.* **95,** 1484-1488 (1991).
3. F. Lepoint-Mullie, N. Voglet, T. Lepoint and R. Avni, *Ultrason. Sonochem.* **8**, 151-158 (2001).
4. P.-K. Choi, S. Abe and Y. Hayashi, *J. Phys. Chem. B* **112**, 918-922 (2008).
5. T. J. Matula, et al., *Phys. Rev. Lett.* **75**, 2602-2605 (1995).

Proceedings of Symposium on Ultrasonic Electronics, Vol. 29 (2008) pp. 267-268
11-13 November, 2008

# Influence of the secondary acoustic radiation from a bubble on the vibration phase of the other bubble

気泡の二次的な音響放射が他気泡の振動位相に与える影響

Takaaki Fujikawa[1‡] Kenji Yoshida[2] and Yoshiaki Watanabe[2]
([1]Facul. Eng., Doshisha Univ.; [2]Facul. Life & Medi. Sci., Doshisha Univ.)
藤川貴彬[1‡], 吉田憲司[2], 渡辺好章[2] ([1]同志社大 工; [2]同志社大 生命医科)

## 1. Introduction

Various ultrasonic techniques using bubbles have been developed in recent years. It is necessary to clarify the bubble dynamics for the developments of these techniques. In the previous researches, the dynamics of a single bubble has been investigated experimentally and theoretically. However the dynamics of multiple bubbles is still unknown in detail.

In acoustic field, a bubble vibrates synchronizing with a surrounding pressure variation. The vibrating bubble shows the secondary acoustic radiation. When the two bubbles are located in closely, the secondary acoustic radiation influences the phase and the amplitude of the vibration of other bubble. [1] In this study, we try to clarify the effect of the secondary acoustic radiation on the bubble vibration. We optically observed the behavior of two bubbles, focusing on the interactive force between two bubbles. Based on the analysis of the direction of the interactive force, we investigate the influence of the secondary acoustic radiation on the bubble vibration phase.

## 2. Theory of the interactive force

The interactive force called the secondary Bjerknes force acts between two vibrating bubbles. The direction of the interactive force is determined by the relation of vibration phases of bubbles. In this section, we explain the interactive force between two bubbles.

### 2.1 The Secondary Bjerknes force

Two bubbles of bubble 1 and bubble 2 linearly vibrate in phase $\varphi_1$ and $\varphi_2$. In this case, the interactive force acting between two bubbles is represented as

$$\langle F \rangle = -\frac{2\pi\rho {R_{10}}^3 {R_{20}}^3 \omega^2}{D^2} \varepsilon_{10}\varepsilon_{20} \cos(\varphi_1 - \varphi_2), \quad (1)$$

where < > is the time integration for one driving ultrasound wave cycle, $\rho$ is density of liquid, $R_{10}$ and $R_{20}$ are the equilibrium radii of the bubbles, $\varepsilon_{10}$ and $\varepsilon_{20}$ are the vibration amplitudes of the bubbles, $\omega$ is the angular frequency of an external sound, and $D$ is the distance between the centers of the bubbles.

In the Equation (1), we can understand that the direction of $F$ is decided by vibration phase difference "$\varphi_1$-$\varphi_2$".

### 2.2 Vibration phase difference "$\varphi_1$-$\varphi_2$"

Assuming that there is no influence of secondary acoustic radiation from the bubble on the other bubble vibration, $\varphi_1$ and $\varphi_2$ are determined only by $\omega$, $R_{10}$ and $R_{20}$. [2] We explain the phase $\varphi$ in detail. In the case of "$R_0 > R_r$", $\varphi$ equals 0, and in the other case of "$R_0 < R_r$", $\varphi$ equals $\pi$. [2] $R_r$ is the resonance radius of a free bubble. When both the initial radii $R_{10}$ and $R_{20}$ are larger than $R_r$ or smaller than $R_r$, $\varphi_1$-$\varphi_2$ equals 0. As the results, the attractive force acts between two bubbles. When $R_{10}$ (or $R_{20}$) is larger than $R_r$ and $R_{20}$ (or $R_{10}$) is smaller than $R_r$, the repulsive force acts since $\varphi_1$-$\varphi_2$ equals $\pi$. It should be noted that the direction of $F$ doesn't depend on $D$ when the secondary acoustic sradiation doesn't influence the bubble vibration.

Considering this influence of the secondary acoustic radiation from the bubble, "$\varphi_1$-$\varphi_2$" is represented as

$$\varphi_1 - \varphi_2 = \tan^{-1}\frac{B_1}{A_1} - \tan^{-1}\frac{B_2}{A_2} . \quad (2)$$

The detailed equation is described in Ref. [1]. In the Equation (2), $A$ and $B$ are the functions of $D$, $R_{10}$, $R_{20}$, and $\omega$. Therefore, "$\varphi_1$-$\varphi_2$" is determined by those parameters. It should be noted that the direction of $F$ depends on $D$ in addition to $R_{10}$, $R_{20}$, and $\omega$. Examining the dependence of the direction of interactive force on $D$, therefore, we can investigate the effect of the secondary acoustic radiation on phase difference between bubbles vibrations.

## 3. Observation procedure

Focusing on the direction of interactive force between two bubbles, we observed the behaviors of two bubbles using a high-speed video camera. The observation system is described in Ref. [3].

dth0106@mail4.doshisha.ac.jp

**Figure 1** shows the structure of the experimental cell. The electronic signal is input to the transducer bonded to the acrylic cylindrical container. In this cell, the standing wave is formed. The bubble is adhered to polymer film at the antinode of the standing wave. Below the adhesion bubble, an oxygen bubble is generated by electrolytes of water. In this experiment, the direction of the interactive force is decided by the movement of the oxygen bubble.

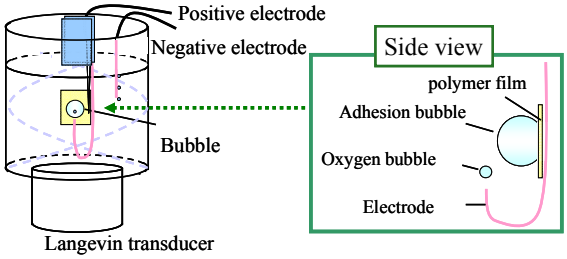


Fig.1 Experimental cell.

## 4. Observation result and discussion

### 4.1 Influence of the secondary acoustic radiation

We observed the bubble behavior in several conditions for $D$. $R_{a0}$ is lager than $R_r$, and $R_{f0}$ is smaller than $R_r$. $R_{f0}$ is initial oxygen bubble radius. **Figure 2** shows the observation results of the bubble behaviors. In this condition, the repulsive force should act between the bubbles, assuming that there is no influence of the secondary acoustic radiation on the bubble vibration. Figures 2 (a-1) and (b-1) show the observed images before irradiating the ultrasound; also Fig.2 (a-2) and (b-2) are the observed images during the ultrasound irradiation. In Fig.2 (a), (b), $D$ are 690μm and 445μm respectively. The irradiated ultrasound pressure at the bubble position is 3kPa. From the series of Fig.2 (a), we can confirm that the repulsive force acted between these bubbles. Contrary to our expectation, we can see that the attractive force acted between these bubbles in Fig.2 (b). As these results, it is clearly demonstrated that the direction of $F$ depends on $D$. In other words, the secondary acoustic radiation influences the bubble vibration.

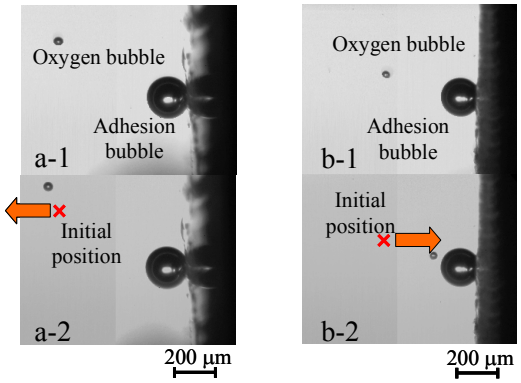


Fig.2 Interactive force between two bubbles.

### 4.2 Qualitative discussion

Dependence of the direction of $F$ on $D$ was observed only in specific condition for bubble size. We observed bubble behavior in various $D$ and $R_{a0}$. $R_{a0}$ is initial adhesion bubble radius.

**Figure 3** shows the experimental result. The white circle plots show the attractive force, the black circle plots show the repulsive force, the gray square plots show the direction of $F$ was unknown, and the dashed line shows the condition for contact of the two bubbles.

In Fig.3, the experimental result shows that the attractive force acts in $R_{a0} < 100$μm. The repulsive force acts in $R_{a0} > 140$μm. On the other hand, these results show that the direction of the interactive forces depend on $D$ in the range of $R_{a0}$ from 100μm to 140 μm. We discuss why the dependence of direction of $F$ on $D$ appears in specific radial conditions. In $R_0=R_r$, pressure amplitude of acoustic wave radiated by a bubble is significantly large. In this experimental condition, $R_r$ is 100μm. Therefore, we supposed that the dependence of direction of $F$ on $D$ appears when $R_{a0}$ is near the resonant condition.

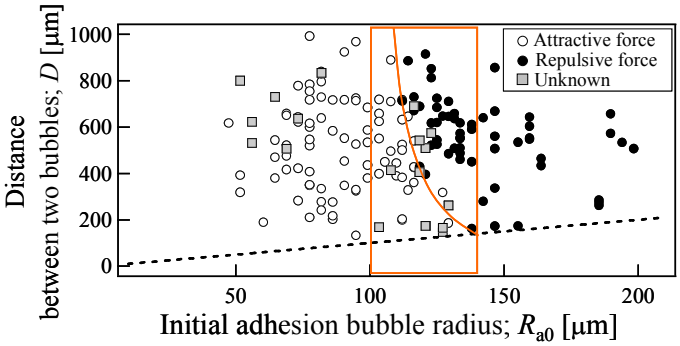


Fig.3 Direction of interactive force in $R_{a0}$- $D$ plane.

## 5. Conclusion

In this paper, we optically observed the behavior of two bubbles using a high-speed video camera, focusing on the direction of the interactive force between two bubbles. As the results, it was confirmed that the direction of the interactive force depends on the distance between two bubbles. Therefore, it was verified that the acoustic wave radiated by the bubble effect on the vibration phase of the other bubble.

## References

1. Masato Ida, Phys.Rev.E, 67, 056617, 2003.
2. T.G.Leighton, “The Acoustic Bubble”, ACADEMIC PRESS, 1994.
3. K. Yoshida *et al.* : Jpn. J. Appl. Phys. **47** (2008) 4200.

2P6-5

Proceedings of Symposium on Ultrasonic Electronics, Vol. 29 (2008) pp. 269-270
11-13 November, 2008

# Collapsing behaviors of two bubbles adhered to the rigid wall in an ultrasonic field: Simultaneous generation of micro flows

超音波場における二つの壁面付着気泡の崩壊挙動：同時発生する複数の微小流

Kenji Yoshida[1†] and Yoshiaki Watanabe[1] ([1] Facul. Life & Med. Sci., Doshisha Univ.)
吉田憲司[1†]，渡辺好章[1]（[1]同志社大　生命医科）

## 1. Introduction

In ultrasonic cleaning technique and sonoporation which is gene thrapy technique using ultrasound, cleaning effects and gene introduction are considered to be enhanced by effects of bubbles driven by ultrasound. In case of a bubble near a rigid material or tissue in an acoustic field, the bubble typically shows a "non-spherical vibration" which is induced due to effects of the material near the bubble. Since the dynamics of this non-spherical vibration have been still unknown, further detailed understanding should be necessary. In previous studies on a collapse of a single bubble adhered to a rigid material or soft gel, detailed bubble behaviors and its dependence on bubble size have been examined.[1,2] However, there are few reports on behaviors of multi bubbles near a material. In the case of multi bubble, interactive force acting among bubbles which is called secondary Bjerkens force should induce non-spherical vibration in addition to the effects of a material near bubbles.

In order to examine effects of interaction on non-spherical vibration of bubbles near a rigid material, we observed behaviors of two bubbles adhered to a quartz glass, using a high-speed video camera with maximum recording rate $10^6$ fps. As results, we confirmed that non-spherical vibrations of two bubbles are different from that of single bubble. In particular, interesting bubble behaviors such as a simultaneous generation of several micro flows are observed. In this paper, we discusse effects of interaction between two bubbles on bubble behaviors.

## 2. Experiment system

We observed bubble behaviors using high-speed video camera (Shimadzu HPV-1). The detailed system for observation was described in Ref [1,2]. **Figure 1** shows the arrangement of two bubbles and quartz glass in observation cell. A bolted Lagevine transducer was attached to the bottom of an acrylic cylindrical cell with a diameter of 60mm. A quartz glass with a height of 10mm, a width of 10mm and a thickness 2mm was inserted in the cell. Then, two bubbles are adhered to the surface of the quartz glass. The initial radii $R_o$ of bubbles are from 70 to 450μm. The initial distance L between two bubbles is from 0 to 650μm. Here, L is defined as the distance from a center of a bubble to that of the other bubble. The bubble behaviors were observed from top or side face of bubbles under an irradiation of ultrasound with center frequency 27 kHz and maximum sound pressure 100 kPa.

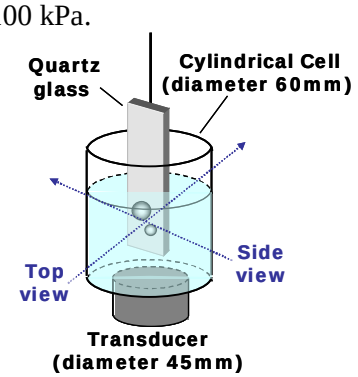


Fig.1 Observation cell.

## 3. Results

When normalized initial distance between two bubbles $L/(R_{1o}+R_{2o})$ were shorter than 1.5, observed results demonstrated that collapse behaviors of two bubbles were far different from that of a single bubble. Focusing on "process of bubble deformation" and "generation of micro flow", the differences are discussed.

### 3.1 Process of bubble deformation

In case of a single bubble, previous research showed that the bubble kept axial symmetry shape until the split though it vibrated non-spherically.[1] Here, the axis of symmetry is perpendicular to the rigid surface through the center of the bubble. In

case of two bubbles, we observed that bubbles lost axis symmetric shape until the split of bubbles. This is probably because attractive or repulsive force caused by interaction between bubbles affects the bubble deformation.

**Figure 2(a),(b)** show observed results. Bubble behaviors were observed from side face of bubbles. The observed times of obtained pictures are displayed on each picture. The input time of an electrical signal to the transducer is 0sec. In Fig.2 (a), we confirmed that the top portion of each bubble moved toward the other bubble. Then, the surface of each bubble opposite to the other bubble was fluctuated. This deformation process clearly indicated that the attractive force acted between bubbles. In Fig.2 (b), we could confirm that two bubbles lost the axis symmetric shape. The smaller bubble showed violent non-spherical vibration and moved away from the larger bubble. The Larger bubble showed the surface fluctuation which appeared only in the portion near the smaller bubble. The movement of smaller bubble indicates that the repulsive force acted between bubbles. Therefore, we suppose that bubbles lost axial symmetric shape due to the repulsive force.

### 3.2 Micro-flows generations

We observed specific generations of micro flows which followed above-mentioned fluctuation of bubble surface induced by interaction. Sometimes, we clearly confirmed simultaneous generation of several micro flows. This micro flows were generated in the direction parallel or oblique to the surface of quartz glass. In case of a single bubble, a micro flow was generated in the direction normal to rigid surface.[1]

Figure 2 demonstrates an observed result of the simultaneous generation of several micro flows. Bubble behaviors were observed from the top face of bubbles. After ultrasound irradiation, smaller bubble showed violent non-spherical vibration. On the other hand, the larger bubble almost did not vibrate. Then, a micro flow seemed to be generated into the smaller bubble [see picture (a)]. After the generation of this flow, the surface of larger bubble near smaller one expanded locally [see picture (b)]. When this local expanded portion contracted, a micro flow generated into the larger bubble [see picture (c)]. This local surface fluctuation propagated on the larger bubble surface. Then several micro flows simultaneously generated into larger bubble [see picture (d)].

## 4. Conclusions

In order to examine effects of interaction on behaviors of bubbles near a rigid material, we observed behaviors of two bubbles adhered to a quartz glass, using a high-speed video camera. When two bubbles were significantly near, it was indicated that the interaction between bubbles significantly affected "process of bubble deformation" and "generations of micro flows".

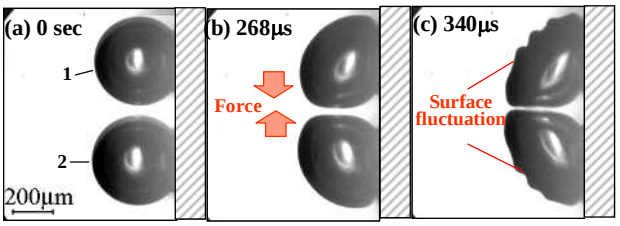


(a) Under action of attractive force.

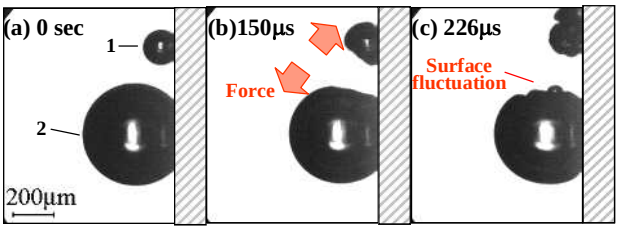


(b) Under action of Repulsive force.

Fig.2 Deformation induced by interaction. (a) $R_{1o}$ and $R_{2o}$ are 212μm and 243μm respectively. $L/( R_{1o} + R_{2o})$ is 1.37. (b) $R_{1o}$ and $R_{2o}$ are 97μm and 281μm respectively. $L/( R_{1o} + R_{2o})$ is 1.3.

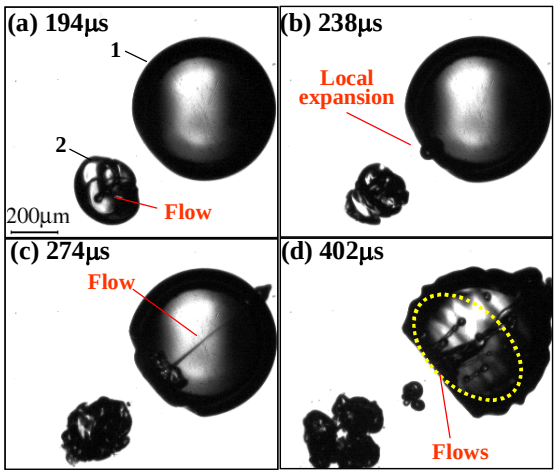


Fig.4 Several micro-flows generation. $R_{1o}$ and $R_{2o}$ are 338 μm and 110μm respectively. $L/( R_{1o} + R_{2o})$ is 1.26.

### References

1. S.Nakatani *et al.*: Jpn. J. Appl. Phys. **47** (2008) 3904.
2. K. Yoshida *et al,*: Jpn. J. Appl. Phys. **47** (2008) 4200

2P6-6

Proceedings of Symposium on Ultrasonic Electronics, Vol. 29 (2008) pp. 271-272
11-13 November, 2008

# FEM Analysis of Piezoelectric Resonance Characteristics on the Geometrical Configuration of a Sonochemical Reactor

ソノケミカル反応容器の音場設計における圧電共振特性の FEM 解析

Nagaya Okada[1†], Masanori Sato[1] and Yoshiyuki Asakura[1] ([1] HONDA ELECTRONICS CO., LTD.)
岡田長也 [1†]，佐藤正典 [1]，朝倉義幸 [1] （[1] 本多電子）

## 1. Introduction

Recently, chemical effects and physical effects caused by ultrasonic cavitation have been studied widely. The physical factors for the reaction field have been elucidated by many researchers, clarifying the relationship of chemical action to the shape of the sonochemical reactor, the shape and placement of the transducer, etc. However no investigation has been focused on measuring ultrasonic energy distribution for the industrial scale sonochemical reactors.

In order to have an industrial application of sonochemical action, the important factors that affect cavitaiton include ultrasonic frequency, acoustic power, ambient temperature, ambient pressure, and so on. Many researchers have investigated the frequencies ranging from 20 to 1200 kHz. It was widely noted that the sonochemical reaction efficiency was improved at a high frequency region from several 100 kHz. In these experiments, the irradiation volume ranged from 10 to 500 ml. Asakura et al. examined a sonochemical efficiency for a frequency of 45 kHz was improved using cylindrical sonochemical reactor in 70 mm diameter at a liquid height of 500 mm [1]. This result suggests that precise condition setting of sonochemical field may improve sonochemical efficiency value even at a low frequency. At the low frequency region, the distribution of ultrasonic energy attributed by input acoustic power especially can be changed significantly according to the size and shape of the sonoreactors as well as the height of the water. Hence the degree of chemical and mechanical effects in each position becomes an obstruction to a precise control.

This study presents an impedance of a transducer dependence on the geometrical configuration of a sonochemical reactor cell. The impedance of the transducer changed significantly when the standing wave field was resonant [2]. The sound field was generated under several configurations of sound sources and reflectors. The dependence between the impedance of the transducer and the sound pressure distribution in the sonochemical reactor was calculated by using the Finite Element Method (FEM). A sound pressure field was calculated when a few pressure antinodes exist in a sonochemical reactor cell using the most simplified case.

E-mail: nagaya@honda-el.co.jp †

## 2. Simulation model

In the present study, the commercial available FEM software has been utilized (ANSYS, ANSIS Inc.). In the software, the sound field analysis and piezoelectric transducer analysis can be calculated at a same time.

The calculations have been performed for a rectangular cell of 56 mm x 56 mm x 100 mm in internal dimensions and a cylindrical cell with 56 mm in diameter filled with water at 20 ºC. A bolt-clamped Langevin type transducer (BLT transducer) with a diameter of 45 mm was attached to the bottom of the cells. From the symmetry of the cylindrical cell, a 2-D plane mode has been considered in the calculation. For the rectangular reactor, 1/4 of the total 3-D volume model has been considered. As a boundary condition, the applied pressure is assumed as 0 at the inner surface of reactor's wall and the liquid surface. The frequency of the BLT transducer and the liquid height were chosen on setting of processing conditions to exist a few sound pressure antinodes. The impedance of the BLT transducer was evaluated as a function of the liquid height.

## 2. Results and discussion

The calculated spatial distribution of the pressure amplitude is shown as a function of the liquid height in **Fig.1**. The BLT thickness was decided as the frequency was 25 kHz at the liquid height of 70 mm. The calculation was worked out by maintaining this BLT thickness, thus the driving frequency of 25 kHz. In **Fig.1**, the calculated picture shows only a half of the 2-D plane mode,

and the right side of the picture is the reactor's wall. A striped pattern shows a sound pressure antinodes's existence. The pressure amplitude field at the liquid height of 80 mm is the most stable, and the field is disturbed depending on changes in liquid height.

**Figure 2** shows the resonant frequency and the impedance of the BLT transducer as a function of the liquid height. The resonant frequency decreases as a liquid height increases and the impedance at the liquid height of 80 mm is changed abruptly. This result suggests the degree of the resonant in the cell can be read the change by the change of the impedance.

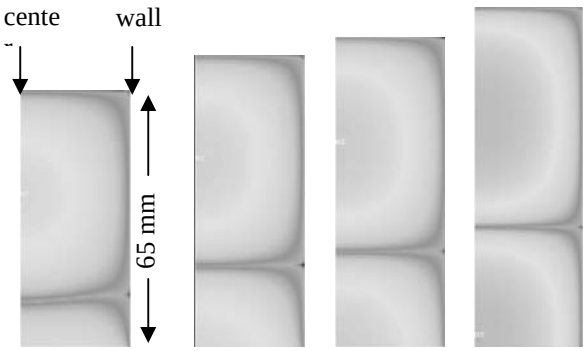


Fig. 1 Calculated spatial distribution of the pressure amplitude. The liquid height of 80 mm is the most stable on sound pressure field.

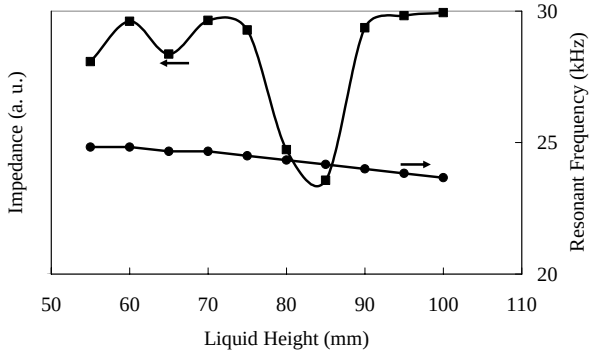


Fig. 2 Dependence of the liquid height on calculated resonant frequency and impedance of the BLT transducer driving at 25 kHz.

In **Fig.3**, the calculated result for the case at driving frequency of 34 kHz is shown. The sound pressure antinodes increase on the liquid height increasing. The pressure field at the liquid height of 70 mm and 97 mm is more stable than the liquid height at 65 mm and 90 mm, respectively. The resonant frequency and the impedance are shown in **Fig.4**. The calculated result indicates that the impedance is changed when the degree of resonant is changed. However, not all the data explain this phenomenon. The impedance value is changed abruptly at the liquid height of 100 mm because the impedance value is strongly affected by the resonant frequency changing. The gradient of resonant frequency curve is not constant at this liquid height and it makes more difficult to determine of the best state.

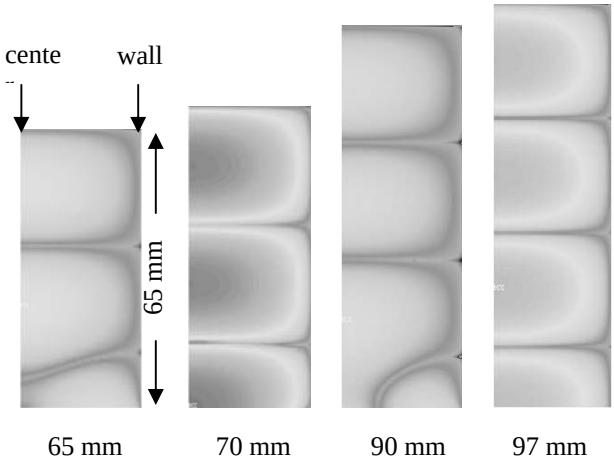


Fig. 3 Calculated spatial distribution of the pressure amplitude. The liquid height of 80 mm and 97 mm are better stable on sound pressure field.

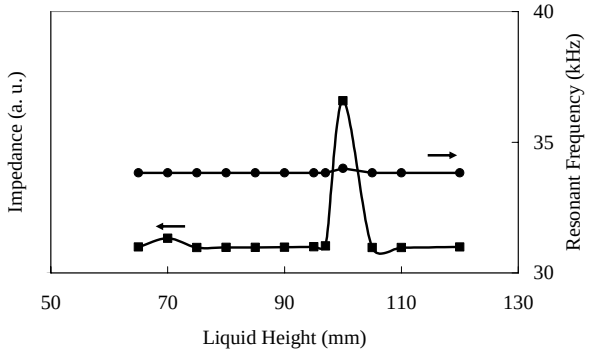


Fig. 4 Dependence of the liquid height on calculated resonant frequency and impedance of the BLT transducer driving at 34 kHz.

## 3. Conclusion

The impedance of the transducer dependence on the sound pressure field condition was evaluated using the FEM method. The results suggest that the degree of the resonant in the cell can be read the change by the change of the impedance. It must be helped very much to understand the optimal design of the sonochemical reactor cell.

## References

1. Y. Asakura, T. Nishida, T. Matsuoka, S. Koda: Ultrason. Sonochem.**15** (2008) 244.
2. Y. Asakura and S. Koda: Ultrasonic Technology **5** (2007) 55 [in Japanese].

Proceedings of Symposium on Ultrasonic Electronics, Vol. 29 (2008) pp. 273-274
11-13 November, 2008

# The Intensity of MBSL in Aqueous Solutions at 2.4 MHz
超音波霧化中の多泡性ソノルミネッセンス

Hisashi Harada†, Naohiro Iwata and Keisuke Shiratori (Facult. Sci. Eng., Meisei Univ.)
原田久志‡, 岩田尚大, 白鳥啓介 （明星大 理工）

## 1. Introduction

It is known that the high frequency oscillator (> 1 MHz) provides liquid mist. This effect has received much attention for the possibility of practical use. Former paper, we confirmed the illumination originates from cavitation during ultrasonic irradiation at 2.4 kHz [1]. In recent years, we have reported relation between the intensity of MBSL (multi bubble sonoluminescence) and sonochemical reactivity at 200 kHz [2]. In this presentation, the relation will be discussed in high frequency region.

## 2. Experimental

A Pyrex glass cylindrical tube (volume about 60 ml, diameter 22 mm, length 300 mm) containing saturated gases in pure water (5 ~ 20 ml) was used for experiment. As dissolved gases, Ar, $O_2$, $N_2$, $H_2$, He, air and the mixtures of $O_2$ and $N_2$ were prepared. Each gas was passed through the solution except the air-saturated sample before irradiation. The composition of dissolved gas in the solution at the initial stage of observation was thought similar composition of atmospheric gas in the reactor. The atmospheric gas was analysed by a gas chromatography (Shimadzu, GC8AT). Then, ultrasonic waves were applied from the bottom of the tube attached with ultrasonic atomizer (Honda Electric, HM-303N, 2.4 MHz, DC 24 V / 1.0 A).

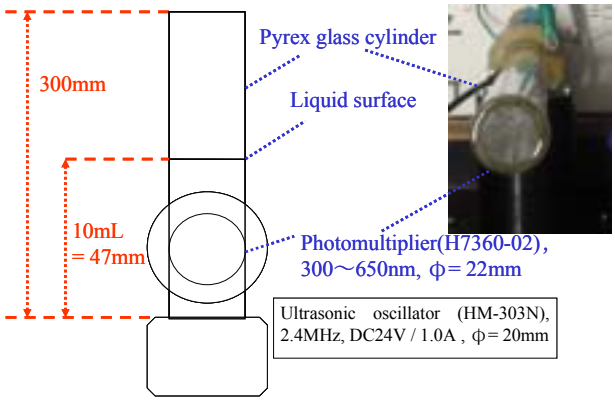


**Fig. 1 Experimental setup for measurement of sonoluminescence**

E-mail address: harada@chem.meisei-u.ac.jp

Intensity of sonoluminescence was measured in the dark box attached with photon counting head (Hamamatsu Photonics, H7360-01) as shown in Fig. 1. Ultrasonic power was estimated by KI method and the rate of rising temperature of solution in the early stage of ultrasonic irradiation (A Standard Method to Calibrate Sonochemical Efficiency of an Individual Reaction System recommended by Japan Society of Sonochemistry) [3].

## 3. Results and discussion

It is known that the intensity of MBSL decreases with increasing frequency [4]. However, MBSL was detected in an air atmosphere even at 2.4 MHz. Fig. 2 indicates the effect of volume of water in the tube on the intensity of MBSL. Clear result was obtained. According to this result, volume of 10 ml of solution was adopted for below examinations.

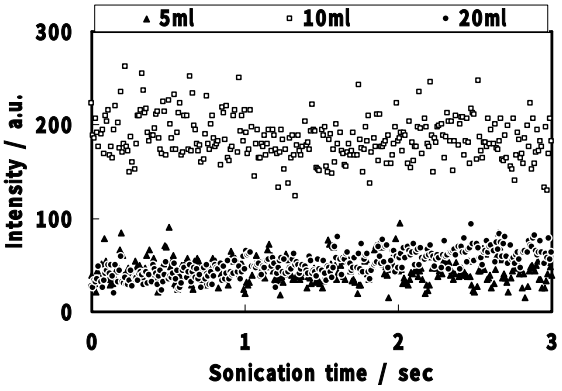


**Fig. 2 Effect of volume of water on MBSL**

Fig. 3 illustrated time dependencies of the intensities of MBSL in various kinds of dissolved gases. The selection of dissolved gas is important for cavitation. Argon was recorded the highest intensity. The intensity followed the order of Ar > Air > $O_2$ > $N_2$ >> He, $H_2$, $CO_2$. In the cases of $H_2$ and $CO_2$, only a little MBSL was detected. In this figure, we note that the intensity of air is higher than those of each element ($O_2$ and $N_2$). Air includes about 20%$O_2$. Thus, composition of air is

the gas mixture of 20%$O_2$ - 80%$N_2$ if minor gases are not considered. In order to confirm the mixed gas effect, MBSL was measured in various ratio of $O_2$ - $N_2$ mixture.

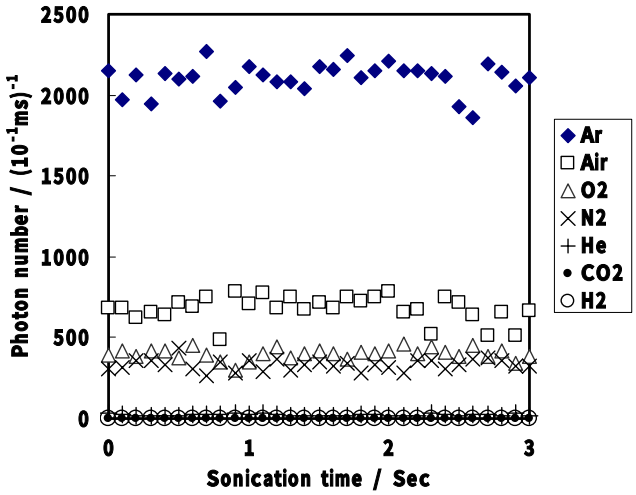


Fig. 3 Effect of dissolved gas on MBSL

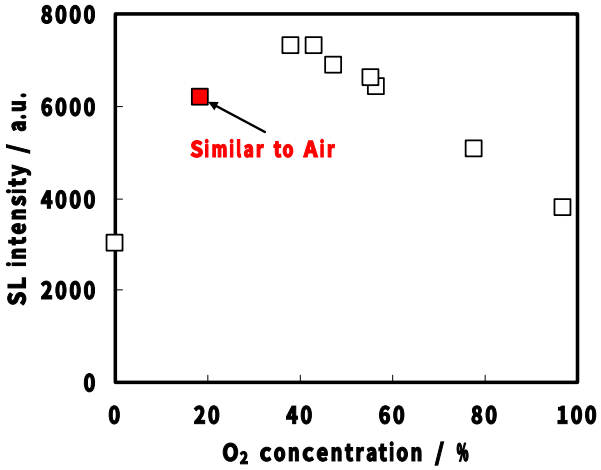


Fig. 4 Mixture gas effect on MBSL

Fig. 4 shows dependence of the intensity of MBSL on $O_2$ concentration in $N_2$ matrix. The intensity increased with $O_2$ concentration below 40% $O_2$. The intensity at 20% $O_2$ was similar to that in air. The maximum intensity was obtained at 40% $O_2$. This ratio is the similar ratio for air. In the region above 40% $O_2$, on the other hand, the higher concentration of $O_2$ was applied, the lower intensity was observed.

As another examination, sonochemical luminescence was performed as shown in Fig. 5. Increasing of illumination was observed in luminol alkaline solution. We also confirmed sonochemical power using by the Standard Method to Calibrate Sonochemical Efficiency in showing experimental section. Therefore, it was certain that not only sonoluminescence but also chemical power was gained even at 2.4 MHz.

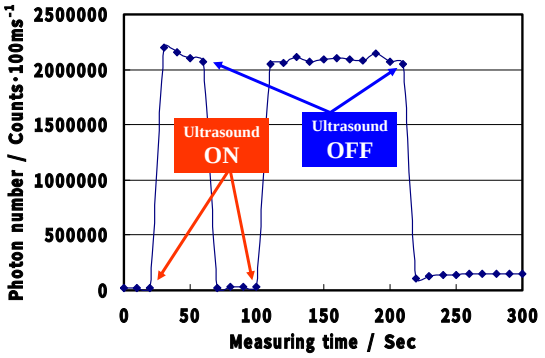


Luminol + $K_3Fe(CN)_6$ in NaOH solution

Fig. 5 Measurement of chemical power

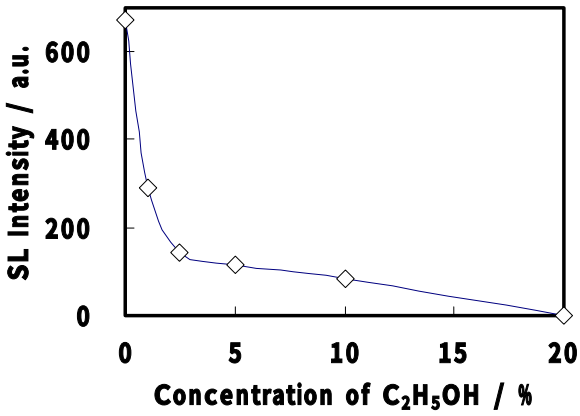


**Fig. 6 Addition effect of ethanol on MBSL**

In the case of producing liquid mist, ethanol solution is often utilized. So, we try to use ethanol in order to obtain MBSL. As shown in figure 6 the intensity was decreasing drastically.

## References


1. H. Harada, H. Yoshida and H. Kato, *11th meeting of European Society of Sonochemistry* (2008, France).
2. H. Harada and H. Kato, *International Symposium on sonochemistry and sonoprocessing* (2007, Kyoto)
3. S. Koda, T. Kimura, T. Kondo and H. Mitome, *Ultrasonics-Sonochemistry*, **10(3)**, 149-156 (2003)
4. P. Kanthale, M. Ashokkumar, F. Grieser, *Ultrasonics-Sonochemistry*, **15**, 143-150 (2008).

2P7a-14

Proceedings of Symposium on Ultrasonic Electronics, Vol. 29 (2008) pp. 275-276
11-13 November, 2008

# Basic Investigation for Detection of Early Cancer by Optically Assisted Ultrasonic Velocity Change Imaging

光アシスト超音波速度変化イメージング法による初期癌検出のための基礎的検討

Hiromichi Horinaka†,Syunsuke Kawakami, Satoshi Ishibashi , Tetsuya Matsuyami, Kenji Wada, and Toshiyuki Matsunaka (Facult. Eng., Osaka Prefecture Univ.)
堀中博道‡，川上俊介，石橋　賢，松山哲也，和田健司，松中敏行（大阪府立大学 工）

## 1. Introduction

In recent years, applications of nano-particles to medical diagnosis and treatment have been actively researched. It is expected that the nano-particles display the cancer distribution in biological tissue because they are easy to accumulate to new blood vessel created by the cancer. However, this method cannot be applied to detection of the early stage cancer because the new blood vessel is not undeveloped. For detection of early cancer, the agent which has an affinity to protein introduced in tumor is expected. The difference of sojourn time of drug in the tumor tissue from that in the normal tissue is also expected to use for detection of early cancer.

The fluorescence labeling methods has been generally used to detect the tumor area in tissue. However, it cannot give the depth information of tumor distribution. To detect of early cancer, the photo-acoustic signal from Photofrin for PDT (Photodynamic Therapy) in tissue mimicking layer was detected.[1)]

We already proposed the optically assisted ultrasonic velocity change method and measured the optical absorption distribution in highly scattering medium. [2,3)] The method has the possibility to apply to detection of the light absorption distribution in depth of biological tissue.

In this study, we apply the optically assisted ultrasonic velocity change method to detect the distribution of medicine which accumulates the cancer tissue in order to develop a new method for detection of early cancer.

## 2. Experimental set-up

Figure 1 shows the experimental set-up and the phantom. The ultrasonic array transducer transmits ultrasonic pulses to the phantom through the transparency standoff. The optical fibers were mounted closer by the array transducer. Three kinds of semiconductor lasers which individually oscillated at wavelength of 660nm, 813nm and 910nm were used as light sources. Moreover, the light of 512nm from the green laser (SHG of Nd:$YVO_4$ laser) was guided by using mirrors to illuminate the phantom.

The center frequency of the ultrasonic pulses was 13MHz. A frame of image consisted of 346 ultrasonic beams. RF echo waveform data measured by the array transducer were stored and transported to the personal computor via the signal processing board. The waveforms of echo pulses of every line was divided into appropriate areas with the width of transmitted pulse. The cross-correlation between the corresponding area of the waveform data measured before and after light illumination was calculated to obtaine the time difference of the echo pulse shift induced by light illumination. The temperature change image was constructed from the ultrasonic pulse shift. The optical absorption distribution was estimated from the temperature change image.[3)]

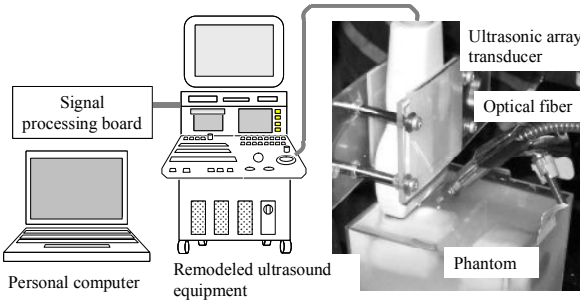


Fig.1 Experimental set-up

## 3. Experimental results

ICG (Indocyanine Green) has been known as the imaging agent for angiographic examination by using the near-infrared light. It was reported that ICG stayed in the tumor tissue for long time. [4)] We apply the optically assisted ultrasonic velocity change method to detect the distribution of the tumor-localizing drug, ICG, in chicken meat. The

E-mail address: horinaka@pe.osakafu-u.ac.jp

phantom structure is shown in Fig. 2 (a). The agar colored by ICG was inserted into the chicken meat. The absorption spectrum of the agar colored by ICG measured by the monochromator was shown in Fig.2 (b). The absorption peak locates around 800nm.

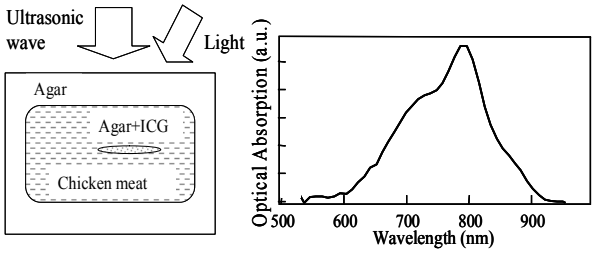


(a) Phantom structure (b) Absorption spectrum of ICG

Fig.2 Phantom structure and optical property of ICG

The normal B-mode images of the phantom were obtained by using the experimental set-up shown in Fig.1. Fig.3 (a) shows the normal B-mode image. The normal B-mode shows boundaries of tissue but does not show the position of agar colored by ICG.

The ultrasonic velocity change images were measured by using four lasers with oscillation wavelength of 532nm, 660nm, 813nm and 910nm. The light emitted from the optical fiber was diffused. The irradiance of the light in the phantom was set to be below 0.5 W/cm$^2$ in consideration of the skin exposure limit.

Figure 3 (b) shows the ultrasonic velocity change images obtained under the light of 813nm at exposure time 15s, 30s and 45s. The grayscale bar at the right of this figure shows the temperature change corresponding to the velocity change of the ultrasound waves. The ultrasonic velocity change image shows the distribution of ICG in the chicken meat.

Figure 3 (c) shows the ultrasonic velocity change images obtained under the light of 910nm on the same irradiance of the light as Fig. 3 (b). The distribution ICG does not appear in Fig.3 (c).

The difference between Fig.3 (b) and (c) is thought to attribute to the spectrum of Fig.2 (b). The distribution area of objective agent is thought to be distinguished from those of biological materials by measuring the dependence of the ultrasonic velocity change image on wavelength.

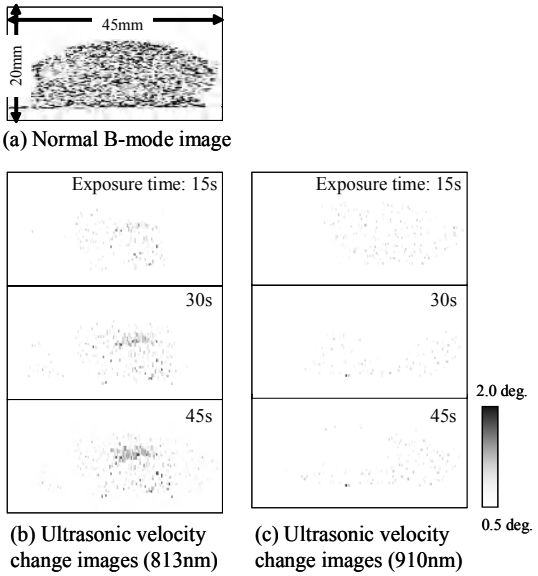


(a) Normal B-mode image

(b) Ultrasonic velocity change images (813nm) (c) Ultrasonic velocity change images (910nm)

Fig.3 Normal B-mode image and ultrasonic velocity images of the phantom

## 4. Conclusion

The optically assisted ultrasonic velocity change method was applied to detect the distribution of medicine which accumulates the cancer tissue in order to develop a new method for detection of early cancer. The phantom was prepared from the chicken meat and the agar colored by ICG which is usually used as fluorescence label. The light wavelength of 813nm in the absorption band of ICG was used to illuminate the phantom. The ultrasonic velocity change image showed the distribution area of ICG in the chicken meat. The depth profile of ICG distribution, which cannot be obtained by fluorescence labeling methods, was displayed. Experimental results showed that the optically assisted ultrasonic velocity change method has the potential to detect early cancer.


## Acknowledgment

This research was partially supported by the Nakatani Foundation of Electronic Measuring Technology Advancement.


## References


1. H. Mukoda, S. Sato, H. Ashida and T. Arai : The Review of Laser Engineering, **32** (2004) 645 (in Japanese)
2. H. Horinaka, T. Matsunaka et al.: Jpn. J. Appl. Phys, **41** (2002) 3555
3. H. Horinaka, T. Matsunaka et al. : Electronics Letters, **43** (2007) 1254
4. T. Ohta, Y. Abe, T. Miura and T. Sato : NIPPON ACTA RADIOLOGIA 2002, **62**, 284 (in Japanese)

2P7a-15

Proceedings of Symposium on Ultrasonic Electronics, Vol. 29 (2008) pp. 277-278
11-13 November, 2008

# Small Calculi Detection for Medical Acoustic Imaging with Correlation between Ultrasonic Echo Signals

医用超音波イメージングにおけるエコー信号間の相関を用いた微小結石検出法

Hirofumi Taki[1‡], Tetsuya Matsuda[1] and Toru Sato[1] ([1] Graduate School of Informatics, Kyoto Univ.)
瀧宏文[1‡]，松田哲也[1]，佐藤亨[1]（[1]京大 情）

## 1. Introduction

Calculus detection in screening the breast of women is important to differentiate marignant from benign masses. Despite several advances of acoustic imaging, medical acoustic imagers have insufficient capability for small calculus detection in comparison to X-ray. Therefore the improvement of the ability to detect calculus in acoustic imaging is strongly desired to serve an effective and low-cost screening technique without ionizing radiation.

In this paper, we propose a novel method to detect small calculi utilizing cross-correlation between RF signals behind the range of a measurement point, and then evaluate the effectivity using computer calculation based on the finite element method.

## 2. Cross-correlation of RF signals behind a measurement point

The proposed calculus detection method employs the cross-correlation of acoustic RF signals behind a measurement point. **Figure 1** shows the schema of this process. The cross-correlation value behind a measurement point is expressed as follows,

$$r(x+\frac{\Delta X}{2}, z) = \max_{l} G(x, z, l)$$

$$G(x, z, l) = \frac{\sum_{z'=z_1}^{z_2} g(x, z')g(x+\Delta X, z'+l\Delta Z)}{\sqrt{\sum_{z'=z_1}^{z_2} |g(x, z')|^2 \sum_{z'=z_1}^{z_2} |g(x+\Delta X, z'+l\Delta Z)|^2}}$$

where $x$ and $z$ are the lateral and vertical components of a measurement point on a B-mode image, g($x$,$z$) is the acoustic RF signal at P($x$,$z$), $\Delta X$ is the interval of scan lines, $\Delta Z$ is the range interval, $Z_1$ and $Z_2$ are the minimum and maximum of the z coordinates in a region of interest (ROI) behind the measurement point P($x$,$z$).

The calculus detection of the proposed method consists of three steps. First, we select points of high echo power, positions with a possibility of the existence of a calculus. We then calculate the cross-correlation value behind each selected point. When a small calculus exists in a acoustic beam, the waveform changes behind the calculus by several causes, as shown in **Fig. 2**. Therefore we predict the existence of a calculus from the decrease of the cross-correlation value.

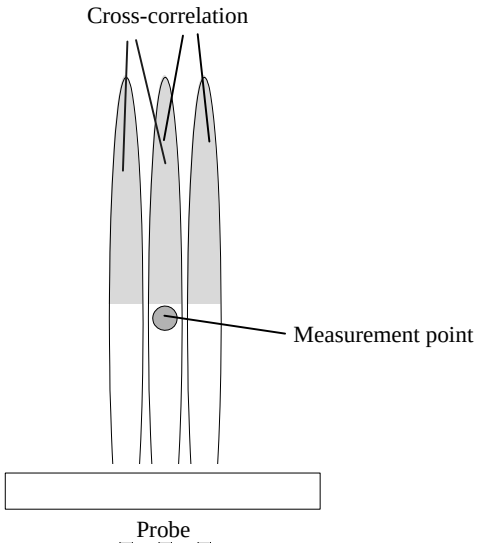


Fig. 1 Cross-correlation between RF signals of adjacent scan lines for calculi detection.

## 3. Simulation model

To evaluate the effect of the proposed calculus detection method, we use a simulated digital tissue map, as shown in **Fig. 3**. The formation of the map is as follows; the skin is 2mm in thickness, muscle with minute fat droplets is located under the skin, a calculus 0.5mm wide is set at the center for a 10mm depth, and a connective tissue layer 1mm thick is located for a 15mm depth.

---

taki@sys.i.kyoto-u.ac.jp

A probe 19.7 mm wide is set at the center on the skin. The probe has 33 elements 0.5mm wide, and the element gap is 0.1mm. 16 elements are activated simultaneously to form a scan beam. We calculate the RF signals utilizing PZFlex, a computer simulation tool based on the finite element method [1, 2].

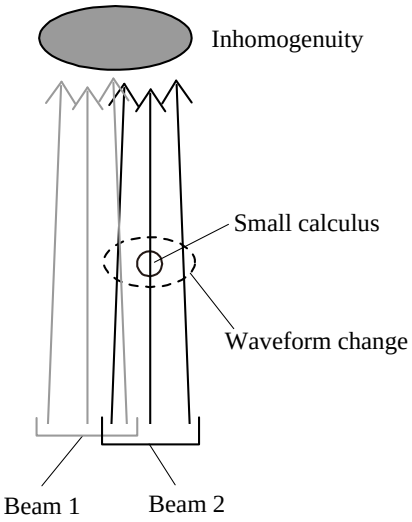


Fig. 2 Schema of the decrease of the cross-correlation value when a small calculus exists in a scan line. The waveform of an ultrasound pulse changes after passing through the calculus, and thus the cross-correlation value behind a calculus decreases.

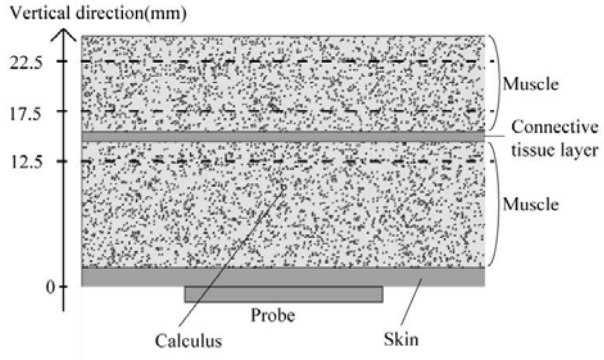


Fig. 3 Digital tissue map used in this study. A calculus 0.5mm wide set at the center for a 10mm depth.

## 4. Result

**Figure 4** shows the cross-correlation values and their average minus twice the standard deviation when a calculus of 0.5mm wide exists at the center, where the ROIs for the cross-correlation values are at the depth of 15mm and 20mm, and the summation interval in the vertical direction is 5mm. The cross-correlation values at the center, the position of the small calculus, decreases considerably. This indicates that the proposed calculus detection method has an ability to detect small calculi sensitively.

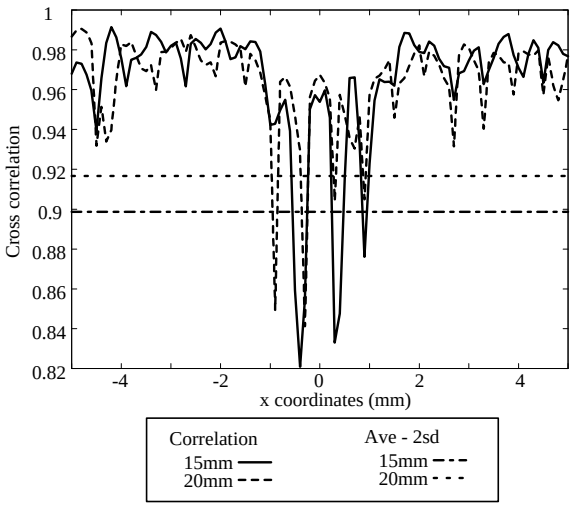


Fig. 4 Schema of the decrease of the cross-correlation value when a small calculus exists in a scan line. The waveform of an ultrasound pulse changes after passing through the calculus, and thus the cross-correlation value behind a calculus decreases.

**Acknowledgment**

This work is partly supported by the Research and Development Committee Grants of the Japan Society of Ultrasonics in Medicine, Japan and the Innovative Techno-Hub for Integrated Medical Bio-imaging Project of the Special Coordination Funds for Promoting Science and Technology, from the Ministry of Education, Culture, Sports, Science and Technology (MEXT), Japan.

**References**

1. J.A. Hossack and G. Hayward: IEEE Trans. Ultrason. Ferroelect. Freq. Contr. **38**(1991) 91.
2. R. Lerch, IEEE Trans. Sonics Ultrason. **SU37**(1990) 233.

2P7a-16

Proceedings of Symposium on Ultrasonic Electronics, Vol. 29 (2008) pp. 279-280
11-13 November, 2008

# Experimental study of high-resolution ultrasonic imaging for multiple target detection with frequency domain interferometry

周波数領域干渉計法による複数目標検出における
高分解能超音波イメージングの実験検討

Tomoki Kimura‡, Hirofumi Taki, Takuya Sakamoto and Toru Sato (Graduate School of Informatics, Kyoto Univ.)
木村智樹‡, 瀧宏文, 阪本卓也, 佐藤亨 （京都大 情報学）

## 1. Introduction

To improve diagnostic technique for metabolic syndrome such as diabetes mellitus, we need high-resolution imaging technique for a layer structure of a carotid wall. In this study we apply a radar technique, frequency domain interferometry (FDI), to medical ultrasonic imaging.

## 2. High-resolution imaging with FDI

### 2.1. The processing methods of FDI

We estimate the interval of multiple targets within a range gate using the phases of signals at different frequencies. The phase difference between two signals from different targets is proportional to the product of the frequency and the target interval. Thus the phase difference varies with the frequency of a signal, as depicted in Fig. 1. The variance of the phase difference between two signals at different frequencies is proportional to the product of the frequency difference and the target interval. Therefore we can estimate the target interval utilizing the variance of the phase difference. To obtain a range profile, we calculate correlation values between signals at different frequencies. We then integrate the correlation values with weighting function for phase correction.

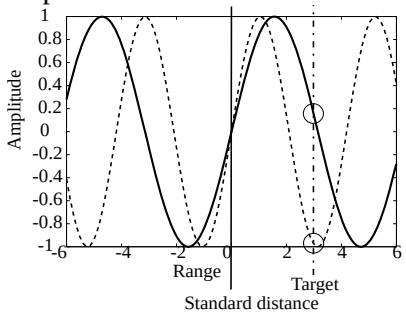


Fig. 1 Schema of the phases of the signals at different frequency

### 2.2. Capon method

The beamformer method scans all distances within a range gate. When multiple targets exist within a range gate, the resolution of the beamformer method deteriorates because of the interference by the targets at other positions. Therefore we use the Capon method, minimizing the contribution from other distances subject to a constant response at a desired distance[1].

### 2.3. Suppressing the coherent interference by frequency averaging

We assume multiple coherent interferences are in the echo from a single range gate. Additionally we also assume that the target intervals are constant while receiving the echo from a range gate. Under this assumption, the cross correlation between the signal from the desired distance and the coherent interference is nonzero. The Capon method selects the weighting function to minimize the sum of signals, and thus results in the cancellation of the signal from the desired distance. To solve this problem, we suppress the correlation of coherent interferences by a frequency averaging technique. The phase relation of those signals change differently according to their respective target distances. Thus it is possible to suppress the correlation by averaging the correlation at several frequencies. In this point, frequency averaging uses the same principle as spatial averaging. Two averaging techniques have been proposed for suppression of the correction[2, 3]. Uniform frequency averaging (UFA) averages the correlation in uniform weights, and adaptive frequency averaging (AFA) in controlled weights to suppress the correlation completely. The resolution of AFA is generally higher than that of UFA.

## 3. Study of experimental data

---

tcfts440@yahoo.co.jp

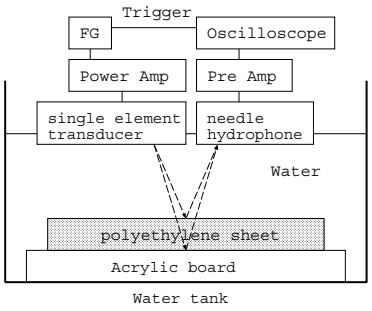


Fig. 2 Schema of the experiment.

**Figure 2** shows the schema of the experiment of this study. Target is polyethylene sheet 0.05mm thick. Transmit waveform is a monocycle pulse, the center frequency is 8MHz, sampling frequency is 500MHz.The echo consists of two backscattering waves from the front and back of the polyethylene sheet. We detect two waves from the echo using FDI, and then estimate the thickness of the sheet. For a computational simulation of this experiment of the two targets case, we make the pseudo echo

$$s_1(t) = as_0(t) + bs_0(t-\tau) + n(t) \qquad (5)$$

where $s_0(t)$ is the echo from acrylic board, a/b is amplitude ratio of the input signal, $\tau$ is the time delay resulting from the thickness of the sheet, and $n(t)$ is white noise. **Figure 3** shows the waveform of a pseudo echo, where a/b = 0.493, $\tau$ = 0.051μs and S/N = 38.3dB. **Figure 4** shows the normalized brightness distribution of the pseudo echo given by the beamformer method, the Capon method with UFA and that with AFA. In this study, 26 signals of different frequencies are utilized. The frequencies are selected from 1.5 to 14.0MHz, and the sampling interval in the frequency domain is 0.5MHz. It is difficult to separate the echo employing the beamformer method. Utilizing Capon method two edges are detected clearly and beam half-value widths of two edges are 3.09, 1.54μm in UFA and 3.37, 1.24μm in AFA. Estimation error in thickness is 1.84 μm in UFA and 2.30 μm in AFA. In the ideal case without noise, we can estimate the correct echo power from amplitude ratio.

Figure 3 shows the waveform of the polyethylene echo with the time-windowing and smoothing. **Figure 5** shows the normalized brightness distribution of this signal. In this case, we use echo from acrylic board as a reference wave and we use the same frequencies and the number of frequency averaging as those of the numerical computation. It is difficult to separate the echo employing the beamformer method. Utilizing Capon method, two edges are detected and estimation error in thickness is 2.16μm in UFA and 0.91μm in AFA.

**Acknowledgment**

This work is partly supported by the Innovative Techno-Hub for Integrated Medical Bio-imaging Project of the Special Coordination Funds for Promoting Science and Technology, from the Ministry of Education, Culture, Sports, Science and Technology (MEXT), Japan.

**References**

1. L.Smaini, H.Luce, M.Crochet, and S.Fukao: J.Atmos.Oceanic Technol. **19** (2001) p.954.
2. O.L.Frost: IEEE ICASSP. **86** (1986) p.2499.
3. K.Takao and N.kikuma: IEEE Trans. Antennas Propagat. **AP-35** (1987) p.1389.

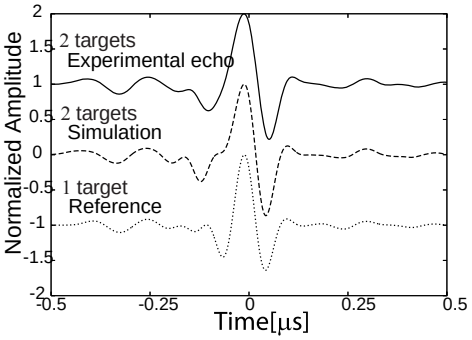


Fig. 3 The echo from a polyethylene sheet 0.05 mm thick, the pseudo echo $s_1(t)$, and the echo from an acrylic board.

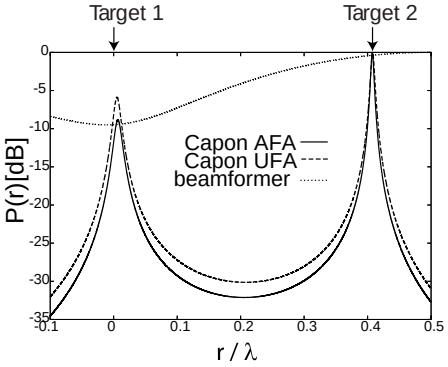


Fig. 4 The normalized brightness distribution from a pseudo echo in the case that two targets are separated by 0.41 λ. Target distances are estimated using the beamformer method, the Capon method with UFA, and the Capon method with AFA.

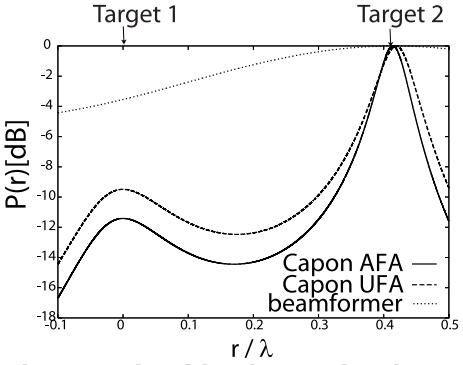


Fig. 5 The normalized brightness distribution from a polyethylene echo. (The parameters are same as in Fig. 4)

2P7a-17

Proceedings of Symposium on Ultrasonic Electronics, Vol. 29 (2008) pp. 281-282
11-13 November, 2008

# Beamformer Design to Shield Noise Sources
ノイズ源を遮蔽するビーム設計

Mariko Yamamoto[1†], Shin-ichiro Umemura[2] and Takashi Azuma[1] ([1] CRL Hitachi, Ltd.; [2]Facult. Eng., Tohoku Univ.)
山本真理子[1‡], 梅村晋一郎[2], 東 隆[1] ([1]日立 中研; [2]東北大 工)

## 1. Background and purpose

Strong reflectors are noise sources for imaging living body. Dynamic range of living body becomes generally between about 40 and 60 dB with strong reflectors in the visual field as a diaphragm or bones. Sidelobe of these strong reflector reduces contrast solution in a wide range. It often inhibits visibility of hypo-echoic structure like blood vessels and cysts extremely. Uniform sidelobe reduction method is attained with beamform optimization which minimizes the difference of ideal beam shape and actual beam shape is already reported [1].

But with existing method, in some case, it's difficult to design mainbeam -to- sidelobe intensity ratio larger than strong reflector-to- tissue background reflectivity ratio. We propose a beamformer design to selectively inhibit sidelobe in direction of strong reflector. To realize our method, we optimize not only apodization weight but also delay time based on constrained least square. We demonstrated our method by image simulation.

## 2. Proposed algorithm

Our method expects following steps on imaging.

1. Get a data for calculating desirable beam shapes (Pre-scan).

2. Calculate desirable beam shapes by detecting positions and intensities of reflectors to avoid.

3. Calculate apodization data to make beams which fit in well with desirable shapes.

4. Scan with calculated apodization data and make an image.

When strong reflector is positioned as **Fig.1** (a), we define desirable beam shapes as Fig.1 (b). Direction of main beam shifts as scan lines but that of inhabitation region are fixed on strong reflector's position to shield noise source. With these beam forms, we calculate beamforming datas to scan body. Fig.1(c) is a view of beam shapes to scan body. They are made with beamforming data calculated with Fig.1(b).

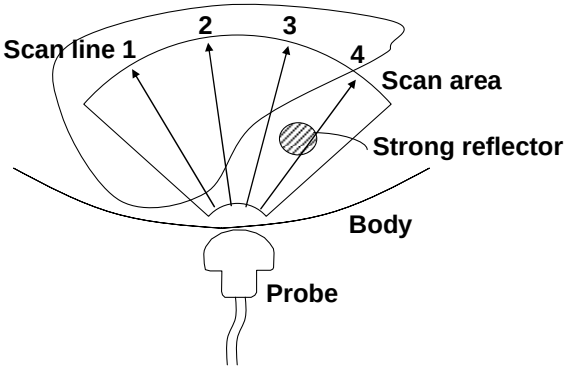


(a) Positioning of tissues and a imager

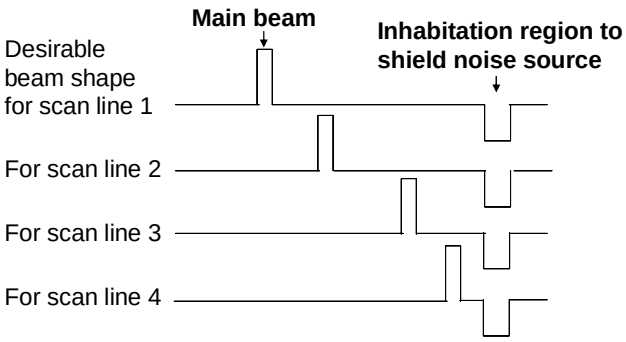


(b) Desirable beam shapes

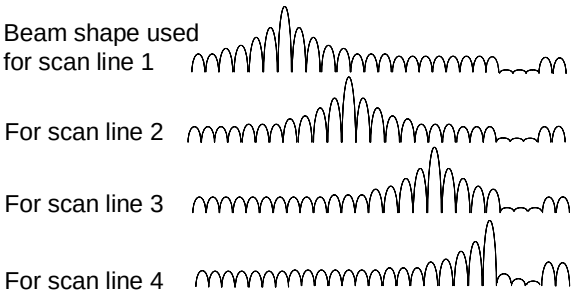


(c) Actual beam shapes by calculated apodizations

Fig. 1. Concept diagram of our process

mariko.yamamoto.td@hitachi.com

We defined apodization weight and delay time of elements of probes as beamforming data. It's a complex number. Optimization algorithm of beamforming data to get beams which fit in well with desirable shapes is as follows.

We expressed beamfoeming data as a vector **p** and a transform from beamfoeming data to beam shape as a matrix **T**. With these expression, beam shape **B** becomes

$$\mathbf{B} = \mathbf{Tp}. \tag{1}$$

Precisely, **T** is a matrix like

$$T = \begin{pmatrix} e^{jL_{11}/v/t} & \cdots & e^{jL_{1N}/v/t} \\ \vdots & \ddots & \vdots \\ e^{jL_{M1}/v/t} & \cdots & e^{jL_{MN}/v/t} \end{pmatrix}. \tag{2}$$

**T**'s elements describes phase sifts calculated by distance between each elements (j=1,…,N) to each position of field (i=1,…,M) **Lij**. When desirable shape is described with vector **W**, fitness with desirable shape is evaluated as

$$\|\mathbf{WB}\|^2 = \mathbf{B}^\dagger \mathbf{W}^\dagger \mathbf{WB} \tag{3}$$

and transmitting power is evaluated as

$$\|\mathbf{p}\|^2 = \mathbf{p}^\dagger \mathbf{p}. \tag{4}$$

And now, constrained least square

$$\delta\left(\|\mathbf{WB}\|^2 + \lambda \|\mathbf{p}\|^2\right) = \mathbf{0} \tag{5}$$

A is applied to get a apodization to form best-fitted beam shape under constant beam power. And problem is reduced to an eigenvalue problem

$$\mathbf{T}^\dagger \mathbf{W}^\dagger \mathbf{WTp} = \lambda \mathbf{p}. \tag{6}$$

So we can get a complex beamforming data to make beam which best-fit with desirable shape by inserting transfer function as **T**, inserting desirable beam shape as **W** and solving eigenvalue problem (6). An eigenvector for maximum eigenvalue is used as beamforming data to scan.

## 3. Result

**Fig.2** shows a simulation results calculated with our complex beamforming data. Imaging object is shown in Fig.2 (a). It contains 3 hypo-echoic cyst (-30.5dB, -34.0dB, -40.0dB) and laminar strong reflector (0dB) in background tissue (-30dB). Radius of each cyst is almost double of beam width. Example of beam shape of existing/our method is shown in Fig2 (b-1)/(b-2). 1-D beams are used for ease of calculation. Simulated image with existing/our method is shown in Fig.2 (c-1)/(c-2). On existing image, fog made by side-lobes of strong reflector is present and especially, visibility of inside of the cyst is degraded. On the other hand, on our image, fog is suppressed and the visibility of inside of cysts found improved. With these results, we assume our method is superior on imaging live body with strong reflector like bones, especially observation of structure inside of blood vessels or cysts.

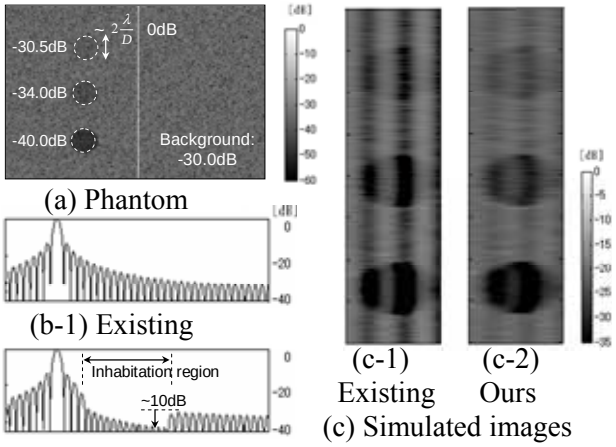


Fig.2 Simulation result

## 4. Conclusion

We proposed an beamformer design to selectively inhibit sidelobe in direction of strong reflector. Optimized complex beamforming data is obtained as an eigenvector of a matrix which was made from desirable beam shape and beamforming data - to - beam field transfer matrix. With this optimization , noise shield can be realized. We demonstrated our method by image simulation.

## References

1. K.Ranganathan et al: IEEE trans. on ultrason., Ferroelect., Freq. Contr., **50**(1) (2003) 15.

2P7a-18

Proceedings of Symposium on Ultrasonic Electronics, Vol. 29 (2008) pp. 283-284
11-13 November, 2008

# Optimum Quadratic Filters for Nonlinear Ultrasonic Imaging

Pornchai Phukpattaranont† and Chusak Limsakul (Facult. Eng., Prince of Songkla Univ.)

## 1. Introduction

The state-of-the-art pulse-echo ultrasound imaging systems exploit nonlinear behavior from interaction between acoustic energy and media to improve spatial and contrast resolution. Some nonlinearities are generated by ultrasound contrast agents (UCAs) [1] while others are formed by the propagation of sound in tissue [2]. We have validated the use of a quadratic filter (QF) for separating the linear and quadratic components of the beamformed radio frequency (RF) data in pulse-echo ultrasonic imaging [3]. Based on the understanding of the QF in the frequency domain in [4], the novel QF design is formulated and preliminary evaluation is given in [5]. In this paper we present details on parameter adjustment in the QF design for the improvement of imaging quality.

## 2. Theory

The design of QFs for capturing the second order nonlinearities is performed in frequency domain. The linear-phased QF is designed based on the sum of two 2D Gaussian filters where their centers are placed at the maximal contrast-to-tissue ratio of UCA over surrounding tissue. In the design, parameters are varied and investigated in order to achieve the best filter for enhancing imaging quality both in terms of contrast and spatial resolution. Our goal in the design is to calculate coefficients of the QF, $h(n_1, n_2)$, from the frequency response given by

$$H(e^{j\omega_{1k}}, e^{j\omega_{2l}}) = G(\omega_{1k}, \omega_{2l}) e^{j\phi(\omega_{1k}+\omega_{2l})} \qquad (1)$$

where $G(\omega_{1k}, \omega_{2l})$ represents the desired magnitude response based on the 2D Gaussian filters and $\phi(\omega_{1k}, \omega_{2l})$ is the phase response. Parameters to be optimized are as follow: the center of Gaussian filter, the rotation angle ($\theta$), the width of the passband along the cross-diagonal ($\sigma_x$) and diagonal orientations ($\sigma_y$). Please see [5] for details.

In the design, the centers of the Gaussian functions are positioned at frequency pairs where the contrast-to-tissue (CTR) ratio is maximal along the main diagonal of 2D frequency plane. The bandwidth of filter is independently determined to optimize spatial resolution. Therefore, the design approach offers two degrees of freedom in maximizing the CTR and spatial resolution simultaneously. This avoids the inherent tradeoff between contrast and spatial resolution when linear filters are used (e.g. in second harmonic imaging). After the filter coefficients $h(n_1, n_2)$ are obtained, the QF image is produced by applying the quadratic filter coefficients to the beamformed RF data throughout the standard B-mode image to estimate the quadratic component

$$y(n) = \sum_{k_1=0}^{N-1} \sum_{k_2=0}^{N-1} h(k_1, k_2) x(n-k_1) x(n-k_2). \qquad (2)$$

## 3. Results and discussion

We investigate and evaluate the proposed design with RF data acquired from a flow phantom (Model 524; ATS Laboratories, Inc., Bridgeport, CT) containing flow channels embedded in rubber-based tissue mimicking material. The contrast agent, BR14 (Bracco Research S.A., Geneva, Switzerland), was used. While UCA with 1:4000 dilution was circulated through the 6-mm channel, UCA with 1:10000 dilution was circulated through the 4-mm channel. The B-mode image is shown in **Fig. 1**(Top Left). The strength of echoes from UCA with 1:4000 dilution in the 6-mm flow channel (CTR = 5.5 dB) is higher than those from UCA with 1:10000 dilution in the 4-mm flow channel (CTR = 2.9 dB).

**Fig. 2** (Right) shows the magnitude of 2D frequency responses of the QFs under investigation. The centers of Gaussian function are at frequency (-2, 2) and (2, -2) MHz. Other parameters, i.e., ($\sigma_x$, $\sigma_y$, $\theta$) for the QF1, QF2, and QF3 are (1.1, 0.55, $-\pi/4$), (0.55, 0.55, $-\pi/4$) and (0.55, 1.1, $-\pi/4$), respectively. Fig. 2 (Left) shows the corresponding coefficients of the QFs. The size of the QF1, QF2, and QF3 are 37, 47, and 37, respectively. The corresponding QF images are shown in Fig. 1 with the CTR values of 23.8, 25.2, and 16.1 dB. Although the CTR of QF2 is highest, there is loss of axial resolution compared with that from the QF1.

Additional study on resolution is carried out using the images from a quality assurance phantom. **Fig. 3** shows the B-mode image of the quality assurance phantom and the QF images resulting from the same QF kernels used to generate QF images of the flow phantom in Fig. 1.

---

E-mail address: porncahi.p@psu.ac.th

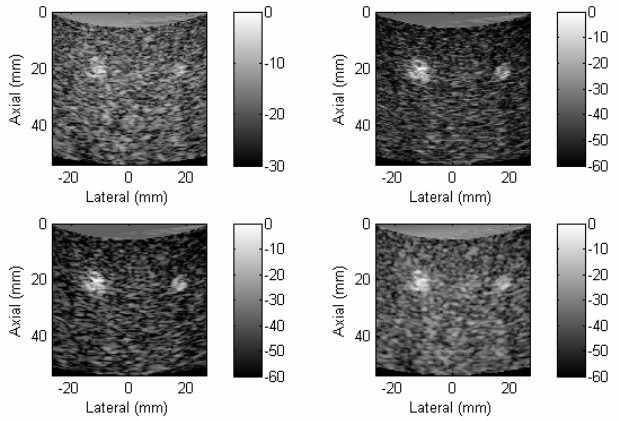


Fig. 1 Top Left: B-mode image of a flow phantom. Images from the QF1, QF2, and QF3 are shown at Top Right, Bottom Left, and Bottom Right, respectively.

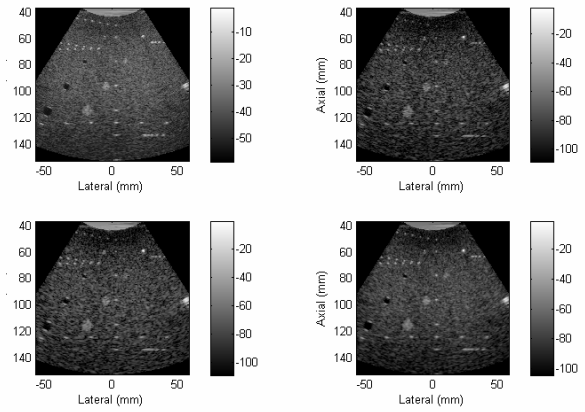


Fig. 3 Top Left: B-mode image of a quality assurance phantom. The images from the QF1, QF2, and QF3 are shown at Top Right, Bottom Left and Bottom Right, respectively.

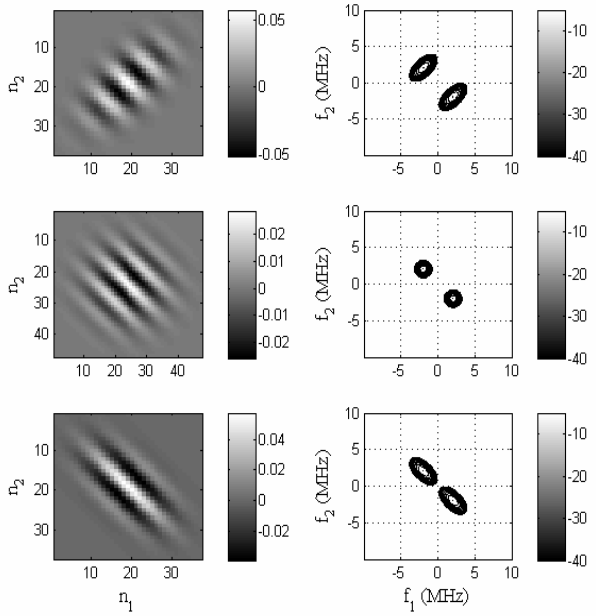


Fig. 2 Left: Coefficients of the QF. Right: The magnitude of 2D frequency response of the QF.

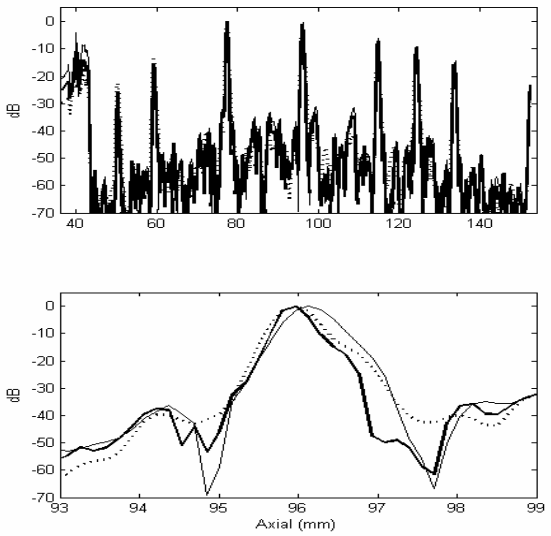


Fig. 4 Axial lines through the center of the quality assurance phantom. Thick: The QF1. Thin: The QF2. Dash: The QF3.

**Fig. 4** shows axial lines through the center of the quality assurance phantom. It can be seen that the axial resolution of the QF1 image is better than that from the QF2 and QF3. Based on the demonstrating results, we conclude that the QF with wider bandwidth in cross-diagonal orientation provides the QF image with better axial resolution.

**Acknowledgment**

The authors thank Professor Emad S. Ebbini for his suggestions and support in this work. In addition, this research project was funded by a grant from the Thailand Research Fund and Commission on Higher Education through Contract No. MRG5080287.

**References**

1 P. J. A. Frinking, A. Bouakaz, J. Kirkhorn, F. J. Ten Cate, and N. de Jong: Ultrasound Med. Biol. **26** (2000) 965.
2 M. A. Averkiou: Proc. IEEE Ultrasonic Symp., 2000, p. 1563.
3 P. Phukpattaranont and E. S. Ebbini: IEEE Trans. Ultrason., Ferroelect., Freq. Contr., **50** (2003) 987.
4 P. Phukpattaranont and K. Chetpattananondh: Proc. Symp. Ultrason. Elec, 2005, p. 281.
5 P. Phukpattaranont, T. Nilmanee, C. Limsakul, and E. S. Ebbini: Proc. IEEE Ultrasonic Symp, 2007, p. 2211.

2P7a-19

Proceedings of Symposium on Ultrasonic Electronics, Vol. 29 (2008) pp. 285-286
11-13 November, 2008

# Tissue Boundary Imaging Based on Eigenvalue Decomposition
# 固有値分解による組織境界イメージング

Hironari Masui[1†], Takashi Azuma[1] and Kazuaki Sasaki[2]
([1] Hitachi CRL, [2]Tokyo Univ. of A&T)
増井裕也[1‡], 東隆[1], 佐々木一昭[2] ([1]日立 中研; [2]農工大 農)

## 1. Introduction

Defining the boundary between a tumor region and surrounding normal tissue is essential for non- and minimally invasive therapies. Tissue strain imaging was effective for tissue characterization [1], but it involves a computational complexity. That is possible to be transformed to color map. Tissue boundary on the color map is not always clear becouse of nonlinearity of transformation [2]. Several groups have studied the vector maps of tissue motion to investigate the elasticity of tissue [3].

We have proposed a new method of ultrasonic straingraphy based on detecting spatial discontinuity in the tissue motion vector, estimated by the correlation of images between sequential frames [4,5]. To transform from a vector map to a scalar one, we tried a variety of parameters: vector length or angle, etc. However tissue boundary is not necessarily clearly depending on the situation because vector length or angle do not sufficiently reflect information of vector map.

In order to obtain adequate scalar map, eigenvalue decomposition technique is applied. First of all, a vector map in ROI (region of interest) is converted into a complex matrix by regarding component x as real part and componet y as imaginary part. Secondly, eigenvalue decomposition is applied to the complex matrix. The feature of mixed vector pattern is possible to be extracted by decomposing as eigenvalue components. Consequently, boundary imaging is adequately performed.

A VX2 tumor implanted in the liver of a rabbit were chosen to test our new method. The boundary between the tumor and the normal tissue surrounding it was not clearly detected in B-mode images, but it could clearly be seen with the method we propose.

## 2. Boundary imaging method

The outline flowchart for tissue boundary imaging is shown in **Figure 1**. The image frames were obtained from an EUB-8500 ultrasonic scanner (Hitachi Medical Corp., Tokyo, Japan) and hand-held fixing linear array probe EUP-L54M (Hitachi Medical Corp., Tokyo, Japan). The probe was operated at a frequency of 9 MHz.

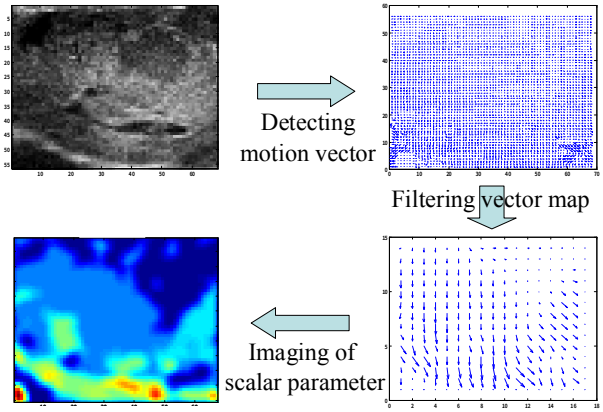


Fig. 1 Outline flowchart

A motion vector is detecting from two image frames based on block matching method [6]. A window array was set in each frame to measure motion. If the window was too small, the reliability of the motion vector that was detected was insufficient. If the window was too large, the correlation between consecutive frames was lost caused by deformation in the window. A window size of 30×30 pixels was selected based on consideration of this tradeoff. The best region for matching was found from a search area of 50×50 pixels set in the next frame by searching the minimum points for subtraction, absolution, and summation in the results. A VX2 tumor implanted in a rabbit liver were imaged as an experiment. Since the VX2 tumor could be moved by respiratory motion, pushing with an ultrasound probe was unnecessary in these cases.

After the tissue motion vector was mapped, an image processing, which is the moving average technique, applied to vector map. We set ROI at a size of speckle caused by ultrasonic measurement. In order to detect spatial discontinuity in the motion vector, an scalar map is imaged by using eigenvalue decomposition.

**Figure 2** is a flowchart for computing scalar component. A window (ROI) array was set in each

vector map to obtain scalar map.

A vector map in ROI is converted into a complex matrix by regarding component x as real part and component y as imaginary part. A complex matrix (m×m) is generated as follow:

$$\mathbf{A} = \begin{pmatrix} A_{11X} + iA_{11Y} & A_{12X} + iA_{12Y} & \cdots & A_{1mX} + iA_{1mY} \\ A_{21X} + iA_{21Y} & \cdots & \cdots & A_{2mX} + iA_{2mY} \\ \cdots & \cdots & \cdots & \cdots \\ A_{m1X} + iA_{m1Y} & \cdots & \cdots & A_{mmX} + iA_{mmY} \end{pmatrix}. \quad (1)$$

Eigenvalue decomposition is applied to the complex matrix.

$$\mathbf{A}\mathbf{p}_k = \mathbf{A}\lambda_k (k \le m)$$
$$\lambda_k : \text{eigenvalue(complex number)} \quad (2)$$
$$\mathbf{p}_k : \text{eigenvector } (m \times 1).$$

Eigenvalues are obtained. A scalar value is determined from the eigenvalues. Maximum absolute value of eigenvalues is selected as scalar one in this paper.

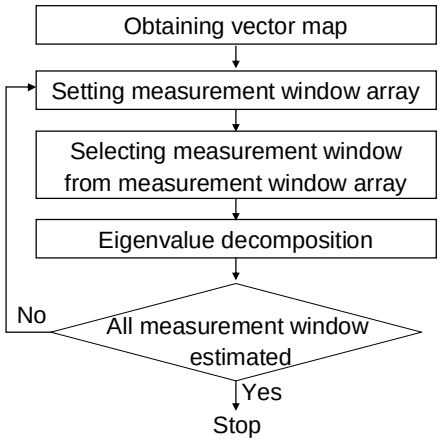


Fig. 2 Flowchart for computing scalar component

## 3. Experimental result

**Figure 3** shows a B-mode image and vector map of tissue motion for the VX2 tumor implanted in rabbit liver.

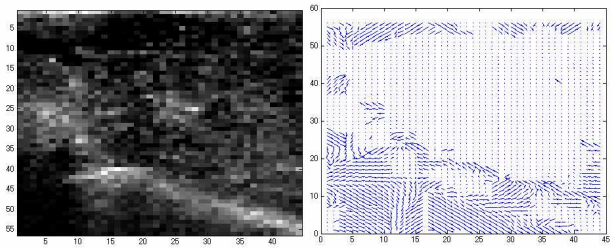

(a) B-mode image (b) vector map

Fig. 3 VX2 tumor implanted in rabbit liver

**Figure 4** shows the scalar component computed from the vector map. **Figure 4(b)** is obtained by eigenvalue decomposition. A window size of 3×3 pixels was selected on trial. For comparison, tensor imaging computed under the same conditions is shown in **Figure 4(a)**. The tensor imaging shows the disconnected boundary between the tumor and surrounding normal tissue, while **Figure 4(b)** shows the boundary which is clearly detected.

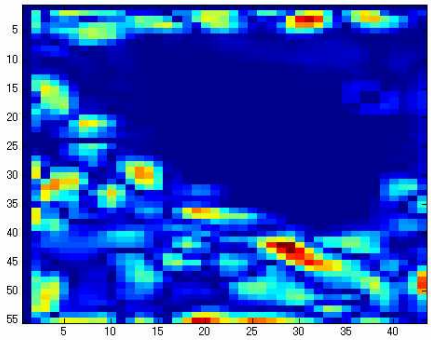

(a) Tensor imaging

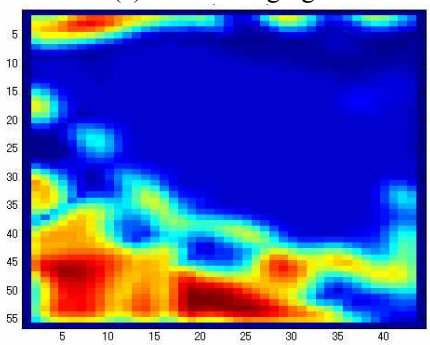

(b) Eigenvalue decomposition

Fig. 4 Scalar components computed from vector map

## 4. Conclusion

We proposed the boundary imaging method based on eigenvalue decomposition. Eigenvalue is sufficientry reflect information of vector map. This method has possibiity of obtaining fine structure of tumor.

## References


1. T. Shiina et al.: J. Med. Ultrason. **29** (2002) 119.
2. N. Nitta et al.: IEICE **J84-A** (2001) 1405 (in Japanese).
3. Y. Yamashita and M. Kubota: Proc. IEEE Ultrason. Symp. (1990) 1371.
4. T. Azuma et al.: Proc. IEEE Ultrason. Symp. (2006) 2040.
5. H. Masui et al.: Proc. Symp. Ultrason. Electron. **28** (2007) 429.
6. H. Yoshikawa et al.: Jpn. J. Appl. Phys. **45** (2006) 4754.

2P7a-20

Proceedings of Symposium on Ultrasonic Electronics, Vol. 29 (2008) pp. 287-288
11-13 November, 2008

# Reconstruction of shear modulus with mechanical source

## ずり弾性率と力源の再構成

Chikayoshi Sumi†, Sayaka Suekane (Facult. Sci. Tech. Eng., Sophia Univ.)
炭親良‡，末包明夏 （上智大 理工）

### 1. Introduction

We have developed various strain-measurement based shear modulus reconstruction methods, e.g., 1-dimensional [1] and multidimensional (2D and 3D) [1-3] methods. For a multidimensional reconstruction, Methods A to C [2,3] use a mean normal stress as an unknown, whereas Method F [1] uses a typical Poisson's ratio. In a dynamic deformation case, a density can also be reconstructed together. In addition, in Methods A to C and F, by using an iterative solution (e.g., conjugate gradient method) with no references, a shear modulus reconstruction being dependent of the initial estimate of the iterative solution can be obtained (Method D), whereas by using a quasi-reference shear modulus (e.g., unity) instead of an absolute shear modulus, a relative shear modulus reconstruction can be achieved (Method E) [4,5]. Both Methods D and E are useful when the target tissue is deeply situated (e.g., liver, heart) because no geometrical artifacts are yielded. Although all 3D reconstructions can deal with arbitrary mechanical sources (e.g., high intensity focus ultrasound, static compressor, vibrator, heart motion, pulsation etc.) existing outside a region of interest (ROI) [i.e., external sources], the existence of a mechanical source in the ROI [i.e., an internal source] make the Methods impossible to achieve the reconstruction of shear modulus.

In this study, we extend the reconstruction methods such that arbitrary internal mechanical sources (i.e., expressed as a static or dynamic pressure or a force vector) can be reconstructed together with the shear modulus [5-7]. However, because in 1D and 2D reconstructions, both the internal and external mechanical sources will affect the shear modulus and source reconstructions as in solo shear modulus reconstruction [1-3] (i.e., due to the low dimensionalities), we also evaluate the effects of the mechanical source conditions (size, intensity, frequency etc.) on such low dimensional reconstructions.

c-sumi@sophia.ac.jp

### 2. Methods

Basically, dynamic deformation cases are dealt with. As mechanical source models, a pressure or force vector can be dealt with. Thus, strictly, the number of unknowns cannot be larger than three. Thus, if necessary, a typical density value will be used, or the more equations will be obtained under the assumption that the mechanical source is stationary.

### 3. Simulations

A tissue phantom (50 mm side cube) and mechanical sources were simulated using successive-over-relaxation method. For instance, a spherical source (5 mm dia.) that partially overlapped a spherical region having a different shear modulus from that of the surrounding region (e.g., 2 vs 1 x $10^5$ N/m$^2$) is used.

For a static deformation case, the unknowns are a mechanical source and for Method F, a shear modulus and for Methods A to C, a mean normal stress and a shear modulus. For Methods A to C, because a mechanical source can be considered to be dealt with by combining with a mean normal stress, in these cases, we refer to the Methods as Methods A' to C'. Furthermore, the inertia can also be combined with the mean normal stress and the mechanical source (The Methods are referred to as Methods A" to C").

As mechanical sources, (i) a pressure p, (ii) a force component in a depth direction and (iii) a 3D force vector were dealt with.

In a similar way, dynamic cases were also dealt with. Here, only the reconstructed images obtained in static cases are shown.

As the results obtained by Method F, for mechanical source (i) to (iii), a shear modulus was able to be reconstructed with a high accuracy (**Fig. 1a**). However, mechanical sources were not able to be accurately reconstructed (omitted).

However, when using Methods A to C, for (i) to (iii), all the shear modulus, the mechanical sources

and the mean normal stresses were reconstructed with high accuracies (**Fig. 1b**).

Interestingly, for (i) to (iii), Methods A' to C' yielded accurate shear modulus reconstructions (**Fig. 1c**). Methods A' to C' are also effective methods.

For 3D reconstructions, internal mechanical sources was able to be reconstructed together. After the solo shear modulus reconstructions using external sources [1-3], internal sources can also be reconstructed using the strain tensor data. In contrast, in 1D and 2D reconstructions, the use of a small mechanical source yields smaller shear modulus values than the original.

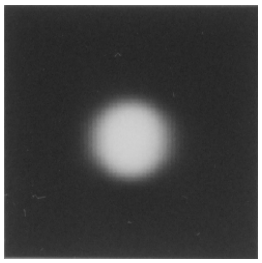


(a) Method F

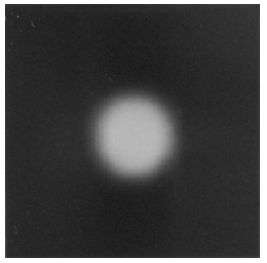



(b) Method C

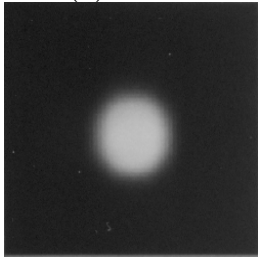


(c) Method C'

Fig. 1. Reconstructions obtained when a mechanical source (i) exist in an ROI.

## 4. Discussions and conclusions

We succeeded in the shear modulus reconstructions even when internal mechanical sources exist in an ROI by allowing the simultaneous reconstruction of the mechanical sources. The reconstruction will also allows the estimation of point spread function [6]. For 1D and 2D reconstructions, mechanical sources should be large. Other results obtained including experimental ones will also be reported.

The reconstruction of the mechanical source can be used for designing US beamformer for US imaging, controlling tissue deformation (i.e., elasticity imaging) and high intensity focus ultrasound (HIFU) treatment [6,8]. For such reconstructions, an accurate tissue tracking algorithm (i.e., our developed phase matching algorithm [1]) should be used.

We should also mention the case where the reconstruction target is a stress tensor [5,7]. As described above, mean normal stress can be reconstructed. Hydrostatic pressure in fluid can also be reconstructed together with fluid parameters in the same manner [5,7]. Thus, other stress tensor components can be evaluated using the reconstructed mechanical properties and mean normal stress or hydrostatic pressure together with the measured deformations.

## References


1. C. Sumi et al.: IEEE Trans UFFC **52** (2005) 1670.
2. C. Sumi et al.: IEEE Trans UFFC **53** (2006) 2416.
3. C. Sumi et al.: IEEE Trans UFFC **54** (2007) 2394.
4. C. Sumi et al.: Acoustical Imaging **29** 2007 (in press).
5. C. Sumi et al.: Acoust Sci Tech (under review).
6. C. Sumi et al.: IEEE 2007 Int Ultason symp, 1557.
7. C. Sumi: USA patent application 11/334,089, Jan. 18, 2006 (JP-2005-14774, Jan. 21, 2005).
8. C. Sumi et al.: Jpn J Appl Phys **47(5B)** (2008) 4137.

Proceedings of Symposium on Ultrasonic Electronics, Vol. 29 (2008) pp. 289-290
11-13 November, 2008

# Characterization of Ultrasound Generated Protein Microbubbles: From Production to Destruction

Judy Lee‡, Atsuya Towata, Kyuichi Yasui, Teruyuki Kozuka, Toru Tuziuti and Yasuo Iida (National Institute of Advance Industrial Science and Technology ( AIST))

## 1. Introduction

Protein microbubbles have generated substantial interest over the years due to their diverse biomedical applications such as echo or magnetic resonance contrast agents and as a vehicle for targeted drug deliveries. The production of microbubbles is important in terms of the size distribution, concentration and shell thickness and strength. These characteristics can govern the microbubble's scattering properties and more importantly destruction by dissolution or ultrasound. Destruction by ultrasound can be detrimental for echo contrast agent purposes, but beneficial for applications such as drug release. In this study, bovine serum albumin microspheres were generated by high intensity ultrasound and the importance of solution temperature was investigated. The destruction of microbubbles by dissolution and ultrasound is also discussed.

## 2. Method

Bovine serum albumin (BSA) microbubbles were produced by sonicating 5 wt% of BSA under a high intensity ultrasonic horn (Branson Ultrasonics, D450, 20 kHz) at a power of ≈ 200 W/cm² for 10 seconds. The BSA microbubbles were confirmed by labeling with the fluorescent dye rhodamine B isothiocyanate (RBITC) and viewed under UV illumination with a microscope equipped with an Olympus U-MSWG2 filter (appropriate for RBITC). The bubble size distributions were characterized by Coulter® Multisizer™ II analyser fitted with a 100 μm aperture and confirmed with light microscopy images. Different size distributions can be isolated by allowing the microbubbles to rise in a vial and collecting either the top or bottom fraction after a certain period of time. A microbubble size distribution of around 10 μm was used in this study. Destruction of BSA microbubbles by ultrasound were performed by immersing a glass vial containing 5 mL of microbubble solution in a liquid filled vessel with either a 727 kHz or 2 MHz transducer fitted at the bottom. A driving power of 40 W, measured by a power meter, was used.

## 3. Results and Discussion

*Production*: A typical light microscopy image of ultrasound generated BSA microbubbles is shown in Fig. 1(a). The BSA shells were confirmed by incubating the microbubbles in RBITC dye (Fig. 1(b)). A fluorescence image of a BSA shell from a collapsed microbubble, depicted in Fig. 1(c), shows a very thin shell of less than 1 μm.

It has been shown in the literature that the generation of BSA protein microbubbles is due to the cross-linking of cysteine groups to form disulfide bridges by superoxide radicals generated by sonication[1]. However, it was found in this study that microbubbles were produced even under high shear homogenization. It can be observed in Fig. 2 that the number of microbubbles produced increases with increasing solution temperature, but the size distribution is not significantly affected. To obtain a high yield of microbubbles, the solution temperature needs to be near the protein denaturation temperature (62°C for BSA[2]).

*Destruction:* Protein microbubbles can collapse via diffusion of gas across the shell into the surrounding liquid[3]. This rate is accelerated in degassed mediums. To observe the behavior of the BSA shell during microbubble dissolution, fluorescent labeled BSA microbubbles were injected in mildly degassed water and the collapse of a 10 μm BSA microbubble is captured by a CCD

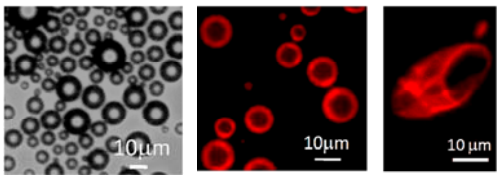


Fig. 1: (a) Light microscopy image of BSA microbubbles. (b) and (c) Fluorescence image of RBITC labeled microbubbles.

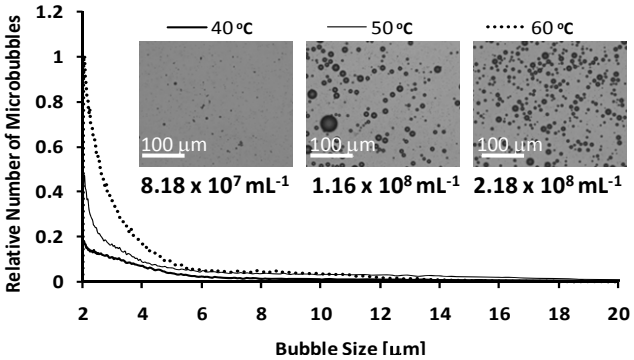


Fig. 2: Effect of solution temperature on the concentration and size distribution of BSA microbubbles produced from 10 second sonication.

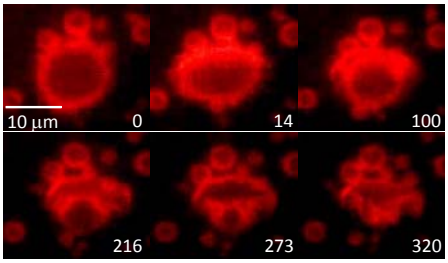


Fig. 3: Selecterd frames from a frame rate of 30f/s documenting the collapse of a 10 µm bubble due to the diffusion of gas in a degassed medium.

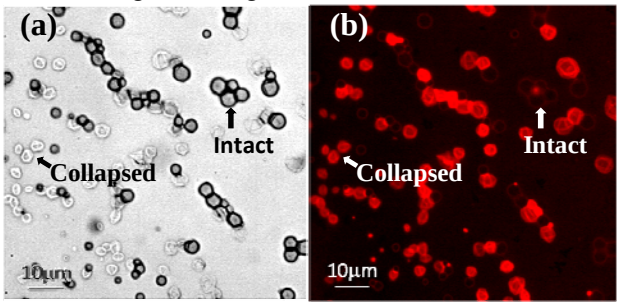


Fig. 4: (a) Light illumination showing microbubbles that has been dried on a glass plate. (b) Same sample as (a) but showing fluorescence emission from microbubbles that were not cross-linked by glutaraldehyde.

camera (Fig.3). Initially the microbubble is spherical, but deviates from sphericity (frame 0) as gas slowly diffuses out from the microbubble core. This diffusion lowers the pressure inside the microbubble and causes the shell to buckle (frame 14). Frames 100 to 320 illustrate the collapse of the shell as the microbubble deflates through a small rupture caused by the buckling. The same collapse of microbubbles was observed when a layer of microbubble is dried on a glass plate.

BSA microbubble shell can be strengthened by increasing shell thickness or with a cross-linking agent such as glutaraldehyde (GA), which cross-links the amine group of lysine. The effect of GA on the strength of the microbubble shell is demonstrated in Fig. 4. A mixture of microbubbles with and without GA cross-linking is dried on a glass plate. In order to distinguish between the two different microbubbles, microbubbles that were not cross-linked were fluorescent labeled with RBITC. Fig. 4(a) is an image of the dried sample mixture viewed under normal light illumination. It shows that some microbubbles have collapsed, while others appear to be still intact. The same sample was illuminated under UV to identify microbubbles without GA cross-linking (Fig. 4(b)). It can be observed by comparing the two images that microbubbles that did not collapse during drying were microbubbles with shells cross-linked by GA.

The destruction of BSA microbubbles with an average size of around 10 µm by ultrasound is shown in Fig. 5. At a frequency of 727 kHz and power of 40 W, bubbles around 10 µm were destroyed in 60 sec leaving few bubbles around

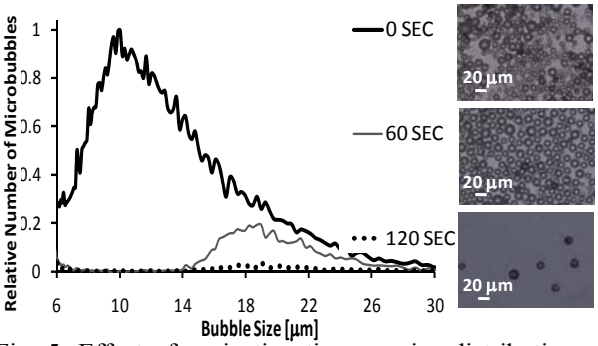


Fig. 5: Effect of sonication time on size distribution of microbubbles (727 kHz with an applied power of 40 W).

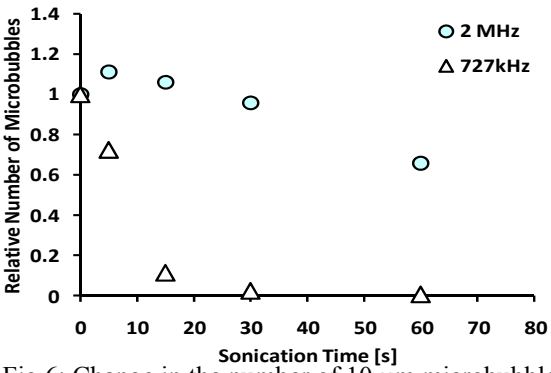


Fig.6: Change in the number of 10 µm microbubbles as a function of sonication time at a power of 40 W.

20 µm as confirmed by the light microscopy images. These larger bubbles were destroyed with longer sonication times. The destruction of 10 µm microbubbles as a function of time for 727 kHz and 2 MHz is shown in Fig. 6. It shows that microbubbles were completely destroyed by 727 kHz in 30 sec, whereas only 30 % were destroyed by 2 MHz after 60 sec. This effect may be due to large microbubbles having a lower resonance frequency. It has been shown that when driven at resonance, microbubbles undergo large expansions which lead to fragmentation of protein shells[3]. However, it is also known that the pressure threshold for acoustic cavitation increases with increasing frequency. This may also contribute to the lower number of microbubbles destroyed at 2 MHz compare to 727 kHz.

**Acknowledgement**

This work is supported by the JSPS Postdoctoral Fellowship program and the Ministry of Education, Culture, Sports, Science and Technology of Japan.

**References**

1. M. W. Grinstaff and K. Suslick: Proc. Natl. Acad. Sci. USA 88 (1991) 7708.
2. M. Ruegg, U. Moor, and B. Blanc: J. Dairy Res. 44 (1977) 509.
3. P. A. Dayton, K. E. Morgan, A. L. Kilibanov, G. H. Brandenburger, and K. W. Ferrara: IEEE Trans. Ultrason., Ferroelectr., Freq. Contr. 16 (1999) 220.

2P7b-2

Proceedings of Symposium on Ultrasonic Electronics, Vol. 29 (2008) pp. 291-292
11-13 November, 2008

# Study of effect in active path selection of fluid microcapsules to the variation of ultrasound emission at the bifurcation point

流路分岐部における照射超音波の変化に対するマイクロカプセルの流路選択効率の検討

Yusuke Muramatsu[1‡], Sawami Ueda[1], Ryusuke Nakamoto[1], Yusuke Nakayashiki[1], Kohji Masuda[1], and Ken Ishihara[2] ([1] Tokyo Univ. Agri.& Tech.; [2]Ehime Univ.)
村松悠佑[1‡], 上田沢美[1], 中元隆介[1], 中屋敷悠介[1], 桝田晃司[1], 石原謙[2]（[1]東京農工大; [2]愛媛大）

## 1. Introduction

Making use of the phenomena that microcapsules or microbubble of μm order collapse themselves after ultrasound emission near their resonant frequency, physical DDS (Drug Delivery System) has been proposed[1,2]. To minimize the side effect of medication, drug should affect to the target area, not to other parts inside human body. Though recent mainstream of DDS is focused on the gene transduction by using gene vector, it takes time and cost to develop for each object. The microcapsules, which can contain the specified drug inside the shell, have the possibility to correspond to various kinds of medications. The distribution of the capsules is easily recognized by echogram (B-mode image) because the brightness of echogram varies according to the density of capsules. However, it was difficult to enhance the efficiency of medication because the capsules diffuse after the injection, where motion of the capsules in the blood flow cannot be controlled. In this paper we describe our attempt for active path selection of microcapsules in the artificial blood vessel by acoustic radiation force[3].

## 2. Experiment

We used microcapsule F-80E(Matsumoto Oil, Japan) which shell is made of PVC(polyvinyl chloride) with specific gravity as 0.0225 and average of diameter as 99.2 [μm]. We sieved it as the range of diameter is from 65 to 73 [μm] because of the limitation of magnification in the microscope. Also we have prepared the artificial blood vessel, which is made of PEG(polyethylene glycol), including the Y-form bifurcation as **Fig.1**. The external size is 50x80x10 [mm] and inner diameter of the path is 2 [mm]. The axis of the transducer is set 50 [deg] to *x*-*y* plane and 60 [deg] to *y*-*z* plane as shown in **Fig.2**. Defining the point O as the intersection of three paths, the points P, Q and R indicate 1, 2 and 3[mm] upper from O, respectively.

---

masuda_k@cc.tuat.ac.jp

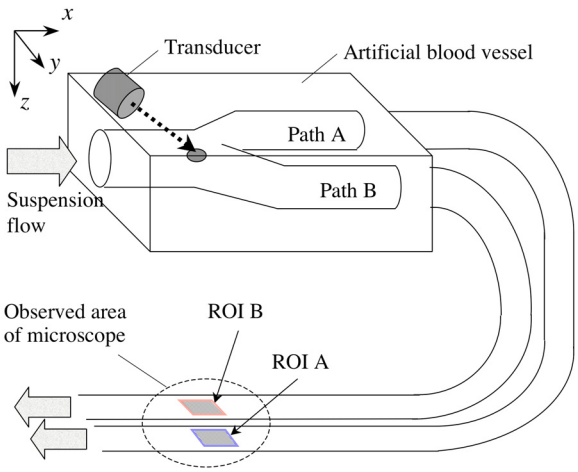


**Fig.1** Experimental setup including artificial blood vessel.

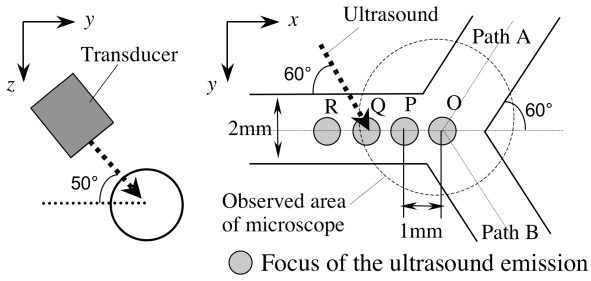


**Fig.2** Schematic view of the artificial blood vessel

To evaluate the amount of capsules which passes through each path, we have extended two lower courses by using semi-transparent tube and established the observed area which includes them in the same view as shown in **Fig.1**. By using a microscope (BX50, Olympus, Japan), optical image of observed area is recorded.

## 3. Results

**Fig.3** shows microscopic images of the area, which are captured by using high-speed camera Phantom-V4.2 (Nobby tech Co. Ltd, Japan) with interval time as 2 [ms]. To measure the capsules

amount, we established two square regions of interest in each course (ROI A, ROI B) and calculated the brightness average. The brightness in a region decreases according to the number of capsules inside. Thus we defined the shadow index as the following equation to evaluate the amount of capsules in the ROI.

$$\text{shadow index} = REF - \frac{\sum_{x=0}^{m}\sum_{y=0}^{n} f(x.y)}{S} \qquad (1)$$

Where $f$ is brightness of the ROI, $REF$ is brightness average without capsules and $S$ is area of the ROI. Then we have confirmed the relation between shadow index and capsules density.

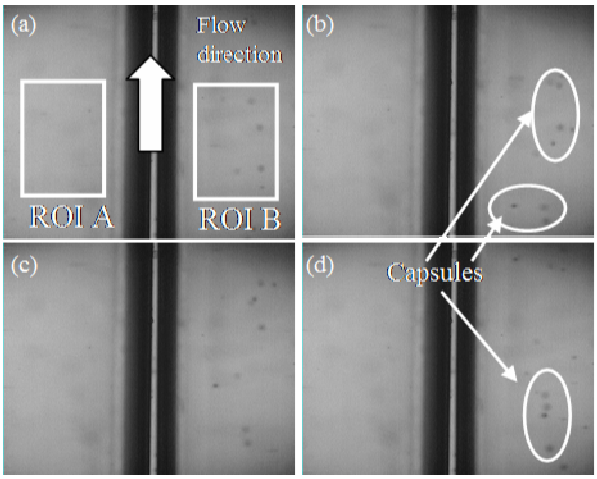


**Fig.3** Time series images of the observed area by 500 [fps] after injection of capsules suspension with ultrasound emission.

Capsules suspension passed through the ROI without ultrasound and calculated the average of shadow index for 15 [frames] (duration 30 [ms]) for various flow velocities. As the result shown in **Fig.4**, using the density in capsules as 0.15-0.25 [g/L], significant change of density can be detected.

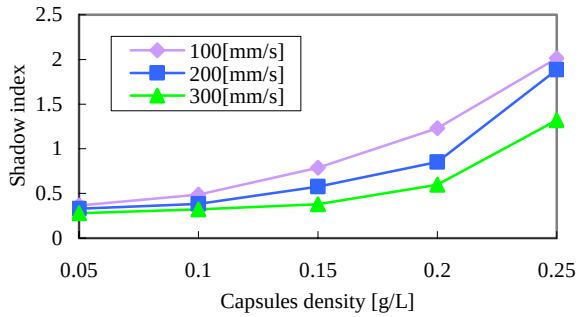


**Fig.4** Shadow index versus capsules density.

We measured the shadow indices in two ROIs using various conditions in emission of sinusoidal ultrasound. When frequency as 1 [MHz], sound pressure as 160 [kPa], flow velocity as 100 [mm/s] and capsules density as 0.2 [g/L], ultrasound was focused at points O, P, Q shown in **Fig.2**. **Fig.5** shows the value of shadow indices for each focused point.

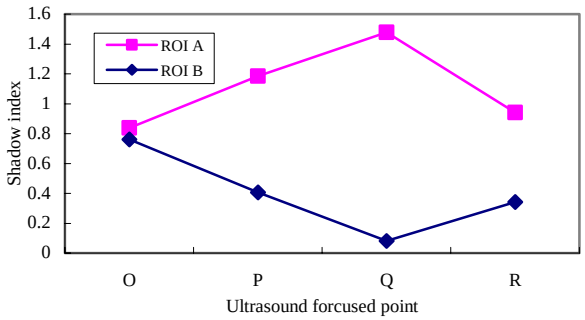


**Fig.5** Capsules path selection efficiency depending on the ultrasound focused position.

When the ultrasound was focused at point O, there was no difference between two ROIs. However, more than 90 [%] of capsules were introduced to path B when the ultrasound was focused at point Q. Thus focused point of ultrasound emission and the shape of the bifurcation should be considered to realize active path selection of capsules.

## 4.Discussion

In this study, we used the microcapsules which size is 63～75[μm] which cannot be applied to *in vivo* experiment. Because acoustic radiation force is proportional to the volume of capsules, it should be 1/100 when the diameter of capsules is several microns. Thus the blood velocity to be applied this technique is limited to few [mm/s]. Therefore we have to devise the minimization of the artificial blood vessel and its observation system.

## 5.Conclusions

In this study, we have experimented and considered to realize active path selection of microcapsules at a bifurcation of the artificial blood vessel. We are going to apply the experiment by varying other parameters and to investigate the mechanism of this phenomena.

## References


1. D. Koyama, W. Kiyan and Y. Watanabe：Jpn. J. Appl. Phys. 43 (2004) 3215-3219.
2. Y. Yamakoshi and M. Koganezawa：Jpn. J. Appl. Phys. 44 (2005) 4583-4587
3. Y. Muramatsu, K. Masuda, S. Ueda, K. Ishihara：Proc. Symp. Ultrason. Electron, Vol.28, (2007), 407-408.

2P7b-3

Proceedings of Symposium on Ultrasonic Electronics, Vol. 29 (2008) pp. 293-294
11-13 November, 2008

# Bi-frequency driven transducers for multi-frequency ultrasonic imaging

多周波超音波イメージングのための二周波駆動振動子

Natsuki Yoshizumi[1†], Shigemi Saito[2], Daisuke Koyama[3], Kentaro Nakamura[3] and Iwaki Akiyama[1] ([1] Facult. Eng., Shonan Inst. of Tech.; [2]School of Marine Sci. and Tech., Tokai Univ.; [3]Precision. and Intelligence Lab., Tokyo Insttiute of Tech.)

吉住夏輝 [1‡], 斎藤繁実 [2], 小山大介 [3], 中村健太郎 [3], 秋山いわき [1] ([1] 湘南工大 工; [2] 東海大 海洋; [3] 東工大 精研)

## 1. Introduction

Wideband ultrasonic system can effectively reduce the speckle noise on echographic images by applying the frequency compound technique[1]. The authors developped ultrasonic transducers[2-8], which form multiple frequency beams based on the nonlinear acoustic propagation. The transduceres transmit ultrasonic puleses, which consist of frequency componets $f_1$ and $f_4$, which is the quad frequency of $f_1$. As secondary waves, $f_2$, $f_3$ and $f_5$ are generated by the nonlinear interaction through the medium. They are the second harmonic of the $f_1$, the differece between $f_1$ and $f_4$, and the sum of $f_1$ and $f_4$, respectively. Generally, it is difficult to excite the ultrasonic pulses of the fundamental vibration mode and the higher-order vibration mode of even numbers simultaneously by a single transducer. This problem can be solved by adopting double layer for the structure of the transducer. We can determine thickness of the layers and select electrodes suitable for the each modes so that the desired vibration modes are excited efficiently. In this report, we mesured profiles of the ultrasonic beams which are formed by two different type of bi-frequency driven transducers, and compare them.

## 2. Bi-frequency Driven Transducers

**Fig.1** shows double layered transducers we propose. As shown in Fig.1 (a), one consists of a ploy vinylidene fluoride (PVDF) layer and a lead zirconate titanate (PZT) layer. The PVDF film is boded on a surface of the PZT disc. Ultrasonic pulses are radiated from the aperture of 20 mm in diameter. Curvature radius of the transducer is 70 mm, thus the pulses are focused at center of the curvature. The resonance frequency of the PZT disc and the PVDF film are 2 MHz and 7 MHz, respectively. Another is a double layered PZT that is made by a sinter as an integral structure shown in Fig.1 (b). The upper PZT is 600 μm thick and the lower PZT is 210 μm thick. Electrodes are formed at top surface, bottom surface and between upper and lower PZTs. The PZT is cut out in an octagon shape from a square PZT plate, 16 mm on a side. An acoustic lens is bonded at the bottom surface, and radiated ultrasonic pulses are focused at distance of 50 mm from the bottom surface of the PZT.

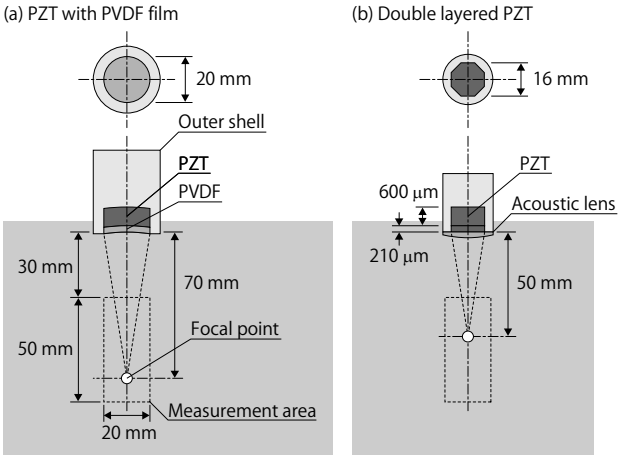


Fig.1 Configuration of the proposed transducers.
(a) PZT with PVDF film
(b) Double layered PZT

## 3. Multi-frequency Beam Measurements

We measure multi-frequency ultrasonic beams formed by the bi-frequency driven transducers. Ultrasonic signals of 2 MHz and 8 MHz are generated by a digital-to-analog converter and input to the transducers. The ultrasonic waves radiated from the transducers are detected with a needle type hydrophone (Force Institute) moving in a range of 20 mm by 1 mm steps in the radial direction and a range of 50 mm by 2 mm steps in the axial direction as shown in Fig.1, and sampled by an 8 bit digital oscilloscope (LeCroy 9370CL). Rate of the analog-to-digital conversion is 50 MS/s. In one measurement, 5000 points sampled data are obtained. To improve S/N ratio, we perform 64 times average on the oscilloscope. Sound pressure levels of the each frequency components ($f_1$, $f_2$, $f_3$, $f_4$, $f_5$) are calculated by fast Fourier transform (FFT).

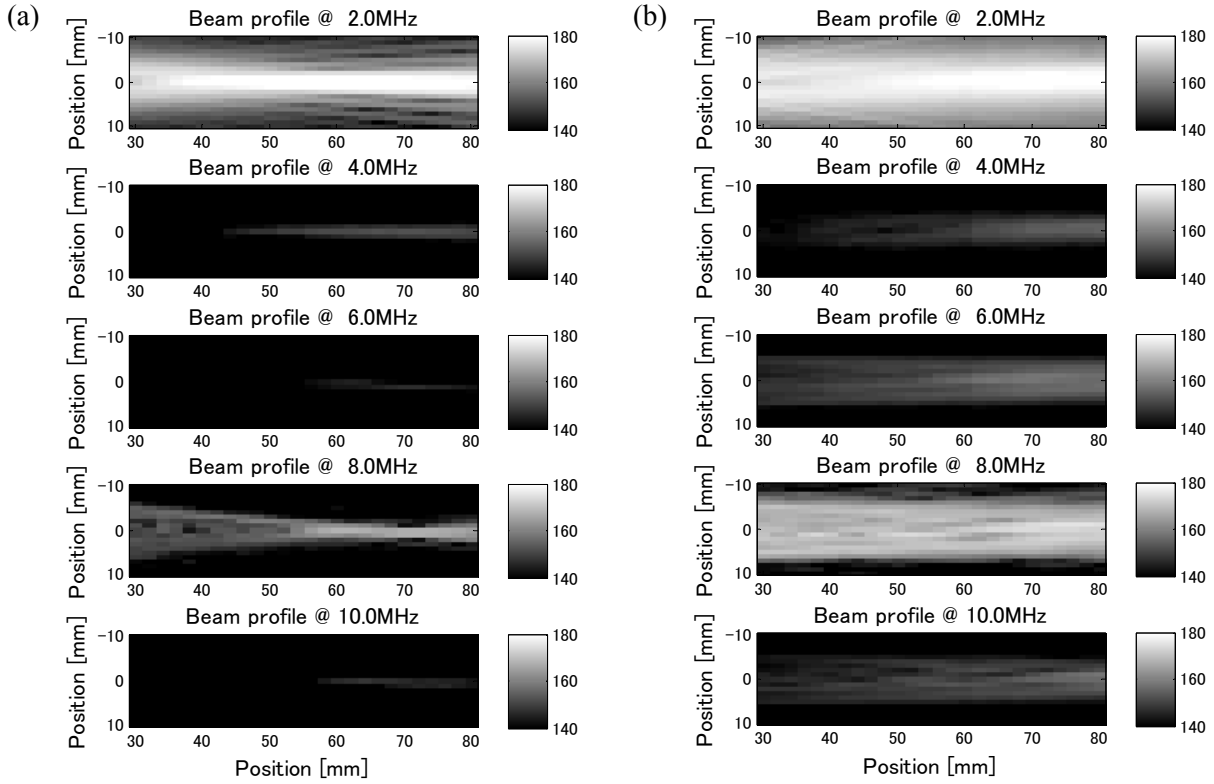


Fig.2 Multi-frequency ultrasonic beams.

(a) PZT with PVDF film

(b) Double layered PZT

## 4. Results and Discussion

Beam profile of each frequency radiated from the bi-frequency driven PZT with PVDF film transducer is shown in **Fig.2** (a). Frequency components 2 MHz and 8 MHz are applied to the PZT layer and PVDF layer, respectively. Similarly, Fig.2 (b) shows results of the double layered PZT transducer. Frequency components 2 MHz and 8 MHz are applied to the top electrode and the intermediate electrode, respectively. The bottom one is common and set to grand.

Multi-frequency ultrasonic beams are formed on the both results. In addition, the secondary waves increase through the propagation. From the former result, the beams are focused at the designed position, and its width is narrow compared to the latter result.

## 5. Conclusion

We proposed two different structure of transducer that can transmit two frequency ultrasonic pulses, and confirmed multi-frequency beams generation by the transducer.


## Acknowledgment

This work was in part supported by KAKENHI (20300181).


## References


1. P.A. Magnin, O.T. Vonramm and F.L. Thurstone: Ultrason. Imaging **4** (1982) 267.
2. I. Akiyama, H. Yamamoto, G. Ohashi, and A. Ohya: Proc. IEEE Ultrasonics Symp. (2003) 1642.
3. I. Akiyama, H. Yamamoto, G. Ohashi, and A. Ohya: Proc. 18th Int. Cong. Acoustics (2004) 163.
4. I. Akiyama, H. Yamamoto, G. Ohashi, and A. Ohya: Acoustical Imaging **27** (2004) 651.
5. I. Akiyama, A. Ohya and S. Saito: Jpn. J. Appl. Phys. **44** (2005) 4631.
6. I. Akiyama, S. Saito, and A. Ohya: Proc. Symp.Ultrasonic.Electronics (2006) 141

7.I. Akiyama, S. Saito, and A. Ohya: J. Acoust. Soc. Am. **120** (2006) 3026.

8. I. Akiyama, S. Saito, and A. Ohya: J. Med. Ultrasonics **33** (2006) 71.

Proceedings of Symposium on Ultrasonic Electronics, Vol. 29 (2008) pp. 295-296
11-13 November, 2008

# High-Amplitude and Long-Burst Pulse Transmission Array Probe for Phase-Conversion Molecular Imaging

超音波分子イメージングのための高出力アレイプローブ

Takashi Azuma[1†], Shiho Sonoda[1], Ken-ichi Kawabata[1] and Shin-ichiro Umemura[2]
([1] Hitachi Central Research Laboratory; [2]Facult. Eng., Tohoku Univ.)
東　隆[1‡], 薗田志保[1], 川畑健一[1], 梅村晋一郎[2]　([1]日立中研; [2]東北大 工)

## 1. Introduction

In phase-conversion ultrasonic molecular imaging [1], tissue-selective nano-droplets are converted to contrast microbubbles by using higher power ultrasound than that transmitted from a conventional imaging array. Developing wideband imaging arrays capable of phase-conversion ultrasonic molecular imaging is useful since many developed imaging sequences will be available immediately after phase-conversion. Since the sensitivity of an array decreases as a result of the breakdown after the transmission of phase-conversion ultrasonic molecular imaging, the limitations of duration and amplitude need to be overcome before an array for a phase-conversion ultrasonic molecular imaging can be used. We carried out various experiments and numerical simulations to investigate the breakdown process.

In our previous study, a conventional array using two PZT layers was broken after driving with 16 cycle pulses at 50 V caused. In this study, we measured breakdown conditions and breakdown process of an imaging array in cooling condition. By chnaging thermal boundary condition, it is expected that the thermal effect to breakdown process will be clear, and cooling effect to increase the limitation of transmission ultrasound energy.

## 2. Material and method

We measured the electric impedances by using a 4294A impedance analyzer (agilent) and the round trip response of array elements in an imaging array, whose center frequency is 7.5MHz, by using 5900PR pulser-receiver (panametrics) after high-amplitude and long burst transmission. These results were compared with the impedance and waveform calculated by PZFlex, a finite element code, by assuming several different ways of breakdown.

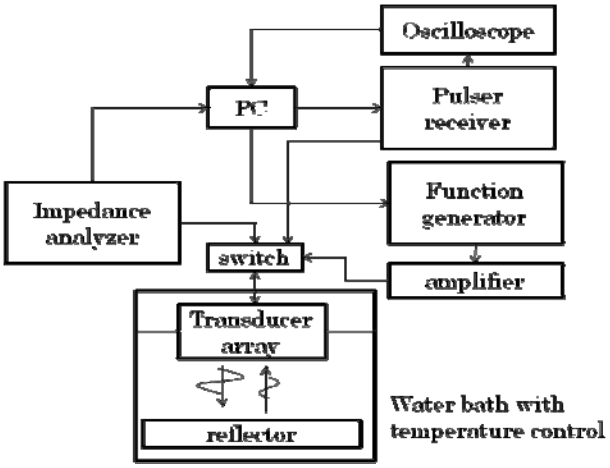


Fig.1　Experimental setup

## 3. Results and discussions

Breakdowns of the array occurred after driving with 100 cycle pulses at 160 V. This single PZT layer array could transmit higher power than two PZT layer array before breakdown. Mechanical Q values were increased with duration length during this breakdown process as shown in Fig.2 and Fig.3. Fig.2 shows results of impedance measurements and Fig.3 shows results of round-trip response. Fig.4 shows cooling of backing layer of transducer array improved the limitation of transmission energy from the transducer array. The experimental result was consistent with the simulation result assuming the peeling of the adhesive between PZT and the matching layer.

These results indicated that suppressing increases in temperature is also essential for phase-conversion ultrasonic molecular imaging using this improved array. Our simulation study has already showed that a new transducer structure that uses a heat conducting acoustic isolation layer on a metal block that was designed to inhibit this type of breakdown while maintaining the wide bandwidth required for imaging. Experimental results of the

---

takashi.azuma.sa@hitachi.com

thermal breakdown after phase-conversion ultrasonic molecular imaging transmission from our proposed structure probe will also be discussed.

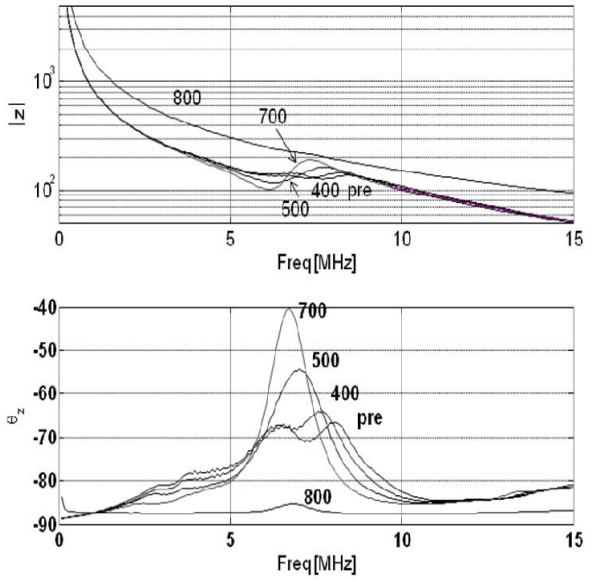


Fig.2 electric impedance after 120V driving. Numbers in the graph indicate cycle numbers of driving burst waves.

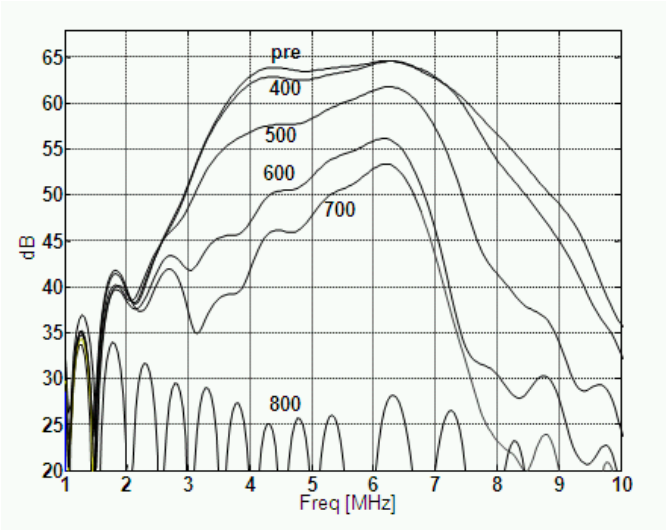


Fig.3 Round-trip responses after 120V driving. Numbers in the graph indicate cycle numbers of driving burst waves.

## 4. Conclusion

To prevent the peeling between matching layer and PZT, heat conductance around PZT should be improved. These experimental results indicate that the cooling effect improve the limitation of transmission energy. These results also suggest that improvement of heat conductance in a transducer array using acoustic isolation layer will be useful for phase-conversion ultrasonic molecular imaging.

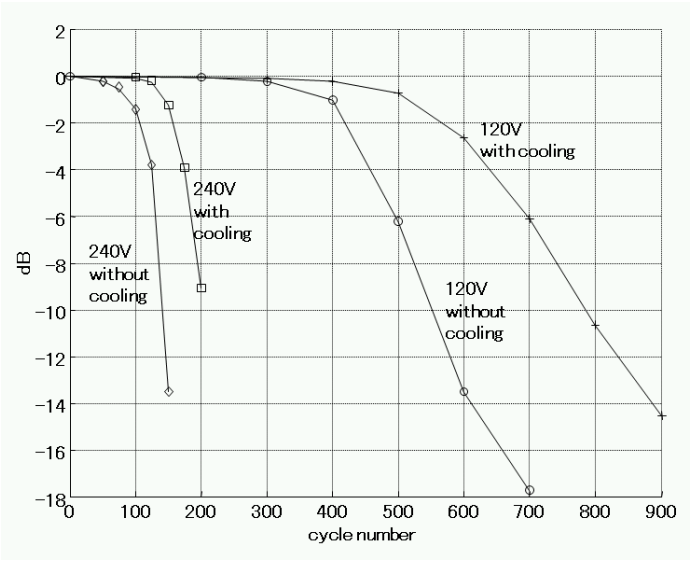


Fig.4 Sensitivity change of round-trip responses caused by breakdown

**Acknowledgment**

Part of this work was supported by the New Energy and Industrial Technology Development Organization, Japan.

**References**

1. **K. Kawabata, et al, IEEE Ultrason. Symp. (2006) 517-520.**
2. **T. Azuma, et al, IEEE Ultrason. Symp. (2006) 836-839.**

Proceedings of Symposium on Ultrasonic Electronics, Vol. 29 (2008) pp. 297-298
11-13 November, 2008

# Comparison of sound pressure distribution analysis with scale up experiment for small ultrasonic acoustic lens probe

微小超音波プローブ用音響レンズに関するスケールサイズ実験と解析の音場特性比較

Fumitaka Naitou[1‡], Sayuri Matsumoto[2], Mari Takahashi[1], Takenobu Tsuchiya[1] and Nobuyuki Endoh[1] ([1]Facult. Eng., Kanagawa Univ. , [2]PARI)
内藤 史貴[1‡], 松本 さゆり[2], 高橋 茉里[1], 土屋 健伸[1], 遠藤 信行[1]（[1]神奈川大学 工,[2]港空研）

## 1. Introduction

Many researchers are studying about underwater ultrasonic high–resolution imaging system. Authors have studied about the characteristics of convergence field of acoustic lens for developing the underwater image system[1-5]. In this study, we propose a small ultrasonic probe composed with an acoustical lens for diagnosys and therapy. The lens is designed by ray theory, and effective diameter of the acoustical lens is 40mm. We measured the characteristic of convergence field of acoustical lens in water tank. Size of lens is 4 times to final ultrasonic probe because of preliminary study. And, we analysis acoustic field by FDTD method

## 2. Experimental setup and analysis model

Figure 1 shows measuring system to obtain convergence field of acoustical lens. The distance between sound source and center of acoustic lens is 700mm. A burst-pulse of 10 cycles at 2.0MHz is radiated from the transducer whose diameter is 10mm and center frequency is 2.0MHz. The sound field distribution behind the lens was measured by a hydrophone whose diameter is 0.6mm. Diameter and effective diameter of the lens is 58mm and 40mm, and first plane of lens is flat. Material of lens was acrylic resin. Acoustic refraction index of acrylic is 0.53, and theoretical values of focal point is 291.3mm from the first lens plane. The aspheric surface equation of 2nd lens plane is shown in Eq. (1) The lens was fixed by lens holder.

$$X_{B2}(Y) = \frac{Y^2/(136.5)^2}{1+\sqrt{1-(1+(-0.5597))Y^2/(136.5)^2}}$$

Figure 2 shows analysis model to calculate convergence field by FDTD method in cylindrical coordination using symmetrical property. Calculated sound fields by 2DFDTD do not coincide with that of actual 3D lens. However, we can get result of similar to three dimension analysis by using cylindrical coordination using symmetrical property. A virtual sound source was used for reduction of calculation time. The distance between virtual sound source and the first plane of lens is 40mm. The configuration of the virtual sound source is circle of 660mm in curvature. It was assumed that a burst-pulse of 10cycle at 2.0MHz was radiated from virtual sound source.

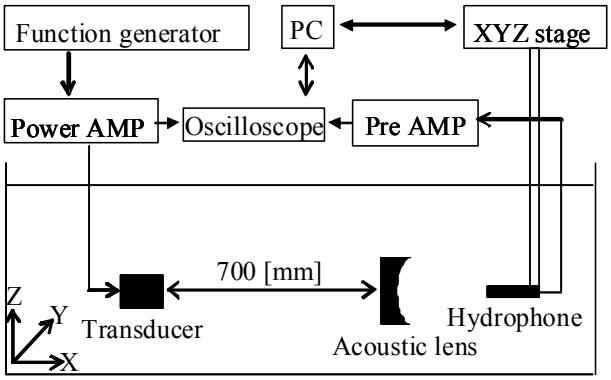


Fig. 1 Block diagram of measurement

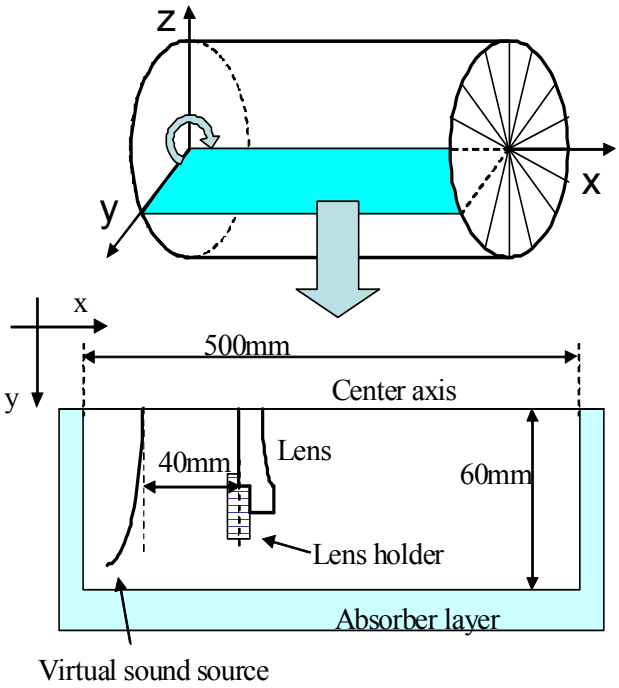


Fig.2 Calculation model for FDTD simulation

E-mail ; r200770074yx@kanagawa-u.ac.jp

Calculated step size of in analytic area is 0.0375mm. Sound velocity of water was calculated by Greenspan's equation at 18.0 deg. C, and sound velocity of lens was reported in previous work[6]. The lens holder is considered a rigid body.

## 3. Result

On-axis sound pressure of measurement and analysis result are shown in Fig.3 Comparison of measurement to analysis results, measured minimum value positions agreed well with analysis results. Focal point of measurement and analysis is 316mm and 310mm. Measurement and analysis beam pattern of transverse axis of focal point are shown in Fig.4. In the graph, beam width and beam pattern are about the same. Sound field distribution with cross section for axial distance in focal point are shown in Fig. 5. We can see that measurement and analysis result are convergence at the center. Comparison of characteristics of lens between experimental results and analysis results is shown in Table 1. All graphs are normalized by focal point sound pressure. Beam width is range of 0dB to -3dB.

## 4. Conclusion

We designed acoustic lens for small ultrasonic prove, and measured and calculated convergence field by the acoustic lens. Comparison between measurement and analysis result, it was almost the same. And beam pattern of transverse axis of focal point too. In future work, we will research incident angle dependency of convergence field of acoustic lens. Therefore, we will be simulating 3DFDTD of Cartesian coordinate system without cylindrical coordinate system.

Table 1 Comparison of characteristics of lens between experimental results and analysis results

| | measurement | analysis |
|---|---|---|
| Focal point | 316mm | 310mm |
| Beam width | 5.5mm | 5.6mm |


**Acknowledgments**

This study was partly sponsored by High-Tech Research Center Project from Kanagawa University and the Ministry of Education, Culture, Sports, Science and Technology, Japan 2007, Grand-in-Aid for Scientific Research (20500429) in 2008 and 2009.


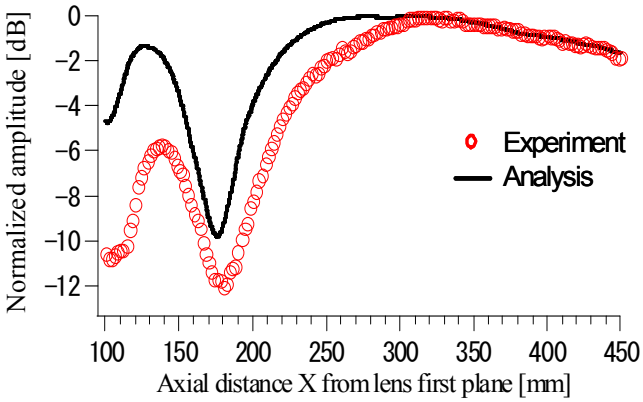


Fig. 3 On-axis sound pressure

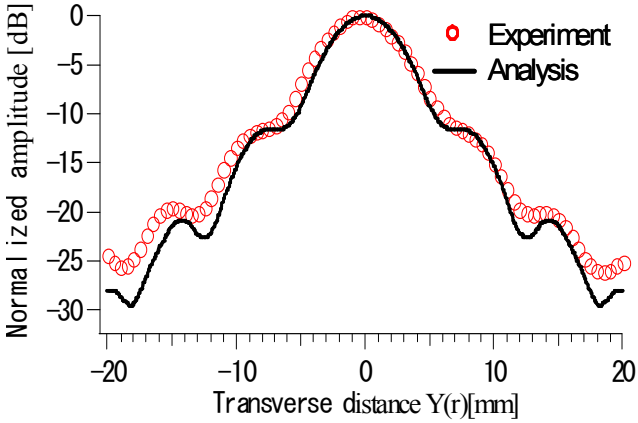


Fig. 4 Beam pattern of focal point

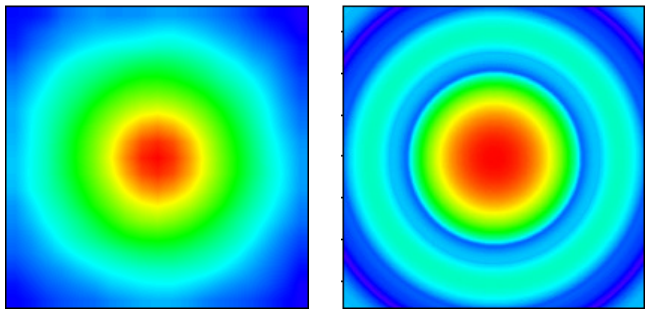

(a)Measurement (b)Analysis

Fig. 5 Sound field distribution with cross section for axial distance in focal point


**References**

1) S. Matsumoto, T. Tsuchiya, T. Anada and N. Endoh : Proc. of European Conf. on Underwater Acoustics, 2006, p.57.

2) S.Matsumoto, H.Takeyama, T.Tsutiya, T.Anada and N.Endoh : Proc. of Meeting of the Marine Acoustics Society of Japan, 2007, p.57.

3) S.Matumoto,Y.Shin,T.tsuchiya,T.Anada,N.Endoh and H.takeyama : USE2007 **28** (2007)479.

4) F.Naitou, S.Matsumoto, Y.Shin, T.Tsutiya, T.Anada and N.Endoh : Proc. of Meeting of the Marine Acoustics Society of Japan, 2008, p.33.

5) Y.Shin, S.Matsumoto, T.Tsutiya, T.Anada and N.Endoh : Proc. of Meeting of the Marine Acoustics Society of Japan, 2007, p.25

2P7b-6

Proceedings of Symposium on Ultrasonic Electronics, Vol. 29 (2008) pp. 299-300
11-13 November, 2008

# Effect of edge mode resonance on directivity of small ultrasound probe fabricated with Lead Zirconate Titanate polycrystalline film deposited by hydrothermal method

水熱合成法による PZT 多結晶膜を用いた小型超音波プローブの指向性に対するエッジモード共振の影響

Tomohito Hasegawa[1†], Minoru Kuribayashi Kurosawa[1] and Shinichi Takeuchi [2]
([1] Tokyo Tech.; [2]TUY.)
長谷川智仁 [1†]，黒澤実 [1]，竹内真一 [2] ([1] 東工大 総理工; [2] 桐蔭大 医工)

## 1. Introduction

Recently, miniature and high-frequency ultrasound probes are widely having studied for medical applications. Piezoelectric ceramics or piezoelectric polymer films are used as piezoelectric materials for the miniature high-frequency ultrasound probes. Piezoelectric polymer films show wide-band frequency characteristics but have the problem of low transmission sensitivity. Ultrasound probes using piezoelectric ceramics show high transmission sensitivity. However, piezoelectric ceramics are brittle, and the probe using them has narrow-band frequency characteristics.

We reported the fabrication of needle-type miniature hydrophones and ultrasound transducers using hydrothermally synthesized PZT polycrystalline films[1][2]. It was confirmed that these films had wide-band frequency characteristics with sensitivities in the megahertz band. It is thus thought that these films can be used to for miniature ultrasound probes with wide-frequency band characteristics. In the last report, the fabrication methods of a miniature ultrasound probe and the transmission and reception characteristics were evaluated [3]. Here, we report the results of our measurement of the probe's reception and transmission directivity.

## 2. Experiment method

The directivity of the miniature ultrasonic probe was measured in a water tank. Schematic diagram of the reception directivity measurement method (a) and the transmission directivity (b) are drawn in Fig. 1. The input signal to a transmitter was 15 cycles of burst wave. The burst wave was obtained by a function generator and a power amplifier; 200 $mV_{0\text{-}P}$ output signal from the function generator was amplified by 55 dB using the power amplifier. The received signal was amplified using a pre-amplifier in a pulser-receiver, and then measured with a oscilloscope. Directivity was measured from 90 to –90 degrees at intervals of 2 degrees. The directivity was measured at the frequencies of 5, 10, 15, and 20 MHz. The distance between the transmitter and the receiver was kept far enough to maintain the far field condition. The experimental results were compared with the directivity function calculated from far field radiation patter of a circular piston.

### A. Directivity measurement of reception

The effective element diameter of the ultrasound probe of the sound source was 6.35 mm, and center frequency was 15 MHz. The miniature ultrasound probe and the PVDF hydrophone for a comparison were used for receiving. The diameter of each effective element was 0.6 mm. The distance from an acoustic radiation surface to the probe was 150 mm. The probe was fixed to the theta axis, and directivity was measured by measuring the voltage while rotating the theta axis centering around a sound reception surface.

### B. Directivity transmission measurement

A miniature ultrasound probe with an effective element diameter of 0.6 mm was used for the sound source. The PVDF hydrophone was used for reception. The distance from the acoustic radiation surface to the PVDF hydrophone was 15 mm. The miniature ultrasound probe was fixed to the theta axis, and directivity was measured by measuring the voltage while rotating the theta axis centering around an acoustic radiation surface.

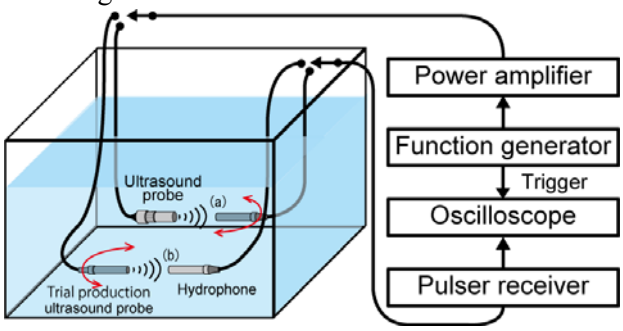


Fig. 1 Directive measurement system

†tomohito.hasegawa@ip.titech.ac.jp

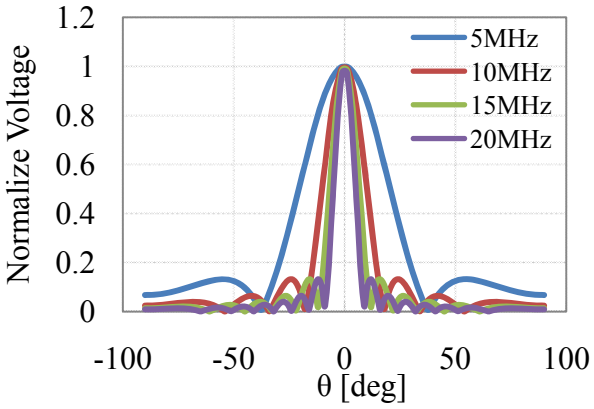


Fig. 2 Theory value of transmission and reception directivity

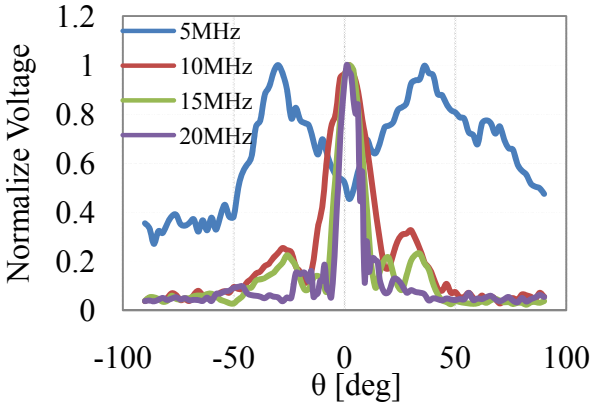


Fig. 3 Transmission directivity of miniature ultrasound probe

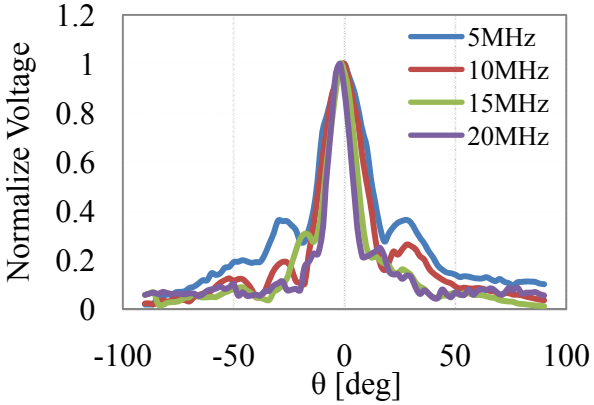


Fig. 4 Receiving directivity of miniature ultrasound probe

## 4. Results

The transmission and the receiving directivity theoretical value are shown in Fig. 2. The transmission directivity of the miniature ultrasound probe is shown in Fig. 3.

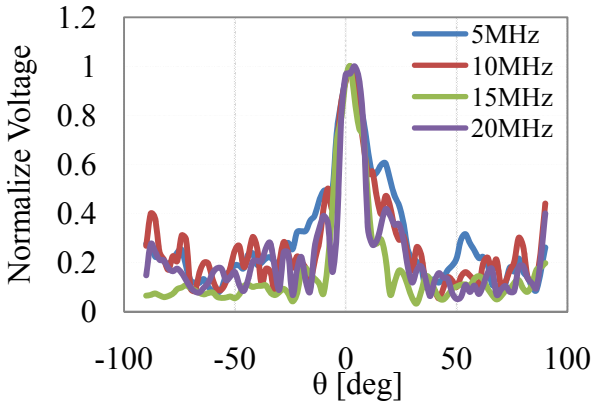


Fig. 5 Receiving directivity of PVDF hydrophone

The receiving directivity of the miniature ultrasound probe and the PVDF hydrophone is shown in Figs.4 and 5. Except for that at 5 MHz, the experimental reception directivity was similar to the theoretical experimental values, i.e., those obtained with the PVDF hydrophone or with the miniature ultrasound probe. At 5 MHz, measured directivity was sharper than that of the theoretical value. Likewise, in transmission directivity, the theoretical and experimental values were similar to each other except at 5 MHz, at which main directivity was low.

## 5. Conclusion

As for the directivity of the miniature ultrasound probe, the theoretical value and the experimental value were in good agreement for both reception and transmission at 10, 15, and 20 MHz. However, at 5 MHz, the theoretical value and the experimental value differed greatly in both transmission and reception. This can be attributed to the effect of the resonance mode of the diameter direction; namely, edge mode. In future works, the vibrational distribution of the end surface of a miniature ultrasound probe is scheduled to be measured with LDV.

**Acknowledgment**

This work was supported by a Grant-in-Aid for Japan Society for the Promotion of Science Fellows.

**References**

1. M. Ishikawa, M. Kurosawa, E. Akito, and S. Takeuchi : Jpn. J. Appl. Phys. 44 (2005) 4342.
2. H. Kitsunai, N. Kawashima, S. Takeuchi, M. Ishikawa, M. Kurosawa, E. Odaira : Jpn. J. Appl. Phys. 45 (2006) 4688.
3. T. Hasegawa, H. Kitsunai, A. Endo, N. Kawashima, S. Takeuchi, M. Ishikawa, and M. K. Kurosawa : Jpn. J. Appl. Phys. 46 (2007) 4801.

Proceedings of Symposium on Ultrasonic Electronics, Vol. 29 (2008) pp. 301-302
11-13 November, 2008

# Mechanical Properties of Low Attenuation Silicone Rubber Acoustic Lens Material Doped with Zinc Oxide for Medical Echo Probe

酸化亜鉛を添加したシリコーンゴム製低減衰音響レンズの機械強度特性

Noriko Yamamoto[1†], Yohachi Yamashita[2], and Kazuhiro Itsumi[1] ([1]Corporate Research and Development Center, Toshiba Corp., [2]Toshiba Research Consulting Corp.)
山本紀子[1†]，山下洋八[2]，逸見和弘[1] （[1]（株）東芝　研究開発センター，[2]東芝リサーチコンサルティング（株））

## 1. Introduction

Silicone (Q) rubber has been the predominant acoustic lens material for the medical array probe application since 1970[1)] because it is safe to use for the human body, has a suitable sound velocity ($c$) ($c$~ 1000 m/s), and a reasonably low $\alpha$ ($\alpha$~ 0.3 dB·mm$^{-1}$·MHz$^{-1}$). However, the acoustic impdance ($Z$) of pure Q rubber is approximately $0.97 \times 10^6$ kg·m$^{-2}$·s$^{-1}$, which is considerably different from the $Z$ of human tissue ($Z = 1.5 \times 10^6$ kg·m$^{-2}$·s$^{-1}$) at 37 °C. Therefore, to obtain the $Z$ of Q rubber close to that of human tissue, $SiO_2$ powder has been doped into the Q rubber. Since $SiO_2$ has a low density ($\rho$), $2.2 \times 10^3$ kg·m$^{-3}$, dopant contents 35 vol% in Q rubber are necessary for obtaining a $Z$ of higher than $1.4 \times 10^3$ kg·m$^{-3}$. As a result, $SiO_2$ -doped Q rubber shows large $\alpha$ > 0.9 dB·mm$^{-1}$·MHz$^{-1}$ and poor mechnical properties.

Recently, the authors have reported the acoustic properties of high temperature vulcanization (HTV) Q rubber doped with high-$\rho$ dopants ($\rho$ = 9.2), $Yb_2O_3$. The HTV Q rubber with $Yb_2O_3$ nanopowder dopant having an average particle size of 8 nm shows the low $\alpha$, appropriate $Z$, and high mechanical properties. However, the rubber has low mechanical tear strength less than 30 N/mm for practical application, and bio-compatibility was uncertain.[2,3)] The ZnO has also high-$\rho$ ($\rho$ = 5.6), and is stable procurement and bio-compatible material. In this report, the effect on acoustic and mechanical properties of ZnO-doped HTV Q rubber has been studied to develop a reliable low-$\alpha$ lens material for medical array probe applications.

## 2. Measurements and Results

### *2.1 Acoustic and mechanical properties*

The ZnO powder of the particle size of 30 nm was added to the millable type HTV Q rubber,[3)] which was used as the base material in this study. To realize several $Z$ values of lens, the ZnO powder dopant contents in Q rubber were varied. Table I lists the acoustic and mechanical properties of the base HTV Q rubber, two $Z$ types of ZnO-doped HTV Q rubbers (sample 1 and 2), and the conventional lens material Q rubber (Ref.). The base HTV Q rubber material contains about 10 vol% of 20 nm-particle-size of fumed $SiO_2$ powder. Thus, ZnO powder vol% is shown without $SiO_2$ in Table I. All the acoustic properties were measured at 37 °C, and each mechanical property was measured at room temperature in according with JIS K6253, K6252 and K6264-2. Both ZnO-doped samples had lower attenuation coefficient $\alpha$ than the conventional lens rubber. Tear strengths and elongation of ZnO-doped samples were about 3 times bigger than those of the conventional rubber. The rubber, which has high tear strength and elongation generally shows strong rub resistance. At Table I, this tendency was also appeared in the abrasion loss; ZnO-doped samples indicated about 1/3 compared to that of the conventional rubber.

Table I. Acoustic and mechanical properties of HTV Q rubbers.

| Sample | Base | 1 | 2 | Ref. |
|---|---|---|---|---|
| Dopant | $SiO_2$ | ZnO† | ZnO† | $SiO_2$ |
| Dopant content (vol%) | 10 | 12.4 | 15.4 | 23 |
| Rubber density (g/cm$^3$) | 1.09 | 1.61 | 1.73 | 1.4 |
| Acoustic velocity (m/s)* | 955 | 849 | 839 | 1039 |
| Acoustic impedance $Z$* ( × 10$^6$ kg·m$^{-2}$·s$^{-1}$) | 1.04 | 1.38 | 1.46 | 1.45 |
| Tear strength (N/mm) | 24 | 46 | 43 | 16 |
| Elongation (%) | 430 | 590 | 560 | 170 |
| Abrasion Loss (g) | 0.034 | 0.072 | 0.125 | 0.362 |

*Measured at 37°C / †$SiO_2$ is also included in the base Q rubber

### *2.2 Rubbing scanning test*

The ZnO-doped rubber sample 2 and conventional lens rubber were shaped in acoustic lens for use of rubbing scanning experiment. Using the abrasion tester (the color fastness to

abrasion test machine according as JIS L0849), fixture part was modified and two pieces of lens shaped sample were settled. Figure 1 illustrates the motion of the abrasion tester. Settled two samples were same type and were rubbed same direction as ultrasonic diagnostic scanning. On the stage, 15-mm-width waterproof sandpaper (AWA P600) was placed. Ultrasonic diagnostic jelly (SONO JELLY (M), Toshiba Medical Supply Co., LTD.) was applied on the sandpaper and samples. The abrasion test was executed 800 times of back and forth motion; each 200 times, SONO JELLY was added, and each 400 times, sandpaper was renewed. The abrasion loss rates on the initial sample weight showed 0.83% in ZnO-doped sample 2 and 1.68% in conventional rubber. Figure 2 shows the cross-section profiles of the lens shaped samples. The ZnO-doped sample kept round lens shape even after the rubbing test, in contract, the conventional rubber was planed. Therefore, using the ZnO-doped HTV Q rubber predicts a long-life acoustic lens.

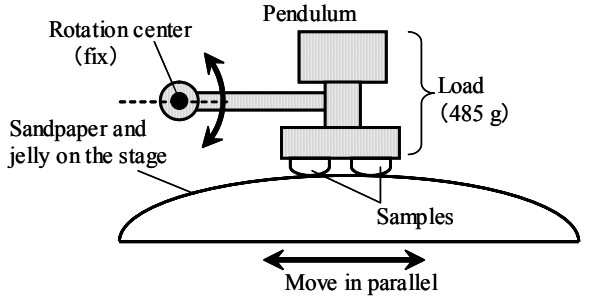


Fig. 1. Motion of abrasion tester.

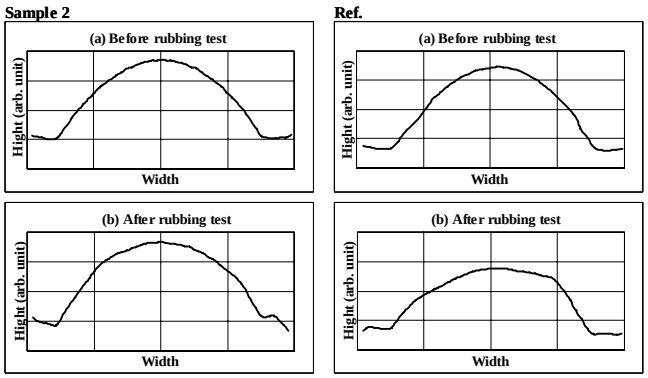


Fig. 2. Lens profiles of (left) ZnO-doped rubber and (right) conventional rubber (a) before and (b) after rubbing scanning test.

## 3. Discussion

Figure 3 shows SEM microstructures of ZnO-doped HTV Q rubber (a) and conventional rubber (b). Neither large pores nor agglomerations were seen in ZnO-doped rubber. The additive ZnO powder was in spherical shape, because of that caused high and uniform dispersibility in the Q rubber. The rubber strength is decided by how much of the breaking origins in the material. Because of ZnO-doped rubber has fewer pores and agglomerations, and the shape of ZnO powder is spherical, there is little chance of breaking origination. Further, ZnO is also used as vulcanization accelerator so that made the HTV Q rubber mechanical properties more strength.

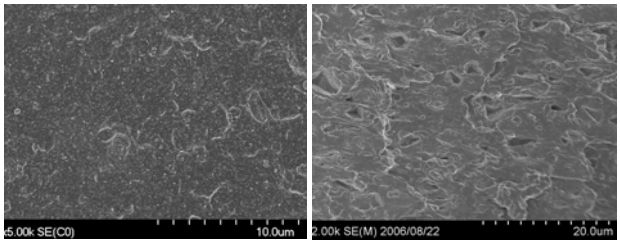


Fig. 3. SEM images of (a) ZnO-doped rubber (× 5000) and (b) conventional rubber (× 2000).

## 4. Conclusions

The ZnO-doped high temperature vulcanization (HTV) Q rubbers for acoustic lens materials were investigated. Their acoustic and mechanical properties were compared to evaluate their use as an acoustic lens material for medical ultrasonic probe application and the following results were obtained.

(1) Compared with conventional rubber, ZnO-doped HTV Q rubber showed 3 times higher tear strength and elongation and abrasion loss was 1/3.
(2) The rubbing scanning test evidenced that ZnO-doped rubber lens has excellent rub resistance.
(3) Spherical shaped powder ZnO and its effects of vulcanization acceleration to the base rubber contribute high mechanical strength of ZnO-doped rubber.

## References

1. K. Iinuma and M. Hashimoto: Proc. 26th Conf. Medical Ultrasonics, Tokyo, 1974, Jpn. J. Med. Ultrason., 28 (1974) Suppl. 26, p. 119 [in Japanese].
2. Y. Yamashita, Y. Hosono, N. Yamamoto, and K. Itsumi: Jpn. J. Appl. Phys. **46** (2007) L851.
3. Y. Yamashita, Y. Hosono, N. Yamamoto, and K. Itsumi: Jpn. J. Appl. Phys. **47** (2008) 4132.

Proceedings of Symposium on Ultrasonic Electronics, Vol. 29 (2008) pp. 303-304
11-13 November, 2008

# A novel cleaning equipment using ultrasonic waveguide mode
# 導波路管型超音波洗浄機用振動子の試作

Kazunari Suzuki[1,2‡] , Ki Han[1] , Shoichi Okano[1] , Jyunichiro Soejima[1]
and Yoshikazu Koike[2] ([1]KAIJO CO., LTD.; [2]Facult. Eng.,Shibaura Inst.of Tech.)
鈴木一成 [1,2‡]，潘毅 [1]，岡野勝一 [1] ，副島潤一郎 [1]，小池義和 [2]（[1] カイジョー; [2] 芝浦工大 工）

## 1. Introduction

There is a great demand for ultrasonic cleaning, not only in the advanced semiconductor/FPD cleaning process but also in the substrates for HDD or photovoltaic manufacturing process. The authors have been investigating a spouting megasonic cleaning equipment (Spot type shower) [1,2]. This equipment is possible to installed in the piece by piece type cleaner. However, distance between megasonic nozzle and substrate should be set up within 20mm to obtain optimum cleaning effect. Therefore, it takes a lot of spaces on substrate to set up the nozzle and arm.[3] In this report, we proposed a novel cleaning equipment using ultrasonic waveguide mode (we call MEGATUBE). By applying the input power to the PZT, ultrasonic wave can be traveled along the waveguide. It is possible to supply ultrasonic apart from PZT. We showed the prototype transducer using waveguide, and propagation characteristics were investigated.

## 2. Transducer using ultrasonic waveguide mode

The transducer using a waveguide consists of a PZT attached with a vibration plate, reflection nozzle (SUS316L), and a waveguide (quartz) as shown in **Fig.1**. These parts were installed in a case and sealed by packing. Cleaning solution (DI water or chemicals) is supplied from a case and throughout the waveguide. Reflection nozzle has been applied to the spot type shower.[4] Ultrasonic waves generate from PZT (vibration area is 15mm in diameter) are reflected between PZT and reflection nozzle, waves are converged towards the center of the nozzle and emitted together with solution flowing. A waveguide connected with reflection nozzle has a removable structure. We can select the waveguide that has a different length or bend shape according to the purpose.

We tried a simulation of wave propagation using Cellular Automata.[5] **Fig.2** shows propagation in the waveguide filled with water. Ultrasonic waves are generated from vibration area (φ15) at 950 kHz. Waves propagate in the waveguide have a periodic waveguide mode. Wave data shows the sound pressure at center of Y-axis. Period of sound pressure along X-axis is under consideration.

---

kz-suzuki@kaijo.co.jp

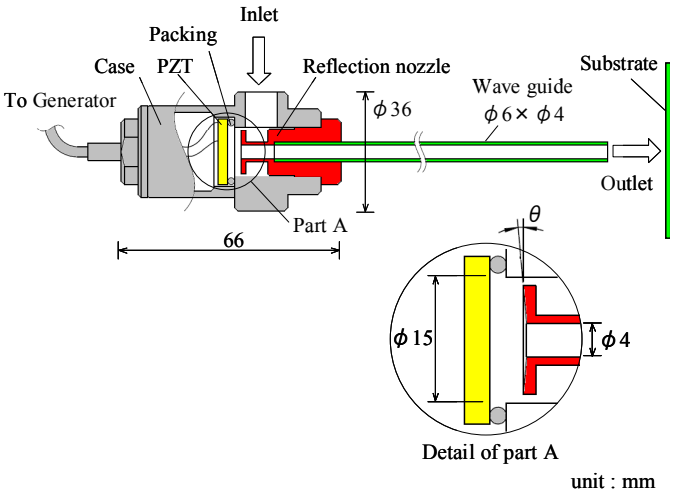


Fig.1 Configuration of the waveguide type transducer

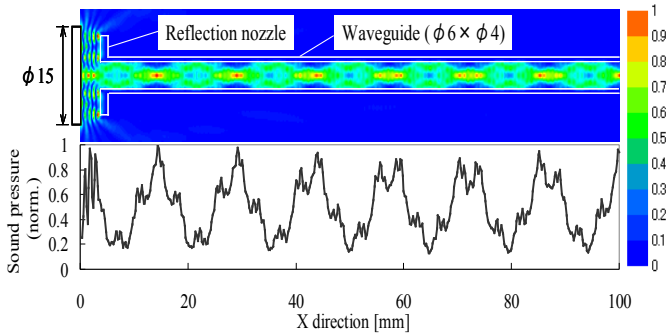


Fig.2 Propagation in the waveguide predicted by Cellular Automata

## 3. Sound pressure measurement by hydrophone

Sound pressure was measured using a quartz rod hydrophone probe (Honda elec. HUS-5). As shown in **Fig.3**, cleaning solution (DI water) spouting from waveguide will reach at the hydrophone and output voltage is measured by oscilloscope (Lecroy wave Jet 354). Rectify processing and 30Hz low-pass filter was applied by PC to concern the change of output voltage due to solution flowing. Ultrasonic generator (KAIJO 28101) is connected to the transducer and generate at 950 kHz. Flowing rate is controlled at 1L/min and dissolved $O_2$ concentration of DI water is at 7~8ppm.

First, spot type transducer which has no waveguide[3] was evaluated. The output voltage of hydrophone was measured changing the output power of generator. As shown in **Fig.4**, the larger output voltage could be obtained with the larger output power, and output voltage becomes 0.17mV at 30W.

Next, waveguide type transducer was evaluated. The output voltage of hydrophone was measured changing the length of waveguide, and output power is fixed at 30W. As shown in **Fig.5**, the output voltage decreases depend on the length of waveguide, and output voltage becomes 0.10mV at 500mm, it decreases in 41% against the spot type. Between the length of 100mm and 500mm, output voltage decreases in 42%. One of a factor in this phenomenon is absorption of ultrasonic in water. Coefficient of absorption in water is $25\times10^{-3}$ at 1MHz,[6] and decrease in distance 400mm is calculated with 1%. Therefore, there is a great different with measurement result. Influence of dissolved gas in water or absorption of ultrasonic in waveguide made of quartz should be concerned.

The output voltage of hydrophone was measured changing the bend angle of waveguide, waveguide length is 200mm, bend radius is 60 mm, and output power is fixed at 30W. As shown in **Fig.6**, the output voltage is almost same depend on the angle of waveguide, and obtained output voltage is 0.12mV approximately

## 4. Conclusion

We showed the prototype transducer using waveguide, and propagation in waveguide predicted by Cellular Automata has a continuous waveguide mode. At the sound pressure measurement using hydrophone the output voltage decreases depend on the length of waveguide, at 500mm in length, it decreases in 41% against the spot type. The output voltage is almost same depend on the angle of waveguide. Therefore, we can expect the stable cleaning effect when using waveguide which has a bend shape.

**References**


1. H. Suzuki, K. Ichikawa and S. Takahashi : Kaijo Technical Report. 9 (1999) p.8.
2. K. Suzuki : Kaijo Technical Report. 12 (2003) p.33.
3. K. Suzuki, K. Han, S. Okano, J. Soejima and Y. Koike : USE 2008 Symp. Ultrasonic Electronics. (2008). [To be presented]
4. S. Takahashi : Official report of patent, No. 3256198 (2002)
5. T. Komatsuzaki, H. Sato, Y. Iwata and S.Morishita : Transactions of JSCES(1999) Paper No.19990017.
6. J. Saneyoshi, Y. Kikuchi, and O. Nomoto: Ultrasonic technical handbook (1966) p.921


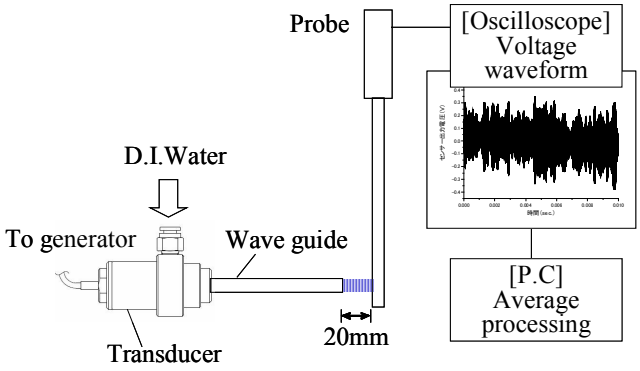


Fig. 3 Schematic diagram of sound pressure measurement using hydrophone probe

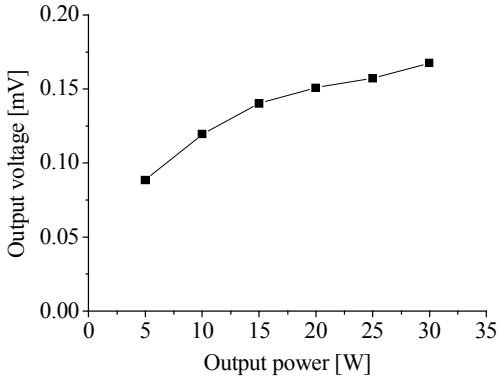


Fig. 4 Dependence on the output power at spot type

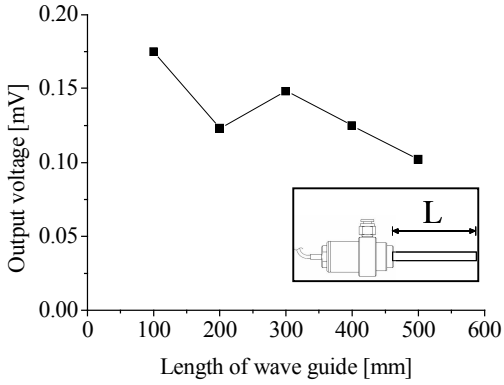


Fig. 5 Dependence on the length of waveguide

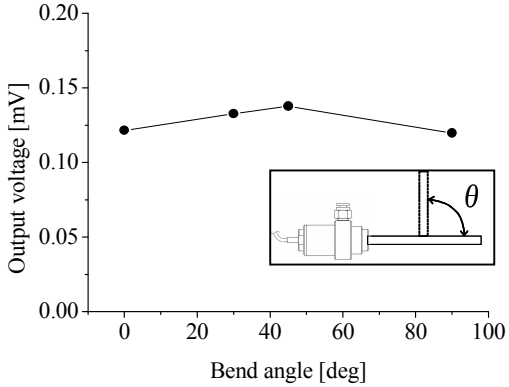


Fig. 6 Dependence on the bend angle of waveguide

2P8-2

Proceedings of Symposium on Ultrasonic Electronics, Vol. 29 (2008) pp. 305-306
11-13 November, 2008

# Nucleation Enhancement of Al alloys by High Intensity Ultrasound

Jeong IL Youn[1‡], Byoung IL Kang, Beom Suk Han[2] and Young Jig Kim[1]
([1] School of Advanced Materials Science and Engineering, Sungkyunkwan Univ.,
[2] Vehicles Research and Development, Korea Automotive Technology)

## 1.Introduction

Ultrasound is well known as a tool used in medicine for fetal imaging, in underwater range finding or in the non destructive testing of metals for flaws. However, the ultrasound with high intensity energy could be used in melting and casting process to obtain fine-grained ingot. In order to obtain fine-grained microstructure, the nucleation frequency has to be increased and grain growth must be restrained. Various processes, such as rapid cooling, melts stirring, and inoculation, have been used for obtaining fine grains. The high intensity ultrasound has been implied to increase the nucleation frequency during solidification of metal melts. It has been shown that the injection of high intensity ultrasound vibration into aluminum alloy during its solidification can eliminate columnar dendritic structure, refine the equiaxed grains, and under some conditions, produce globular non dendritic grains [1,2]. Mechanisms for grain refinement under ultrasonic vibration have been proposed but they are still arguable [3]. In addition, the process application of high intensity ultrasound vibration for grain refinement of ingot mainly has been focused on solidification or semi-liquid region of metal alloy. However, in this way, ultrasound injection for fine-grained ingot could not be applied to normal casting processes, i.e. sand casting, permanent mold casting, and die casting.

In this study, high intensity ultrasound process, it is named as Sono-processing, was tested as a refinement process of primary alpha and silicon phase in hypo- and hyper-eutectic Al-Si alloy, A356 and A390 alloy, respectively. The present investigation attempts to evaluate the effect of ultrasound vibration on microstructure, which was cast to be injected ultrasound vibration energy into the full alloys melts.

## 2. Experimental procedure

A356 and A390 aluminum alloys were cast in the laboratory. The chemical composition for these alloys is given in **Table I**.

younj1@skku.edu

Table I. Chemical composition of A356 and A390 aluminum alloy (mass%)

| Element | A356 | A390 |
|---|---|---|
| Si | 6.9 | 16.9 |
| Cu | 0.2 | 4.3 |
| Mg | 0.4 | 0.5 |
| Mn | 0.1 | 0.1 |
| Fe | 0.1 | 0.1 |
| Al | Bal. | Bal. |

**Fig. 1** shows the ultrasound injection system of 20 kHz with the power output up to 840 W for metal melts. The system comprised of an ultrasonic generator, a transducer of PZT type, booster and radiator horn. The most important thing in this apparatus was a cooling system for PZT transducer which was not worked at high temperature. The molten alloy injected ultrasound was poured into the permanent mold heated at 150 $^{o}$C and then,

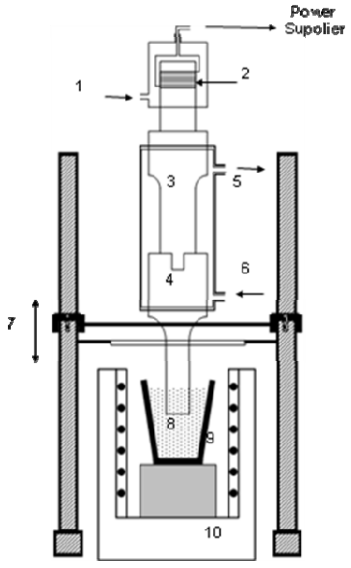


1.Cooling air in, 2.PZT 3.Booster horn, 4.Radiator horn, 5.Cooling water out, 6.Cooling water in, 7.Elevator, 8.Melts, 9.Graphite crucible, 10.Electric resistance furnace

Fig. 1 Schematic diagram of apparatus for ultrasound injection into metal melts

pouring temperature was about 700±10 $^{o}$C and 750±10 $^{o}$C at A356 and A390 alloy, respectively.

### 3. Results and discussions

The optical micrographs of the samples from castings made with and without high intensity ultrasound injection into alloys melts are shown in **Fig. 2 and 3**. The microstructure refinement, especially primary alpha phase, could not be achieved in A356 alloy with simply ultrasound injection into alloy melts as shown in Fig. 2 (a) and (b). However, the influence of ultrasound on the microstructure in A390 alloy is very clear as shown in Fig. 3 (a) and (b). Primary silicon of A390 alloy with ultrasound injection into melts was very small and dispersed uniformly in alloy matrix. In previous study, it has been reported that the microstructure refinement could be achieved by ultrasound vibration only during solidification of melts, and there is no effect on nucleation enhancement by just melts vibration [4]. The same result gets in this experiment on A356 alloy. Compared with A356 alloy, however, A390 alloy shows the nucleation enhancement by ultrasound vibration of melts only. Based on these experiments results, solute cluster hypothesis could be suggested. Until now, the microstructure refinement by ultrasound injection

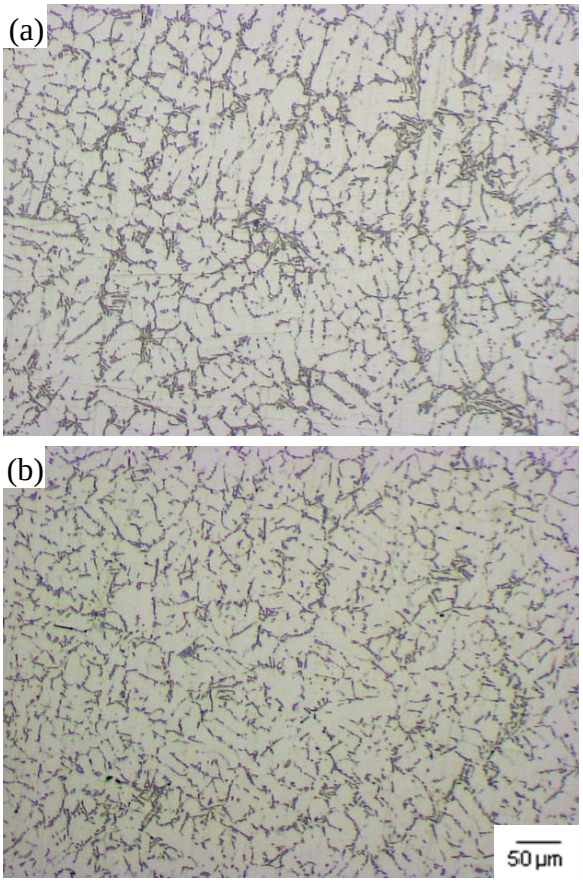


Fig. 2 Microstructure of A356 alloy; (a) without and (b) with ultrasound injection for 10 min.

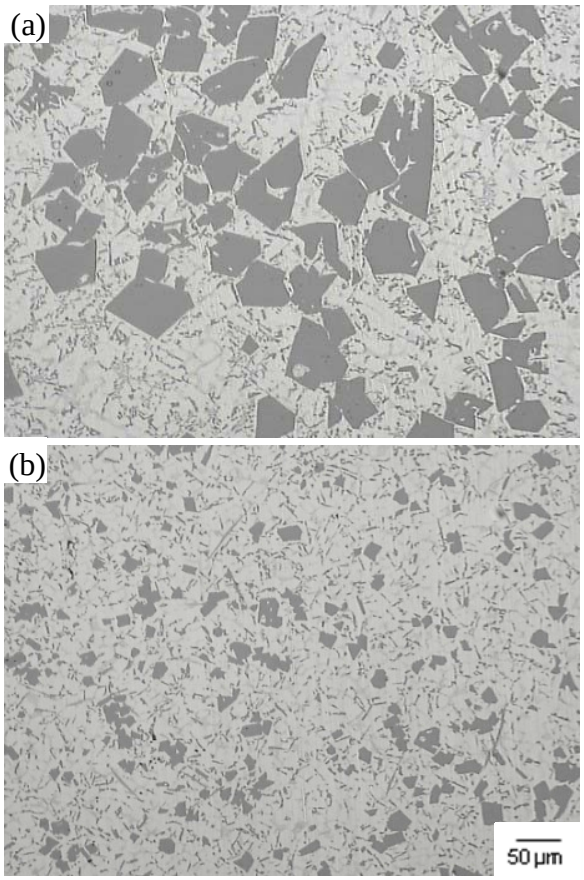


Fig. 3 Microstructure of A390 alloy; (a) without and (b) with ultrasound injection for 10 min.

could be explained only in terms of break of dendrite arms during solidification and/or formation of nuclei by cavitation effect. However, solute cluster hypothesis suggests that the microstructure refinement can be achieved by uniformity of solute cluster in melts as a chemical composition, and in result, nucleation enhancement can be promoted by high intensity ultrasound.

### 4. Conclusion

The present investigation attempts to evaluate the effect of ultrasound vibration on the microstructure of hypo- and hyper-eutectic Al-Si alloys. The microstructure refinement could be achieved by ultrasound injection into metal melts as a chemical composition. The refinement mechanism could be explained by solute cluster hypothesis.

**References**

1. X. Jian, T.T. Meek and Q. Han : Scripta Mater. **54** (2006) 893.
2. Y.L. Li and et al : Mat. Sci. and Eng. A. **487** (2008) 518.
3. J. Campbell : Int. Met. Review. **2** (1981) 71
4. Y. Osawa and et al : J. JFS **71** (1999) 98

2P8-3

Proceedings of Symposium on Ultrasonic Electronics, Vol. 29 (2008) pp. 307-308
11-13 November, 2008

# Ultrasonically Induced Enhancement in Treatment of Livestock Waste Sludge

Jiho Park[1], Young Uk Kim[1†], Jong-Sub Lee[2], Mian Chen Wang[3](1Dept. of Civil & Env. Eng., Myongji Uni., [2]Dept. of Civil & Env. Eng., Korea Uni., [3]Dept. of Civil & Env. Eng., The Pennsylvania State Uni.)

The effect of ultrasound on total mass, dewaterability, turbidity, and coliform counts of livestock waste sludge was investigated. The study involved laboratory tests and pilot plant experiment under various test conditions including sonication time, ultrasonic energy level, and sludge volume. Laboratory test results showed that sonication caused a decrease in sludge particle size, capillary suction time, and coliform counts. Pilot plant experiment results showed that ultrasonic treatment significantly improved dewaterability, and reduce the volume, mass, and water content of sludge.

KEYWORDS: ultrasound, sludge, livestock waste, sludge disposal, sludge dewaterability, pilot plant

The rapidly increasing quantities of sludge produced in livestock waste treatment facilities may cause serious and direct impacts on public health. Because the cost associated with sludge handling and disposal is highly dependent on the volume and water content of the sludge, there is a great interest in developing techniques for reducing sludge volume. A technique that has received considerable attention is sonication. A number of studies have investigated the beneficial effect of treating the sludge with ultrasound before the sludge reaches the digesting tank to increase soluble Biochemical Oxygen Demand (BOD).[1-2)] There are also studies investigating the effectiveness of ultrasound on the dewaterability of sewage sludge by changing the floc structures and microorganism surface properties.[3-4)]

The primary focus of this study is to investigate the effectiveness of ultrasound in enhancing the dewaterability of sludge as a post - treatment process. In addition to dewaterability, the effect of sonication on coliform counts and capillary suction time was investigated. Meanwhile, pilot plant tests were performed to investigate the potential application of the laboratory experimental findings.

The test sludge was obtained from a treatment plant of livestock waste in Kimpo, Korea. After sampling from an anaerobic digestion tank, the test sludge samples were prepared at a constant solids concentration. The sludge was ultrasonically treated in a bath-type ultrasonic processor(Chosun, Model CS-1000, 36×36×36(cm)) under various test conditions. The piezo ceramic transducer of 50mm diameter and 85mm height was used to produce ultrasound that was tuned at 28kHz. The applied ultrasound energy level was expressed in terms of the specific supplied energy parameter which is defined as follows:

$$I_{US} = \frac{P \times t}{Vol} \qquad (1)$$

In which, $P$ is the consumed ultrasonic power(kW), $Vol$ is the total volume of the sludge sample(liter) and $t$ is the ultrasonic irradiation time(minutes). During the test, the time required for water coming out of sludge to travel a certain distance through filter paper(whatman 17CHR) was measured using a CST(capillary suction time) tester. All measurements were done in triplicate under the same conditions, and the average values were used for the subsequent analysis.

The pilot plant experiment was performed using the specially developed large scale ultrasonic bath processor. The processor, shown in Figure 1, had a diameter of 1m and a height of also 1m. The experiment was conducted using a maximum power of 6kW with 28kHz ultrasonic wave frequency, and the specific supplied energy parameter($I_{US}$) was maintained around 30. The reason for the chosen value will be discussed in the later. The test sludge was first treated with ultrasound, and was then dewatered using a centrifuge machine. After dewatering, the mass, water content, and volume of the dewatered sludge were measured.

[1†]E-mail: yukim@mju.ac.kr

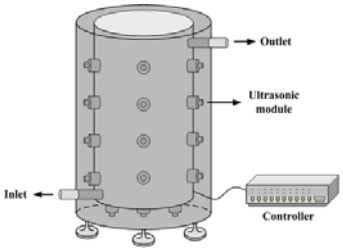


Fig. 1. Large scale ultrasonic processor

Figure 2 shows the change in CST(capillary suction time) with $I_{US}$. CST was measured to evaluate sludge dewatering behaviors according to changes in particle size. CST indicates how fast sludge can release its water. Usually, a long CST means a high cake specific resistance. In the figure, a decrease in CST with increased $I_{US}$ is clearly seen. Based on the definition of $I_{US}$, the results indicate that CST reduction is influenced not only by ultrasound power but sonication time and sludge volume as well. The results also reveal that sludge flocs were both separated and disintegrated by ultrasonic treatment, resulting in the increased filterability.

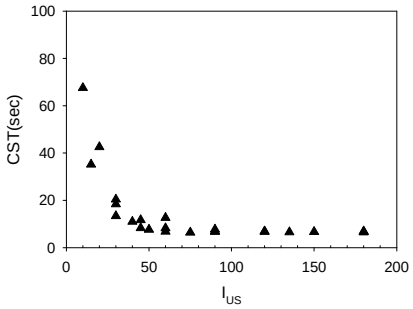


Fig. 2. Capillary suction time

Coliform count is a commonly - used bacterial indicator to determine the sanitary quality of food and water. Figure 3 shows that coliform counts decrease with increasing $I_{US}$ at a trend resembling that of previous figures. Coliform counts decrease drastically and remain almost constant as ultrasonic energy increases. Thus, in addition to dewaterability, ultrasound can also affect the sanitary quality of livestock waste sludge considerably.

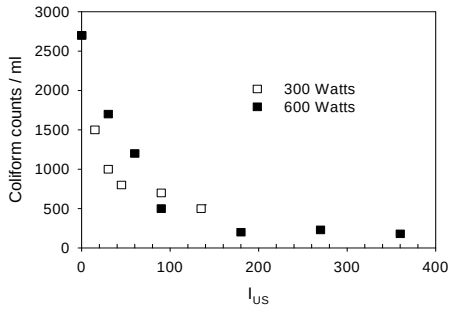


Fig. 3. Coliform counts vs. $I_{US}$

The pilot plant experiment shows considerable difference in the total volume of sludge both with and without sonication as illustrated in Figure 4. These results indicate clearly that ultrasonic energy reduces not only the volume of sludge, but also its mass and water content.

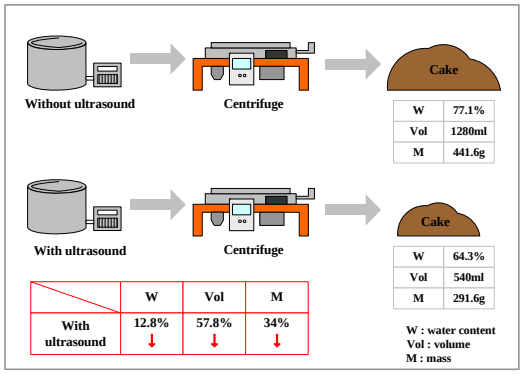


Fig. 4. Cake reduction due to ultrasound

The pilot plant experiment was conducted to investigate potential field applications of these research findings. In conclusion, ultrasonic treatment is a useful tool for enhancing sludge dewaterability thereby reducing the amount of sludge released from livestock waste treatment facilities.

This study was gratefully supported by Korea Research Foundation Grant (KRF – 2005 – 202 - D00504).

## References

1. J. A. Müller: Wat. Sci. & Tech. **44**(2001) 121.
2. U. Neis, K. Nickel and A. Tiehm: Wat. Sci. & Tech. **42**(2000) 73.
3. Y. Kim and B. Kim: Jpn. J. Appl. Phys. **42**(2003) 5898.
4. Y. Kim, J. Ha, G. Kim and S. Na: Jpn. J. Appl. Phys. **45**(2006) 311.
5. L. H. Mikkelsen and K. Keiding: Wat. Res. **36**(2002) 2451.
6. A. Tiehm, K. Nickel, M. Zellhorn, and U. Neis: Wat. Res. **35(**2001) 2003.

2P8-4

Proceedings of Symposium on Ultrasonic Electronics, Vol. 29 (2008) pp. 309-310
11-13 November, 2008

# Estimation of Sound Energy Distribution for the Design Optimization of Large-Scale Sonoreactors

Younggyu Son[1‡], Myunghee Lim[1], Ik-Beom Park[2], Mingcan Cui[1], Jeehyeong Khim[1†]
([1] Department of Civil, Environmental and Architectural Engineering, Korea University; [2]Gyeonggi-do Institute of Health and Environment)

## 1. Introduction

Numerous cavitation events including the formation, oscillation and implosive collapse of bubbles occur continuously an locally in micro-scale as ultrasonic wave over 20 kHz travels in the aqueous phase. It is believed extreme conditions such as high temperature over several thousand degrees Kelvin and high pressure over 1000 atmospheres are formed inside cavitation bubbles. During the oscillation and the collapse of cavitation bubbles these severe conditions lead to removals of organic pollutants related to pyrolysis and radical oxidations inside bubbles and adjacent regions.

Many previous studies have shown that a wide variety of organic pollutants including chlorinated compounds, phenols, and endocrine disrupting compounds can be effectively degraded using ultrasound alone and combination with other advanced oxidation processes such as ultraviolet, ozone, hydrogen peroxide and so on. The common working volumes of sonoreactors which have been reported in the literature are in small scale ranged to only several hundred milliliters, related to probe type and cup horn type. For the industrial application of ultrasound, researches on large-scale sonoreactors were rarely done.

This present study was designed to evaluate the performance of a large-scale sonoreactor under various conditions. The specific objectives of this investigation were to quantify the sonochemical reactions and to optimize the geometry of sonoreactors.

---

hyeong@korea.ac.kr

## 2. Materials and methods

The sonoreactor used in this study consisted of an acrylic reactor and an ultrasonic transducer module (Mirae Ultrasonic Tech.) placed at the bottom. The transducer module contained nine PZT transducers and could produce ultrasound of 35, 72, 100 and 170 kHz frequency. The maximum power of the transducer module was 400 W. The reactor was filled with distilled water of 60 L.

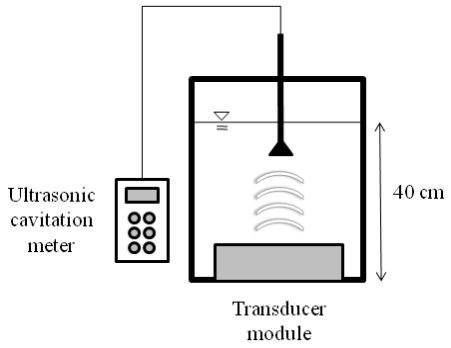


Fig. 1 Schematic of the large- scale sonoreactor

An ultrasonic /megasonic cavitation meter (ppb pb-502) was used for the analysis of cavitation energy in the sonoreactor. This instrument could detect the collapse of the cavitation bubbles as they imploded on the surface of a probe. As a result, it could display the energy density of cavitation as a unit of W/cm$^2$. The diameter of the probe was 5 cm.

When ultrasound is applied to an aqueous potassium iodide (KI) solution, triiodide ion ($I_3^-$) can be liberated from the iodine ion. The amount of triiodine ion liberated can then be used for the quantification of a sonochemical reaction as sonochemical efficiency (SE), as follows:

$$SE = \frac{C_I}{P_{US}\, t_{US} / V_I} \qquad (1)$$

where $C_I$ is the liberated triode ion concentration, $P_{US}$ is the cavitation energy, $t_{US}$ is the irradiation time and $V_I$ is the aqueous volume. In this study, the concentration of KI was 0.1 M, the irradiation time was 10 min., and the amount of liberated iodine was measured at 350 nm using a UV/VIS spectrophotometer (Analyticjena SPECORD 40). Hydrogen peroxide was measure using the KI method.

## 3. Results

Cavitation energy was measured along the liquid height, which was irradiation distance. **Fig. 2** shows cavitation energy distributions for 80, 160, 240 and 320 W of input electrical energy. Measured cavitation energy decreased from at the position of 5 cm to the position of 10 cm. However cavitation energy increased after 10 cm as the height of liquid increased and then decreased again drastically near liquid surface. No evidence of cavitation- energy attenuation was not found here.

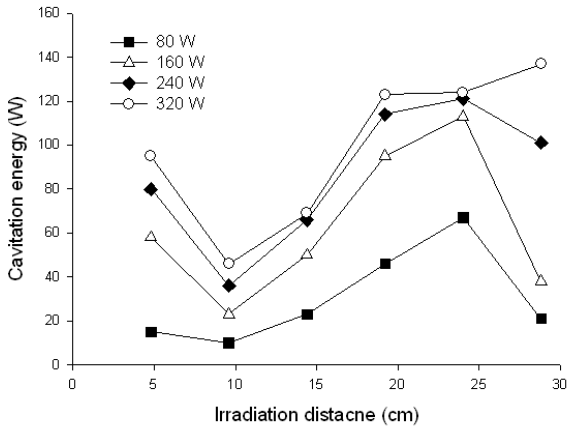


Fig. 2 Cavitation energy distributions for 80, 160, 240 and 320 W in the large-scale sonoreactor

**Fig. 3** shows the relationship between averge input electrical energy and average cavitation energy for 35 kHz. The empirical relationships (eq. 2) was obtained using a quadratic curve fitting skill. This was successfully achieved ($R^2$ was 0.9969).

$$Cavitation\ energy = -0.0016(input\ energy)^2 + 1.4459(input\ energy) \quad (2)$$

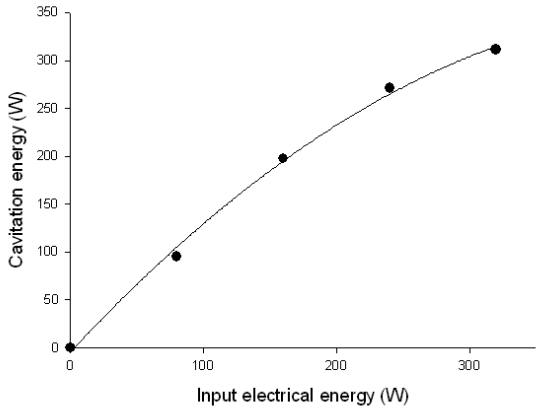


Fig. 3 Relationship between input electrical energy and measured cavitation energy for 35 kHz


## Acknowledgements

This study is supported by the Ministry of Environment, Republic of Korea as "The Eco-technopia 21 project" (no. 061-081-042).


## References


1. Y. G. Adewuyi, Ind. Eng. Chem. Res. **40** (2001) 4681.
2. L. H. Thompson and L. K. Doraiswamy, Ind. Eng. Chem. Res. **38** (1999) 1215.
3. T. J. Mason and J. P. Lorimer, Applied Sonochemistry-The Uses of Power Ultrasound in Chemistry and Processing, Wiley-VCH Verlag GmbH, Weinheim, 2002.
4. T. G. Leighton, The Acoustic Bubble, Academic Press, London, 1994.
5. Y. Asakura, T. Nkshida, T. Matsuoka and S. Koda Ultrason. Sonochem. **15** (2008) 244.

Proceedings of Symposium on Ultrasonic Electronics, Vol. 29 (2008) pp. 311-312
11-13 November, 2008

# Extraction of Metal Species from Contaminated Soils Utilizing Supercritical $CO_2$ and Ultrasound

Ik B. Park, Younggyu Son (Korea University), Il S. Song, Kyung H. Na, Jongchan Kim (Gyeonggi-do Institute of Health and Environment) and Jeehyeong Khim† (Korea University)

## 1. Introduction

Supercritical Fluid Extraction (SFE) is the process of separating the extractant from the sample matrix using supercritical fluids such as carbon dioxide ($CO_2$) etc., as the extracting solvent. Recently, supercritical fluids comprising a chelating agent have been proposed for chelation and dissolution of metals and metal oxides without the use of either organic solvents or aqueous solutions [1]. Currently the most commonly used supercritical fluid is $CO_2$ due to its low critical parameters (31.1 ℃, 7.4 MPa), high diffusivity, non-toxicity and low viscosity. Though supercritical $CO_2$ has been applied successfully for the extraction of organic compounds in industry, the direct extraction of metal ions using pure supercritical $CO_2$ was found to be inefficient, due to the charge neutralization requirement and the weak solute-solvent interaction [2]. In order for heavy metals to be dissolved in $CO_2$, the metals must be present as electrically neutral complexes. If a suitable chelating agent is chosen, a $CO_2$–soluble organic chelating agent will produce a metal complex that can be extracted easily into supercritical $CO_2$ from sample matrices [3]. This chelation-SFE might be a promising technology for the treatment of metal-contaminated soil materials. Moreover, ultrasound has been widely applied in chemical, pharmaceutical, medical and food industries etc., and enhances the rate and the efficiency of the extraction process using ultrasound in combination with SFE [4]. The main purpose of this study is to identify and evaluate the extraction efficiency of metal species for contaminated soils using supercritical $CO_2$, a chelating agent and ultrasound.

## 2. Materials and Methods

*Chelating agent*

The chelating agent used in this study is Cyanex 272, as shown in Fig. 1, which contains 85% bis (2,4,4-trimethylpentyl)phosphinic acid, and was obtained from Cytec Inc., Canada.

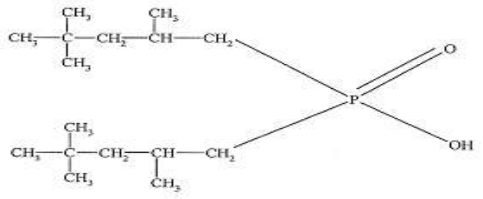

Fig. 1 Chemical structure of the chelating agent.

*Soil samples*

The soil samples were commercially available sand obtained from Joomoonjin, Republic of Korea, with 0.5 wt% of organic content and was sieved through a 1 mm sized mesh. An ICP-spiking solution (AccuStandard, Inc., USA), containing 15 metal species of Sb, As, Ba, Be, Cd, Cr, Co, Cu, Pb, Ni, Se, Ag, Tl, and V, was spiked into the soil material and was mechanically mixed in order to achieve a homogeneous state. It was then aged for 7 days at room temperature.

*Chelation-SFE-ultrasound system*

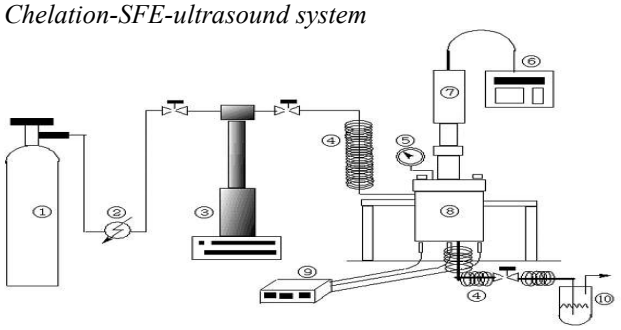

① $CO_2$ cylinder ② condenser ③ syringe pump ④ heating coil ⑤ pressure gauge ⑥ ultrasonic power generator ⑦ ultrasonic transducer ⑧ high-pressure extractor ⑨ temperature controller ⑩ separator

Fig. 2 Schematic diagram of the experimental system.

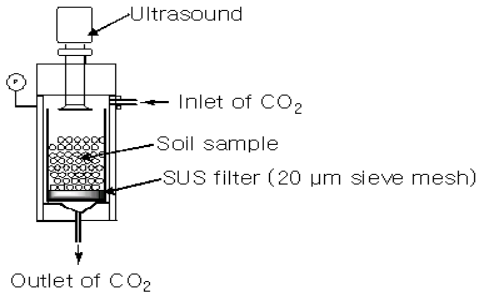


Fig. 3 Structure of the high pressure extractor.

---

hyeong@korea.ac.kr

The chelation-SFE-ultrasound system consists of two units, an SFE unit and an ultrasonic unit, which are equipped on top of the extractor as shown in Fig. 2 and Fig. 3. The system consists of a $CO_2$ cylinder, a syringe pump and its cooling unit, an SUS extractor (130 mL), a power generator, an ultrasonic transducer, and a separator. High purity $CO_2$ (>99:999%, Daesung Co. ROK) used as the supercritical solvent was compressed to the desired operating pressure by the syringe pump (model 260D, ISCO Inc., Lincoln, NE) with a controller (series D, ISCO Inc.). $CO_2$ was then sent into the high pressure extractor containing 10g of soil sample and 1 mL of Cyanex 272 as a chelating agent. The extractor was heated to the desired extraction temperature by a temperature controller. In addition, the horn type ultrasonic processor (20 kHz, Sonics & Materials, VCX 750) installed on top of the extractor supplied a power of 316 W/cm$^2$ with pulse on (3 sec) and off (3 sec) when operating the system. The valves and tubes at the exit of the extractor were heated to 343 K to avoid condensation by the heating coil. The extracted metal species was captured by 60 mL of separator.

## 3. Experimental Results and Conclusion

The soil samples were digested for 20 min in a microwave digester (MARS-5, CEM) with $HNO_3$ (70%) at a temperature of 180 ℃. The subsequent solutions were analyzed by the ICP-AES (inductively coupled plasma-atomic emission spectrometer, Vista-pro, Varian Inc., USA). The concentrations of the metal species for original and spiked soil samples were measured as shown in Table 1.

Table 1 Conc. of metal species for original and spiked soil

| Metal species | Conc. of original soil (mg/kg) | Conc. of spiked soil (mg/kg) |
|---|---|---|
| Ag | 0.434 | 4.798 |
| As | 0.440 | 14.818 |
| Ba | N.D. | 86.110 |
| Be | N.D. | 7.738 |
| Cd | N.D. | 15.302 |
| Co | N.D. | 31.298 |
| Cr | N.D. | 83.728 |
| Cu | N.D. | 77.352 |
| Ni | N.D. | 40.254 |
| Pb | 0.510 | 31.172 |
| Sb | 1.066 | 1.148 |
| Se | N.D. | 6.698 |
| Tl | N.D. | 7.558 |
| V | 0.112 | 48.746 |
| Zn | 1.942 | 74.500 |

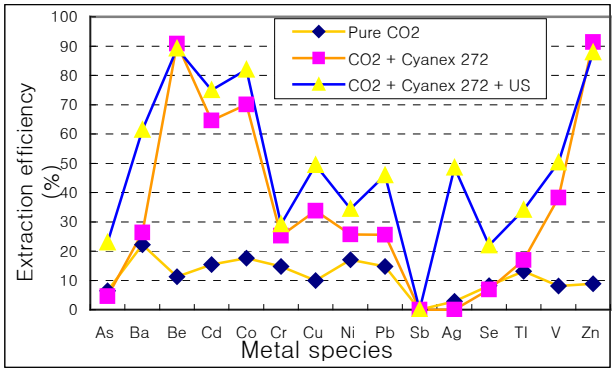


Fig. 4 Comparison of extraction efficiency of metal species from the soil samples using pure $CO_2$, $CO_2$ + Cyanex 272, and $CO_2$ + Cyanex 272 + Ultrasound.

The series of experiments were conducted to establish the influence of supercritical pure $CO_2$, $CO_2$ + Cyanex 272, and $CO_2$ + Cyanex 272 + Ultrasound, for the soil samples of pH 4.10. The experimental conditions were fixed at 40℃, 16 MPa, 10 min static and then 20 min dynamic extraction time, a flow rate of 3 mL/min $CO_2$, and an ultrasound of 316 W/cm$^2$ at 20 kHz with a duty ratio of 50 % and a period of 6 s. In addition, the ultrasound was applied during the 10 min static time and then during the first 5 min of 20 dynamic extraction time. As indicated in Fig. 4, the extraction efficiency of metal species showed in the ascending order of pure $CO_2$ < $CO_2$ + Cyanex 272 < $CO_2$ + Cyanex 272 + Ultrasound for most of the metals. The extraction of metal ions by only supercritical $CO_2$ was confirmed to be inefficient because of the charge neutralization requirement and the weak solute-solvent interaction. Since the active component of Cynanex 272 is a phosphinic acid, the metals (with the exception of As, Be, Sb, Ag, Se and Tl), were extracted through a cation exchange mechanism. Using ultrasound with a chelating agent (Cyanex 272) could substantially enhance the extraction efficiency, as suggested in previous literature [5], by facilitating mass transport which helps to move the solubilized metal or metalloid species into the supercritical fluid phase. A further study will be carried out for the important parameters controlling chelation-SFE-ultrasound system such as chelating agent type, water content, pH, temperature, pressure, soil matrix and sonication time.

## References


1. C. Kersch, M.J.E. van Roosmalen, G.F. Woerlee and G.J. Witkampc: Ind. Eng. Chem. Res. **39** (2000) 4670.
2. S. A. Fatah, M. Goto, A. Kodama and T. Hirose: J. of Supercritical Fluids, **28** (2004) 21.
3. F. Chang, H. Kim, B. Joo, K. Park and H. Kim: J. of Supercritical Fluids, **45** (2008) 43.
4. T.I. Trofimov, M.D. Samsonov, S.C. Lee, N.G. Smart and C.M. Wai: J.Chem Technol.Biotechnol **76** (2001) 1223.
5. C.M. Wai and Y. Enokida: U.S. Patent 7,128,840 B2 (2006).

2P8-6

Proceedings of Symposium on Ultrasonic Electronics, Vol. 29 (2008) pp. 313-314
11-13 November, 2008

# Optimization of Ultrasound Irradiation for the Soil Washing of Diesel-Contaminated Fine Particles

Beomguk Park‡, Jihoon Cha, Younggyu Son, Myunghee Lim and Jeehyeong Khim†
(Dep. of Civil, Environ. and Architect. Eng. Korea Univ., Korea)

## 1. Introduction

The soil washing process is an innovative clean-up method used in soil remediation technologies. It can effectively remove many types of pollutants including petroleum hydrocarbons and heavy metals and the treatment process can be finished within a relatively short period.[1)]

The aim of conventional soil washing process is the separation fine particles from bulk soil. Because most pollutants in soil are concentrated on fine particles and these fine particles commonly tend to be attached to coarser particles. [1), 2)]

Ultrasound, which is applied in many industrial fields has recently been extensively investigated for use in the soil washing process. The application of ultrasound causes acoustic cavitation that produces a high speed microjet, a shock wave and a micro-streaming due to the asymmetric collapse on the surface of the soil. These can enhance transportation rates. [3)]

Previous studies on ultrasonic soil washing typically focused on the parameters of ultrasound, soil and pollutants such as power intensity, initial concentration, particle size etc.[4),5)] Most researchers used particles that were larger than 0.1mm and that had a high efficiency using conventional soil washing processes and ultrasound. However, in comparison to coarse particles, fewer studies have been carried out on fine particles that are contaminated with a high concentration of pollutants. The purpose of this study is to estimate a removal efficiency in soil washing process according to frequency, power and mixing for removing diesel from contaminated fine particles by using the ultrasound.

---
hyeong@korea.ac.kr

## 2. Experimental Procedures

Experiments were carried out on the diesel contaminated soils. Granite soil, which is very common in Korea, was used after being air-dried and sieved. Particles which pass through a # 200 were used. Diesel fuel was purchased from a gas station in Seoul, Korea. The diesel was dissolved in n-pentane.

The mixture was then added to the soil and made homogenous. Initial concentrations of diesel in the soil were 10,000mg/kg. An ultrasound radiation experiment was then carried out after the n-pentane in the soil was completely evaporated.

A bath type sonicator (Flexonic, Mirae Ultrasonic Tech., Korea) with a frequency of 35, 170 kHz and 100, 200W power was used. A mixture of 5mg contaminated soil and 15mL water was added into a 400mL cylindrical bath reactor to prevent compaction and was ultrasonically irradiated for 10min while mixing at 100-200 rpm. The reaction temperature was kept constant at 25±2℃ by a water cooling system.

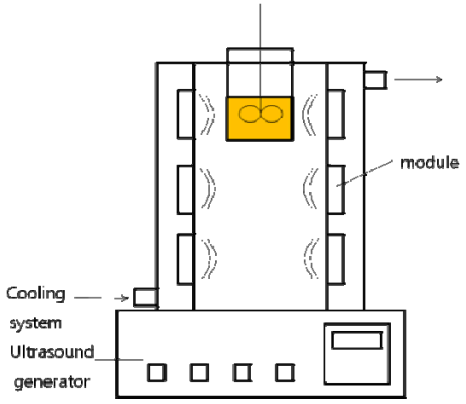


**Fig. 1.** Scheme of ultrasonic bath and reactor

After sonication, the mixtures were placed into a centrifuge in order to separate the solid and liquid phases. A 5 g sample of soil was placed into a beaker and anhydrous sodium sulfate was added to

remove moisture. The soil sample was then extracted with 100mL of dichloromethane. The diesel concentration was then measured for total petroleum hydrocarbon (TPH) with a GC-FID (Agilent, 6890N, USA).

### 3. Result and Discussion

An investigation was carried out on the optimum conditions of ultrasonic soil washing for remediation of fine particles contaminated with diesel. The removal efficiency of sonication is shown in Fig. 2. The removal efficiency of diesel on 35 kHz is higher than 170 kHz in a low rotation frequency (100W-100rpm, 200W-100rpm). In a high rotation frequency, the efficiency is almost the same (100W-200rpm, 200W-200rpm). This is because the energy input at a high power and mixing is sufficient to achieve maximum removal using ultrasound and mixing.

The rotational frequency effect is more efficient than the power effect. However, a comparison of quantitative physical energy is required.

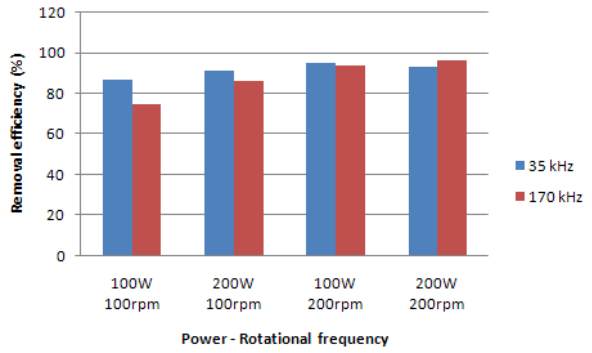


**Fig. 2.** Removal efficiency according to frequency, power, and rotational frequency

Initially, in order to consider energy, we measured the increasing temperature according to time to compare the cavitation energy in less direct ways. The results are shown Fig. 3.

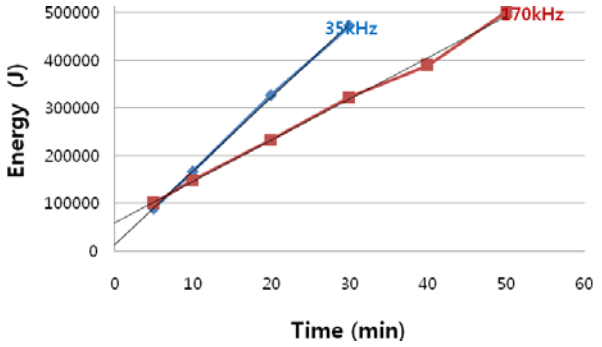


**Fig. 3.** Cavitation energy according to frequency

The reaction temperature increased according to sonication time. Despite the same electronic energy input, the cavitation energy differed from frequency. Low frequency is a more effective way to transfer energy from electronic energy to cavitation energy than high frequency. Therefore, the removal rate of diesel is higher in low frequency than in high frequency with the lower rotational frequency (100 rpm).


### Acknowledgments

This subject is supported by Ministry of Environment, Republic of Korea as “The Eco-technopia 21 project” (no. 061-081-042).


### References


1. T.J. Mason, A. Collings and A. Sumel : Ultrason. Sonochem. **11** (2004) 205.
2. R.G.Sheets and B.A. Bergquist : J. Hazard. Material. **66** (1999) 137.
3. A.F. Collings, A.D. Farmer, P.B. Gwan, A.P. Sosa Pintos and C.J. Leo : Minerals Engineering **19** (2006) 450.
4. S. Na, Y. Park, A. Hwang, Y. Kim and J. Khim : Jpn. J. Appl. Phys. **46** (2007) 4775.
5. D. Feng and C. Aldrich : Adv. Environ. Res. **4** (2000) 103.
6. I. Hua and M.R. Hoffmann : Environ. Sci. Technol. **31** (1997) 2237.

2P8-7

Proceedings of Symposium on Ultrasonic Electronics, Vol. 29 (2008) pp. 315-316
11-13 November, 2008

# Compaction of Soft Magnetic Composite Powder using Ultrasonic Vibrations

超音波振動を用いた絶縁被膜鉄粒子の圧縮成形

Shinichi Kikuchi[1‡], Daisuke Koyama[1], Kentaro Nakamura[1] and Hyun-Lok Cha[2]
([1] P & I Laboratory , Tokyo Inst. of Tech.; [2]KITECH)
菊池慎一[1‡]，小山大介[1]，中村健太郎[1]，Hyun-Loc Cha[2]（[1]東工大 精研；[2]KITECH）

## 1. Introduction

To fabricate efficient electromagnetic motors being based on the optimized design, a technique to produce three-dimensionally-shaped magnetic core is required. The metal powder compaction method is a promising candidate for making arbitrary shaped cores. However, it is difficult to increase the density and uniformity using conventional pressing machine. This results in low magnetic efficiency and low mechanical strength. To overcome this problem, we propose to introduce ultrasonic vibrations in the compacting process. We expect the increase in the density of the compressed powder. Also, we expect to reduce the friction between the die and the work being based on the report which showed that high frequency vibrations have such effects to lower the friction coefficient even though the vibration amplitude is around 1-10 microns[(1)]. In this report the effects of ultrasonic vibrations on the compaction rate are experimentally studied under higher previous study.

## 2. Soft magnetic composite powder

Soft Magnetic Composite(SMC) powder is iron powder which is covered with insulating film. We used SMC550 with the particle size of 120 μm and SMC500 with the particle size of 150 μm[(2)].

## 3. Compaction molding system

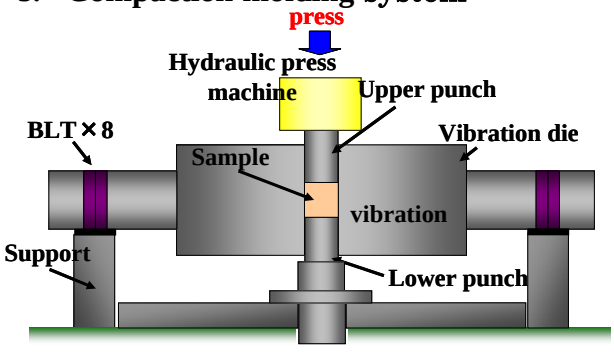


Fig.1 Compacting system.

kikuchi.s.ac@m.titech.ac.jp

Compaction system is shown in **Fig. 1**. SMC powder set in the compacting part of the vibration die's center is compressed by a hydraulic pressing machine. Methods of the application of the ultrasonic vibration are

(1)radial vibrations of the compaction die at 28 kHz,
(2)longitudinal vibrations of the upper and lower punches at 40 kHz, and
(3)both (1) and (2) .

In this report, we focus on the 28-kHz radial vibration method and compression experiment using it.

## 4. Radial vibration die

The fabricated vibration system and the vibration mode are shown in **Figs. 2 and 3**. The die is made of SKH-9 steel, and operated in the fundamental

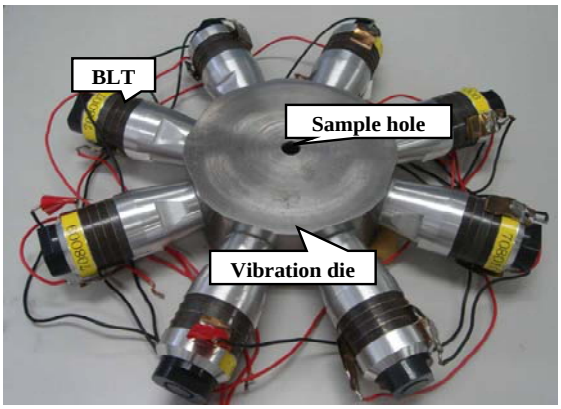


Fig. 2 the 28-kHz radial vibration system.

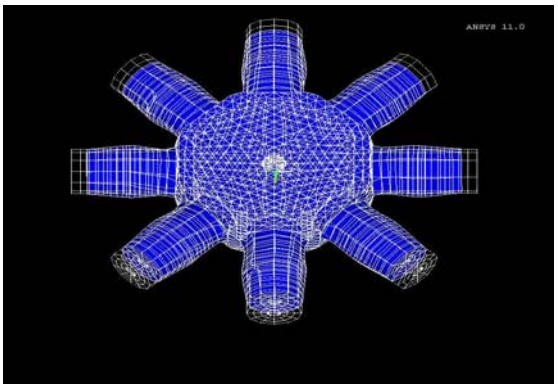

Fig. 3 Radial vibration mode by ANSYS.

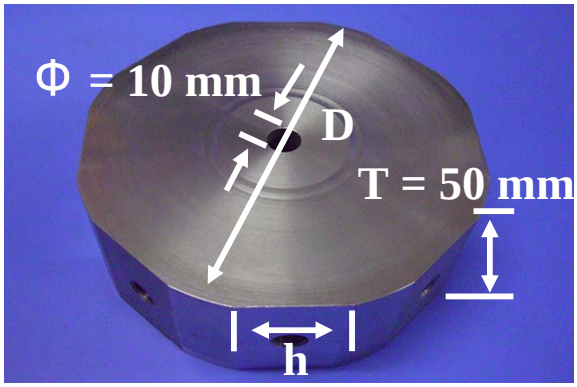


Fig.4 Vibrating compaction die.

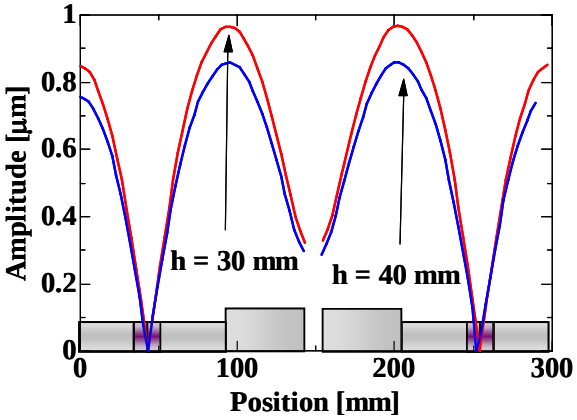


Fig. 5 Vibration distribution in the radial direction.

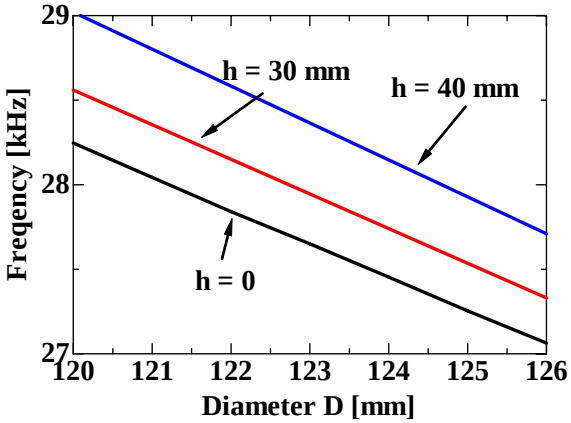


Fig. 6 Relationship between the diameter of die and the resonance frequency for the radial mode.

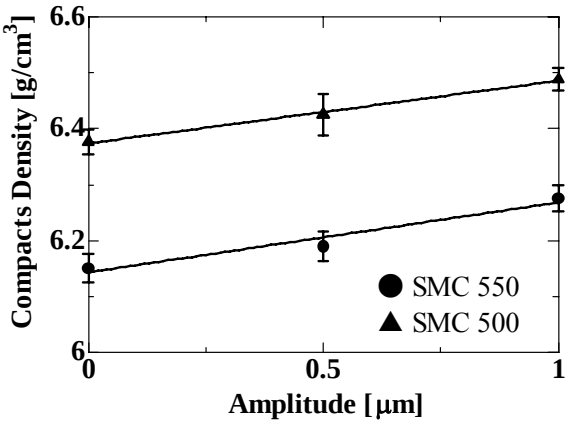


Fig. 7 Density vs. the vibration amplitude of the compaction die.

radial mode. It has a 10-mm-diameter compacting part in the center and eight bolt-clamped Langevin PZT transducers 30 mm in diameter. Using finite element analysis, the shape of the die as shown in **Fig. 4** was determined, where a large vibration amplitude can be obtained on the inner surface of the center hole at the frequency of 28 kHz. A couple of examples with the numerical results are shown below. The vibration distributions in the radial direction for different joining areas are shown in **Fig. 5.** The resonance frequency of the vibration die as a function of the width of joining area is shown in **Fig. 6**. From these results, we chose 30 mm for the width of joining area and 123 mm for the diameter of the vibration die. Impedance characteristics of the radial vibration die were measured across the input of the transducer with 8-parallel connection the resonance frequency is 28.12 kHz, the free motional admittance is 30 mS, and the quality factor is 140.

## 5. Results of compression experiment

Relationship between the sample density and the vibration amplitude of the vibration die is shown in **Fig. 7**. The compacting static pressure is 300 MPa constant. The compacting time is 8 sec. The density increases with the vibration amplitude of the vibration die.

## 6. Discussion and Conclusion

We developed a 28-kHz ultrasonic radial vibration die for powder compaction enhancement. The apparent increase in the density due to the ultrasonic vibration application has been confirmed for a medium range static pressure in the experiment using SMC. We shall design upper and lower vibration punch which are excited by a 40-kHz ultrasonic longitudinal vibration, and carry out compression experiment using it.

## 7. References

1. J. Tujino, Y. Atumi, T. Ueoka, J. Yamamoto and K.Wakasaki: Proc. Spr. Meet. Acoust. Soc. Jpn. pp. 617-618 (1982) (In Japanese).
2. http://www.hoganas.con/japan/

2P8-8

Proceedings of Symposium on Ultrasonic Electronics, Vol. 29 (2008) pp. 317-318
11-13 November, 2008

# Comparison of Magnetic Properties of SMC Motor Core Fabricated by Ultrasonic Vibration Compaction

Hyun Rok Cha[1†], Shinichi Kikuchi[2], Seoung Kyu Jeon[1], Sung Ho Lee[1], Cheol Ho Yun[2] and Kentaro Nakamura[2] ([1] Facult. Eng., KITECH.; [2]Facult. Eng., Tokyo Tech.)

## 1. Introduction

Recently, Soft Magnetic Composite(SMC) cores for reactor, transformers and various kind of motor have drawn great attention among researchers of magnetic and electric industry. The SMC is ferro-magnetic powder particles surrounded by an electrical insulating layer. This charateristic has advatage in a motor desing such as compact and light-weight, because the magntic core has higher degree of freedem in shape compare to the core made out silicon steel. Also it has lower loss and superior magnetic properties than laminated silicon steel at high frequency range since the insulation coating of every particle gives very small eddy current paths inside a particle. Generally it was produced by cold compaction.[1] However, it is difficult to remove the compresed core from the die without break after compaction process since the pressure for the compaction process is extremly high.[1,2] To overcome this problem, we propose to introduce ultrasonic vibrations to the die to reduce the friction.

In this paper, the SMC motor core was fabricated by ultrasonic vibration compaction. Magnetical properties and electrical propertis are investiged.

## 2. Experimental Procedure

For this research, ultrasonic vibration press was prepared. Fig.1. shows the arrangement of the ultrasonic vibration press. It is consisted of an upper and lower punch, vibration compacting die design for operating 20kHz half wavelength longitudinal vibration and a press frame with a hydraulic static compacting pressure source. The vibration die consists of vibration source with six bolt-clamped Langevin type PZT transducers and support fixture. The die is driven by 1kw high speed bipolar amplifier

To review the possibility of SMC application to general motors, it is adopted for high speed motor. Fig 2 shows the construction of the tested motor and shape of fabricated SMC core. The powder specimens for SMC core are used Somaloy 550KE, 550, 500( Höganäs AB) respectively.

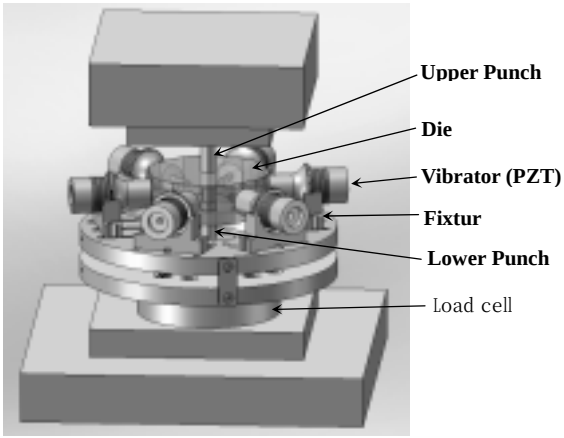


Fig. 1 The arrangement of ultrasonic vibration press

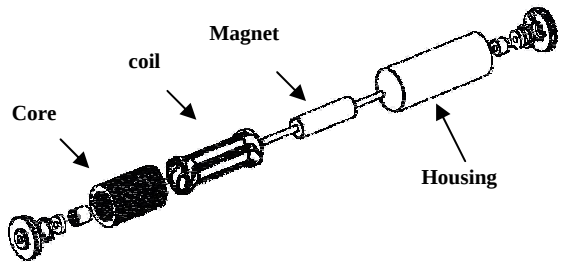


Fig. 2 The construction of the tested motor

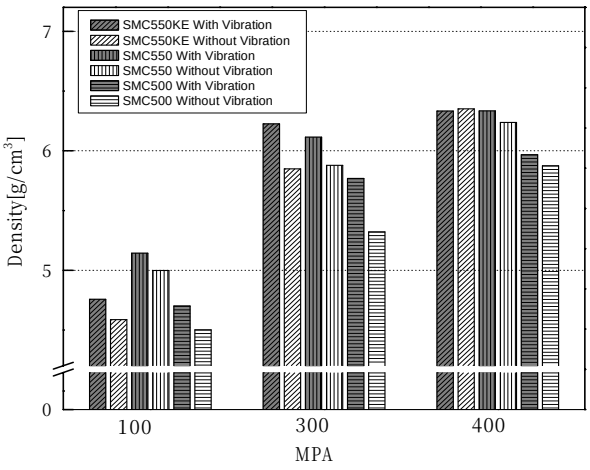


Fig. 3 The compact density obtained by ultrasonic acting and conventional compaction

---

1.Korea Institute of inductiral technology : hrcha@kitch.re.kr

2.Tokyo institute of tecnolgy : knakamur@sonic.pi.titech.ac.jp

They are cold pressed from 100 to 400MPa using proposed ultrasonic vibration press and then heat-treated. The heat treatment temperature was gradually increased with speed of 4℃/min up to 500℃ and then held for 1 hour in atmospheric condition.

Motor performance analysis was carried out by dynamometer (WB100). In order to analyze the magnetic property, Iron loss & Hysteresis characteristic analyzer (MPG100D) was used.

### 3. Results and Discussion

Fig.3. shows the compact density obtained by ultrasonic acting and conventional compaction of SMC specimen under the pressure of 100, 300 and 400MPa respectively. As shown, the compact density increased after ultrasonic acting. Especially, the compact density of the ultrasonic compacted SMC550 under the pressure 300MPa was 5.5g/㎤, while that of conventionally compacted composite was 5.2 g/㎤.

Fig.4. shows the iron-loss according to frequency with and without vibration action. As shown, the iron-loss of SMC core is totally decreased by ultrasonic action. The values of hysteresis loss are more than eddy current loss in total iron-loss when we increased the frequency. Generally, the hysteresis loss can be reduced by improving the stressed regions.[1] It means that the ultrasonic action has a possibility to improve the stressed regions during compaction action.

The appearance of a prototype motor and assembled SMC core was shown in figure 5.

Fig.6. shows the results of dynamic motor performance having SMC core both ultrasonic treated and no treated one. The results clearly shows that the motor efficiency and torque is dramatically increased by using ultrasonic vibration die. The ultrasonic treated SMC motor shows a higher motor efficiency by more than 9% under the rated speed of 24,000rpm.

### 4. Conclusions

In this research, Ultrasonic vibration press was introduced to improve the magnetic prosperity. The proposed method increased density about 2~5%, improved magnetic properties and increased motor efficiency more than 9%.

### References


1. H. Shokrollahi and K. Janghorban : J. Mater. Processing. Tech (2007).
2. Jiromaru Tsujino and Haruo Suzuki: Jpn. J. Appl. Phys. 31 (1992) pp 290-293.


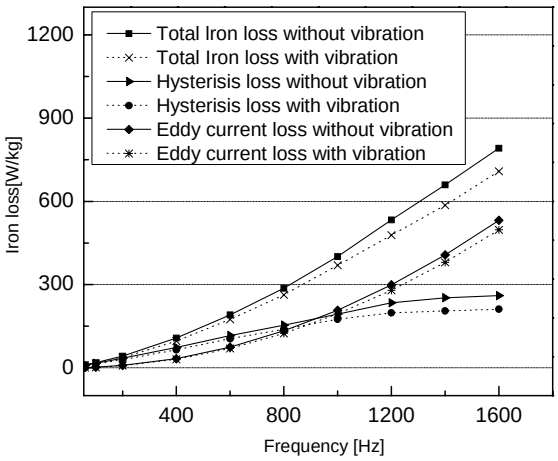


Fig. 4 The iron-loss according to frequency with and without vibration action

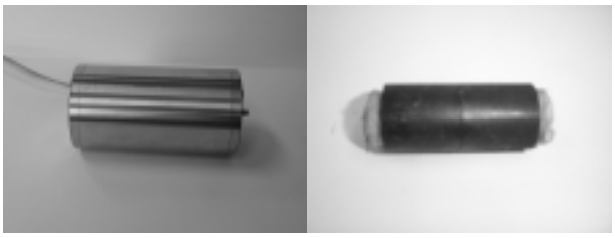

(a) (b)

Fig. 5 The appearance of a prototype motor and assembled SMC core (a): Motor Ass'y, (b): Core Ass'y

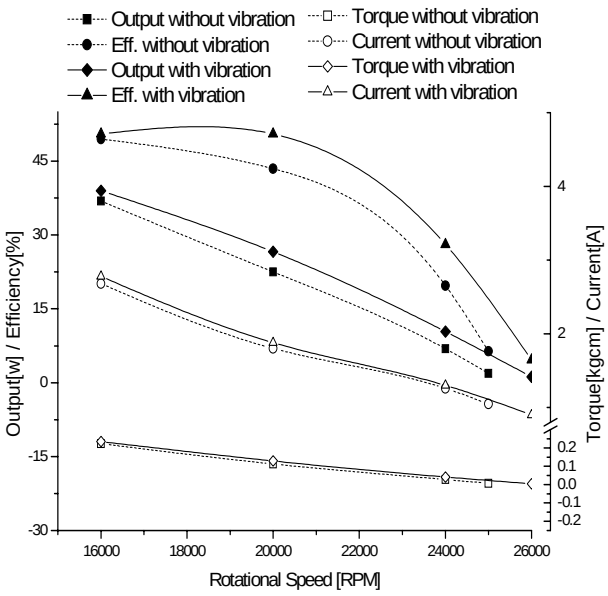


Fig. 6 The results of dynamic motor performance having SMC core both ultrasonic treated and no treated one

2P8-9

Proceedings of Symposium on Ultrasonic Electronics, Vol. 29 (2008) pp. 319-320
11-13 November, 2008

# Room-Temperature Ultrasonic Bonding of Semiconductor Thin-Dies with Die Attach Films on Glass Substrates

Siu Wing Or*, Sui Yin Wong, and Ho Chi Wong (The Hong Kong Polytechnic University)
Yiu Ming Cheung and Ping Kong Choy (ASM Assembly Automation Ltd.)

## 1. Introduction

The revolutionary reduction in thickness (<75 μm) of semiconductor dies in the recent years has imposed a significant limitation on conventional conductive epoxy-based die bonding as a result of the failures caused by epoxy overflow, coverage, spread-out, and its induced die tilt. The state-of-the-art thermocompressive bonding of thin-dies in form of wafer-back laminates with die attach films (DAFs) is not subject to such fluidic problems at the expense of requiring a high bonding temperature, a long bonding time, and a large bonding pressure [1]. The process window of high bonding temperature and pressure, together with the low throughput due to long bonding time, exerts a great challenge to the advance of the thin-die bonding technology. In this paper, a novel ultrasonic thin-die bonding technique is proposed to improve the process window and to increase the throughput compared to the state-of-the-art thermocompressive thin-die bonding technique. The proposed technique is essentially based on the proper transmittal of ultrasonic vibration energy generated from a piezoelectric ultrasonic transducer to softening, plasticizing, and adhering the DAFs between the associated thin-dies and their substrates.

## 2. Setup and Working Principle

Fig. 1 shows the in-house automated equipment model for the ultrasonic thin-die bonding. The equipment model basically consists of a 40 kHz, 500 W piezoelectric ultrasonic transducer and its ultrasonic signal generator, a vision system, a three-axis linear motion system, a pressure control system, and a thermal management system. Fig. 2 illustrates the photograph and schematic diagram of a standard test specimen used in the present study.

The test specimen has a thin-die of 8 mm long, 6 mm wide, and 50 μm thick laminated with a 10 μm thick DAF and the thin-die-DAF laminate is to be bonded on an 1 mm thick glass substrate. The reasons for selecting glass as the substrate are: (1) It is transparent and the bond quality can be inspected visually immediate after each bonding; and (2) this chip-on-glass (COG) configuration represents one of the most important configurations in modern semiconductor packages.

In a bonding operation, the glass substrate is first held by a vacuum-based, temperature-controlled worktable, and a thin-die-DAF laminate is picked and placed onto the glass substrate. Second, the specimen is pressed by the transducer with a pressure, and the ultrasonic energy is applied by the transducer through the thin-die to softening and plasticizing the DAF so as to adhere the thin-die and the glass substrate. Comparing to the state-of-the art thermocompressive thin-die bonding, this ultrasonic thin-die bonding technique essentially requires much lower temperature and shorter time to be described in Section 3.

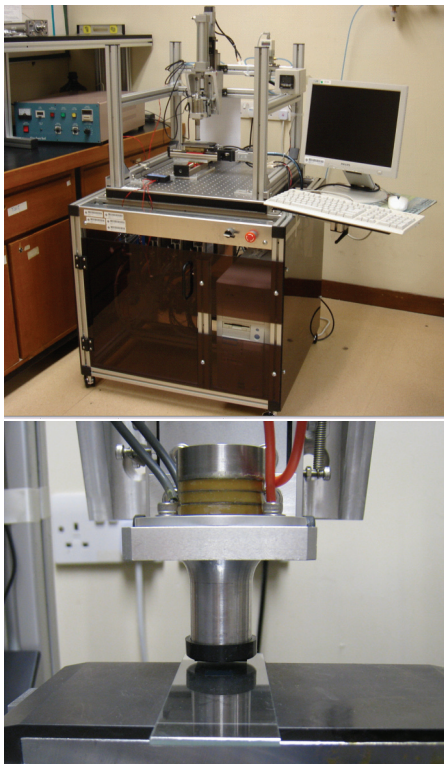

Fig. 1. The in-house automated equipment model for the ultrasonic thin-die bonding (top) and the zoom-in view of the 40 kHz, 500 W piezoelectric ultrasonic transducer (bottom).


Fig. 2. Photograph (left) and schematic diagram (right) of a standard test specimen used in the present study.

* E-mail: eeswor@polyu.edu.hk

## 3. Ultrasonic Bonding Studies

Based on the equipment model and the test specimens, a series of experiments were performed to investigate the effect of introducing ultrasonic vibration energy on the reduction of bonding temperature, bonding time, and void formation in the ultrasonic thin-die bonding process. The voids formed along the bond interfaces were visually inspected using a digital optical microscopy technique and the percentage of void formed was recorded. The ultrasonically bonded test specimens were compared with the thermocompressively bonded test specimens in terms of bonding temperature, bonding time, and percentage of voids formed.

Table 1 shows some typical results of the proposed ultrasonic thin-die bonding and the state-of-the-art thermocompressive thin-die bonding. It is clear that the use of ultrasonic energy is capable of establishing the quantitatively good bondability with less than 10 % voids at a lower bonding temperature of 80 ºC and a shorter bonding time of 1.5 s (Specimen A) as compared with the thermocompressive bonding of 160 ºC bonding temperature and 2 s bonding time (Specimen B). By using the same bonding time of 2 s, it can even realize the technologically important and physically interesting room-temperature thin-die bonding (Specimen C) with void formation less than 10 %. Interestingly, the voids associated with this room-temperature ultrasonic bonding are >50 % reduced from the thermocompressive bonding at 120 ºC with 2 s (Specimen D).

## 4. Conclusion

We have developed a novel ultrasonic thin-die bonding technique and its associated piezoelectric ultrasonic transducer and prototype equipment model to improve the process window and to increase the throughput limited intrinsic in the state-of-the-art thermocompressive thin-die bonding technique. Room-temperature ultrasonic bonding of thin-die-DAF laminates on glass substrates has been successfully achieved using 2 s bonding time with less than 10 % voids. To obtain comparable results, it has been found that bonding temperature in excess of 120 ºC is generally required in the thermocompressive process.


## Acknowledgment

This work was supported by the Innovation and Technology Fund of the Hong Kong Special Administrative Region (HKSAR) Government under Grant No. GHP/003/06.


## Reference


1. A.C.C. Chong and Y.M. Cheung, "Post-bond Compression Process for Bonding Thin-Die on BT Substrate using Thermoplastic Adhesive Tape," *Proc High Density Microsystem Design and Packaging and Component Failure Analysis, 2005 Conference, June 2005*, pp. 1-6.


Table 1: Comparison of ultrasonic and thermocompressive thin-die bonding results for the test specimens.

| Specimen | Bonding Technique | Bonding Temperature (ºC) | Bonding Time (s) | Percentage of Void Formed (%) | Optical Micrograph |
|---|---|---|---|---|---|
| A | Ultrasonic Bonding | 80 | 1.5 | 5 | 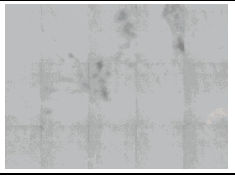 |
| B | Thermocompressive Bonding | 160 | 2 | 5 | 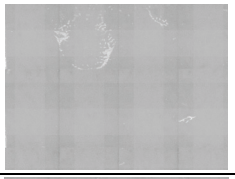 |
| C | Ultrasonic Bonding | Room Temperature | 2 | 9 | 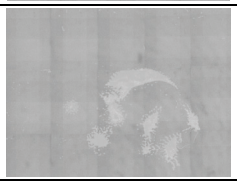 |
| D | Thermocompressive Bonding | 120 | 2 | 20 | 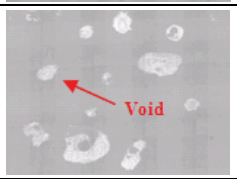  |

2P8-10

Proceedings of Symposium on Ultrasonic Electronics, Vol. 29 (2008) pp. 321-322
11-13 November, 2008

# Design of Ultrasonic Horn for Microelectronic Parts – Material Dependence

Minseok Bae‡, Young H. Kim (Korea Science Academy)
Jeong-Hoon Moon (Dept. of Mechanical Eng., Suwon Science College)
Kyung-soo Kim (Changjo Engineering Co.)

## 1. Introduction

High-density packaging technologies are continuously developed for high-performance microelectronic parts. For example, micro-pitch terminals or flip chips without a plastic package are employed for the miniature electronic devices. However, it is hard to bond those small and high-density devices with traditional soldering process. In addition, lead-free bonding technology is required for environment. To address those problems, ultrasonic bonding technique has been developed [1].

It is essential to analyze vibration modes and resonance frequency of ultrasonic horn to obtain good bonding quality. FEA (Finite Element Analysis), that can be used various scientific and engineering fields to simulate complex situation, can be also used to analysis ultrasonic horn [2].

Vibration modes and eigen frequencies of the ultrasonic horns are dependent on horn materials. Hence, choosing the best horn material is needed to obtain high-quality ultrasonic bonding.

In this research, ultrasonic bonding horns with various horn materials are designed using FEA. COMSOL 3.4 is used for analyzing eigen modes and frequency response of each horn [3].

## 2. Design Criteria

**Fig. 1** shows a schematic diagram for ultrasonic bonding of IC chip on a substrate. Transverse vibration is needed to bond IC chip on a substrate. To cause transverse vibration of IC chip, ultrasonic horn should have longitudinal motion. If ultrasonic horn vibrates other direction, IC chip can be damaged or bonding will not be succeeded. Therefore, longitudinal modes were considered for an appropriate bonding. Resonant frequency of the longitudinal mode was tuned near 40 kHz.

Typical vibration modes near the longitudinal mode of a 59×28×14mm$^3$ rectangular block were obtained. **Fig. 2** shows the desired vibration mode and two nearest modes of the block. The longitudinal mode should be separated from other nearest modes, or proper bonding quality cannot be obtained [4].

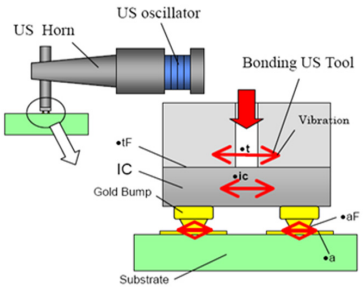


Fig. 1 Schematic diagram of IC chip bonding.

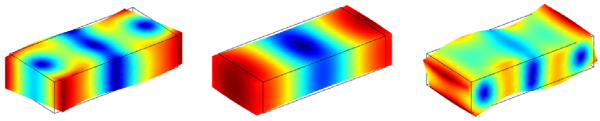

(Nearest mode) (Desired mode) (Nearest mode)

Fig. 2 Vibration modes of a rectangular block.

## 3. Properties of Horn Materials

Vibration modes and resonant frequencies are determined by horn materials and horn dimensions. Therefore, horn dimensions should be changed for different horn materials. In the present work, three horn materials are used for ultrasonic horn design. The mechanical properties of those materials were measured before FEA. Speeds of longitudinal and transverse waves were measured using pulse-echo setup, and densities were by Archimedes principle. The measured mechanical properties of three horn materials are listed in **Table 1**.

Table 1 Mechanical properties of horn materials.

| Materials | Density (g/cm$^3$) | Elastic Moduli (GPa) Young's | Shear | Poisson's Ratio |
|---|---|---|---|---|
| JPN | 7.688 | 196 | 74.6 | 0.312 |
| SKD11 | 7.708 | 217 | 84.5 | 0.280 |
| SKH | 8.110 | 234 | 91.4 | 0.285 |

## 4. FEA of ultrasonic horns

It has four steps to design ultrasonic horns: (1) Basic horn structure, (2) Add 2 fixtures & grip fixtures, (3) Add welding tip, and (4) Add suction hole.

After final step, vibration modes were separated about 3 kHz. The vibration mode and dimensions of final model are shown in **Fig. 3** and **Table 2**. Resonant frequencies of final models are in **Table 3**. Three horn materials showed well-separated

bms1991@empal.com

resonant frequencies.

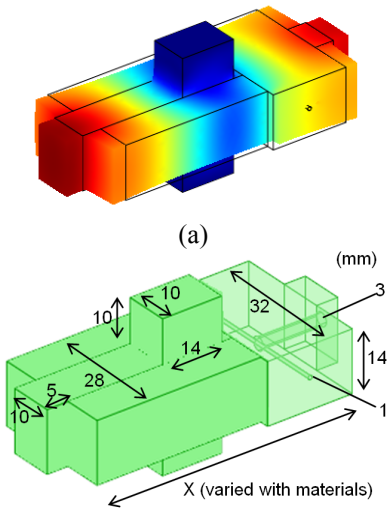


Fig. 3 Desired mode & dimensions of final welding horn.

Table 2 Length of x for four horn materials.

| Horn materials | JPN | SKD11 | SKH |
|---|---|---|---|
| X (mm) | 59 | 62 | 63 |

Table 3 Resonant frequencies of final designed horns.

| Horn Materials | Resonant frequencies (kHz) | | |
|---|---|---|---|
| | Before | Desired | Behind |
| JPN | 36.88 | 39.75 | 42.53 |
| SKD11 | 36.99 | 39.96 | 43.46 |
| SKH | 36.81 | 39.84 | 43.53 |

## 5. Frequency response analysis of the horn

Frequency response analysis for 30.0 kHz to 50.0 kHz frequency range of JPN horn was also obtained by FEA (**Fig. 4**). The maximum x-direction displacement appears at about 39 kHz and it showed good agreement with resonance frequency. Calculated Q factor is about 4.88. This result shows it can be nicely used to obtain proper transverse motion of a chip.

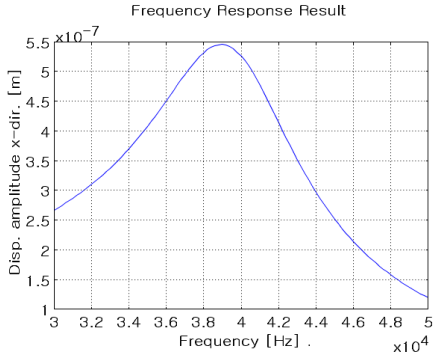


Fig. 4 Frequency response result of JPN horn.

## 6. Evaluation of manufactured ultrasonic horns

Ultrasonic horns designed by FEA were fabricated. Different horn materials cause different size of the horns. Simulated resonance frequencies and measured resonant frequencies were compared in **Table 4**. Measured one showed good agreements with simulated one.

Table 4 Resonant frequencies of manufactured horns.

| Horn Materials | Resonant frequencies (kHz) | |
|---|---|---|
| | Simulated | Measured |
| JPN | 39.75 | 40.90 |
| SKD11 | 39.96 | 39.80 |
| SKH | 39.84 | 40.07 |

Ultrasonic bonding results are shown in **Fig. 5** and **Fig. 6**. Chip size was $6\times10mm^2$ and gold bump size was $100\times100um^2$. Silicone base with gold coating was used. Flatness of horn and chip was not proper, so some portions were only bonded. However, bonding quality can be improved with more accurate alignment in mechanical system.

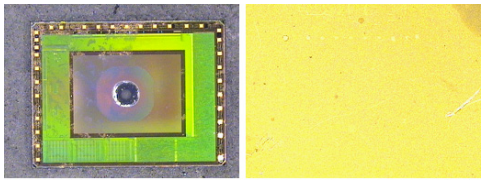

Fig. 5 US bonding results-chip and base-JPN horn.

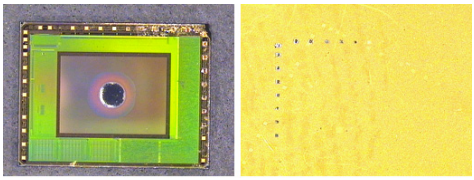

Fig. 6 US bonding results-chip and base-SKH horn.

## 7. Conclusion

Ultrasonic welding horn using various horn materials has been designed by FEA with material constants measured by experiment. Two projections on both side of horn and two fixtures on the node of horn separated resonant frequencies of neighbor vibration modes. Designed ultrasonic horns were fabricated. As results, resonant frequency of fabricated horn showed good agreement with designed frequency. Primary bonding test with fabricated horn shows feasible results.

## References

1. J. Tsujino, Y. Harada, S. Ihara, K. Kasahara, M. Shimizu, T. Ueoka: Ultrasonics, 42 (2004) 125.
2. L. Parrini, Ultrasonics, 41 (2003) 261.
3. COMSOL AB, COMSOL version 3.4 (2007)
4. J.A. Gallego-Juarez, E. Riera, V. M. Acosta-Aparicio: Nonlinear Acoustics- Fundamentals and Applications (ISNA 18), 18th International Symposium

Proceedings of Symposium on Ultrasonic Electronics, Vol. 29 (2008) pp. 323-324
11-13 November, 2008

# Precision measurement of convergence characteristic of single aspheric acoustic lens

単一非球面音響レンズの収束特性の精密計測

Sayuri Matsumoto[1], Yuichi Shin[2†], Fumitaka Naito[2], Takenobu Tsuchiya[2], Nobuyuki Endoh[2] and Norihide Takeyama[3]([1]PARI , [2]Facult. Eng., Kanagawa Univ. , [3]Genesia)
松本 さゆり [1]，進 雄一 [2†]，内藤 史貴 [2]，土屋 健伸 [2]，遠藤 信行 [2]，武山 芸英 [3]
（[1]港空研，[2]神奈川大学 工，[3]ジェネシア）

## 1. Introduction

Underwater around port facilities or port area, an acoustic imaging tool, that could be used in low transparency water or during night, is needed to check undertaking construction for safety, to monitor suspicious individuals or objects for security and to look damage in the wake of disaster. We have been studying about a high resolution imaging SONAR system including acoustic lenses. For a higher performance lens system design, it is necessary to investigate acoustic lens characteristics. We reported measured temperature dependencies of acoustic lens material [1], measured characteristics of acoustic lens designed by OpTaliX [2], that is an optical lens software, and analysis of convergence field calculated by FDTD method [3]. In previous work, it was disagreement between measured and calculated acoustic lens (Lens B) characteristic results on the image plane. In this study, we re-measured sound pressures around the convergent region precisely, compared them with calculated results by FDTD method considered the experimental condition.

## 2. Experimental set up

Equations (1) and (2) define the first and the second planes of acoustic lens as shown in Fig.1.

$$Z_1(X) = \frac{X^2/(-364.6)}{1+\sqrt{1-(1+(-16.00))X^2/(-364.6)^2}} + (-2.052\times10^{-8})X^4 \cdots (1)$$

$$Z_2(X) = \frac{X^2/(84.92)}{1+\sqrt{1-(1+(-0.1030))X^2/(84.92)^2}} + (1.927\times10^{-8})X^4 \cdots (2)$$

Acoustic lens is made of acrylic resin, and its relative refraction index is 0.532. Effective diameter and image plane distance, that is from a aperture plane to image point, of the lens are approximately 150 mm and 164 mm, respectively. Beam width at the image plane of the lens by OpTaliX is approximately 2 mm. Figure 2 shows an acoustical lens characteristics measurement system in a tank. The tank size of distance, width, and depth are 1.5 m, 1.5 m and 1.0 m, respectively. The origin of coordinate system is defined on a center of the aperture plane. X, Y, and Z axis are along sound axis, transverse, and depth direction, respectively.

Then the acoustic lens was set at 1290 mm apart from a transducer. A burst wave that has 10 wave cycles was projected by the transducer (1 MHz center frequency, 25Φ diameter) in water. Sound

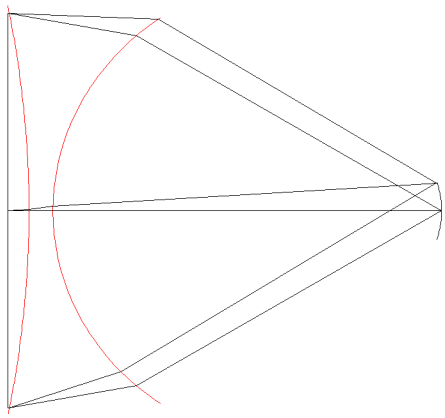

Fig.1 Lens B Design.

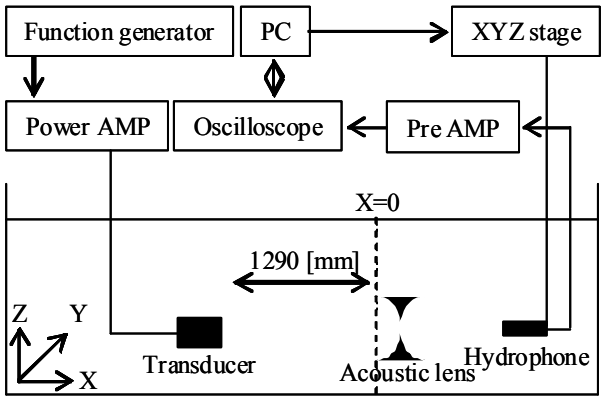


Fig.2 Lens Performance Measurement System

pulse was refracted by lens then received by a hydrophone. Described above experiments were conducted at a water temperature of 22.6 degrees.

## 3. Measured result and study

Figure 3 shows a measured distribution of sound pressure along X axis as red circle. For comparison of mention above and FDTD simulated result as blue line showns in the same figure. Those data sets were normalized by the maximum value of each data. The maximum point that is to say an image plane distance of 180mm in the experiment was good agreement with 181mm in the simulation. Figure 4 shows distributions of sound pressure along Y axsi through a convergent region. Graph legends are the same in Fig. 3. At this point, define a beam width on an image plane as a half bandwidth, measured and simulated beam width are 5.5 mm and 4.5 mm, respectively. Both results agreed rather well in an error range.

Then we compared measured image plane distances and beam widths with designed them by OpTaliX. The measured image plane distance was 16 mm far from designed it of 164 mm. The difference seemed to be caused source positions; it was assumed that a source is located at infinity from lens in designing, but at finite distance from lens in measuring. The measured beam width was 2.5 mm larger than designed it of 2.0 mm. Those two differences seemed to be made a spherical aberration.

## 4. Conclusion

In this study, we re-measured the characteristic of sound pressure through the acoustic lens designed by OpTaliX based on ray theory. The measured results were good agreement with FDTD simulated them that considered measuring condition. Moreover we compared measured results with designed them, reviewed the differences.

In future work, we will study the differences in details.


## Acknowledgments

This study was partly sponsored by High-Tech Research Center Project from Kanagawa University and the Ministry of Education, Culture, Sports, Science and Technology, Japan from 2005 to 2008, Sasagawa Scientific Research Grant (18-320M) from the Japan Science Society in 2006, Grand-in-Aid for Scientific Research (20500429 and 20686059).


## References


1. Shin, Matsumoto, Tsuchiya, Anada, Endoh: Proceedings of MASJ07, pp. 25 (2007)
2. Matsumoto, Shin, Tsuchiya, Anada, Endoh, Takeyama: Proceedings of USE07, 479-480(2007).
3. Naito, Shin, Matsumoto, Tsuchiya, Endoh: Proceedings of MASJ08, pp. 33 (2008)
4. Keen, Pidsley, Proceedings of UAM, Crete, GREECE (2007).
5. Mori, Ogasawara, Nakamura, Proceedings of UAM, Crete, GREECE (2007).
6. Matsumoto, Tsuchiya, Anada, Endoh: Proceedings of USE06, 29-30 (2006).
7. Matsumoto, Tsuchiya, Anada, Endoh: Proceedings of UAM, Crete, GREECE (2007).
8. Optenso,【OpTaliX】Reference Manual (6.15-1),（Optenso, Germany, 2004）pp. 493.
9. T. Anada et al, Jpn. J. Appl. Phys. **41**, 3509, 2002.


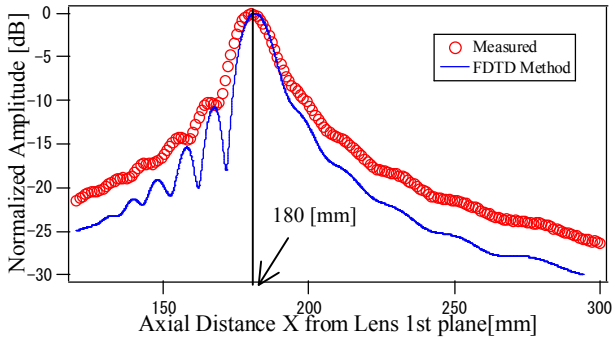


Fig.3 Measured and Simulated Acoustic Fields along Axis X

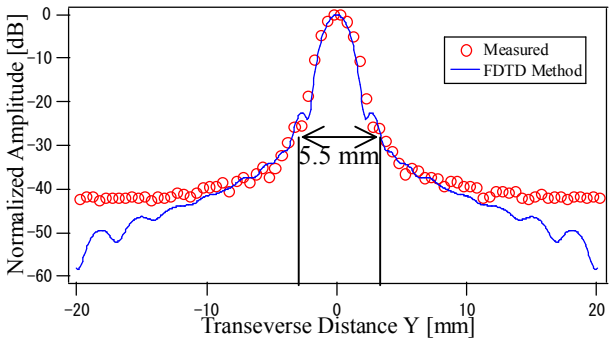


Fig.4 Measured and Simulated Acoustic Fields along Axis Y

2P9-2

Proceedings of Symposium on Ultrasonic Electronics, Vol. 29 (2008) pp. 325-326
11-13 November, 2008

# Sound Pressure Field Focused by Aplanatic Acoustic Lens for Ambient Noise Imaging

周囲雑音イメージングのためのアプラナート音響レンズの集束音場

Kazuyoshi Mori[1†], Hanako Ogasawara[1], Toshiaki Nakamura[1], Yuji Sato[2], Takenobu Tsuchiya[3] and Nobuyuki Endoh[3] ([1]National Defense Academy; [2]Univ. Tsukuba; [3]Kanagawa Univ.)

森　和義[1†]，小笠原英子[1]，中村敏明[1]，佐藤裕治[2]，土屋健伸[3]，遠藤信行[3]　([1]防衛大学校; [2]筑波大; [3]神奈川大)

## 1. Introduction

Buckingham *et al*. developed a new method which views ambient noise as a sound source rather than a hindrance and which is neither passive nor active sonar. This method is called ambient noise imaging (ANI).[1] Some systems have been built for ANI. In the first generation, the Acoustic Daylight Ocean Noise Imaging System (ADONIS), consisting of a 3 m diameter spherical reflector and having an array of 126 hydrophones attached to the focal surface, was built by Epifanio and Buckingham *et al*.[2] In the second generation, the Remotely Operated Mobile Ambient Noise Imaging System (ROMANIS), consisting of a 2-D sparse array of 504 hydrophones fully populating a 1.44 m circular aperture, was built by Venugopalan *et al*. Both systems successfully detected silent target objects using snapping shrimp noises.[3]

On the other hand, an acoustic lens system would be a powerful choice for realizing ANI, because such a system would not require a large receiver array and a complex signal processing unit for two-dimensional beam forming, which could reduce the size and cost of the system. In our past studies, we analyzed a sound pressure field focused by an acoustic lens system constructed for an ANI system with a single spherical biconcave lens using the 2-D and 3-D Finite Difference Time Domain (FDTD) method and the small scale trial in water tank. Our aim was the development of a lens with a resolution similar to the beam width of ROMANIS, which is 1 deg at the frequency of 60 kHz. These results showed that the lens with a aperture diameter of 2.0 m has the sufficient resolution.[4, 5]

In this study, an aplanatic lens correcting the aberrations is applied to ANI system. We analyzed the sound pressure distribution focused by the acoustic aplanatic lens using the 3-D FDTD method. We then compared the analysis results of –3 dB areas with those of the spherical lens.

## 2. Design of Aplanatic Lens for ANI system

An absolutely aplanatic lens must satisfy the following three conditions. First, both surfaces of lens are aspherical. Secondly, the lens must satisfy "the principle of equal optical path" in order to concentrate rays of normal incidence completely. The principle of equal optical path means that the optical paths of all rays are equal when they originate at the same source, even if they refract at any surface. In the present case, this includes any optical paths equal to the central optical path because all rays are focused at the same point. Thirdly, "Abbe's sine-condition" must be satisfied for all points of incidence. A coma aberration is removed in a paraxial area when Abbe's sine-condition is satisfied without a spherical aberration.

Yoshida[6] developed a numerical method for designing aplanatic lenses which satisfy the above three conditions in the case of optical convex lenses. Sato *et al*. applied this method to the design of an acoustic aplanatic lens. They evaluated the convergence characteristics of the biconcave and biconvex aplanatic acoustic lenses analyzed using the ray path and the sound pressure distribution obtained by the 2-D FDTD method.[7]. In a designing process for ANI system, the authors compared sound pressure fields focused by some aspherical lenses including an aplanatic lens using the 2-D FDTD method.[8]

In this study, the aplanatic lens was designed as the following conditions; the aperture diameter is 2.0 m, the focal length is 2.5 m, and the center thickness is 0.05 m. The lens shape and the ray paths are shown in **Fig. 1**. The rays concentrate on each different point at the incidence angles of 0 deg and 7 deg. In these cases, both spherical and comma aberrations are corrected. However, the rays do not concentrate on a point because this lens has a small comma aberration at 15 deg.

† kmori@nda.ac.jp

### 3. Results and Conclusion

The sound pressure distribution focused by the aplanatic lens was calculated using the 3-D FDTD method. The beam pattern is compared with that of the spherical lens in **Fig. 2**. In the case of the aplanatic lens, the width of main-lobe is slightly narrow and the peak level is large as compared with the spherical lens. The side-lobe level of the aplanatic lens is smaller than that of the spherical lens. The –3 dB area, whose pressure is 3 dB lower than the maximum at the image point, is used for evaluating the directional resolution of the lens, the same as the 3 dB beam width. The –3 dB areas are shown in **Fig. 3**. Each –3 dB area of aplanatic lens is smaller than that of spherical lens. These results suggest that the aplanatic lens has fine resolution as compared with the spherical lens by correcting the spherical and comma aberrations. We have a plan to measure the sound pressure field focused by an aplanatic lens on a small scale trial in water tank. The experimental results using the lens of 1/5 scale will be compared with these analysis results.

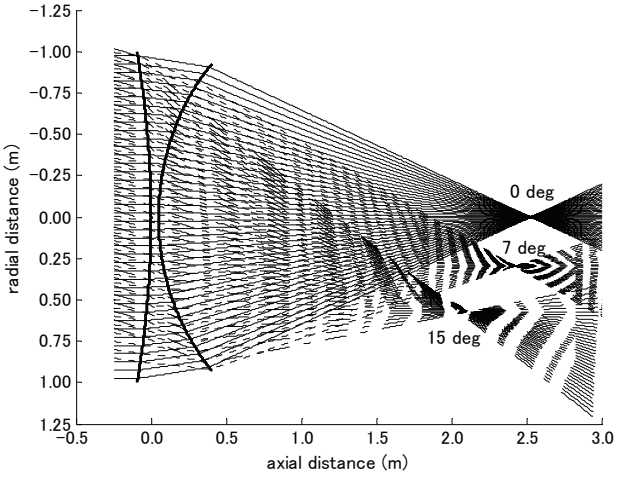


Fig. 1 Lens shape and ray diagrams.

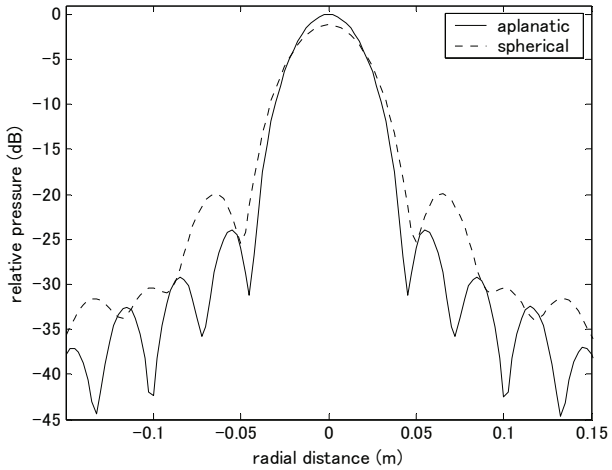


Fig. 2 Beam patterns of normal incidence.

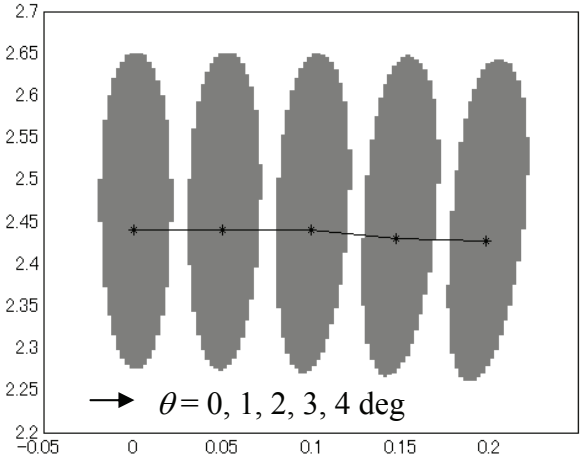


(a) spherical lens

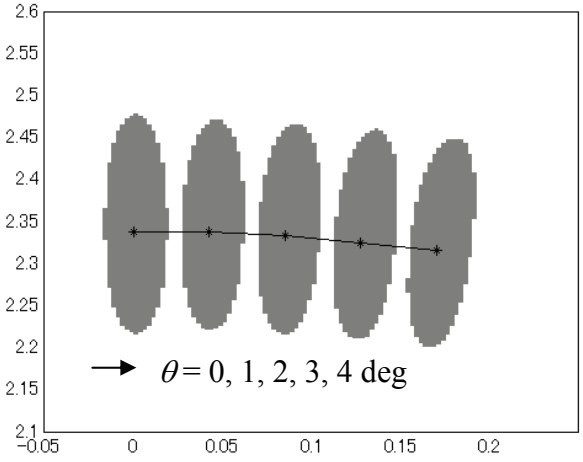


(b) aplanatic lens

Fig. 3 Comparison of –3 dB areas. (horizontal: radial distance, vertical: axial distance, $\theta$ : incidence angle)

### References


1. M. J. Buckingham, B. V. Verkhout and S. A. L. Glegg: Nature, **356** (1992) 327.
2. C. L. Epifanio, J. R. Potter, G. B. Deane, M. L. Readhead and M. J. Buckingham: J. Acoust. Soc. Am., **106** (1999) 3211.
3. P. Venugopalan, M. A. Chitre, E. T. Tan, J. Potter, K. T. Beng, S. B. Ruiz and S. P. Tan: Proc. Oceans 2003 Marine Technology and Ocean Science Conf. (2003) CD-ROM.
4. K. Mori, A. Miyazaki, H. Ogasawara, T. Yokoyama and T. Nakamura: Jpn. J. Appl. Phys., **45** (2006) 4834.
5. K. Mori, H. Ogasawara, and T. Nakamura: Jpn. J. Appl. Phys., **47** (2008) 4344.
6. S. Yoshida: Tohoku-daigaku Kagaku-keisoku Kennkyuu-syo Houkoku, **6**(3) (1958) 123. [in Japanese]
7. Y. Sato, A. Miyazaki, K. Mori, and T. Nakamura: Jpn. J. Appl. Phys., **46** (2007) 4982.
8. K. Mori, H. Ogasawara, and T. Nakamura: to be published in Acoustical Imaging, **29** (2008).

Proceedings of Symposium on Ultrasonic Electronics, Vol. 29 (2008) pp. 327-328
11-13 November, 2008

# FEM Analysis of low frequency and wideband array composed of disk bender transducers having differential connections
# 差動接続を用いた屈曲円板型低周波送波器アレイの広帯域化に関する FEM 解析

Mitsuru Yamamoto†, Takeshi Inoue, Hiroshi Shiba and Yuta Kitamura (NEC Corporation)
山本満†，井上嵩梓，芝博史，北村佑太　（NEC）

## 1. Introduction

In recent years, it has become necessary to transmit in low frequency and wideband frequency for underwater sonar systems of oceanic development and investigation. To address this need, we had developed a disk bender transducer with dual radiation surface which utilized two piezoelectric ceramic disks operating in an unstiffened mode as high-power, miniature, light weight and low-frequency transducer. However this disk bender transducer had the defect that the frequency bandwidth was narrow because the radiation surfaces were small and the acoustic load was small. Its fractional bandwidth became 10-20% at most. Then, we studied the technology that made it to wideband by two or more differential connections of the disk bender transducers by using finite element method (FEM) analysis. The wider fractional bandwidth more than 100% was found being able to be achieved from the result of the analysis for differential connections of the three disk bender transducers operating in different resonance frequencies each other.

## 2. Construction of disk bender transducer

The plane and cross-sectional views of the disk bender transducer are shown in Fig. 1. The transducer has two bender vibration disks. Each vibration disk consists of a metal plate and a piezoelectric ceramic disk polarized in the thickness direction. Each piezoelectric ceramic disk is firmly bonded to the metal disk with an epoxy resin adhesive, in a circular depression of the metal disk. The two vibration disks are connected by an elastic plate and clamped together with eight bolt-nut assemblies with elastic springs. In actual operation, when a voltage is applied to two piezoelectric ceramic disks, they vibrate in phase in the radial direction, which results in bending vibrations in each vibration disks.

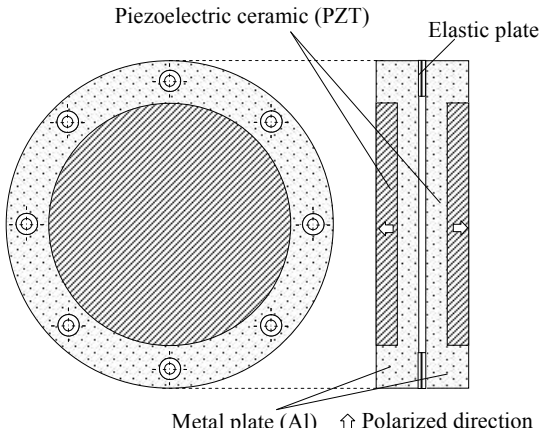


Fig. 1　Plane view and cross-sectional view of a disk bender transducer.

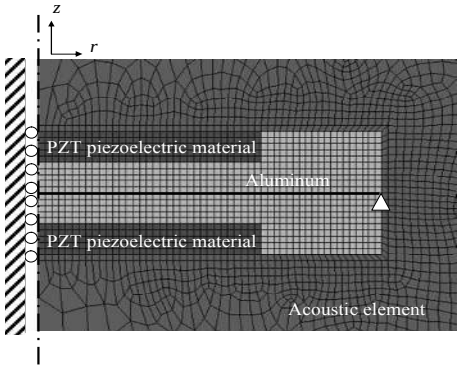


Fig. 2　Transducer simplified model for FEM analysis.

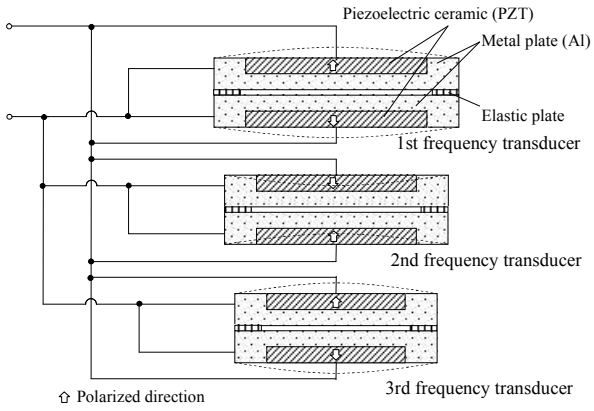


Fig. 3　Chart of connecting wires of low frequency and wideband array composed of disk bender transducers having differential connections.

E-mail: m-yamamoto@dq.jp.nec.com

## 3. Analysis model

FEM analysis model of the transducer is shown in Fig. 2. For the purposes of simplifying the analysis, we used transducer z-axis symmetric model and simple support model ignored eight bolt-nut assemblies and the elastic plate. It is no problem in a relative evaluation of transmitted voltage response (TVR) though the resonance frequency is different in the analytical result of such a model.

Figures 3 and 4 show the chart of connecting wires and concentrated constant equivalent circuit for the disk bender transducer array having differential connections, respectively. In Fig. 3, the polarized direction of the piezoelectric ceramic for the 2nd frequency transducer is opposite in them for another transducers. In Fig. 4, this shows the equivalent circuit model with the transformer turn ratio of -1:1. Because the transformer works effectively, the array composed of the three disk bender transducers shown in Fig. 4 functions as the multiple mode filters, and can obtain the bandwidth which is more than three times than that of an individual transducer. In the equivalent circuit in Fig. 4, mutual impedance was disregarded for the simplification.

## 4. Analysis results

Figure 5 shows the calculated results of TVR when changing the diameter of the disk bender transducer. The thicknesses of those transducers were assumed to be constant in 0.042λ, and the diameter of a piezoelectric ceramic was defined as 65% for the whole diameters of the transducers. The peak values of the TVR do not change so much though the resonance frequency decreases as the diameter grows. Moreover, it is understood that Q value becomes a rising narrowband while making to the low frequency.

Figure 6 shows TVR for the array composed of the three transducers having differential connections. In figure, plots are shown in TVR of each transducer and line is shown in TVR when the voltage of out-of-phase was applied in the 2nd frequency transducer. The peak values at three resonance frequencies are almost the same and it is obtained -6dB fractional bandwidth of 100%.

## 5. Conclusion

The underwater performance of low frequency and wideband array composed of disk bender transducers having differential connections were calculated by FEM. These analytical results demonstrated that this transducer array has a low-frequency and wide-bandwidth performance. The possibility that the wideband characteristic of 100% or more is obtained was shown by a differential connection of three disk bender transducer array.

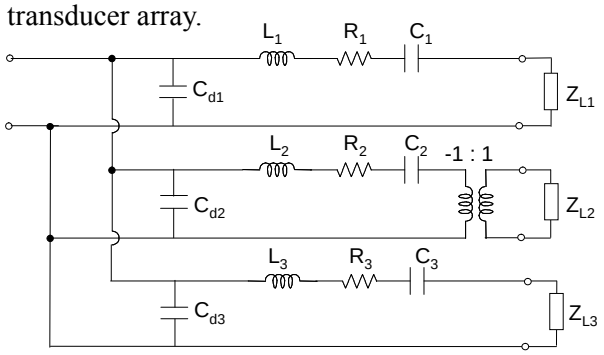


Fig. 4 Concentrated constant equivalent circuit for the disk bender transducers array having differential connections.

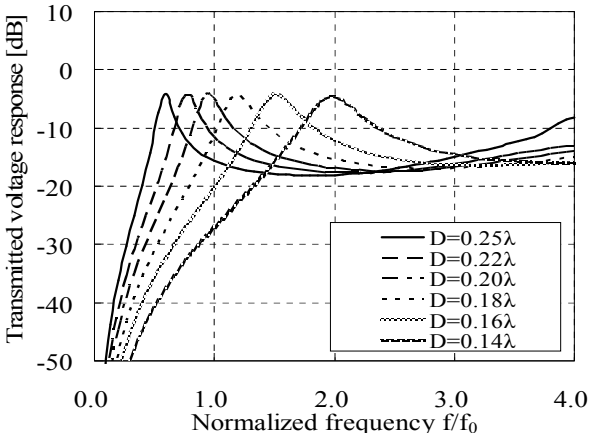


Fig. 5 Theoretical transmitted voltage response by FEM analysis when changing the diameter of the disk bender transducer.

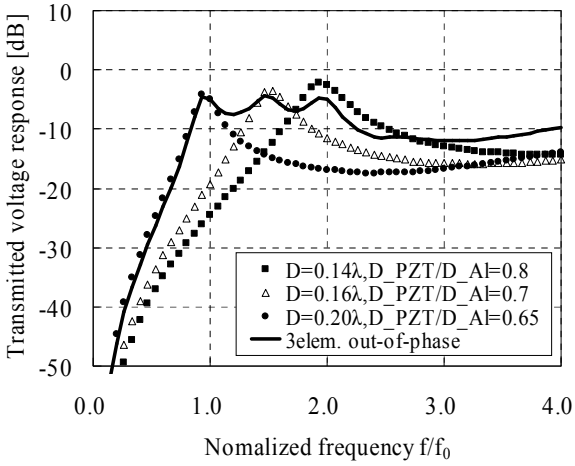


Fig. 6 Transmitted voltage response for the transducers array having differential connections calculated by FEM analysis.

## References

1. M. Yamamoto, Y. Hama, H. Shiba, N. Watari and T. Inoue: J. Acoust. Soc. Jpn. **15**, 5(1994) 311.
2. M. Yamamoto, H. Ishimura, Y. Hama and T. Inoue: Jpn. J. Appl. Phys. **37** (1998) 3161.

2P9-4

Proceedings of Symposium on Ultrasonic Electronics, Vol. 29 (2008) pp. 329-330
11-13 November, 2008

# Optimal Design of a Barrel Stave Flextensional Transducer

Hoeyong Kim and Yongrae Roh†
(Kyungpook National University, Korea)

## 1. Introduction

Flextensional transducer can be classified into 7 classes according to its operation principle, and class I is known to have the most stable structure for deep underwater applications due to its concave shell [1]. The concave class I transducer is often called barrel stave transducer. Many researches have been done on the design of the transducer structure. Systematic investigation, however, has been quite rare [2]. Therefore, in this study, we analyzed and designed the barrel stave flextensional transducer to achieve the widest frequency bandwidth by considering all the cross-coupled effects of structural variables.

## 2. Modeling of a barrel stave flextensional transducer

The structure of a class Ⅳ flextensional transducer is described in **Fig. 1** that shows a finite element model constructed with the ANSYS®. Harmonic and transient analyses were performed with the model. Main structural components are a piezoceramic stack in the middle of the transducer, a metallic flange to support the whole structure and a flexible concave shell surrounding the whole structure. Dimensions and geometric shape of these are of significant influence on the transducer performance as evidenced in previous reports on other types of flextensional transducers. Hence, this work focuses on the analysis of the effects of these variables and the determination of the optimal combination of these variables to have the widest frequency bandwidth. Properties of the materials composing the transducer are listed in **Table 1**.

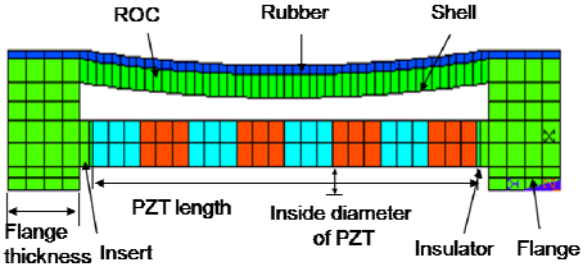


Fig. 1 Finite element model of the transducer

†yryong@knu.ac.kr

Table 1 Material properties of each part of the transducer

| | Density (kg/m3) | Young's Modulus (Pa) | Poisson's ratio |
|---|---|---|---|
| Insert, Flange | 2,710 | 68.9E9 | 0.30 |
| Insulator | 2,900 | 80.0E9 | 0.25 |
| Shell | 1,900 | 27.4E9 | 0.25 |
| Rubber | 1,100 | 3.0E7 | 0.49 |
| Ceramic stack | PZT-4 | | |

## 3. Analysis of the transducer performance

In order to compare the transducer performance for different combinations of the structural variables, a basic transducer model was constructed to have the dimensions in **Table 2**. The basic model was established to let the transducer operate at 7.5 kHz and have a typical geometry in use. Variation ranges of major design variables were also established as in **Table 3** considering practical applicability of the transducer. Over the range, the response of the transducer was investigated through harmonic analyses with the model in Fig. 1. Results of the calculation were analyzed to find the relationship between the variables and the following performance factors: bandwidth ($\Delta f$), center frequency ($f_c$), and transmitting voltage response (TVR). **Fig. 2** is an illustrative result that shows the change of the $\Delta f$ in relation to the shell thickness. Fig. 2 shows that the bandwidth can be maximized at a specific shell thickness. Similar relationships were derived for all the other variables.

Table 2 Basic geometry of the transducer

| | |
|---|---|
| Shell thickness ($x_1$) | 7 mm |
| Flange thickness ($x_2$) | 24 mm |
| Flange length ($x_3$) | 37 mm |
| PZT length ($x_4$) | 139 mm |
| ROC (radius of curvature) ($x_5$) | 410 mm |
| Rubber thickness | 2 mm |
| PZT Thickness | 10 mm |
| Inside diameter of PZT | 5 mm |

Table 3 Variation range of the structural variables of the transducer

| Structural variables | Variation range(mm) |
|---|---|
| Shell thickness | 5 ~ 9 |
| Flange thickness | 18 ~ 30 |
| Flange length | 31 ~ 43 |
| PZT length | 118 ~ 160 |
| ROC (radius of curvature) | 320 ~ 500 |

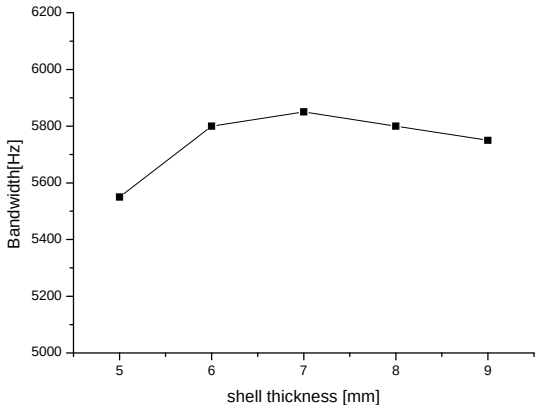


Fig. 2 Variation of performance in relation to shell thickness.

Based on the results, fc, TVR, and $\Delta f$ of the transducer were derived as functional forms. Formulation of the performance was carried out by means a second order multiple regression model and a commercial software SAS® [3]. The goal of present work is to design a transducer structure to have the widest possible bandwidth while satisfying given constraints simultaneously. Hence, the combination of the structural variables was optimized to minimize the target function in Eq. (1) while satisfying the two constraints in Eq. (2).

$$\text{Target function: Minimize } T = \frac{1}{\Delta f} \quad (1)$$

$$\text{Constraint: } f_c - 100 \text{ Hz} \le f_c \le f_c + 100 \text{ Hz}$$
$$TVR_{peak} \ge T_0 \text{ dB} \quad (2)$$

For the minimization of the target function, SQP-PD (Sequential Quad-ratic Programming Method of Phenichny and Danilin) method was used because of its high convergence rate [4]. **Table 4** shows the results of the optimization. **Fig. 3** is the corresponding performance of the optimized transducer. Compared with the initial basic model, the optimized structure shows a wider bandwidth while its center frequency and TVR level meet given specifications.

Table 4 Result of the optimization

| variable | Optimized Value |
|---|---|
| $x_1$ (mm) | 6 |
| $x_2$ (mm) | 29.94 |
| $x_3$ (mm) | 43 |
| $x_4$ (mm) | 118 |
| $x_5$ (mm) | 320 |

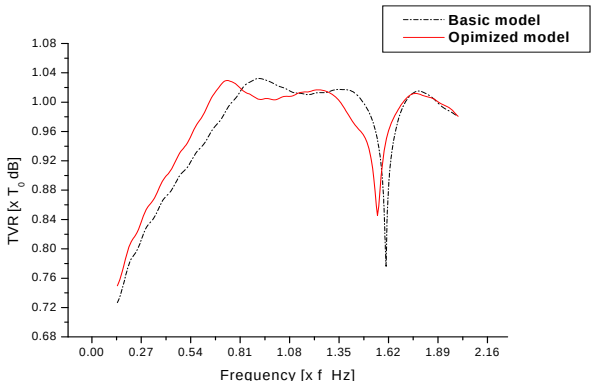


Fig. 3 TVR spectrum of the basic and optimized models

## 4. Conclusions

The structure of a barrel stave flextensional transducer was designed to achieve the widest bandwidth while satisfying other constraints simultaneously. In comparison with conventional analytic and finite element methods, the design method in this paper can consider all the cross-coupled effects of design variables and can determine the detailed geometry of the transducer with great efficiency and rapidity.


## Acknowledgment

This work was supported by Defense Acquisition Program Administration and Agency for Defense Development in Korea.


## References


1. S. C. Butler, J. L. Butler, A. L. Butler, and G. H. Cavanagh: J. Acoust. Soc. Am. 102 (1997) 308.
2. K. J. Kang and Y. R. Roh: J. Acoust. Soc. Am. 114 (2003) 1454.
3. R. E. McKeighen: IEEE Trans. UFFC 43(1996) 63.
4. D. A. Pierre, *Optimization theory with applications* (Dover Publications, New York, 1986).

2P9-5

Proceedings of Symposium on Ultrasonic Electronics, Vol. 29 (2008) pp. 331-332
11-13 November, 2008

# Analysis of the effect of reflected wave from sonar-dome on radiation impedance for cylindrical array

Jungsoon Kim[1‡], Moojoon Kim[2], Kanglyeol Ha[2], Heeseon Seo[3] and Cheeyoung Joh[3]
([1]Dept. of Multimedia Eng., Tongmyong Univ.; [2]Dept. of Physics, Pukyong Univ.; [3]6th R&D Institute, Agency for Defense Development)

## 1. Introduction

In designing underwater sonar system, such as Hull-Mounted Sonar, the radiation impedance is very important design factor because it is associated to the radiation power of the system and the mutual interference force among the vibrating elements[1]. In a practical system, the sonar has a dome to protect the arrayed elements from the underwater environment such as flow resistance and shock pressure. However, the acoustic wave from the elements is reflected on the surface of the dome, and its effect on the radiation impedance cannot be ignored [2].

In this study, to analyze the effect of the reflected wave on the radiation impedance, we introduced a model which two vibrating elements are mounted on an infinite planar rigid baffle and a plane reflector exists in front of the baffle. Using this model, the variation of the radiation impedance with the distance between the elements, the separation from the reflector, the driving frequency, and the complex reflection coefficient of the reflector are calculated. In the calculation, the Ring function is introduced to evaluate the acoustic pressure distribution by the reflector[3].

## 2. Theory

If a transducer array is consisted of $N$ elements on the rigid baffle, the total radiation impedance of the $n$-th element is expressed as follows[2];

$$Z_n = \sum_{m=1}^{N} Z_{mn} \frac{u_m}{u_n} \quad , \tag{1}$$

where, $u_m$ and $u_n$ are vibrating velocity of the $m$-th and $n$-th element, respectively. $Z_{mn}$ is the mutual radiation impedance between the two elements. The total radiation impedance with a reflector in front of the array is represented by following equation.

$$Z_n = \sum_{m=1}^{N} \left( Z_{mn} + Z'_{mn} \right) \frac{u_m}{u_n}, \tag{2}$$

where,

$$Z'_{mn} = \frac{1}{u_m} \int_{S_n} p'_{mn} dS_m .$$

---

kimmj@pknu.ac.kr

$S_n$ is the vibrating area of the $n$-th element, $dS_m$ is the minute area of the $m$-th element. $p'_{mn}$ is the reflected sound pressure from the reflector.

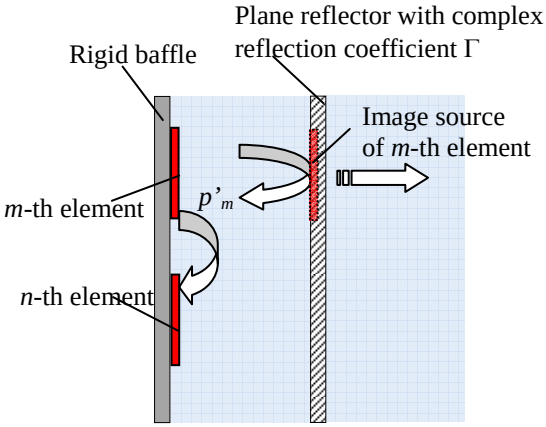


Fig. 1. Calculation model.

We assume that a plane reflector which has a complex reflection coefficient $\Gamma$ is placed in front of the two piston sources mounted on an infinite planar baffle, as shown in **Fig 1**. The sound pressure radiated by $m$-th element is reflected from the reflector, that is to generate the virtual image of the $m$-th element on the reflector. The sound pressure from the virtual image can be given by,

$$p'_{mn} = \frac{j\rho ck}{2\pi} u_m \Gamma \int_{S'_m} \frac{\exp(-jkl)}{l} dS'_m . \tag{3}$$

Here, $\rho$ is the density, $c$ is the sound velocity and $k$ is the wave number of the medium. $l$ is the distance between $dS'_m$ in the virtual image of the $m$-th element and $dS_n$ in the $n$-th element. Therefore, the radiation impedance between the two elements can be represented by,

$$Z'_{mn} = \frac{j\rho ck}{2\pi} \Gamma \int_{S'_n} \int_{S'_m} \frac{\exp(-jkl)}{l} dS'_m dS_n . \tag{4}$$

For example, we assumed that the two identical circular piston sources with the radius $a$ are mounted with the separation $d$ on the baffle and the reflector is separated from the baffle by $z$. Using the Ring function[3], the mutual radiation impedance is given as follows;

$$Z'_{mn} = j2\pi\rho ck\Gamma \int_{x_N}^{x_F} xR_2(x) \int_{r_N}^{r_F} R_1(r,x) \exp(-jkr) dr dx \tag{5}$$

here, $r_F = \sqrt{(a+x)^2 + z^2}$, $x_F = b + d$,

$$r_N = \begin{cases} \sqrt{(a-x)^2 + z^2}, x > a \\ z \quad , 0 \le x \le a \end{cases}, \quad r_N = \begin{cases} b-d, d > b \\ 0, 0 \le d \le b \end{cases}$$

$$R_1(x) = \frac{1}{\pi}\cos^{-1}\left(\frac{x^2 - a^2 - z^2 + r^2}{2x\sqrt{r^2 - z^2}}\right),$$

$$R_2(x) = \frac{1}{\pi}\cos^{-1}\left(\frac{x^2 + d^2 - b^2}{2xd}\right).$$

If $0 \le x \le a$ *and* $z \le r \le \sqrt{(a-x)^2 + z^2}$, $R_1(r, x) = 1$ and when $0 \le d \le b$ *and* $0 \le x \le b - d$ then $R_2(r, x) = 1$.

## 3. Calculation Results

To investigate the variation of the radiation impedance by the reflected wave from the sonar-dome, the radiation impedance for various *z*, *d*, *ka* and $\Gamma$ are calculated by using Eq. (2) and Eq. (5).

When $ka = 1.54$, the variation of the radiation impedance for various *z* and Γ is shown in **Fig. 2**. In this figure, the *x*-axis is normalized by the wavelength $\lambda$. When $d = 0$, $R'_{mm}$ and $X'_{mm}$ mean the real part and the imaginary part of the self-radiation impedance, respectively, considering the effect of the reflected wave from the reflector. And, when $d \neq 0$, $R'_{mn}$ and $X'_{mn}$ mean the real part and the imaginary part of the mutual-radiation impedance, respectively, considering the same effect.

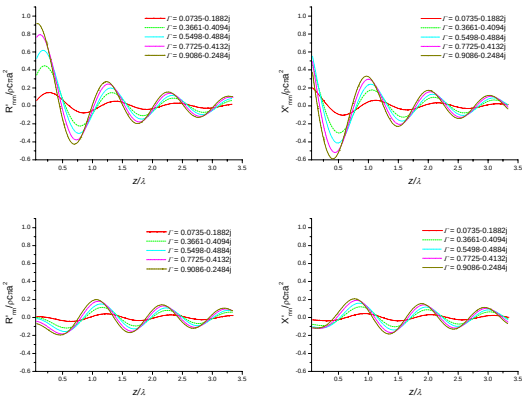


Fig. 2. The variation of the self- and mutual-radiation impedance considering the reflected wave from the reflector at *z* for various Γ .

The amplitude of variation of the self-radiation impedance gradually decreased according to *z*. However, the variation of the self- and mutual-radiation impedance is dramatically changed as Γ increased.

**Figure 3** shows the change of the total radiation impedance with *d* for various Γ in case of

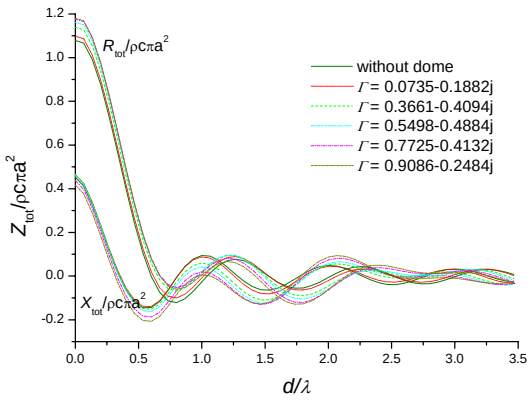


Fig. 3. The total radiation impedance considering the reflected wave with *d* for various Γ.

$ka = 1.54$ and $z = 1.2\lambda$. In these results, the difference between the resistance and the reactance of the total radiation impedance increases with reflection coefficient Γ.

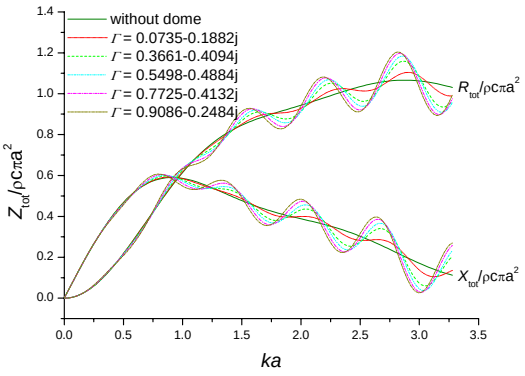


Fig. 4. The total radiation impedance variation with *ka*.

The total radiation impedance variation with *ka* for various Γ shows in **Fig. 4**. The difference between the result of with and without dome increases according to Γ and *ka* in the given range.


## Acknowledgment

This work was supported by Agency for Defense Development of Korea, 2007.


## References


1. T. Yokoyama, T. Asami, K. Mori, T. Nakamura and A. Hasegawa: Jpn. J. Appl. Phys. **43** (2004) 3154.
2. Takashi Ikeda and Tetsuo Miyama: The Journal of the Acoustical Society of Japan, **33**(1977) 342.
3. Shigeo Ohtsuki: The Journal of the Acoustical Society of Japan, **30**(1974) 76.
4. Lawrence E. Kinsler, Austin R. Frey Alan B. Coppens James V. Sanders: *Fundamentals of acoustics* ( John Wiley & Sons, 1980) p.124.

2P10-7

Proceedings of Symposium on Ultrasonic Electronics, Vol. 29 (2008) pp. 333-334
11-13 November, 2008

# Numerical simulation of sound field in time domain using a combination of FDTD method and boundary integral equation method

FDTD 法と境界積分方程式法の結合解法による音場シミュレーション

Takao Tsuchiya and Atsushi Kumagai (Doshisha Univ.)†
土屋隆生，熊谷篤志 (同志社大) †

## 1. Introduction

Large-scale numerical simulation of sound field in time domain has sometimes come to be required in the field of the architectural acoustics or the acoustic imaging. The geometrical sound field analysis is usually applied to the large-scale simulation, but it is difficult to achieve high accuracy because the wave nature cannot be included in the analysis. On the other hand, the wave nature can be included in the wave acoustic analysis such as the finite difference time domain (FDTD) method[1,2], but the huge amount of computation resources is generally required to reduce the numerical dispersion error or the numerical dissipation error.

To cope with the computation resource and the numerical accuracy, the numerical method using a combination of the finite element method (FEM) and the boundary integral equation method has been proposed[3]. In this method, the FEM is applied to the small domain in which the wave analysis is required, and the boundary integral equation method is applied to the other large field to obtain the response at the required point. Using the combination method, it is possible to achieve high accuracy in the large-scale simulation. In this paper, the combination method is applied to the simulation of the acoustic imaging. The FDTD method is applied to the small domain in which targets are located. The reflected waves from the targets are calculated by the Kirchhoff boundary integral equation method. Some numerical demonstrations are made in the two dimensional field.

## 2. Theory

Two dimensional acoustic field is considered as shown in **Fig.1**. The field is divided into two domains; one is the FDTD domain $\Omega_f$ and the other is the domain to be solved by the boundary integral equation method $\Omega_b$. A virtual boundary $\Gamma$ is assumed between two domains. The transducer is located in $\Omega_b$, and the targets are located only in the FDTD domain.

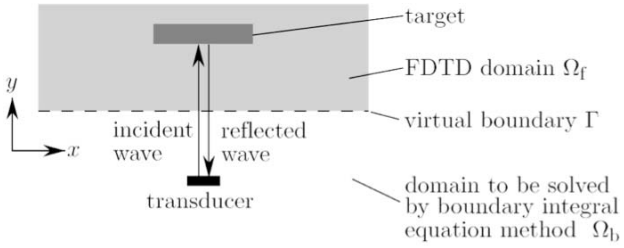


Fig.1 Two dimensional model.

The calculation procedure is as follows;

1) Calculate the incident wave for the input of FDTD method on the virtual boundary $\Gamma$ based on the fundamental solution of 2-D sound field.

2) Analyze the wave propagation in $\Omega_f$ by the FDTD method and obtain the responses on $\Gamma$.

3) Calculate the reflected wave at the receiving point by the Kirchhoff boundary integral equation.

### 2.1 Calculation of incident wave

The fundamental solution of 2-D sound field is given as follows[4]

$$\varphi_2(d,t) = \int_{-\infty}^{\infty} \frac{\delta(t-r/c)}{4\pi ct}\,dz = \frac{H(t-d/c)}{2\pi\sqrt{t^2-(d/c)^2}} \qquad (1)$$

where $r$ is distance between point source along line source and observation point, $c$ is sound speed, $\delta$ is Dirac's delta function, $d$ is distance between line source and point on the virtual boundary and $H$ is Heviside step function. The input wave on the virtual boundary is calculated as

$$p_i = \int_0^{\infty} \frac{\partial f}{\partial \tau}\varphi_2(d,t-\tau)\,d\tau = \frac{\partial f}{\partial \tau} * \varphi_2(d,t) \qquad (2)$$

where $f$ is driving waveform at the source. The input waves are calculated at the FDTD grid points on the virtual boundary, and the wave propagation in the FDTD domain is then calculated.

### 2.2 Calculation of reflected wave

The reflected waves from the target are calculated on the virtual boundary by the FDTD method. In the 3-D case, the response at the receiving point is calculated by the following Kirchhoch boundary integral equation[5].

ttsuchiy@mail.doshisha.ac.jp

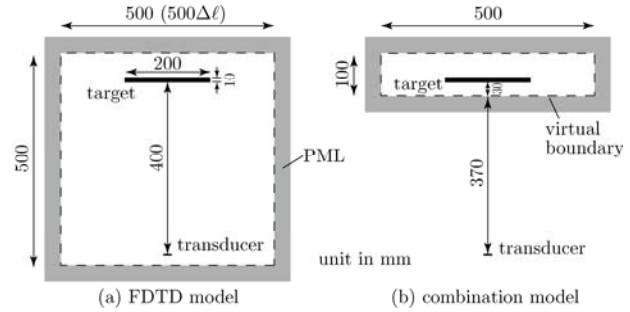

Fig.2 Numerical models.

$$p_o = \frac{1}{4\pi}\int_\Gamma \left[\frac{1}{r}\frac{\partial p_\Gamma}{\partial n} + \frac{1}{r}\frac{\partial r}{\partial n}\left(\frac{p_\Gamma}{r} + \frac{1}{c}\frac{\partial p_\Gamma}{\partial t}\right)\right] d\Gamma \qquad (3)$$

where $n$ denotes the normal line direction. In the 2-D case, the response is expressed as

$$p_o = \int_\Gamma \left[\varphi_2(\bar{r},t) * \frac{\partial p_\Gamma}{\partial n} + \frac{\partial \bar{r}}{\partial n}\frac{\varphi_2(\bar{r},t)}{ct} * p_\Gamma + \frac{1}{c}\frac{\partial \bar{r}}{\partial n}\varphi_2(\bar{r},t) * \frac{\partial p_\Gamma}{\partial t}\right] d\Gamma \qquad (4)$$

where is $\bar{r}$ the distance between the virtual boundary and the receiving point.

## 3. Numerical experiments

To verify the validity of the present method, some numerical examinations are made for the sound propagation in water. 2-D models are considered as shown in **Fig.2**. Figure (a) shows the FDTD model and (b) shows the model for the combination method. The grid spacing $\Delta\ell$ and the time step $\Delta t$ are chosen to be 1mm and 0.33 $\mu$ s, respectively where CFL number is 0.5. The sound speed $c_0$ is 1500m/s and the medium density $\rho_0$ is 1000kg/m$^3$. The domain is surrounded with the five-layered PML. A single-shot pulse of differential Gaussian shape is applied to the transducer of 20mm in length. A target of 200mm in length, 10mm in width and 2000kg/m$^3$ in density is located in each model.

**Figure 3** shows the calculated sound pressure waveforms reflected from the target. Figure (a) shows the waveform when the transmitted pulse width is 16.6 $\mu$ s and (b) 6.6 $\mu$ s. The two calculated results well agree in the long pulse width,

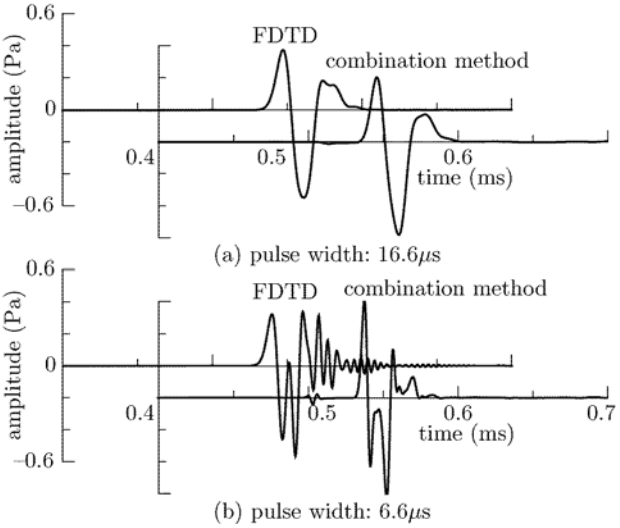

Fig.3 Calculated waveforms reflected from the target.

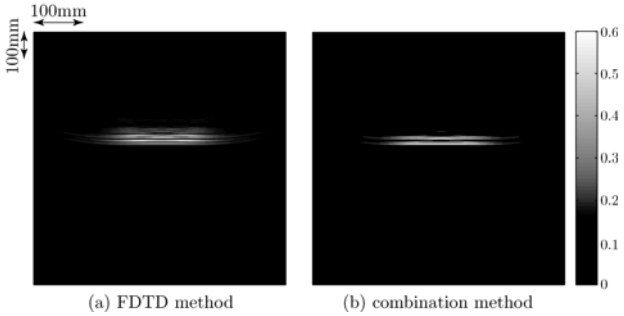

Fig.4 B-mode images of one target.

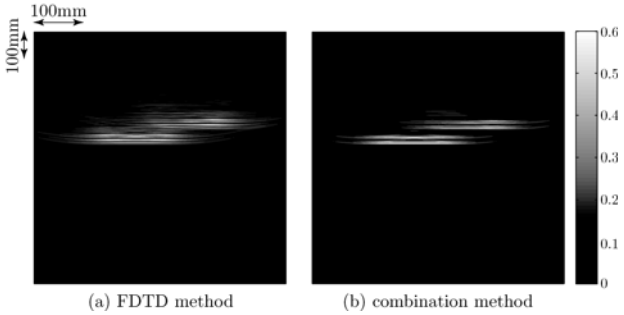

Fig.5 B-mode images of two targets.

although the waveform calculated by FDTD method collapses in the short pulse width because of the numerical dispersion error. On the other hand, the numerical dispersion error hardly appears in the result by the combination method because it does not occur in the boundary integral equation method.

To achieve a high-resolution image in acoustic imaging, a short width pulse is necessary as much as possible. However the indistinct image is obtained by the FDTD method using the short width pulse because of the numerical dispersion. **Figure 4** shows the B-mode images of the target obtained by scanning the transducer. The image obtained by the FDTD method is indistinct, while that by the combination method is clear. **Figure 5** shows the case of two targets. By the FDTD method it is difficult to distinguish each target, while the two targets can be sharply distinguished by the combination method. It is found that the present combination method is suitable for the large-scale simulation.

## References

1. Y. Saito, T. Tsuchiya and N. Endoh: Jpn. J. Appl. Phys. **45**, 5B (2006) 4693.
2. M. Sato: Jpn. J. Appl. Phys. **45**, 5B (2006) 4453.
3. S. Bunya and S. Yoshimura: J. Acoust. Soc. Jpn. **58**, 12 (2002) 738 (in Japanese).
4. M. D. Greenberg: *Application of Green's functions in science and engineering* (Prentice-Hall, New Jersey 1971).
5. Archi. Inst. Jpn.: Prediction of sound field in rooms: Theory, application and recent development (Archi. Inst. Jpn., Tokyo 2001).

2P10-8

Proceedings of Symposium on Ultrasonic Electronics, Vol. 29 (2008) pp. 335-336
11-13 November, 2008

# Phase Shift Keying Modulation with Impulse Response for Ultrasonic Communication

通信系のインパルス応答を考慮した PSK 変調方式

Tadashi Ebihara[1‡], Keiichi Mizutani[2], Naoto Wakatsuiki[1], Koichi Mizutani[1], and Koichi Morikawa[3] ([1]Univ. Tsukuba; [2]Tokyo Tech.; [3]Univ. Tsukuba)

海老原格[1‡], 水谷圭一[2], 若槻尚斗[1], 水谷孝一[1], 森川浩一[3] ([1]筑波大院・シス情工; [2]東工大院・理工; [3]筑波大・工シス)

## 1. Introduction

Recently, there has been an increase of research in ultrasonic communication especially in underwater environment[1-4], because radio communication in underwater environment is a challenging task due to the rapid attenuation of the electromagnetic spectrum. In contrast, ultrasonic communication in the air is not so often used because they attenuate rapidly in the air. However, use of ultrasonic to communicate in the air is effective in short-range communication[5-7]. An audible frequency acoustic communication method using ubiquitous speakers and microphones has advantages like availability of commercial audio devices for and no regulation in frequencies.

On the other hand, existence of impulse response distorts the waveform notably in the air ultrasonic communication. To perform communication with low error rate, it is necessary to ensure sufficient symbol time For example, there are preceding studies that considers the relationship between the length of symbol time and bit-error rate (BER)[8]. Unlike the high-frequency communication that is able to ensure information transmission rate with sufficient symbol time, there is a problem for low-frequency communication to balance transmission rate and symbol time. To achieve balance competing goals for transmission rate and symbol time, reducing the affection of impulse response is necessary.

This study was aimed at designing new phase shift keying (PSK) modulation for low-frequency communication in the air. By inserting guard time (GT) between symbols, it is possible to reduce the affection of impulse response in communication system.

## 2. Modulation and system fabrication

*2.1 PSK modulation method with impulse response*

PSK is a digital modulation technique whereby the phase of a carrier frequency is shifted to represent a digital “1” or “0” state as follows,

$$\left.\begin{aligned} s_0(t) &= A\sin 2\pi f_c t \\ s_1(t) &= -A\sin 2\pi f_c t \end{aligned}\right\},\ 0 \le t \le T, \qquad (1)$$

ebihara@aclab.esys.tsukuba.ac.jp

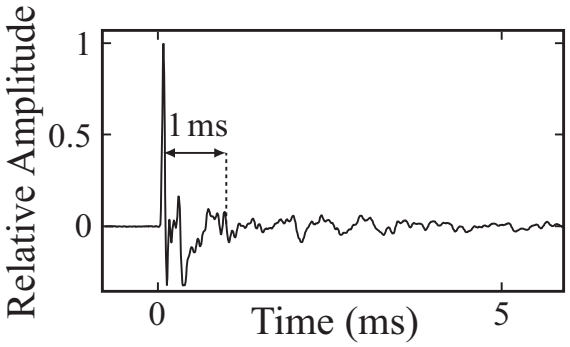


**Fig.1** Impulse response observed from performance evaluation system.

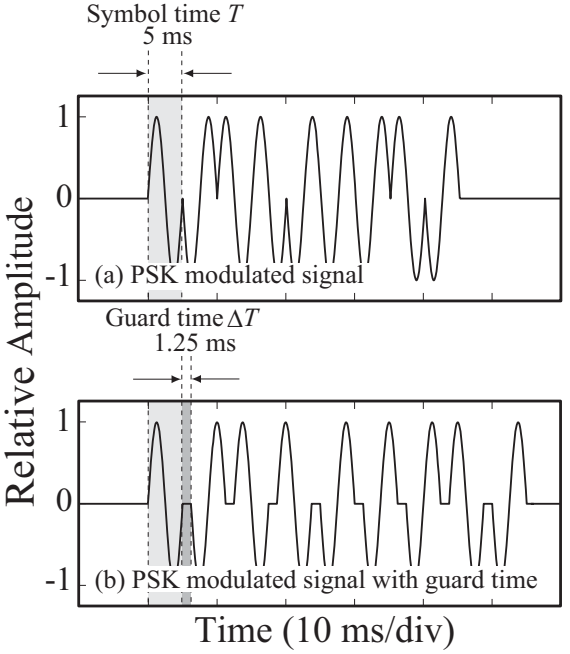


**Fig.2** PSK modulated signal and PSK modulated signal with GT to reduce the affection of impulse.

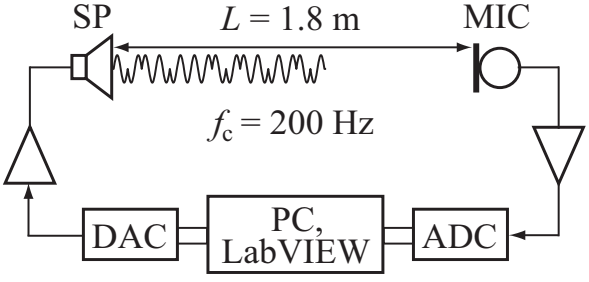


**Fig.3** Block diagram of a performance evaluation system of acoustic communication in the air.

where $s_0$ is a signal when data bit is "0", $s_1$ is "1", $A$ is a signal amplitude, and $T$ is a symbol time. However, precipitous phase shifting distorts signal due to impulse response as shown in **Fig.1**, especially in bit-inverting point because impulse response of communication system and transmitted signal are convoluted. To avoid this problem, we suggest inserting GT between symbols as follows

$$\left.\begin{aligned} s_0(t) &= A\sin 2\pi f_c t\big|_{0\le t\le T} + 0\big|_{T\le t\le T+\Delta T} \\ s_1(t) &= -A\sin 2\pi f_c t\big|_{0\le t\le T} + 0\big|_{T\le t\le T+\Delta T} \end{aligned}\right\}, \quad (2)$$

where $\Delta T$ is GT. From these expressions, PSK modulated signal and PSK modulated signal with GT are shown in **Fig.2**. Figure 2 (a) shows PSK modulated signal where $T$ is 5 ms, and Fig.2 (b) shows PSK modulated signal with GT where $T$ is 5 ms and $\Delta T$ is 1.25 ms, because notably impulse response can be observed within 1 ms in Fig.1. By inserting GT between symbols, we can avoid the problem from impulse response more effectively.

*2.2 Performance evaluation system*

We consider the performance evaluation system for digital communication in the air as shown in **Fig. 3**. This evaluation system consists of a personal computer (PC), digital to analog and analog to digital converter (DAC, ADC), a speaker amplifier (SP Amp), a loudspeaker (SP), a microphone (MIC), a microphone amplifier (MIC Amp), and a sound propagation path. Transmission signal is created and modulated by LabVIEW in PC. Amplified transmitted signal from SP which is controlled by DAC, propagates the channel and is received by MIC. Amplified received signal through ADC is added to white Gaussian noise and demodulated by LabVIEW in PC.

## 3. Experimental Results

The SP (FF-70EG, Foster) and the MIC (WM-62PC, Panasonic) were placed face-to-face in an anechoic chamber at the distance of 1.8 m. The SP and MIC were controlled through DAC and ADC (6062E, National Instruments) by the PC. The transmitted data, whose length was 16 bit, was created randomly. Bi-phase shift keying (BPSK) was used for modulation. The carrier frequency was 200 Hz and GT was 1.25 ms, in order to avoid the impulse response effect in evaluation system as shown in Fig. 1. The experiment was performed by changing signal-to-noise ratio (SNR). We define *SNR* as follows

$$SNR = 10\log_{10}\left(E_S / E_N\right), \quad (3)$$

where $E_S$ is received signal power and $E_N$ is additive white Gaussian noise (AWGN) power, which was added to the received signal in PC. Through this experiment, BER was calculated in each SNR.

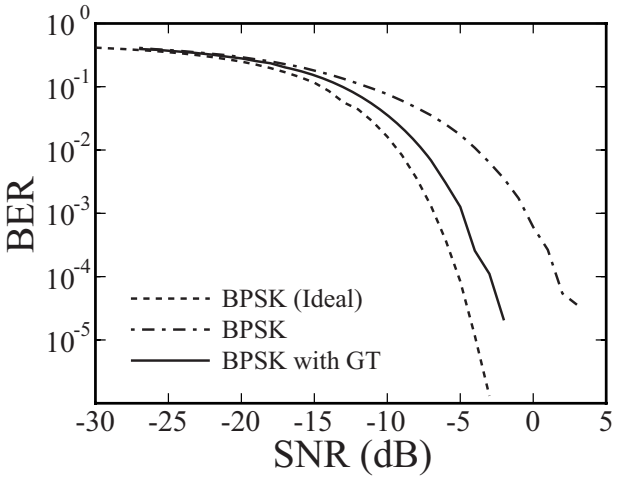


**Fig.4** BER performance of BPSK modulated signal and BPSK modulated signal with GT observed in performance evaluation system.

Figure 4 shows the BER performance in case that the transmitted signal is as shown in Fig.2 (a), and Fig.2 (b). Ideal performance was drawn in dot-line, experimental result from BPSK was in chain line, and experimental result from BPSK with GT was drawn in continuous line. In the simulation, we do not consider about signal distortion caused by impulse response of performance evaluation system, and the received signal is ideally transmitted through AWGN channel. From Fig.4, BPSK with GT achieves BER $10^{-3}$ at -5 dB when normal BPSK achieves at -0.5 dB. Moreover, when SNR is -5 dB, BER of BPSK with GT is about $10^{-3}$, and normal BPSK is about $10^{-2}$. The obtained results from Fig.4 suggest that by inserting GT between symbols, we can improve SNR at same BER about 4 dB, and BER at same SNR about 10 times. Consequently, by inserting GT between symbols, it is possible to reduce the affection of impulse response in communication system.

## 4. Conclusion

New PSK modulation method to reduce the affection of impulse response was proposed. By inserting guard time whose length is 25% of symbol time, we could improve BER at same SNR effectively. Considering relationships between transmission rate and symbol time is our future work.

## References

1. M. Stojanovic: IEEE J. Oceanic Eng. 21 (1996) 125.
2. H. Ochi *et al.*: Jpn. J. Appl. Phys. **39** (2000) 3184.
3. M. McCord *et al.*: J. Acoust. Soc. Am. **115** (2004) 2507.
4. Y. Watanabe *et al.*: Jpn. J. Appl. Phys. **44** (2005) 4717.
5. A. Ward *et al.*: Trans. IEEE. Personal Com. **4** (1997) 42.
6. N. Priyantha *et al.*: Proc. MOBICOM (2000) 32.
7. L. Chuan *et al.*: Trans. IEEE. Ultrason. **55** (2008) 908.
8. K. Mizutani *et al.*: Jpn. J. Appl. Phys. **44** (2005) 4541.

2P10-9

Proceedings of Symposium on Ultrasonic Electronics, Vol. 29 (2008) pp. 337-338
11-13 November, 2008

# Locality of Area Coverage on Acoustic Communication in Air using Differential Phase Shift Keying

差動位相偏移変調を用いる空中音響通信における
通信領域の局所性

Keiichi Mizutani[1‡], Tadashi Ebihara[2], Naoto Wakatsuki[2] and Koichi Mizutani[2]
([1] Tokyo Institute of Technology; [2] University of Tsukuba)
水谷圭一[1‡]，海老原格[2]，若槻尚斗[2]，水谷孝一[2]　([1] 東工大院 理工; [2] 筑波大院 シス情工)

## 1. Introduction

Acoustic communication in underwater environment has often been studied[1-5]. In contrast, acoustic communication is not often used in air environment, because airborne sound is not very effective compared with electromagnetic waves, particularly for long-distance communication[6, 7]. The disadvantages include the problem of attenuation and slow propagation velocity. However, it may be rather effective for short-range communication such as acoustic beacon systems for autonomous robots in small area[8]. An example of the autonomous robot control system using acoustic beacons is shown in **Fig. 1**. To setup the beacons close to each other, each communication area coverage of each beacon is required to be limited. Therefore a localization of acoustic communication may be effective for the above system.

In this paper, we experimentally evaluate a locality of area coverage on digital acoustic communication in air using differential phase shift keying (DPSK). At first, a propagation loss performance is evaluated using one transmitter and one receiver in environmental noise of constant level. Next, influences of interference from another transmitter are evaluated using two transmitters and one receiver.

## 2. System Fabrication

The experimental system using DPSK digital acoustic communication is fabricated as shown in **Fig. 2**. This consists of two transmitters, one receiver and environmental noise source. Transmitter consists of a PC, a digital-to-analog converter (DAC) and a loudspeaker (SP). Receiver consists of a PC, an analog-to-digital converter (ADC) and a microphone (MIC). Architecture of the environmental noise source is same as the transmitter. White Gaussian noise is transmitted from SP with constant level at the receiver. The transmitter, the receiver and the environmental noise source share the PC and software programs although these are independent in practical application. Therefore, the clock of each component is naturally synchronized.

mizutani@mobile.ee.titech.ac.jp

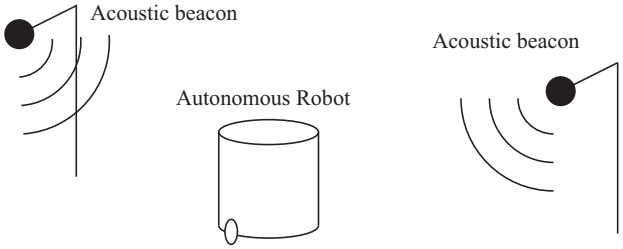


Fig. 1 Example of the autonomous robot control system using acoustic beacons.

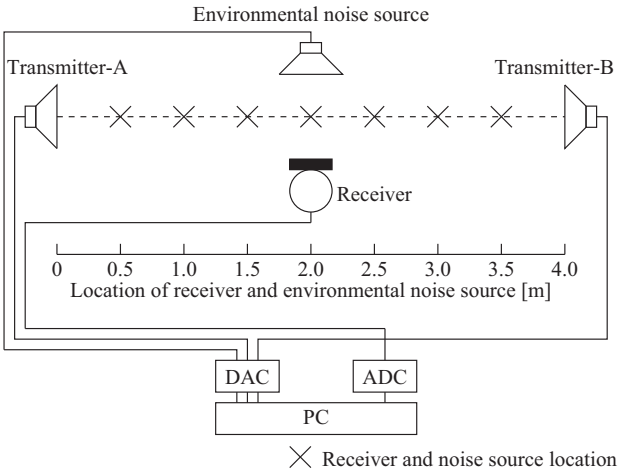


Fig. 2 System fabrication of the experiment system using DPSK digital acoustic communication and location of the two transmitters, the receiver and the environmental noise source.

## 3. Experiment and Evaluation

The location of the two transmitters and the receiver is shown in **Fig. 2**. Distance between the transmitters A and B is fixed to 4.0 m and these are setup face-to-face. The receiver and the environmental noise source are located at 0.5, 1.0, 1.5, 2.0, 2.5, 3.0 and 3.5 (m) from the transmitter-A, and bit-error-rate (BER) is evaluated at the each evaluation point. Transmitted power of the transmitters-A and -B are configured so that signal-to-noise-ratio (SNR) becomes -4.0, 0, 4.0, 8.0

and 12.0 (dB) at the middle point of the transmitters-A and -B. Carrier frequency is 10 kHz, one-symbol time is 0.8 ms, and modulation scheme is differential binary phase shift keying (DBPSK), which are the same as our previous experiment[8].

At first, BER performances are evaluated by emitting the transmission signal from only one transmitter-A or -B. Area coverage of the transmitter is more limited as environmental noise level becomes high. In this case, the cell radius is 0.9, 2.3 and 3.2 (m) under SNR is -4.0, 0 and 12 (dB) respectively if the BER is taken as $10^{-2}$ at the cell edge.

**Figure 5** shows the BER performance under condition that both of the transmitters-A and -B work. The signals from transmitter-B are independent of that from transmitter-A and the receiver tries to demodulate signals from the transmitter-A. BER performance deteriorates and cell radius is limited when the transmitted power of the transmitters-A and -B becomes high because transmitted waves emitted from undesired transmitter interferences in desired communication. However, under low SNR condition, BER performances are same whether another transmitter works or not because the environmental noise becomes dominant in such a situation. In this case, the cell radius is 0.9 and 1.3 (m) under SNR is -4.0 and 0 (dB) respectively if the BER at the cell edge is taken as $10^{-2}$.

## 4. Conclusions

Locality of acoustic communication using DBPSK was experimentally evaluated. The cell radius of the transmitter could be limited under low SNR condition. If another transmitter works, the cell radius was limited by effect of the interference from another transmitter. The cell radius to distance between the transmitter-A and -B was 22.5 % under SNR was -4.0 dB if the BER at the cell edge was taken as $10^{-2}$.

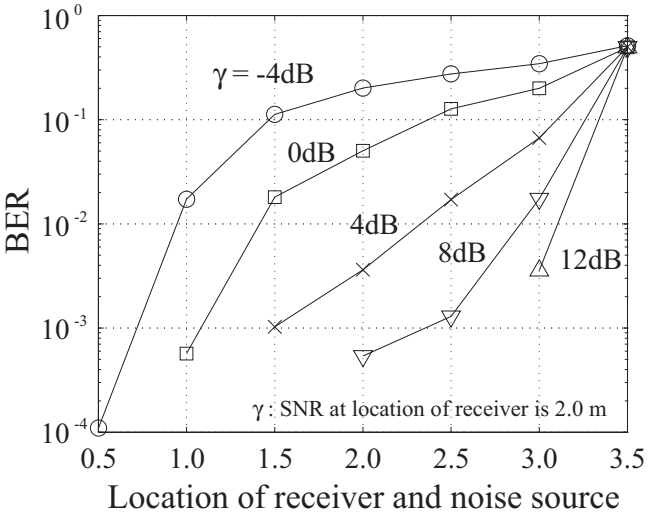

Fig. 3 BER performance with only transmitter-A.

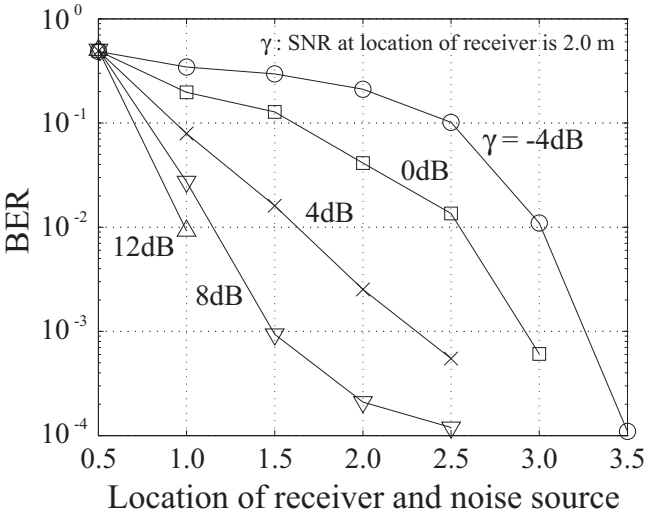

Fig. 4 BER performance with only transmitter-B.

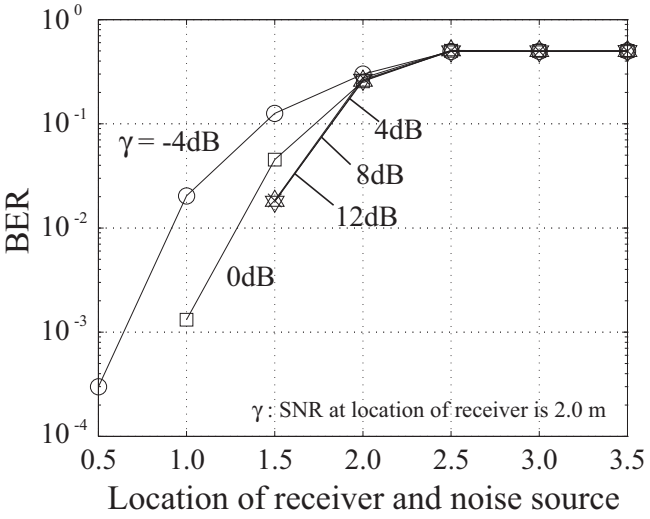

Fig. 5 BER performance with transmitters-A and -B.


**References**

1. D. P. Konstantakos, C. C. Tsimendis, A. E. Adams and B. S. Sharif: IEE Proc. Commun.. **152** (2005) 1031.
2. T, Kikuchi, H. Saito, T. Tsuchiya and Y. Hiyoshi: Jpn. J. Appl. Phys. **44** (2005) 4708.
3. S. Lee, K. C. Park, J. R. Yoon and P. H. Lee: Jpn. J. Appl. Phys. **46** (2007) 4971.
4. H. Ochi and T. Fukuchi: Jpn. J. Appl. Phys. **46** (2007) 4961.
5. T. Shimura, H. Ochi and Y. Watanabe: Jpn. J. Appl. Phys. **46** (2007) 4956.
6. H. R. Beom and H. S. Cho: Robotica **13** (1995) 243.
7. L. Kleeman: Robotica **13** (1995) 87.
8. K. Mizutani, N. Wakatsuki and K. Mizutani: Jpn. J. Appl. Phys. **46** (2007) 4541.

2INV1

Proceedings of Symposium on Ultrasonic Electronics, Vol. 29 (2008) pp. 339-340
11-13 November, 2008

# High Temperature Ultrasonic Probes and Their Potential Applications
# 高温超音波プローブ及びその応用可能性

Cheng-Kuei Jen † and Makiko Kobayashi (Industrial Materials Institute, National Research Council Canada)
任正魁†，小林牧子 （工業材料研究所　カナダ国立研究所）

## 1. Introduction

Ultrasonic nondestructive evaluation (NDE) of materials, parts and structures [1-4] has played a vital role in many industries involving improvement of reliablity, safety, service life extension, maintenance cost reduction, etc. Increasingly ultrasound is used for structural health monitoring (SHM) [3,5,6] for aerospace components, nuclear and electrical power plants, petroleum plants, engines, etc. For aerospace sector SHM facilitates condition based maintenance to estimate the remaining useful life on a continuous basis and also enable modern light-weight aircraft designs with increased safety and cost reductions. Also due to the high demand on non-stop supplying of energy, SHM and NDE are crucial to extend the life span of every nuclear power, electric power and petroleum plant, and land based engines, the time span between two adjacent showdowns for plant and engine inspections and also each shutdown time. Furthermore, globle market demands high quality products manufactured by cost-effective technologies and technical specifications are increasingly advanced and precise. The required quality control for these manufacturing technologies desires on-line process diagnostics (OPD) [4,7]. Ultrasound is one attractive OPD approach. This study involves NDE, SHM and OPD using ultrasound at high temperatures (HT) [1-7].

## 2. HT transducers and buffer rods approaches

Two approaches to achieve HT ultrasonic measurements are used. One is to use HT thick (>30μm) film ultrasonic transducers (UTs) made by a sol-gel spray fabrication process [3,5,6,8]. It consists of six main steps: (1) preparing high dielectric constant solution, (2) ball milling of piezoelectric ceramic powders to submicron size, (3) film spraying using slurries from steps (1) and (2) to produce a layer of piezoelectric composite ceramic film, (4) heat treatment to produce a solid film, (5) corona poling to obtain piezoelectricity, and (6) top electrode fabrication. Steps (3) and (4) are used multiple times to produce proper piezoelectric film thickness for optimal ultrasonic operating frequencies. In this operating frequencies. investigation lead-zirconate-titanate (PZT) solution is used for step (1). Piezoelectric PZT, bismuth titanate (BIT) and lithium niobate (LN) powders are used for the fabrication of HT piezoelectric composite film PZT/PZT, BIT/PZT and LN/PZT ultrasonic transducers (UTs) to operate reliably up to 150°C, 450°C, 750°C, respectively. They can be directly coated and used as integrated UTs (IUTs). If the substrate is thin, then such HT UTs can be made as flexible UTs (FUTs) [8]. All HT IUTs and FUTs can be used for SHM and NDE of objects with curved surfaces [3,5,6,8].

Another approach involves the use of HT delay line buffer rods. In this investigation clad buffer rods consisting of core and cladding [2,7] and non-clad buffer rods [1,3,9] are used. The advantages using buffer rods is that the temperature of the probing end can be much higher than the UT end. The well known issues to use the long delay line buffer rods are the presence of spurious echoes due to one or more of: mode conversion, wave reverberation and diffraction within the rod of finite diameter. These echoes are unwanted because of their possible interference with the desired signals from the measured sample. These noises can be reduced significantly using clad geometry [2,7] and tapered and/or thread shapes [9], thus signals with high signal-to noise ratio (SNR) can be obtained. In this study only longitudinal (L) waves are used.

## 3. Different HT UTs and ultrasonic probes

The evaluation of the ultrasonic strength of all HTUTs and probes will be based on a commercially available EPOCH (model LT) pulser-receiver device which has receiver gain up to 100dB. This handheld device is commonly used in the NDT industry. The electrical contacts during all measurements were carried out using a spring-loaded two- pin probe. **Fig.1** shows a 79μm thick BIT/PZT film IUT deposited onto a steel substrate of 12.7 mm thick and measured by the EPOCH device at 400°C. At 400°C 47.4dB gain, out of the available 100 dB receiver gain was used to produce the 1st echo reflected from the end of

---

Cheng-kuei.jen@cnrc-nrc.gc.ca

the plate. The centre frequency and the 6dB bandwidth are 5.5MHz and 4.6MHz respectively. **Fig.2** shows that the HT IUTs shown in **Fig.1** are used as sensors incorporated into mold (or die) inserts for OPD of polymer injection molding (IM) [7] and light-weight metal IM or die casting.

Fig.1BIT/PZT IUT at 400°C.

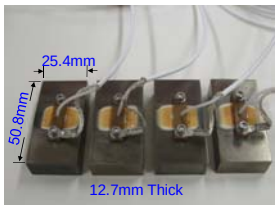


Fig.2 Four HT IUTs

**Fig.3** shows the HT measurement setup of a FUT having a ~70µm thick BIT/PZT film deposited onto a 38µm thick stainless steel which is bonded onto a 12.7mm thick steel substrate using a metallic adhesive at 303°C. The measured ultrasonic data gone through a high pass filter is presented in **Fig.4**. $L^n$ is the nth round trip L echo through the plate thickness The centre frequency and the 6dB bandwidth of the $L^1$ echo at 300°C were 10.7MHz and 8.2MHz, respectively. Using EPOCH 69dB out of the available 100dB receiver gain was used.

Fig.1BIT/PZT FUT at 303°C.

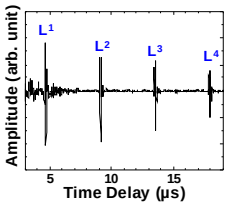


Fig.4 Signals at 300°C.

When a clad buffer rod consists of a 12.7mm steel core and 1mm thick stainless steel cladding as shown in **Fig.5** is used together with a 106µm thick 150°C PZT/PZT IUT deposited onto its one end, the measurement setup shown in Fig.6 demonstrates that the probing end of the clad rod can operate at a higher temperature (182°C). If the length is longer, the probing temperature can be higher. In **Fig.6** at 151°C only 10dB out of the available 100dB receiver gain of EPOCH was used. At 150°C the centre frequency and the 6dB bandwidth of the $L^1$ echo were 7.0MHz and 5.9MHz, respectively.

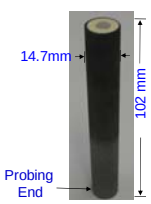


Fig.5 PZT/PZT IUT on a clad rod.

Fig.6 PZT/PZT UT at 151°C.

**Fig.7** and **Fig.8** show thick PZT/PZT and BIT/PZT film IUT onto two non-clad tapered rods and a clad steel buffer rod, respectively. Their center frequencies are near 5MHz. The former two are used for OPD of polymer extrusion [7] without the need of any cooling. It may be used from the feed hopper down to the extruder die. The latter is used as the immersion HT UT for the remaining wall thickness profile measurement of the container inside the 450°C molten zinc. The steel wall thickness is normally 60mm. Thickness reduction is caused by the corrosion which may be unpredictable due to uneven heating profile. Such thickness measurement is one of the most important NDE for hot-dip galvanization industry.


Fig.7 PZT/PZT IUT with non-clad rod.

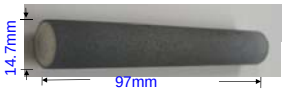


Fig.8 BIT/PZT IUT with clad rod

## 4. Conclusions

HTUTs including BIT/PZT and PZT/PZT IUTs or FUTs made by sol-gel sprayed techniques can be used for SHM and NDE purposes. Together with metal plate, clad and non-clad buffer rod delay lines they can be used as mold (or die) insert sensors for OPD of polymer or metal IM and polymer extrusion, and container wall thickness profile measurement in molten zinc.

## References

1. T. Arakawa, K. Yoshikawa, S. Chiba, K. Muto, and Y. Atsuta: NDT&E. **7** (1992) 263-272.
2. C.-K. Jen, J.-G. Legoux and L. Parent: NDT&E **33** (2000) 145-153.
3. M. Kobayashi and C.-K. Jen: Smart Mat. Structures **13** (2004) 951-956.
4. S.P. Kelly, D. Babcock, I. Atkinson, C. Gregory and K.J. Kirk: Proc. IEEE Ultrasonics Symp. (2007) 904-908.
5. M. Kobayashi, C.-K. Jen, Y. Ono, K.-T. Wu and I. Shih: Jpn. J. Apl. Phys. **46** (2007) 4688-4692
6. Q. Liu, K.-T. Liu, M. Kobayashi, C.-K. Jen and N. Mrad: Smart Struct. Mat. **17** (2008) 045023.
7. C.-K. Jen, Z. Sun, J. Tatibouët and Y. Ono: Chap.3 in Ultrasonic and Advanced Methods for NDT, World Scient. Publ. NJ (2007) 57-77.
8. M. Kobayashi, C.-K. Jen and D. Lévesque: IEEE Trans. UFFC **53** (2006) 1478-1485.
9. C.-K. Jen, L. Piche and J.F. Bussiere: J. Acoust. Soc. Am. **88** (1990) 23-25.

2INV2

Proceedings of Symposium on Ultrasonic Electronics, Vol. 29 (2008) pp. 341-342
11-13 November, 2008

# Bubbles and Ultrasound: A New Partnership for Medical Imaging

Peter N. Burns
(Departments of Medical Biophysics and Radiology, University of Toronto)

An enduring challenge in medical imaging has been the detection and imaging of perfusion at the capillary level of the circulation. It is here, across the hundreds of millions of microscopic vessels in tissue, that exchange of oxygen and nutrients that sustains viability takes place. Knowledge of the integrity of perfusion in the myocardium is central to the understanding of acute heart disease, in the brain of stroke and less obviously, in a cancer of the proliferation of blood vessels known as angiogenesis. A technique that can image perfusion offers an aid to both the diagnosis of heart disease, stroke and cancer and their treatment and subsequent monitoring. Contrast imaging for ultrasound seeks to provide such a method.

After more than 20 years of development and a somewhat hesitant start, microbubbles have finally come of age as a contrast agent for ultrasound. The bubbles themselves comprise small spheres of a gas with low solubility in blood - such as a perfluorocarbon - stabilised by a thin shell layer of a flexible, biocompatible material. This is typically a lipid, though proteins and polymers are also used. The diameter of the resulting encapsulated bubble is about 3-5 μm, slightly smaller than a red blood cell. A suspension of bubbles in water is injected into a peripheral vein in the arm or hand. A typical whole body human dose is only about few million bubbles, about the same as the number of red blood cells in a single microlitre of blood. Partly because of this extremely low dose, injections of microbubbles are very well tolerated and have an excellent safety record.

The objective of perfusion imaging in ultrasound is to detect and segment the component of the echo due to blood and use this to form a real-time image of the distribution of blood vessels. While Doppler works well as a way of identifying blood where there is sufficiently fast flow in relation to tissue movement, in the vast majority of the vascular system, the blood is moving at a speed comparable to natural tissue motion. The blood-born bubbles provide a distinct acoustic ‘label’ for the identification of the vascular echo that is independent of flow velocity: the challenge for contrast imaging is to create a method for its detection and display. It is a fortuitous and unintended consequence of the choice of the size of bubble that it displays a radial resonance between about 3 and 5 MHz, which lies in the diagnostic range of ultrasound frequencies. Solving an equation first conceived by Lord Rayleigh one hundred years ago suggests that bubbles may undergo resonant excursions of several radii in a diagnostic ultrasound field: this nonlinear resonant oscillation provides the key for the detection and separation their echo from the much greater energy from the surrounding tissue. Unlike their air-filled predecessors, typical perfluorocarbon bubbles can be driven into nonlinear oscillation which lasts over seconds or even minutes, creating a steady stream of harmonic echoes. A class of imaging methods have been developed that exploits the coherence of these echoes over many pulses. Unlike tissue structures, which give rise to echoes that simply mirror the incident pulse, bubbles respond differently to the phase and amplitude of each pulse they experience. It is therefore a relatively simple matter to make an imaging method that differentiates between tissue and these bubbles: one simply sends a sequence of pulses of differing phases and amplitudes. On receiving the echoes from this sequence, the receiver combines them in a way that ensures that the ‘mirror-like’ echoes from tissues combine to zero. What is left is then some combination of the nonlinear components of the bubble echo. Precisely what nonlinear components are produced by a sequence of pulses can be determined mathematically. For example, keeping the amplitude of the pulse constant but changing the phase of alternate pulses by 180 degrees (known as *pulse inversion* imaging) produces an echo with even order harmonics. On the other hand, keeping the phase constant and changing the amplitude (known as *power modulation* imaging) detects odd and even order nonlinear components, though at some cost to the signal-to-noise ratio. Combinations of amplitude and phase offer specific advantages. Almost all diagnostic systems now use some form of this multipulse modulation processing in their contrast-specific imaging modes. As long as the peak negative pressure is kept low (less than about

---

Burns@sri.utoronto.ca

100kPa) so that the bubble is not disrupted by the pulses, real time imaging of perfusion can be achieved in many organ beds, including the myocardium, liver, kidney, skin, prostate and breast, even in the presence of tissue motion. Whereas the technology for bubble imaging in commercial ultrasound systems has stabilised over the past few years, clinical applications are currently experiencing expansion, especially in tumour imaging, which in turn presents new challenges for imaging methodology.

At least 3 million clinical contrast studies have been performed to date worldwide: clinical applications have focused on areas in which ultrasound already plays an important diagnostic role. In cardiology, contrast can aid visualisation of the endocardium, especially important in wall motion studies, and has been shown to improve the accuracy of stress echo. It can also image and measure myocardial perfusion in real time, at rest and with stress, with spatial resolution superior to the current nuclear medicine standard. In radiology, perfusion can be imaged in many organs, but work has concentrated on the liver, where contrast can help characterise focal lesions with an accuracy comparable to contrast-enhanced CT and MRI. It also aids in lesion detection, in real time guidance of interventions such as radiofrequency ablation and in monitoring response to new cancer therapies. In tumour imaging, the target is the angiogenic, or proliferating network of blood vessels that sustains a developing cancer. Not only has the identification of these vessels proven an important way to distinguish a malignant from a benign lesion, the vessels themselves have become the objective of a new class of molecular therapies that aim to inhibit angiogenic formation. Such anti-agiogenic or vascular-disrupting drugs have the effect of shutting down the tumour circulation and inhibiting further growth. They do not in themselves kill cancer cells, so the tumour often responds without shrinking in size, hence the need for a functional test to determine drug response. Quantitative flow measurement with bubbles is achieved by infusing the agent to a steady level, then using a few high mechanical index pulses to disrupt and clear the image plane of bubbles following which measurement of its replenishment offers a unique way to quantify microvascular flow and perfusion volume. Models of the process are in development to help improve accuracy.

Current development of the bubbles themselves focuses on two main areas. In the first, the potential for functional information yielded by the bubbles is increased by active targeting to a specific cellular or molecular process. Thus a bubble attaches itself to the cells lining blood vessels (endothelial cells) which are involved in a disease process such as inflammation (in atherosclerosis) or proliferation (in cancer). This is achieved by attaching ligands to the surface of the lipid shell, such as a peptide and an antibody. Antibodies to factors such as VCAM, a marker of inflammation and VEGF receptor, a marker of vascular proliferation, have already been shown to effectively make bubbles ‘stick’ selectively to the endothelial surface. This form of molecular imaging has potential applications in identifying the target and the effectiveness of new therapies. In the second application, the bubbles are used as a potentiator of the therapy itself. Bubbles can concentrate and lower the threshold for thermal tissue damage in HIFU treatments. They can also have the effect of opening or permeabilising the endothelial layer, allowing drugs to pass through into a region of tissue selected by the ultrasound beam. The drugs can be circulating in the bloodstream, or incorporated into the bubbles themselves. In the latter case, plasmid DNA, which cannot survive in the blood, can be carried in the bubble shell and released by acoustic disruption. Oscillation of the free gas near the cell membrane permeabilises it and allows the DNA to enter the cell. Both endothelial cells and myocytes have been successfully transfected in this potentially new form of gene therapy.

These new applications pose many interesting challenges to ultrasound imaging technology: Can we quantify the number of bound bubbles? Can we detect single bubbles bound to a single cell? Can we distinguish bound from free bubbles acoustically? Can we scale bubble-specific imaging to higher frequencies? Answering such questions will assure that ultrasound imaging of bubbles remains a rich field of enquiry in the foreseeable future.

2E7a

Proceedings of Symposium on Ultrasonic Electronics, Vol. 29 (2008) pp. 343-344
11-13 November, 2008

# Separation of Nonlinear Ultrasound Signals Based on Second-Order Volterra System Identification

Pornchai Phukpattaranont† (Facult. Eng., Prince of Songkla Univ.)

## 1. Introduction

We propose to investigate the application of a system identification based on a second-order Volterra filter (SVF)[1] to separate nonlinear signals from a nonlinear pulse-echo ultrasound. In other words, we identify a nonlinear pulse-echo system (NPS) consisting of multiple scattering point targets (**Fig. 1.** upper block diagram) with the SVF consisting of linear and quadratic kernels (Fig. 1. lower block diagram). The objective is to apply the approach on medical ultrasound applications, e.g. ultrasound imaging enhancement and nonlinearity parameter B/A estimation. This paper is focused on developing an efficient implementation of the input-output based system identification. In addition, the preliminary evaluation results of the approach are demonstrated and discussed.

## 2. Nonlinear Pulse-Echo System

In this section, we present a model used to produce radio-frequency (RF) lines from a nonlinear pulse-echo system (NPS). **Fig. 2** shows a diagram of a pulse-echo RF line generated from media with different nonlinearity parameter B/A. The NPS model combines capabilities of the Field II program [2] with the Khokhlov Zaboloskaya Kuznetsov (KZK) equation [3]. The pulse-echo RF data are generated in three steps: First, the spatial impulse responses in transmissions are produced from solutions of the KZK equation. Second, when linear propagation and weak scattering are assumed, the received RF pulse-echo signal resulting from the interaction of the transmitted pulse and a scatterer is determined. Third, a received pulse-echo RF line is obtained by a weighted addition of received RF signals from all scatterers in the region of interest.

## 3. SVF System Identification

Identification of quadratic nonlinear system algorithm is based on a digital method of modeling quadratically nonlinear systems with general random input discussed in [4]. Representation of the SVF in the frequency domain in term of the discrete Fourier transform (DFT) of $y(n)$ can be expressed as

E-mail address: porncahi.p@psu.ac.th

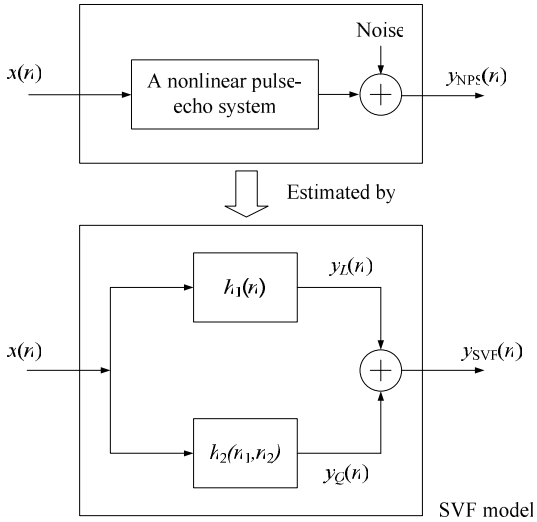


Fig. 1 Identification of a nonlinear pulse-echo system (NPS) using a SVF model.

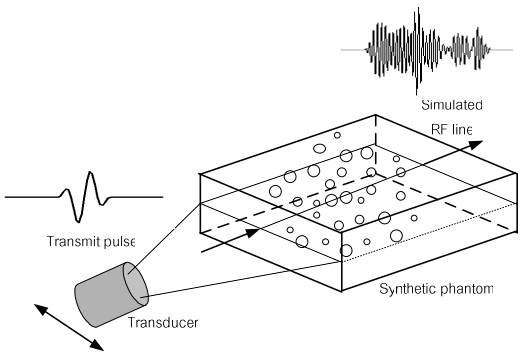


Fig. 2 A diagram showing the generation of an RF line from a nonlinear pulse-echo system (NPS).

$$Y(f_k) = H_1(f_k)X(f_k) + \sum_{\substack{i,j=-(M-1) \\ i+j=k}}^{M} H_2(f_i, f_j)X(f_i)X(f_j) \qquad (2)$$

where the linear transfer function $H_1(f_k)$ and the quadratic transfer function $H_2(f_i, f_j)$ are unknown. $M$ is the length of input sequence divided by two. Kim and Power [4] proposed a general DFT-based solution for the system identification problem using higher-order spectra. We skip the details of the algorithm, but state that (2) can be written in matrix form:

$$Y(f_k) = \mathbf{x}^T\mathbf{h}, \qquad (3)$$

where the vector **h** contains the coefficients $H_1(f_k)$ and all $H_2(f_i, f_j)$: $i+j=k$. To solve the variable **h**, both

sides of (3) are multiplied from the left by $\mathbf{x}^*$ and the expectation operator is applied resulting in

$$\mathbf{f} = \mathbf{Gh}, \quad (4)$$

where $\mathbf{f} = E[\mathbf{x}^* Y(f_k)]$and $\mathbf{G} = E[\mathbf{x}^* \mathbf{x}^T]$. After the linear and quadratic frequency responses are determined, inverse discrete Fourier transforms (IDFTs) are applied to obtain the linear impulse response $h_1(n)$ and the quadratic kernel $h_2(n_1, n_2)$.

## 4. Results and discussion

The parameters used in simulation are as follows. The impulse response of the transducer is a Gaussian-modulated sinusoidal pulse with center frequency 3 MHz and fractional bandwidth 60 %. The sampling frequency is 40 MHz. A single focus at 70 mm is used in both transmission and reception. The synthetic phantom is composed of scattering particles located at uniform random positions in a 20 mm × 3 mm × 1 mm volume and Gaussian distributed scattering strengths are assigned to those particles.

To determine coefficients of linear and quadratic kernels, we form a system of linear equations (Equation (4)) using average of frequency responses resulting from 64 pseudorandom binary sequences and their corresponding outputs from the NPS. While each pseudorandom binary sequence is composed of 150 data points, each pulse-echo line from the NPS consists of 256 data points. Gaussian white noise is added to pulse-echo data to achieve the SNR of 50 dB. After the SVF kernels are identified, we transmit a 3-cycle sinusoidal pulse at 2 MHz with a Hanning weighting to both systems, i.e., the NPS and the SVF for validation.

**Fig. 3** shows a simulated RF line from the NPS using the dotted line. The pulse duration is approximately 2.8 mm. In addition, the corresponding spectra of time waveforms in the top panel are displayed in the bottom panel. The 2nd harmonics is clearly observed at 4 MHz. It can be seen that the linear kernel appropriately predicts the linear output in the fundamental energy band (around 2 MHz). On the other hand, the quadratic kernel captures energy primarily in the 2nd harmonic and low frequency bands corresponding to second order nonlinearity covering the whole transducer bandwidth. This is the advantage of the SVF approach over other static models such as linear bandpass filters whose the sensitivity to nonlinear separations is fixed to some specific frequencies, e.g. the 2nd harmonic.

In addition, we found that the regularization based on the truncated singular value decomposition (TSVD) can reduce the number of input sequences used in identification algorithm as

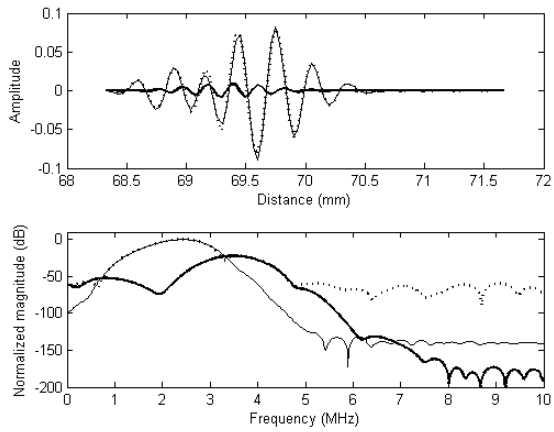


Fig. 3 Comparison of the pulse-echo line from the NPS (dotted) with the linear plus quadratic output from the SVF model (solid).

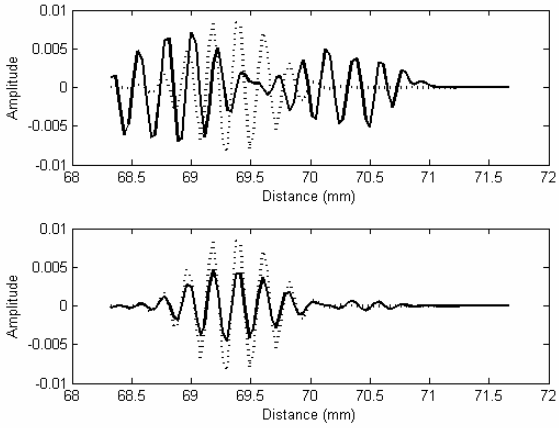


Fig. 4 Quadratic outputs from the algorithm without (Top) and with (Bottom) TSVD regularization when the number of input sequences is decreased from 64 to 16.

shown in **Fig. 4**. Its advantage is to make the identification approach more practical. The study on computational complexity reduction is ongoing research.


## Acknowledgment

This research is funded by a grant from Thailand Toray Science Foundation and Faculty of Engineering, Prince of Songkla University through Contract No. ENG-51-2-7-02-0004-S.


## References


1 G.. L. Sicuranza: Proc. IEEE. **80** (1992) 1263.
2 J. A. Jensen and N. B. Svendsen: IEEE Trans. Ultrason., Ferroelect., Freq. Contr. **39** (1992) 262.
3 Y. S. Lee and M. F. Hamilton: J. Acoust. Soc. Am., **97** (1995) 906.
4 K. I. Kim and E. J. Powers: IEEE Trans. Acoust., Speech, Signal Processing, **36** (1988) 1758.

2E7b

Proceedings of Symposium on Ultrasonic Electronics, Vol. 29 (2008) pp. 345-346
11-13 November, 2008

# Assessment of microelastic properties of bone using scanning acoustic microscopy : a face-to-face comparison with nanoindentation

Pascal Laugier[1] , Fabienne Rupin [1], Davy Dalmas[2], Françoise Peyrin[3], Kay Raum[4], Etienne Barthel[2], Amena Saïed[1]

[1] UPMC Univ Paris 06, CNRS UMR 7623, LIP, F-75006, Paris, France
[2] Unité Mixte CNRS/Saint-Gobain " Surface du Verre et Interface " UMR 125, Saint-Gobain Recherche, F-93303, Aubervilliers, France
[3] ESRF/CREATIS, F-38043 Grenoble, France
[4] Q-BAM Group, Dept. of Orthopedics, Martin Luther University of Halle-Wittenberg, 06097 Halle, Germany

Corresponding author: Pascal Laugier, E-mail: laugier@lip.bhdc.jussieu.fr

## Introduction

There are a number of motivations for investigating the micromechanical properties of bone, such as (i) investigating relationships between micro-elastic bone properties and collagen and mineral, (ii) providing insights into the structure-function relationships, (iii) providing inputs for numerical models to predict macroscopically derived ultrasonic attenuation or speed of sound (or mechanical) properties or to predict the strain at the cellular level. Nanoindentation is currently the only established mechanical tool for the direct assessment of elastic properties at the microscopic level. However, because the measurements are limited to spots (i.e., are taken at discrete levels), comprehensive evaluations of the heterogeneous microstructure are not possible. Scanning acoustic microscopy (SAM) is an appealing technology because of its scalability that makes it suitable to assess elastic properties at various scales. SAM is used with a set of calibration materials with known acoustic impedance. The signal reflectivity from the surface can be converted into an acoustical impedance value which is well modeled as the square root of the product of the local mass density and local stiffness coefficient in the test direction. When the local density (or mineralization) is documented, such as with micro-computed tomography (μ-CT), for example, the stiffness coefficient can be computed and subsequently, tissue-level elastic modulus can be extracted from acoustical impedance measurements . As an extension of previous SAM studies reported by our group, this work aimed at validating acoustic microscopy as a modality to map elastic modulus at the tissue-level [1-4].

## Material and methods

Toward this goal a face-to-face comparison was conducted between SAM and nanoindentation estimates of elastic modulus. Three embedded transverse sections taken from female human femoral mid-diaphysis were explored by 200MHz-SAM (8μm-spatial resolution). The acoustical tissue elastic modulus Ea of cortical bone was obtained by combining acoustical impedance and bone density derived from degree of mineralization of bone (DMB) provided by Synchrotron μ-CT (10-μm-spatial resolution) [3], assuming a Poisson's ratio of 0.3. Nanoindentation measurements (2-μm-depth indents) were done in 2 line scans (30 indents each at 30-μm-interval) across the radial direction extending from the peripheral to the inner layers of each anatomical quadrant. The indentation depth was selected in order to ensure the same volume probed with the three techniques. After SAM acquisition, nanoindentation was performed using a commercial instrument (Nano-XP) with a Berkovich tip. Tests were performed at room temperature under dry conditions. The strain rate was constant during the experiments (0.05 s-1) and indentation depth was fixed to 2 μm in order to obtained residual indents observable with the SAM resolution (approximately 8-10 μm) and similar probed volume in both case. When the tip was at the maximum penetration, the load was maintained constant during 150 s.
Ea was compared to nanoindentation estimates of elastic modulus En and to DMB. Before any indentation measurements were made, regions of interest were measured with the SAM. After nanoindentation tests were completed, the same regions of interest were imaged again with SAM to visualize the location of residual indents. The Synchrotron μ-CT scans were performed afterwards. The SAM images from before and after nanoindentation and DMB maps were digitally matched using a custom developed image fusion and analysis software to match positions a which Z, E and DMB were measured. Optical examination of the sample surface with an optical microscope allowed to classify indents as being taken in the interstitial tissue or in the osteonal tissue. Indents that fell into a canal (PMMA) were systematic excluded from the analysis.

**Results**

Comparison between Ea and En performed on homogeneous calibration materials (aluminium, PMMA and polycarbonate) of known Poisson ratio (ν) yielded a difference of less than 1%. Results for the bone samples, indicated in the Table 1, are in general agreement with published results.

All variables were significantly correlated, however, a higher correlation was found between Z and DMB ($R^2$=0.53) than between En and DMB ($R^2$=0.38). In addition, Z was best predicted with a multiple regression model including both the density and the modulus En ($R^2$=0.73). These results reflect the influence of density on the acoustical impedance. A good correlation was observed between En and Z ($R^2$=0.65, RMSE=1.9 Gpa). We assume that the 35% of the variability of En which could not be explained by Z might be attributable to unknown local variation of the Poisson's ratio. Similarly, differences between Ea and En (Table 1) may likely be due to the fixed assumed value of the Poisson's ratio (ν=0.3), while values comprised between 0.15 and 0.45 have been reported in the literature.

Despite these differences, a highly significant linear correlation between Ea and En was found ($R^2$=0.63, $p<0.001$, RMSE=1.8 GPa) suggesting that SAM can be reliably be used as a modality to quantitatively map the local variations of tissue-level bone elasticity.

**Discussion and conclusion**

Quantitative SAM displays properties of bone in high resolution 2-D images, whereas nanoindentation provides measurements at discrete levels. SAM is a valuable tool to provide data on the spatial distribution of micro-elastic bone properties (stiffness) but an appropriate and accurate measurement or model of the density is required to correct the acoustical impedance data and extract an accurate value of the stiffness. Experimental and theoretical issues must be further considered for the comparison between SAM and nanoindentation : *(i)* measurements are taken under different experimental conditions (dry and quasi-static measurements for nanoindentation, dynamic measurements in immersion with SAM) ; this may affect the visco-elastic response of the specimens and ultimately the measured moduli ; *(ii)* usual hypothesis include isotropy, homogeneity and fixed Poisson's ratio value. Further work is required to elucidate the impact of these hypothesis of on the outcome of the calculation of the acoustic and nanoindentation moduli.

Table 1 : measured values

| Tissue type | Z (Mrayl) | Ea (GPa) | En (GPa) | DMB(g.cm-3) |
|---|---|---|---|---|
| Osteonal | 8.5±1.8 | 31±12 | 18.4±2.9 | 0.92±0.09 |
| Interstitial | 10.2 ±1.1 | 42±8 | 21.4±2.0 | 0.99±0.06 |
| All | 9.1±1.7 | 35±12 | 19.5±3.0 | 0.95±0.08 |

## References


1. Raum K, Reisshauer J, Brandt J. Frequency and resolution dependence of the anisotropic impedance estimation in cortical bone using time-resolved scanning acoustic microscopy. J Biomed Mater Res A. 2004 Dec 1;71(3):430-8.
2. Hofmann T, Heyroth F, Meinhard H, Fränzel W, Raum K. Assessment of composition and anisotropic elastic properties of secondary osteon lamellae. J Biomech. 2006;39(12):2282-94.
3. Raum K, Cleveland RO, Peyrin F, Laugier P. Derivation of elastic stiffness from site-matched mineral density and acoustic impedance maps. Phys Med Biol. 2006 Feb 7;51(3):747-58.
4. Raum K, Leguerney I, Chandelier F, Talmant M, Saïed A, Peyrin F, Laugier P. Site-matched assessment of structural and tissue properties of cortical bone using scanning acoustic microscopy and synchrotron radiation muCT. Phys Med Biol. 2006 Feb 7;51(3):733-46.

# USE2008

The 29th Symposium
on
ULTRASOIC
ELECTRONICS

Thursday, November 13, 2008

Proceedings of Symposium on Ultrasonic Electronics, Vol. 29 (2008) pp. 347-348
11-13 November, 2008

# Development of Ultraviolet-Excitation Photothermal Microscope and Observation of Non-Stained Biological Cells
紫外励起光熱変換顕微鏡の開発と無染色生細胞の観察

Noriyuki Fujii‡ and Akira Harata
(Dept. of Mol. and Material Sciences, Kyushu Univ.)
藤井宣行‡, 原田明 （九大院総理工）

## 1. Introduction

One of the Ultimate goals of analytical biochemistry is to detect certain target molecules in a living cell and to observe molecular behavior *in-situ*. A fluorescence microscope is powerful tool for biological imaging with which the distributions of fluorescent substances are observed with ultrahigh sensitivity up to the single-molecule detection level. Unfortunately, the greater parts of biologically important chemicals, such as amino acids, nucleotides, proteins, hormones, and so on, are nonfluorescent. Thus, it is desirable to develop ultrasensitive imaging methods for nonfluorescent compounds in and around a living cell, so we aim to develop imaging methods for it by improving performance of photothermal spectroscopic method[1].

Photothermal spectroscopy is one of the most sensitive detection methods for nonfluorescent chemical species in a liquid solution. The thermal lens method, one of the photothermal methods, is suitable for observing substances in biological cells because it is based on the optical excitation and optical detection of photothermal effects, and is easy to use in combination with optical microscopy.

We have designed a new photothermal microscope using the third harmonics of the Ti:sapphire laser as the excitation light source[2]. Position-selective observation is achieved with newly equipping a CCD system to the microscope, and distortion of photothermal image is discussed in observing non-stained yeast cells (5μmΦ in diameter) as target.

## 2. Experimental methods

**Figure 1** shows the schematic illustration of the experimental setup for ultraviolet-excitation microscopic photothermal lens imaging. The third harmonic of a Ti:sapphire laser was used as the excitation light source. A thermal lens was generated in a sample on a slide glass using

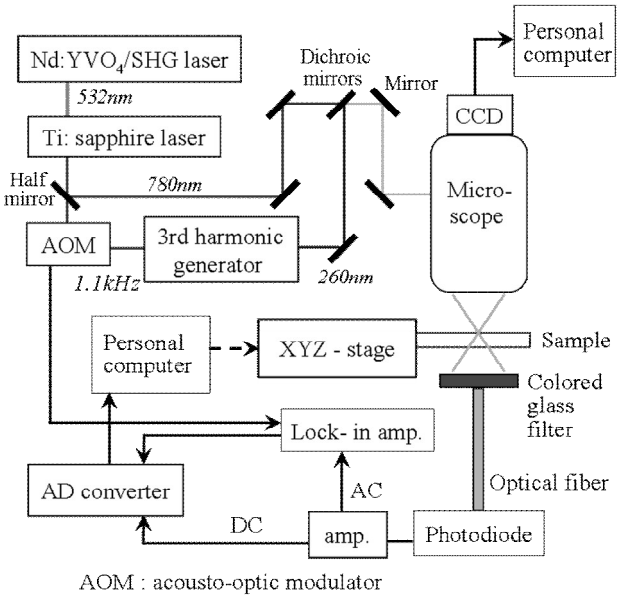


Figure.1 Experimental setup for ultraviolet-laser excitation microscopic photothermal lens imaging. The photothermal lens signal is obtained from the AC output of the photodiode; the transmitted light intensity is monitored with DC output.

the third harmonics (260nm, < 1mW). The thermal lens signal was probed with the fundamental emission (780nm, < 3mW) of the Ti:sapphire laser. Both excitation and probe laser beams were focused using a reflection objective lens (magnification, × 20; numerical aperture, 0.38). The excitation beam was intensity-modulated at 1.0 kHz with an acousto-optic modulator. The probe beam was passed through the sample. The light intensity at the probe beam center was monitored with a photodiode connected to an optical fiber. A colored glass filter set between the sample and the optical fiber blocked the excitation beam. The thermal lens signal monitored with a lock-in amplifier was obtained from the AC output. The photothermal amplitude $Q$ and phase $P$ are calculated using

$$Q = \sqrt{S_{IP}{}^2 + S_{OP}{}^2}$$

$$P = \arctan\left(S_{OP}/S_{IP}\right)$$

hr-n-fujii@mms.kyushu-u.ac.jp

, where $S_{IP}$ and $S_{OP}$ are the in-phase and out-of-phase signal intensities, respectively. The DC output of photodiode was used to monitor transmitted light intensity.

The sample was set on an XYZ-mechanical stage that was computer-controlled using laboratory -made software. Typically, a $60 \times 60 \mu m^2$ area was obtained in 1μm scanning steps. Position -selective observation is achieved with newly equipping a CCD system to the microscope. Accuracy of the x-y position was better than 3μm.

The samples used were yeast cells in the air or glycerin on quartz plates. These cells were not stained. When we used yeast cells with glycerin, the sample was covered with a quartz cover slip.

## 3. Results and Discussion

**Figure 2** shows photothermal images of yeast cells. Image (a) was an image of yeast cells in the air and (b) was in glycerin. The contrasts of these images reflect the intensity of photothermal lens signals. Both A and B in these images show CCD images of the scanned areas ($60 \times 60 \mu m^2$).

White area in the CCD image A is due to scattered probe beam. Three black spots are CCD images of 3 yeast cells. It can be observed from the images A and (a) that the positions of the high photothermal lens signals correspond to those of the yeast cells. This means that we could get the photothermal lens signals of the yeast cells with ultraviolet-laser excitation beam. However, the photothermal lens signals show non-spherical shape, though a yeast cell has a spherical shape. It is considered that the difference in refractive index between a yeast cell and the air caused distortion of the shape.

In Fig. 2(b), photothermal image of yeast cells in glycerin, some differences can be seen from image (a). First, photothermal lens signals were not always observed even where we could see a yeast cell in image B (CCD image). The signals were obtained at two areas, though there were four yeast cells in image B. It is suggested that photothermal lens signals of some yeast cells could not be obtained because of the height distribution: Each cells in glycerin seems to be in a different height above the quartz cover slip. Second, thermal lens signals accompanied with a ghost signals. In a transmitted light image observed simultaneously (not shown), there were no change in the transmitted light intensities at the position of the ghost signal. The reasons why the ghost signals are obtained are under investigation.

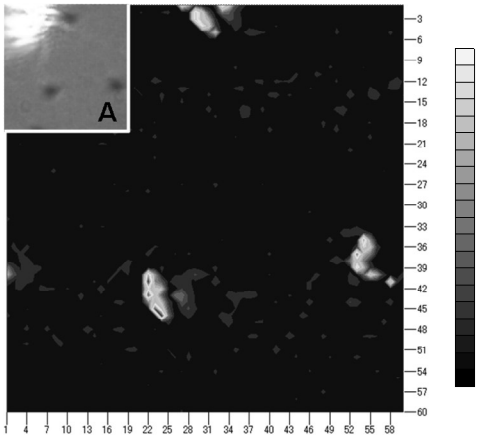


(a)

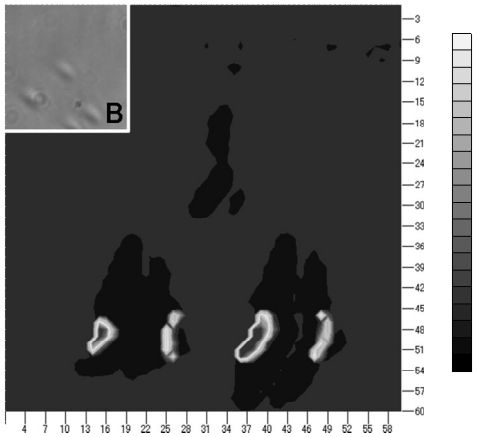


(b)

Figure.2 Photothermal amplitude images of yeast cells. Area size is $60 \times 60 \mu m^2$. Circumstances of yeast cells are (a) the air and (b) glycerin. Both A and B in this images show CCD images of scanned areas, respectively.

## 4. Conclusion

For observation of non-stained biological cells**,** we have developed an ultraviolet-excitation photothermal microscope, with which position -selective observation of photothermal images of yeast cells in both the air and glycerin are successfully carried out. Position of the photothermal images well corresponded to that of the CCD images. Although some distortions of the cell shape as well as ghost are observed at the present stage, it is expected that this method has great potential for the *in-situ* microscopy of non-stained biological cells.

## References

1. A. Harata, in 'Nano Biophotonics: Science and Technology', Elsevier BV, pp. 73-92 (2007)
2. A. Harata, T. Matuda, S. Hirashima: Jpn. J. Appl. Phys. **46** (2007) 4561

3J2b-2

Proceedings of Symposium on Ultrasonic Electronics, Vol. 29 (2008) pp. 349-350
11-13 November, 2008

# Imaging of Electromagnetic Properties via Ultrasound Waves
超音波による電気・磁気特性の画像化

Kenji Ikushima[1], Hiraku Toida[2] and Susumu Komiyama[2] ([1]Dept. Appl. Phys., Tokyo Univ. of A & T; [2]Dept. Basic Science, Univ. of Tokyo)
生嶋健司[1]，樋田啓[2]，小宮山進[2]　([1]東京農工大　工; [2]東大院　総合文化)

## 1. Introduction

Ultrasound technique is widely used to nonivasively image human bodies and material structures. However, the majority of existing applications is restricted to diagnosing elastic properties of the targets; viz., electromagnetic properties are not probed. Piezoelectric imaging techniques are highly developed in scanning probe microscope systems,[1,2] but only surface analysis is targeted. Recently, we have proposed and demonstrated a distinguishing method of probing electromagnetic properties of matters via acoustic-wave excitation.[3] In this scheme, electro- or magneto-mechanical response of materials is detected through acoustically stimulated electromagnetic (ASEM) radiation. Measurements of such radiation are performed in wireless operation of acoustic-wave devices,[4,5] but detection of extremely weak ASEM radiation from materials to be studied has been untackled.[6] Utilizing a pulsed ultrasound technique, we proved that electromagnetic waves are emitted from a variety of materials when they are acoustically stimulated and that the emission takes place even without the mechanical resonance condition. The signal is found in bones, woods, plastics, and ferrites as well as a standard piezoelectric material of GaAs.[3] In this paper, we present imaging results of the ASEM method for GaAs and a pure iron foil.

## 2. Experiment

**Figure 1** depicts the measurement setup.[3] A target sample is placed in a focused zone at a distance (about 40 mm) from a 10 MHz transducer, in which rectangular 50 ns wide pulses are applied at a repetition rate of 200 Hz by a pulser/receiver (Panametrics-NDT, 5077PR). Noting the ultrasound velocity in water (1500 m/s), ASEM radiation emitted by the sample is temporally separated by 27 μs from the apparent signal attributed to the transducer, allowing unambiguous and sensitive detection of true signal. The signals are detected via loop antenna tuned to the center frequency of ultrasound waves with a bandwidth of about 200 kHz. ASEM waves picked up by the antenna are fed to low-noise preamplifiers (a total gain of 97 dB) and averaged over pulses by using a digital oscilloscope. By moving the transducer with an XYZ stage, the focal point scans over the whole area of samples. Two-dimensional (2D) pictures of ASEM radiation on picowatt levels are thus obtained.

e-mail address: ikushima@cc.tuat.ac.jp

## 3. Results

**Figure 2** shows an ASEM image of semiconductor crystals, in which piezoelectric materials are selectively visualized. The samples are GaAs (110), GaAs (100) and nonpiezoelectric silicon crystal. The signals are detected with loop antenna (i) (Fig.

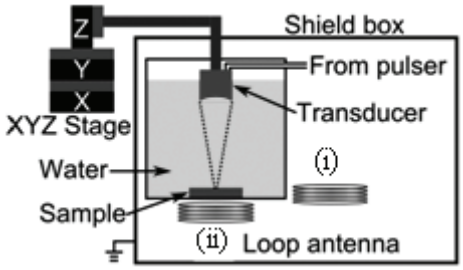


Fig.1 Schematic diagram of measurement setup.

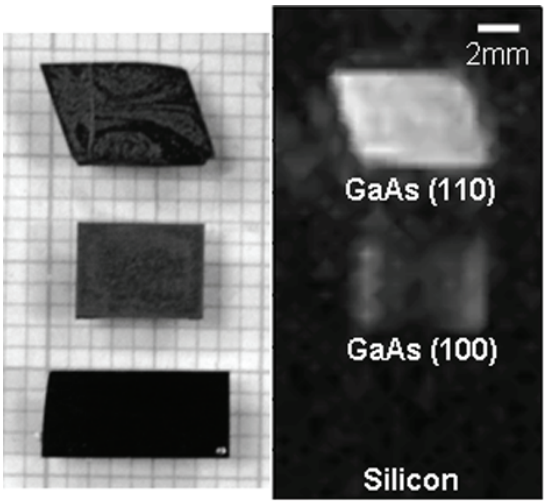


Fig.2 Photograph (left) and ASEM image (right) of GaAs (110), GaAs(100) and Si(100) plates.

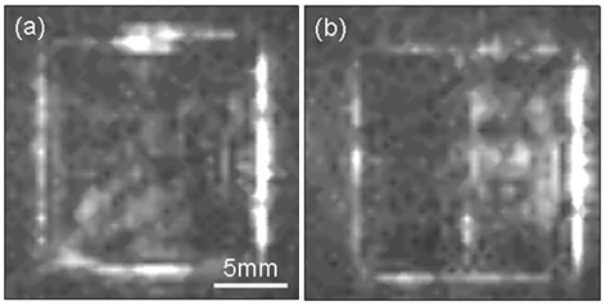


Fig.3 ASEM image of an iron foil: Original sample (a) and one after folded (b).

1). Longitudinal acoustic waves are expected to generate ASEM waves in GaAs when their wave vector $\boldsymbol{k}$ is parallel to the piezoelectric axis of <110>. Thereby, ASEM signals at GaAs (110) plate are definitely larger than ones at GaAs (100) plate. Changing antenna configuration, we also found that radiation distribution of GaAs (110) signals is well explained by the interpretation of piezoelectric polarization. The spatial resolution of about 0.6 mm is determined by focal size of ultrasound waves. Owing to the ubiquity of electromechanical coupling in matters, this measurement method may find broad application in noncontact material evaluation.

In addition to piezoelectricity, magnetomechanical coupling can be an origin of ASEM radiation. **Figure 3 (a)** and **3(b)** show images of a 0.1 mm thick iron foil. The signals are detected by loop antenna (ii). As seen in Fig. 3 (a), ASEM radiation is found to occur along the sample edges, suggesting the presence of magnetization. We suppose that the observed signal arises from the aligned magnetic domains induced by external stress or distortion when the iron foil is clipped. To confirm the interpretation, we introduced external distortion by folding the foil in the middle. The radiation emerges along the middle line as shown in Fig. 3 (b).

## 4. Conclusion

We have demonstrated a unique method of detecting and imaging electromagnetic response induced by ultrasound waves. The method will make it possible to implement nondestructive tomographic imaging of electromagnetic properties in matters as well as to obtain 2D spatial profiles.

**Acknowledgment**
This work was supported by Industrial Technology Research Grant Program in 2006 from New Energy and Industrial Technology Development Organization (NEDO) of Japan.

**References**

1. A. Gruverman, O. Auciello and H. Tokumoto: Annu. Rev. Mater. Sci. **28** (1998) 101.
2. S. V. Kalinin, E. Karapetian and M. Kachanov: Phys. Rev. B **70** (2004) 184101; S. V. Kalinin, B. J. Rodriguez, S. Jesse, T. Thundat and A. Gruverman: Appl. Phys. Lett. **87** (2005) 053901.
3. K. Ikushima, S. Watanuki and S. Komiyama: Appl. Phys. Lett. **89** (2006) 194103.
4. H. Ogi, H. Hiho and M. Hirao: Appl. Phys. Lett. **88** (2006) 141110.
5. M. Thompson, S. M. Ballantyne, L.-E. Cheran, A. C. Stevenson and C. R. Lowe: Analyst (Cambridge, U. K.) **128** (2003) 1048.
6. Studies of EM radiation originated from piezoelectricity of rock are reported in geophysical researches, but the EM signals are produced by rock fracture or high-pressure experiments. For instance, S. Yoshida and T. Ogawa: J. Geophys. Res. **109** (2004) B09204.

3J2c-1

Proceedings of Symposium on Ultrasonic Electronics, Vol. 29 (2008) pp. 351-352
11-13 November, 2008

# Ultrasonic Measurement of Closed Stress Corrosion Crack Depth Using Subharmonic Phased Array

サブハーモニック超音波フェーズドアレイ SPACE を用いた閉じた応力腐食割れの計測

Yoshikazu Ohara[1†], Hiroaki Endo[1], Tsuyoshi Mihara[2] and Kazushi Yamanaka[1]
([1]Tohoku Univ.; [2]Univ. Toyama)
小原良和[1†]，遠藤宏明[1]，三原毅[2]，山中一司[1]（[1]東北大工; [2]富山大工）

## 1. Introduction

Nonlinear ultrasound has a potential of becoming a primary means of evaluating closed cracks, and subharmonic waves[1-4] with half-frequency of input wave are particularly useful because of its excellent selectivity for closed cracks and high temporal resolution. Thus far, we have developed a novel imaging method, subharmonic phased array for crack evaluation (SPACE)[5,6], on the basis of subharmonic waves and phased array algorithm. In this study, we form more than 10 mm deep stress corrosion crack (SCC), and image the SCC in three positions using SPACE. Subsequently, we precisely compare the SPACE images with the optical images, and examine the relation between optically- and SPACE-measured crack depths.

## 2. Subharmonic Phased Array for Crack Evaluation (SPACE)

Figure 1 shows the present implementation of SPACE. Sensors are a $LiNbO_3$ single-crystal transmitter for generating intense ultrasound and a receiving array for focusing on reception. By inputting an intense ultrasound, fundamental waves are scattered and subharmonic waves are generated at open and closed parts of cracks, respectively. These waves received by the array sensor are digitally filtered at fundamental and subharmonic frequencies. Subsequently, they are phase shifted following delay laws and thereafter are summed. Fundamental and subharmonic images can indicate the open and closed parts of cracks, respectively.[5,6]

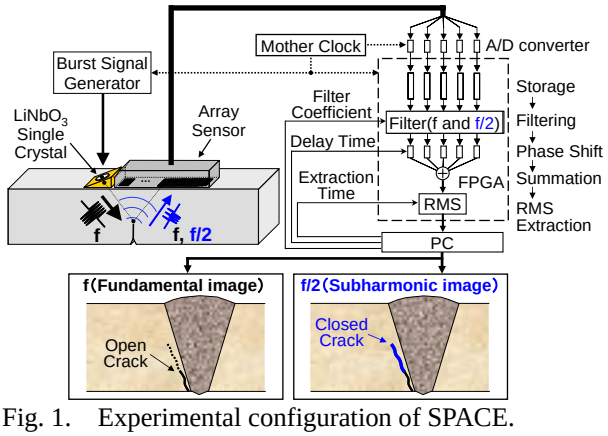


Fig. 1. Experimental configuration of SPACE.

## 3. Formation of a deep SCC

Although more than 10 mm deep SCCs have been observed in atomic power plants, it is difficult to form such a deep SCC in the laboratory owing to the low growth rate. In this study, we used new method to form such a deep SCC.[6] First, we formed approximately 10 mm deep fatigue crack in an austenitic stainless steel specimen (SUS304 sensitized under 600 ºC for 4 h) with $K_{max}$=28 and $K_{min}$=0.6 MPa $\sqrt{m}$ using a three-point bending fatigue test. Subsequently, we extended the SCC from the tip of the fatigue crack in a solution of 30 wt % $MgCl_2$ at 90 °C for 650 h and at a nominal bending stress of 124 MPa (Fig. 2).

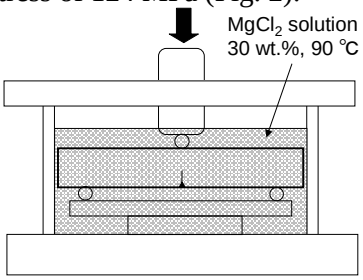


Fig. 2. Experimental setup for SCC formation.

## 4. Imaging of the SCC with SPACE

To precisely visualize the branched SCC, we applied SPACE to the SCC at three positions. The input signal was a three-cycle burst of a 7 MHz sinusoidal wave with a 10.3 $nm_{p-p}$ amplitude. We used 64 elements in an array sensor with the center frequency of 5 MHz. Furthermore, we selected a configuration to receive both forward- and back-scattered waves from cracks, and focused on reception with 0.1 mm step. Fig. 3 shows the fundamental and subharmonic images of the SCC at positions A, B and C. A variety of crack images were visualized depending on the positions. This shows that the SCC was complexly branched. Note that the crack tips were deeper in subharmonic images than in fundamental images at all positions. This suggests that the tip of the SCC was closed.

After the measurement, the specimen was sliced to thin plates to optically examine the depths and distributions of the SCC (Fig. 4(a)). Fig. 4(b)

shows an optical image of the cross sections. It was observed that the SCC was complexly branched from the tip of the fatigue crack. Note that the SCC was extended diagonally to the fatigue crack. This might be interpreted by assuming that the origin of the SCC generation is a slip band in the high shear stress area around the crack tip (Fig. 4(c)), although SCC is generally extended under tensile stress.

To precisely compare SPACE images with cross sections, we superimposed the optical crack image on the SPACE images (Fig. 3(d) and (e)) as shown in Fig. 5. The crack tip in the optical image was deeper than that in the fundamental image (a). This causes the underestimation of crack depth. In contrast, the crack tip in subharmonic image (b) was deeper than that in optical image. This suggests that subharmonic image can visualize optically-unobservable closed crack.

To examine the measurement accuracy of SPACE, the relationship between optically- and SPACE-measured crack depths is shown in Fig. 6. The underestimation was reduced to be less than 1 mm in the subharmonic images, whereas it was 1.6 mm at the maximum in the fundamental images. Thus we demonstrated that SPACE is useful in reducing the underestimation of crack depths.

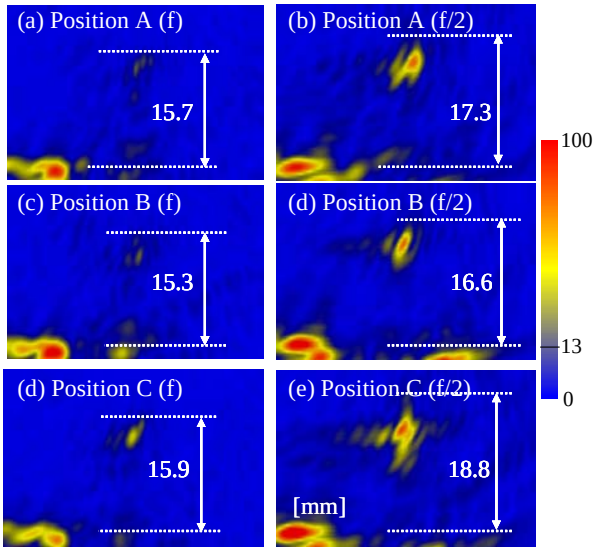


Fig. 3. Dependence of the SPACE images of the SCC on the measurement positions. (a) Fundamental and (b) subharmonic images at position A. (c) Fundamental and (d) subharmonic images at position B. (e) Fundamental and subharmonic images at position C.

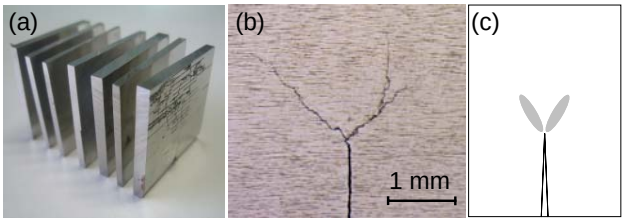


Fig. 4. Optical observation of the specimen. (a) The cut specimen to optically examine the SCC distribution. (b) The optical image of the cut cross section. (c) Schematic illustration of shear stress field around crack tip.

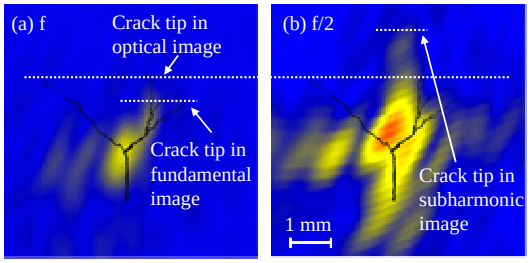


Fig. 5. Superimposition of the optical crack image on the SPACE images. (a) Fundamental and (b) subharmonic images.

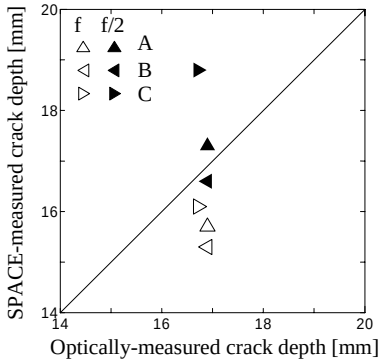


Fig. 6. Relationship between optically- and SPACE-measured crack depths of the SCC.

## 5. Conclusions

We formed more than 10 mm deep SCC, and precisely imaged the complexly-branched SCC at three measurement positions using SPACE. After the measurement, we cut the specimen, and discussed the origin of the SCC extension. We superimposed the optically-observed crack images on the SPACE images. This suggests that subharmonic image can visualize optically-unobservable closed crack. By examining the relationship between optically- and SPACE-measured crack depths, we demonstrated that SPACE is useful in reducing underestimation of crack depths.

**Acknowledgment** This work was supported by Grants-in-Aid for Science Research from the Ministry of Education, Culture, Sports, Science and Technology of Japan, and by Japan Nuclear Energy Safety Organization.

**References** 1) K. Yamanaka, T. Mihara and T. Tsuji: Jpn. J. Appl. Phys. **43-5B** (2004) 3082. 2) M. Akino, T. Mihara and K. Yamanaka: Rev. Prog. QNDE **23** (2004) 1256. 3) R. Sasaki, T. Ogata, Y. Ohara, T. Mihara and K. Yamanaka: Jpn. J. Appl. Phys. **43-5B** (2004) 3082. 4) Y. Ohara, T. Mihara and K. Yamanaka: Ultrasonics **44** (2006) 194. 5) Y. Ohara, T. Mihara, R. Sasaki, T. Ogata, S. Yamamoto, Y. Kishimoto and K. Yamanaka: Appl. Phys. Lett. **90** (2007) 011902. 6) Y. Ohara, S. Yamamoto, T. Mihara, K. Yamanaka, Jpn. J. Appl. Phys. **47-5B** (2008) 3908.

Proceedings of Symposium on Ultrasonic Electronics, Vol. 29 (2008) pp. 353-354
11-13 November, 2008

# A Detection of Nonlinear Components of Lamb Wave Generated from Closed Cracks Using Double-Layered Piezoelectric Transducer

二層型圧電振動子を用いた
閉じた亀裂から発生する Lamb 波の非線形成分の検出

Makoto Fukuda‡ and Kazuhiko Imano (Faculty Eng. & Resource Sci., Akita Univ.)
福田誠‡，今野和彦（秋田大 工学資源）

## 1. Introduction

Ultrasonic waves have been widely used in the non-destructive evaluation (NDE) of several materials[1,2]. Recently, harmonic ultrasonic waves have been employed as new tools for testing materials[3-5]. When materials are loaded with external force, closed cracks are generated in materials. This phenomenon can be one cause of the generation of nonlinear propagation of sound. Closed cracks detection with subharmonic ultrasonic waves has been studied[5].

The authors have recently presented a double-layered piezoelectric transdcuer (DLPT) in aligning polarization direction and subharmonic components generating from plastic-deformed metal rods have been detected[6,7]. In this study, Lamb waves in a glass plate using our system are generated and subharmonic components of Lamb waves generating from closed crack in the glass plate are detected.

## 2. Double-layered piezoelectric transducer

A double-layered piezoelectric transdcuer (DLPT) composed from a pair of $PbTiO_3$ transducers with the same characteristics (resonance frequency $f_0$). The two transdcuers are stacked and bonded to one another in aligning polarization direction. The resonance frequency of the DLPT is $f_0$ when the DLPT is connected in parallel; however, it is $f_0/2$ when the DLPT is connected in series. It is possible to improve the receiving sensitivity of the subharmonic components.

In order to generate S0-mode Lamb wave in glass plate ($c_L$ = 5800 m/s, $c_T$ = 3300 m/s) effectively, ultrasonic waves are transmitted from DLPT via a wedge (epoxy resin: $c_W$ = 2500 m/s).

The frequency-admittance characteristics of the DLPTs, having the wedge, connected in parallel and in series, as shown in **Figs. 1(a)** and **1(b)**, respectively. An effective fundamental pulse waves transmission (1 MHz) is obtained when the DLPT is electrically connected in parallel, while an effective subharmonic pulse waves reception (500 kHz) is obtained when the DLPT is connected in series.

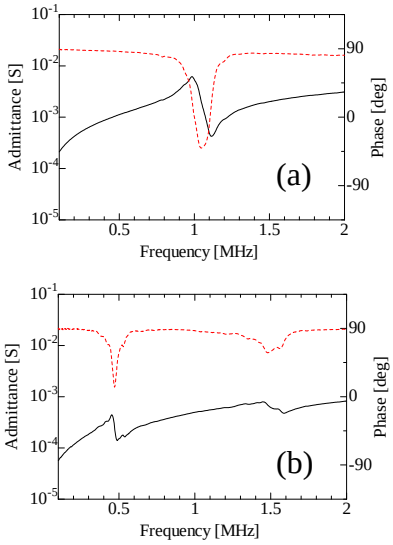


Fig. 1. Frequency-Admittance characteristics of DLPT electrically connected (a) in Parallel and (b) in series. Solid lines indicate the absolute value of admittance and dotted line the phase of admittance.

## 3. Experimental methods

The system for generating Lamb waves and detecting subharmonic components using DLPT is shown in **Fig. 2**. The thickness of the glass plate was 5.4 mm, and nanometer-order width of crack existed in center of the glass plate. It has been reported that second harmonic waves have been generated from this glass plate and have been detected in our eariler paper[3].

Transmission signals were generated using a function generator, and their amplitudes were amplified to 150 V with a high-frequency power amplifier. When DLPT was driven, DLPT was connected in parallel electrically. Ultrasonic pulse waves were transmitted in the glass plate via the wedge, and then Lamb waves were launched in the glass plate. Lamb waves were reflected at the edge of the glass plate. The reflected Lamb waves were received by DLPT connected in series electrically.

‡e-mail: mfukuda@gipc.akita-u.ac.jp

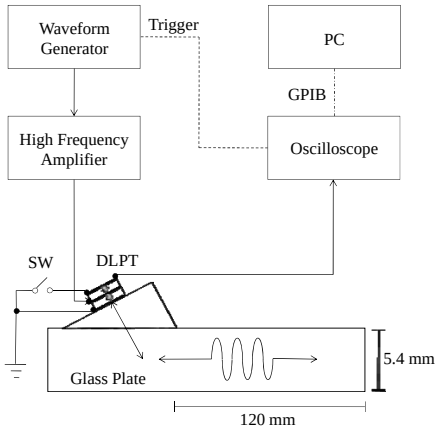


Fig. 2. Experimental setup.

The electrical connection of DLPT was automatically controlled by an analog switch. Finally, the received pulse waves were digitized and fed to a personal conputer via a general purpose interface bus (GPIB).

## 4. Results and discussion

**Figures 3(a)** and **3(b)** show the waveform and its spectrum received by our system from "no crack area" of the glass plate, respectively. Wavelet transform for the received waveform is carried out as shown in **Fig.4**. Lapping dispersion curves of group velocity of Lamb wave in glass over result of wavelet transform, Fig.4 confirmed that the waveform generated from DLPT was S0-mode Lamb wave. Subharmonic components were slightly detected, however subharmonic components were approximately 40 dB smaller than fundamental components. Subharmonic components would be generated by contact acoustic nonlinearity (CAN) at DLPT-wedge and/or wedge-glass because the subharmonic components were detected from "no crack area".

On the other hand, **Figs 3(c)** and **3(d)** show the result of "closed crack area". Subharmonic components detected from "closed crack part" were increased approximately 5 dB compared with "no crack area". Change of amplitude of subharmonic components will indicate the existance of the closed crack.

In order to apply our system to NDE, subharmonic components generation/detection of another mode of Lamb wave and imaging of cracks will be required.

## 5. Conclusions

A generation of Lamb wave in the glass plate and a detection of subharmonic components generated from the closed cracks using DLPT with the layers having the aligning polarization direction was demonstrated. Subharmonic components were detected approximately 5 dB at "no crack area" compared with "closed crack area".

In futute work, subharmonic components generation and detection of another mode of Lamb wave using DLPT will be required. Moreover, several application that are imaging of cracks and a comparison between fundamental components and nonlinear components for imaging using our system will be carried out.

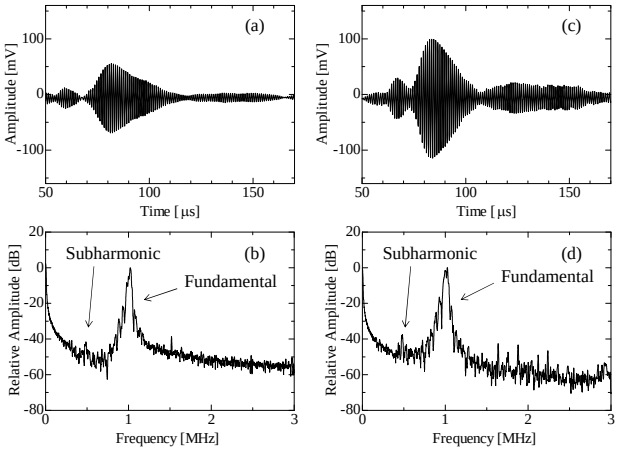


Fig. 3. (a) The received waveform and (b) its spectrum in no-crack area. (c) The waveform and (d) its spectrum in closed crack area.

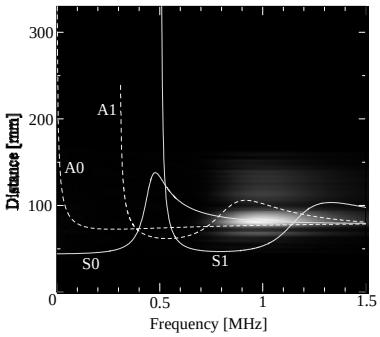


Fig. 4. Dispersion curves of group velocity of Lamb wave in glass and result of wavelet transform of received waveform.

## References

1. K. Imano: IEICE Electr. Exp. **4** (2007) 340.
2. M. Watanabe, M. Nishihira and K. Imano: Jpn. J. Appl. Phys. **45** (2006) 4565.
3. K. Imano and A. Muto: Sozai Busseigaku Zasshi **20** (2007) 12 [in Japanese].
4. K. Kawashima, M. Murase, K. Shibata and T. Ito: Mater. Trans. **48** (2007) 1202.
5. Y. Ohara, T. Mihara and K. Yamanaka: Ultrasonics **44** (2006) 194.
6. M. Fukuda and K. Imano: accepted to Acoust. Sci. & Tech.
7. M. Fukuda, M. Nishihira and K. Imano: Jpn. J. Appl. Phys. **46** (2007) 4529.

3J6-1

Proceedings of Symposium on Ultrasonic Electronics, Vol. 29 (2008) pp. 355-356
11-13 November, 2008

# Observation of bubble population phenomena in sonochemical reactor

超音波反応槽内における気泡構造形成過程の観察

Yasuo Iida, Atsuya Towata, Kyuichi Yasui, Teruyuki Kozuka, Toru Tuziuti, and Judy Lee (National Institute of Advanced Industrial Science and Technology (AIST))
飯田康夫，砥綿篤哉，安井久一，小塚晃透，辻内　亨，ジュディー・リー

## 1. Introduction

Single bubble dynamics have been theoretically and experimentally discussed in detail throughout the life of the bubble. However, the dynamics of the multibubble system in the real sonochemical reactors have been seldom studied experimentally because of its complexity. In the multibubble system, we should take into account the population phenomena of bubbles; bubble-bubble interaction, spatial structure, size distribution, and their number. Sonoprocessing has been applied in industry because of its unique features. We know that the efficiency can be proportional to the number of active bubbles, however we have little knowledge on the control of the number of bubbles and their distribution in the reactor. We can find some pioneering works upon this problem [1-3]. The authors have reported the direct observation of bubble dynamics in the microreactor to confine bubbles under the observation field of a microscope [4, 5]. In this paper, we have tried to directly determine the temporal development of the population phenomena in sonochemical reactors; Bubble size distributions were directly observed by laser diffraction method. Bubble dynamics in cavitation fields have been taken by a high-speed video camera. A series of SL images were taken by an intensified CCD camera. We will discuss the bubble structure in multibubble system from the sound field dynamics, such as standing/travelling wave ratio and the related radiation forces, and the bubble dynamics, such as initiation, coalescence, fragmentation and flow of bubbles. Both dynamics are mutually affecting each other and leading to the inhomogeneous distribution of bubbles in a sonoreactor.

## 2. Experimental

The ultrasound was emitted from a ceramic transducer (50mm diameter) through a stainless base fitted to the bottom of a glass vessel (100x100x120mm) which contained 1L of solution. The bubble size distribution was measured with a laser diffraction particle size analyzer (Nikkiso, Aerotrac SPR 7340). As the ultrasound waves deflect the probing laser beam, bubble size was determined during the off time of the pulsed ultrasound irradiation. The bubble motions were observed with a high-speed video camera (Photoron, FASTCAM-512PCI). The sonoluminescence (SL) images were captured by an intensified CCD camera (Andor Technology, model DH501-18F-01).

## 3. Results and discussion

**Figure 1** shows the development of the bubble size distribution by the sequential burst of ultrasound. The cavitation bubbles have grown to 20 μm of D50 by the first train of 20000 waves of ultrasound (100ms) via the coalescence phenomena. The size of the bubbles decreased and some dissolved away during the OFF period. In the following burst of ultrasound, both the size and the number of bubbles increased and the D50 reached 150μm at the 9th burst. It was also shown that the population growth was dependent on the burst sequence. The long ON time and short OFF time effectively increased the size and the number of bubbles. It should be noted that the active bubbles are in the range of 1-10μm for the ultrasound frequency used. The overgrown bubbles will be expelled from the system as degas bubbles. Therefore, the coalescence in this direction should be negative to the activity of sonochemical reactions. On the other hand, the coalescence in the first burst will help the tiny (dark) cavitation bubbles from the fate of dissolution up to the rectified diffusion limit [6]. Therefore, the coalescence in this direction is positive to the activity of sonochemical reactions. Video images captured by the high-speed video camera supported the population phenomena of the bubbles observed with the particle size analyzer.

The active bubble structures in multibubble system were studied by a series of SL images taken by an intensified CCD camera. **Figure 2** shows SL structures at different dissolved oxygen (air) concentrations in water at 448 kHz and 22 W. The

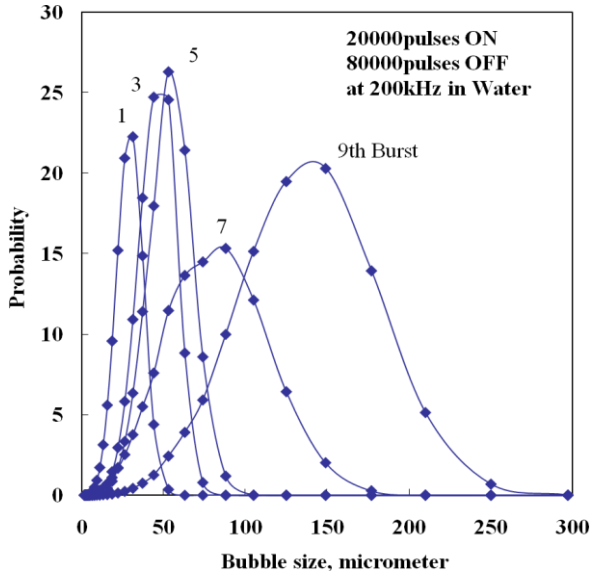


Fig. 1 The development of the bubble size distribution by the sequential burst of ultrasound.

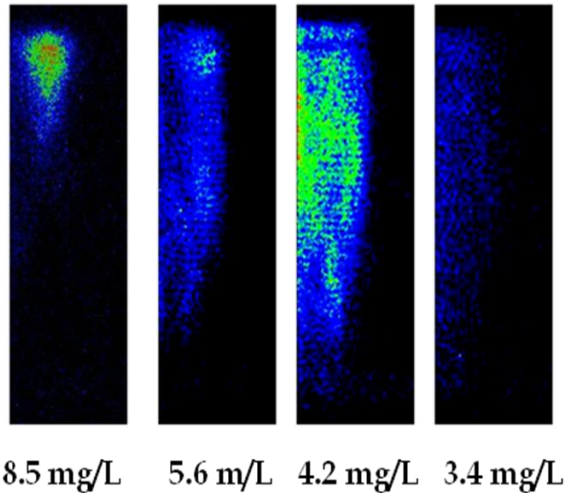


Fig. 2 Sololumonescence structure at different dissolved oxygen concentration. Continuous sonication at 448 kHz and 22 W.

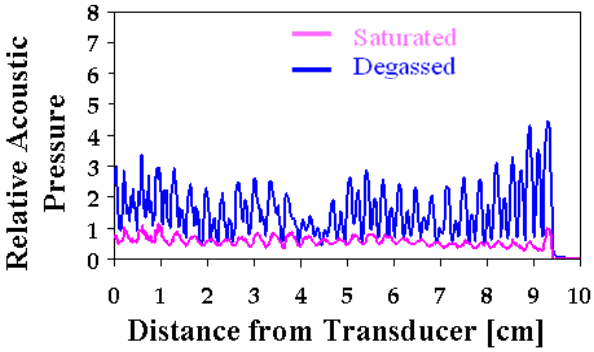


Fig. 3 : Acoustic pressure distribution at 448 kHz, relative to the first antinode at the liquid surface for saturated water.

acoustic pressure distributions were also obtained along the centre of the reactor (**Figure 3**). The observed active bubbles structures are determined by the interacting dynamics of sound field and bubbles. The locations to where bubbles might migrate and accumulate under radiation forces are controlled by the sound field structure. Bubble accumulation will in turn affect the local sound field through the processes of absorption, scattering and shielding. These will in turn affect the bubble size distribution through their influence on the processes of coalescence and fragmentation. In all, the strong SL near the liquid surface at higher air content could be due to the damping of standing waves by large coalesced bubbles and the increase in the transport of active bubbles to the liquid surface by the radiation force from traveling wave component. The increase in the SL intensity at the mild air content can be attributed to an increase in the number of active bubbles due to inhibition of bubble coalescence and also an increase in the local acoustic pressure due to the lower attenuation effect. The increase in the local acoustic pressure caused an expansion in the active cavitation areas.

**Acknowledgment**
This work is supported by a Grant from the Ministry of Education, Culture, Sports, Science and Technology, Japan.

**References**

1. A. Henglein, R. Ulrich and J. Lillie, J. Am. Chem. Soc., 111 (1989) 1974.
2. J. Lee, M. Ashokkumar, S. Kentish and F. Grieser, J. Am. Chem. Soc., 127 (2005) 16810.
3. J. Lee, S. E. Kentish and M. Ashokkumar, J. Phys. Chem. **B, 109** (2005) 5095.
4. Y. Iida, T. Tuziuti, K. Yasui, K. Towata and T. Kozuka, Ultrason. Sonochem., **14** (2007) 621.
5. J. Lee, T. Tuziuti, K. Yasui, S. Kentish, F. Grieser, M. Ashokkumar and Y. Iida, J. Phys. Chem. **C, 111** (2007) 19015.
6. C. C. Church, J. Acoust. Soc. Am., **83** (1988) 2210.

Proceedings of Symposium on Ultrasonic Electronics, Vol. 29 (2008) pp. 357-358
11-13 November, 2008

# Effects of ultrasound exposure time on dispersion of nanometer-sized diamond particles

超音波照射時間の変化によるナノダイヤモンド微粒子の分散への影響

Takeyoshi Uchida[1†], Tsuneo Kikuchi[1] Takahiro Aoki[2] Norimichi Kawashima[2] and Shinichi Takeuchi[2] ([1]NMIJ・AIST; [2]Facult. Biomedical Eng., Toin Univ.)
内田武吉[1‡]，菊池恒男[1]，青木貴宏[2]，川島徳道[2]，竹内真一[2]（[1]産業技術総合研究所; [2]桐蔭横浜大 医工）

## 1. Introduction

Recently, various forms of nanotechnology have been studied, including application of such technology to the development of fullerene or carbon nanotubes. Our study focuses on the improvement of dispersion stability of nanometer-sized diamond particles having a primary particle size of about 5 nm[1-3]. Diamond particles of this type are normally used for the ultra-fine polishing required by medical or other types of precision equipment. For example, when texturing a hard disk substrate, the texturing profiles affect the final magnetic properties in the longitudinal direction of the disk. However, the diamond particles aggregated to about 5 μm remain present immediately after manufacturing. The aggregated diamond particles cause the scratch on the substrate. Therefore, technology for dispersion to the primary particle size is needed.

In this study, we attempted the dispersion of nanometer-sized diamond particles by ultrasound exposure. Before now, the diamond particles have been disaggregated to average particle size of about 100 nm in standing wave sound field[4]. Also, the dispersion stability of such diamond particles was improved by high oxidation ability of active oxygen species generated by ultrasound exposure. However, despite the improvement, the diamond particles are not disaggregated to the primary particle size. Therefore, we need to evaluate the various conditions of ultrasound exposure for disaggregating to primary particle size. We report the effects of variations to ultrasonic exposure times in this paper.

## 2. Experimental method

Figure 1 shows the configuration of our employed ultrasound exposure system, which consists of a stainless-steel vibrating disk (2 mm thickness, 180 mm diameter) with a bolt clamped Langevin-type transducer (HEC-45402, Honda Electronics Co., Ltd.). The transducer was placed at the bottom of a water tank（70 mm long, 70 mm wide, 150 mm high). 30 mg of diamond particles were added to 500 mL of distilled water, and the diamond suspension was stirred thoroughly. Ultrasound was irradiated to the diamond suspension by use of the ultrasound exposure system shown in Fig. 1. A standing wave sound field was then formed in the water tank.

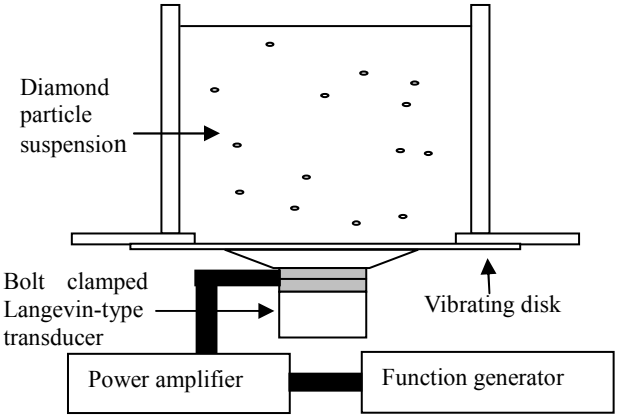


Fig. 1 Acoustic dispersion system for improvement of disaggregation and surface modification of nanometer-sized diamond particles

In this paper, the diamond suspension was exposed to ultrasound at 150 kHz. Average sound pressure in water tank; i.e., the average value of sound pressure distribution at height of 10 mm from the vibrating disk, was controlled to 70 kPa. The loop of the standing wave sound field was located at the height of 10 mm from the vibrating disk. The height of the diamond suspension in water tank was 100 mm. Ultrasound exposure time was within the range of 20 s to 1200 s. Average particle size and particle size distribution of the diamond particles after ultrasound exposure were measured by means of a size distribution measuring system (LS230 Beckman Coulter).

## 3. Experimental results

Figures 2 and 3 show the effects of ultrasound exposure time on average size and particle size distribution of nanometer-sized diamond particles.

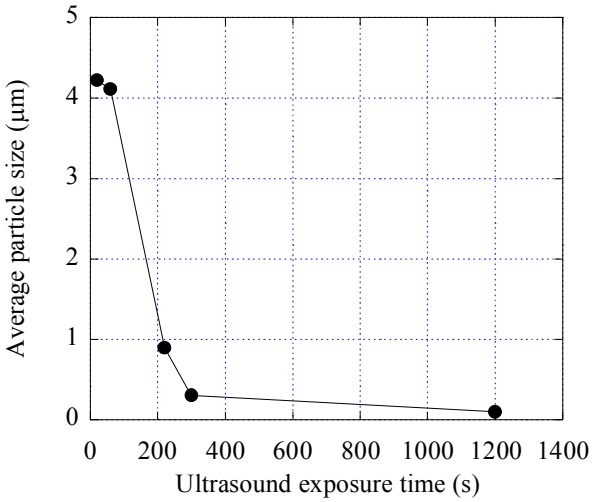


Fig. 2 Relationship between ultrasound exposure time and average particle size of nanometer-sized diamond particles

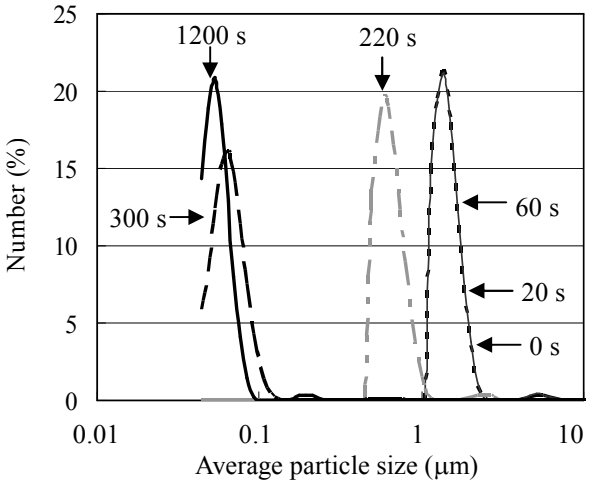


Fig. 3 Change in particle size distribution of nanometer-sized diamond particles by ultrasound exposure

The average particle size of the diamond particles decreased with increasing ultrasound exposure time. Deposition of the diamond particles was observed at 20 s and 60 s, and the average particle size produced by those ultrasound exposure times remained unchanged from average particle size before ultrasound exposure. Also, diamond particles disaggregated to an average particle size of about 100 nm at 300 s and 1200 s. These results indicate that average particle size of the diamond particles can be controlled by varying ultrasound exposure time.

Next, particle size distribution of the diamond particles was measured under increasing ultrasound exposure time. Particle size distribution at 20 s and 60 s remained unchanged from the particle size distribution before ultrasound exposure. Furthermore, as shown in Fig. 3, particle size distribution at 1200 s shows smaller particle sizes than those observed at 300 s. However, because our size distribution measuring system has a lower measurement limit of 40 nm, results below that level could not be measured, so it is possible that the diamond particles exposed to 1200 s have been disaggregated to an average particle size and particle size distribution less than the lower measurement limit.

## 4. Summary

We studied changes in average particle size and particle size distribution of nanometer-sized diamond particles caused by variations in ultrasound exposure time. The diamond particles had a primary particle size of about 5 nm, but aggregated to about 5 μm immediately after manufacture. Particles of this type were exposed to ultrasound at 150 kHz in water tank, and ultrasound exposure time was varied over a range of 20 s to 1200 s.

Our results show that average particle size and particle size distribution of the diamond particles changed with increasing ultrasound exposure time. At exposure times of 300 s and 1200 s, the diamond particles had an average particle size less than about 100 nm. Furthermore, at 300 s and 1200 s, the diamond particles had a narrow particle size distribution in the nanometer range.

In our future work, changes to the zeta potential of nanometer-sized diamond particles by increased ultrasound exposure time will be measured as well, because zeta potential affects the dispersion stability of diamond particles. The dispersion mechanism of the diamond particles by ultrasound exposure will also be considered.

## References

1. V. L. Kuznetsov, A. L. Chuvilin, Y. V. Butenko, I. Y. Malkov, V. M. Titov: Chem. Phys. Lett, **222** (1994) 343.
2. A. E. Aleksensky, M. V. Baidakova, M. A. Yagovkina, V. I. Siklitsky, A. Y. Vul, H. Naramoto, V. I. Lavrentiev: Diamond and Related Materials,**13** (2004) 2076.
3. A. V. Gubarevich, S. Usuba, Y. Kakudate, A. Tanaka, O. Odawara: Jpn. J.Appl. Phys, **43** (2003) L920.
4. T. Uchida, A. Hamano, N. Kawashima, S. Takeuchi: Jpn. J. Appl. Phys. **44** (2005) 4553.

Proceedings of Symposium on Ultrasonic Electronics, Vol. 29 (2008) pp. 359-360
11-13 November, 2008

# V 型超音波モータを用いた高速高分解能ステージ

High speed and quick response precise linear stage system using V-shape transducer ultrasonic motors

阿隅一将 [1,2†]，福永了一 [1]，藤村健 [1]，黒澤実 [2] ([1] 太平洋セメント; [2] 東工大)
Kazumasa Asumi[1,2†], Ryouichi Fukunaga[1] ,Takeshi Fujimura[1] and Minoru Kuribayashi Kurosawa[2]
([1]Taiheiyo-Cement Corp., [2]Tokyo Inst. of Tech.)

Maximum speed of 1.5m/s and 1nm positioning accuracy ultrasonic motors have been minimized and developed. By using a V-shape transducer ultrasonic motor, a 10kg weight massive stage was driven. The stage speed reached at 0.2m/s with controlled maximum acceleration of 3m/s$^2$ for thrust of 30N. For the high speed and precise positioning, the driving mode of the transducers changed from a resonance frequency drive, an impact inertial drive and a DC drive depending on the required speed, acceleration, positioning stroke and resolution. The stage was driven 20mm distance from an initial position in static condition with 1 nm resolution within 350ms.

## 1. はじめに

超音波モータは、磁場を発生しない、ボールねじやギアなどの機構が不要となりコンパクトにできること、などから電子線を使用する測長 SEM や電子線描画装置などの半導体製造装置のステージの駆動機構として注目されている。しかし、小型の超音波モータの研究は多い[1,2,3]ものの、高速かつ高分解能な超音波モータの研究は少ない。筆者らはこれまでに、高速かつ高分解能であるランジュバン振動子を 2 個用いた V 型超音波モータについて報告してきており[4,5,6]、1.5m/sec 以上の速度と 1nm の分解能を両立している。本報告では、比較的大きかった V 型超音波モータの小型化を試みた。また小型化した V 型超音波モータを用いて、可動部 10kg のステージを駆動し、特性を測定した結果を報告する。

## 2. V 型超音波モータの小型化

新規に作成した小型の V 型超音波モータを **Fig.1** に示す。V 型超音波モータは、ランジュバン振動子 2 個を 90° V 型に配置してその端部を結合させた形状をしている。この振動子は Head Block 先端が前後に振動する「対称モード」と左右に振動する「非対称モード」があり、これら 2 つの振動が結合させるように設計されている。圧電素子には、電極間 7 層の一体焼成型のハード系 PZT を各 2 個計 4 個用いている。特性を落とさずに小型化するため、圧電素子の大きさはそのままとした。Head Block を極力小さく設計し、ナットに振動速度の遅いリン青銅を用いたことによって、ナット長を短くした。

**Fig.2** にナット長を変えた時の各モードの共振周波数を示す。超音波モータの駆動に必要な「対称モード」と「非対称モード」以外にも共振が現れた。FEM 解析とモータの振動を実測した結果からこの共振は Head Block が上下に振動するモードであることがわかった。この振動を回避するためナット長を 21mm とした。

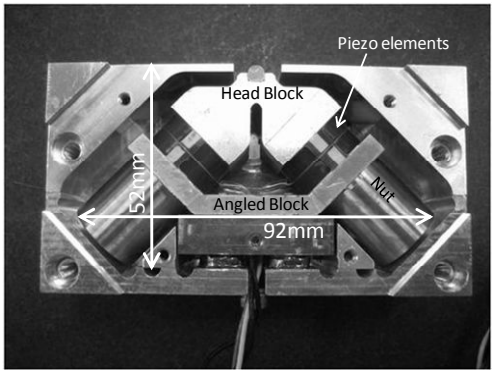


Fig.1 New design for minimization of V-shape motor.

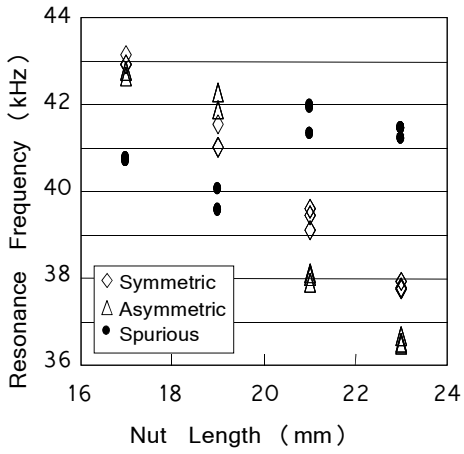


Fig.2 Resonance frequencies shift by changing nut length.

## 3. 小型化した V 型超音波モータの特性

小型化した V 型超音波モータについて、速度と推力を測定した。可動部 1kg ステージを用い、38.5kHz で 100Vrms を印加した時の速度と加速度を測定し、推力を算出した。**Fig.3** にその結果を示す。最高速度は 1.5m/sec を超え、推力は 40N を示し、旧来の大きな V 型超音波モータと遜色ない値が得られた。また、DC 電圧駆動で 10nm のステップ駆動を行った結果を **Fig.4** に示す。位置センサには分解能 0.2nm のリニアスケール

† kazumasa_asumi@taiheiyo-cement.co.jp

を用いている。1nm 程度の分解能が得られ、10nm のステップ駆動が行えていることがわかる。

## 4. 10kg ステージ駆動特性

可動部 10kg のステージを速度 200mm/sec、加速度 3m/sec$^2$、加加速度 90m/sec$^3$ の S 字制御を行い、20mm 駆動した結果を **Fig.5** に示す。コントローラは、はじめ共振周波数で駆動する高速モードを用い、移動プロファイル終了後、慣性駆動に切り替えて位置を追い込み、さらに DC 電圧で微動位置決めを行うよう、各駆動モードが自働で切り替わるようにプログラムした[6]。Fig.5 から約 350msec で±1nm に整定できていることがわかる

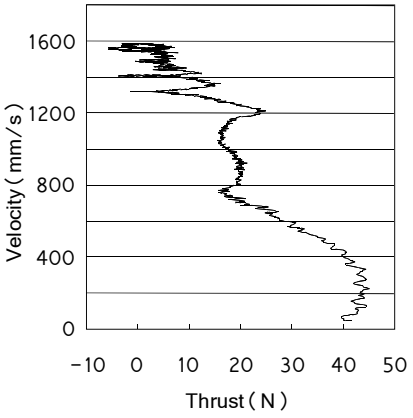

Fig. 3 Thrust-speed of V-shape motor

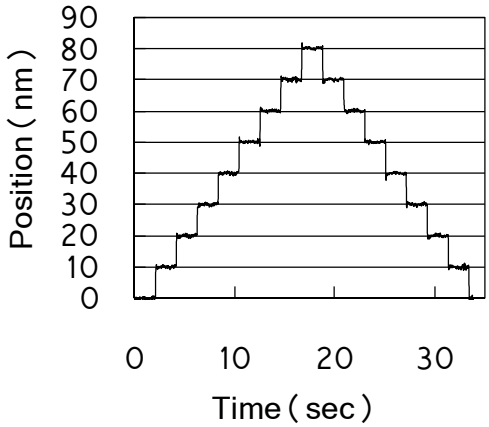

Fig. 4 Step positioning of 10 nm.

## 5. まとめ

V 型超音波モータの小型化を行い、速度や分解能を落とさずに約 40%の小型化を実現した。速度は 1.5m/sec 以上、分解能は 1nm 程度であった。小型化した V 型超音波モータを可動部 10kg のステージを駆動したところ 20mm 駆動で約 350msec で±1nm に静定することができた。

## 引用文献


1. T. Kanda, A. Makino, Y. Oomori and K. Suzumori; ” A Cylindrical Micro-Ultrasonic Motor Using Micromachined Bulk Piezoelectric Vibrator with Glass Case”, Jpn. J. Appl. Phys. 45 (2006) pp. 4764-4769
2. H. Tamura, K. Kawai, T. Takano, Y. Tomikawa, S. Hirose, and M. Aoyagi; “Diagonally Symmetric Form Ultrasonic Motor Using LiNbO3 Plate”, Jpn. J. Appl. Phys. 46 (2007) pp. 4698-4703
3. Y. Doshida, S. Kishimoto, K. Ishii, H. Kishi, H. Tamura, Y. Tomikawa, and S. Hirose; “Miniature Cantilever-Type Ultrasonic Motor Using Pb-Free Multilayer Piezoelectric Ceramics”, Jpn. J. Appl. Phys. 46 (2007) pp. 4921-4925
4. M. K. Kurosawa, O. Kodaira, Y. Tsuchitoi, and T. Higuchi, “Transducer for high speed and large thrust ultrasonic linear motor using two sandwich-type vibrators,” IEEE Trans. on Ultrason. Ferroelectrics, and Freq. Cont., vol.**45**, no. 5, pp. 1188-1195, 1998.
5. 阿隅一将, 福永了一, 黒澤実, “V-shape 2 bolt clamped Langevin-type transducer ultrasonic linear motor”, 信学技報, US2006-91, PP.31-36, (2006-12)
6. K. Asumi, T. Fujimura, R. Fukunaga and M. K. Kurosawa: "Improvement of the low speed controllability of a V-shaped, two bolt-clamped Langevin-type transducer, ultrasonic linear motor", Proc. of Symp. on Micro-Nano Mechatronics and Human Science, MHS2007, pp. 377-382, Nagoya, 2007.11


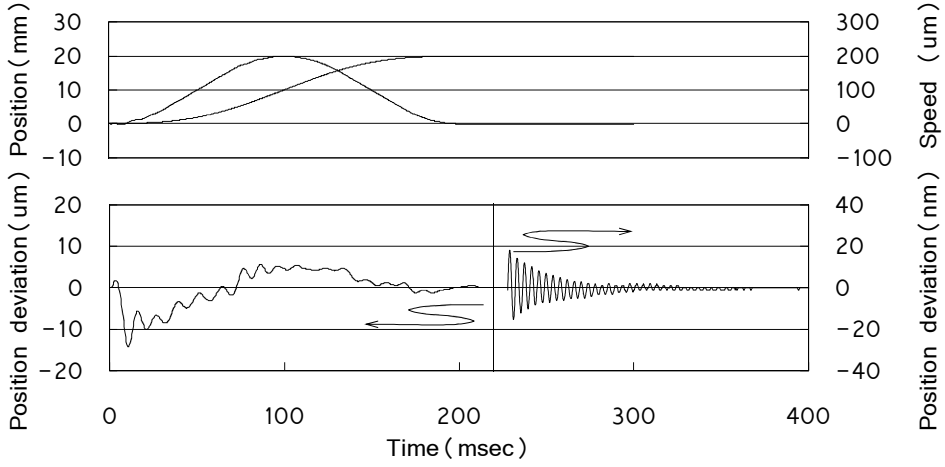

Fig. 5 10 kg stage motion.

Proceedings of Symposium on Ultrasonic Electronics, Vol. 29 (2008) pp. 361-362
11-13 November, 2008

# Application of a novel cleaning equipment using ultrasonic waveguide mode to the post CMP cleaning - Cleaning efficiency of spot type shower -

# 導波路管型超音波洗浄機用振動子の CMP 後洗浄への適用 −スポット型振動子の洗浄評価−

Kazunari Suzuki[1,2], Ki Han[1†] , Shoichi Okano[1] , Jyunichiro Soejima[1] and Yoshikazu Koike[2] ([1]KAIJO CO., LTD.; [2]Facult. Eng.,Shibaura Inst.of Tech.)
鈴木一成 [1,2]，潘毅 [1†]，岡野勝一 [1] ，副島潤一郎 [1]，小池義和 [2]（[1] カイジョー; [2] 芝浦工大 工）

## 1. Introduction

Alongside recent efforts to increase processing speeds of semiconductor devices, Al patterns have been replaced with Cu. As CMP has been used to form multilayer circuit, edge and back side cleaning becomes important to remove contamination perfectly at post CMP cleaning. The authors have been investigating post CMP cleaner that installed spouting megasonic cleaning equipment (Spot type shower).[1)] On the other hand, we proposed a novel cleaning equipment using ultrasonic waveguide mode (we call MEGATUBE).[2)] This equipment has a waveguide connect with transducer which has a same structure of spot type. By applying this equipment, it is possible to supply ultrasonic for edge and back side of substrate. However, it is concerned to decrease the cleaning effect caused from waveguide size. Firstly, we showed cleaning efficiency of spot type and relationship between dissolved gas concentration were investigated.

## 2. Cleaning equipment for the post CMP

Chemical-mechanical planarization commonly abbreviated CMP, is a technique used in semiconductor fabrication for planarizing a wafer. After CMP, the number of particles over 0.20μm diameter is about $1\sim4\times10^4$ per 8inch wafer. Brush scrub cleaning is applied on this surface to remove these particles. After that, wafer will carry to the spin cleaning unit, precise cleaning by spot type shower with megasonic (generate at 950kHz), rinse by DI water and spin dry will be applied.

Spot type shower consists of a PZT attached with a vibration plate, and reflection nozzle (SUS316L), as shown in **Fig.1**. These parts were installed in case and sealed by packing. Cleaning solution (DI water or chemicals) is supplied from a case and throughout the waveguide. Ultrasonic waves generate from PZT (vibration area is 15mm in diameter) are reflected between PZT and reflection nozzle, waves are converged towards the center of the nozzle and emitted together with liquid flowing.

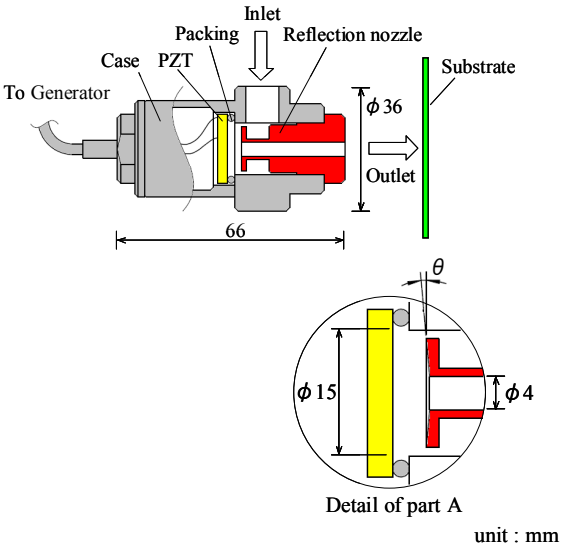


Fig.1 Configuration of the spot type transducer

We proposed a novel cleaning equipment using ultrasonic waveguide mode.[2)] This equipment has a waveguide connect with transducer which has a same structure of spot type. The waveguide has a removable structure, we can select the waveguide that has a different length or bend shape according to the purpose.

**Fig.2** shows an advantage of waveguide type transducer applied to the spin cleaning unit. At the spot type, distance between nozzle and substrate should be set up within 20mm to obtain optimum cleaning effect. Therefore, it takes a lot of spaces on substrate to set up the transducer and arm. On the other hand, at the waveguide type, there is no need to set up the transducer and arm, so there is a free space on substrate. By applying the input power to the PZT, ultrasonic wave can be traveled along the waveguide. It is possible to supply ultrasonic apart from PZT. And using the waveguide which has a different length or bend shape, it is possible to supply ultrasonic for edge and back side of substrate.

---

kz-suzuki@kaijo.co.jp

## 3. Cleaning efficiency of spot type shower

### 3.1 Output power and cleaning time

As a reference to the waveguide type transducer, particle removal efficiency (PRE) using spot type was evaluated. $SiO_2$ particles were prepared as contamination and put uniformly on wafer surface. The number of particles on wafer surface is counted by Inspection device (KLA-Tencor SP-1) and 0.20μm diameter is about $1\times10^4$ per 8inch wafer after contamination. DI water was used as cleaning solution. Flowing rate is controlled at 1L/min and dissolved $N_2$ concentration in DI water is at 20ppm.

At the post CMP cleaning process high rate of particle removal have been required. **Fig.3** shows a relationship between PRE and output power of spot type changing the cleaning time 10sec to 50sec. The larger PRE could be obtained with the larger output power, and PRE of 90% is obtained at 20W and 20sec or more.

### 3.2 Dissolved gas concentration

At the megasonic cleaning, dissolved gas concentration or kind of dissolved gas in cleaning solution have an influence on PRE.[3] The influence of dissolved $N_2$ gas concentration in DI water was carried out. **Fig.4** shows a result changing the output power 15W to 30W. In case of cleaning after 20 sec was investigated. At 12ppm of $N_2$ gas concentration, PRE becomes maximum in each output power. It is thought to have a relation with existence of cavitation. FFT analysis was carried out to confirm existence of cavitation using a hydrophone probe (KAIJO 19001D). DI water spouting from the waveguide will reach at the hydrophone and output voltage is measured by oscilloscope. **Fig.5** shows FFT analysis result of output voltage at 12ppm and 30W. From this result, harmonics(2f) and sub-harmonics(1/2f) were confirmed. They show existence of cavitation in DI water.

## 4. Conclusion

We proposed an application of waveguide type transducer to the post CMP cleaning. As a reference to the waveguide type transducer, particle removal efficiency using spot type was evaluated, and PRE of 90% is obtained at 20W and 20sec or more. The influence of dissolved $N_2$ gas concentration in DI water was carried out, and PRE becomes maximum at 12ppm. Particle removal efficiency using waveguide type transducer will be investigated.

**References**


1. S. Okano, T. Echigo, T. Osawa, T. Takano and O. Takahasi : Kaijo Technical Report. 11 (2001) p. 26.
2. K. Suzuki, K. Han, S. Okano, J. Soejima and Y. Koike : USE 2008 Symp. Ultrasonic Electronics. (2008).[To be presented]
3. K. Tsukamoto : IDEMA Japan News 43 (2001) p. 7.


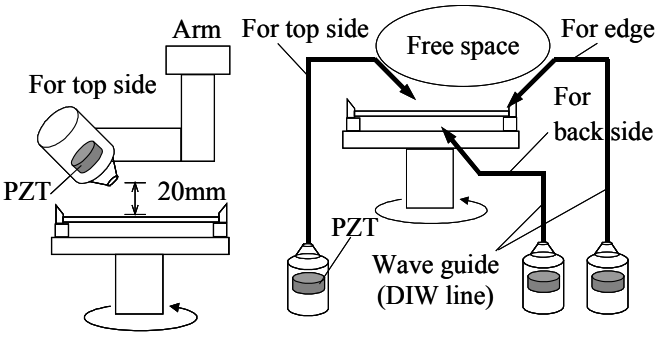


(a)Spot type (b)Waveguide type

Fig.2 Application of waveguide type transducer to the spin cleaning unit

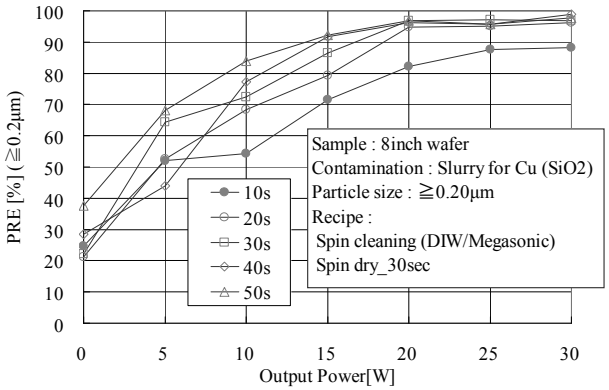


Fig. 3 Output power dependence on particle removal efficiency changing the cleaning time

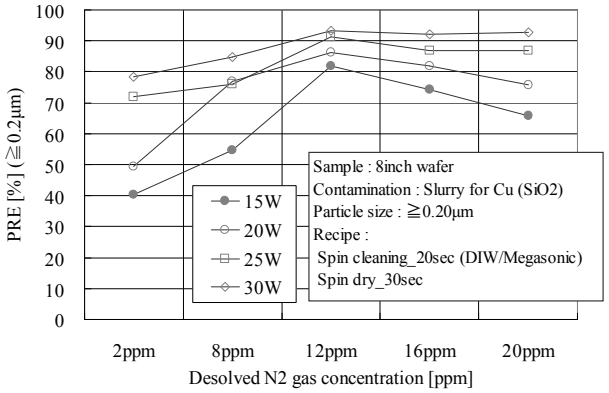


Fig. 4 Dissolved $N_2$ gas concentration dependence on particle removal efficiency changing the output power

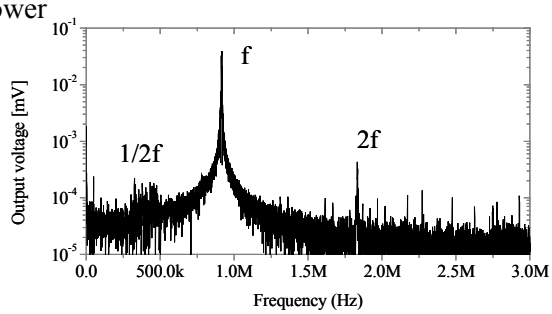


Fig. 5 FFT analysis result of a hydrophone probe output (12ppm, 30W)

3J8-3

Proceedings of Symposium on Ultrasonic Electronics, Vol. 29 (2008) pp. 363-364
11-13 November, 2008

# Properties of Lead-Free Piezoelectric Ceramics and Its Application to Ultrasonic Cleaner

無鉛圧電セラミックスと超音波洗浄機への応用

Tonshaku Tou[1†], Yuki Hamaguti[1], Yuichi Maida[1], Haruo Yamamori[1], Kazutoshi Takahashi[2], Yoshimitsu Terashima[2], ([1]Honda Electronics Co., Ltd.; [2]Fuji Titanium Industry Co., Ltd. )

董敦灼[1†]，浜口佑樹[1]，舞田雄一[1]，山森春男[1]，高橋和利[2]，寺嶋良充[2] ([1]本多電子; [2]富士チタン工業)

## 1. Introduction

$Pb(Zr,Ti)O_3$ (PZT) piezoelectric materials have been widely used in actuators, sensors, resonators and ultrasonic transducers because of its superior piezoelectric properties. However, the toxicity of lead oxide causes environmental contamination. Therefore, it is necessary to develop lead-free piezoelectric ceramics. Although the piezoelectric properties of $(Bi_{0.5}Na_{0.5})TiO_3$-based ceramics have been investigated by many researchers [1,2], there is not report about the properties which can be used as a transducer for ultrasonic cleaner. We have developed a new lead–free piezoelectric ceramics $(Bi_{0.5}Na_{0.5})TiO_3$-$BaTiO_3$-$(Bi_{0.5}Na_{0.5})(Mn_{1/3}Nb_{2/3})O_3$ which has good piezoelectric properties. [3] In this paper, the high power characteristics of the ceramics was reported. The properties of a bolt-clamp Langevin transducer (abbreviated as BLT) using the ceramics was investigated. The cleaning effect of ultrasonic cleaner using the BLTs was evaluated.

## 2. Experimental methods

A conventional process of ceramic engineering was used to prepare the sample. The commercially available $Bi_2O_3$, $Na_2CO_3$, $BaCO_3$, $TiO_2$, $Nb_2O_5$ powders, all of purity at least 99.0% were used as raw materials. After the corresponding metal oxides of the prescribed amount being mixed by ball milling, $0.82(Bi_{0.5}Na_{0.5})TiO_3$-$0.15BaTiO_3$-$0.03(Bi_{0.5}Na_{0.5})(Mn_{1/3}Nb_{2/3})O_3$ was synthesized by heating at 850°C for 2 hours, and then pulverized. After formed at 190 MPa, sintered at 1150°C for 2 hours and machined, cylinder sample of 34 mm in external diameter, 14 mm in internal diameter and 5 mm in thickness was obtained. For the evaluation of high power characteristics, strip sample of 43 mm in length, 7 mm in width and 1 mm in thick was fabricated by the same process. In order to measure the electrical properties, silver paste was coated to form electrodes on both sides of the sample, and subsequently fired at 600°C for 30 min. The samples were polarized under 3 kV/mm bias at 120°C in a silicon oil bath for 20 min.

Cylinder sample was used to fabricate bolt-clamp Langevin transducer (BLT) as shown in Fig.1. It consists of two piezoelectric elements and two metal blocks clamped at each end. In order to evaluate the cleaning effect, 15 BLTs were assembled to a metal tank as 600 W type cleaner.

The piezoelectric properties of the samples were measured by using an impedance analyzer (HP4194A). After measured the vibration velocity of strip sample, electrical transient response[4] was used to evaluate high power characteristics. A ultrasonic sound pressure meter (Honda electronics HUS-5) was used to measure the intensity of ultrasound of the cleaner. A aluminum foil of 0.01 mm in thick was used to examine the erosion effect of the cleaner.

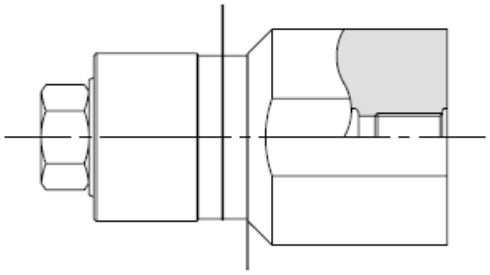

Fig.1 Schematic diagram of the bolt-clamp Langevin transducer (BLT).

## 3. Results and Discussion

Table 1 shows the dielectric and piezoelectric properties of lead-free ceramics. Compare to commercial hard PZT (Honda electronics HC-50GS), we expect that lead-free ceramics can be used to ultrasonic cleaner. Figure 2 shows the mechanical quality factor Qm of strip sample as a function of vibration velocity. Both Qm decreased with an increase in vibration velocity. However,

---

ttou @honda-el.co.jp

Table 1. Properties of lead-free ceramics

| | kt (%) | Qm | $d_{33}$ (pC/N) | $\varepsilon_{33}^T/\varepsilon_0$ | tan $\delta$ (%) | Tc (°C) |
|---|---|---|---|---|---|---|
| Lead-free | 41 | 500 | 110 | 520 | 0.66 | 260 |
| Hard PZT | 45 | 1100 | 290 | 1200 | 0.50 | 320 |

kt: coupling factor, Qm: mechanical quality factor, $d_{33}$: piezoelectric constant, $\varepsilon_{33}^T/\varepsilon_0$: dielectric constant, tan $\delta$ : dielectric loss, Tc: Curie point.

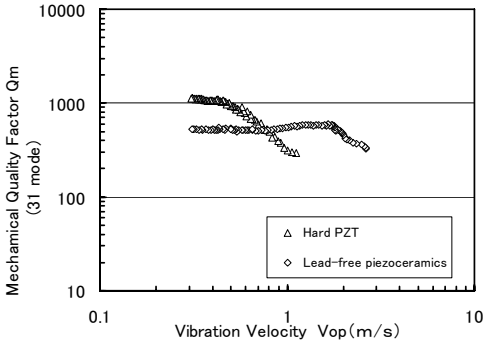


Fig.2. Variation of the mechanical quality factor $Q_m$ with the vibration velocity.

Qm of hard PZT decreased rapidly when the vibration velocity was over 0.5 m/s. On the other hand, Qm of lead-free ceramics did not change rapidly when the vibration velocity was less than 1.8 m/s. The result suggests that lead-free ceramics is suitable for the application of high power. Figure 3 shows the vibration velocity of vibration surface of the BLT as a function of input electric power. The frequency of the BLT is 28 kHz. The vibration velocity of BLT using lead-free piezoelectric ceramics was larger than that of commercial hard PZT at the same input power although both of them increased with an increase in power. It suggests that the power loss in lead-free BLT is smaller than that in leaded BLT. This result is correspondent to the relationship between Qm vibration velocity as shown in Fig.2.

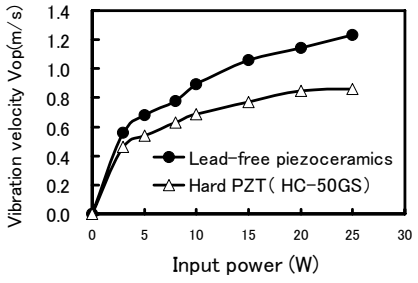


Fig.3. Variation of the vibration velocity of BLT (Bolt-clamp Langevin Transducer) with the input power.

Figure 4 shows the intensity of ultrasound of cleaner as a function of the distance from bottom of the tank. Although they changed in the same way, the intensity of ultrasound of cleaner using lead-free piezoceramics is higher than that of hard PZT. Figure 5 shows the erosion area of a aluminum foil after it was sunk into the tank for 1 minute. The erosion area was resulted from the cavitation of ultrasound. Because cavitation plays an important role to remove contaminants, the result suggests that the clean effect of cleaner using lead-free is equivalent to hard PZT.

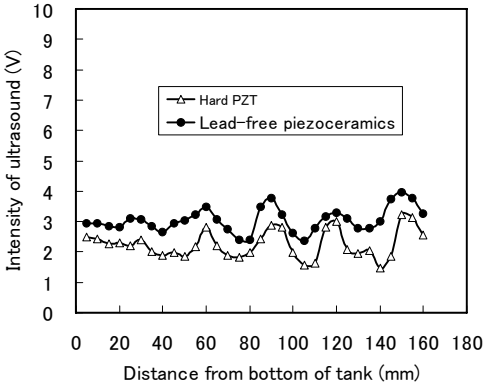


Fig.4. Variation of the intensity of ultrasound of the cleaner with distance from the bottom.

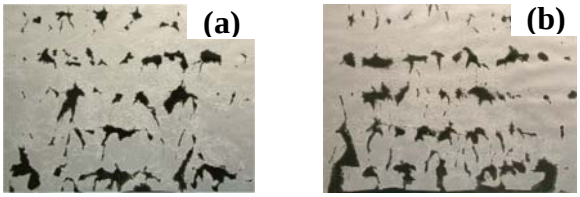


Fig.5. Erosion area of aluminum foil after sunk into the tank of cleaner. (a) Hard PZT, (b) lead-free piezoceramics.

## 4. Conclusions

Lead–free ceramics $0.82(Bi_{0.5}Na_{0.5})TiO_3$-0.15 $BaTiO_3$-0.03$(Bi_{0.5}Na_{0.5})(Mn_{1/3}Nb_{2/3})O_3$ has been developed and applied successfully to ultrasonic cleaner. The cleaner has a high clean effect which is good for commercial application.

## References


1) T. Takenaka, K. maruyama, K. Sakata, Jpn. J. Appl. Phys., **30** (1991)2236.
2) H. Li, C. Feng, P. Xiang, Jpn. J. Appl. Phys., **42** (2003) 7387.
3) T. Tou, Y. Hamaguti, Y. maida, H. Yamamori, K. Takahashi, Y. Terashima: Japan Patent 4044944 (2008).
4) M. Umeda, K. Nakamura, S. Ueha, Jpn. J. Appl. Phys., **37** (1998) 5322.

3J8-4

Proceedings of Symposium on Ultrasonic Electronics, Vol. 29 (2008) pp. 365-366
11-13 November, 2008

# Acoustic Characteristics of High Frequency Ultrasound Probe using Piezoelectric Film Deposited by Aerosol Deposition Method エアロゾルデポジション法による PZT 膜を用いた高周波超音波プローブの音響特性

Akito Endo‡, Jun Akedo (AIST ), 遠藤聡人‡, 明渡純 (産業技術総合研究所)

## 1. Introduction

In recent years, microscopical texture is diagnosed using a 20 MHz to about 40 MHz. The reason for using a high frequency ultrasound is for improving distance resolution[1) 2)]. In order to improve lateral resolution according to it, the small ultrasonic transducer of 100 μm or less is needed. However, the sensor was miniaturized, when it became the number of high frequency further, attenuation was large, sound pressure required for an ultrasonic diagnosis was not obtained, but the big subject that penetration distance (visual field depth) was insufficient occurred.

The aerosol deposition (AD) method is the deposition process also with an easy detailed pattern by not choosing the substrate quality of the material [3)], but being able to form easily a piezoelectric film 1 μm to 100 μm or more without adhesion layer, and using a metal masker. Therefore, by this research, the PZT film deposited by the AD method annealing temperature differs considered the influence which it has on the sound pressure of a high frequency ultrasound from10 MHz to 60 MHz.

## 2. Experimental Procedure

### 2.1 depositing condition and material property for PZT films

The diameter 3 mm and thickness 0.5 mm alumina substrate was used for the substrate for depositing a PZT film. Ti/Pt was deposited on the substrate using RF spatter as a lower electrode. The thickness of a lower electrode deposited 50nm of titanium as a glue layer, deposited 600nm of platinum as a electrode layer on titanium, and Ti/Pt were deposited the thickness of 650nm on the alumina substrate. The raw material used as a starting PZT powder (Zr/Ti = 52/48) was the commercially available powder (PZT-LQ: niobium-modified PZT; Sakai Chemical Ind.) with average particle size of 0.3 nm were used as starting powder.

The deposited PZT film was annealed at 600 ℃, 700 ℃, and 850 ℃ in air . Because, This was a low annealing temperature which is the feature of the conventional AD film at 600 ℃ which a piezoelectric property recovers, it was taken as to 850 ℃ at which lead does not evaporate. Annealing time of each PZT films were fired for 30 minutes. Each annealing temperature and the film thickness are about 30 μm. And each PZT films were poled at 250 ℃ at 30 kV/cm for 20 minutes and at 250 ℃ at 30 kV/cm for 20 minutes in air.

Acoustic velocity is considered to be about 3210 m/s from report that the density and Young's modulus of PZT deposited by the AD method are about 7.76 g/cm$^3$ and 80 GPa[4)]. Therefore, in λ/4 resonance, the resonance frequencies of the deposited PZT films are considered to be near about 27 MHz to 29 MHz.

The dielectric permittivity (ε) and loss (tan δ) of the each PZT film (at 0.5 V) were measured using an impedance analyzer (HP4194) at 100 kHz. The dielectric permittivity (ε) and loss (tan δ) of the deposited PZT film annealed at 600 ℃, 700 ℃, and 850 ℃The dielectric permittivity (ε) and loss (tan δ)of the deposited PZT film annealed at 600 ℃, 700 ℃, and 850 ℃ were ε :774, 780, 1030, and tan δ 3.98 %, 3.91 %, 2.89 %.

### 2.2 Experimental setup of ultrasound using fabricated probe

The frequency response characteristic was measured by the short pulse drive of each ultrasonic probe and the frequency characteristic of sound pressure was measured using the needle type hydrophone (HNP-400, ONDA). The signal from a function generator was amplified with power amplifier (75W250W, Amplifier Research) with amplification 50dB, and was impressed to the ultrasound probes. The transmitted ultrasound propagated underwater and received by the needle type hydrophone. The received signal is amplified by a preamplifier(AH-2010-100, ONDA) with an amplification of 20 dB, and is displayed on an oscilloscope (TDS2022B,Tektronix). In consideration of the Fresnel region, the probe and the hydrophone were installed in 10 mm distance.

## 3. Results and Discussion

The frequency characteristics of the sound pressure using each ultrasound probe is shown in Fig.1. As for the resonance frequency of each ultrasonic probe, from the frequency characteristics of the sound pressure, the resonance frequencies as λ/4

thickness mode were near 26 MHz to 27 MHz. And, the fluctuation in sound pressure is greatly found to all ultrasound probes. The maximum sound pressures of the ultrasonic probe using a PZT film at 600 ℃, 700 ℃, and 850 ℃ were 574 kPa, 1MPa, and 803 kPa. When each ultrasonic probes were compared, the ultrasonic probe using a PZT film at 600 ℃ has irradiated only the maximum sound pressure of 139 kPa at 40.5 MHz in high frequency band from 40 MHz to 60 MHz. However, the ultrasonic probe using a PZT film at 700 ℃ has resonance frequencies of 40 MHz, 47 MHz, and near 55.5 MHz, and was set to 341 kPa, 384 kPa, and 248 kPa in high frequency band from 40 MHz to 60 MHz. The sound pressure of the ultrasonic probe using the PZT film at 850 ℃ was become to 423 kPa at 40 MHz and the almost same sound pressure as the ultrasonic probe using the PZT film at 700 ℃ was shown.

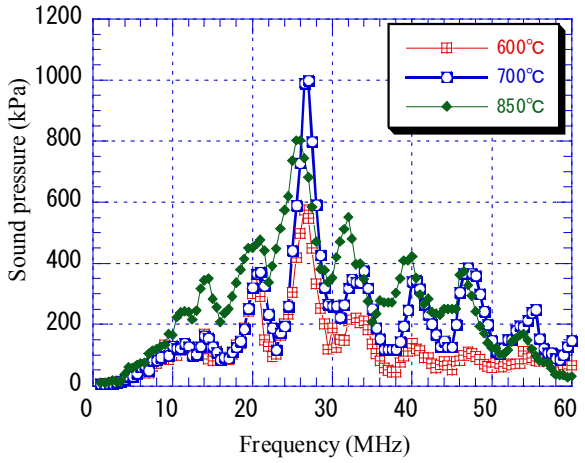


Fig. 1 The frequency characteristics of the sound pressure using each ultrasound probes

The transmission characteristics of ultrasound probe using the PZT fired at 700 ℃, were investigated using the impulse response by a pulse drive. In order to investigate the frequency response of the ultrasonic probe, the pulse of about 18 ns of pulse width of amplitude 30.2 V was used. The received waveforms and power spectrum of an received ultrasound which were irradiated from the ultrasonic probes using a PZT film at 700 ℃ is shown in Fig. 2. They were found that the center frequencies were 27.1 MHz and the each fractional bandwidth (-3 dB) were 2.5 %.

## 4. Conclusion

In the frequency characteristic of sound pressure, the ultrasound probe using a PZT film at 700 ℃ was able to irradiate the ultrasound of 1 MPa at 27 MHz. Moreover, in the high frequency from 40 MHz or 60 MHz, the ultrasonic probe using the PZT film at 850 ℃ showed the value of the high sound pressure of 423 kPa at 40.5 MHz. Moreover, the sound pressure was overall high in the frequency of 10 MHz to about 50 MHz.

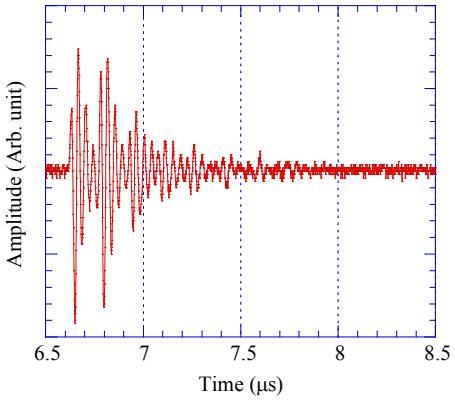


(a)

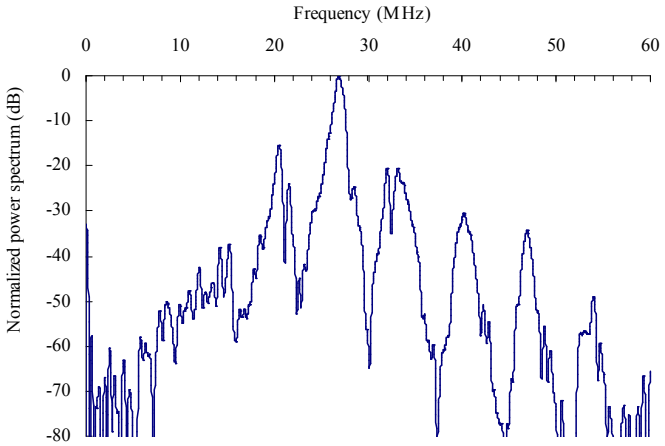


(b)

Fig. 2 (a) Received waveform and (b) normalized power spectrum of the irradiated ultrasound by the ultrasonic probes using PZT film annealed at 700 ℃.

**Acknowledgement**

This research was supported by the New Energy and Industrial Technology Organization (NEDO) .

**Referance**

1) M.Ishikawa, M. K. Kurosawa, A. Endo, S. Takeuchi, Jpn. J. Appl. Phys., 44 (2005) 4342
2) D. M. Mills and S.W. Smith: IEEE Trans. Ultras. Ferroelectr. and Freq. Control 49 (2002) 1005.
3) J. Akedo and M. Lebedev: Appl. Phys. Lett. 77 (2000) 1710
4) T. Miyoshi: Jpn. J. Appl. Phys. **46** (2007) 7018.

3P2b-1

Proceedings of Symposium on Ultrasonic Electronics, Vol. 29 (2008) pp. 367-368
11-13 November, 2008

# Visualization of the Wavefronts of Ultrasound Passed through Bovine Bones

牛骨を透過する超音波波面の可視化による検討

Masahiro Ohno (Facult. Eng., Chiba Inst. Tech.)
大野正弘（千葉工大・工）

## 1. Introduction

Ultrasonic diagnosis of osteoporosis has attracted much attention in recent years.[1)-5)] In the standard measurement system thus far reported,[2)] ultrasound was radiated towards a certain site of a limb (e.g., wrist) and the transmitted component was detected to determine the values of sound velocity and attenuation, which are believed to be correlated with the value of bone density. However, wave propagation in human bones, which have non-uniformly rounded surfaces as well as complicated inner structures such as trabecular networks of cancellous bones, may not be a simple process. If aberration is generated in the ultrasonic field, errors will be introduced into the values to be determined, into that of attenuation in particular. To improve the precision of diagnosis, the spatial structure of the ultrasonic fields passing through such bones must be investigated. For this purpose, we have tried to observe the wavefronts of ultrasonic beams passed through bovine bones by the use of schlieren visualization technique.

## 2. Experimental Setup

**Fig. 1** shows the fundamental part of the experimental setup, which simply consists of a bone sample immersed in water and an ultrasonic transducer irradiating ultrasonic waves towards it. Two kinds of ultrasonic transducers were used, one of which had a center frequency of 1.03 MHz and a radiation area of 10 mm in diameter, the other 3.5 MHz and 13 mm. Both of them had flat surfaces. Ultrasound was irradiated in tone-burst waveforms the duration of which was longer than 20 cycles. A 500 W power amplifier was used to boost the voltage applied to the transducer. To visualize the ultrasonic field distribution, this setup was placed in a standard schlieren system the optical axis of which was oriented in the Z direction. The light source was a Xe stroboscopic lamp having an irradiation time as long as 180 ns, which was sufficiently short to visualize the wavefronts of ultrasound both at 1.03 MHz and 3.5 MHz. The light was monochromized by inserting a wavelength filter centered at 500 nm.

ohno.masahiro@it-chiba.ac.jp

The experiment was carried out in the following manner. First, ultrasonic field distribution was visualized and recorded without the bone sample. Next, several bone samples, cortical or cancellous, were inserted in the ultrasonic path, then the images of the ultrasonic waves transmitted through them were recorded. Since the attenuation of the ultrasound due to the insertion of the bone was considerably high, irradiation power of the ultrasound was set much higher in the latter case. All the schlieren images were taken by detecting zeroth order light (non-diffracted light). This method is suitable for the present study, because it allows any wavefront deformation to be visualized as darkening against a bright background, while the method by detecting the diffracted light permits only a limited part of the wavefront deformation to appear in the picture owing to the pinhole's selectivity to the diffracted light.

All the bone samples used were bovine bones. Marrow part in the cancellous bone was removed beforehand, and a special care was taken so as to replace the hollow area of the trabecular structure by water.

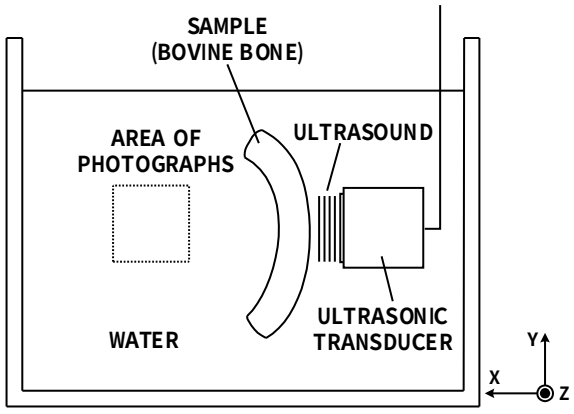


Fig. 1 Experimental Configuration

## 3. Experimental Results

**Fig. 2** shows the experimental results for the ultrasonic frequency of 1.03 MHz. All the images show the field distribution in a 10 mm-squared area 25 mm apart from the transducer surface. Fig. 2 (a) shows the ultrasonic field in a free space (without samples), which represents an undisturbed but

slightly diffracted wavefront pattern. Figs. 2 (b) and (c) are the wavefronts after propagating through a 7 mm-thick cortical bone. Fig. 2 (b) is the result when the ultrasound passed through the central part of the cortical bone, which shows a slight deformation (rounding) of the wavefronts. Fig. 2 (c), the result for the case when the ultrasound traveled through the peripheral part of the cortical bone, represents stronger wavefront bending and a beam deflection. The result for a cancellous bone is shown in Fig. 2 (d). The thickness of the sample was 18 mm. The schlieren image shows small deformation, even smaller compared to the field in a free space.

**Fig. 3** shows the results for the 3.5 MHz ultrasound. At this frequency, wavefronts were severely deformed after the beam had passed through, even the central part of, the cortical bone (Fig. 3(b)). On the other hand, wavefronts emerging from the cancellous bone (Fig. 3(c)) were as straight as those in the free space. However, it should be noted that the cancellous bone used in this experiment was much thinner (7 mm) than that used in the experiment at 1.03 MHz. No image was obtained for an 18 mm-thick cancellous bone at 3.5 MHz because of the high ultrasonic attenuation.

## 4. Summary

The structure of ultrasonic waves that had passed through bovine cortical or cancellous bones has been observed by using the shilieren visualization technique. Wavefront deformation in the results for cortical bones can be attributed to the refraction at the curved interface between the bone and water. On the other hand, results for the cancellous bones, which showed small deformation, need further investigation to be fully accounted for. At present, we consider that the trabecular structure of the cancellous bone did generate a large amount of scattered waves, but they were hardly observable by the schlieren system because they diverged from various points in the bone, and, resultantly, the remaining portion of the ultrasound was effectively visualized.

## References


1) I. Mano *et.al.*: Jpn. J. Appl. Phys. **46** (2007) 4858.
2) I. Mano *et.al.*: Jpn. J. Appl. Phys. **45** (2006) 4700.
3) T. Otani: Jpn. J. Appl. Phys. **44** (2005) 4578.
4) A. Hosokawa *et.al.*: Jpn. J. Appl. Phys. **36** (1997) 3233.
5) T. J. Haire and C. M. Langton: Bone **24** (1999) 291.


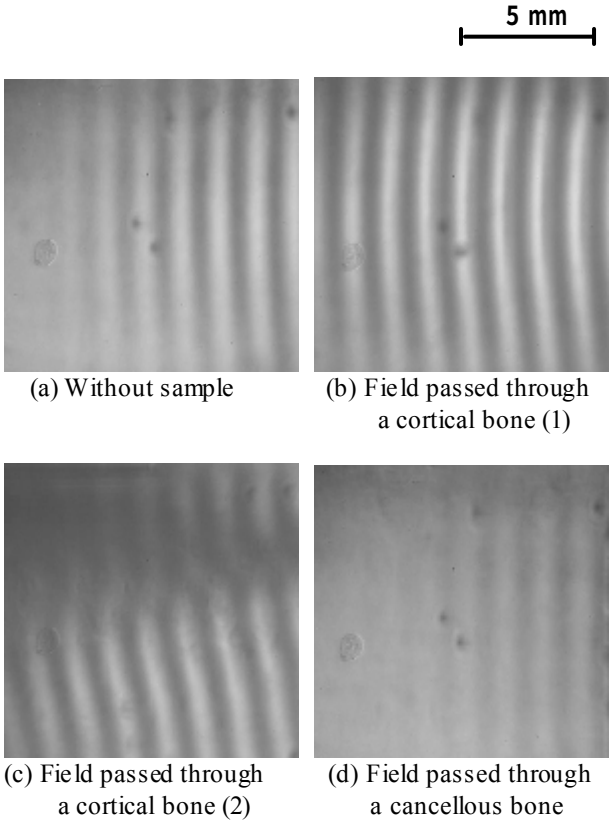


Fig. 2 Schlieren images of ultrasonic fields at 1.03 MHz.

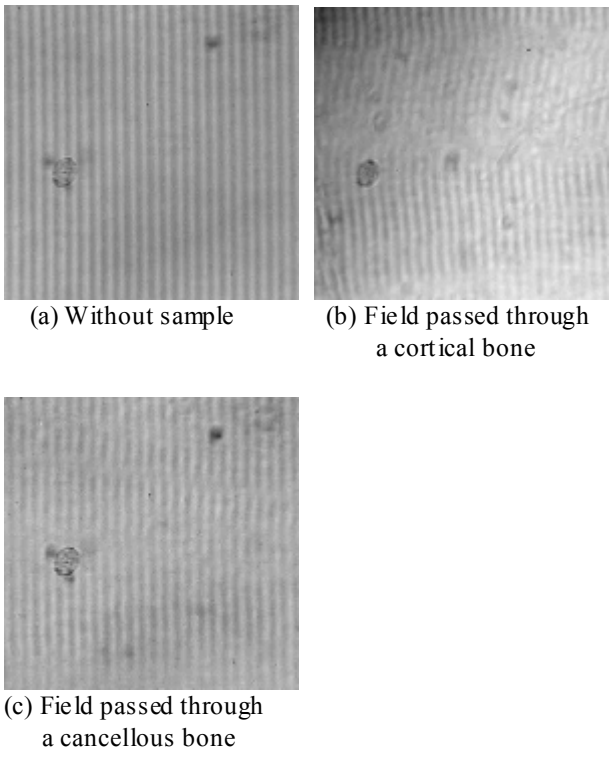


Fig. 3 Schlieren images of ultrasonic fields at 3.5 MHz.

Proceedings of Symposium on Ultrasonic Electronics, Vol. 29 (2008) pp. 369-370
11-13 November, 2008

# 超音波 CT 法による内臓脂肪測定のファントム評価実験

# Phantom evaluation experiment of ultrasound CT for visceral fat measurement

川本幸一郎‡, 山田晃, 田村美希（農工大院 生物シ応用科）
Koichiro Kawamoto, Akira Yamada, Miki Tamura (Grad. Bioappl. and Sys. Eng., Tokyo Univ. of A&T)

Sound speed reconstructive imaging for the human abdomen using transmission type computed tomography was studied, aiming at the measurement of the visceral fat area for the metabolic syndrome diagnosis. In this paper, examinations were made to verify the validity and precision of the visceral fat area measurement based on experiment using a phantom specimen of human abdomen. As a result, it was demonstrated that the reproducibility of the image and precision of the visceral fat measurement was almost satisfactory, which can serve as the metabolic syndrome diagnosis.

## 1. Introduction

With the escalation of the public medical expenses, importance of the preventive medical care of adult deceases was recognized. Under the circumstances, Japanese government introduced the metabolic syndrome examination as the health diagnosis from Apr. 2008. For this purpose, we have been studying the ultrasound tomographic reconstruction of the abdominal sound speed image aiming to measure the visceral fat area[1,2]. In this paper, examinations were made to verify the validity and precision of the visceral fat area measurement based on experiment using a phantom specimen of human abdomen.

## 2. Principle of the visceral fat measurement

For the imaging of the human body abdominal medium, the transmitter and receiver facing pair transducers are arranged on the body surface. Travel time of the waves transmitted through the abdominal medium for different observation paths were collected. We assume that the travel time is proportional to the path integral of the inverse sound speed of the medium along the connecting path between the transmitter and receiver based on the straight path propagation model. On this assumption, tomographic calculations are made to obtain the unknown cross-sectional sound speed $c(x,y)$ of the target medium knowing the travel time data $T_m$ for the multiple obaservation paths $m$=1-$M$. We assumed that the highy distorted waves, including those transmitting through the spinal cord, does not satisfy the straight ray propagation assumption. Hence, these diorted waves are excluded from the tomographic calculation.

It is noted that the abdominal sound speed of the fat region, which is around 1450m/s, is much lower than the average value of the soft tissues of 1520m/s. On the other hand, the sound speed of protein regions including muscle, intestine and kidney, which is above 1550m/s, is much higher than the average value. The fact enables us to estimate the fat areas from the reconstructed abdominal cross sectional sound speed image. Here, in order to serve the technique to the metabolic syndrome diagnosis, visceral fat regions should be discriminated from the subcutaneous fat region. To this end, border between the subcutaneous and visceral region is estimated using the marked points obtained along the high sound speed abdominal muscle regions in the reconstructed image. Using the border information thus obtained, visceral fat regions are separated from the subcutaneous ones and visceral fat area can be finally measured.

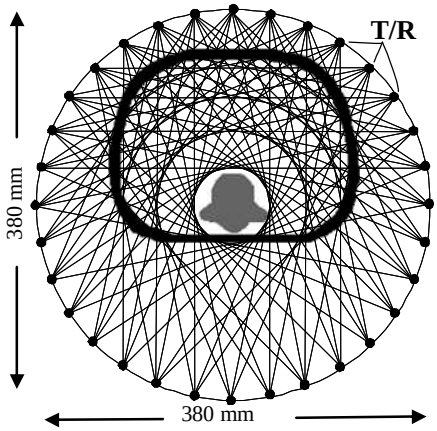


Fig.1 Transmitter/receiver arrangement and propagation path.

## 3. Evaluation experiment

### 3.1 Transducer/receiver arrangement

As shown in Fig.1, a facing pair of ultrasound transmitter and receiver (with frequency band 10-500[kHz] and aperture diameter 40[mm]) are moved along the abdominal peripheral circular boundaries with diameter $D$ =380[mm]. The transmitter is moved at 32 equiangular points and the receiver is moved along 16 equiangular points

yamada@cc.tuat.ac.jp

along the circular boundaries. With the combination of these transmitter and receiver points, measurements are made along $M$ = 96 paths.

### 3.2 Phantom

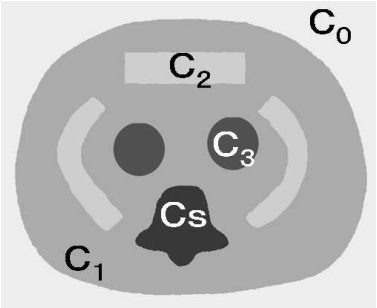


Fig.2 Sample specimen arrangement used in experiment

An abdominal mimicking phantom was prepared as shown in Fig.2,. A urethane wall ultrasound abdominal phantom (CIRS: Model 57, 275x200 [mm]) having a plastic spinal cord pillar was used as a container. At the circumference region, high speed polyethylene glycol objects were embedded as abdominal muscle regions, where 8% concentration glycerin was added to adjust the sound speed with $c_2$=1575m/s. In the interior part, food oil objects with sound speed $c_3$=1450 m/s were embedded as visceral fat regions. Between the objects, ultrasound gel with sound speed $c_1$=1500 m/s was filled.

### 3.3 Result and discussion

Using the travel time observation data for the abdominal phantom described above, a sound speed image was reconstructed as shown in Fig.3(a). In addition to that, the images using the simulation data were compared based on the ideal straight ray propagation calculation and the rigorous finite difference methods, as shown in Fig.3(b) and (c), respectively. The experimental result in (a) is little bit degraded compared to the theoretical ones in (b) and (c). Especially, the degradation of the image in the subcutaneous region is evident. This is caused by the lack of the path data and can be improved if more number of path data around subcutaneous region is incorporated. Another cause of the degradation is due to the defects of the phantom specimen such as the misalignment of the object, or the mixture of the air bubbles at the object interface. On the whole, however, it was demonstrated that the reproducibility of the image was almost satisfactory, especially for the purpose of the visceral fat area measurement.

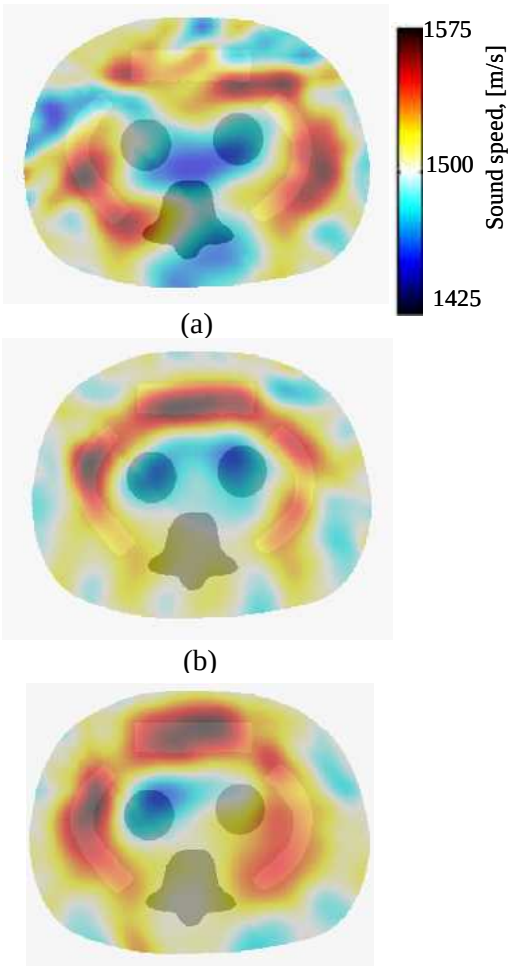


(a)

(b)

(c)

Fig.3 Reconstructed sound speed image of the abdominal phantom: (a) image using the measured data, (b) image using the simulated data based on the straight ray propagation model, (c) same as in (b) based on the finite difference calculation. The reconstructed colored sound speed images are superimposed with the predetermined gray-scale image.

### References

1. A.Yamada, K.Nogami, “Ultrasound travel time tomography for the sound speed abdominal imaging”, 2007 Int. Conf. Ultrasonic CD-ROM, Vienna, Austria, 89 (Apr. 2007).
2. K.Nogami, A.Yamada, “Evaluation experiment of ultrasound CT for the abdominal sound speed imaging”, Jpn.J.Appl.Phys., 46, 7B,4820-4826 (2007).

Proceedings of Symposium on Ultrasonic Electronics, Vol. 29 (2008) pp. 371-372
11-13 November, 2008

# 直角四方向観測型超音波逆散乱トモグラフィ
# Quadrangular View Ultrasound Inverse Scattering Computed Tomography

山田晃†（農工大院 生物シ応用科）
Akira Yamada (Grad. Bioappl. and Sys. Eng., Tokyo Univ. of A&T)

Ultrasound inverse scattering imaging technique from the quadrangular observation data configured with four linear array probes was proposed, aiming at a practical and versatile inverse scattering imaging system featuring lower cost and higher-speed data acquisition. In the present method, backward and sideward scattering wave data as well as the conventional forward scattering data were incorporated in the reconstruction calculations based on the Fourier slice theorem. From the simulation examinations, validity of the method was demonstrated, despite the difficulty of the inverse problem due to the limited quadrangular observation view as well as the finite aperture of the linear arrays.

## 1. Introduction

Ultrasound inverse scattering computed tomography is expected to be useful to the application for the medical diagnosis and non-destructive inspection.[1] For the realization of the technique, large-scale ring array data acquisition systems had ever been developed.[2] The method has difficulties that data collections are required from great number of view directions around the object, therefore, hardware cost becomes very high, in addition to that, great number of data observation prevents the high speed data acquisition. To resolve the problem, we had proposed a square array system placing four linear arrays at the perimeter of the target region.[3] In this method, wide band multifrequency scattering components were incoprporated in the resonctrcuiton procedure, to make it possible to reconstruct the image by using few number of view data around the qudrangular illumination directions. There was, however, a room for improvements, since only the forward scattering data were used. In this paper, backward and sideward scattering wave data as well as the conventional forward scattering data are incorporated in the reconstruction calculations. As a result, it is realized to reconstruct the image only by using four quardranguar view data.

## 2. Principles

Four linear array transducers are arranged along a square side around the target as shown in Fig.1. When emitting pulsed plane waves from one of the linear array, forward, backward, rightward and leftward scattering waves are observed along the each square side arrays. We propose an inverse scattering method using only four sets of illumination view data which is collected by emitting the waves from each quadrangular direction.

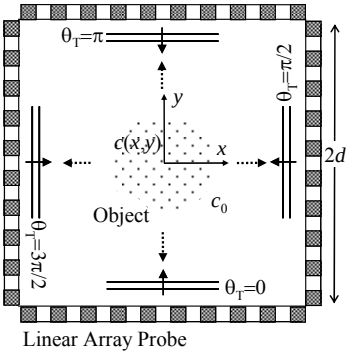


**Fig.1** Data observation geometry using four linear arrays along square perimeter of the object.

As preprocessing of the received wave, the scattered wave component $\phi(t)$ is obtained by subtracting the incident wave $\phi_i(t)$ from the net observation wave $\phi_{net}(t)$ ($\phi=\phi_{net}-\phi_i$), after that temporal angular frequency components $\phi_\omega$ is extracted by the Fourier transform of $\phi$. We consider the problem to obtain the object's parameters $o(x,y)$ from the observation $\phi_\omega(x')$ along the array axis $x'$ at $y'=d$ . Here, $o(x,y)$ is defined with respect to the sound speed $c(x,y)$ of the medium, and the background constant sound speed $c_0$ as $o(x,y)=c_0^2/c(x,y)^2-1$. To this end, $\phi_\omega(x')$ is Fourier transformed with respect to $x'$ to obtain $\Phi_\omega(K_x')$. Data $\Phi_\omega(K_x)$ is related with the object function according to the following Fourier diffraction slice theorem under the weak scattering Born approximation.

$$\Phi_\omega(K_x-k_0\sin\theta_T, y=d)e^{-id\sqrt{k_0^2-(K_x-k_0\sin\theta_T)^2}} = \frac{i}{2}k_0^2\frac{O(K_X,K_Y=\sqrt{k_0^2-(K_x-k_0\sin\theta_T)^2}-k_0\cos\theta_T)}{\sqrt{k_0^2-(K_X-k_0\sin\theta_T)^2}}, \quad (1)$$

yamada@cc.tuat.ac.jp

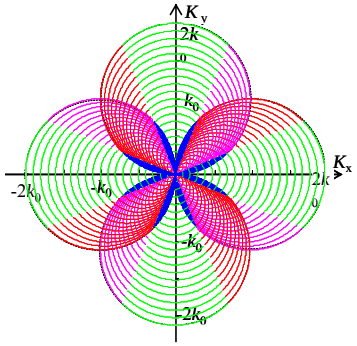


**Fig.2** Contour plots of the data in the Fourier plane with multi-frequency wave illumination from quadrangular direction.

where, $k_0=\omega/c_0$ is the wave number, $\theta_T$ is the transmitter direction and $O(K_x, K_y)$ is the two dimensional spatial Fourier transform of the object $o(x,y)$ with respect to $(x, y)$ .

Equation (1) states that Fourier plane data can be obtained from the receiver array at $y=d$ over the locus of the upper half semicircles centered at $(k_0\sin\theta_T, -k_0\cos\theta_T)$ and radius $k_0$. It is noted that aperture observation angle $\theta_s$ is less than $\pi/4$ because of the square aperture of the receiver arrays. Consequently, obtainable locus of the data becomes quarter circles. By changing the temporal angular frequency over the range $0<\omega<\omega_0$, the quarter circular arc data with varying radius $(=k_0)$ can be obtained. These quarter circles are drawn for the different observation view, i.e., using the collected data along $y=+d$, $y=-d$, $x=+d$ and $x=-d$. As a result, Fourier plane data can be fulfilled within the entire circle with radius $2k_0$ as shown in Fig.2. By executing the inverse Fourier transform of the data $O(K_x, K_y)$, the object function $o(x,y)$ (i.e., the sound speed $c(x,y)$) can finally be obtained.

## 3. Simulation Test

In order to demonstrate the validity of the method described above, simulation test examinations were carried out. As a numerical phantom specimen, cylindrical object with radius $a$=6 mm and sound speed variation 0.1% is considered at the arbitrary position in the target region. Four linear array probes: each one is 64 mm long having 128 elements with 0.5 mm spacing, which is quarter wavelength at the fundamental frequency 750 kHz. They are placed along the square perimeters (64 mm x 64 mm) of the object. The sets of data for the quadrangular illumination with different frequency component in the range lower than $f$=750 kHz were calculated. They were mapped over the Fourier plane. Figure 3(a) shows the gray scale image of the log amplitude of $O(K_x,K_y)$ in the Fourier plane. On the other hand,

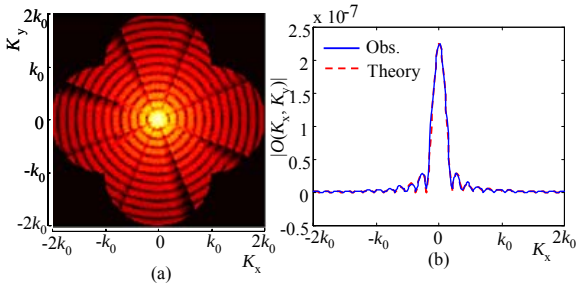


**Fig.3** Calculated object function: (a) gray scale image of $\log(|O(K_x,K_y)|)$ on Fourier plane and (b) cross sectional profile of $|O(K_x,K_y)|$ on $K_x$ axis (solid line show the result from the scattered data, dotted line from the theory).

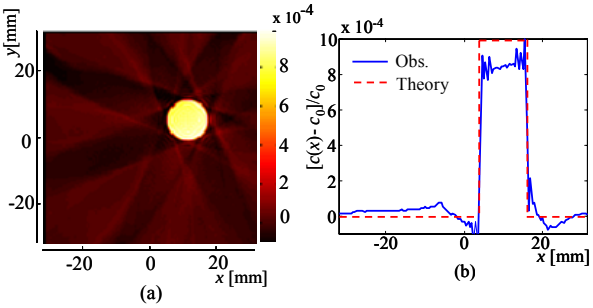


**Fig.4** Reconstructed sound speed image of the cylindrical object: (a)gray scale image on $(x,y)$ plane, (b)cross-sectional image on $x$-axis. Results from the scattered data (solid line) are compared to the theory (dotted line).

Fig.3(b) shows the cross sectional plot of the same data along $K_x$ axis, where the results (solid line) are compared with the theory (dotted line). We can see that the data is in accordance with the theory, although there are a few part of missing regions in particular directions. Finally, carrying out inverse Fourier transform calculation, sound speed image $c(x,y)$ was reconstructed as shown in Fig.4, where (a) shows the gray scale image on $(x,y)$ plane, and (b) shows the cross sectional plot on $x$ axis. Results with solid line are compared with the theory with dotted red line. The reconstructed sound speed value is slightly lower caused by the missing of the data in the Fourier plane. Except this, overall reproducibility of the reconstructed image is fairly good both in shape and sound speed value.

## References


1. A. Yamada and K. Kurahashi: Jpn. J. Appl. Phys., **32**, (1993) 2507.
2. M. P. Andre, H. S. Janee, P. J. Martin, G. P. Otto, B. A. Spivey and D. A. Palmer: Int. J. Imag. Syst. Tech., **8**(1997) 137.
3. A.Yamada and S. Yano: Jpn. J. Appl. Phys., **8A**, (2004) 5582.

Proceedings of Symposium on Ultrasonic Electronics, Vol. 29 (2008) pp. 373-374
11-13 November, 2008

# Improvement of Vibrational Distribution Measurement of Piezoelectric Devices based on Image Processings

画像処理に基づいた圧電デバイス振動変位分布測定法の改良

Kentaro Tachibana, Yasuaki Watanabe, Noriyuki Imaeda, Shigeyoshi Goka, Takayuki Sato and Hitoshi Sekimoto (Graduate School of Science and Engineering, Tokyo Metropolitan University)
橘 健太朗，渡部泰明，今枝憲幸，五箇繁善，佐藤隆幸，関本 仁（首都大院 理工）

## 1. Introduction

Measuring the vibration mode shape is very important when designing piezoelectric devices. We have developed many methods for visualizing mode shapes that combine surface speckle interferometry and image-processing techniques for high-frequency resonators[1-4]. The methods all involve irradiating the surface of a roughly finished device with a collimated laser beam and capturing images of the speckle field generated on the surface with a video camera.

We reported an improved laser speckle method that increases detection sensitivity using stroboscopic laser irradiation and estimates the absolute vibration displacement [5-8]. This method was based on a simple surface-interferometric model and statistical operations for the interference intensity of the speckle images. We applied this method to a burst wave device excitation system using two lasers with different wavelengths[9].

We explain how we improved upon the above mentioned laser speckle method and system. The unique features of this method include 1) concurrent irradiation of the two-lasers that use a polarization-controlled optical mixer, 2) improved displacement measuring accuracy and range achieved through exclusion of the interference coefficient g from the displacement calculation, and 3) linearization of two-dimensional correlation images to "net" vibrational displacement distributions, which enable an absolute displacement estimation on the entire surface of the devices, using the data from partial surfaces measurements.

## 2. Measurement system

**Figure 1** is a block diagram of the measurement system with two lasers and burst wave device excitation. The basic hardware setup was the same as [9].

bobo@esys.eei.metro-u.ac.jp

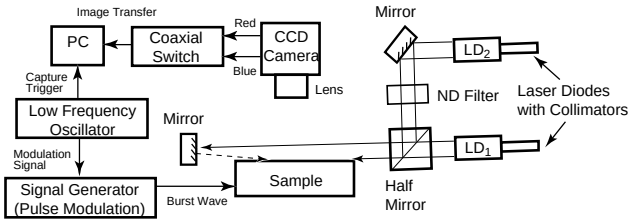


Fig. 1 Experimental setup of full-field in-plane motion visualization system using burst resonator excitation and two lasers.

In this system a half mirror was placed to mix the collimated laser beams. To avoid the CCD saturation and to equalize the detection sensitivity for each laser, a natural density (ND) optical filter was used. The azimuth angles of the lasers were each adjusted to obtain the maximum detection sensitivity for the in-plane vibrational displacement.

## 3. Improved displacement measuring accuracy

In the burst-wave excitation system, the difference in speckle brightness caused by the interference condition between the resonator-resting and -driving states is approximately given by

$$\Delta I = \gamma\left(1-\frac{\sin 2kdx}{2kdx}\right). \qquad (1)$$

Here, $k = 2\pi/\lambda$, where $\lambda$ is the wavelength of the laser diode, $\gamma$ is the interference factor of the fringes, and $dx$ is the vibrational displacement of the resonator. In this equation, we assume that $dx$ changes linearly. In the proposed method, $\gamma$ is not required to calculate the vibrational displacement.

To improve the order of approximation, we introduced the third order polynomial function to approximate the 2nd term in the parentheses in (1).

$$\frac{\sin 2kdx}{2kdx} = \alpha dx^3 + \beta dx^2 + \eta dx + 1, \qquad (2)$$

where $\alpha$, $\beta$, and $\eta$ are constants and can be derived by determining $\lambda$ and the approximation range of the vibrational displacement. By rearranging (1) and (2), the differences in optical intensities $\Delta I_s$ for

two lasers can be obtained. We can thus obtain the absolute vibrational displacement using the following equation,

$$dx = \frac{-B + \sqrt{B^2 - 4AC}}{2A} \tag{3}$$

where

$$\begin{cases} A = p\Delta I_1 \alpha_2 - \Delta I_2 \alpha_1 \\ B = p\Delta I_1 \beta_2 - \Delta I_2 \beta_1 \\ C = p\Delta I_1 \eta_2 - \Delta I_2 \eta_1 \end{cases},$$

and $p = \lambda_1 / \lambda_2$.

## 4. Transformation of images

In our previous method, we found areas with approximately the same vibrational amplitude in test resonators from the two-dimensional correlation images over the entire surface of the resonators, and then we estimated the vibrational displacement in each marked area [8,9].

We propose a new vibrational distribution estimation algorithm for deriving whole vibrational displacement over the entire surface of the resonator using partial displacement measurement and two-step transformations of the two-dimensional correlation images.

1) The differential interference intensity for resonator- resting and resonator-driving states is given by the inverse transformation of the correlation equation based on the probability theory.

2) The vibrational amplitude is obtained by substituting the above differential interference intensity into the inverse function of (1).

## 4. Experimental results

On the basis of our method, we estimated the measured absolute vibrational amplitude [7]. Five hundred image pairs were accumulated and averaged to reduce the CCD and environmental noises.

**Figure 2** shows the measured in-plane displacement vs. the absolute displacement. The dotted line represents the ideal characteristics. It is clear from Fig. 2 that the measurement error of +25 nm was observed at 60 to 100 nm. However, the minimum measurable value was expanded to 20 nm compared to 50 nm reported in the previous paper [9]. This improvement is a consequence of applying higher order polynomial expression to the interference relation. The maximum measurable value of 160 nm is limited by the wavelength of the violet laser

**Figures 3**(a) and (b) show the experimental results of full-field in-plane motion of fundamental TS-mode in a 16 MHz quartz crystal resonator. It is clear from the figures that the proposed image transformation method gives the linear mode shape from the 2D correlation image.

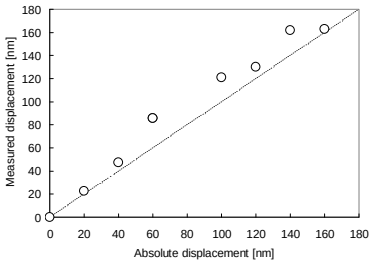


Fig. 2 Experimental results of displacement measurement.

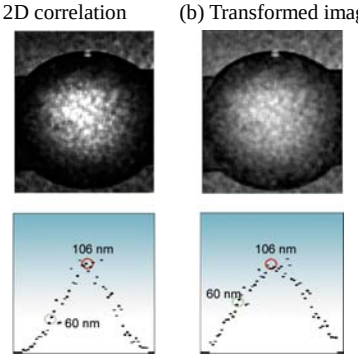


Fig. 3 Experimental results of in-plane motion of quartz resonator.

## 5. Conclusions

We have improved the mode shape visualization method, which is based on a novel two-dimensional image transform; and simultaneous device irradiation with two lasers with different wavelengths.


## Acknowledgment

This work was partially supported by Grant-in-Aid for Scientific Research (C), No. 20560399, MEXT, Japan.


## References


1. Y. Watanabe, Y. Shikama, S. Goka, T. Sato and H. Sekimoto: Jpn. J. Appl. Phys. **40** (2001) 3572.
2. Y. Watanabe, T. Tominaga, T. Sato, S. Goka and H. Sekimoto: Jpn. J. Appl. Phys. **41** (2002) 3313.
3. Y. Watanabe, T. Sato, S. Goka and H. Sekimoto: Proc. IEEE Ultrasonic Symp., 2002, pp. 928.
4. Y. Watanabe, S. Goka, T. Sato and H. Sekimoto: IEEE Trans. Ultrason. Ferroelectr. and Freq. Control **51** (2004) 491.
5. Y. Watanabe, K. Tsuno, T. Tsuda, S. Goka, T. Sato and H. Sekimoto: Proc. 2004 Annu. Symp. Freq. Control, 2004, pp. 591.
6. Y. Watanabe, K. Tsuno, T. Tsuda, S. Goka and H. Sekimoto: Jpn. J. Appl. Phys. **44** (2005) 4440.
7. Y. Watanabe, T. Tsuda, S. Ishii, S. Goka and H. Sekimoto: Jpn. J. Appl. Phys. **45** (2006) 4585.
8. Y. Watanabe, S. Ishii, S. Goka, H. Sekimoto, M. Kato and T. Tsuda: Proc. 2006 Annu. Symp. Freq. Control, 2006, pp.554
9. Y. Watanabe, N. Imaeda, S. Ishii, S. Goka, T. Sato and H. Sekimoto: Proc. 2007 Annu. Symp. Freq. Control, 2007, pp.160-163.
10. Y. Watanabe, H. Kitabori, S. Goka, T. Sato and H. Sekimoto: Trans on IEICE, **J86-C** (2003) 1337.
11. Y. Watanabe, T. Sato, S. Goka and H. Sekimoto: Acoust. Sci. & Tech. **23** (2002) 284.

3P2b-5

Proceedings of Symposium on Ultrasonic Electronics, Vol. 29 (2008) pp. 375-376
11-13 November, 2008

# Visualization of elastic waves by photorefractive imaging method

フォトリフラクティブ映像法による弾性波の可視化

Takahiro Miura[1†], Makoto Ochiai[1], Yoshikazu Ohara[2] and Kazushi Yamanaka[2]
([1] Power Systems Company, Toshiba Corp.; [2]Tohoku Univ.)
三浦崇広[1†]，落合誠[1]，小原良和[2]，山中一司[2] （[1]東芝　電力システム社; [2]東北大 工）

## 1. Introduction

Recently, nondestructive testing (NDT) is increasingly important because of social demand for structural reliability, manufacturing-quality assurance, etc. Ultrasoinc testing (UT) is commonly adapted to NDT, but it is difficult to reduce the inspection time due to contact of transducers and limitated inspection area. The real-time photoractive (PR) imaging [1] of 2D ultrasonic waves has a potential of reliable and high-speed inspection, though it has not been applied to diffraction and scattering at defects.

The authors improved the PR imaging by the phase difference (PD) method[2]. In this work we apply it to diffraction analysis of travelling waves at a slit with high signal to noise ratio (S/N).

## 2. Principle of PD method

The phase of a signal optical beam $I_S$ reflected or scattered from a vibrating object is given as

$$\delta_s = \delta_1 \sin(\omega_s t + \varphi_s) = 4\pi\xi/\lambda \sin(\omega_s t + \varphi_s)$$

where $\xi, \omega_s, \varphi_s, \lambda$ are the vibration amplitude, angler frequency, the phase and the optical wavelength, respectively. The phase of the reference beam $I_R$ is modulated as $\delta_R = \delta_2 \sin(\omega_R t + \varphi_R)$, by using an electro-optic modulator (EOM), where $\delta_2$ is the modulation amplitude, $\omega_R$ is the angler frequency and $\varphi_R$ is the phase. The signal and reference beams form a diffraction grating in the PR crystal. The reference beam is diffracted to form an image, but a small fraction of the signal beam is also transmitted as a background $I_B$ which degrade the S/N of images. However, the intensity of image in the PD method is [2],

$$\begin{aligned}\Delta I &= I(\varphi_R^+) - I(\varphi_R^+ + \pi) \\ &= 8 I_R e^{-\alpha L/\cos\theta} (\Gamma L/2)^2 \times M^2 J_0(\delta_1) J_1(\delta_1) \\ &\quad J_0(\delta_2) J_1(\delta_2) \cos(\Psi - \varphi_s + \varphi^+)\end{aligned} \quad (1)$$

where $\alpha$ is the optical absorption coefficient, $L$ is the thickness of the diffraction grating, $2\theta$ is the angle between the signal and reference light, $\Gamma$ is the two-wave mixing coefficient, $M$ is the visibility of the interference fringe, $J_n$ is the Bessel function of the first kind, $\Psi = \tan^{-1}(\Omega\tau)$, $\Omega = \omega_S - \omega_R$ is the frequency difference and $\tau$ is the photorefractive response time. It is important to note that Eq (1) gives higher sensitivity than in conventional PR method, since the background $I_B$ is removed by subtraction in the right hand side.

## 3. Experimental setup

**Figure.1** shows an experimental setup. The laser beam was divided into two beams with the polarized beam splitter (PBS). One beam irradiated the PRC, whose phase is modulated by the EOM, as the reference beam. The other beam irradiated the specimen, and the signal beam reflected or scattered from the specimen irradiated the PRC after image transfer by 2 camera lenses.

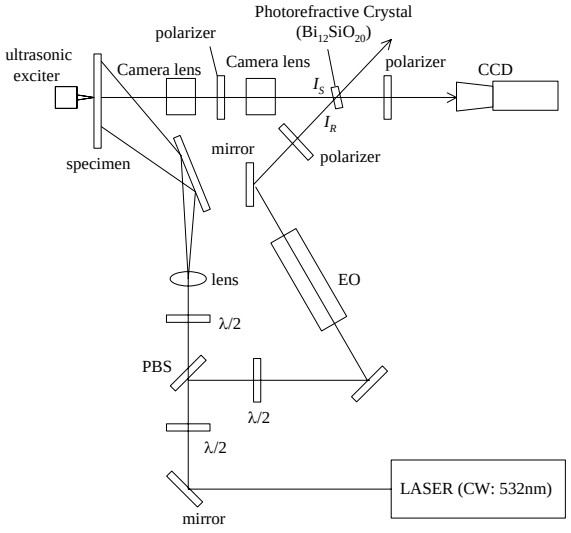


Fig. 1 Experimental setup

The imaging area was ϕ30-40mm. The signal and reference beams interfered each other in the PRC to form a diffraction grating, and therefore the reference beam was diffracted by the grating and acquired as an interference image by a CCD camera

For large area inspection, it is important to

takahiro.miura@toshiba.co.jp

detect traveling waves propagating to wide area rather than standing waves confined within boundaries. In this study, we use a copy paper 0.1mm in thick as a tentative specimen. The CCD camera image of specimen surface is shown in **Fig. 2**. The paper had a slit (tear) with 12mm length shown in the lower right part of the image. Ultrasonic wave was excited at the center of the image by a piezoelectric transducer. The excitation frequency was 48kHz and the reference beam frequency was modulated to 47.999kHz, and therefore the difference frequency Ω=1Hz. Induced ultrasonic amplitude measured by heterodyne interferometer was about ±12nm.

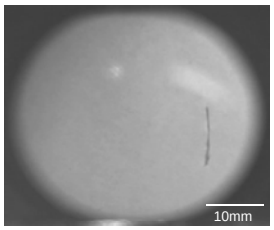


Fig. 2 Image of paper surface

Total laser power was 0.8W, the signal beam power was 22μW and the reference beam power was 2.1mW at the front of BSO crystal. The integration time of the CCD camera was 100ms.

### 3. Result

**Figure 3** shows PD images of traveling waves on the paper, which it was electrically driven with different phase of the reference beam modulation.

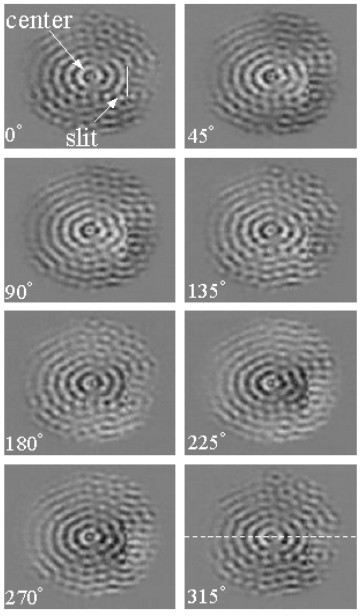


Fig. 3 Traveling waves on the paper

It is clear that traveling waves were generated concentrically on the paper by piezoelectric transducer. The traveling wave reached the slit, and changed its direction due to diffraction at the slit.

**Figure 4** shows magnified image at the slit. In the PD method image (Fig.4(a)), it is clear that the phase of the traveling waves was changed at the slit as indicated between the allows. For sensitivity improvement, we averaged the PD method image for 10 cycles as shown in Fig.4(b). It is clearer because high spatial frequency noises were removed by the averaging.

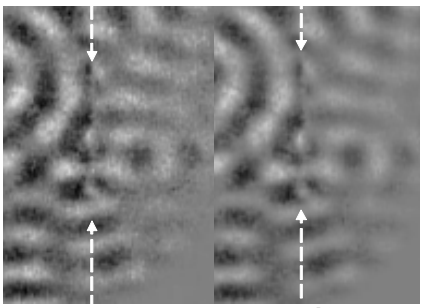


Fig. 4 Magnified image at the slit. (a) PD method image. (b) Averaged PD method image for 10 cycles.

**Figure 5** shows an amplitude profile along the dotted line in Fig. 3 (315° ) through the center of concentric traveling wave (350 pixel), and the slit position (450 pixel). At the position of slit (450 pixel), the traveling wave was disappeared, in contrast to at the position of 250 pixel where there was no slit.

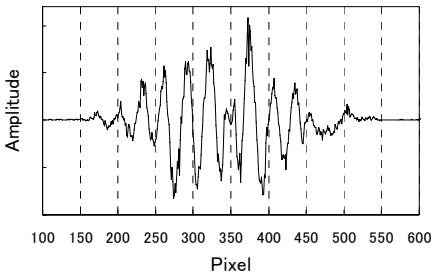


Fig. 5 Amplitude profile of traveling waves

### 4. Conclusion

We applied the PD method, including that using an improved signal analysis, to imaging of diffraction behavior of traveling ultrasonic waves on a paper, and observed clear phase change at a slit. We will apply this technique to inspection of metal structures in the future.

### References

1. K. L. Telschow, V. A. Deason: Ultrasonics 40(2002)1025-1035.
2. K. Yamanaka, K. Aizu, S. Sakai, A. Mizukami and H. Cho: Key Engineering Materials. 261-263 (2004) 969-974.

Proceedings of Symposium on Ultrasonic Electronics, Vol. 29 (2008) pp. 377-378
11-13 November, 2008

# Imaging of surface acoustic wave reflection and focusing using circular, ellipsoidal and parabolic boundaries

円、楕円、放物線境界での表面音響波の反射や収束のイメージング

Motonobu Tomoda [1†], Oliver B. Wright [1], Kosei Ueno [2], Yoshiaki Nishijima [2], Saulius Juodkazis [2], and Hiroaki Misawa [2] ([1] Graduate School of Engineering, Hokkaido University; [2] Research Institute for Electronic Science, Hokkaido University)

友田基信 [1†]，Oliver B. Wright [1]，上野貢生 [2]，西島喜明 [2]，Saulius Juodkazis [2]，三澤弘明 [2]（[1] 北海道大学大学院工学研究科；[2] 北海道大学電子科学研究所）

## 1. Introduction

Gigahertz surface acoustic waves (SAW) are now in common use in filters inside cellular phones. SAW's are also put to use for the nondestructive testing of the thickness or elastic properties of thin films. SAW's can be confined on the surface of a substrate in resonator configurations often making use of interdigital electrode technology.[1] The best way to investigate fundamental SAW behavior in such confined geometries is by imaging the acoustic wave field. Real time imaging brings the additional advantage of allowing the evolution of the wave field to be studied in two dimensions.

By exploiting a nondestructive and noncontact optical SAW excitation and imaging technique,[2-4] we investigate the real time propagation of SAW in confined or partially confined geometries. In particular we image the reflection and focusing of gigahertz SAW's using microscale circular, ellipsoidal and parabolic boundaries in a crystalline silicon substrate.

## 2. Imaging system

**Fig. 1** shows a schematic diagram of the imaging system. The method is based on the optical pump and probe technique, making use of a Sagnac interferometer and an optical scanning system.[4] We make use of a mode-locked Ti:Sapphire femtosecond laser system that delivers ~100 fs duration infrared optical pulses at a repetition rate of 80.4 MHz (one pulse every 12.4 ns). We operate with pump and probe pulses at wavelengths of 415 nm and 830 nm, respectively. An acousto-optic modulator (AOM) is used to chop the optical pump beam at 1 MHz. The pump pulse energy ~ 0.1 nJ, selected at about half the damage threshold, is focused to a ~2 $\mu$m diameter spot on the sample surface using a (50×) microscope objective lens. This pump pulse generates SAW's at frequencies up to ~1 GHz, with a typical SAW pulse duration ~1 ns. The optical probe beam passes through a optical delay line and then into the Sagnac interferometer.[4] The probe spot position can be scanned in two dimensions over the sample surface by controlling a two-axis rotating mirror. After each pump optical pulse, two probe pulses are reflected from the sample and pass back into the interferometer for measurement of their phase difference, approximately proportional to the outward velocity of the sample surface. Synchronous detection of the interferometer output from a photodetector is achieved with a lock-in amplifier referenced to the pump chopping frequency. The typical surface displacements measured are ~10 pm. It takes approximately 5 minutes to obtain a 100 $\mu$m×100 $\mu$m raster scan

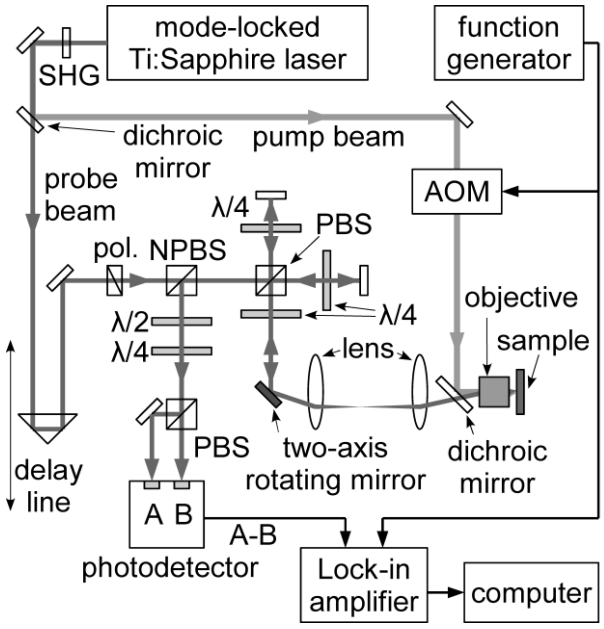


Fig. 1. Schematic diagram of the imaging system. SHG: second harmonic generation crystal, AOM: acousto-optical modulator, pol.: polarizer, NPBS: non-polarizing beam splitter, PBS: polarizing beam splitter, λ/4: quarter-wave retarder, and λ/2: half-wave retarder.

e-mail address: mtomoda@eng.hokudai.ac.jp

image with a 1 $\mu$m step. Animations up to 12.4 ns can be obtained by varying the delay time between the pump and the probe pulses.

### 3. Samples

Micro-fabrication methods including lithography and dry etching are used to make the samples. The samples are fabricated on a silicon (100) wafer by plasma dry etching using a $SF_6$ and $C_4F_8$ gas mixture. The use of two gases ensured etching of structures with vertical side walls. The etching was carried out in a sequence of etching ($SF_6$) and passivation ($C_4F_8$) steps in alternation. The overall etching rate was ~1 $\mu$m min$^{-1}$, ensuring speedy preparation. Grooves of depth and width ~10 $\mu$m are formed in the shape of circles, ellipsoids and parabolas. The sample is then coated with a polycrystalline chromium film of thickness ~40 nm by rf sputtering to enhance the optical pump pulse absorption and probe pulse reflection. Optical reflectivity images of the circular and parabolic boundaries are shown in **Fig. 2 (a)** and **(c)**.

### 4. Results and discussion

SAW propagation images for these samples were obtained as animations with 30 frames over 12.4 ns. We show in **Figs. 2 (b)** and **(d)** typical SAW images for circular and parabolic shape boundaries.

The silicon (100) surface shows fourfold rotational symmetry in its linear elastic properties. SAW's propagating along [010] (and in equivalent symmetry directions) are Rayleigh-like modes.[5] SAW's propagating along [011] (and in equivalent symmetry directions) are pseudo-SAW modes.[5] Due to the very thin Cr film, our measured propagation velocities ~5 km s$^{-1}$ are very close to the values for bulk Si.[6] The slight difference in SAW and PSAW velocities produces slight deviations from circular wave fronts, as is evident at 6.2 ns in **Fig. 2 (b).**

In **Fig. 2 (b)**, corresponding to a circular resonator, the anisotropy of the substrate causes the reflected SAW wave front at 18.6 ns to be square shaped, after which time the waves focus to a point in a symmetrical position with respect to the optical pump spot (the black spot in the figure). In **Fig. 2 (d)** corresponding to a parabolic boundary, the SAW pulses are excited near the focus. The reflected wave fronts are approximately straight. We also have made animations of SAW's inside elliptical boundaries, and have observed that SAW's excited near one focus converge to the second focus. We are at present investigating precisely how the Si anisotropy affects the evolution of the wave front shapes on reflection.

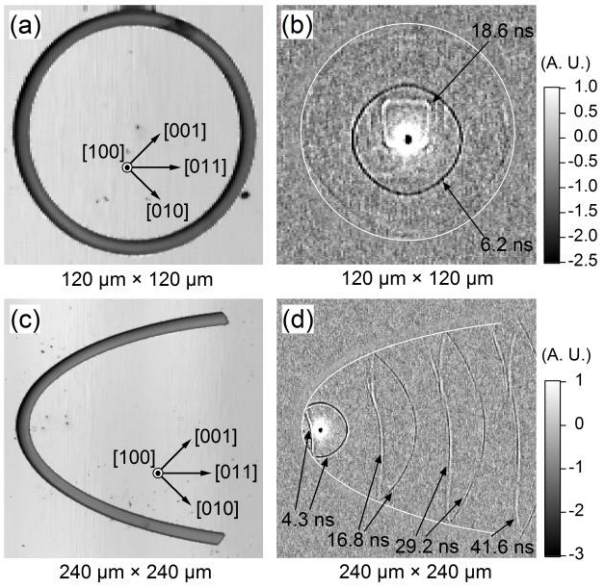


Fig. 2. (a) Optical reflectivity image of a circular resonator of internal diameter 100 $\mu$m. (c) Optical reflectivity image of a sample with a parabolic boundary. The substrate is a Si (001) covered with a 40 nm polycrystalline Cr film. (b), (d) snapshots of the SAW propagation corresponding to the samples of (a) and (c), respectively. The times after pumping are indicated by the arrows.

### 5. Conclusions

In conclusion we have observed SAW reflection and focusing using microscale circular, ellipsoidal and parabolic boundaries in a crystalline silicon substrate. Further work of interest involves increasing the optical excitation energy in order to produce nonlinear acoustic resonances in microscale cavities. Imaging the waves in real time should allow novel effects to be categorized, such as shock waves or instabilities.

### References


1. R. Weigel *et al.*: IEEE Trans. Micro. Theory Tech. **50** (2002) 738.
2. Y. Sugawara *et al.*: Phys. Rev. Lett. **88** (2002) 185504.
3. O. B. Wright, O. Matsuda and Y. Sugawara: Jpn. J. Appl. Phys. **44** (2005) 4292.
4. T. Tachizaki *et al.*: Rev, Sci. Inst. **77** (2006) 043713.
5. R. E. Vines, M. R. Hauser and J. P. Wolfe: Z. Phys. B **98** (1995) 255.
6. H. Coufal *et al.*: J. Acoust. Soc. Am. **95** (1994) 1158.

Proceedings of Symposium on Ultrasonic Electronics, Vol. 29 (2008) pp. 379-380
11-13 November, 2008

# Real-time imaging of GHz acoustic waves on bulk acoustic resonators

バルク音響振動子における GHz 音響波伝搬の
実時間イメージング

Takashi Fujikura[1‡], Osamu Matsuda[1], Oliver B. Wright[1], Jeremy Masson[2] and Sylvain Ballandras[2]
([1] Grad. Sch. Eng., Hokkaido Univ., Sapporo, Japan; [2] FEMTO-ST, Besancon, France)
藤倉崇[1‡], 松田理[1], Oliver B. Wright[1], Jeremy Masson[2], Sylvain Ballandras[2]
([1] 北海道大 工; [2] FEMTO-ST, Besancon, France)

## 1. Introduction

Acoustic devices are indispensible for wireless communication systems. In particular, surface acoustic wave (SAW) devices are widely applied in the telecommunications industry. Film bulk acoustic resonators (FBAR) are under development because of their compact construction[1]. For high frequency operation up to several GHz, FBAR's make use of the thickness resonance of thin piezoelectric films. To evaluate such filters, electrical measurement and mathematical simulation are useful tools. Another tool is the imaging of surface vibration, allowing the vibrational modes to be directly accessed.

Both optical and local probe methods for imaging bulk acoustic resonances and SAW on FBAR's have been reported[2-5]. These studies are useful for understanding the device acoustics and reveal leakage of acoustic waves from the device. Such measurements have been carried out in the frequency domain, and the frequency range has been limited to relatively narrow bands for each investigation.

Here we propose a wideband time-resolved technique to increase the frequency range of the measurements on FBAR devices, based on an ultrafast optical imaging technique combined with electric excitation. The electrical excitation is synchronized with the ultrashort probe laser pulses. Acoustic waves over a broad frequency range (100 MHz-2.5 GHz) are excited and imaged. By the use of Fourier transforms, we extract the acoustic wave amplitude at each frequency and the acoustic dispersion relation.

## 2. Experimental setup

The experimental setup is shown in **Fig. 1**. We use an optical pump and probe technique and a common-path interferometer[6]. The FBAR, shown in **Fig. 2**, consists of a thin film of AlN of thickness 2 $\mu$m, and is coated with a Pt electrode[7]. The fundamental resonance frequency is 120 MHz, with resonances up to the GHz range.

We use a mode-locked Ti:Sapphire laser of

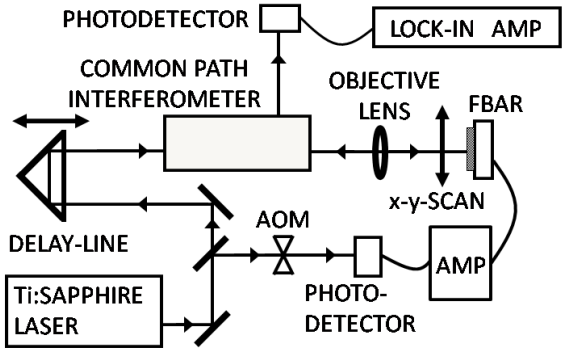


Fig. 1 Experimental setup

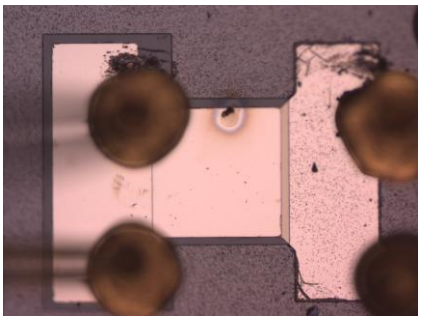

Fig. 2 Optical micrograph of the FBAR

central wavelength 830 nm, pulse duration ~200 fs, and repetition rate 76 MHz. The laser beam is divided into two, one for the probe light and another for use in a high bandwidth (~3 GHz) photodetector. The photodetector output is fed to a wideband amplifier whose output is connected to the FBAR device. The electrical pulses driving the FBAR are thus synchronized to the probe optical pulses. The excitation optical beam before the photodetector is modulated at 1 MHz for purposes of synchronous detection using a lock-in amplifier at this frequency. The probe light beam passes through a variable (up to 4 m) delay line. Sets of two probe pulses separated by a time interval of 100 ps are focused to a ~2 $\mu$m spot on the sample with a ×50 objective lens, and are raster scanned over its surface. The reflected probe pulses enter a

common-path interferometer where they are combined for detection of optical phase variations that are directly proportional to the normal velocity of the sample surface. The displacements of the sample surface are resolved to ~1 pm resolution. The typical image size is 220 $\mu$m × 220 $\mu$m, with an acquisition time of 20 min. To form an animation we measure 60 images over the ~13 ns interval between optical (or electrical) pulses.

### 3. Experimental results

We have obtained images over the frequency range 100 MHz-2.5 GHz. Typical results in the time domain are shown in **Fig. 3**.

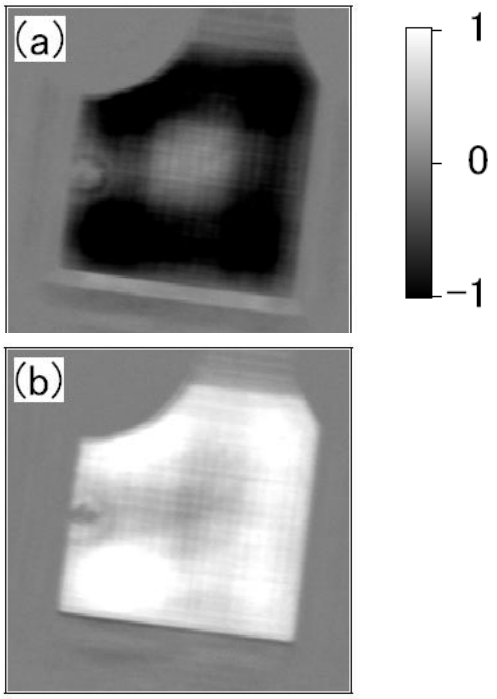


Fig. 3 Experimental time-resolved surface vibration images for a 220 $\mu$m × 220 $\mu$m region of the FBAR. (a) and (b) correspond to a time difference of 6790 ps.

The mode patterns seen correspond to a combination of surface acoustic and bulk acoustic waves. The temporal Fourier transfoms (not shown) are used to obtain the mode patterns at frequency intervals of 76 MHz. In addition to the bulk thickness resonances periodic in the fundamental resonance frequency, we also observe SAW resonances and SAW leakage from the device (though not very clear in Fig. 3 outside the region of the FBAR due to the poor contrast).

### 4. Conclusions

We have demonstrated the real-time imaging of electrically-excited acoustic waves over a wide frequency range in bulk acoustic resonators by means of an ultrafast optical technique. This imaging system should prove useful for the evaluation of acoustic devices which operate in the GHz region .


### Acknowledgment

We are grateful to P. Muralt for the fabrication of the FBAR samples.


### References


1. R. Weigel, D. P. Morgan, J. M. Owens, A. Ballato, K. M. lakin, K. Hashimoto, and C. C. W. Ruppel: IEEE Trans. Micro. Theory Tech. **50** (2002) 738.
2. J. V. Knuuttila, P. T. Tikka, and M. M. Salomaa: Opt. Lett. **25** (2000) 613.
3. K. Kokkonen and M. Kaivola: Appl. Phys. Lett. **92** (2008) 063502.
4. J. E. Graebner, B. P. Barber, P. L. Gammel, and D. S. Greywall: Appl. Phys. Lett. **78** (2001) 161.
5. H. Safar, R. N. Kleiman, B. P. Barber, P. L. Gammel, J. Pastalan, H. Huggins, L. Fetter, and R. Miller: Appl. Phys. Lett. **77** (2000) 136.
6. T. Tachizaki, T. Muroya, and O. Matsuda: Rev. Sci. Instrum. **77** (2006) 043713.
7. J. Masson, G. Martin, R. Boudot, Y. Gruson, S. Ballandras, A. Artieda, P. Muralt, B. Belgacem, and L. Chomeloux: Proc. IEEE Frequency Control Symposium, (2007) p.741.

3P2b-8

Proceedings of Symposium on Ultrasonic Electronics, Vol. 29 (2008) pp. 381-382
11-13 November, 2008

# Real time imaging and dispersion behavior of Lamb waves in an elastic wedge

くさび構造におけるラム波伝播の実時間イメージングと分散解析

Shinnosuke Matsueda†, Motonobu Tomoda, Osamu Matsuda and Oliver B. Wright
(Graduate School of Engineering, Hokkaido University)
松枝真之介†，友田基信，松田理，Oliver B. Wright　（北海道大学大学院工学研究科）

## 1. Introduction

Flexural acoustic waves in plates, namely Lamb waves, show dispersion depending on the plate thickness.[1] They can be used for the nondestructive testing of plates or pipes, for example. Lamb waves are also expected in plates of non-uniform thickness, in which case their propagation becomes much more complex.[2] In particular, in a quadratic wedge the propagation time diverges as a wave packet approaches the sharp end at normal incidence, producing the so-called 'acoustic black hole' effect in which the wave is not reflected, at least in theory for a perfect wedge.

In order to elucidate this phenomenon more clearly, we implement a real time surface acoustic wave imaging technique at frequencies up to ~1 GHz with ~1 $\mu$m lateral and ~1 ps temporal resolution.[3-5] This nondestructive and noncontact method is based on the optical pump and probe technique that makes use of ultrashort laser pulses and interferometric detection of surface displacement. From the spatiotemporal Fourier transforms of our data we can also derive the acoustic dispersion relation and images of the acoustic propagation at individual frequencies.[6]

## 2. Samples

Gold wedges of various shapes are prepared by rf sputtering, making use of a programmable shutter on a translation stage inside the vacuum chamber. The substrate is a commercial silicon nitride membrane with a thickness of 2 $\mu$m (as shown in **Fig. 1**). The thickness of the gold wedge typically changes from 6 $\mu$m to zero over a length of ~200 $\mu$m in quadratic fashion.

e- mail address: matsueda@eng.hokudai.ac.jp

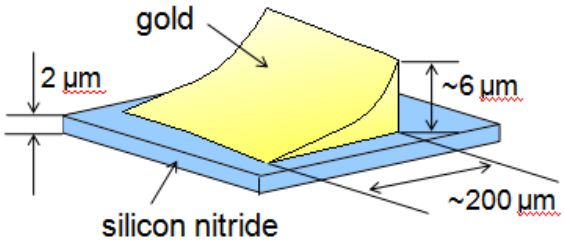


Fig. 1 Schematic diagram of a gold wedge on a silicon nitride membrane.

## 3. Imaging method

**Fig. 2** shows the measurement setup. We use a mode-locked Ti:sapphire laser of repetition rate 80.4 MHz (one pulse every 12.4 ns), a pulse width of 200 fs and a centre wavelength of 830 nm. The 830 nm beam is used for probing and a second harmonic (415 nm) beam is used for pumping. The pump optical pulses are focused on to the sample to a ~2 $\mu$m circular spot or to a line of width ~2 $\mu$m through a ×50 microscope objective. This excites Lamb wave pulses at frequencies up to ~1 GHz. Delayed probe light pulses are focused to a ~1 $\mu$m spot through the same objective lens. Changes in surface displacement are measured in a Sagnac interferometer by

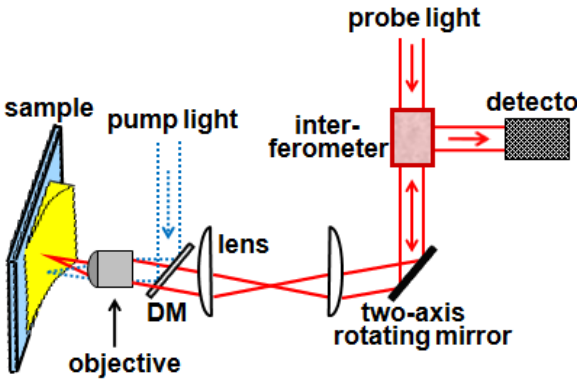


Fig. 2 Measurement setup
DM: dichroic mirror

monitoring the difference in phase between two probe light pulses as a function of the delay time between the pump and probe pulses.[5] The probe light spot is scanned in two dimensions over the sample surface using a two-axis rotating mirror. It takes 20 minutes to obtain a 200 $\mu$m × 200 $\mu$m raster scan image with a 1 $\mu$m step. In this way animations of the Lamb wave propagation can be viewed over the ~12.4 ns interval between pump pulses.

## 4. Results and discussion

We have detected Lamb waves in our structures propagating in all directions on the sample surface. We show in **Fig. 3** a typical Lamb wave image for the gold wedge sample. We observe both fast and a slow Lamb waves. These are analogous to the symmetric and antisymmetric modes in a single-component plate.[1] By taking the Fourier transform we were able to derive the dispersion relations of both modes. These dispersion relations were found to depend on the imaged region on the wedges.

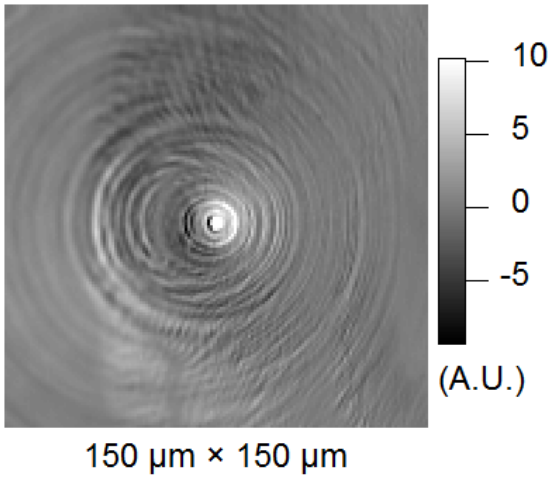


Fig. 3 Snapshot of Lamb waves on a gold wedge on a silicon nitride membrane. The left hand quarter of the image corresponds to the bare membrane. The gold wedge becomes gradually thicker towards the right (see Fig. 1).

## References

1. B. A. Auld: “Acoustic Fields and Waves in Solids”, Vol. II, Wiley, New York (1973)
2. V. V. Krylov and R. E. T. B. Winward: J. Sound Vib. **200** (2007) 43
3. Y. Sugawara, O. B. Wright, O. Matsuda, M. Takigahira, Y. Tanaka, S. Tamura and V. E. Gusev: Phys. Rev. Lett. **88** (2002) 185504
4. O. B. Wright, O. Matsuda and Y. Sugawara: Jpn. J. Appl. Phys. **44** (2005) 4292
5. T. Tachizaki, T. Muroya, O. Matsuda, Y. Sugawara, D. H. Hurley and O. B. Wright: Rev. Sci. Instrum. **77** (2006) 043713
6. Y. Sugawara, O. B. Wright and O. Matsuda: Appl. Phys. Lett. **83** (2003) 1340

3P2b-9

Proceedings of Symposium on Ultrasonic Electronics, Vol. 29 (2008) pp. 383-384
11-13 November, 2008

# Temperature Distribution Measurement in Rectangular Space by Acoustic Computerized Tomography Using Projection Data of Unequal Angular Intervals

不等角間隔投影データを用いた音響トモグラフィ法による矩形空間内部温度分布計測

Ayumu Minamide‡, Koichi Mizutani, and Naoto Wakatsuki (Univ. Tsukuba)
南出歩‡，水谷孝一，若槻尚斗 (筑波大院・シス情工)

## 1. Introduction

Temperature distribution measurement is very important in various fields, such as, for temperature control in greenhouse[1], comfort in office[2]. Thus, suiable measurement methods are required, and investigated. Among these, acoustic computerized tomography (A-CT) method[3,4] is applied to measure temperature distribution. This method is based on Radon transform. Measuring times of flights (TOFs) of acoustic waves between acoustic transducers, reciprocal of sound velocity distribution is reconstructed by the A-CT method. The A-CT method has several advantages, for example, noncontact measurement, effective use of the space, large-scale space measurement.

However not to do linear scanning and lotational scaninng, the transducers are hitherto located at equal intervals along circumference of measurement space, and pseudo linear scanning and lotational scanning whose angular intervals are equal are easily done. However, many applications are in rectangular spaces. It is inefficient to take circular arrangements of the transducers in the rectangular spaces. Since outside of the circular space could not be measured and the advantage of the effective use of the space is lost. Thus, we try to locate the acoustic transducers along the sides of the rectangular space. This causes a problem that projection data could not be obtained at equal angular intervals. Because inverse Radon transform is integral of direction of angle, projection data of unequal angular intervals could not be simply used for summation instead of the integration. In this paper, we propose new A-CT method to use projection data of unequal angular intervals. In this method, the projection data of unequal angular intervals in $r$-$\theta$ space are interpolated in two-dimension, so that the data of equal intervals are obtained. By numerical simulation, we confirm the usefulness of the proposing method.

minamide@aclab.esys.tsukuba.ac.jp

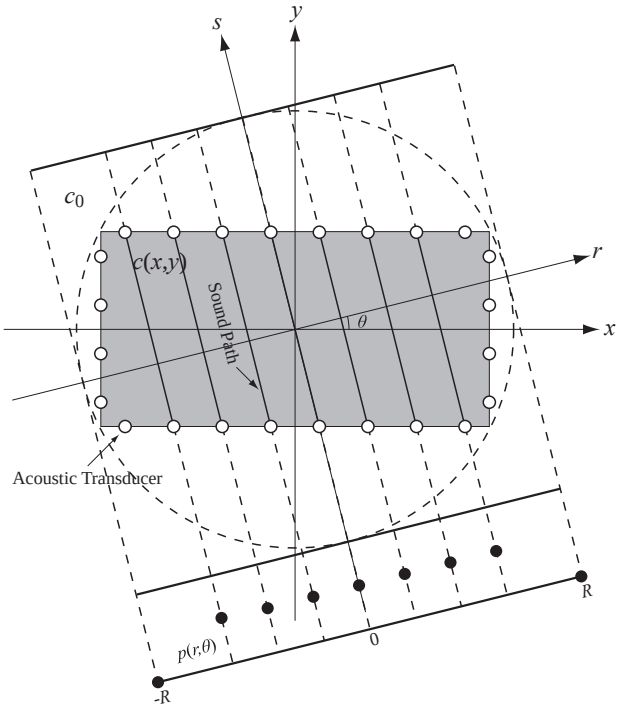


**Fig. 1** Principle of A-CT in rectangular space.

## 2. Principle

**Figure 1** depicts principle of A-CT method in rectangular space. 24 acoustic transducers are located at equal intervals along the sides of the rectangular space. Ordinary A-CT method obtains dense projection data by interpolating TOFs of parallel sound paths at $r$-axis. To use all sound paths and solve the problem of unequal angular intervals, projection data are mapped to $r$-$\theta$ surface, and interpolated at the $r$-$\theta$ surface. By the two-dimensional interpolation, all sound paths are used for reconstruction and projection data of equal angular intervals are obtained. In this paper, biharmonic spline interpolation method[5] is employed. This method is often used to illustrate contour line map from scattered data by artificial satellites. The proposed A-CT method makes a smooth curved surface from various points. Thus, biharmonic spline interpolation method is to be effective.

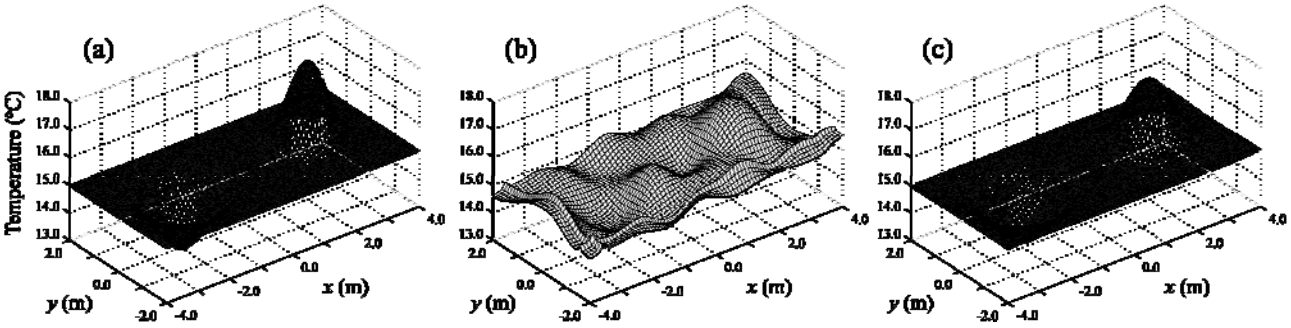


**Fig. 2** Exact and reconstructed temperature distributions. (a) Exact distribution. (b) Reconstructed from projection data of 45 ° equal angular intervals. (c) Reconstructed by the proposed method.

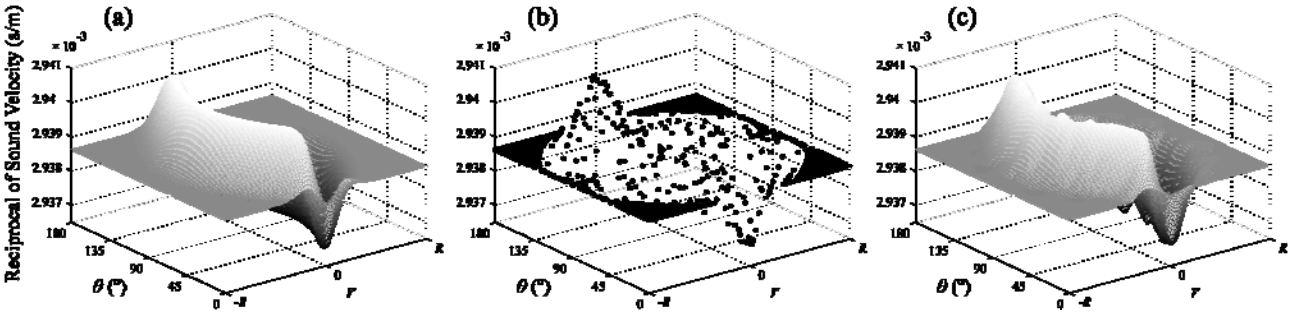


**Fig. 3** Exact, acquired, and interpolated projection data at $r$-$\theta$ surface. (a) Exact projection data. (b) .Original projection data. (c) Interpolated projection data.

### 3. Numerical Simulation

By the numerical simulation, we confirm the usefulness of the proposed method. **Figure 2** presents exact and reconstructed temperature distributions. Figure 2(a) presents exact temperature distribution in rectangular space. The size of the rectangular space is 8.0 × 4.0 ($m^2$). The temperature distribution is given by two Gaussian functions, and base temperature is 15.0 °C. One Gaussian whose 1/e width is 1.4 m and peak value is 18.0 °C, is located at (2.0 m, 0.0 m). The other is located at (-2.0 m, 0.0 m) and 1/e width is 1.8 m. The peak value is 13.0 °C. Figure 2(b) is the distribution reconstructed by ordinary A-CT method using 45 ° equal angular intervals. RMS error of the reconstructed distribution is about 0.32 °C. Peak values are about 13.73 °C at (-1.9 m, 0.1 m) and about 16.59 °C at (2.0 m, -0.1 m). Figure 2(c) is the distribution reconstructed by the proposed method. 180 projection data are used for reconstruction. The RMS error is about 0.09 °C. Peak values are about 13.21 °C at (-2.0 m, 0.0 m), and about 17.37 °C at (2.0 m, 0.0 m). **Figure 3** presents exact, acquired, and interpolated projection data at $r$-$\theta$ surface, respectively. By biharmonic spline interpolation, a smooth curved surface is obtained from Fig. 3(b), as shown in Fig. 3(c).

Since Fig. 2(b) is reconstructed from only 4 projection data, large artifacts accrue. In contrast, Fig. 2(c) is reconstructed from 180 projection data, and the artifacts decrease. Moreover, peak values approach to those of the exact distribution, and RMS error decreases.

### 4. Conclusion

By the numerical simulation, we confirmed the usefulness of the proposed method. Interpolating projection data of unequal angular intervals at $r$-$\theta$ surface, the proposed method could use all projection data. Therefore, peaks of the reconstructed distribution approach to those of the exact distribution, and RMS error decreases. As future work, experimental verification will be scheduled.


### Acknowledgment

This work was supported in part by a Grant-in-Aid for Scientific Research (B) (No. 17380149) from the Japan Society for the Promotion of Science.


### References


1. Georgios K. Spanomitsios: J. agric. Engng Res. **80** (2001) 251.
2. Sami Karjalainen, and Olavi Koistinen: Building and Environment, **43** (2007) 2880.
3. G. Höfelmann, H. O. Luck and P. Becker: J. Aerosol. Sci. **23** (1992) 51.
4. A. Minamide, K. Mizutani, and N. Wakatsuki: Jpn. J. Appl. Phys. **47** (2008) 3967.
5. Sandwell, David T: Geophysical Research Letters, Vol. 14, No. 2, (1987) 139.

3P2c-1

Proceedings of Symposium on Ultrasonic Electronics, Vol. 29 (2008) pp. 385-386
11-13 November, 2008

# Piezoelectric oscillator sensor to detect damages in a structure

Hyeoksang Kwon‡, Byungsoo Kim and Yongrae
(Kyungpook National University, Korea)

## 1. Introduction

Recent research activities on structural health monitoring (SHM) led to the development of smart sensors and integrated sensing systems in the fields of mechanical, aeronautical and civil engineering [1]. Low-cost smart sensors are key ingredients for wide adoption of the structural health monitoring technology. In particular, the electro-mechanical impedance based technique, which uses smart piezoelectric ceramic (PZT) materials, has emerged as a powerful technique for SHM [2]. This paper presents the feasibility of a piezoelectric oscillator sensor to detect the damages in structures for the SHM purpose. The oscillator sensor is composed of an electronic feedback oscillator circuit and a piezoelectric vibrator to be attached to a structure of interest. Damage to the structure causes a change of the impedance spectrum of the structure, which results in a corresponding change of the resonant frequency of the PZT patch [3]. The oscillator sensor can instantly detect the frequency change in a very simple manner. Feasibility of the piezoelectric oscillator sensor is verified with a sample aluminum plate where artificial cracks of different depth are imposed in sequence. Validity of the measurement is confirmed through comparing the experimental data with the results of finite element analysis (FEA) of the plate.

## 2. Finite element analysis

Influence of the damages on a simple structure was analyzed by the finite element method with a commercial software package, ANSYS. The FEA model contained a small PZT patch attached to an aluminum plate as the SHM sensor. The sensor in this work utilized a lateral vibration mode of the PZT patch. Damage to the plate leads to the change of the electromechanical impedance of the plate, which in turn results in corresponding change of the resonant frequency of the PZT patch. Hence observation of the resonant frequency can identify the crack geometry. Through the FEA, the change of the lateral mode resonant frequency of the PZT patch was investigated in relation to the number of cracks of a certain length and then similar analysis was performed in relation to the length of cracks assuming a single crack was present on the plate.

‡hyeoksang.kwon@gmail.com

According to the results in **Fig. 1**, the resonant frequency of the PZT patch decreased in proportion to both the length and the number of cracks. After a certain threshold length, the resonant frequency showed almost linear decrease in proportion to the crack length. For a short crack, increase of the crack number did not have much influence on the resonant frequency of the PZT sensor. However, for a relatively longer crack, the number of cracks had significant influence on the resonant frequency.

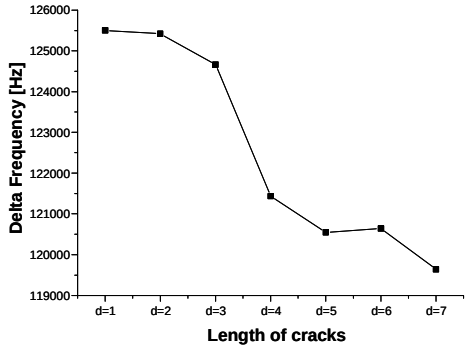


(a)

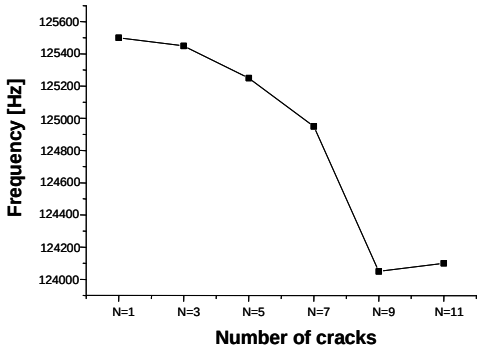


(b)

Fig. 1 Resonant frequency of the PZT sensor vs. (a) crack length and (b) crack number

## 3. Oscillator sensor experiment

Experimental oscillator sensor was fabricated with a feedback oscillation circuit and a PZT patch attached to an aluminum plate as shown in **Fig. 2**. The oscillator circuit was tuned to the lateral mode resonant frequency of the PZT element and was used to feedback the resonant signal in response to the structural condition. Response of the sensor was observed while artificial cracks of different depth were imposed in sequence. PZT is a typical

piezoceramic generating electricity in response to an external force. However, the PZT is inherently also a pyroelectric material that generates electricity in response to its environmental temperature change. During the measurement, if the PZT sensor encounters a change of its environmental temperature, the sensor generates corresponding electricity, which will be confused with the real electric signals caused by structural damages. For resolution, a dual sensor system was employed, which consisted of a reference sensor and a real sensor. The reference sensor was bonded to a small aluminum plate, and the small aluminum plate was exposed to the same environment as that for the big experimental plate specimen. The small aluminum plate with the reference sensor did not have any cracks and was stored close to the experimental specimen. The experimental specimen, thus the real sensor, was open to the effects of both the cracks and the environment while the reference plate, thus the reference sensor, was open to the effect of the environment only. Difference of the sensor signals reflected the effect of the cracks only. **Fig. 3** is the results of the measurements with the PZT oscillator sensors. As expected from the FEA results, the oscillator sensor showed changes in its oscillation frequency in proportion to the length and the number of the cracks. These results agreed well with the results of the FEA, and confirmed the validity of the present piezoceramic oscillator sensor.

However, as illustrated in Figs. 1 and 3, the response of the sensor leveled off after a certain length and number of cracks. Since each crack is apart from its adjacent crack with a constant distance, a larger number of cracks mean that latter cracks are farther from the PZT patch. Hence, Figs. 1 and 2 can be interpreted as that the PZT oscillator sensor is not so sensitive to distant cracks as it is to near cracks. The response of the oscillator sensor is limited to the area near the PZT patch, thus only local measurement is possible with the oscillator sensor. For distant cracks, more active method should be devised

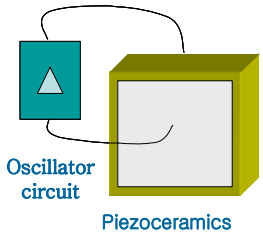


(a)

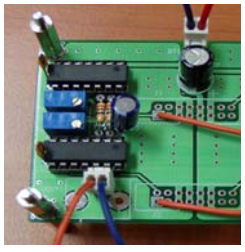

(b)

Fig. 2 Oscillator sensor; (a) schematic structure of the sensor (b) photograph of the oscillator circuit

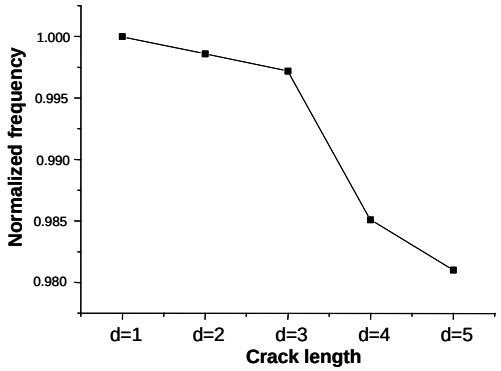


(a)

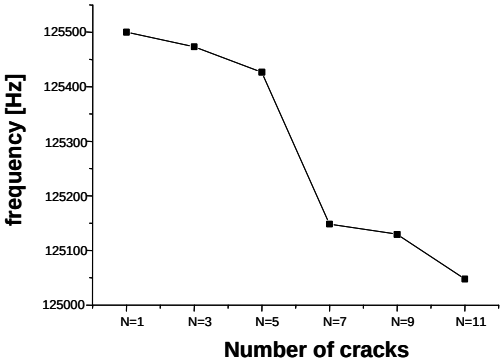


(b)

Fig. 3 Oscillation frequency change in relation to the (a) crack length and (b) crack number

## 4. Conclusions

The feasibility of the piezoelectric oscillator sensor was verified to detect the damages in structures. The oscillator sensor was composed of an electronic feedback oscillator circuit and a piezoelectric lateral mode vibrator attached to the structure of interest. The oscillator sensors could instantly detect the resonant frequency change of the piezoelectric patch in response to the change in the length and the number of cracks in the experimental sample plate. Validity of the measurement was confirmed through comparing the experimental data with the results of the FEA of the plate with cracks.

## Acknowledgment

This work was supported by by Smart Infra-Structure Technology Center (SISTeC), KAIST, Korea.

## References

1. K. K-H. Tseng, and A. S. K. Naidu:. *Smart Mater. Struct.* 11 (2002) 317.
2. W. T. Yeung and J. W. Smith: *Engineering Structures.* 27 (2005) 685
3. S. H. Park, C. B. Yun and Y. R. Roh: *J. NDT&E Int.* 40 (2007) 71.

3P2c-2

Proceedings of Symposium on Ultrasonic Electronics, Vol. 29 (2008) pp. 387-388
11-13 November, 2008

# Investigation on the reflection and transmission of Lamb waves across a rectangular crack

Byungsoo Kim‡, Hyeoksang Kwon and Yongrae
(Kyungpook National University, Korea)

## 1. Introduction

The scattering of a Lamb wave at the boundary of damages has attracted the attention of many researchers, and different methods have been reported as the tool to analyze the phenomenon [1, 2]. Most of these methods, however, have the problem that the field information like displacements and stresses at crack boundaries is presented with a single matrix that is called a global matrix. The dimension of the global matrix is likely to increase dramatically with the number of crack, thus it is almost prohibiting to analyze multiple cracks. In this paper, the repeated and sequential scattering in the crack is regarded as a summation of numerous scattering cycles, and is divided into three independent processes. Each scattering cycle is composed of two of the three processes. Instead of the single big global matrix, several small local matrices are composed, and the mode matching technique is applied to each process [1]. Reflection and transmission coefficients of a multimode Lamb wave across the crack are calculated with these local matrices per each scattering cycle. Enforcement of proper boundary conditions, normalization, and superposition of the transmitted and reflected waves from all the scattering cycles lead to the overall steady state responses at the crack boundary.

Properties of the scattered wave are highly influenced by the geometry of the crack, thus clear analysis of the dimensional effects of the crack allows more accurate evaluation of structural damages. Hence, the efficacy of the method in this paper is illustrated by investigating the effects of crack dimensions on the Lamb wave scattering. The overall reflection and transmission coefficients are analyzed in terms of the width and depth of the crack. Plate thickness is adjusted so that only the $S_0$ and anti-symmetric mode $A_0$ can exist as the incident wave at a given frequency.

## 2. Scattering mechanism

A rectangular crack of width ($g$) and depth ($d$) in a plate is presented in **Fig. 1**. If an incident wave ($W_i$) strikes $I_1$ and $I_2$ boundaries, some portion of its energy is reflected back in $R_1$, and remained portion is transmitted to $R_2$.

‡z9810029@gmail.com

When the transmitted wave strikes the boundaries $I_3$ and $I_4$, some portion of that wave is reflected back in $R_2$ while the other portion is transmitted to $R_3$. The reflected wave strikes the boundaries $I_1$ and $I_2$ again, and some portion is transmitted to $R_1$ while the other portion is reflected to $I_3$ and $I_4$, and so on. These scattering processes occur again and again, and accordingly generate transmitted and reflected waves to $R_3$ and $R_1$, respectively, until no energy is left in $R_2$. The scattering mechanism can be divided into three independent processes as shown in Fig. 1. $W_i$ is the incident wave, $W_r$ is the reflected wave, and $W_t$ is the transmitted wave. If a cycle is defined as the combination of the processes to generate a reflected wave in $R_1$ ($-x$ direction) and a transmitted wave in $R_3$ ($+x$ direction), the first cycle comprises processes 1 and 2, the second cycle comprises processes 3 and 2, and so on.

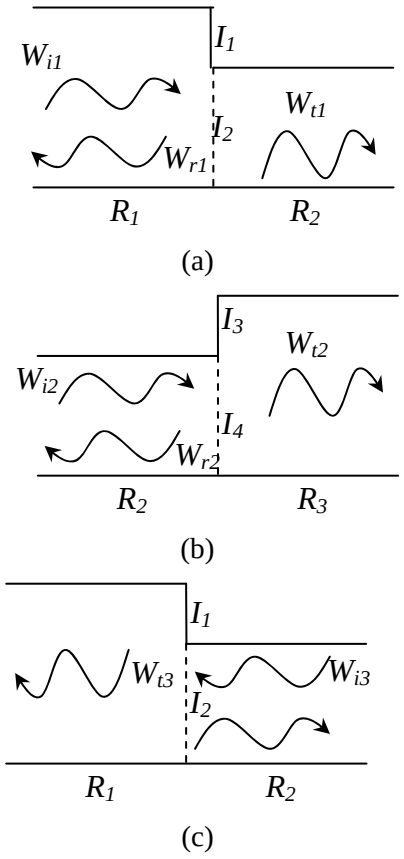


Fig. 1 The scattering mechanism: (a) process 1, (b) process 2, and (c) process 3.

## 3. Analysis

The analysis scheme is applied to an aluminium plate. Driving frequency is 100 kHz. Thickness of the plate ($H$) is 5 mm, and the size of the crack embedded in the plate is changed by varying the depth ($d$) from 0.5 mm to 4 mm and by varying the width ($g$) from 0 mm to 14 mm, respectively. In the steady state response, the first scattering cycle consists of the processes 1 and 2, and the next cycle consists of the processes 3 and 2, and so on. The reflection and transmission coefficients become more and more close to those of steady state responses as the iteration number of scattering increases. For an incident wave of $S_0$ or $A_0$ modes, the coefficients were calculated in terms of the crack geometry, $d$ and $g$, and are presented in **Figs. 2** and **3**. Fig. 2 shows that the magnitudes of transmission and reflection coefficients induced by $S_0$ incidence decrease and increase, respectively, as the depth ($d$) of a crack increases, whereas they are not affected so much by the width ($g$) of a crack. In contrast to the case of $S_0$ incidence, it is shown in Fig. 3 that the magnitudes of the coefficients induced by $A_0$ incidence are relatively sensitive to the variation of $g$ as well as $d$, and they are fluctuating in a certain pattern and have many points of inflection. As expected, the responses of $A_0$ incidence are more sensitive to the geometric variation of the crack than that of $S_0$ incidence because the wave length of $A_0$ is much smaller than that of $S_0$. In the case of the crack width close to '0', similar mode conversion was reported by Flores-López *et al* [3].

## 4. Conclusions

The local matrix scheme in this paper allows quantitative examination of the characteristics of the Lamb waves scattered by a defect in a much simpler manner than traditional methods. The technique is applicable to assess the health of a structure for ultrasonic non-destructive testing purposes [4].


## Acknowledgment

This work was supported by by Smart Infra-Structure Technology Center (SISTeC), KAIST, Korea.


## References


1. A. Lakhtakia, V. V. Varadan and V. K. Varadan: *J. Acoust. Soc. Am.* **80** (1986) 311.
2. A. Gunawan A and S. Hirose: *J. Acoust. Soc. Am.* 115 (2003) 996.
3. M. A. Flores-López M A and R. D. Gregory: *J. Acoust. Soc. Am.* 119 (2006) 2041.
4. S. H. Par, C. B. Yun, Y. R. Roh and J. Lee: *Smart Materials and Structures* 15 (2006) 957.


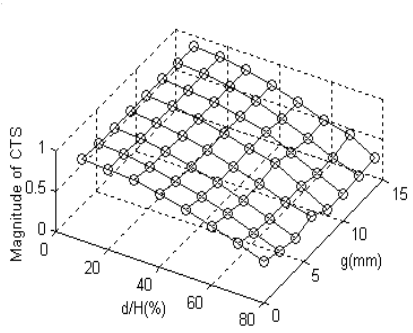


(a)

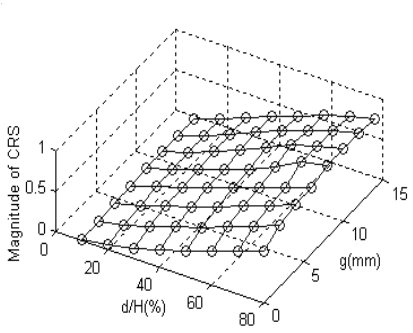


(b)

Fig. 2 Reflection and transmission coefficients when an $S_0$ mode wave is incident; $d/H$ (%) is the ratio of crack height/plate thickness: (a) transmission coefficient of $S_0$, (b) reflection coefficient of $S_0$

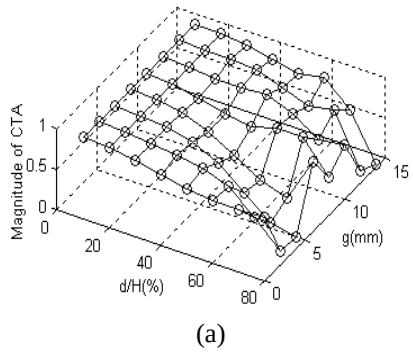


(a)

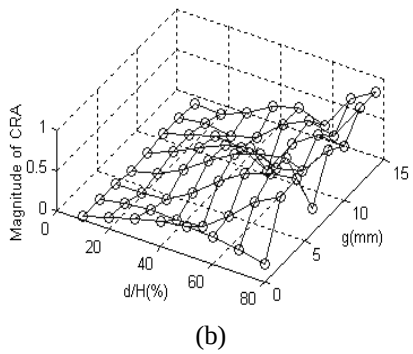


(b)

Fig. 3 Reflection and transmission coefficients when $A_0$ mode wave is incident; (a) transmission coefficient of $A_0$, (b) reflection coefficient of $A_0$

3P2c-3

Proceedings of Symposium on Ultrasonic Electronics, Vol. 29 (2008) pp. 389-390
11-13 November, 2008

# Acoustical Detection of Internal Cracks of Square Billets

# 角鋼片の内部欠陥の超音波による検出

Hideto Mitsui[1‡], Koichi Mizutani[1], Naoto Wakatsuki[1] and Masaki Yamano[2] ([1] Univ. Tsukuba; [2] Sumitomo Metal Industries,Ltd. )
三井秀人[1‡], 水谷孝一[1], 若槻尚斗[1], 山野正樹[2] ([1]筑波大院・シス情工；[2]住友金属・総技研)

## 1. Introduction

The detection of defects in screws and coils is difficult because of their complicated shapes. So it is important to detect internal cracks of billets before screws and coils are manufactured. In addition, the accuracy for the ultrasonic testing of the billets is required to be improved the quality of manufactures[1)]. The detection of internal cracks of billets mainly uses the pulse echo method although there are other methods for the ultrasonic testing[2,3)]. This method has some difficulties for treating elastic wave and mode transformation caused by the cracks. And the detection is inaccurate in some case because this method is easily affected by the shape and the direction of the cracks.

In this paper, we propose a method for a reconstruction of internal cracks using times of flights of longitudinal wave. It is possible to reconstruct the internal cracks using the sound velocity calculated from the times of flights of longitudinal wave. The crack detection is numerically tested based on the simulation of the wave propagation using the transmission-line matrix (TLM) method.

## 2. Principle of measurement

*2-1. Measurement of times of flights of longitudinal wave*

We detected internal cracks using times of flights of longitudinal wave. Longitudinal wave is the fastest elastic wave. First received wave is always longitudinal wave regardless of the condition of the area. This method can avoid the influences of other waves and mode transformation.

**Figure 1** shows transmitted wave and diffracted wave from a crack. Figure 1(a) shows the no crack case. In Fig. 1(b), incident wave is diffracted by the crack because that is cavity. $p_T$ is transmitted wave, and $p_D$ is diffracted wave from the crack. **Figure 2** shows times of flights of $p_T$ and $p_D$. Times of flights of $p_D$ are longer than that of $p_T$. Then, a sound velocity of the crack part is lower than the around area. Difference of the sound velocity makes possible to measure with or without the crack.

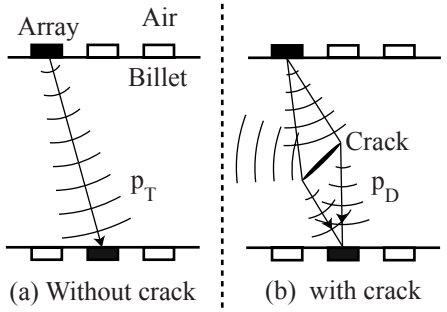


Fig.1 Transmitted wave ( $p_T$ ) and diffracted wave from a crack ( $p_D$ )

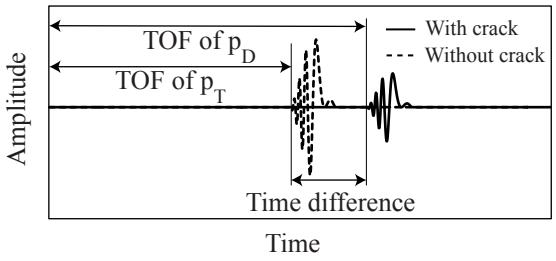


Fig.2 Times of flights (TOF) of $p_T$ and $p_D$

*2-2. Reconstruction of internal cracks using the Matrix method* [4)]

A measurement area is partitioned into ($m$, $n$) cells. The relationship between times of flights of longitudinal wave and the sound velocity is given by

$$\mathbf{T} = \mathbf{L} \cdot \mathbf{X} , \qquad (1)$$

where **T** is the times of flights of longitudinal waves, **L** is the lengths passing through the cells and **X** is the inverse number of the sound velocities in the cells. Sound paths are approximated by lines connecting the transmitters and receivers. The number of the sound paths accords with that of measured data. The number of cells is $m \times n$. **T** and **X** are column vectors whose sizes are equal to the number of the sound paths, **L** is a matrix whose size is (the number of the sound paths × the number of the cells). Solving eq. (1) yields,

$$\mathbf{X} = \mathbf{L}^{+} \cdot \mathbf{T} , \qquad (2)$$

mitsui@aclab.esys.tsukuba.ac.jp

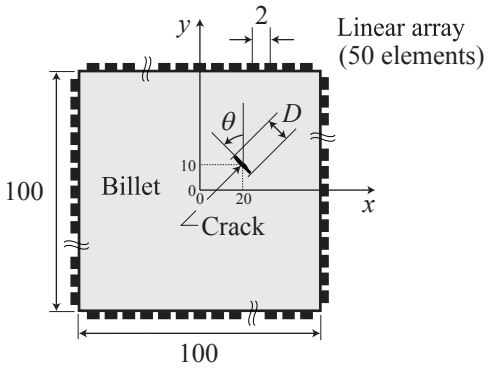


Fig.3 Simulation field of billet and internal crack

where $\mathbf{L}^+$ is a generalized inverse of $\mathbf{L}$. It is possible to reconstruct an apparent sound velocity distribution, which is expected to be related to the internal cracks

## 3. Simulation results

The simulation of the wave propagation uses the TLM method[5,6]. The TLM method is based on the Huygens' principle, which gives the time domain solution of the wave field. This study uses potential wave in view of only longitudinal wave. Other waves such as shear waves and surface waves are neglected.

**Figure 3** shows a simulation field of a billet and an internal crack. The billet is assumed to be steel (the sound velocity is 5900 m/s, the density is 7700 kg/m$^3$). The size of the billet is 100 mm square. The center of the billet is taken as the origin. The crack is located at 20 mm to $x$-axis and 10 mm to $y$-axis. The depth of the crack is $D$ mm, the width is 0.2 mm and the direction is $\theta$°. Linear arrays are set all around the billet. Each array has 50 elements, and the element pitch is 2 mm. The length of the array is 100 mm. The sampling frequency is 50.0 MHz. The transmitted signals are down chirp signals of 2.0 ± 1.0 (MHz).

**Figure 4** shows the images of internal crack reconstructed from the simulation when $D$ is 10 mm. Figure 4(a), (b), (c) and (d) show the results of $\theta$ = 0, 30, 60 and 90°, respectively. The locations of reconstructed crack in Fig.4 are in accord with those of the crack of the simulation field. Therefore, the internal crack can be detected exactly regardless of the direction of the crack. The direction of the crack conforms with $\theta$. The depth of the crack is approximately equal to $D$. **Figure 5** shows the images reconstructed from the simulation when $\theta$ is 60° with various depth $D$. Figure 5(a) and (b) respectively show the results of $D$ = 5 and 2 mm. The detection of the location of crack in Fig. 5 is as accurate as that in Fig. 4. Since the wavelength of the transmitted signals is 3 mm, it is possible to detect internal crack even if the depth of the crack is shallower than the wavelength.

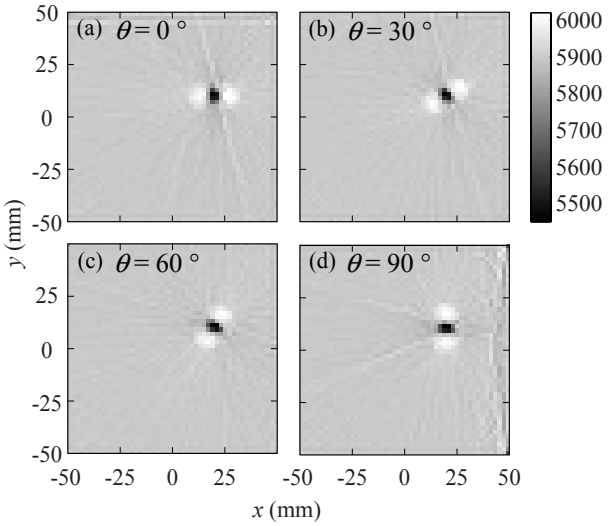


Fig.4 The images of internal crack reconstructed from the simulation. $D$ = 10 mm. (a), (b), (c) and (d) show results of $\theta$ = 0, 30, 60 and 90 °

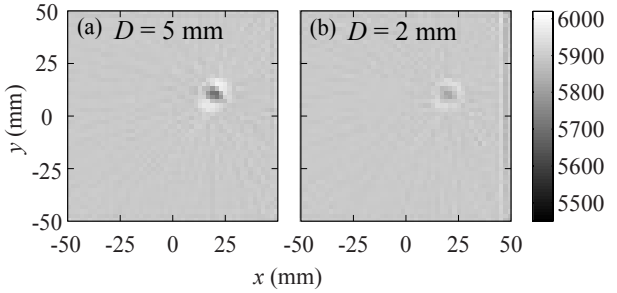


Fig.5 The images reconstructed from the simulation. $\theta$ = 60°. (a), (b) show results of $D$ = 5, 2 (mm)

## 4. Conclusions

Through the simulations, the location of internal crack could be detected exactly regardless of the shape and the direction of the crack. This is expected to be useful for the ultrasonic testing. The determination of the direction and shape of the crack remains as future work. The treatment of elastic waves as vector wave is also planned.

**References**

1. H.Yamaguchi, N.Matsubara, K.Fujisawa and S.Matsumoto: ISIJ. **70** (1984) 1210.
2. M.Ohno, T.Kato, A.Kokubo and K.Yamamoto: Jpn. J. Appl. Phys. **44** (2005) 4421.
3. R.Sasaki, T.Ogata, Y.Ohara, T.Mihara and K.Yamanaka: Jpn. J. Appl. Phys. **44** (2005) 4389.
4. K.Sawamura, K.Mizutani, Kashiwazaki and I.Odanaka: The 26th Symposium On Ultrasonic Electronics (2005) 237.
5. P.B.Johns and R.L.Beurle: Proc. IEE, vol.118, No.9 (1971) 1203.
6. W.J.R.Hoefer and P.P.M.So: John Wiley & Sons (1991)

3P2c-4

Proceedings of Symposium on Ultrasonic Electronics, Vol. 29 (2008) pp. 391-392
11-13 November, 2008

# Visualization and modal analysis of guided waves from a defect in a pipe

Nor Salim Bin Muhammad, Takahiro Hayashi, Morimasa Murase, and Shoji Kamiya
(Faculty of Engineering, Nagoya Institute of Technology)

## 1. Introduction

In our previous study, a robot arm and laser Doppler vibrometer were used for visualizing reflected waves in two regions around defect from a large number of waveforms measured on the surface of pipe [1]. To acquire more information of the propagated wave from defect, guide waves in the whole circumference of pipe around defect are visualized in this study to demonstrated the components of in plane and out of plane vibrations occur in the pipe surface respectively. We also further improved the visualized inspected areas by applying two difference signals processing emphasizing the signal of reflected wave and eliminating the incident wave excited from the used magnetostrictive transducer [3].

## 2. Laser scanning technique

In order to visualize guided wave propagation on a surface of an object, we collect waveforms at many points on the surface of the object with sufficiently small distance compared to the laser wavelength. The entire system is controlled by a PC as described in Fig.1, where the robot arm is controlled to move the focal point of laser beam according to scanning locations and to tilt the laser beam to the determined directions. At the same time axisymmetric torsional mode, T(0,1) is excited at frequency 70 kHz from a magnetostrictive transducer which attached enclosing the pipe circumference to vibrate the pipe.

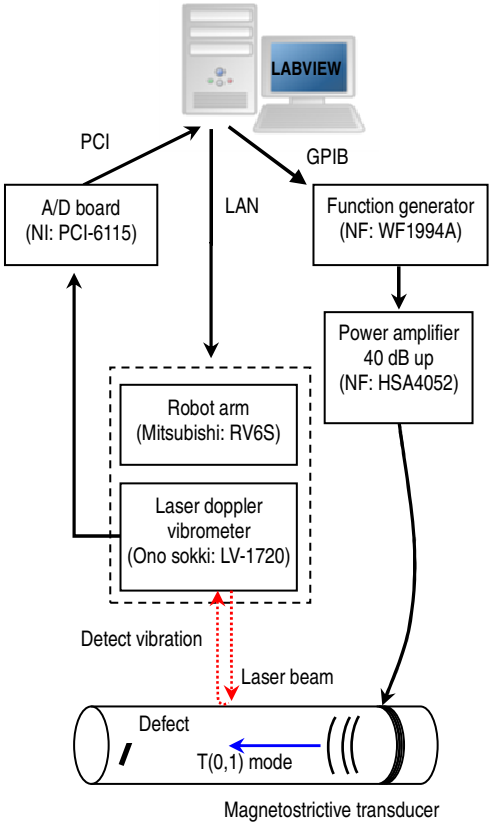


Fig.1 Laser scanning system

This paper presents guided wave inspections of test pipes which have two different artificial defects on the surface of aluminum pipes with dimensions of 4 m in length, 110 mm in outer diameter and 3.5 mm in thickness. The artificial defects on the pipe surfaces are shown in Fig.2 which Fig.2(a) consists of a file notch stretching in the circumferential direction and Fig.2(b) shown a file notch stretching in the oblique direction at angle of about 45° to the horizontal direction. Both defects were made in the size of about 40 mm in length, 10 mm in width and 2 mm in depth using a file at 500 mm from end of the pipe.

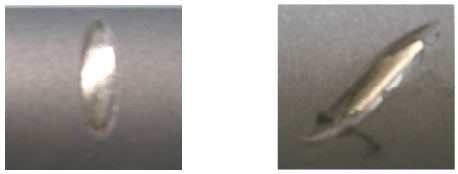

(a) Circumferential defect (b) Oblique defect

Fig.2 Artificial defects made on pipe surfaces

The enclosed surfaces on pipe circumference are scanned at many points on retro-reflection tapes attached on 12 of the scanning regions as shown in Fig.3 to improve the reflection of laser beam when scanning the surface of pipes [1].

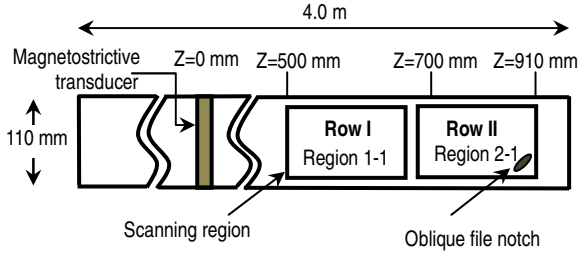


(a) Configuration of test pipe

E-mail address: chd16510@stn.nitech.ac.jp

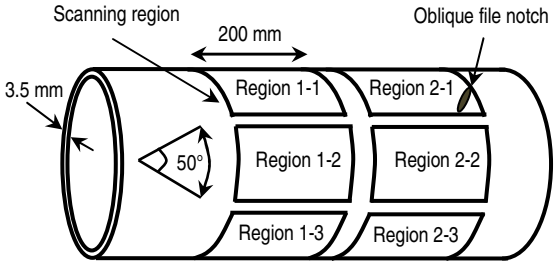


(b) Scanning regions on pipe surface

Fig.3 Visualized guided wave propagations

Fig.3(a) illustrates the location of magnetostrictive transducer, scanning regions and defect on the pipe. RF signals of guided waves were collected in the scanning area along 50° of circumferential and 200 mm of longitudinal direction in each scanning area as shown in Fig.3(b). Then, the collected RF signals from each scanning region on pipe surface was visualized in time framed images and regroup as a large image which demonstrate the simultaneous vibration of reflected wave from defect at each scanning position.

## 3. Emphasizing reflected wave from defect

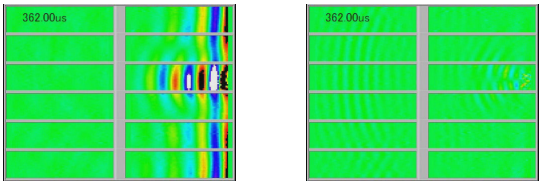


(a) In plane vibration modes (b) Out of plane vibration modes

Fig.4 Emphasized reflected wave from circumferential defect in pipe.

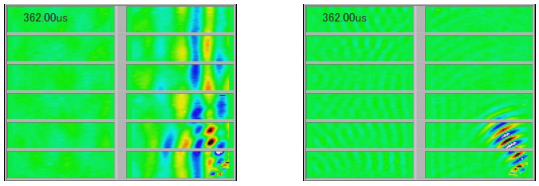


Fig.5 Emphasized reflected wave from oblique defect in pipe.

The visualized propagation of reflected wave for each mode can be obtained directly from simultaneous vibration at each scanning location. On the contrary, identification of existing defect is still difficult since the visualized image does not clearly demonstrate the propagation of reflected wave from defect. This is caused by the insignificant amplitude of reflected wave compare to incident wave and also interference of the incident wave to the reflected wave. Visualized guided wave propagations from the emphasized reflected wave are shown in Fig.4 and 5 where the propagation of stripes representing the behaviors of reflected and excited incident wave which is still remained in the visualized in plane vibration modes.

## 4. Elimination of incident wave

In the second signal prosessing technique used in this study, we eliminate the incident wave to make the propagation uncomplicated and easy to understand. The visualized images from these waveforms are shown in Fig.6 and 7 where the excited incident wave is successfully removed from the in plane vibration modes.

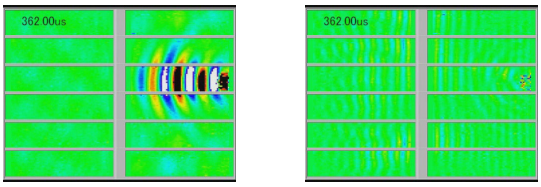


(a) In plane vibration modes (b) Out of plane vibration modes

Fig.6 Simplified reflected wave from circumferential defect.

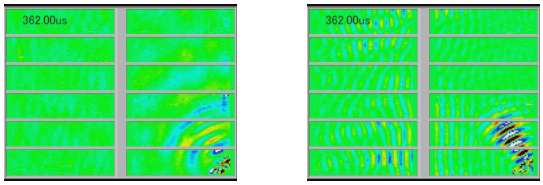


(a) In plane vibration modes (b) Out of plane vibration modes

Fig.6 Simplified reflected wave from oblique defect.

## 5. Conclusions

The incident wave of an axisymmetric torsional mode and reflected waves from defects are clearly shown for whole circumference of pipes. The visualization results exhibit the profiles of the reflected waves associate with the orientation and shape of defects on the pipe surface. This is proved as the reflected waves from circumferential defect propagate in circumferential direction of the pipe in opposite direction to incident waves and reflected waves from oblique defect propagate inclined at angle 45° according to the orientation of defect in opposite direction to incident waves.

**References**

1. T. Hayashi, Y. Kojika, K. Kataoka and M. Takikawa : *Review of progress in QNDE* **27A** (2007) pp.178-184.
2. S. Yashiro, J. Takatsubo, H. Miyauchi and N. Toyama : NDT & E International **41**(2) (2008) pp.137-144.

3P2c-5

Proceedings of Symposium on Ultrasonic Electronics, Vol. 29 (2008) pp. 393-394
11-13 November, 2008

# Defect detections of pipes using guided waves generated by an efficient transduction method with a reflector
# 反射体を利用した高効率ガイド波励起検出法による欠陥の検出

Hideo Nishino, Keiji Ogura and Kenichi Yoshida (The Univ. of Tokushima)
西野秀郎, 小倉圭二, 吉田憲一 （徳大院）

## 1. Introduction

Guided waves propagating in the axial direction of pipe [1, 2] have been anticipated for an efficient nondestructive inspection tecnique because of their capability of long range propagation. But in the case of pipes having high propagation attenuations, e.g., buried- and embedded-pipes, the propagation distances and inspection area become extremely short due to their energy leakge to the surrunding materials. Therefore an improvement of transduction efficiency of guided wave is one of the invariable and continuous themes for the exploitation of the guided wave inspection. The authors proposed an efficient transduction method with wave reflectors [3]. Efficient transduction has been realized by using the reflector located at an optimum axial position apart from the sensor. While a similar method that can be applied only at the pipe edge has been already reported [4], our method has been able to be applied to any position of the pipe. In this paper, experimetal investigations of defect detections by the efficient method are described. Experiments were carried out with the piezoelectric ring sensor system. Sensitivity with the reflector for defect detections was 2 – 2.5 times larger than that without the reflector.

## 2. Principle of the efficient transduction [3]

In general setting of the ring-shaped sensor for guided wave generation, guided waves are generated in both sides along the axis of the pipe, here we call those waves left- and right-propagating waves, respectively. When the ring-shaped reflector fixed around the pipe is located just right side of the sensor, the right-propagating wave reflects at the reflector and its propagating direction is changed (As a matter of fact, multiple reflection is occurred between the sensor and reflector). These two waves are overlapped each other. When the distance L between the sensor and the reflector equals the $n\lambda/2$ ($\lambda$:wavelength of guided wave), amplitude of the guided wave increases due to the interference. As for the efficient detection, a similar manner of the interference is took place either.

## 3. Experimental verification of defect detection

Figure 1 shows the experimental appartus. A 60.5 mm outer diameter and 4 mm thick aluminum (Al) pipe was used as a specimen. The ring-shaped piezoelectric transducer system was employed. Nowadays, this system and the magneto-strictive sensor (MsS) system are de fact standard systems for guided wave inspection. The piezoelectric system is consisted of two sets of eight piezoelectric elements. The elements of each set are located at 45° interval on circumferential position of the pipe. The two sets were respectively used as a generator and a reciever as shown in Fig.1. 2 mm thick lead (Pb) plate was sandwitched between an iron hose-fixing belt and the pipe surface was used as the reflector in the experiments. Gaussian enveloped tone-burst signals were used to generate the T(0,1) mode guided waves. The measured propagation velocity was 3120 m/s. The frequency was 50 kHz ($\lambda$ = 62 mm).

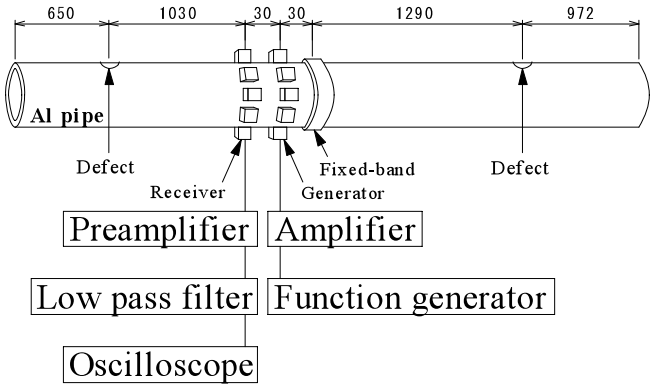


**Fig. 1 Schematic illustration of experimental apparatus**

In order to compare the sensitivities with and without the reflector, following experimental procedure was carried out. (1) The reflector was set as shown in Fig. 1 then the propagation direction was left. In this setting, the artificial defect was gradually increased (about 0.05 mm step) at the left side and was inspected. (2) The reflector was released then the propagation direction was both side. The other defect was introduced at the right side and was also inspected in the same manner of (1). The artificial defects were produced by the small grainder as shown in Fig. 2.

## 4. Results

Time domain signals generated and detected by the piezoelectric system at the defect having 1.65 mm depth (cross-sectional loss: 3.06%) with and without the reflector were shown in Figs. 3 and 4, respectively. It was confirmed that the amplitude

nishino@me.tokushima-u.ac.jp

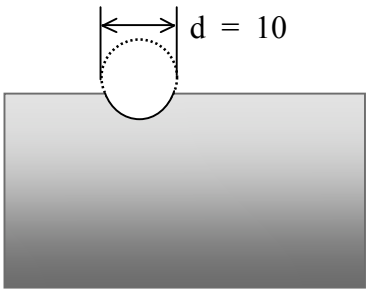


Fig. 2 Schematic side view of a pipe and defect.

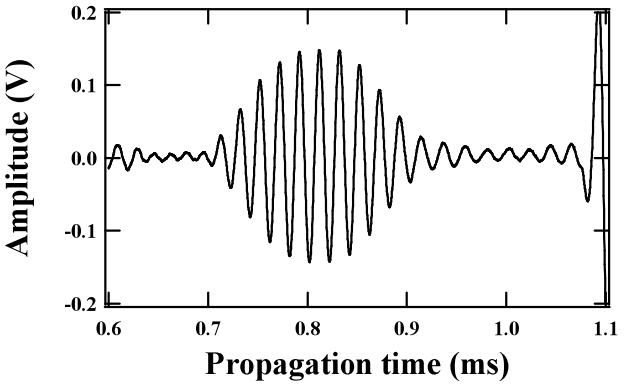


Fig. 3 Time domain signal obtained with the reflector.

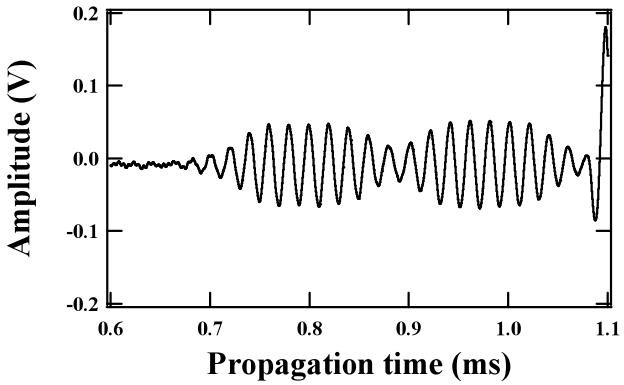


Fig. 4 Time domain signal without the reflector. The first wave packet indicates the signal of the left side defect which had already introduced in the previous experiment with the reflector.

obtained with the reflector was 2.5 times larger than that without the reflector. Enveloped time domain signals with the reflector for the different cross sectional losses (0% - 3.06%) are shown in Fig. 5. It was confirmed that the amplitude was obviously increased with increasing the cross sectional loss. Amplitude obtained with the piezoelectric transducer system as a function of cross sectional loss was shown in Fig. 6. Circles and squares in Fig. 6 indicate the amplitudes with and without the reflector, respectively. The minimum cross sectional loss that could be obtained with and without reflector was almost same at around 0.5%.

## 5. Conclusions

Evaluations of an efficient guided wave method with a reflector for defect detections were carried out by using the piezoelectric sensor system. It was confirmed that the sensitivities of the method with the reflector were 2 - 2.5 times larger than those without the reflector.

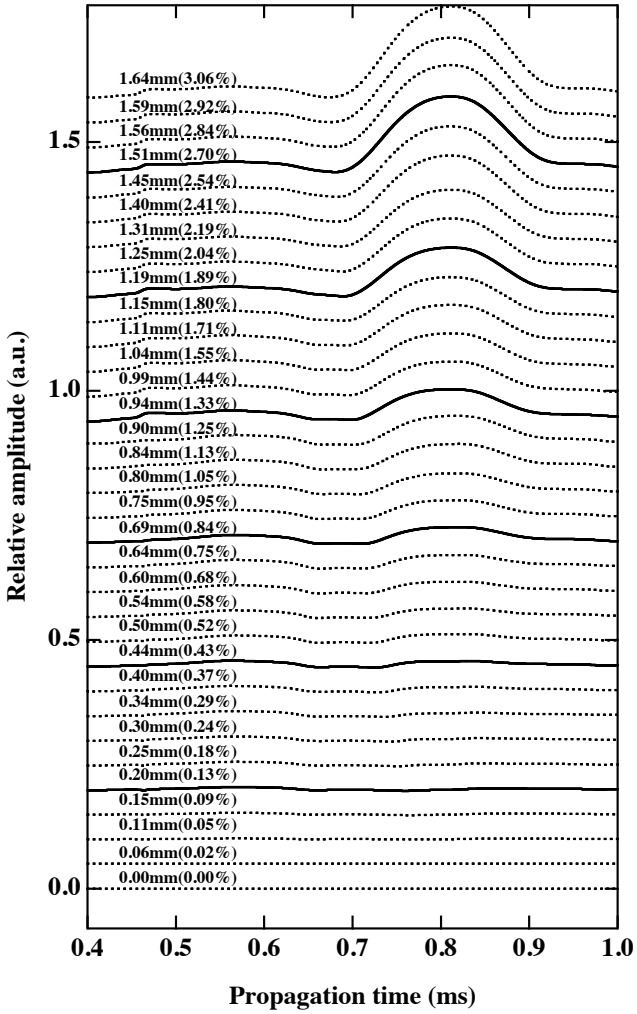


Fig. 5 Enveloped signals for different depth defects.

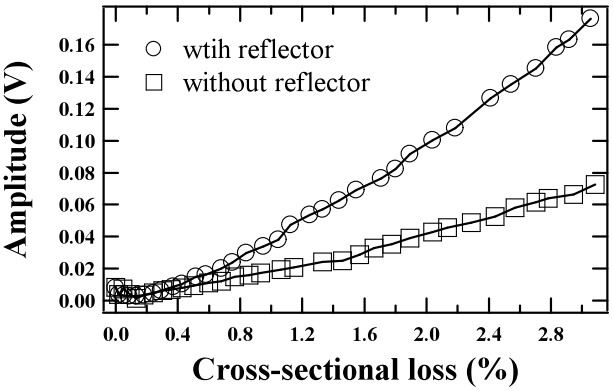


Fig. 6 Amplitude as a function of cross sectional loss.


## Acknowledgement

This work was done as a part of the Nuclear and Industrial Safety Agency (NISA) Project on Enhancement of Ageing Management and Maintenance of Nuclear Power Plants.


## Reference


1. J.L.Rose, Ultrasonic wave in solid media (Cambridge univ. press, Cambridge 1999).
2. H. Nishino et al, JJAP 40 (2001) 354.
3. H. Nishino et al, Proc. ICM&P 2008, accepted.
4. T. Yamasaki et al, Proc. 3rd US-Jpn symp Adv. Appl. and Capabil. in NDE (2005) 426.

3P6-8

Proceedings of Symposium on Ultrasonic Electronics, Vol. 29 (2008) pp. 395-396
11-13 November, 2008

# Biodiesel production from virgin and waste oils using ultrasonic reactor in pilot scale

Le Tu Thanh†, Kenji Okitsu, Yasuhiro Sadanaga, Norimichi Takenaka, Hiroshi Bandow (Osaka Prefecture University)

## Introduction

Currently, most of the biodiesel fuel (BDF) is produced by the transesterification reaction of oils with methanol in the presence of alkaline catalysts using mechanical stirring method at temperature 50-65°C [1]. This method consumes much energy because reactants must be heated up to desired temperature to occur the reaction, and also requires rather long reaction time (1-4 hours). Many studies have been done to reduce the production cost such as by the use of waste oil [2], various catalysts [3], continuous process [4]. Ultrasound irradiation can stimulate the reaction at room temperature, and the reaction time can become much shorter than mechanical stirring, therefore energy can be saved. In this study, BDF production in the pilot scale was performed by circulation process under low frequency ultrasound (20 kHz) with the input power of 1 kW. Effect of various process parameters such as the amount of KOH, molar ratio of oil to methanol and also reaction time were investigated.

## Experimental procedure

### *Materials and apparatus*

Canola oils were of commercial edible grade. Waste vegatable oils were those after domestic use, collecteted by municipal activities, and settled to remove food remainning in the oils. Potassium hydroxide (95.5%) and methanol (99%) were purchased from Wako Pure Chemical Industries.
Dr. Hielscher ultrasonic transducer model UIP 2000 having a frequency of 20kHz and total power of 1kW was used as an ultrasound source, and connected to a reactor with the working volume of 3L. System to separate glycerin and crude biodiesel fuel (BDF), and to purify BDF was designed by Kimura Chemical Plants Co., Ltd with the capacity of 100L/one batch process.

### *Procedure*

The experimental setup system is schematically depicted in Fig.1. In each experiment, 54L oil and methanol in a given molar ratio containing KOH were fed to the reactor and a circulation tank by a pump. The feeding ratio of reactants was controlled by a valve system. After 10 minutes, all reactants were transferred to the circulation tank. Feeding valves for oil and methanol were closed, and the circulation valve was opened. Then the circulation of the reactants was curried out for 60 minutes. The reaction mixture was settled overnight to separate glycerin, excess methanol, and crude BDF. The crude BDF was purified by washing 3 times with tap water (water to BDF: 20% v/v), and dried by heating up to 65°C with a mild flushing of a dry air under reduced pressure at 520torr.

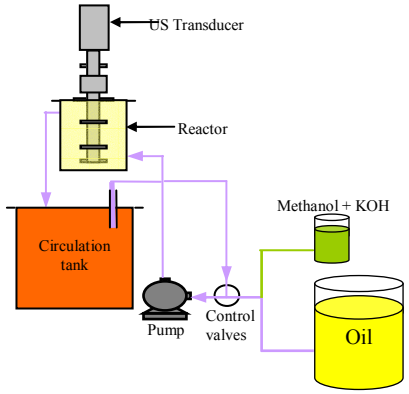


Fig.1 Schematic diagram of the setup of ultrasonic circulation process for BDF production

### *Analysis*

Reactant and products were determined by HPLC (Shimadzu LC-6A HPLC pump with RID 10A detector). The column used was Cadenza CD-C18, 25cmx3.0mm with 4μm particle. Mobile phase was an acetone/acetonitrile: 70/30 v/v, with a flow rate of 0.4ml/min. Using the standard chemicals, triolein, diolein, monoolein and methyl oleate (from Sigma Aldrich Corporation), calibration was made for the quantification of triglycerides (TGs), diglycerides (DGs), monoglycerides (MGs), and fatty acid methyl esters (FAMEs). 5mL samples were taken from the circulation tank, and neutralized by 1ml of $H_3PO_4$ 5% aqueous solution to stop reaction. About 70mg sample was diluted in 10ml of the mobile phase and injected to HPLC.

## Results and discussion

### *Changing of concentration of reactants versus time*

Figure 2 shows the progress of transesterification reaction for canola oil. The concentration of KOH was 0.7%, and the oil/methanol molar ratio was 1:5. In the initial stage of the reaction, conversion of TGs and

also the yield of FAMEs were rapid. The rate then decreased and approached to equilibrium in about 50 min; after 70min, TGs and FAMEs concentration were 2.5% and 95%, respectively. The highest concentration of MGs and DGs were observed in the first 10 min reaction. The changing of the reactant and products in the waste oil was almost the same as canola oil.

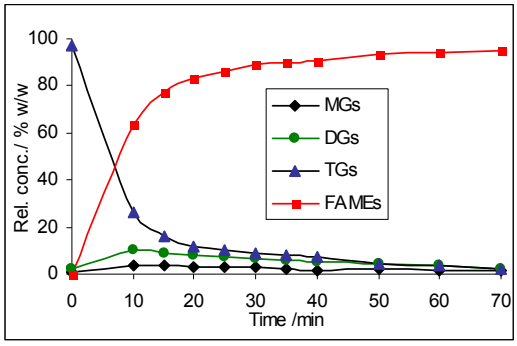


Fig.2 Time profile of reactant and products for transesterification reaction of canola oil to FAMEs with molar ratio of oil to methanol 1:5, KOH 0.7%

*Effect of KOH catalyst amount*

In the experiments done in this study, concentration of KOH was in the range of 0.5-1.0 % w/w (KOH to oil). The effect of catalyst amount on the conversion efficiency is shown in Fig.3. The maximum conversion of FAMEs achieved 95% at 0.7% of KOH. Increasing amount of catalyst led to the formation of soap, and thus washing and purifying BDF became difficult. However, optimal concentration of KOH was 1% in the case of waste oil containing high concentration of free fatty acid (FFA about 1.7%).

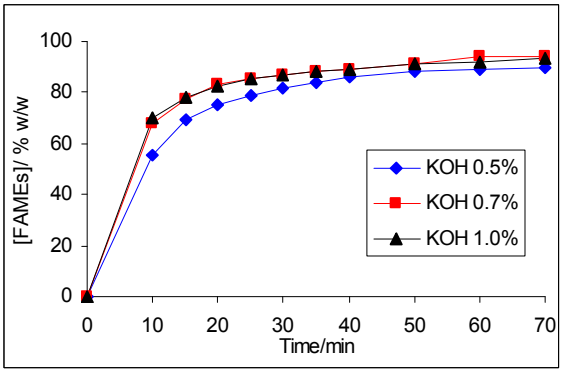


Fig.3 Effect of KOH catalyst amount on the conversion of FAMEs. Molar ratio of oil to methanol was 1:5

*Effect of molar ratio of methanol to oil*

An excess amount of methanol is necessary for the transesterification of TGs and methanol. Because the transesterification is an equilibrium reaction, the lager amount of methanol can enhance the methanolyis to result in the equilibrium favorable to methyl ester (FAMEs). The optimal conversion of FAMEs achieved was 95% at the molar ratio of oil to methanol being 1:5 (Fig.4). It is note worthy the results show the lower the molar ratio the faster the conversion in the initial stage of the reaction (10min). This fact may imply that under ultrasound irradiation at the initial stage with small amount methanol, small size droplet of methanol was formed rapidly and easily dissolved in oil phase leading to emulsion, so that the reaction could take place rapidly.

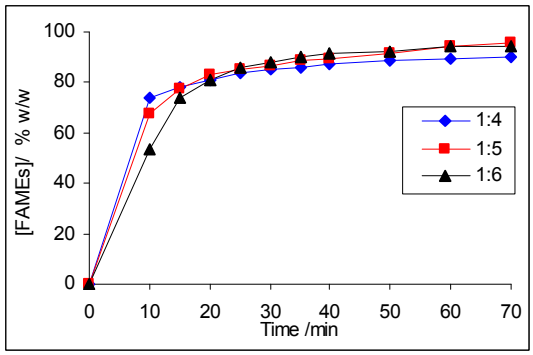


Fig.4 Effect of the molar ratio of oil to methanol on the conversion of FAMEs. Concentration of KOH was 0.7%

The chemical compositions in BDF products obtained in this study are summarized in Table 1.

Table 1: Main components of BDF products

| Oil | Oil:MeOH | KOH% | MGs | DGs | TGs | FAMEs |
|---|---|---|---|---|---|---|
| Canola | 1:4 | 0.7 | 1.1 | 3.1 | 2.6 | 93.2 |
| Canola | 1:5 | 0.7 | 0.5 | 1.9 | 1.3 | 96.3 |
| Canola | 1:5 | 0.5 | 1.2 | 2.4 | 2.3 | 94.1 |
| Canola | 1:6 | 0.7 | 1.5 | 2.8 | 1.3 | 94.4 |
| Waste | 1:5 | 1.0 | 1.5 | 2.5 | 4.0 | 91.6 |

## Conclusion

The above results show that transeterification reaction of virgin and waste oils with methanol in the presence of catalyst KOH assisted by ultrasound is very efficient. This process saves energy consumption, reduces reaction time as well as soap formation. The optimal conditions are found as molar ratio to oil to methanol 1:5; amount of KOH 0.7% and 1% for virgin and waste oils, respectively. Under these conditions, the yield of FAMEs archives 96.3% for virgin oil and 91.6% for waste oil.

## References

1. A.S. Ramadhas, S. Jayaraj, C. Muraleedharan: Fuel **84** (2005) 335-340.
2. A.V. Tomasevic, S.S. Siler-Marinkovic: Fuel Process. Tech. **81** (2003) 1-6.
3. S. Gryglewicz: Biores. Tech. **70** (1999) 249-253.
4. C. Stavarache, M. Vinatoru, Y. Maeda, H. Bandow: Ultrasonics Sonochem., **14** (2007) 413-417.

3P6-9

Proceedings of Symposium on Ultrasonic Electronics, Vol. 29 (2008) pp. 397-398
11-13 November, 2008

# Ultrasonic Soil Washing with Surfactants for the Remediation of Diesel-Contaminated Soil

Jihoon Cha‡, Beomguk Park, Younggyu Son, Mingcan Cui, Jeehyeong Khim†
(Department of Civil, Environmental and Architectural Engineering, Korea University)

## 1. Introduction

Sites that have been contaminated by petroleum hydrocarbons (PHCs) have been recently reported [1-5]. Soil contamination with PHCs has been caused by the leakage of underground storage tanks in various sites such as gas stations, military bases, and industrial complexes etc. Soil remediation can lead to long term contamination of ground water through rainfall, if it is not timeously removed [1].

There are various remediation technologies that can be used for soil remediation (e.g. vapor extraction, pump and treat, flushing, washing etc.)Of these technologies, soil washing takes the shortest time to process and shows the highest efficiency. Recently, a number of researchers have used ultrasound for the remediation of soil (heavy metals, diesels, etc.) [1-5]. Ultrasound causes physical effects (microjet, microstreaming, shock wave) by cavitation. These effects can enhance the mass transfer from the solid phase to the liquid phase.

In studies on ultrasonic irradiation, research has been carried out on the efficiency of diesel removal depending upon a variety of variables (soil and liquid ratio, power intensity, surfactants etc.) [1-6]. However, minimal research has been conducted on the relationship between power intensity and reaction time when inserting the same type of energy.

In this study we compared the effects of diesel removal in soil polluted by diesel, with the same input energy (different power intensities and reaction times). The effect of surfactant on the removal of diesel was then examined.

## 2. Experimental procedures

The sonoreactor used herein consists of a stainless steel reactor, pentagon shape and ultrasonic transducer module (Mirae Ultrasonic Tech.) placed on the reactor wall. Each transducer module contained three PZT transducers (Tamura corp.) and could produce ultrasounds of 35, 72, 110 and 170 kHz. The maximum power of the transducer module was 500 W. The reactor was filled with 5 L of tap water. A 50 mL reactor cell containing contaminated soil and washing water was submerged in a sonoreactor. Fig. 1 shows a schematic of the experimental apparatus.

Jumunsin sand was sieved using a mesh size ranging from 30 to 40 and the range of particle size was therefore 0.4~0.6 mm. The soil was contaminated with diesel (using n-pentane) for 15 days. The initial concentration of diesel in the soil was 7,000 mg/kg.

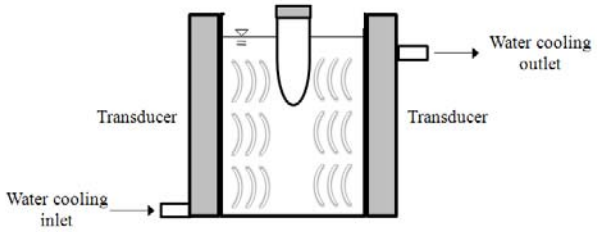


**Fig. 1** Schematic of reactor

An ultrasound irradiation experiment was carried out after the n-pentane in the soil had completely evaporated. The bath type sonicator (Flexonic, Mirae Ultrasonic Tech.) with a frequency of 35 kHz and 50, 100, 200, and 400 W of power was used. A mixture of 10mg contaminated soil and 20mL water was added into a 100mL cylindrical bath reactor and sonicated for 5, 10, 20 and 30 min. Observations of the effect of the surfactant were conducted using sodium dodecyl sulfate (SDS) 20mM. The reaction temperature was kept constant at 25±2℃ by a water cooling system.

After sonication, the sample was placed into a centrifuge operated at 4000 rpm in order to separate solid and liquid phases. The diesel concentration in

---

hyeong@korea.ac.kr

the solid phase was then extracted by using dichloromethane and measured for total petroleum hydrocarbon content (TPH) with a GC-FID (Agilent, 6890).

## 3. Results and Discussion

To determine the optimal condition of irradiation for ultrasonic soil washing, various sets of input power and irradiation times were applied in the case of 35 kHz. The results shown in **Fig. 2** revealed that removal efficiencies were almost the same for the four combinations when the total input energy was constant.

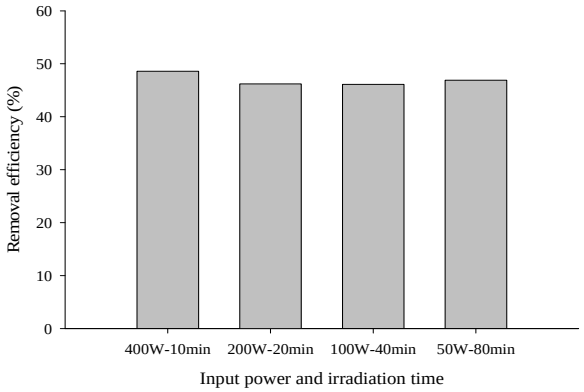


**Fig. 2** Diesel removal efficiency for various combinations of input power and irradiation times

**Fig. 3** shows the diesel removal efficiency for various input powers. Irradiation time was 30 min. As input power increased, the removal efficiencies increased. However, the improvement of removal efficiency was not as significant as expected. This indicated that while a certain amount of pollutants could be readily desorbed from the soil using ultrasound, diesel removal was not effectively enhanced as the input ultrasonic energy increased.

As shown in **Fig. 4**, the addition of surfactant could effectively improve removal efficiency. Surfactants could be promoted by the mass transfer of hydrophobic compounds into a hydrophilic phase and the cavitation event could occur more violently due to bubble coalescence inhibition.

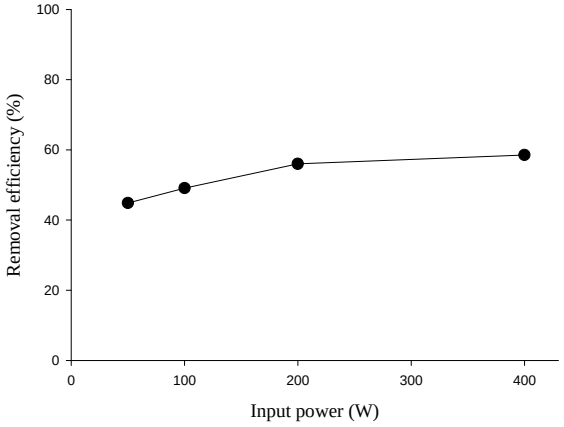


**Fig. 3** Diesel removal efficiency for various input powers

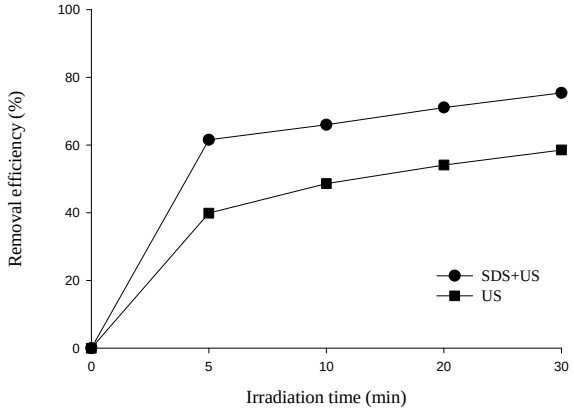


**Fig. 4** Diesel removal efficiency for only ultrasound and combination of ultrasound and surfactant


## Acknowledgments

This subject is supported by Ministry of Environment, Republic of Korea as “The Eco-technopia 21 project” (no. 061-081-042).


## References


1. G. J. Price and M. McCollom : Ultrasonics Sonochemistry **2** (1995) S67.
2. D. Feng and C. Aldrich : Advances in Environmental Research **4**(2000) 103-112
3. D. Feng, L. Lorenzen, C. Aldrich and P. W. Máre : Minerals engineering **14** (2001) 1093.
4. Y. U. Kim and M. C. Wang : Ultrasonics 41 (2003) 539.
5. S. Na, Y. Park, A. Hwang, Y. Kim and J. Khim : Jpn. J. Appl. Phys **46** (2007) 4775.
6. A. Collasiol, D. Pozebon and S. M. Maia : Anal. Chim. Acta **518** (2004) 157.

3P6-10

Proceedings of Symposium on Ultrasonic Electronics, Vol. 29 (2008) pp. 399-400
11-13 November, 2008

# Relationship between the lactic fermentation promoted by ultrasound and the fermentation temperature
# 超音波による乳酸発酵促進と発酵温度との関係

Satoshi Koyama† and Nobuyoshi Masuzawa (Musashi Institute of Technology)
小山聡†，増澤信義（武蔵工業大学）

## 1. Introduction

Various kinds of food processing using lactic acid bacteria are carried out. Among them, yoghurt and kefir are representative products. By adding lactic bacteria to milk, they are produced through lactic acid fermentation[1,2]. We have carried out the studies on the promotion of fermentation by irradiating ultrasound in this process[3,4]. Up to now, the following is the result of our study. Fermentation promotion with ultrasound is dependent on the frequency and the sound pressure of irradiating ultrasound[5,6]. However, mechanism of promotion effect has not been made clear yet. One of ultrasonic actions is temperature rise by the absorption of ultrasonic energy. In this study, we experimentally examined in the fermentation temperature of the lactic acid fermentation and the influence of temperature rise with ultrasonic irradiation.

## 2. Relationship between fermentation temperature and temperature rise with ultrasonic irradiation

It is known that the lactic acid fermentation is strongly dependent on the fermentation temperature. Fermentation temperature of kefir used in this study is appropriate around 20～30°C from the notice delivered from the company. We made an experiment in order to know the optimum fermentation temperature in the case of no ultrasonic irradiation. Solidification time with ultrasonic irradiation is compared with solidification time without ultrasonic irradiation near the optimum temperature. We examine the relationship between the fermentation temperature and promotion effect of the lactic acid fermentation.

It is considered that if the temperature of the milk rises with ultrasonic irradiation, the fermentation is promoted and solidification time is shortened below the optimum temperature and the fermentation is suppressed and solidification time is lengthened above the optimum temperature. If the promotion of the lactic acid fermentation does not relate to temperature rise, it is considered that behavior of the lactic acid bacterium is activated by other effects of ultrasonic irradiation.

## 3. Measurement method

Water is filled into a water tank made of acrylic resin, and water temperature is kept constant within ±0.1°C using a circulation-type temperature regulator. 500 ml of milk in a bag of thin polyethylene was placed in the tank. By adding 1 g of inoculum bacteria to the milk, the mixture is agitated. Defining this moment as the beginning of fermentation, pH is measured in every one hour. The colloid particles become insoluble when lactic acid fermentation advances and pH drops. The time when fermentation is achieved (solidification) is defined as the time when pH becomes 5.0, which is the pH of a kefir product. Ultrasonic frequencies were changed by installing vibration systems of different frequencies. The frequencies were 20, 150 and 250 kHz. In order to avoid the effects of standing waves, sound absorber material was placed at the both sides of the tank and opposite the vibration system. The sound pressure is 10 kPa constant.

Sound pressure is measured beforehand using sonic meter SM1000 (Shinka Industry). The inoculum used in this study is a highly activated kefir fungus of Nakagaki Co. made by the freeze-drying process. 1000 ml paper-packed milk with 3.5% milk fat was used.

## 4. Measured results

At first we made experiment in order to obtain the optimum fermentation temperature without ultrasonic irradiation. Figure.1 shows the result of the experiment. As shown, the optimum temperature is 29°C. It is considered that solidification time is shorted below 29°C and lengthened above 29°C with ultrasonic irradiation. Since the absorption of ultrasound in the milk is dependent to the ultrasonic frequency, temperature rise is dependent to the ultrasonic frequency. In the frequency range, the more frequency is high, the

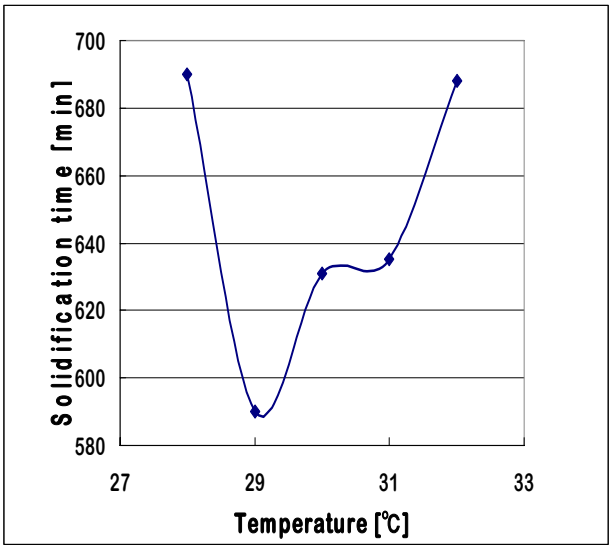


Fig.1. Solidification time dependent on temperature in the case of no ultrasonic irradiation

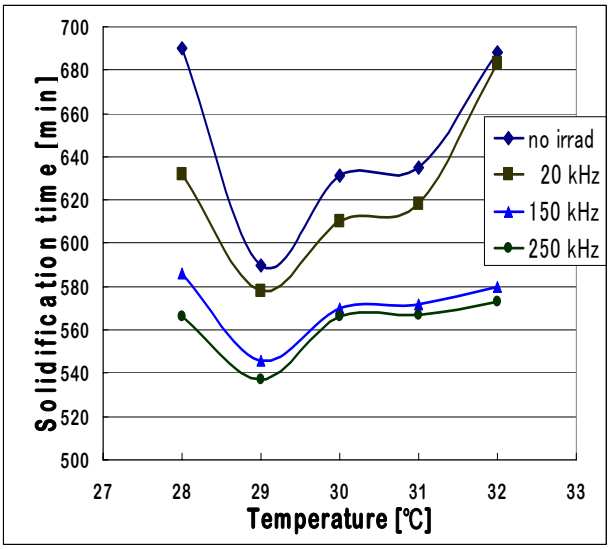


Fig.2. Solidification time dependent on temperature in the case of ultrasonic irradiation

more absorption is high. Therefore we made experiments by changing ultrasonic frequencies.

Figure.2 shows the solidification time when the frequency is changed. Solidification time with ultrasonic irradiation is shorter than that of no irradiation in respective temperature. The more frequencies are high, the more solidification times are short. If temperature rise with ultrasonic irradiation influences promotion of fermentation, the lactic acid fermentation is suppressed above 29$^{o}$C. All the data, however, show the lactic acid fermentation is promoted with ultrasonic irradiation in the measured temperature range.

It is obvious that temperature rise with ultrasonic irradiation does not influence promotion of the lactic fermentation. Temperature rise is not a main cause of promotion of fermentation with ultrasound and ultrasonic effect dependent on frequency is large in the measurements in this study. This is considered that cause of the promotion might be expansion of chemical site with stirring effect of ultrasound.

## 5. Comculusions

In this study, we experimentally examined on the relationship between promotion of fermentation and temperature rise with ultrasonic irradiation. As a result, it was found that temperature rise with ultrasonic irradiation influences promotion of the lactic fermentation very little.

## References

1. Y. Uchimura and S. Okada: *Nyusankin Jikken Manuaru* (Experiment Manual on Lactic Bacteria) (Asakura-shoten, Tokyo 1992) p.1 [in Japanese]
2. Nyusankin-kenkyu shudankai: *Nyusankin-no Kagaku-to Gijutsu* (Science and Technology of Lactic Bacteria) (Gakkai-shuppan-senta, Tokyo 1986) p.226 [in Japanese]
3. N. Masuzawa and E. Ohdaira: “Attempts to Shorten the Time of Lactic Fermentation by Ultrasonic Irradiation” Jpn. J. Appl. Phys. **41** (2002) 3277-3278
4. N. Masuzawa, A. Kimura and E. Ohdaira: “Ultrasonic Monitoring of the Progress of Lactic Acid Fermentation” Jpn. J. Appl. Phys. **42** (2003) 2963-2964
5. T. Shimada, E. Ohdaira and N. Masuzawa: “Effect of Ultrasonic Frequency on Lactic acid Fermentation Promotion by Ultrasonic Irradiation” Jpn. J. Appl. Phys. **43** (2004) 2831-2832
6. K. Katayama and N. Masuzawa : “Frequency dependence of promotion degree in lactic fermentation promotion using sound and ultrasound” *Proc. .The thirteenth International Congress on Sound and Vibration* (2006) RS98-752 pp. 1-8

3P6-11

Proceedings of Symposium on Ultrasonic Electronics, Vol. 29 (2008) pp. 401-402
11-13 November, 2008

# Enhancement in removal efficiency of tannins in livestock wastewater using ultrasound/ozone

Junghyun Lim, Eunju Cho, Mingcan Cui, Myunghee Lim and Jeehyeong Khim†
(Department of Civil, Environmental and Architectural Engineering, Korea University)

## 1. Introduction

In piggery wastewater treatment, there are many steps that can be used to enhance processing efficiency. There is little doubt that biological processes will be continued as base treatments. However, biological treatments cannot be applied to large molecules and are toxic to microorganisms due to their resistance to biological processes.[1] Tannins are highly distributed in organic compounds in piggery wastewater and in molecules that are too large for biodegradation. They have an adverse affect on different organisms ranging from toxic effects on animals to growth inhibition of microorganisms.[2] Therefore, other processes are needed to increase removal efficiency. Advanced processes based on chemical oxidation may be a satisfactory option for biological treatment of non-degraded wastewater.

Many researchers have reported oxidation of poly-phenolic compounds using ultrasound, ozone and a combination of these.[3] A combined operation of sonolysis and ozonation shows synergistic effects in contaminated wastewater. The mechanism of combination may be summarized in two ways.[4] First, the physical effects of ultrasound can enhance $O_3$ diffusion so that the specific area of $O_3$ bubbles can be increased. Second, cavitation produced by ultrasound can generate more OH radical formations, and increase diffusion efficiency.[5] While reports have been presented on the effects of using ozonation to degrade tannins, they do not include the effects of ultrasound and ultrasound/ozonation.

The effects of ultrasound, ozone and their combination were therefore investigated in this study. Three different results will be presented for the effects of total organic carbon (TOC) and the concentration of tannins.

---

hyeong@korea.ac.kr

## 2. Materials and Methods

Tannin (molecular form: $C_{76}H_{52}O_{46}$, molecular weight: 1701.23 g; minimum assay: 90.0%) was purchased from Yakuri Pure Chemicals. All samples were sonicated for 1 h in a bath-type sonicator (Flexonic, Mirae Ultrasonic Tech.) with 170 kHz and 400W. Ozone was produced from pure oxygen (minimum purity 99.99%) using an ozone generator (LAB 2B, Triogen), yielding 2 g $h^{-1}$ $O_3$. A schematic diagram of the experimental set-up is shown in Fig. 1. The experiments were carried out in a 200 mL reactor which was initially filled with 500 mg $l^{-1}$ synthetic tannins. The experimental temperature was maintained at 25 ±3°c, using a cooling water system.

All samples were filtered using a 0.45㎛ Whatman filter and were then analyzed. The removal of organic carbons via mineralization was monitored by the Sievers 5310C Laboratory Total Organic Carbon Analyzer (GE Analytical Instruments, Inc.) equipped with a 900 Autosampler System (GE Instruments). The concentration of tannins was measured by the standard methods. [6]

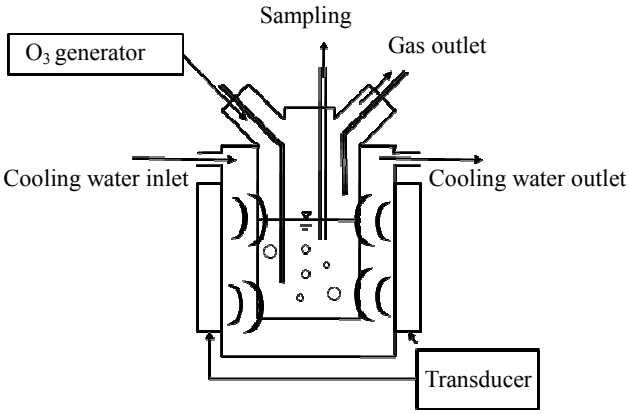


**Fig. 1** Schematic diagram of the experimental set-up

## 3. Results and Discussion

Experiments were performed with ozonation alone, ultrasound alone and the combined US/$O_3$ system in

order to investigate the synergistic effects. As shown in Fig. 2, the synergistic action of $O_3$ and ultrasound degradation was presented during the first hour by 80 % as compared to the ozonation and sonolysis alone, which showed 60 % and 5 %, respectively. Ozonation alone was relatively more effective than ultrasound for tannins reduction, but the combination of the two processes showed a synergistic increase in the overall process rate. This could indicate that the cavitation event accelerates ozonation effects. Therefore, despite there being quite a low efficiency when ultrasound is used alone, the effects of ultrasound show that when it is combined with ozonation it is effective in accelerating the reduction of tannins. This result concurs with other works where poly-phenolic compounds were degraded by US/$O_3$, US and $O_3$ alone.[7)]

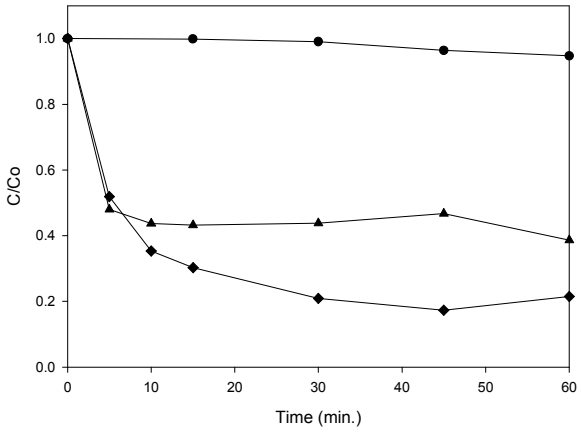


**Fig. 2.** Comparison of individual and combined schemes for tannins degradation ( 0.100 L, 25 ± 3°c, [$C_{76}H_{52}O_{46}$] = 0.3 mM); ●, US only (170 kHz, 400 W);▲, $O_3$ only ( 1 g $L^{-1}$);◆, US + $O_3$)

All of the total organic carbon samples were monitored and the data is shown in Fig. 3. The simultaneous application of ultrasound and ozone resulted in significantly enhanced tannins mineralization. The use of ultrasound alone on tannins resulted in a limiting mineralization of almost zero percent after 60 min. Similarly, ozone alone could only reduce TOC by about 20%.

In contrast, when the combination processes were applied, the extent of mineralization exceeded 35%. When sonicated solutions are bubbled with $O_3$ gases, the thermal decomposition of $O_3$ (g) in the cavitation bubbles leads to enhanced OH radical and $H_2O_2$ yields. Furthermore, the cavitation induced ultrasound increased the specific area of $O_3$ bubbles prior to an accelerated reaction.

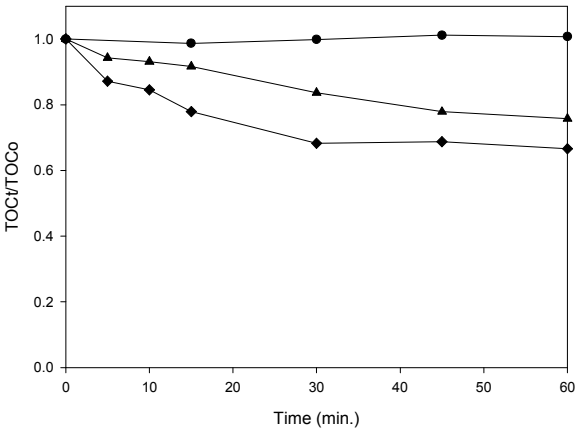


**Fig. 3.** TOC degradation for tannins with individual and combined schemes (0.100 L, 25 ± 3°c, [$C_{76}H_{52}O_{46}$] = 0.3 mM); ●, US only (170 kHz, 400 W);▲, $O_3$ only ( 1 g $L^{-1}$);◆, US + $O_3$)

Based on these experiments, sonolysis on tannins degradation and mineralization is quiet low but when combined with ozonation, significant synergistic effects are indicated.

**Acknowledgment**

This work was supported by the Korea Science and Engineering Foundation (KOSEF) grant funded by the Korea government (MOST) (No. R01-2007-000-20886-0)

**References**

1. Scalbert, A. : Phytochemistry **30** (1991) 3875.
2. Cui MC : MS thesis. (2007)
3. Saroj DP, Kurmar A., Bose P., Tare V. and Dhopavkar V. : wat. Res. **39** (2005) 1921.
4. Ince NH, Tezcanli G. Belen R and Apikyan IG : Appl. Catal. B: environ. **29** (2000) 167.
5. Tezcanli GG and Ince NH : Ultrasonics **42** (2004) 603.
6. APHA, Standard Methods for the Examination of Water and Wastewater, 20th ed., 1998.
7. Destaillats H, Colussi A. J., Joseph JM and Michael R. Hoffmann : J. Phys. Chem. A **104** (2000) 8930.

3P6-12

Proceedings of Symposium on Ultrasonic Electronics, Vol. 29 (2008) pp. 403-404
11-13 November, 2008

# The Effect of Sonication on Chlorine Disinfection in the Inactivation of E.coli

Hoang Lam Pham[1], Hyunjun Kim[1], Myunghee Lim[1], Iordache Ioan[2], Jeehyeong Khim[1]
([1] Dep. of Civil, Environ. and Architec. Eng., Korea University; [2] Nat. Res. and Development Inst. for Cryogenics and Isotopic Technologies, Romania)

## 1. Introduction

Chlorination has been widely used as a method for water disinfection in terms of pathogen control. However, it is found that chlorination can cause potential problems for human health because of the formation of disinfection byproducts (DPBs) that are considered to be carcinogenic for humans, such as trihalomethanes (THMs) and haloacetic acids (HAAs), etc [3]. DBPs produced in water are caused by the reaction between chlorine and organic matters [2]. Therefore, chlorine concentration must be controlled in order to prevent the formation of DPBs.

Ultrasonic irradiation has been recently investigated for bacterial inactivation because it has proven to be effective when sonicating alone as well as when combining with other disinfection methods such as UV, $H_2O_2$, $O_3$, chlorine. In chlorination, low frequency ultrasound showed highly synergic effects in pretreatment[4] and in a simultaneous treatment with a short sonicationtime.[1]

The aim of this study is to investigate the effect of ultrasonic irradiation in chlorine disinfection at different powers and irradiation times on the chlorine demand of the inactivation of E.coli.

## 2. Materials and methods

A NaOCl solution of 8% (JunSei, Japan) was used to produce a chlorine solution of 0.6±0.02 mg/l as free chlorine. The final free chlorine concentrations were verified by the DPD colorimetric method.

E.coli suspension (KCTC 2441) was prepared by a 24h growth at 37°C in an incubator in a LB broth (Difco). Bacteria were prepared at the initial concentration of $6x10^5$ cells $cm^{-3}$ for experiments. Serial dilutions and standard plate counts were used as the number of bacteria. Results were reported as a percentage of the surviving colony forming units per milliliter (CFU $cm^{-3}$).

In the case of chlorine alone, a 10 mL solution including bacteria was added to a 190 ml free chlorine solution. The residual free chlorine was then measured using the DPD colorimetric method. For the combination of chlorination and ultrasound, the solution including bacteria and free chlorine was sonicated in a 20 kHz probe system (vibra-cell 750, Sonics &Materials, USA).

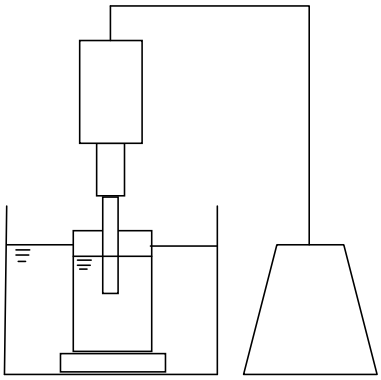

**Fig. 1** Schematic system of ultrasound probe

The chlorine demand is calculated by the following:

Chlorine demand (chlorine alone)
= initial concentration – residual (1)

Chlorine demand (Chlorine with ultrasound)
= initial concentration – residual
– chlorine loss in sonication (2)

The loss of chlorine due to sonication was determined by the sonication of a free chlorine solution without bacteria.

## 3. Results and discussion

**Fig. 2** shows the chlorine demand of chlorination

hyeong@korea.ac.kr

alone and chlorination with sonication. The ultrasonic power was 225W and irradiation time was 2 min.

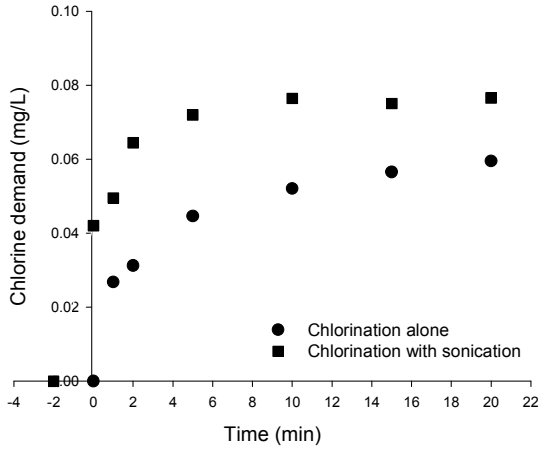


**Fig.2.** Chlorine demand of chlorination alone and chlorination with sonication

The result shows that the chlorine demands in the case of the combination are higher than those of chlorination alone for all periods of monitoring times. However, the differences in chlorine demand decreased as time increased. A higher chlorine demand in the case of chlorination with sonication indicated that inactivation of bacteria could be improved by ultrasound due to microjet, microstreaming and enhancement of mass transfer.

To evaluate the effect of sonication time in the case of chlorination with sonication, 2 min and 5 min of sonication time were applied in the condition of 225 W, as shown in **Fig. 3**.

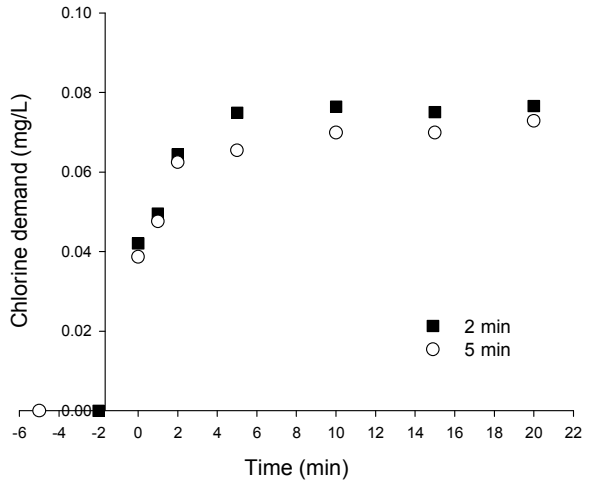


**Fig. 3** Chlorine demand for 2 min and 5 min sonication

The chlorine demand of 5 min sonication was lower than that of 2 min sonication, indicating that a longer time period of sonication (5 min) had an adverse effect on chlorination. Duckhouse *et al*. reported similar results and they explained that excess sonication could result in the re-agglomeration of dead cells, which could then protect the living cells from further disinfection.

**Fig.4** shows the effect of irradiation power for the chlorine demand in the condition of 2 min irradiation for the inactivation of *E-coli*. Chlorine demand increased as ultrasonic power increased. However, the case of the application of 300 W was not significantly enhanced compared to that of 225 W. Therefore, 225 W might be the optimum input power condition in this case.

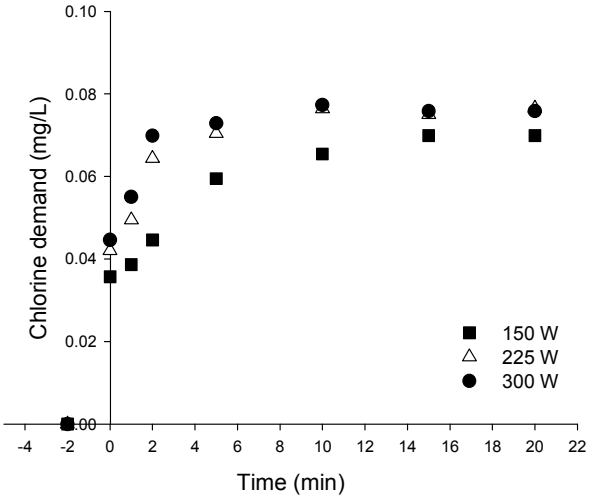


**Fig. 4** Chlorine demand for different powers in the condition of 2 min irradiation


## Acknowledgments

This work was supported by the Korea Science and Engineering Foundation (KOSEF) grant funded by the Korea government (MOST) (No.R01-2007-000-20886-0)


## Reference


1. H. Duckhouse , T.J. Mason, S.S. Phull and J.P. Lorimer : Ultrasonics Sonochemistry **11** (2004) 173.
2. M.S. Siddiqui, G.L. Amy and B.D. Murrhy : Water Res. **31** (1997), 3098.
3. S.W. Krasner, H.S. Weinberg, S.D. Richardson, S.J. Pastor, R. Chinn, M.J. Sclimenti, G.D. Onstad and A.D .Thruston : Environ. Sci. Technol. **40** (2006), 7175.
4. T.Blume , U.Neis : Ultrasonics Sonochemistry **11** (2004) 333–336.

3P6-13

Proceedings of Symposium on Ultrasonic Electronics, Vol. 29 (2008) pp. 405-406
11-13 November, 2008

# The Effects of Power Density and Irradiation Time for Ultrasonic Inactivation of E. coli

Hyunjun Kim[‡,1], Hoang Lam Pham[1], Myunghee Lim[1], Mingcan Cui[1], David Elena[2], Jeehyeong Khim[†,1]
(Dep. of Civil, Environ. and Architec. Eng. Korea Univ[1].,
Nat. Res. and Development Inst. for Cryogenics and Isotopic Technologies, Romania[2])

## 1. Introduction

Chlorination is the most common disinfection method, which utilizes chemicals such as chlorine and its products (ex. NaOCl). This is because chlorination is inexpensive and effective for the inactivation of bacteria and viruses. However, there are a number of problems associated with chlorination, which include its reaction with dissolved chemicals and the production of harmful by-products such as trihalomethanes (THMs), producing unpleasant odors etc. [1]. Because of these problems, alternative methods such as ozonation and ultraviolet irradiation have been investigated and the application of ultrasound in disinfection has recently been investigated by a number of reserchers [1,2,3,4].

When ultrasound is irradiated in an aqueous phase, cavitation bubbles are produced. The collapse of the cavitation bubble produces localized high pressure and temperature resulting in damage to the bacterial cell wall, the deagglomeration of bacterial clusters, and the generation of oxidants such as OH radicals and hydrogen peroxide which attack the chemical structure of the bacterial cell wall [2].

Many reserchers have reported on the influential factors affecting cavitation bubbles and combinations of other disinfection methods (ex. chlorination, UV irradiation, ozonation) in water and wastewater desinfection using ultrasound [1,3,4]. While these studies included the influence of power density, there was a diffculty incomparing high power density-short time irradiation with low power density-long time irradiation in the efficiency of disinfection.

---

hyeong@korea.ac.kr

The aim of this study is to investigate the efficiency of inactivation for E. coli by changing the power density and irradiation time at a constant input energy.

## 2. Material and Experimental method

*E. coli* KCTC (2441) was used in this test and was grown in a LB broth (Difco) which was sterilized by autoclaving. Prior to performing the disinfection experiment, 20mL of LB medium was inoculated and incubated at 37ºC for 24h. The broth was then centrifuged at 4000rpm for 10min and the E. coli cells were separated from the broth and washed twice with a phosphate buffered saline (PBS, pH 7.2).

To adjust the initial concentration of E. coli suspension at approximately 4-5×$10^7$ cells/ml, a PBS solution was added to the E. coli suspension. The volume of bacterial solution for the experiment was 100ml.

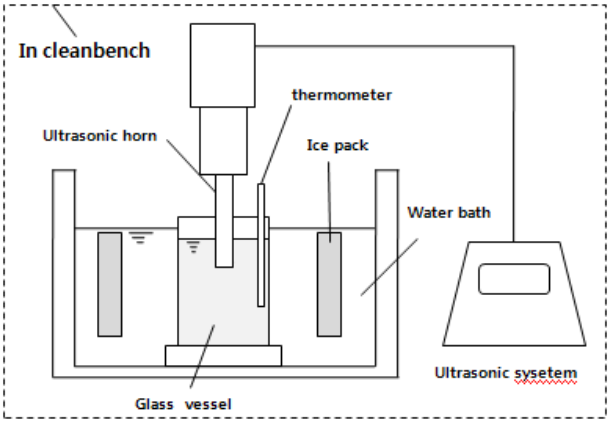


**Fig. 1** Schematic of experimental set-up

The experimental set-up is depicted schematically in Fig. 1. A glass vessel was placed in a water bath. The water temperature was controlled

at 20~25ºC using ice packs during ultrasound irradiation.

The ultrasound system (Vibra-cell 750, Sonics & Materials) was a horn-type and operated at a constant frequency of 20kHz. All equipments were placed on a clean bench.

The ultrasound system was operated at different powers and irradiation times in order to investigate the relationship between power density and irradiation time interval for efficiency of disinfection. Table 1 shows the variation of sound power, power density and irradiation in the experiment.

Serial dilution and the plate counting method were used as the method of analysis. A desoxycholate agar broth (Difco) was used in the plate counts.

**Table 1** Variation of sound power, power density and irradiation time at 20kHz , volume 100ml

| **Total power (W)** | **150** | **225** | **300** |
|---|---|---|---|
| **Power density (W/ml)** | **1.5** | **2.25** | **3.0** |
| **Irradiation time interval (min)** | **15** | **10** | **7.5** |

### 3. Results and Discussion

Fig. 2 shows the effect of total power in disinfection. When the total power was higher, the efficiency of inactivation was higher in the E. coli. This result was similar to that obtained in previous research [5]. However, the gap of removal between the result at 225W and 300W was smaller than that at 150W and 225W, because an increase of vibrational amplitude occurs in the decoupling between the vibrational tip and the bacterial solution and the energy transfer decreases [6].

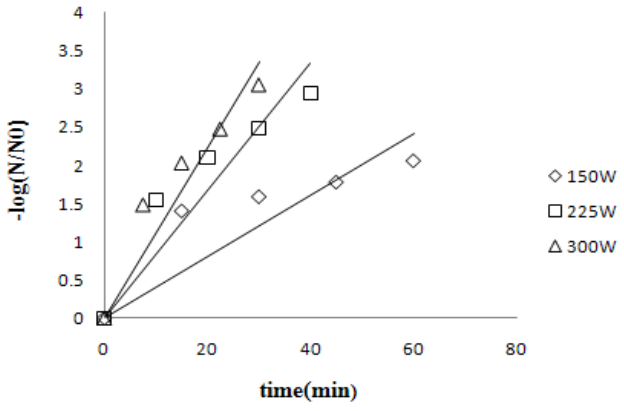


**Fig. 2** Effect of ultrasonic input total power in inactivation of E. coli

The variations of input energy calculated by multiplying the power-density and the irradiation time were 1350, 2700, 4050, and 5400 J/mL. Fig. 3 shows the effect of input energy in the inactivation of E. coli.

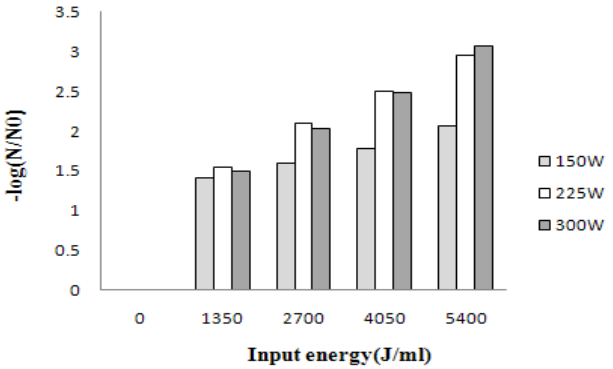


**Fig. 3** Effect of ultrasonic input energy in inactivation of E. coli

The result at 1350 J/mL was the same for different total powers. As input energy increased, the results at 225W and 300W were the same and their results were higher than at 150W. From this result, it is possible that, at a critical power, this could be removed at certain bacterial concentrations. Below the range, the same energy results in ineffectiveness.


### Acknowledgments

This work was supported by the Korea Science and Engineering Foundation (KOSEF) grant funded by the Korea government (MOST) (No. R01 - 2007 - 000 - 20886-0)


### References


1. H. Duckhouse, T. J. Mason, S. S. Phull and J. P. Lorimer: Ultrason. Sonochem. 11 (2004) 173.
2. A. Antoniadis, I. Poulios, E. Nikolakaki, and D. Mantzavinos: J. of Hazard. Mater. 146 (2007) 492.
3. E. Joyce, S. S. Phull, J. P. Lorimer, and T. J. Mason: Ultrason. Sonochem. 10 (2003) 315.
4. T. Blume and U. Neis: Ultrason. Sonochem. 11 (2004) 333.
5. K. Masaki, O. Ryota, S. K. Naomi, T. Kouhei and Y. Toshikuni: Biotechnol. Prog. 21 (2005) 897.
6. I. Hua, R. H. Hochemer, and M. R. Hoffmann: Environ. Sci. Techol. 29 (1995) 2790.

3P6-14

Proceedings of Symposium on Ultrasonic Electronics, Vol. 29 (2008) pp. 407-408
11-13 November, 2008

# Biodegradability Enhancement in Ultrasound-assisted Oxidation for the Removal of Dye

Eunju Cho‡, Junghyun Lim, Mingcan Cui, Younggyu Son and Jeehyeong Khim
(Department of Civil, Environmental & Architectural Engineering, Korea University)

## 1. Introduction

In industrial wastewater, dyes are almost non-biodegradable because they consist of various high molecules. It is therefore difficult to remove dyes by using aerobic treatment or short-term anaerobic treatment [1]. In particular, reactive dyes are very soluble in water, rendering it difficult to degrade organic dye using a conventional absorption or activated sludge process [2].

Sonochemical degradation is applied to the removal of the organic pollutants in aqueous solutions by the cavitation effect. Recently, a combination of ultrasound and advanced oxidation processes (AOPs) was investigated for enhancing removal rate. Among these processes the combination of Fenton's oxidation and ultrasound has an effective removal rate. This process has a synergy effect based on the reaction of ferrous ion with sonochemically produced $H_2O_2$ and it was reported to enhance the sonochemical degradation [3].

The main objective of this study is to analyze the feasibility of decolorization and mineralization by combining the sonochemical process with the Fenton process.

## 2. Materials and method

C.I. Reactive Black 5 (Remazol Black B; MW = 991.8 g $mol^{-1}$) was obtained from DyStar in 80-85% purity. A hydrogen peroxide solution (34.5% w/w, extra pure) and $FeSO_4 \cdot 7H_2O$ (extra pure) were obtained from the Samchun Chemical Co.

The sonolysis equipment was a Flexonic (Mirae Ultrasonic Tech.) with a frequency of 35 kHz and a 400 W energy input. A reactor volume was 100mL. A specially designed ultrasonic machine is presented Fig. 1. The temperature was fixed at 20-25℃ during the ultrasound irradiation. Samples of the dye solution were taken out at 15 minute intervals. All samples were filtrated using a Syring filter (0.45 μm) from Whatman.

The UV-spectra of dye solution was measured using a UV-spectrophotometer Specord 40 from Analytik Jena. The maximum absorbance wavelength ($\lambda_{max}$) of C.I. Reactive Black 5 could be found at 597 nm from the spectra.

hyeong@korea.ac.kr

Accordingly, the concentration of the dye solution in the reaction at different reaction times was determined by measuring the absorption intensity at $\lambda_{max}$ = 597 nm and from a calibration curve.

Total organic carbon (TOC) measurements of samples were determined with a Sievers 5310C Laboratory TOC analyzer and a Sievers 900 Autosampler (GE).

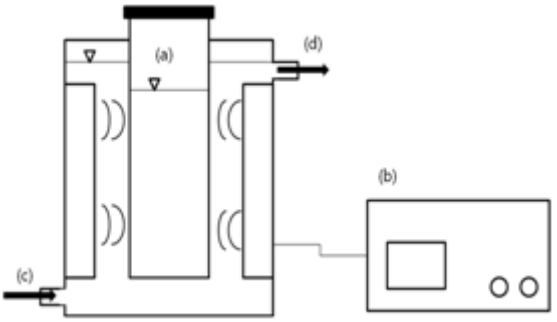


**Fig. 1** Experimental set up (a) reactor, (b) sonicator, (c) cooling water inlet, (d) cooling water outlet

The initial concentration of dye was 10~100 mg $L^{-1}$. The ratio of concentration between $H_2O_2$ and $FeSO_4$ was one to four, and the concentration of $H_2O_2$ was 120 mg $L^{-1}$. Before the experiment, $FeSO_4$ was dissolved in a solution for 1 hour, and $H_2O_2$ was injected in a solution immediately prior to the experiment. During the Fenton process, the sample was well mixed using a stirrer.

## 3. Results and discussion

The degradation of C.I. Reactive Black 5 was carried out using three different approaches under the following conditions : (1) Sonochemical process, (2) Fenton process, (3) Sonochemical + Fenton process. Fig.2 shows the decolorization observed of all the processes according to reaction time. After 60min reaction in the Sonochemical process and Fenton process, the removal of C.I. Reactive Black 5 amouted to 5% and 80%, respectively. When the reaction in the Sonochemical was combined with the Fenton process, the C.I. Reactive Black 5 was almost removed within 15 min.

Lin et al. [4] studied the decoloration of acid dye by Sonochemical combined with the Fenton process, and observed that the degradation efficiency was increased by more than only one process. During

ultrasonic irradiation, the shockwaves created by cavitation can accelerate the reaction time. Because ultrasound in the combined process is utilized for the cleaning of the ferrous iron surface. Therefore, the process of ultrasonic cavitations results cleans ferrous iron, and accordingly more reactant surface area was formed for further surface reactions. However, after 45 min, the removal efficiency of acid dye did not increase. It is assumed that the Fenton process rapidly reacts with $H_2O_2$ during the first reaction, while the reaction rate almost changed after the first reaction because $H_2O_2$ was slowly created by ultrasound. Therefore, the degradation occurs at a slow speed.Our results also show that after 15 min the removal rate of reactive dye had not changed.

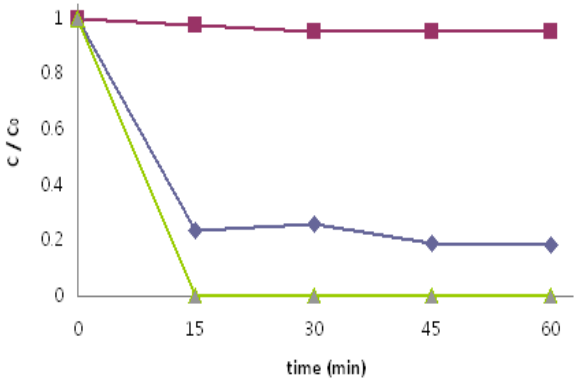


**Fig. 2** Degradation of C.I. Reactive Black 5 (■ : Sonochemical process, ◆ : Fenton process, ▲ : Sonochemical + Fenton process), reaction condition - $H_2O_2$ = 120mgL$^{-1}$ ; $H_2O_2$:$FeSO_4$ = 1:4 ; $[dye]_0$ = 100mgL$^{-1}$; frequency = 35kHz; power = 400W

The mineralization carried out of C.I. Reactive Black 5 is shown in Fig. 3, where the Fenton process and the Sonochemical process combined with the Fenton process are compared. Although 80% of decolorization was achieved after 1 h for the Fenton process, the removal ratio of TOC was almost 20%.

The minimal change of TOC is due to the presence of imediates such as methanoate, nitrite, oxalate. As a result, the organic carbon still remained as intermediate [5]. In the case of the combination process (Fenton+US) the removal ratio of TOC was 50% within 60min. This concurs with results obtained by Inoue et al. [6]. Inoue et al. [6] used additives ($Fe_2SO_4$) to enhance the degradation of TOC. Therefore, the combination process of Fenton and ultrasound can be used as an effective degradation of reactive dyes and TOC.

The degradation rate of dye is dependent on the initial concentration. A lower initial concentration of degradation rate is more rapid than a higher initial concentration. S. Vajnhandl et al. [5] showed that the apparent decolorization rates decreased with an increase in the initial concentration.

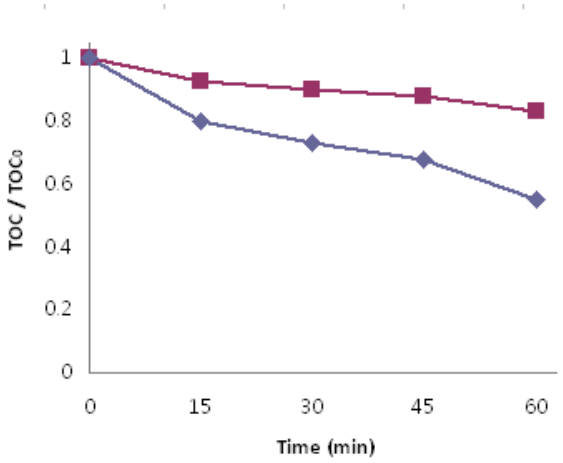


**Fig. 3** The mineralization of C.I. Reactive Black 5 (■ : Fenton process, ◆ : Sonochemical + Fenton process ) , reaction condition - $H_2O_2$ = 120mgL$^{-1}$ ; $H_2O_2$:$FeSO_4$ = 1:4 ; $[dye]_0$ = 100mgL$^{-1}$; frequency = 35kHz; power = 400W

**Acknowledgments**

This work was supported by the Korea Science and Engineering Foundation (KOSEF) grant funded by the Korea government (MOST) (No. R01-2007-000-20886-0)

**References**

1. A. Rehorek, M. Tauber, and G. Gübitz : Ultrasonics Sonochemistry **11** (2004) 177.
2. Lin S.H. and Peng C.F. : Environmental Technology 16 (1995) 693
3. H. Zhang, Y. Zhang and D. Zhang : Color. Technol. **123** (2006) 101.
4. J. Lin, X. Zhao, D. Liu, Z. Yu, Y. Zhang and H. Xu : J. Hazard. Mater. **157** (2008) 541.
5. S. Vajnhandl and A. M. Le Marechal : J. Hazard. Mater. **141** (2007) 329.
6. M. Inoue, Y. Masuda, F. Okada, A. Sakurai, I. Takahashi and M. Sakakibara : Wat. Res. **42** (2008) 1379.

3P6-15

Proceedings of Symposium on Ultrasonic Electronics, Vol. 29 (2008) pp. 409-410
11-13 November, 2008

# Physicochemical elucidation of cavitation bubble interfacial region

キャビテーションバブル気液界面領域の物理化学的解明

Ben Nanzai‡, Kenji Okitsu, Norimichi Takenaka, Hiroshi Bandow
(Osaka Prefecture University, Department of Engineering)
南齋勉‡, 興津健二, 竹中規訓, 坂東博 (阪府大院工)

## 1. Introduction

It is known that powerful ultrasonic irradiation in a liquid brings about the formation, growth and collapse of micro gas bubbles. During the collapse, local reaction zone of extremely high pressure (several hundred atmospheres) and temperature (several thousand degrees) are produced due to the quasi-adiabatic collapse[1] while the bulk liquid temperature hardly changes. This process is known as acoustic cavitation bubbles. In aqueous solutions especially, the reactive OH radicals and hydrogen atoms[2] are formed from the sonolysis of water vapor.

LAS tends to accumulate at the interface of cavitation bubbles due to their amphiphilic property, and do not evaporate into the cavitation bubble because of their low volatility derived from anionic state. Therefore, from the sonolysis of LAS, it is anticipated that the relation between cavitation bubbles and LAS molecules, and the behavior of LAS molecules toward the interface of bubbles can be estimated.

In previous reports, the sonolysis of surfactant has examined, however, the degradation rate behavior has not considered systematically yet. Therefore in this study, the relationship between sonochemical degradation rates of LASs and the initial LAS concentration was investigated systematically.

## 2. Experiment

Aqueous solutions of three anion surfactants, sodium p- octylbenzenesulfonate (LAS $C_8$), sodium p- nonylbenzenesulfonate (LAS $C_9$) and sodium p-dodecylbenzenesulfonate (LAS $C_{12}$) were adjusted from 15 μM to 3000μM.

Ultrasound irradiation was carried out using a 65 mmø oscillator (Kaijo 4611type; MFG. No.37G4) and an ultrasonic generator (Kaijo TA-4021type; Lot. No.19G9, frequency; 200 kHz), which was operated at 200 W. A 60 mL Ar-saturated aqueous solution containing each LAS compound was sonicated in a water bath, which was maintained at 20°C by a cold water circulation system.

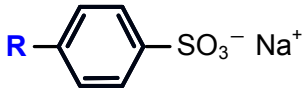


R : $C_8H_{17}$
sodium p-octylbenzenesulfonate (LAS $C_8$)

$C_9H_{19}$
sodium p-nonylbenzenesulfonate (LAS $C_9$)

$C_{12}H_{25}$
sodium p-dodecylbenzenesulfonate (LAS $C_{12}$)

**Fig. 1** Structural formula of LAS Cn. “n” is carbon number of the alkyl chain.

The concentration of each compound in aqueous solution was monitored by HPLC. The initial rate of degradation (within 10 min) was estimated on the basis of the average of several experimental runs. Since it was reported that the rate of sonolysis obey pseudo first-order kinetics, the LASs concentrations as the sonication time was approximated by exponential function and their derivative value at zero sonication time was adopted as the degradation rate used for the analysis of the obtained data.

## 3. Results and Discussion

In Fig.2, the initial degradation rates of LASs are plotted as a function of initial solute concentrations. At the concentration below 100 μM, it can be also seen that the degradation rates of all compounds increased linearly with increasing initial solute concentration. This increase is due to the increasing of surface excess of LASs molecules and it is indicated that LASs molecules transport rapidly to the interface of cavitation bubbles.

At high concentration, the degradation rates increased with increasing the initial concentration, and then they passed the peak at different concentration and decreased. Moreover, the degradation rate of LAS with the longer n-alkyl

nanzai@chem.osakafu-u.ac.jp

chain turned downward at lower concentration. That is, LASs with longer n-alkyl chain length has the peak at lower initial LAS concentration and lower degradation rate.

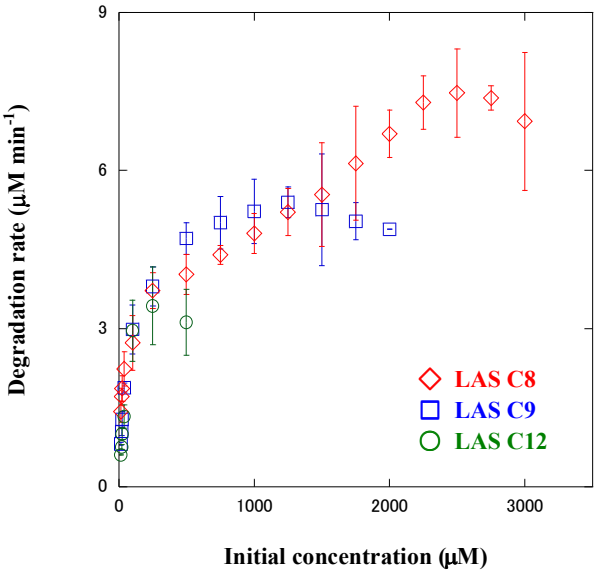


**Fig. 2** Relationship between the concentration of LASs and their initial sonochemical degradation rate.

Here, it is necessary to consider what affected on the initial LASs concentration and the degradation rate at each peak. It is proposed that micelle was formed at effective reaction zone via the accumulation onto the interfacial region. That is, the LAS concentration of effective reaction zone might to reach the CMC and this concentration seemed to affect on the peaks of degradation rate. For the verification of this assumption, the relationship between the degradation rate and CMC of each LAS should be considered. The CMC values were estimated by electric conductivity method because the literature data were varied from test to test. In this estimation, the concentration with inflection point was defined as the CMC.[3] Subsequently, the relationship between CMC and each LAS degradation rate at the concentration of peak was shown in Fig. 3. The linear relation can be seen among these plots. These results seemed to be indicated several meanings. In the each case, it was suggested that the maximum degradation rates were related with the CMC value. That is, though it was indicated that the accumulation ratios were almost same when the initial bulk concentration of each LAS was same, the maximum accumulation ratio was derived from CMC. Here, in addition to above description, one more phenomenon could be suggested as the reasons for the decrement of degradation rate in Fig. 2. The concentration of effective reaction zone was reached CMC and micelle was formed. Destaillats et al. proposed that micelle formation reduced the apparent sonochemical efficiency by isolating the free surfactant monomers from gas/liquid interface of the cavitation bubbles. Thus, micelles could be considered a good "shelter" from direct sonochemical effects.[4] Hence, the degradation rate decreased with increasing initial LAS concentration over CMC because more micelles were formed at the effective reaction zone.

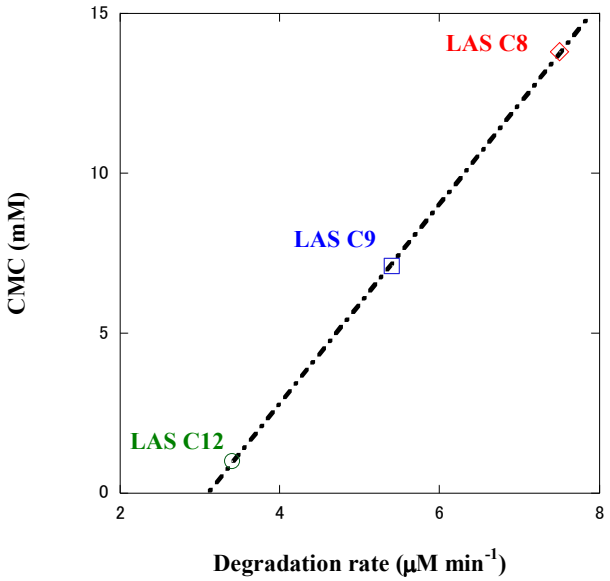


**Fig. 3** Relationship between degradation rates which have peaks in Fig. 2 and CMC of each LAS.

## 4. Conclusion

The initial degradation rate of each LASs had a peak respectively. It was suggested that these peaks had some relations with CMC of each LAS. The linear relation between them was confirmed and accumulation ratio was estimated as 5.5 times.


## Acknowledgment

This work was funded by the Sasakawa Scientific Research Grant from The Japan Science society.


## References


1. W.B. McNamara III, Y.T. Didenko and K.S. Suslick: J. Phys. Chem. B **107** (2003) 7303.
2. A.E. Alegria, Y. Lion, T. Kondo and P. Riesz: J. Phys. Chem. **93** (1989) 4908.
3. M. Manabe, H. Kawamura, A. Yamashita and S. Tokunaga: J. Colloid Interface Sci. **115** (1987) 147.
4. H. Destaillats, H.M. Hung, and M.R. Hoffmann Environ. Sci. Technol. **34** (2000) 311.

3P6-16

Proceedings of Symposium on Ultrasonic Electronics, Vol. 29 (2008) pp. 411-412
11-13 November, 2008

# Sonochemical degradation of phenol and cyclohexanol in mixed solution

混合溶液中におけるフェノールとシクロヘキサノールの超音波分解

Kenta Ishikawa‡, Ben Nanzai, Kenji Okitsu, Norimichi Takenaka, Hiroshi Bandow(Osaka Prefecture Univ.)
石川健太‡，南齋勉，興津健二，竹中規訓，坂東博 （大阪府立大学）

## Introduction

When the high intensity ultrasonic wave is irradiated to solution, micro bubbles which are called cavitation bubbles generate with high temperature and high pressure. It is reported that the sonochemical reaction happens at the inside of cavitation bubbles and their interface.

Here, the site where the sonochemical reaction takes place is defined as "Effective Reaction Zone" (Fig.1) [1]. LogP was found to be the representative parameter for understanding the hydrophobic properties of compounds. It is reported that the larger the value of LogP of solute becomes, the easier the molecules are gathered in the cavitation bubble interface and the decomposition speed grows [2].

In this work, The competing reaction of phenol and cyclohexanol as which the value of LogP was almost the same was considered. Moreover, the radical scavenge abilities were compared in the sonication for each single solute system of the phenol and cyclohexanol.

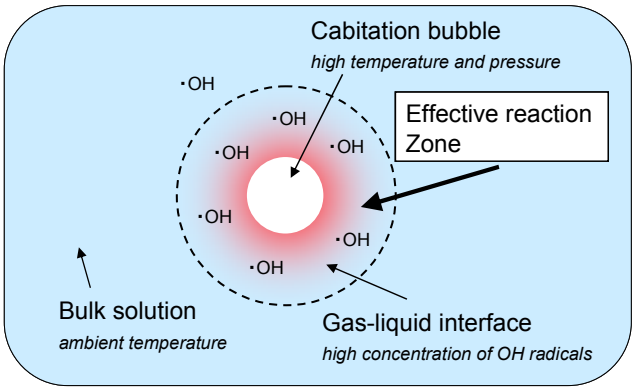


Fig. 1. Effective reaction zone where the sonochemical reaction take place.

## Experimental

Ultrasound irradiation was carried out using a 65 mmϕ oscillator (Kaijo 4611type; MFG. No.91F2) and an ultrasonic generator (Kaijo TA-4021type; Lot. No.19G9, frequencuy; 200 kHz), which was operated at 200 W. A 60 mM Ar-saturated aqueous solution containing phenol and cyclohexanol was sonicated in a water bath, which was maintained at 20°C by a cold water circulation system (TAITECCP-150R). When single solute system of the phenol and cyclohexanol, the concentration of each solution were prepared from 0 μM to 500 μM. In the case of mixed solution, the concentration of phenol was prepared to 100 μM, and the concentration of cyclohexanol was prepared from 0 μM to 500 μM. Hydrogen peroxide yields were measured by the KI method using a Spectrophotometer (U-3300). The concentration of phenol was monitored by a high-performance liquid chromatograph (HPLC : Shimadzu LC-20AT, SPD-20AV) with UV detection at 222 nm using a ODS column with a mobile phase of acetonitrile/water (40:60 v/v) flowing at 0.3 mL $min^{-1}$.

kea0820@chem.osakafu-u.ac.jp

## Results and Discussion

OH radicals are formed from water pyrolysis in the collapsing hot bubbles (Reaction 1).

$H_2O \rightarrow \cdot OH + \cdot H$ (1)

The reaction between OH radicals which are generated from Reaction 1 produce hydrogen peroxide (Reaction 2)

$\cdot OH + \cdot OH \rightarrow H_2O_2$ (2)

During the sonochemical treatments of radical scavenger in water, radical scavenger reacts with OH radical and Reaction 2 is inhibited.

To compare the radical scavenge abilities, the amount of the hydrogen peroxide generation was shown in Fig.2. It could be seen that the radical scavenge ability of cyclohexanol was higher than that of phenol.

The values of LogP are 1.46 for phenol, and 1.23 for cyclohexanol. In addition, reaction rate constants of OH radical with phenol are $6.6\times10^9$ L $mol^{-1}$ $s^{-1}$ and with cyclohexnol is less than $6.6\times10^9$ L $mol^{-1}$ $s^{-1}$ (reaction rate constant of OH radical with cyclohexanol is expected from the value of heptanol, 1-hexanol and 1-heptanol). Expecting

from two values of LogP and reaction rate constant of OH radical, the radical scavenge abilities of phenol should be higher than that of cyclohexanol. It was considered that it was related to the molecular structure of phenol and cyclohexanol. Phenol has the π electron and cyclohexanol has the sterically-bulky structure. Thus, for phenol, it was suggested that electronic repulsion with the π electron was caused when the phenol molecules started to be gathered on the cavitation bubble interface.

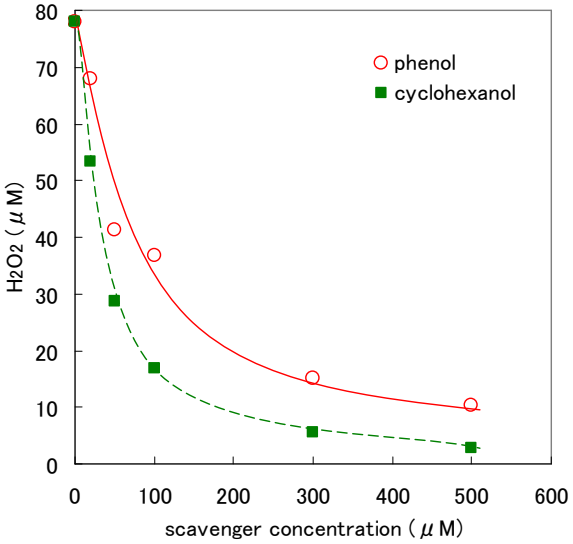


Fig.2. Changes in concentration of the sonochemically formed hydrogen peroxide in phenol and cyclohexanol aqueous solutions.

Surface tension was measured as an index of the gathering easiness of gas-liquid interface. This result showed that there was practically no change in the surface tention of each compound compared with that of water at low concentration. On the other hand, the surface tension of cyclohexanol has become much smaller than phenol as the concentration of solution was high. From this result, cyclohexanol molecule was gathered easily on the interface compared with phenol and it was considered that the π electron repulsion effect of phenol was larger than the effect of the sterically-bulky structure of cyclohexanol. However, whether the solute was densely gathered in the interface at the low concentration is not elucidated.

Phenol and cyclohexanol were sonicated in the mixture solution. This result was shown in Fig. 3. It can be seen that the decomposed amount of phenol hardly changed up to the concentration of cyclohexanol was 20 μM but it decreased as the concentration of cyclohexanol increased. From this result, it was considered that the "effective reaction zone" was densely distributed more than 20 μM and the molecules of phenol competed with cyclohexanol to react OH radicals in this range of the concentration. Thus, the molecules of phenol were densely gathered in the "effective reaction zone" at low concentration. It was suggested that the electronic repulsion from the π electron of phenol was effective at low concentration.

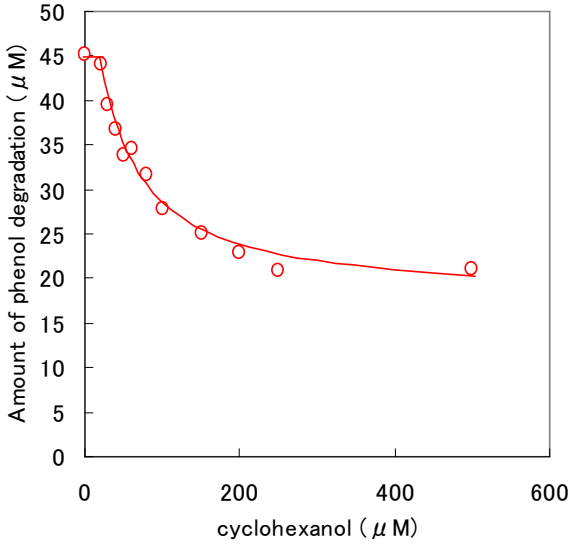


Fig. 3. Sonochemical degradation of phenol as a function of cyclohexanol concentration.

## Conclusions

The radical scavenge abilities of cyclohexanol was higher than that of phenol. It was suggested that this results related to the electronic repulsion from the π electron of phenol.

## References

[1] K. Okitsu, K. Iwasaki, Y. Yobiko, H.Bandow, R. Nishimura and Y. Maeda : Ultrason. Sonochem. **12** (2005) 255.

[2] B. Nanzai, K.Okitsu, N. Takenaka, H. Bandow and Y. Maeda : Ultrason. Sonochem. **15** (2008) 478.

3P6-17

Proceedings of Symposium on Ultrasonic Electronics, Vol. 29 (2008) pp. 413-414
11-13 November, 2008

# Sonolysis of dicarboxylic acids in aqueous solution

炭素数及び不飽和度の異なる各種ジカルボン酸水溶液の超音波化学反応

Rei Moriya†, Yukio Naruke, Hisashi Tanaka, and Hisashi Harada (College Chemistry, Grad. School, Meisei Univ.)
守谷怜‡，成毛由紀夫，田中寿，原田久志（明星大院 理工）

## 1. Introduction

It is important for sonochemical process to produce cavitation during sonic wave irradiation. Acoustic cavitation leads to localize spots of high temperatures and pressures. Thermal and radical fields for chemical reaction are prepared inside and around the cavitation. Different reaction paths are considered at each reaction site. Volatile compounds go into cavitation babbles. Non-volatile materials, on the other hand, stay around the babbles. The other day, we have already reported about chemical reaction of volatile compound [1]. We have also examined chemical reaction paths of dicarboxylic acids around the cavitation area [2]. Those acids, as probe compounds for reactions around bubbles, are non-volatile and water-soluble. Furthermore, products are simple and easy detectable.

In this paper, we discussed the difference of products when various carbon numbers of reactants were prepared. We also try to examine the difference in behavior between with and without double bond.

## 2. Experimental

### *2.1. Materials (Reactants)*

Series of dicarboxylic acids were prepared. Those are oxalic acid (HOOC-COOH), malonic acid (HOOC-($CH_2$)-COOH), succinic acid (HOOC-($C_2H_4$)-COOH), maleic acid (*cis type including double bond*, HOOCHC:CHCOOH), and fumaric acid (*trans type including double bond*, HOOCHC:CHCOOH). We used extra pure grade reagents (Wako Pure Chemicals) without further purification. Each acid was dissolved into water. Concentration and volume of trial samples are 8-10 mM (mainly 8.62 mM) and 30-100 $cm^3$ (mainly 100 $cm^3$), respectively.

### *2.2. Sonochemical reaction*

A Pyrex glass short-neck Kjeldahl flask (actual volume approximately 300 $cm^3$, mainly 296 $cm^3$) was used as a reactor. The glass reactor containing the reactant solutions was sonicated using an ultrasonic generator at 25℃. It was placed in a temperature-controlled water bath (EYELA) all the time. Almost all trials were carried out under irradiation of 200 kHz (Kaijo, 200W). Sonolysis was also tried to perform at other frequencies. Before sonication, pure argon gas (Ar) was passed through the reactant solution in order to expel the air. Then the glass reactor was sealed when it was filled with Ar. Saturated gas in the solution plays an important role in the sonochemical reaction. In our cases, we supposed the solution was saturated with Ar.

07m2016@chem.meisei-u.ac.jp

### *2.3. Analysis*

The amounts of gaseous products in the reactor were determined by using a gas chromatograph (Shimadzu, GC8A). Liquid products in the solution, on the other hand, were detected by using a liquid chromatograph (Shimadzu, LC10A).

Hydrogen peroxide in the solution was analyzed by means of a colorimetric technique (Nacalai Tesque, Titanium sulfate solution for detection of hydrogen peroxide, and JASCO, V530).

## 3. Results and discussion

### *3.1. Decomposition of saturated materials*

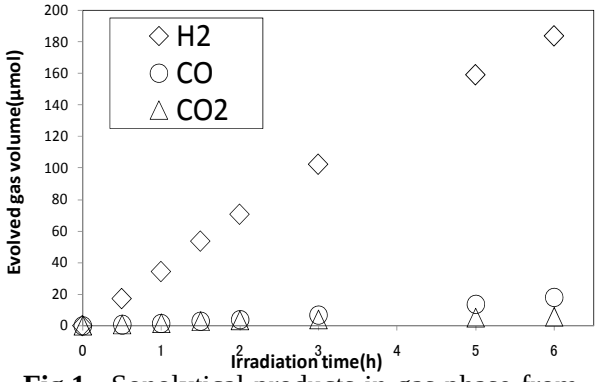


**Fig.1** Sonolytical products in gas phase from succinic acid solution at 25℃

Figure 1 shows gaseous reaction products from succinic acid solution under 200kHz ultrasound in an Ar atmosphere. Hydrogen ($H_2$),

carbon monoxide (CO) and carbon dioxide ($CO_2$) were produced. Similar products were obtained in all reactant solutions in this our work. The rates of production, of course, were different. Hydrocarbons could not be detected. In the case of malonic acid, a little amount of methane has detected after long time irradiation. Thus production of another compounds will be expected. Products in liquid phase will be examined in near future.

Although it is not clear in this figure, the production rate of $CO_2$ decreased with irradiation time. The production rate of CO, on the contrary, increased with irradiation time.

Reduction of $CO_2$ during sonication was considered [3], as indicated below equation.

$$CO_2 + H_2 \text{ (or } 2H) \rightarrow CO + H_2O \text{ --- (1)}$$

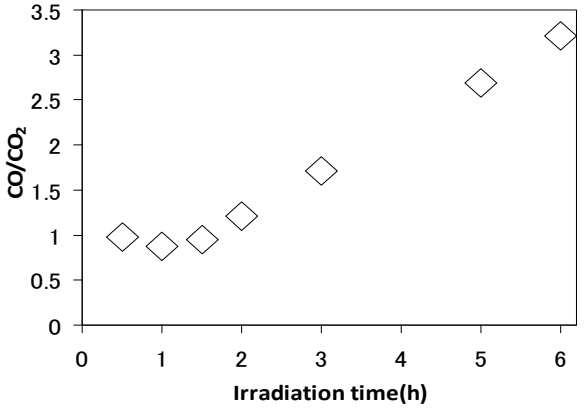


**Fig.2** Time dependence of ratio of CO to $CO_2$

Figure 2 illustrates the ratio went up with irradiation time. This figure also shows CO was evolved even at the early stage of sonication. Namely, we note that CO is produced not only the reduction of $CO_2$ but also the direct decomposition of reactant. Thus, the reaction rate has to be estimated from total amount of carbon compounds.

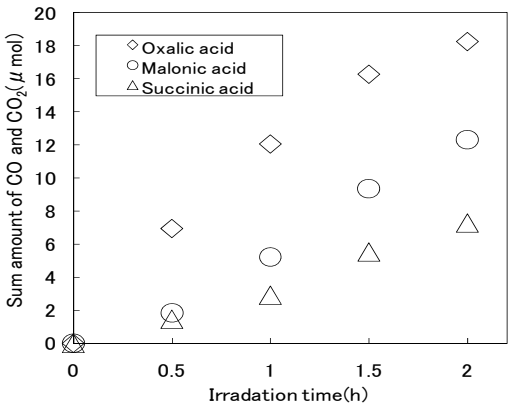


**Fig.3** Effect of length of carbon chain on chemical reactivity

In order to confirm the relation between chemical reactivity and carbon number (carbon chain length), the sum amount of CO and $CO_2$ produced during sonication in each reactant solution is shown in Fig. 3. Oxalic acid recorded the highest reactivity. The order of reactivity was inverse relation to the number of carbon in the molecule.

### *3.2. Deference of rates between saturated and unsaturated materials*

In the case of dicarboxylic acids of carbon number over 3, there are unsaturated same carbon number acids. For example, in the case of 4-carbon compounds, fumaric acid and maleic acid are corresponding to succinic acid. Each of them is isomer.

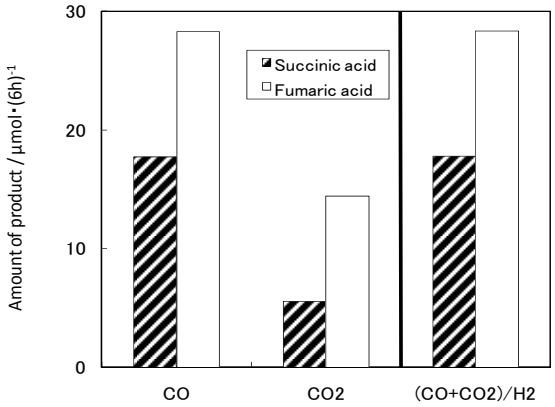


**Fig.4** Comparison of sonolytical rates between saturated and unsaturated dicardoxylic acids

Figure 4 indicates the comparison of the sum amount of CO and $CO_2$ produced after 6 hours sonication between succinic acid and fumaric acid. Because both compounds have different hydrogen number, the ratios of carbon products (CO and $CO_2$) to $H_2$ produced were also illustrated in this figure. It is seen that unsaturated compound is more reactive than saturated one. We will report the reactivity for another unsaturated 4-carbon compound (maleic acid) in the presentation site.

**References**

1. H, Harada, A. Yoneyama, Y. Ikeda and K. Yasui: Proc., 10th Meeting of the European Society of Sonochemistry. (2006) p.59.
2. Y. Naruke, H. Tanaka and H. Harada: Proc., 14th Photocatalyst Symposium. (2007) p.94.
3. H. Harada: Ultasonics-Sonochemistry. **5** (1998) 73.

3P6-18

Proceedings of Symposium on Ultrasonic Electronics, Vol. 29 (2008) pp. 415-416
11-13 November, 2008

# Effect of Agitation Condition on Performance of Sonochemical Reaction

超音波化学反応性能に及ぼす攪拌条件の影響

Keiji Yasuda†, Kazumasa Matsuura and Hirotoshi Horizoe (Facult. Eng., Nagoya Univ.)
安田啓司‡，松浦一真，堀添浩俊（名古屋大 工）

## 1. Introduction

In order to apply sonochemical methods to on-site wastewater treatment, the enhancement of sonochemical reaction is necessary. It has been reported that the superposition of ultrasonic fields(1) or the liquid mixing(2) increased the sonochemical reaction rate. However, there are few studies from the reactor engineering for the enhancement of sonochemical reaction.

In this study, for different ultrasonic fields, the effect of agitation condition on performance of sonochemical reaction are examined.

## 2. Experimental

**Fig. 1** shows the outline of the experimental apparatus. The reactor was made of transparent acrylic resin. The dimensions were 120 mm in length, 120 mm in width and 350 mm in height. Four PZT ultrasonic transducers were attached at the bottom, lower, middle and upper of the reactor. The ultrasonic frequency was 486 kHz. The effective electric power applied to one transducer was changed from 0 to 50 W. The propeller ($\phi$ 60 mm) or turbine ($\phi$ 75 mm) type of agitator was used. The agitator was inserted from top of reactor. The distance between reactor bottom and agitator was 140 mm. The revolution rate of agitator was changed from 0 – 200 rpm.

The samples were potassium iodide (KI) and tetraphenylporphine tetrasulfonic acid (TPPS) aqueous solution. The initial concentrations of KI and TPPS were 0.1 mol/L and 3.3 μ mol/L, respectively. The sample volume was 4.5 L. The concentration of triiodide ion ($I_3^-$) produced after 30 min sonication or TPPS concentration after 60 min soncation was measured by using ultraviolet and visible spectrometer.

## 3. Results and discussion

**Fig. 2** shows the effect of electrical power to one transducer on the $I_3^-$ concentration for different positions of transducers. For the single irradiation, the $I_3^-$ concentration by using bottom transducer is

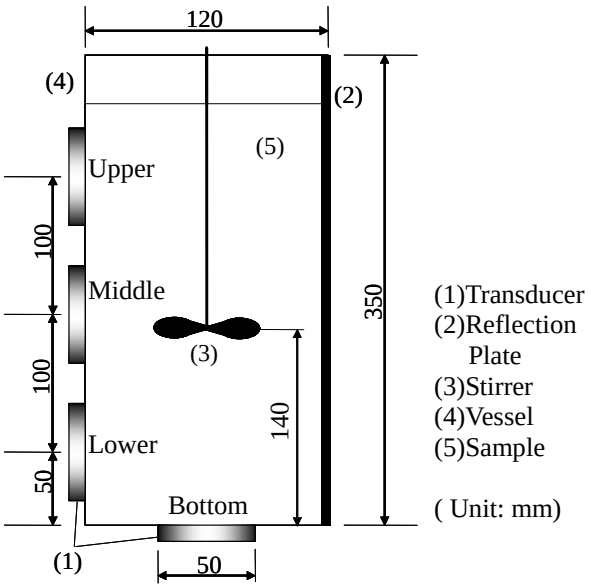


Fig.1 Outline of experimental apparatus

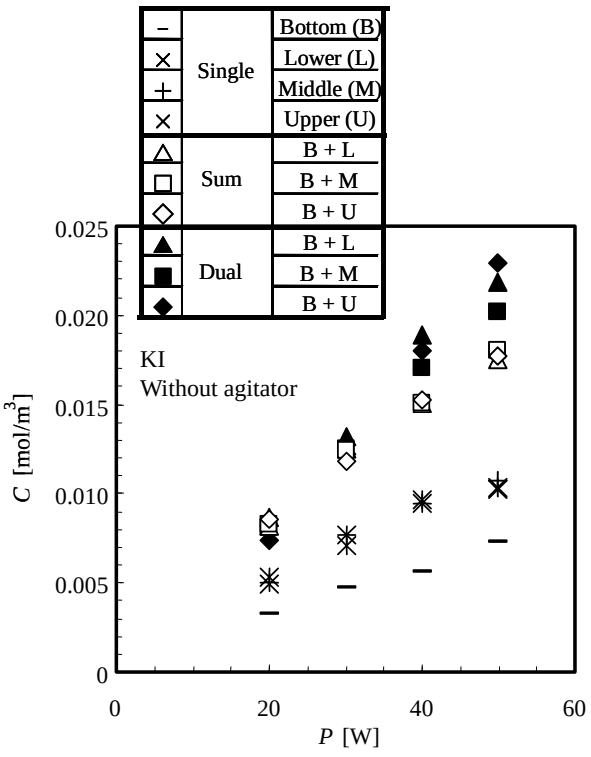


Fig.2 Effect of electrical power to one transducer on the $I_3^-$ concentration for different positions of transducers

lower than those by using lower, middle and upper transducers. This is because the fountain at liquid surface inhibits the formation of standing wave in reactor. In the cases of high electric input power to transducer, the $I_3^-$ concentration for dual irradiation is higher than the sum of $I_3^-$ concentrations for single irradiation. It is considered that the area of sonochemical reaction fields increases by the superposition of ultrasonic fields. For the dual irradiation at $P$ = 50 W, the $I_3^-$ concentration by using upper transducer is higher than those by using bottom and middle transducers. It is considered that the liquid surface is easy to form standing wave by using bottom transducer.

**Fig. 3** shows the effect of electrical power to transducer on ratio of TPPS decomposition conversion with agitator. The ordinate indicates the decomposition conversion ratio of with agitator to without agitator. The ratio of TPPS decomposition conversion increases with electrical power. It is considered that at high ultrasonic intensity, the standing wave is difficult to break by agitation.

**Fig. 4** shows the effect of revolution rate on ratio of TPPS decomposition conversion or $I_3^-$ concentration for single irradiation from bottom with agitator. In the case of propeller type agitator, the ratios of TPPS decomposition conversion and $I_3^-$ concentration increase with revolution rate. The ratio of TPPS decomposition conversion is higher than that of $I_3^-$ concentration. It is considered that the agitation enhances the supply of TPPS to reaction filed since TPPS concentration is much lower than KI concentration. In case of turbine type agitator, on the other hand, the ratio of $I_3^-$ concentration decreases with revolution rate. This is because the bottom of turbine type agitator, which has flat plate, reflects ultrasound and the degree of reflection decreases by revolution of agitator.

**Fig. 5** shows the effect of revolution rate on ratio of TPPS decomposition conversion or $I_3^-$ concentration for dual irradiation with agitator. The data for irradiation from bottom are almost same as those for dual irradiation. In the case of TPPS, the excessive agitation decreases decomposition conversion. This is because the area of standing wave becomes small by liquid turbulence. In the case of KI, on the other hand, the dependence of $I_3^-$ concentration on revolution rate is small. From these results, it is obvious that the agitation is effective for low concentration sample.


**References**

1. R. Feng et al: Ultrason. Sonochem., **9** (2002) 231.
2. K. Yasuda et al.: J. Chem. Eng. Jpn. **32** (1999) 347.


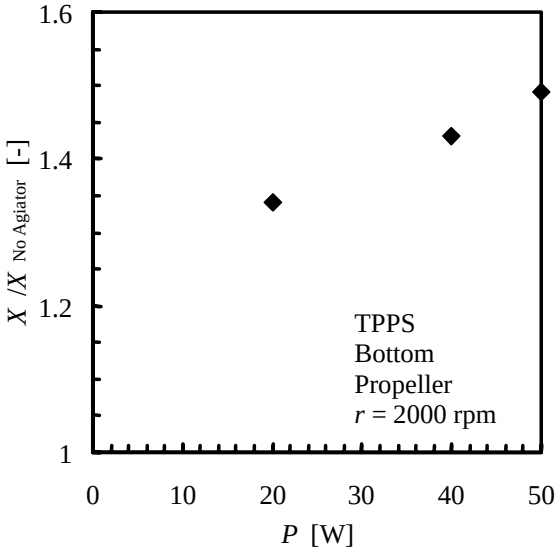


Fig.3 Effect of electrical power to transducer on ratio of TPPS decomposition conversion with agitator

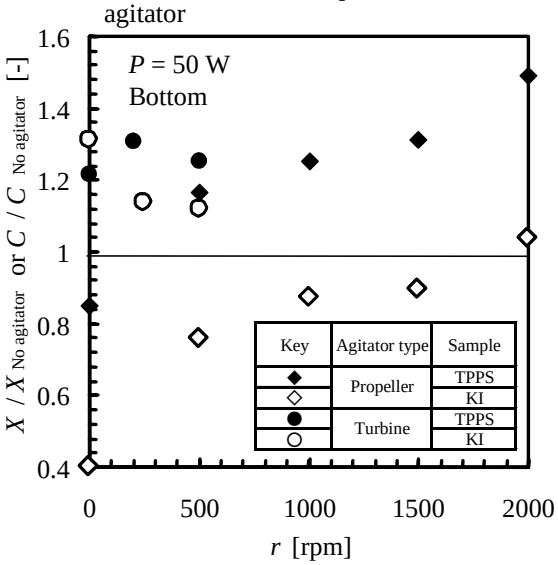


Fig.4 Effect of revolution rate on ratio of TPPS decomposition conversion or $I_3^-$ concentration for single irradiation from bottom with agitator

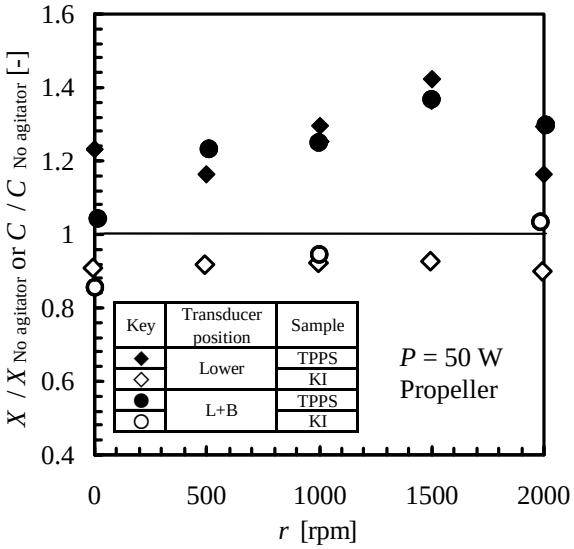


Fig.5 Effect of revolution rate on ratio of TPPS decomposition conversion or $I_3^-$ concentration for dual irradiation with agitator

3P6-19

Proceedings of Symposium on Ultrasonic Electronics, Vol. 29 (2008) pp. 417-418
11-13 November, 2008

# Effect of Hydrogen Peroxide and Frequency on Sonochemical Degradation of Phenol

Myunghee Lim‡, Younggyu Son, Mingcan Cui, Jeehyeong Khim† (Dep. of Civil, Environ. and Architec. Eng. Korea Univ.)

## 1. Introduction

The chemical effects of ultrasound enhance chemical reactivity through cavitation. Sonication of aqueous solutions produces the formation, growth and collapse of cavitation bubbles. The collapse of the cavitation bubble results in a localized high temperature (5000 K) and pressure (1000 atm) [1].

The main reaction mechanisms are radical reaction (·O, ·H, ·OH, etc.) and pyrolysis. Volatile compounds were directly volatilized on the inside of the cavitation bubble and were decomposed by high temperature and pressure. However, non-volatile compounds barely diffused into the bubble, and were therefore indirectly degraded by radicals in the bulk solution or interface of bubbles.

Phenol, a hazardous chemical in the priority pollutant list [2], was studied for its sonochemical degradation. To enhance the degradation rate of phenol, various attempts have been made for the application of high frequency ultrasound [3], combinations of oxidants/additives [3, 4, 5] and integration with ultraviolet rays [1].

In this study, an investigation was carried out on the effect of hydrogen peroxide and frequency on the degradation of phenol and total organic carbon (TOC).

## 2. Experimental Procedures

The sonochemical reaction was carried out in a 300 mL pyrex bottle (the reactor total volume 500 mL) containing the solution. The pyrex bottle reactor was emerged in an acryl reactor, as shown in Fig. 1. The reaction temperature was maintained at 16~18℃ by using a cooling water system. The ultrasound of 35 kHz, 1 MHz, and 240 W were applied in a bath type ultrasonic system (Frexonic, Mirae Ultrasonics Tech.).

---

hyeong@korea.ac.kr

High-purity phenol (Samchun) was used and the initial concentration was 0.05 mM. 0.0018 mM of hydrogen peroxide (Samchun) was added to the phenol solution.

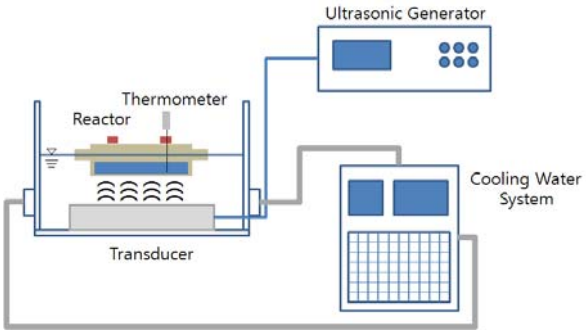


Fig. 1 Schematic of sonochemical reactor

1 mL of liquid was analyzed by the direct photometric method (5530D, standard methods for the examination of water and wastewater, 20th edition, APHA) every 5 min. Hydrogen peroxide was detected by the iodometric method [6]. The total organic carbon (TOC) concentration was measured by a TOC analyzer (SEIVERS 5310C laboratory analyzer, GE).

## 3. Result and discussion

The concentration change of phenol is shown in Fig. 2. A more rapid degradation of phenol occurred during sonolysis at 1 MHz than at 35 kHz. At a higher frequency, the power of the cavitation effect decreased. Therefore, the cavitation event occurring at a low frequency is more violent and efficient on the inside of the cavitation bubble.

However, at a high frequency the acoustic period is shorter and the size of the cavitation bubble decreases. Consequently, most of the formed radicals have sufficient time to recombine. Therefore, a high frequency results in a high hydrogen peroxide concentration in aqueous solutions, which can cause higher degradation rates

of non-volatile compounds (ex. phenols) than at a low frequency.

In addition to the hydrogen peroxide in phenol solution, the concentration of phenol was decreased above 90% within 30 min (Fig. 3 (a)). On the other hands, in the case where only the ultrasound process was applied, the same degradation rate of phenol was obtained within 120 min (1 MHz, Fig. 2). Therefore, the addition of hydrogen peroxide can enhance the degradation of phenol. This concurs with other results previously obtained [7].

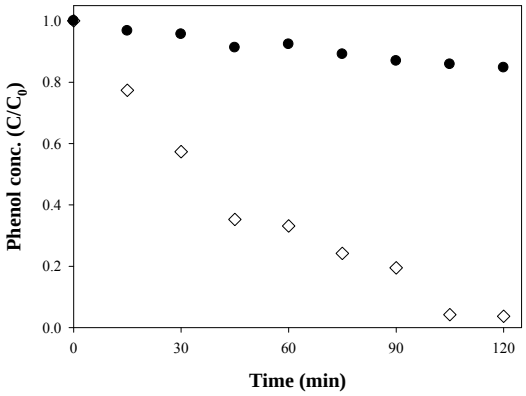


Fig. 2 Concentrations of phenol with sonication time

(● : 35 kHz, ◇ : 1 MHz)

Hydrogen peroxide was individually added two times (initially, and after 15min). As soon as it was placed in the hydrogen peroxide, the TOC concentration also decreased. The hydrogen peroxide concentration also directly decreased (Fig. 3 (b)). This result was the same for different frequencies.

In previous research [7, 8], additives in phenols solution (hydrogen peroxide and $Fe_2SO_4$) were used to enhance the degradation of TOC.

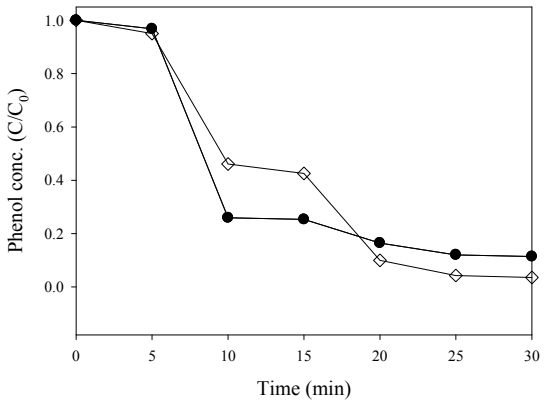


(a)

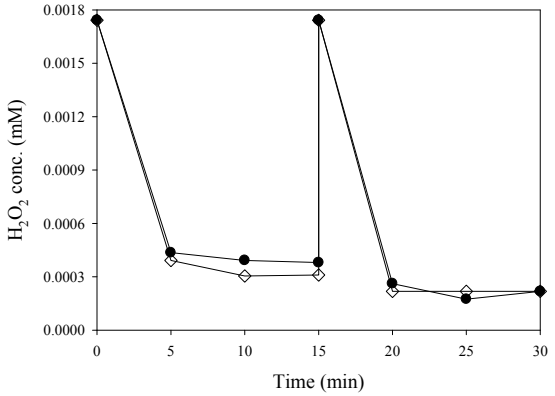


(b)

Fig. 3 Concentrations of phenol and hydrogen peroxide with sonication time ((a) phenol with hydrogen peroxide, (b) hydrogen peroxide)

(● : 35 kHz, ◇ : 1 MHz)

Therefore, a high concentration of $H_2O_2$ or some catalysts ($Fe_2SO_4$) and a combination of AOPs (advanced oxidation processes) are required for the degradation of TOC.

**Acknowledgements**

This subject is supported by Ministry of Environment, Republic of Korea as "The Eco-technopia 21 project" (no. 061-081-042).

**References**

1. Y. Chen and P. Smirniotis : Ind. Eng. Chem. Res. **41** (2002) 5958.
2. USEPA, National Recommended Water Quality Criteria (2006).
3. M. H. Entezari, C. Petrier and P. Devidal : Ultrasonics Sonochemistry **10** (2003) 103.
4. M. Kubo, K. Matsuoka, A. Takahashi, N. shibasaki-Kitakawa and T. yonemoto : Ultrasonics Sonochemistry **12** (2005) 263.
5. C. Wu, X. Liu, D. We, J. Fan and L. Wang : Wat. Res. **35** (2001) 3927.
6. M. A. Beckett and I. Hua : J. Phys. Chem. A. **105** (2001) 3796.
7. J. Lin, C. Chang, J. Wu and Y. Ma : Wat. Sci. Tech. **34** (1996) 41.
8. M. Inoue, Y. Masuda, F. Okada, A. Sakurai, I. Takahashi and M. Sakakibara : Wat. Res. **42** (2008) 1379.

3P6-20

Proceedings of Symposium on Ultrasonic Electronics, Vol. 29 (2008) pp. 419-420
11-13 November, 2008

# Effects of gas content in a liquid on the threshold for free radical production

液体中の含有気体が超音波照射下の
フリーラジカル発生閾値におよぼす影響

Kengo Okada[1†], Nobuki Kudo, Mariame A. Hassan[2], Takashi Kondo[2] and Katsuyuki Yamamoto[1] ([1] Graduate School of Information Science and Technology, Hokkaido Univ.; [2] Univ. of Toyama)

岡田健吾[1]，工藤信樹[1]，ハッサン マリアム アリ[2]，近藤隆[2]，山本克之[1]
([1]北大院 情報；[2]富山大 医)

## 1. Introduction

Ultrasound contrast agents, which are suspensions of microbubbles of several microns in diameter, have been utilized for noninvasive ultrasound diagnostic imaging and therapy[1)]. Exposure to ultrasound increases the risk for adverse effects of production of free radicals such as hydroxyl (OH) radicals. It is known that the efficiency of free radical production depends not only on acoustic parameters such as pulse duration (PD) and duty ratio[2)] but also on non-acoustic parameters such as degree of gas saturation and addition of microbubbles[3)]. However, the contributions of dissolved gas and microbubbles to free radical production are still unclear.

In this study, effects of gas contents on the thresholds of PD and pulse repetition frequencies (PRF) for free radical production were investigated. The thresholds of PD were evaluated using four test solutions with different gaseous conditions: air-saturated and degassed solutions with and without microbubbles.

## 2. Materials and methods

The experimental system used in this study consisted of a water bath filled with degassed water and a flat-face ultrasound transducer immersed in the bath with its radiating surface facing up (**Figure 1**). A dish was placed on the transducer, and 3 ml of a test solution was gently poured into the dish. The test solution was exposed to 1-MHz ultrasound of 0.1 $MPa_{p-p}$ in pressure amplitude for 5 minutes at various PDs and PRFs. The colorimetric assay of liberated $I_2$ from KI-starch solution[4)] was used for detecting $H_2O_2$, which is produced by the recombination of two OH radicals. The change in color of the solution caused by $H_2O_2$ was quantified as absorbance at a wavelength of 555 nm. The absorbance of a test solution directly correlates to amount of free radical production.

okada@bme.ist.hokudai.ac.jp

An air-saturated and a degassed solution were prepared by leaving KI-starch solutions in bottles at atmospheric pressure and at 40-mmHg pressure, respectively. Microbubbles of 20 μm in diameter with shells consisting of polyvinylidene chloride-acrylonitryl copolymer (F-30E, Matsumoto Yushi-Seiyaku) were added to both the air-saturated and degassed solutions at a concentration of 1 mg/ml just before sonication.

## 3. Results and discussion

**Figure 2** shows a comparison of the amounts of free radicals produced in the four test solutions exposed to ultrasound of 5 ms in PD and 100 Hz in PRF. Amounts of free radical produced in the air-saturated test solutions were larger than those in the degassed test solutions regardless of the presence or absence of microbubbles. Addition of microbubbles increased the amount of free radical produced in the degassed test solution but had no effect in the air-saturated test solution. This result shows that dissolved gas has a dominant effect on free radical production.

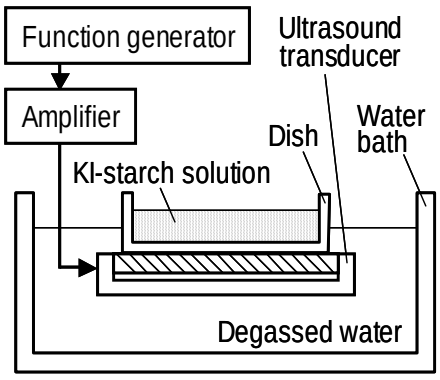


Fig. 1. Experimental setup used in the experiments.

In order to determine the thresholds of PD and PRF, we evaluated the relationship between PD and amount of free radicals produced at various PRFs. **Figure 3** shows the results in the air-saturated test solution without microbubbles. The amount of free radicals produced increased linearly with increase in PD at fixed PRF. The threshold of PD at a certain PRF was determined from the intersection of a least-squares regression line (shown as a dashed line in the figure) with the x-axis. The threshold line for this solution for free radical production was then obtained as a function of PDs and PRFs.

The threshold lines for the other three test solutions were obtained in the same way as that described above. **Figure 4** shows a summary of the threshold lines for the four test solutions. All of the threshold lines had the same trend: PD decreased with increase in PRF. The lines for the degassed test solutions had higher threshold PDs at all PRFs than did those for the air-saturated test solutions regardless of the presence or absence of microbubbles. Microbubbles caused a decrease in the threshold in degassed test solution but not cause in the air-saturated test solution. These results show that dissolved gas has a dominant effect also on the thresholds.

## 4. Conclusion

To understand the underlying concepts required for the determination of thresholds for free radical production, the effects of dissolved gas and microbubbles on the thresholds of PD and PRF were investigated. Dissolved gas has a more dominant effect than that of microbubbles on both the amount of free radicals produced and the threshold.


## Acknowledgment

This work was partially supported by a Grant-in-Aid for Scientific Research, Japan Society for the Promotion of Science and was conducted as a part of a project of the Research and Development Committee Program of the Japan Society of Ultrasonics in Medicine.


## References


1. C. M. H. Newman and T. Bettinger: Gene Ther. **14** (2007) 465.
2. A. Henglein, R. Ulrich and J. Lilie: J. Am. Chem. Soc. **111** (1989) 1974.
3. D. L. Miller and R. M. Thomas: Ultrasound Med. Biol. **21** (1995) 1059.
4. T. Kondo and G. Yoshii: Ultrasound Med. Biol. **11** (1985) 113.


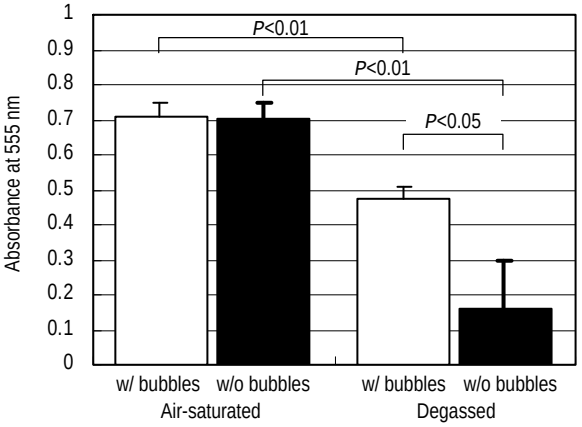


Fig. 2. Comparison of the amounts of free radicals produced in air-saturated and degassed solutions with and without microbubbles. Bars and error bars show the mean ± S.D. (n=4).

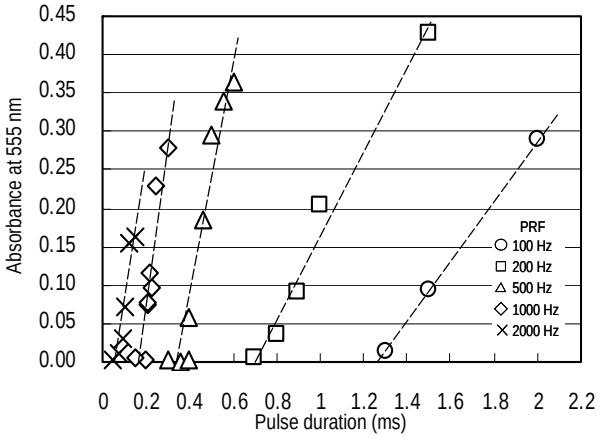


Fig. 3. Relationship between PDs and amounts of free radicals produced in air-saturated test solution without microbubbles.

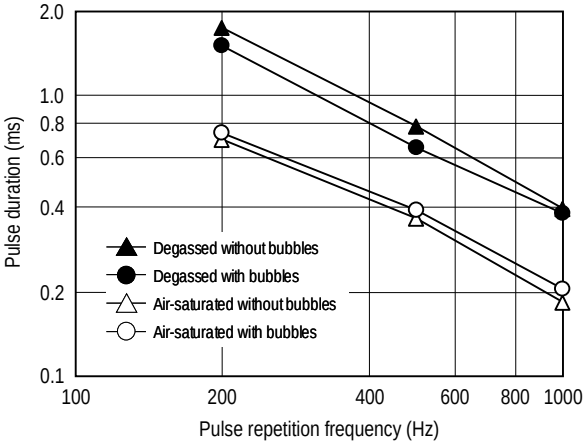


Fig. 4. Thresholds of PDs and PRFs for free radical production in air-saturated and degassed test solutions with and without microbubbles.

Proceedings of Symposium on Ultrasonic Electronics, Vol. 29 (2008) pp. 421-422
11-13 November, 2008

# Improvement of Tissue Strain Uniformity and Elastogram by Compression Optimizing

加圧方法最適化による組織内歪み均一性の向上及びelastogramの改善

Shizuka Sato†, Takayuki Sato, Sayuki Aiura, Yasuaki Watanabe, Shigeyoshi Goka and Hitoshi Sekimoto ( Tokyo Metropolitan Univ.)
佐藤翔†，佐藤隆幸，相浦紗雪，渡部泰明，五箇繁善，関本仁 （首都大　理工）

## 1. Introduction

A tissue-strain distribution by compressing the model is reflected directly in an image of tissue-stifness distribution in Elastography. In this study, we develop the simulation tool which optimize the tissue-strain distribution using a damper and a concave compression board. We set thickness of damper, Young's modulus and curvature radius of concave compression board as parameters and consider the strain flatness in lateral direcion as optimizing index.

## 2. FEM simulation

It is assumed that when a model with a flat surface is compressed, damper reduce the large strain caused by the edge of compression board is reduced by using a damper, and as the result, the tissue strain uniformity is expected to improve in the observed region. In this study, we calculate the strain distribution of an object consisted of three layers as shown in Figure 1 under the compression using Finite Element Method (FEM).

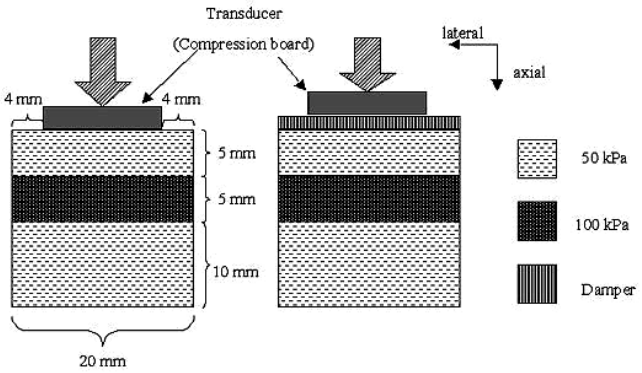


Fig. 1　Simulation model

### 2.1 Compression with damper using a flat board

We calculated the strain flatness with and without damper, which is 50 kPa in Young's modulus and has 3 mm thickness in order to confirm the effect of insertion of the damper. Figure. 2 shows ratio of the strain under the center line to the strain under the left line and that is regarded as strain flatness. It is desirable that strain ratio is closed to 1, and Figure 2 shows that the strain ratio is improved remarkable in the shallow region.

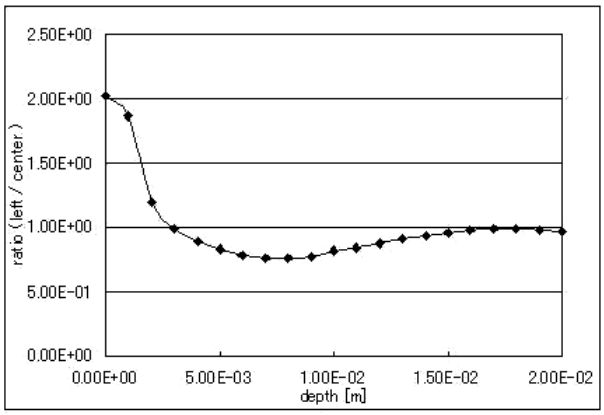


(a)

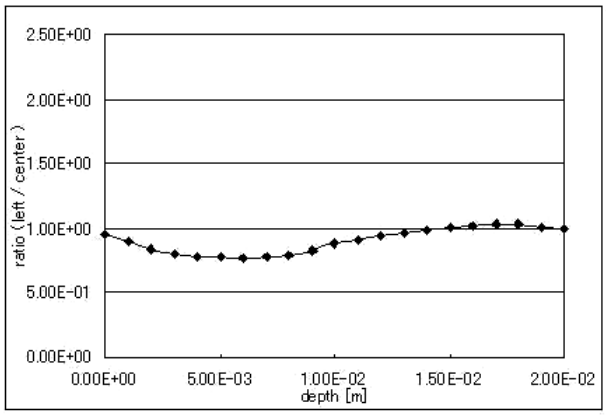


(b)

Fig. 2　Strain ratio between center line and left line
(a)No damper (b)With damper

---

shizuka@esys.eei.metro-u.ac.jp

### 2.2 Compression using a concave board

As the result shown in Figure 2, the strain ratio is lower than 1 in the region from 3 to 15 mm depth, regardless of the insertion the damper. To improve such low strain ratio, we use the compression board which has a concave surface.

The result shown in Figure 3 is conducted by changing the curvature radii of 500, 1000, 1500 and 2000 mm of the concave compression board, in addition to the insertion of the damper (50kPa, 3mm in thickness). This result illustrates that the curvature radii of 500, 1000, 1500 and 2000 mm contribute in improving strain flatness.

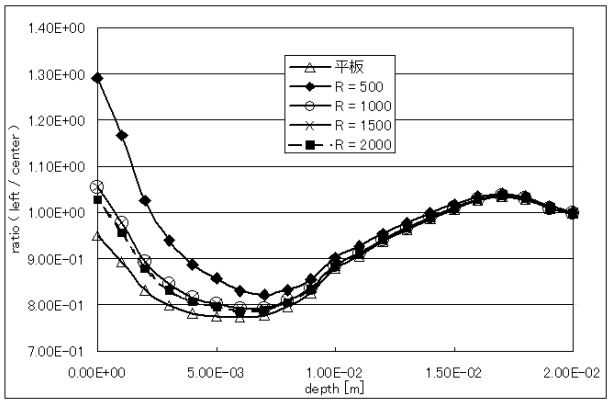


Fig. 3 Strain ratio using a concave compression board

### 3. FDTD simulation

According to the strain distribution obtained by FEM analysis, the wave motion analysis of the pre- and post-compression tissue based on FDTD method was performed to produce an elasticity image, which is necessary for screening of the compression optimizing.

The wave motion analysis is also performed on the drawn in Figure 1. The scatterers were randomly arranged in the tissue at the rate of 1%. The tissue is given the 1% compression in the axial direction, and the echo signals of the pre- and post-compression are collected.

### 4. Cross correlation processing

Executing 1-dimentional cross correlation process between the corresponding echo signal lines of the pre- and post- compression, an elasticity distribution image can be obtained.

For elasticity image, the stiffer region generally leads the higher correlation value. Figure 4 shows the obtained image of elasticity distribution drawn in a grayscale. The whiter region indicates the higher correlation value, namely, the harder region. As shown in Figure 4, it is found that the stiff layer is described as a highly-correlated region than the soft layer.

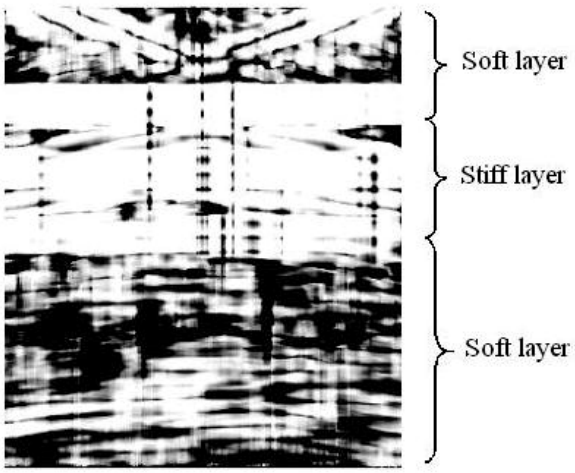


Fig. 4 Image of strain distribution

### 5. Conclusion

We tried to optimize the tissue compression using FEM simulation in order to improve the strain nonuniformity of compressed tissue which causes degradation of elastogram. As the results, it is possible to improve the strain flatness along the lateral direction by the insertion of the damper and using the concave board in the numerical experiments. In order to improve the quality of simulation image, FDTD method simulation should be improved.

### Reference

1. M.O'Donnell, et al., IEEE Trans. Ultrason., Ferroelect., Freq.Contr. **44** (1997)1304-1319.

Proceedings of Symposium on Ultrasonic Electronics, Vol. 29 (2008) pp. 423-424
11-13 November, 2008

# Optimization of Apodization Function For Lateral Modulation
横方向変調の最適化

Chikayoshi Sumi†, Yuuichi Komiya and Shinya Uga
(Facult. Sci. Tech. Eng., Sophia Univ.)
炭親良†，小宮勇一，宇賀真也 (上智大 理工)

## 1. Introduction

We have realized the beamformings [1-3] for accurately measuring tissue or blood displacement/velocity vectors or strain tensors [4] using multidimensional cross-spectrum phase gradient method (MCSPGM), and multidimensional autocorrelation and Doppler methods (MAM and MDM). The beamformings are realized by using the steerings of the multiple beams and apodizations. In [1-4], we reported several lateral cosine modulation methods (LCMMs) that use different apodization functions in addition to the multidirectional synthetic aperture method (MDSAM) and the multiple transmitting method (MTM). As shown, the coherent superimposition of the steered beams performed in LCMM has a higher potential for realizing a more accurate measurement of displacement vector than the synthesizing of the displacement vector using the accurately measured axial displacements performed in MDSAM and MTM. However, in LMMs, MDSAM and MTM can also be used to obtain plural steered beams. If necessary, plural transducers are also used (for instance, for heart). These modulations can also be used for B-mode imaging [1-3].

For these beamformings, in [1,3], we also reported more proper apodization functions than that using Gaussian functions we proposed previously, i.e., those using parabolic functions and Hanning windows. The uses of the proper functions realize the echo data having wider lateral bandwidths and higher signal-to-noise ratios (SNRs). Moreover, we also reported an optimization method [1,2] for obtaining the best apodization function in a least squares sense. That is, the best approximated designed point spread function (PSF) can be obtained.

We have also started to report the research for the best PSF. First, in order to gain the insight about the ideal shape of the PSF, the accuracies of the 2D displacement vector measurements were compared by using simulated rf-echo data that have PSFs with lateral envelopes, i.e., Gaussian function (GA), Hanning window (HA) and parabolic function (PA). Next, for the three PSFs used, by calculating the PSFs and spectra using a typical type transducer model and the apodization functions respectively obtained using the optimization method and Fraunhofer approximation, we'll also compare the accuracies of the realized PSFs.

c-sumi@sophia.ac.jp

## 2. Ideal shape of PSF

We simulate laterally modulated echo data using the PSFs having lateral envelopes, i.e., GA, HA and PA. For the three PSFs having a same energy, the order of the full width half maximums (FWHMs) is, PA > HA > GA, whereas that of the lengths of their foots is, GA > HA > PA [2,3]. The PSFs that have a same beamwidth are also used. For both cases, the accuracies of the 2D displacement vector measurements are evaluated. Rigid motions and strains (0.1 to 4 percent) are respectively simulated. The typical ultrasound (US) frequencies are used (1, 3.5 and 5 MHz). The lateral modulation frequencies are set at the same as those of US frequencies. The SNRs of the simulated echo data range form 10 to 30 dB.

For LCMMs, the order of the measurement accuracies was, PA > HA > GA. For only an axial strain case, for instance, see **Fig. 1**, i.e., SDs of measured lateral displacements when US frequency, 3.5 MHz; $\sigma_x$ (of 2D GA) = $\sigma_y$ = 0.4 mm; window sizes used in MCSPGM, 1.6 × 1.6 or 3.2 × 3.2 mm; echo SNR, 20 dB. Similar results were obtained for axial displacement measurements (omitted). For LCMM, a PSF having a wider FWHM was ideal. Long foots are extra. Such a PSF yields a high echo SNR and a large spectrum of the center frequency.

## 3. Accuracies of realized PSFs

Next, for the three PSFs used, the PSFs and spectra are calculated using Field II. For GA, the lateral SD $\sigma_y$ of 0.6 and 0.8 mm were used under the conditions of US speed, 1,500 m/s; US

frequency, 3.5 MHz; modulation frequency (fy), $1/\lambda$ mm$^{-1}$; and modulation depth, 30 mm. For the three PSFs, Fraunhofer approximation was used such that the corresponding apodization functions that yielded the same intensity of a transmitted US could be obtained. The transducer parameters used were of element size, $\lambda$; height, 5.0 mm; and the space between elements was 0.1 mm. The beam pitch was 0.1 mm.

All the obtained apodization functions were able to approximate the three PSFs. See **Fig. 2**, i.e., the PSFs obtained for GA and PA and **Fig. 3(a)**, i.e., the lateral profile for PA ($\sigma_y$ of 0.8 mm, and GA and HA omitted). For the respective three PSFs, the corresponding same shapes of US pulses were used, although the respective shapes should be optimized together with the apodization functions.

Furthermore, for the three PSFs, optimizations of the apodization functions were performed on the basis of a least squares estimation [2]. The conjugate gradient method was used, in which the respective apodization functions obtained by Fraunhofer approximation were used as the initial estimates (specifically, only two main lobes were used). See **Fig. 4**, i.e., the PSFs of the GA and PA and **Fig. 3(b)**, i.e., the lateral profile for PA. As shown, the optimizations significantly increase the lateral bandwidths [see Fig. 3(a) vs 3(b)]. However, the optimization used also made the foots of the PSFs slightly longer.

## 4. Better PSF obtained by nonlinear optimization

Thus, we obtain the insights of the best PSF that can be obtained using all the insights about the ideal PSF and the accuracy of the practical beamforming. The foots of apodization function should be cut as shown in **Fig. 5a** [5]. The better optimization can be realized, for instance, by involving a nonlinear manner, i.e., cutting procedure of the foots of the apodization function at each iteration. This allows the decrease of the channels or the confine the effective aperture. The obtained apodization function and PSF are shown in **Fig. 5b** to **5d**. The better PSF than PA (i.e., the best PSF) will be designed or depicted [2]. The described procedure can also be used for the optimization of the transmitted US pulse shape. Such obtained beamforming parameters can also be used for the best B-mode imaging.

## References


1. C. Sumi: Jpn. J. Appl. Phys., **47(5B)** (2008) 4137.
2. C. Sumi: IEEE 2007 Int Ultason symp, 1557.
3. C. Sumi: IEEE Trans UFFC (in press).
4. C. Sumi: IEEE Trans on UFFC **55** (2008) 24.
5. C. Sumi: 2008 Acost Soc Jpn Fall meeting.


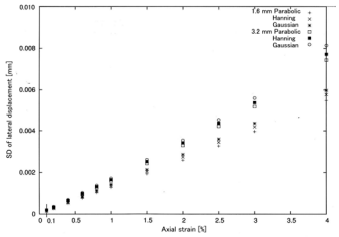


Fig. 1. SDs of lateral displacements measured on simulated rf-echo data.

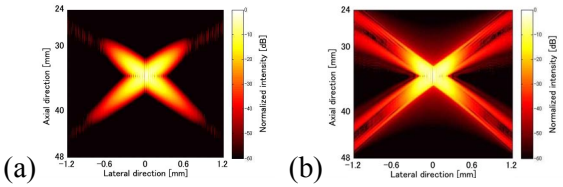


(a) (b)

Fig. 2. PSFs obtained using the apodization functions obtained by Fraunhofer approximation (FA). (a) GA and (b) PA.

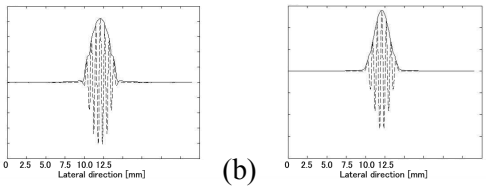


(a) (b)

Fig. 3. For PA, lateral profiles of PSFs obtained by (a) FA and (b) Optimization.

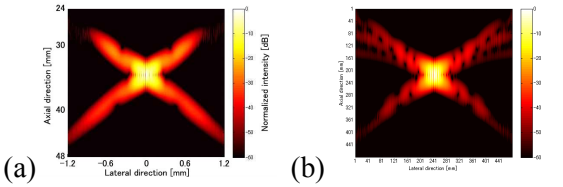


(a) (b)

Fig. 4. PSFs obtained by optimization. (a) GA and (b) PA.

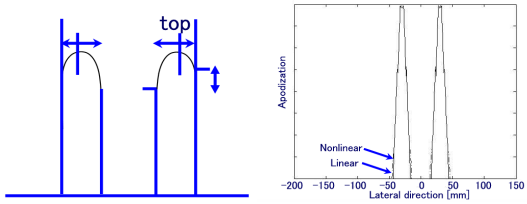


(a) Schematic of apodization. (b) Optimized for PA.

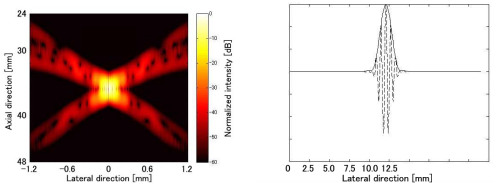


(c) PSF for PA (d) Lateral profile for PA

Fig. 5. Nonlinear optimization.

3P7a-3

Proceedings of Symposium on Ultrasonic Electronics, Vol. 29 (2008) pp. 425-426
11-13 November, 2008

# Lateral modulation and displacement vector measurement using hyperbolic scan by virtual beam forming

# 仮想ビームでの双曲線走査による横方向変調と変位ベクトル計測

Kengo Kondo[1†], Makoto Yamakawa[2] and Tsuyoshi Shiina[3] ([1] Grad. Sch. of Sys. and Inf. Eng., Univ. of Tsukuba; [2]Grad Sch. of Eng., Kyoto Univ. ; [3]Grad Sch. of Med., Kyoto Univ.)

近藤健悟 [1‡]，山川誠 [2]，椎名毅 [3] （[1] 筑波大 シス情; [2] 京都大 工; [3] 京都大 医）

## 1. Introduction

Various methods measuring multidimensional displacement have been developed. Generally the accuracy of measured displacement vector is high in beam direction, while it is low in lateral direction because the point spread function constituted by RF signals represents acoustically-oscillated pattern in beam direction but not in lateral direction. Lateral modulation method was proposed by Jensen et. al. [1] for blood flow measurement. The method generates lateral ocsillating RF signal, which enables us to attain high-accuracy measurement of lateral displacement. However, this modulation method realizes the RF signal as designed below center of aperture, consequently it causes distorted RF far from center of aperture. The distorted RF causes a loss of the linearity of point spread function. We propose a method to solve the distortion by designing a suitable beam scan path.

## 2. Lateral Modulation Method

Lateral modulation method generates lateral oscillating waves by using specific apodization function in linear scan. The function is inverse Fourier transform of product of cosine function and rectangular [1] or Gaussian [2] window function, i.e. two delta functions convoluted by sinc or Gaussian function. A lateral frequency of the modulated RF depends on lateral positions of the two delta function and a depth, thus the apodization function is varied with the depth in order to keep a constant lateral frequency.

We propose a hyperbolic scan method in order to improve the PSF. The hyperbolic scan is realized continuously focus on a hyperbola using synthetic aperture beamforming approach. Lateral modulation can be simplified as superposition of two spherical waves, which are transmitted from two point sources corresponding to peaks of apodization. Phase difference between the spherical waves are equivalent on any points of a hyperbola with foci the source of spherical waves, because a hyperbola is the locus of points such that the distances of a point from the foci differ from each other by a constant amount. An apodization function is superposition of two Gaussian functions with peak points at one quarter from both ends of the aperture respectively, and is constant with depth.

## 3. Displacement Vector Measurement

We propose a 2D Combined Autocorrelation (2D-CA) method which can measure 2D displacement vector. The method is an enhanced method of Combined Autocorrelation (CA) Method [3], which has been proposed as a 1D displacement measurement method with high accuracy and wide dynamic range for tissue elasticity imaging. The 2D-CA method estimates displacement vector as follows:

1. Calculate rough (wavelength per step) displacement by 2D template matching.
2. Separate lateral and axial oscillations of RF by heterodyning demodulation [4].
3. Shift signal by rough displacement obtained by step 1 to avoid aliasing, then measure accurate lateral and axial phase shifts by autocorrelation (Doppler) method respectively.
4. Transform phase shifts in axial direction along hyperbola and lateral direction to displacement components in x-y coordinate.

## 4. Simulation Results

We evaluated the availability of the method by simulation. The lateral modulation is applied to a point scatterer model in order to observe point spread function. Generated RFs by lateral modulation are shown in **Fig. 1** and **2**. Below center of aperture (lateral position $x$=0mm), 2D-RFs are correctly generated as designed in both method. On the other hand, far from center of aperture (lateral position $x$=20mm), generated RF is distorted in conventional lateral modulation method (linear

scan), while it is not distorted as designed in our proposed method (hyperbolic scan). The result shows that the proposed method yields the same PSF pattern at any points regardless of the lateral position or the depth.

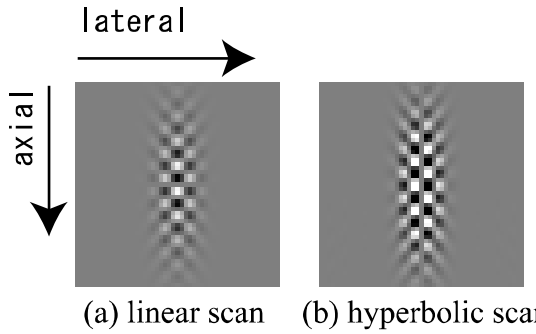


Fig. 1 Lateral modulated RF at depth 50mm, $x$=0mm

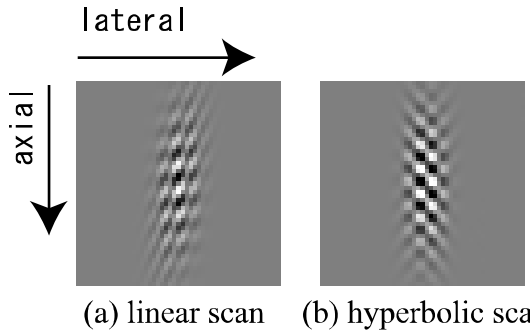


Fig. 2 Lateral modulated RF at depth 50mm, $x$=20mm

Next, a model which expands uniformly in the lateral direction, $x$, was used for estimating the displacement by the proposed 2D-CA method as shown in **Fig. 3(a)**. Results of simulation for conventional and proposed lateral modulation are shown in **Fig. 3(b)** and **(c)** respectively. **Figure 3(b)** shows that the farther from center of aperture ($x$=0), the larger error of estimated value in conventional method. It corresponds to the result of PSF simulation. **Figure 3(c)** shows that proposed method correctly estimated the lateral displacement even in the area far from the center, consequently the accurately measurable region is wider compared with the conventional method.

Expansion of cylindrical model as mimic left ventricular was also simulated as **Fig. 4** and displacement vector distribution was estimated by the 2D-CA with hyperbolic scan. **Figure 5** shows that displacement vector components estimated by the proposed hyperbolic scan method highly coincides with the ideal image.

## 5. Conclusion

We proposed a new lateral modulation method which indicates uniform PSF in whole image. A uniform PSF is very useful for measuring displacement vector. Beam scanning paths located on hyperbola make a uniform PSF pattern. The validity of the hyperbolic scan method was shown by simulation. The effectiveness of 2D-CA method with hyperbolic scan was also shown by simulation on displacement vector estimation. In the next stage, we are going to verify the availability of proposed method by phantom experiments.

## References


1. J. A. Jensen and Peter Munk: IEEE Trans. Ultrason., Ferroelect., Freq. Contr. **45** (1998) 837.
2. H. Liebgott, A.Basarab, D. Loizeau, J. E. Wilhjelm. J. A. Jensen, P. Delachartre: Proc IEEE Ultrason. Symp. (2006) 2168
3. T. Shiina, M. M. Doyley and J. C. Bamber: Proc. IEEE Ultrason. Symp. (1996) 1331.
4. M. E. Anderson: Proc. IEEE Ultrason. Symp. (2000) 1487.


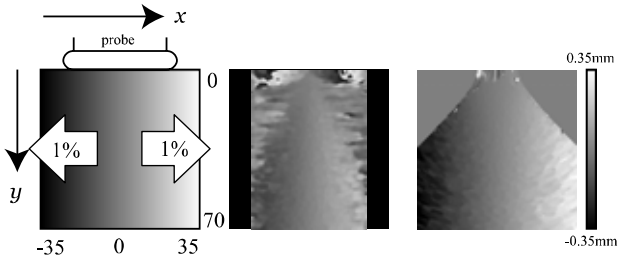


Fig. 3 A model of lateral-direction deformation and estimated displacements

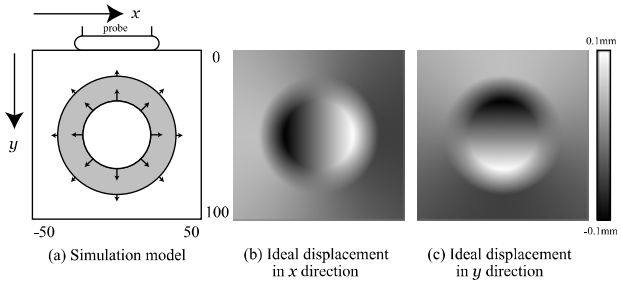


Fig. 4 Cylindrical simulation model

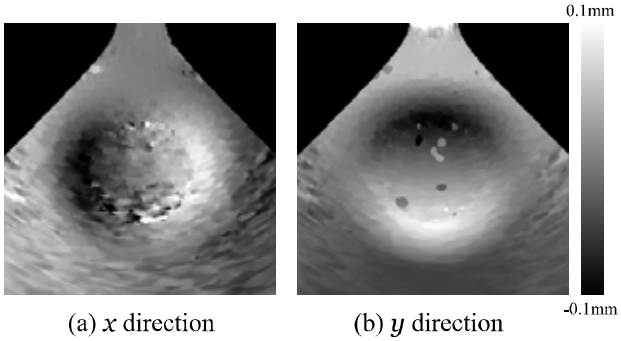


Fig. 5 Estimated displacement by 2D-CA method with hyperbolic scan

Proceedings of Symposium on Ultrasonic Electronics, Vol. 29 (2008) pp. 427-428
11-13 November, 2008

# Experimental Evaluation of High-Speed 2D Motion Vector Measurement by Combining Synthetic Aperture Array Processing with Constrained Least Squares Method

配列型合成開口処理と制限付き最小二乗法を用いた高速二次元変位ベクトル推定精度の検討

Ryouta Yokoyama[1‡], Shin-ichi Yagi[1], Kiyoshi Tamura[2] and Masakazu Sato[3] ([1] [1]Grad. Sch. of Inf. Sci., Meisei Univ., [2] Alpka Co., Ltd., [3]Microsonic Co., Ltd.)
横山亮太[1‡]，八木晋一[1]，田村清[2]，佐藤正和[3]（[1]明星大院 情報; [2]アロカ（株）,[3]マイクロソニック（株））

## 1. Introduction

Dynamic elastography could be a promissing tool of diagnostic imaging for clinical tissue characterization, in which various types of complex tissue oriented structures and their high-speed dynamics [1,2] are revealed by the advanced algorithm of processing signals from a measurement system, beyound conventional static elastography.

Ultra-high speed ultrasonic imaging can be maximally realized by a single trasmission of pulsed ultrasonic field from a tansducer aperture without any beam scanning by introducing synthetic aperture (SA) array signal processing. In order to develop ultra-high speed dynamic elastography we adopted an integrated combination of SA technology and alternate generations of virtual point sources controlled by exciting arrayed elements of the same transducer. This combination successfully realized each successive dynamical distribution of 2-dimensional motion vectors at ultra-high frame rate from 2-dimensional echo frames which were saved in real-time across a tissue phantom [3,4].

For the next step toward an accessible ultra-high speed elastograpy the verification of measured local phase change in accuracy and variance has to be analyzed, which is required to calculate local displacement vector components. Thus, the spatio-temporal performance of conventional cross-correlation method was compared with the constrained least squares method [5] for SA reconstructed echo data at 4000 frames per second from a tissue phantom where a transient shear wave is propagating across the medium.

## 2. Measurement System

The experimental system setup of transducer and tissue phantom to obtain 2-dimensional motion vector distributions which reflect the traveling of transient shear wave caused by pulsed excitation of a wideband electrodynamic transducer (Labworks ET-132-203, DC-11kHz) are shown in **Fig. 1**.

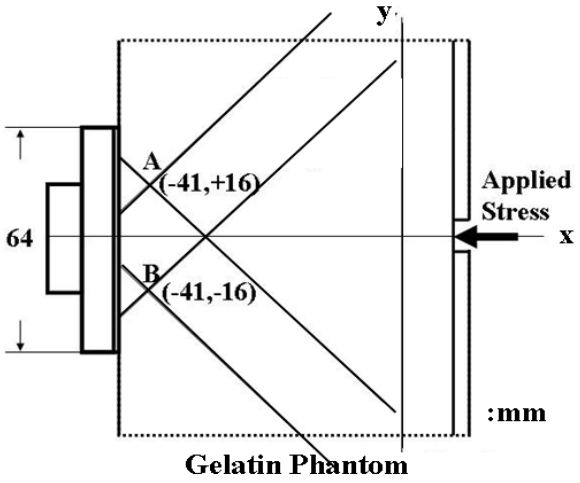


Fig. 1 Experimental setup for external stress input and alternate irradiations by two virtual point sources A and B across a 1 % gelatin phantom including 1 % fine starch powder.

The linear array transducer has 256 elements with 0.25 mm lateral pitch and 13 mm elevational width and 3.0 MHz center frequency with 2 MHz bandwidth. The each element is controlled to generate alternate virtual point sources which realize local phase change estimate in different directional evaluations through SA processing, and connected to A-D converter (30 MHz, 12-bits) with a huge individual cache memory.

The SA processing with matched filtering is carried out in spatial frequency domain for parallel signal processing in practical stage by

$$Q(k_x, k_y) = e^{-j(\sqrt{k^2 - k_u^2}X + k_u Y)} S(k_u, \omega) P^*(\omega),$$

where $S(k_u, \omega)$ is 2-dimensional Fourier transform of received analytic echo signal s(u,t) on an array

‡ e-mail:yoko@con.ei.meisei-u.ac.jp

element (X,Y+u) shifted from the array center (X,Y), which is scattered from distributed target reflectivity q(x,y). P(ω) is a spectrum of transmitted pulse from the point sources. The reconstructed complex echo frame p(x,y) with optimum resolution is obtained by 2-dimensional inverse Fourier transform of $Q(k_x,k_y)$.

## 3. Estimate of Instantaneous Local Phase Change

Primarily the instantaneous local phase change $\Delta\phi(x,y)$ between SA reconstructed successive echo frames $p_1(x,y)$ and $p_2(x,y)$ was evaluated by the following complex spatial cross-correlation method.

$$\Delta\phi(x,y) = \tan^{-1}\frac{\left\langle \mathrm{Im}\{p_1^*(x,y)\,p_2(x,y)\}\right\rangle_{\in R}}{\left\langle \mathrm{Re}\{p_x^*(x,y)\,p_2(x,y)\}\right\rangle_{\in R}},$$

where $\langle\ \rangle_{\in R}$ denotes the spatial average around the local point (x,y) corresponding to the point spread function of SA processing system.

The next step is to confirm the previous evaluation using 2-dimensional expansion of the constrained least square method which was firstly proposed by Kanai [5] for the ill-posed problem.

$$\Delta\phi(x,y) = \tan^{-1}\frac{\left\langle \mathrm{Im}\{p_1^*(x,y)\,p_2(x+\delta_x,y+\delta_y)\}\right\rangle_{\in R}}{\left\langle \mathrm{Re}\{p_x^*(x,y)\,p_2(x+\delta_x,y+\delta_y)\}\right\rangle_{\in R}},$$

$\delta_x$ and $\delta_y$ are satisfied to minimize the constrained least square error around the local point (x, y) in the following equation.

$$\alpha_{\min}(\delta_x,\delta_y) = 1 - \frac{2\,|\left\langle p_1^*(x,y)\,p_2(x+\delta_x,y+\delta_y)\right\rangle_{\in R'}|}{\left\langle |\,p_x(x,y)\,|^2 + |\,p_2(x+\delta_x,y+\delta_y)\,|^2\right\rangle_{\in R'}},$$

where $\langle\ \rangle_{\in R'}$ indicates the spatial averaging taken around local position (x,y) and $(x+\delta_x,y+\delta_y)$.

## 4. Experimental Data

The estimated area is set around the system origin of x-y coordinate, in which the center of the array transducer is located at (X,Y)=(-50 mm,0 mm). The evaluation data along the center axis (y=0) are shown in **Fig. 2**, where the selected ranges of spatial averaging area R and R' are +/-0.8 mm(:x), +/-0.75 mm(:y) and +/-0.4 mm(:x), +/-0.75 mm(:y) respectively. The maximized phase change at the far right is representing the transient stress input, within 1 ms of frame interval and the entirely smoothed distribution of local phase change $\Delta\phi(x,0)$ on the small background motions are observed where each $\alpha_{min}$ was appeared almost at the origin of the concave characteristics, as shown in **Fig. 3**.

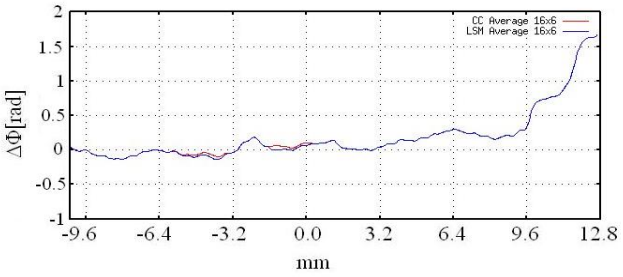


Fig. 2 The comparison of local phase change evaluations by conventional cross-correlation method and constrained least square method within a frame interval (1 ms).

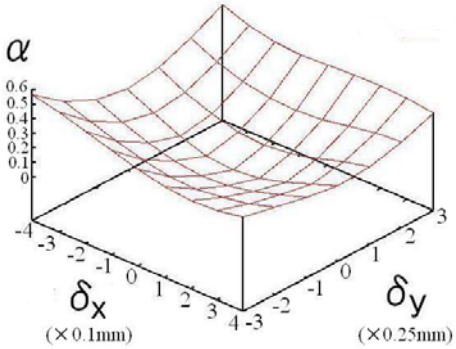


Fig. 3 Typical distribution $\alpha(\delta_x,\delta_y)$ of constrained least square errors in Fig. 2 shows the minimum at the original positions of successive two echo frames.

## 5. Conclusion

The estimated instantaneous local phase change across a tissue phantom by conventional cross-correlation method showed no significant difference from the data obtained the constrained least square method. However the more precise parameter changes for measurements seems to be required to check the overall system performance.


## Acknowledgment

This work was partly supported by Foundation for Positive Health Promotion of Japan 2007.


## References


1. H. Kanai: 2006 IEEE Ultrason. Sympo. Proc., pp. 760-763, 2006.
2. H. Kanai: IEEE Trans. Ultrason., Feroelect., Freq. Contr., vol. 51, no. 11, pp. 1931-1942, 2005.
3. S. Yagi, A. Sanuga, K. Tamura and M. Sato: 2006 IEEE Ultrason. Synmo. Proc., pp.1205-1208, 2006.
4. S. Yagi, A. Sanuga, K. Tamura and M. Sato: Acoustic Imaging vol. 29, pp.45-50, 2008.
5. H.Kanai, M. Sato, Y. Koiwa and N. Chubachi: IEEE Trans. Ultrason., Ferroelct., Freq. Contr., vol. 43, no. 5, pp. 791-810, 1996.

Proceedings of Symposium on Ultrasonic Electronics, Vol. 29 (2008) pp. 429-430
11-13 November, 2008

# Elastography Using Graph Cuts
# グラフカットを用いた弾性イメージング

Naoto Akazawa†, Kan Okubo, Norio Tagawa (Tokyo Metropolitan Univ., Faculty of System Design)
赤澤直人‡, 大久保寛 , 田川憲男（首都大 システムデザイン）

## 1. Introduction

In recent years, graph cuts (GC) algorithm has emerged as an increasingly useful tool for many computer vision and image processing problems[1] . This technique treats the segmentation problem as an energy minimization problem; it optimizes the energy function to solve the problem.

Meanwhile, elastography is examined as a new application of ultrasound in medical diagnostic imaging. This method utilizes signals observed in different situations (for example, with / without additional static pressure ). Therefore, it is expected that we can apply GC algorithm to Elastography successfully.

In this paper, we examined the effectiveness of elastography using GC algorithm. As a result, it is clarified that we can obtain appropriate displacement estimation at every region by elastography using GC.

## 2. Calculation models

**Figure 1** shows the simulation model. We assume the following conditions: three objects having different elasticity are placed in front of a sound source. Each object reflects an echo signal which is different from each other in regard to the amplitude. We don't consider propagation parameters (dispersion or attenuation) of medium.

In this study, we set up that a center frequency is 40 MHz and a band width is 4 MHz for a transmitted FM chirp signal on the source. The pulse width is 4 μs with the sampling rate of 500 MHz.

We prepare three ideal data for simulation under the above conditions. The data are following three signals: $X(t)$, echo signal reflected from objects; $X'(t)$, reflected echo signal with static compression; $A(t)$ transmitted wave signal for matched filter. Total points of $X(t)$ is 16384, and $X'(t)$ has identical points. **Figure 2** depicts Schematic diagram of simulation. For $X(t)$ and $X'(t)$, white gaussian noise of 10% dynamic range ratio is added respectively.

---

† E-mail: naoto.akazawa@n-akazawa.org

## 3. Graph cuts (GC) algorithm

GC is utilized to seek the label $B$ that minimizes the energy $E(B)$. Relation equations in GC are given as

$$E(B) = E_{smooth}(B) + E_{data}(B) \quad (1)$$

$$E_{data}(B) = \sum_{n \in N} \left| X(B_n) - X'(B_n) \right| \quad (2)$$

$$E_{smooth}(B) = \sum_{(n,n+1) \in N} \kappa Potts(B_n, B_{n+1}) \quad (3)$$

$$Potts(B_n, B_{n+1}) = \begin{cases} 0 \mid_{B_n = B_{n+1}} \\ 1 \mid_{B_n \neq B_{n+1}} \end{cases} \quad (4)$$

$\kappa$ is smoothing parameter. Now, we use Potts model and expansion move algorithm for GC.

The graph model of GC is shown in **Fig. 3**. The initial allocation of the node is deriven as displacement data $B(t)$.

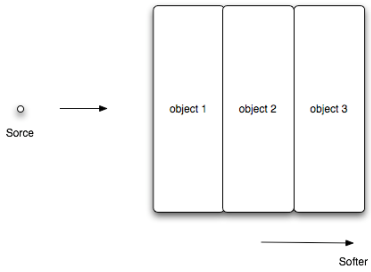


Fig. 1 Simulation model

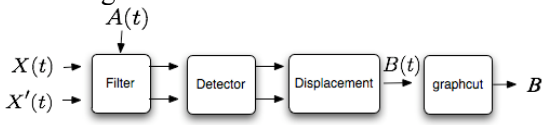


Fig. 2 Simulation dialog

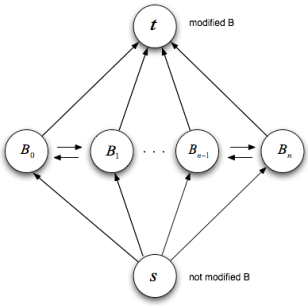


Fig. 3 Graph model for graph cut

## 4. Calculated results and discussions

In Fig. 1, amplitude signals reflected from each object object1 is assumed as follows; 1.0 for object1, 0.5 for object2 and 0.25 for object3. In $X(t)$, the region of echo signal from object1 is from 4000 to 8000, the region of object2 is from 8000 to 12000, and the region of object3 is from 12000 to 16384. Additionally, in $X'(t)$, the regions of object1, object2 and object3 are respectively shifted by 300 points, 400 points and 500 points, in contrast to $X(t)$.

**Figure 4** illustrates a waveform of the received signals from the boundary of each medium. **Figure 5** shows detected signals of $X(t)$ and $X'(t)$ compressed by $A(t)$. Next, initial allocation of node cost $B(t)$ is plotted in **Fig. 6** obtained by simple correlation.

**Figure 7** indicated the label data $B$ obtained using GC at $\kappa$=100. This result of the displacement has enough precision. **Figs. 8 and 9** show the results at $\kappa$=10 and $\kappa$=200, respectively.

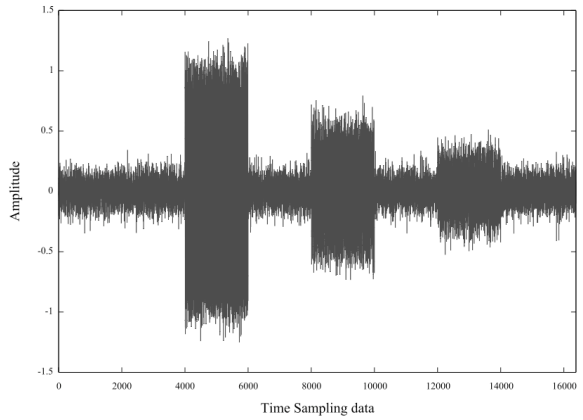


Fig. 4 Received echo signal

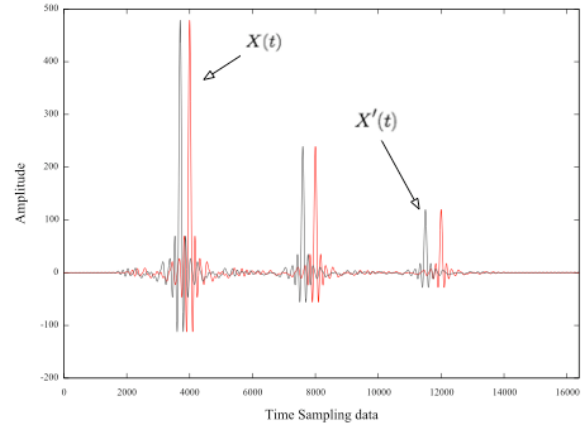


Fig. 5 Detected complession signal

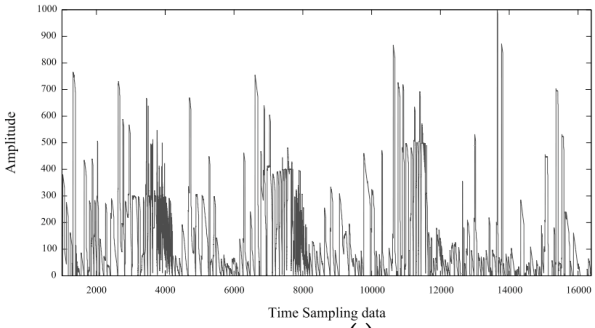


Fig. 6 Sample data $B(t)$ for graph cut

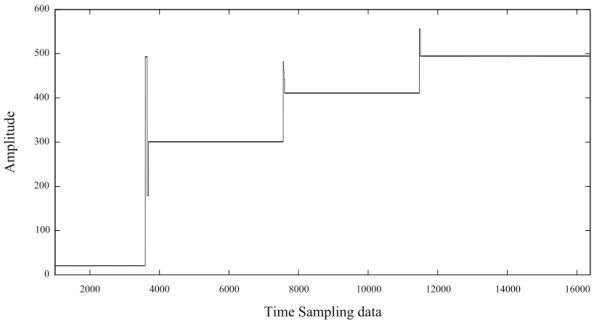


Fig. 7 Result at $\kappa$=100

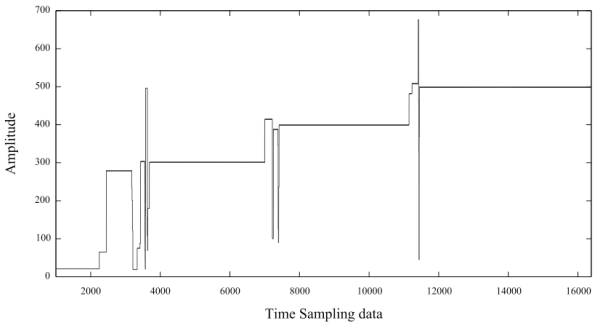


Fig. 8 Result at $\kappa$=10

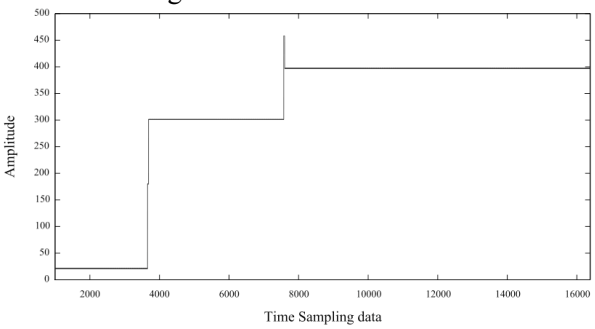


Fig. 9 Result at $\kappa$=200

## 4. Conclusions

This study has made a basic examination for elastography based on GC algorithm. Our simulation confirm the feasibility of the proposed technique. In near future, we intend to apply elastography by harmonic components using graph cut.

**References**

1. Hiroshi Ishikawa: IEEE Computer Society Conference on Computer Vision and Pattern Recognition (1999) p.1132.

Proceedings of Symposium on Ultrasonic Electronics, Vol. 29 (2008) pp. 431-432
11-13 November, 2008

# Precise Tissue Elasticity Reconstruction Based on Detection of Small Displacements

微小変位検出に基づく精細組織弾性イメージング

Sayuki Aiura, Takayuki Sato, Shizuka Sato, Yasuaki Watanabe and Hitoshi Sekimoto
(Graduate School of Science and Engineering, Tokyo Metropolitan University)
相浦紗雪, 佐藤隆幸, 佐藤翔, 渡部泰明, 関本仁 （首都大学東京大学院 理工）

## 1. Introduction

While biopsy is the gold standard for the diagnosis of malignant breast lesions, its invasive procedures are painful for the patient. For noninvasive diagnosis, the elasticity image from ultrasound echo data can be used to determine the tumor type with objective criteria. Thus the ultimate goal of ultrasound imaging is to image the absolute elasticity modulus precisely.

Most elastography methods primarily involve the imaging of strain fields in soft tissue. Elastograms are created by comparing ultrasonic echo data obtained before and after a slight compression of the tissue. However, the quantitative modulus images created by elastography are expected to provide a more accurate method for the discrimination of cancers from benign masses. Because the strain images represent only relative information within the sampled tissue, research groups have reported a variety of ways to create modulus images [1-2]. We have also taken steps to develop an absolute elasticity modulus measurement system using the data from a precision balance and radio frequency echo data in **Figure 1**.

In this paper we propose an approach for reconstructing precise elasticity modulus images in simulation. Because breast tumors have various shapes, hardnesses, and mobilities, the creation of accurate images encounters two problems. First, when the tissue is disturbed concentrated loads are applied to the boundaries, particularly around the irregular form of an invasive lesion. This causes stress concentration, and makes the normal tissue around the boundaries appear stiffer than in actuality [3]. Secondly, it is difficult to demonstrate the boundaries between normal tissue and an invasive lesion of simlar elasticity. Both problems limit the effectiveness of elasticity modulus imaging in its current state. Therefore as a first step to improving the method, we introduce a detection scheme that shows how the boundaries move with the compression for mobility control and estimates the small displacements around the boundaries.

---

sabo@esys.eei.metro-u.ac.jp

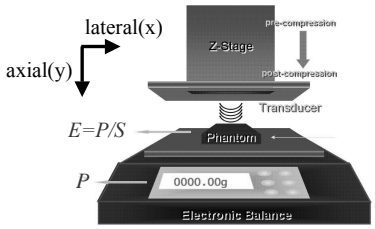


Fig. 1 Measurement system

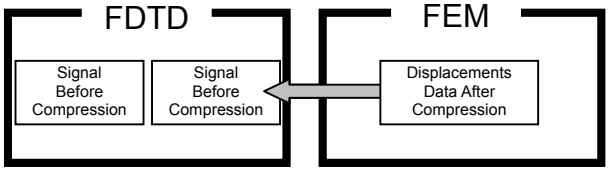


Fig. 2 Approach to the simulation

## 2. Methods

*Theory*

To evaluate the credibiliy of the experiment using the developed measurement system in **Figure 1**, we observe the moment of boundaries in simulation by two methods.

To generate ultrasound-like signals for the simulation, the finite-difference time-domain method (FDTD) is employed. The expressions for it are obtained as:

$$P^{n+\frac{1}{2}}(i,j) = P^{n-\frac{1}{2}}(i,j) + k\frac{2\Delta t}{2\Delta x}\left\{\dot{u}_x^{\,n}\left(i+\frac{1}{2},j\right) - \dot{u}_x^{\,n}\left(i-\frac{1}{2},j\right)\right\} - k\frac{2\Delta t}{2\Delta y}\left\{\dot{u}_y^{\,n}\left(i,j+\frac{1}{2}\right) - \dot{u}_y^{\,n}\left(i,j-\frac{1}{2}\right)\right\} \quad (1)$$

$$\dot{u}_x^{\,n+1}\left(i+\frac{1}{2},j\right) = \dot{u}_x^{\,n}\left(i+\frac{1}{2},j\right) - \frac{1}{\rho}\frac{2\Delta t}{2\Delta x}\left\{P^{n+\frac{1}{2}}(i+1,j) - P^{n+\frac{1}{2}}(i,j)\right\} \quad (2)$$

$$\dot{u}_y^{\,n+1}\left(i,j+\frac{1}{2}\right) = \dot{u}_y^{\,n}\left(i,j+\frac{1}{2}\right) - \frac{1}{\rho}\frac{2\Delta t}{2\Delta y}\left\{P^{n+\frac{1}{2}}(i,j+1) - P^{n+\frac{1}{2}}(i,j)\right\} \quad (3)$$

Here, $P$ denotes the estimated sound pressure, $u_x$ the estimated lateral particle velocity, $u_y$ the estimated axial particle velocity, $k$ volume elasticity, $n$ the number of the time steps and $i$ and $j$ are the number of points in the lateral and the axial directions respectively.

Prospective displacements on the plane are predicted with the finite element method (FEM) using the expression below,

$$\begin{Bmatrix}\sigma_x\\ \sigma_y\\ \tau_{xy}\end{Bmatrix}=\frac{E}{(1+v)(1-2v)}\begin{bmatrix}1-v & v & 0\\ v & 1-v & 0\\ 0 & 0 & \frac{1}{2}(1-2v)\end{bmatrix}\begin{Bmatrix}\frac{\partial u_x}{\partial x}\\ \frac{\partial u_y}{\partial y}\\ \frac{\partial u_x}{\partial x}+\frac{\partial u_y}{\partial y}\end{Bmatrix} \quad (4)$$

where $\sigma_x$ and $\sigma_y$ are the axial and lateral stress, $\tau_{xy}$ is x-y shear stress, $u_x$ and $u_y$ are the axial and lateral displacement, $E$ is Young's modulus, and $v$ is Poisson's ratio.

In the simulation, the postcompression FDTD signals are adjusted according to the FEM displacement data result. **Figure 2** illustrates this approach to the simulation.

*Simulation*

**Figure 3** shows a simulation model that consists of a normal breast tissue model with 10mm(axial) × 3.5mm(lateral) plane and a harder cubed inclusion whose side is 5mm on the plane. This tissue model is based on a measurement system constructed of a 192ch/10MHz transducer generating a 10MHz frequency echo and a precision balance in **Figure 1**, and the corner of the inclusion are derived from the whole plane for the following the movement at the corner of the inclusion that may cause stress concentration. The inclusion and adjacent tissues both have same thickness.

Young's modulus of the inclusion is set to 60kPa and of the surrounding tissue to 30kPa. Poisson's ratio is provided as 0.42 on the model. 1% compression of the model height to the axial direction is applied to the top of the model.

All elements are set to 0.05mm(a)×0.05mm(l) on the model for FEM. For FDTD eleven 10 MHz acoustic waves are transmitted from the top of the model to axial direction and the reflections are received at the transmitter just above the corner of the inclusion. The markers with extremly-hard stiffness are set in the model to stimulate the amplitude increment of the reflected waves. One marker is located at 6 elements off the upper and right sides of the inclusion and the other is on. We observe the movement of the markers to obtain the small displacement around the boundaries.

## 3. Results

In Fig. 4, the estimated waves at the receiver are shown with the time delays indicating that the markers move differently in different stiffnesses of the tissue. The time difference between the delays of the signals, 35 nsec, allows commercially available measurement systems, e.g. oscilloscopes, to obtain tolerable echoes for detecting small

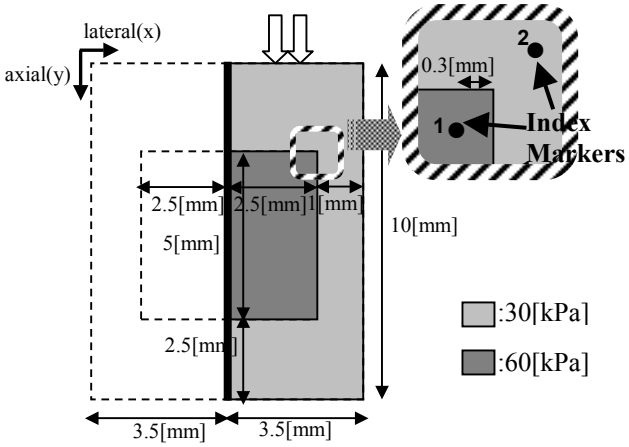


Fig. 3 Simulation tissue model

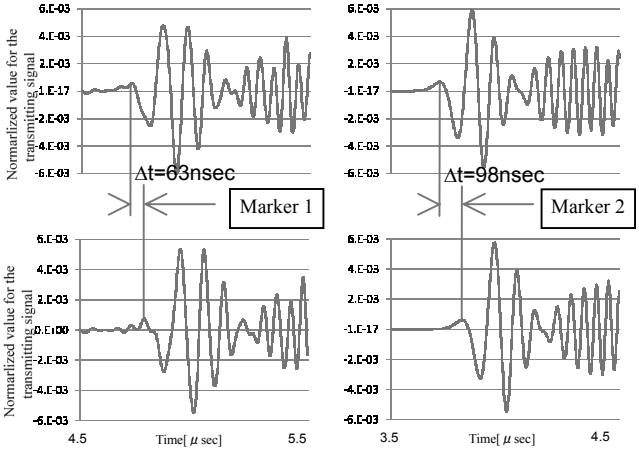


Fig. 4 Estimated waves in simulation

displacements in the experiment. The result shows the possibility for imaging the precise elasticity modulus around the boundaries between different elastic properties of the tissue and under conditions which give rise to irregular concentration.

## 4. Conclusion

In conclusion, the detection scheme described in this article is confirmed to reconstruct elasticity modulus images more precisely. We are now developing an iterative finite element inverse algorithm focusing on the boundaries with mesh optimization to improve upon the elasticity imaging result and preparing a phantom experiment where the algorithm is used for imaging.

## References

1. M. Yamakawa and T. Shiina: Jpn. J. Appl. Phys. **44** (2005) pp. 4567-4577

2. J. Li, Y. Cui, M. Kadour and J. A. Noble: IEEE Trans. UFFC **55** (2008) pp. 319-326

3. E. E. Konofagou, T. Harrigan and J. Ohir: Ultrasonics **38** (2000) pp. 400-404

3P7a-7

Proceedings of Symposium on Ultrasonic Electronics, Vol. 29 (2008) pp. 433-434
11-13 November, 2008

# Development of Ultrasound Breast Imaging System
超音波乳腺画像の採取・表示システムの開発

Satoshi OZAWA[1‡], Hokuma SAITO[2],Masakazu SATO[3], Hiroshi KITUNAI[3], Takasuke IRIE[3], Masasumi YOSHIZAWA[2], Kan OKUBO[1], Norio TAGAWA[1], Hiromu YOKOI[4] and Nobuyuki HONDA[5], ([1] Facult. System Design , Tokyo Metropolitan Univ.; [2] Tokyo Metropolitan College; [3] Microsonic Co., Ltd.; [4] Yokoi Orthopedic Clinic; [5] Teramoto Memorial Hospital)
小沢智志[1‡]，斎藤北茉[2]，佐藤正和[3]，橘内洋[3]，入江喬介[3]，吉沢昌純[2]，大久保寛[1]，田川憲男[1]，横井浩[4]，本田伸行[5]（[1]首都大 システムデザイン；[2]都立高専 ものつくり工；[3]マイクロソニック 開発部；[4]横井整形外科；[5]寺元記念病院）

## 1. Introduction

To date, the ultrasound is paid to attention as a method for diagnosis of cancer. The diagnosis method of breast cancer that increases in recent years includes mammography diagnosis and ultrasound diagnosis. Mammography diagnosis uses radiation to image the breast gland. Therefore, frequent applications are not preferable. In this study, ultrasound diagnosis with little harm for human body is taken up. The equipment to rotate a ultrasonic probe mechanically and to acquire images automatically has been developed recently. Integrating this equipment, ultrasound imaging system is examined, and developed. The proposed system is shown in **Fig. 1**.

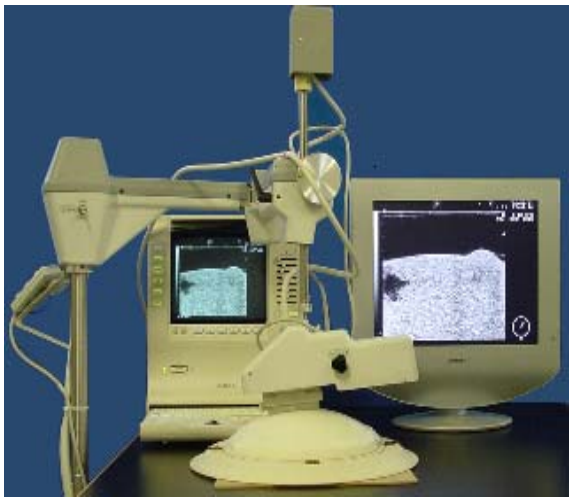

Fig. 1 Ultrasound diagnostic equipment.

## 2. Image collection

In the imaging process, at first the ultrasonic probe is rotated around a nipple on a breast to get the B-mode images in the inner part of a breast, and next, the probe is rotated apart from a nipple to image the outer part of a breast. An example of the phantom image collected by the system is shown in **Figs. 2** and **3**.

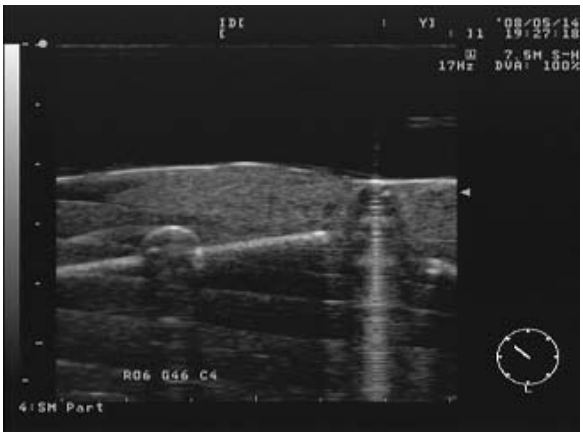

Fig. 2 Example of B-mode image of phantom at inner part.

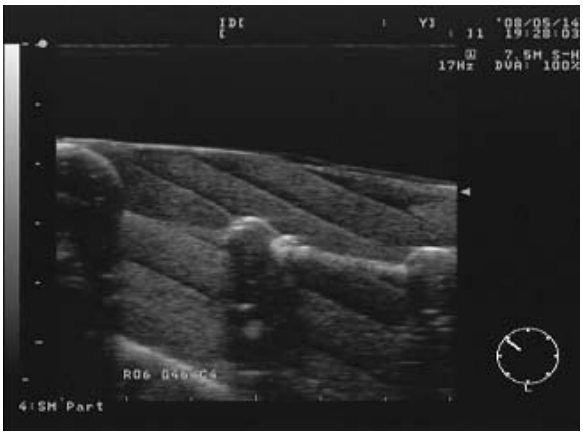

Fig. 3 Example of B-mode image of phantom at outer part.

## 3. Image processing for C-mode imaging

The cross-sectional B-mode image of a whole breast should be composed of the four B-mode images already collected like Figs. 2 and 3 and forming a line. Actually, after selecting the four images from the all collected images, the overlapped regions in the each image are cut down, and these are combined like **Figs. 4** and **5**.

To generate C-mode images, the voxel image representation is adopted, and the three-dimensional image is generated by inserting the above mentioned cross-sectional images into the voxel data region. The C-mode images are generated by picking out the values of the voxels positioned at the desired depth from the breast surface. The examples are shown in **Figs. 6** and **7**.

## 4. Discussions and conclusions

From the phantom images shown in Figs. 5 and 7, it can be confirmed that the proposed imaging system has no geometric distortion. Additionally, from the actual breast images shown in Figs. 4 and 6, it is obvious that this system is effective for examination of breast cancer. In Fig. 6, the position of the cancer is easy to be known.

In this study, we generate the cross-sectional images by confirming the optimal layout of the four images by eyes. As a future work, including the image selection for generating the cross-sectional images, we construct the algorithm by which all processing is done automatically based on the pattern recognition strategy.

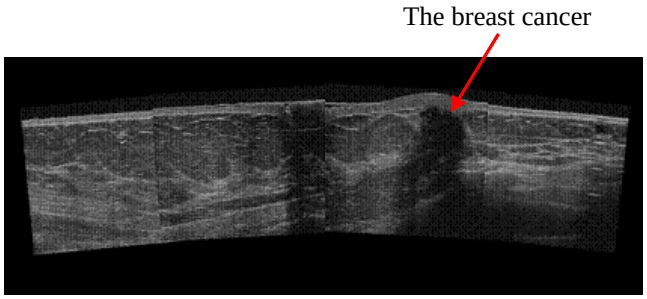


Fig.4 Example of cross-sectional image of breast.

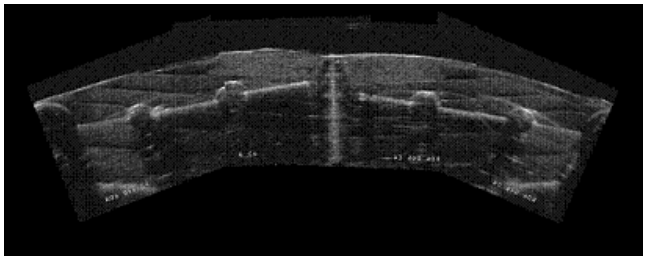

Fig.5 Example of cross-sectional image of phantom.

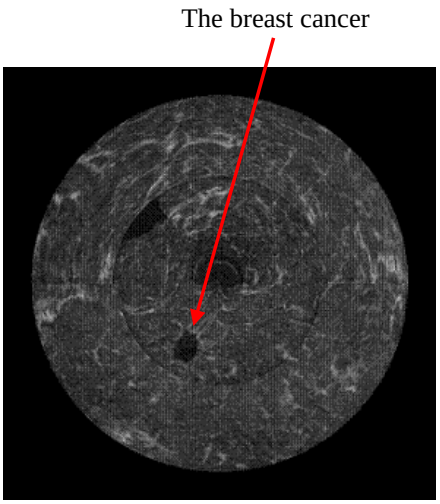


Fig.6 Example of C-Mode image of breast.

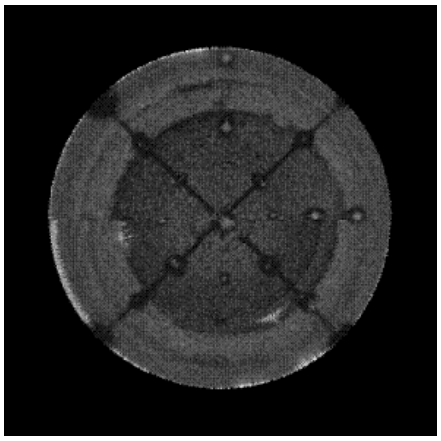

Fig.7 Example of C-Mode image of phantom.

## References

1. T. Irie, H. Asaba, J. Anzai, H. Yokoi, and N. Honda: Jpn. Soc. of Ultrasonics in Medicine **75** (2002) S443.
2. N. Honda, H. Yokoi, T. Irie, and J. Anzai: Jpn. Soc. of Ultrasonics in Medicine **79** (2006) S214.
3. H. Yokoi, et al.: Jpn. Soc. of Ultrasonics in Medicine **42** (1983) 627-628.

3P7a-8

Proceedings of Symposium on Ultrasonic Electronics, Vol. 29 (2008) pp. 435-436
11-13 November, 2008

# Evaluation of Preprocessing Operations for the Extraction of Fine Blood Vessels from Ultrasound Images

# 超音波画像における細径血管抽出のための前処理手法の評価

Yasuaki Osawa, Masayasu Ito
(Tokyo Denki Univ., Grad. School of Science. and Tech.)
大澤康明, 伊東正安（東京電機大学・理工）

## 1. Introduction

This paper is concerned with an image processing technique, which extracts fine blood vessels from an ultrasound image as accurate as possible using the noninvasive imaging system developed before[(1)].

It is not difficult to detect a large blood vessel in an ultrasound image, since the brightness or the echo level of the blood vessel can be differentiated easily from that of neighbor tissues. On the other hand, the small blood vessels show little difference in brightness from the neighbors. Besides, their contours are not clear due to the speckle noise and thus preprocessing is essential to our purpose. So far various smoothing and enhance methods have been proposed elsewhere. We examined an adaptive morphological operation in image processing and found that it can smooth and enhance the image at the same time [(2)].

There exist many types of morphological operations applied to the ultrasound image preprocessing. They use different types of structuring elements. Typical structuring element is of a constant type and the others are of more functional ones. We tried a morphological operation of fuzzy type and adaptive ones of two different structuring elements; triangular type and Gaussian type. In this paper, we compare the new adaptive morphological operation with the conventional ones developed before and we will evaluate them. We use the post processing techniques for extracting the contour of fine blood vessels reported before[(1)].

Ultrasound images are accessed from the developed non-invasive imaging and diagnostic system for ultra fine blood vessels [(3)]. It scans the region of 1[cm]×1[cm]×3[cm] using 30MHz transducer and 128 successive cross sectional images are stored for processing.

07smj03@j.dendai.ac.jp ito@re.ccs.dendai.ac.jp

## 2. Preprocessing

We already reported that morphological operations are less affected by image quality and equipment, when the introduced structuring element is dependent on the local image. In this research, the following four filters are used. The first and second ones are adaptive morphological filters with different structuring elements: triangular and Gaussian type. The third is a fuzzy morphological filter, which uses the fuzzy logic. The fourth is a normal morphological filter. Now closing and opening morphological operations result in successive 128 smoothed cross sectional images with enhanced edges. The size and appropriate parameters of the structural element of these morphological operations were decided by an evaluation function called separability.

## 3. Comparison of morphological operations

Here we introduced four evaluation indices; separability, gradient, brightness difference between the inner and outer regions, and blood vessel extraction rate. Table.1 shows evaluated values averaged around the extracted contours of relatively large blood vessels after each of the four operations is executed in the preprocessing. Separability is calculated from the inner and interclass variances in the spatial image of cylindrical region (radius 7 pixels, length 7 pixels). Strip of 3 by 7 pixels is given to the evaluation region for gradient and brightness difference,. Blood vessel extraction rate is the percent of the number of contour-extracted

frames to the total processed frames. Note here that all the other indices are obtained from the extracted contours. Similarly, we evaluated the extracted small blood vessels as shown in Table 2.

Fig. 1 shows how the original noisy ultrasound image is smoothed and enhanced by the preprocessing methods. Here only the profile of the white line in the blood vessel (Fig. 2) is shown for reference. Fig. 3 shows a 3D view of the extracted blood vessels using Gaussian type adaptive morphological operation.

| | normal | adaptive | fuzzy | Gauss |
|---|---|---|---|---|
| Separability | 0.713 | 0.713 | 0.712 | 0.713 |
| Gradient | 7.921 | 7.981 | 7.994 | 7.914 |
| Brightness difference | 36.19 | 36.92 | 35.98 | 37.14 |
| Blood vessel extraction rate | 0.68 | 0.914 | 0.766 | 0.961 |

Table.1 Evaluated indices of four filters applied to large blood vessel

| | normal | adaptive | fuzzy | Gauss |
|---|---|---|---|---|
| Separability | 0.691 | 0.683 | 0.686 | 0.695 |
| Gradient | 8.332 | 8.306 | 8.67 | 8.444 |
| Brightness difference | 42.51 | 38.38 | 43.22 | 42.92 |

Table.2 Evaluated indices of four filters applied to small blood vessel

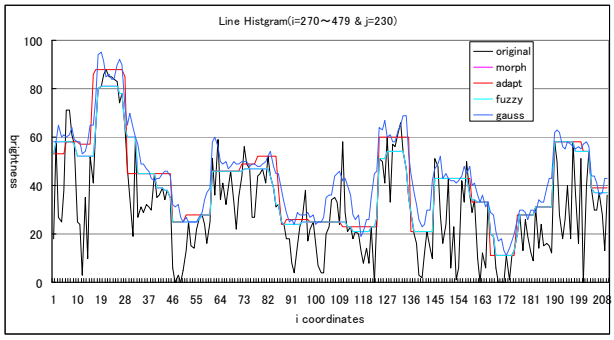


Fig 1 Profiles of the processed images

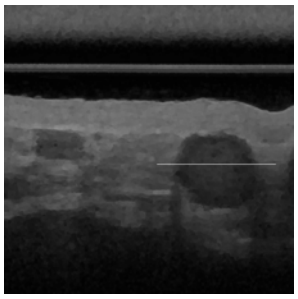

Fig.2 Preprocessed ultrasound image

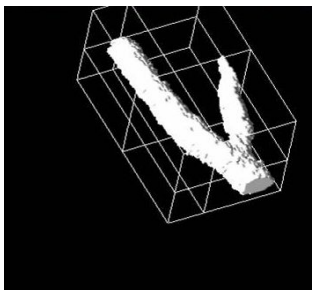

Fig.3 3D image of an extracted blood vessel

## 4. Conclusion

From Table 1, we can conclude that the adaptive morphological operation is a very useful preprocessing tool for image segmentation such as contour extraction purpose. Little difference is observed among the evaluation indices of the four methods, when the contour extraction succeeds. The structuring element of Gaussian type gives more moderate smoothing and enhancement effect to the noisy ultrasound image than the others. We observe that it becomes easy for the artifact due to the acoustic shadow to be removed in the post processing stage. We can say at this stage that the Gaussian adaptive morphological operation is superior to the others.

In the future we will analyze the function of various adaptive structuring elements mathematically and find a total evaluation function from preprocessing to post processing.


## Acknowledgment

This work was supported in part by a grant from the TDU Frontier R & D Center and in part by the Regional Industry Revitalization Project, Bureau of Economy, Trade and Industry.


## References


1. Masayasu Ito, Yuzuru Saito, Yasuaki Osawa: Evaluation of Preprocessing Operations for the Extraction of Fine Blood Vessels from Ultrasound Images, Proceeding of Symposium on Ultrasonic Electronics, Vol.28,(2007), pp.393-394,14-16 November, 2007.

2. M.Tsubai, M.Ito:Control of Variable Structuring Element on Adaptive Mathematical Morphology for Boundary Enhancement of Ultrasound Images, Trans. Information and System, Vol.86-D-II, NO.6,pp.895-907, 2003.

3. M. Ito, A. Yamada, K. Kato,K. Kobayashi,N. Kuroshima," Development of ultrasound imaging and diagnostic system for fine blood vessel structure., Proc. of 11th Congress of WFUMB, Ultrasound in medicine and biology, 32,5S,278, May,(2006)

Proceedings of Symposium on Ultrasonic Electronics, Vol. 29 (2008) pp. 437-438
11-13 November, 2008

# Visualization of intersection points of motion vectors in left ventricle by processing successive echograms

# 断層像の動画像処理による左心室運動ベクトルの交点描出法とその応用

Rui Takahashi‡, Kohji Masuda, Takashi Yoshinaga, Hirotaka Matsuura and Shun Uchibori
( Graduate School of BASE, Tokyo Univ. of Agri. & Tech. )
高橋累‡，桝田晃司，吉永崇，松浦宏尚，内堀駿 （東京農工大 BASE）

## 1. Introduction

Now heart disease is the 2nd most common cause of death in Japan. To find and diagnose heart disease as possible as early, echography (ultrasonography) is indispensable equipment in cardiovascular diagnosis due to its noninvasiveness, real-time observation and ease of carry. On the other hand, examination with echography greatly depends on the expertise and experience of an operator because of its blurriness and low spatial resolution. Comparig with other organs, echocardiogram (echogram of heart) includes motion information more than the construction. Thus the recognition software[1,2] in motion pattern of heart on echocardiogram may help for a quatitative diagnosis independent to the operator.

Considering the short-axis view of heart, which extracts the plane perpendicular to the axis of the artery, a normal ventricular wall expands and contracts concentrically on echogram. To evaluate the synchronicity of motion in the heart, the tissue doppler imaging (TDI) technique is available and already integrated with echography. However, because the TDI has anisotropy in motion detection, it is not suitable for comprehensive evaluation of motion function. Therefore, we have developed a software to recognize the synchronous motion of heart by calculating intersection points between the instantaneous velocities of ventricular wall derived from optical flow method[3].

## 2. Method

The video stream of echocardiogram was captured by 8bit and 30fps by using the digital echography (Toshiba AplioXV). Then the motion vectors between frames were calculated by optical flow method (time interval 33ms), where brightness is more than the threshold. Next the *x*-*y* coordinate system was applied to divide it into small square areas which side is $\sigma$ pixel as shown in **Fig.1**.

masuda_k@cc.tuat.ac.jp

Defining the area which is *a*-th in the *x* direction and *b*-th in the *y* direction is defined as $A_{ab}$, the area velocity of $A_{ab}$ is calculated by averaging all the vectors inside the area. Here we established $\sigma = 15$ pixel and $P = Q = 30$ $(0 < a < P, 0 < b < Q)$.

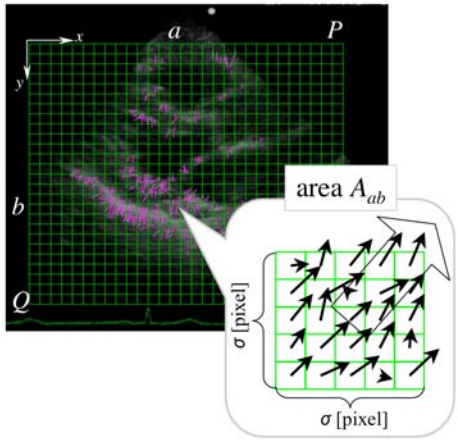


Fig.1 Division of the echogram into small areas and calculation of the area velocity.

Because the shape of left ventricle in a normal heart reveals circle, prolongations of motion vectors in the area velocities concentrate in the center of the left ventricle if it contracts concentrically. And if there is local malfunction caused by the disease as myocardial infarction, prolongations of vectors make their intersections dispersedly. Thus we aimed to reveal the intersection points which are derived from motion vectors in the area velocities to evaluate the comprehensive motion function of the heart.

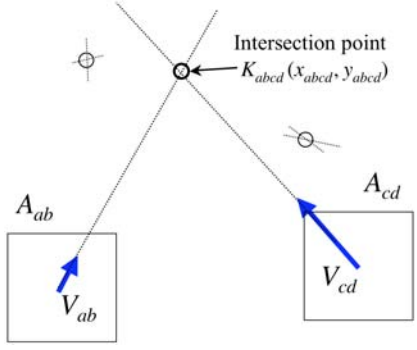


Fig.2 Definition of the intersection point.

**Fig.2** shows the definition of the intersection point $K_{abcd}$ which is created by the vector $V_{ab}$ of the area $A_{ab}$ and the vector $V_{cd}$ of the area $A_{cd}$. The coordinates of intersection points are calculated by all of the combination between different two motion vectors. Here to reduce calculation time, the motion vectors are prolonged to the positive direction in the systolic phase as shown in **Fig.3** (a). On the other hand, in the diastolic phase, the motion vectors are prolonged to the negative direction by recognizing the motion phase from the electrocardiography (ECG). Then the instantaneous distribution of the intersection points is obtained as **Fig.3** (b).

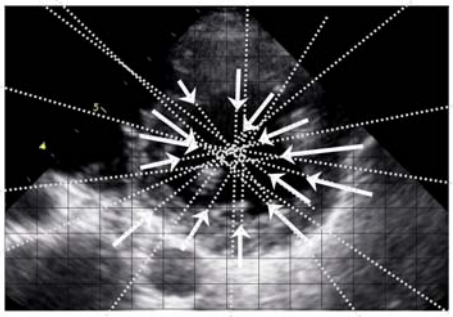

(a) The area velocities with their prolongations.

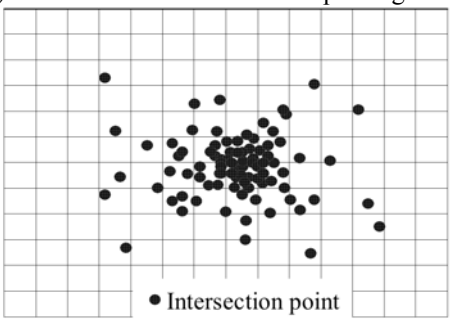


(b) Distribution of the intersection points.

Fig.3 Elucidation of the intersection points.

Moreover, because there is no quantitative information in the distribution, the weight coefficient is calculated to cumulate the frequency in each pixel according to the magnitude of the vectors. In the intersection point $K_{abcd}$ ($0 < a,c < P$ and $0 < b,d < Q$), the weight coefficient $W_{abcd}$ is defined as the summation of the absolute values and memorized as the arrangement ($K_{abcd}$, $W_{abcd}$). Then the weight coefficient in each pixel is summarized and newly defined as $W(x,y)$. However, since $W(x,y)$ is proportion to the number of the motion vectors, it should be normalized by the number of the maximum intersection points. Thus dividing $W(x,y)$ by $N(N\text{-}1)/2$, where $N$ is the total number of the vectors, the quotient is finally defined as $I(x,y)$, which is named as the intersection index. **Fig.4** shows the distribution of intersection index, where $I(x,y) > 1.25$, in the myocardial infarction patient in the systolic phase. Because of the asynchrony in the ventricle motion, the shape of $I(x,y)$ was distorted.

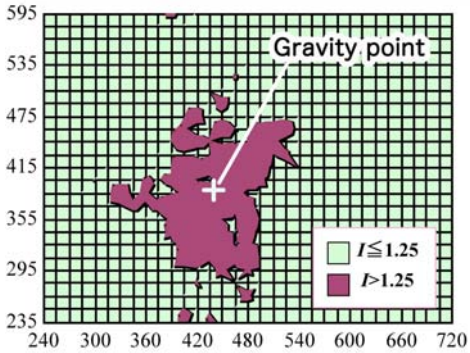


Fig.4 The distribution of the intersection index in MI patient (70y.o., M) and its gravity point.

## 3. Results

We have compared the distribution of the intersection index through every frame among normal subjects and heart disease patients. **Fig.5** shows the trajectory of the gravity point of the intersection index during a heartbeat. The fluctuation of the gravity point in the heart disease patients is easily distinguished from the normal subjects. In the normal hearts the gravity points concentrate in a small region.

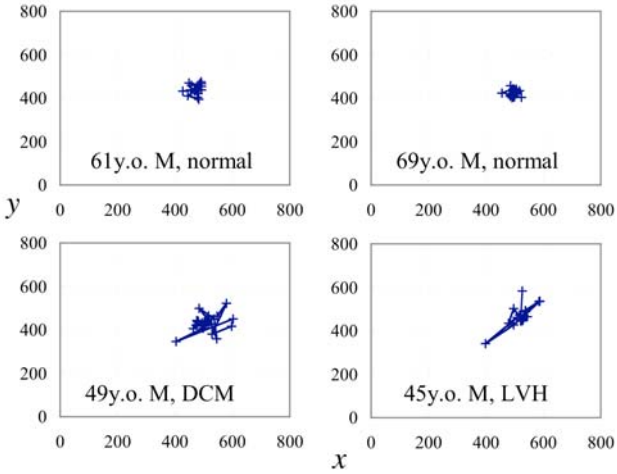


Fig.5 Trajectories of the gravity point during heartbeat in two normal subjects and two heart disease patients.

## 4. Conclusions

We developed a new method to visualize the synchronicity of motion in the heart by introducing the intersection index. We are going to enhance the accuracy of this method for quantitative evaluation.

## References

1. G.E.Mailloux, et al, IEEE Trans. Med. Imaging, vol.8, no.2, pp.143-153, 1989.
2. T.S.Denney, Jr. and J.L.Price, IEEE Trans. on Image Processing, vol.3, no.2, pp178-191, 1994.
3. K.Althoff, et al, IEEE Computers in Cardiology, Vol 27, 2000.

3P7a-10

Proceedings of Symposium on Ultrasonic Electronics, Vol. 29 (2008) pp. 439-440
11-13 November, 2008

# Application of independent component analysis to speckle reduction in liver echo image

# 肝エコー画像におけるスペックルリダクションへの独立成分解析の適用

Tadashi Yamaguchi[1†], Hiroki Suyari[2] ([1] Research Center for Frontier Medical Engineering, Chiba Univ.; [2]Grad.Sc. of Advanced Integration Science, Chiba Univ.)
山口匡[1‡], 須鎗弘樹[2] ([1] 千葉大 CFME; [2] 千葉大 融合科学)

## 1. Introduction

The speckle reduction method that doesn't depend on the depth attenuation etc. is requested in medical ultrasonics field.

In this research, it is examined to separate a speckle and other signals by using independent component analysis (ICA) for information observed by using ultrasonic diagnostic equipment. Subject disease of this research is the liver fibrosis. Targets are normal livers (in vivo) and fibrotic livers (in vivo and in vitro). We analyze the relationship between the characteristic of the signal that observed by US equipment and the result of separation by ICA.

## 2. Basics of application of ICA to ultrasonic image

ICA is already applied in medical field such as brain wave analysis with multi channel, segmentation of brain function in f-MRI and color component separation in optical measurement of skin although the relation between the processing result and phenomena is indistinct in either measurement. In order to apply ICA to an ultrasonic image, it is necessary to examine some causes of generating and independency of echo signals. The most fundamental feature of the ultrasonic image of liver is a speckle. Speckle is the result of interference with reflected wave from a lot of scatterers, and it is irrelevant noise to tissue structure. In diseased liver such as fibrosis, much minute diseased tissues are intermingled, and echo from the diseased tissue obseaved with speckle. Since these signals are short in time, it is buried in a speckle and it is difficult to detect by visual observation (**Fig. 1**). However, since these are the direct reflective waves from diseased tissue, they have the feature that it has been independent of the speckle which is an interference noise (**Fig. 2**).

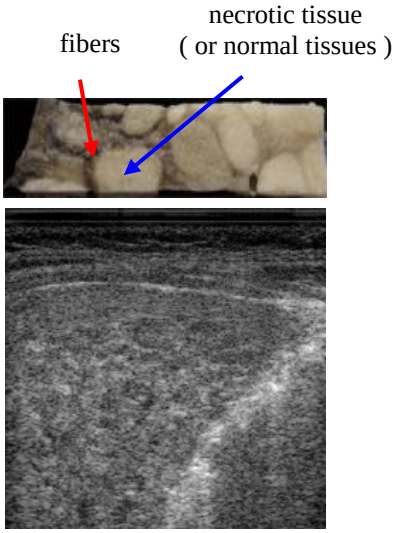


Fig.1 Image of liver fibrosis

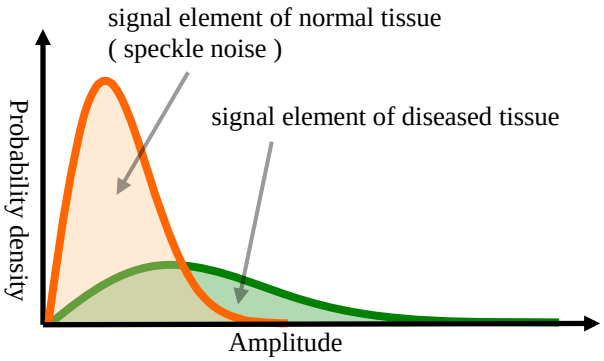


Fig.2 Elements of echo signal in liver fibrosis

In order to separate two independent ingredients by ICA, the signal which observed the same phenomenon simultaneously in two or more positions is required. Then, we examined a means to prepare two simultaneous observation signals used as inputs to ICA. It is some methods of changing observation conditions in the same subject and acquiring two echo images (RF signal), and a method of using the ingredient approximated to the speckle contained in the image for separation as the 2nd image.

---

yamaguchi@faculty.chiba-u.jp

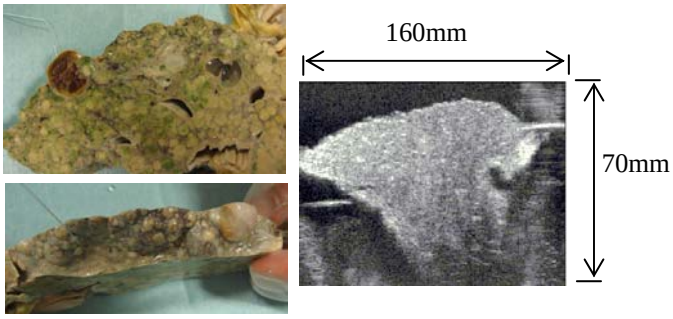


(a) specimen (b) original echo image
Fig.3 Example of human fibrotic liver specimen.

### 3. Result of ICA

It was comfirmd that the gain of the echo image used for an input seldom influences the judgment of independency by basic examination. On the other hand, it was estimated that the influence of the irradiation frequency which is one of the main causes for determining the characteristic of a speckle is large. Then, irradiation frequency was changed to one human liver specimen, two echo images were observed, and it was considered as the input of ICA (**Fig.3**). Echo data of fibrotic liver were assumed by using ultrasonic diagnostic equipment and a convex scanning probe (Toshiba Medical Systems co. modified SSA-770A and PVT-375AT). The focus depth was 40 mm and the gain was assumed to be 80. The sending and receiving frequency was 4.0 MHz and 6.0 MHz, respectively.

**Figure 4** shows the relult of ICA in human liver specimen. Although the speckle has occurred in the whole image in an output 1, the minute characteristic structures are detected at the edge and parenchymatous liver part in the output 2. These minute structures were in agreement with the fiber structure of a liver specimen. The amplitude distribution characteristic of the output 1 could be mostly approximated by the Rayleigh distribution, and it was confirmed that only the speckle ingredient had been extracted ideally.

### 4. Conclusion

The setting methods of the observation conditions in ultrasonic diagnostic equipment differ in neither a sound, nor brain waves, etc., and are not necessarily completely in agreement with the theory of ICA. However, it is possible to apply ICA to speckle reduction effectively by determining observation conditions on the basis of the character of a speckle. Ideally, it is desirable by irradiating with two or more signals simultaneously to observe many observation signals at once.

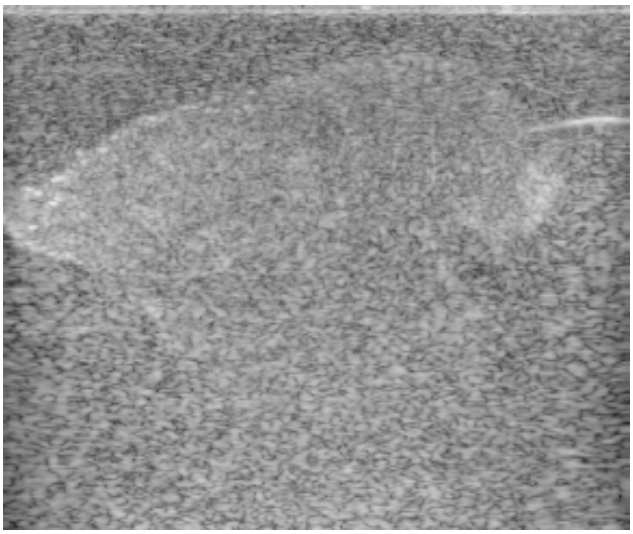

(a) Output 1

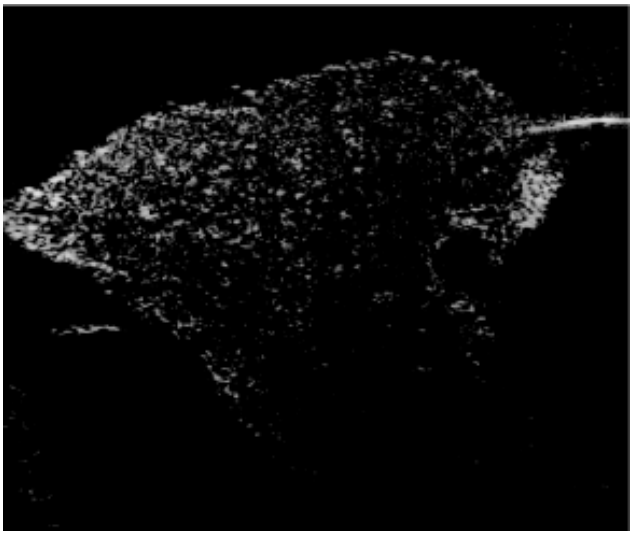

(b) Output 2

Fig.4 Result of ICA in human fibrotic liver specimen.

**References**

1. H. Shimura, T. Yamaguchi, H. Suyari and H. Hachiya : IEICE Rep. **US2006-15** (2006) 1. [in Japanese]

3P7a-11

Proceedings of Symposium on Ultrasonic Electronics, Vol. 29 (2008) pp. 441-442
11-13 November, 2008

# Influence of Blood Vessel Wall Motion on Shear Rate Estimation in Blood Flow

血流内のずり速度推定における血管壁運動の影響

Naotaka Nitta (Inst. for Human Sci. & Biomed. Eng., AIST)
新田尚隆 （産総研 人間福祉医）

## 1. Introduction

Relationships between the intravascular wall shear stress in flow dynamics, and the progress of arteriosclerosis plaque generation have been clarified by some studies [1]. Since the shear stress is defined by multiplying the viscosity by the shear rate, it is important that both factors can be estimated accurately [2-3]. Among them, the shear rate is an important factor to determine the estimated shear stress distribution. Hence, some investigations to improve the accuracy of shear rate estimation are conducted [4]. However, the finding with respect to the influence of blood vessel wall motion on shear rate estimation in blood flow is insufficient. Therefore, in this study, with the aim of the optimal wall filter design for the shear rate estimation, the above influence is investigated.

## 2. Shear rate estimation

Shear rate is defined as the derivation of velocity profile as follows.

$$v_r(x) = \frac{dv(x)}{dx} \qquad (1)$$

where $v_r(x)$, $v(x)$ and $x$ indicate the shear rate, velocity vector and depth direction, respectively.

## 3. Simulation

**Fig.1** shows the simulated radio frequency (RF) signal with a center frequency of 10 MHz and a signal-to-noise ratio (SNR) of 20 dB. This signal is produced by convolving the scatterer (600 particles/mm$^3$) and a pulse with 6 waves, and includes echoes from the walls and blood cells. Blood vessel has a radius of 2 mm and its luminal center lies at a depth of 15 mm from the surface of an ultrasonic probe. Blood flow is assumed to be a parabolic shape with a peak velocity of 0.2 m/s, and the ultrasonic beam incident angle is set to 60 degree. In order to measure the velocity, the successive 8 pulses are transmitted at a pulse repetition frequency (PRF) of 5 kHz.

---

n.nitta@aist.go.jp

In order to investigate the influence of blood vessel wall motion on shear rate estimation in blood flow, the dilative and contractive wall motions are added. Here, the dilative and contractive rates are defined as a ratio of the wall displacement during two pulses transmission interval, which corresponds to a reciprocal of PRF, to the initial diameter of lumen, and the motions from -0.4 % (contraction) to 0.4 % (dilation) are induced.

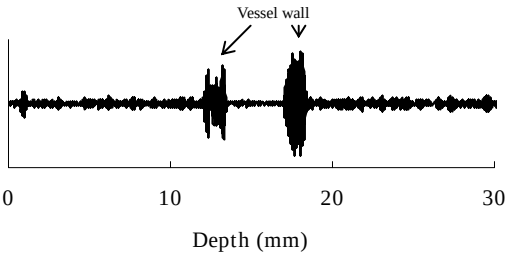


Fig.1 RF signal from the vessel wall and blood cells.

## 4. Results

**Fig.2** shows the results of estimated (a) velocity and (b) shear rate profiles during dilation, respectively. Here, the velocity profiles were estimated by the autocorrelation method without any wall filter, and the shear rate profiles were estimated by differentiating the above velocity profiles using the differential window width of 0.6 mm.

**Fig.3** shows the results of estimated (a) velocity and (b) shear rate profiles during contraction, respectively. In **Fig.2**(a) and **Fig.3**(a), the wall motions were estimated beside the velocity profiles, and as predicted easily, the resultant shear rate profiles in **Fig.2**(b) and **Fig.3**(b) included two false peaks beside the desirable shear rate.

**Fig.4** shows the summarized evaluation results with respect to root mean square error (RMSE) of (a) velocity and (b) shear rate estimations, respectively. It should be noted that the RMSE exhibits an asymmetry property. That is, the RMSE in dilation is smaller than that in contraction. These findings are useful for designing the optimal wall filter in estimating the shear rate.

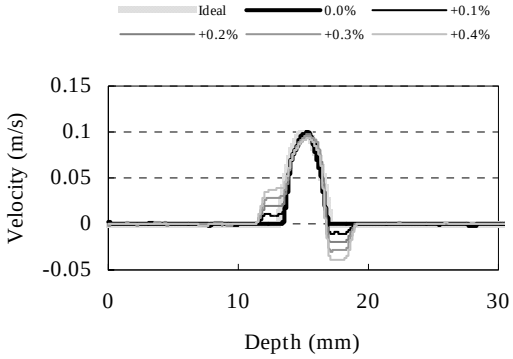


(a)

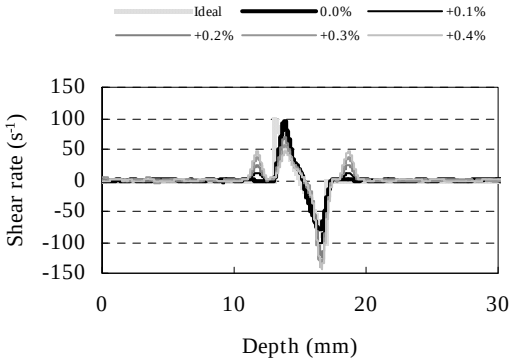


(b)

Fig.2 Estimated (a) velocity and (b) shear rate profiles during dilation.

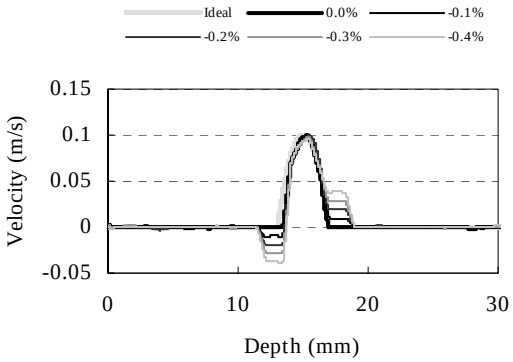


(a)

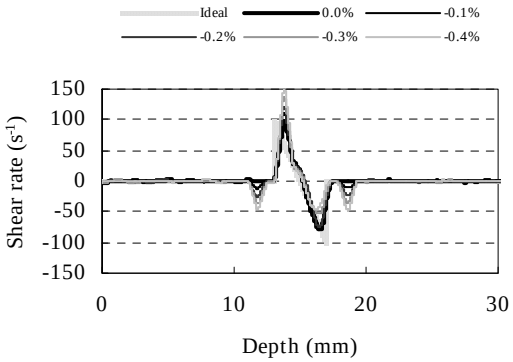


(b)

Fig.3 Estimated (a) velocity and (b) shear rate profiles during contraction.

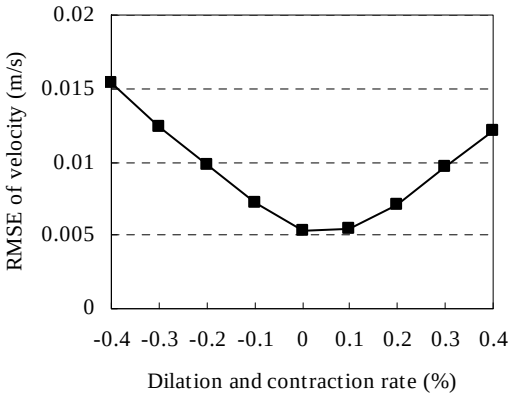


(a)

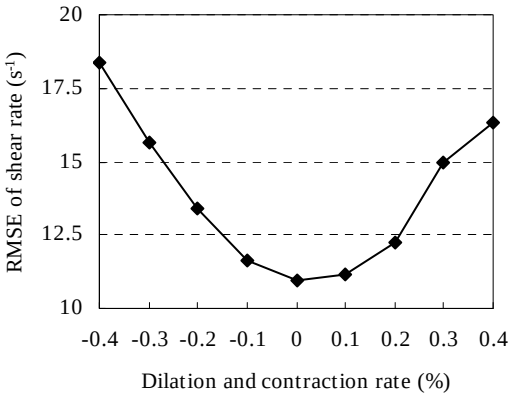


(b)

Fig.4 RMSE of (a) velocity and (b) shear rate estimations.

## 5. Conclusion

In this study, the influence of blood vessel wall motion on shear rate estimation in blood flow was investigated. These findings are useful for designing the optimal wall filter in estimating the shear rate.

**References**

1. H.M. Honda, T. Hsiai, C.M. Wortham: Atherosclerosis. **158** (2001) 385.
2. N. Nitta, K. Homma : Trans. J. Soc. Med. Biol. Eng. **44** (2006) 190.
3. N. Nitta, K. Homma : Jpn. J. Appl. Phys. **44** (2005) 4602.
4. N. Nitta, N. Takeda : Jpn. J. Appl. Phys. **47** (2008) 4209.

3P7a-12

Proceedings of Symposium on Ultrasonic Electronics, Vol. 29 (2008) pp. 443-444
11-13 November, 2008

# Accuracy Evaluation for High-Frequency Ultrasonic Measurement of Viscoelasticity of Radial Arterial Wall by Basic Experiments

高周波超音波を用いた橈骨動脈壁粘弾性計測法の基礎実験による精度評価

Kazuki Ikeshita[1†], Hideyuki Hasegawa[2,1] and Hiroshi Kanai[1,2] ([1]Grad. School of Eng., Tohoku Univ.; [1]Grad. School of Biomedical Eng., Tohoku Univ.)
池下和樹[1]，長谷川英之[2,1]，金井　浩[1,2]（[1] 東北大院 工; [2] 東北大院 医工）

## 1. Introduction

The endothelial dysfunction is considered to be an initial step of atherosclerosis[1]. Additionally, it is reported that the smooth muscle, which constructs the media of the artery, changes its characteristics owing to atherosclerosis[2]. Consequently, it is important for early preventive treatment to noninvasively assess the endothelial function and the mechanical property of the media which is mainly composed of smooth muscle.

For the evaluation of the endothelial function, there is a conventional technique for measurement of the transient change in the inner diameter of the brachial artery caused by flow-mediated dilation (FMD) after the release of avascularization[3]. For more sensitive and regional evaluation, we developed a method for direct measurement of the change in the elasticity of the intima-media region due to FMD[4,5]. Additionaly, we proposed a new noninvasive method for measurement the transient change in the stress-strain relationship owing to the FMD at the radial artery for measurement of mechanical property of the media[6].

From the stress-strain relationship, the viscoelasticity of the intima-media region using the least-square method to investigate the transient change in the viscoelasticity due to FMD. In this study, the accuracy of the method of measuring the viscoelasticity of radial arterial wall was evaluated by basic experiments.

## 2. Principles

### 2.1 Measurement of stress-strain relationship of the intima-media region in the radial arterial wall

To noninvasively assess the stress-strain relationship of the intima-media region of the radial arterial wall, it is necessary to measure waveforms of the change in thickness (strain) and the blood pressure (stress) continuously. The minute change in the thickness of the radial arterial wall, $h(t)$, at time $t$ during a cardiac cycle was measured by the *phased-tracking method*[7]. To obtain the change in thickness, the velocities of the artery wall boundaries A (lumen-intima) and B (media-adventitia) were estimated. The change in thickness, $\Delta h(t)$, between two different depths, $d_A$ and $d_B$, in the arterial wall along an ultrasonic beam was obtained from the difference between displacements, $x(t; d_A)$ and $x(t; d_B)$, at these two positions as follows;

$$\Delta\hat{h}(t) = \hat{x}(t; d_A) - \hat{x}(t; d_B) = \int_0^t \{\hat{v}(t; d_A) - \hat{v}(t; d_B)\}\mathrm{d}t, \qquad (1)$$

where ^ means an estimate.

The blood pressure waveform $p(t)$ was simultaneously and continuously measured by a sphygmometer which automatically optimizes the position of the sensor for blood pressure measurement. Therefore, we could obtain the stress-strain relationship noninvasively.

### 2.2 Viscoelasticity estimation of arterial wall using least-square method

The smooth muscle constructs the media and it is the main source of the viscoelasticity of the vessel wall[8]. By assuming the Voigt model as a viscoelastic model of the intima-media region, the stress-strain relationship is given by

$$\hat{\tau}(t) = E_s\gamma(t) + \eta\dot{\gamma}(t) + \tau_0, \qquad (2)$$

where $\hat{\tau}(t)$ is the stress and $\gamma(t)$, $\dot{\gamma}(t)$, $E_s$, and $\eta$ are strain, strain rate, static elasticity, and viscosity coefficient, respectively. The measured strain $\gamma(t)$ is the incremental strain due to the pulse pressure, whereas the measured stress includes the bias stress (diastolic blood pressure). Therefore, $\tau_0$ is added to the right-hand side of eq. (2) as the bias stress corresponding to diastolic pressure.

The parameters in eq. (2), $E_s$, $\eta$, and $\tau_0$, are estimated using the least-square method by minimizing the mean squared error, $\alpha$, between the measured and model stresses $\tau(t)$ and $\hat{\tau}(t)$.

### 2.3 Procedure for basic experiment

In the basic experiment (**Fig. 1**), ultrasonic RF echoes (transmit: 22 MHz) were acquired at a

E-mail:{kanai, hasegawa, ikeshita}@us.ecei.tohoku.ac.jp

sampling frequency of 66.5 MHz for 2 s and a frame rate was about 160 Hz. In this experiment, we used a linear type probe which scans 127 positions. Two different homogeneous cylindrical phantoms made from silicone rubber were measured. The elastic moduli of these phantoms have been already measured (phantom A: 490 kPa and phantom B: 750 kPa). The wall thickness was 1 mm. The change in internal pressure, $\Delta p(t)$, which was applied using a flow pump, was measured by a pressure sensor. The transient change in stress-strain relationship during a cardiac cycle was obtained from the measured change in thickness, $\Delta h(t)$, and the internal pressure $\Delta p(t)$.

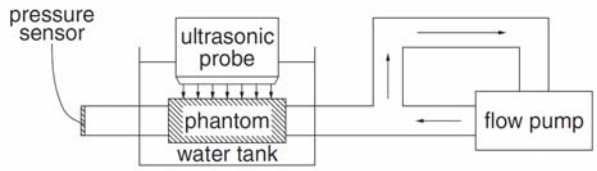


Fig. 1 Schematic diagram of basic experiment.

## 3. Results

**Figure 2(a)** shows a B-mode image of the silicone rubber phantom A. The lines *k* and *l* show tracking points assigned at the outside and inside edges of the anterior wall of the silicone rubber. **Figure 2(b)** and **2(c)** show the estimated velocities of these edges. The distance between *k* and *l* was set at 1 mm.

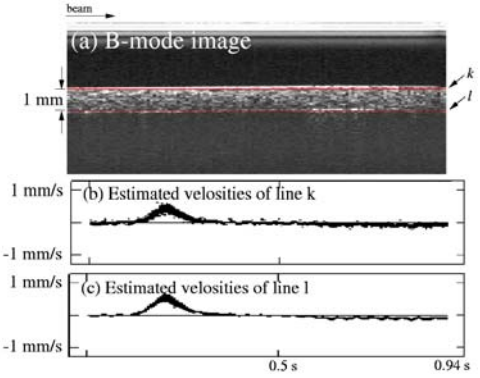


Fig. 2 (a) B-mode image of the silicone rubber. (b) and (c) Estimated velocities at lines *k* and *l* obtained at 127 ultrasonic beam positions.

The accuracy of the estimation of the viscoelasticity depends on the accuracy of the measurement of the velocity of the wall. By assuming the constant movement of homogeneous phantom, the accuracy of the estimated velocities can be evaluated by the standard derivation among velocities obtained at 127 beam positions. The averaged standard derivation $\bar{\sigma}$ is expressed as

$$\bar{\sigma} = \frac{1}{N}\sum_{n=1}^{N}\sigma(t), \qquad (3)$$

$$\sigma(t) = \sqrt{\frac{1}{M}\sum_{m=1}^{M}\{v_h(t+T_s) - \bar{v}_h(t)\}^2},$$

where $M$, $N$, $v(t)$ and $\bar{v}(t)$ are the number of beams, the number of data in one cycle of the flow pump, measured velocity and mean velocity spatially averaged for 127 beam positions, respectively. The averaged standard deviation $\bar{\sigma}$ for phantoms A and B were 0.0486 mm/s and 0.0464 mm/s, respectively. These are 4.7% and 6.3% of the maximum velocities.

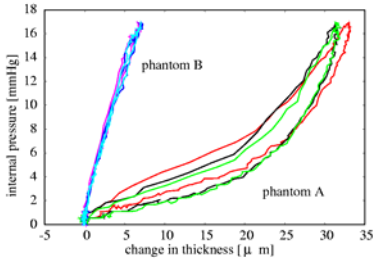


Fig. 3 Stress-strain relationship of phantoms A and B.

**Figure 3** shows the stress-strain relationships of phantoms A and B obtained at a beam position. The slope and area of the stress-strain loop show the elasticity and ratio of elastic modulus and loss modulus. From the Fig. 3, the elasticity of phantom A is smaller than that of phantom B, and the viscosity of phantom A is larger than that of phantom B.

We estimated the static elasticity $E_s$ and viscosity $\eta$ from the stress-strain relationship. The average and standard deviation of static elasticity and viscosity coefficients of phantom A and B were 223.7±143.1 kPa, 992.1±1293.6 kPa, 1.44±1.47 kPa•s and 0.69±4.48 kPa•s.

## 4. Conclusion

In this study, from the measured stress-strain relationship, we estimated the viscoelasticity of the silicone rubber noninvasively. This method has a potential for the noninvasive measurement of viscoelasticity of the arterial wall. However, the proposed method still requires the improvement of the measurement of strain rate.

## References

1. R. Ross: N. Engl. J. Med. **340** (1996) 115.
2. Y. Matsuzawa: Jpn. J. Clin. Med. **51** (1993) 1951.
3. M. C. Corretti, et al.: J. Am. Coll. Cardiol. **39** (2002) 257.
4. H. Hasegawa, et al.: J. Med. Ultrason. **31** (2004) 81.
5. T. Kaneko, H. Hasegawa and H. Kanai: Jpn. J. Appl. Phys. **46** (2007) 4881.
6. K. Ikeshita, H. Hasegawa and H. Kanai: Jpn. J. Appl. Phys., **47** (2008) 4165.
7. H. Kanai, et al.: IEEE Trans. Ultrason. Ferroelectr. Freq. Control, **43** (1996) 791.
8. K. Hirata et. al.: JSME Mechanical Engineer's Handbook C6. JSME, Tokyo, Japan (1998) 147.

3P7a-13

Proceedings of Symposium on Ultrasonic Electronics, Vol. 29 (2008) pp. 445-446
11-13 November, 2008

# Optimization of Window Size and Search Region in 2D Correlation Function for Assessment of Regional Myocardial Contraction and Relaxation

心筋収縮拡張特性計測における 2 次元相関窓長と探索領域の最適化

Yasunori Honjo[1†], Hideyuki Hasegawa[2, 1] and Hiroshi Kanai[1, 2] ([1] Grad. School of Eng., Tohoku Univ.; [2] Grad. School of Biomedical Eng., Tohoku Univ.)
本庄泰徳[1]，長谷川英之[2, 1]，金井　浩[1, 2]　([1] 東北大院 工; [2] 東北大院 医工)

## 1. Introduction

Methods for imaging of 2-D strain rate in the heart wall are useful for quantitative evaluation of the regional heart function. The 2-D strain rate and heart wall motion have been estimated by an algorithm, speckle tracking and so on. However, important parameters in the algorithm, the optimal sizes of a region-of-interest (ROI) and search region, have not been thoroughly investigated.

In this study, the optimal values of these important parameters were determeind, and the 2-D heart wall motion was estimated by 2-D cross-correlation between RF echoes.

## 2. Principles

### 2.1 2D cross-correlation function

In this study, 2-D displacement was estimated by 2-D cross-correlation between RF echoes. The correlation coefficient $r_n(\Delta N, \Delta l, \Delta d)$ at the axial and lateral shifts, $\Delta d$ and $\Delta l$, is calculated from RF signal $\mathrm{rf}_n(l, d)$ at depth $d$ and beam position $l$ in the $n$-th frame as follows:

$$r_n(\Delta N, \Delta l, \Delta d) = \frac{1}{A}\sum_{i=l-L/2}^{l+L/2}\sum_{j=d-D/2}^{d+D/2}\{\mathrm{rf}_n(i, j)\cdot \mathrm{rf}_{n+\Delta N}(i+\Delta l, j+\Delta d)\}, \quad (1)$$

$$\left(A=(L+1)(D+1)\sigma_{n,l,d}\sigma_{n+\Delta N,l+\Delta l,d+\Delta d}\right)$$

where $\sigma_{n,l,d}$ is the standard deviation of the RF signal $\mathrm{rf}_n(l, d)$ in an ($L\times D$) ROI. RF signals in the ROI in the $n$-th frame are compared with those in the ($n + \Delta N$)-th frame. The ROI in the ($n + \Delta N$)-th frame is shifted by $\Delta d$ and $\Delta l$ in the axial and lateral directions relative to those in the $n$-th frame.

### 2.2 Reconstructive interpolation

One of the problems in the estimation of 2-D strian rate is the anisotropic spatial resolution. The spatial resolution in the lateral direction is much lower than that in the axial one. The coasely sampled 2D cross-correlation function is an inexact estimator of the location of the peak. Therefore, in order to overcome this problem, sampled correlation function was interpolated to improve the precision of displacement estimation by means of reconstructive interpolation [1].

This method is a time-domain technique based on analog signal reconstruction theory. It is possible to interpolate the sampled cross-correlation function at an arbitrary time by means of low-pass filteration. The interpolated cross-correlation function $r(t)$ is expressed as follows:

$$r(t) = \sum_{n=-N_c/2}^{N_c/2} r(nT_s)\mathrm{sinc}\left[\frac{\pi(t-nT_s)}{T_s}\right] w_h\left[\frac{\pi(t-nT_s)}{T_s}\right], \quad (2)$$

where $T_s$ is the sampling interval, $N_c$ is the number of the sampled cross-correlation function, and $w_h$ is the Blackman window.

## 3. Determination of optimal parameters

### 3.1 Determination of the size of a search region

At first, one of the important parameter, the optimal size of a search region, was determined to successfully track the 2-D heart wall motion.

The size of a search region can be rephrased as the number of sampled points, the length of cross-correlation function. Therefore, the effect of the number of sampled correlation function was investigated by means of a simulated sinusoidal wave. Waveforms sampled at intervals of $\theta_s$=3～120 degrees were interpolated by reconstructive interpolation so that the sampling interval became 3 degrees.

**Figures 1(a)** and 1(b) show the differences $\varepsilon(\theta_s)$ between the peak positions of true and sampled correlation functions evaluated at the different number of sampled point $N_c$. The differences $\varepsilon(\theta_s)$ is defined using peak positions $P_0$ and $P_{\theta s}$ of true and interpolated correlation functions as follow:

$$\varepsilon(\theta_s) = \frac{P_{\theta_s} - P_0}{P_0}, \quad (2)$$

---

E-mail: (kanai,hasegawa,honjo)@us.ecei.tohoku.ac.jp

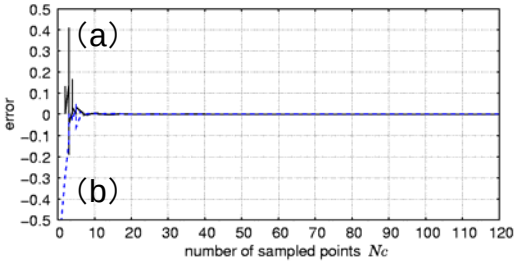


Fig. 1: Error $\varepsilon(\theta_s)$ between the interpolated peaks and the true peaks of correlation functions between simulated sinusoidal functions (a) $P_0$=1, (b) $P_0$=-1.

As shown Fig. 1, the error decreased sufficiently at a number greater than 8 sampling points. The size of a search region should set as narrow as possible because there may be several regions in the post frame which have echo patterns similar to that in the ROI in the previous frame when the size of the search region is too large. Therefore, the size of the search region $N_c$ was determined to be 8 (8 degree $\times$6 mm).

### 3.2 Determination of the size of a ROI

To determine the optimal size of an ROI, ROIs with different sizes ($l \times d$) = ((1.5～7.5 degree)$\times$(0.1～3.1 mm)) were examined. The 2-D displacement of an ROI in the IVS was estimated by 2-D cross-correlation function using ROIs with different sizes. The reliabilities of the axial and lateral displacements obtained by 2-D tracking were evaluated using correlation coefficients between displacements estimated by the 2-D method and corresponding displacements obtained by the 1-D method in two different measurements [2].

As shown in Fig. 2(a), correlation coefficient is totally high (0.9~0.95). This result shows the axial displacement can be estimated accurately by 2-D tracking with any size of an ROI. On the other hand, Fig. 2(b) shows different tendency compared with Fig. 2(a). The distribution of correlation coefficients showed a dominant peak at a size of an ROI of (4.5 deg$\times$2.1 mm). Therefore, in this study, the size of an ROI was determined to be (4.5 deg$\times$2.1 mm).

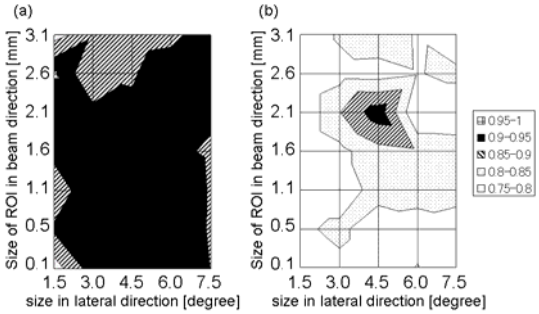


Fig. 2: Cross-correlation coefficients (a) between the axial displacement estimated by the 2-D method and reference and (b) between the lateral displacement estimated by the 2-D method and reference.

## 4. *In vivo* experiment

The motion of an arbitrary region in the interventricular septum (IVS) was estimated by 2-D tracking. The 2-D cross-correlation function was calculated between two consecutive frames. The size of a search region was routinely determined by the length corresponding to 8 number of beams (8 degree$\times$6 mm). The size of an ROI was set at the determined optimum size (lateral axial) = (4.5 deg $\times$2.1 mm).

**Figures 3(a)** and 3(b) show the lateral and axial displacements, respectively. Displacements estimated by the 2-D method (solid line) were compared with those estimated by the established method, 1-D phase-sensitive method (dashed line) [2]. These displacements by the 2-D method well corresponded to the references by the 1-D phase-sensitive method. Figure 3(c) shows that two-dimensional IVS motion obtained by the 2-D correlation function. The IVS moved to the apical side during cardiac systole and then, it began to return to the original position during diastole.

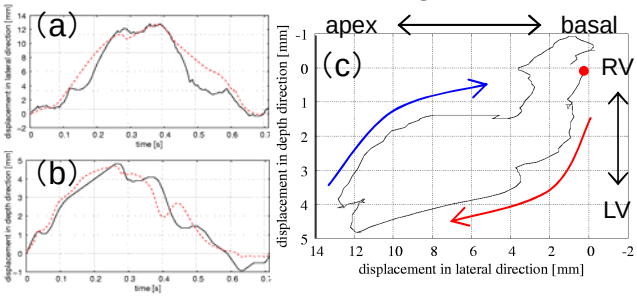


Fig. 3: (a) Displacement in the lateral direction. (b) Displacement in the axial direction. (c) 2-D displacement

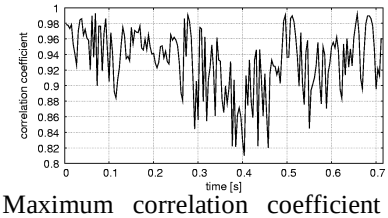


Fig. 4: Maximum correlation coefficient during one cardiac cycle.

## 5. Conclusion

Regional heart wall motion was measured at high temporal and spatial resolutions. As shown Fig. 4, maximal correlation coefficients during one cardiac cycle was more than 0.6 [3], and i*n vivo* experimental results show the possibility of this method for measurement of two-dimensional heart motion to assess the regional myocardial strain rate.

### References

1. I. Cespedes et al.: Ultrason. Imaging. **17** (1995) pp. 142-171.
2. H. Kanai et al.: IEEE Trans. UFFC., **43** (1996) pp. 791-810.
3. I. Akiyama et al.: Trans. IEICE., D-**71** (1988) pp. 733-736.

3P7b-8

Proceedings of Symposium on Ultrasonic Electronics, Vol. 29 (2008) pp. 447-448
11-13 November, 2008

# Problems in Deriving the Soft-Tissue Thermal Index(TIS) Using $I_{SPTA}$ in the Near Field

# 近距離音場における $I_{SPTA}$ を用いた Soft-Tissue Thermal Index(TIS)算出の問題点

Masahiro Yoshioka‡ (NMIJ, AIST)
吉岡正裕‡（産総研）

## 1. Introduction

The thermal index (TI) and mechanical index (MI) are indices used for evaluating medical diagnostic ultrasonic equipment. IEC 62359 is the international standard for deriving TI and MI[1)]. TI gives information about the temperature rise in tissue caused by ultrasonic absorption and it is defined as the ratio of the acoustic output power at a specified point to that required to raise the temperature at that point by 1 ˚C for a specific tissue model. The soft-tissue thermal index (TIS) is a TI that is appropriate for soft tissues and it is derived from the measured values for the ultrasonic output power and intensity radiated in water. In this report, problems in deriving the TIS using the spatial-peak temporal-average intensity in the near field are investigated.

## 2. Derivation of TIS[1)]

### 2.1 Procedure for deriving TIS

The procedure for deriving the TIS of IEC 62359: 2005 differs according to the radiating area of the ultrasonic transducer $A_{aprt}$ (cm$^2$) used. In this report, the derivation for the case $A_{aprt}$ > 1 cm$^2$ is considered. $z$ (cm) is the depth from the tissue surface contacted by the ultrasonic transducer as shown in **Fig. 1**. The acoustic output power contributing to tissue temperature rise $P_P(z)$ (mW) is given by Eq. (1).

$$P_P(z) = \min\left\{P_\alpha(z), I_{SPTA\alpha}(z)\times 1\text{cm}^2\right\} \quad (1)$$

$$P_\alpha(z) = P\times 10^{-\alpha z f_{awf}/10} \quad (2)$$

$$I_{SPTA\alpha}(z) = I_{SPTA}(z)\times 10^{-\alpha z f_{awf}/10} \quad (3)$$

Where $P$ (mW) is the acoustic output power at the radiation surface of the transducer, $I_{SPTA}(z)$ (mW/cm$^2$) is the spatial-peak temporal-average intensity in the plane at a depth $z$ in water, $f_{awf}$ (MHz) is the ultrasonic frequency and $\alpha$ = 0.3 (dB/cm/MHz) is the acoustic attenuation coefficient of tissue. $z_S$ (cm) is the depth having the highest value of $P_P(z)$ in the range satisfying $z \geq z_{bp}$ (cm). $z_{bp}$ is the minimum depth for measuring $I_{SPTA}(z)$ and it is given by the following equation.

masahiro.yoshioka@aist.go.jp

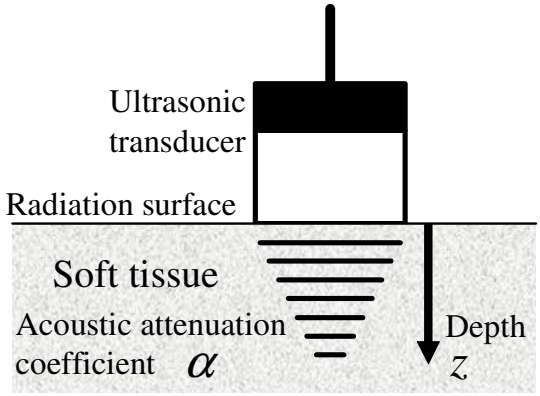


Fig. 1 Illustration of soft tissue being irradiated by ultrasound waves from a transducer in contact with the surface of the soft tissue.

$$z_{bp} = 1.5D_{eq} = 1.5\sqrt{\pi A_{aprt}/4} \quad (4)$$

Where $D_{eq}$ (cm) is the equivalent aperture diameter of the ultrasonic transducer. Considering that the temperature increase is greatest at the depth $z_S$, the TIS is given by:

$$\text{TIS} = \frac{P_P(z_S) f_{awf}}{C_{TIS}}, \quad (5)$$

where $C_{TIS}$ (= 210 mW·MHz) / $f_{awf}$ is the acoustic output power for raising the tissue temperature by 1 ˚C.

### 2.2 Perfusion assumption

As eq. (5) shows, $P_P(z)$ is the critical parameter for deriving the TIS. It is obtained in IEC 62359 by applying a perfusion assumption (with a heat perfusion length of 1 cm); specifically, if the beam area is less than 1 cm$^2$, the acoustic output power controls the temperature rise and if it is greater than 1 cm$^2$, the intensity controls it. In eq. (1), which is used to derive $P_P(z)$, the beam area is judged to be less than 1 cm$^2$ or not by comparing $P_\alpha(z)$ and $I_{SPTA\alpha}(z) \times 1$ cm$^2$.

## 3. Problems in deriving TIS

### 3.1 Derivation of $z_S$

In this report, a 3.5-MHz ultrasonic transducer with a 1.4-cm-diameter plane circular surface (radiating area of 1.5 cm$^2$) used for general

medical diagnostic ultrasonic equipment is considered. The parameters $P_\alpha(z)$ and $I_{SPTA\alpha}(z) \times 1$ cm$^2$ of the ultrasonic transducer are derived from ultrasound pressure distributions, which are calculated numerically using the Rayleigh integral solution[2]. The calculation results are plotted in **Fig. 2**. From eq. (4), $z_{bp}$ is found to be 2.1 cm, and consequently $z_S$ = 2.1. However, as Fig. 2 shows, $P_P(z)$ increases as $z$ decreases below $z_S$. Moreover, the tissue temperature rise is highest at depths close to the radiation surface when the ultrasonic frequency and the curvature radius of the transducer are high, as shown in Fig. 2[3,4]. Since the depth at which the temperature rise is greatest $z_S$ is an important parameter for users of medical diagnostic ultrasonic equipment, it is problematic if $z_S$ cannot be accurately determined. To overcome this problem, it is necessary to reduce $z_{bp}$ to a depth close to the radiation surface.

### 3.2 Derivation of TIS in the near field

Because the beam area at a depth close to radiation surface is the same as the radiation surface area, the beam area of a transducer with $A_{aprt}$ = 1.5 cm$^2$ will be greater than 1 cm$^2$. However, as Fig. 2 shows, there are some depths $z$ at which $P_\alpha(z) < I_{SPTA\alpha}(z) \times 1$ cm$^2$. The TIS is overestimated in this case. This overestimation is due to estimating the beam area by comparing $P_\alpha(z)$ and $I_{SPTA\alpha}(z) \times 1$ cm$^2$. This method for estimating the beam area can be applied only in the far field. Moreover, the acoustic output power in the range of 1 cm$^2$ cannot be derived as $I_{SPTA\alpha}(z) \times 1$ cm$^2$ in the near field.

The TIS should be thus derived using the spatially averaged intensity for 1 cm$^2$ in the near field. Since the value of the spatially averaged intensity depends on the location of the 1-cm$^2$ region, in this report, $I_{SATA1\times1}(z)$ is defined as the maximum spatial-average temporal-average intensity for 1 cm$^2$ at a depth $z$. It is proposed that the TIS be derived using $P'_\alpha(z)$ instead of $P_\alpha(z)$ using the following equations.

$$P_P'(z) = I_{SATA1\times1\alpha}(z) \times 1\text{cm}^2 \qquad (6)$$

$$I_{SATA1\times1\alpha}(z) = I_{SATA1\times1}(z) \times 10^{-\alpha z f_{awf}/10} \qquad (7)$$

The calculation results of $I_{SATA1\times1\alpha}(z)$ for the ultrasonic transducer described in Section 3.1 are plotted in Fig. 2. $z_S$ and the TIS when the sound pressure on the radiation surface of this transducer is 10 kPa are compared in the following three derivation methods.

1) $z_{bp}$ = 2.1 cm, using $P_P(z_S)$ of eq. (1) (method of IEC 62359: 2005): $z_S$ = 2.1 cm, *TIS* = 0.104
2) $z_{bp}$ = 0.3 cm, using $P_P(z_S)$ of eq. (1): $z_S$ = 0.4 cm, *TIS* = 0.157
3) $z_{bp}$ = 0.3 cm, using $P_P'(z_S)$ of eq. (6): $z_S$ = 0.3 cm, *TIS* = 0.106

Method 2) is the case when the hydrophone for measuring the intensity is as close as possible to the ultrasonic transducer, in contrast with method 1) described in IEC 62359: 2005. Using method 2), $z_S$ is found to close to the radiation surface, reflecting the same as the tendency as the tissue temperature rise[4]. Therefore, the TIS is derived from the acoustic output power $P_\alpha(z)$; however, the beam area is greater than 1 cm$^2$. In method 3), which uses $I_{SATA1\times1}(z)$ instead of $I_{SPTA\alpha}(z)$ that method 2) uses, $z_S$ is also found to be close to the radiation surface and the TIS is calculated to be 0.67 times that in method 2). Because the ratio of the two TISs given by methods 2) and 3) is according to 1 cm$^2$ / $A_{aprt}$ = 0.65, it is considered that the overestimation of the TIS can be removed by using spatial-averaged intensity rather than the spatial-peak intensity.

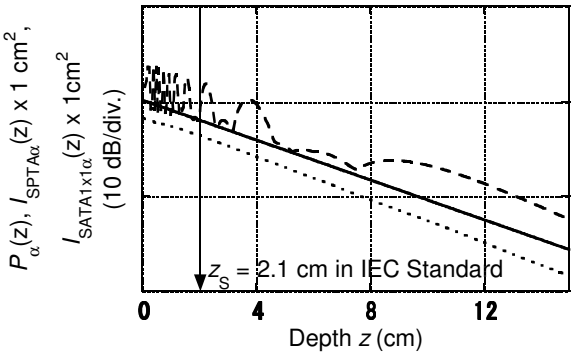


Fig. 2 $P_\alpha(z)$ (solid line), $I_{SPTA}(z) \times 1$ cm$^2$ (broken line) and $I_{SATA1\times1}(z) \times 1$ cm$^2$ (dashed line) for 3.5-MHz ultrasonic field radiated from 14-mm-diameter plane circular transducer.

## 4. Summary

When deriving the TIS using IEC International Standards, the depth of the highest temperature rise cannot be accurately determined and the acoustic power in the range of 1 cm$^2$ cannot be derived as $I_{SPTA\alpha}(z) \times 1$ cm$^2$ in the near field. In order to overcome these problems, a derivation using the spatial-averaged intensity for 1 cm$^2$ is proposed.


### Acknowledgment

The author expresses gratitude to the members of Japanese National Committee of IEC/TC87 (Ultrasonics) for useful discussions.


### References


1. IEC 62359: 2005.
2. G. R. Harris: J. Acoust. Soc. Am. **70** (1981) 10.
3. M. G. Curley: IEEE Trans. U.F.F.C., **40** (1993) 59.
4. O'Brien and D. S. Ellis: IEEE Trans. U.F.F.C., **46** (1999) 1459.

3P7b-9

Proceedings of Symposium on Ultrasonic Electronics, Vol. 29 (2008) pp. 449-450
11-13 November, 2008

# Basic Verification of the Tissue Effect of An Ultrasonically Activated Scalpel

超音波凝固切開装置の生体作用の基礎検討

Masaru Oya[1†], Tadashi Yamaguchi[2], Hideki Hayashi[2], and Hiroyuki Hachiya[3]
([1]Graduate school of Advanced Integration Science, Chiba Univ.; [2]Resarch Center for Frontier Medical Engineering, Chiba Univ.; [3]Graduate School of Sci. and Eng., Tokyo Institute of Technology)
大屋優[1‡], 山口匡[2], 林秀樹[2], 蜂屋弘之[3]（[1]千葉大 融合科学; [2]千葉大 CFME; [3]東工大 理工）

## 1. Introduction

Ultrasonically activated scalpel is used widely in laparoscope-assisted surgery, but it is concerned that it may give undesirable damage to the surrounding tissues during surgical operation by mechanical effect of sound.
In this paper, we present the vibration distribution of the blade using laser Doppler vibrometer. We observe the generation of cavitation bubble in the water and discuss the sound propagation and the bioeffect of sound in water.

## 2. Ultrasonically activated scalpel

Ultrasonically activated scalpel is a surgical instrument which can perform incision and coagulation simultaneously. The active blade at the tip is the specification which vibrates on the frequency of 55.5 kHz. Incision is mechanically performed by repeating that the vibrating blade extends an organization locally beyond an elastic limit. Coagulation is performed when the frictional heat by vibration of a blade carries out heat denaturation of the protein in a living body tissue. A blade is roughly divided hook blade and laparoscopic coagulating shears (LCS). Hook blade can perform incision by making a blade press to an organization, and if a flat portion is pressed, it can also perform coagulation. And LCS can hold an organization in the pad portion and active blade portion which vibrate at high speed, and can perform incision and coagulation simultaneously.

## 3. Measurement of vibration distribution

In the blade portion in contact with a living body tissue, in order to know what kind of vibration is actually excited, the equipment was operated in the air and vibration distribution was measured using the scanning laser Doppler vibrometer (Polytec PVS-400). Measurement results are shown in **Fig.1** and **Fig.2**. The gray scale images correspond to the velocity component which is normal to the image plane. **Figure 1** shows that, in the ball type blade, the whole surface of the ball is vibrating uniformly. **Figure 2** shows that bending-type vibration is excited on the front face of LCS, and uniform vibration is excited on the end face of LCS.

Fig.1 Measurement result of ball type blade

(a) The front face of LCS

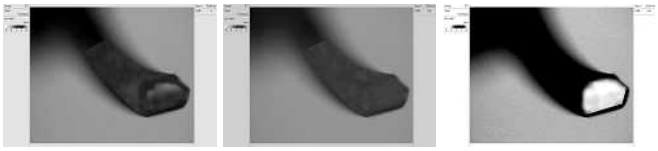

(b) The end face of LCS

Fig.2 Measurement results of LCS

## 4. Observation of cavitation bubbles

When the cavitation bubbles collapse, they force liquid energy into very small volumes. Although the collapse of a cavity is a relatively low-energy event, highly localized collapses can erode metals over time, and damage tissues. It is important to observe where cavitation bubbles generate.
We observed the generation of cavitation bubbles around the blade in degassed water. We lighted up the water from side of the water tank, and took photographs using a high speed camera (Casio EXILIM EX-F1).
**Figure 3** shows cavitation bubbles near the ball type blade and LCS. In these cases, the ultrasonically activated scalpel worked with

masaru-oya@graduate.chiba-u.jp

maximum output. It was observed that the amount of cavitation bubbles increases as we increased output of the equipment. In ball type blade, bubbles were generated from upper and lower part of blade shown in **Fig.3 (a)**. The generating position changed irregularly in the circumferential direction. Since the vibration distribution of ball blade is almost uniform, the generating position of these cavitation bubbles changes irregularly. In LCS, bubble generation mainly from the blade end was observed, shown in **Fig.3 (b)**. The bubbles that generated near the blade are carried by acoustic streaming.


(a) Ball type blade (b) LCS

Fig.3 Cavitation.bubble from blades.

## 5. Acoustic pressure in the water

To estimate the ultrasound exposure of the tissue, it is necessary to measure the acoustic field around the blade of an ultrasonically activated scalpel. We measured the acoustic pressure emitted from the blade in degassed water using hydrophone. The hydrophone was fixed at the point of 30 mm from the blade tip where cavitation bubbles exist, The peak negative acoustic pressure is an important parameter because it relates to the occurrence of cavitation.

**Figure 4** shows the received sound waveform from the LCS and its frequency analysis result. In **Fig.4 (b)**, we observed 55.5 kHz component which is the driving frequency of this equipment. In **Fig.4 (b)** and **(d)**, a frequency component near 10 kHz can be observed. This frequency component was observed when the cavitation bubbles generate. Then this frequency component and the generation of bubbles are related, but the detailed mechanism of acoustic wave emission is examined. We observed almost same frequency components in ball type blade.

**Figure 5** shows the results of sound pressure measurement. The measured sound pressure is smaller than the sound pressure required for cavitation. It is thought that cavitation bubbles generated locally near the blade, and the bubbles are carried by the flow of the acoustic streaming.

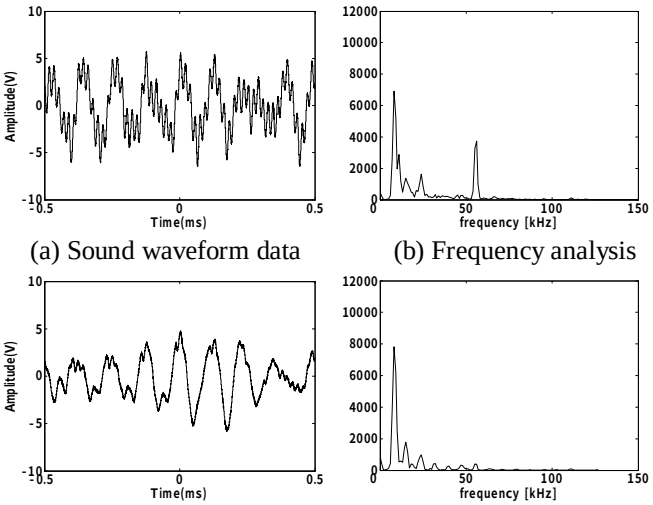


(a) Sound waveform data (b) Frequency analysis

(c) Sound waveform data (d) Frequency analysis

Fig.4 Sound waveform and its spectrum (LCS)

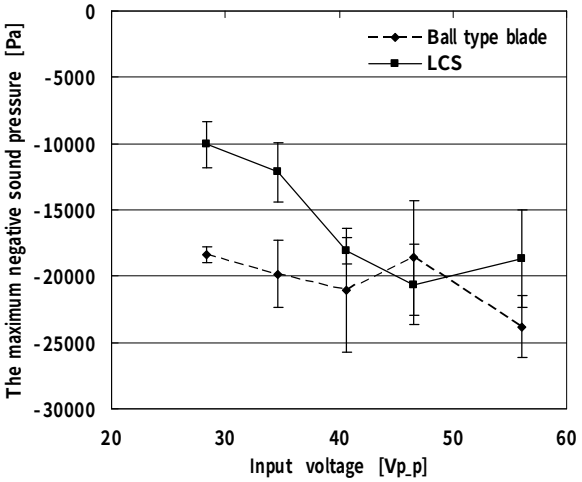


Fig.5 The result of sound pressure measurement

## 6. Conclusion

In this paper, we measure acoustic characteristics of the ultrasonically activated scalpel to estimate the bioeffect. We measured the vibration distribution of the blade of the equipment using laser Doppler vibrometer. We observed the generating bubbles and sound pressure near the blade in the water. Cavitation bubbles generated locally near the blade, and it is thought the collapse of bubbles is also localized near the blade.

## References

1. Satoshi Tamura: Jpn. J. Appl. Phys. **45** (2006) 2842.
2. Steven D. McCarus: Physiologic mechanism of the Ultrasonically Activated Scalpel. The Journal of the American Association of Gynecologic Laparoscopists: Vol. 3, No.4, 601-608, 1996

3P7b-10

Proceedings of Symposium on Ultrasonic Electronics, Vol. 29 (2008) pp. 451-452
11-13 November, 2008

# Development of Area Image Sensing Method for Puncture Needle Type Ultrasonography
# 穿刺型超音波顕微鏡用面走査手法の開発

Masasumi Yoshizawa†, Ryuuji Emoto, Hirotaka Kawabata (Tokyo Metropolitan College of Industrial Technology), Takasuke Irie (Microsonic Co., Ltd.), Kouichi Itoh (Hitachi-Omiya Saiseikai Hospital) and Tadashi Moriya (Professor Emeritus of Tokyo Metropolitan Univ.)
吉澤昌純‡，江本龍二，川畑宏貴（都立産技高専），入江喬介（マイクロソニック（株））， 伊東紘一 （常陸大宮済生会病院），守屋正（首都大名誉教授）

## 1. Introduction

Since the acoustic characteristics of living organisms are known to vary according to their organic composition, minute structural differences, and other factors,[1] an acoustic microscope has been applied to biological tissue characterization. Many imaging methods for acoustic characteristics such as the measurement of the speed of sound or acoustic impedance have been developed for acoustic microscopes. They are useful for intraoperative pathological examination because staining is not required. In particular, since acoustic impedance can be used to visualize a surface without slicing a biological tissue, it may be applied to endoscopic ultrasonography.[2] However, no suggestions for the sensing device and scanning mechanism for endoscopic ultrasonography have been made.

For endoscopic ultrasonograpy to faciliate tissue diagnosis, we are developping the puncture needle-type ultrasonography. Previously, we demonstrated an imaging method for the acoustic impedance difference for puncture needle-type ultrasonography using a thin rod with the focusing end face.[3] However, no suggestions for the scanning mechanism have been made. In this paper, we describe an area image sensing method for the acoustic impedance difference for puncture needle-type ultrasonography using a thin rod.

## 2. Principle

Figure 1 shows the schematic of the equipment for the puncture needle-type ultrasonography. The measurement principle of the method was previously reported.[3] The principle of the proposed scanning method in this case is based on the movements of the end point of the lever as shown in Fig.2. In Fig.2, a thin rod is placed on the fulcrum. When the end point A rotates clockwise forming a circle, the point B moves counter clockwise also forming a circle. By sensing the surface of the sample as a function of the angle ($\theta$), two dimensional scanning can be done.

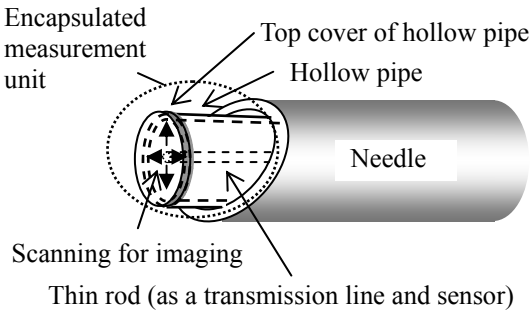


Fig. 1. Basic concept for puncture needle-type ultrasonography.

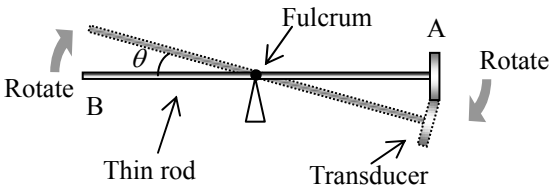


Fig. 2. Basic concept for area image sensing method..

## 3. Experiment and results

Figure 3 shows the schematic diagram of the measurement. In this research, for the first step to conform the method, the thin rod was moved horizontally. Figure 4 shows the measurement system for horizontal scanning. In this experiment, a fused quartz rod with a diameter of 0.84 mm and a length of 74 mm as shown in Fig. 3 was connected to a transducer with a center frequency of 9.0 MHz. The ends of the fused quartz rod were flat polished. A burst wave having an amplitude of 5 V from peak to peak, a center frequency of 8.4 MHz, and a pulse width of 43 cycles was applied. An aluminum plate was used as a sample.

Figure 5 shows the normalized amplitude of the interference signal as a function of distance from center. Those data were obtained by measuring four times in different directions (right

yoshizawa@acp.metro-cit.ac.jp

and left). The phase difference becomes constructive interference condition when the distance from center is 1.9 mm by simple arithmetic. The amplitude envelope of the interference signal has a peak when the length of the distance from the center is approximately 1.9 mm, as expected. This means that the method performs the desired operation.

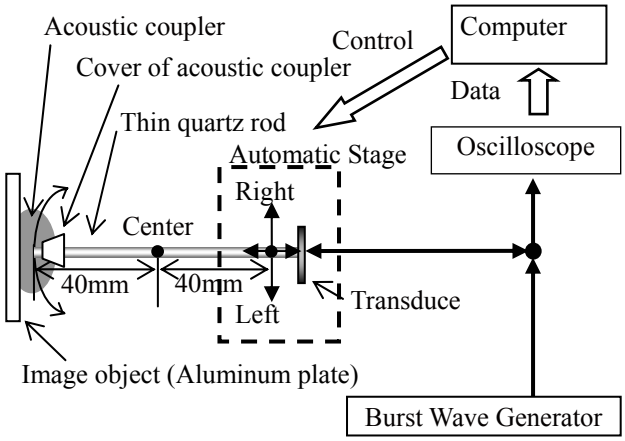


Fig. 3. Schematic diagram of measurement.

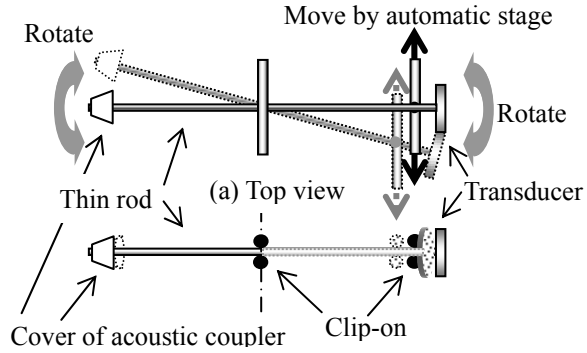


(b) Side view

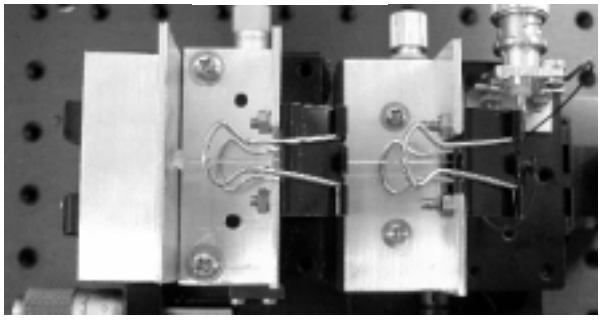

(c) Picture of top view

(d) Picture of side view

Fig. 4. Measurement system for horizontal scanning.

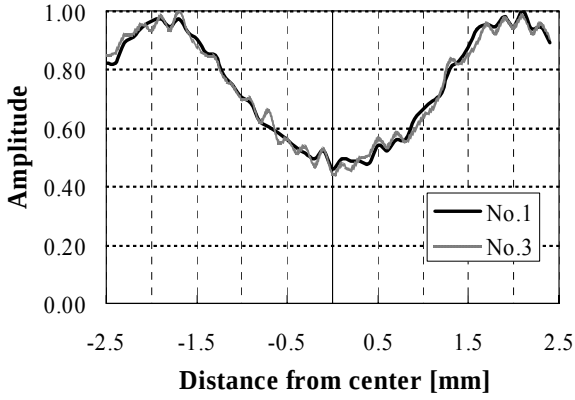


(a) Left direction

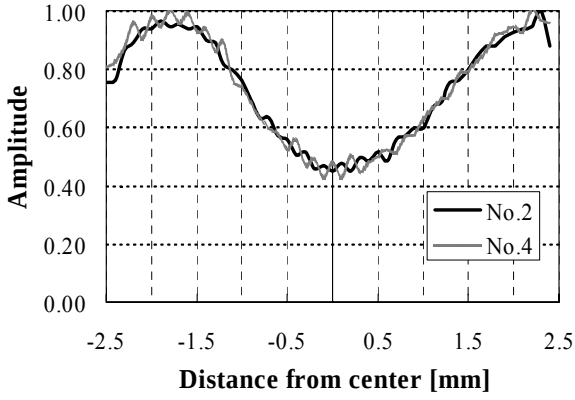


(b) Right direction

Fig. 5. Normalized amplitude of interference signal as a function of distance from center.

## 4. Conclusions

In order to develop an area image sensing method for the acoustic impedance difference for puncture needle-type ultrasonography using a thin rod, we confirmed experimentally that the proposed scanning method can be used for the area image sensing.

## Acknowledgment

This study was partially supported by the Adamant Kogyo Company Limited.

## References

1. R. C. Chivers: Ultrasound Med. Biol. **7** (1981) 1.
2. Y. Saijo, E. S. Filho, H. Sasaki, T. Yambe, M. Tanaka, N. Hozumi, K. Kobayashi, and N. Okada: IEEE Trans. Ultrason. Ferroelectr. Freq. Control **54** (2007) 1571.
3. M. Yoshizawa, T. Irie, K Itoh, and T. Moriya: Jpn. J. Appl. Phys. **47** (2008) 4176.

3P7b-11

Proceedings of Symposium on Ultrasonic Electronics, Vol. 29 (2008) pp. 453-454
11-13 November, 2008

# Inline Transmitter/Receiver System without Direct Receiving of Transmitted Signals

送信信号の直接受信を回避可能なインライン送受信システム

Masayuki Tanabe†, Kan Okubo and Norio Tagawa (Facult. System Design, Tokyo Metropolitan Univ.)
田邉将之‡，大久保寛，田川憲男 （首都大システムデザイン）

## 1. Introduction

It is important to obtain more fine images with high spatial resolution and signal-to-noise ratio (SNR) in ultrasound medical imaging, especially in intravascular ultrasound (IVUS).[1,2] To realize higher spatial resolution, tissue harmonic imaging (THI)[3,4] and the pulse compression technique (PCT)[5] have been introduced. We have continuously examined frequency modulation (FM) chirp PCT from the viewpoint of fundamental study,[6-8] and already proposed an inline transmitter/receiver system for IVUS, which uses both of the THI and the PCT.[9] In this system, a Pb(Zn1/3Nb2/3)O3-PbTiO3 single crystal (PZN-PT) is used as a transmitter, and a polyvinylidene fluoride (PVDF) film placed on the transmission side of the PZN-PT is used as a receiver, and another PVDF film placed on the reverse side of the PZN-PT is used as a refenence. A PZN-PT is suitable for a transmitter because of its transmitting performance, although its bandwidth is narrow[10]. On the other hand, a PVDF is suitable for a receiver since its bandwidth is effectively wide enough to receive harmonic components.[11,12] When a PVDF film in front of the PZN-PT receives a transmitted signal and an echo signal at the same time, by extracting the difference signal between the both signals each of which is received by the each PVDF film, echo signal can only be obtained. In the previous study, we investigated the effectiveness and the feasibility of canceling system. However, in consideration of the practical use of this system, the reference PVDF should avoid receiving echo signal, i.e., it has to receive only tansmitted signal in order to cancel the transmitted signal mixed into the signals received by the reciver PVDF. In this study, we newly propose an inline transmitter/receiver system which has no undesirable echo signals.

## 2. Structure of proposed system

A diagram of the inline transmitter/receiver system with canceling function and the proposed structures to avoid receiving undesirable echo signals are shown in **Fig. 1**. In this system, PVDF films are used as not only a transducer but also a matching layer. PVDC films are used as an insulator in consideration of the actual system.

### 2.1 Type-1

A reflecting mirror is put on the side of the reference PVDF film; it is set at the left side of the PZN-PT as shown in Fig. 1 (b), and can efficiently reflect the transmitted signal passing through the reference PVDF film toward –*y*-direction so as to decrease the undesirable echo signals.

### 2.2 Type-2

A reflecting mirror is put on the side of the receiver PVDF film being at the upper side of the PZN-PT as shown in Fig. 1 (c), and reflects the transmitted toward +*x*-direction and we use echo signals for imaging. This type may lower SNR in imaging against the type-1 because of the reflection efficiency of the mirror, but we can rotate the mirror instead of the transmitter/receiver for rotational IVUS imaging and hence, a slip ring is not required.

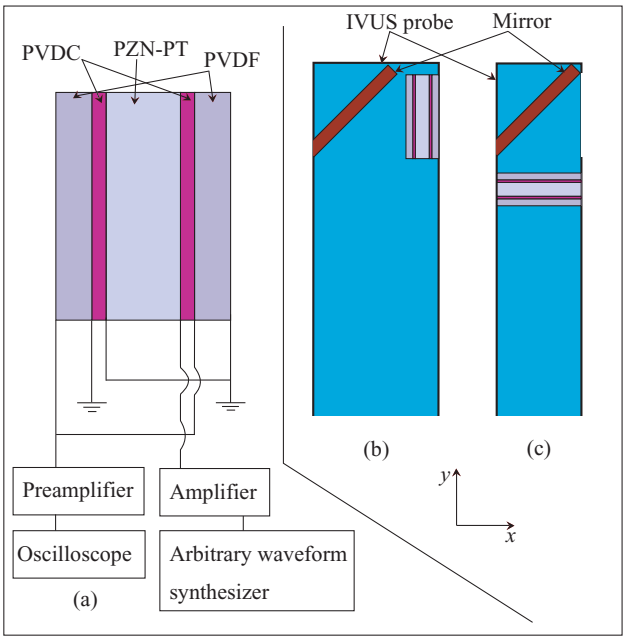


Fig.1 (a) A diagram of inline transmitter/receiver system with canceling function, and proposed structures; (b) type-1 and (c) type-2

---

Email: masatanabe@gmail.com

## 3. Experiments

In this study, PZFLEX, a standard finite element method (FEM) simulator for ultrasound propagation, is used for the 2-dimensional simulations. We examined the received difference voltages between two PVDF films using the proposed two structures. A sine wave, frequency of 20 MHz, duration of $\lambda$, voltage of 40 Vp-p is appiled to the PZN-PT as a transmitted pulse. The thickness of PZN-PT, PVDC and PVDF are 90, 11 and 23.75 μm, respectively. The distance between the target stainless steel and the IVUS probe is 0.5 mm.

## 4. Results and Discussion

**Figure 2** shows the difference voltage between two PVDF films using the type-1 structure with or without a target stainless steel. 28.0 mV*p-p* echo signal from the target stainless steel is obtained, and is sufficiently larger than the echo signal reflected directly from the mirror.

**Figure 3** shows the difference voltage between two PVDF films using the type-2 structure. In this figure, 7.4 mV*p-p* echo signal from the target stainless steel was obtained at approximately 2.2 μs, and 0.73 mV*p-p* echo signal reflected directly from the mirror is obtained from 0.7 μs. The echo signal from the mirror is undesired for imaging, and therefore we will reduce the signal as a future work.

## 5. Conclusion

Through these results, we confirmed the feasibility of two types of proposed system. In near future, we will examine a shape of the reflecting mirror and apply these systems to the PCT and THI.

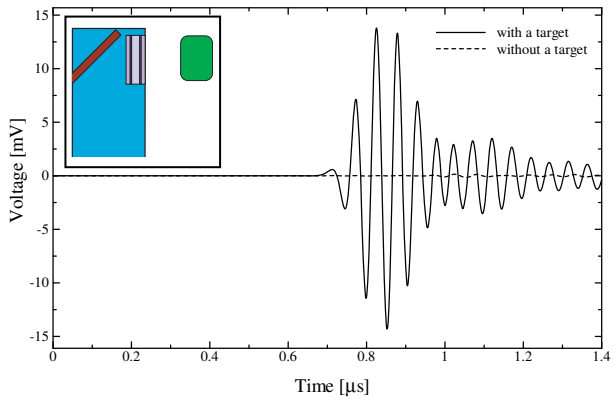


Fig. 2: Difference voltage between two PVDF films using Type-1 structure with a target stainless steel (solid line) and without a target one (broken line)

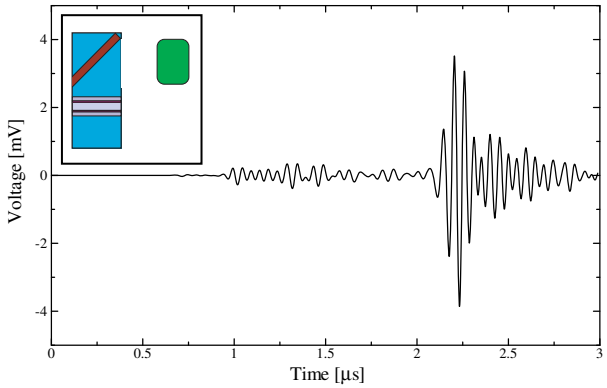


Fig. 3: Difference voltage between two PVDF films using Type-2 structure with a target stainless

## References


1. I. H. Mita, H. Kanai, Y. Koiwa, M. Ichiki, and F. Tezuka: Jpn. J. Appl. Phys. **40** (2001) 4753.
2. Y. Saijo, A. Tanaka, N. Owada, Y. Akino, and S. Nitta: Ultrasonics **42** (2004) 753.
3. F. N. Demirbilek and Y. Yamakoshi: Jpn. J. Appl. Phys. **42** (2003) 342.
4. M. E. Frijlinl, D. E. Goertz, L. C. A. van Damme, R. Krams, and A. F. W. van der Steen: IEEE Trans. Ultrason. Ferroelectr. Freq. Control **53** (2006) 1844.
5. D. Y. Kim, J. C. Lee, S. J. Kwon, and T. K. Song: Proc. IEEE Ultrasonics Symp., 2001, p. 1477.
6. Y. Tonegawa, N. Tagawa, and T. Moriya: Jpn. J. Appl. Phys. **43** (2004) 3076.
7. Z. Hu, T. Moriya, and Y. Tanahashi: Jpn. J. Appl. Phys. **40** (2001) 3896.
8. Z. Hu, N. Tagawa, and T. Moriya: Jpn. J. Appl. Phys. **39** (2000) 3233.
9. M. Tanabe, K, Okubo and N. Tagawa: Jpn. J. Appl. Phys. **47** (2008) 4149.
10. J. Jin, K. K. Rajan, and L. C. Lim: Jpn. J. Appl. Phys. **45** (2006) 8744.
11. T. Tamura, Y. Yoshida, H. Inoue, and K. Murata: Jpn. J. Appl. Phys. **41** (2002) 3295/
12. I. Akiyama, A. Ohya, and S. Saito: Jpn. J. Appl. Phys. **44** (2005) 4631.

3P7b-12

Proceedings of Symposium on Ultrasonic Electronics, Vol. 29 (2008) pp. 455-456
11-13 November, 2008

# Matching Layer Function of PVDF Receiver in Inline Transmitter/Receiver System

インライン送受信システムにおいて受信機として用いるPVDFの整合層機能

Makoto Miyata†, Masayuki Tanabe, Kan Okubo and Norio Tagawa (Facult. System Design, Tokyo Metropolitan Univ.)
宮田誠‡，田邉将之，大久保寛，田川憲男 （首都大システムデザイン）

## 1. Introduction

It is important to obtain high resolution and high signal-to-noise ratio ultrasonic medical images, especially in intravascular ultrasound (IVUS). [1,2] For this purpose, tissue harmonic imaging (THI) [3,4] and the pulse compression technique (PCT) [5] have been appiled for IVUS. In preliminary study, we have proposed an inline transmitter/ receiver system for IVUS which uses THI and the PCT, and confirmed that the each assertion is effective.[6-9] In this system, a $Pb(Zn_{1/3}Nb_{2/3})O_3$-$PbTiO_3$ single crystal (PZN-PT) is used as a transmitter, a polyvinylidene fluoride (PVDF) film placed on the transmission side of the PZN-PT is used as a receiver, and another PVDF film placed on the reverse side of the PZN-PT is used as a reference receiver in order to prevent the transmitted signal mixing with the echo signal. We have examined the PVDF's receiving capacity for harmonic components with various thicknesses of 28, 52, and 110 mm. However, the measurement results are sensitive to the experimental conditions and the fabrication of the transmitter/receiver system; hence, we have obtained no unequivocal conclusion. This study's ojective is to clarify the suitable thickness of the PVDF films in consideration of the total performance for pulse compression imaging through FEM simulations.

## 2. System Structure and Matching Layer

### 2.1 Structure of inline transmitter/receiver system

A diagram of the proposed system is shown in **Fig. 1**. A PVDF film used as a receiver works also as a matching layer. PVDC films are used as an insulator in consideration of the actual inline system. The thicknesses of the PZN-PT and the PVDC are 90 and 11 μm respectively.

### 2.2 Matching layer function of PVDF

The PVDF receiver can be used also as a matching layer between the PZN–PT layer and water, with which the catheter is filled. The acoustic impedance of the matching layer, $Z_m$, placed between two materials whose acoustic impedances are $Z_1$ and $Z_2$ respectively, is formulated as $Z_m = \sqrt{Z_1 \cdot Z_2}$. The acoustic impedance of PZN-PT is 23 Pa･s/m$^3$ and that of water is 1.52 Pa･s/m$^3$. Therefore, the ideal acoustic impedance of the matching layer in this system is approximately 5.91 Pa・s/m$^3$, and a PVDF having an acoustic impedance of 4.02 Pa･s/m$^3$ can be used as a matching layer appropriately. A matching layer should have a thickness of λ/4, in which λ indicates the wavelength in a matching layer. In this study, we transmit an FM chirp signal with a central frequency of 20 MHz, and speed of sound of a PVDF is 2260 m/s. Hence, the wavelength of the central frequency is approximately 113 μm, and the suitable thickness of the PVDF film is 28.25 μm for this matching layer.

## 3. Experiments

In this study, PZFLEX, a standard finite element method (FEM) simulator for ultrasound propagation, is used for the simulations. To evaluate the suitable thickness of the PVDF film for the both functions as a matching layer and a receiver, we

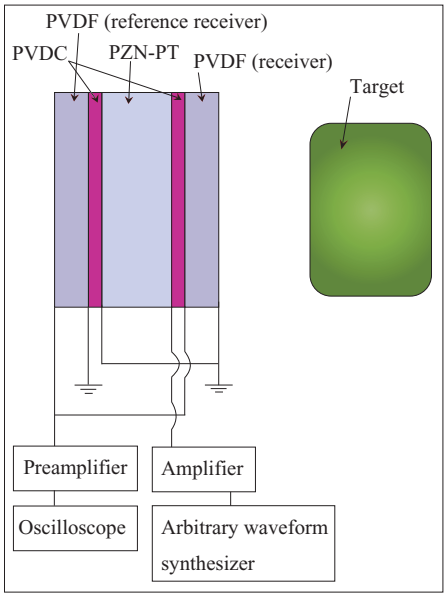


Fig. 1 : Proposed inline transmitter/receiver system.

macoto.miyata@gmail.com

examined the voltage of the echo signals received by the PVDF with varying the thickness of both the PVDF films simultaneously. In these simulations, an FM chirp signal with a central frequency of 20 MHz, a bandwidth of 4 MHz, a pulse width of 5 μsec with the Hamming window, is used as a transmitted pulse. The thickness of the PVDF is varied from 9.5 to 104 μm.

In our inline system, the transmitted signal is expected to be mixed into the received signals. Hence, by connecting the leading wires of both PVDF films shown in Fig. 1, the directly received transmitted signals of both PVDF films are canceled and the desirable echo signal can be extracted. In consideration of the actual usage of this system, in these simulations, we evaluate the echo signals extracted by the above canceling function.

## 4. Results

**Figure 2** shows the results of the voltages of the echo signals with respect to the thickness of the PVDF film. From this figure, it can be confirmed that the theoretically suitable thickness of 28.25 μm is almost the best value. In **Fig. 3**, the received waveforms with some thicknesses around 28.25 μm are shown.

## 5. Conclusions

Through simulations, we confirmed that the thickness of the PVDF film should be selected with respect to the frequency used for imaging, especially for the fundamental imaging. For the harmonic imaging, we will verify the suitable thickness of the PVDF film.

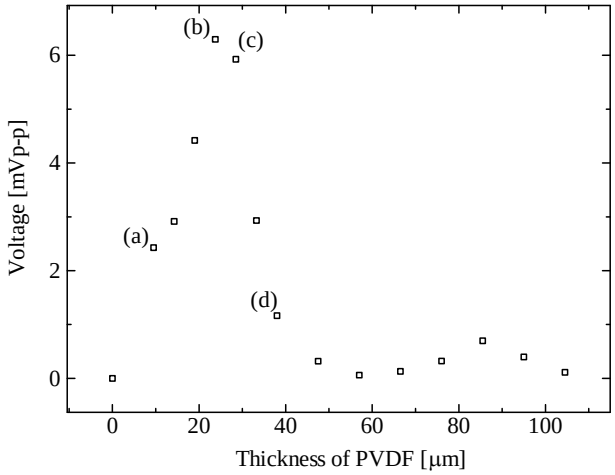


Fig. 2 : Voltages of echo signals received by PVDF film with various thicknesses.

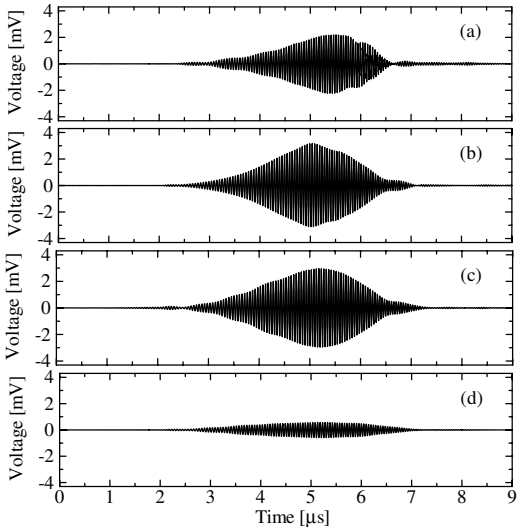


Fig. 3 : Instances of waveforms received by PVDF film with thickness of (a) 19 μm, (b) 23.75 μm, (c) 28 μm and (d) 38 μm respectively.

## References


1) H. Mita, H. Kanai, Y. Koiwa, M. Ichiki, and F. Tezuka: Jpn. J. Appl. Phys. **40** (2001) 4753.
2) Y. Saijo, A. Tanaka, N. Owada, Y. Akino, and S. Nitta: Ultrasonics **42** (2004) 753.
3) F. N. Demirbilek and Y. Yamakoshi: Jpn. J. Appl. Phys. **42** (2003) 342.
4) M. E. Frijlinl, D. E. Goertz, L. C. A. van Damme, R. Krams, and A. F. W. van der Steen: IEEE Trans. Ultrason. Ferroelectr. Freq. Control **53** (2006) 1844.
5) D. Y. Kim, J. C. Lee, S. J. Kwon, and T. K. Song: Proc. IEEE Ultrasonics Symp., 2001, p. 1477.
6) Y. Tonegawa, N. Tagawa, and T. Moriya: Jpn. J. Appl. Phys. **43** (2004) 3076.
7) Z. Hu, T. Moriya, and Y. Tanahashi: Jpn. J. Appl. Phys. **40** (2001) 3896.
8) Z. Hu, N. Tagawa, and T. Moriya: Jpn. J. Appl. Phys. **39** (2000) 3233.
9) M. Tanabe, S. Xie, N. Tagawa, T. Moriya, and Y. Furukawa: Jpn. J. Appl. Phys. **46** (2007) 4805.

3P7b-13

Proceedings of Symposium on Ultrasonic Electronics, Vol. 29 (2008) pp. 457-458
11-13 November, 2008

# Three-dimensional Scatterer-size Estimation in Dissected Human Lymph Nodes Using High-frequency Ultrasound

Jonathan Mamou[‡, a)], Alain Coron [b)], Masaki Hata [c)], Junji Machi [c)], Eugene Yanagihara [c)], Pascal Laugier [b)], and Ernest J. Feleppa [a)]

[a)] F. L. Lizzi Center for Biomedical Eng. Riverside Research Inst., New York, NY, USA
[b)] UPMC Univ Paris 06, UMR 7623, LIP, Paris, F-75005, France, and CNRS, UMR 7623, LIP, Paris, F-75006, France
[c)] University of Hawaii and Kuakini Medical Center, Honolulu, HI, USA

## 1. Introduction

High-frequency (i.e. >15 MHz) ultrasound (HFU) research is attracting considerable interest because the short wavelengths (e.g., 100 μm at 15 MHz) and small focal-zone beam diameters of HFU provide fine-resolution images. Studies have demonstrated the unique ability of HFU systems to image shallow or low-attenuation tissues for biomedical applications. For example, HFU already has been successful for small-animal [1], ocular [2], intravascular [3], and dermatological imaging [4].

Most human lymph nodes have sizes ranging from 2 to 8 mm in diameter, although sometimes larger sizes are encountered, e.g., in the case of node-filling metastatic cancers. Therefore, lymph nodes typically are small enough to be imaged using HFU.

Quantitative ultrasound (QUS) is being investigated by several research groups, and many tissue parameters have been estimated. This study focuses on QUS methods to estimate scatterer size from the spectrum of the radio-frequency (RF) echo signals. This method is derived from the theoretical framework of ultrasound scattering established by Lizzi et al. [5] for biological tissues and subsequently expanded by him and others [6]. Using frequency-dependent information derived from RF backscattered signals allows quantitatively assessing tissue micro-structural properties and relating them to histological properties. Our hypothesis is that scatterer-size estimates may help to differentiate between cancer-containing nodes and cancer-free nodes.

## 2. Methods

Lymph nodes were dissected from patients with histologically proven primary cancers (e.g., breast, colorectal, and gastric cancers) at the Kuakini Medical Center (KMC) in Honolulu, HI. De-identified patient information was coded and sent to Riverside Research Institute (RRI) in New York, NY. Pathologists at KMC provided RRI with a tracing of the boundary of each cancerous region in every histological section for each node.

After excision by the surgeon, dissected nodes were brought to the pathologist for gross preparation. Then, individual, manually defatted, fresh lymph nodes were placed in a water bath containing isotonic saline (0.9% sodium chloride) at room temperature and scanned individually. Ultrasound data were acquired with a focused, single-element, transducer (PI30-2-R0.50IN, Olympus NDT, Waltham, MA) with an aperture of 6.35 mm and a focal length of 12.7 mm. The transducer had a center frequency of 25.6 MHz and a minus-6-dB bandwidth that extended from 16.4 to 33.6 MHz. The transducer was excited by a Panametrics 5900 pulser/receiver unit. The RF echo signals were digitized at 400 MHz. The spacing between adjacent A-lines was 25 μm. A 3D scan of each lymph node was obtained by scanning adjacent planes every 25 μm to uniformly cover the entire lymph node.

After 3D ultrasound scanning was completed, a 3D segmentation algorithm was used to detect the boundaries of the residual fat layer and of the actual lymph-node tissue.

Following 3D segmentation, scatterer-size estimates were computed using 3D cylindrical regions of interest (ROIs) of 1-mm diameter and 1-mm length. Scatterer sizes were only estimated when the ROI was entirely in the tissue region found by the 3D segmentation algorithm. Each individual RF-segment spectrum within the ROI was compensated for attenuation. The spectra of each RF segment within one ROI were averaged and log compressed. A calibration spectrum was obtained from a planar reflector and subtracted from the ROI spectrum to obtain a normalized spectrum. The normalized spectrum was fit to a Gaussian scattering model [6], and the fit parameters were inverted to obtain scatterer-size estimates. The optimization bandwidth was varied for each ROI based on a local SNR estimator. The optimization bandwidth for ROIs having

satisfactory SNR was chosen larger than that used for ROIs having less satisfactory SNR. Using the largest optimization bandwidth possible is advantageous because theory predicts that the standard deviation of the scatterer-size estimates is inversely proportional to the optimization bandwidth.

Adjacent ROIs overlapped by 90% in 3D. Scatterer-size estimates were color-coded and overlaid over conventional B-mode images for display. The scatterer-size parametric images had a voxel size of 0.1 x 0.1 x 0.1 mm because of the 90% overlap.

## 3. Results

The results presented here pertain to the illustrative case of a 64-year-old male patient who was diagnosed with stage-3 colon cancer. Four lymph nodes were obtained from this patient during colon-cancer surgery. Three of the dissected nodes were determined to be negative for metastatic cancer and the fourth node was determined to be positive. **Figure 1** shows cross-sections through the 3D ultrasound volume of one of the negative nodes augmented by the color-coded scatterer-size estimates and the segmentation results. The segmented fat region and lymph-node tissue regions are inside a red and green boundary, respectively. For this lymph node, the scatterer-size estimates had an average of 21.5 μm and a standard deviation of 4.19 μm.

## 4. Conclusions

The methods proposed herein currently are being used on many (>100) human lymph-node acquisitions. Our expectation is that because scatterer-size estimates describe microstructure within the tissue, clinically useful differences should exist between estimates for metastatic and non-metastatic regions of lymph nodes.


## Acknowledgment

This work was supported by NIH grant CA100183.


## References


1. D. H. Turnbull: Methods Mol. Biol. **135** (2000) 235.
2. R. H. Silverman, J. A. Ketterling, J. Mamou and D. J. Coleman: Arch Ophthalmol. **126** (2008) 94
3. Y. Saijo, A. Tanaka, N. Owada, Y. Akino, and S. Nitta: Ultrasonics. **42** (2004) 753
4. M. Vogt M and H. Ermert: IEEE Trans. Ultrason. Ferroelectr. Freq. Control. **54** (2007) 1551
5. F. L. Lizzi, M. Greenebaum, E. J. Feleppa, M. Elbaum and D. J. Coleman: J. Acoust. Soc. Am. **73** (1983) 1366
6. M. L. Oelze, J. F. Zachary, and W. D. O'Brien, Jr.: J. Acoust. Soc. Am. **112** (2002) 1202


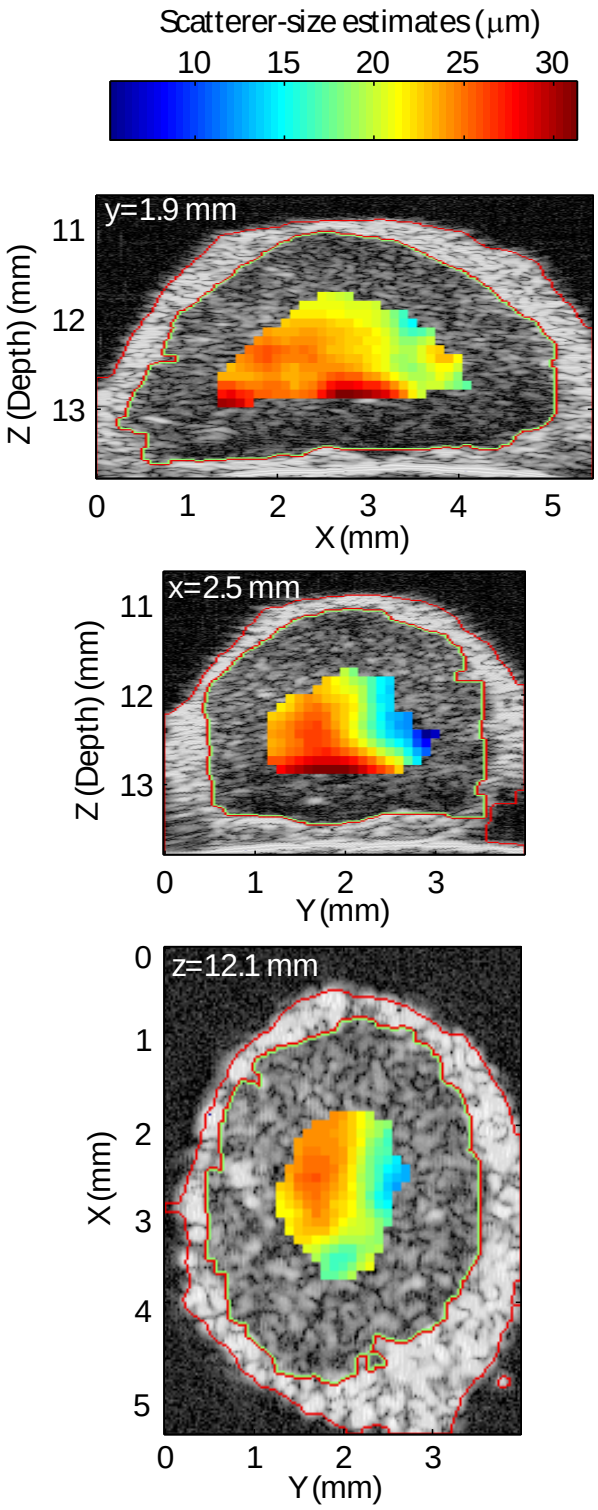


Fig. 1 Cross-section through a lymph-node processed with a 3D segmentation algorithm and a scatterer-size estimation routine. Segmentation results are visible as the green and red boundaries surrounding fat and lymph-node tissue, respectively. Scatterer-size information was color-coded and overlaid over the conventional B-mode cross-sections.

3P7b-14

Proceedings of Symposium on Ultrasonic Electronics, Vol. 29 (2008) pp. 459-460
11-13 November, 2008

# Frequency dependence of ultrasonic properties of bovine cortical bone samples

Guillaume Haïat[†1], Magali Sasso[2], Salah Naili[2] and Mami Matsukawa[3]
[1] CNRS, Université Paris 7, Laboratoire de Recherches Orthopédiques, UMR CNRS 7052 B2OA, 10 avenue de Verdun, 75010 Paris, France, [2] Laboratoire de Biomécanique et Biomatériaux Osteo-Articulaires, UMR CNRS 7052 – Université Paris 12, Créteil, France.[3]: Laboratory of Ultrasonic Electronics, Doshisha University, Kyotanabe, Kyoto-fu 610-0321, Japan

## 1. Introduction

Quantitative ultrasound (QUS) techniques are used for bone assessment and estimation of fracture. Cortical bone makes up for the compact part of bone, mainly found in the shaft of long bones and in the envelope of short bones.

The development of axial transmission techniques enables the assessment of cortical bone. Cortical bone is determinant in bone fragility since it supports most of the load of the body, represents 80% of the skeleton mass and is primarily involved in most of osteoporotic fractures. However, ultrasonic propagation in cortical bone is intricate and the mechanisms involved in wave propagation are still poorly understood. The main parameter of interest in axial transmission is speed of sound (SOS). Cortical bone is a dispersive media and only few studies have focused on the understanding of wave attenuation and velocity dispersion in cortical bone.

The objective of the present work is to demonstrate the feasibility of Broadband Ultrasonic Attenuation (BUA) and velocity dispersion measurements in bovine cortical bone and to appraise its dependence on bone mass, microstructure and anatomical location.

## 2. Material and methods

Three left femurs of 36-months old cows were used in the present study. Parallelepipedic samples (4~11mm side) were cut all along the bone axis and circumference. First, the femur was cut into 5 rings. Then, from each ring, 8 samples were taken in the anterior, posterior, medial, lateral and in the four oblique parts of the bone. Bone Mineral Density (BMD) was measured by dual X-ray absorptiometry (QRD-1000, Hologic) in the axial direction. Cortical bone microstructure was assessed using optical microscopy images of bone sections cut from the top axial surface of each sample. Samples were manually classified into 4 microstructures: plexiform (Pl), Haversian (H), porotic (Po) mixed (M) microstructures (made of combined microstructures) [1, 2].

The plexiform microstructure is made of lamellae having the vascular plexus sandwiched within. Lamellae have a 100~200 µm thickness. Haversian microstructure is made of osteons which are aligned in the axial direction. Osteons diameter is 150~300 µm. Porotic microstructure can be found at parts were muscles adhere and has the largest pores size comprised between 50 and 300 µm.

Bone samples were assessed in a normal saline solution (NSS) stabilized at 25±0.1°C. A pair of 8 mm diameter self-made broadband polyvinylidene (PVDF) transducers was used. Each sample was evaluated 4 times with repositioning in the axial, radial and tangential directions.

BUA and dispersion were evaluated from ultrasonic measurements using a substitution method. We used a single sinusoidal pulse for the excitation of transducer. It enables the BUA and dispersion measurements. The frequency dependent attenuation coefficient and phase velocity are derived from the ratio of the spectrum of the signal transmitted through bone and through NSS by correcting from transmission and diffraction effects [3]. BUA (respectively dispersion) is defined as the slope of the frequency dependent attenuation (respectively phase velocity) and is evaluated on a 1 MHz-wide frequency range centred around 4 MHz.

## 3. Results and discussion

On the 1 MHz restricted bandwidth, the attenuation coefficient and phase velocity are quasi linear with frequency, which shows the feasibility of BUA and dispersion measurements.

The value of the averaged standardized coefficient of variation is equal 11.4% for BUA measurements and the value of the averaged coefficient of variation is equal 1 m/s/MHz for dispersion measurements.

ANOVA analysis revealed a significant directional effect for BUA ($p<0.002$) but not for dispersion measurements. Significant anatomical effects were found for BUA ($p<0.005$) and dispersion ($p<0.05$) measurements. BUA values in the three directions are significantly positively correlated to BMD ($R^2 = 0.44$, $p<10^{-5}$ in the axial direction) but when considering plexiform microstructure only, no correlation is found between BUA and BMD.

Velocity Dispersion values in the three directions are significantly positively correlated to BMD ($R^2 = 0.4$, $p<10^{-5}$ in the axial direction).

---

†: guillaume.haiat@univ-paris-diderot.fr

Interestingly, negative values of velocity dispersion were found for 9 sample and directions for the first time, mostly in the tangential direction and for mixed microstructure. Negative values might be explained by interferences of two pulses propagating at different wave speed in the mixed microstructure, leading to a “mixed mode” configuration [4].

Figure 1 shows the relationship between BUA and dispersion measurements for the different directions. The solid line shows the results predicted using the Kramers-Kronig relationship [5, 6] which predict a slope of the dispersion as a function of BUA higher than what is observed experimentally. These discrepancies may be due the limited bandwidth [7] and to the interference effects described above.

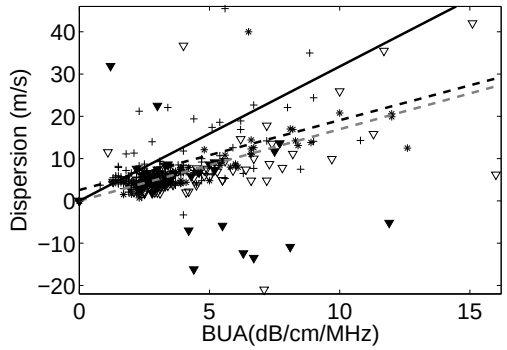


Fig. 1 Dispersion *vs* BUA values in the range from 3.5 to 4.5 MHz for all directions. Crosses (respectively stars) correspond to the axial (resp. radial) direction. Full triangles correspond to samples of mixed microstructure in the tangential direction and hollow triangles correspond to other sample in the tangential direction. The full line shows results obtained using the Kramers-Kronig relationship.

The present study is the first extensive study of BUA and dispersion around 4 MHz in cortical bone. The results obtained in this study compares well with results found in the literature in terms of BUA [8-11] [12] and dispersion [8] [10], although much less samples were considered in these previous studies.

The dependence of BUA on the direction may be due to scattering effect, because osteons and lamellae are oriented in the axial direction. The transmitted wave crosses fewer pores when it propagates in the axial direction and is therefore less attenuated. In addition, BUA values obtained for each kind of microstructure are similar to the repartition of pores size in each microstructure (8~12$\mu$m in plexiform, 20~50$\mu$m in Haversian and 50~300$\mu$m in porotic) which may determine the scattering regime.

Visco-elasticity may also contribute to attenuation in cortical bone. Interstitial tissue between osteons and lamellae is known to have a visco-elastic behavior (see for instance [13]). Interstitial tissue is more prominent in Haversian than in plexiform microstructure which may also contribute to higher BUA in Haversian microstructure. In the future, more interest should be placed in assessing the effect of hydroxyapatite crystallite orientation on BUA and dispersion, as it was done recently for velocity measurements [14]

These promising results show that BUA and dispersion might be complementary parameters to investigate cortical bone quality with axial transmission devices. More details on this work can be found in [15-17].

**Acknowledgment**

Part of this study was supported by the Academic Frontier Research Project on "New frontier of Biomedical engineering Research" of Doshisha University. Mami Matsukawa would like to thank the Bilateral joint projects supported by JSPS and CNRS. . Magali Sasso would like to thank the University Paris 12 -Val de Marne (‘‘Conseil Scientifique’’) for support during her stay at the Laboratory of Ultrasonic Electronics, Doshisha University, Japan.

**References**

[1] Y. Yamato, H. Kataoka, M. Matsukawa, K. Yamazaki, T. Otani, and A. Nagano, Japanese Journal of Applied Physics **44** (2005), 4622.

[2] Y. Yamato, M. Matsukawa, T. Otani, K. Yamazaki, and A. Nagano, Ultrasonics **44** (2006), 233.

[3] P. Droin, G. Berger, and P. Laugier, IEEE Transactions on Ultrasonics, Ferroelectrics, and Frequency Control **45** (1998), 581.

[4] K. R. Marutyan, M. R. Holland, and J. G. Miller, J Acoust Soc Am. **120** (2006), EL55.

[5] M. O'Donnell, E. T. Jaynes, and J. G. Miller, J Acoust Soc Am **63** (1978), 1935.

[6] M. O'Donnell, E. T. Jaynes, and J. G. Miller, J Acoust Soc Am **69** (1981), 696.

[7] K. R. Waters, M. S. Hughes, G. H. Brandeburger, and J. G. Miller, J. Acoust. Soc. Am. **108** (2000), 556.

[8] R. S. Lakes, H. S. Yoon, and J. L. Katz, Journal of Biomedical Engineering **8** (1986), 143.

[9] C. M. Langton, A. V. Ali, C. M. Riggs, J. A. Evans, and W. Bonfield, Clinical Physics and Physiological Measurement **11** (1990), 243.

[10] S. Lees and D. Z. Klopholz, Ultrasound in Medicine and Biology **18** (1992), 303.

[11] S. Han, J. Rho, J. Medige, and I. Ziv, Osteoporosis International **6** (1996), 291.

[12] L. Serpe and J. Rho, Journal of Biomechanics **29** (1996), 963.

[13] R. S. Lakes and J. L. Katz, J Biomech **12** (1979), 679.

[14] Y. Yamato, M. Matsukawa, T. Yanagitani, K. Yamazaki, H. Mizukawa, and A. Nagano, Calcif Tissue Int. **82** (2008), 162.

[15] M. Sasso, G. Haïat, Y. Yamato, S. Naili, and M. Matsukawa, in press, Ultrasound Med Biol (2007).

[16] M. Sasso, G. Haïat, Y. Yamato, S. Naili, and M. Matsukawa, J Biomech **41** (2008), 347.

[17] G. Haiat, M. Sasso, S. Naili, and M. Matsukawa, J Acoust Soc Am. (in press).

3P7b-15

Proceedings of Symposium on Ultrasonic Electronics, Vol. 29 (2008) pp. 461-462
11-13 November, 2008

# Influence of multiple scattering and of absorption on velocity dispersion in trabecular bone

Guillaume Haïat[†1], Alain Lhémery[2], Frédéric Padilla[3], Pascal Laugier[3] and Salah Naili[4]
[1] CNRS, Université Paris 7, Laboratoire de Recherches Orthopédiques, UMR CNRS 7052 B2OA, 75010 Paris, France, [2] Commissariat à l'énergie Atomique, LIST, Gif-sur-Yvette, France.
[3]: CNRS, Université Paris 6, Laboratoire d'Imagerie Paramétrique, UMR 7623 15, rue de l'école de Médecine 75006 Paris [4] Laboratoire de Biomécanique et Biomatériaux Osteo-Articulaires, UMR CNRS 7052 – Université Paris 12, Créteil, France.

## 1. Introduction

Quantitative ultrasonic (QUS) techniques are now widely used clinically for the diagnostics of osteoporosis. In particular, Speed of Sound (SOS) measurements are highly correlated with bone mineral density and bone strength for bovine and human specimens. Most of the anatomical sites assessed with QUS techniques are composed of trabecular bone, which consists in an anisotropic, heterogeneous and two phase medium made of a network of interconnected elastic rods or plates (the trabeculae) filled with a viscous fluid-like medium (the marrow). Despite their routine clinical use, the physics of ultrasonic propagation through trabecular bone and the mechanisms responsible for the variation of the ultrasonic velocity with bone properties still remain unclear.

Of particular interest is the question of velocity dispersion. Unlike most soft tissues in which the phase velocity has been shown to be an increasing function of frequency, negative values of the velocity dispersion have been measured in trabecular bone [1-6] and remain poorly explained physically.

In the past, numerous aspects of ultrasonic bone characterization have been investigated and several theoretical models have been applied to the ultrasonic propagation through cancellous bone including Biot or Schoenberg. Some models considering the scattering of the ultrasonic wave on the trabeculae modeled as infinite cylinders have been developed assuming independent [7] as well as multiple scattering [8, 9].

Such approaches led to the prediction of negative and positive values of the velocity dispersion according to the microstructure, but the physical determinants of velocity dispersion could not be estimated. Moreover, a recent work by Marutyan et al. [10] shows that negative value of the dispersion in trabecular bone can arise from interference between fast and slow longitudinal wave modes as predicted by the Biot theory. However, the Biot theory presents several shortcomings in that it requires a large number of parameters (tortuosity, permeability, viscous characteristic length, power index, etc.) that are not known with accuracy.

Negative velocity dispersion has been previously predicted by multiple scattering theories to model composite material [11]. However, it has not been used so far in order to predict and understand such phenomena in trabecular bone. The aim of this paper is to propose a model predicting the frequency dependence of the phase velocity as well as their physical determinants by considering a simple biphasic description of trabecular bone, where the trabeculae are assumed to be identical and parallel and by taking into account multiple scattering phenomena. Therefore, a 2D homogenization model accounting for the coupling of absorption and multiple scattering effects is employed to calculate the dependence of phase velocity on frequency and bone properties.

## 2. Theory

The problem of multiple scattering of waves by a set of scatterers is a classical problem of theoretical physics, initially solved in the 1940's [12]. Some of these theories were developed in order to describe a two-phase material composed of oriented fibers in a matrix. Among these theories, the quite recent one developed by Yang and Mal [13] known as the generalized self-consistent method relies on the description of the heterogeneous medium as being constituted of three cylindrical phases. This three-phase description is combined with the classical multiple-scattering theory originally derived by Waterman and Truell [14] for spherical scatterers and then modified to account for the cylindrical symmetry. The idea of a three-phase modelling approach is to describe the homogeneous effective medium by considering three concentric cylinders.

In this paper, the model developed by Yang and Mal [13] is adapted in order to model trabecular bone as a two-phase medium composed of randomly distributed elastic infinite cylinders corresponding to the trabeculae saturated with water (for *in vitro* experiments) and to bone marrow (for *in vivo* experiments).

Here, the axes of all scatterers are assumed to be perpendicular to the plane of incidence of the

[†]: guillaume.haiat@univ-paris-diderot.fr

ultrasonic wave, this situation corresponding to a 2D model.

Bone material properties were taken from the literature. We have included in our model absorption phenomena, which was not done in the original model. The attenuation coefficient at 600 kHz in bone and marrow was also taken from the literature [15]. The frequency dependence of phase velocity for each medium was obtained by applying the local Kramers-Kronig relationships [16].

The surrounding medium is an artificial synthetic medium that represents the overall effective homogeneous elastic medium to be determined. Radius $a$ is that of the scatterer and radius $b$ is related to the average free path of scattered waves in water and depends on bone volume fraction ($BV/TV$) and on $a$ through:

$$b = \frac{a}{\sqrt{BV/TV}} \qquad \text{Eq. (1)}$$

Moreover, the density $\rho_e$ of the effective medium is a simple function of $BV/TV$ and is given by:

$$\rho_e = BV/TV\ \rho_w + (1\text{-}BV/TV)\ \rho_t. \qquad \text{Eq. (2)}$$

The computation of phase velocity is performed for 10 values of $f$ between 400 and 800 kHz. The value of the velocity dispersion is then obtained through a least square regression analysis of the phase velocity as a function of the frequency.

## 3. Results and discussion

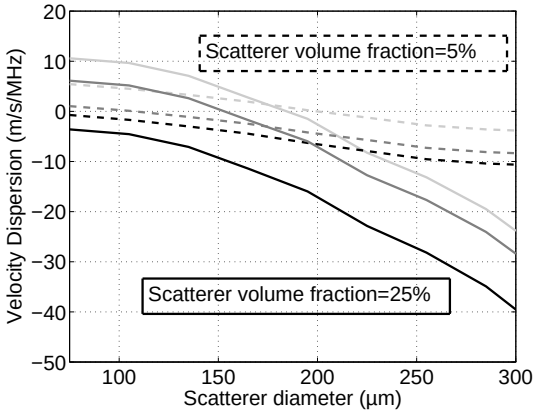


Fig. 1 Simulated velocity dispersion around 600 kHz as a function of BV/TV. The solid and dashed lines correspond respectively to results obtained with a scatterer diameter of 300 and 75 µm. Black lines correspond to results obtained by neglecting all viscoelastic effects; dark grey (respectively ligth grey) lines correspond results obtained by considering viscoelastic effects in the scatterer only (respectively in the scatterer and in the matrix).

In order to test and validate the model on a simple configuration corresponding to the 2D approximation of our model, the results were successfully compared with the experimental results obtained by Wear in [17] with trabecular bone-mimicking phantoms [18] (data not shown)..

Figure 1 shows the variation of dispersion as a function of BV/TV for relatively thin and thick scatterer diameters. The order of magnitude of velocity dispersion values spans within the range obtained experimentally [5]. When considering no absorption, the velocity dispersion is always negative. However, when absorption is accounted for in the trabeculae (dark grey lines), an increase of dispersion depending on BV/TV is found. Moreover, taking into account absorption in the marrow (light grey lines) leads to an increase of dispersion, which is independent of BV/TV. Velocity dispersion is a decreasing function of the scatterer diameter due to the increase of the scattering cross section. When absorption is taken into account, weak (respectively high) scatterer diameters lead to positive (respectively negative) dispersion values. Most experimental values of dispersion are negative, which seems to indicate that the contribution of scattering phenomena would be more important than that of viscous absorption. More details on this work can be found in Ref. [18].

**References**


[1] K. A. Wear, IEEE Trans. Ultrason. Ferroelect. Freq. Contr. **48** (2001), 1079.

[2] R. Strelitzki and J. A. Evans, Eur. J. Ultrasound **4** (1996), 205.

[3] P. H. F. Nicholson, G. Lowet, C. M. Langton, J. Dequeker, and G. Van der Perre, Phys Med Biol **41** (1996), 2421.

[4] K. Wear, Ultrasound. Med. Biol. **26** (2000), 641.

[5] P. Droin, G. Berger, and P. Laugier, IEEE Trans. Ultrason. Ferroelec. Freq. Contr. **45** (1998), 581.

[6] G. Haiat, F. Padilla, R. O. Cleveland, and P. Laugier, IEEE Trans. Ultrason. Ferroelec. Freq. Contr. **53** (2006), 39.

[7] K. A. Wear, J. Acoust. Soc. Am. **115** (2004), 66.

[8] F. Luppé, J. M. Conoir, and H. Franklin, J. Acoust. Soc. Am. **111** (2002), 2573.

[9] F. Luppé, J. M. Conoir, and H. Franklin, J. Acoust. Soc. Am. **113** (2003), 2889.

[10] K. R. Marutyan, M. R. Holland, and J. G. Miller, J. Acoust. Soc. Am. **120** (2006), EL55.

[11] V. K. Varadan, Y. Ma, and V. V. Varadan, J. Acoust. Soc. Am. **80** (1986), 333.

[12] L. L. Foldy, Phys Rev **67** (1945), 1415.

[13] R. B. Yang and A. K. Mal, J. Mech. Phys. Solids **42** (1994), 1945.

[14] P. C. Waterman and R. Truell, J. Math. Phys. **2** (1961), 512.

[15] S. A. Goss, R. L. Johnston, and F. Dunn, J. Acoust. Soc Am. **64** (1978), 423.

[16] M. O'Donnell, E. T. Jaynes, and J. G. Miller, J. Acoust. Soc. Am. **69** (1981), 696.

[17] K. A. Wear, J. Acoust. Soc. Am. **118** (2005), 1186.

[18] G. Haiat, A. Lhémery, F. Renaud, F. Padilla, P. Laugier, and S. Naili, J Acoust Soc Am (in revision).

3P7b-16

Proceedings of Symposium on Ultrasonic Electronics, Vol. 29 (2008) pp. 463-464
11-13 November, 2008

# Estimation of *in vivo* cancellous bone elasticity

*in vivo* 海綿骨弾性定数の評価

Takahiko Otani[1†], Isao Mano[2], Toshiyuki Tsujimoto[3], Tadahito Yamamoto[4], Ryota Teshima[4], and Hiroshi Naka[5] ([1]Facult. Sci. Eng., Doshisha Univ.; [2]OYO Electric Co., Ltd.; [3]Horiba, Ltd.; [4]Facult. Med., Tottori Univ.; [5]Facult. Med., Osaka City Univ.)

大谷隆彦[1‡], 真野功[2], 辻本敏行[3], 山本真人[4], 豊島良太[4], 中弘志[5] ([1]同志社大 理工; [2]応用電機㈱; [3]㈱堀場製作所; [4]鳥取大 医; [5]大阪市立大 医)

## 1. Introduction

The primary purpose of measuring bone status is to assess fracture risk in medical examination. However, mechanical or breaking strength is obtained only by the destructive testing. The destructive testing is not appropriate for medical assessment or medical diagnosis. It is generally agreed that Bone Mineral Density (BMD) or bone mass density is a good predictor of fracture risk. The effect of decreasing bone density (a symptom of osteoporosis) is greater for cancellous bone than for dense cortical bone, because cancellous bone is metabolically more active. Accordingly, bone density is assessed or measured at a site with a high volume fraction of cancellous bone to estimate the onset of osteoporosis. For the purpose of assessment of bone status or bone quality in a sense of mechanical strength, it is better to add a mechanical parameter concerning bone quality to the bone density. Mechanical parameters relating to mechanical strength, ultimate strength, yield strength, and elastic limit, are not obtainable by nondestructive way. The only obtainable parameter by nondestructive way is elasticity. Estimation of *in vivo* cancellous bone elasticity and the dependence of elasticity on bone density is discussed.

## 2. Methods

In the cancellous bone, two longitudinal waves, the fast and slow waves, propagate along a trabecular orientation. The propagation speed of fast wave increases with mass density of cancellous bone and the amplitudes of fast and slow waves transmitted through cancellous bone depend considerably and differently on the mass density[1-2]. In our previous studies, the propagation process for an ultrasonic wave through *in vivo* measurement site containing cancellous bone was formulated for both fast and slow waves[3] and a new ultrasonic bone densitometer, prototype LD-100, has been developed to assess the bone status by measuring mass density [mg/cm$^3$] and elasticity [GPa] of cancellous bone on the basis of the fast and slow waves[4]. Prototype LD-100 has been aimed to have a function comparative to that of peripheral quantitative computed tomography (pQCT, a microfocus X-ray system), and measurement site is set at the same site of pQCT, at the distal end of radius, to realize a direct comparison of measured cancellous bone density between the ultrasonic and radiological methods in the same unit [mg/cm$^3$]. Bone mineral density or bone mass density of cancellous bone was evaluated by the attenuation of transmitted slow wave and elasticity of cancellous bone was evaluated by the propagation speed of fast wave and the bone mass density. 175 volunteers from 22 to 87 years old (average age 59.0 years old). They consisted of 54 men (average age 57.9 years old) and 121 women (average age 59.5 years old). After obtained informed consent, all measurements were carried out.

totani@oyoe.jp

## 3. Results and discussion

Each subject was measured by ultrasonic method, prototype LD-100 and also by radiological method, pQCT (Stratec XCT-960). Cancellous bone densities measured by slow wave attenuation are shown in **Fig.1**. Measured densities are expressed in bone mineral density. Measured propagation speeds of fast wave in cancellous bone are shown in **Fig.2** as a function of bone volume fraction $V_f$. According to measured results in Fig.2, the fast wave speed is approximately expressed by a linear equation, except in the vicinity of $V_f = 0$, as

$$c_4 = m\rho_4 + n = m\left(\rho_{bt} V_f\right) + n \quad (1)$$

where $c_4$ : propagation speed of fast wave
$\rho_4$ : apparent mass density
$\rho_{bt}$ : material density of bone tissue (trabecular bone tissue)
$V_f$ : bone volume fraction (BV/TV)

Since the fast wave propagates in trabecular structure of cancellous bone, the elasticity for

longitudinal wave is evaluated by the fast wave speed and the apparent mass density of cancellous bone. Elasticity $E_4$ of trabecular structure is expressed by

$$E_4 = \rho_4 \, c_4^{\,2} \qquad (2)$$
$$= \alpha \, \rho_4^{\,3} + \beta \, \rho_4^{\,2} + \gamma \, \rho_4$$

Cancellous bone is comprised of a trabecular network with soft tissue (bone marrow) in the pore spaces. If the cancellous bone density decreases to zero, the elasticity of cancellous bone (with bone marrow *in situ*) should approach to the elasticity of bone marrow (2.0GPa). Thus, the elasticity $E_c$ of cancellous bone with bone marrow *in situ* is expressed by the sum of the elasticity of trabecular structure and bone marrow as

$$E_c = \left(\rho_{bt} V_f\right) c_4^{\,2} + E_{bm}\left(1 - V_f\right) \qquad (3)$$
$$= \rho_4 \, c_4^{\,2} + E_{bm}\left(1 - V_f\right)$$

where $E_{\mathrm{bm}}$ : elasticity of bone marrow

Estimated elasticities of cancellous bone of subjects are shown in **Fig.3**. Estimated relation given by eq.(3) is also represented in the figure.

*Remarks and summery*

1) The bone density and the elasticity of cancellous bone are evaluated on the basis of clear causality concerning fast and slow waves.
2) Measured values
   (a) Bone mass density (or bone mineral density) in [mg/cm$^3$] and bone volume fraction (BV/TV) in [%], which is compatible with measured value in [mg/cm$^3$] obtained by the X-ray CT system.
   (b) Elasticity of cancellous bone in [GPa].
   Measured *in vivo* elasticities : 2.2-5.4GPa
   average 2.9GPa
   lowest 2.1GPa (BV/TV = 5%)
   (water 2.2GPa)
   (bone marrow 2.0GPa)
3) Elasticity of cancellous bone is approximately expressed by a third degree function of bone density. In case bone density decreases to zero, elasticity of cancellous bone with bone marrow *in situ* approaches to that of bone marrow.

**References**


1. A. Hosokawa and T. Otani : J. Acoust. Soc. Am. **101** (1997) 558.
2. A. Hosokawa and T. Otani : J. Acoust. Soc. Am. **103** (1998) 2718.
3. T. Otani,: Jpn. J. Appl. Phys. **44**, (2005) 4578.
4. I. Mano, K. Horii, S. Takai, T. Suzaki, H. Nagaoka and T. Otani,: Jpn. J. Appl. Phys. **45**, (2006) 4700.


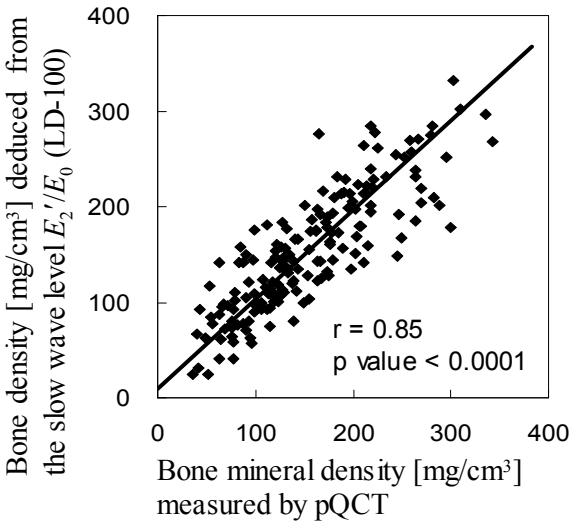


Fig.1 Bone density deduced from slow wave level and bone mineral density measured by pQCT.

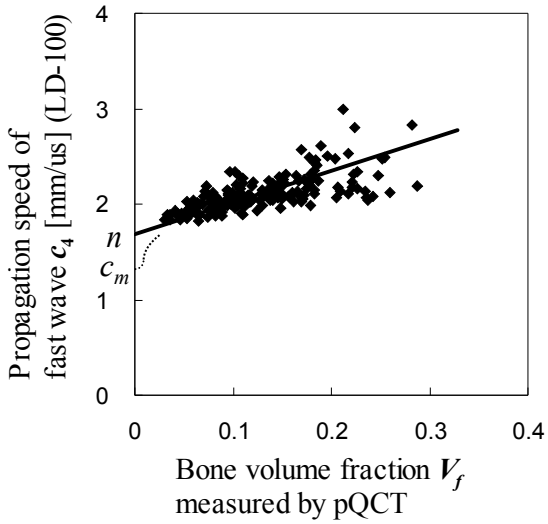


Fig.2 Propagation speed of fast wave and bone volume fraction measured by pQCT.

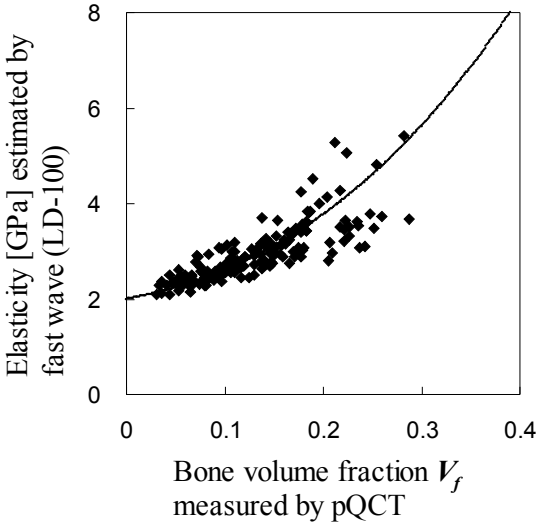


Fig.3 Elasticity corresponding to fast wave and bone volume fraction measured by pQCT.

3P7b-17

Proceedings of Symposium on Ultrasonic Electronics, Vol. 29 (2008) pp. 465-466
11-13 November, 2008

# Anisotropy of longitudinal ultrasound velocity and HAp orientation in bovine cortical bone

ウシ皮質骨中の超音波縦波音速の異向性と HAp 結晶配向

Yuichiro Yaoi[1†], Kazufumi Yamamoto[2], Takahiko Yanagitani[3],
Mami Matsukawa[1], Kaoru Yamazaki[2] and Akira Nagano[2]
([1] Doshisha Univ.; [2]Hamamatsu Univ. Sch. Med. ; [3]Nagoya Inst. Tech.)
矢追佑一郎 [1‡]，山本和史 [2]，柳谷隆彦 [3]，松川真美 [1]，山崎薫 [2]，長野昭 [2]
([1] 同志社大; [2] 浜松医大 整形外科; [3] 名工大)

## 1. Introduction

Quantitative ultrasound (QUS) is a good method to measure elastic properties of bone, which is expected to be an innovative technique to evaluate bone quality. One problem of this method is the comparatively low measurement accuracy, which seems to come from the complicated wave properties in bone, due to the multiscale heterogeneous and anisotropic elasticity. For example, the cortical bone mainly consists of hexagonal hydroxyapatite (HAp) crystallites and type I collagen. Elastic properties of the bone are strongly affected by the preference of HAp crystallites, because elastic modulus of HAp crystallites is more than 80 times larger than that of type I collagen[1)]. We have investigated the distribution of ultrasonic longitudinal wave properties in the cortical part of bovine femur, considering the microstructure and the HAp crystallites orientation[2) 3)]. In this study, then, the anisotropy of ultrasound wave velocity (SOS) and the HAp crystallites orientation are experimentally investigated in detail, using cylindrical specimens obtained from the bovine cortical bone.

## 2. Materials and Methods

A left femur was obtained from a 32-month-old bovine. Three ring-shaped cortical bone samples were obtained from the mid-shaft. Four cylindrical specimens (diameter 11mm) were taken from one ring sample as shown in **Fig. 1**.
Measurements of longitudinal wave speeds were performed using a conventional ultrasonic pulse technique as shown in **Fig. 2**. A PVDF focus transmitter (diameter 20 mm, focal length 40 mm) and a flat PVDF receiver (diameter 10 mm) were used in this experiment. The beam width at the half maximum values of the wave amplitude was approximately 1.5 mm at the focal point. Both PVDF transducers were mounted coaxially with distance of 60 mm in degassed water at 22.0±1.0 ℃. A single sinusoidal signal with a center frequency of 1 MHz and amplitude of 50 $V_{p\text{-}p}$ was applied to the transmitter. The longitudinal wave propagated through water, sample and water. The flat transducer received the wave, and converted it into the electrical signal. The received signal was amplified by a 40-dB preamplifier and visualized in an oscilloscope. The measured specimen was placed in the focal zone of the sound field. The direction of the ultrasound incident wave was perpendicular to the side surface of the cylindrical specimen. The measurements were done at each rotation angle of 5 degrees.

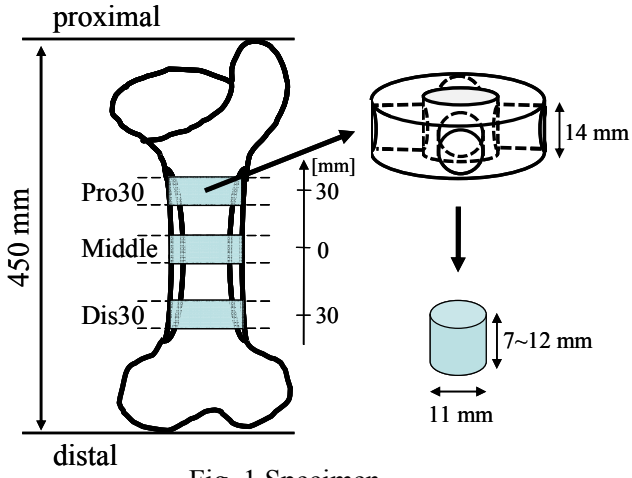


Fig. 1 Specimen.

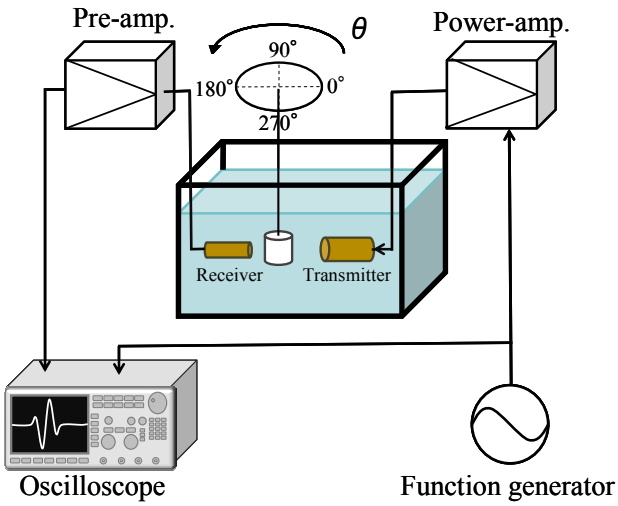


Fig. 2 Ultrasound measurement system.

yuichiro_y0306@hotmail.co.jp

The crystalline orientation of the sample was determined by XRD pole figure analysis (Philips, X-Pert Pro MRD). X-ray source (Cu-K$\alpha$, generated at a tube conditions of 45 kV and 40 mA) irradiated the sample surface through the parallel beam optics with 0.3 mm x 3 mm slit. The X-ray irradiated area was always smaller than the sample surface area in this optics.

### 3. Results and Discussions

**Figure 3** shows the velocity data of a specimen obtained from the anterior part of the middle sample. The 0 degree indicates the axial direction and the 90 degree indicates the tangential direction. Velocity changed due to the rotation angle. Four specimens in the same ring showed similar tendency of velocity, which were higher in the axial direction. However, the direction where the fastest wave velocity was observed was inclined 5 to 10 degrees from the axial direction. **Figure 4** shows the anisotropy of ultrasound wave velocity at each part in the middle specimens. **Figure 5** shows (0002) pole figure measured from the anterior specimen. From the pole-figure of X-ray diffraction analysis, the highly concentrated pole was clearly observed. This pole concentration indicates that the crystalline c-axes are oriented to the similar direction. We also found the small tilt of c-axis direction from the bone axis, which was in agreement of the velocity data. There is a possibility that the small tilt of the direction of the fastest wave seems to be dependent of the HAp crystallites orientation.

### 4. Conclusion

We have investigated the anisotropy of ultrasound wave velocity and the HAp crystallites orientation. We have found that the directions of the fastest velocity and the c-axis of the HAp crystallites orientation are a little inclined from the bone axis.


### Acknowledgment

Part of this work was supported by a Grant-in-Aid for Scientific Research (B) from JSPS and the bilateral joint project between JSPS and CNRS.


### References


1. R. S. Gilmore et. al.: J.Mater.Sci. **17** (1982) 1131.
2. Y. Yamato et. al.: Calcif. Tissue Int. **82** (2008) 162.
3. K. Yamamoto et. al.: Jpn. J. Appl. Phys. **47** (2008) 4096.


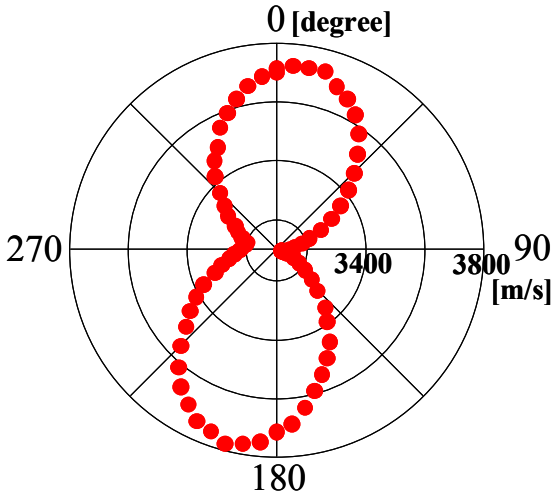


Fig. 3 Anisotropy of ultrasound velocity in the anterior part of the middle sample. Velocity difference from 3100 m/s was adopted to emphasize the anisotropy.

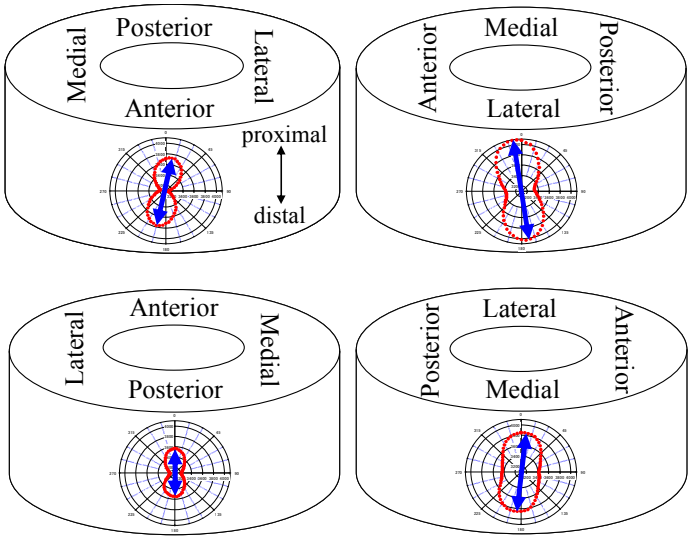


Fig. 4 Anisotropy of ultrasound wave velocity in the middle sample of bovine femur.

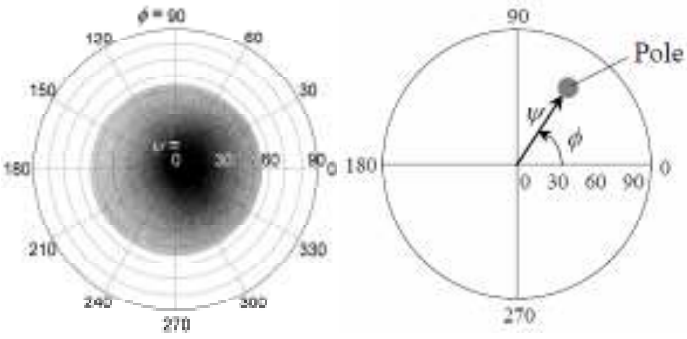


Fig. 5 (0002) pole figure in the anterior part of the middle sample, with the explanation of angles.

3P7b-18

Proceedings of Symposium on Ultrasonic Electronics, Vol. 29 (2008) pp. 467-468
11-13 November, 2008

# The effect of soft tissue on the ultrasonic wave propagation in cancellous bone

海綿骨中の軟組織が超音波の伝搬に与える影響

Takashi Saeki [1†], Tomohiro Kubo[1], Mami Matsukawa[1] and Yoshiki Nagatani[2]
([1] Doshisha Univ.; [2]Kobe City College of Technology)
佐伯崇 [1‡]，久保智宏 [1]，松川真美 [1] ,長谷芳樹 [2]（[1] 同志社大学; [2] 神戸市立工業高等専門学校）

## 1. Introduction

Longitudinal ultrasonic wave propagating in cancellous bone separates into two waves, fast and slow waves. The fast wave mainly propagates in the trabeculae bone. BV/TV (bone volume fraction) and anisotropy of cancellous bone have strong effects on the propagation phenomena of fast wave. On the other hand, the slow wave mainly propagates in the soft tissue. Several studies have been performed to understand the nature of these wave propagation phenomena [1-2]. Most of the former investigations were in vitro studies using the cancellous bone filled with water. However, for in vivo application of ultrasonic technique, it is necessary to study the effect of actual soft tissue (marrow) among cancellous bone upon the wave propagation.

In this study, then, we have investigated the ultrasonic properties of bone marrow, whose ultrasonic properties have not been evaluated precisely. Considering the properties, we have investigated wave propagation in the cancellous bone filled with the marrow, especially focusing on the studies through both experiment and the FDTD simulation.

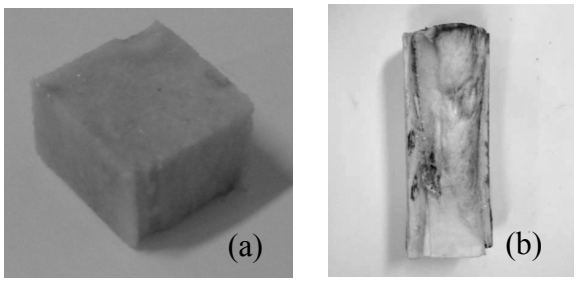


Fig.1 Cancellous bone in the epiphysis and bone marrow obtained from the diaphysis.

## 2. Specimen

The bone mainly consists of cortical bone, cancellous bone and bone marrow. Cancellous bone is filled with marrow. We obtained specimens from left 25-month-old bovine femur. As shown in Fig.1a, bone marrow fills the pores among trabecular structure. The specimen size was 20×20×9 mm.

saeki@usl.doshisha.ac.jp

In addition, as shown in Fig.1b, we removed the marrow from the femoral diaphysis to measure ultrasonic properties.

## 3. Ultrasonic measurements

At first, we have measured the ultrasonic properties of the bone marrow with a conventional ultrasonic pulse technique. By changing the length of the sample marrow, we obtained velocity and attenuation in the temperature range from 20 ℃ to 39 ℃.

We next measured the cancellous bone filled with marrow or water. The measurements were performed using an acoustic tube shown in Fig. 2. This acoustic tube was filled with water.

Here, we used self made transducers using PVDF film (Toray, thickness 40 μm). The applied electrical signal was 1 cycle of sinusoidal wave at 1 MHz. The received signals were amplified 40dB by a preamplifier (BX-31, NF Corporation) and measured by an oscilloscope (TDS5000 Tektronix Japan, Ltd.). Water and specimen were deaerated in a vacuum camber for 2 hours before measurement.

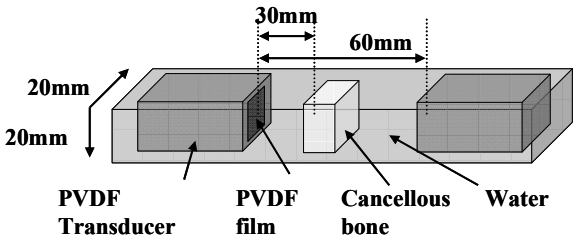


Fig.2 Configuration of an acoustic tube

## 4. FDTD Simulation

The followings are the governing equations for the 3-dimensional elastic FDTD method for the isotropic medium related to the x direction [3]:

$$\frac{\partial \sigma_{xx}}{\partial_t} = (\lambda + 2\mu)\frac{\partial v_x}{\partial_x} + \lambda\frac{\partial v_y}{\partial_y} + \lambda\frac{\partial v_z}{\partial_z} \quad (1)$$

$$\frac{\partial \sigma_{xy}}{\sigma t} = \mu\left(\frac{\partial v_x}{\partial_y} + \frac{\partial v_x}{\partial_x}\right) \quad (2)$$

$$\frac{\partial v_x}{\partial t} = \frac{1}{\rho}\left(\frac{\partial \sigma_{xx}}{\partial_x} + \frac{\partial \sigma_{xy}}{\partial_y} + \frac{\partial \sigma_{zx}}{\partial_z}\right) \quad (3)$$

We simulated wave propagation in the cancellous bone using X-ray CT image of an actual cancellous bone. Figure 5 shows an example of the image obtained by X ray CT (SMX-160CT-SV3 Shimadzu, Kyoto). The spatial resolution was 60.7 μm. Here, the total simulation field was 21.6×21.6 ×17.2 mm. The size of cancellous bone was 21.0 × 21.0 × 9.0 mm. The time increment for the simulation was 5 ns. As shown in Fig.6, the initial particle velocity was given at the top of the simulation model assuming a plane transmitter. The experimentally measured waveform was used for the initial wave.

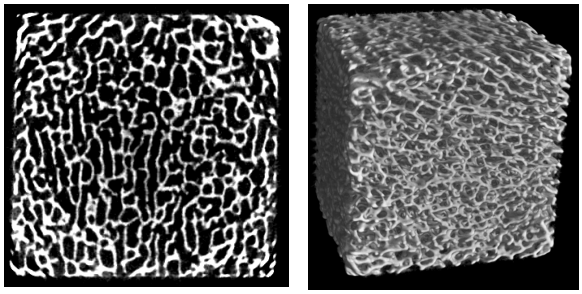

Fig.5 X-ray CT image of cancellous bone.

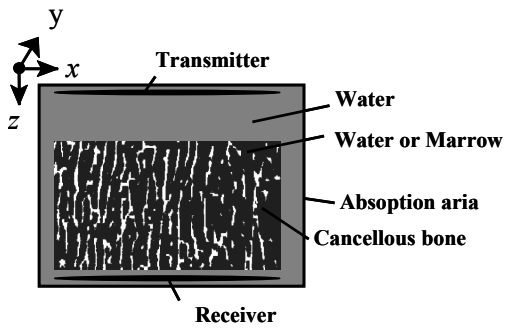


Fig.6 FDTD simulation model.

## 5. Results and discussions

We have measured bone marrow samples obtained from the different bovine femora. The averaged wave velocity of the marrow was almost 1440m/s at 36 °C. Figure 7 shows the temperature dependence of wave velocity in two samples. The velocity values were similar with the reported data of El-Sariti et.al. One interesting result is the comparatively low velocity in the marrow. The attenuation in the bone marrow was also measured.

Next, we have compared the wave propagation in the cancellous bone from experimental and simulation studies. In both results, we can confirm the clear separation of incident wave to the fast and slow waves. The amplitudes of the waves were dramatically changed in the experiments, especially in case of bone filled with bone marrow. One reason for this seems to come from the effect of frictional loss at the interface of trabeculae and soft tissue, which cannot be considered in the FDTD simulation.

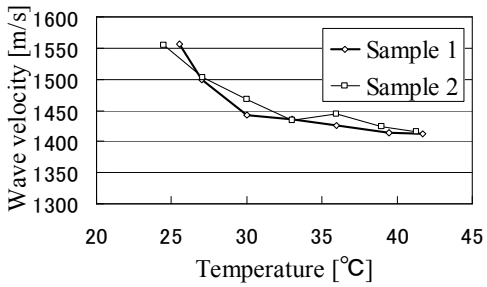


Fig. 7 Temperature dependence of observed wave velocity.

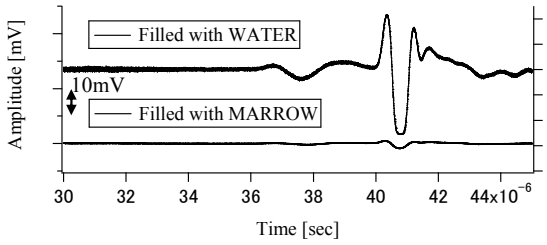


Fig. 8 Experimentally observed waveform passed through specimen.

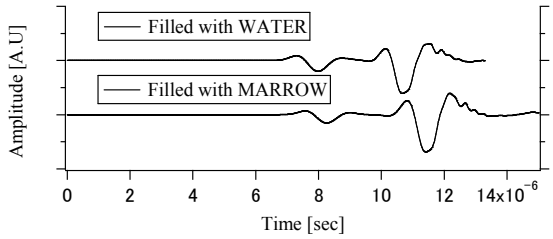


Fig.9 Simulated waveform passed through the specimen.

## 6. Conclusion

Ultrasonic wave propagation in the bovine cancellous bone was investigated, considering the ultrasonic properties in bone marrow. From the comparison between experiments and simulations, the possible strong effect of frictional loss at the solid bone- soft tissue interfaces was pointed.

## References

1. A. Hosokawa, and T. Otani, J. Acoust. Soc. Am, **101** (1997) 558.
2. A. Hosokawa, et.al., Jpn. J. Appl. Phys., **36** (1997) 3233.
3. Y. Nagatani et.al., Jpn. J. Appl., Phy., **44** (2006) 4622.
4. A. El-Sariti et.al., Ultra. Med. Bio. **32** (2006)985.

3P7b-19

Proceedings of Symposium on Ultrasonic Electronics, Vol. 29 (2008) pp. 469-470
11-13 November, 2008

# Influence of Trabecular Elements on Fast and Slow Wave Propagations in Oblique Directions to Layers of a Stratified Trabecular Phantom

層状構造海綿骨ファントム中を斜方向伝搬する高速波・低速波における骨梁要素の影響

Atsushi Hosokawa† (Dept. Elect. & Comp. Eng., Akashi Nat. Coll. Tech.)
細川篤† （明石高専 電気情報）

## 1. Introduction

Ultrasound characteristics in bone depend on not only the material but also structural properties. Because the ultrasound waves propagating in bone reflect these properties mixedly, estimating the bone properties from their parameters is very difficult. In order to realize accurate bone assessment using ultrasound techniques, therefore, the influence of bone structure must be clarified. In particular, cancellous bone can largely affect the propagation of ultrasound waves owing to complexity of the innner trabecular structure. The macroscopic trabecular orientation is closely related to the ultrasound propagation through cancellous bone, and a unique phenomenon that two longitudinal waves, called as “fast and slow waves”, propagate in the oriented trabecular direction can be observed.[1] However, the influence of trabecular microstructure on the fast and slow waves is not sufficiently clear.

In the previous study,[2] the influence of minor trabecular rods on the fast and slow wave properties was investigated by using stratified trabecular phantoms. In this study, the influence on these properties in oblique directions to the stratified layers was experimentally investigated.

## 2. Stratified trabecular phantoms

Based on a stratified model composed of periodically alternating solid and fluid layers,[3] the stratified trabecular phantom was previously developed.[2] In this trabecular phantom, as shown in **Fig. 1**, the minor trabecular rods were arranged perpendicular to the major trabecular plates. As the purpose of this study was to investigate the influence of trabecular elements (but not material properties), the practical phantom was generated using brass plates and cylindrical rods. The spaces between the trabecular (brass) plates were filled with degassed water as substitute for bone marrow. Assuming bovine cancellous bone, the plate thickness and space were determined to be 0.2 and 1 mm, respectively. The final thickness of the phantom was 10 mm. For comparison, the phantom without the rods was also generated.

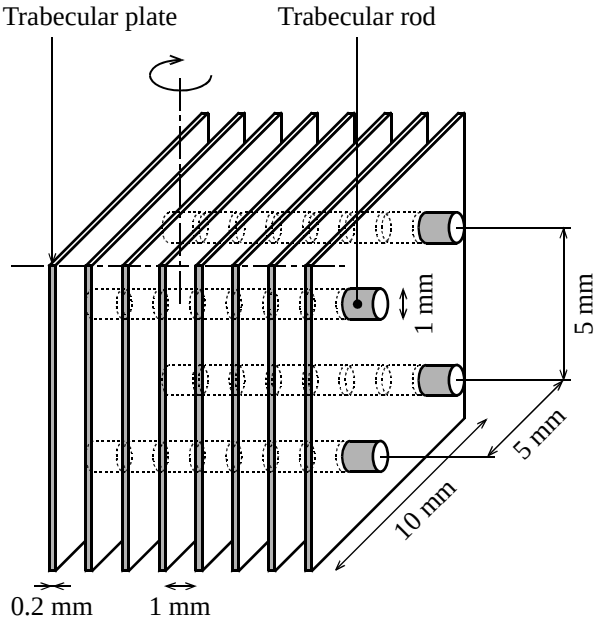


Fig. 1 Geometry of a stratified trabecular phantom.

## 3. Calculating method of propagation speed[4]

At oblique incidence on the surface of a solid specimen in a fluid, an ultrasound wave is refracted according to Snell’s law. If the time difference of the ultrasound wave with and without the specimen is $\Delta t$, the wave speed in the solid $v_s$ is given by

$$\left(\frac{v_s}{v_f}\right)^2 = \left[1+\left(\frac{v_f \Delta t}{d}\right)^2 - 2\left(\frac{v_f \Delta t}{d}\right)\cos\theta_i\right]^{-1}, \quad (1)$$

where $v_f$ is the speed in the fluid, $d$ is the specimen thickness, and $\theta_i$ is the incident angle. The refracted angle $\theta_r$, that is the propagation angle in the specimen to the thickness direction, is given by

$$\tan\theta_r = \frac{\sin\theta_i}{\cos\theta_i - \left(v_f \Delta t / d\right)}. \quad (2)$$

hosokawa@akashi.ac.jp

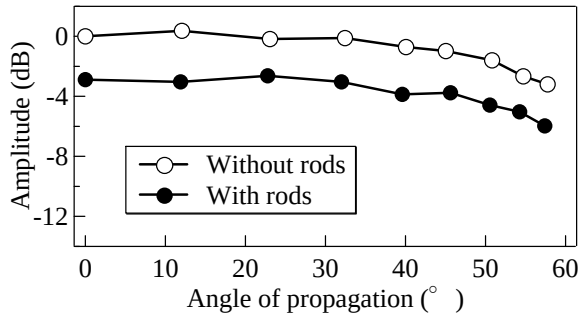


(a) Fast wave

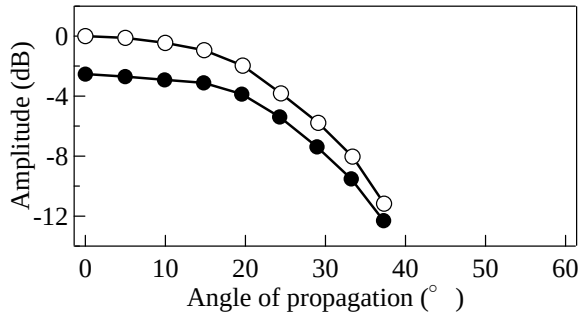


(b) Slow wave

Fig. 2 Fast and slow wave amplitudes in stratified trabecular phantoms without and with trabecular rods vs. propagation angle to trabecular plates.

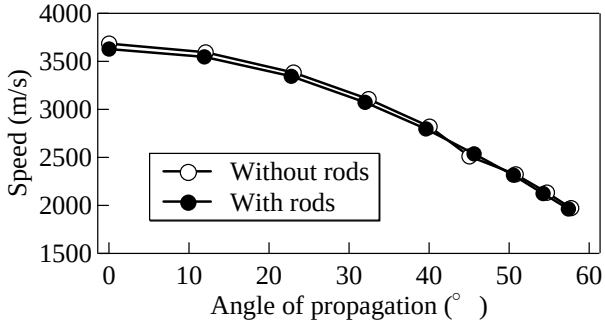


(a) Fast wave

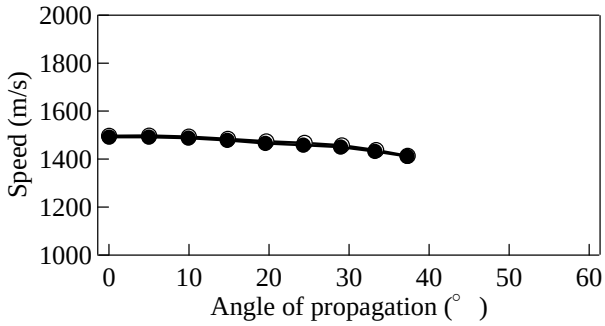


(b) Slow wave

Fig. 3 Fast and slow wave speeds in stratified trabecular phantoms without and with trabecular rods vs. propagation angle to trabecular plates.

## 4. Experimental results

Fast and slow waves propagating through stratified trabecular phantoms without and with trabecular rods were experimentally observed in water. The trabecular phantoms were rotated on the axis parallel to the trabecular plates and perpendicular to the trabecular rods, as shown in Fig. 1. For each wave, the peak-to-peak amplitude and the propagation speed were measured as a function of the propagation angle to the trabecular plates.

Firstly, the measured results of the fast and slow wave amplitudes are shown in **Fig. 2**. Similarly with the previous results,[2)] it can be observed that both amplitudes are attenuated by the influence of the trabecular rods. This influence on the fast wave amplitude is not significantly changed with the propagation angle, whereas the slow wave amplitude is less influenced at higher propagation angles. Next, the measured speeds of the fast and slow waves are shown in **Fig. 3**. The fast wave speed in the trabecular phantom with the trabecular rods is slightly slower than that without the trabecular rods. This difference seems to disappear at higher propagation angles. The obvious difference in the slow wave speed, on the other hand, cannot be found.

## 5. Conclusions

The influence of minor trabecular rods was experimentally investigated for the fast and slow wave propagations at oblique angles to the layers of the stratified trabecular phantom. The experimental results showed that the influence on the slow wave amplitude largely depended on the propagation angle, that is the propagation direction.

**Acknowledgment**

This study was supported by a Grant-in-Aid for Young Scientists (B) (19700393) from MEXT, and in part, by a Grant-in-Aid for Scientific Research (B) (19360189) from JSPS, by the Academic Frontier Research Project on “New Frontier of Biomedical Engineering Research” of Doshisha University and MEXT, and by JSPS and CNRS under the Japan-France Research Cooperative Program.

**References**

1. A. Hosokawa and T. Otani: J. Acoust. Soc. Am. **101** (1997) 558.
2. A. Hosokawa: Jpn. J. Appl. Phys. **47** (2008) 4170.
3. M. Schoenberg: Wave Motion **6** (1984) 303.
4. R. E. Smith: J. Appl. Phys. **43** (1972) 2555.

3P7b-20

Proceedings of Symposium on Ultrasonic Electronics, Vol. 29 (2008) pp. 471-472
11-13 November, 2008

# Introduction of "Digital Elastic Model of Human Body" for 3-D FDTD Simulation - Elastic Wave Propagation in Human Body -

体内音場解析のための"ディジタル人体弾性モデル"実現に向けて

Yoshiki Nagatani[1‡], Atsushi Hosokawa[2], Takefumi Sakaguchi [3], Mami Matsukawa [4], and Yoshiaki Watanabe [4] ([1] Kobe City College of Technology; [2] Akashi National College of Technology; [3] Nara Medical University; [4] Doshisha University)

長谷芳樹 [1‡], 細川篤 [2], 阪口剛史 [3], 松川真美 [4], 渡辺好章 [4] ([1] 神戸市立工業高等専門学校; [2] 国立明石工業高等専門学校; [3] 奈良県立医科大学; [4] 同志社大学)

## 1. Backgrounds and Objectives

There are many previous studies about numerical simulations focusing on specific area of human body. As comparative studies between simulations and experimental measurements, our group has also worked on behaviours of ultrasonic waves in cortical bones, cancellous bones, bone marrows [1-6], and sound distributions in human heads [7,8]. However, the simulation technique of elastic wave propagation including entire human body is not established yet. The development of precise and accurate "*Digital Elastic Model of Human Body*" would be an useful tool in medical, welfare, and engineering fields: e.g. giving us new point of view and validating safeness on developing new medical equipments, diagnosis simulators for young doctors etc.

As a preliminary work, therefore, we constructed the elastic model of entire human body for three-dimensional simulation of wave propagation.

## 2. Simulation Model: Digital Elastic Body

As a model, the make data in the "Realistic High-Resolution Whole-Body Voxel Models" constructed by Nagaoka *et al.* was used [9]. The model describes consisting tissues of normal Japanese person with the resolution of 2 mm.

Using the model, elastic properties of the tissues are assigned to water, fat, cortical bone, bone marrow, and air. The elastic coefficients and attenuation of cortical bone and bone marrow used are experimentally measured values [4,6]. The bottoms of both feet are assumed to be immersed in water. **Figures 1(a)(b)** show the projected figures of density distribution of 3-D "*Digital Elastic Model of Human Body* " model. The brighter area indicates the tissue with higher density.

## 3. Simulation Technique: Elastic FDTD Method

In this study, the elastic three-dimensional finite-difference time-domain (FDTD) method was used. In order to reflect the absorption effect, the values of the normal and shear stresses are attenuated in each calculation step of propagation. The frequency dispersion of attenuation was not considered [5]. In this simulation, the elastic anisotropy of the solid portion was not considered. The stress and particle velocity were calculated


**Figure 1** Projected figures of three-dimensional "*Digital Elastic Model of Human Body*."

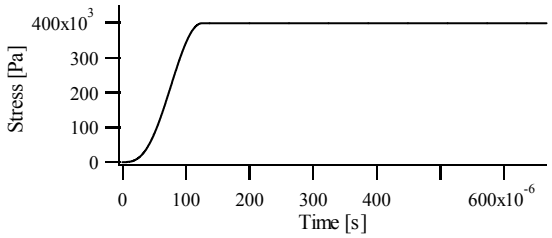


**Figure 2**: Initial normal stress put into square surface at the bottom of right heel.

nagatani@kobe-kosen.ac.jp

alternately both in the spatial and time domains, which was called “the leapfrog method [10].” The applicability of the program used has been confirmed in our previous studies [1,2].

**Figure 2** shows the initial stress, a quarter cycle of a sinusoidal wave with Hanning window. It was applied to the square surface of 40×40 mm at the bottom of right heel shown in Figs. 1(a)(b). One step in walking movement of a person of 65 kg in weight was assumed.

## 4. Results and Discussions

**Figures 3(a)(b)(c)** show the screenshots of the normal stresses on the diagonal surface shown in Fig. 1(a) as a dotted line, which includes tibia and femur. Figure 3(c) shows the separation of single wave into several parts.

**Figure 4** shows the received waveform at point C in Fig. 3(a) which is inside the distal end of the femur. The first waves with small amplitude may have passed through solid part of the tibia. After the waves, multiple scattered waves can be seen.

The changes of peak amplitudes from point A to D are shown in **Fig. 5**. The decrease of peak amplitude may be caused by the multiple reflections caused by the complex structure of bone. It should be checked precisely in the future work.

## 5. Conclusion

Using the “*Digital Elastic Model of Human Body*”, the capability of elastic wave simulation inside human body was confirmed. The multiple reflected waves was seen while its propagation in human leg model.

## Acknowledgment

This study was supported by the Grant-in-Aid for Young Scientists (B) (20791218) of the Ministry of Education, Culture, Sports, Science and Technology. This study was partly supported by bilateral joint project between JSPS and CNRS, in addition to the Academic Research Frontier project of Doshisha University and Ministry of Education, Culture, Sports, Science and technology in Japan.

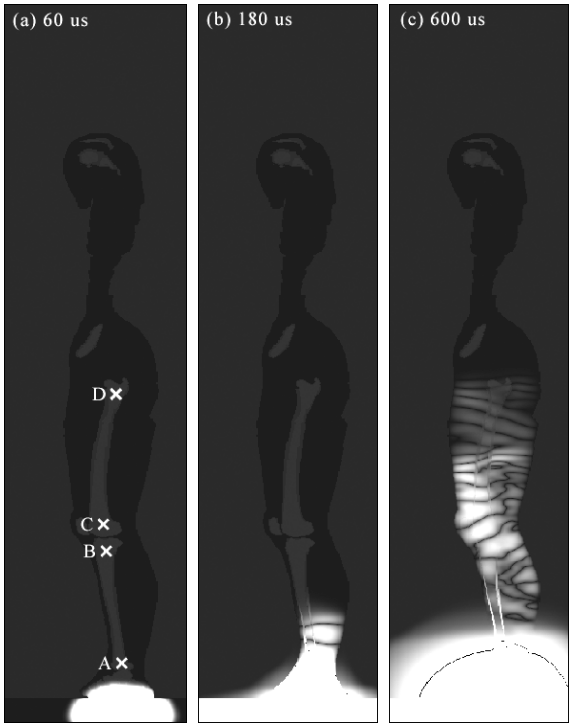


**Figure 3**: Screenshots of normal stresses in simulation model at each moment.

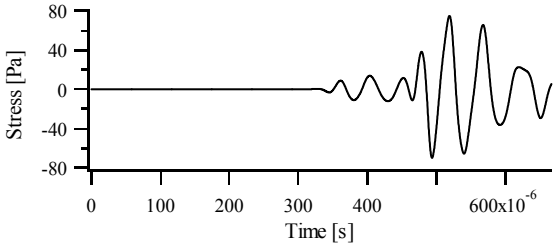


**Figure 4**: Received waveform at point C.

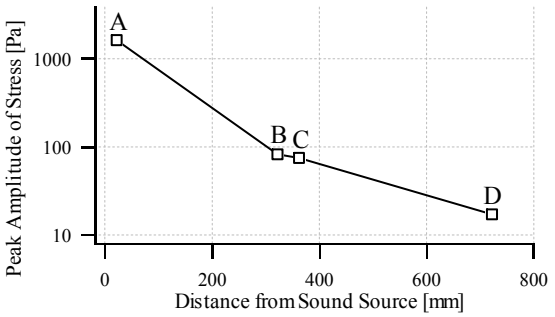


**Figure 5**: The changes of peak amplitudes from point A to D.

## References

1. Y. Nagatani, H. Imaizumi, T. Fukuda, M. Matsukawa, Y. Watanabe, and T. Otani, Jpn. J. Appl. Phys., Vol. 45 No.9A (2006) 7186-7190.
2. Y. Nagatani, K. Mizuno, T. Saeki, M. Matsukawa, T. Sakaguchi, and H. Hosoi, Ultrasonics (2008). [in press]
3. A. Hosokawa, Jpn. J. Appl. Phys., Vol. 47 No.5A (2008) 4170-4175.
4. Y. Yamato, M. Matsukawa, T. Yanagitani, K. Yamazaki, H. Mizukawa, and A. Nagano, Calcified Tissue International, 82, No.2 (2008) 162-169.
5. K. Yamamoto, Y. Yaoi, Y. Yamato, T. Yanagitani, M. Matsukawa, and K. Yamazaki, Jpn. J. Appl. Phys., Vol.47, No.5 (2008) 4096-4100.
6. T. Saeki, M. Matsukawa, and Y. Nagatani, IEICE Technical Report, US2008-23 (2008) 5-9.
7. T. Sakaguchi, T. Hirano, Y. Watanabe, T. Nishimura, H. Hosoi, S. Imaizumi, S. Nakagawa, and M. Tonoike, Jpn. J. Appl. Phys., Vol. 41 No.5A (2002) 3604-3608.
8. Y. Tanikaga, T. Sakaguchi, and Y. Watanabe, Proceedings of Forum Acusticum, Sevilla (2002).
9. T. Nagaoka, S. Watanabe, K. Sakurai, E. Kunieda, S. Watanabe, M. Taki, and Y. Yamanaka, Physics in Medicine and Biology, Vol.49 (2004) 1-15.
10. K. S. Yee, IEEE Transactions on Antenna and Propagation, AP-14, No. 3 (1966) 302-307.

3P8-11

Proceedings of Symposium on Ultrasonic Electronics, Vol. 29 (2008) pp. 473-474
11-13 November, 2008

# A Study on Structure of Joined Surfaces on Ultrasonic Joining of Au by use of Surface Acoustic Wave Device

弾性表面波素子による金接合における接合状態の検討

Kengo Naruse†[1], Kiyomi Mori[2] and Yuji Watanabe[2*]
(Seidensha Electronics Co., Ltd[1], Takushoku Univ., Faculty of Engineering[2])
成瀬健悟†[1]，森きよみ[2]，渡辺裕二[2*]（精電舎電子工業(株)[1]，拓殖大学 工学部[2]）

## 1. Introduction

We are studying the ultrasonic joining of Flip-chip type package of IC by use of surface acoustic wave (SAW) device.[1),2)] In the previous study, we carried out ultrasonic gold foil (Au:99.95%) joining by using a SAW device at 2.50 MHz. As the result, we confirmed that the SAW joining avoids damage of joined specimens and it has wider joining space at higher frequency. In addition, we use the SAW device of standing wave type for joining of Au. Therefor, we consider that joined specimens are influenced by the wavelength of SAW propagation, and we assume that it is joined at loop points of standing wave of SAW. In this paper, we describe the structure of joined surfaces and distribution of joined parts on the ultrasonic joining of Au foil.

## 2. Construction of the SAW joining system

Figure 1 illustrates the SAW device that is used in this study. The substrate of the SAW device is 128°-rotated Y-cut X-propagating $LiNbO_3$ and the dimensions of the substrate are a length of 30 mm, a width of 90 mm and a thickness of 10 mm. Using the substrate, we designed a 2.5 MHz SAW resonator.[3),4)] Since the acoustic velocity of the SAW of the substrate is 4000 m/s, one wavelength is 1.6 mm. Therefore, the width of every electrode finger and the gap width between electrode fingers were both designed as 0.4 mm. In addition, we designed the apertures to be 15.2 mm and the length of propagation path to be 9.2 mm, so we obtained 15.2×9.2 $mm^2$ as a joining area. Moreover, we arranged two sets of inter digital transducer (IDT) and one set of reflector set on the both end on the substrate. The electrical power was supplied by a power amplifier. The practical natural frequency of the SAW device fabricated was 2.422 MHz when aluminum was vapor-deposited for the electrodes. Figure 1(a) shows the top view of the SAW device. As shown in the figure, vibration velocity at the measuring point was monitored by using a laser Doppler vibrometer. Figure 1(b) shows the side view of the SAW device. As shown in Fig. 1(b), static pressure induced by a dead load from a steel rod is supplied to the specimens being joined, which are put on the SAW device. In addition, polytetrafluoroetylene (PTFE) film and polyimide (PI) film are placed between a steel rod and the SAW device in order to protect heat conduction to the steel rod. The films are also used as like as a cushion to supply static pressure to Au foil uniformly.

For the excitation of SAW during the joining, we use gated waves with 2.422 MHz of carrier frequency, 0.5 ms of duration time and 0.5 ms of interval time. The signal is used in order to avoid destruction of the substrate by heating.

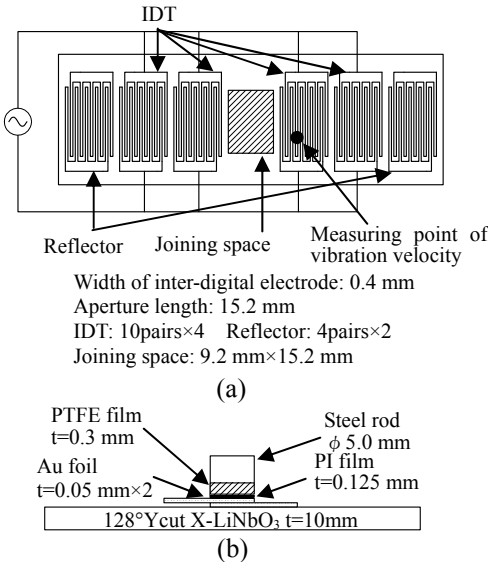


Fig.1. Schematic diagram of construction of SAW joining system. (a) Top view and (b) Side view (t: thickness $\phi$ : diameter)

## 3. Result of Microscope Observation of Structure of Joined Surfaces

Material characteristics of Au foil are shown in Table 1. Conditions of SAW joining are shown in Table 2. Here, two pieces of Au specimens are overlapped for 3.2 mm. It is equivalent to two wavelengths of SAW. Thin PI films are put between the specimens and electrodes in order to make isolation. And we did the tensile test of the joined specimens, which are joined under the conditions of Table 2. For the fractured specimens, we observed

*E-mail address: u2watana@es.takushoku-u.ac.jp

Table1. Characteristics of Au foil.

| Material | Au foil(99.95%) |
|---|---|
| Melting point(℃) | 1337 |
| Material strength(MPa) | 130.3(99.99%)[5)] |
| Material size(mm) | 10×2×0.05 |

Table2. Conditions of SAW joining.

| Specimens | Au foil(99.95%)<br>Thickness 0.05 mm<br>Two sheets piled |
|---|---|
| Frequency of SAW joining | 2.422 MHz |
| Area of joined part($mm^2$) | 2×3.2 |
| Vibration velocity(m/s) | 1.7 |
| Supplied voltage($V_{p-p}$) | 200 |
| Static pressure(MPa) | 22.0 |

the fractured surfaces by using a scanning electron microscope (SEM). The results are shown in Figs. 2(a) – 2(e).

Figure 2(a) shows the surface of Au foil. Figures 2(b) and 2(c) show the fractured surfaces of joined part. By comparing with Fig. 2(a), we can see roughness on the surfaces in Fig. 2(b) and 2(c).The roughness means that the specimens were joined at these areas. Moreover, roughness can be seen on the whole surface. Therefore, we understand that joined part is not joined only at loop point of the standing wave of SAW.

Moreover, we can see that the roughness near the center of a joined surface of the specimen is large and deep. On the other hand, the roughness on the circumference of it is small. The expanded view of roughness in the circle A and circle B of Fig. 2(b) are shown in Figs. 2(d) and 2(e). From the figures, we can clearly see the difference in the size of roughness. Therefore, we can conclude that the joint strength near a center is strong and the circumference is weak. On the reason, we guess that the center of the joining area is joined first by contact pressure. Therefore, the other area can not be joined well, because relative motion between upper and lower film is very low. As the result, it is difficult to remove oxidized layer and contaminant of the joined surface by ultrasonic vibration. The fact shows that the static pressure is not supplied to the specimen uniformly.

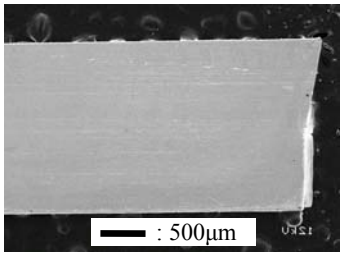


(a) Surface of Au foil.

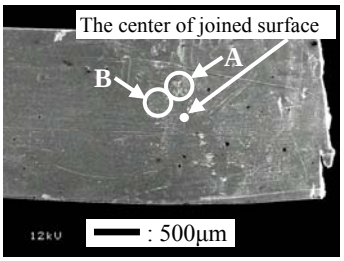


(b) The joined surface of the foil of SAW device side.

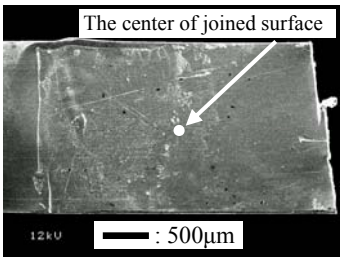


(c) The joined surface of the foil of pressed side.

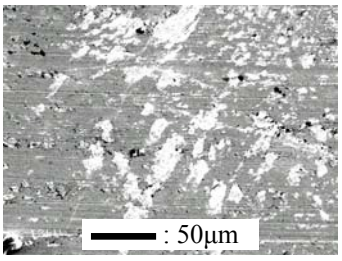


(d) The expanded view in circle A of Fig. 2(b).

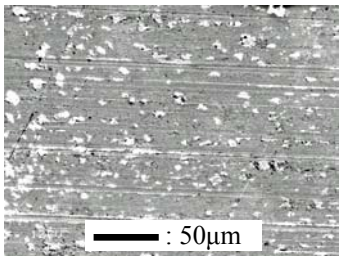


(e) The expanded view in circle B of Fig. 2(b).

Fig.2. Observation of surface of specimens by SEM.

## 4. Conclusions

The structure of joined surfaces on ultrasonic joining of Au foil by SAW device was studied. As the result, we confirmed that the distribution of joined part is irrelevant to the wavelength. Furthermore, we guess that static pressure is not supplied uniformly. As the next step, we will study on relationship between distribution of static pressure and joined part.

**Acknowledgment**

This study was supported by Mr. K. Asakura of Takushoku Univ., Faculty of Engineering.

**References**

1. K. Naruse, K. Mori and Y. Watanabe : Jpn. J. Appl. Phys. Vol.**47** (2008) pp.4305-4308
2. K. Naruse, K. Mori and Y. Watanabe : Proc. Symp. Ultrason. Electron., Vol.**28**,(2007)pp345-346.
3. T. Kojima: Doctoral Dissertation, Tohoku Univ. 1988 [in Japanese]
4. J. S. P. S. Surface Acoustic Wave 150th Committee: Surface Acoustic Wave Technology Handbook (Ohmsha, 1991), p.161 [in Japanese].
5. The Japan Institute of Metals ”Metals data book” p.165 [in Japanese].

Proceedings of Symposium on Ultrasonic Electronics, Vol. 29 (2008) pp. 475-476
11-13 November, 2008

# Study on the sound source and the reflector to generate strong acoustic field for levitation

超音波浮揚における強力音場生成のための音源および反射板の検討

Teruyuki Kozuka†, Kyuichi Yasui, Toru Tuziuti, Judy Lee, Atsuya Towata and Yasuo Iida (National Institute of Advanced Industrial Science and Technology (AIST))
小塚晃透‡，安井久一，辻内亨，ジュディー・リー，砥綿篤哉，飯田康夫 （産総研）

## 1. Introduction

Using a standing wave field generated between a sound source and a reflector, it is possible to trap small objects at nodes of the sound pressure distribution in air. In order to trap and manipulate object stably, the force should be strong enough.

In the previous paper, higher sound pressure in a standing wave field was achieved using a concaved reflector than that using a flat one[1]. In the present paper, a sound field was generated under a flat or concave reflector, and the sound field has been studied both by experimental measurement and numerical calculation. The calculated result agrees well with the experimental data. In the best condition, a steel ball of 2.0 mm in diameter was levitated in air.

## 2. Calculation of the sound field

A standing wave field was generated between a sound source and a reflector in air. The sound source is a cylindrical bolted Langevin type transducer with a horn of 20 mm, 25 mm or 30 mm in diameter, and the frequency is 28.0kHz. The entire surface vibrated equally in phase with a constant displacement amplitude of 30 $\mu m_{p\text{-}p}$ for all the horns. The reflector is circular glass plate of 45 mm in diameter and the surface is flat or concave. The focal length of concaved reflector is 51.9 mm or 77.85 mm. The reflector was parallel to the sound source and placed at 52 mm from the sound source. The sound speed $c_0$ is 344.0 m/s, the density $\rho_0$ is 1.2 kg/m$^3$.

The direct sound pressure $p_d$ from the sound source surface $F_0$ is calculated by the Rayleigh's formula.

$$p_d = \mathrm{j}\frac{\rho_0 c_0 v_0}{\lambda}\exp(\mathrm{j}\omega t)\iint_{F_0}\frac{\exp(-\mathrm{j}kr_0)}{r_0}\mathrm{d}F_0 \quad , \quad (1)$$

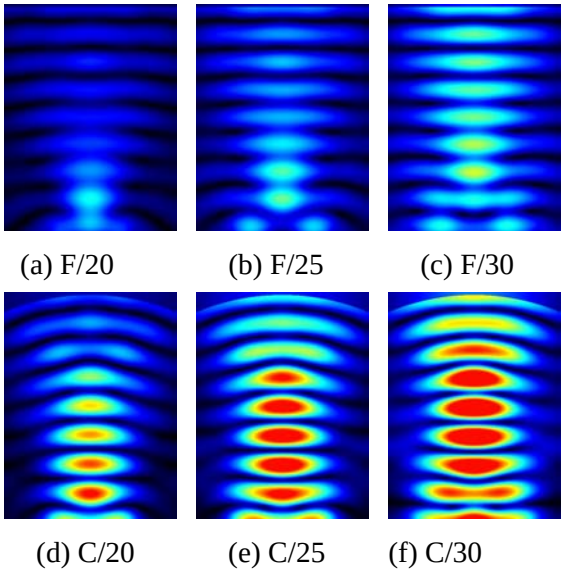

(a) F/20 (b) F/25 (c) F/30

(d) C/20 (e) C/25 (f) C/30

Fig.1 Calculated sound pressure distribution. F: Flat reflector, C: Concaved reflector, /20, /25, /30: Sound source diameter [mm].

where $v_0$ is velocity of a vibrating plate at the sound source, $\lambda$ is wave length, $\omega$ is angular frequency, $t$ is time, $k$ is wave number and $r_0$ is the distance between an arbitrary point on $F_0$ and the observation point.

When there is an object in the sound field, the reflected waves are generated from the object. In the present case, there is a reflector in front of the sound source. The reflected sound pressure from the reflector is calculated by integrating the original sound velocity at the reflector surface $F_1$. Moreover, the second reflected wave on $F_0$ and the third reflected wave on $F_1$ are calculated by the similar equations. The sound pressure distribution on the standing wave field is calculated by adding the sound pressures. Figure 1 shows the calculated total sound pressure with a flat or concave reflector for various sound source diameters. The focal length of the concaved reflector is 51.90 mm. When the sound source diameter is larger, the sound pressure is higher. With the concave reflector, the sound pressure is higher than that with a flat one.

kozuka-t@aist.go.jp

The particle in the sound field is forced from the anti-node to the node. According to Nyborg and Gor'kov, the force acting on a small sphere due to radiation pressure can be given by the following equation, provided the radius $a$ of the sphere is sufficiently small compared to the wave length $\lambda$:

$$F = V\left[D\nabla\langle e_k\rangle - (1-\gamma)\nabla\langle e_p\rangle\right] \qquad (2)$$

Where $V=(4/3)\pi a^3$, $D=3(\rho_s-\rho_0)/(2\rho_s+\rho_0)$, $\langle e_k\rangle$ and $\langle e_p\rangle$ are the time averaged kinetic energy and potential energy of sound acting on the small sphere, respectively.

Figure 2 shows calculated force on a particle along the sound beam axis. The particle is made of steel ($a$=1.0 mm, $\rho$=7874 kg/m$^3$). The force is stronger when the sound source diameter is larger. The local maximum force in the 3rd cycle from the sound source are 0.15 mN, 0.30 mN and 0.39 mN for the sound sources of $\phi$20 mm, $\phi$25 mm or $\phi$30 mm in diameter, respectively, when the reflector is concave with 51.9 mm in focal length. When the reflector is concave, the force is higher than that for a flat reflector. When the sound source diameter is 25 mm, the force is 0.04 mN, 0.30 mN or 0.23 mN with the reflector of flat, concaved with 51.9 mm or 77.85 mm focal length, respectively.

## 3. Experiment

The experimental setup is the same as that of the calculation except that the pin-hole was opened at the center of the reflector and that a thin wire was through the hole. The wire was jointed to a steel ball and a weighting machine. It measured the steel ball weigth along the sound beam axis in the standing wave field. Figure 3 shows the result of measurement for about 22 mm from the sound source. The steel ball weight is 33 mg without sound, and the value -33 mg means that it is levitated. The maximum weight in the 3rd cycle are 28 mg, 70 mg and 65 mg which corresponds to the force of 0.15 mN, 0.30 mN and 0.39 mN, when the sound source is $\phi$20 mm, $\phi$25 mm or $\phi$30 mm in diameter, respectively, with the concave reflector of 51.9 mm in focal length.

The influence of the sound source size and reflector form is the same as the calculate result. However the experimentally measured force is larger than the calculated one. This may be an error of an experiment.

## 4. Conclusion

A sound field was generated under a flat or concave reflector, and the sound field has been studied both by experimental measurement and numerical calculation. A steel ball of 2.0 mm in diameter was levitated in air.

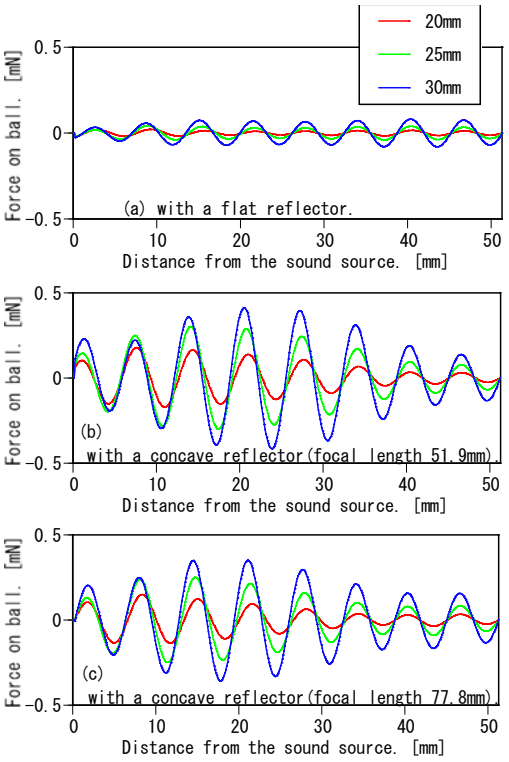


Fig. 2. Calculated force on steel ball along the sound beam axis.

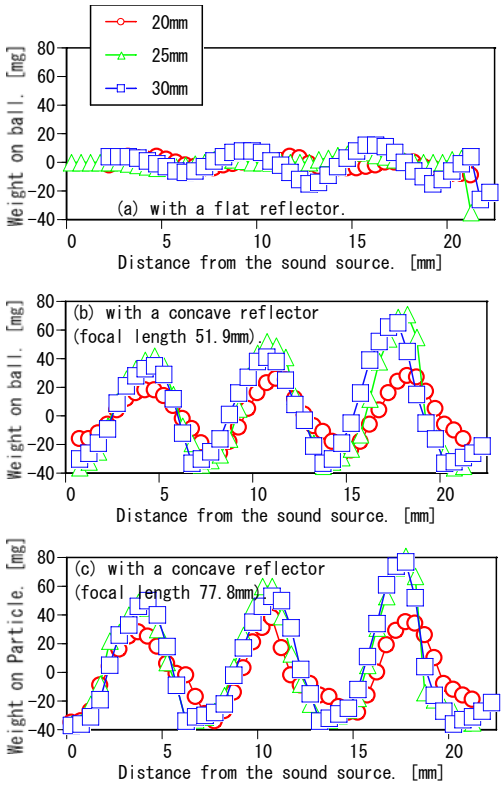


Fig. 3. Measured force on steel ball along the sound beam axis.


## Acknowledgment

This work was supported by KAKENHI19560248.


## References


1. T. Kozuka et. al.:Jpn. J. Appl. Phys. **47** (2008) 4336.

3P8-13

Proceedings of Symposium on Ultrasonic Electronics, Vol. 29 (2008) pp. 477-478
11-13 November, 2008

# Aerial Ultrasonic Source Using Stripe-Mode Transverse Vibrating Plate with Jutting Driving Point
# 凸端駆動による縞モードたわみ振動板型空中超音波音源

Hikaru MIURA , Hitoshi ISHIKAWA† (Coll. of Sci. & Tech., Nihon University)
三浦　光，石川　整†　（日大 理工）

## 1. Introduction

As acoustic sources emitting strong acoustic waves in air, ultrasonic sources using a stripe-mode rectangular transverse vibrating plate[1] or a lattice-mode square transverse vibrating plate[2] have been used. Because these sources are based on the resonance of transverse vibration, their electric-acoustic conversion rate is as high as 90%, which is a merit. However, the driving point of these acoustic sources is at the center of the vibrating plate, which interferes with the emission of acoustic waves in air and restricts the utilization of the acoustic sources as devices such as deodorizers. In this study, a vibrating plate with a new shape was developed to enhance the effectiveness of acoustic sources. Namely, the stripe-mode rectangular transverse vibrating plate was improved such that the driving point was outside the plate. This is hereafter called a stripe-mode transverse vibrating plate with a jutting driving point.

The following were experimentally examined. ①The length of the side parallel to the node line of the transverse vibrating plate at which the plate is preferably driven in the stripe mode. ②The driving conditions when the length between the driving point and the edge of the vibrating plate is varied. ③The effect of varying the surface area of the vibrating plate by changing the length of the side perpendicular to the node line of the vibrating plate.

## 2. Acoustic Source

**Figure 1** shows the outline of an aerial ultrasonic source using a stripe-mode transverse vibrating plate with a jutting driving point. As shown in the figure, a 20kHz bolt-clamped Langevin-type ultrasonic transducer is connected using screws to an exponential horn (diameter at the thick end, 70mm; diameter at the thin end, 10mm; amplification ratio, 7.0; made of duralumin) used as an amplifier, to which a 1/2-wavelength resonance rod (diameter, 10mm; made of duralumin) for controlling the longitudinal vibration frequency is connected. The tip of the rod is connected with the stripe-mode transverse vibrating plate with the jutting driving point (plate thickness, 3mm; made of duralumin) using a screw.

## 3. Design of Vibrating Plate

**Figure 2** shows an example of the stripe-mode transverse vibrating plate with a jutting driving point. The dotted lines in the figure represent the node lines of the vibrating plate. The length d between the nodes in the stripe mode is expressed as

$$d = \sqrt{\frac{\pi C_D h}{2f}} \qquad (1)$$

miura@ele.cst.nihon-u.ac.jp, Real-giant@hotmail.co.jp

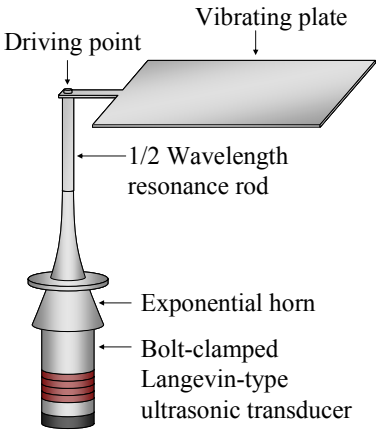

Fig.1 Outline of an ultrasonic source.

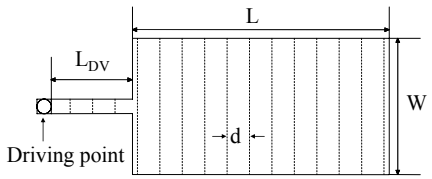

Fig.2 Outline of vibrating plate ($N_L$=12).

Here, $C_D$ is a material-specific constant, h is the plate thickness, and f is the frequency when the stripe mode appears at resonance. By substituting $C_D$=1.509kHz・mm, h=3mm, and f=19.8kHz, which are obtained on the basis of the preliminary examination, into eq.(1), d=18.86mm is obtained. The lengths of the sides perpendicular and parallel to the node line of the vibrating plate, L and W, respectively, are expressed as

$$L = (N_L - 0.5)d \qquad (2)$$

$$W = N_w d \qquad (3)$$

Here, $N_L$ is the number of nodes and is a natural number, and $N_W$ may have a noninteger value. Moreover, $L_{DV}$ in Fig. 2 is the length between the driving point and the edge of the vibrating plate.

$$L_{DV} = N_i d \qquad (4)$$

Here, $N_i$ may have a noninteger value.

## 4. Length of Side Parallel to Node Line of Vibrating Plate

In the case of a vibrating plate with the driving point at its center, $N_W$ is an odd natural number[1]. In order to realize smooth driving of the stripe-mode transverse vibrating plate with the jutting driving point, $N_W$ was experimentally examined. In the experiment, when $N_L$ and $L_{DV}$ were fixed at 12 and 3.0, respectively, and $N_W$ was changed in 0.1 steps between 4 and 6, the electric impedance of the acoustic source was measured when the stripe mode was observed at resonance. The result is shown in

**Fig.3**. The figure reveals that the impedance is large only at $N_W$=5.0 and is small at other values of $N_W$. Therefore, it is effective to set $N_W$ to be an odd natural number for the stripe-mode transverse vibrating plate with the jutting driving point, similar to the vibrating plate with the driving point at its center.

## 5. Length between Driving Point and Edge of Vibrating Plate

In order to realize smooth driving of the stripe-mode transverse vibrating plate with the jutting driving point, $L_{DW}$ was also experimentally examined. In the experiment, when $N_L$ and $N_W$ were fixed at 12 and 5.0, respectively, which were determined on the basis of the above result, and $N_i$ was changed in 0.1 steps between 1 and 3, the electric impedance of the acoustic source was measured when the stripe mode was observed at resonance. The result is shown in **Fig.4**. The figure reveals that $N_i$ fluctuates within a certain period and the impedance is large at $N_i$=1.9 and 2.9. Therefore, it is effective to set $L_{DV}$ with a fractional part of 0.9.

## 6. Examination of Vibrating Plate with Various Surface Areas

In the case of a vibrating plate with a driving point at its center, $N_L$ is an even number[1]. $N_L$ was also examined experimentally. In the experiment, $N_W$ and $L_{DV}$ were fixed at 5.0 and 2.9, respectively, on the basis of the above results, and $N_L$ was changed in steps of 1 from 1 to 32 to examine. The stripe mode was not observed at resonance at $N_L$=15, 18, 21, 24, 27, and 30. At other values of $N_L$, the stripe mode was observed at resonance.

## 7. Quality Factor

For values of $N_L$ at which the stripe mode was observed at resonance, an admittance loop was observed by changing the frequency. The quality factor was calculated for values of $N_L$ at which the stripe mode was observed at resonance. The result is shown in **Fig.5**. In the figure, the quality factor is small when $N_L$ is 5 or less, even though the stripe mode is observed at resonance. However, when $N_L$ is 6 or more, the quality factor, although slightly fluctuating, essentially remains constant at approximately 1,000. Therefore, it was found to be desirable to fabricate the stripe-mode transverse vibrating plate with the jutting driving point by setting $N_L$ to be 6 or more.

## 8. Conclusions

In order to realize smooth driving of the stripe-mode transverse vibrating plate with the jutting driving point, the numerical value of $N_W$ and $N_i$ of the vibrating plate was varied to experimentally elucidate its optimal condition. As results, the following were clarified: effective to set $N_W$ to be an odd natural number, similar to the case of the stripe-mode square transverse vibrating plate, and effective to set $L_{DV}$ with a fractional part of 0.9. From the above results, the area of the vibrating plate was experimentally examined by varying the length of the side perpendicular to the node line of the vibrating plate under the conditions of $N_W$=5.0 and $L_{DV}$=2.9. As a result, it was found that $N_L$ should be at least 6, but not a multiple of 3 greater than or equal to 15.

When a stripe-mode transverse vibrating plate with a jutting driving point is fabricated under the above conditions, it is possible to smoothly drive the plate in the stripe mode at resonance.

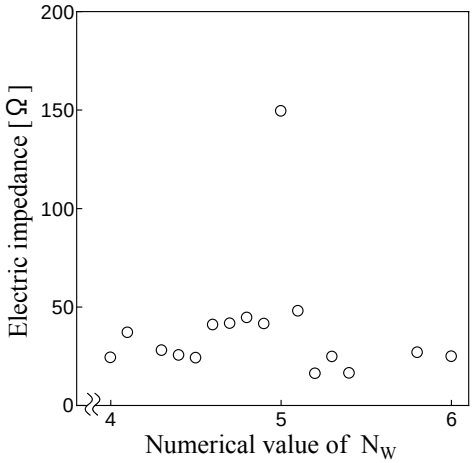


Fig.3 Relationship between numerical value of $N_W$ and electric impedance.

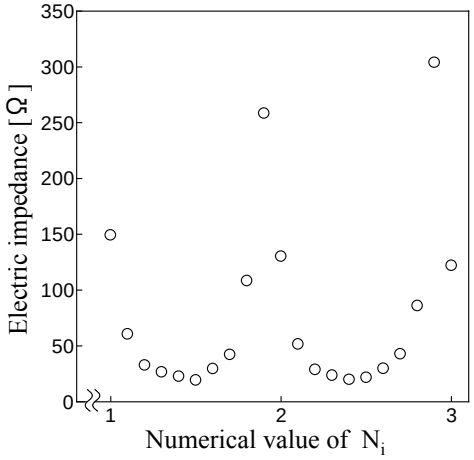


Fig.4 Relationship between numerical value of $N_i$ and electric impedance.

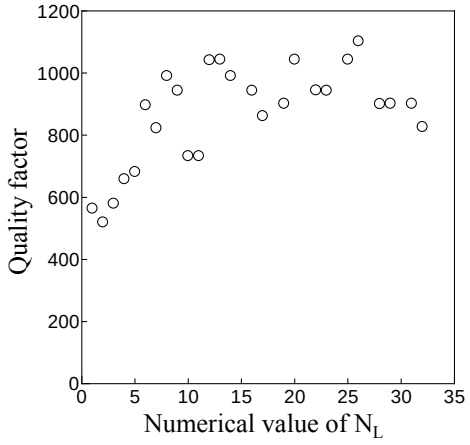


Fig.5 Relationship between numerical value of $N_L$ and quality factor.

## References


1. H. Yamane and M. Kawamura: Nihon Onkyo Gakkai-Shi **32** (1976) 83 [in Japanese].
2. H. Miura: Nihon Onkyo Gakkai-Shi **50** (1994) 677 [in Japanese].

Proceedings of Symposium on Ultrasonic Electronics, Vol. 29 (2008) pp. 479-480
11-13 November, 2008

# Examination of Method for Judging Heat Receiving of Mortar by Using Aerial Ultrasonic Waves Having Finite Amplitudes.
# 有限振幅の空中超音波を用いてモルタルの受熱を判定する方法の検討

Youichi Ito, Naoto Asakura† (Sci. and Tech., Nihon Univ.)
伊藤洋一，朝倉直人† (日大・理工)

## 1. Introduction

We excited a mortar sample exposed to heat in a non-contact way [1] by using high-intensity aerial converging ultrasonic waves (20 kHz) with finite amplitude, and determined the influence of the heat receiving by analyzing the vibrations of the mortar sample. This report discusses the relationship between irradiation intensity of the sound waves and the vibration velocity for a mortar sample exposed to heat, with the converging point of the ultrasonic waves coincident with the surface of the mortal sample. It also discusses the possibility of determining the state of the mortar sample exposed to heat by analyzing the harmonic vibrations (40 to 100 kHz) of the sample produced by irradiating the sound waves with finite amplitude.

## 2. Sound Source and Experimental Method

Figure 1 shows the schematic view of the experimental device. We used the point-converging acoustic source with stripe-mode vibration plate to generate high-intensity aerial ultrasonic waves with finite amplitude.[2] The ultrasonic waves radiated by this sound source converged into a circular section 10mm in diameter 140mm from the opening of the sound source, and provided intensive ultrasonic waves of about 4000 Pa at the supplied power of 50 W. In the experiment, the center on the surface of the mortar sample was made to coincide with the converging point O of the radiated sound waves, as shown in Fig. 1. The sample was continuously irradiated with ultrasonic waves, and vibration displacements on the sample face irradiated with the sound waves were measured using a laser Doppler displacement meter. Table Ⅰ gives the detailed characteristics of the mortar samples used for the experiment. We used a mortar sample (MS20) at the

yitoh@ele.cst.nihon-u.ac.jp

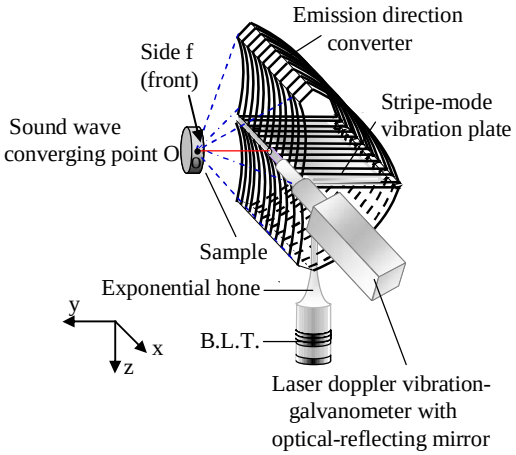


Fig. 1 Ultrasonic source and device used for experiment.

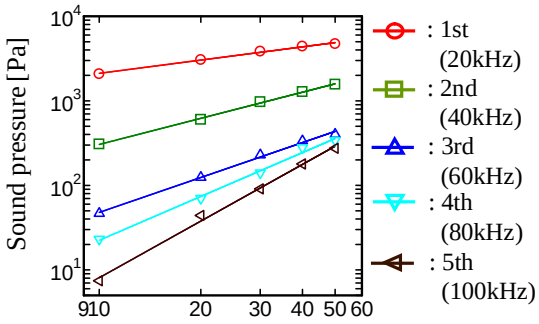


Fig. 2 Characteristics of ultrasonic waves at the converging point.

Table Ⅰ Details of samples.

| mortar | normal (MS20) | 500 ℃ (MS500) | 1000 ℃ (MS1000) |
|---|---|---|---|
| diameter [mm] | 49.96 | 50.46 | 50.50 |
| thickness [mm] | 21.42 | 19.84 | 19.52 |
| weight [g] | 91.08 | 76.88 | 71.48 |
| volume [m³] | 4.197 ×10⁻⁵ | 3.966 ×10⁻⁵ | 3.908 ×10⁻⁵ |
| density [kg/m³] | 2170 | 1939 | 1829 |

normal temperature (20 ℃) as well as the samples exposed to the atmosphere at 500 ℃ (MS500) and 1000 ℃ (MS1000) respectively for about 30 minutes.

### 3. Characteristics of Irradiated Sound Waves and Vibration Velocity Characteristics of Mortar Samples

Figure 2 shows the relationship between the sound pressure and the power supplied to the sound source, measured on the face (at point O) of the sample. Because the sound waves with finite amplitude was used, the fundamental to fifth harmonic waves (20 kHz to 100 kHz) were produced, as shown in the figure. Figures 3 and 4 show the vibration velocity characteristics of the samples MS20 and MS1000 respectively. The figures indicate that two samples vibrated at the frequencies corresponding to the fundamental and harmonic sound waves respectively. In comparison between the harmonic components of the two samples, it was found that the sample MS1000 had a vibration velocity increasing at a higher rate than the sample MS20, as the sound pressure was higher.

### 4. Determination rate of Vibration and Influence of Heat Receiving

Figure 5 shows the relationship between the vibration velocity at the fundamental frequency and the harmonic component rate (distortion rate) for each sample. The figure indicates that each of the samples had a higher distortion rate as a higher electric power was supplied, that it had a higher distortion rate as the exposure to heat had a greater influence on the sample. If the same electric power is supplied to the sound source, each of the samples had a higher distortion rate as the exposure to heat had a greater influence on the sample. It is obvious that samples had different distortion rates.

### 5. Conclusions

When a mortar sample was excited in a non-contact way by using high-intensity aerial point-converging ultrasonic waves (20 kHz) with finite amplitude, the sample vibrated at the frequencies corresponding to the fundamental and harmonic sound waves respectively. Moreover, it was revealed that the sample's ratio of vibration velocity at harmonics to that at the fundamental frequency depended on the influence that the exposure to heat had on the sample. It is also obvious that the sample had a ratio of vibration velocity depending on the influence of the exposure to heat. Therefore, it may be possible to determine how much a mortar sample is exposed to heat.

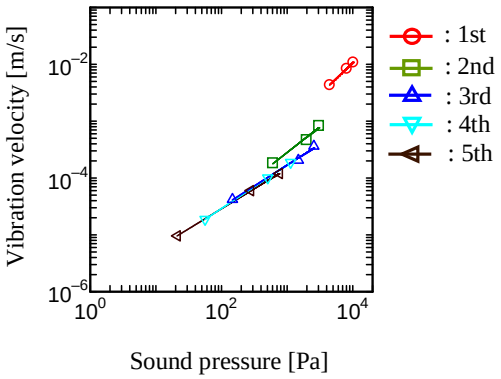


Fig. 3 Relationship between sound pressure and vibration velocity of sample MS20 at the converging point.

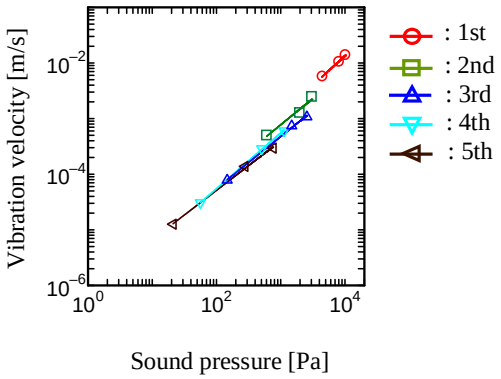


Fig. 4 Relationship between sound pressure and vibration velocity of sample MS1000 at the converging point.

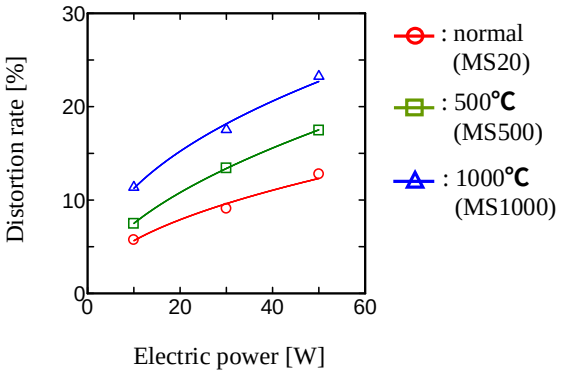


Fig. 5 Relationship between Electric power and Distortion rate.

### References

1. Y. Ito, A. Oosumi and N. Asakura: Jpn. J. Appl. Phys. **47** (2008) 4292.

2. Y. Ito: J. Acoust. Soc. Jpn. **46** (1990) 383-390.

3P8-15

Proceedings of Symposium on Ultrasonic Electronics, Vol. 29 (2008) pp. 481-482
11-13 November, 2008

# Linearly convergent Type Aerial Ultrasonic Source with Changeable Incidence Angle of Sound Waves and Its High-Intensity Sound Field.

音波の入射角度を変更できる線集束空中超音波音源とその音場

Youichi Ito† (Sci. and Tech., Nihon Univ.)
伊藤洋一† (日大・理工)

## 1. Introduction

It is considered that the method of utilizing the acoustical radiation force of high-intensity aerial ultrasonic waves may be used to retain any small solid object or liquid on the surface of an object within the specific long and narrow region in the non-contact way. [1] In this research, we used the linearly convergent type aerial ultrasonic source [2] that had been developed. To use this method, it was indispensable to form a standing-wave ultrasonic field along the surface of an object. However, the existing method of emitting sound waves from a sound source could not form any standing-wave sound field along the surface of an object. Thus, we developed the method of changing the incident angle of a converged sound waves relative to the surface of an object by combining the conventional linearly convergent type sound source with a new emission direction converter.

## 2. Principle and Characteristics of Sound Source

The conventional linearly convergent type ultrasound source comprises the combination of a stripe-mode flexible vibration plate and a emission direction converter A, as shown in Fig. 1, and can make linearly convergent the sound waves radiated from the both faces of the vibration plate so that the length of the converged sound wave is almost equal to that of the vibration plate. The converter A comprises the same number of isolating plates as that of nodal lines on the stripe-mode vibration plate, and the parabolic reflecting plates inserted between the isolating plates. A new convergent-type sound source is provided by combining the direction converter B. Figure 2 shows the cross-sectional views of the converters A and B placed on the both faces of the vibration plate respectively. The converter B has the same number of isolating plates as the converter A, and two types of parabolic reflecting plate b and c are placed between the isolating plates. The two parabolic reflecting plates have different focal lengths from each other, though they have their focal point at the point O and their tops on the axis z. Therefore, the sound waves radiated from the vibration plate will

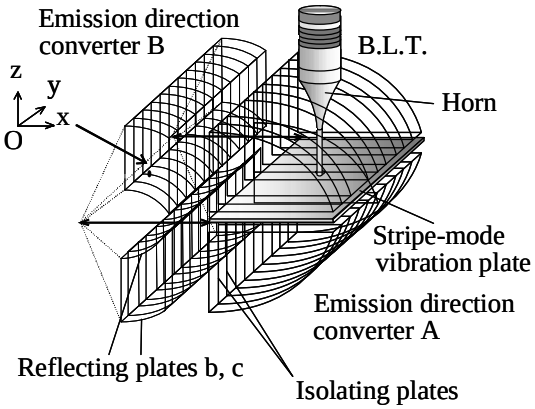


Fig. 1 Schematic sketch of new linearly convergent ultrasonic source.

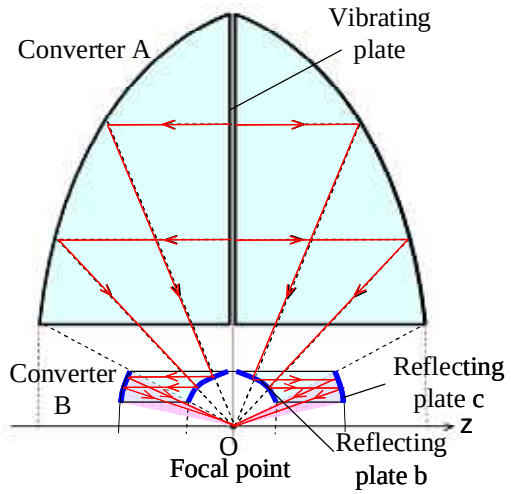


Fig. 2 Arrangement of two converters and converging of the ultrasonic waves.

yitoh@ele.cst.nihon-u.ac.jp

be reflected by the reflecting plate a to go toward the focal point 0, and then reflected by the reflecting plate b to propagate in the direction along the axis z. Subsequently, the sound waves reflected by the reflecting plate c will be incident into the focal point 0 in the same phase, and converge.

Next, the basic characteristics of the linearly convergent type sound source (frequency: 19.0kHz, electric input power: 2W) will be described. The solid lines as shown in Fig. 3 (a) to (c) indicate the sound waves converging characteristics of the sound source comprising only the converter A. The dot lines as shown in Fig. 3 indicate the sound waves converging characteristics of the sound source comprising the converters A and B. The figure indicates that the sound waves radiated from the vibration plate linearly converged. Here, the results as shown in Fig. 3(b) are compared with each other. The figure indicates that the wavelength in the direction z is about 56mm for the solid line and about 25mm for the dot line. Considering these wavelengths as those in the direction z in the sound field that is formed when two plane waves are obliquely incident in the directions opposed to each other, the incident angle relative to the axis z is about 72º in solid line and about 44º in dot line. This means that the incident angle of the sound waves converging into the convergent point can be changed by combining the converter A with the converter B. The higher standing-wave ratio in the sound field, as shown by the dot line, indicates that a good standing-wave sound field is formed along the surface of an object.

### 3. Conclusion

We proposed a new method of changing the incident angle of the converged sound waves emitted by the linearly convergent type aerial ultrasonic source, tentatively made the model of the system using this method, and experimentally demonstrated the method. The results indicate that it was possible to change the incident angle of the converged sound waves emitted by the conventional linearly convergent type sound source (19 kHz). We also confirmed that it was possible to form the desired standing-wave sound field.

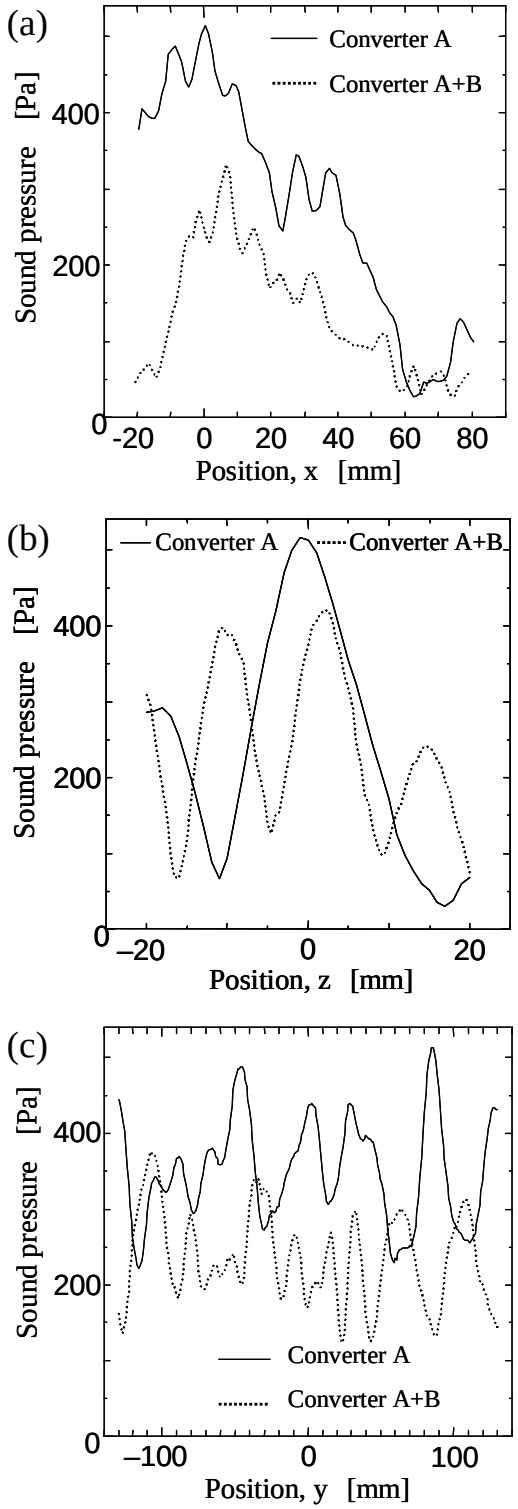


Fig. 3 Distribution of sound pressure in the vicinity of the converging point. (a): in the direction of the x-axis, (b): in the direction of the z-axis, (c): in the direction of the y-axis.

### References

1. Y. Ito, A. Oosumi and N. Asakura: Jpn. J. Appl. Phys. **47** (2008) 4292.
2. Y. Ito: J. Acoust. Soc. Jpn. **42** (1986) 621-629.

3P8-16

Proceedings of Symposium on Ultrasonic Electronics, Vol. 29 (2008) pp. 483-484
11-13 November, 2008

# Applying diverging tube for the low temperature drive on the loop-tube type thermoacoustic system

ループ管型熱音響システムの低温度差駆動に向けた分岐管の利用

Takahiro Ishino[1‡], Shin-ichi Sakamoto[2], Masahiro Nishikawa[3], and Yoshiaki Watanabe[4]
([1,3,4] Doshisha University; [2] University of Shiga prefecture)
石野貴廣[1‡]，坂本眞一[2]，西川昌宏[3]，渡辺好章[4]（[1,3,4] 同志社大; [2] 滋賀県立大）

## 1. Introduction

Global warming, which results from greenhouse gas emissions, has become a major task confronting human society. In fact, large quantities of greenhouse gases generated to drive cooling systems have been exhausted by wasteful systems. To make efficient use of waste energy, we specifically examine the loop-tube[1], which is a thermoacoustic cooling system that can use waste energy effectively as a driving energy source. A loop-tube is an applied thermoacoustic phenomenon[2]: a loop-tube converts heat energy to and from sound energy.

## 2. Theory

The stack is the most important device in this system. The loop-tube is driven by forming an extreme temperature difference at the tops and bottoms of a stack at the prime mover. Temperature differences should exist at a low temperature to use waste energy effectively at comparatively low temperatures at factories and other installations. For driving by low temperature differences, it is particularly important to improve energy conversion efficiency. Therefore, it is necessary to adjust the phase difference between the pressure and particle velocity at a prime mover stack[3]. We use the method of a loop-tube with a diverging tube. A boundary condition by which the particle velocity slows in the divergence path is added for the cross section in the divergence part extension. According to this boundary condition, the sound field is controlled to generate the node of the particle velocity, which is the antinode of pressure in the divergence part. Consequently, the phase difference between the pressure and the particle velocity at a prime mover stack is adjusted. This report specifically describes the effect that the installation position of diverging tube exerts on the sound field.

## 3. Experimental system and method

A block diagram of the measurement system is illustrated in **Fig. 1**. For the effect of diverging tube, heat pump was not set. Tops of the stack were defined to be 0 m. The tube center is the axis; clockwise was defined as the positive direction. The system was constructed with a stainless steel tube of 1.01 m length, 0.5 m width, and 3.62 m total length. Its inner diameter was 42 mm. The system was filled with air at atmospheric pressure. The stack was a 50-mm-long honeycomb ceramic with a channel radius of 0.47 mm. A spiral type electrical heater inserted at the upper part of a stack served as the heat source; a heat exchanger to keep the room temperature was placed at the lower part of a stack. The inner diameter of the diverging tube was equal to that of the loop-tube: 42 mm. The loop-tube's length from the upper side to the lower side was 0.4 m, as depicted in Fig. 1. Diverging-tube connecting positions of four kinds were changed so that the position from the heater to the upper part of the diverging tube side was 1.79 m, 1.89 m, 1.99 m, or 2.09 m.

Heating power of 330 W was supplied for 600 s using a heater. Pressure sensors (PCB Inc.) were set on this system wall to measure the sound pressure in the loop-tube. Furthermore, the temperature of the upper part of a stack was measured using K-type thermocouples. Measurements of sound pressure and temperature started when heat energy was supplied. They were carried out for 900 s.

The pressure, the phase difference between the pressure and particle velocity, and the amount of sound intensity in this system were calculated using the two-sensor power method with pressure measurement results[4,5].

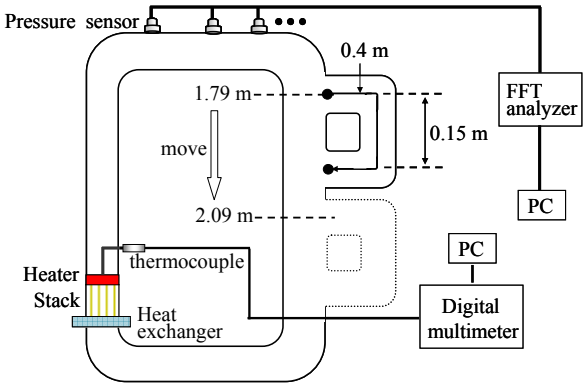


Fig. 1 Diagram of measurement system.

## 4. Results and discussion

**Figure 2** shows the distribution of the sound intensity with and without a diverging tube in the system. **Fig. 3** depicts the change of temperature at the upper part of a stack. Fig. 2 shows that the amount of sound intensity with a diverging tube in the system is higher than that of the non-diverging tube. The sound intensity was highest when we set up a diverging tube at the position of 1.99 m. At this position, the conversion efficiency from heat energy to sound energy in the stack improved by about 18 times compared to that of the non-diverging tube. In addition, the temperature of the top of a prime mover stack was decreased about 500°C, from 845°C to 345°C, compared to that of the non-diverging tube. It is considered that the energy conversion improvement is major factor to induce low temperature. The sound field in the loop tube was adjusted by the diverging tube. Therefore, the phase difference in the stack approached an appropriate phase difference at which the heat exchange occurred efficiently. **Fig. 4** portrays the distribution of sound pressure in the loop-tube with and without the diverging tube. That figure shows clearly that the sound field was controlled so that the antinode of the sound pressure, the node of particle velocity, was excited in the divergence part. The phase difference distribution was controlled similarly. The phase difference between the pressure and the particle velocity at the prime mover stack was adjusted to improve the energy conversion efficiency.

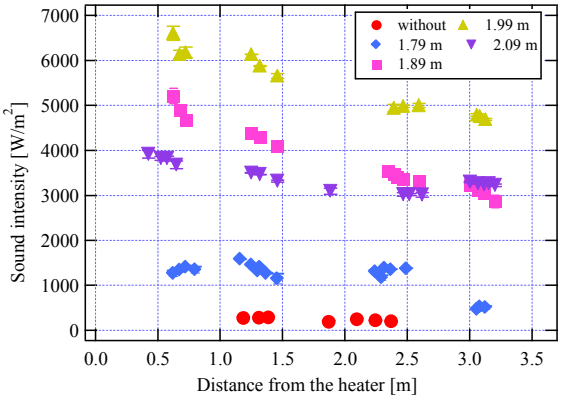


Fig. 2 Distribution of sound intensity in loop-tube.

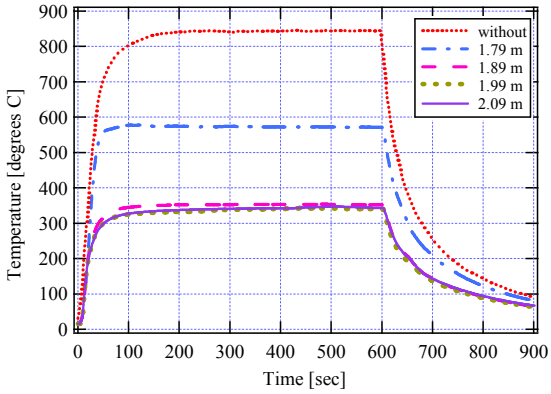


Fig. 3 Temperature variation of top of a stack.

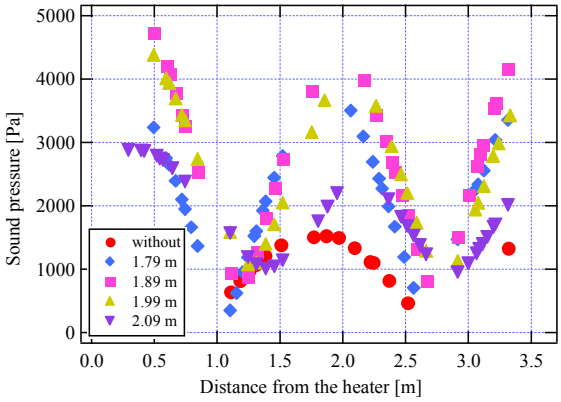


Fig. 4 Distribution of sound pressure in loop-tube.

## 5. Conclusions

This report described a design method of a loop-tube type thermoacoustic cooling system with a diverging tube for low temperature driving. By adjusting the installation position of the diverging tube, the conversion efficiency from heat energy to sound energy in the stack was improved by about 18 times. As a result, the device was driven by the low temperature difference; the steady temperature of the top of the prime mover stack was decreased about 500°C. This method adjusted the phase difference in the prime mover stack to perform heat exchange efficiently between the working gas and the stack wall.


## Acknowledgment

This research was partially supported by a Ministry of Education, Culture, Sports, Science and Technology Grant-in-Aid for Young Scientists (B), 2007


## References


1. S. Sakamoto *et al*. :Jpn. J. Appl. Phys. **45** (2006) 9257.
2. G. W. Swift : J. Acoust. Soc. Am. **84** (1998) 1145-1180.
3. P. H. Ceperley :Acoust. Soc. Am. **66** (1979) 1508.
4. A. M. Fusco, W. C. Ward, and G. W. Swift, J. Acoust. Soc. Am. **91**(4) (1992) 2229–2235.
5. T. Biwa, Y. Ueda, T. Yazaki, and U. Mizutani, Cryogenics **41** (2001) 305–310.

Proceedings of Symposium on Ultrasonic Electronics, Vol. 29 (2008) pp. 485-486
11-13 November, 2008

# Effect of lamination mesh on energy conversion from sound to heat in thermoacoustic system

熱音響システムにおいて積層メッシュが音から熱へのエネルギー変換に及ぼす影響

Atsushi Sakaguchi[1†], Shin-ichi Sakamoto[2], Tsuji Yoshiyuki[1] and Yoshiaki Watanabe[1]
([1] Doshisha Univ., [2] Univ. of Shiga Pref.)
坂口敦[1‡], 坂本眞一[2], 辻良行[1], 渡辺好章[1]（[1]同志社大, [2]滋賀県立大）

## 1. Introduction

A loop tube is a thermoacoustic cooling system. The loop tube consists of a prime mover and a heat pump. Heat energy is converted to sound energy at the prime mover and sound energy is converted to heat energy at the heat pump by application of the thermoacoustic effect[1–3]. A stack having very narrow channels is in the prime mover and the heat pump. We have studied energy conversion in the stack of the heat pump using an acoustic tube with a connected compression driver, for example, a loudspeaker, etc. A previous work[4] suggested that the best insertion position of the stack is uniquely determined when the driving frequency and channel radius of the stack are varied under identical $\omega\tau$[4, 5], which is the parameter controlling energy conversion. Furthermore, the best insertion positions approach the acoustic tube's center by decreasing the value of $\omega\tau$. These results demonstrate that the value of $\omega\tau$ can be a useful index of the insertion position of the ceramic stack.

For practical application of the loop tube, it is important to improve its energy conversion efficiency. Increasing the number of stack channels is effective to increase the thermal boundary layer in which energy conversion between the oscillating gas and the stack wall occurs. In addition, reducing the channel radii of the stack increases the number of channels. Consequently, reducing the channel radii of the stack is equivalent to increasing the thermal boundary layer. It is difficult for a ceramic stack to reduce the channel radii of the stack because of presently used manufacturing techniques. Therefore, we use a lamination mesh which is formed by piling up stainless mesh pieces to reduce the channel radii of the stack; however, the cooling property of the lamination mesh remains unclear and the value of $\omega\tau$ using the lamination mesh cannot be calculated. This study investigates cooling characteristics of the lamination mesh and examines the value of $\omega\tau$ and the channel radius of the lamination mesh.

## 2. Theory

The parameter $\omega\tau$ is expressed by the following equation [5].

$$\omega\tau = \omega\frac{r^2}{2\alpha} \qquad (1)$$

In that equation, $r$ denotes the channel radius of the stack and $\alpha$ is the thermal diffusivity, and $\omega$ is the angular frequency of the sound wave. When temperature of the working gas is constant, $\omega\tau$ depends on only the resonant frequency and the channel radius of the stack.

## 3. Experimental setup

A block diagram of the measurement system is shown in **Fig. 1**. The loudspeaker was put into one side of the acoustic tube; the other side is a closed end. The driving frequency is set as 100 Hz to generate a one-wavelength mode. In this experiment, meshes of three types were used, the mesh numbers of the lamination meshes—the number of meshes per inch—were 10, 20, and 40. The lamination mesh thickness is 15.0 mm; the laminating pattern is random. The loudspeaker side of the acoustic tube is defined as forward. The closed end side is defined as backward. Backward of the lamination mesh is defined as the insertion position of the lamination mesh and a measurement point of the temperature change. The insertion position of the lamination mesh was moved from 1.60 to 1.85 m. The temperature change was measured using a K-type thermocouple.

## 4. Results

**Figure 2** presents temperature measurement results. This figure shows that every temperature

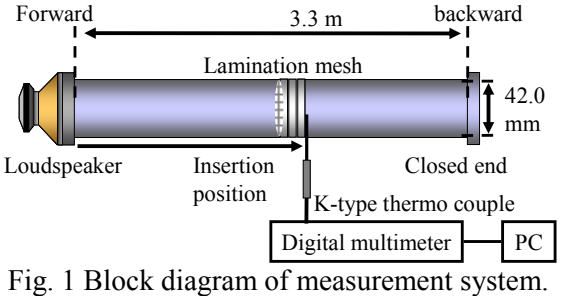


Fig. 1 Block diagram of measurement system.

measurement is a temperature decrease. A three-dimensional approximate curve was calculated, as shown in **Fig. 3**, to estimate each peak position of the temperature decrease. From these results, the peak positions of each lamination mesh were observed. The peak positions of 10, 20, and 40 mesh were 1.74, 1.70, and 1.66 m.

## 5. Discussion

Peak positions were normalized by the length of the acoustic tube to simplify these results. As it turns out, normalized peak positions of 10, 20, and 40 mesh were 0.527, 0.515, and 0.503. Therefore, the normalized peak positions come closer to center of the acoustic tube because of the increased mesh number. An increasing mesh number is similar in its effect to a reduction of channel radii. Furthermore, from eq. (1), reducing the channel radii is equivalent to decreasing the value of $\omega\tau$. Consequently, the normalized peak positions come closer to the center of the acoustic tube because of the decrease in $\omega\tau$. In the previous work[4], the normalized peak positions of the ceramic stack come closer to the center of the acoustic tube by decreasing the value of $\omega\tau$. The experimental results reveal a tendency resembling that shown by a ceramic stack.

In addition, values of $\omega\tau$ using the lamination mesh were estimated from the previous work and experimental results. **Figure 4** shows results of previous work related to the normalized peak position under each value of $\omega\tau$ using a ceramic stack and relevant experimental results. Results show that $\omega\tau$ of 10, 20, and 40 mesh were approximately 1.3, 1.0, and smaller than 1.0. Moreover, channel radii of the lamination mesh were calculated from these values of $\omega\tau$. Channel radii of the lamination mesh using 10, 20, and 40 mesh were approximately 0.3, 0.2, and smaller than 0.2 mm. These results suggest that the same design method is adaptable to the use of a lamination mesh and a ceramic stack.

## 6. Conclusion

Experiments were carried out by changing the mesh number and the insertion position of the lamination mesh using the acoustic tube to measure the cooling characteristics of the lamination mesh. The experimental results reveal a tendency similar to that of a ceramic stack. Values of $\omega\tau$ and the channel radius of the lamination mesh were estimated in the previous work. Results presented herein suggest that the same design method can be adapted to use of the lamination mesh and a ceramic stack.


## Acknowledgment

This research was partially supported by a Ministry of Education, Culture, Sports, Science and Technology Grant-in-Aid for Young Scientists (B), 2007


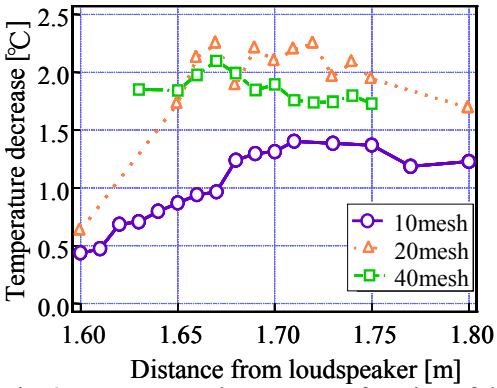


Fig. 2 Temperature decrease as a function of the stack distance from the loudspeaker.

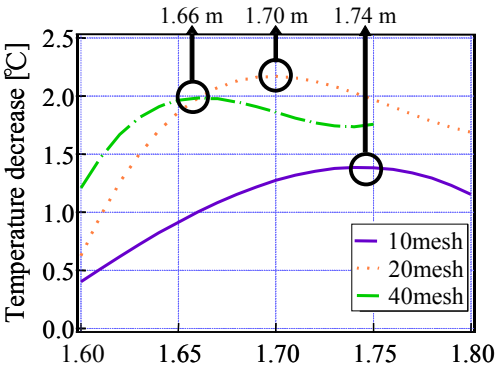


Fig. 3 Temperature decrease as a function of the stack distance from the loudspeaker (three-dimensional approximated curve).

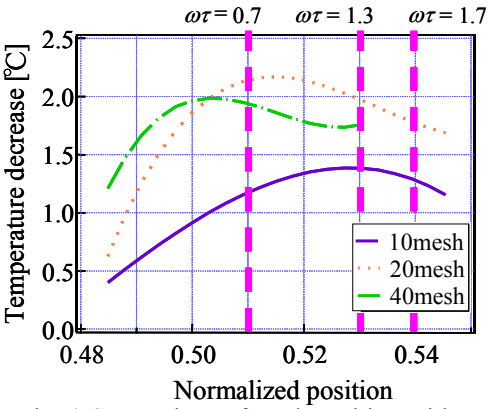


Fig. 4 Comparison of stack position with $\omega\tau$.

## References


1. P. H. Ceperley, J. Acoust: Soc. Am. 77 1239-1244 (1985)
2. S. Backhaus, G. W. Swift: Nature 339, 335-338 (1999)
3. S. Sakamoto, Y. Watanabe: Acoust. Sci. & Tech., 27(6), 361-365(2006)
4. Y. Tsuji, S. Sakamoto, T. Ishino, Y. Watanabe, J. Senda: Jpn. J. Appl. Phys. 47, 4231-4264(2008)
5. A. Tominaga: Netsuonkyo-kougaku-no-kiso (Fundamentals of Thermoacoustics), (Utidaroukakuho, Tokyo, 1998) pp. 117 [in Japanese].

3P8-18

Proceedings of Symposium on Ultrasonic Electronics, Vol. 29 (2008) pp. 487-488
11-13 November, 2008

# The Effect of Membrane Insert Position on the Acoustic Field in a Thermoacoustic System

# 熱音響システムにおいて薄膜の設置位置が管内音場に与える影響

Masahiro Nishikawa[1†], Shin-ichi Sakamoto[2], Takahiro Ishino[3] and Yoshiaki Watanabe[4]
([1,3] Facult. Eng., Doshisha Univ.; [2] Facult. Eng., The Univ. of Shiga prefecture; and [4] Facult. Life and Med. Sci., Doshisha Univ.)
西川昌宏[1‡], 坂本眞一[2], 石野 貴廣[3], 渡辺好章[4]
([1,3]同志社大 工; [2]滋賀県立大 工; [4]同志社大 生命医科)

## 1. Introduction

Although progress in science and technology has brought us many amenities, it has depleted natural energy resources. From the standpoint of grobal emvironment conservation, the issue of fossil fuel depletion is especially important, but switching to alternative fuels has social, economic, and technological problems. Therefore we focus on efficent use of energy, and study the practical application of the thermoacoustic cooling system which can utilize waste heat. The system uses the thermoacoustic phenomenon[1] which enables interconversion between heat and sound energy.

In this report, we conducted an experiment with membrane varying its position for the purpose of adjusting the acoustic field in the loop-tube type thermoacoustic system and discussed its effect.

## 2. Theory

**Figure 1** shows the schematic view of the loop-tube and a photograph of a stack. The thermoacoustic phenomenon realize heat energy transport by heat exchange between medium and the channel walls in the stack, and simultaneous medium oscillation. Phase difference between sound pressure and particle velocity affects energy transport in the stack. It is known that energy conversion efficiency from heat to sound reaches its maximum when the phase difference nearly equals to 0 degree[2,3] at the prime mover. Therefore the phase difference becomes important when the phenomenon is used.

In the loop-tube, the prime mover produces the medium's self-oscillation. The wave length of the sound equals to the total length of the loop-tube. Node of particle velocity and antinode of sound pressure distribution are observed near the prime mover.

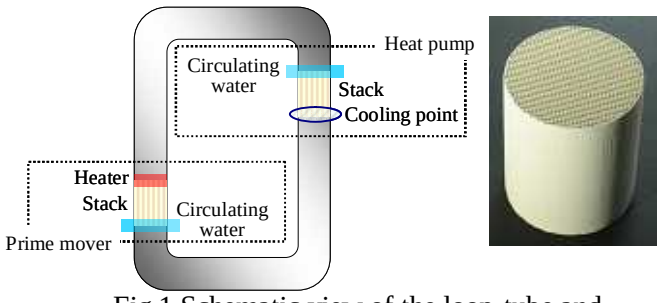


Fig.1 Schematic view of the loop-tube and a photograph of a stack.

When a membrane is inserted to the loop-tube, it adds a new boundary condition which makes particle displacement smaller to the insert position. Particle velocity is in proportion to particle displacement; therefore membrane insertion shifts the acoustic field along the tube axis, and the distribution of phase difference.

## 3. Experiment

**Figure 2** shows the experimental system. We compared acoustic fields varying in insert position of membrane above the prime mover to the acoustic field without membrane. The heat pump was eliminated from the experimental system to simplify the observation. Measuring points were defined clockwise with the axis centered in the tube and a HHEX set at 0 mm. The membrane was made of L-LDPE and its thickness was 0.06 mm. The system was constructed with stainless tube of 2800 mm in total length and the inner diameter was 42 mm. The thickness of the stack was 50 mm and the radius of stack channels was 0.47 mm. Air was filled in the system at the atmosphere pressure. The HHEX was a spiral type electric heater at the top side of the stack. The room temperature HEX was made of copper and the temperature was kept consistent by circulating water. Heat input energy from HHEX was 330 W.

The measuring time was 1000 seconds, with the heat supplied for the first 600 seconds only. 8 pressure sensors were set on the inner wall of the tube to observe acoustic field in the system, and obtained data was used to determine distribution of sound pressure, particle velocity, phase difference between them, and sound intensity by two-sensor power method[4].

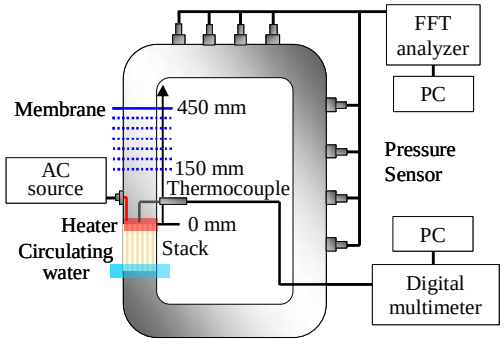


Fig.2 Block diagram of the experimental system.

## 4. Results and Discussion

**Figure 3** shows the distribution of sound intensity at 400 seconds after heat supply started. Dashed thick line in **Fig.3** indicates each position of the membrane. The most remarkable point in this figure is that the sound intensity increased as the membrane was moved closer to the prime mover in this measurement range. The three possible reasons are as follows:

The first reason is the adjustment of phase difference between sound pressure and particle velocity at the position of the prime mover by shifting distribution of phase difference. The distribution of phase difference shown in **Fig.4** indicates that the phase difference at the prime mover came close to a suitable value as described in Chapter 2 "Theory."

The second reason is decrease in viscous resistance in the channels of the stack caused by the shift of distribution of particle velocity. **Fig.5** shows the distribution of particle velocity at 400 seconds after heat supply started. This figure indicates that as the membrane was moved closer to the prime mover, the node of particle velocity distribution came to the prime mover. As a result, particle velocity in the stack channels decreased to reduce viscous resistance.

The last reason is decrease in viscous resistance in the stack channels caused by thinning of viscous boundary layer. Due to the aforementioned two reasons, the energy conversion efficiency from heat to sound was improved to thin the viscous boundary layer. As a result, temperature of top side of the stack decreased, and the viscous resistance decreased.

As an addional insight in **Fig.3**, there were increases in sound intensity distribution when the membrane was at 150 and 200 mm. It suggests that membrane insertion caused suppression of mass flow[2,5] in this system to improve the energy conversion efficiency from heat to sound.

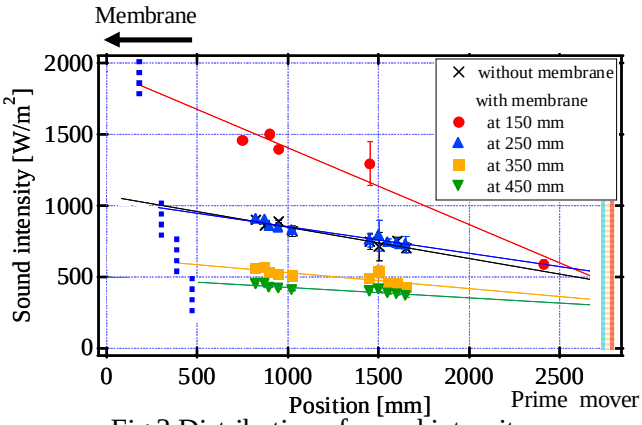


Fig.3 Distribution of sound intensity; at 400 sec. after heat supply started.

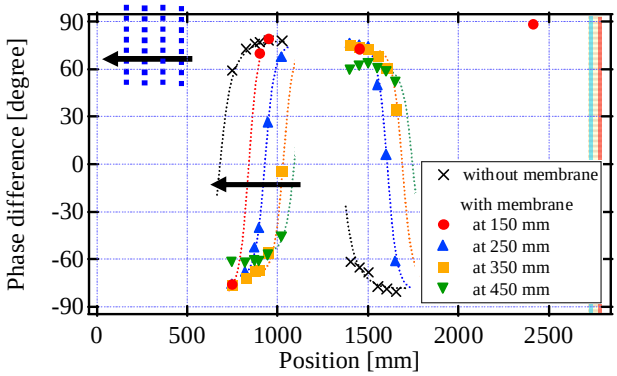


Fig.4 Distribution of phase difference between sound pressure and particle velocity; at 400 sec. after heat supply started.

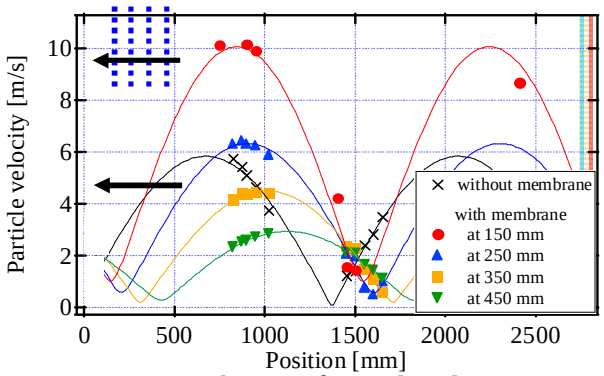


Fig.5 Distribution of particle velocity; at 400 sec. after heat supply started.

## 5. Conclusions

Our experiment was aimed at adjustment of acoustic field, especially phase difference between sound pressure and particle velocity in a loop-tube type thermoacoustic cooling system.

We focused on the change in distribution of phase difference when insert position of the membrane was varied at certain input heat energy.

It was found that the sound intensity increased as the insert position of the membrane became closer to the stack. This was due to higher energy conversion efficiency from heat to sound. It is considered that the improvement of the efficiency was achieved by the adjustment of phase difference between sound pressure and particle velocity at prime mover, and decrease in viscous resistance in the stack channels.


## Acknowledgment

This research was partially supported by a Ministry of Education, Culture, Sports, Science and Technology Grant-in-Aid for Young Scientists (B), 2007.


## References


1. A. Tominaga: (Uchida roukakuho, Tokyo, 1998.)[in Japanese]
2. Y.Imamura, S.Sakamoto and Y.Watanabe, Jpn. J. Appl. Phys., 46(7A), 4417-4420, 2007.
3. P. H. Ceperley, Acoust. Soc. Am. 66 (1979) 1508.
4. Andrew M.Fusco, William C. Ward, and Gregory W. Swift, J. Acoust. Soc. Am. 91(4), (1992)
5. S.Sakamoto, T.Tsujimoto and Y.Watanabe, Jpn. J Appl. Phys. 38, (1999).



(dth0155[†1],dth0118[3])@mail4.doshisha.ac.jp,
(ssakamot[2],kwatanab[4])@mail.doshisha.ac.jp

3P8-19

Proceedings of Symposium on Ultrasonic Electronics, Vol. 29 (2008) pp. 489-490
11-13 November, 2008

# Rotation Phase Analysis of Surface Particle Motion of Coiled Waveguide for Flexural Ultrasound Wave

屈曲超音波伝搬路における表面粒子運動の回転位相解析

Ryo Tanaka†, Masayuki Tanabe, Kohei Tomoda, Kan Okubo and Norio Tagawa
(Faculty of System Design, Tokyo Metropolitan Univ.)
田中亮‡，田邉将之，友田耕平，大久保寛，田川憲男（首都大システムデザイン）

## 1. Introduction

We have developed a traveling wave-type miniature ultrasonic motor using a helical coiled waveguide as a stator, which is called CS-USM (Coiled Stator Ultrasonic Motor)[1], and have already applied it to an IVUS (Intravascular Ultrasound) probe.[2-4] In this motor, the elliptical motion of the surface particle due to the flexural ultrasonic waves rotates the rotor, which can be placed adjacently inside or outside the stator, via the frictional force. For high frequencies, rotational directions of both of the inner rotor and the outer rotor are consistent with those of usual traveling wave-type ultrasonic motor. However, for low frequencies, the outer rotor rotates inversely. In the previous studies, we examined the rotational direction of the surface particle motion of a coiled waveguide for low frequencies, and we clarified that the direction at the inner surface and the direction at the outer surface are the same, which is not realized by a straight-line waveguide.[5,6] In this study, we examine the rotation phase at the both surfaces through simulations.

## 2. Methods

In this study, using the PZFlex, which is a standard FEM simulator for ultrasound propagation, and modeling a helical coiled waveguide with a stainless steel wire, we simulate the surface particle motion due to traveling flexural waves at both of the inner and the outer surfaces for low frequencies.

In the simulations, the density of the stainless steel wire is set as 7910 $kgm^{-3}$, the sound speed of longitudinal wave is 5790 m/s, and the sound speed of transverse wave is 3100 m/s. The width and the thickness of it are set respectively as 0.3 mm and 0.1 mm, and the inner diameter of the helical coiled structure is 0.3 mm.

## 3. Results

**Figure 1** shows the direction of the surface particle's motion qualitatively. **Figure 2** shows the actual loci of the surface particle obtained through simulations for the low frequency of 0.3 MHz. In this figure, "r-dir" indicates the radial direction of the coil, and "θ-dir" indicates the direction of wave propagation. The loci are decomposed into the r-dir component and the θ-dir component, and these are analyzed as a time series in **Fig. 4** to examine the rotation phase. In Fig. 2, "t = 46.62 μs" and "t = 53.21 μs" indicate respectively the start and end time of the time series shown in Fig. 4, and the locus drawn by solid and thick line corresponds to the such time series. Similarly, **Fig. 3** shows the results of the motion for the high frequency of 3 MHz. From Figs. 2 and 3, we can confirm that the rotation direction of the outer surface for low frequencies is reverse to that for high frequency.

As mentioned above, Fig. 4 shows time series representation of the surface particle motion for 0.3 MHz, and **Fig. 5** shows that for 3 MHz. In the both figures, "$D_r$" indicates the r-dir component and "$D_\theta$" indicates the θ-dir component. Fig. 5 indicates that, for high frequencies, the particle motion properties at both surfaces are completely equal to that caused by the anti-symmetric mode of the Lamb wave, i.e., there are no difference between the coiled structure and the straight-line structure. On the other hand, the coiled structure influences the property for low frequencies. From Fig. 4, it can be confirmed that the rotation phases at the both surfaces are almost the same in addition to the rotational direction.

## 4. Discussions and Conclusions

In a coiled waveguide for low frequencies, the motion phase along the surface normal direction coincides with that of the anti-symmetric mode in a straight-line waveguide, but the rotation direction at the outer surface equals to that of the symmetric mode. These properties indicate that the complicated wave mode exists. It is desirable to investigate the detail and the microscopic mechanism of this mode.

---

Email: tanaka.ryo.9.11@gmail.com

**Acknowledgment**

This work was supported by the research funds from KONICA MINOLTA MEDICAL & GRAPHIC, INC.

**References**

1. T. Moriya, Y. Akano and Y. Furukawa: IEEE Ultrasonics Symp. (2005) 1546.
2. S. Xie, M. Tanabe, N. Tagawa, T. Moriya and Y. Furukawa: IEEE Ultrasonics Symp. (2006) 1301.
3. M. Tanabe, S. Xie, N. Tagawa, T. Moriya and Y. Furukawa: Jpn. J. Appl. Phys. **46** (2007) 4805.
4. M. Tanabe, S. Xie, N. Tagawa, T. Moriya: Jpn. J. Appl. Phys. **47** (2008) 4262.
5. S. Xie, M. Tanabe, N. Tagawa and T. Moriya: IEEE Ultrasonics Symp. (2007) 2284.
6. S. Xie, M. Tanabe, K. Okubo, N. Tagawa and T. Moriya: Jpn. J. Appl. Phys. **47** (2008) 4271.

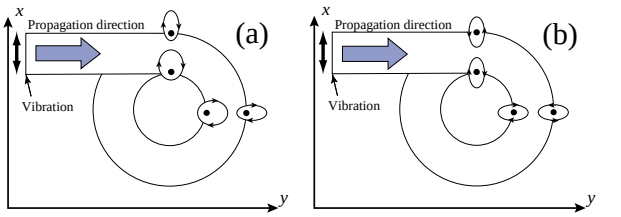


**Fig. 1** Outline of surface particle's rotation with a helical coiled waveguide. (a) Low frequencies. (b) High frequencies.

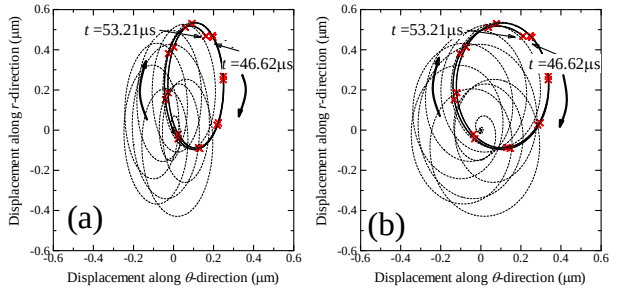


**Fig. 2** Analytical result of surface particle motion for low frequencies at (a) outer surface and (b) inner surface.

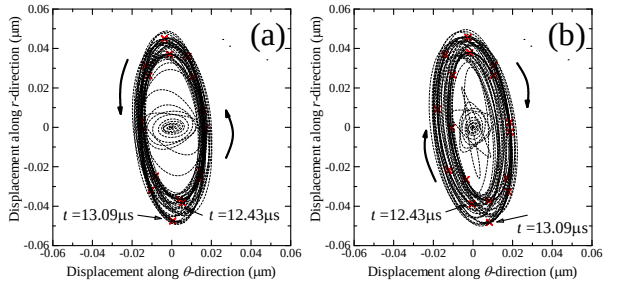


**Fig. 3** Analytical result of surface particle motion for high frequencies at (a) outer surface and (b) inner surface.

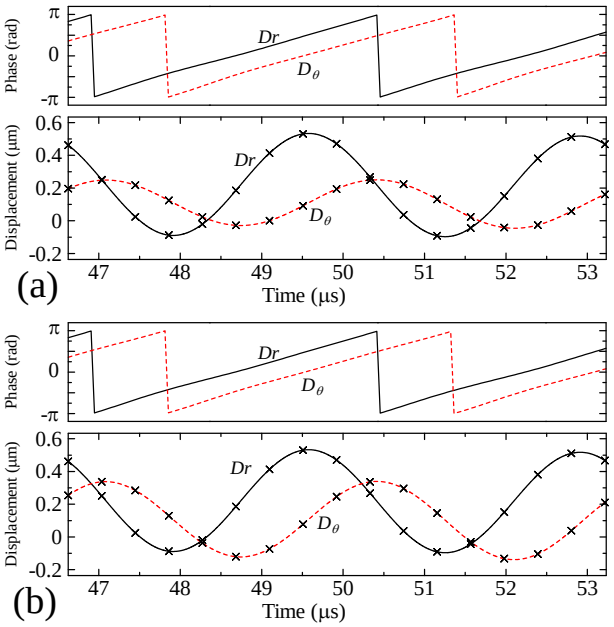


**Fig. 4** Time series representation of surface particle motion for low frequencies by decomposing locus in Fig. 2 into two components. (a) indicates outer surface and (b) indicates inner surface.

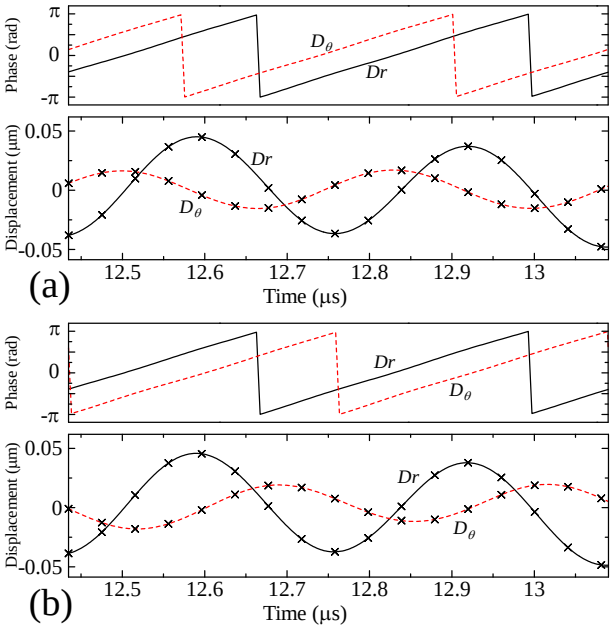


**Fig. 5** Time series representation of surface particle motion for high frequencies by decomposing locus in Fig. 3 into two components. (a) indicates outer surface and (b) indicates inner surface.

Proceedings of Symposium on Ultrasonic Electronics, Vol. 29 (2008) pp. 491-492
11-13 November, 2008

# Development of precise rotation manipulator of a ball based on resonant vibration of cantilever

カンチレバーの共振を利用した
球体の精密回転マニピュレータの開発

Teruyuki Tomita[1, 2‡], Toshihiro Tsuji[1, 2] and Kazushi Yamanaka[1, 2]
([1] Tohoku Univ., [2] JST,CREST)
冨田輝之[1, 2‡], 辻俊宏[1, 2], 山中一司[1, 2] ([1] 東北大, [2] JST,CREST)

## 1. Introduction

Precise rotation manipulator of a ball is required for observation of surface structures or for machining. Rotation control with 3-axes has already been achieved using multiple vibration modes of a cylinder [1]. In this work, we propose an alternative geometry, a cantilever manipulator, suitable for installation into narrow gaps or for integrated mass production by micro electromechanical systems (MEMS) technology. The cantilever has resonant vibrations such as deflection (D), lateral bending (LB), and torsion mode [2-5]. In principle, it is also suitable for batch deposition of thick piezoelectric films [6,7]. In this study, we develop a ball manipulator driven with cantilevers, and applied it to observation of a ball SAW device used for high sensitivity gas sensor and chromatographs [8,9].

## 2. Principle

The principle of the manipulation is shown in **Fig.1**. The D mode rotates the ball around the Y-axis in the direction of counter clock wise, since the ball is lifted due to the inertia during tapping by the cantilever, such as in the ultrasonic force microscopy [2]. The LB mode rotates it around the Z-axis. The rotation direction is dependent on the direction of differential friction force of a point contact. Moreover, various rotation axes will be realized using two or more cantilevers by controlling the amplitude and phase of excitation signal of each cantilever, independently.

## 3. Experimental setup

We fabricated three cantilevers manipulator (**Fig.2 (a)**), with a width of 2mm and a length of 25mm ([100] direction), cut from a 0.5 mm thick Si wafer. The end of the cantilever was glued to a 4mm-square, 1mm thick PZT vibrator and it was glued to a thick Cu substrate. **Fig.2 (b)** shows the manipulator supporting a LGS ball SAW device with a diameter of 3.3mm.

a7tm5621@stu.material.tohoku.ac.jp

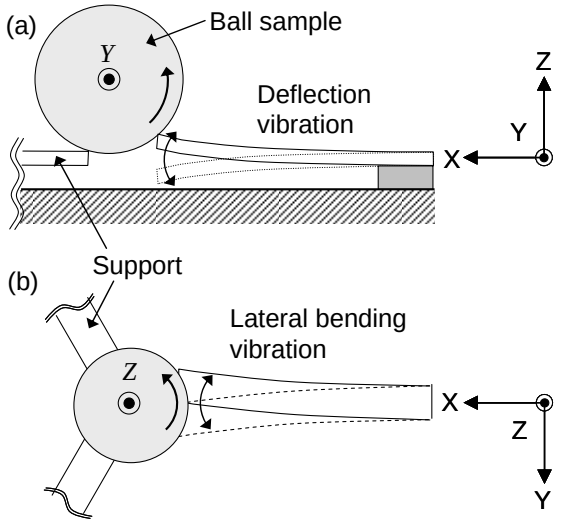


Fig. 1 Principle of rotation of a ball using cantilever. (a) Deflection mode. (b) Lateral bending mode.

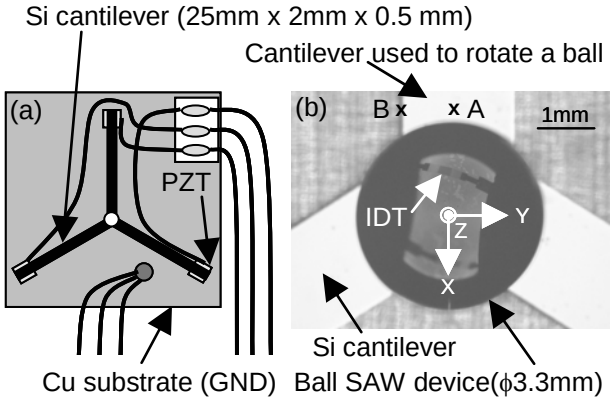


Fig. 2 Manipulator with three cantilevers. (a) Schematic illustration. (b) Ball SAW device on the manipulator.

## 4. Vibration spectra of the cantilever

We measured vibration spectra of the cantilever at positions A and B shown in Fig.2 (b) with excitation amplitude of 2.24V. In **Fig.3 (a)** dashed and solid curves represent noncontact spectrum and contact spectrum to a ball SAW device at position A, respectively. The 3rd D (D3) mode was identified from the theoretical analysis of free resonance frequency, assuming Young's modulus, Poisson's

ratio, and density of Si to be 166GPa, 0.22, and $2.33x10^3kg/m^3$, respectively. When the ball contacted the cantilever, the resonance frequency increased from 22.20kHz to 24.13kHz and Q factor decreased from 42.0 to 19.0. The low-frequency-shift is explained by a tapping contact of the cantilever [3]. **Fig.3 (b)** shows the spectra measured at position B. The 2nd LB (LB2) mode [4,5] was identified from similar analysis. When the ball contacted the cantilever, resonance frequency increased from 28.73kHz to 29.81kHz and Q factor decreased from 80.7 to 21.6. These changes may be useful for monitoring of contact and surface/subsurface state of the balls [5].

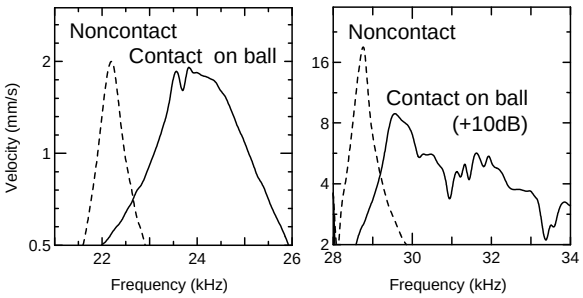


Fig. 3 Vibration spectra of free end of a cantilever. (a) Deflection vibration. (b)Lateral bending vibration.

## 5. Manipulation of a ball SAW device

We observed the rotation of a ball. When we drove the manipulator at the D3 mode, the ball was rotated around the Y-axis at 23.70kHz and 100V. The rotation direction was consistent with the principle shown in Fig.1 (a). When we drove the manipulator at the LB2 mode, the ball was rotated around the Z-axis at 29.70kHz and 100V. The rotation direction was clockwise.

Next, we tried to decrease the rotation speed, by driving intermittently using burst wave signal with duration $n_b$ cycles and interval $n_i$ cycles shown in **Fig.4**. We rotated a ball SAW device for microscope observation of the IDT and surface condition of crystal ball around it (**Fig.5**).

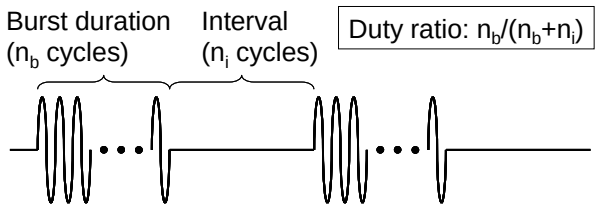


Fig. 4 Schematic illustration of burst wave excitation signal.

Figs.5 (a-c) show the manipulation using the LB2 mode. Duty ratio of the burst was 9.1% and the ball was rotated around the Z-axis. Figs.5 (d-e) show the manipulation using the D3 mode. Duty ratio of the burst was 33.3% and the ball was rotated around the Y-axis, centering the IDT in the view of microscope. Thus, the desired manipulation was achieved.

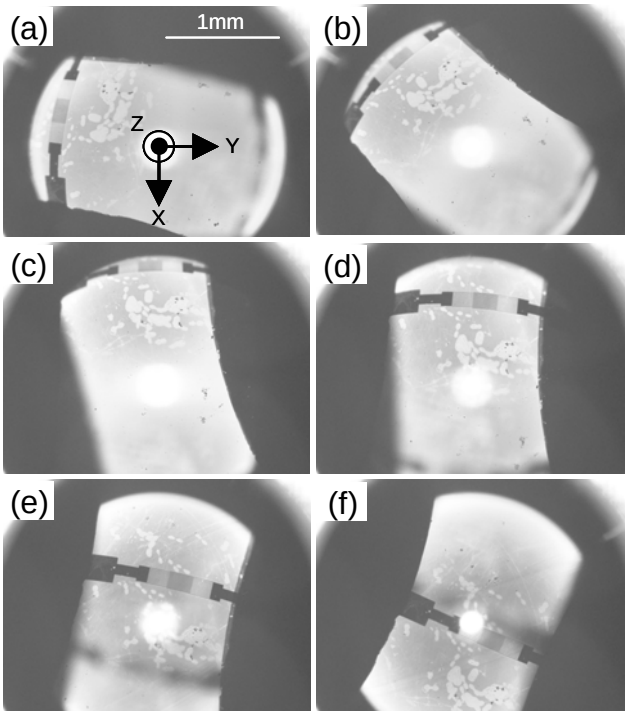


Fig. 5 Rotation of a ball SAW device. (a) At start. (b) After LB2 mode for 2.2s from (a). (c) After LB2 mode for 4.4s from (a). (d) After D3 mode for 3s from (c). (e) After D3 mode for 6s from (c). (f) After D3 mode for 9s from (c).

## 6. Conclusion

We proposed a cantilever manipulator and rotated a ball SAW device both around the Y and the Z-axes using deflection and lateral bending vibration, respectively. This manipulator may be mass-produced by and applied to MEMS processes.

### References

1. Y. Gouda, K. Nakamura, and S. Ueha: Ultrasonics **44** (2006) e617.
2. K.Yamanaka, H. Ogiso, O. Kolosov: Appl. Phys. Lett. **64** (1994) 178.
3. K. Yamanaka, A. Noguchi, T. Tsuji, T. Koike, and T. Goto: Surf. Interface Anal. **27** (1999) 600.
4. T. Tsuji, K. Kobari, S. Ide, and K. Yamanaka: Proc. Symp. Ultrason. Electron. **27** (2006) 185.
5. K. Yamanaka, K. Kobari and T. Tsuji: Jpn. J. Appl. Phys. **47** (2008) 6070.
6. J. Akedo, and M. Lebedev: Appl. Phys. Lett. **77** (2000) 1710.
7. M. Nakazawa, M. Tabaru, K. Nakamura, S. Ueha, and A. Maezawa: Jpn. J. Appl. Phys. **46** (2007) 4466.
8. K. Yamanaka, S. Ishikawa, N. Nakaso, N. Takeda, D. Y. Sim, T. Mihara, A. Mizukami, I. Satoh, S. Akao, and Y. Tsukahara: IEEE Trans. Ultrason. Ferroelectr. Freq. Control **53** (2006) 793.
9. N. Iwata, T. Abe, T. Tsuji, T. Mihara, S. Akao, and K. Yamanaka: Jpn. J. Appl. Phys: **46** (2007) 4532.

3P8-21

Proceedings of Symposium on Ultrasonic Electronics, Vol. 29 (2008) pp. 493-494
11-13 November, 2008

# Loudspeaker by Ultrasonic motors and it's control system
# 超音波モータを用いたスピーカの制御方法

YusukeMasuda [1†], KeigoHigashida [1], Syunsuke Chiba [1], Hirokazu Negishi [2], Juro Ohga [3], Kazuaki Maeda [4] and Hajime Kubota [1] ([1] Chiba Institute of Tech; [2] MIX Acous Lab; [3] MIX Acous Lab/Shibaura IT; [4] TOA.)
増田裕輔 1‡, 東田啓吾 1, 千葉俊輔 1, 根岸廣和 2, 大賀寿郎 3, 前田和昭 4, 久保田一 1
(1 千葉工大 工; 2MIX 音研; 3MIX 音研/芝浦工大; 4TOA)

## 1. Introduction

Piezoelectric ultrasonic motor is known for their use in precise positioning apparatus in IC manufacturing plants.

It is our proposal to utilize this motor as a driver of a loudspeaker for low frequency reproduction, exploiting its high mechanical impedance. Introduction of ultrasonic motor seems to overcome common shortcomings of ordinary electrodynamic loudspeakers[1].

This report covers results of our recent measurements and evaluation of our most recent prototype.

## 2. The principle of Ultrasonic motor and its driving method Principle

USR60E3 by Shinsei Kogyo is used in our prototype[2]. **Fig.1** shows the cut out photo which shows the location of piezoelectric actuator, teethed stator and metallic rotor. Principle of ultrasonic motor is familiar to the participants of this symposium therefore only basic reminder is shown is **Fig.2**

Two asynchronous 40-45 kHz sine waves of the same frequency are needed in order for a USR60 to generate progressive wave.

### 2.1Driving method

The revolution velocity of the motor is varied by changing the amplitude of the progressive wave on stator surface. In order to do this, amplitude, frequency, or phase difference of the two sine waves can be modulated. Relationship between loudspeaker output and amplitude modulation input was found to be non-linear, but those for frequency and phase difference are not yet studied. In order to reverse the direction of rotation, the phase difference between the two input signals simply has to be reversed.

Masuda_1983@hotmail.com

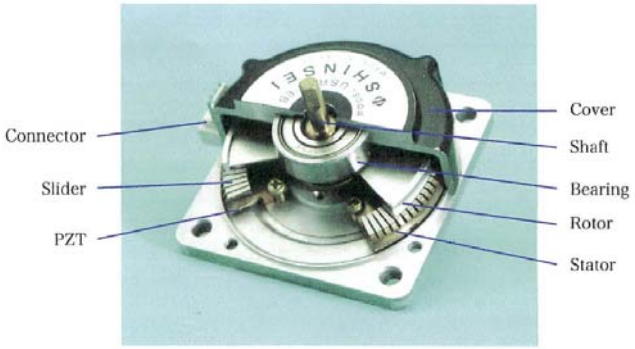


**Fig 1 Ultrasonic motor USR60E3**

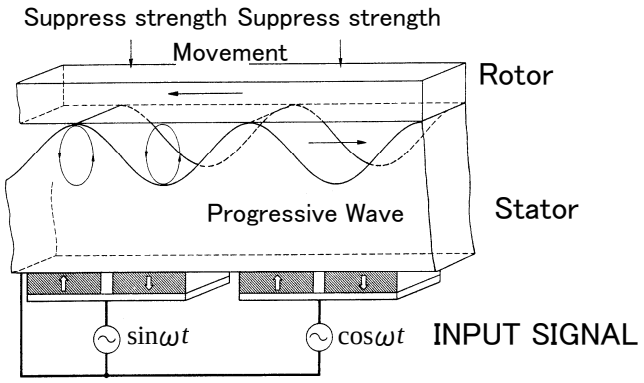


**Fig 2 Driving principle**

### 2.2Frequency Modulation

**Fig. 3** explains the relationship between input frequency and revolution speed. The motor exhibits linearity in the area of 41-42+ kHz but gradually levels off after 42+ kHz. The loudspeaker utilizes this linear region for its operation. Minor deviation is observed in No.10475 which hit top speed around 39.5 kHz. This was the only brand-new motor which could account for the reason for this difference.

### 2.3Phase difference modulation

Phase difference vs. rotational speed is shown in **Fig. 4**. It is apparent that except for -5 to +5

degree region, linearity in change is observed in between -30 to +30 degrees. In case of driving reciprocal type loudspeaker, -5 to +5 degree area should be skipped from the modulation.

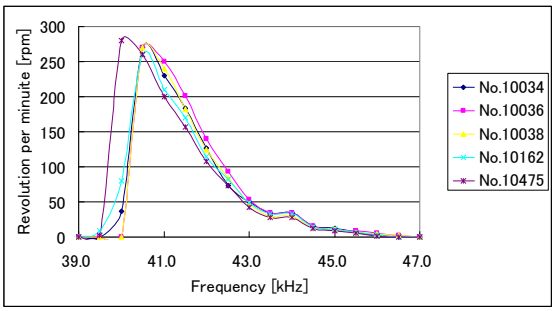


**Fig 3 Input signal frequency vs. RPM**

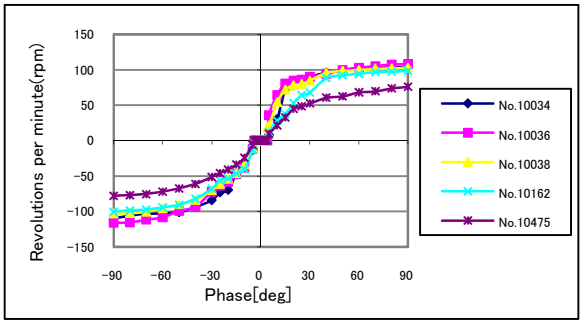


**Fig 4 Input signal phase difference vs. RPM**

## 3. Configuration of the latest prototype loudspeaker

**Fig. 5** shows the latest, dual motor model. Two motors are introduced to achieve linear modulation and cone type radiator is connected to give reciprocal motion. Frequency modulation is chosen to control the motor[3].

One motor is bolted on to solid base to give bias rotation and the other motor is connected directly to the same shaft and is also linked to the cone radiator. The second motor is counter driven at the same speed as the first to keep the cone stationary. When either or both motor(s) is(are) modulated by audio signal, the linear region mentioned above is utilized to move the cone. This approach is named as the dual motor de-spin model.

The frequency characteristics of the dual motor de-spin model loudspeaker is compared with that of a conventional dynamic model using the same cone in **Fig. 6**. The dual motor de-spin model outperforms in low frequency region.

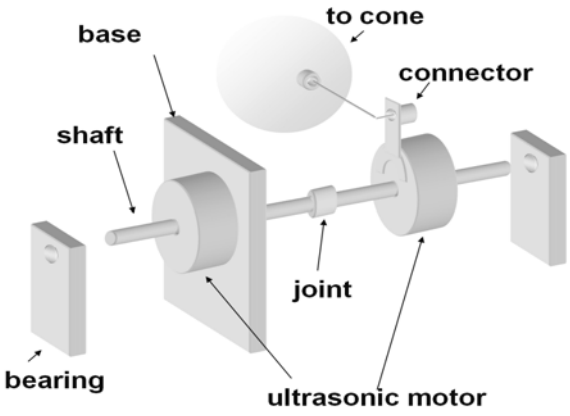


**Fig5 Dual motor model**

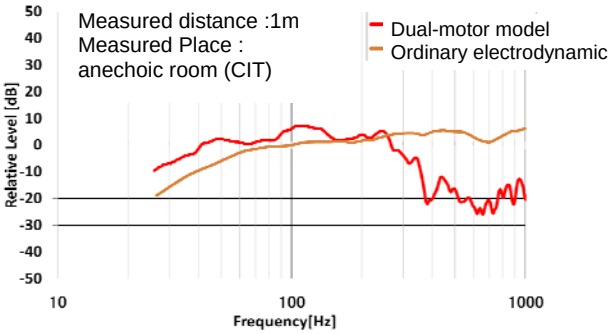


**Fig 6 Output sound pressure frequency response**

## 4. Conclusion

The dual motor de-spin model which utilizes two ultrasonic motors was proposed, prototyped and demonstrated its practicality. This loudspeaker is useful for low frequency sound reproduction.

Further study will be carried out in order to improve performance by re-examining the roles of two motors and the connecting mechanism between them.

References:

1. J. Ohga, H. Negishi, T. Sashida, K. Maeda: “A loudspeaker utilizing ultrasonic motor”, JASJ Vol.62, No.11. P813-818, 2006

2. T. Kenjo, T. Sashida: “Introduction to Ultrasonic Motor” Oxford Press

3. J. Ohga, H. Negishi, K. Maeda: “A novel speaker driven by Ultrasonic motor”, Special presentation, Spring conference, 2008 The Oceanographic Society of Japan,

3P8-22

Proceedings of Symposium on Ultrasonic Electronics, Vol. 29 (2008) pp. 495-496
11-13 November, 2008

# Evaluating the Efficacy of Counterweight Structure in Improving the Performance of Linear Ultrasonic Motors

Chaodong Li† and Jian Jin (School of Mechanical & Electronic Engineering and Automation, Shanghai University, China)

## 1. Introduction

Linear ultrasonic motors have a very good application value for high precision mechanisms. With the development of science and technology, humanoid robots, insect robots, precision machines and biogenic medical devices need the actuators as small as possible. Currently, many kinds of linear ultrasonic motors have been developed. Because of the large transverse dimension, it is difficult to be used in reality. There are only a few miniaturized piezoelectric linear ultrasonic motors that based on resonance principle. Such as P-653 motor (PI Co., Germany), SQUIGGLE motor (New Scale Co., USA), L1B4 motor [1] and two types which are proposed by the authors [2,3]. According to the author's experience, the smaller the motor is, the worse the output characteristic is. The main reason is that the transverse vibration strength which is the acceleration altitude is not enough. The Langevin type transducer is mature enough and has been widely used in the field of ultrasonic engineering. It can amplify the output amplitude through the concentrator. In order to increase the vibration on driven side and decrease the vibration on un-driven side, counterweight structure is applied in the design of linear ultrasonic motor by using the structure of Langevin type transducer for reference. We hope to find a new way to solve the problem of linear ultrasonic motor miniaturization mentioned above.

## 2. The effect of Langevin type transducer with concentrator to increase the working end amplitude

The ultrasonic concentrator (horn) is a part of power ultrasonic Langevin type transducer. It is used to enlarge the amplitude on working end of ultrasonic transducer. And the efficiency of ultrasonic machining is increased. There are many kinds of concentrators that enlarge the amplitude, such as conical, exponential, stepped and so on. The sections of them are all reduced gradually from joined end to working end [4]. According to the A. Iula etc's work, hollow structure can also enlarge the amplitude [5]. The ratio of operative side amplitude to free side one A=v2/v1 is an important parameter of concentrator. The longitudinal

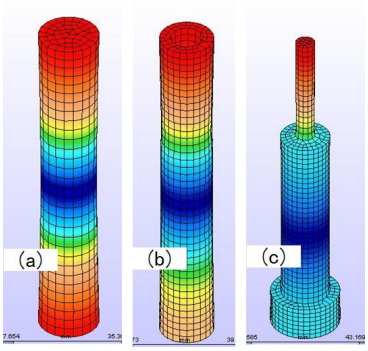


Fig. 1 Examples of first longitudinal vibration mode Ratios of front and back velocity amplitude are, (a):434/434=1.00; (b):538/374=1.44; (c):987/312=3.16

vibration amplitude ratios are different for the shaft with different shape. **Fig. 1** illustrates the first longitudinal vibration modes for different shape. They all have the same volume. FEM analysis is carried out. The amplitude ratios are 1.00, 1.44 and 3.16 respectively. Langevin type transducer is a sandwiched structure. The front metal cover can be used as transmitting ultrasonic energy, while the back one is used as the counterweight. These two parts are designed in different structures to enlarge the working end amplitude. The vibration of free end can be decreased. So does the concentrator work.

## 3. The effect of counterweight structure for linear ultrasonic motor to increase the operative side amplitude

According to the operation principle of ultrasonic concentrator, the structure of linear ultrasonic motor can be modified. With the same free side amplitude, the operative side amplitude is the larger the better.
A plate type structure is cited here. **Fig. 2** (a) and (b) show the first and the second vibration modes for the plate type oscillator with a dentation in the middle of the body. The ratio of the operative side (top of the dentation) amplitude along the anticipant output direction to the maximum amplitude of the free sides is defined as the valid amplitude ratio. The valid amplitude ratios in **Fig. 2** are 0.59 and 0.33 respectively. After the same counterweight is added on each side of the body, as shown in **Fig. 3**, the valid amplitude ratios are 0.83 and 0.47 respectively. The valid amplitude ratio is increased for both the two output directions.
A diamond hollow structure is developed

† E-mail: eastward@sh163.net

(equivalent to add a negative counterweight), as shown in **Fig. 4**. The rectangular counterweight is added on each side of the micro linear ultrasonic motor. The profile size of the motor is 28 mm×5 mm×7 mm. The operative side is the top of the dentation. **Figure 5** gives the non-counterweight one. **Figure 6** gives the solid one with the same volume and a simple shape. A comparison of the two motor structures indicates that the operative side amplitude of the former motor (**Fig. 4**) is increased for both the two driving directions. The efficiency of structure design is proved. And the output characteristics are improved.

## 4. Conclusion

According to the simulation results, the linear ultrasonic motor with counterweight structure or hollow structure (negative counterweight) can achieve better output characteristics.


## Acknowledgment

This work was supported by the National High-Tech Research and Development Program of China (863 Program) (2007AA04A212) and Shanghai Leading Academic Discipline Project (Y0102).


## References


1. Taegone Park, Beomjin Kim, etc : Jpn. J. Appl. Phys. **41** (2002) 7139.
2. C. Li, D. Shao and J. Xu : Proc. of IEEE Ultrasonics Symposium. (2006) 2265
3. C. Li and H. Yao：Proc. of Actuator 08 (2008) 607.
4. Yiquan Yuan: *Principle of Modern Ultrasonics and Its Applications* (Nanjing University, China, 1996) p.6. (in Chinese)
5. A. Iula, L. Pareniti, M. Pappalardo and N. Lamberti : Proc. of IEEE Ultrasonics Symposium. (2005) 1534.


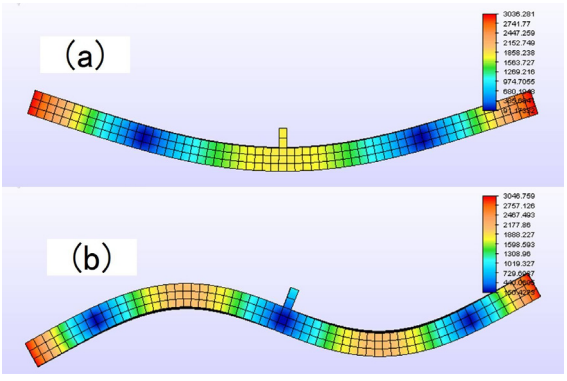


Fig. 2 The first and second bending vibration modes of plate shaped vibrator
Valid amplitude ratios are, (a):1800/3036=0.59; (b):1003/3046=0.33

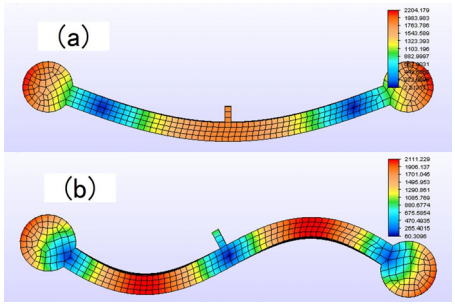


Fig. 3 The bending modes of the vibrator with counterweight
Valid amplitude ratios are, (a):1821/2204=0.83; (b):952/2043=0.47

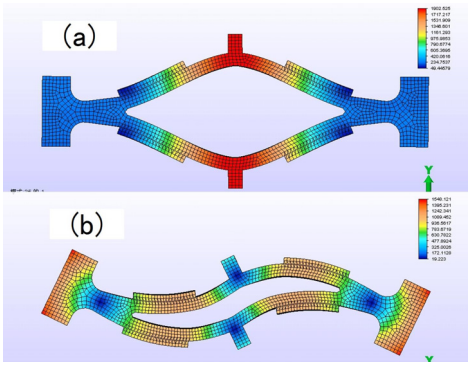


Fig. 4 The bending modes of the vibrator with rectangular counterweight and diamond hollow structure
(a): relative amplitude in the top of dentation is 1902
(b): valid amplitude ratio: 511/1548=0.33

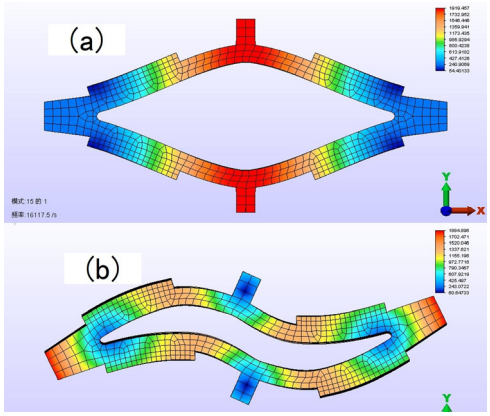


Fig. 5 The bending modes of the vibrator with diamond hollow structure
(a): relative amplitude in the top of dentation is 1919
(b): valid amplitude ratio: 400/1884=0.21

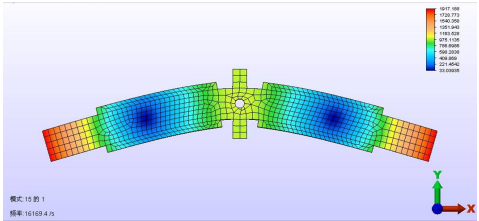

Fig. 6 The first bending vibration mode of plate shaped vibrator with a simple structure
relative amplitude in the top of dentation is 997

3P8-23

Proceedings of Symposium on Ultrasonic Electronics, Vol. 29 (2008) pp. 497-498
11-13 November, 2008

# Preload Control of High-speed Ultrasonic Actuator and Equivalent Circuit Analysis

高速回転超音波アクチュエータの予圧制御と等価回路解析

Manabu Aoyagi[1†], Maiko Seki[2], Takehiro Takano[2], Hideki Tamura[3] and Yoshiro Tomikawa[3] ([1] Facult. Eng., Muroran Inst. Tech.; [2] Facult. Eng., Muroran Inst. Tech.; [2] Facult. Eng., Yamagata Univ.)

青柳学[1†], 関舞子[1], 高野剛浩[2], 田村英樹[3], 富川義朗[3] ([1] 室蘭工大 工; [2] 東北工大 工; [3] 山形大 工)

## 1. Introduction

An L-shaped ultrasonic actuator which has simple preload mechanism using a flat spring has been proposed and it has high-speed revolution characteristics.[1)] High-speed rotation of a rotor can be realized at low preload, but its risetime becomes longer. It is hard to make the chracteristic of high-speed revolution with short risetime. However, if a preload can rapidly change from large to small for an accelaration phase, the risetime will become shorter, because the revolution speed and torque can be changed with the preload.
The purpose of this study is to shorten the risetime of a rotor revolution by a preload control with maintaining maximum revolution. This paper reports some experimental results and equivalent circuit which can be used on a comartial circuit simurator and which can consider variable preload.

## 2. Principle and construction

**Figure 1** shows the basic construction of stator of L-shaped ultrasonic actuator. This stator excites two couple vibration modes of longitudinal vibration and bending one, as shown in **Fig.2**. The tip of stator gives a push to a rotor and it revolves fast in both directions.

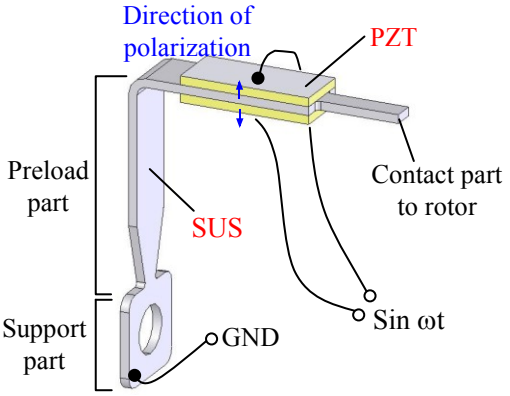


Fig.1 Basic construction of the stator of L-shaped ultrasonic actuator.

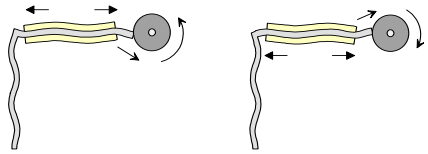

Fig. 2 Coupled vibration modes.

## 3. Preload control

The stator is fixed on a support jig with a hinge and a multilayer piezoelectric actuator (MPA) arranged as shown in **Fig.3**. The MPA moves the stator and changes preload. Therefore, preload can be controlled electrically.

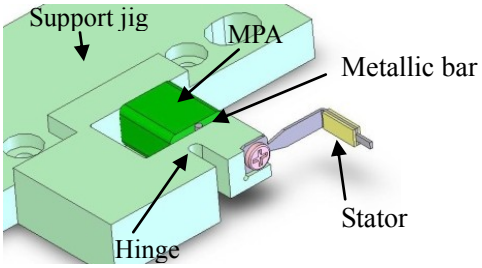


Fig.3 Construction of an L-shaped ultrasonic actuator with preload control MPA.

## 4. Experimental results

Revolution speed and risetime are changed by preload voltages which are applied to MPA, as shown in **Fig.4**. When preload was 80V, the shortest risetime was obtained. After many experimental considers, it was found that the effective drive method for highspeed revolution with short risetime was to suddenly drop the preload voltage from 80V to zero at 92ms after starting. **Figure 5** shows transient responses with preload control and without one. Their maximum revolution speeds were almost the same, but the risetime became shorter by 37.6% compared to without preload control.

---

maoyagi@mmm.muroran-it.ac.jp

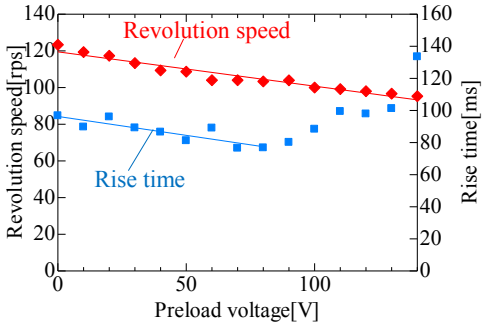


Fig.4 Revolution speed and rise time as a function of preload voltage.

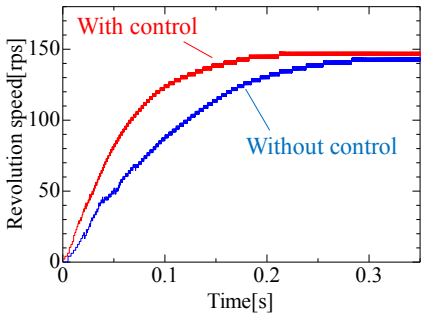


Fig.5 Comparison of transient response of revolution speed by presence of preload control.

## 5. Equivalent circuit

Several equivalent circuits of ultrasonic actuator have been proposed.[2-4] However, their simulations are not necessarily easy. The equivalent circuit of L-shaped ultrasonic actuator is shown in **Fig.6**. Friction force and slip are expressed with two pair of voltage controlled voltage source and diode. This circuit can be simulated by a commercial circuit simulator. Preload is expressed by DC power source. By changing the voltage of the DC power source, revolution characteristics under preload control will be easily simulated. **Figures 7 and 8** are normal force and thrust to a rotor, respectively. In the case of large preload, it is found that the mean values of normal force and thrust are also large.

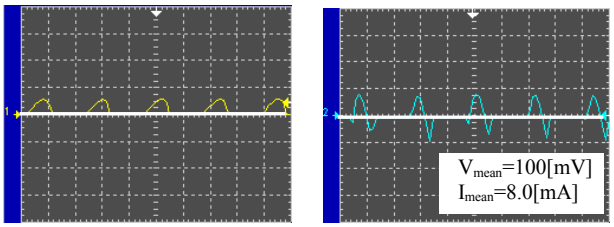


(a) Normal force $V_n$. (b) Thrust $V_t$.

Fig.7 Outputs at small preload.

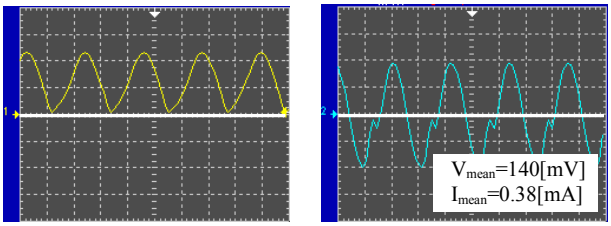


(a) Normal force $V_n$. (b)Thrust $V_t$.

Fig.8 Outputs at large preload.

## 4. Summary

A rise time can be shorter by an electrical preload control with maintaining maximum revolution speed. The proposed equivalent circuit has possibility to easily simulate the performance of preload control.


### Acknowledgment

This work was partially supported by a Grant-in-Aid for Scientific Research (No.19016001) on Priority Areas No.438 from the Ministry of Education, Culture, Sports, Science, and Technology.


### References


1. N. Kawashima, et.al: IEIECE Technical Report, **US2006-46** (2006)17.
2. T. Sashida and T. Kenjo: *An Introduction to Ultrasonic Motors* (Clarendon Press, Oxford, 1993) p.89.
3. S. Ueha and Y. Tomikaw: *Ultrasonic Motors, -Theory and Applications* (Clarendon Press, Oxford, 1993) Chap.7.
4. M. Aoyagi and Y. Tomikawa: Jpn. J. Appl. Phys. **36** (1995) 2752.


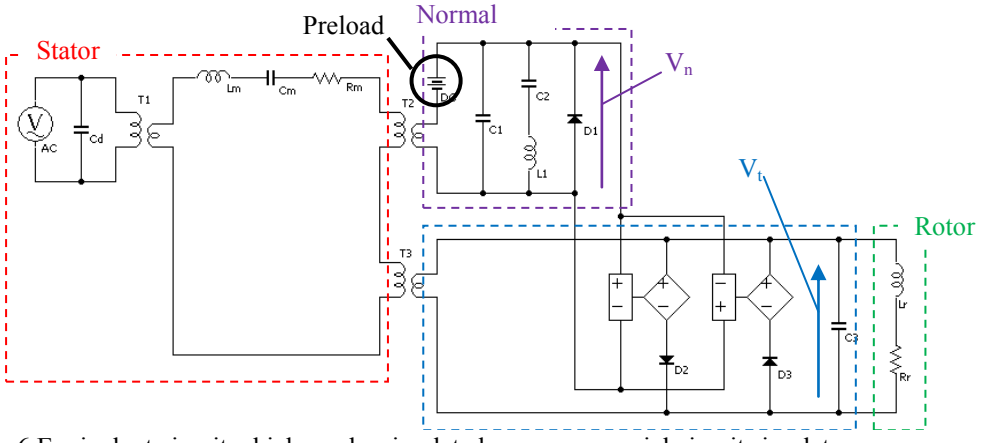


Fig.6 Equivalent circuit which can be simulated on a commercial circuit simulator.

Proceedings of Symposium on Ultrasonic Electronics, Vol. 29 (2008) pp. 499-500
11-13 November, 2008

# A new type of rectangular plate type linear ultrasonic motor using a double mode piezoelectric vibrator of the first longitudinal mode and the first flexural mode

縦１次屈曲１次多重モード利用矩形板型超音波モータ

Ryouichi Fukunaga, Kazumasa Asumi, Ryouta Asakura, Yutaka Inada (TAIHEIYO CEMENT CORPORATION)
福永　了一‡、浅倉綾太、阿隅　一将、稲田　豊（太平洋セメント株式会社）

## 1. Introduction

An ultrasonic motor (USM) directly drives the rotor by friction without clutches or brakes, and so is characterized by a simple structure and a small size. By making use of this feature, the USM is finding such applications as in the vibration compensation mechanism of a camera. Of all others, a mechanism that combines the first longitudinal and first flexural modes with a rectangular plate as shown in Fig. 1 was proposed by Tomikawa, et al.,[1] and has widely been studied using piezoelectric ceramics[2] and single crystals.[2] Further, as for the system combining the first longitudinal (L1) and first flexural (F1) modes, the use of a cylindrical piezoelectric device was proposed, and progress is expected in the future.[4]

There is, however, no report on the ultrasonic motor using the multiplex L1 and F1 modes with a rectangular plate. If such a motor is realized, it is expected that we can lower the driving frequency using a lower order mode, and realize a smaller sized ultrasonic motor. Here, an ultrasonic motor using the multiplex L1 and F1 modes with a rectangular plate is developed and the characteristics are measured.

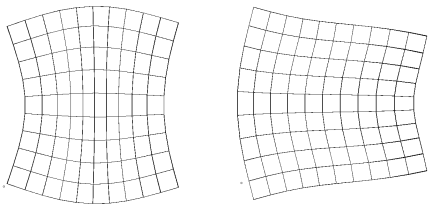

Fig1. Longitudinal and Flexural modes

## 2. Determination of side ratio of rectangular plate and the behavior of L1-F1 mode

The study of the multiplex mode vibrator with a rectangular plate was analyzed by Jumonji, et al.[5] in detail.

Using the FEM analysis (Piezo Plus of Wave Research), the authors extracted the aspect ratio where the L1 and F1 modes of a rectangular plate degenerate. Figure 2 shows the simulation result on the side ratio vs. the resonance frequency assuming L = 20 mm. It was found that the degeneration occurs at around 70 kHz with W = 21. For the L1-F1 vibrator using the piezoelectric ceramics polarized across the rectangular plate thickness as shown in Fig. 2, the electrodes with two subdivisions are placed on one side and an earth electrode is placed on the other.

Figure 2 suggests that the degeneration between L1 and F1 modes occurs at the side ratio of around W/L = 1.05.

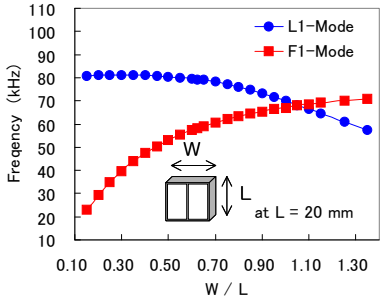


Fig2. Frequency spectrum of a rectangular plate

In the L1-F1 type USM, a driving chip is mounted in the one central part of a short side, and there could be two driving methods of single-phase driving and two-phase driving. This time, a sliding chip is adhered onto the central part of a short side, and the frequency-speed and the field-speed characteristics are evaluated with two-phase driving.

## 3. Trial fabrication of ultrasonic motor

### 3.1 Fabrication of an USM sample

A single-plate ceramic material (using the material “NA” of Nihon Ceratec) is used for the piezo-ceramic vibrator as shown in Fig. 3.

Single-plate ceramic material is processed into a plate of 20 x 18.3 x 3 mm. Silver is applied by printing for the electrodes with two subdivisions in the one surface of 20 x 18.3 mm and the electrode covering the entire area on the other side, and the sample is baked at 850˚C. Then, polarization is uniformly accelerated by the electric field of 2 kV/mm in the silicone oil of 120˚C to obtain a

piezo-ceramic vibrator. The resonance frequency was 76.8 kHz in the L1 mode and 77.1 kHz in the F1 mode. Alumina ceramic material (A995 of Nihon Ceratec) of half cylinder type was adopted for the sliding chip.

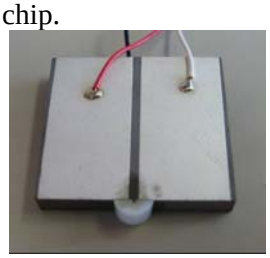

Fig.3 Piezoceramic vibrator
(20×18.3×3mm)

### 3.2 Measurement of force-velocity characteristics

To measure the force-velocity characteristics, the driving system is prepared by pressure-contacting the USM onto an alumina plate (processed A995 of Nihon Ceratec) with the mirror-polished side surface of a precision linear table. It is hung with a weight using a fixed pulley, and the position is measured using a glass scale (encoder; BL55-RE of Sony).

## 4. Experimental results

Figure 4 shows the frequency-traveling speed characteristics. It is found that the maximum speed is 130mm/s at the driving frequency of 77 kHz and the two-phase input of 90 Vrms.

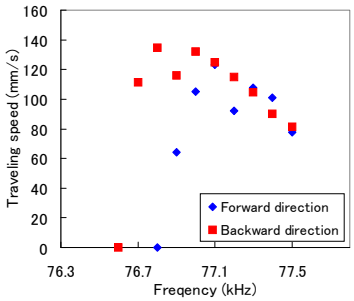


Fig.4 Traveling speed vs frequency characteristic
（No Load、at 90Vrms input）

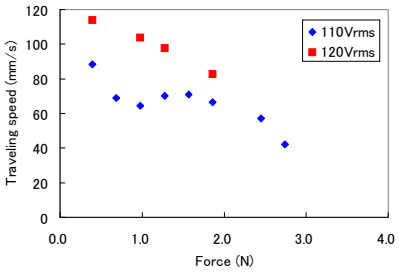


Fig.5 Traveling speed vs force characteristic（at 77kHz）

Figure 5 shows the force-traveling speed characteristics. It is shown that the maximum force of 2.8 N is obtained with the input of 110 Vrms. From the force-efficiency characteristics as shown in Fig. 6, the maximum efficiency was 1.8%.

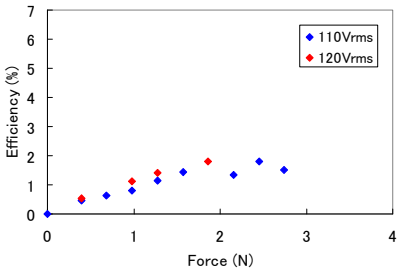


Fig.6 Efficiency characteristic
（at 77kHz）

## 5. Summary

An ultrasonic motor using the L1-F1 mode with the rectangular plate is fabricated.

Using a piezo-ceramic vibrator of 20 x 18 x 3 mm, the maximum speed of 130 mm/s at the input voltage of 90 Vrms, maximum force of 2.8N at the input voltage of 110 Vrms gaining the maximum efficiency of 1.8% are obtained. To improve efficiency, a newer electrode structure shall be advised and tested in the future.

Characteristics of the efficiency in this fabricated motor is not so high. Therefore, it is necessary to consider another type of electrode configuration that enables the longitudinal movement and improve the efficiency.

The ultrasonic motor of this type is characterized by a simple electrode structure and a relatively low driving frequency, and will find applications by making use of an easily realizable small size. Therefore, it is expected that the USM with a rectangular piezo-ceramic vibrator and the L1-F1 multiplex driving mode will have a promising future.

## Acknowledgement

The discussions with Professor Takano, Tohoku Institute of Technology, and Professor Emeritus Tomikawa at Yamagata University are greatly appreciated. The FEM analysis by Mr. Shunsuke Tsunoda, Nagaoka University of Technology, is also appreciated.

## References

1. .Tomikawa, .Ogasawara, .Sugawara, .Chikano,T.Takano, : IEICE trans US87-5 （1987）
2. Y. Tomikawa, T. Takano and H.Umeda : Jpn. J. Appl. Phys. Vol. 31 (1992) pp 3073-3076
3. H.Tamura, K.Kawai, T.Takano, : Jpn. J. Appl. Phys. Vol.32, No9B, pp4190-4193
4. H. Kanasugi, T. Maeno, :ICA 2007, Madrid ULT-09-015
5. H.Jyumonji : IEICE trans Vol.53-A No.4 pp176-183

3P8-25

Proceedings of Symposium on Ultrasonic Electronics, Vol. 29 (2008) pp. 501-502
11-13 November, 2008

# Elastic holding mechanism for ultrasonic motors
超音波モータの弾性保持機構

Naotake Inoue‡ and Takaaki Ishii (Univ. of Yamanashi)
井上尚武‡, 石井孝明（山梨大院）

## 1. Introduction

Basically, ultrasonic motor should be supported at the nodal positions to avoid vibration suppression. However, it is very difficult to support ultrasonic motors because nodal points do not always appear on their surfaces. Therefore several kinds of holding mechanisms using rubber are sometimes employed to isolate motor's vibration. The rubber mount mechanisms are relatively easy to design and easy to use, however the motor's vibration is partially suppressed and vibration energy is dissipated. In addition, vibration mode will change and eventually motor characteristics will deteriorate.

In this report, an effective holding mechanism using resonance is proposed for the ultrasonic motor. The holding parts are designed to resonate at the same frequency as the motor's one. Hence this method can hold ultrasonic motor at the anti-nodal positions which means ultrasonic motor's vibration mode remains unchanged. This kind of trial had been proposed using longitudinal vibration[1]. In this research, both longitudinal and bending vibrations are designed to be the same resonance frequencies, and the effect of this holding mechanism will be discussed.

## 2. Design of the ultrasonic motor

An ultrasonic linear motor using 1st longitudinal vibration mode and 2nd bending vibration mode is used in this experiment[2,3]. Fundamental shape of the motor and the longitudinal and bending modes used for this motor are shown in figures 3 and 4. By controlling the excitation of these two vibration modes, we can obtain elliptical motion on the edge of the ultrasonic motor. Then the ultrasonic motor will be realized.

The resonance frequencies of the longitudinal and bending vibration modes have to be almost the same value to obtain elliptical vibration efficiently. The dimensions of the ultrasonic motor are important for the resonance frequencies. Length, width and thickness have to be optimized to obtain desired frequencies.

In this experiment, around 50 kHz is employed for the resonance frequencies to realize small sized ultrasonic motor. The piezoelectric ceramics will be bonded onto the stainless steel, and then unimorph type vibrator will be used for the experiments. Finite element method (ANSYS) is used for the design.

## 3. Design of the holding mechanism

The fundamental design for the holding mechanism is illustrated in figure 1. Simple structure having the same resonance frequency as motor's one is employed. One side of the holding part is attached to the motor and another side of the part is fixed. These parts have to be vibrated at the same frequency and the same amplitude. Three points on the side of the motor are used for holding the motor as shown in figure 1.

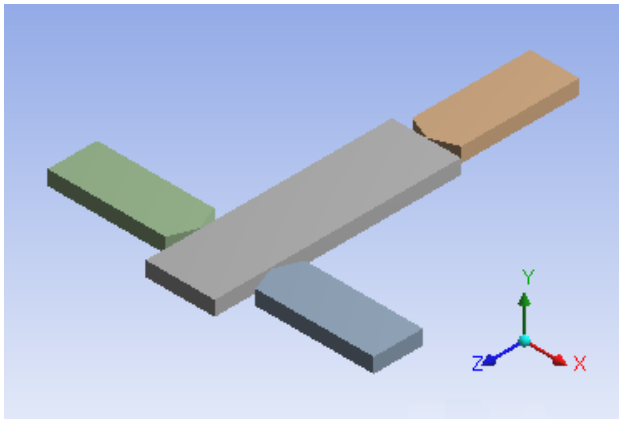


Fig. 1 Fundamental design of the proposed holding mechanism.

The fundamental holding mechanism is explained as follows.

For the longitudinal vibration of the motor, two holding parts attached to the motor perpendicular to the axial direction vibrate in bending mode associated with the longitudinal vibration of the motor as shown in figure 4. A holding part attached to the motor parallel to the axial direction vibrates in longitudinal mode associated with the longitudinal vibration of the motor as shown in figure 4.

For the bending vibration of the motor, two holding parts attached to the motor perpendicular to the axial direction vibrate in longitudinal mode associated with the bending vibration of the motor as shown in figure 5. A holding part attached to the motor parallel to the axial direction vibrates in bending mode associated with the bending vibration of the motor as shown in figure 5.

Three contact positions will vibrate in bending

mode which cause contact angle change, the shape of the holding parts has to be designed as point contact or line contact. Stainless steel will be used for the holding parts.

## 4. Analysis results

The vibration modes were analyzed by using FEM.

First, an ultrasonic motor was designed to vibrate both in 1st longitudinal vibration and 2nd bending vibration at the same frequency. 1st longitudinal vibration mode is shown in figure 2, and 2nd bending vibration mode is shown in figure 3.

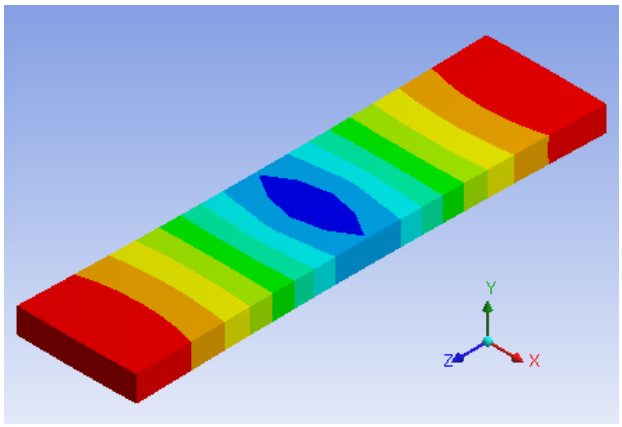


Fig. 2 Longitudinal vibration mode of the ultrasonic motor.

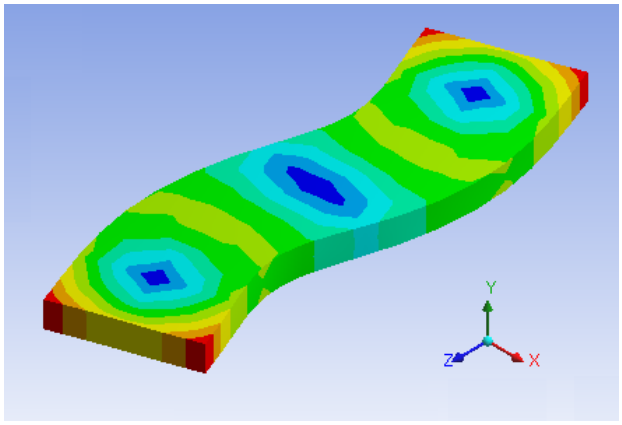


Fig. 3 Bending vibration mode of the ultrasonic motor.

These analyses were curried out under the conditions of free. In these analyses, simple structure of the ultrasonic motor consists of only piezoelectric ceramics is used.

The ultrasonic motor with holding mechanism is shown in figures 4 and 5. As explained in the previous section, holding parts vibrate associated with the motor's vibration. Since the resonance frequencies of the longitudinal and bending vibrations are designed to be the same, vibration excited in the ultrasonic motor does not affected by the holding mechanism.

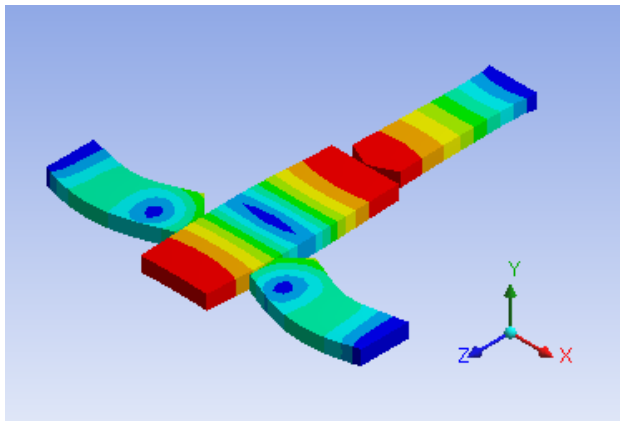


Fig. 4 Longitudinal vibration mode of the ultrasonic motor with holding mechanism.

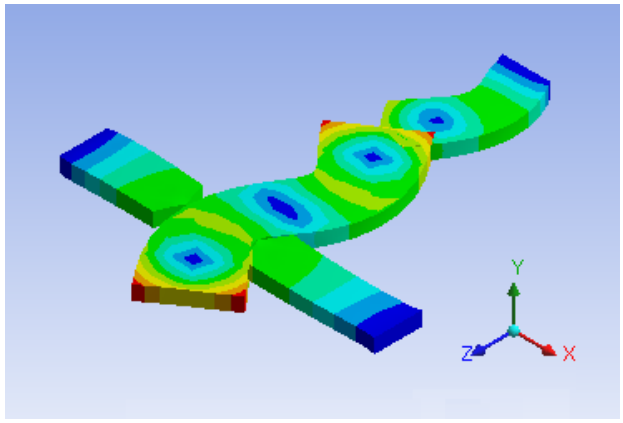


Fig. 5 Bending vibration mode of the ultrasonic motor with holding mechanism.

## 5. Future plan

It will be necessary to fabricate the ultrasonic motor and the holding mechanism. And the feasibility of this proposal has to be confirmed. The ultrasonic motor with unimorph type structure will be fabricated and will be used for the experiments. The structure is different from the one analyzed in the previous section, however, the concept can be applied and the elastic holding mechanism will be realized.

## References

1. Cheol-Ho Yun, Takaaki Ishii, Kentaro Nakamura, Sadayuki Ueha and Koji Akashi: Jpn. J. Appl. Phys. 41 (2002) pp. 3261-3266
2. Hideki Tamura, Kyousuke Shibata, Manabu Aoyagi, Takehiro Takano, Yoshiro Tomikawa, and Seiji Hirose: Jpn. J. Appl. Phys. 47 (2008) pp. 4015-4020
3. Manabu Aoyagi, Fumihiro Suzuki, Yoshiro Tomikawa and Ichiro Kano: Jpn. J. Appl. Phys. 43 (2004) pp. 2873-2878

3P8-26

Proceedings of Symposium on Ultrasonic Electronics, Vol. 29 (2008) pp. 503- 504
11-13 November, 2008

# Design of a Two-dimensional Array of Multi-Degree-of-Freedom Ultrasonic Micro Motors

多自由度超音波マイクロモータの 2 次元アレイ化設計

Yasuyuki Goda, Daisuke Koyama, and Kentaro Nakamura
(P&I Laboratory, Tokyo Inst. of Tech.)
合田泰之、小山大介、中村健太郎 （東工大 精研）

## 1. Introduction

Current applications of Multi-Degree-of-Freedom (MDOF) actuator exist mainly in manufacturing process such as robot arms and grippers. Most of these MDOF actuators are based on electromagnetic force and air pressure. Meanwhile, ultrasonic type has advantages in silent operation, simple structure, small size, and having a holding force. Ultrasonic MDOF actuator has been prototyped using a combination of a longitudinal vibration and two orthogonal bending vibrations of a rod[1]. In this study, we propose a simple structure of MDOF ultrasonic actuator suitable for miniaturization into millimeter-size. We previously proposed the structure of MDOF ultrasonic actuator suitable for fabricating on a substrate with the minimum number of PZT elements[2] and obtained three axes rotation of a ball rotor. Also, the authors investigated the integration of the actuators into 2-D array, and fabricated an X-Y stage with 2 x 2 array actuators. But we could not operate each actuator independently because of the vibration coupling between the actuators via the substrate. In this paper, we propose a new structure for decreasing the coupling and discuss the frequency design of the stator and the array.

## 2. Structure and operation principle

This actuator consists of a ceramic cylinder and a thin PZT ring fixed on a substrate as shown in **Fig. 1**. The PZT ring is uniformly polarized in thickness direction, and its electrode is divided into four parts. We can excite two orthogonal horizontal vibrations and one longitudinal vibration as shown in **Fig. 2** by selecting the electrodes. The horizontal vibration is excited by applying anti-phase voltages on the two electrodes across the cylinder, while the longitudinal one is stimulated by in-phase drive of the four electrodes. The substrate has two layers: upper layer consists of an insulant for making the wiring of all the hot electrodes and lower layer consists of a metal for the ground connection.

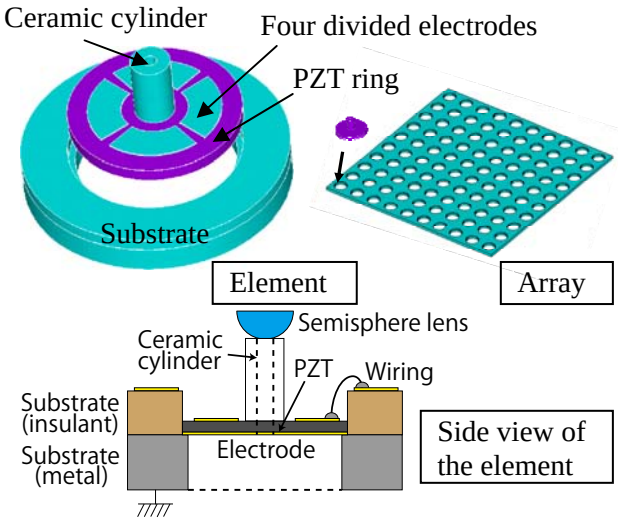


Fig. 1 Proposed structure of the MDOF ultrasonic actuator and the composition of the array.

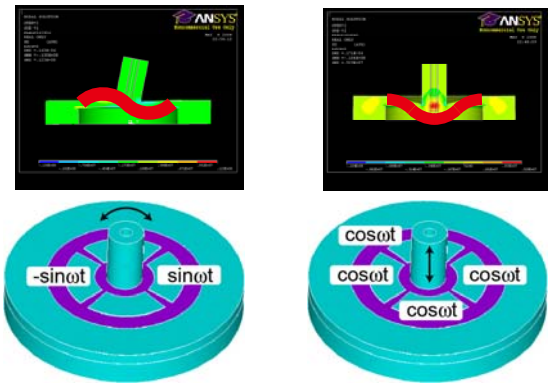


Fig. 2 Vibration modes of the stator and how to apply the voltages to the electrodes to excite each vibration. (A) shows the horizontal vibration mode and (B) shows the longitudinal vibration mode of the stator.

## 3. Resonance frequency design

There are two steps for designing the array actuator: first one is stator design and the second one is de-coupling design. For the stator model shown in **Fig. 3(A)**, using Finite Element Analysis (FEA), the resonance frequencies are calculated for the periphery of the lower disk under the fixed

E-mail: gouda@sonic.pi.titech.ac.jp

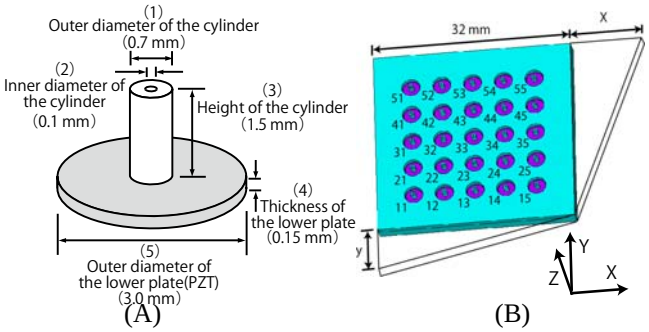


Fig. 3 Analysis model of (A) the stator and (B) the array. About the stator model, the round of the PZT is perfectly in the fixed condition.

condition. The condition is assumed to be equivalent to the case in which the lower disk is mounted on the substrate. Effects of five parameters ((1) outer diameter, (2) inner diameter, and (3) height of the cylinder, and (4) thickness and (5) outer diameter of the lower plate (PZT)) on the resonance frequencies are studied. **Figure 4** shows the results. We decided the inner diameter and the thickness of the lower part as 0.4 mm and 0.3 mm, respectively, from the reasons of fabrication process. The outer diameter of the lower part is decided as 3.0 mm from the number of the actuators to be arrayed and the substrate size. The other two parameters are decided under the consideration of the de-coupling.

Next, we analyzed the vibration amplitudes for X, Y, and Z directions for 25 stators. When the horizontal vibration is excited in No. 11 actuator, unnecessary vibration (X, Y, and Z-vibrations) of other 24 stators reached to 27 %. In the case of longitudinal vibration excitation to No. 11, unwanted vibration was 52 %. In the previous structure, there was higher vibration coupling in the case of longitudinal vibration. These unwanted vibrations are enhanced by the standing wave between the parallel edges of the substrate. We changed the length of one of the parallel edges. The results for difficult Xs and Y=0 are summarized in Table 1. The unnecessary vibration level reduced to 48 % when X=1.5 mm. If Y is changed to 3.2 mm, the vibration is decreased to 39 %.

## 4. Conclusions

We proposed a new fabrication of the MDOF ultrasonic actuator and decided sizes of the stator. From FEA result, unwanted vibrations were reduced by tilting edges of the substrate that had been parallel.


## Acknowledgment

A part of this study was supported by the Grant-in-Aid for Scientific Research of Japan Society for the Promotion of Science, #17360038.


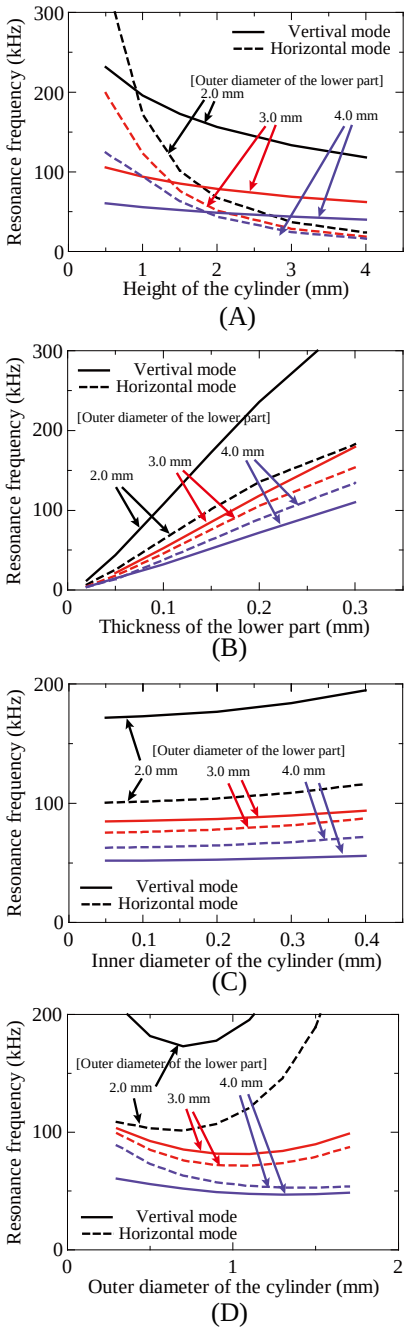


Fig. 4 Resonance frequencies against each four parameters with change of the outer diameter of the lower part.

Table 1 Percentages of unnecessary vibration amplitude against the excited vibration amplitude with the change of the substrate length.

| (mm) | X=0 | X=1.5 | X=3.2 | X=6.4 |
|---|---|---|---|---|
| Y=0 | 52% | 48% | 63% | 60% |

## References


1. Takafumi Amano, et al., Proc. IEEE Int. Ultrasonic Symp., pp.667-670, 1998.
2. Gouda, et al., IEICE technical report, US-Vol.106, No. 440, pp. 1-6, 2006

3P8-27

Proceedings of Symposium on Ultrasonic Electronics, Vol. 29 (2008) pp. 505- 506
11-13 November, 2008

# A self-running ultrasonically levitated 2D stage
# 自走式超音波浮上２次元ステージ

Daisuke Koyama† and Kentaro Nakamura (Precision and Intelligence Laboratory, Tokyo Institute of Technology)
小山大介†，中村健太郎（東京工業大学　精密工学研究所）

## 1. Introduction

Ultrasonically levitated stage utilizing the near-field acoustic levitation have several advantages compared with air bearing and magnetic systems such as a simple configuration, low-profile and silence in operation. The authors have been investigating the non-contact ultrasonically levitated stages: the sliding table with two triangular cross-sectional beam [1] and the bidirectional slider with the aluminum rectangular frame [2]. In our previous work [3], the ultrasonically levitated linear slider for a self-running sliding stage was investigated. This paper deals with the 2D version of the self-running ultrasonically levitated stage.

## 2. Configuration of the stage

We propose the ultrasonically levitated 2D stage, in which the four self-running non-contact bidirectional linear sliders [3] are installed. **Fig. 1** shows the configuration of the element slider. The slider has a simple structure: it consists of an aluminum vibrating plate (30×10×1 mm) and a PZT element (10×10×1 mm). When the flexural vibration is excited along the vibrating plate, the slider on the flat substrate can be levitated with the small distance compared with the wavelength in air due to the acoustic radiation force from the own vibrating plate. The flexural standing wave excited along the slider is asymmetric in the length direction of the slider by attaching the PZT element on the edge of the vibrating beam, and the sound pressure distribution in the air gap between the slider and the flat substrate is also asymmetric. The acoustic streaming is induced in such asymmetric acoustic standing wave field, and the slider can move in the same direction as the acoustic streaming due to the kinematic viscosity force of air. By changing the driving frequency, the flexural vibration mode of the slider can be controlled and the moving direction of the slider can be changed.

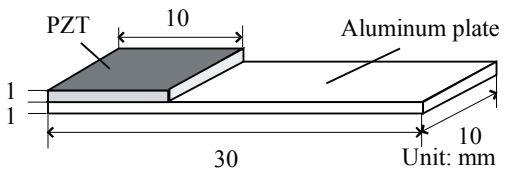


Fig. 1 A self-running ultrasonically levitated linear slider [3].

The configuration of the proposed 2D stage is shown in **Fig. 2**. By cutting the 1-mm-width lines on the aluminum plate (60×60×1 mm), four element sliders are integrated. In this version, the vibrating plate is a cantilever-type and the PZT plates are attached on the fixed-end of the vibrating plates. The 2D stage has four linear sliders, two pairs both in x and y directions, shown in Fig. 1.

## 3. 2D Stage performance

By controlling the input voltages to each PZT element, the channels 1 to 4 in Fig. 2, the stage performance was investigated. When the stage was set in the guide rail to restrict the stage moving direction to a linear motion in the x-direction, the straight back-and-force motion could be achieved by controlling the driving frequencies and input voltages to the channels 1 and 3. The straight motion in the y-direction could be also achieved by the control of the inputs to the channels 2 and 4. The driving condition of each channel, in which the stage could move in each direction, is summarized in **Table 1**. The vibration distribution of the stage was measured by an LDV in the driving condition which the stage moved to the positive direction of the x-axis (**Fig. 3**). The positions of PZT elements are also shown. The vibration mode of the vibrating plate on the channel 1 was the lattice flexural mode and the vibration displacement amplitude is larger

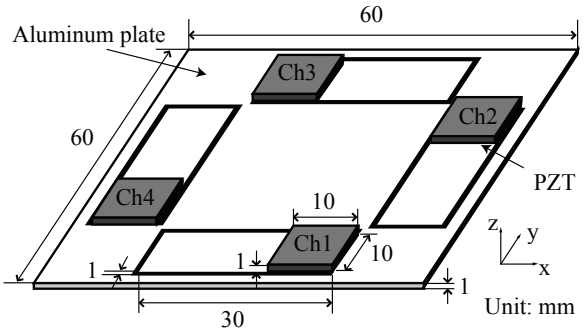


Fig. 2 Proposed self-running ultrasonically levitated 2D stage.

†dkoyama@sonic.pi.titech.ac.jp

Table 1 Driving condition of each channel (○, 80$V_{pp}$ at 69 kHz; △, 80 $V_{pp}$ at 68 kHz; ×, no input).

| | Ch 1 | Ch 2 | Ch 3 | Ch 4 |
|---|---|---|---|---|
| pos. x-direction | ○ | × | ○ | × |
| neg. x-direction | △ | × | △ | × |
| pos. y-direction | × | ○ | × | ○ |
| neg. y-direction | × | △ | × | △ |

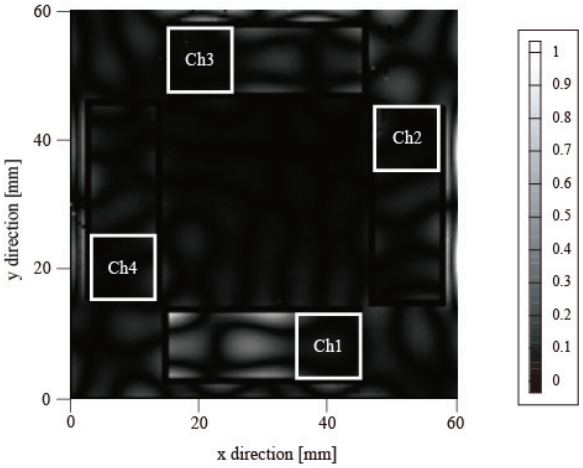


Fig. 3 Vibration distribution of the stage at 69 kHz.

than that of the other channels. The vibrating plate on the channel 1 will contribute mainly to the thrust of the stage since the vibration mode on the channel 1 and the moving direction of the stage correspond to that of our previous slider [3] shown in Fig. 1. Likewise, the thrust forces of the stage moving in the negative-x, positive-y and negative-y-directions originate the flexural vibration on the channels 3, 2 and 4, respectively. The difference of each resonance frequency is attributed to the individual difference and the bonding condition of the PZT elements. Under the condition in which the stage was moved in the positive-x-direction, namely only the channels 1 and 3 were excited with the same voltages at 69 kHz, the levitation distance of the stage was measured by using a digital microscope (VH-8000 and VH-Z450, Keyence, Japan). The levitation distance of 6.3 μm was obtained with the maximum vibration amplitude of 4.7 μm.

The thrust characteristics of the stage were investigated in the same condition. The thrust was measured by inclining the stage and balancing the thrust and the fraction of stage's weight. **Fig. 4** shows the relationship between the input voltage and the thrust. The experimental values and the error bars indicate the averaged values of 5 times and the standard deviations. The stage could not be levitated with the driving voltage under 40 $V_{pp}$ due

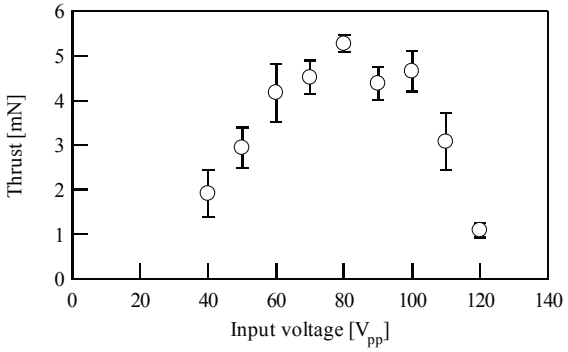


Fig. 4 The stage thrust vs. the input voltages to the channels 1 and 3.

to the small vibration amplitude. When the stage was excited with the driving voltage of 40 to 80 $V_{pp}$, the thrust could be increased with the input voltages. With over 80 $V_{pp}$, the thrust was decreased with the increase of the input voltage, and the maximum thrust of 5.3 mN could be obtained with 80 $V_{pp}$. Since the levitation distance increases with the input voltage, namely the vibration amplitude, the acoustic streaming is decreased and the thrust is also decreased by increasing the input voltage [1]. In the case that the vibration amplitude is decreased, the acoustic streaming is also decreased due to the effect of the viscosity boundary layer. Therefore the thrust of the stage has the optimum value against the input voltage.

**4. Conclusions**

The 2D self-running ultrasonically levitated stage was investigated. The stage consists of four vibrating plate, which is the same configuration as our previous bidirectional slider. By controlling the input voltages of the four channels, the moving direction of the stage could be controlled. The levitation and thrust properties were investigated, and the maximum thrust of 5.3 mN could be obtained with the input voltages of 80 $V_{pp}$.

**Acknowledgment**

This work was partially supported by Fluid Power Technology Promotion Foundation, Electro-Mechanic Technology Advancing Foundation and the Ministry of Education, Science, Sports and Culture, Grant-in-Aid for Scientific Research on Priority Areas, No. 438, 2008.

**References**

1. Koyama et al.: IEEE Trans. Ultrason., Ferroelect., Freq. Contr. **54** 3 (2007) 597.
2. Koyama et al.: IEEE Trans. Ultrason., Ferroelect., Freq. Contr. **54** 11 (2007) 2337.
3. Koyama et al.: IEEE Trans. Ultrason., Ferroelect., Freq. Contr. **55** 8 (2008) 1823.

3P8-28

Proceedings of Symposium on Ultrasonic Electronics, Vol. 29 (2008) pp. 507-508
11-13 November, 2008

# Effects of Gap Distance on Revolution Speed of Non-Contact Type Ultrasonic Motor using Flexurally Vibrating Disk

屈曲振動円板を用いた非接触型超音波モータの回転速度特性に及ぼすギャップ長の影響

Yasuhiro Yamayoshi†, Tomohiro Nakagawa, Hideki Tamura and Seiji Hirose
(Facult. Eng., Yamagata Univ.)
山吉康弘†，中川友裕，田村英樹，広瀬精二 （山形大 工）

## 1. Introduction

Ordinary ultrasonic motors utilize the mechanical friction force to get the driving force. Consequently, they have a disadvantage that the contact surfaces between the stator and rotor wear out by friction. On the other hand, we first proposed a non-contact type ultrasonic motor [1]. It is not using the friction force because the rotor rotates in non-contact with the stator by maintaining the small air gap between the stator and rotor. Recently, the non-contact ultrasonic motor with a rotor levitated by radiation pressure had reported [2]. In these motors, the rotor over the flexurally vibrating stator rotates by the acoustic streaming induced in the gap space between the stator and rotor. These are promising as a long life, high-speed and small-sized motors. However, the effects of a gap distance on the characteristics of these motors have been little investigated in detail. This paper reports the effects of a gap distance on the revolution speed of the non-contact type ultrasonic motor using a flexurally vibrating disk.

## 2. Construction of motor

**Fig. 1** shows the construction of the non-contact type ultrasonic motor using a flexurally vibrating disk. The rotor made by an acrylic resin with 2 mm thickness rotates together with the ϕ0.9 mm shaft supported by the ball bearing and pivot tip. A gap distance between the stator and rotor can be adjusted by sliding the shaft up and down. In the motor with the levitated rotor, the levitating distance of the rotor depends on the mass of the rotor and the vibration velocity of the stator but in this motor, a gap distance is always kept constant. **Fig. 2 (a)** shows the vibration patterns of the stator. The resonant mode ($B_{13}$) has three nodal lines and one nodal circle of a $0.85D_s$ diameter. Two degenerating resonant modes are driven with the different phases by 90 degrees to excite a circumferential flexurally traveling wave. **Fig. 2 (b)** shows the structure and driving condition of the stator. The stator is constructed by bonding an aluminium disk with the same diameter and a thickness of $t_A$ and a lead zirconate titanate (PZT) disk with a 30 mm outside diameter, 1 mm inside diameter and 0.15 mm thickness polarized in the direction of thickness. Four fan-shaped electrodes for exciting two $B_{13}$ modes are formed to the under surface of the PZT disk using both photolithography and wet etching techniques. **Fig. 3** shows the resonant frequencies of the stators and gap space as a function of the rotor diameter. They are calculated by the finite element method (FEM) analysis taking account of the interaction between piezoelectric materials, structure and the acoustic space surrounding them. The sound pressure pattern in the gap space is illustrated in Fig. 3. According to the graph, the resonant frequency of the gap space is in inverse proportion to the rotor diameter. The resonant frequencies of the stator with $t_A$ = 0.4 mm

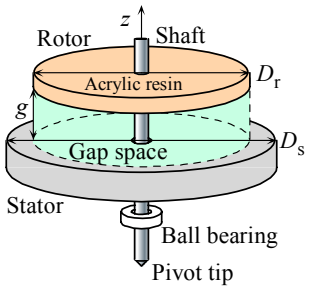


Fig. 1 Construction of non-contact type ultrasonic motor using a flexurally vibrating disk.

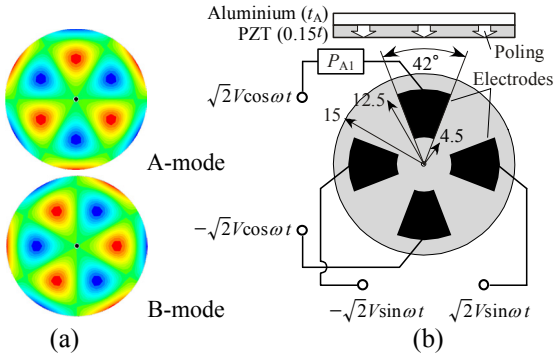


Fig. 2 Vibration patterns (a) and structure and driving condition (b) of stator.

yamayosi@yz.yamagata-u.ac.jp

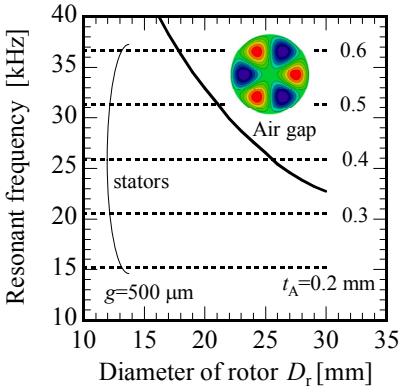


Fig. 3 Resonant frequency of stators and gap space as a function of rotor diameter calculated by FEM.

and the air gap are equaled at about $D_r$ = 26 mm. However, the resonant frequency of the stator with $t_A$ = 0.3 mm is not equaled to the air gap resonance within $D_r$ = 30 mm. When the resonant frequencies of the stator and air gap are equaled, the intense sound pressure is caused in the gap space by the resonant effect of the air gap. As a result, it has been considered that the rotor rotates with a higher revolution speed [3].

## 3. Experimental results

The characteristics of the revolution speed at several gap distance are measured under the constant input power ($P_{A1}$ = 60 mW) using two stators and the rotors with a different diameter. **Table 1** presents the equivalent circuit constants of two stators measured under the low vibration velocity. **Fig. 4** shows the rotation energy $E_r$ of the rotor as a function of the rotor diameter to compare the experimental results of the rotors with the different diameter. $E_r$ is calculated by $J(2\pi\Omega/60)^2/2$, where $J$ and $\Omega$ are moment of inertia and revolutions per minute of the rotor. The measured results of the stators with $t_A$ = 0.4 and 0.3 mm are shown in Fig. 4 (a) and (b), respectively. In case of $g$ = 500 and 200 μm in Fig. 4 (a), the maximum revolution speed is obtained at the rotor of $D_r$ = 26 mm. It is considered that the air in gap space is resonating then because the both resonant frequencies of the stator and air gap are nearly equaled as shown in Fig. 3. In case of the narrower gap like 100 and 50 μm, the rotatable range of rotors extends to a small diameter. In Fig. 4 (b), the rotors hardly rotate in case of a 500 and 200 μm gap

Table 1 Equivalent circuit constants of stators.

| $t_A$ [mm] | mode | $f_r$ [kHz] | $Q$ | Capacitance ratio $\gamma$ |
|---|---|---|---|---|
| 0.4 | A | 25.903 | 106 | 33.5 |
| | B | 25.922 | 101 | 33.3 |
| 0.3 | A | 21.538 | 84 | 33.0 |
| | B | 21.523 | 82 | 31.3 |

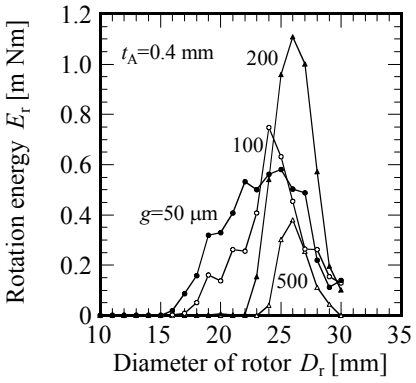


(a) $t_A$ = 0.4 mm

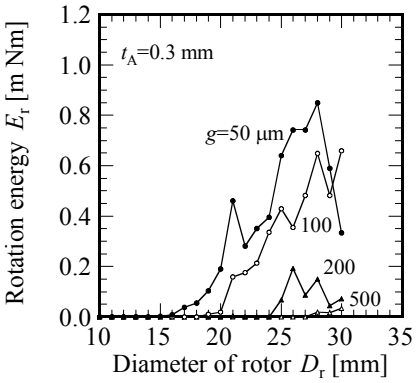


(b) $t_A$ = 0.3 mm

Fig. 4 Rotation energy of rotor depending on rotor diameter.

because the stator resonance is not equaled to the resonance of the air gap as shown in Fig. 3. However, in case of the narrower gap, the rotors come to obtain a high-speed rotation in a diameter in wide range.

## 4. Conclusion

The revolution speed of the non-contact type ultrasonic motor using a flexurally vibrating disk were measured at several gap distance. The results of the presented study demonstrated that it is necessary to satisfy the resonant condition of the air gap in case of the comparatively wide gap but the motor with the narrower gap can obtain a higher speed rotation on the wide conditions.

**Acknowledgment**
This work was partially supported by Grant-in-Aid for Scientific Research, 20920023 on Japan Society for the Promotion of Science (JSPS).

**References**

1. Y. Yamayoshi and S. Hirose: Technical Report of IEICE. **US91-41** (1991) 15 [in Japanese].
2. J. Saito, J. R. Friend, K. Nakamura and S. Ueha: Jpn. J. Appl. Phys. **44** (2005) 4666.
3. Y. Yamayoshi, S. Sone, S. Hirose and H Nakamura: Technical Report of IEICE. **US93-46** (1993) 39 [in Japanese].

3J7a-1

Proceedings of Symposium on Ultrasonic Electronics, Vol. 29 (2008) pp. 509- 510
11-13 November, 2008

# A High-Performance Spatio-Temporal Displacement Smoothing Filter for Myocardial Strain Imaging

心筋歪みイメージングのための高性能の時空間的変位平滑化フィルター

Shuhui Bu[1 †], Tsuyoshi Shiina[2], Makoto Yamakawa[3], and Hotaka Takizawa[1]
([1]System Info. Eng., Univ. Tsukuba; [2]Faculty of Med., Kyoto Univ.; [3]Faculty of Eng., Kyoto Univ.)
布 樹輝[1†], 椎名 毅[2], 山川 誠[3], 滝沢 穂高[1]
([1]筑波大 システム情; [2]京都大 医学科; [3]京都大 工学研究科)

## 1. Background

Accurately assessing local myocardial strain is important for diagnosing ischemic heart diseases because decreased myocardial motion often appears in the early stage. We previously proposed a new method of 3-D myocardial motion tracking and visualization of the invariant of a full strain tensor using a 2-D phased array. The feasibilities of the proposed methods were evaluated by numerical simulations[1]. However, the strain calculation is very sensitive to noise, which causes low spatial resolution in the strain image. For overcoming the problem, we have proposed a new displacement smoothing filter based on dynamic grid interpolation (DGI) method[2] for reducing the noise in strain calculation.

Typically, when the scanning frame-rate is high, the correlation coefficient, which is calculated from autocorrelation method, will be high. But only using two consecutive frames' phase-shift data, the displacements' dynamic range is low. Therefore, the strain calculation will be affected by the noise. In this study, in order to improve the accuracy of myocardial strain imaging, we extend the proposed DGI method, that more than 2 frames' data can be processed. The displacement vectors are tracked and smoothed. From the simulation results, we can conclude that our method can provide more accurate myocardial strain image.

## 2. Method

In this system, a 2-D transducer acquires echo data from the myocardium by volumetric sector scanning. Radio frequency (RF) signals for each scan line are received at all elements in the probe. The phase-shifts at every measuring point between several consecutive frames are calculated by the combined autocorrelation method (CAM) or the extended combined autocorrelation method (ECAM), and the displacement vectors are calculated by WPGM from obtained phase-shifts. At the same time, the myocardium meshes are generated from the segmented myocardial boundaries, and the displacement vectors in each mesh's node are interpolated by bilinear interpolation, and their coordinates are also translated from Cartesian coordinates to cylinder coordinates. The displacement data is smoothed by DGI in spatial dimension, and the displacement data are also tracked and smoothed in temporal dimension. Finally, the strain tensors are calculated from the tracked displacement vectors for improving the accuracy.

In the DGI method, the displacement vectors in all sampling nodes are defined as $\vec{u} = (u_r, u_c)$, where $u_r$ is radial direction's displacement component and $u_c$ is circumference direction's displacement component. Virtual springs are attached at each mesh node in radial and circumference directions, respectively. Through the virtual springs, revising displacements $\vec{\varepsilon} = (\varepsilon_r, \varepsilon_c)$ are introduced, and an overall error function is defined as:

$$
\begin{aligned}
e(\varepsilon_r, \varepsilon_c) = & \sum_{i=1}^{n}\sum_{j=1}^{m}\left[(\varepsilon_r^{\,i,j})^2 + (\varepsilon_c^{\,i,j})^2\right] \\
& + \sum_{i=1}^{n}\sum_{j=1}^{m-1}\frac{E_{rr}^{i,j}}{2}(u'_r{}^{i,j+1} - u'_r{}^{i,j})^2 \\
& + \sum_{i=1}^{n-1}\sum_{j=1}^{m-1}\frac{G_{rc}^{i,j}}{2}\left[(u'_r{}^{i+1,j+1} - u'_r{}^{i+1,j}) - (u'_r{}^{i,j+1} - u'_r{}^{i,j})\right]^2 \\
& + \sum_{i=1}^{n-1}\sum_{j=1}^{m}\frac{E_{cc}^{i,j}}{2}(u'_c{}^{i+1,j} - u'_c{}^{i,j})^2 \\
& + \sum_{i=1}^{n-1}\sum_{j=1}^{m-1}\frac{G_{cr}^{i,j}}{2}\left[(u'_c{}^{i+1,j+1} - u'_c{}^{i,j+1}) - (u'_c{}^{i+1,j} - u'_c{}^{i,j})\right]^2
\end{aligned}
$$

where $m$ is the radial direction's node number, $n$ is the circumference direction's node number, and $u' = (u'_r, u'_c)$ is the revised displacement vectors.

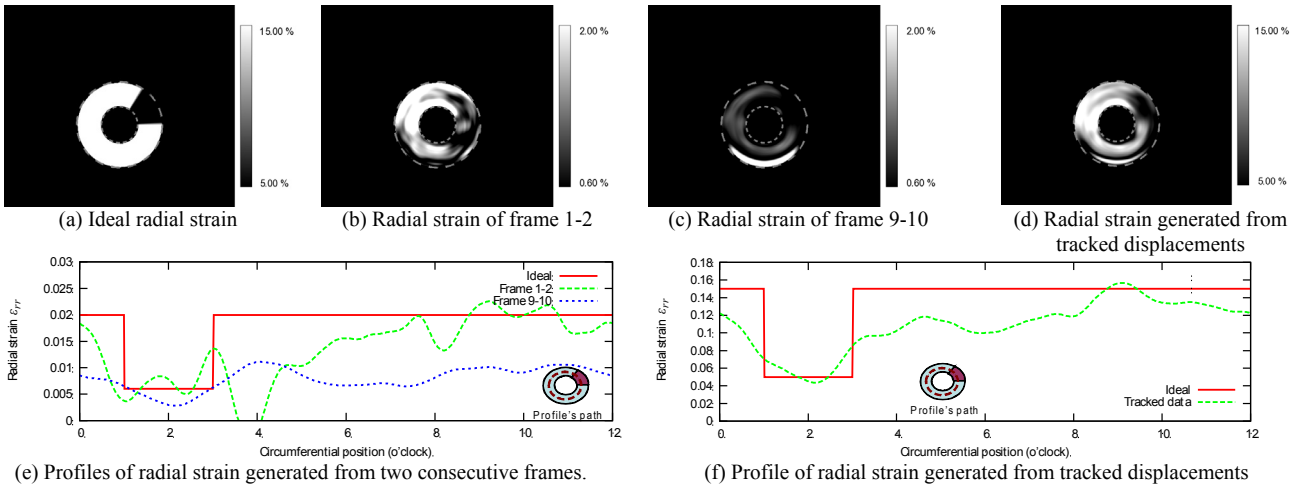


(a) Ideal radial strain (b) Radial strain of frame 1-2 (c) Radial strain of frame 9-10 (d) Radial strain generated from tracked displacements

(e) Profiles of radial strain generated from two consecutive frames. (f) Profile of radial strain generated from tracked displacements

Fig. 1 Resulting images and profiles

By minimizing the error function, the revised displacements, which combine original and revising displacements at each mesh node, are obtained. The virtual spring's pseudo-elasticity parameters $E^{i,j}{}_{rr}$ and $E^{i,j}{}_{cc}$ control the axial displacement revision. The pseudo shear elasticity parameters $G^{i,j}{}_{rc}$ and $G^{i,j}{}_{cr}$ control the shear direction's revising effect.

For further improving the smoothing effect, the elasticity parameters are automatically adjusted based on the noise level. For displacement data, because the error fluctuated around the true value, if the displacement error of one sampling node is large, the difference between its neighbor's displacements will also be large. Based on this, a displacement error function is defined as

$$\sigma_{rr}^{i,j} = \left| \frac{u_r^{i,j+1} - 2u_r^{i,j} + u_r^{i,j-1}}{h_r^{i,j} + h_r^{i,j+1}} \right|,$$

$$\sigma_{cc}^{i,j} = \left| \frac{u_c^{i+1,j} - 2u_c^{i,j} + u_c^{i-1,j}}{h_r^{i,j} + h_r^{i+1,j}} \right|,$$

$$\sigma_{rc}^{i,j} = \sigma_{rc}^{i,j} = \frac{\sigma_{rr}^{i,j} + \sigma_{cc}^{i,j}}{2}.$$

$h_r$ and $h_c$ is distance between adjacent node in radial and circumference direction, respectively. The pseudo-elasticity parameters for each sampling node are mapped by sin function from $E^{min}$ to $E^{max}$ based on the above functions as

$$E^{i,j} = \sin\left(\frac{\sigma^{i,j} - \sigma^{\min}}{\sigma^{\max} - \sigma^{\min}} \frac{\pi}{2}\right)(E^{\max} - E^{\min}) + E^{\min}.$$

After the displacement vectors are revised, the displacement vectors are tracked by combine previous and current two frames' revised displacement. Finally, the strain tensors are calculated from the tracked and smoothed displacement vectors.

## 3. Simulation

The performance of our proposed method is evaluated by numerically simulating the short-axis imaging of a 3-D myocardial model. The hypothetic infarcted wall is located around 1 to 3 o'clock. The maximum radial strain in a normal wall is set to be 15% and 5% in an infarcted wall. The total scanned frame number is 30. The short-axis twisting is set to 4.5 degrees. The 2-D transducer's outer diameter is 20 mm. The ultrasonic pulse has a center frequency of 3.75 MHz, and the fractional bandwidth is 40%. The signal-to-noise ratio is set to 10 dB. The optimized pseudo-elasticity parameters, which control the smoothing, are set in the range of 20 to 2800 in the radial direction and 20 to 800 in the shear direction.

## 4. Results and Conclusions

The resulting images and profiles are shown in Figure 1. Figure 1(a) shows the ideal radial strain. Figure 1(b) shows the radial strain generated from frames 1-2, and figure 1(c) shows the radial strain generated from frames 9-10. Figure 1(d) shows the radial strain generated from tracked displacements. Figure 1(e) shows the profiles of radial strain generated from consecutive two frames, and figure 1(f) shows profile of radial strain generated from tracked displacements. The average accuracy of images generated from consecutive two frames is 60.27%, and the accuracy of image (d), which is generated by our proposed method, is 33.50%. From the resulting images and evaluating parameters, we can see that even the SNR is low, our proposed method can output accurate and stable myocardial strain image.

## References

1. N.Nitta and T. Shiina, 2003 IEEE Ultrasonics Symp., pp. 1258-1261.
2. S. Bu, T. Shiina, M. Yamakawa, and H. Takizawa: IEEJ Transactions, pp.1732-1742, vol.127, no.10, 2007.

3J7a-2

Proceedings of Symposium on Ultrasonic Electronics, Vol. 29 (2008) pp. 511-512
11-13 November, 2008

# Examination of Parameters Depending on Scatterer Density for Quantification of Liver Fibrosis

肝線維症の定量化のための散乱体密度に依存するパラメータの検討

Hiroshi Eduka[1‡], Tadashi Yamaguchi[2], Naohisa Kamiyama[3], and Hiroyuki Hachiya[4]
([1] Graduate school of Advanced Integration Science, Chiba Univ.; [2]Resarch Center for Frontier Medical Engineering, Chiba Univ.; [3]Toshiba Medical Systems Co.; [4]Graduate School of Sci. and Eng., Tokyo Institute of Technology)
江塚大史[1‡]，山口匡[2]，神山直久[3]，蜂屋弘之[4]（[1]千葉大 融合科学; [2]千葉大 CFME; [3]東芝メディカルシステムズ; [4]東工大 理工）

## 1. Introduction

Various studies about tissue characterization (TC) that used probability density function (PDF) of echo envelopes have been performed[1]. In the case of enough scatterer density, such as the normal liver tissue, the PDF of echo envelopes can be approximated by Rayleigh distribution. On the other hand, in the heterogeneous medium, such as the liver fibrosis, the PDF of echo envelopes will not obey Raylergh distribution. In this case, it is known that the PDF can be approximated by K, Weibull or Nakagami distribution. However, it is difficult to characterize tissue properties by only these distribution functions.

In this research, we examined relationships between the scatterer density and the PDF of echo envelopes of heterogeneous medium with computer simulation and *in vivo* data. Parameters to estimate scatterer density of fiber tissue is calculated by Q-Q probability plot in simulation data, and we examined possibility of the quantification of the actual liver fibrosis.

## 2. Quantitation method of heterogeneity

Generalization of amplitude characteristic evaluation of echo envelopes was tried by the computer simulation. Simulation models were made by mixing a high scatterer density part of 20-200 scatteres/resolution-cell that assumed fiber tissue to the medium of density enough to generate the speckle (10 scatters/rc). As a result, the fiber tissue and the normal liver which generates a speckle were intermingled. The mixture rate of the high density part is 8-40% in the whole of ROI. The amplitude characteristic of echo envelopes was derived from the result of Q-Q probability plot. In

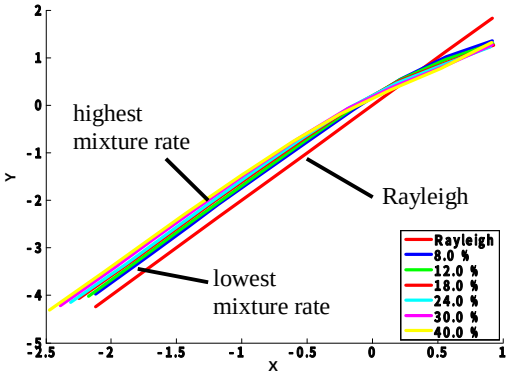


Fig.1 Results of Q-Q probability plot in simulation data of homogeneous and heterogeneous media.

Q-Q probability plot, Rayleigh distribution is expressed by the straight line with the gradient of two[2,3].

**Figure 1** shows the results of Q-Q probability plot in the case of 60 sc/rc were mixed in homogeneous media with different mixture rate. The value of curvature of the results of Q-Q probability plot was increased with rise of the mixture rate of the high scatterer density part. It is thought that change of the value of curvature in change of the rate of the signal of a high echo to the signal of a low echo which constitutes a speckle.

Then, we approximated the result of the Q-Q plot in two different straight lines, and proposed those slopes and intersection coordinates as indexes of the mixture rate of a high echo signal. The slopes was calculated by $\tan^{-1}\theta_1$ in low amplitude part and $\tan^{-1}\theta_2$ in high amplitude part (**Fig.2**).

---

eduka@graduate.chiba-u.jp

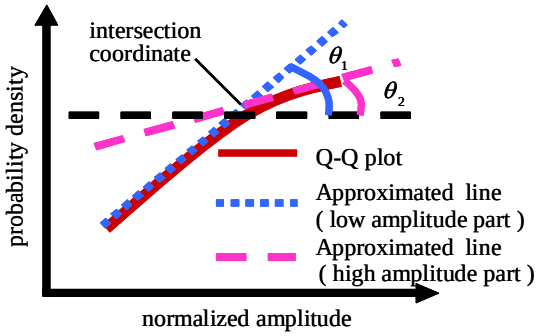


Fig.2 Parameters which evaluate a mixture rate of high scatterer density part.

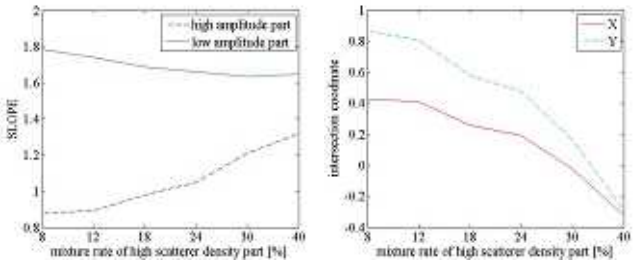


(a) (b)

Fig.3 Change of the parameter accompanying the mixing rate of high scatterer density part (60 scatters/rc). (a) Change of slope. (b) Change of intersection coordinates.

## 3. Evaluation of parameters by computer simulation

**Figure 3** shows change of parameters accompanying change of the rate of mixture of a high scatterer density part (60 sc/rc). The slope of low amplitude part decreased slightly with increase of the mixture rate. On the other hand, the slope of high amplitude part decreased greatly with increase of the mixture rate. It has high correlation with intersection coordinates, and these parameters had special combination corresponding to the mixture rate of high scatterer density part.

These features were similarly observed, when changing scatterer density from 20 to 200 scatters/resolution-cell at a fixed mixture rate.

## 4. Application to *in vivo* data of liver fibrosis

The combination of the parameter determined by the simulation was applied to clinical data. Echo data sets (*in vivo*) of liver fibrosis were classified by Shin-Inuyama classification as the result of biopsy.

**Figure 4** shows the original echo data sets and results of applying our estimation method with four parameters. The result which the part presumed to be high scatterer density as compared with the speckle was dyed red is shown below to the original data of each degree of pathological change advance.

In F0 which is normal liver, the dyed part is only walls of portal veins or a vein. In F1 in early stages of a pathological change, a small number of dyeing part is observed in the edge and parenchymatous part of liver. The quantity of the dyeing part increased and diffused with advance of a pathological change as same as the feature of liver fibrosis.

## 5. Conclusion

From the result of simulation, the parameters obtained from Q-Q probability plot changed depending on the scatterer density and the mixture rate, and showed the combination of the respectively characteristic parameters. It is thought that the stage of liver fibrosis can be quantified by estimating the scatterer density by using the combination of these parameters.

## References

1. Maartje M. Nillesen, et.al. : Ultrasound Med. Biol. **34** (2008) 674.
2. T. Yamaguchi, H. Hachiya, et.al. : Jpn. J. Appl. Phys. **44** (2005) 4615.
3. H. Yamada, et.al. : Journal of Hepatology **44** (2006) 68.

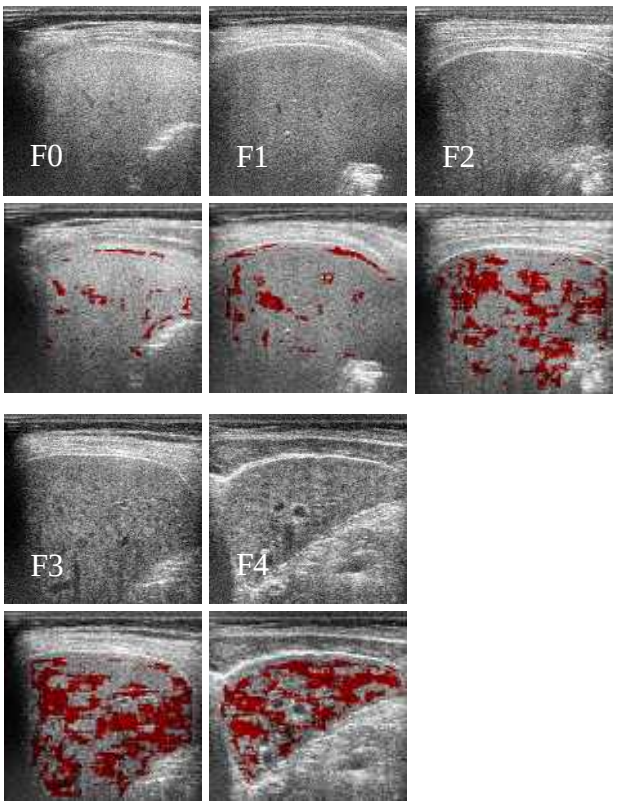


Fig.4 Parametric imaging for liver fibrosis.

3J7a-3

Proceedings of Symposium on Ultrasonic Electronics, Vol. 29 (2008) pp. 513-514
11-13 November, 2008

# Measurement of Scatterer-Size Dependent Frequency Characteristics of High Frequency Ultrasonic Echoes for Assessment of Red Blood Cell Aggregation

赤血球凝集度評価を目指した超音波散乱波の周波数特性の散乱体サイズ依存性の計測

Nobutaka Saitoh[1†], Hideyuki Hasegawa[2,1] and Hiroshi Kanai[1,2] ([1] Graduate School of Eng. Tohoku Univ.; [2]Graduate School of Biomedical Eng., Tohoku Univ.)
齋藤靖好 [1]，長谷川英之 [2,1]，金井　浩 [1,2]　([1] 東北大院　工; [2] 東北大院　医工)

## 1. Introduction

Red blood cell (RBC) aggregation, which is one of the determinants of blood viscosity, plays an important role in blood rheology. RBC aggregation is formed by adhesion of RBCs because electrostatic repulsion between RBCs weakens as protein and saturated fatty acid in blood increase. Excessive RBC aggregation promotes various circulatory diseases in the clinical situation, such as atherosclerosis, hypercholesterolemia, diabetes, thrombosis and so on [1,2]. Therefore, noninvasive assessment of RBC aggregationis highly required. The purpose of this studyis to establish a noninvasive and quantitative method for assessment of RBC aggregation.

## 2. Method

RBC is a very small ultrasonic scatterer whose radius is 4 μm at most, and amplitudes of scattered RF echoes are very small. To assess the level of RBC aggregation, the power spectra of echoes are calculated using the fast Fourier transform (FFT) and the RF echoes are analyzed in the frequency domain.

The spectrum of nonaggregating RBCs obeys Rayleigh behavior [3,4], which means that the power of scattered wave is proportional to the fourth power of frequency. By dividing the measured power spectrum by that of echo from a silicone plate, the frequency response of transmitting and receiving transducer are removed from the measured power spectrum [5]. Then, the frequency range used for normalization was determined because the ultrasonic pulse used in this study has a finite frequency band width. The reproducibility function $|\hat{\gamma}_0(f)|^2$ [6] is used to determine the effective frequency band of the transducer.

E-mail:nsaitoh@us.ecei.tohoku.ac.jp

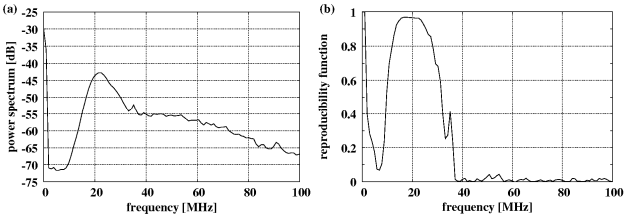


Fig. 1. (a) Power spectrum from Silicone plate, (b) The reproducibility function.

$$|\hat{\gamma}_0(f)|^2 = \frac{\left|\sum_{i=1}^{M} S_i(f)\right|^2}{M\sum_{i=1}^{M}|S_i(f)|^2}, \qquad (1)$$

where $S_i(f)$ and $M$ show the power spectrum of an RF signal and the number of acquisitions of RF signals, respectively. Figure 1(a) shows the power spectrum that is averaged over 100 power spectra $S_i(f)$ of RF signals from a silicone plate, and Fig. 1(b) shows the reproducibility function $|\hat{\gamma}_0(f)|^2$. The frequency band, in which the reproducibility function was greater than 0.9, was used for normalization.

In Rayleigh scattering, the normalized power spectrum changes linearly with respect to the logarithmic frequency and scatterer's effective radius can be estimated from the intercept. In non-Rayleigh scattering, on the other hand, the spectral slope decreases as the scatterer's effective radius increases. Therefore, it is possible to assess the RBC aggregation from the spectral slope and intercept value.

## 3. Basic experiment using microspheres

The employed ultrasound diagnostic system (UD-1000, Tomey, Japan) was equipped with a mechanical scan probe at a center frequency of 40 MHz (wavelength λ is about 40 μm). Ultrasound RF echoes were acquired at a sampling frequency of 1

Table 1. Microspheres' diameter and experimental results.

| | particle diameter [μm] | slope [/$\log_{10}$ f] | intercept [no dimension] |
|---|---|---|---|
| (1) | 5±2 | 4.08 | −29.4 |
| (2) | 11±3 | 3.33 | −23.8 |
| (3) | 15±5 | 2.52 | −18.1 |
| (4) | 30±10 | −0.67 | 4.51 |

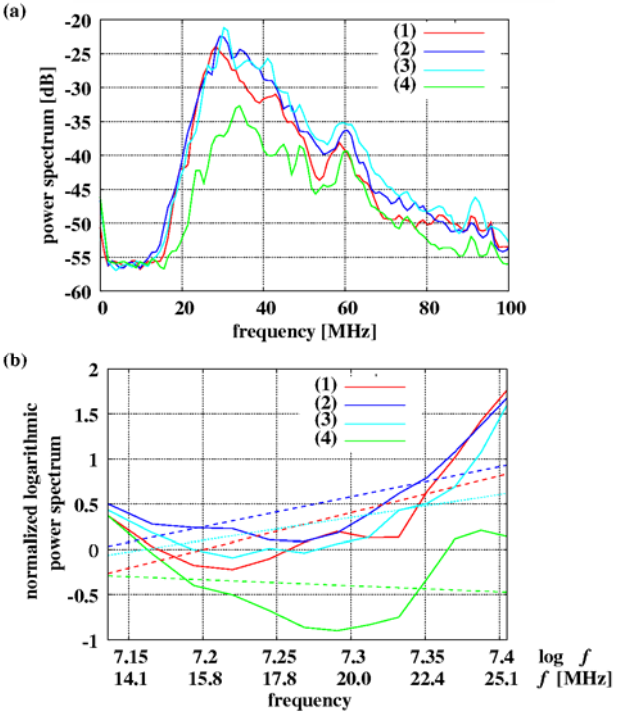


Fig. 2. (a) Power spectrum obtained for microspheres, (b) Normalized power spectrum and least-mean-squared regression lines.

GHz and 100 power spectra were averaged to reduce the influence of noise. Table 1 shows measured objects which have deferent scatterers' radius. These microspheres simulated RBC and RBC aggregation. Figure 2(a) shows the averaged power spectra of echoes from the microspheres. Figure 2(b) shows the normalized power spectrum. The spectral slope and intercept values were shown in Table 1. In Fig 2(b), the normalized power spectrum of a larger scatterer showed smaller spectral slope.

## 4. *In vivo* experiment

Figure 3(a) shows the power spectrum from the lumen of the vein at dorsum manus of a 23-year-old healthy male and Fig. 3(b) shows the normalized power spectrum and least-mean-squared regression line. The spectral slope and intercept were determined to be 3.75 and -27.6, respectively. RBC diameter is 8 μm at most and this value of radius is between those of microspheres (1) and (2). Therefore, the spectral slope of echoes from RBC was close to that of microsphere (1) and (2). These results show that the Spectral slope is related to the scatterer's radius.

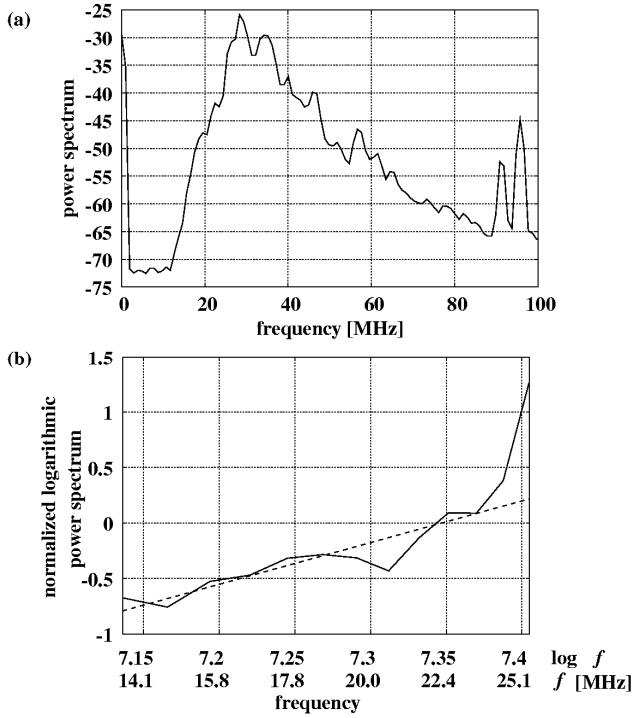


Fig. 3. (a) Power spectrum obtained for the vein, (b) Normalized power spectrum and least-mean-squared regression lines.

## 5. Conclusion

The effective radius of nonaggregating RBC was estimated *in vivo* using spectral parameters. The increase of scatterer's radius led to decrease of the spectral slope. These results show the possibility of the proposed method for the assessment of RBC aggregation.


## Acknowledgment

We would like to appreciate Tomey corporation for their cooperation on the use of the diagnostic equipment.


## References


1. D. G. Paeng, et al.: *Ultrasound Med. Biol.* **30** (2004) 45.
2. A. Amaratene, et al.: *IEEE Ultrason. Symp.* (2005) 874.
3. M. F. Insana, et al.: *J. Acoust. Soc. Am.* **87** (1990) 179.
4. G. Cloutier, et al.: *J. Acoust. Soc. Am.* **122** (2007) 645.
5. F. L. Lizzi, et al.: *J. Acoust. Soc. Am.* **73** (1983) 1366.
6. H. Kanai: *Spectrum Analysis of Sound and Vibration* (Corona Publishing Co., Ltd., Tokyo, Japan, 1999) (in japanese)

3J7a-4

Proceedings of Symposium on Ultrasonic Electronics, Vol. 29 (2008) pp. 515-516
11-13 November, 2008

# An analysis of the pulse wave for the blood vessel evaluation
# 血管壁評価に向けた脈波解析

Masashi Saito†, Mami Matsukawa, Yoshiaki Watanabe (Doshisha University)
齋藤雅史‡，松川真美，渡辺好章（同志社大）

## 1. Introduction

Arteriosclerosis disease has become a problem in this aging society. The pulse wave velocity (PWV) method is one of the diagnostics techniques for arteriosclerosis under the incipience condition[1]. The velocity of the pulse wave which propagates in the blood vessel wall is analyzed with this technique. This is because viscoelastic characteristics of the blood vessel change by the arteriosclerosis disease[1]. In addition to the velocity changes, the pulse waveform itself changes due to the viscoelastic characteristics. This change of the waveform is not mainly used now. We then focus on the changes of the waveform to extract wave information of the viscoelastic property of the blood vessel. Of course, our purpose is to screen the symptom of incipient arteriosclerosis by the pulse wave. Therefore, we suggest a simple technique for the evaluation of the wave.

## 2. Methods

*Signal Processing and Computational Techniques*

The pulse wave is the displacement wave caused by the inner pressure wave which propagates in the blood vessel. This pressure wave is composed of the incident wave and the reflected wave. The incident wave is a pulsed wave caused by the blood flow which comes from the constriction of the heart. The reflected wave is generated by the reflection of the incident wave at the peripheral arteries. Because the reflected wave propagates to the peripheral artery, it strongly depends on the viscoelasticity of the vessel wall. Therefore, the evaluation of the blood vessel seems possible by using this reflected waveform. The incident waveform becomes important to estimate the reflected wave. **Figure 1** shows the outline for the estimation of the incident wave.

At first, the changes in sectional area of the blood vessel were estimated as a function of time with the observed blood flow velocity waveform. Here, the equation of continuity and the motion equation of one dimension fluid model was used[2]. Next, the waveform of inner pressure was presumed from the relationship between changing sectional area and pressure in the blood vessel[2]. To convert from the inner pressure to displacement, generalized Voigt model was used. In this case, the viscoelastic shear properties were obtained from the reference[3]. The senior subjects' shear elasticity constants were estimated 2.5 times with the value of young subjects. After the estimation of incident wave, the reflection waveform was obtained from the difference between this incident wave and the observed pulse wave.

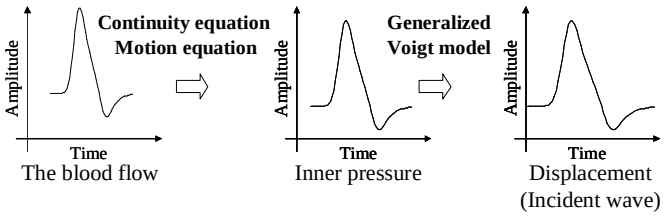


(i) Estimation of the incident wave.

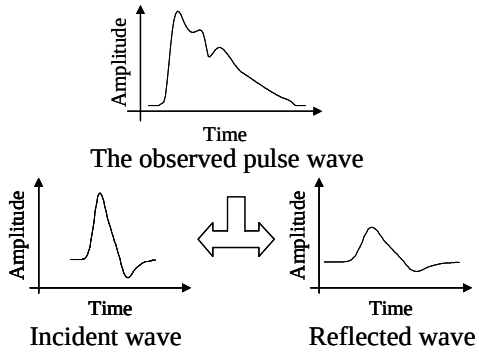


(ii) Separation technique.

Fig.1 Estimation of the reflected wave.

*Measurement of the pulse wave and Blood Flow*

The electrocardiogram and the pulse wave at the left common carotid artery of the healthy young subjects (10 persons) and senior subjects (7 persons) were measured. **Figure 2** shows the measurement system. A mechano-cardiogram system (FUKUDA DENSHI, MES-1000) was used for the measurement. The electrode was installed on both hands and feet to measure the electrocardiogram. The amorphous pulse wave sensor (FUKUDA DENSHI, TY-501A) was used to measure the pulse wave. To measure these data during the resting state, subjects refrained from meal, exercise and smoking. They got lying down for ten minutes in the room at 22℃. Then, the measurement was started. The measurement period was 60 seconds.

After the pulse wave measurement, we measured an electrocardiogram and the blood flow velocity at left common carotid artery during the resting state. A probe (TOSHIBA, PLT-1204AT center frequency 12MHz) of ultrasonic diagnostic equipment (TOSHIBA, Aplio SSA-700A) was used for the measurement. The measurement period was 5 seconds.

mmatsuka@mail.doshisha.ac.jp

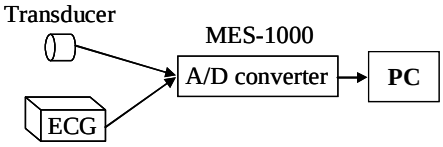

Fig.2 Measurement system.

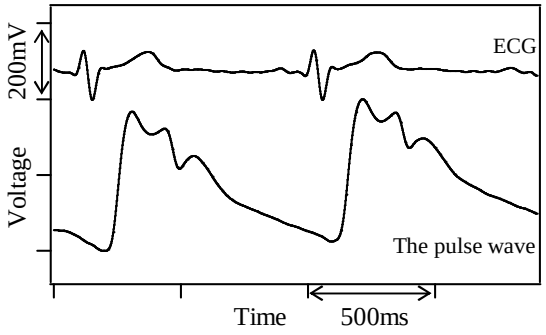

(i) 24 years old.

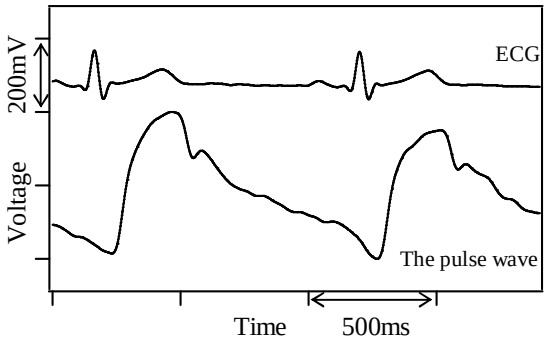

(ii) 73 years old.

Fig. 3 Observed waveforms of the pulse wave.

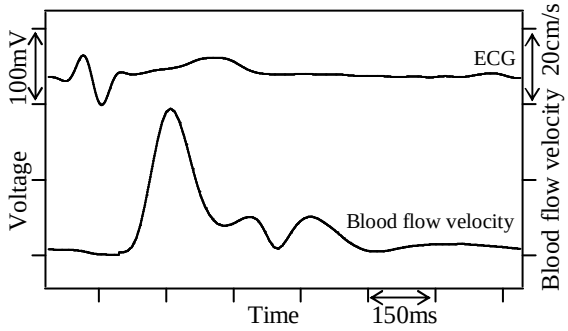

(i) 24 years old.

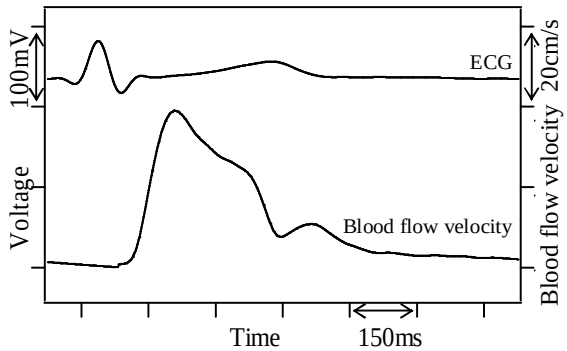

(ii) 73 years old.

Fig. 4 Observed waveforms of blood flow velocity.

## 3. Results and Discussion

**Figure 3** shows examples of the observed pulse wave. **Figure 4** shows the observed blood flow velocities. The incident wave was estimated from the blood flow velocity. The observed pulse waveform was then separated into the incident wave and the reflected wave. **Figure 5** shows the results of separated waves normalized by the amplitude of the incident waves. As shown in Fig. 5, the amplitude of the reflected wave in the senior subject is larger than that of the young subject. This tendency was similar with the data of other subjects. Because senior subjects' vessel walls seem to be harder, the influence of the wave attenuation is probably small.

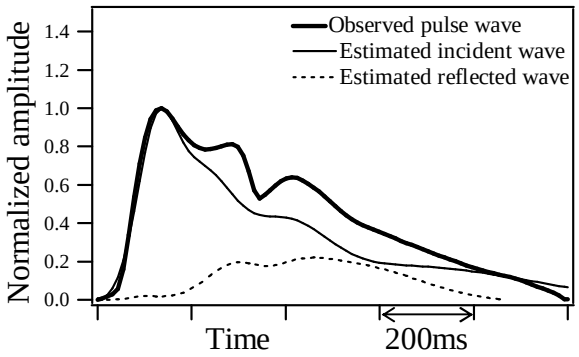

(i) 24 years old.

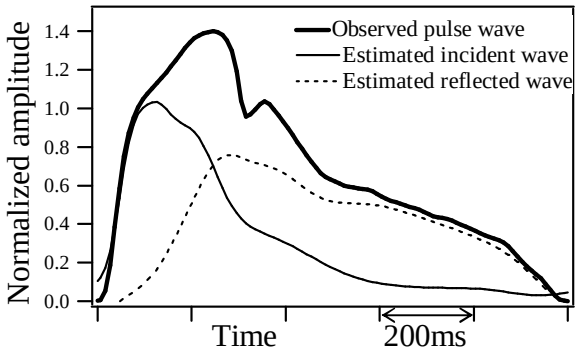

(ii) 73 years old.

Fig. 5 Results of wave separation.

## 4. Conclusion

A simple technique to evaluate the pulse wave is proposed. From the comparison between young and senior subjects, we found changes in the reflected wave due to the age. The viscoelastic characteristics of the blood vessel wall changes owing to the age. Therefore, there is a possibility that the property of the vessel wall can be evaluated with this simple technique.

## References

1. W. W. Nichols, "McDonald's Blood Flow In Arteries," Hodder Arnold, 2005.
2. T. Kitawaki, et. al. "The analysis of upper arm pressure pulse waveform if the systemic artery using the one-dimensional numerical model," JSFM, C2-1, 2004.
3. N.Katakura, et. al. "The effect of molecular weight of polymer on viscoelastic properties of tissue conditioners," JSDMD, 7(3), 439-443, 1988.

3J7b-1

Proceedings of Symposium on Ultrasonic Electronics, Vol. 29 (2008) pp. 517-518
11-13 November, 2008

# Micro bubble adhesion to target wall by ultrasonic wave frequency sweep method

超音波の周波数走査法によるターゲット壁への微小気泡の付着

Yoshiki Yamakoshi†, Takashi Miwa (Graduate school of Eng., Gunma Univ.)
山越　芳樹‡, 三輪　空司（群馬大院工学研究科）

## 1. Introduction

Permeability enhancement that promotes drug injection through cell membrane by ultrasonic wave is an useful means in future drug delivery system which uses micro bubbles as payload vehicles. Mechanical effects such as surrounding liquid flow which is caused by micro bubble forced oscillation and micro jet which is produced by bubble destruction enhance the permeability of the cell membrane. Since these effects increase in the vicinity of the bubble, the bubbles are placed close to the surface of the target in the permeability enhancement. In addition, the bubbles have to cover over the target surface because the mechanical effect of one bubble is spatially restricted. Group of UC Davis has proposed a sophisticated method which adheres micro bubbles to the blood vessel wall using ultrasonic traveling wave1). This method has a feature that the bubble adhesion is carried out mechanically by an acoustic radiation force, however the bubbles adheres only to the wall of traveling direction of the ultrasonic wave in this method.

We have proposed a method of self-adhesion of micro bubbles to the target wall using ultrasonic pumping wave2). The acoustic radiation force between actual bubble and the mirror bubble, which is produced by bubble nonlinear oscillation, acts as a trapping force to the bubble.

In this paper, a method of micro bubble adhesion to the target wall by frequency sweep of the pumping ultrasonic wave is proposed.

## 2. Bubble adhesion to target wall by ultrasonic wave frequency sweep method

Figure 1 shows basic idea of proposed micro bubble adhesion by frequency sweep of ultrasonic pumping wave. First, an ultrasonic pumping wave is applied to the target (Fig.1 (a)). The sound pressure of the pumping wave is chosen lower than the threshold of the bubble destruction though it is enough to generate a nonlinear vibration of the bubble. The neighboring bubbles aggregate by the secondary Bjerknes force which is an acoustic radiation force between oscillating micro bubbles

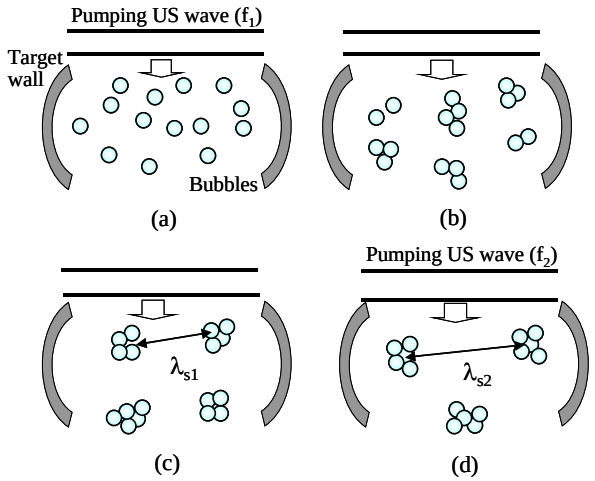


Fig.1　Bubble adhesion to target wall by frequency sweep of ultrasonic pumping wave.

(Fig.1 (b)). The secondary Bjerknes force also aligns the bubbles with almost the same interval. This interval relates with the wavelength of the secondary wave radiated from the bubbles (Fig.1 (c)). Then, the frequency of the ultrasonic pumping wave decreases from frequency $f_1$ to $f_2$ ($f_2<f_1$). Since the frequency of the secondary ultrasonic wave decreases from $nf_1$ to $nf_2$ where n is order of harmonic wave, the interval between neighboring bubbles expands with the expansion of the wavelength of the secondary wave (Fig.1 (d)). A large amount of bubbles reaches the target wall by repeating the procedure which consists of the frequency sweep from $f_1$ to $f_2$ followed by rapid frequency change from $f_2$ to $f_1$.

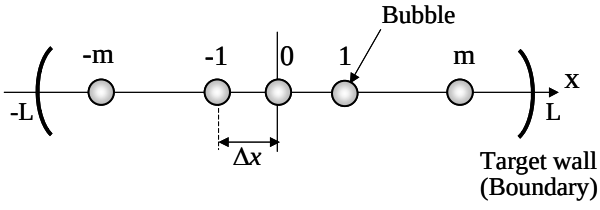


Fig.2 Schematic diagram of the bubble movement by frequency sweep of the ultrasonic pumping wave.

Let us consider a condition for the bubble to reach the target wall. Figure 2 shows a model under consideration. We assume that 2m+1 bubbles align along x axis and they move either in x or in –x directions by the frequency sweep. The secondary

e-mail:yamakosi@el.gunma-u.ac.jp

Bjerknes force $F_B$ between two bubbles with an interval of x is given by 3)

$$F_{B,n} = -2\pi R_1^3 p_{I0} R_{\varepsilon,n} \frac{p_{1,n}}{x} k_n \sin\left(k_n x + \theta_{R,n}\right) \quad (1)$$

where $R_1$ : equilibrium radius of bubble, $p_{I0}$ : sound pressure of the pumping wave, $R_{\varepsilon,n}$ : radial displacement of n-th order nonlinear volumetric oscillation of bubble. $p_{1,n}$, $k_n = 2\pi/\lambda_n$ and $\theta_{R,n}$ : sound pressure, wave number and relative phase of n-th order nonlinear secondary ultrasonic wave, respectively. In eq.(1), it is assumed that n-th order harmonic oscillation is dominant among harmonic oscillations. Since the Bjerknes force is a sinusoidal function, the bubbles are trapped at the positions where the following conditions are satisfied.

$$F_{B,n} = 0 \quad and \quad \partial F_{B,n}/\partial x < 0 \quad (2)$$

From eqs.(1) and (2), interval between the neighboring bubbles $\Delta x$ is given by

$$\Delta x = \lambda_n - \left(\theta_{R,n}/2\pi\right)\lambda_n \quad (3)$$

If the frequency of the ultrasonic pumping wave is swept from $f_1$ to $f_2$ where $f_2<f_1$, it might be considered that the frequency of the nonlinear secondary ultrasonic wave is swept from $nf_1$ to $nf_2$. This frequency sweep expands the bubble alignment. The positions of m-th bubble for the pumping wave frequencies $f_1$ and $f_2$ are given by

$$x_m(f_1) = m\left(1-\left(\theta_{R,n}/2\pi\right)\right)\lambda_{n,1}$$
$$x_m(f_2) = m\left(1-\left(\theta_{R,n}/2\pi\right)\right)\lambda_{n,2} \quad (4)$$

where $\lambda_{n,1}$ and $\lambda_{n,2}$ are the wavelength of the nonlinear secondary waves, respectively.

From eq.(4), displacement of m-th bubble is

$$dx_m = x_m(f_2) - x_m(f_1) = m\left(1-\frac{\theta_{R,n}}{2\pi}\right)\left(\lambda_{n,2}-\lambda_{n,1}\right) \quad (5)$$

Equation (5) shows that the displacement of m-th bubble increases with increase of number of aligned bubbles. Once the bubble reaches the target wall, it is impossible to expand the whole of the bubble alignment any more, because the Bjerknes force acts as a repulsive force between bubbles. To collect the bubbles of more amount at the wall, the frequency is swept from $f_1$ to $f_2$ followed by rapid change of the frequency from $f_2$ to $f_1$.

## 3. Experiment

Experimental set-up is shown in fig.3. Micro bubble flow cell is 3 mm in width, 1mm in depth and 40 mm in length. Two concave ultrasonic transducers are adopted to introduce the ultrasonic pumping wave. Dynamics of micro bubbles are observed by microscope with CCD camera.

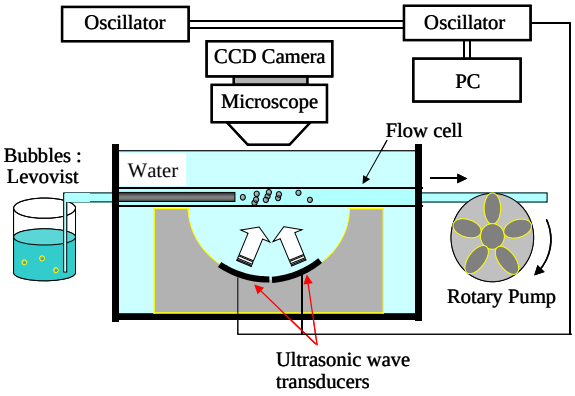


Fig.3 Experimental set-up.

Figure 4 shows an experimental result. Figs.4(a)-(c) are the ultrasonic pumping wave is set to 3MHz, 3.5MHz and 4MHz, respectively. Fig.(d) is a result of frequency sweep from 4MHz to 3MHz. An ultrasonic wave contrast agent (Levovist) is used as micro bubbles.

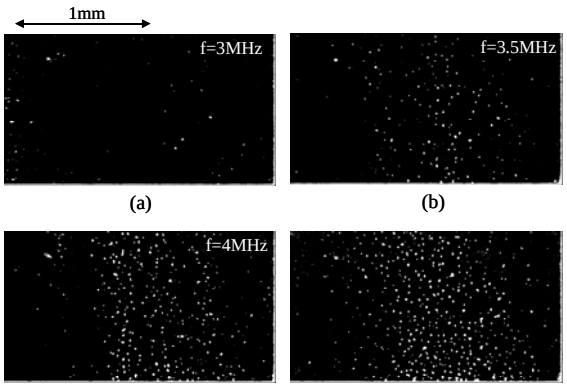


Fig.4 Experimental result.

## 4. Discussions

To concentrate the micro bubbles at the target wall, frequency sweep of ultrasonic pumping wave is proposed. Amount of bubbles at the wall increases by repetition of the frequency sweep. Experiment is carried out using Levovist micro bubbles.

## References

1. A. Lum, M. Borden, P. Dayton, D. Kruse, S. Simon, and K. Ferrara: J. Controlled Release **111** (2006) 128.
2. Y.Yamakoshi and T.Miwa, Jpn. J. of Appl.Phys. **47** (2008) 4127.
3. Y.Yamakoshi and T.Miwa, Jpn. J. of Appl.Phys. **46** (2007) 4847.

3J7b-2

Proceedings of Symposium on Ultrasonic Electronics, Vol. 29 (2008) pp. 519-520
11-13 November, 2008

# Ultrasound Based Multi-Functional Imaging Using Size Dependent Characteristics of Phase Change Nano Droplet

相変化ナノ液滴の粒径による音響特性の違いを用いた多機能超音波イメージング

Rei Asami†, Takashi Azuma and Ken-ichi Kawabata
(Central Research Lab., Hitachi Ltd.)
浅見玲衣‡，東隆，川畑健一　((株)日立製作所　中央研究所)

## 1. Introduction

Accuracy of imaging based diagnosis could synergistically improve with simultaneous allocation of multiple molecular targets. Concurrent visualization of multiple targets requires distinguishable probes and an image acquisition method which can simultaneously handle signals from each probe. We aim to provide such an image acquisition method with ultrasound and our novel contrast agent phase-change nano droplets (PCND), submicron sized liquid droplets which turn into highly echogenic microbubbles upon ultrasound pulse application [1]. Combined with real-time image acquisition of ultrasound scanner, the method would lead to a clinically applicable multi-targeted molecular imaging system.

**Figure 1** illustrates the basic principle of PCNP mechanism, which enables localized in-situ microbubble generation further to be utilized as a therapeutic sensitizer [2] after visualization. PCND is composed of mixture of low boiling point and high boiling point perfluorocarbon stabilized by surfactant lipids and polymers, shown in **Fig. 2.**

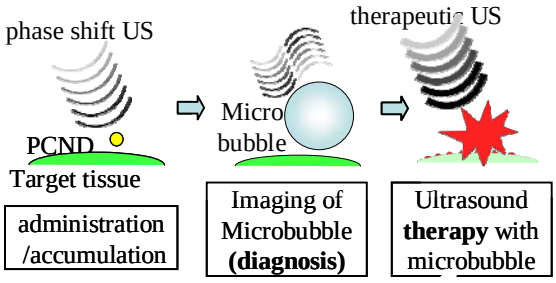


**Figure1: PCND Mechanism**

Our aim is to establish either separately inducible or visualize-able droplets for multi-targeted molecular imaging system by altering its perfluorocarbon and stabilizing lipids contents. In this study, we focused on changing two main parameters, size and perfluorocarbon mixing ratio, of all parameters possibly affecting acoustic characteristics of PCND, and investigated their acoustic characteristics. Specifically, acoustic pressure necessary for phase change induction and acoustic response at the timing of and after microbubble generation are investigated.

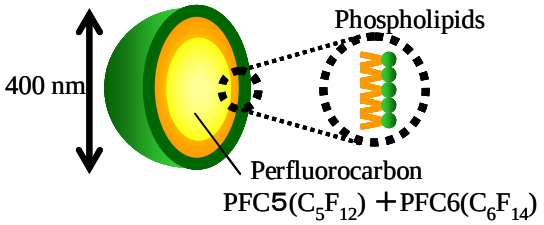


**Figure2: PCND Structure**

## 2. Methods

PCND is prepared with varying perfluorocarbon (PFC) mixture and emulsifier at varying PFC to emulsifier ratio, and emulsified at 20 MPa. Laser diffraction particle size analyzer is used for particle characterization. PCND dispersion is suspended in polyacrylamide gel phantom, which is placed in water bath at 37℃ for ultrasound application at frequency of 8 and 4 MHz, 4 cycles, and varying amplitude for phase change induction. Acoustic characteristics of induced microbubbles are investigated acoustically using pulsar-receiver. For acquiring acoustic characteristics during phase change induction, ultrasound at 3.2 MHz, 500 cycles and 85V is used and acoustic response was gathered by hydrophone.

## 3. Results and Disucussion

Two different monodisperse PCND suspensions were produced with average diameter of 170, and 700 nm (**Fig.3)**. At 4 and 8 MHz, sound pressure threshold for phase change induction of small PCND were higher than large PCND by a factor of 1.8 and 1.5, respectively (**Fig.4**). When resonance frequency of generated microbubbles is measured, small group resulted in about 2.8 MHz whereas

large group resulted in 1.2 MHz, suggesting the size difference of resulted bubbles.

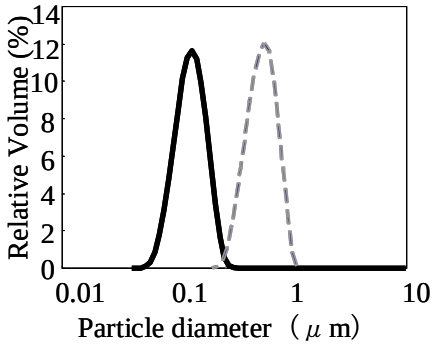


**Figure 3 : Particle distribution of PCND**

Solid line represents small PCND (mean diameter at 170nm) and dashed line represents large PCND (mean diameter at 700nm)

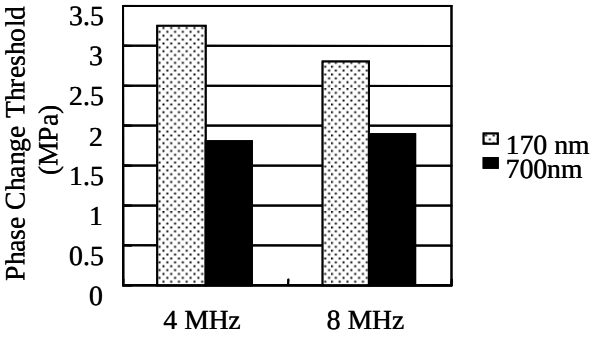


**Figure 4: Phase Change threshold for different sized PCND at 4 and 8 MHz**

FFT Spectra of acoustic signal acquired upon application of phase change ultrasound at 3.2 MHz are shown in **Fig.5**. In both small and large samples, peaks are observed at fundamental frequency as well as the second and the third harmonics. Relative amplitude of the second harmonic components of small group is significantly higher than that of large group (indicated by an arrow in Fig. 5). $1.5^{th}$ harmonic component is particular in small group (indicated by parenthesis in Fig. 5).

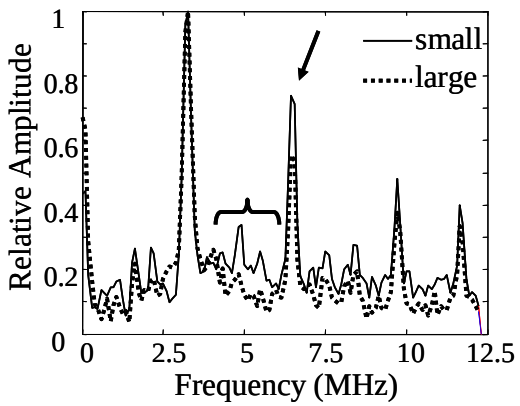


**Figure 5: FFT Spectra of Acoustic Signal emitted upon phase change US application**

When the proportion of ultrasonically inactive high boiling-point PFC (perfluorohexane) is increased within the same size, the threshold for phase change induction increased dramatically as shown in **fig 6**.

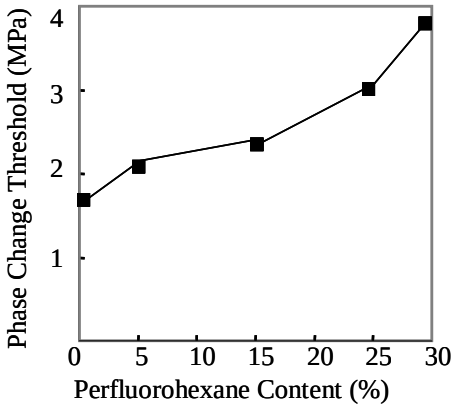


**Figure 6:Phase change threshold change**

These suggest that phase change could be induced selectively for different sized PCND according to the ultrasound amplitude with varying frequencies. Significant difference observed from emitted acoustic signal suggests that selective visualization could be done by appropriate filtering in frequency domain. However, it should be noted that not just acoustic characteristics but also other important characteristics such as pharmacokinetics of the drug could very likely be altered by size difference. As a solution, above results suggests that alternation of proportion of high boiling point PFC could potentially function as a mimic of PCND size difference. Amplitude modulation of ultrasound, thus, has a potential to visualize distinguishable PCND separately with an adequate image processing.

**Acknowledgment**

This work is entrusted by the New Energy and Industrial Technology Development Organization (NEDO), Japan.

**References**

1. K. Kawabata *et al*, Jpn J Appl Phys, **44** (2005) 4548.

2.. S. Umemura, et al, IEEE Trans. Ultrason.,Ferroelect., Freq. Contr, **52** (2005) 1690

Proceedings of Symposium on Ultrasonic Electronics, Vol. 29 (2008) pp. 521-522
11-13 November, 2008

# Calorimetric Method for Measuring High Ultrasonic Powers Using Distilled Water as the Heating Material: Eliminating the Effects of Acoustic Streaming, Viscous Heating and Thermocouple Position

## 純水を発熱体とするcalorimetry法による超音波パワー計測 －諸問題を軽減する水温測定法の提案－

Tsuneo Kikuchi, Takeyoshi Uchida (NMIJ/AIST)
菊池恒男，内田武吉（NMIJ/産総研）

### 1. Introduction

In this paper, we propose a calorimetric method for calibrating ultrasonic powers higher than 100 W. This method is an alternative to using radiation force balance (RFB) [1,2]. We report that the ultrasonic power measured using this method agrees well with that measured by the primary standard of NMIJ. We also demonstrate that acoustic streaming, viscous heating and the thermocouple position do not affect this measurement method.

### 2. Experimental method and results

Fig. 1 shows a schematic figure of the experimental setup. To avoid multiple reflections between the water surface and the transducer, the waterbath was tilted at an angle of about 30 deg., and the reflector was placed on the water surface. A cylindrical waterbath was used for a 1-MHz, 20-mm-diameter PZT transducer with an air-backing. The waterbath had an inner diameter of 150 mm and a depth of 90 mm. The amount of water used was about 1600 $cm^3$. A thermocouple (Takara) was used to measure the water temperature.

Conventionally, ultrasonic power has been estimated by taking the derivative of the water temperature rise as a function of time[4]. However, the time dependence of the temperature rise, is strongly affected by the thermocouple position (see Fig. 2). As Fig. 2 shows, steep temperature rises are observed at the time when the ultrasound is switched on (labeled “Ultrasound ON” in Fig. 2). This phenomenon is known as *viscous heating* [3] and is caused by ultrasonic

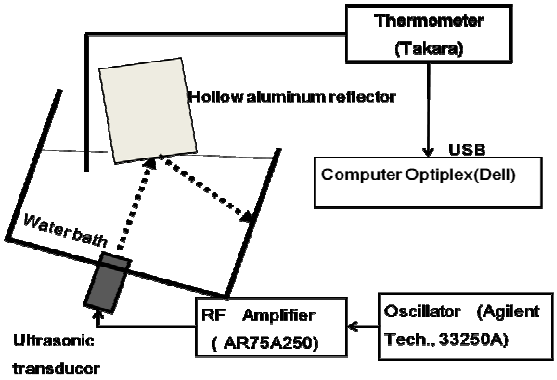


Fig. 1 Schematic diagram of the calorimetric measurement system.

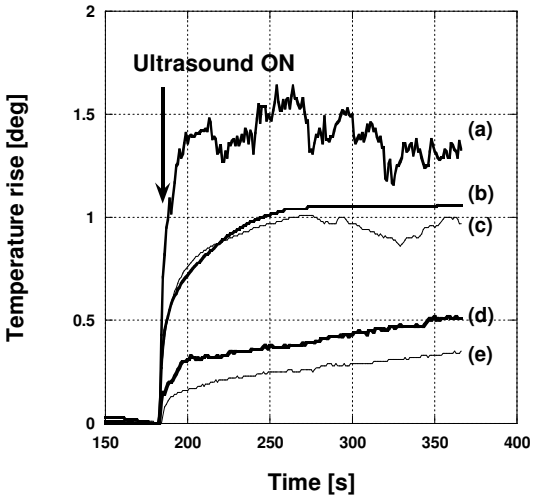


Fig. 2 Examples of water temperature as a function of time for ultrasonic irradiation at 1 MHz.

irradiation of the thermocouple. If the thermocouple is placed in the ultrasonic beam, the temperature rise becomes unstable as shown by curve (a) in Fig. 2. Viscous heating is observed in the low-frequency range, even

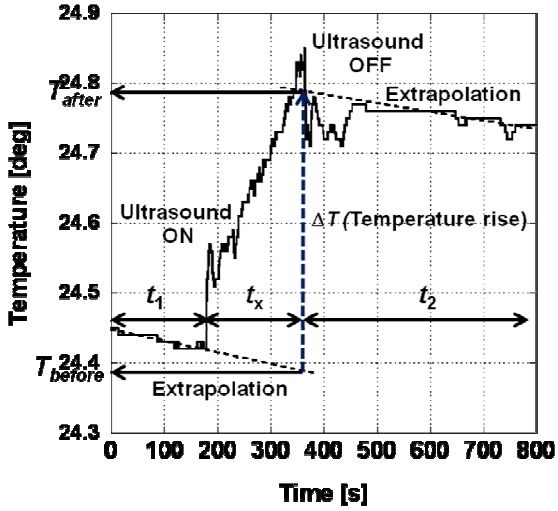


Fig. 3 Method of measuring the temperature rise caused by ultrasonic irradiation.

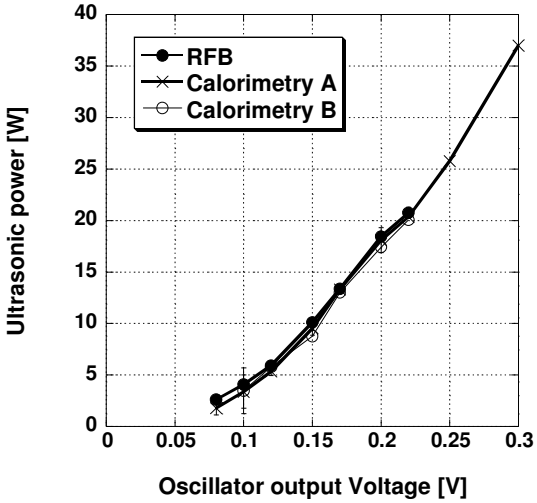


Fig. 4 Measured ultrasonic power by RFB and calorimetry at 1 MHz without multi-reflection.

when the thermocouple is located outside of the ultrasonic beam, due to diffraction. To overcome these problems, we measured the water temperature before and after ultrasonic irradiation, as shown in Fig. 3.

Ultrasound irradiation begins at a time $t_1$ after the measurement starts. The water temperature measurement continues for a time $t_2$ after the irradiation finishes. By assuming that the drift in the water temperature between $t_1$ and $t_2$ are sufficiently small, both temperature variations can be approximated by linear regression and are extrapolated to the time when the ultrasonic irradiation finishes. Here, the temperature rise caused by ultrasonic irradiation is defined as the difference between the two temperatures $T_{\text{before}}$ and $T_{\text{after}}$.

The ultrasonic power $P$ can be calculated by the equation (1):

$$P=(T_{\text{after}}-T_{\text{before}})/t_x \, C_p M \quad (1)$$

where $C_p$ is the heat capacity of water (4.2 [J $K^{-1}$ $g^{-1}$]) and $M$ is the mass of water. In the actual measurements, $t_1$, $t_2$ and $t_x$ are given by $t_1$=$t_x$=180 s and $t_2$=480 s.

As Fig. 4 shows, the measurement results at 1 MHz agree well with those of the radiation force balance method. The two sets of measurements labeled A and B in Fig. 4 were obtained after performing a full reset of the measurement system. These results demonstrate that this method does not require the thermocouple to be aligned.

### 3. Summary

In this study, we proposed a calorimetric method for measuring ultrasonic power that involves measuring the water temperature before and after ultrasonic irradiation. By using this method, problems associated with ultrasonic radiation including acoustic streaming, viscous heating and setting reproducibility can be removed. In the future, we intend to use this method to develop a standard for measuring the ultrasonic power.

### References

[1] T. Kikuchi, T. Uchida, Proc. Spring Meet. Acoust. Soc. Japan, 1323-1324, 2008 [in Japanese].

[2] T. Kikuchi and T. Uchida, Proc. Autumn Meet. Acoust. Soc. Japan, 1231-1232, 2007 [in Japanese].

[3] A. Shaw, *et al*., Ultrasound in Med. & Biol., Vol.25, No.1 (1999), 121-132..

[4] S. Koda, *et al*., Ultrasonic Technology, Vol.16, No.4 (2004) 1-5 [in Japanese].

3J7b-4

Proceedings of Symposium on Ultrasonic Electronics, Vol. 29 (2008) pp. 523-524
11-13 November, 2008

# Viscoelasticity Estimation of Soft Tissue for Estimation of Heat Generation in Application of Ultrasonic Surgical Knife

超音波メス使用時の発熱量推定のための
軟組織の粘弾性特性推定

Naoki Suzuki[1†], Hideyuki Hasegawa[2,1] and Hiroshi Kanai[1,2] ([1] Graduate School of Engineering, Tohoku Univ.; [2] Graduate School of Biomedical Engineering, Tohoku Univ.)

鈴木直貴[1]，長谷川英之[2,1]，金井　浩[1,2]　([1] 東北大院　工; [2] 東北大院　医工)

## 1. Introduction

In this study, we investigated the ultrasonic surgical knife which is one of the medical treatment technologies with ultrasound. The ultrasonic surgical knife can cut soft tissues using ultrasound vibrations and it can cut a soft tissue and stop bleeding by coagulation at the same time. The ultrasonic knife can coagulate proteins at a comparatively low temperature compared with other surgical knives such as the laser surgical knives, and it is a great advantage to prevent undesirable injury to patients together with the effect of stopping bleeding. The improvement of patients' QOL (Quality of Life) is becoming more and more important in recent years [1]. However, effects of the ultrasound vibration of the blade on the soft tissue have not been revealed thoroughly so far. The detailed investigation on the influence of the tip vibration of the blade would be useful for the improvement of safety and the optimization of efficiency of the ultrasonic surgical knife.

## 2. Principle

The biological tissue is a viscoelastic body, and a mechanical model (Fig. 1(a)) is assumed as a model of the soft tissue in this report. When an ultrasonic knife is driven by a simple harmonic signal, the stress σ also becomes a simple harmonic. In this case the stress-strain relationship shows a hysteresis property illustrated in Fig. 1(b) because there is phase delay θ of strain γ from stress σ. Stress σ and strain γ expressed by the mechanical model are given by

$$\sigma = m\frac{d^2\gamma}{dt^2} + G\gamma + \eta\frac{d\gamma}{dt}, \qquad (1)$$

$$\gamma = \frac{\sigma_0}{\sqrt{G - m\omega^2 + \left(\frac{\omega\eta}{G}\right)^2}}\sin(\omega t - \theta), \qquad (2)$$

$$\theta = \tan^{-1}\left(\frac{\omega\eta}{G - m\omega^2}\right), \qquad (3)$$

where $m$, $G$ and $\eta$ are the equivalent mass, static elastic modulus and viscosity coefficient, respectively. When elastic modulus $G$ and viscosity constant $\eta$ are estimated, the calorific value and the change in the stress-stress relationship due to temperature increase can be estimated prior to application of the ultrasonic knife by contacting it with soft tissue.

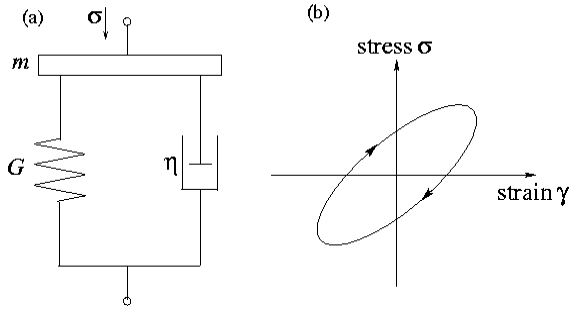


Fig. 1 (a) Mechanical model. (b) Stress-strain relationship.

## 3. Method

In this study, elastic modulus $G$ and viscosity coefficient $\eta$ of an object were estimated by considering the equivalent circuit of an object and an ultrasonic knife. Stress σ and strain rate $\dot{\gamma}$ (=dγ/dt) correspond to the voltage and electric current in the corresponding electric circuit, respectively. Admittance characteristics $Y(\omega)$ of the knife with and without being contacted with the object were measured using a network analyzer (HP8751A). Equivalent mass $m$, elastic modulus $G$ and viscosity coefficient $\eta$ correspond to the measured inductance $L$, inverse of capacitance $C$ and resistance $r$ of the equivalent circuit of the object, respectively. The experiments were conducted for silicone rubber (elastic modulus 48.8 kPa) and a soft tissue (chicken breast muscle).

---

E-mail : suzuki@us.ecei.tohoku.ac.jp

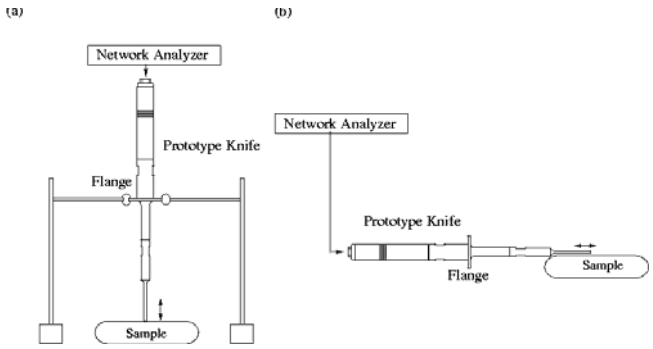


Fig. 2 Experimental setup. (a) End of tip contacts. (b) Side of tip contacts.

## 4. Result

Admittance characteristics $Y(\omega)$ of the ultrasonic knife without load, loaded by soft tissue, and loaded by silicone rubber were measured as shown in Figs. 3(a) and 3(b). The changes in resonance frequency $f_0$ and the size of the radius of the admittance circle were measured. Resistance $\hat{r}_a$, capacitance $\hat{C}_a$, and inductance $\hat{L}_a$ of the soft tissue and silicone were obtained by comparing the admittance of the equivalent circuit without load with that with load.

Resistance $\hat{r}_a$ and capacitance $\hat{C}_a$ of the soft tissue were estimated to be 15.4 Ω and 1.77 nF, respectively, and those of resistance $\hat{r}_a$ and capacitance $\hat{C}_a$ of the silicone rubber were 20.4 Ω and 3.75 nF, respectively. The capacitance of the soft tissue was about twice larger than that of silicone rubber. Therefore, elastic modulus $G$ of the soft tissue was estimated to be 98 kPa by referring to elastic modulus $G$ of silicone rubber (48.8 kPa) because the inverse of capacitance corresponds to the elastic modulus. The estimated elastic modulus of soft tissue (98 kPa) was in good agreement with that reported in literature (100 kPa [2]).

The inverse of capacitance and resistance of soft tissue when the end of the tip contacted with the tissue was nearly triple larger than those when the side of the tip contacted. When the end of the tip contacted, the tip induced the normal strain in the tissue. Such deformation is dependent on complex Young's modulus $E+j\lambda$. On the other hand, the shear strain induced by the contact of the side of the tip with the tissue was dependent on the complex shear modulus $G+j\eta$. When a material is incompressible, $E=3G$ and $\lambda=3\eta$ [3]. The experimental results showed these relationships because a soft tissue is almost incompressible.

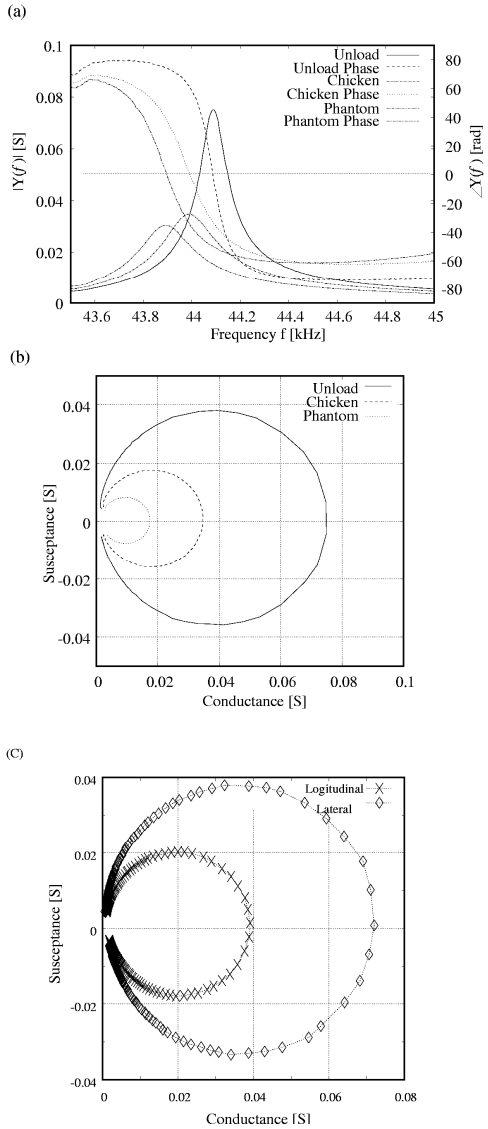


Fig. 3. (a) Admittance $Y(\omega)$ and (b) admittance circle when the end of the tip contacted. (c) Admittance circles of chicken muscle when the end and side of the tip contacted.

## 4. Conclusion

In this report, the equivalent electricity resistance, inductance and capacitance of the soft tissue were measured with a network analyzer. It will be possible to assess the calorific value in the application of an ultrasonic knife by enabling the estimation of viscosity coefficient η by further investigations.

## References

1. T. F. Molnar, *et al.*, *Eur. J. Cardio-Thorac. Sung.*, **26** (2004) 1192.
2. M. Saitoh, Biological Engineering, Corona Publishing Co., Ltd, Tokyo, Japan (1985) 17. (in Japanese)
3. T. Nakagawa, Rheology, Iwanami Publishing Co., Tokyo, Japan (1978) pp.22-23. (in Japanese)

# Author Index (* First Author)

ISSN 1348-8236

# Proceedings

## of Symposium on

# ULTRASONIC ELECTRONICS

# Vol. 29

## USE2008

The 29th Symposium
on
ULTRASONIC
ELECTRONICS

Nov.11-13, 2008 Sendai, Japan

URL: http://www.use-jp.org